S. Ted Treves *Editor*

Pediatric Nuclear Medicine and Molecular Imaging

Fourth Edition

Springer

Pediatric Nuclear Medicine and Molecular Imaging

S. Ted Treves
Editor

Pediatric Nuclear Medicine and Molecular Imaging

Fourth Edition

Springer

Editor
S. Ted Treves, MD
Joint Program in Nuclear Medicine
Department of Radiology
Harvard Medical School
Boston, MA
USA

Division of Nuclear Medicine and
Molecular Imaging
Department of Radiology
Brigham and Women's Hospital
Boston, MA
USA

Division of Nuclear Medicine and
Molecular Imaging
Department of Radiology
Boston Children's Hospital
Boston, MA
USA

Associate Editors
Frederic H. Fahey, DSc
Joint Program in Nuclear Medicine
Department of Radiology
Harvard Medical School
Boston, MA
USA

Division of Nuclear Medicine and
Molecular Imaging
Department of Radiology
Boston Children's Hospital
Boston, MA
USA

Frederick D. Grant, MD
Joint Program in Nuclear Medicine
Department of Radiology
Harvard Medical School
Boston, MA
USA

Division of Nuclear Medicine and
Molecular Imaging
Department of Radiology
Boston Children's Hospital
Boston, MA
USA

Department of Radiology
Brigham and Women's Hospital
Boston, MA
USA

ISBN 978-1-4614-9550-5 ISBN 978-1-4614-9551-2 (eBook)
DOI 10.1007/978-1-4614-9551-2
Springer New York Heidelberg Dordrecht London

Library of Congress Control Number: 2014937664

Printed on acid-free paper

Springer is part of Springer Science+Business Media (www.springer.com)

To my children Olivia, Blake, Alex and Erik and my wife Nancy.

Foreword

Just as we have realized the benefits of improved instrumentation with SPECT and the introduction of PET into pediatric practice, we are reminded that administered radionuclides are not without inherent hazard. Authority to address this dilemma has been assigned to the general editor of this volume who, with his colleagues, has responsibility for the nuclear imaging part of the *Image Gently* program. Their philosophy, copied from the canon of health physics, is to keep radiation exposure from nuclear medical procedure to as low as reasonably appropriate (ALARA) in order to maintain diagnostic accuracy, i.e., to maximize the gain to hazard ratio. Their commitment to this principle should assure pediatricians, their patients and families that the use of nuclear imaging in children is justified and beneficial.

This fourth edition, with many chapters written by Ted Treves as well as other authorities, exhibits the several additions recently made to pediatric nuclear medicine and calls attention to advances in instrumentation, including combined anatomical and functional imaging (PET/SPECT-CT/MRI), and radio-pharmaceutical chemistry that have been applied to a number of childhood disorders including those of the brain, the GU and GI systems, as well as neuroendocrine and other tumors.

In oncology, FDG-PET, which reflects the aerobic glycolysis of tumors, has assumed a lead role. Meanwhile, newer ^{18}F-labeled compounds that assess other manifestations of cancer and provide greater specificity are being brought into pediatric practice. The uses of these modalities, which aid in formulating more unambiguous diagnosis and providing more rapid indicators of response to therapy, are being explored.

At the same time, in the laboratory, the availability of high-resolution animal imaging equipment coupled with the development of new agents based on the molecular pathophysiology of disease allows us to glimpse a future that is certain to be greater in scope and complexity than the present.

All of this makes and will make pediatric nuclear medicine a much more demanding discipline than it was at the time the first edition of this text was published. To the extent that past is prologue, and with the knowledge of what is now being developed, we can anticipate a continued life for this and future editions.

Boston, MA, USA — S. James Adelstein, MD, PhD

Preface

When I first began my career as a pediatric nuclear medicine physician over 42 years ago, I could never have imagined the incredible advances that have taken place in the field; nor could I have imagined that I would have played even the smallest role in bringing this nascent imaging discipline to the fore of the radiologic sciences. Today, nuclear medicine offers critical diagnostic and treatment capabilities that benefit children. In recent years, nuclear medicine has evolved to include molecular imaging.

As the founder and chief of the Division of Nuclear Medicine and Molecular Imaging at Boston Children's Hospital (1970–2011), I have witnessed breathtaking technological advancements that have had impressive clinical impact – changes that have translated swiftly into improved patient care and outcomes. This amazing progress has enriched the field and led us now to the innumerable opportunities that lie ahead.

It has been nearly 30 years since the first edition of *Pediatric Nuclear Medicine* was published. It has been followed by a new edition nearly every decade since, updating the changes and advances within the field. This edition is entitled *Pediatric Nuclear Medicine and Molecular Imaging* to reflect the development and progression of the field during the last decade. I have been very fortunate to have contributions from colleagues all over the world, whose expertise and experiences enrich this edition. It has been exciting and a pleasure to once again assemble the current principles of pediatric nuclear medicine and share with readers new developments in this fourth edition.

The unique features and capabilities of pediatric nuclear medicine and molecular imaging significantly contribute to the diagnosis of many diseases in children. Pediatric nuclear medicine procedures reveal physiological processes *in vivo*. They permit early detection of disease, help patient management and therapeutic decisions, and have become increasingly important tools to follow the success of therapy or to assess progression of disease. Nuclear medicine provides information about the patient's condition by physiological, sensitive, rapid, safe and minimally invasive means. Therefore, diagnostic nuclear medicine procedures are well suited for the evaluation of pediatric patients. Nuclear medicine reveals unique information about the patient's condition not easily obtained or even possible with other diagnostic methods.

In this new edition, my collaborators and I hope to update readers about the well-established applications of pediatric nuclear medicine while incorporating essential developments of the past decade. Given ongoing

advances in technology and clinical practice, it is anticipated that further developments will be incorporated into pediatric nuclear medicine and molecular imaging in the foreseeable future. There is no question that the increased use of PET/CT and SPECT/CT has influenced the practice of nuclear medicine in children. Multimodality image fusion and hybrid imaging are recognized as important aspects of the field, and this information is incorporated in the appropriate chapters. This book is designed to ensure that all aspects of functional imaging of pediatric nuclear medicine are covered and emphasized. Following the tradition of the first three editions, this book focuses primarily on pediatric aspects of nuclear medicine and, therefore, it is important to note that *it is not intended* to provide an in-depth multimodality review of all pediatric imaging.

Most chapters from the third edition have been thoroughly revised or entirely re-written and new chapters have been added as well. The first chapter covers general aspects of pediatric nuclear medicine, followed by chapters on pediatric sedation and general anesthesia, pediatric imaging variants, central nervous system including cerebrospinal fluid, thyroid diagnosis musculoskeletal system, hepatobiliary system, lymphatic system, parathyroid imaging, cardiopulmonary system, gastrointestinal system, genitourinary system, infection and inflammation, oncologic disorders, instrumentation, measurement of glomerular filtration rate, image processing, radiation doses, and risk. Finally, there is a chapter on molecular imaging in pediatrics.

Radionuclide therapies in thyroid disorders and neuroblastoma with ^{131}I in children have also been incorporated in this edition. A characteristic of pediatric nuclear medicine is that normal values in children are difficult to obtain, as healthy patients cannot be studied easily with these techniques due to ethical and other inherent concerns relating to the use of radioactive materials. However, whenever possible, an effort is made to incorporate normal values within the appropriate chapters.

Clinical investigation in children is necessary in order to advance the understanding and derive the maximum benefit of nuclear medicine in pediatrics. However, as stated previously, radioisotope research in children, although possible, is quite limited in scope and depth. On the other hand, the use of small animal imaging provides the opportunity to explore, in serial non-destructive testing, mechanisms of disease, elucidation of biokinetics, pharmacology and metabolism in appropriate animal models. The use of such multimodality and multidisciplinary facilities provides ways to explore, discover and innovate on many issues related to pediatric disorders in ways not possible otherwise. This approach can enable exploration of problems and ideas that originate from the bench to the bedside and from the bedside to the bench.

In recent years, interest in the potential risks from radiation exposure to pediatric patients from the use of imaging methods employing ionizing radiation has increased. This has been a concern of members of the scientific community, government, lay press and the general public. This has led to the formation of the Image Gently campaign (www.imagegently.org). The mission of the campaign is to raise awareness, educate and advocate for the need to promote radiation protection for children worldwide. This edition adheres

to this mission and includes ways to communicate potential radiation risk to patients, families and members of the healthcare team. In addition, this book discusses means to optimize pediatric radiopharmaceutical administered doses and to reduce patient radiation exposure.

We sincerely hope this fourth edition of *Pediatric Nuclear Medicine and Molecular Imaging* will be a valuable resource to physicians, students, nurses, technologists and others involved in the care of pediatric patients.

Boston, MA, USA S. Ted Treves, MD

Acknowledgements

I would like to express my deepest and most sincere thanks to all my colleagues and friends who, in one way or another, have contributed in making *Pediatric Nuclear Medicine and Molecular Imaging* a reality.

First, I would like to thank my Associate Editors, Frederic Fahey, PhD, and Frederick Grant, MD, for their tireless work, encouragement, senses of humor, collegiality and friendship.

I owe an enormous thanks to all the contributors to this edition, all of whom have provided state-of-the art chapters, and helped to make this edition informative and current. The effort and sacrifice of time each of them has made amidst demanding work schedules does not go unnoticed.

I would also like to mention all the members of the Harvard Medical School – Joint Program in Nuclear Medicine (JPNM). The professional friendship, collaboration and support all of you have given to me over the years has been truly remarkable. This unique program has sustained and nurtured the growth of nuclear medicine at Harvard and beyond. Over the years, many JPNM residents and fellows have participated in research in pediatric nuclear medicine and their contributions are mentioned in chapters in this book.

I would like to recognize and give a very special thanks to S. Jim Adelstein, MD, PhD, for his unwavering support, encouragement, advice and friendship over my years at Harvard. It was most fitting that Jim made the introductory remarks when I received the de Hevesy Award during the Annual Meeting of the 2013 SNMMI in Vancouver, BC, since it was Jim who brought me to Harvard in 1970. I consider this award the highlight of my career, and I am honored and humbled by this recognition of the SNMMI.

There are also many friends and colleagues at Boston Children's Hospital who have provided support and friendship over the last four decades for which I am eternally grateful. I would like to recognize and thank the former Chairmen of Radiology, Drs. Neuhauser, Kirkpatrick, Kirks, Lebowitz and Taylor, for their support and encouragement, which enabled the creation and development of a very unique and state-of-the-art nuclear medicine unit at Boston Children's Hospital. The success of the nuclear medicine program at Boston Children's Hospital is due in great part to the unparalleled efforts of a world-class team of dedicated clinicians, scientists and technologists with whom I have had the privilege to work. The Boston Children's Hospital program included the clinical unit as well as the research unit, of which the radiopharmaceutical research laboratory and the Small Animal Imaging

Laboratory have been a part. Special thanks to Drs. Fred Fahey, Fred Grant, Alan Packard and Robert Mulkern for their commitment to help develop the Boston Children's Hospital Small Animal Imaging Laboratory. With the encouragement and support of Dr. George Taylor, former Chair of Radiology at Children's, I had the privilege along with my colleagues to have been the founder of the first laboratory of its kind at Boston Children's Hospital.

Over many years, Royal Davis provided personnel and organizational leadership to ensure smooth technical operations in the nuclear medicine unit at Boston Children's Hospital, which led to excellence and quality in service as well as helped promote innovations and facilitated clinical and laboratory research work. Many technologists have contributed to the quality of the work that over the years has led to many of the examples of images included in this book. Their dedication to patient care, patience, and compassion in working with children and their families cannot be emphasized enough. Technologists include Joanne Louis, Vicky Kourmouzi, Stephen Laffin, Diane Itrato, Westley Evans, Jennifer Keezer, Peter Morriss, Leah Oberg, Erin Snay, Victoria Dune, Katelynn Laffin, Natasha Ditoro, Monique Stevens, Tracy Tetrault, Erin Kistler, Teresa DiBona, Daniel Speredolozzi and others. Our nurses Del Spangler and Marie Callahan provided expert care, comfort and compassion to many of our patients. Child Life Specialist Tricia Ashe provided help in the preparation of patients and parents, provided explanations, appropriate distractions and toys and educational materials. Karl Mitchell and Xinhua Cao helped in the development of excellent computer software dedicated to pediatric nuclear medicine with excellent display designs that make viewing and interpretation of complex data more efficient and intuitive. Their work has been critical to imaging and non-imaging systems integration. Along with Chuck Hornberger, they all provided invaluable assistance in clinical database research, image registration and fusion. In addition, Amanda Baker, Marie Vitello, and Anthony Falone provided expert research data coordination.

A very special thanks to Nancy Drinan whose work behind the scenes helping to draft and edit grant applications has been tireless. I would also like to thank David Zurakowsky, PhD for his many contributions in the planning and analysis of many research projects.

Fred Fahey, DSc, has provided outstanding physics support and has been a professional and research mentor to many faculty, fellows, residents and technologists.

The Pediatric Nuclear Medicine Research Laboratory under the direction of Alan Packard, PhD, including Jason Dearling, PhD, Shaohui Zhang, PhD, and Vamsidhar Akurathi, PhD. – I thank you for the dedication and energy you bring to your work towards discovery and innovations.

I owe enormous thanks to Brian Schott for his help during the preparation of this work. Brian has shown incredible dedication and extraordinary patience through many aspects of work, including going through multiple drafts and versions of the various chapters, effectively communicating with our contributors, their staffs, and with Springer. Brian's meticulous attention to detail and commitment to this project has made my work more bearable.

Thanks to Jennifer Duane for assistance during the early planning and communications with contributors to this book.

Most importantly I would like to thank Nancy, and our children, Erik, Alex, Blake and Olivia, for their patience, understanding, love and support, which enabled me to focus on this work.

Finally, I would like to express my deepest appreciation to the courageous young patients and their remarkable families from whom I have learned the most and to whom I owe the greatest debt of gratitude.

Boston, MA, USA S. Ted Treves, MD

Contents

Contributors

S. James Adelstein, MD, PhD Joint Program in Nuclear Medicine, Department of Radiology, Harvard Medical School, Boston, MA, USA

Department of Radiology, Brigham and Women's Hospital, Boston, MA, USA

Zvi Bar-Sever, MD Faculty of Medicine, Tel-Aviv University, Tel-Aviv, Israel

Department of Nuclear Medicine, Schneider Children's Medical Center, Petach-Tikva, Israel

Blaise F.D. Bourgeois, MD Department of Neurology, Harvard Medical School, Boston, MA, USA

Department of Neurology, Boston Children's Hospital, Boston, MA, USA

Harry T. Chugani, MD Department of Neurology, Wayne State University School of Medicine, Detroit, MI, USA

Department of Neurology, PET Center, Children's Hospital of Michigan, Detroit, MI, USA

Heike Elisabeth Daldrup-Link, MD, PhD Department of Radiology, Pediatric Radiology Section, Lucile Packard Children's Hospital, Stanford School of Medicine, Stanford, CA, USA

Laura Drubach, MD Joint Program in Nuclear Medicine, Department of Radiology, Harvard Medical School, Boston, MA, USA

Division of Nuclear Medicine and Molecular Imaging, Department of Radiology, Boston Children's Hospital, Boston, MA, USA

Department of Emergency Medicine, Boston Children's Hospital, Boston, MA, USA

Georges El-Fakhri, PhD Joint Program in Nuclear Medicine, Department of Radiology, Harvard Medical School, Boston, MA, USA

Division of Nuclear Medicine and Molecular Imaging, Center for Advanced Medical Imaging Sciences, Department of Radiology, Massachusetts General Hospital, Boston, MA, USA

Frederic H. Fahey, DSc Joint Program in Nuclear Medicine, Department of Radiology, Harvard Medical School, Boston, MA, USA

Division of Nuclear Medicine and Molecular Imaging, Department of Radiology, Boston Children's Hospital, Boston, MA, USA

Sanjiv Sam Gambhir, MD, PhD Department of Radiology, Department of Bioengineering, Molecular Imaging Program at Stanford (MIPS), Stanford University School of Medicine, Stanford, CA, USA

Department of Materials Science and Engineering, Stanford University School of Engineering, Stanford, CA, USA

Michael J. Gelfand, MD Section of Nuclear Medicine, Department of Radiology, Cincinnati Children's Hospital Medical Center, Cincinnati, OH, USA

Frederick D. Grant, MD Joint Program in Nuclear Medicine, Department of Radiology, Harvard Medical School, Boston, MA, USA

Division of Nuclear Medicine and Molecular Imaging, Department of Radiology, Boston Children's Hospital, Boston, MA, USA

Department of Radiology, Brigham and Women's Hospital, Boston, MA, USA

Arin K. Greene, MD, MMSc Department of Surgery, Harvard Medical School, Boston, MA, USA

Department of Plastic and Oral Surgery, Boston Children's Hospital, Boston, MA, USA

Robert Howman-Giles, MB BS, MD, FRACP, FAANMS, DDU Discipline of Imaging and Discipline of Paediatrics and Child Health, Faculty of Medicine, University of Sydney, Sydney, Australia

Department of Nuclear Medicine, The Children's Hospital at Westmead, Sydney, Australia

Alun G. Jones, PhD (Deceased) Department of Radiology, Harvard Medical School, Boston, MA, USA

Leonard B. Kaban, DMD, MD Department of Oral and Maxillofacial Surgery, Harvard School of Dental Medicine, Boston, MA, USA

Department of Oral and Maxillofacial Surgery, Massachusetts General Hospital, Boston, MA, USA

Alvin Kuruc, MD, PhD Global Macro GFX, Investment Banking, Credit Suisse, London, UK

Matthew E. Lawler, DMD Department of Oral and Maxillofacial Surgery, Harvard School of Dental Medicine, Boston, MA, USA

Department of Oral and Maxillofacial Surgery, Massachusetts General Hospital, Boston, MA, USA

Ruth Lim, MD Department of Radiology, Harvard Medical School, Boston, MA, USA

Department of Radiology, Massachusetts General Hospital, Boston, MA, USA

Kevin London, BHB, DipSci, MBChB, DCH, MM(Clin Epi), FRACP Discipline of Paediatrics and Child Health, Faculty of Medicine, Universtiy of Sydney, Sydney, Australia

Department of Nuclear Medicine, The Children's Hospital at Westmead, Sydney, Australia

William A. Lorenzen, MS Department of Radiation Safety, Boston Children's Hospital, Boston, MA, USA

Reid A. Maclellan, MD, MMSc Department of Surgery, Harvard Medical School, Boston, MA, USA

Department of Plastic and Oral Surgery, Boston Children's Hospital, Boston, MA, USA

Michael Manfredi, MD Department of Pediatrics, Harvard Medical School, Boston, MA, USA

Gastrointestinal Procedure Unit, Division of Gastroenterology, Hepatology and Nutrition, Boston Children's Hospital, Boston, MA, USA

Keira P. Mason, MD Department of Anaesthesia, Harvard Medical School, Boston, MA, USA

Department of Anesthesiology, Perioperative and Pain Medicine, Boston Children's Hospital, Boston, MA, USA

Wolfgang Peter Mueller, MD Department of Nuclear Medicine, University Hospital of the LMU, Ludwig-Maximilians-University of Munich, Munich, Germany

Alan B. Packard, PhD Joint Program in Nuclear Medicine, Department of Radiology, Harvard Medical School, Boston, MA, USA

Division of Nuclear Medicine and Molecular Imaging, Department of Radiology, Boston Children's Hospital, Boston, MA, USA

Christopher J. Palestro, MD Department of Radiology, Hofstra North Shore-LIJ School of Medicine, Hempstead, NY, USA

Division of Nuclear Medicine and Molecular Imaging, Department of Radiology, North Shore Long Island Jewish Health System, New Hyde Park, NY, USA

Zachary S. Peacock, DMD, MD Department of Oral and Maxillofacial Surgery, Harvard School of Dental Medicine, Boston, MA, USA

Department of Oral and Maxillofacial Surgery, Massachusetts General Hospital, Boston, MA, USA

Thomas Pfluger, MD Department of Nuclear Medicine, University Hospital of the LMU, Ludwig-Maximilians-University of Munich, Munich, Germany

Randy P. Prescilla, MD Department of Anaesthesia, Harvard Medical School, Boston, MA, USA

Department of Anesthesiology, Perioperative and Pain Medicine, Boston Children's Hospital, Boston, MA, USA

Heinrich Schelbert, MD Department of Molecular and Medical Pharmacology, David Geffen School of Medicine at UCLA, Los Angeles, CA, USA

Division of Nuclear Medicine, Department of Molecular and Medical Pharmacology, Ronald Reagan UCLA Medical Center, Los Angeles, CA, USA

Susan E. Sharp, MD Department of Radiology, Cincinnati Children's Hospital Medical Center, University of Cincinnati College of Medicine, Cincinnati, OH, USA

Barry L. Shulkin, MD, MBA Division of Nuclear Medicine, Department of Radiological Sciences, St. Jude Children's Research Hospital, Memphis, TN, USA

Michael Stabin, PhD Department of Radiology and Radiological Sciences, Vanderbilt University Medical Center, Nashville, TN, USA

S. Ted Treves, MD Joint Program in Nuclear Medicine, Department of Radiology, Harvard Medical School, Boston, MA, USA

Division of Nuclear Medicine and Molecular Imaging, Department of Radiology, Boston Children's Hospital, Boston, MA, USA

Division of Nuclear Medicine and Molecular Imaging, Department of Radiology, Brigham and Women's Hospital, Boston, MA, USA

Roger F. Uren, MBBS, MD, FRACP, DDU Discipline of Medicine, University of Sydney, Sydney, Australia

Department of Nuclear Medicine and Diagnostic Ultrasound, Royal Prince Alfred Hospital Medical Centre, Sydney, Australia

Katherine A. Zukotynski, MD Department of Medical Imaging, Sunnybrook Health Sciences Centre, University of Toronto, Toronto, ON, Canada

Joint Program in Nuclear Medicine, Department of Radiology, Harvard Medical School, Boston, MA, USA

Department of Radiology, Brigham and Women's Hospital, Boston, MA, USA

General Aspects of Pediatric Nuclear Medicine

1

S. Ted Treves and Frederick D. Grant

Pediatric nuclear medicine is a very interesting, dynamic, and exciting field. Nuclear medicine contributes to the diagnosis of many diseases in children. Well-established procedures reveal physiological processes *in vivo*, permit early detection of disease, help patient management and therapeutic decisions, and provide an important tool to follow the success of therapy or to assess progression of disease. One of the reasons that nuclear medicine in pediatric patients remains successful is that nuclear medicine studies provide unique information about the patient's condition that cannot be obtained easily (or sometimes at all) with other diagnostic methods. Some nuclear medicine procedures require pharmacologic interventions. Examples include the administration of furosemide, acetazolamide, phenobarbital, cholecystokinin analog, and dobutamine.

Pediatric patients, with their wide range of body size, physical and psychological developmental changes, and medical disorders, present unique challenges. Patients in pediatric nuclear medicine range in weight from premature infants to young adults reaching adult weight. It has been said that children are not small adults, and even in nuclear medicine "one size does not fit all" [1, 2].

As a consequence, nuclear medicine physicians and members of the team frequently need to adapt to these challenges and often need to customize studies and personalize care. Diagnostic nuclear medicine procedures are well suited for the evaluation of pediatric patients because they are physiological, sensitive, minimally invasive, and safe.

An important advantage of nuclear medicine procedures in the first year of life is that they are extremely safe. Radiopharmaceuticals contain only trace amounts of material and are nontoxic and nonallergenic. The total mass of material that is administered is very small and is administered in a very small volume (typically <1.0 mL). The small administered mass and volume of material means that radiopharmaceuticals do not produce a hemodynamic or osmotic effect. For example, a patient who is allergic to iodine can safely receive ^{123}I-NaI or ^{123}I-MIBG without fear of an allergic reaction because the actual mass of

S.T. Treves, MD (✉)
Joint Program in Nuclear Medicine,
Department of Radiology,
Harvard Medical School, Boston, MA, USA

Division of Nuclear Medicine and Molecular Imaging,
Department of Radiology, Boston Children's Hospital,
Boston, MA, USA

Division of Nuclear Medicine and Molecular Imaging,
Department of Radiology, Brigham and Women's Hospital,
Boston, MA, USA
e-mail: ted_treves@HMS.harvard.edu

F.D. Grant, MD
Joint Program in Nuclear Medicine,
Department of Radiology, Harvard Medical School,
Boston, MA, USA

Division of Nuclear Medicine and Molecular Imaging,
Department of Radiology, Boston Children's Hospital,
Boston, MA, USA

Department of Radiology,
Brigham and Women's Hospital, Boston, MA, USA
e-mail: frederick.grant@childrens.harvard.edu

S.T. Treves (ed.), *Pediatric Nuclear Medicine and Molecular Imaging*,
DOI 10.1007/978-1-4614-9551-2_1,

Table 1.1 Comparison of mass and volumes for certain radiopharmaceuticals and contrast agents. Example in a 1-year-old

	Volume (mL)	Mass (mg)
^{99m}Tc-MDP	0.06	0.64
^{99m}Tc-DMSA	0.03	0.22
^{99m}Tc-MAG_3	0.10	1.1
Gd-DTPA	2.0	940
Optiray 320	20	6,400

iodine that is administered is exceedingly small and well below the threshold needed to trigger an allergic reaction. The volume and mass of a radiopharmaceutical that is administered is significantly lower than for MRI and CT contrast agents. For example, the volume of ^{99m}Tc-MDP solution administered to a 1-year-old patient weighing 10 kg is 0.06 mL, and the administered mass of material is 0.64 mg. In comparison, for the same 1-year-old, the volume of Gd-DTPA (Magnevist, Bayer) administered for an MRI scan is 2.0 mL, and the mass is 940 mg. The volume of ioversol (Optiray 320™ Covidien) administered for a CT scan is 20 mL, and the mass is 6,400 mg. Thus, the administered volume for ^{99m}Tc-MDP is 20–200-fold less than for MRI or CT contrast agents, and the administered mass is more than a thousandfold less. Other radiopharmaceuticals are listed in Table 1.1.

A characteristic of pediatric nuclear medicine is that normal values in children are difficult to find, as normal patients cannot be studied easily with these techniques due to ethical and other concerns relating to the use of radioactive materials.

Also, the wide range of disorders, body sizes, and developmental stages of pediatric patients requires patient-centered care with considerations regarding individualized adjustments of imaging methodology, dosimetry, and interpretation. Physicians and technologists working in pediatric nuclear medicine should be familiar with children, their varied behavior, and the disorders that affect them. Dealing with pediatric patients adds a level of complexity compared to adult nuclear medicine patients. Pediatric nuclear medicine procedures are "people-intensive." Many procedures that in an adult setting can be conducted adequately by a single technologist may require two technologists (or a technologist and an aide) in children. More time and patience is necessary when dealing with children than with adults. Despite the best efforts of staff, procedures in children usually take longer than in adults (sometimes as much as twice as long).

Formal training and experience in pediatric nuclear medicine allows medical professionals to adjust the practice of nuclear medicine to meet the medical and personal needs of pediatric patients. For example, at centers experienced in the care of children, patient sedation for pediatric nuclear medicine studies is used less frequently than in less specialized centers. Also, image quality in specialized centers is frequently superior to those from nonspecialized institutions.

The nuclear medicine team should adjust the procedures in order to address the clinical problem to be investigated. The goal of every pediatric nuclear medicine study is to obtain the best diagnostic yield while employing the highest technical standards in the shortest period of time, with the lowest patient radiation exposure.

The Consultation

Pediatric nuclear medicine studies should begin with evaluation of the diagnostic question, review of prior medical history, and assessment of the needs and concerns of the patient and family. Obtaining a clear description of the clinical question being asked is of utmost importance in guiding the procedure. Although current medical information systems treat the request for a nuclear medicine study as an "order," the patient will be better served if the requesting clinician and nuclear medicine physician treat this as a request for a consultation. As a consultant, the nuclear medicine physician can determine the most appropriate study to answer the clinical question and can optimize the nuclear medicine study to the physical and physiological development of the pediatric patient. If the nuclear medicine consultant determines that the examination requested is not appropriate to address the problem in question or that another type of examination is indicated, he or she

should communicate such concern to the referring physician in order to select a more appropriate examination or to avoid an unnecessary examination. Whenever possible, questioning parents and patients about the clinical history and symptoms, or an appropriately directed physical examination, should be considered integral parts of the nuclear medicine study as sometimes important relevant information may be gathered that may not be available on the original request.

Before proceeding with a nuclear medicine study, a female adolescent or young adult should be asked if she might possibly be pregnant. If the post-menarche patient does not know if she is pregnant, it is prudent to wait until the next menstrual period or to perform a pregnancy test. If the patient is pregnant, it is advisable to consult with the referring physician about the need for the test at this time and to evaluate the potential risks and benefits of performing the test (or not). Asking a young woman if she is pregnant, however, can be a very delicate matter, and it needs to be handled with care and sensitivity. This can be difficult, and it can be worse if the parent does not know that the young woman is sexually active. Sometimes it is necessary to consult with the referring physician about the best way to handle the situation given each individual family situation. If the mother of the patient having an examination is pregnant, she should be instructed on how to avoid or reduce her radiation exposure.

Optimal results are obtained when the physician and the technologist review the case and consult in order to determine if any aspect of the examination requires special attention. It is highly desirable that previous imaging studies be readily accessible to the nuclear medicine physician. Knowledge of potentially conflicting imaging tests already scheduled is essential when planning the study. Planning several studies in the same day requires careful scheduling, so the patient experience can be streamlined. It is important to determine if the patient had been given radiographic contrast during the past few days as contrast can produce shielding artifacts on the nuclear medicine images. It is also important to determine, before the test, if the patient may require sedation and if there are any special precautions. In addition, knowledge of patient medications that may interfere with the nuclear medicine study is important for successful interpretation and results.

Optimal pediatric nuclear medicine practice requires the use of modern equipment, appropriate radiopharmaceutical administered doses, updated techniques, displays, and advanced image processing software. In the modern era, nuclear medicine results should be reported promptly to the referring physician. Results of image analysis should be available immediately after the studies are completed so results can be reported rapidly and within a clinically useful time. The report should be clear and concise, and it must address the clinical question(s) being asked. Rapid and efficient electronic access to nuclear medicine images and reports facilitates communication with referring physicians and can help improve patient care.

Interaction with Patients and Families

Parents are naturally concerned about what is going to happen to their child. The word nuclear can be concerning to some patients and parents. It is important that the nuclear medicine physician and other members of the nuclear medicine care team be accessible to patients, parents, and referring physicians to help explain the low radiation exposures and physiological nature of nuclear medicine examinations [3].

Patients and families should be given information about what the anticipated nuclear medicine procedure will entail. If possible, the patient's family should be contacted by a member of the nuclear medicine staff a day or two in advance to confirm the appointment and to discuss the test. For example, it is important that families understand necessary patient preparation, the anticipated duration of the study, and whether it may be necessary to return later the same day or on a later day. Many parents find it helpful if information about nuclear medicine studies and departmental procedures is posted on the hospital or department website. It is useful to provide referring physicians' offices with brochures explaining common nuclear medicine tests (Appendix 1).

Fig. 1.1 Young patient with a nuclear medicine technologist after a study was completed. Establishing a good rapport with the patient can be helpful in assuring patient cooperation

The first contact, whether by phone or in person, is important and should include a clear and honest explanation of the procedure. Physicians and technologists should make a concerted effort to inform patients (whenever possible) and parents personally about the examination. Every pediatric patient must be treated as an individual with individual emotional and physical needs. Children who are prepared can be more cooperative, often facilitating the examination for everyone involved. Patients should be told what they will see, hear, feel, and, most importantly, what they will be expected to do. For example, they should be informed of an impending injection, the injection site, if there will be any pain, and any other appropriate explanations all of which tend to help reduce anxiety. Children have highly developed imaginations, and their fantasies can be anxiety provoking. It is important to keep in mind a child's developmental level when giving information and defining expectations during the procedure. Explanations and words should be chosen accordingly to ensure proper understanding of the information being given. It is sometimes helpful to explain the procedure to the child at least twice, first outside the imaging room where the child may feel less threatened and then in the imaging room. Throughout the examination, the technologist should provide reassurance and positive verbal reinforcement to enhance the child's sense of mastery (Figs. 1.1 and 1.2).

In most instances, children of all ages benefit from having a parent, relative, or a familiar staff person in the imaging room. Typically, children between the ages of 8 and 36 months may suffer separation anxiety if removed from their parents. Older children may tolerate separation, but most will prefer the presence of a familiar person. Younger children may be comforted by a favorite toy or stuffed animal that they have with them during the examination (Fig. 1.3). This should be permitted so long as it does not interfere with the test. Some children can cope better with the examination when they are alone rather than with their parents. Many adolescents may prefer privacy and independence, while other adolescents will still want a parent with them during the study. Children and teenagers with extensive medical or hospital experience may have strong feelings about whether or not parents stay in the examination room, and these desires should be respected (Fig. 1.4) [1].

Fig. 1.2 A young girl walking toward the examining room accompanied by her mother and a nuclear medicine technologist

Fig. 1.3 The patient is allowed to hold a favorite toy while undergoing a nuclear medicine scan. The toy did not interfere with the test. The technologist is supporting the child by talking to her

Fig. 1.4 Both parents and the child are watching TV while the patient is undergoing a ^{99m}Tc-DMSA SPECT. Watching TV or a favorite program while imaging is proceeding can have a calming effect

Physical Environment

Ideally, the physical environment of the nuclear medicine department should support patient comfort as well as patient, family, and personnel safety and efficient workflow. Making a department accessible and friendly for children requires extra attention to the design and workflow of the department. Space is needed for patient reception and waiting, imaging, a radiopharmaceutical administration room, an examination room, a radiopharmacy, a technologist workspace or room, and a consultation/reading room. Ideally, the radiopharmacy and administration/examination room should be in close proximity to each other, while reception and waiting areas should be located away from the examination rooms. The consultation/reading room and the technologist work area should be easily accessible to nuclear medicine personnel and referring physicians. Emergency supplies should be readily accessible.

Waiting Room

Most children undergoing nuclear medicine examinations are outpatients, and careful scheduling can reduce waiting time for patients and parents. However, in practice, parents and families almost always experience some waiting before, during, and after an examination. Some studies may require extended waiting in the department after administration of the radiopharmaceutical (e.g., examinations using FDG). Other studies require the patient to return one or more times after initial imaging. Parents and other family members may wait for a few minutes to several hours while the patient is undergoing an examination. The waiting room should be spacious, friendly, comfortable, attractively decorated, and well lit, and seating should be sufficient to accommodate family members. The waiting room should be supplied with plenty of appropriate reading materials and toys as well

Fig. 1.5 A waiting room in nuclear medicine. There is abundant space for the family to wait for the patient, and there are plenty of toys, a blackboard, a TV, and other materials to help entertain the family and the siblings. There are plenty of reading materials including information about nuclear medicine and its tests. The reception desk is low to allow children to view what is behind it

as information about parking, nuclear medicine, and other subjects appropriate for patients and their families. The reception desk should be at a writing height, so children can see the receptionist and are not intimidated by a tall counter (Fig. 1.5).

Radiopharmacy

The radiopharmacy should be well equipped with lead-shielded cabinets (for SPECT and PET radiopharmaceuticals), a hood, a sufficient counter space, an appropriate safety equipment, an exhaust for volatile or gaseous materials, and a laminar flow hood. The room itself should be under negative air pressure. In departments that prepare radiopharmaceuticals, the radiopharmacy should be compliant with the requirements of section 767 of the US Pharmacopeia. Some institutions do not have a radiopharmacy, and, in this case, radiopharmaceuticals are provided by commercial vendors. Therefore, these centers do not need an elaborate in-house radiopharmacy. Radioactive storage and calibration equipment should be provided however. Data entry tools for radiopharmaceuticals and other pharmaceuticals should be provided in the nuclear medicine facility. The radiopharmacy should have sufficient space for supplies as well as for storage and disposal of radioactive materials. In addition, storage space is needed for nonradioactive supplies.

Radiopharmaceutical Administration: Examination Room

Busy pediatric nuclear medicine departments should have at least one room for administration of radiopharmaceuticals so that imaging rooms are free for performing studies. This room, which should allow for privacy, is also used to talk to patients and parents and to conduct directed physical examinations. The administration/examination room ideally should be adjacent to the radiopharmacy. This room also can be used for the administration of ^{131}I for the treatment of hyperthyroidism or thyroid cancer. Patients undergoing FDG-PET studies require special planning as they will need an area for waiting during the 1-h uptake period after FDG administration. Keeping this room at 24° centigrade has been shown to markedly reduce FDG uptake in brown adipose tissue, and it may be helpful for the patient to acclimate in this room for at least 30 min prior to FDG administration [4]. With the increased use of CT with PET, there is a need for

Fig. 1.6 An example of a modern gamma camera/SPECT/CT system (© COPYRIGHT Siemens Healthcare 2013)

space for the administration of oral contrast agents.

Imaging Rooms

Examining rooms should be designed so that they are friendly, attractive, and sufficiently spacious to contain the equipment, permit proper examination, allow sufficient privacy, and allow for the presence of the patient's parents in the room. Examining rooms should be flexible in design and adaptable to the changing technology in nuclear medicine (Figs. 1.6 and 1.7). Some useful attributes of a nuclear medicine exam room include:

1. Sufficient general ambient light as well as dimmers in order to be able to provide a soothing effect (some children fall asleep during the examination).
2. Ceiling-mounted spotlight for illuminating the injection site or catheterization fields.
3. Ceiling-mounted hangers to hold bottles or bags for intravenous infusion.
4. Ceiling-mounted heating lamps.
5. Telephone with a cancelable bell; emergency numbers must be posted clearly on the telephone.
6. Oxygen and vacuum outlets, preferably wall-mounted and within easy reach from the patient's head on the examination table.
7. Exhaust for safe disposal of radioactive gases (xenon-133 for ventilation studies).
8. Small TV mounted over the examining table within easy view of the patient; a video player to play appropriate programming for the patient.
9. Sufficient space to house associated electronic equipment, such as electrocardiographs, electroencephalograph, anesthesia monitoring equipment, and external physiological detectors.
10. Doors wide enough to permit safe access to regular and special patient beds.
11. Room designed to permit safe maneuvering of the patient's bed in relation to all the equipment around the patient.

Performing the Study

The technologist should examine patients for metallic objects that can shield gamma radiation (e.g., keys, belt buckles, coins, jewelry). Once the first images are obtained, any diapers, clothing, or gauze contaminated with radionuclides should be removed and the area reimaged. Contaminated skin should be thoroughly washed, monitored, and reimaged. Once the examination is completed, the physician and the technologist should review and evaluate the quality and adequacy of

Fig. 1.7 A modern PET/CT system (© COPYRIGHT Siemens Healthcare 2013)

the study and determine if additional imaging is necessary. Depending on the initial result, the physician may need to reexamine the patient and the clinical data before the patient is discharged. When appropriate, the physician may recommend additional anatomic imaging to clarify an abnormal finding or to try to increase the specificity of a scintigraphic finding.

Proper patient positioning to avoid motion artifacts is essential for a good examination. Because most nuclear medicine imaging requires the patient to remain still for a relatively long period, immobilization techniques to help patients remain still during imaging are commonly used. Sandbags, adhesive tape, a papoose wrap with blanket, Velcro straps, and contoured pillows may be employed, depending on the size, age, condition, and activity of the patient. Newborns usually find swaddling comforting. In addition to these immobilization techniques, it is sometimes necessary for a technologist or an aide to hold a patient in position during imaging. Imaging artifacts resulting from holding patients by hand should be anticipated, recognized on the image, and, if possible, avoided. In some cases, the nuclear medicine physician needs to mark the patient's skin over a lesion to help guide biopsy or surgery as in the case of a thyroid nodule, an osteoid osteoma, a sentinel node, etc. Technologists often need to talk, support, encourage, and distract the child while ensuring that the gamma camera is set up and functioning correctly. With a quiet environment, dim lights, and care, some children fall asleep during long examinations. Watching television or a DVD can be an effective "sedative" and can help distract and relax some patients (and parents) during the examination. In some cases, immobilization alone is not successful, and sedation is required in order to avoid multiple sedations during the day of the patient's visit (see Chap. 2).

In our experience, children less than 1 year of age only need sedation in less than 3 % of cases, mainly for brain or whole body SPECT or PET [2]. Sedation should only be used when absolutely necessary. The type and dose of sedative used must be individualized and should be

decided in consultation with the referring physician or pediatric anesthesiologist. Some large institutions have specialized pediatric imaging sedation guidelines and dedicated teams of nurses and anesthesiologists that manage all sedation and anesthesia for imaging. When administering sedatives to patients, potential side effects such as aspiration and respiratory arrest should be anticipated and appropriate means of treatment made available. Sedation or general anesthesia can affect many physiological processes, including cerebral metabolism, myocardial function, renal blood flow, and specific functions such as cerebrospinal fluid flow and cardiovascular shunt flow.

With the increased use of single photon emission computed tomography (SPECT) and positron emission tomography (PET), the use of sedation has increased. Sedation or general anesthesia should be planned in advance of the patient's visit to nuclear medicine. It is important to assess the appropriateness of the patient for sedation or general anesthesia before the study. Proper advance instructions about eating, diet, and any other preparation should be communicated clearly to the patient or family. Similarly, outpatients need to be informed about their need to meet discharge criteria after sedation or general anesthesia and the time commitment that may be needed. Importantly, if the patient needs more than one imaging procedure in the same day, sedation scheduling should be appropriately coordinated (see Chap. 2).

Imaging Infants and Young Children

Pediatric nuclear medicine plays an important role in the evaluation of the majority of organs and systems in the body in children less than 1 year of life. Imaging patients in this age group is one of the most interesting and challenging aspects of this medical specialty, as the clinical problems encountered in patients during the first year of life are rather unique in terms of the disorders involved, extra care needed, and special imaging requirements. Successful imaging of neonates and infants requires special care and patience. Although imaging protocols should be standardized as much as possible, studying this population often requires that the nuclear medicine specialist diverge from routine protocols by altering radiopharmaceutical doses, imaging technique, or type and number of images needed in order to optimize the imaging approach and the specific diagnostic task at hand.

During growth and development in the neonate and infant, radiopharmaceutical kinetics can be different from those in the older child or the adult. These characteristics must be kept in mind during interpretation of nuclear medicine studies. Newborns and infants have relatively slower renal radiopharmaceutical kinetics, lower renal function, lower glomerular filtration rate (see Chap. 14), faster washout of radioactive gases from the lungs, faster circulation times, and faster lymphatic flow than adult patients. Another example of differences in radiopharmaceutical biodistribution occurs in the developing brain. Similarly, in children the concentration of ^{99m}Tc-methylene diphosphonate (MDP) in growth centers is relatively high.

Babies and infants experience rapid growth and development that are reflected on nuclear medicine studies. The pulmonary capillary bed in the very young child has a smaller number of arterioles than the older child. Gradually, with growth and maturation, physiological processes and radiopharmaceutical kinetics and biodistribution reach adult levels (Figs. 1.8, 1.9, 1.10, and 1.11) [2, 5].

Instrumentation and Equipment

Collimators

Collimator selection for individual types of examinations is important, and awareness of the characteristics of various collimators helps optimize imaging. Collimation in pediatric nuclear medicine should favor high- and ultrahigh-resolution-type collimators. Magnification scintigraphy with the pinhole collimator provides the highest spatial resolution images routinely

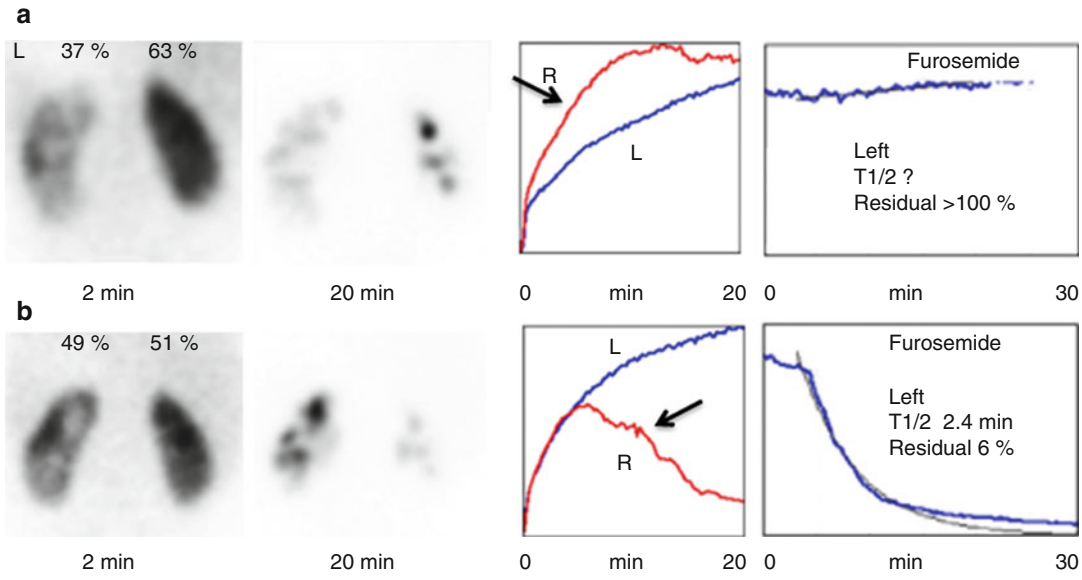

Fig. 1.8 MAG3 studies from a 3-month-old boy. (**a**) Early study reveals 63 % of the total renal function in the right kidney which is normal. Note the prolonged time-to-peak from the right renal time-activity curve and a very high residual at 20 min post-tracer administration (*red curve* and *arrow*). (**b**) Study done 2 months after left pyeloplasty without any intervention in the right kidney shows a normal right kidney time-activity curve and normal drainage (*red curve*=R). The right kidney shows maturation with a normal time-activity curve (*red curve* and *arrow*). *The blue curve* is form the left kidney as the *red curve* is from the right kidney

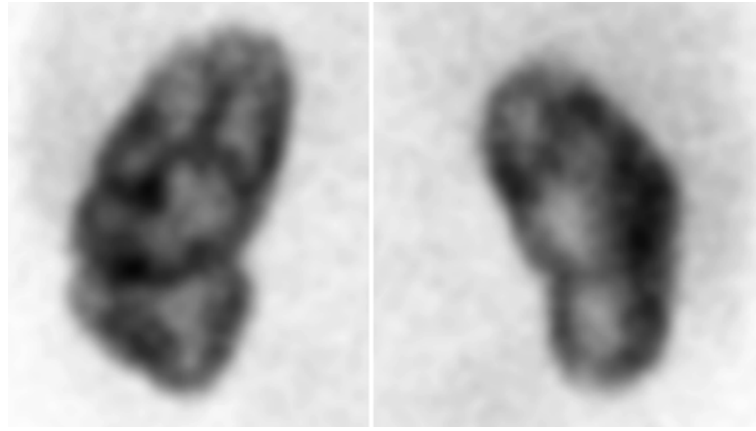

Fig. 1.9 ^{99m}Tc-DMSA pinhole images of the kidneys from a 6-week-old male showing normal fetal lobations that should not be confused with cortical defects

available with gamma cameras, and in selected applications it is an indispensable technique for imaging small body parts in children (see Chap. 28). Pinhole images using an insert of a small aperture (3–4 mm) in infants undergoing ^{99m}Tc-DMSA renal scans or ^{99m}Tc-MDP bone scans are of excellent quality even in the smallest patients. However, the pinhole collimator has the lowest sensitivity of any of the routinely used collimators used with the gamma camera, particularly with the smaller apertures, and the images can take several minutes to acquire which can be

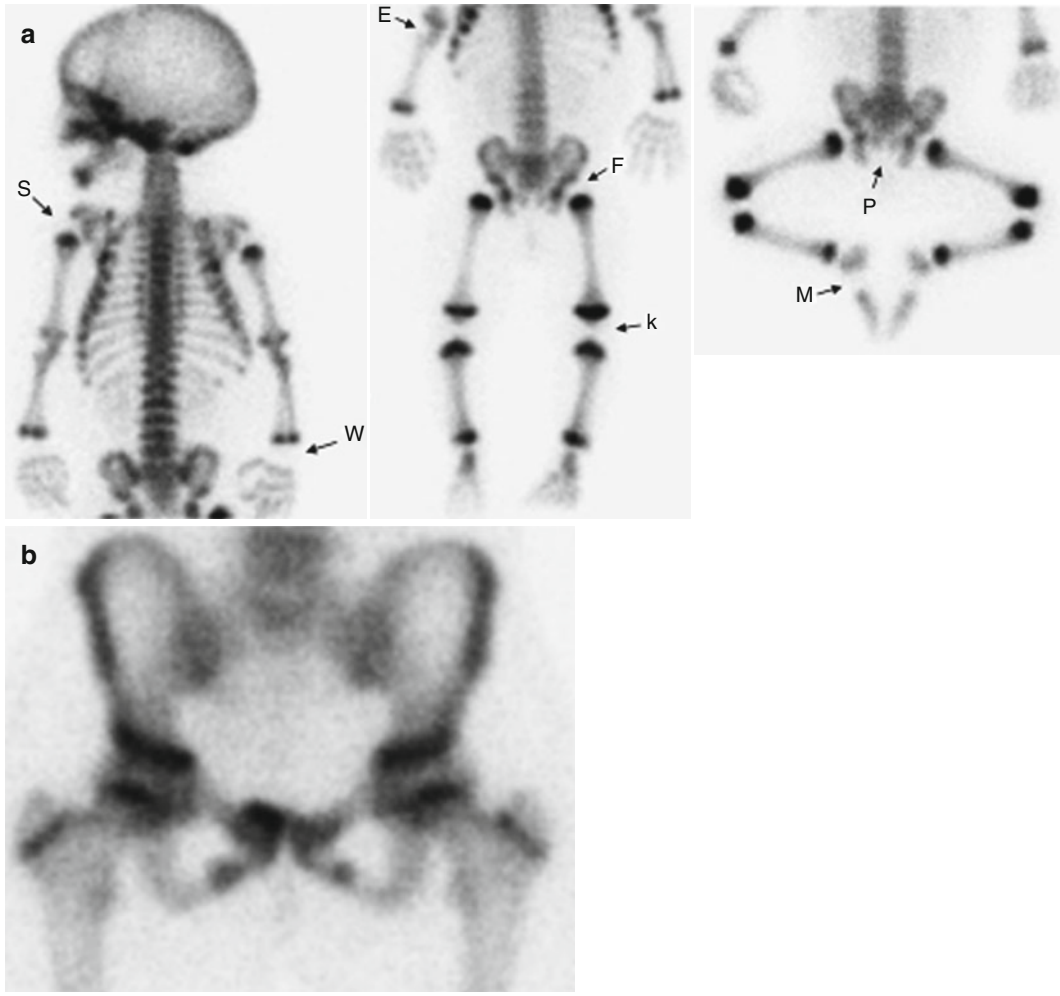

Fig. 1.10 ^{99m}Tc-MDP skeletal scans. (**a**) One-month-old baby. Absent tracer uptake in non-ossified centers. *S* shoulder, *W* wrist, *E* elbow, *F* femoral head, *K* knee, *P* pubis, *M* mid foot. (**b**) A 10-year-old patient showing open ischiopubic synchondroses

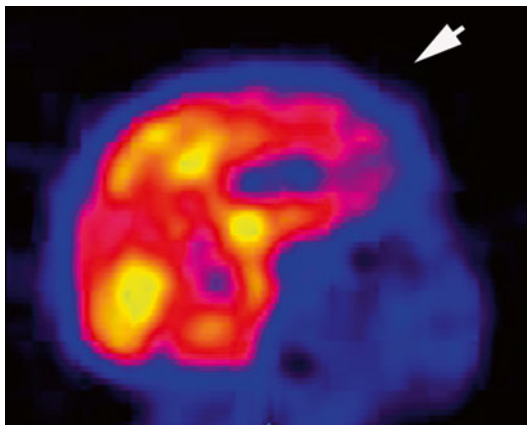

Fig. 1.11 Brain immaturity. ^{99m}Tc-ECD brain SPECT from a newborn showing relatively low cerebral perfusion in the anterior sensorimotor aspect of the brain (*arrow*)

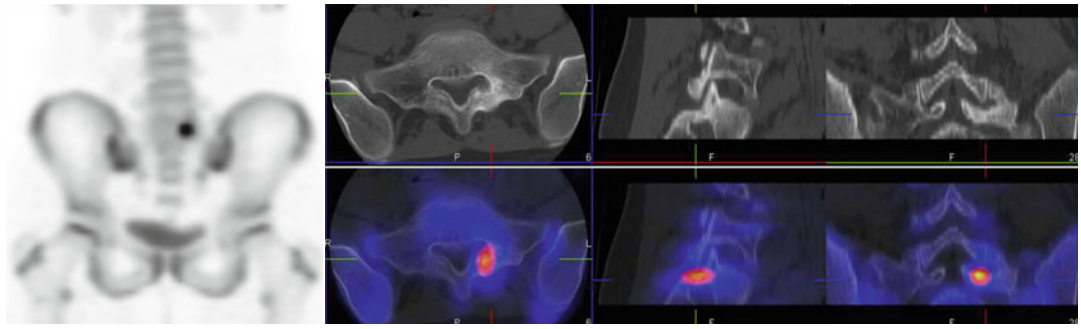

Fig. 1.12 Stress changes in the pars interarticularis. *Left*: MIP of the pelvis. *Right*: ^{18}F-NaF PET and CT fusion. Selected slices reveal intense fluoride uptake in the region of the right L5 pars. On CT, there is a linear defect through the right L5 pars interarticularis

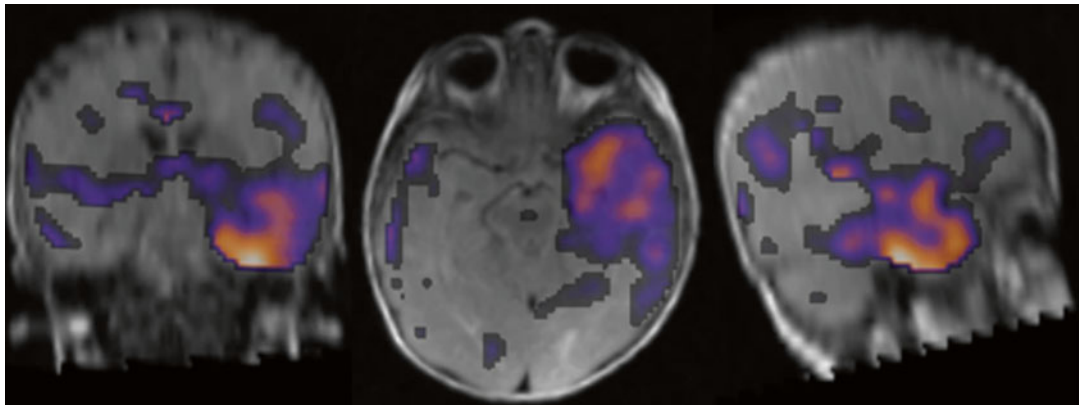

Fig. 1.13 ^{99m}Tc-ECD perfusion brain SPECT. Ictal minus interictal perfusion SPECT has been subtracted and fused to an MRI. There is differential ictal increase of cerebral blood flow in the left temporal lobe

rather difficult with children. Mobile cameras can be used for the evaluation of patients in operating rooms, intensive care units, recovery rooms, interventional radiography suites, and catheterization laboratories.

Image Fusion and Systems Integration

Image fusion overlays two or more three-dimensional (3D) image sets of the same or different imaging modality that are in the same orientation in the same space. Anatomic and functional imaging are complementary, and appropriate image registration and fusion software should be easily available. The introduction of hybrid PET/CT and SPECT/CT scanners has sparked increasing use and interest in image fusion. This hardware approach to image fusion often needs to be complemented by software adjustments on the images when patients move between the PET or SPECT and the CT. The PET/CT and SPECT/CT scanners limit image fusion to two modalities. Electronic image fusion, however, does not depend exclusively on hybrid instrumentation. Image fusion enables the direct comparison of function and structure [SPECT and MRI], function and function (SPECT and FDG-PET), structure and structure (MRI and CT), etc. (Figs. 1.12, 1.13, 1.14, 1.15, and 1.16).

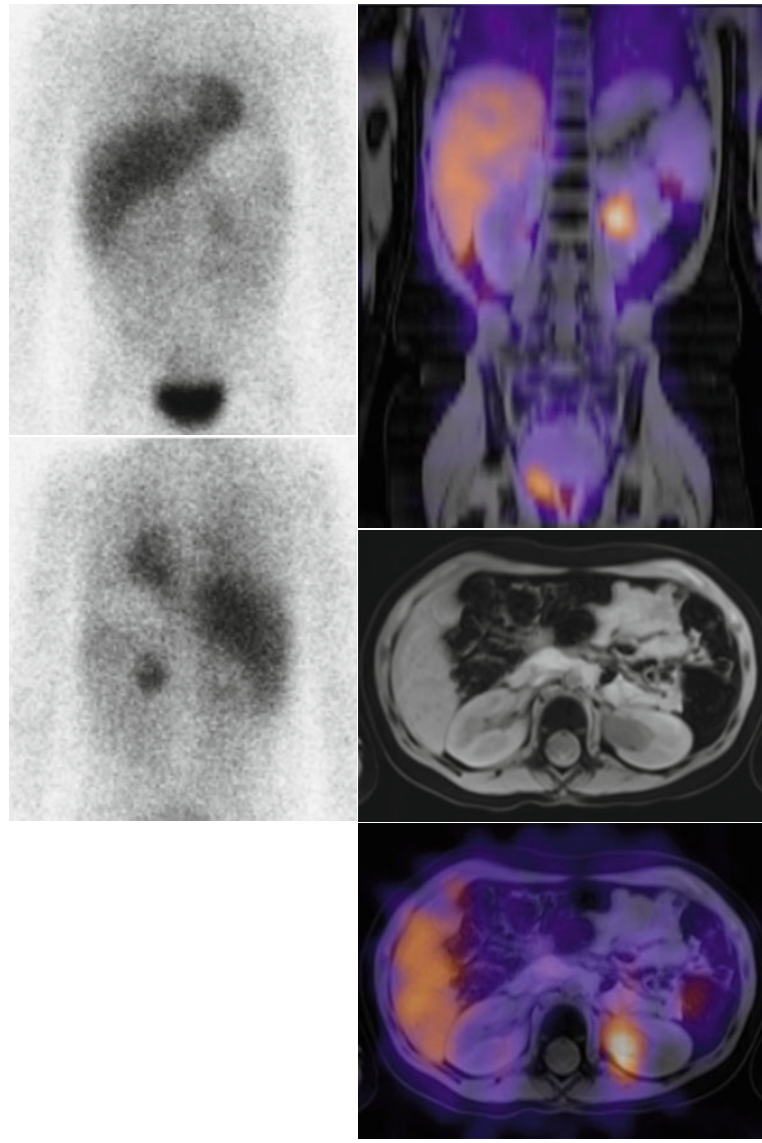

Fig. 1.14 A 3-year-old girl with neuroblastoma after chemotherapy and surgery. Fusion of ^{123}I-MIBG SPECT and MRI demonstrates retroperitoneal MIBG accumulation only in a dilated renal pelvis which was determined not to be a metastasis

With advances in electronic communications, computer processing power, high-capacity networks, and the wider acceptance of imaging standards, image fusion is rather easy to obtain and is now within the reach of routine practice. With the increasing sophistication of picture archiving and communication systems (PACS), all imaging methods can be viewed on most modern workstations. More recently, PET/MRI scanners are being introduced in practice. These systems show promise for the assessment of a variety of disorders and have the advantage over PET/CT of not utilizing X-rays, therefore resulting in lower radiation exposure to the patient. At present, PET/MRI systems are rather expensive and may not be within the reach of most institutions. However, electronic image fusion is very effective and does not require

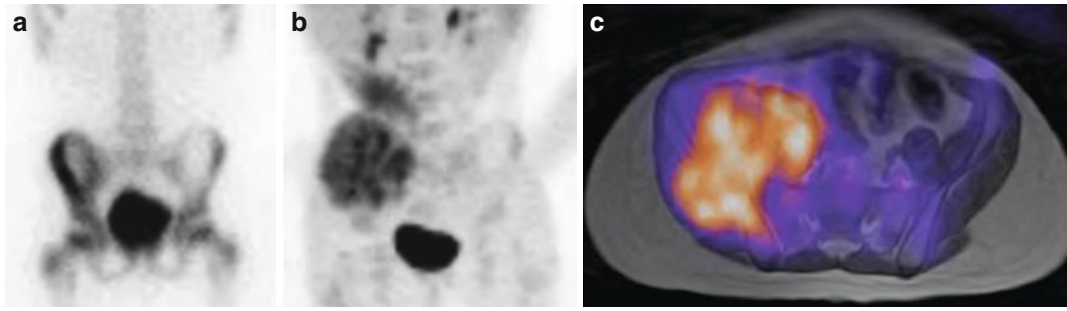

Fig. 1.15 Ewing sarcoma. (**a**) ^{99m}Tc-MDP bone scan shows increased tracer uptake in the left iliac bone, left acetabulum, and proximal femur. (**b**) ^{18}F-FDG MIP shows a larger region of increased tracer uptake also involving the soft tissue component of the tumor. (**c**) ^{18}F-FDG fused to an MRI allowing to correlate increased metabolism within the tumor mass

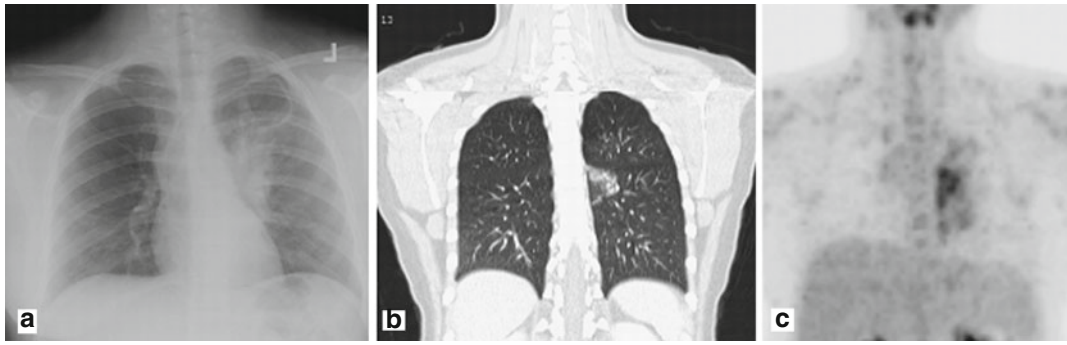

Fig. 1.16 ^{18}F-FDG uptake in pneumonia. A 13-year-old girl following chemotherapy and radiation therapy for Hodgkin's lymphoma presented with 5 days of fever and cough. (**a**) The chest X-ray revealed left lower lobe pneumonia. (**b**) A selected coronal computed tomography (CT) slice also reveals a lesion in the left thorax. (**c**) The ^{18}F-FDG-PET reveals increased tracer uptake in the same region, indicating active inflammatory disease extending beyond the visible CT lesion

the investment in these expensive devices. Electronic image fusion of brain studies (SPECT/MRI, PET/MRI) is relatively easy, while image fusion of body images obtained with the patient in different anatomic positions may be more difficult.

It is common that pediatric patients referred for PET or SPECT have had a CT study in the recent past. In these cases it is advantageous to use the CT already obtained and fuse it with the PET or the SPECT, thus avoiding additional CT exposures (see Chap. 31).

Radiopharmaceutical Administration

Routes of radiopharmaceutical administration include intravenous, oral, inhalation, subcutaneous, intradermal, instillation, and intrathecal.

Intravenous Administration

Intravenous injection is the most frequent route of radiopharmaceutical administration and

warrants special attention. In advance of tracer administration, a tray lined with absorbent paper should be prepared for each patient dose. This tray should contain disposable gloves, skin antiseptic, needles, gauze, the radiopharmaceutical dose, adhesive tape, and a tourniquet. The radiopharmaceutical syringe should be shielded, clearly labeled with the name of the patient, the name of the tracer, the dose, the date and time of calibration, and the volume.

When dealing with venous access in small infants, there is no substitute for an experienced nuclear medicine technologist, nurse, or physician. Volume and site of injection are important. A 23–25-gauge needle of the butterfly type can be used. A disposable T-type connector with a one-way valve permits rapid injection of the tracer followed by a saline flush. The radiopharmaceutical should be in a small volume (0.2–0.5 mL) of solution. Premature and newborn infants may require smaller volumes (0.1–0.2 mL). A large vein, such as an antecubital vein, is usually adequate to permit rapid administration of the radiopharmaceutical and the saline flush. Other veins may be used as long as they can tolerate the rapid bolus and the saline flush. Patients usually lie supine for the injection. The site of injection should not overlap the area of interest. Once an appropriate vein is identified, a tourniquet is applied and the skin is cleaned with an antiseptic. The tubing is filled with sterile saline. The extremity is immobilized or held by an aide if necessary, and the vein is entered. As soon as blood return occurs, the tourniquet is released. If there is no free retrograde venous flow into the tube of the butterfly needle, no attempt should be made to inject the radiopharmaceutical, and another injection site should be identified.

After successful venous entry, the needle should be carefully secured in place with adhesive tape. One should check once more to make sure that there is free flow into the vein. It is good practice to flush the tubing with a small volume (1–3 mL) of normal saline before injecting the tracer. The radiopharmaceutical should then be injected and the tubing flushed with normal saline.

Injection technique varies for static and dynamic studies. The injection speed for static studies can be delivered slowly, and a rapid bolus injection is not needed. For dynamic studies requiring high temporal resolution, a proximal injection site, a small volume of radiopharmaceutical solution, and a rapid speed of injection are important for successful examination.

Radiopharmaceutical Dose Adjustment

In nuclear medicine, dosing of radiopharmaceuticals in the adult population is roughly standardized. Pediatric radiopharmaceutical doses should be determined by the minimum amount necessary to ensure satisfactory examination in a reasonable period of time. Administered doses in pediatric nuclear medicine have been developed by experience, taking into account the body mass, absorbed radiation dose, type of examination, available photon flux, instrumentation, and examination time. High doses (which do not result in improved diagnostic sensitivity or accuracy) or low doses (which do not permit adequate examination) should be considered unnecessary radiation exposures. The amount of radioactivity administered to a child for a nuclear medicine procedure should be adjusted according to the patient's body weight or other expressions of body size. Several methods for the determination of radiopharmaceutical doses in children have been used. The resulting calculated doses using these various methods have varied considerably among the different approaches [6]. Also, administered doses of radiopharmaceuticals in children have varied considerably even among pediatric institutions. In the past, there has been no standardized approach to scaling the administered radiopharmaceutical doses in children (Fig. 1.17).

More recently, the North American Expert Consensus Guidelines for Pediatric Administered

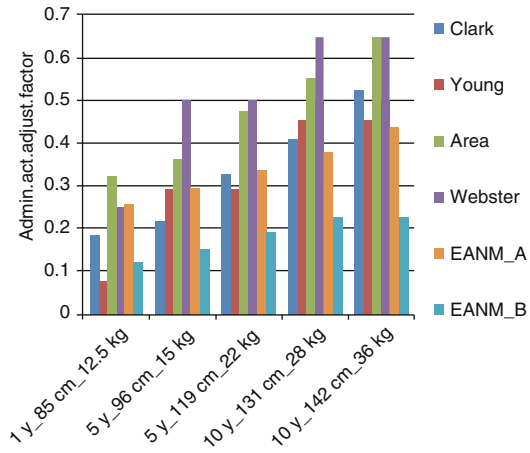

Fig. 1.17 Various methods used to calculate pediatric radiopharmaceutical administered doses

Radiopharmaceuticals have been developed and approved by the Society of Nuclear Medicine and Molecular Imaging (SNMMI), the American College of Radiology (ACR), and the Society for Pediatric Radiology (SPR) and were published recently and widely disseminated by the Image Gently Campaign [7, 8]. In addition the European Association of Nuclear Medicine has developed and published a Dosage Card that closely resembles the North American Guidelines [9].

Estimations of administered doses of activity for pediatric patients that are based on adult dose corrected for body weight or body surface area are generally good guides for children over 1 year of age. Premature infants and newborns require special consideration, and the concept of minimum total dose should be considered. Minimum total dose can be defined as the minimum dose of radiopharmaceutical below which the study would likely be inadequate regardless of the patient's body weight or surface area. The minimum dosage is determined by the type of study: dynamic or static. As a general rule, dynamic studies require a higher dose of tracer than do static studies. Matching the acquisition framing rate with the timing of the physiologic process to be investigated also allows for an optimal determination of administered tracer dose in cases such as hepatobiliary or dynamic renal imaging.

Radionuclide Therapy

Therapy with internally administered radionuclides is employed less often in children than in adults. However, in the past few years there seems to be an increase in the use of this treatment method in children. The most frequently performed radionuclide therapy in children is with ^{131}I in patients suffering from hyperthyroidism refractory to medical treatment and those who refuse surgery. Reasons for the increase in the use of ^{131}I treatment for hyperthyroidism include undesirable side effects from medical therapy or lack of patient compliance with treatment. Another use of ^{131}I is for the treatment of patients with metastatic papillary carcinoma of the thyroid (see Chap. 5).

During the past few years, treatment of neuroblastoma has included therapy with intravenous ^{131}I-MIBG. ^{131}I-MIBG therapy has become popular, and centers have developed specific programs to deal with this method of treatment. One approach utilizes a single, relatively high dose of the agent and requires in-hospital admission with patient isolation. This is the most frequently utilized approach. Another method employs smaller-fractionated doses of the same agent, which does not require hospitalization (see Chap. 20).

Radiation Exposure and Risk

The objective of pediatric nuclear medicine is to obtain the best diagnostic information employing the highest quality imaging in the shortest period of time and with the lowest patient radiation exposure. In general, nuclear medicine procedures involve exposure to low levels of ionizing radiation, and the diagnostic value of these procedures when used appropriately far outweighs potential radiation risk (see Chap. 31).

Appendix 1: Example of a Patient/Parent Brochure About a Nuclear Medicine Procedure

Bone Scan in Nuclear Medicine

What is a bone scan? A bone scan is an image that shows bone blood flow, metabolism, and cell activity in the bones. There are two types of bone scans – planar and 3D (SPECT).

Why bone scans at this hospital? Our department of nuclear medicine is committed to providing a safe, comfortable, and child-friendly atmosphere with specialized:

- Nuclear medicine physicians with expertise in interpreting bone scans in children of all ages
- Technologists with experience imaging children
- Equipment adapted for pediatric use
- Protocols that keep radiation exposure as low as possible while assuring high image quality

When is a bone scan needed? A bone scan can detect very small changes in your child's bones, even ones that may not be seen on regular X-rays. Bone scans can detect subtle injuries, stress changes, or small fractures that may result from intense playing or sports activity as well as infection or inflammation.

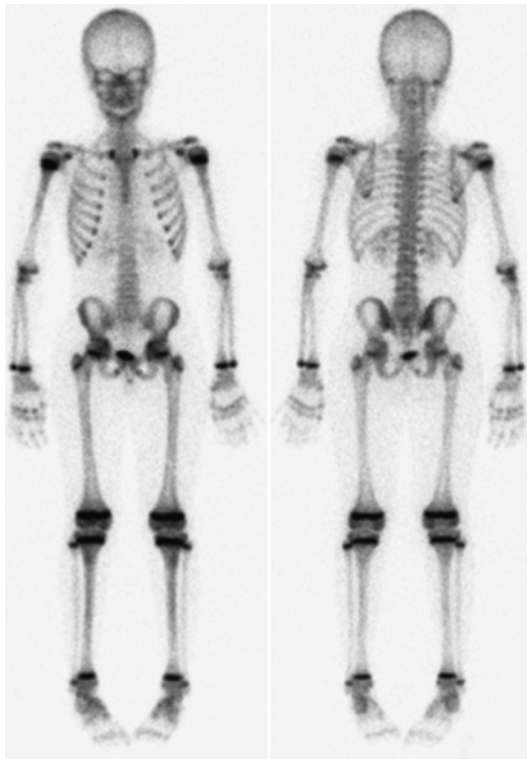

How should I prepare for a bone scan? There is no special preparation needed for this test. However, between the injection of the radiopharmaceutical and the scan, there is a 3–4-h waiting period. In addition, the scan time is approximately 30–60 min. Please schedule your day accordingly.

How is a bone scan obtained? Scans are obtained using special cameras called gamma cameras. Before the images are taken, a tiny volume of a radiotracer (radiopharmaceutical, ^{99m}Tc-MDP) is injected in one of your child's veins using a very small needle (smaller than the needles used for blood tests). Two-minute pictures showing blood flow to the bones may be obtained while the tracer is injected. The actual images of the bones are obtained approximately 3–4 h after the injection of the tracer.

After the injection, your child can continue with his or her normal activities while waiting for the scan to begin. When you return to nuclear medicine, the bone scan is obtained. Your child will lie on an imaging table, and the camera will slowly move around his or her body as several pictures are taken. The camera does not touch your child and does not produce radiation. It is very important that your child remains still during the imaging in order to obtain the best quality images. The number of images obtained and the total imaging time will vary depending on the diagnosis under consideration, although the average imaging time is about 1 h. Some of the images are three-dimensional (3D), and such images are also evaluated by "slicing" the image through different planes.

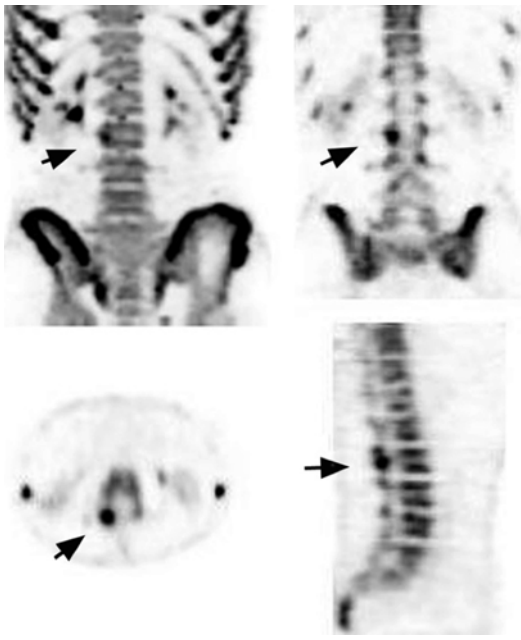

Bone scan in a young gymnast with back pain. His X-rays were normal, but you can see that on the bone SPECT, there is stress injury in the spine (arrows). The picture on the right upper quadrant is a volume-rendered image, while the others are slices of the 3D image. The slices help localize the lesion

What happens after the bone scan? Once the pictures are ready, the nuclear medicine physician will evaluate them and will produce and send a report to your child's doctor. You will be free to leave and your child can resume normal activity.

What about radiation exposure? Your child will be exposed to a very small amount of radiation that is within the lower range of what is received from routine diagnostic imaging procedures that use X-rays. Nuclear medicine has been used on babies and children for more than 40 years with no known adverse effects from the low doses employed. We are committed to ensuring that your child receives the smallest radiation dose needed to obtain the desired result. Our doctors balance the medical benefits of any imaging test with potential radiation risks even if these are minuscule.

More information about nuclear medicine radiation safety can be found on the Image Gently website (www.imagegently.org).

This pamphlet is written to provide patients, parents, and caregivers with information about bone scans and radiation exposure. This information should not be used as a substitute for the advice from your doctor. If you are concerned or have any unanswered questions, you should talk with a nuclear medicine physician before the study begins.

References

1. Treves ST. Pediatric nuclear medicine/PET. 3rd ed. New York: Springer; 2007.
2. Treves ST, Baker A, Fahey FH, et al. Nuclear medicine in the first year of life. J Nucl Med. 2011;52(6):905–25.
3. Fahey FH, Treves ST, Adelstein SJ. Minimizing and communicating radiation risk in pediatric nuclear medicine. J Nucl Med. 2011;52(8):1240–51.
4. Zukotynski KA, Fahey FH, Laffin S, et al. Seasonal variation in the effect of constant ambient temperature of 24 degrees C in reducing FDG uptake by brown adipose tissue in children. Eur J Nucl Med Mol Imaging. 2010;37(10):1854–60.
5. Heyman S. Toxicity and safety factors associated with lung perfusion studies with radiolabeled particles. J Nucl Med. 1979;20(10):1098–9.
6. Treves ST, Davis RT, Fahey FH. Administered radiopharmaceutical doses in children: a survey of 13 pediatric hospitals in North America. J Nucl Med. 2008; 49(6):1024–7.
7. Gelfand MJ, Parisi MT, Treves ST. Pediatric radiopharmaceutical administered doses: 2010 North American consensus guidelines. J Nucl Med. 2011;52(2):318–22.
8. Treves ST, Parisi MT, Gelfand MJ. Pediatric radiopharmaceutical doses: new guidelines. Radiology. 2011;261(2):347–9.
9. Lassmann M, Biassoni L, Monsieurs M, Franzius C. The new EANM paediatric dosage card: additional notes with respect to F-18. Eur J Nucl Med Mol Imaging. 2008;35(9):1666–8.

Sedation and General Anesthesia

2

Randy P. Prescilla and Keira P. Mason

Infants and young children who are scheduled for nuclear medicine imaging studies often require sedation, and those with complicated medical conditions will require general anesthesia. There are several indications for sedation in nuclear medicine: Sedation can reduce patient motion during prolonged image acquisitions, facilitate a procedure which requires patient response to command and cooperation (e.g., voiding during a radionuclide cystogram) and minimize discomfort, anxiety, or pain [1]. Appropriate sedation is even more essential in neonates and infants, since they require special care, patience, adaptation, experience, and skillful hands. Infants undergo rapid growth and development, and sedative and radiopharmaceutical distribution and kinetics may vary from that of older children and young adults. Newborns and infants have a lower glomerular filtration rate, faster circulation, and faster pulmonary wash-in and washout of radioactive gases than older children [2].

Sedation is the most common technique of ensuring immobility in infants, children, and the developmentally compromised who are unable to remain motionless on their own. In rare circumstances, anesthesia services are required to ensure the safety of the patient and the surrounding people. In general, the relative contraindications to sedation include an allergy to the sedatives utilized, a prior adverse reaction to sedation, history of a difficult endotracheal intubation or difficulty providing positive pressure ventilation via mask, uncontrolled gastroesophageal reflux, and a patient who has significant cardiac or respiratory compromise [3] (Table 2.1). This chapter will review established sedation guidelines and recommendations, the logistics of setting up a sedation and anesthesia program, patient selection and sedation-related risk factors and adverse events, a review of the more commonly utilized sedatives, and the challenges of providing sedation and anesthesia in the nuclear medicine setting.

The Depths of Sedation

The tenets of sedation rely on the ability to deliver sedation to a targeted depth and to be able to identify the achieved levels. The term "conscious sedation" is no longer acknowledged as appropriate terminology nor is it recognized as an indicator of depth of sedation. The Joint Commission, American Academy of Pediatrics (AAP), and American Society of Anesthesiologists (ASA)

R.P. Prescilla, MD (✉) • K.P. Mason, MD
Department of Anaesthesia,
Harvard Medical School, Boston, MA, USA

Department of Anesthesiology,
Perioperative and Pain Medicine,
Boston Children's Hospital,
Boston, MA, USA
e-mail: randy.prescilla@childrens.harvard.edu;
keira.mason@childrens.harvard.edu

S.T. Treves (ed.), *Pediatric Nuclear Medicine and Molecular Imaging*,
DOI 10.1007/978-1-4614-9551-2_2, © Springer Science+Business Media New York 2014

define sedation as a sedation continuum that one can pass through escalating depths, described as minimal, moderate, and deep [4, 5] (Fig. 2.1). These depths of sedation rely on a subjective assessment of the patient's response to verbal, tactile, and painful stimuli to predict the patient's risk of respiratory and cardiovascular compromise. The associated risks with each level of the sedation continuum are assumed but have never been validated.

Table 2.1 Relative contraindications to sedation

Active uncontrolled gastroesophageal reflux
Active uncontrolled vomiting
Current (or within the past 3 months) history of apnea requiring an apnea monitor
Active current respiratory issues that are different from the baseline status (pneumonia, exacerbation of asthma, bronchiolitis, respiratory syncytial virus)
Unstable cardiac status (life-threatening arrhythmia, abnormal cardiac anatomy, significant cardiac dysfunction)
Craniofacial anomaly, which could make it difficult to effectively establish a mask airway for positive pressure ventilation, if needed
History of adverse or paradoxical events occurring following administration of barbiturate or chloral hydrate
Allergy to barbiturates or chloral hydrate
History of failed sedation in this institution's radiology department

From Mason et al. [3] with permission

Guidelines for Sedation Practice, Monitoring, and Qualifications

The practice of sedation has become a controversial topic over the past decade, as non-anesthesiologists have become sedation providers. Topics of debate include the sedatives appropriate for administration by non-anesthesiologists, the depth of sedation that is safe for non-anesthesiologists to achieve, the training and credentialing appropriate for non-anesthesiologists, and the reimbursement for non-anesthesiologists. In 2002, the American Society of Anesthesiologists (ASA) updated the 1995 document of *Practice Guidelines for Sedation and Analgesia by Non-anesthesiologists* [6, 7]. The purpose of this document was to "allow clinicians to provide their patients with the benefits of sedation/analgesia while minimizing the associated risks" [6]. These guidelines are consistent with the most recent updates of 2006 by the American Academy of Pediatrics (AAP) of *The Guidelines for Monitoring and Management of Pediatric Patients During and After Sedation for Diagnostic and Therapeutic Procedures* [4, 8–10]. Both the AAP and ASA guidelines were intended to standardize sedation practice in order to minimize the practice variance which has existed in the past [11].

The Joint Commission has also established standards for sedation and anesthesia care and, recently, in 2007, established recommendations

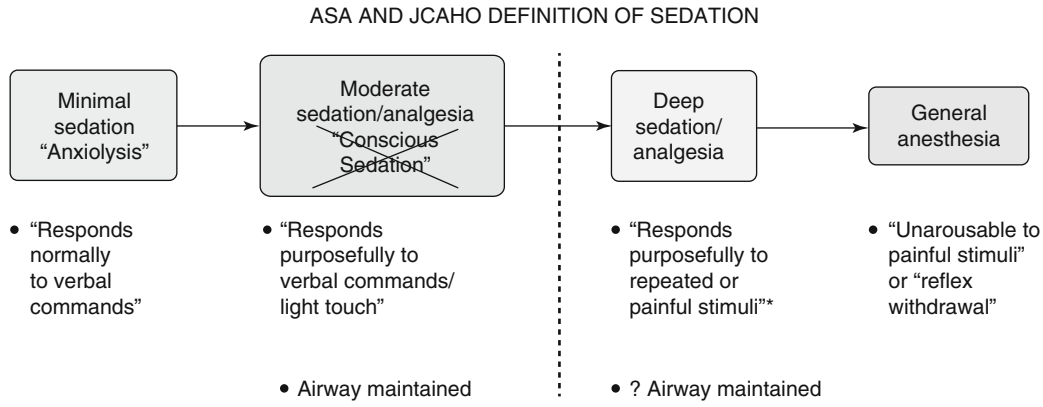

Fig. 2.1 ASA and JCAHO definition of sedation (From Kaplan et al. [5] with permission). * Reflex withdrawal from a painful stimuluis is NOT considered a purposeful response

for the minimal training and qualifications expected of sedation providers: "Individuals administering moderate or deep sedation and anesthesia must be qualified and have the appropriate credentials to manage patients at whatever level of sedation or anesthesia is achieved, either intentionally or unintentionally" [12]. With respect to deep sedation, the Joint Commission specified that "individuals must be qualified to rescue patients from general anesthesia and are competent to manage an unstable cardiovascular system as well as a compromised airway and inadequate oxygenation and ventilation" [12]. The Joint Commission does not specify the methods required to validate a provider's rescue skills but instead states that "each organization is free to…determine that the individuals are able to perform the required types of rescue" [12].

More recently, the Centers for Medicare & Medicaid Services (CMS) published in 2009 the *Revised Hospital Anesthesia Services Interpretive Guidelines – State Operations Manual* (*SOM*) *Appendix A.7, 8*, which mandated that deep sedation be identified as anesthesia services. Deep sedation was defined as "a drug-induced depression of consciousness during which patients cannot be easily aroused but respond purposefully following repeated or painful stimulation. The ability to independently maintain ventilatory function may be impaired. Patients may require assistance in maintaining a patent airway, and spontaneous ventilation may be inadequate. Cardiovascular function is usually maintained" [12]. In 2010, the CMS limited the administration of deep sedation to an anesthesiologist, nonanesthesiologist physician, dentist, oral surgeon, podiatrist, certified registered nurse anesthetist (CRNA), or anesthesia assistant [13, 14]. One year later, these guidelines were revised in *Pub. 100–07 State Operations Provider Certification* which revised Appendix A of 42 CFR 482.52 and acknowledged that individual hospitals may establish their own policies with respect to the qualifications of sedation providers, provided that national guidelines of one or more specialties are followed [14].

Setting Up a Sedation and Anesthesia Service

The Department of Radiology/Nuclear Medicine generally depends on the services of other specialties to provide sedation or anesthesia [15]. Frequently, these services are provided by departments of anesthesia, pediatrics, hospital medicine, emergency medicine, or intensive care medicine [16–20]. Each institution and health care facility must determine which specialists can be credentialed to administer sedation services.

In 2004, the ASA first issued guidelines for the delivery of anesthesia in locations outside of the operating room. This *statement on nonoperating room anesthetizing locations* sets a minimum standard for these anesthetizing locations and, essentially, the expectation that they be similar to that of the operating room. Although these expectations may seem obvious, they are not always easy to meet in the Department of Radiology/Nuclear Medicine. For example, anesthetizing locations are expected to have a source of wall oxygen along with a means for removal of waste anesthesia gases. Older nuclear medicine suites, however, were not designed with anesthesia services in mind; many were designed prior to the ASA guidelines of 2004. Accommodation of anesthesia services has, for these sites, required that renovation and engineering services reconfigure these sites. As radiology units strived to become more efficient, they have found that the capability to recover patients postanesthesia within their department offsets the inefficiency of transporting patients to remote anesthesia recovery areas. However, even recovery sites remote to the operating room must provide identical postanesthesia care. This care requires additional resources, as there is the expectation that "appropriate post-anesthesia management should be provided. In addition to the anesthesiologist, adequate numbers of trained staff and appropriate equipment should be available to safely transport the patient to a postanesthesia care unit" [21]. To facilitate coordination between the Department of Radiology/Nuclear Medicine and the outside

services that provide anesthesia and sedation, it is preferable to appoint a director(s) of Radiology/Nuclear Medicine Anesthesia and Sedation. This professional(s) should have a commitment to promoting safe and efficient care to all radiology patients through collaboration with the radiology/nuclear medicine physicians, nurses, and technologists. As the technology and image techniques in the field of radiology advance, it is important that this director(s) remains current with these advances and proactively plans with the nuclear medicine physicians and technologists whenever specific imaging techniques require specialized anesthesia management.

Patient Selection

The American Academy of Pediatrics advocates five safety goals for sedation: (1) guard the patient's safety and welfare; (2) minimize physical discomfort and pain; (3) control anxiety, minimize psychological trauma, and maximize the potential for amnesia; (4) control behavior and/or movement to allow the safe completion of the procedure; and (5) return the patient to a state in which safe discharge is possible [4]. Multiple factors are required in order to achieve these goals such as careful patient selection for sedation, credentialing qualified individuals to administer the medications and to rescue from an adverse response, the use of appropriate physiologic monitoring, and the appropriate selection of sedatives and analgesics.

A thorough medical history and review of systems should be documented prior to scheduling a patient and should include pertinent prior surgical, sedative, and anesthetic histories. All current medications and drug allergies must be noted along with relevant clinical consultations and laboratory and clinical studies. To optimize the pre-evaluation and appropriate triage of patients, each patient and family should be directly contacted by a qualified health care professional prior to final scheduling. This direct contact enables the past and current history to be clarified and expounded upon and provides the family with the opportunity to ask questions. Fasting (i.e., NPO) instructions must also be finalized.

Table 2.2 Red flags for sedation

1. Apnea
2. Full-term infant less than 1 month of age (unless an inpatient admitted to the hospital)
3. Respiratory-compromised patients
4. Uncontrolled/unpredictable gastroesophageal reflux or vomiting that poses an aspiration risk
5. Craniofacial abnormality that may make it difficult to establish effective mask airway
6. Cyanotic cardiac disease or unstable cardiac status
7. Painful procedure that may be challenging to provide adequate analgesia without a general anesthetic
8. High-risk procedure that may require presence of an anesthesiologist for resuscitation
9. Procedure that requires absolute immobility only achievable with a general anesthetic
10. Procedure being performed in remote location that is so removed that immediate emergency backup assistance would be virtually impossible
11. Inadequate qualified personnel available to provide safe procedural sedation

In most radiology departments, this triage is performed by a core group of radiology nurses. These nurses also determine with the family and patient which medications, if any, should be continued even on the day of the intended procedure. All conversations and accompanying medical information should be documented in a manner consistent with individual institution policy.

There are no universally accepted criteria for the triage of patients to sedation or anesthesia. There are recommendations, however, which have been developed and followed, identifying "red flags" which warrant further assessment or consultation prior to receiving sedation (Table 2.2).

In general, those patients who are triaged to receive sedation, particularly by non-anesthesiologists, tend to be classified as American Society of Anesthesiologists (ASA) levels I and II and, occasionally, level III (Table 2.3). Children in ASA classes III and IV, those with special needs, anatomic airway abnormalities, or extreme tonsillar hypertrophy, often require additional and individual consideration and often require general anesthesia (as opposed to sedation). These and other patients with complicated medical histories may also warrant prior consultation with other specialties such as cardiology, otolaryngology, pulmonary, or neurology.

Table 2.3 ASA physical status classification

1. A normal healthy patient
2. A patient with mild systemic disease
3. A patient with severe systemic disease
4. A patient with severe systemic disease that is a constant threat to life
5. A moribund patient who is not expected to survive without the operation
6. A declared brain-dead patient whose organs are being removed for donor purposes

Excerpted from http://www.asahq.org/Home/For-Members/Clinical-Information/ASA-Physical-Status-Classification-System of the American Society of Anesthesiologists. A copy of the full text can be obtained from ASA, 520 N. Northwest Highway, Park Ridge, IL 60068-2573

Risks of Sedation and Anesthesia

The risks of sedation and anesthesia include hypoventilation, apnea, airway obstruction, cardiopulmonary arrest, and the morbidity and mortality associated with these events [1, 17, 22–25]. These adverse responses during and after sedation for a diagnostic or therapeutic procedure may be minimized, but not completely eliminated, by (1) a careful pre-procedure review of the patient's underlying medical conditions and consideration of how the sedation process might affect or be affected by these conditions, (2) appropriate drug selection for the intended procedure, (3) presence of an individual with the skills needed to rescue a patient from an adverse response, and (4) appropriate physiologic monitoring and continuous observation by personnel not directly involved with the procedure which allow for accurate and rapid diagnosis of complications and initiation of appropriate rescue interventions [4].

Most Common Medications Used in Pediatric Sedation

Unfortunately, most drugs used for sedation in children do not carry pediatric information that have been reviewed and approved by the Food and Drug Administration. Only a small percentage of drugs approved by the FDA are labeled for pediatric use, with the rest being used where the intent is the "practice of medicine." The published medical literature includes off-label use in pediatrics.

The most common medications currently used to provide sedation in children have recently been reviewed [26]. These include chloral hydrate, pentobarbital, midazolam, dexmedetomidine, ketamine, propofol, ketorolac, morphine, and fentanyl. The mean features of these drugs are presented below.

Chloral Hydrate and Pentobarbital

Historically, chloral hydrate and pentobarbital have been the hypnotics of choice for pediatric sedation [27–30]. Both medications have no analgesic properties. They are useful for non-painful procedures as a sole agent (magnetic resonance imaging, computerized tomography, nuclear medicine). They can also be used with adjuvant analgesics in order to promote a hypnotic, sedative state for interventional procedures. Rates of successful sedation with chloral hydrate and pentobarbital range from 85 to 98 % [31, 32]. Both pentobarbital and chloral hydrate are medications which have almost 100 years of clinical experience. Because of their extended half-life (which approaches 24 h), they have been associated with prolonged recovery times and sedation-related morbidity. Adverse events with these medications include oxygen desaturation, nausea, vomiting, hyperactivity, respiratory depression, and failure to adequately sedate [29, 33].

Chloral hydrate is only available as an oral sedative. Pentobarbital, on the other hand, can be given by various routes; it may be administered intravenously, intramuscularly, and orally. Children less than 1 year of age respond well to these two medications when given in the oral form. Pentobarbital, flavored with cherry syrup, is more palatable and equally effective as chloral hydrate [34]. Comparing the two medications, oral pentobarbital has been associated with fewer respiratory events as compared to chloral hydrate. The incidence of a drop in oxygen saturation during sedation was over seven times higher in patients sedated with oral chloral hydrate compared to those sedated with pentobarbital [3].

Oral pentobarbital has been shown to have similar efficacy and a lower rate of respiratory complications compared with intravenous pentobarbital in infants [35].

Consideration should be given to the use of oral pentobarbital in infants less than 12 months of age, regardless of the presence of an intravenous line. Patients over 1 year of age receive intravenous sedation because it is more predictable and reliable. Pentobarbital is titrated up to 6 mg/kg intravenously to provide sedation and hypnosis. Patients who are on barbiturate therapy (for seizures) can develop tolerance to barbiturates and may receive a higher dose, up to 8 mg/kg body weight.

Midazolam

Midazolam is a short-acting benzodiazepine with sedative, anxiolytic, muscle relaxant, and amnestic effects with rapid onset and short duration of action. It is administered orally, intravenously, intramuscularly, as well as intranasally. Midazolam is usually administered to provide anxiolysis, with accompanying mild sedation. This state usually suffices for short diagnostic procedures, especially in children who are tired, sleepy, or close to their regular nap time. Adverse effects with midazolam include respiratory depression and hypotension, with rare effects including headache, nausea, emesis, cough, and/or hiccups. Contraindications include acute narrow-angle glaucoma, uncontrolled pain, existing central nervous system depression, and shock [36].

Dexmedetomidine

Dexmedetomidine (Precedex; Hospira, Lake Forest, IL) is a highly selective alpha-2 adrenoceptor agonist approved for use in intubated and non-intubated adults. Dexmedetomidine is not approved for pediatric use by the FDA. It is, however, used for pediatric sedation in several settings such as diagnostic radiologic imaging studies and intensive care units.

Dexmedetomidine offers the advantage of providing sedation and analgesia with little respiratory depression and in most a tolerable decrease in blood pressure and heart rate [37]. When administered to adults within clinical dosing guidelines, there are no accompanying changes in resting ventilation [38–40].

It can produce dose-dependent decreases in blood pressure and heart rate as a result of its alpha-2 agonist effect on the sympathetic ganglia with resulting sympatholytic effects [39, 40].

The half-life of dexmedetomidine is shorter than that of pentobarbital and chloral hydrate. A short half-life makes dexmedetomidine easier to titrate, quicker to recover from, and potentially associated with fewer prolonged sedation-related adverse events.

There is literature to support that dexmedetomidine has some analgesic properties [41–43]. It may be useful for select interventional radiology procedures that require sedation and minimal analgesia. It can be particularly effective when supplemented with a local anesthetic during the procedure. In addition, some feel that dexmedetomidine actually mimics some aspects of natural sleep [25].

Although there are no absolute contraindications to dexmedetomidine, the concurrent use of digoxin is often considered a relative contraindication, as it has been associated with extreme bradycardia in children and cardiac arrest in adults [44, 45]. Rarely, dexmedetomidine can cause potentially life-threatening cardiovascular complications in some adults and children [44, 46–49]. The use of dexmedetomidine in nuclear medicine has been recently reported [50].

Ketamine

Ketamine is a rapid-acting dissociative agent that is administered via intravenous, intramuscular, oral, rectal, nasal, epidural, or intrathecal routes. Ketamine can produce a rapid onset of deep sedation and analgesia with minimal respiratory depression and cardiovascular side effects [51, 52]. Ketamine is unique because it provides deep sedation and profound analgesia while still

maintaining airway muscle activity and upper airway patency [53]. Large doses of ketamine can produce a state of general anesthesia.

When given in small bolus doses, ketamine provides analgesia for an average of 30 min. As an infusion, ketamine can produce a continuous state of analgesia which may be titrated up and down in response to (or in anticipation of) the painful stimulus. It is especially useful for patients who will undergo an exceptionally painful procedure, those on long-term treatment with opioids, or those who have a high tolerance to opiates. Ketamine provides an effective alternative to narcotics in these patients.

The use of ketamine for pediatric sedation and analgesia has been described in various nonoperating room settings. Most of the experience with ketamine in children is drawn from emergency medicine and, lately, from interventional radiology.

Hallucinations, delusions, nightmares, and emergence delirium are phenomenon most commonly described as a potential side effect of ketamine; these are more commonly noted in adults [53, 54]. The presence of these adverse events in the pediatric population is controversial [55, 56]. In adults, the concomitant administration of benzodiazepines (midazolam or diazepam) with ketamine has been shown to decrease the incidence of these events. Again, the utility of benzodiazepines in reducing these events in children is controversial [57–59]. Some reports indicate that the addition of benzodiazepines leads to an increased incidence of oxygen desaturation events [60]. Under age 5, there is no definitive evidence that benzodiazepine administration will reduce the hallucinations, delusions, and excitatory behavior that can occur with ketamine. Children over age 5 may benefit from concomitant benzodiazepine administration.

Propofol

Propofol is an intravenous anesthetic approved for use in the induction and maintenance of general anesthesia in children and adults. It has a rapid onset of action, distributed extensively and rapidly cleared from the body. Emergence from anesthesia occurs quickly.

Common adverse events include apnea (children and adults). Other common adverse events in adults include bradycardia, arrhythmias, blood pressure problems, decreased cardiac output, burning/stinging at the site of injection, hyperlipidemia, respiratory acidosis, rash, and pruritus.

Propofol is also used in monitored anesthesia care for deep sedation in intensive care units and areas outside the operating room, including radiology and nuclear medicine suites. There has been an increasing interest by non-anesthesiologists in using propofol as a sedation agent [16–18]. Propofol is commonly administered first via a slowly titrated load to achieve the targeted depth of sedation which is then maintained with a continuous infusion at doses of 100 mcg/kg/min upwards [61]. Propofol administration requires that the sedation provider be proficient and expert in the identification and management of airway compromise: even at low-dosing ranges, the cross-sectional area of the airway at the level of the tongue and epiglottis narrows, and patients can manifest signs of obstruction [62, 63]. There is literature to support that propofol can be as safely administered by gastroenterologists, pediatricians, nurse practitioners, and emergency room physicians as it can be by anesthesiologists [16–18, 64, 65].

Ketorolac and Other Non-opioid Analgesics

Analgesics may be required for procedures in addition to the use of hypnotics, sedatives, or infiltration with local anesthesia. There are a variety of analgesics available. Ketorolac is a nonsteroidal anti-inflammatory drug administered intravenously every 6 h with a maximum of 72 h of administration. A one-time administration of ketorolac may be sufficient to provide analgesia for simple, short nuclear medicine procedures such as cerebral spinal fluid (CSF) flow studies and lymphangiograms.

Intravenous ibuprofen and intravenous acetaminophen were approved for use in the USA in

2009 and late 2010, respectively. However, the current costs of these medications have limited their routine clinical use.

Ketorolac and ibuprofen may inhibit platelet aggregation and prolong bleeding time, which may be an undesirable effect for some conditions. Alternative analgesics include narcotics or ketamine.

Narcotics

The choice of narcotic should depend on the duration of the procedure and the extent of analgesia required. Morphine and fentanyl are the more popular narcotics. Morphine requires approximately 10 min to take effect and has a duration of action of approximately 2 h. Fentanyl works quicker, has 100 times the potency of morphine, and can produce analgesia in minutes. It generally needs to be re-dosed at least every 30–60 min depending on the procedure. Narcotics should be administered prior to (i.e., in anticipation of) the painful stimulus so that adequate analgesia is present at the time of the stimulus.

Respiratory depression is the most common adverse event resulting from narcotic use. In addition, rapid administration of fentanyl may result in rigid chest syndrome. Naloxone is the opioid antagonist indicated for the reversal of opioid-induced respiratory depression. Naloxone, as well as other drugs and equipment for resuscitation, should be readily available in the radiology/nuclear medicine suites.

Combination Therapy

Additional medications increase the risk of adverse events, so the sedation physician or anesthesiologist should be aware of the possible adverse events that may result from the medications administered. Drugs with long durations of action must be allowed to manifest their pharmacologic actions and peak effects before additional doses are considered. The practitioner must know whether the previous dose of any drug has taken full effect before administering additional medications [4]. If the mechanisms of action of concomitant medications are similar, synergistic effects may be potentiated, and the risk of adverse events is magnified. Respiratory depression is a common pathway of adverse events and may result unexpectedly and quickly.

Practitioners must also be cognizant that drug interactions may occur. Drugs such as protease inhibitors, macrolide antibiotics, some azole antifungals, and cimetidine inhibit the cytochrome P450 system, and concomitant use of these medications can result in prolonged sedation with midazolam and other hypnotics that involve the same enzyme systems.

Challenges in Nuclear Medicine

As the availability and introduction of complex imaging studies continue to increase, anesthesiologists and sedation-care providers must maintain their understanding of associated principles, safety, and management concerns for the patients undergoing imaging studies [66]. The unique environment in nuclear medicine presents inherent challenges for providing sedation and the administration of general anesthesia.

Radiation Safety

Unlike other modalities in pediatric imaging, there is a need for enhanced safety around the use of radioactive materials in nuclear medicine. Sedation and anesthesia providers must observe basic radiation safety practices, in the same manner that the nuclear medicine nurses and technologists practice radiation safety. The sedation and anesthesia providers may be required to complete radiation safety training and may be even required to wear dosimeters while working in the area. Exposure to radioactive materials should be minimized. Biologic fluids must be considered as radioactive and must therefore be handled and disposed of appropriately. Spills should be handled in accordance with existing

protocols and reported to the nuclear medicine technologist who will then report the incident to designated radiation safety officers.

Duration and Timing of Procedures

The anticipated duration of the scan will impact on the medical decision on what pharmacologic agent to use (e.g., short-acting versus longer-acting sedative) and the preferred intervention (e.g., intubation versus use of oral airway for general anesthesia). It is therefore essential for all health professionals involved to discuss the expected duration of the imaging study as well as the anticipated recovery plans after sedation or anesthesia.

Unlike other pediatric imaging modalities, nuclear medicine studies require an uptake period following injection of the radioisotope. This uptake period can last from half an hour for brain studies to over an hour for whole-body scans. It may be helpful to contact the sedation or anesthesia provider prior to radioisotope injection, in order to confirm the availability of such services soon after the uptake period.

The degradation process of the isotopes also plays a role in the duration of the scan; as a general rule, the farther the time point of the injection of the isotope to the start of the scan, the longer the subsequent duration of the scan. It is therefore best to perform the scan as soon as the uptake of the isotope is completed (about half an hour for brain studies and an hour for whole-body PET scans). Again, sedation providers or anesthesiologists who are assigned concurrently to other units may need to be reminded in advance in order to ensure proper timing of the initiation of sedation or general anesthesia.

Combination Studies

Combination studies in nuclear medicine require even more careful planning. In centers with positron emission tomography–computerized tomography (PET–CT) scanners, combination studies can be performed without moving the patient. In centers that do not have PET–CT scanners, the patients will need to be transferred to a CT scanner after the PET scan. This may present problems of transporting patients who are intubated or who received short-acting sedating agents. In addition, the intake of oral contrast may be required for abdominal CT scans; in such cases, the patient will need to wake up, drink the oral contrast agent, and wait for at least an hour prior to being re-sedated. Other modalities such as MRI may also be required following nuclear medicine scans. There is a need to coordinate the availability of the subsequent scanners and the staff in order to minimize the duration of sedation and general anesthesia.

There may be requests for additional studies or procedures after a nuclear medicine imaging study. These include non-painful procedures such as blood draws through existing intravenous lines, dressing changes, or echocardiograms. Often, these do not create problems unless the schedule is so tight that no additional time in the scan room is permitted. In such cases, these procedures are best performed in the recovery area or postanesthesia care unit (PACU). Painful procedures such as spinal taps and fluid aspirations may also be requested. In such cases, the decision on whether these procedures can be performed, and if so, the timing, should be made with appropriate discussion prior to the nuclear medicine study. A consensus must also be reached on whether sedation or general anesthesia will be continued after the primary diagnostic scan.

Painful Procedures

Painful diagnostic procedures in nuclear medicine such as cerebral spinal fluid (CSF) flow studies and lymphangiograms may require the administration of analgesic agents to decrease pain and optimize the procedures and scans. Again, the choice of analgesics should depend on the duration of the procedure and the extent of analgesia required. In addition, some diagnostic procedures by themselves do not inflict pain, but due to the underlying condition (e.g., fractures in children who require bone scans), children may

experience severe discomfort or pain during these procedures. In such cases, discussion with the inpatient service may be necessary to ensure the comfort of these patients prior to arrival at the nuclear medicine suite.

Some children will require repeat visits for tests that may cause discomfort or pain, such as radionuclide cystograms. Sedatives that tend to provide amnestic effects, such as midazolam, will be especially helpful for these children.

Bladder Catheterization

Although extended fasting periods and certain medications (e.g., dexmedetomidine) can cause hypotension, the benefits of rehydration prior to and during sedation or anesthesia should be carefully weighed against the potential ramifications of the patient developing a full bladder. The presence of a full bladder may necessitate the need for bladder catheterization for several reasons [67]. First, a full bladder may obscure or cause reconstruction artifacts. The former may constitute a significant problem in oncologic cases where the pelvic area needs to be fully evaluated. Secondly, the urge to void may result in patient discomfort and potential spontaneous voiding with associated spillage of radioactive material. Although bladder catheterization will alleviate these risks, the procedure itself may require the administration of additional sedatives or analgesics. It is therefore essential to have a collaborative discussion prior to the scan, among the sedation provider, the nuclear medicine physician, and the technologist who will be performing the study, in order to create a contingency plan.

Summary

Sedation and general anesthesia are required for certain patients who are scheduled for nuclear medicine imaging. The creation of a credentialed anesthesia and sedation service will enhance the efficiency of the radiology/nuclear medicine department while promoting safe care of pediatric patients. The nuclear medicine setting is unique and poses inherent challenges. There is a need for ongoing discussions among the providers of sedation and anesthesia, the nuclear medicine nurses, technologists, and physicians.

Acknowledgments We wish to thank Joanne Louis, CNMT, for her technical review and Ms. Amanda Buckley for the editorial assistance and preparation of this chapter.

References

1. Mandell GA, Cooper JA, Majd M, Shalaby-Rana EI, Gordon I. Procedure guideline for pediatric sedation in nuclear medicine. Society of Nuclear Medicine. J Nucl Med. 1997;38(10):1640–3.
2. Treves ST, Baker A, Fahey FH, et al. Nuclear medicine in the first year of life. J Nucl Med. 2011;52(6):905–25.
3. Mason KP, Sanborn P, Zurakowski D, et al. Superiority of pentobarbital versus chloral hydrate for sedation in infants during imaging. Radiology. 2004;230(2):537–42.
4. Cote CJ, Wilson S. Guidelines for monitoring and management of pediatric patients during and after sedation for diagnostic and therapeutic procedures: an update. Pediatrics. 2006;118(6):2587–602.
5. Kaplan RF, Cravero JP, Yaster M, Cote C. Chap. 48. Sedation for diagnostic and therapeutic procedures outside the operating room. In: Cote CJ, Lerman J, Todres ID, editors. A practice of anesthesia for infants and children. Philadelphia: Saunders/Elsevier; 2009. p. 1023–48.
6. American Society of Anesthesiologists Task Force on Sedation and Analgesia. Practice guidelines for sedation and analgesia by non-anesthesiologists. Anesthesiology. 2002;96(4):1004–17.
7. Practice guidelines for sedation and analgesia by non-anesthesiologists. A report by the American Society of Anesthesiologists Task Force on Sedation and Analgesia by Non-Anesthesiologists. Anesthesiology. 1996;84(2):459–71.
8. Guidelines for the elective use of conscious sedation, deep sedation, and general anesthesia in pediatric patients. Committee on Drugs. Section on anesthesiology. Pediatrics. 1985;76(2):317–21.
9. American Academy of Pediatrics Committee on Drugs. Guidelines for monitoring and management of pediatric patients during and after sedation for diagnostic and therapeutic procedures. Pediatrics. 1992;89(6 Pt 1):1110–5.
10. Committee on Drugs. American Academy of Pediatrics. Guidelines for monitoring and management of pediatric patients during and after sedation for diagnostic and therapeutic procedures: addendum. Pediatrics. 2002;110(4):836–8.
11. Keeter S, Benator RM, Weinberg SM, Hartenberg MA. Sedation in pediatric CT: national survey of current practice. Radiology. 1990;175(3):745–52.

12. Joint Commission for Accreditation of Hospitals (JCAHO). Operative or other high-risk procedures and/or the administration of moderate or deep sedation or anesthesia. The Comprehensive accreditation manual for Hospitals: official handbook. Oakbrook Terrace: JCAHO; 2007. p. PC-41.
13. Department of Health & Human Services. Centers for Medicare & Medicaid Services. Revised hospital anesthesia services interpretive guidelines – state operations manual (SOM) Appendix A Ref: S&C-10-09-Hospital. Revised 2 May 2010. https://www.cms.gov/SurveyCertificationGenInfo/downloads/SCLetter10_09.pdf. Accessed 14 Feb 2011.
14. Department of Health & Human Services. Centers for Medicare & Medicaid Services. CMS Manual System. Pub. 100–07 State Operations Provider Certification. Transmittal 59. Clarification of the interpretive guidelines for the anesthesia services condition of participation. 21 May 2010. https://www.cms.gov/transmittals/downloads/R59SOMA.pdf. Accessed 20 Jan 2011.
15. McQuattie S. Pediatric PET/CT imaging: tips and techniques. J Nucl Med Technol. 2008;36(4):171–80.
16. Mallory MD, Baxter AL, Yanosky DJ, Cravero JP. Emergency physician-administered propofol sedation: a report on 25,433 sedations from the pediatric sedation research consortium. Ann Emerg Med. 2011;57(5):462–8.1.
17. Cravero JP, Beach ML, Blike GT, Gallagher SM, Hertzog JH. The incidence and nature of adverse events during pediatric sedation/anesthesia with propofol for procedures outside the operating room: a report from the Pediatric Sedation Research Consortium. Anesth Analg. 2009;108(3):795–804.
18. Srinivasan M, Turmelle M, Depalma LM, Mao J, Carlson DW. Procedural sedation for diagnostic imaging in children by pediatric hospitalists using propofol: analysis of the nature, frequency, and predictors of adverse events and interventions. J Pediatr. 2012;160(5):801–6.e1.
19. Mason KP, Fontaine PJ, Robinson F, Zgleszewski S. Pediatric sedation in a community hospital-based outpatient MRI center. AJR Am J Roentgenol. 2012;198(2):448–52.
20. Vespasiano M, Finkelstein M, Kurachek S. Propofol sedation: intensivists' experience with 7304 cases in a children's hospital. Pediatrics. 2007;120(6):e1411–7.
21. American Society of Anesthesiologists. Statement on Nonoperating Room Anesthetizing Locations. http://www.asahq.org/For-Members/~/media/For%20Members/documents/Standards%20Guidelines%20Stmts/Nonoperating%20Room%20Anesthetizing%20Locations.ashx. Accessed 12 March 2013
22. Sanborn PA, Michna E, Zurakowski D, et al. Adverse cardiovascular and respiratory events during sedation of pediatric patients for imaging examinations. Radiology. 2005;237(1):288–94.
23. Maxwell LG, Tobias JD, Cravero JP, Malviya S. Adverse effects of sedatives in children. Expert Opin Drug Saf. 2003;2(2):167–94.
24. Metzner J, Posner KL, Domino KB. The risk and safety of anesthesia at remote locations: the US closed claims analysis. Curr Opin Anaesthesiol. 2009;22(4):502–8.
25. Bhananker SM, Posner KL, Cheney FW, Caplan RA, Lee LA, Domino KB. Injury and liability associated with monitored anesthesia care: a closed claims analysis. Anesthesiology. 2006;104(2):228–34.
26. Prescilla R. Pharmacology and clinical applications of sedatives, analgesics, and adjuncts. In: Mason K, Koka B, editors. Pediatric sedation outside the operating room: a multispecialty collaboration. New York: Springer; 2011. p. 93–122.
27. American Academy of Pediatrics Committee on Drugs and Committee on Environmental Health: use of chloral hydrate for sedation in children. Pediatrics. 1993;92(3):471–3.
28. Ferrer-Brechner T, Winter J. Anesthetic considerations for cerebral computer tomography. Anesth Analg. 1977;56(3):344–7.
29. Greenberg SB, Faerber EN, Aspinall CL, Adams RC. High-dose chloral hydrate sedation for children undergoing MR imaging: safety and efficacy in relation to age. AJR Am J Roentgenol. 1993;161(3):639–41.
30. Greenberg SB, Faerber EN, Aspinall CL. High dose chloral hydrate sedation for children undergoing CT. J Comput Assist Tomogr. 1991;15(3):467–9.
31. Napoli KL, Ingall CG, Martin GR. Safety and efficacy of chloral hydrate sedation in children undergoing echocardiography. J Pediatr. 1996;129(2):287–91.
32. Thompson JR, Schneider S, Ashwal S, Holden BS, Hinshaw Jr DB, Hasso AN. The choice of sedation for computed tomography in children: a prospective evaluation. Radiology. 1982;143(2):475–9.
33. Ronchera-Oms CL, Casillas C, Marti-Bonmati L, et al. Oral chloral hydrate provides effective and safe sedation in paediatric magnetic resonance imaging. J Clin Pharm Ther. 1994;19(4):239–43.
34. Chung T, Hoffer FA, Connor L, Zurakowski D, Burrows PE. The use of oral pentobarbital sodium (Nembutal) versus oral chloral hydrate in infants undergoing CT and MR imaging–a pilot study. Pediatr Radiol. 2000;30(5):332–5.
35. Mason KP, Zurakowski D, Connor L, et al. Infant sedation for MR imaging and CT: oral versus intravenous pentobarbital. Radiology. 2004;233(3):723–8.
36. Macias CG, Chumpitazi CE. Sedation and anesthesia for CT: emerging issues for providing high-quality care. Pediatr Radiol. 2011;41 Suppl 2:517–22.
37. Evers AS, Crowder CM, Balser JR. General anesthetics. In: Brunton LL, Laso JS, Parker KL, editors. Goodman and Gilman's the pharmacological basis of therapeutics. 11th ed. New York: McGraw-Hill; 2006.
38. Hall JE, Uhrich TD, Barney JA, Arain SR, Ebert TJ. Sedative, amnestic, and analgesic properties of small-dose dexmedetomidine infusions. Anesth Analg. 2000;90(3):699–705.
39. Talke P, Lobo E, Brown R. Systemically administered alpha2-agonist-induced peripheral vasoconstriction in humans. Anesthesiology. 2003;99(1):65–70.
40. Talke P, Richardson CA, Scheinin M, Fisher DM. Postoperative pharmacokinetics and sympatholytic

effects of dexmedetomidine. Anesth Analg. 1997;85(5):1136–42.
41. Bamgbade OA. Dexmedetomidine for peri-operative sedation and analgesia in alcohol addiction. Anaesthesia. 2006;61(3):299–300.
42. Jackson 3rd KC, Wohlt P, Fine PG. Dexmedetomidine: a novel analgesic with palliative medicine potential. J Pain Palliat Care Pharmacother. 2006;20(2):23–7.
43. Rich JM. Dexmedetomidine as a sole sedating agent with local anesthesia in a high-risk patient for axillofemoral bypass graft: a case report. AANA J. 2005;73(5):357–60.
44. Berkenbosch JW, Tobias JD. Development of bradycardia during sedation with dexmedetomidine in an infant concurrently receiving digoxin. Pediatr Crit Care Med. 2003;4(2):203–5.
45. Precedex (dexmedetomidine hydrochloride) Hospira, Inc. Lake Forest, IL 60045 USA. http://www.precedex.com/wp-content/uploads/Precedex_PI.pdf. Accessed 12 March 2013.
46. Belleville JP, Ward DS, Bloor BC, Maze M. Effects of intravenous dexmedetomidine in humans. I. Sedation, ventilation, and metabolic rate. Anesthesiology. 1992;77(6):1125–33.
47. Ingersoll-Weng E, Manecke Jr GR, Thistlethwaite PA. Dexmedetomidine and cardiac arrest. Anesthesiology. 2004;100(3):738–9.
48. Scheinin H, Aantaa R, Anttila M, Hakola P, Helminen A, Karhuvaara S. Reversal of the sedative and sympatholytic effects of dexmedetomidine with a specific alpha2-adrenoceptor antagonist atipamezole: a pharmacodynamic and kinetic study in healthy volunteers. Anesthesiology. 1998;89(3):574–84.
49. Venn RM, Bradshaw CJ, Spencer R, et al. Preliminary UK experience of dexmedetomidine, a novel agent for postoperative sedation in the intensive care unit. Anaesthesia. 1999;54(12):1136–42.
50. Mason KP, Robinson F, Fontaine PJ, Prescilla R. Dexmedetomidine offers an option for safe and effective sedation for nuclear medicine imaging in children. Radiology. 2013;267(3):911–7.
51. Way WL, Trevor AJ. Pharmacology of intravenous nonnarcotic anesthetics. In: Anesthesia. 2nd ed. New York: Churchill Livingstone; 1986. p. 813–7.
52. Drummond GB. Comparison of sedation with midazolam and ketamine: effects on airway muscle activity. Br J Anaesth. 1996;76(5):663–7.
53. Fine J, Finestone SC. Sensory disturbances following ketamine anesthesia: recurrent hallucinations. Anesth Analg. 1973;52(3):428–30.
54. Meyers EF, Charles P. Prolonged adverse reactions to ketamine in children. Anesthesiology. 1978;49(1):39–40.
55. Roelofse JA, Joubert JJ, Roelofse PG. A double-blind randomized comparison of midazolam alone and midazolam combined with ketamine for sedation of pediatric dental patients. J Oral Maxillofac Surg. 1996;54(7):838–44; discussion 845–6.
56. Sherwin TS, Green SM, Khan A, Chapman DS, Dannenberg B. Does adjunctive midazolam reduce recovery agitation after ketamine sedation for pediatric procedures? A randomized, double-blind, placebo-controlled trial. Ann Emerg Med. 2000;35(3):229–38.
57. Green SM, Johnson NE. Ketamine sedation for pediatric procedures: part 2, review and implications. Ann Emerg Med. 1990;19(9):1033–46.
58. Hollister GR, Burn JM. Side effects of ketamine in pediatric anesthesia. Anesth Analg. 1974;53(2):264–7.
59. Wathen JE, Roback MG, Mackenzie T, Bothner JP. Does midazolam alter the clinical effects of intravenous ketamine sedation in children? A double-blind, randomized, controlled, emergency department trial. Ann Emerg Med. 2000;36(6):579–88.
60. Sussman DR. A comparative evaluation of ketamine anesthesia in children and adults. Anesthesiology. 1974;40(5):459–64.
61. Frankville DD, Spear RM, Dyck JB. The dose of propofol required to prevent children from moving during magnetic resonance imaging. Anesthesiology. 1993;79(5):953–8.
62. Evans RG, Crawford MW, Noseworthy MD, Yoo SJ. Effect of increasing depth of propofol anesthesia on upper airway configuration in children. Anesthesiology. 2003;99(3):596–602.
63. Reber A, Wetzel SG, Schnabel K, Bongartz G, Frei FJ. Effect of combined mouth closure and chin lift on upper airway dimensions during routine magnetic resonance imaging in pediatric patients sedated with propofol. Anesthesiology. 1999;90(6):1617–23.
64. Pambianco DJ, Vargo JJ, Pruitt RE, Hardi R, Martin JF. Computer-assisted personalized sedation for upper endoscopy and colonoscopy: a comparative, multicenter randomized study. Gastrointest Endosc. 2011;73(4):765–72.
65. Rex DK, Deenadayalu VP, Eid E, et al. Endoscopist-directed administration of propofol: a worldwide safety experience. Gastroenterology. 2009;137(4):1229–37; quiz 1518–29.
66. Veenith T, Coles JP. Anaesthesia for magnetic resonance imaging and positron emission tomography. Curr Opin Anaesthesiol. 2011;24(4):451–8.
67. Roberts EG, Shulkin BL. Technical issues in performing PET studies in pediatric patients. J Nucl Med Technol. 2004;32(1):5–9; quiz 10–11.

PET and PET/CT in Children and Young Adults

3

Frederick D. Grant

The introduction of PET, and especially ^{18}F-FDG PET, has transformed pediatric nuclear medicine. In particular, hybrid imaging with ^{18}F-FDG PET/CT has transformed pediatric nuclear oncology [1–4]. However, PET and PET/CT have a wide variety of pediatric indications [1] including neurology [5, 6], sports medicine and orthopedics [7], pediatric cardiology [8], and infection imaging [9], as well as pediatric oncology. Most PET and PET/CT studies utilize the glucose analogue, ^{18}F-fluorodeoxyglucose (^{18}F-FDG) (Figs. 3.1 and 3.2). Few other PET radiopharmaceuticals have been approved for routine clinical use, and few of those have extensive pediatric experience [6, 10]. One with some pediatric experience is the bone imaging agent [^{18}F] sodium fluoride, which can be used for skeletal imaging of both benign and malignant conditions (Fig. 3.3) [7].

F.D. Grant, MD
Joint Program in Nuclear Medicine,
Department of Radiology, Harvard Medical School,
Boston, MA, USA

Division of Nuclear Medicine and Molecular Imaging,
Department of Radiology,
Boston Children's Hospital, Boston, MA, USA

Department of Radiology,
Brigham and Women's Hospital, Boston, MA, USA
e-mail: frederick.grant@childrens.harvard.edu

Radiopharmaceuticals

[^{18}F] Sodium Fluoride

Fluorine-18 (physical half-life 110 min) is a positron emitter and is the predominant radiolabel for PET radiopharmaceuticals in routine clinical use. It is a cyclotron product typically produced by the nuclear reaction ^{18}O (p,n) ^{18}F and isolated as an aqueous solution of [^{18}F] sodium fluoride. Fluorine-18 may be the ideal PET tracer for medical imaging due to its high specific activity, efficient labeling of a wide variety of PET radiopharmaceuticals, and nearly 2-h half-life. The emitted positron has the lowest kinetic energy (630 keV) of any common PET radionuclide. This limits the positron range before annihilation and may contribute to improved spatial resolution with ^{18}F compared to other PET radionuclides [11].

Fluorine-18 sodium fluoride also may be used as a radiopharmaceutical for skeletal imaging [7]. When used as a bone imaging agent, no further chemical processing is required. The North American consensus guidelines [12] recommend a pediatric dose of 2.22 MBq/kg (0.06 mCi/kg) with a minimum dose of 18.5 mBq (0.5 mCi). After intravenous administration, there is rapid bone uptake of [^{18}F] fluoride as it exchanges with hydroxyl ions on the surface of the hydroxyapatite matrix of bone [13]. Fluorine-18 fluoride is rapidly cleared from plasma, so that within 1 h

S.T. Treves (ed.), *Pediatric Nuclear Medicine and Molecular Imaging*,
DOI 10.1007/978-1-4614-9551-2_3,

Fig. 3.1 Whole-body ^{18}F-FDG PET in a 14-year-old female. A MIP of a whole-body ^{18}F-FDG PET demonstrates a typical pattern of normal physiological uptake of ^{18}F-FDG. Physiological uptake of ^{18}F-FDG is most intense in the brain. Other sites of normal physiological uptake include the liver, tonsils, and gastrointestinal system. Variable uptake can be seen in muscles, including myocardium, skeletal muscle, and small muscles in the larynx and orbits. Due to renal excretion, tracer accumulation usually is seen in the renal collecting system, ureters, and bladder. Physiological uptake in the thymus is more common in pediatric patients than adults

of administration, only about 10 % of the dose remains in the circulation [14].

^{18}F-Fluoro-2-Deoxyglucose

Fluorine-18-fluoro-2-deoxyglucose (^{18}F-FDG) is a glucose analogue labeled with ^{18}F. Fluorine-18-FDG is taken into cells through one of the transmembrane glucose transporters, but does not enter the energy producing metabolic pathways [15]. Insulin-mediated stimulation of expression of some glucose transporters (GLUT-4) will increase cellular uptake of ^{18}F-FDG in insulin-sensitive tissues such as skeletal muscle, liver, and myocardium [16]. Fluorine-18-FDG is phosphorylated by cellular hexokinases, but after monophosphorylation, FDG-6 phosphate cannot be further phosphorylated and is trapped in the cell [17], which provides a mechanism for amplification of the ^{18}F signal. Only a few tissues, such as liver, express sufficient phosphorylase activity to dephosphorylate large amounts FDG-6 phosphate, which permits secretion out of the cell. The North American consensus guidelines [12] recommend a pediatric dose of 3.7–5.2 MBq/kg (0.10–0.14 mCi/kg) for torso/whole-body imaging and 3.7 mBq/kg (0.10 mCi/kg) for brain imaging, with a minimum dose of 37 MBq (1.0 mCi) for all studies.

Other PET Radiopharmaceuticals

Other ^{18}F-labeled PET agents, including ^{18}F-fluoro-L-thymidine, ^{18}F-deoxy-phenylalanine (^{18}F-DOPA), and ^{18}F-dopamine, remain investigational, but may acquire a role for imaging specific oncological or other indications [18]. Other PET radiopharmaceuticals [19], including those labeled with ^{11}C or ^{15}N, have limited pediatric experience, in part due to their short half-lives and the need for ready access to a cyclotron. PET radiopharmaceuticals labeled with ^{68}Ga may have a role in identification and localization of neuroendocrine tumors (see Chap. 20). PET with ^{124}I has been used to image thyroid cancer in adults, but has not been used routinely in children or young adults (see Chap. 5).

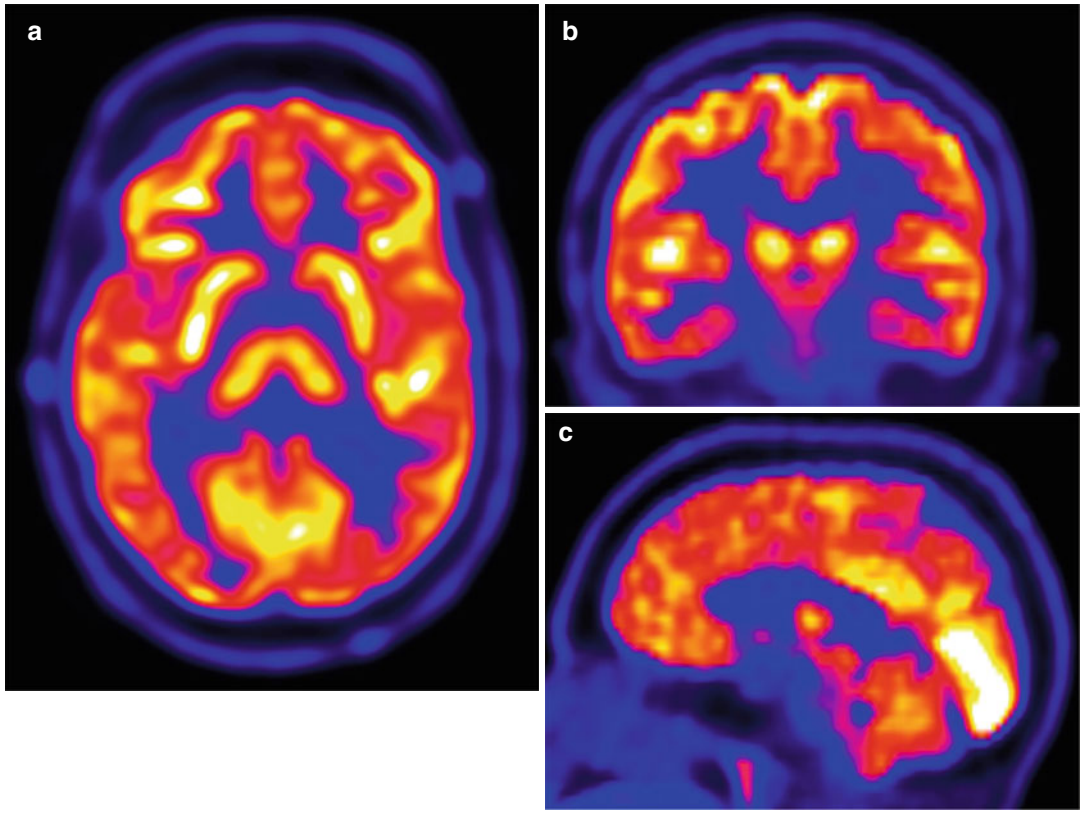

Fig. 3.2 Brain ^{18}F-FDG PET in a 16-year-old male. A brain ^{18}F-FDG PET displayed in axial (**a**), coronal (**b**), and sagittal (**c**) planes demonstrates the normal pattern of ^{18}F-FDG uptake in the brain. Within the cerebral cortex, physiological uptake of ^{18}F-FDG is greater in the gray matter than in the white matter. Uptake in the cerebellum typically is less than in the cerebral cortex. Intense uptake of ^{18}F-FDG also is seen in the striatum. Increased uptake in the visual cortex reflects visual activity during the uptake period

Patient Preparation for ^{18}F-FDG PET and ^{18}F-FDG PET/CT

Patient preparation is important for successful completion of a technically adequate and diagnostically satisfactory PET or PET/CT [20, 21]. Patient and family preparation is of particular importance for ^{18}F-FDG studies [22], but may be less important with PET of the skeleton with [^{18}F] sodium fluoride [23]. Although much information can be provided in a mailing or on a departmental website, individual telephone contact made by a knowledgeable healthcare professional, such as a registered nurse or nuclear medicine technologist, provides an opportunity for individualized education and encouragement. One-to-one contact provides a way for the healthcare professional to answer questions, dispel misunderstandings, identify potential problems that may affect the study, and assess the developmental needs of the patient. For nearly all pediatric patients, family contact with a healthcare professional prior to the study increases the likelihood of a technically adequate and diagnostically successful study.

Pre-study fasting is important before ^{18}F-FDG PET or ^{18}F-FDG PET/CT of the body for an oncological indication [20] or for imaging infection or inflammation [24]. Pre-study fasting may be less important for brain imaging, but most guidelines recommend that it be done [21]. Although rarely performed in children, ^{18}F-FDG PET for myocardial imaging requires enhancement of ^{18}F-FDG uptake in the myocardium [22]. Caloric intake

Fig. 3.3 Fluorine-18-sodium fluoride PET bone scan in a 14-year-old female. A MIP of an ^{18}F-sodium fluoride PET bone scan demonstrates that ^{18}F-sodium fluoride uptake reflects bone turnover in a pattern similar to ^{99m}Tc-labeled diphosphonates, but image quality can be higher with PET acquisition. In pediatric patients, physeal uptake indicates skeletal immaturity

will stimulate insulin secretion, which can increase uptake of ^{18}F-FDG in skeletal and myocardial muscle. For most ^{18}F-FDG PET studies, patients should be fasting for at least 4 h before administration of ^{18}F-FDG and must remain fasting during the 1-h uptake period after tracer administration. This restriction includes caloric intake by nasogastric tube or percutaneous feeding tube. Patients with delayed gastric emptying may need to fast for longer periods to ensure a technically adequate study. Unless the study will be performed with sedation or general anesthesia, patients can continue to drink water before the study. However, they must be instructed to avoid sweetened or caffeine-containing beverages [20, 21]. Even non-nutritive sweeteners may have a mild stimulatory effect on insulin secretion [25]. In patients receiving parenteral nutrition or hydration, all intravenous glucose sources must be discontinued for at least 4 h before ^{18}F-FDG administration. If intravenous hydration must be continued, this can be done with saline-containing solutions, but it is important to confirm that all glucose-containing solutions, including solutions such as D5 Ringer's lactate, have been discontinued.

In infants and young children, adequate fasting can be a challenge and may require coordination of the imaging schedule with the child's eating and sleeping routine. Infants may be breastfed or given a bottle just before the start of the scan. However, this approach is rarely used, as patients usually must have nothing by mouth before undergoing sedation or general anesthesia, which is commonly used in this age group. In older children, allowing a small snack after the uptake period and just before the start of imaging may improve patient cooperation and permit successful completion of a scan. Special attention should be given patients at increased risk of hypoglycemia during prolonged fasting, including infants. Caloric intake still must be restricted before tracer administration and during the ^{18}F-FDG uptake period, but caloric intake after the 1-h uptake period may have little effect on ^{18}F-FDG PET quality. If hypoglycemia is a clinical concern, then a dextrose-containing intravenous solution to maintain adequate blood glucose levels can be started after the 1-h ^{18}F-FDG uptake period.

Elevated blood glucose levels can compete with ^{18}F-FDG for cellular uptake and diminish ^{18}F-FDG uptake in tissues of interest. This effect may be greater when the FDG PET is performed for oncological indications and less when performed to evaluate infection or inflammation [24]. Before ^{18}F-FDG is administered, blood glucose should be checked, typically using a glucometer to test a finger-stick sample of capillary blood. Most guidelines recommend delaying an ^{18}F-FDG PET study if the blood glucose level is greater than 200 mg/dl [20, 21].

Patients with diabetes mellitus can provide special challenges when planning an ^{18}F-FDG PET study. Excess insulin administration may produce hypoglycemia as well as lead to increased nonspecific muscle uptake of ^{18}F-FDG. With inadequate therapy, the resulting hyperglycemia can competitively inhibit tissue uptake of ^{18}F-FDG. Both of these effects can degrade the quality and decrease the diagnostic accuracy of an ^{18}F-FDG PET study. The patient's endocrinologist or primary care physician should be involved in any decision to alter the patient's medical or nutritional regimen. However, if these clinicians are not familiar with the techniques of ^{18}F-FDG PET, they may depend on the nuclear medicine physician to help develop an appropriate plan.

The management approach will depend on whether the patient has type 1 (insulin-dependent) or type 2 (insulin-resistant) diabetes. For most patients with diabetes, scheduling an ^{18}F-FDG PET for early morning will facilitate satisfactory management of blood glucose levels. Patients with type 1 diabetes must continue to receive sufficient insulin to maintain appropriate basal blood insulin levels while fasting. This can be accomplished with either subcutaneous injection of a long-acting insulin (typically at bedtime) or subcutaneous infusion of insulin at a basal rate from an insulin pump. Patients should not take additional pre-meal or sliding scale insulin before the ^{18}F-FDG PET study, as this may result in fasting hypoglycemia and can increase nonspecific muscle uptake of ^{18}F-FDG. Patients demonstrating fasting hyperglycemia may require adjustment of basal insulin doses.

Although type 2 diabetes is more common in adults than in children, increasing numbers of children are developing this disease. Patients with type 2 diabetes have insulin resistance, which can be managed by diet, oral medications, or insulin. With an overnight fast, many of these patients will not develop significant hyperglycemia if they delay taking morning diabetes medications or insulin until midmorning, after completion of an early morning ^{18}F-FDG PET or PET/CT. Treatment with the diabetic drug metformin can been associated with intense ^{18}F-FDG uptake in the colon, and sometimes in the small intestine [26]. Metformin also increases ^{18}F-FDG uptake in skeletal muscle and liver [27]. Although it is used rarely in children, metformin should be discontinued, if possible, two to three days before the ^{18}F-FDG PET study [28]. Some patients will arrive to their scheduled appointment with marked hyperglycemia due to either poorly controlled diabetes or unrecognized nocturnal hyperglycemia. Occasionally, a patient may develop marked hyperglycemia after initiation of glucocorticoid therapy. Ideally, ^{18}F-FDG PET or PET/CT can be postponed while awaiting improved glycemic control, but this may not be possible in all clinical situations.

Depending on the season and climate, brown adipose tissue may be seen in as many as a third of all children having an ^{18}F-FDG PET or PET/CT study (Fig. 3.4). A variety of maneuvers have been used to minimize ^{18}F-FDG uptake in brown adipose tissue. Heating in a warm room for at least 30 min before ^{18}F-FDG administration and for the duration of the uptake period can decrease the incidence of significant uptake in brown adipose tissue from 33 to 9 % [29]. Other interventions have been used in an attempt to decrease ^{18}F-FDG uptake in brown adipose tissue, including oral administration of a low dose of a beta-blocker such as propanolol [30] or a low dose of a benzodiazepine such as diazepam [31], intravenous administration of fentanyl [32], or dietary restriction to a high-fat diet [33] for at least 12 h before the study. Compared to these medical and dietary interventions, pre-study warming avoids the need to assess potential drug interactions or side effects and does not require patient compliance with a special diet. In some institutions, administration of diazepam or fentanyl may be considered sedation and thus require the documentation and consultation needed before any sedation procedure. Regardless of the method used to decrease uptake in brown adipose tissue, it is helpful to instruct patients to avoid cold exposure and to dress warmly while travelling from home for the ^{18}F-FDG PET or PET/CT study.

Intense muscle use prior to ^{18}F-FDG PET will increase uptake of ^{18}F-FDG in the involved muscles (Fig. 3.5). Depending on the indication for the ^{18}F-FDG PET/CT, this may decrease the sensitivity of the study. Therefore, patients should be advised to refrain from heavy physical exertion

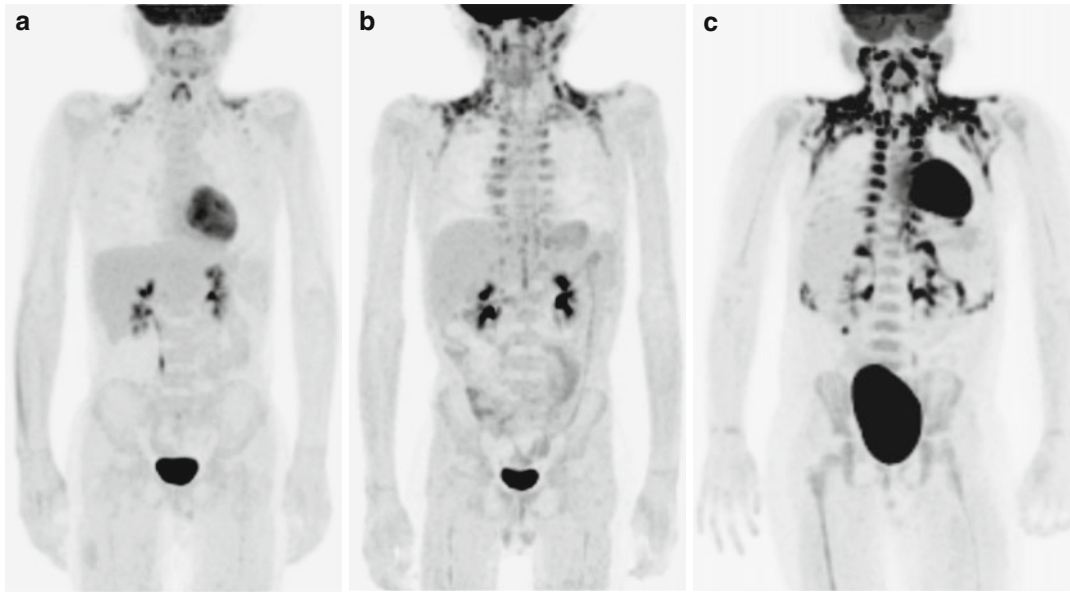

Fig. 3.4 Fluorine-18-FDG uptake in brown adipose tissue. Increased ^{18}F-FDG uptake in brown adipose tissue can be a common finding on ^{18}F-FDG PET of the body. Many pediatric patients may demonstrate a mild degree of brown adipose uptake (**a**), but some may have moderate (**b**) or marked (**c**) uptake. Extensive uptake in brown adipose tissue can obscure sites of pathological ^{18}F-FDG uptake and decrease confidence in study interpretation. A variety of strategies have been used to decrease brown adipose uptake. Note variable myocardial uptake of ^{18}F-FDG, despite similar pretest preparation in all three patients

for at least 24 h before the ^{18}F-FDG PET or PET/CT. Similarly, exercise, repetitive muscle activity, maintaining a static posture, talking, or chewing should be avoiding during the uptake period. In young children, increased uptake may be seen in the muscles of respiration after prolonged crying during the uptake period [34].

Patients should be provided with a quiet environment in which to stay during the uptake period. Although patients may be tempted to use electronic devices, including cell phones, electronic games, or laptop computers, the repetitive hand motion required to operate these devices may result in increased muscle uptake of ^{18}F-FDG. Quiet reading or movie watching usually is not a problem prior to imaging the torso, but patients still need to be encouraged to avoid staying in a single posture requiring prolonged static contraction of neck or back muscles, as this also can result in increased ^{18}F-FDG uptake in affected muscles (Fig. 3.5). In preparation for ^{18}F-FDG PET of the brain [21], the patient should stay in a quiet, dimly lit room for a half an hour before tracer administration and during the uptake period to limit visual stimulation (Fig. 3.2). Ideally, the patients should have limited interaction with others and not talk, speak, or read, but this may not be feasible with every pediatric patient. Depending on the indication for the study, some interaction with caregivers or quiet reading may be allowed or even necessary to gain patient cooperation. Prior to all studies, emotional stimulation should be limited. The indications for ^{18}F-FDG PET and the region of interest will guide the appropriate environment during the uptake period. However, dealing successfully with young children and teenagers requires flexibility to achieve a balance between acquiring an ideal imaging study and provoking an adverse behavioral response to an environment that is sterile or unappealing.

PET Acquisition

The acquisition procedures for pediatric PET and PET/CT depend on the radiopharmaceutical, camera geometry, the clinical indication, and the ana-

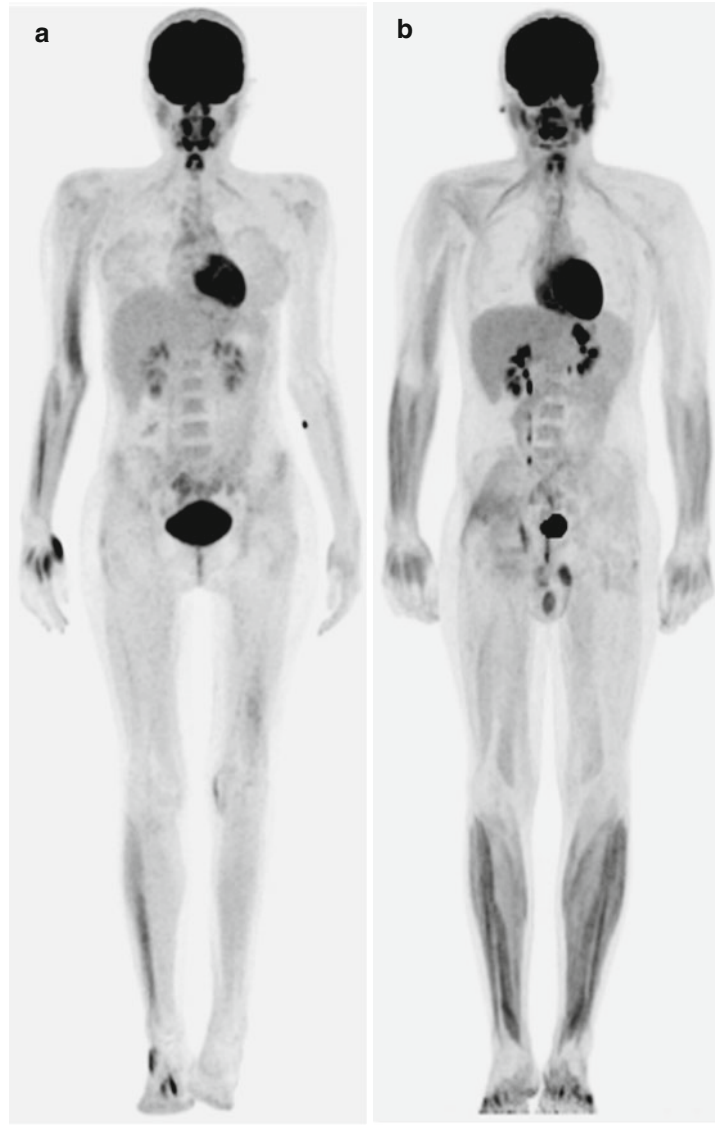

Fig. 3.5 Fluorine-18-FDG uptake in skeletal muscle. Non-pathological muscle uptake can occur with muscle use or exertion before or during the uptake period. (**a**) In a 14-year-old patient with treated synovial cell sarcoma of the left upper leg, increased muscle uptake in the right leg reflects a change in gait and altered weight-bearing. In muscles of the right arm and hand, increased uptake could be related to weight-bearing on a cane, but also reflect use of an electronic entertainment device during the uptake period. (**b**) In a 17-year-old male athlete, diffusely increased uptake throughout the skeletal muscles, but most intense in the lower legs and forearms, was attributed to extreme physical exertion 1 day before the ^{18}F-FDG PET was performed. The patient denied dietary indiscretion, but a similar pattern of uptake can be seen if ^{18}F-FDG PET is performed in a non-fasting patient

tomic region to be imaged. Imaging protocols must be optimized for the equipment available in each department. For example, if a camera detector has septa, images can be acquired in "2-D" mode, while if the septa are retracted or not available on a camera model, then imaging is performed in "3-D" mode [21]. Other camera features, such as time-of-flight circuitry, also can influence acquisition parameters. FDG PET image acquisition in 2-D may require 4–6 min per bed position, while 3-D mode may require 1.5–3 min per bed position. The number of bed positions required to complete a study will depend on the size of the child and camera. Brain imaging typically takes no more than two bed positions, and in small children may require only one bed position.

The uptake period, the time between radiopharmaceutical administration and the start of imaging, depends on the radiopharmaceutical and the clinical indication. Fluorine-18-FDG PET of the torso (base of skull to thighs) or whole body (top of skull to feet) typically is started after a 60-min uptake period. If standard uptake values (SUVs) are to be compared from one study to the

next, then it is critical that the uptake period be very consistent (less than 5 min of variation) from one study to the next [34]. Some authors have advocated a longer uptake period or acquiring a second delayed ^{18}F-FDG PET to better characterize tumors [35], but this has not become routine practice. Other technical factors that may affect the standard uptake value include improper calibration of the dose calibrator and PET camera, subcutaneous infiltration during intravenous administration of tracer, and inappropriate image reconstruction parameters [34].

Fluorine-18-FDG PET of the brain usually is started after a 30-min uptake period [21]. For the occasional patient that needs both brain and body imaging, two approaches are possible. One approach is to start the brain PET after a 30-min uptake. Then, with only a small delay, acquisition of the torso scan can be started 60 min after ^{18}F-FDG administration. However, this approach limits the time a patient may be kept in a heated room as a method to decrease uptake of ^{18}F-FDG in brown adipose tissue. An alternative approach is to acquire the torso or whole-body scan starting at 60 min and then to acquire the brain PET. Imaging for ^{18}F-NaF bone PET begins typically 30–45 min after tracer administration for whole-body or torso imaging, but some departments may wait 90–120 min before acquiring images of the extremities [23].

Special Issues

Some management issues must be considered for all pediatric PET and PET/CT studies. Sedation or anesthesia may be needed in younger patients or patients with intellectual disabilities that may limit adequate cooperation. The preferred approaches and policies for sedation or general anesthesia vary among institutions (see Chap. 2). For other patients, distraction techniques may be sufficient to accomplish a successful study [22]. If sedation or anesthesia will be needed for brain ^{18}F-FDG PET, it should be administered as late as possible after ^{18}F-FDG administration and before imaging [21]. The requirements for sedation or anesthesia may mandate a longer period of fasting than needed for the ^{18}F-FDG PET or PET/CT alone.

The approach to bladder catheterization also varies among institutions. Placement of a bladder catheter will decrease accumulation of excreted tracer in the bladder, which can improve visualization of pelvic pathology on torso or whole-body studies. This is less important in a study limited to the brain. A bladder catheter also prevents the contamination of the scanner bed and patient that can occur if a young patient inadvertently voids during the study. However, if the patient can void before the start of imaging and if torso imaging is performed from the pelvis to head, then only small amount of tracer should be in the bladder when the pelvis is imaged. Placement of a bladder catheter will be unpleasant for the patient and may make an otherwise cooperative child become uncooperative. Some facilities perform bladder catheterization after induction of sedation or anesthesia [22, 36]. However, in patients undergoing conscious sedation, catheterization may arouse the patient and necessitate using deeper sedation than originally planned. In our facility, we routinely do not use bladder catheterization and use it only for patients with known voiding disorders. Rarely, catheterization will be used if a sedated patient is discovered to have a large, filled bladder after imaging has started.

Although pregnancy is not an issue for most pediatric patients, the possibility must be considered in postpubertal girls and young women. Most institutions have standard policies guiding the determination of pregnancy status. At a minimum, postpubertal females should be asked if they might be pregnant. Any patient expressing concern about pregnancy should be able to have a pregnancy test before proceeding with a PET or PET/CT scan. Depending on institutional policies and local statutes and regulations, this may raise issues about patient confidentiality, parental or partner involvement, and the risks and benefits of the scheduled study, which may necessitate involvement of the ordering clinician or primary care provider. Similarly, if a pediatric patient's mother or other family caregiver is pregnant, then special arrangements may be needed for other family members to accompany the patient during the PET or PET/CT study [37].

Image Co-registration

Co-registration with anatomic imaging studies (CT, MR) or with prior PET studies can improve diagnostic accuracy. Nearly all commercially available PET scanners are integrated devices that include both PET and CT capabilities. Thus, PET/CT fusion images can be obtained with a minimum of image manipulation. However, fusion software can be used for co-registration of PET images with a separately acquired CT or MR studies or with a prior PET study. This can be particularly useful with a patient who has had a recent diagnostic CT that was not acquired as a PET/CT. Software co-registration also is becoming more important for planning radiation therapy [38]. For brain PET, such as for evaluation of a seizure disorder or brain tumor, correlative MR studies almost always are available and can be used to create PET/MR fusion images [6]. Elsewhere in the body, PET/MR software co-registration can be helpful for evaluating musculoskeletal tumors or intra-abdominal tumors that may be conspicuous on MR rather than CT. With increased concern about radiation dose, MR is being used more for follow-up and surveillance of pediatric oncology patients. Due to the lower radiation dose, recently introduced hybrid PET/MR scanners may be well suited to pediatric applications [39], but until these reach wider availability (see Chaps. 26 and 27), software co-registration of PET and MR can be used to improve diagnostic certainty while decreasing radiation dose.

PET/CT

The availability of integrated PET/CT scanners provides the possibility that an ^{18}F-FDG PET/CT and diagnostic CT can be acquired as part of the same study and that the diagnostic CT can be used for attenuation correction the ^{18}F-FDG PET. However, implementing this approach in a pediatric department requires careful planning and imaging protocols that can be customized to the medical and developmental needs of each patient. Development of all protocols should be guided by the principle of ALARA [40]. For example, the need for a diagnostic CT may be influenced by other available imaging, such as a recently acquired diagnostic CT or MR.

Depending on the energy settings, the CT acquired as part of a PET/CT study can serve as a stand-alone diagnostic study (with or without intravenous contrast, as indicated), as a "nondiagnostic" study for anatomic correlation, or for attenuation correction only [20]. If appropriately acquired, any of these studies can be used for attenuation correction of the PET, although metallic implants such as pacemakers or prosthetics may create an attenuation artifact.

CT energy settings should be determined based on patient size. An attenuation-only CT can be acquired with an energy of only 16–30 mA, depending on patient size [41]. Any CT scan that is to be used for attenuation correction of an ^{18}F-FDG PET should be acquired with the same patient positioning and with the same breathing pattern as the PET [20]. Thus, a chest CT should be acquired during tidal breathing or with a mid-breath breathhold. Otherwise, misregistration of the attenuation map and ^{18}F-FDG PET may create attenuation artifacts that can decrease the diagnostic accuracy of the PET. However, a chest CT acquired without a full inspiration may have decreased diagnostic accuracy compared to a standard chest CT. Therefore, it may be necessary to acquire multiple chest CT scans, for example, a diagnostic chest CT acquired with a full inspiration and a low-dose attenuation correction CT scan acquired with a mid-breath breathhold. How these scans link to other CT scans of the body will depend on the clinical indication, the need for diagnostic CT imaging of other body regions, and the availability of recent prior imaging. For example, in our institution, we have found that in most patients with lymphoma, it is helpful to perform a diagnostic CT of the "extended neck" that includes the region from the base of the skull to the aorta and is acquired with the arms down and without full lung inspiration. This improves the diagnostic accuracy of both PET and CT, by providing a high-quality diagnostic scan and by facilitating high-fidelity co-registration in a region of the body most likely to have pathological findings.

The appropriate use of intravenous and oral contrast for PET/CT in pediatric patients

remains unclear [20, 34]. The use of either contrast agent implies the acquisition of a diagnostic quality CT scan. However, if a high-quality CT scan is not indicated, then performing one will result in a higher radiation dose than necessary (see Chap. 30). On the other hand, if a diagnostic CT can be acquired as part of the PET/CT study, then this may avoid another separate diagnostic CT and lessen the overall radiation dose to the patient. Some authors have suggested that the use of barium-containing oral contrast may risk attenuation artifacts that can result from minor misregistration between the CT and PET acquisitions. The risk of this may be lower with iodine-containing oral contrast agents, probably as these agents typically are used in diluted form and have a lower density than barium contrast agents, or with a negative contrast agent such as water. If oral contrast agents will be administered before the ^{18}F-FDG PET, then they should be given only with noncaloric, non-sweetened liquids. Similarly, if a CT acquired early during intravenous contrast injection is used for attenuation correction of the PET, then attenuation artifacts may occur around a vessel (e.g., the subclavian vein) containing a transiently high concentration of contrast.

Developing the CT and PET imaging protocols for ^{18}F-FDG PET/CT must be customized for the medical and developmental needs of each patient. For example, in the absence of a specific clinical indication, the routine acquisition of high-energy diagnostic CT throughout the PET field of view is particularly inappropriate in the pediatric population. For each patient, the PET and CT imaging protocol must take into account the clinical indication, the sites of known disease, the information that can be provided by each study, and the goal of limiting radiation exposure.

Normal Patterns of FDG Uptake

Accurate interpretation of ^{18}F-FDG PET and PET/CT requires familiarity with the normal patterns of FDG distribution in children. Normal patterns of physiological uptake and excretion of ^{18}F-FDG should be distinguished from pathological uptake [42–44].

The normal brain demonstrates high ^{18}F-FDG uptake, with the most intense uptake in gray matter and basal ganglia (Figs. 3.1 and 3.2). Glucose provides approximately 95 % of the energy required by the brain [21], and up to 6 % of the administered dose of ^{18}F-FDG may be taken up in the brain [45]. Increased ^{18}F-FDG uptake can be seen with neuronal activation, such as in the visual cortex. This pattern of uptake limits the use of ^{18}F-FDG PET for evaluation of brain tumors as it may be difficult to discriminate uptake in tumor from uptake in nearby normal brain. Similarly, intense uptake in the brain can obscure pathological uptake in the adjacent scalp or skull base.

Normal physiological ^{18}F-FDG uptake is seen in lymphatic tissue in Waldeyer's ring, including the palatine tonsils and adenoids (Fig. 3.1). In children, prominent physiological uptake can obscure disease, while increased uptake in response to an upper respiratory infection can be difficult to distinguish from disease. Symmetrical ^{18}F-FDG uptake is more likely to represent physiological uptake [46]. Mild, and usually symmetrical, ^{18}F-FDG uptake also can be seen in salivary glands and pharyngeal muscles. Laryngeal uptake can range from mild to intense, depending, at least in part on recent talking. As in adults, asymmetrical laryngeal uptake is concerning for pathology, suggesting either FDG-avid local disease or unilateral vocal cord paralysis.

In children, cardiac uptake of ^{18}F-FDG can be variable, and intense myocardial uptake can be seen even after well-documented fasting (Figs. 3.4 and 3.6). Additional dietary interventions, with high-fat, low-carbohydrate diets, to decrease myocardial uptake have been tried in adults [33], especially those with disease located near the heart, but there has been little reported experience using these approaches in children.

Diffuse thymic uptake of ^{18}F-FDG rarely indicates disease in children (Fig. 3.5). This pattern of uptake usually represents age-related physiological activation or post-chemotherapy stimulation (thymic rebound) [47]. Although correlation or co-registration with CT can be used to confirm thymic uptake, the conformation of uptake is

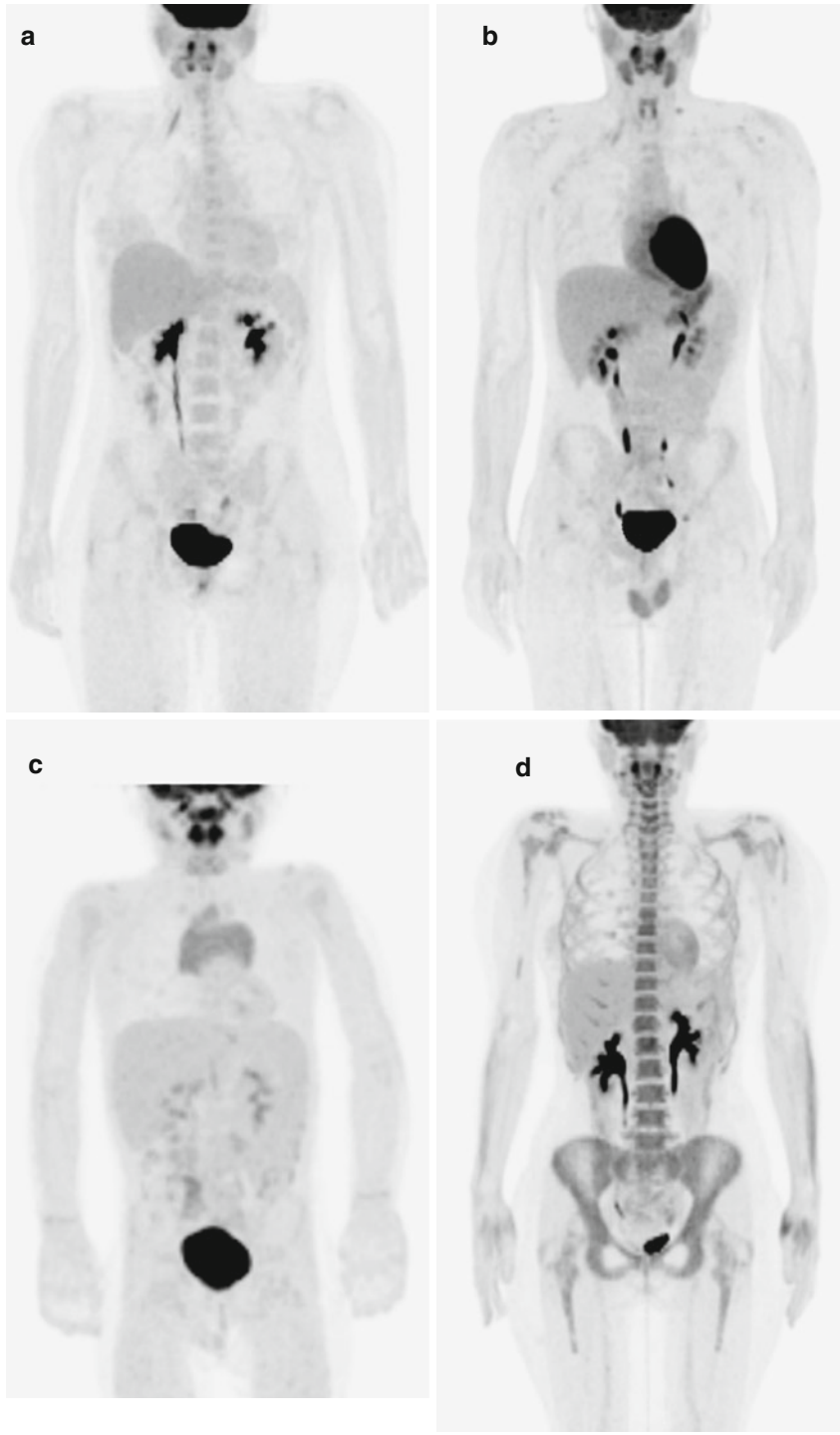

Fig. 3.6 Variable physiological uptake of ^{18}F-FDG. Variable patterns of physiological ^{18}F-FDG uptake can be seen in many organs. (**a**) In postpubertal females, physiological uptake of ^{18}F-FDG is most prominent in the ovaries and fallopian tubes around the time of ovulation and in the uterus at the end of menstrual cycle. (**b**) Mild-to-intense testicular uptake of ^{18}F-FDG can be seen in peripubertal and postpubertal males. (**c**) Thymic uptake of ^{18}F-FDG is as common in pediatric PET. Intense thymic uptake of ^{18}F-FDG also can be seen due to "thymic rebound" after completion of chemotherapy. (**d**) Diffusely increased ^{18}F-FDG uptake in the expected locations of bone marrow typically reflects physiological or pharmacological stimulation of marrow and rarely represents disease involvement of bone marrow

typical of the thymus. Diffuse bone marrow uptake occasionally represents widespread disease, but marrow uptake also is a well-described response to cancer therapy, including physiological rebound after chemotherapy and pharmacological stimulation with colony-stimulating factors used hasten marrow recovery (Fig. 3.6) [42, 48]. On the other hand, focal uptake rarely reflects treatment-related stimulation and raises concern for marrow involvement by disease. Occasionally, diffuse marrow uptake of ^{18}F-FDG can represent incidental nontreatment-related marrow stimulation, such as in response to anemia or a systemic inflammatory process [42].

Normal physiological distribution of ^{18}F-FDG can be seen throughout the gastrointestinal tract [43]. Focal uptake at the gastroesophageal junction is a normal finding, while substantial diffuse or regional uptake along the esophagus more likely represents an inflammatory process, such as posttreatment mucositis. Fluorine-18-FDG uptake by gastric mucosa can be physiological, but also may indicate a pathological neoplastic or inflammatory process. In the small and large intestines, the pattern of ^{18}F-FDG uptake helps distinguish physiological from pathological uptake. Typical physiological ^{18}F-FDG uptake can be multifocal and widespread. A single intense focus of ^{18}F-FDG uptake is worrisome for disease, while regional, segmental, or widespread diffuse intestinal uptake more likely represents an inflammatory process [49]. For example, terminal ileitis may come to attention due to incidental ^{18}F-FDG uptake identified on an ^{18}F-FDG PET/CT.

The urinary system is the usual path of ^{18}F-FDG excretion, so tracer can be seen in the kidneys, renal collecting systems, ureters, and bladder (Fig. 3.1) [43, 50]. Tracer accumulation in ureters usually can be identified by the distinctive contours of the ureters and by correlation with CT. This may be particularly helpful if there is focal urinary tracer accumulation within the urinary collecting system. Tracer accumulation in the collecting system can be minimized by encouraging patient hydration. Although routine use of pharmacological diuresis has been advocated in the past, diuretics are rarely, if ever, used for imaging children [44]. Bladder catheterization may be helpful in selected circumstances, such as in a sedated patient in whom tracer accumulation within the bladder may obscure ^{18}F-FDG uptake in nearby disease. Rarely, collecting system obstruction or hydronephrosis will be identified on ^{18}F-FDG PET or PET/CT. Tracer accumulation in congenital variants such as a dilated renal calyx, an ectopic or horseshoe kidney, or a bladder diverticulum must be recognized to avoid misinterpretation as a site of FDG-avid disease [51]. Persistent uptake in the renal cortex is abnormal and has a broad differential, including infection, infiltrative disorder, and lymphoma.

Physiological uptake of ^{18}F-FDG can be seen in the testes [52], especially in peripubertal and postpubertal young men (Fig. 3.6). In premenarchal females, ^{18}F-FDG uptake should not be seen in the ovaries or uterus. After menarche (Fig. 3.6), ^{18}F-FDG uptake in the ovaries is most intense during follicular genesis and ovulation, while endometrial uptake appears most intense at the end of the menstrual cycle, but also may be increased in the ovulatory phase of the menstrual cycle [53]. Therefore, it can be important to know the menstrual phase to adequately interpret these findings in a female patient.

Increased muscle ^{18}F-FDG uptake can be seen for up to 2 days after heavy exertion or if there is repetitive muscle use during the uptake (Fig. 3.5). Diffusely increased muscle uptake also can be seen in patients who did not fast before ^{18}F-FDG administration. Rarely, widespread muscle uptake represents an inflammatory myositis or rhabdomyolysis. Increased uptake can be seen with compensatory muscle activity, such as increased muscle uptake in a leg after disuse or amputation of the contralateral limb. Increased ^{18}F-FDG uptake is seen with increased use of the accessory muscles of respiration related to respiratory distress or even crying.

Summary

Infants and children provide special challenges to acquiring a technically adequate and diagnostically satisfactory PET or PET/CT scan. Adequate pre-study preparation of the patient and family is

critical. Imaging protocols must pay particular attention to the pediatric spectrum of disease, the developmental needs of pediatric patients, and the goal of minimizing radiation exposure. Interpretation of pediatric ^{18}F-FDG PET and PET/CT requires knowledge of pediatric diseases and an appreciation for the patterns of tracer biodistribution that can be seen in infants and children. Issues such as sedation or anesthesia, rarely a concern in adult nuclear medicine, are a normal part of routine pediatric PET and PET/CT. Protocols and departmental procedures must balance the developmental needs of children with the goal of acquiring a diagnostic imaging study that answers the clinical question. Achieving this goal can be facilitated by trained professional staff, including nuclear medicine physicians, nuclear medicine technologists, registered nurses, and child-life specialists, who have experience in pediatric imaging and a desire to work with infants and children.

References

1. Jadvar H, Connolly LP, Fahey FH, Shulkin BL. PET and PET/CT in pediatric oncology. Semin Nucl Med. 2007;37:316–31.
2. Grant FD, Dubach L, Treves ST. ^{18}F-fluorodeoxyglucose PET and PET/CT in pediatric musculoskeletal malignancies. PET Clin. 2010;5:349–61.
3. Portwine C, Marriot C, Barr RD. PET imaging for pediatric oncology: an assessment of the evidence. Pediatr Blood Cancer. 2010;55:1048–61.
4. Grant FD, Treves ST. Nuclear medicine and molecular imaging of the pediatric chest: current practical imaging assessment. Radiol Clin North Am. 2011;49:1025–51.
5. Patil S, Biassoni L, Borgwardt L. Nuclear medicine in pediatric neurology and neurosurgery: epilepsy and brain tumors. Semin Nucl Med. 2007;37:357–81.
6. Kim S, Salamon N, Jackson HA, Blüml S, Panigraphy A. PET imaging in pediatric neuroradiology: current and future applications. Pediatr Radiol. 2010;40:82–96.
7. Grant FD, Fahey FH, Packard AB, DAvis RT, Alavi A, Treves ST. Skeletal PET with 18F-fluoride: applying new technology to an old tracer. J Nucl Med. 2008;49:68–78.
8. Jadvar H, Alavi A, Mavi A, Shulkin BL. PET in pediatric diseases. Radiol Clin North Am. 2005;43:135–52.
9. Kaste SC. PET-CT in children: where is it appropriate? Pediatr Radiol. 2011;41:S509–13.
10. Weckesser M. Molecular imaging with positron emission tomography in paediatric oncology – FDG and beyond. Pediatr Radiol. 2009;39:S450–5.
11. Levin CS, Hoffman EJ. Calculation of positron range and its effect on the fundamental limit of positron emission tomography. Phys Med Biol. 1999;44:781–99.
12. Treves ST, Parisi MT, Gelfand MJ. Pediatric radiopharmaceutical doses: new guidelines. Radiology. 2011;261:347–9.
13. Wootton R, Doré C. The single-passage extraction of ^{18}F in rabbit bone. Clin Phys Physiol Meas. 1986;7:333–43.
14. Costeas A, Woodward HQ, Laughlin JS. Depletion of ^{18}F from blood flowing though bone. J Nucl Med. 1970;11:43–5.
15. Gatley SJ. Labeled glucose analogs in the genomic era. J Nucl Med. 2003;44:1082–6.
16. The MICAD Research Team. [^{18}F]fluoro-2-deoxy-2-D-glucose. In: Molecular imaging and contrast agent database (MICAD) [internet]. Bethesda: National Center for Biotechnology Information (US); 2004–2012. Bookshelf ID: NBK23335PMID: 20641537.
17. Fowler JS, Ido T. Initial and subsequent approach for the synthesis of ^{18}FDG. Semin Nucl Med. 2002;32:6–12.
18. Vallabhajosula S. ^{18}F-labeled positron emission tomographic radiopharmaceuticals in oncology: an overview of radiochemistry and mechanisms of tumor localization. Semin Nucl Med. 2007;37:400–19.
19. Rice SL, Roney CA, Daumar P, Lewis JS. The next generation of positron emission tomography radiopharmaceuticals in oncology. Semin Nucl Med. 2011;41:265–82.
20. Dulbeke D, Coleman RE, Guiberteau MJ, et al. Procedure guideline for tumor imaging with ^{18}F-FDG PET/CT 1.0. J Nucl Med. 2006;47:885–95.
21. Waxman AD, Herholz K, Lewis DH, et al. Society of Nuclear Medicine procedure guideline for FDG PET brain imaging. http://interactive.snm.org/docs/Society of Nuclear Medicine Guideline for FDG PET Brain Imaging.pdf.
22. McQuattie S. Pediatric PET/CT imaging: tips and techniques. J Nucl Med Technol. 2008;36:171–8.
23. Segall G, Delbeke D, Stabin MG, Even-Sapir E, Fair J, Sajdak R. SNM practice guideline for sodium ^{18}F-fluoride PET/CT bone scans 1.0. J Nucl Med. 2010;51:1813–20.
24. Rabkin Z, Israel O, Keidar Z. Do hyperglycemia and diabetes affect the incidence of false-negative ^{18}F-FDG PET/CT studies in patients evaluated for infection or inflammation and cancer? A comparative analysis. J Nucl Med. 2010;51:1015–20.
25. Liang Y, Steinbach G, Maier V, Pfeiffer EF. The effect of artificial sweetener on insulin secretion. 1. The effect of acesulfame K on insulin secretion in the rat (studies in vivo). Horm Metab Res. 1987;19:233–8.

26. Gontier E, Fourme E, Wartski M, Blondet C, Donardel G, Le Stanc E, Marzarides M, Foehrenbach H, Peckig AP, Alerini JL. High and typical ^{18}F-FDG bowel uptake in patients treated with metformin. Eur J Nucl Med Mol Imaging. 2008;35:95–9.
27. Bybel B, Greenberg ID, Paterson J, Ducharme J, Leslie WD. Increased F-18 FDG intestinal uptake in diabetic patients on metformin: a matched case–control analysis. Clin Nucl Med. 2011;36:452–6.
28. Ozülker T, Ozülker F, Mert M, Ozpaçaci T. Clearance of the high intestinal ^{18}F-FDG uptake associated with metformin after stopping the drug. Eur J Nucl Med Mol Imaging. 2010;37:1011–7.
29. Zukotynski KA, Fahey FA, Laffin S, Davis R, Treves ST, Grant FD, Drubach LA. Constant ambient temperature of 24 °C significantly reduces FDG uptake by brown adipose tissue in children. Eur J Nucl Med Mol Imaging. 2009;36:602–6.
30. Söderlund V, Larsson SA, Jacobsson H. Reduction of FDG uptake in brown adipose tissue in clinical patients by a single dose of propanolol. Eur J Nucl Med Mol Imaging. 2007;34:1018–22.
31. Barrington SF, Maisey MN. Skeletal muscle uptake of fluorine-18-FDG: effect of oral diazepam. J Nucl Med. 1996;37:1127–9.
32. Gelfand MJ, O'Hara SM, Curtwright LA, MacLean JR. Pre-medication to block [^{18}F]FDG uptake in the brown adipose tissue of pediatric and adolescent patients. Pediatr Radiol. 2005;35:984–90.
33. Williams G, Kolodny GM. Method for decreasing uptake of ^{18}F-FDG by hypermetabolic brown adipose tissue on PET. Am J Roentgenol. 2008;190:1406–9.
34. Boellaard R. Standards for PET image acquisition and quantitative data analysis. J Nucl Med. 2009;50: 11S–20.
35. Hustinx R, Smith RJ, Benard F, et al. Dual time point fluorine-18 fluorodeoxyglucose positron emission tomography: a potential method to differentiate malignancy from inflammation and normal tissue in the head and neck. Eur J Nucl Med. 1999;26:1345–8.
36. Roberts EG, Shulkin BA. Technical issues in performed PET studies in pediatric patients. J Nucl Med Technol. 2004;32:5–9.
37. McCarville MB. PET-CT imaging in pediatric oncology. Cancer Imaging. 2009;9:35–43.
38. Scripes PG, Yaparpalvi R. Technical aspects of positron emission tomography/computed tomography in radiotherapy treatment planning. Semin Nucl Med. 2012;42:283–8.
39. Antoch G, Bockisch A. Combined PET/MRI: a new dimension in whole-body oncology imaging? Eur J Nucl Med Mol Imaging. 2009;36:S113–20.
40. Chawla SC, Federman N, Zhang D, et al. Estimated cumulative radiation dose from PET/CT in children with malignancies: a 5-year retrospective review. Pediatr Radiol. 2010;40:681–6.
41. Fahey FH. Dosimetry of pediatric PET/CT. J Nucl Med. 2009;50:1483–91.
42. Gordon BA, Flanagan FL, Dehdashti F. Whole-body positron emission tomography: normal variations, pitfalls, and technical considerations. Am J Roentgenol. 1997;169:1675–80.
43. Shreve PD, Anzai Y, Wahl RL. Pitfalls in oncologic diagnosis with FDG PET imaging: physiologic and benign variants. Radiographics. 1999;19:61–77.
44. Shammas A, Lim R, Charron M. Pediatric FDG PET/CT: physiological uptake, normal variants, and benign conditions. Radiographics. 2009;29:1467–86.
45. Ak I, Stokkel MP, Pauwels EK. Positron emission tomography with 2-[^{18}F]fluoro-2-deoxy-D-glucose in oncology. II: the clinical value in detecting and staging primary tumours. J Cancer Res Clin Oncol. 2000; 126:560–74.
46. Sarji SA. Physiological uptake in FDG PET simulating disease. Biomed Imaging Interv J. 2006;2:e59.
47. Brink I, Reinhardt MJ, Hoegerle S, Altehoefer C, Moser E, Nitzsche EU. Increased metabolic activity in the thymus studied with FDG PET: age dependency and frequency after chemotherapy. J Nucl Med. 2001; 42:591–5.
48. Yao WJ, Hoh CK, Hawkins RA, et al. Quantitative PET imaging of bone marrow glucose metabolic response to hematopoietic cytokines. J Nucl Med. 1995;36:794–9.
49. Tatlidil R, Jadvar H, Bading JR, Conti PS. Incidental colonic fluorodeoxyglucose uptake: correlation with colonoscopic and histopathological findings. Radiology. 2002;224:783–7.
50. Vesselle HJ, Miraldi FD. FDG PET of the retroperitoneum: normal anatomy, variants, pathologic conditions, and strategies to avoid diagnostic pitfalls. Radiographics. 1998;18:805–23.
51. Subhas N, Patel PV, Pannu HK, Jacene HA, Fishman EK, Wahl RL. Imaging of pelvic malignancies with in-line FDG PET-CT: case examples and common pitfalls of FDG PET. Radiographics. 2005;25: 1031–43.
52. Kitajima K, Nakamoto Y, Senda M, Onishi Y, Okizuka H, Sugimara K. Normal uptake of ^{18}F-FDG in the testis: an assessment by PET/CT. Ann Nucl Med. 2007; 21:405–10.
53. Lerman H, Metser U, Grisaru D, Fishman A, Lievshitz G, Even-Sapir E. Normal and abnormal ^{18}F-FDG endometrial and ovarian uptake in pre- and postmenopausal patients: assessment by PET/CT. J Nucl Med. 2004;45:266–71.

Central Nervous System: The Brain and Cerebrospinal Fluid

4

S. Ted Treves, Harry T. Chugani,
Blaise F.D. Bourgeois, and Alvin Kuruc

Part 1: The Brain

S. Ted Treves, Harry T. Chugani,
and Blaise F.D. Bourgeois

The brain is a highly complex organ composed of billions of neurons linked to vast networks. The brain utilizes electrical and neurochemical signals to process information and control behavior.

S.T. Treves, MD (✉)
Joint Program in Nuclear Medicine, Department of Radiology, Harvard Medical School,
Boston, MA, USA

Division of Nuclear Medicine and Molecular Imaging, Department of Radiology,
Boston Children's Hospital,
Boston, MA, USA

Division of Nuclear Medicine and Molecular Imaging, Department of Radiology, Brigham and Women's Hospital, Boston, MA, USA
e-mail: ted_treves@HMS.harvard.edu

H.T. Chugani, MD
Department of Neurology, PET Center,
Children's Hospital of Michigan,
Detroit, MI, USA

B.F.D. Bourgeois, MD
Department of Neurology, Boston Children's Hospital,
Boston, MA, USA
e-mail: blaise.bourgeois@tch.harvard.edu

A. Kuruc, MD, PhD
Global Macro GFX, Investment Banking,
Credit Suisse, London, UK
e-mail: alvin.kuruc@credit-suisse.com

Brain function consumes and produces a great deal of metabolic energy, and it is served by a rich, well-regulated blood supply system [1, 2]. Although great advances in the fields of neurosciences, physiology, physiopathology, neurology, psychiatry, and neuroimaging have been made, our understanding of the brain is still in its infancy. Many imaging tools have been developed to explore the structure and functions of the brain, including computed tomography (CT), structural and functional magnetic resonance imaging (MRI and fMRI), MR spectroscopy (MRS), perfusion-weighted imaging, diffusor tensor imaging (DTI), susceptibility-weighted imaging (SWI), single photon emission computed tomography (SPECT), positron emission tomography (PET), and magnetic source localization using magnetoencephalography (MEG) [3]. These powerful tools have opened the door for the development of new methods for the exploration of the brain in vivo. Changes in local metabolism and activity are often inferred from changes in perfusion. However, although metabolism and perfusion are usually closely linked, this is not always the case. Activity detected by receptor ligands may not relate to either perfusion or metabolism.

This chapter will review methodology of single photon emission computed tomography (SPECT) and positron emission tomography (PET), radiopharmaceuticals, imaging instrumentation, image fusion, and clinical applications. Both SPECT and PET play an important role in the evaluation of the pediatric brain. These methods can depict regional cerebral perfusion, glucose metabolism,

S.T. Treves (ed.), *Pediatric Nuclear Medicine and Molecular Imaging*,
DOI 10.1007/978-1-4614-9551-2_4, © Springer Science+Business Media New York 2014

and other functions and provide maps of the location, quantification, and biokinetics of radiopharmaceutical agents. In addition, these techniques can detect rapid changes due to normal brain activity in different functional conditions or those caused by pharmacologic or cognitive stimulation. During the early 1960s, ^{133}Xe was used to measure regional cerebral blood flow (rCBF) [4]. Because of its relative complexity, this method was limited to a small number of research institutions and therefore did not become widely used. From the late 1960s to the mid-1970s, scintigraphy with ^{99m}Tc-pertechnetate was extensively used for the diagnosis of brain tumors, brain abscess and infections, and subdural hematomas and the assessment of brain death. When CT and MRI became widely available during the 1970 and 1980s, respectively, the use of radionuclide techniques for brain imaging declined dramatically. During the past several years, brain SPECT and PET have experienced significant improvements, and both have found their new place in routine practice. Improvements in the production and distribution of ^{18}F-FDG and better PET systems have facilitated the widespread use of PET. Advances in imaging systems and data processing in SPECT have resulted in systems that are simpler to operate and that yield 3D images of high functional and anatomic resolution.

Each imaging technique has its own strengths and limitations, and it is becoming increasingly natural that physicians and scientists want to combine them in order to take full advantage of the different and often complementary information they provide. Several methods for image registration and fusion are now available in many commercial systems. These methods enable more detailed assessment of functional and anatomic relationships that assist in the interpretation of the images. Current methods enable registration and fusion of two or more 3D image sets. Although the current proliferation of PET/CT systems is impressive, CT image registration is not considered as useful in brain imaging as registration of functional images to MRI and among themselves (SPECT/SPECT, SPECT/MRI, SPECT/PET, PET/MRI, etc.) (Fig. 4.1) [5].

Fused images are frequently very helpful to improve the selection of biopsy sites in order to ensure the highest yield of abnormal tissue to be evaluated. Also, image fusion can assist in guiding surgery and optimizing the targeting of radiotherapy and radiosurgery. Along with improvements in SPECT systems, the availability of single photon emitting radiopharmaceuticals labeled with ^{99m}Tc, such as those that are trapped intracellularly in proportion to rCBF, is being used extensively. For example, ^{99m}Tc-bicisate (ECD) and ^{99m}Tc-hexamethylpropyleneamine oxime (HMPAO) are extensively used for brain SPECT in pediatric patients such as those affected with epilepsy and cerebrovascular disorders (e.g., moyamoya, stroke). Technetium-99m hexakis (2-methoxy-isobutylisonitrile) sestamibi (^{99m}Tc-MIBI) and ^{201}Tl-chloride have been found useful in the assessment of brain tumors following surgery and in radiation therapy to differentiate fibrosis or necrosis from residual tumor or tumor recurrence. The use of ^{18}F-FDG has created renewed interest in PET scanning of the brain in a variety of pediatric disorders such as epilepsy, brain tumors, cerebrovascular disorders, and stroke to name a few. More details about brain imaging radiopharmaceuticals will be discussed within the context of clinical applications.

The future holds almost infinite potential for the discovery and development of radiolabeled molecules of relevance to the study of brain function with SPECT and PET. For example, the potential availability of radiopharmaceuticals that bind to neurotransmitter receptors will encourage research and hopefully further diagnostic opportunities. It is anticipated that in the not-too-distant future, newer tracers will continue to be used in basic research, as well as in basic neuropharmacology research. Ultimately, new agents could be used to define specific patient populations for clinical trials in neurology. As new ligands are developed, it is tempting to speculate that new methods for radiotracer imaging may in the future find their way to join other neuroimaging methods in clinical practice. The variety and type of new and potential ligands are quite large, and a detailed discussion of such newer radiopharmaceuticals is well beyond the scope of this chapter. Ongoing developments in radiopharmaceutical research, imaging methodology, computer science, and clinical research will likely expand the use of

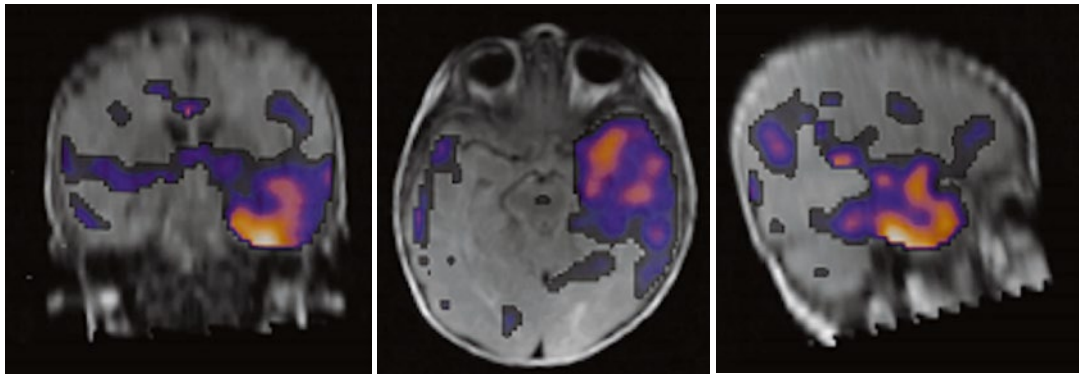

Fig. 4.1 Single photon emission computed tomography (SPECT) and magnetic resonance imaging (MRI) image fusion in a patient with intractable seizures. Ictal minus interictal perfusion SPECT superposed on a brain MRI. The image reflects ictal increase of cerebral blood flow in the left temporal region

nuclear medicine techniques for the investigation of regional brain function in pediatric patients.

Clinical Applications

Clinical applications of brain SPECT and PET in pediatric patients are expected to evolve as new methodology is developed. Table 4.1 lists the indications for radionuclide brain imaging in children. In pediatrics, the most frequent indications for the use of nuclear medicine imaging methods include seizure disorders, cerebrovascular diseases, and brain tumors.

Table 4.1 Indications for radionuclide brain imaging

Epilepsy
Cerebrovascular disease
Infantile spasms
Alternating hemiplegia
Attention deficit/hyperactivity disorder (ADHD)
Complications of extracorporeal membrane oxygenation
Effect of hypothermia and hypoxia
Brain death
Tumors
Rasmussen encephalitis

Normal Brain Development

Ethical considerations make study of normal children with SPECT or PET difficult or almost impossible. Therefore, data on the normal distribution of cerebral perfusion and metabolism in children is scarce. The normal development of the brain affects the distribution of regional cerebral blood flow and metabolism, and this will be reflected on brain SPECT and PET. This is important to keep in mind when evaluating these studies in the youngest patients.

The evolution of cerebral glucose utilization in infants during different stages of development was described by Chugani et al. using PET (Fig. 4.2) [6]. Metabolic activity is initially more intense in the sensorimotor cortex, thalamus, brainstem, and cerebellar vermis; later it involves the parietal, temporal, and occipital cortices, basal ganglia, and cerebellar cortex, and finally, the frontal cortex. More recent studies using higher resolution PET scanners have found that a number of limbic structures (i.e., amygdala, hippocampus, cingulate cortex) also show relatively high glucose metabolism in the newborn period [7]. The development of normal brain in children has also been studied with SPECT using ^{123}I-iodoamphetamine (IMP) and ^{133}Xe, and in general the SPECT studies have confirmed the findings of Chugani and colleagues [6, 8–12].

Childhood Epilepsy

Epilepsy in children is treated with considerable success by medical means. A significant number (20–30 %) of epileptic patients, however, do not respond to drug therapy or remain refractory to this or other medical interventions. Patients with medically refractory partial seizures are referred for surgical resection of epileptogenic cor-

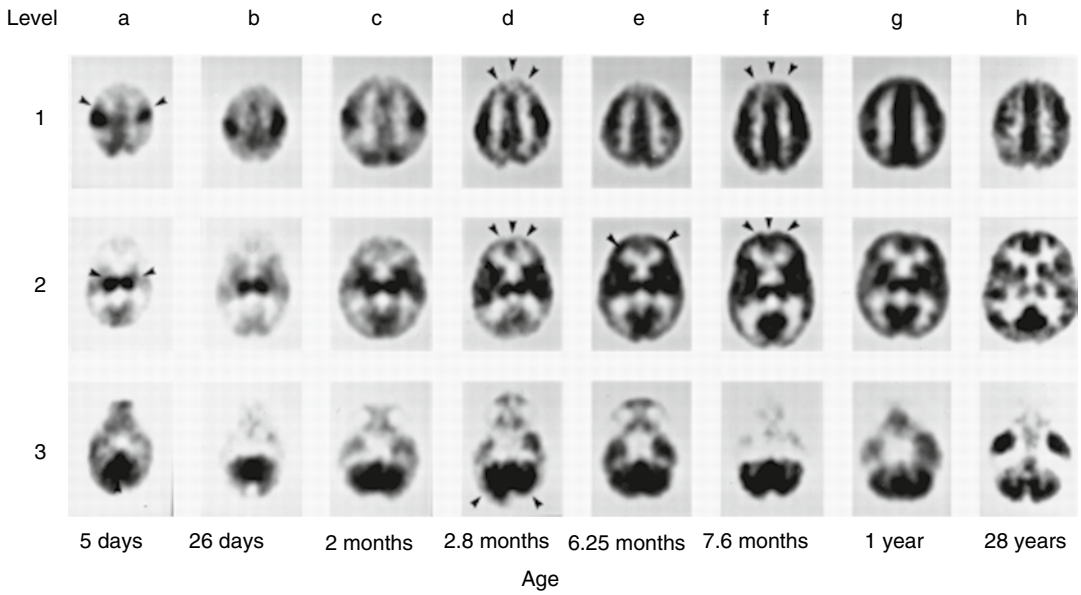

Fig. 4.2 Normal brain development. Fluorodeoxyglucose positron emission tomography (FDG-PET) images illustrating developmental changes in local cerebral metabolic rates for glucose (lCMRGlc) in the normal human infant with increasing age compared to that of the adult (image sizes not on the same scale). Grayscale is proportional to lCMRGlc, with black being highest. In each image, the anterior brain is at the top and the left brain is at the left. (**a**) At 5 days, lCMRGlc is highest in sensorimotor cortex, thalamus, cerebellar vermis (*arrowheads*), and brainstem (not shown). (**b**–**d**) lCMRGlc gradually increases in parietal, temporal, and calcarine cortices, basal ganglia, and cerebellar cortex (*arrowheads*). (**e**) In the frontal cortex, lCMRGlc increases first in the lateral prefrontal regions (*arrowheads*) at around 6 months. (**f**) At around 8 months, lCMRGlc increases in the medial aspects of the front cortex (*arrowheads*) and in the dorsolateral occipital cortex. (**g**) By 1 year the lCMRGlc pattern resembles that of adults (**h**) (From Chugani et al. [6], with permission)

tex. Epilepsy surgery has become a specialized field, and surgical removal or disconnection of a portion of brain believed to contain the epileptogenic focus may control seizures [13, 14]. The patient population involved includes those with seizures in whom structural lesions in the brain can be demonstrated, as well as those patients in whom no lesion in the brain is demonstrated (non-lesional epilepsy). Seizure types that may be treated by surgery include simple partial seizures, complex partial seizures, and secondarily generalized seizures. The largest group of surgical candidates comprises patients with complex partial seizures originating in a temporal lobe. Preoperative evaluation identifies those patients with dysplasias, migrational disorders, tumors, or vascular malformations and can determine whether the epileptic focus is deep (e.g., in the amygdala or hippocampus) or superficial (convexity cortex). Partial seizures of frontal origin and from other extratemporal sites may also be treated surgically when the clinical manifestations and diagnostic studies indicate an epileptic region in a resectable area [15].

When a single epileptogenic focus can be identified, its surgical resection is often followed by cessation of seizures, a reduction of seizure frequency, or a reduction of anti-epileptic doses of medication, all accompanied by an improvement in the quality of life in many patients. Appropriately directed, surgical resection of epileptogenic tissue has resulted in success rates of 55–80 % of patients. Success has been defined as no seizures (some auras may be present) for 2 years after surgery, sometimes with some patients still needing anticonvulsant medication. The postsurgical success is dependent on accurate presurgical localization of epileptogenic foci. Obviously, it would be catastrophic to operate on the wrong site or to overlook a second active focus.

Imaging in Epilepsy

Localization of temporal and extratemporal epileptogenic foci in these patients can be challenging. A battery of tests is employed to verify seizure zone localization. Approaches leading to the localization of ictal cortex begin with noninvasive methods, and depending on the results, they may progress toward more invasive ones. Clinical assessment followed by electrocorticography provide an initial noninvasive approach, but it may not localize the foci and could even be misleading. Brain MRI is the best structural imaging study and can demonstrate mesial temporal sclerosis or other anatomic lesions. However, in some epileptic patients MRI may not reveal anatomic lesions. Furthermore, even if an anatomic lesion is detected on MRI, it cannot detect epileptogenic activity that may extend beyond or be independent of the identified anatomic lesion [16]. Despite great progress in structural neuroimaging, in most specialized epilepsy centers, the epileptogenic focus cannot be localized by MRI scanning in approximately 20–50 % of patients with medically refractory epilepsy. This problem has stimulated efforts to develop functional neuroimaging techniques that can demonstrate transient physiologic disturbances, not just static structural ones.

Perfusion brain SPECT in temporal epilepsy reveals characteristic time-dependent changes in regional cerebral perfusion following a partial seizure. During the earliest postictal period, there is increased perfusion involving the medial temporal lobe, followed by hypoperfusion of the lateral temporal cortex, and later of the entire temporal lobe [17, 18]. Ictal SPECT must be performed with tracer injection at the onset or during the ictal episode. Injections of the tracer postictally will likely demonstrate activation not only of the epileptogenic cortex but also of secondary epileptogenic tissue and this may lead to erroneous conclusions [19]. Much work remains to be done to define the exact time course of propagation of perfusion abnormalities following the seizure, especially in children. Image subtraction techniques (ictal minus interictal perfusion SPECT) with MRI fusion are important to assist in the localization and interpretation of these findings (Figs. 4.3, 4.4, 4.5, 4.6, 4.7, 4.8, 4.9, and 4.10).

Functional abnormalities detected by SPECT or PET are not infrequently accompanied by normal or almost normal CT or MRI scans. In other instances, the perfusion or metabolic abnormalities are seen to extend far beyond the limits of structural lesions. These findings have been demonstrated by several authors using ^{99m}Tc-ECD, ^{99m}Tc-HMPAO, or ^{133}Xe SPECT [20–26].

For the localization of epileptogenic foci, it is generally agreed that ictal SPECT (when successfully accomplished) is better than interictal PET and that interictal PET is better than interictal SPECT. In addition to its wide availability, ictal perfusion brain SPECT has one unique advantage over all other imaging methods. The ^{99m}Tc brain ligands (^{99m}Tc-ECD and ^{99m}Tc-HMPAO) are extracted and trapped intracellularly following their first pass according to rCBF. The tracer remains fixed in the brain for several hours after intravenous administration, permitting imaging at a convenient time following cerebral stimulation. Therefore a "snapshot" of rCBF during specific events can be obtained.

At the moment of injection, the child need not be in or near the camera. It is possible to inject the material through an established intravenous line in a comfortable room while the child's behavior, task performance, and EEG are recorded. SPECT can be obtained when the patient is stabilized, anytime from 0.5 to 6 h following tracer administration (ECD). These advantages are of considerable practical value. Unpredictable events cannot be captured by perfusion studies using CT, PET, or MRI unless they occur while the child's head is in the gantry of the machine. This positioning often provokes anxiety, which may itself alter regional brain function and therefore the pattern seen on perfusion or other functional imaging. Administration of sedatives may affect rCBF. However, since the distribution of SPECT perfusion tracers does not change with time, sedation may be given after tracer injection of perfusion agents (ECD or HMPAO) for the imaging session.

Ictal Perfusion SPECT

Ictal injections are difficult to achieve as they depend ideally on the availability of a

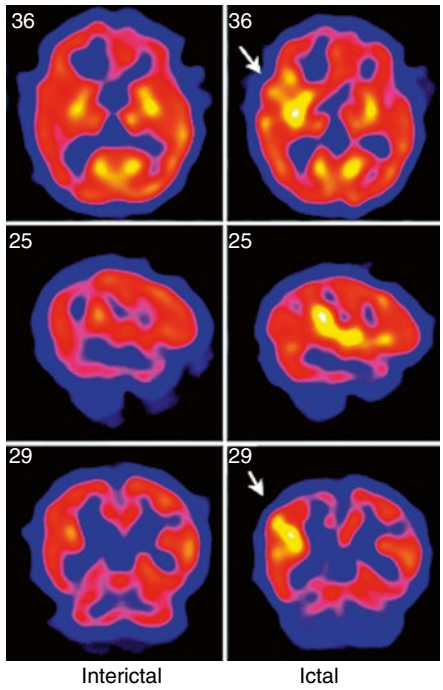

Fig. 4.3 Eight-month-old with intractable seizures. Ictal ^{99m}Tc-ECD SPECT reveals increased brain flow in the epileptogenic zone (*arrows*)

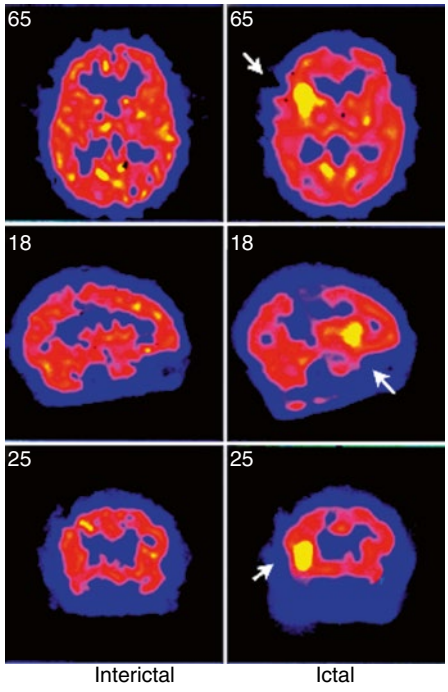

Fig. 4.4 Interictal and ictal ^{99m}Tc-ECD SPECT reveals focal ictal hyperperfusion in the right parietal region (*arrows*)

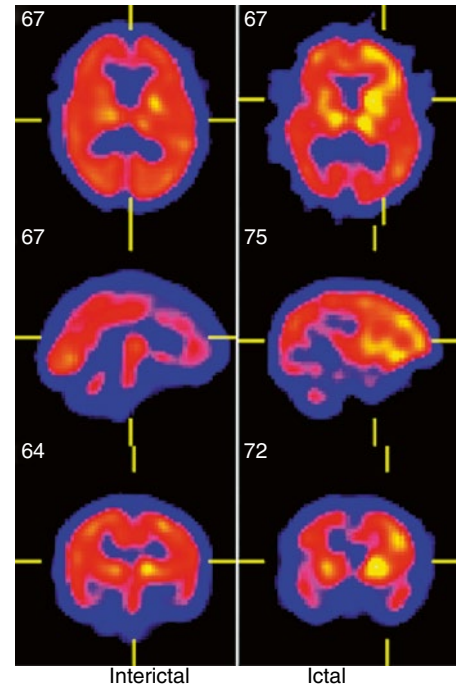

Fig. 4.5 Interictal and ictal ^{99m}Tc-ECD perfusion brain SPECT. A rather large region of hyperperfusion on the left involves the frontal, parietal, and temporal regions. Increased perfusion is also seen in the central structures in the same side

qualified healthcare professional to be at the patient's bedside and be ready to administer the radiotracer at the time of seizure onset [27]. Unfortunately, due to practical considerations, it is not always possible to ensure that a staff member is available to sit next to the patient awaiting a seizure. Therefore, using a special acoustic signal, specialized nurses are called to the patient's room as soon as a seizure occurs, and the tracer is injected as quickly as possible following the onset of the seizure. This limitation makes the yield of true ictal injections lower than it could be. Unfortunately, a number of perfusion brain SPECTs obtained do not reflect true ictal distribution, but rather immediate postictal distribution of the tracer. When this takes place, SPECT is likely to reveal secondary hyperperfused regions in the brain that may extend beyond the initial focus or may even be remote from the initial ictal focus. Therefore, it would be desirable to free up personnel who could ensure that true ictal injections, and therefore truer ictal brain

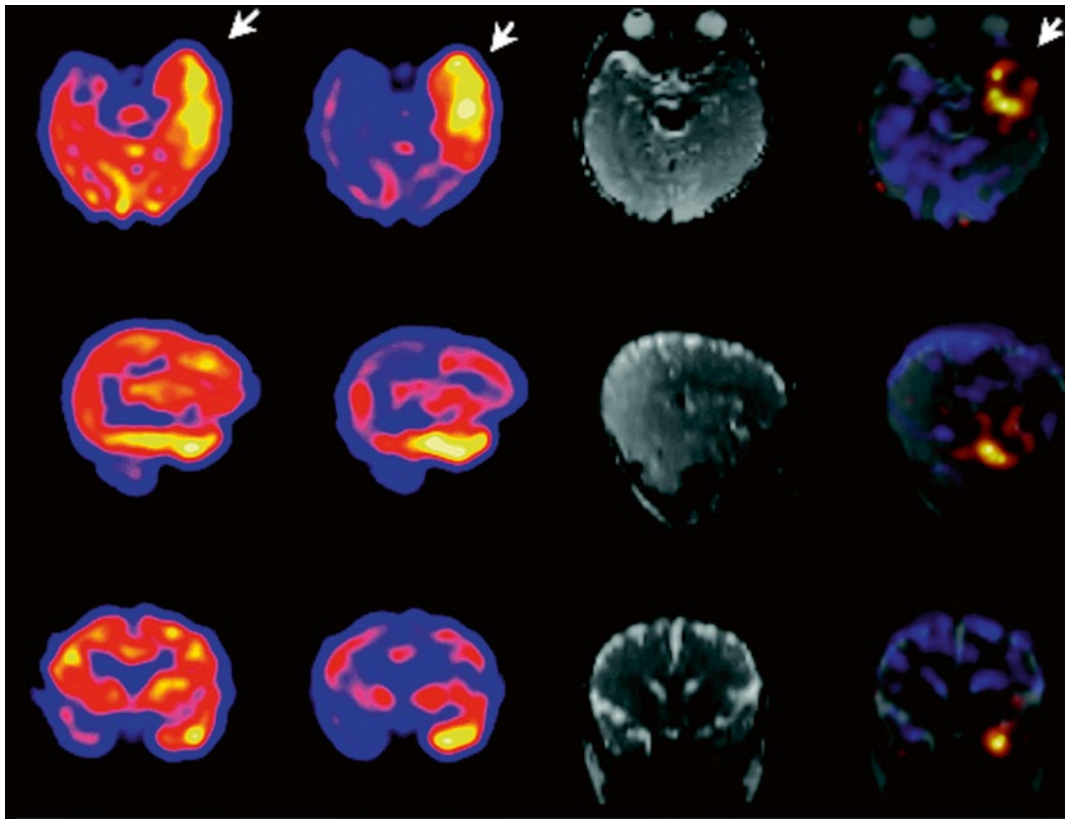

Fig. 4.6 Young child with infantile spasms. The interictal ^{99m}Tc-ECD SPECT reveals relatively increased perfusion in the left temporal lobe, probably indicating activity in this region. The ictal SPECT shows a dramatic increase in perfusion to the left temporal lobe. Note the relative lower intensity in the rest of the brain. Ictal SPECT was subtracted from the interictal SPECT, and the resultant image was superposed ("fused") with the MRI

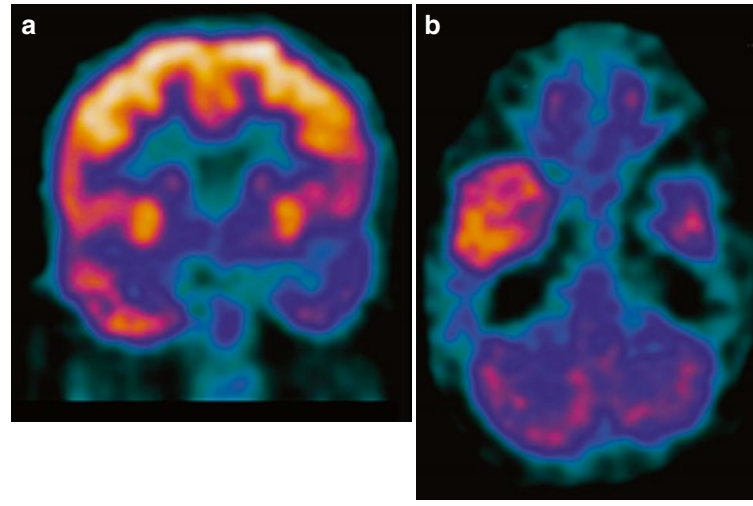

Fig. 4.7 Interictal ^{18}F-FDG PET in a patient with intractable seizures. There is less tracer uptake in the left temporal lobe

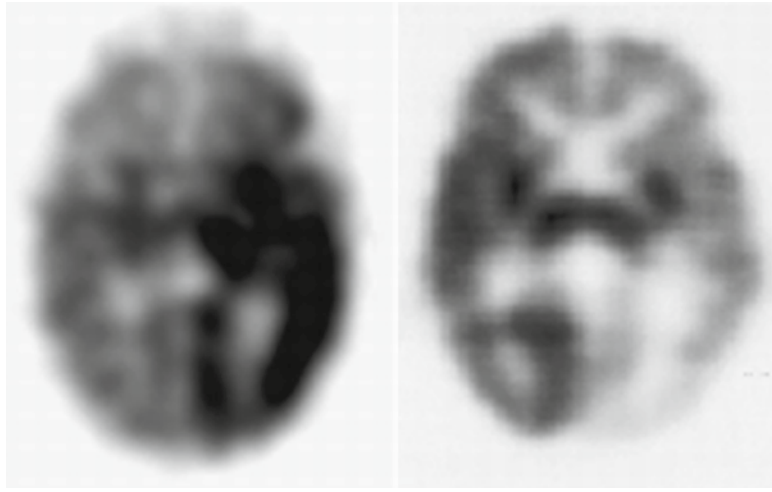

Fig. 4.8 Six-week-old infant with seizures. Patient had recurrent convulsions with the head turning left and stiffening of the right side of the body. A computed tomography (CT) scan at 10 days of age showed evidence of hemorrhage in the left frontal periventricular white matter as well as prominent cortical sulci. Magnetic resonance imaging (MRI) showed subacute hemorrhage in the left caudothalamic groove. An ictal perfusion SPECT reveals high blood flow to almost the entire left hemisphere. An interictal FDG PET reveals marked decrease of tracer uptake in the same regions

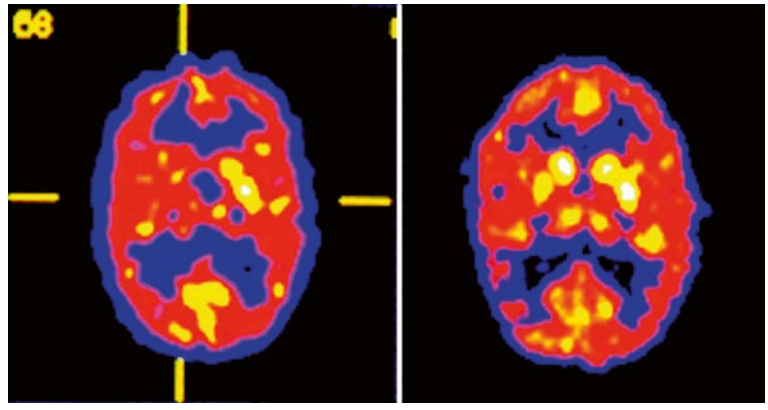

Fig. 4.9 Interictal ^{99m}Tc-ECD SPECT and ^{18}F-FDG PET in the same patient. The asymmetry in tracer uptake is more pronounced on the SPECT

SPECTs, are possible. Although this may be a preferable solution, it may not be practical in most settings.

A multidisciplinary approach should be utilized. This requires excellent coordination and meticulous attention to detail, and this cannot be emphasized enough. The entire process leading to the administration of the radiopharmaceutical to the patient for ictal SPECT should be under the supervision of a nuclear medicine physician with a close collaboration of a team that includes a neurologist, nuclear medicine technologists, specially trained nurses, and radiation safety personnel.

A critical prerequisite is to establish *a secure intravenous line* into the patient in advance of the

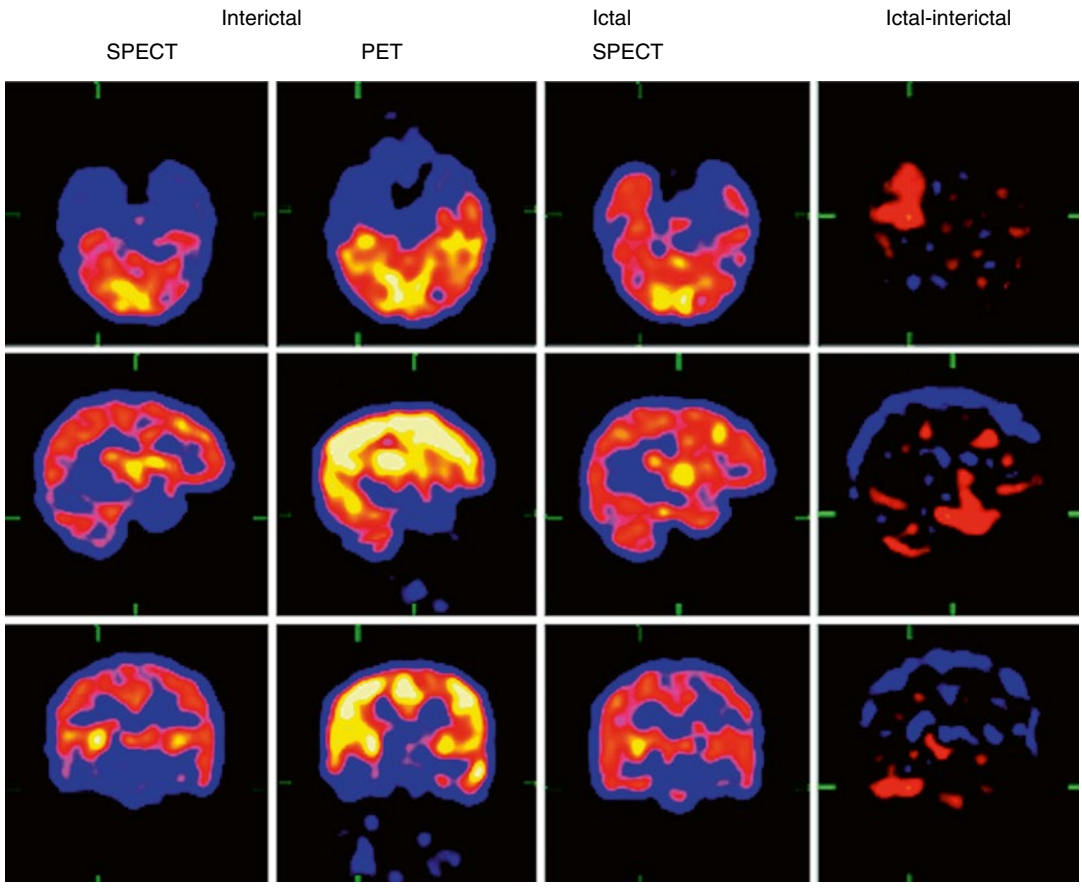

Fig. 4.10 Interictal ^{18}F-FDG PET reveals significant decrease of tracer in the right temporal lobe. This is not as dramatic as on the interictal SPECT. The ictal SPECT clearly demonstrates high perfusion to the right temporal lobe. On the *right panel* are the ictal minus interictal SPECT subtraction images

procedure. This is done with a short intravenous catheter that is secured to the skin with tape and other appropriate precautions, so the line remains patent for the anticipated injection of the tracer during a patient's seizure. The IV access should be kept open with a saline drip. Care must be taken so that patient motion during a seizure will not dislodge the IV access. For the most optimal localization of ictal cortical foci, the patient needs to be injected with the tracer as soon as the seizure starts. Therefore, it is important to make every possible effort to ensure that the tracer is injected at the time of the seizure or a very few seconds (<5 s) after its onset. Figure 4.11a, b show the effect of injecting the patient 30 s and at 2 s after seizure onset (Fig. 4.11a, b). The SPECT obtained with injection at 30 s after seizure onset shows distribution of "ictal" activity within both cerebral hemispheres. Conversely, when the tracer was injected at 2 s following seizure onset, the SPECT demonstrates early seizure activity localized to one hemisphere. If the tracer is injected later (several seconds to a minute after the seizure onset), the resulting distribution will not provide a good localization of epileptogenic cortex. Rather, such distribution will be a postictal distribution showing propagation of the seizure activity focus. In these cases, it is very difficult or impossible to identify the initial ictal focus.

Technetium-99m-ECD or HMPAO is prepared in advance in a dose appropriate to the patient size. The shelf half-life of ^{99m}Tc-ECD is 6 h (HMPAO has a shorter shelf life). The plan is to enable rapid injection of the tracer at the time the patient has a seizure. The activity/volume of radiopharmaceutical in the syringe is calibrated so that if necessary the full dose of the tracer can be given at 6 h after tracer preparation. If the patient experiences a seizure at any time before the 6-h window closes, an appropriate amount of activity in the appropriate volume of the tracer is administered at the time of the seizure. If the patient does not experience a seizure during the 6 h following preparation of the tracer, the tracer is injected for an interictal SPECT, if this was not obtained before.

An Injector System for Ictal SPECT

One of us (STT) designed a simple and convenient injection apparatus to facilitate rapid ictal injections of the brain perfusion radiotracer (^{99m}Tc-ECD or ^{99m}Tc-HMPAO). This simple apparatus is made of Lucite and leaded glass, and it holds two syringes that are placed within the device. One syringe contains the tracer under the leaded glass shield and the other contains a 30 mL saline syringe for flushing the line. A table

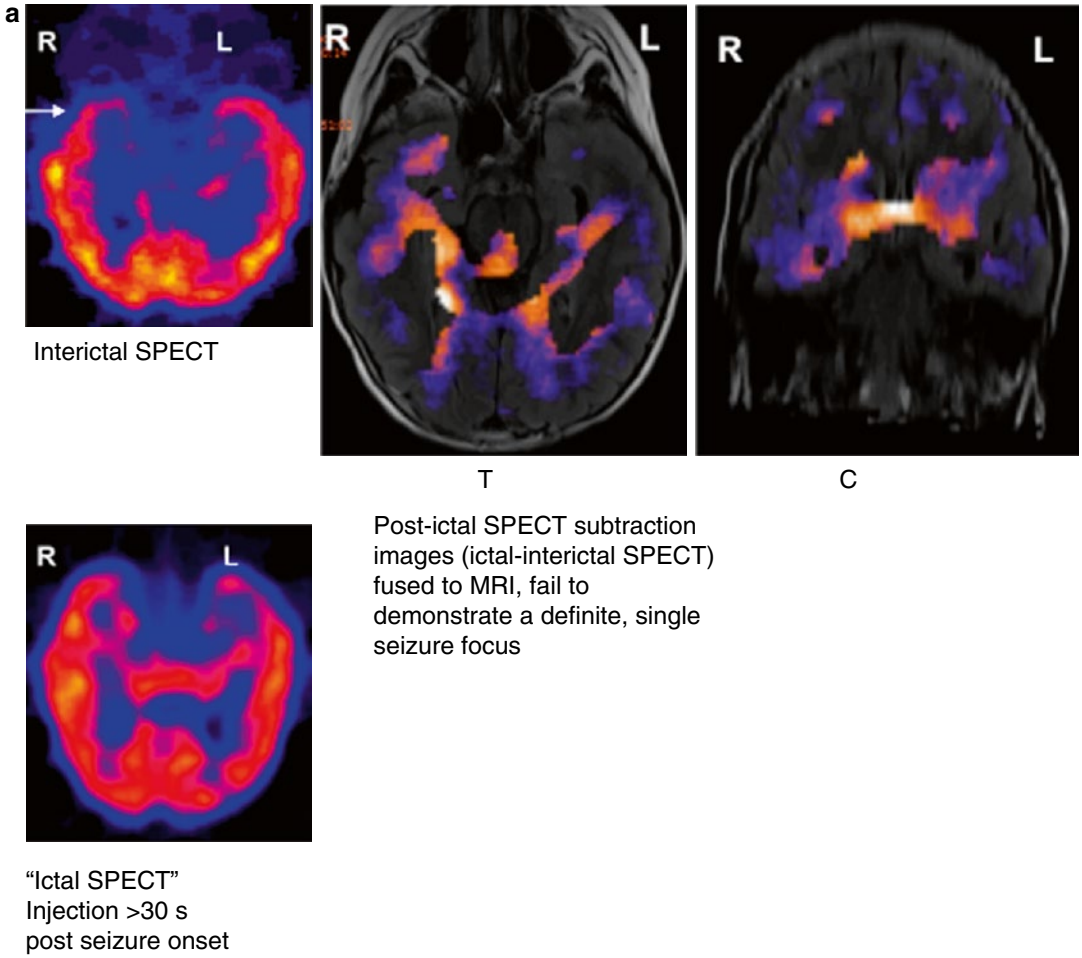

Fig. 4.11 (**a**) Interictal and ictal ^{99m}Tc-ECD SPECT. "Ictal" tracer injection was given >30 s after seizure onset. The ictal minus interictal image shows multiple focal hyperperfusion areas bilaterally *arrow* points to the right temporal lobe (R). (**b**) A repeat ictal SPECT obtained with tracer injected within 2 s of seizure onset reveals focal hyperperfusion in the right temporal lobe (R) (*arrows*)

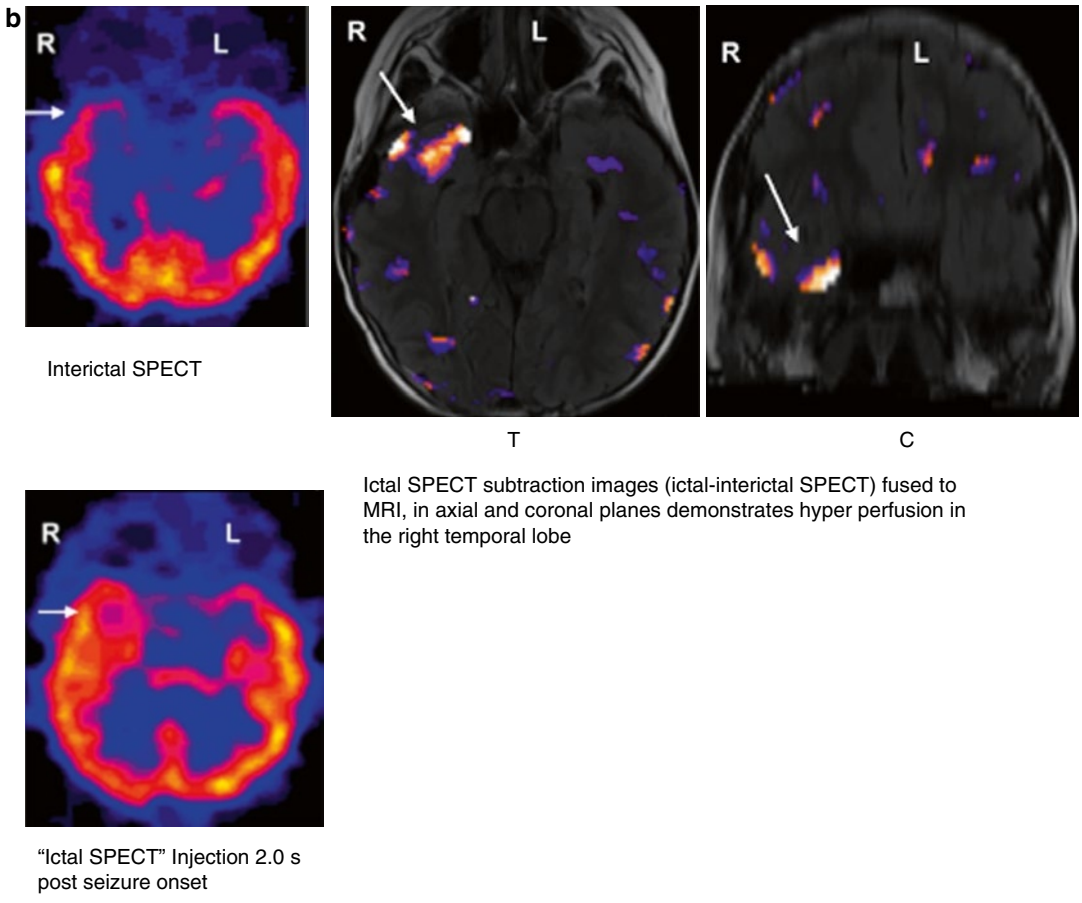

Fig. 4.11 (continued)

listing volumes of tracer to be injected at hourly intervals is placed next to the tracer and flushing syringe, so the nurse or physician can quickly determine the appropriate dose and proceed with the injection. Appropriately sized clamps within the device hold both syringes and another clamp is attached to the IV pole. The tubing is connected so that the saline drip, the radiotracer and the saline flush converge together. It is important to ensure that there is no leakage of fluid and the connectors are tightly secured so that it tolerates the radiopharmaceutical bolus and the saline flush (Fig. 4.12a, b).

The apparatus is delivered to the patient's bedside by a nuclear medicine technologist. At that point the technologist transfers operations to a specially trained nurse familiar with radiation safety and administration of this tracer who will give ictal injections during a seizure event. The entire assembly is checked to ensure that all the connections are done correctly. The line from the injector is connected to the IV tubing and is temporarily closed with a clamp, which is released at the time of tracer administration. At the time when the seizure is detected, the nurse (after double-checking for the volume to be injected) releases the clamp and delivers a bolus of the appropriate volume of the tracer solution which is rapidly followed by the saline flush (usually 10 mL). Following injection, the nurse calls the NM technologist to arrange for patient transport to nuclear medicine, to monitor the area for radioactivity, and to remove the entire apparatus and any tubing.

Positron emission tomography scanning after the injection of ^{18}F-FDG has been widely

used to image regional cerebral glucose metabolism. Since patients must be scanned within minutes of ^{18}F-FDG administration, this technique is impractical for ictal studies. Therefore, the majority of FDG-PET studies in this population are obtained in an interictal state. During the interictal state, PET will generally demonstrate an area of reduced FDG uptake. However, if the patient develops a seizure during the FDG uptake period of 30–40 min, the PET will likely demonstrate focal increase uptake in the epileptogenic zone, particularly if the seizure occurred within the first minutes after FDG administration (Fig. 4.13). This is because during the FDG uptake phase, the blood pool still contains FDG levels sufficient to be taken up by epileptogenic cortex (Fig. 4.14). Interictal PET has a lower sensitivity than ictal SPECT (60 % versus 87 %) in patients with no detectable structural abnormalities.

Computer software allows us to highlight the differences between ictal and interictal perfusion brain SPECT. Subtracted images (ictal minus interictal SPECT) can be superimposed onto the patient's MRI to help pinpoint the seizure focus. This technique is most helpful when MRI scans do not show a structural abnormality [28–30]. However, although ictal SPECT may show the epileptogenic focus, the "epileptogenic zone" (e.g., an area of microdysgenesis) is typically larger than ictal SPECT defined epileptic focus and is delineated on interictal FDG PET (Fig. 4.15).

Typically, patients with intractable seizures are admitted for up to a week into the neuroscience unit under constant clinical, video,

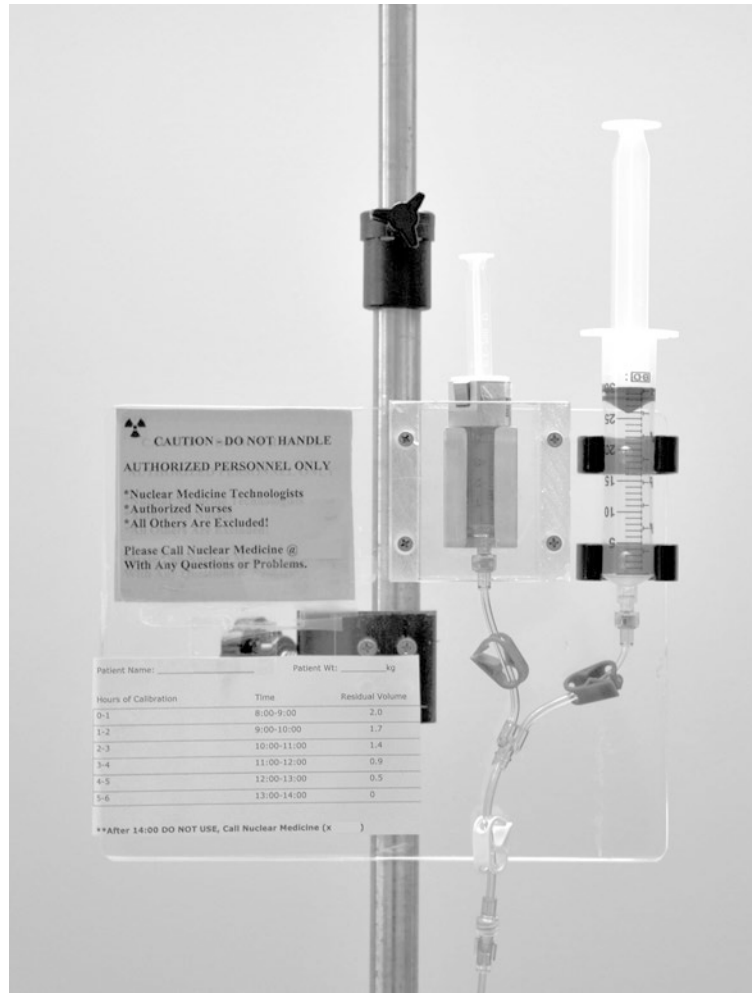

Fig. 4.12 (**a**) Photograph of the injector apparatus used for the ictal administration of the brain perfusion agent. (**b**) Diagram of the injector with explanation of the parts

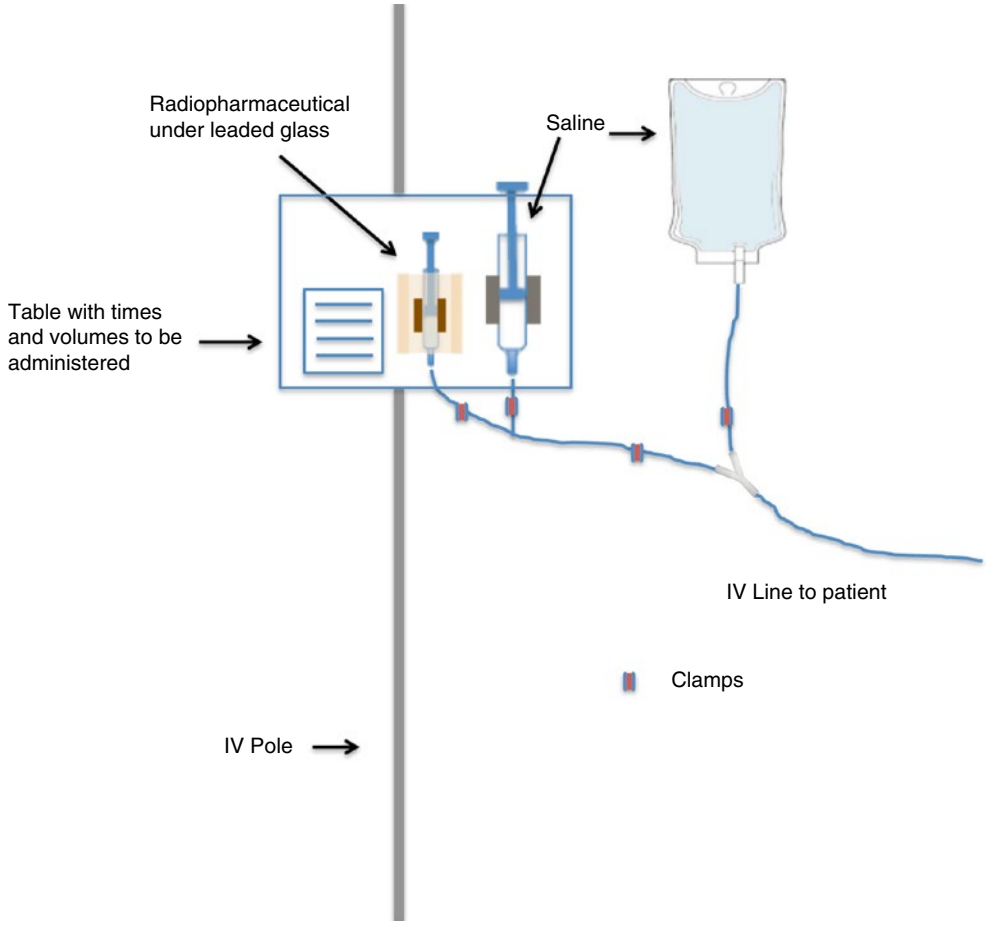

Fig. 4.12 (continued)

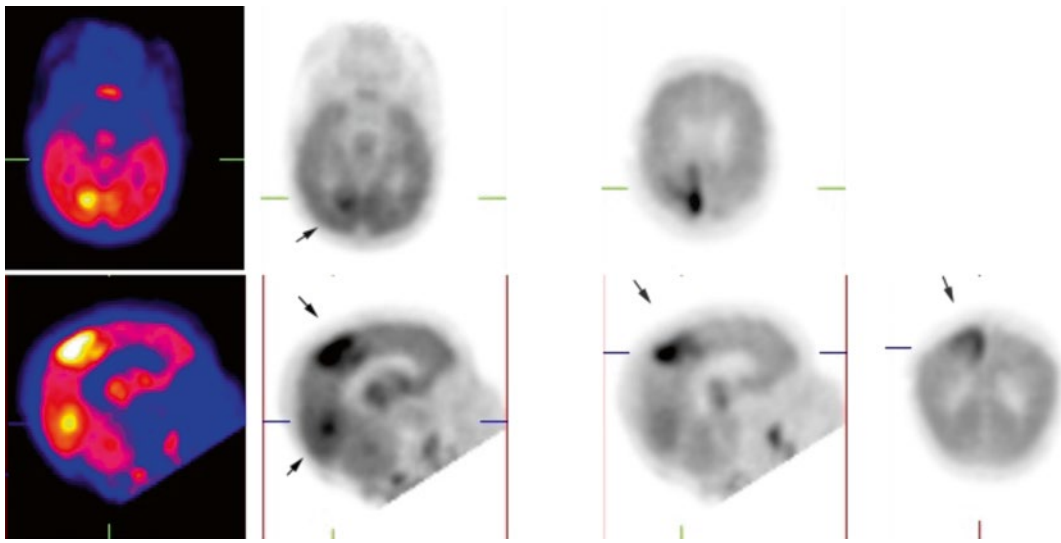

Fig. 4.13 Ictal FDG PET. Soon after the patient was injected with ^{18}F-FDG, he developed a series of seizures. At 1 h following tracer administration, the PET shows focal increased tracer activity within ictal regions in the brain. *Arrows* point to ictal activity in the brain

and surface EEG monitoring. The yield of true successful ictal SPECT requires the coordination of several groups. During the hospital admission time, the patient has an ictal and interictal perfusion SPECT and an interictal PET to assist in the presurgical evaluation. An alternative to ensure a higher yield of ictal injections would be to utilize the EEG signal at seizure onset to trigger the automatic injection of the tracer. In this scenario one would utilize a small automatic pump appropriately attached to the patient. This pump would contain a small volume of appropriately time-precalibrated radiotracer. Our group, in collaboration with members of the epilepsy department at Boston Children's Hospital and colleagues at Massachusetts Institute of Technology, has looked into the development of patient-specific automatic EEG seizure onset detection and the possibility that such seizure onset detection could trigger the injection of the radiotracer into the patient via small automatic injector pumps. Initial work reveals that the signal-processing portion of the research shows promise [31].

More invasive procedures, such as subdural or intraoperative depth electroencephalography (EEG), are utilized to guide surgical resection.

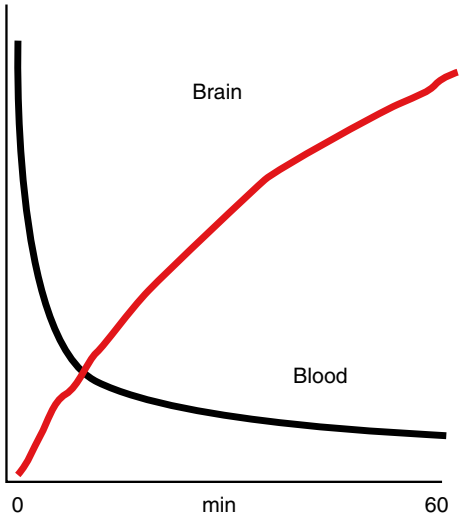

Fig. 4.14 Time-activity curves of FDG in brain and blood over 60 min. If the patient experiences a seizure after the injection of the tracer, blood levels of FDG are available for ictal uptake in brain

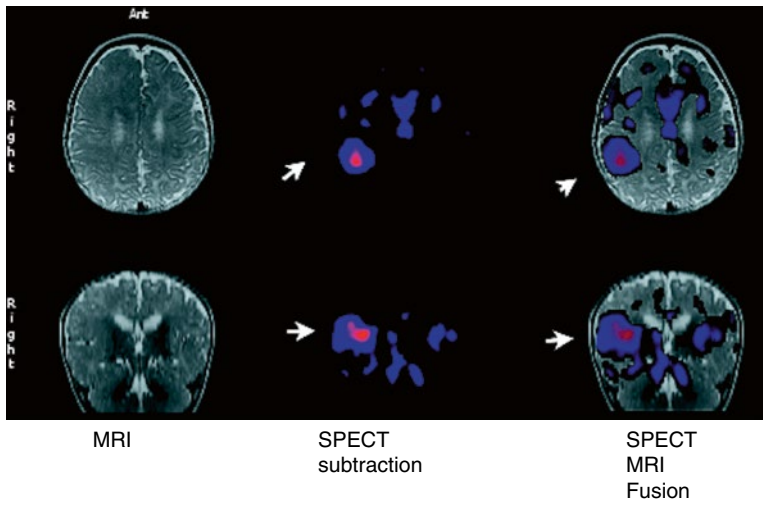

Fig. 4.15 Six-month-old boy with one to two spells/day since birth. More recently he developed five to six seizures in a row over a 2–5-min period, up to five to seven times per day. The electroencephalograph (EEG) was quite active during sleep. The MRI revealed an abnormal gyral pattern in the right frontal and parasylvian regions suggestive of "neuronal migration disorder." An interictal ^{18}F-FDG PET revealed generally decreased tracer uptake in the entire right hemisphere. An interictal ^{99m}Tc-ECD SPECT also revealed generalized decreased perfusion in the entire right hemisphere. An ictal perfusion SPECT showed focal increased perfusion in the right temporoparietal region. Subtraction of ictal and interictal SPECT reveals the regional changes in cerebral perfusion in the right parietal region that are fused with the MRI. *All arrows* point to ictal perfusion in the brain

These procedures are effective, but carry a risk of morbidity and even mortality.

Infantile Spasms

With this entity a characteristic pattern of flexion–extension seizures coming in clusters is associated frequently with profound developmental delay, despite treatment with anticonvulsants and corticosteroids [32]. Both SPECT and PET have been helpful in the assessment of patients with infantile spasms. Both have shown that in these patients several patterns of focal altered distribution of perfusion and glucose uptake can be found. Chugani et al. have identified a subgroup of children with infantile spasms who harbor focal cortical malformations or dysplastic lesions [33, 34]. In these patients FDG PET reveals marked, focal areas of cortical hypometabolism. These areas of functional abnormality, not seen on structural imaging, concur with electrographic abnormalities and can be treated by focal cortical resection.

Perfusion brain SPECT also shows striking focal cerebral perfusion abnormalities in infantile spasms. Abnormalities involve the temporal or parietal lobe but can involve the entire supratentorial cortex. These changes can be single or multiple and unilateral or bilateral. The extent and intensity of these abnormalities appear greater than is noted in most patients with other forms of partial epilepsy. In infantile spasms the PET and SPECT findings, when taken in conjunction with clinical and electrographic data, are suggestive of, but not specific for, the diagnosis [35]. Patients can reveal definite focal cortical ictal hyperperfusion. Activation of subcortical structures can be found in some cases. A diffuse pattern can be present on ictal SPECT. In patients who have a focal PET or SPECT abnormality, surgical resection is followed by marked improvement in seizure frequency and in some even a normal developmental course. Thus functional imaging has revealed a previously unsuspected abnormality in these children and has influenced the development of a therapy with the possibility of alleviating the otherwise dismal developmental outcome (Fig. 4.6) [34, 36–39].

Tuberous Sclerosis

Multiple cortical tubers are characteristic of tuberous sclerosis complex. Seizures often originate from a single tuber, making excisional surgery a therapeutic option for intractable patients. In certain cases these regions can be removed surgically in the hope of providing better seizure control and improving developmental outcome. Ictal and interictal perfusion SPECT can help identify an area of the brain from which seizures are originating. A SPECT may reveal regions consisting of comma-shaped areas surrounding hypoperfused areas in the candidate tuber. A PET or SPECT can be superimposed over corresponding MRI of the brain. In this way the brain's structure or specific tubers can be identified in terms of perfusion or metabolic activity. This aids the neurologist and surgeon in determining who might benefit from seizure surgery [40]. Studies using the PET tracer α-[^{11}C]methyl-L-tryptophan have found that epileptogenic tubers show increased uptake while nonepileptogenic tubers show decreased uptake (Fig. 4.16). PET is performed in the interictal state and can be very helpful to the epilepsy surgery team in selecting suitable candidates for surgery [41, 42].

Cerebrovascular Disease of Childhood

Although more common than previously realized, cerebrovascular disease in children is relatively much rarer than in adults and tends to occur in the context of an underlying anatomic abnormality (e.g., congenital heart disease) or systemic disease (e.g., sickle cell hemoglobinopathy) [43]. Perfusion brain SPECT is making contributions to our understanding of pathogenic mechanisms in a variety of the childhood cerebrovascular disorders.

Moyamoya Disease

Moyamoya is a rare disorder of uncertain etiology that leads to irreversible blockage of a main blood vessel to the brain as it enters into the skull. This disorder occurs predominantly in children and in adults during the third to fourth decades of life. Moyamoya is characterized by an angiographic pattern of supraclinoid internal carotid artery stenosis, followed ultimately by a luxuri-

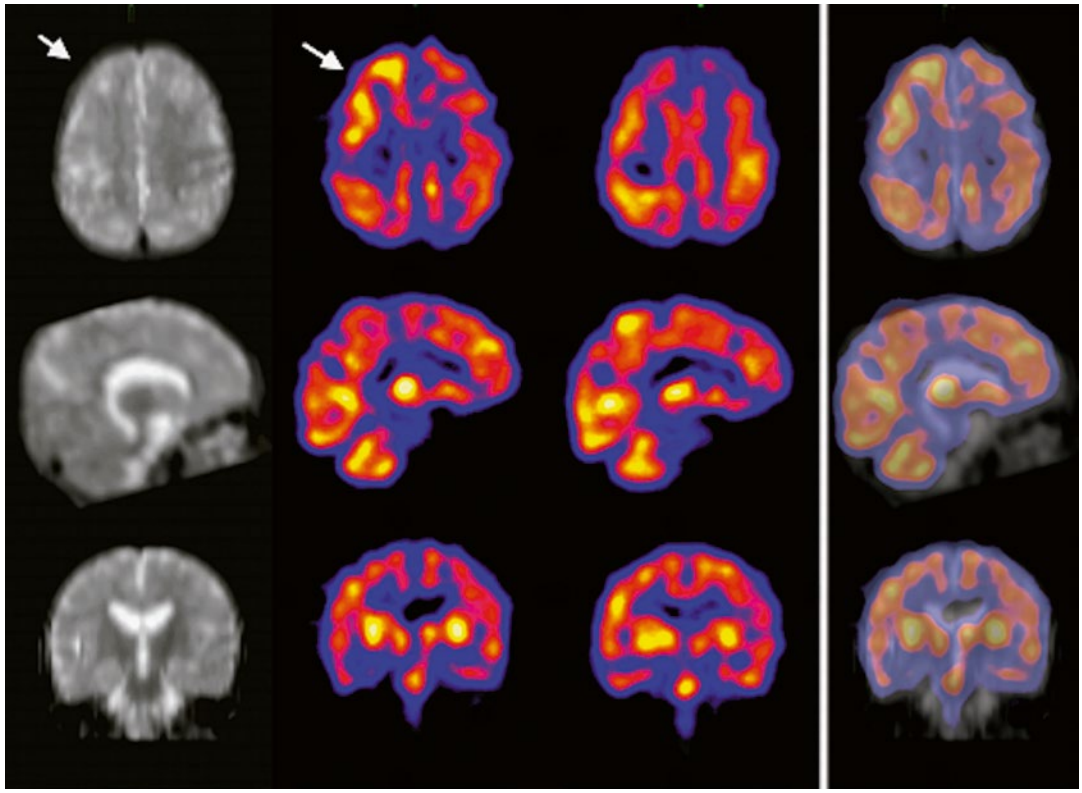

Fig. 4.16 Three-year-old boy with tuberous sclerosis and intractable seizure disorder. The MRI shoes multiple tubers. The interictal ^{99m}Tc-ECD perfusion SPECT reveals grossly irregular tracer distribution with apparent reduction within the tubers. The ictal SPECT reveals increased perfusion surrounding the tubers (*arrows*)

ant pattern of collateral vascularization. This angiographic appearance has been likened to a puff of cigarette smoke (from the Japanese translation) [44]. Moyamoya tends to cause strokes or seizures. Once the process of vascular occlusion begins, it tends to continue despite medical management. Repeated strokes can lead to severe functional impairment or even death. Surgery can produce good results. Therefore, it is important to recognize these lesions and treat them early. Serial cerebral perfusion studies using ^{123}I-IMP were found to document accurately the changes in cerebral blood flow that occur during the course of the disorder [45]. The SPECT abnormalities were partly congruent with MRI and CT findings but showed larger perfusion defects than those revealed by the other modalities. Hence brain SPECT offers an effective way of following the natural history of moyamoya disease, and its noninvasive nature may offer an attractive alternative to serial arteriography. Single photon emission computed tomography may play an important role in evaluating the success of proposed treatments for the disorder, such as superficial temporal artery–middle cerebral artery bypass [46].

Once a diagnosis of moyamoya is suspected by CT or MRI, the next step is usually an angiogram to confirm the diagnosis and to see the anatomy of the vessels involved. Often nuclear medicine studies such as SPECT are used to demonstrate the decreased blood and oxygen supply to areas of the brain involved with moyamoya disease. The neurosurgeon would decide what type of operation is best suited for the patient. Several operations have been developed to treat moyamoya. They have in common the objective of bringing blood to the brain by bypassing the areas of vascular obstruction. The moyamoya vessels and the involved brain are

very sensitive to changes in blood pressure, blood volume, and the relative amount of carbon dioxide in the blood. Studies using acetazolamide (Diamox) a vasodilator that increases cerebral blood flow (by 50–100 % within 20–30 min) are helpful in identifying the vascular reserve of involved territories before surgery. The lack of flow augmentation indicates a loss of autoregulation and inadequate vascular reserves (Fig. 4.17).

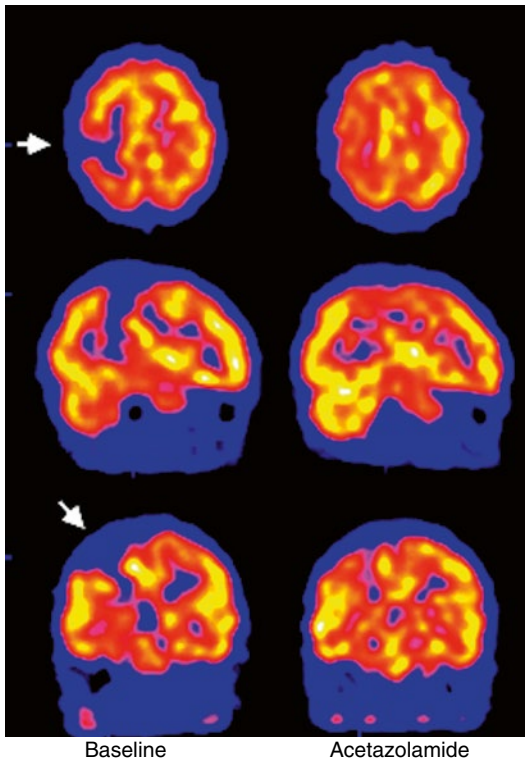

Fig. 4.17 Patient with moyamoya. The baseline ^{99m}Tc-ECD SPECT reveals markedly focal decreased perfusion (*arrows*). A repeat SPECT following the administration of acetazolamide reveals improved perfusion in the affected regions. This patient was considered a good candidate for revascularization

Other Forms of Childhood Cerebrovascular Disease

Using ^{99m}Tc-HMPAO SPECT, Shahar et al. described the scintigraphic findings in 15 infants and children presenting with a variety of cerebrovascular disorders [47]. They correlated these findings with clinical, EEG, and radiologic abnormalities. Focal rCBF changes were found in all patients. In some patients, SPECT abnormalities occurred in the absence, or before the detection, of radiologic changes. This experience is an example of the importance of SPECT as a sensitive early detector of functional brain abnormality in pediatric cerebrovascular disease (Figs. 4.18 and 4.19).

Alternating Hemiplegia

Alternating hemiplegia is a rare neurologic disorder that develops in childhood, usually before the age of 4 years. The disorder is characterized by recurrent but temporary episodes of paralysis on one side of the body as well as other transient neurologic symptoms affecting eye movements, limbs, or facial muscles. One form of the disorder, identified recently, has a favorable outlook. It occurs primarily at night, when a child awakens, and is apparently related to migraine. These children have no other mental or neurologic impairments. In more serious cases symptoms may include mental impairment, balance and gait difficulties, excessive sweating, and changes in body temperature. Seizures can occur. Sleep helps in the recovery from the periods of paralysis, but the paralysis can recur upon waking. There is frequently relief in response to the calcium-entry blocker flunarizine [48].

Perhaps reflecting the temporally fluctuating quality of the symptoms, brain SPECT findings by different groups of investigators in this entity have been variable and at times contradictory. Perfusion

Fig. 4.18 ^{99m}Tc-ECD SPECT in a child following a stroke

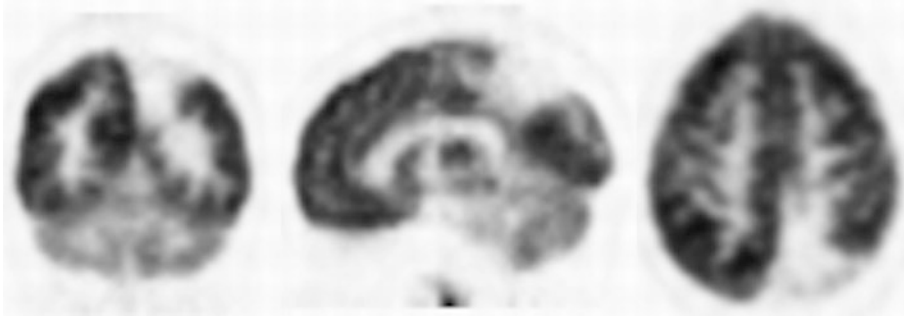

Fig. 4.19 ^{18}F-FDG-PET appearance in a patient with a rupture of an arteriovenous malformation

brain SPECT showed ictal hypoperfusion of the relevant hemisphere with interictal normalization [49]. Mikati et al. defined the familial occurrence and apparent autosomal dominant inheritance of this entity [50]. In this paper SPECT and EEG failed to show abnormalities of cortical perfusion during hemiplegia compared to nonhemiplegic periods. More recently, however, several patients with alternating hemiplegia have shown striking abnormalities in regional cerebral perfusion at both the cortical and subcortical levels. No characteristic distribution in the perfusion abnormality is evident so far in these patients, however.

Attention Deficit/Hyperactivity Disorder

Attention deficit/hyperactivity disorder (ADHD) is the most common neurobehavioral disorder in children, estimated to affect between 4 and 12 % of all school-aged children. The chief features of ADHD are inattention, hyperactivity, and impulsiveness, and this disorder is often associated with substantial impairments, including low self-esteem, poor family and peer relationships, school difficulties, and academic underachievement [51]. A series of studies by Lou et al. using ^{133}Xe suggested a pattern of hypoperfusion of striate and periventricular structures, with sensorimotor cortical hyperperfusion [52, 53]. This pattern tended to reverse after administration of methylphenidate, a commonly prescribed medication that improves attention and academic performance in some ADHD youngsters. This pattern is consistent with some neurophysiologic models of the disorder and with ^{18}F-FDG-PET studies in adult ADHD [54]. This study noted that four regions, primarily in the premotor and sensorimotor cortex, showed a significant decrease in local cerebral metabolic utilization of glucose, suggesting a corresponding regional dysfunction. In a later study in ADHD adolescents, glucose metabolism was significantly reduced in six brain regions, including the left anterior frontal lobe [54, 55].

SPECTs in children and adolescents with ADHD have shown regions of hypoperfusion in the temporal lobes, frontal lobes, and basal ganglia. These findings can be bilateral [56]. There are problems inherent in obtaining consistent imaging results in patients during rest, which may range from extreme stress in a hyperactive child to another in somnolence. Effective treatment of ADHD may be associated with increases in perfusion in the prefrontal cortex and caudate nucleus. In addition, it is difficult to obtain optimal controls, or the experimental groups are too small to yield statistically valid results [57–60]. A lot of work remains to be done in the investigation of changes detected in brain images in ADHD. The lack of a sufficient number of observations and studies with inadequate controls can yield contradicting or confusing results [59, 61, 62]. Functional MRI holds promise for future study of rCBF [58]. Infrared spectroscopy may be useful alternatives in some investigations [63, 64]. Both PET and SPECT will remain important primary means of evaluating the neuropharmacology of the brain [65, 66]. The focus of these techniques may be in the study and exploration of central catecholamines and dopamine receptors and dopamine release [67–75]. Other conditions that have been studied with SPECT and PET include childhood dysphasias, cerebral palsy, autism, schizophrenia, and depression [35, 37, 76–90].

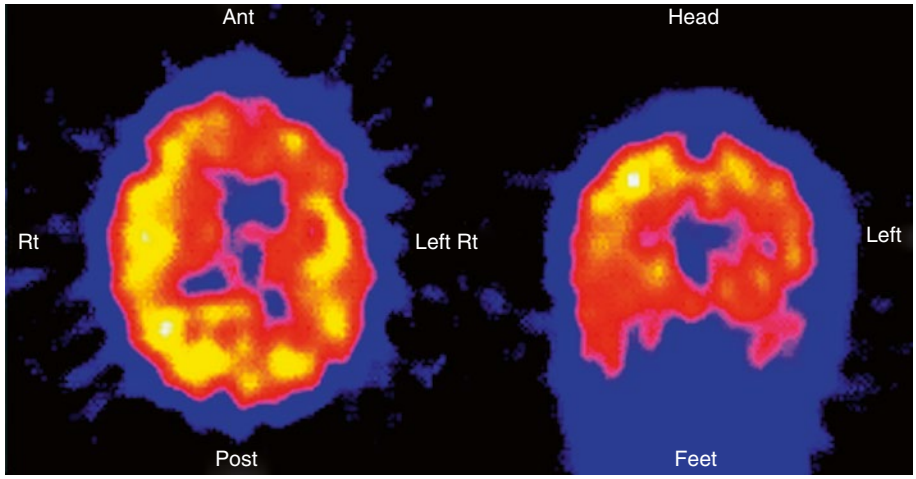

Fig. 4.20 Effect of hypothermia on regional cerebral blood flow. The ^{99m}Tc-HMPAO SPECT reveals marked hypoperfusion of the left frontal, temporal, and parietal regions

Complications of Extracorporeal Membrane Oxygenation

In newborns undergoing extracorporeal membrane oxygenation (ECMO) for refractory respiratory failure, perfusion brain SPECT has been used to investigate the status of cerebral perfusion following the surgical interventions associated with ECMO, involving permanent or temporary occlusion of the right common carotid artery or the major cervical veins. In 7 of 13 children, significant perfusion defects in either the ipsilateral or contralateral hemisphere were documented, whereas only two patients showed abnormalities on ultrasonography, CT, or MRI. SPECT can demonstrate rCBF deficits not detectable by structural imaging modalities that may be of major importance to the neurodevelopmental outcome of such infants [91]. However, although a normal SPECT scan is more likely to predict a normal neurodevelopmental outcome, an abnormal SPECT scan does not predict an abnormal outcome in these infants [92].

Effect of Hypothermia and Hypoxia

Surgical repair of complex congenital heart disease in very small children is possible today because of advances in anesthesia and techniques of hypothermia with hypoxia. This method, however, carries a risk of brain damage. A known complication of hypothermia with hypoxia is the choreoathetosis syndrome (CAS) [93]. We studied eight patients suffering from CAS following deep (<20 °C) hypothermic circulatory arrest or low-flow bypass during cardiac surgery during the neonatal period. Single photon emission computed tomography showed striking focal rCBF abnormalities at both the cortical (frontal, parietal, and temporal cortices) and subcortical (anterior basal ganglia) levels in seven of these eight patients. The distribution of the perfusion abnormalities was not predictable from clinical examination. In these patients, CT and MRI were normal or showed only generalized nonspecific abnormalities. These cerebral perfusion abnormalities may have important implications for developmental outcome in these children (Fig. 4.20) [94].

Developmental and Neuropsychiatric Disorders

Behavioral function studies with SPECT have been done predominantly using perfusion radiopharmaceuticals such as ^{133}Xe [52, 53, 57] and ^{99m}Tc-HMPAO. Oxygen-15 PET and ^{133}Xe SPECT can both allow multiple measurements in the same patient. A serious drawback of these methods, however, is that the patient must be in the field of view of the detectors while the tracer is administered. In this circumstance, multiple affective states, such as anxiety and anger, may exist at the moment of radiopharmaceutical injection, so "baseline" behavioral states cannot be assured

while imaging these patients. As mentioned above, the unique advantage of ^{99m}Tc-ECD and ^{99m}Tc-HMPAO is that once they are taken up, there is lack of significant redistribution within the brain.

Brain Tumors

Tumors of the central nervous system are the greatest challenge in pediatric oncology [95]. Worldwide, approximately 30,000–40,000 children develop CNS tumors each year, and the majority does not survive. Brain tumors are the second most frequent malignancy of childhood as well as the most common solid tumor in children. Brain tumors are the second leading cause of cancer-related deaths in children under age 20. Leukemia remains the leading cause of cancer-related deaths in children. Each year, approximately 4,200 children in the United States alone are diagnosed with a brain tumor [96].

The incidence of malignant brain tumors appears to have increased steadily over the past few years. It is not clear if this is due to a true increase in incidence, improved diagnosis, or increased reporting of cases [97]. Children, age 0–19, had the highest 5-year survival rate at 66 % between 1973 and 2004. That survival rate diminishes as age increases, down to 5 % for persons age 75 and older [98].

While approximately 60 % of children with brain tumors survive at least 5 years from the time of diagnosis, this figure has improved only slightly in the past 25 years. Approximately 50 % of brain tumors in children are infratentorial, with 3/4 of these located in the cerebellum or fourth ventricle. Common infratentorial tumors include cerebellar astrocytoma, medulloblastoma, ependymoma, brainstem glioma, and atypical teratoid/rhabdoid tumors. Approximately 20 % of supratentorial childhood brain tumors are in the sellar or suprasellar region and/or in other areas of the cerebrum or diencephalon (Table 4.2). These include astrocytomas, craniopharyngiomas, and diencephalic and germ cell tumors [99].

The presenting symptoms in brain tumors in children include headaches, seizure, vomiting, ataxia, visual problems such as diplopia or blurred vision, and school or behavioral problems (reading, concentration, memory, poor school attendance). The hope of new approaches to treatment of childhood brain tumors increases the importance of developing accurate methods for the accurate assessment of the viability and extent of the tumors and for the assessment of residual disease after therapy.

Table 4.2 Supratentorial tumors

Other supratentorial tumors
Low-grade cerebral hemispheric astrocytoma or glioma
High-grade or malignant astrocytoma
Mixed glioma
Oligodendroglioma
Primitive neuroectodermal tumor
Ependymoma
Meningioma
Choroid plexus tumors
Pineal parenchymal tumors
Neuronal and mixed neuronal glial tumor
Metastasis (rare) from extra-neural malignancies

From [99]

Imaging

The roles of nuclear medicine in the evaluation of brain tumors include diagnosis, localization and detection of local extent and metastatic disease, assistance with therapy planning, and follow-up and assessment of the effect(s) of therapy. The nuclear medicine techniques used for the assessment of brain tumors mainly include SPECT and PET.

Both MRI and CT have high sensitivity and specificity in the diagnosis of brain tumors in children. These techniques frequently cannot differentiate radiation effect from residual or recurrent brain tumor [100, 101]. Functional imaging (SPECT or PET), on the other hand, can detect the presence of active tumors. In combination with MRI, this ability is useful for diagnosing residual brain tumor following therapy and differentiating between recurrent tumor and radiation necrosis.

Image Fusion

Three-dimensional multimodality image registration and fusion are very important complements to brain SPECT and PET. By combining functional and anatomic information in the same

3D volume, image fusion of CT, MRI, PET, and SPECT images provides more accurate and precise localization of disease and assists with therapy planning and assessment [102]. Clinical applications of SPECT and PET in brain tumors include (a) assessment of degree of malignancy and staging, (b) treatment planning, (c) prognosis, (d) assessment of response to therapy, (e) detection of tumor recurrence, and (g) localization of ictal cortex in postsurgical seizures.

Radiopharmaceuticals

SPECT Radiopharmaceuticals. Tumor-avid agents are normally excluded from normal brain by the blood–brain barrier and concentrate in active tumor tissue. Current SPECT radiopharmaceuticals can image brain tumor activity, cerebral perfusion, and molecular localization and kinetics. These include agents for tumor localization. Currently, the most common agents in this group are ^{201}Tl (TlCl2) and ^{99m}Tc-MIBI. Thallium-201 is a potassium analogue. It enters the cell via Na^+/K^+ ATPase pump. It localizes in lung cancer, breast cancer, melanoma, lymphoma, glioblastoma, etc. Thallium-201 uptake correlates with Ki-67 (mitotic index) and PCNA (proliferating cell nuclear antigen, marker for S phase). It accumulates in gliomas in proportion to tumor aggressiveness. Thallium-201 has been used in differentiating benign from malignant tumors, tumor grading, response to chemotherapy, and differentiating necrosis from recurrent tumor [103]. Thallium-201 uptake can also be seen in recent hemorrhage, recent radiation, posttreatment granulation, neovascularity, and infection (Fig. 4.21).

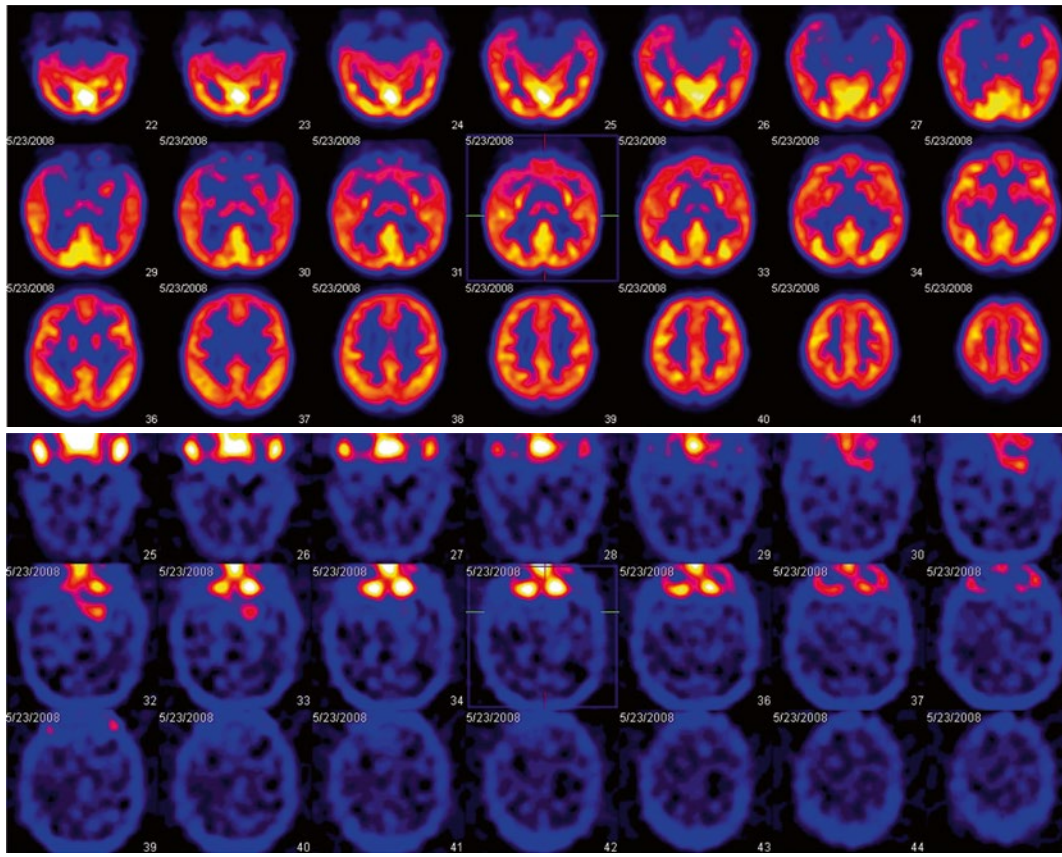

Fig. 4.21 Five-year-old boy with epilepsy and enlarging left temporal lobe mass on MRI. Brain FDG PET shows increased uptake in a left temporal lobe mass. Brain thallium SPECT confirms focal uptake in the left temporal lobe mass

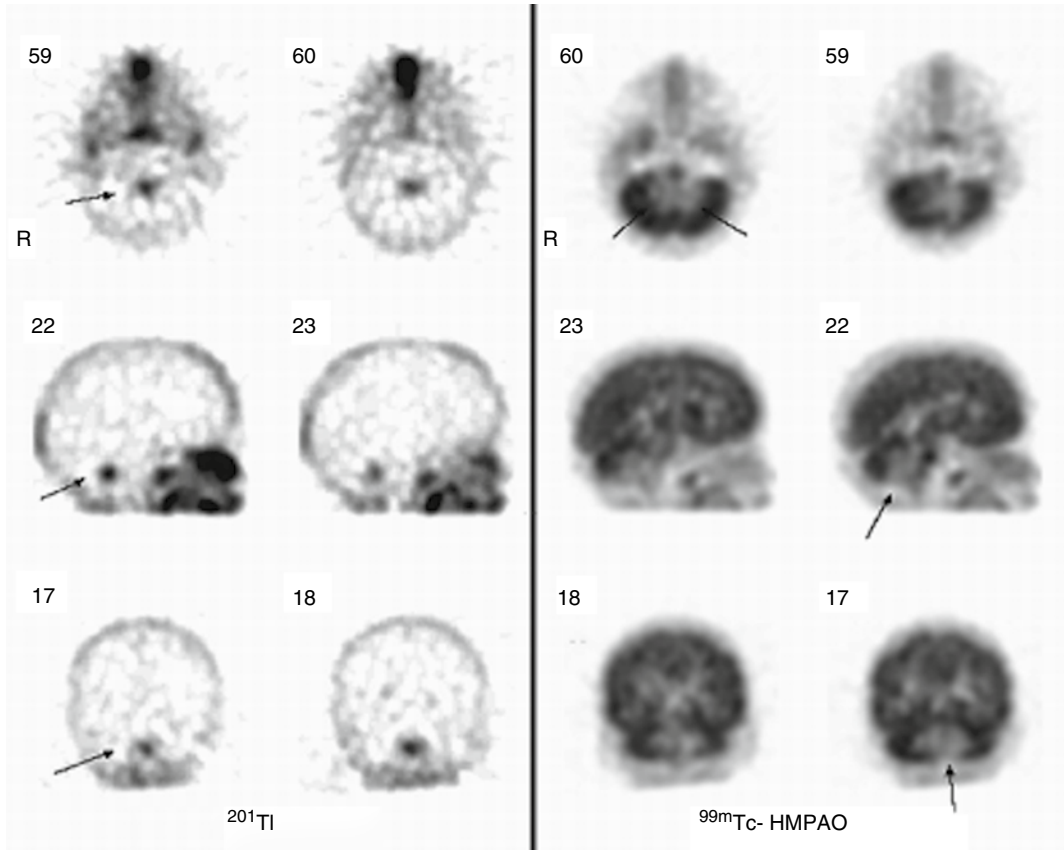

Fig. 4.22 Ependymoma in the posterior fossa in a 4-year-old boy. He was evaluated for the possibility of residual or recurrent tumor following a course of radiation therapy. Thallium-201 SPECT shows intense uptake of tracer in the tumor (*arrows*) (*left*). ^{99m}Tc-HMPAO SPECT reveals a well-defined region of decreased perfusion corresponding to the field of radiation therapy (*right*)

Technetium-99m-MIBI SPECT has been used to assess the viability of brain tumors in children [104, 105]. Technetium-99m-MIBI is a myocardial perfusion agent that has also been found to concentrate in several tumors including brain tumors. Its bio-distribution in brain tumors is similar to that of ^{201}Tl with two main differences. One difference is that it provides a higher photon flux resulting in better images. Early experience with ^{99m}Tc-MIBI SPECT for the assessment of brain tumor viability showed consistent uptake of this agent in brain tumors [105]. The tumor-to-normal brain ratio for tracer uptake of ^{201}Tl and ^{99m}Tc-MIBI exceeds those reported for the most tumor-avid PET agent, ^{11}C-L-methionine, or for the SPECT amino acid analogue ^{123}I-α-methyl-paratyrosine [106]. Another difference is that ^{99m}Tc-MIBI also localizes in the normal choroid plexus. This characteristic may prevent diagnosis of adjacent tumor activity. Choroidal plexus uptake of ^{99m}Tc-MIBI cannot be blocked by perchlorate (Figs. 4.22, 4.23, 4.24, 4.25, 4.26, and 4.27) [107–110].

Radiopharmaceuticals that image cerebral perfusion include ^{99m}Tc-ECD and ^{99m}Tc-HMPAO. These concentrate in normal brain as well as in some tumors are rarely used the assessment of brain tumors. Molecular imaging SPECT radiopharmaceuticals include ^{123}I-MIBG which can be used for the assessment of neuroblastoma metastasis in brain, ^{123}I-Tyrosine to image cell proliferation, ^{99m}Tc-Annexin V to image apoptosis and a_vb_3 receptor imaging in angiogenesis.

PET Radiopharmaceuticals. Currently, the most commonly utilized PET radiopharmaceuti-

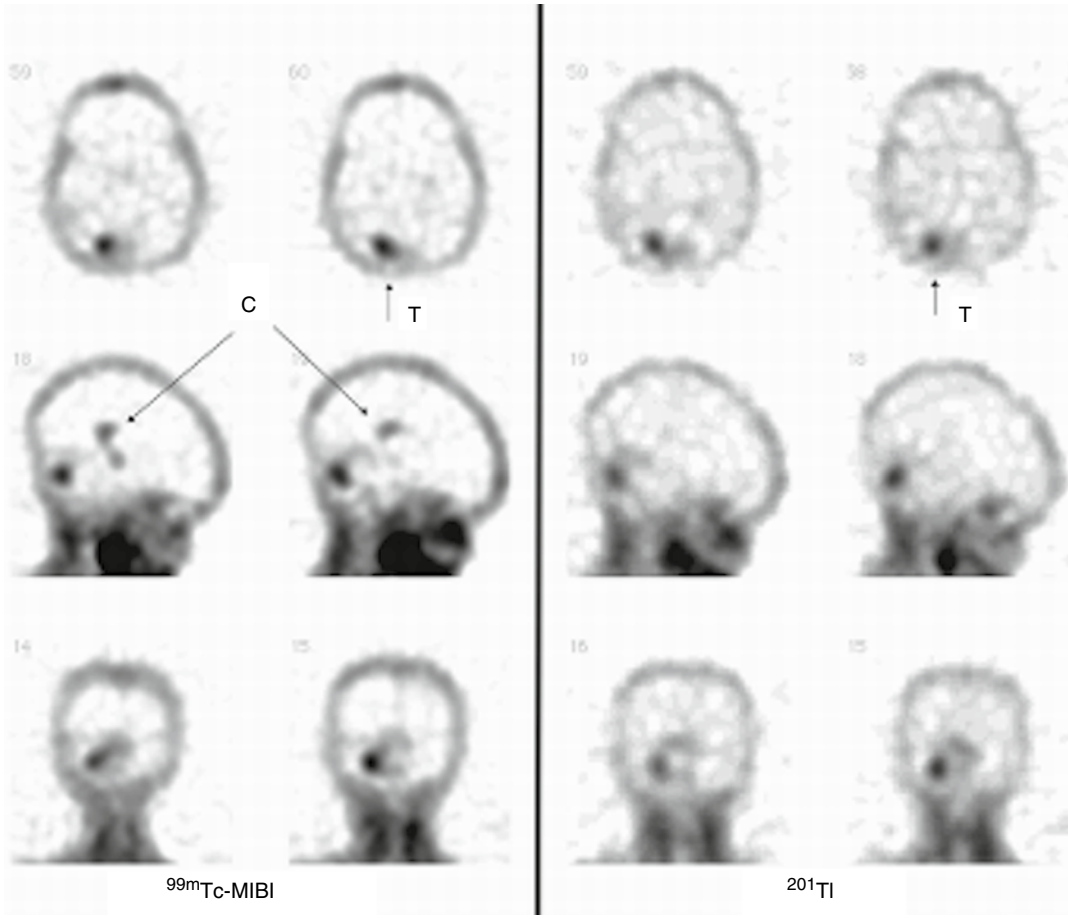

Fig. 4.23 Posterior fossa tumor. This 4-year-old girl had a partially resected cerebellar astrocytoma. *Left*: ^{99m}Tc-MIBI brain SPECT reveals an intense focus of increased tracer uptake in the posterior fossa corresponding to active tumor. In addition, there is normal ^{99m}Tc-MIBI uptake in the choroid plexus (*C*). *Right*: ^{201}Tl SPECT defines the region of active tumor. Unlike ^{99m}Tc-MIBI, however, ^{201}Tl does not concentrate in the choroid plexus

cal for the assessment of brain tumors is ^{18}F-FDG. Increased FDG uptake is seen in high-grade tumors. Factors that contribute to increased FDG uptake include the number of viable cells, tumor blood flow, hexokinase activity, inflammation/infection, and acute or subacute inflammation following radiation therapy. Decreased FDG uptake can be seen with low-grade tumors, necrosis, effective treatment, and chronic radiation therapy. As early as 1982, DiChiro et al. demonstrated that tumor glycolysis rate increases with high grade of malignancy and that the histologic grade of glioma correlated with glycolytic activity on FDG PET [111]. These authors found that 60/60 high-grade gliomas showed increased FDG uptake while in low-grade gliomas only 4/40 showed FDG uptake.

In a retrospective review of 58 biopsy-proven brain tumors, Delbeke et al. demonstrated that in 32 high-grade and 26 low-grade, both primary and metastatic, the sensitivity was 94 % and the specificity was 77 % of FDG PET [112]. Cutoff levels of 1.5 for the tumor-to-white matter FDG uptake ratio and 0.6 for the tumor-to-cortex ratio are useful in the differentiation of low-grade from high-grade gliomas with PET.

Evaluating response to therapy with FDG PET includes qualitative visual image interpretation after FDG uptake reaches a plateau. To reduce the effect of inflammation and edema

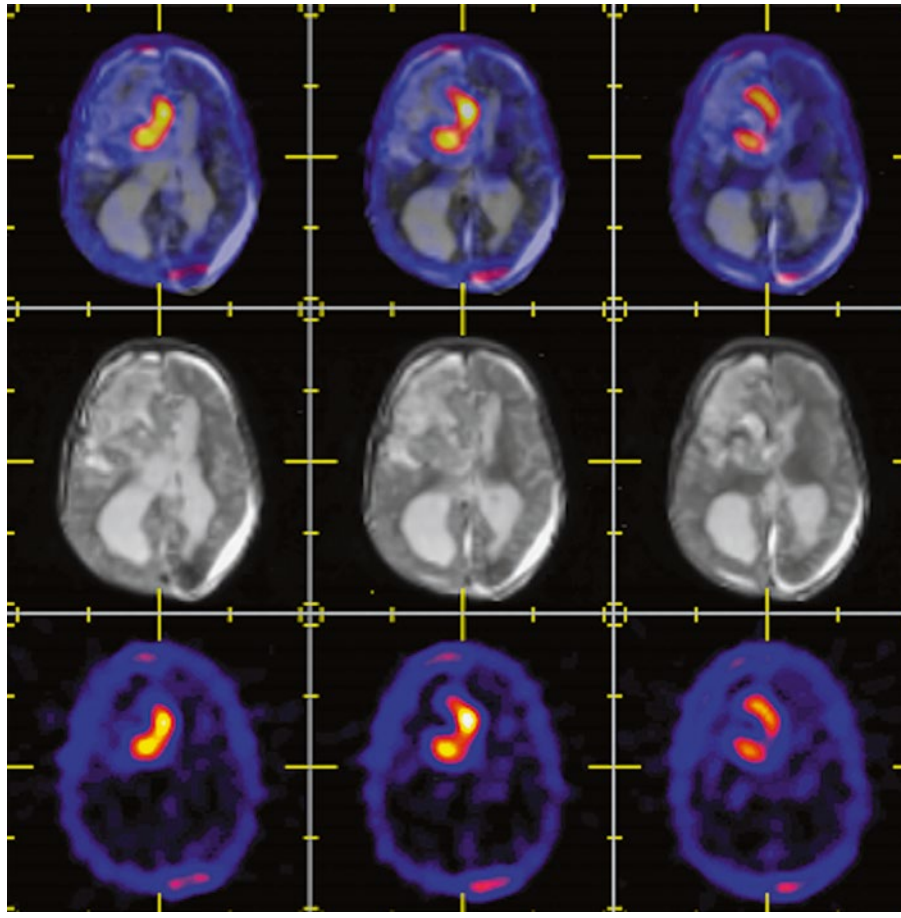

Fig. 4.24 Metastatic neuroblastoma in the brain. *Top row*: MRI/^{201}Tl fusion showing anatomic–functional relations. *Middle row*: selected MRI slices depicting extensive abnormality in the right frontoparietal region. *Bottom row*: selected ^{201}Tl brain SPECT revealing tracer uptake in the tumor (Images obtained with the assistance of I. Haboush and K. Mitchell)

post-therapy, PET is usually carried out approximately 3 months following therapy. Another approach is semiquantitative—that is, determination of the standard uptake ratio (SUV) or a "tumor-to-normal tissue ratio." Quantitative measure of local glucose utilization in mg of glucose per minute per 100 g of tissue would be useful, but this is not done in routine practice. Ideally, the assessment should be done on a 3D volume.

A major limitation of FDG in the assessment of brain tumors is the uptake of FDG in normal brain. This often prevents the detection and clear assessment of brain tumors. A method that can improve tumor lesion detection is the use of delayed FDG PET imaging. Normally, FDG imaging of the brain starts at 60 min following intravenous injection. It is often difficult to differentiate FDG uptake in tumor from normal cortex. Spence and co-workers have shown that the tumor-to-brain ratios increase if imaging is delayed for 3–4 h following tracer administration (Fig. 4.28) [113–115].

PET tumor agents that are normally excluded from the brain present a better alternative to FDG. In addition to FDG other PET agents relevant to the assessment of brain tumors include the following: ^{18}F-fluoroethyltyrosine (FET), ^{18}F-fluorophenylalanine (FDOPA), and

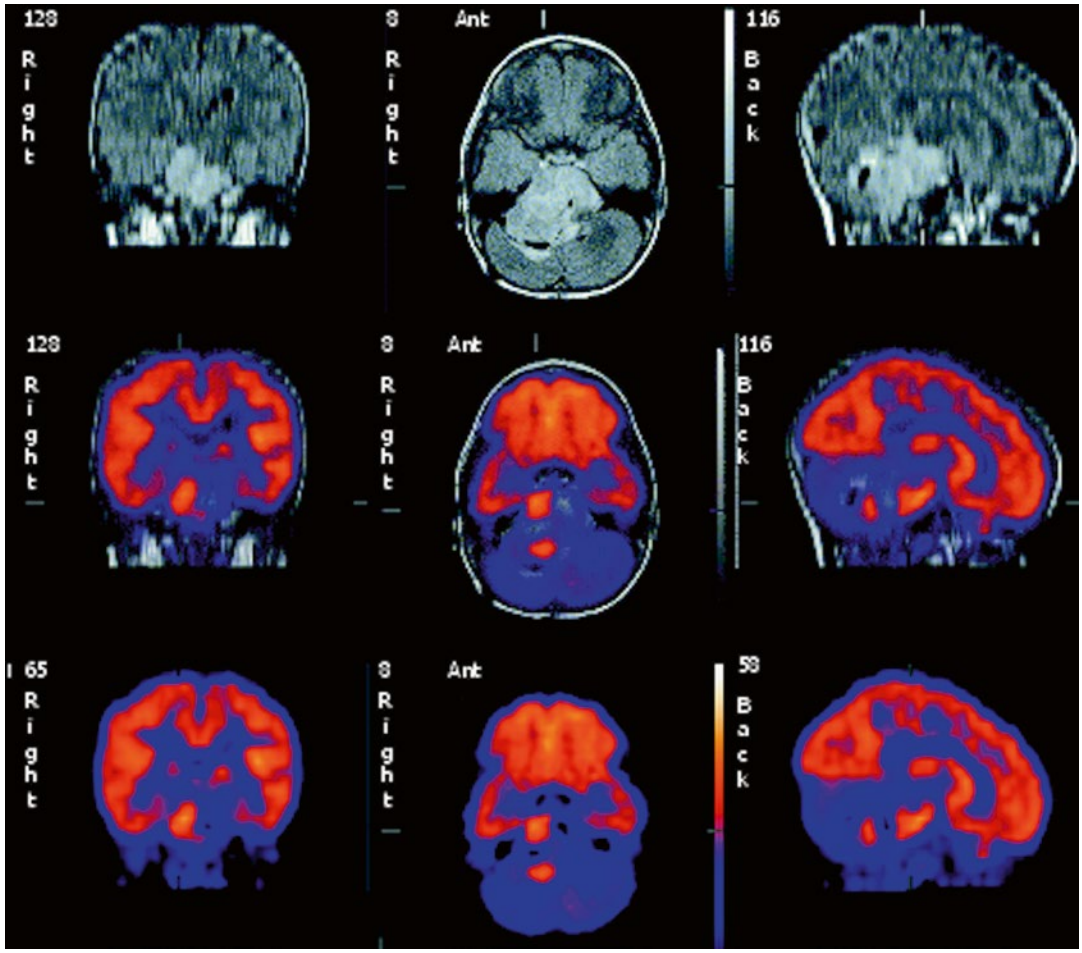

Fig. 4.25 Large brain tumor well seen on the MRI. Within the large tumor, there are two distinct foci of ^{18}F-FDG uptake that may indicate active residual tumor

^{11}C-methylmethionine. These agents depend on amino acid transport. Agents for cell proliferation include ^{18}F-L-thymidine (FLT), ^{18}F-fluorouridine, ^{11}C-choline, and ^{18}F-choline.

FLT was originally developed as an antiviral agent for the treatment of HIV. It is taken up into cells and phosphorylated via thymidine kinase 1 (TK). Its uptake is related to DNA synthesis and cell proliferation. FLT can be effective in distinguishing residual tumor from posttreatment fibrosis or necrosis after resolution of acute inflammation due to the treatment. FLT PET seems to be predictive of overall survival in treated patients with recurrent gliomas [116]. Comparing FDG and FLT, Van Waarde et al. demonstrated that FLT can be effective in differentiating tumor activity from inflammation in rats. Therefore, it is possible that posttreatment evaluation could be done earlier with FLT than with FDG (Fig. 4.29) [117].

FET is a brain tumor imaging agent that shows promise in the diagnosis and assessment of tumor response to therapy. In patients with suspicion of recurrent glioma, FET sensitivity was 93 % and specificity was 100 % [118]. Fluoro-DOPA labeled with ^{18}F has been shown to concentrate in active brain tumors and is more sensitive than FDG. Wei Chen and collaborators demonstrated excellent brain tumor images with fluoro-DOPA with a higher sensitivity (96 %),

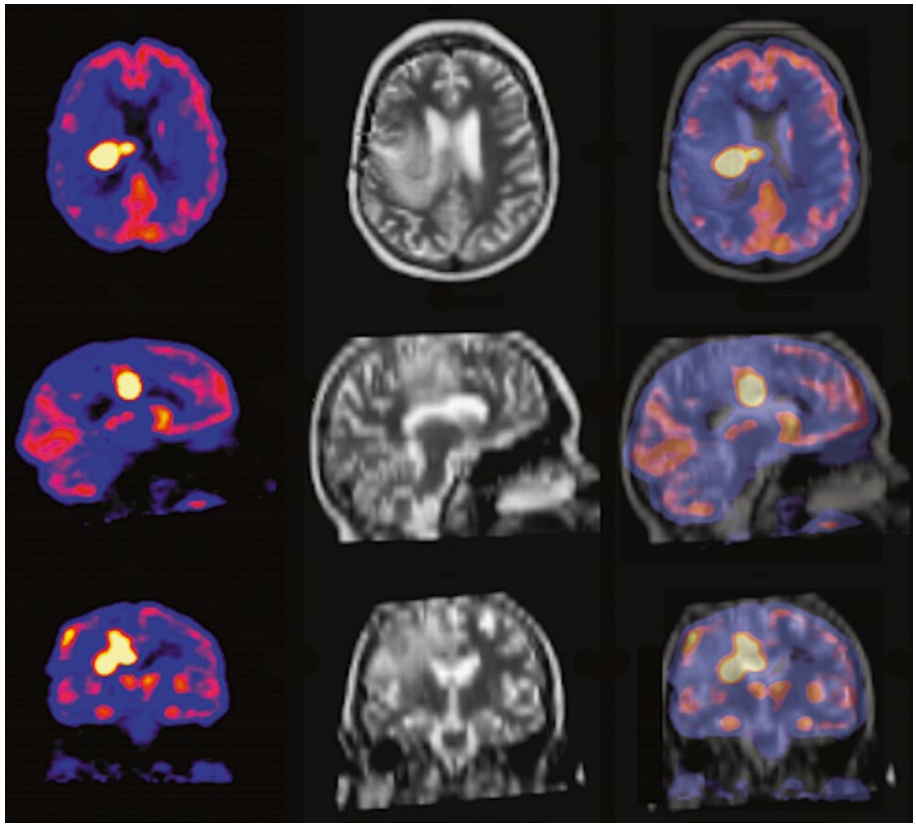

Fig. 4.26 Brain tumor showing intense uptake of ^{18}F-FDG. The tumor uptake is more intense than normal gray matter

higher positive predictive value, and higher negative predictive value than with FDG [119].

Assessment of tumor blood flow and hypoxia can be determined with ^{15}O-H_2 O, and ^{18}F-FMISO or ^{64}Cu-ATSM, respectively. Other radioisotopes that could be used to label promising molecules or compounds include ^{68}Ga (68 min, 830 keV), ^{124}I (4.2 d, 820 keV), and ^{94m}Tc (52 min, 1.0 MeV). The fundamental tracers ^{11}C (half-life = 20 min), ^{13}N (half-life = 10 min), and ^{15}O (half-life = 2 min) can be useful for neuro-oncologic assessments. However, they require on-site cyclotron and extensive on-site chemistry. Their use is limited to large research centers, and therefore, they are not amenable to routine clinical use. Nuclear medicine, including SPECT and PET, can be useful for planning surgery and radiation therapy and for the assessment of conventional and experimental chemotherapy treatments (Fig. 4.30) [120–124].

Postsurgical Seizures

Seizures may be present following tumor resection. These seizures may be new or they may be residual. In these cases, either perfusion SPECT or PET can be utilized in the localization of ictal cortex. For example, Fig. 4.31 shows an FDG PET in a patient that had seizures following resection of an anaplastic astrocytoma (Fig. 4.31). Ictal minus interictal subtraction SPECT can reveal areas of ictal cortex following tumor resection surgery.

Brain Death

Cerebral radionuclide angiography followed by planar scintigraphy with ^{99m}Tc-pertechnetate has been frequently used in patients with an equivocal clinical diagnosis of brain death. Experienced observers can make a satisfactory determination as to the presence or absence of cerebral perfusion (Figs. 4.32, 4.33, and 4.34).

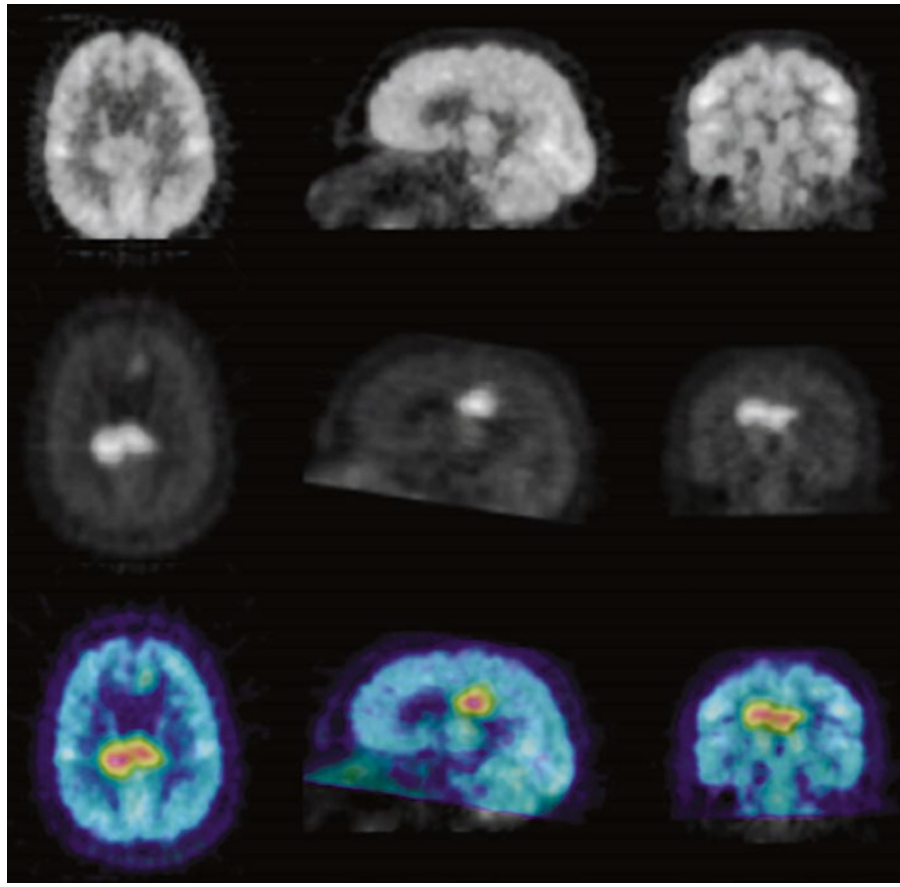

Fig. 4.27 Brain tumor: carbon-11 (^{11}C) methionine versus ^{18}F-FDG. *Top*: ^{18}F-FDG brain PET that faintly outlines tumor uptake. Tracer within the normal brain matter tends to make diagnosis of active tumor difficult. *Center*: ^{11}C-methionine brain PET shows the region of tumor activity quite clearly. *Bottom*: fused ^{18}F-FDG and ^{11}C-methionine PET (Courtesy of Dr. Alan Fischman, MD, PhD, Massachusetts General Hospital, Boston, MA, USA)

Single photon emission computed tomography using ^{99m}Tc-ECD or ^{99m}Tc-HMPAO, or radioiodinated amphetamine, has been used as an adjunct in the assessment of brain death [125]. It is probable that these radiopharmaceuticals allow superior definition of posterior fossa or subtler supratentorial perfusion abnormalities. Brain perfusion agents can be used for cerebral radionuclide angiography followed by planar scintigraphy or brain SPECT. In addition to the characteristic of perfusion agents for the assessment of the brain and the cerebellum, with them, one may obviate the need to repeat a study should there be equipment or other technical failure [126–128].

Radiopharmaceuticals

The development of SPECT and PET radiopharmaceuticals for imaging different aspects of brain function has been, and continues to be, the focus of considerable effort. But despite this effort, very few compounds have been approved for human use at this time [3, 129–131].

Perfusion Radiopharmaceuticals

Two ^{99m}Tc radiopharmaceuticals are used for the assessment of regional cerebral perfusion. The distribution of both of these compounds within the brain reflects rCBF. Tracer distribution is

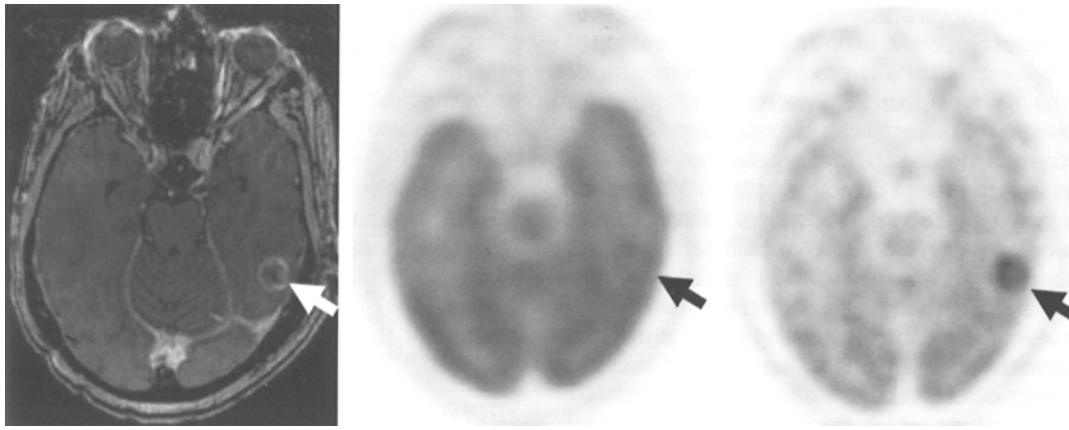

Fig. 4.28 A 69-year-old man with non-small cell lung cancer metastatic to the left temporal lobe 6 months after chemoradiotherapy, with increasing size on MRI (*left*); arrow indicates the lesion. Lesion SUVmax increased from 4.7 to 7.5 between early phase images (*center*) performed 1 h after FDG tracer injection and delayed-phase images (*right*) performed 5.5 h later. In contrast, the SUVmax of the surrounding gray matter decreased from 3.9 to 2.9. The change in the lesion to surrounding gray matter ratio over time was 146 %, compatible with viable metastasis as opposed to radiation necrosis (From Horky and Treves [115], with permission)

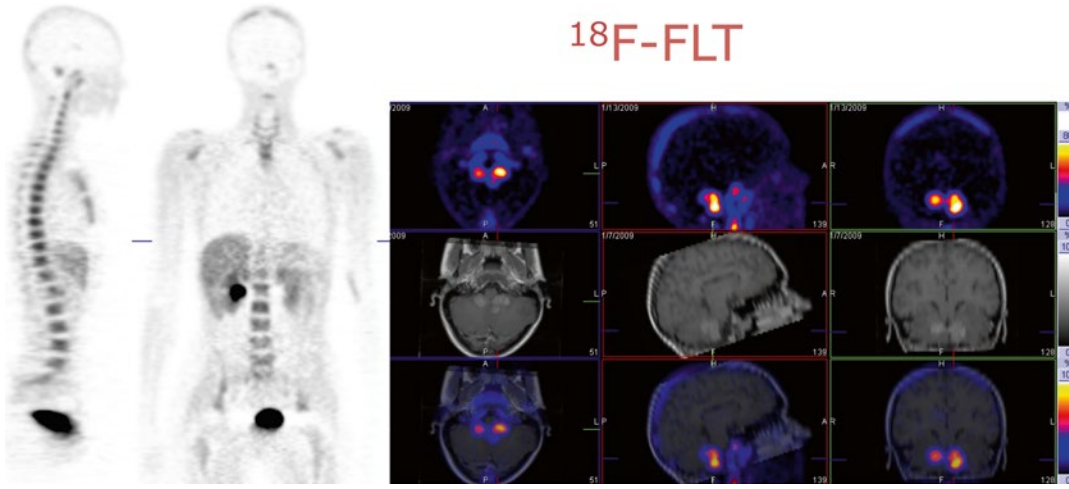

Fig. 4.29 ^{18}F-FLT in a patient with a brain tumor. The *left side* of the figure shows distribution of the tracer in the body (bones, kidneys, and liver, as well as within the brain tumor). The *right side* of the figure shows intense FLT uptake in the brain tumor

essentially fixed after uptake, and there is very little redistribution or efflux over a period of several hours. This combination of properties is important because it allows the tracers to be used to obtain a "snapshot" of rCBF at the time of injection.

Technetium-99m-ECD

Technetium-99m-bicisate, also known as ^{99m}Tc-ECD (Neurolite, Bristol–Myers Squibb Co.), is a neutral, lipophilic compound that rapidly concentrates in the brain following intravenous injection, with a total brain uptake of

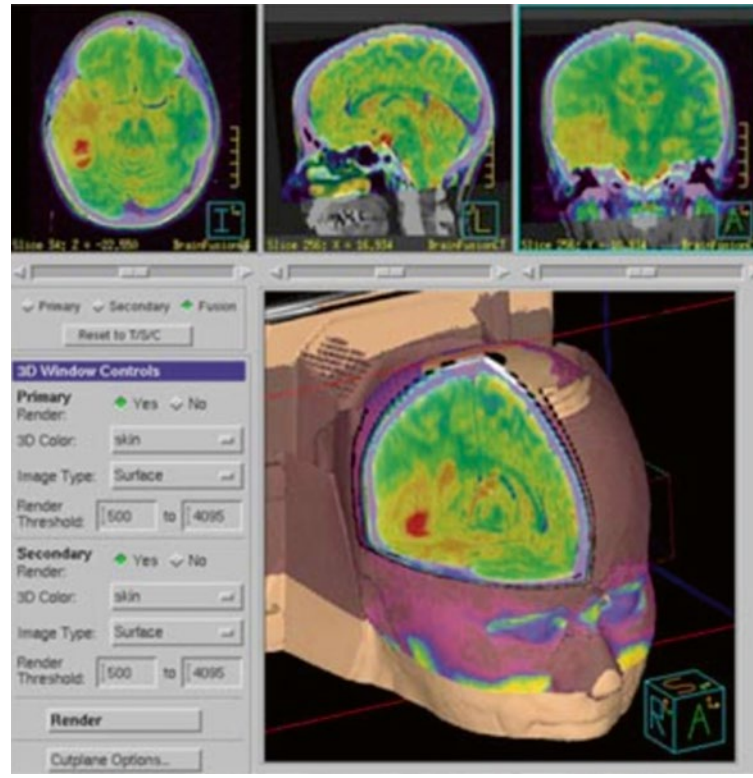

PET/CT, EBROC

Fig. 4.30 Surgical planning with PET/CT, EBROC (From [124])

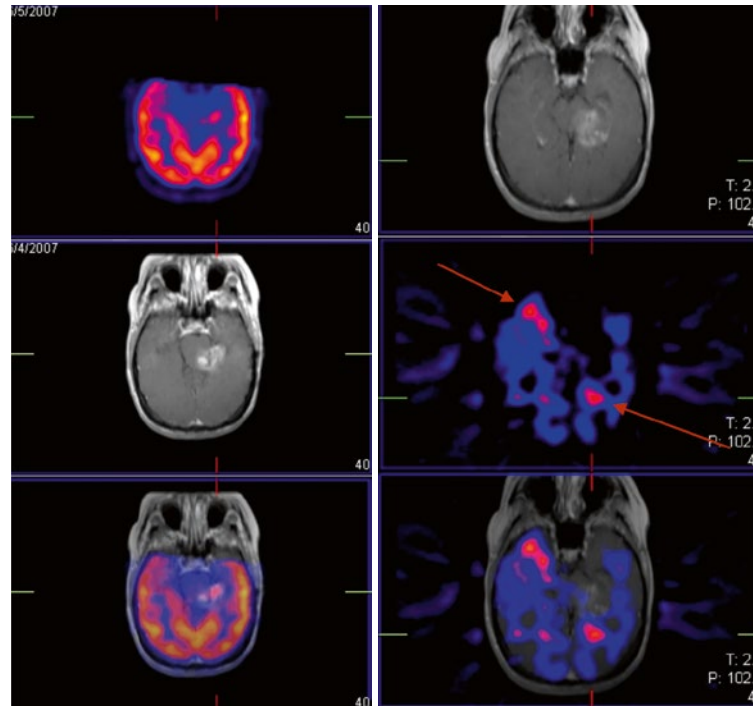

PET/MR

Ictal - inter-ictal
^{99m}Tc ECD SPECT/MR

Fig. 4.31 Seizures following resection of left temporal ganglioglioma, chemotherapy, and radiation in a 19-year-old patient

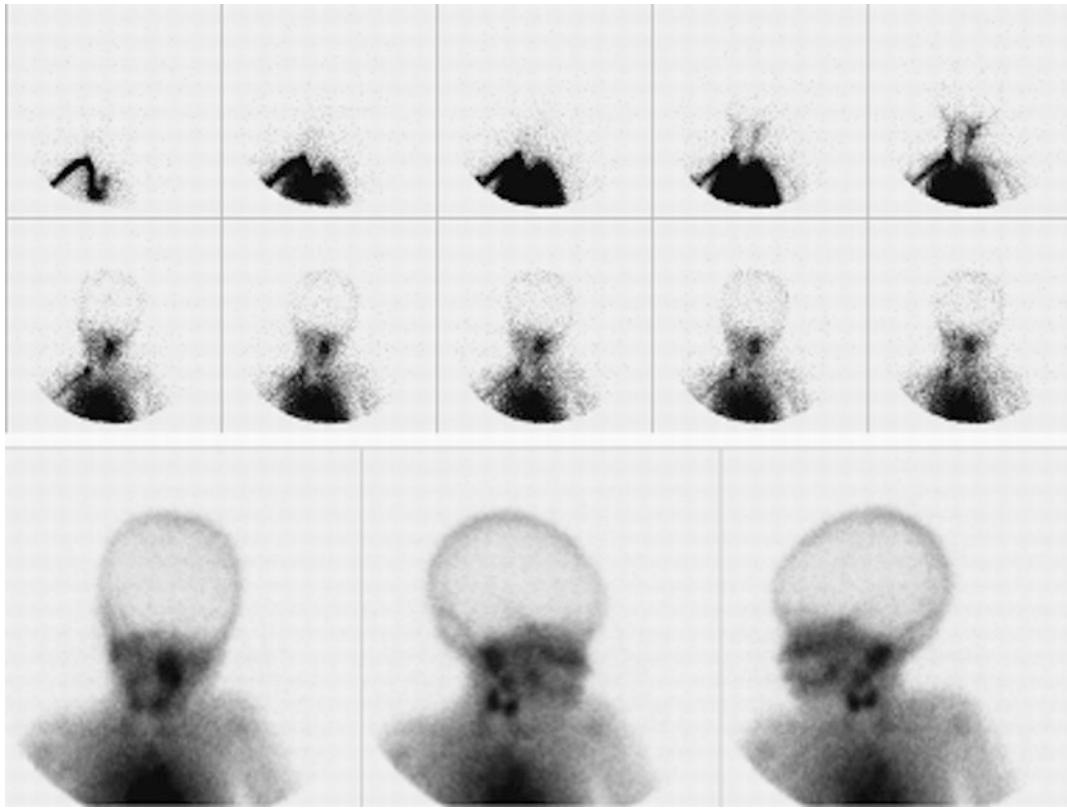

Fig. 4.32 *Top*: a ^{99m}Tc-pertechnetate cerebral radionuclide angiogram reveals no evidence of intracranial blood flow. *Bottom*: anterior and lateral images of the head confirm the absence of intracranial blood flow

approximately 6 % of the administered dose. The activity washes out of the brain quite slowly over time, which allows static imaging. The major organs of retention other than the brain include the gallbladder, kidneys, and liver. The primary route of excretion is the urinary tract, and approximately 50 % is cleared by the kidneys within the first 2 h after administration. Approximately 11 % of the tracer is eliminated via the gastrointestinal tract over 48 h. This agent has advantages over ^{99m}Tc-HMPAO: a longer (6-h) shelf life and more rapid blood clearance [132]. The longer shelf life provides for more clinical flexibility because the dose can be prepared ahead of time without concern about decomposition. Another favorable characteristic of ECD is the relatively lower uptake by soft tissues of the head as compared to HMPAO. ECD can be used to obtain ictal images of regional cerebral perfusion [25, 133, 134]. Certain paroxysmal disorders in which this technique might also be used include migraine or transient cerebral ischemic episodes.

Technetium-99m-HMPAO

Technetium-99m-exametazime, also known as ^{99m}Tc-HMPAO (Ceretec, Amersham Co., Arlington Heights, IL), is also a neutral lipophilic compound that is rapidly cleared from the blood after intravenous injection [135]. Brain uptake is 3.5–7.0 % of the injected dose within 1 min after administration. Approximately 15 % of the initial cerebral uptake is cleared within 2 min, and the rest is retained for 24 h. The remainder of the dose is distributed throughout the body, particularly in the muscles and soft tissues. Approximately 30 % of the administered tracer activity is found in the gastrointestinal tract a few minutes after injection, and approximately 50 % is eliminated by this route in 24 h. Approximately 40 % of the tracer activity is eliminated in the urine within

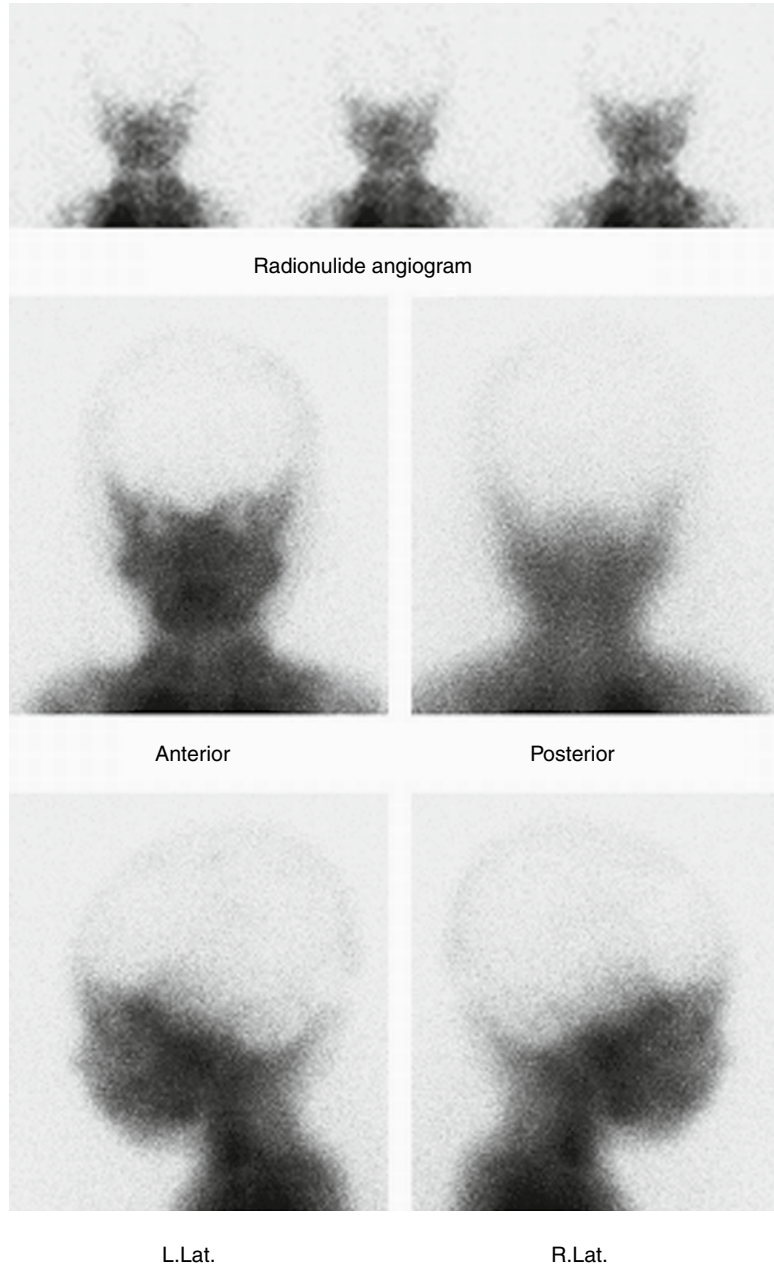

Fig. 4.33 Selected images from a ^{99m}Tc-ECD cerebral radionuclide angiogram (*top*) reveal no evidence of intracranial flow. Static images obtained following administration of the tracer reveal (*middle*) no evidence of tracer uptake in the brain substance. A SPECT (*bottom*) confirmed this finding. The patient was considered brain dead"

48 h. The original formulation of ^{99m}Tc-HMPAO was subject to radiolytic decomposition, which limited its shelf life to 30 min, but the current, stabilized version has a longer shelf life [136, 137].

Iodine-123–Iodoamphetamine

In the past, the radiolabeled amine *N-isopropyl-p-*^{123}I-iodoamphetamine (^{123}I-IMP, Spectamine) was used to evaluate cerebral perfusion during pediatric onset seizures. In contrast to ^{99m}Tc-HMPAO and ^{99m}Tc-ECD, ^{123}I-IMP undergoes substantial redistribution within brain tissue over time, which makes it less useful than the ^{99m}Tc rCBF agents for localizing seizure foci [138]. This radiopharmaceutical is currently not commercially available in the United States.

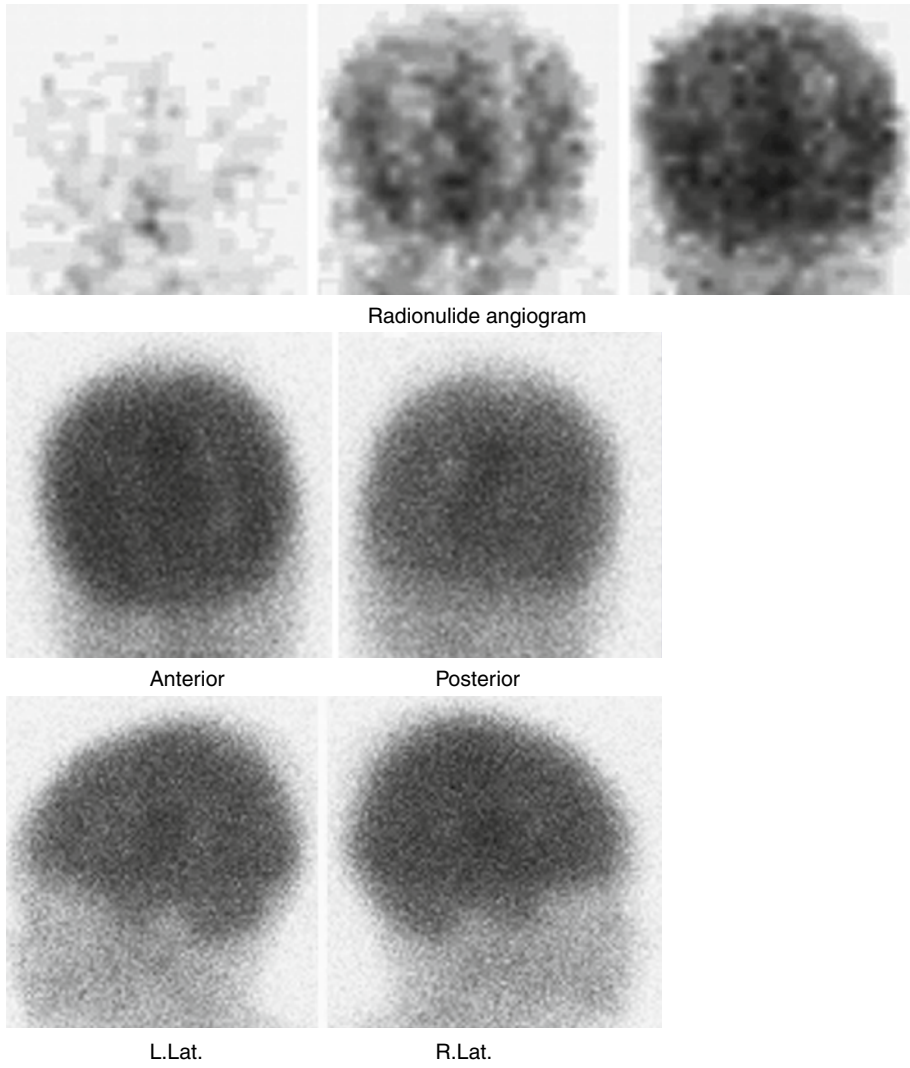

Fig. 4.34 This patient was being evaluated for the possibility of brain death. A ^{99m}Tc-ECD study reveals evidence of intracranial flow in the regions of the anterior and middle cerebral artery territories (angiogram, *top*). Four static images obtained soon after tracer injection reveal evidence of intracranial blood flow (*bottom*)

Xenon-133

Xenon-133 has been used for the characterization of rCBF, but it has fallen into disuse since the introduction of the ^{99m}Tc agents [139–141].

Tumor-Avid Radiopharmaceuticals

Fluoro-2-Deoxyglucose

The use of ^{18}F-labeled 2-deoxyglucose (^{18}F-FDG) has greatly expanded in recent years with the development of nationwide distribution networks that provide this agent to sites that do not have access to on-site cyclotrons. Fluorine-18 FDG accumulates in the brain (and elsewhere) as a function of glucose metabolism, which is typically increased in malignant tissues. It is, however, less than optimal for imaging brain tumors because its high uptake in the normal brain complicates the differentiation of tumor from normal brain [129]. It also accumulates in inflammatory lesions, which may complicate interpretation of post-therapy images [142].

Usual administered dose: 150 μCi/kg (5.5 MBq/kg) with a minimum dose of 1 mCi (37 MBq) and a maximum dose of 10 mCi (370 MBq).

Thallium-201

Thallium-201 (^{201}Tl), although primarily used as a myocardial perfusion agent (see Chap. 7), has also been used for imaging tumors, including those in the brain, where its low uptake in normal brain provides high contrast between the lesion and the normal brain [103, 143]. The tracer accumulates in active tumor tissue within a few minutes after intravenous injection and remains within the tumor for some time, allowing static imaging.

Thallium-201 accumulates in gliomas, medulloblastomas, and oligodendrogliomas and may be useful in evaluating the histologic grade of astrocytomas [144]. An important caveat to the use of ^{201}Tl for tumor imaging is that uptake may also occur in nonneoplastic lesions within the brain [145].

Usual administered dose: 0.03–0.05 mCi (1.11–1.85 MBq)/kg body weight; minimum dose 0.5 mCi (18.5 MBq), maximum dose 2.0 mCi (74 MBq).

Technetium-99m-MIBI and ^{99m}Tc-Tetrofosmin

Technetium-99m-MIBI (Sestamibi, Cardiolite, Bristol–Myers Squibb, N. Billerica, MA) and ^{99m}Tc-tetrofosmin (Myoview, GE Healthcare, Boston, MA) are lipophilic, cationic, ^{99m}Tc complexes that were developed as myocardial perfusion agents (see Chap. 7). As is the case with the myocardial perfusion agent ^{201}Tl, ^{99m}Tc-MIBI was found to accumulate in brain tumors, and similar behavior has been observed for ^{99m}Tc-tetrofosmin [146–148]. The ^{99m}Tc agents typically provide higher tumor-to-normal brain ratios and better definition of tumor margins than ^{201}Tl. Both tracers accumulate in the (normal) choroid plexus, which may complicate interpretation of paraventricular lesions [105, 148]. This uptake is not seen with ^{201}Tl.

Usual administered dose: 0.3 mCi (11.1 MBq)/kg body weight; minimum dose 1 mCi (37 MBq), maximum dose 20 mCi (740 MBq).

Carbon-11-Labeled Methionine

A promising radiopharmaceutical for imaging neurologic tumors is ^{11}C-labeled L-methionine (^{11}C-MET) [131, 144]. Its use, however, is limited to sites with on-site cyclotrons because of the short half-life of ^{11}C (20 min). Radiation-absorbed doses for these radiopharmaceuticals are given in Chap. 28.

Receptor-Specific Radiopharmaceuticals

The evaluation of receptor distribution within the brain is proving to be a valuable research tool, with a large number of studies targeting a variety of receptors and their functional response to various disease states. Virtually all of these are PET studies carried out in the research setting, primarily with ^{11}C-labeled analogues of known receptor agonists and antagonists. The success of the ^{18}F-FDG distribution network has prompted efforts to develop ^{18}F-labeled versions of several of these tracers, but none of these are commercially available at this time.

Iodinated agents (^{123}I) have been developed which target several different neuroreceptors including γ-aminobutyric acid (GABA) and dopamine [149]. At the present time, however, none of these compounds are commercially available in the United States.

Developing ^{99m}Tc receptor-specific radiopharmaceuticals is even more challenging because of the need to incorporate a chelating agent into the molecule without disrupting receptor binding. A ^{99m}Tc-labeled dopamine transporter (DAT) agent has been developed, but it is not commercially available at this point [150, 151].

Radiopharmaceuticals Normally Excluded from the Brain

Technetium-99m-pertechnetate, ^{99m}Tc-diethylenetriamine pentaacetic acid (DTPA), and ^{99m}Tc-glucoheptonate were used extensively in the past for cerebral radionuclide angiography (CRA) and planar brain imaging. However, these agents are seldom used now for this purpose.

Usual administered doses: 0.2 mCi/kg (7.4 MBq/kg); minimum dose 10 mCi (370 MBq), maximum dose 20 mCi (740 MBq).

Imaging Methods

Cerebral Perfusion SPECT

Image quality is dependent on meticulous attention to detail. It is especially important to ensure that the detectors are positioned as close to the head as possible and that patient movement is minimized. Care is taken to reduce patient anxiety about the intravenous injection of the tracer. Injection of perfusion tracers should be done in a quiet environment to minimize anxiety and distractions. A butterfly-type needle should be inserted intravenously and secured with tape. The intravenous line is kept open with normal saline. After a few minutes, when the patient is more relaxed, intravenous injection of the tracer should proceed. A few minutes after intravenous injection of the tracer, the patient is positioned supine on the imaging table. The patient's head should be positioned and firmly secured. Imaging preference is for a multi-detector gamma camera system or a dedicated system, and it should be equipped with ultrahigh-resolution collimators. An example of SPECT recording is as follows: Using a multi-detector system, each detector rotates 360° around the patient's head. Each detector acquires 128×128 images. Total imaging time is approximately 20 min. Very young children and children who are unable or unwilling to cooperate may require sedation. Sedation may affect brain activity and is usually given after injection of the tracer.

Methods for Perfusion Brain SPECT

1. Single controlled baseline study – To facilitate interpretation of results, it is highly desirable to attempt uniformity of conditions at the time of tracer injection. Care is taken to reduce to a practical minimum: patient anxiety, sensory stimulation, and motor activity, as these factors alter the rCBF and therefore the perfusion patterns on brain SPECT. Thus it is essential to ensure that the procedure is explained and the intravenous access established in advance. From a few minutes before until at least 5 min after tracer injection, the patient should be encouraged to engage in a simple task, such as staring at a spot on the wall of a quiet, dimly lit room. Image recording may proceed thereafter.
2. Ictal study – This study is best performed in collaboration with a specialized epilepsy unit offering constant EEG monitoring and video-telemetry. Intravenous access is established. As soon as possible after the onset of seizure activity, an appropriate dose of tracer is given. Preferably, the tracer is administered during the actual ictal event. SPECT may begin a few minutes later, or it may be delayed until seizures are under control.
3. Activation study – This type of study is conducted in the same way as the controlled baseline study, except that the patient is instructed to perform a specific task from a few minutes before until approximately 5 min after tracer injection. The task may involve repetitive visual, auditory, or somatosensory stimulation, a repetitive motor task, or a psychological test depending on the issue of interest. Such a study is exemplified by the work of Woods et al., and a useful general review has been provided by George et al. [83, 152].
4. Two studies in the same day – It is possible to perform two perfusion brain SPECT studies during the same day. The total dose is split such that one-third is given for the first study, and two-thirds of the dose is given for the second study. The second injection may be given immediately after the first SPECT, or it may be delayed for a few minutes or a few hours. Residual tracer activity from the first injection is present on the second SPECT, but it is overwhelmed to some extent. It is possible to subtract residual tracer activity, which requires decay correction, image reorientation, and registration. Final image and comparison may be enhanced by normalization and subtraction of registered images.

Radiopharmaceutical Dosimetry (^{99m}Tc-HMPAO and ^{99m}Tc-ECD)

1. Single-dose studies
   (a) Dose: 0.2–0.3 mCi (7.4–11.1 MBq)/kg body weight
   (b) Minimum dose 1.0 mCi (37 MBq)
   (c) Maximum total dose 10–20 mCi (370–740 MBq)
2. Split-dose studies
   (a) First study: 0.2 m Ci (7.4 MBq)/kg body weight
      (i) Minimum dose 1.0 mCi (37 MBq)
      (ii) Maximum dose 10 mCi (370 MBq)
   (b) Second study: 0.4 mCi (14.8 MBq)/kg body weight
      (i) Minimum dose 2.0 mCi (74 MBq)
      (ii) Maximum dose 20 mCi (740 MBq)

Tumor Perfusion SPECT

Approximately 5 min after intravenous injection of ^{201}Tl or ^{99m}Tc-MIBI, the patient is positioned supine on the SPECT imaging table with the detector(s) placed as close to the patient's head as possible. The patient's head is secured firmly, and then imaging continues exactly as for perfusion SPECT.

Cerebral Radionuclide Angiography and Planar Scintigraphy

For cerebral radionuclide angiography (CRA), the patient is given oral potassium perchlorate 6 mg/kg 30 min prior to tracer injection. Alternatively, sodium perchlorate is given at the time of injection when ^{99m}Tc-sodium pertechnetate is used. Perchlorate is not necessary if ^{99m}Tc-DTPA or ^{99m}Tc-glucoheptonate is used. The radiotracer is administered as a rapid intravenous bolus. The study is usually recorded in the anterior projection, with the gamma camera fitted with a high-sensitivity parallel hole collimator. The CRA is recorded at one frame per second for 60 s using a 128 × 128 matrix. Immediately after the CRA, planar scintigraphic static images, including anterior and lateral views, are obtained for 300,000–500,000 counts on a 256 × 256 matrix format.

Part 2: Cerebrospinal Fluid[1]

S. Ted Treves, Alvin Kuruc

Sensitive, elegant assessments of normal and abnormal cerebrospinal fluid (CSF) dynamics can be obtained with relatively straightforward planar scintigraphy. It is used as a diagnostic tool for disorders affecting the CSF. The introduction of CT and MRI has resulted in a significant reduction in the use of radionuclide cisternography [153]. The method continues to be used in conjunction with clinical examination, structural imaging, and other neurologic procedures in children to aid in the evaluation of selected clinical problems, such as evaluation of shunt function, assessment of the delivery of chemotherapeutic agents, localization of leaks, and in evaluation of the hydrocephalic patient. Radionuclide cisternography provides accurate quantification of CSF dynamics.

Cerebrospinal Fluid

Normal Cerebrospinal Fluid Physiology

Radionuclide cisternography permits observation of the flow, mixing, and absorption of CSF. Cerebrospinal fluid is produced primarily by the choroid plexus (CP), which is located within the lateral third and fourth ventricles. From here the fluid courses into the basal cisterns; it passes along discrete spinal and cranial subarachnoid pathways to its eventual destination over the

[1]Some of the concepts and portions of the wording in this part of the chapter were contributed by K. Welch, M.D., formerly professor of surgery at Harvard Medical School and chairman of the Department of Neurosurgery at Boston Children's Hospital, and by L.A. O'Tuama, M.D., who was coauthor of this chapter in the second edition of *Pediatric Nuclear Medicine*.

convexities of the cerebral and cerebellar hemispheres. Resorption into the systemic venous circulation occurs through the arachnoid villi and granulations [154, 155].

Although the transvenous pathway is thought to be the major route of CSF absorption, several studies suggest that lymphatic vessels associated with cranial and spinal nerves within the subarachnoid spaces provide an alternative pathway of CSF absorption [156, 157]. These accessory routes may also be important when the usual routes of CSF egress are compromised. Winston et al. reported that the surgical correction of orthopedic abnormalities in a child with congenital dysfunction of the spinal cord was followed by acute elevation of the intracranial pressure, perhaps reflecting interference with the spinal accessory pathway for CSF circulation [158].

The rate of CSF turnover is faster in children than in adults. As measured by ventriculocisternal perfusion, however, no significant difference has been noted between CSF formation in adults (0.37 mL/min) and children up to 13 years of age (0.35 mL/min) [159, 160]. Lorenzo et al. and Page et al. did note lower formation rates in newborns and younger children [154, 161].

It is firmly established that CSF is formed by a secretory process, as shown, inter alia, by the difference in electrolyte concentration between CSF and plasma ultrafiltrates [155, 162, 163]. Several discrete enzyme systems play a role in the formation process, primarily Na^+/K^+-activated adenosine triphosphatase (ATPase) but also adenylate cyclase and carbonic anhydrase [154, 164–166]. For comprehensive reviews of these topics, the reader is referred to authoritative reviews by Cserr, Netsky and Samruay, Milhorat, Wright, Davson et al., and Spector and Johanson [155, 167–171].

Abnormal Cerebrospinal Fluid Physiology

An imbalance between the normal rates of production and removal of CSF results in a progressive increase in the total volume of CSF, known generically as hydrocephalus. Hydrocephalus is caused by a relative obstruction of CSF absorption and, rarely, by overproduction.

Diminished Absorption

The most common cause of hydrocephalus in the neonate is congenital malformation. In infants and older children, hydrocephalus is caused by trauma, inflammation, bleeding, or intracranial tumor. In most cases, CT or MRI of the brain distinguishes extraventricular from intraventricular obstructive hydrocephalus. Difficult cases may be solved by radionuclide cisternography.

With hydrocephalus, there is an active, progressive increase in the size of spaces containing CSF. In infants, open sutures allow for an increase in the volume of the ventricles initially with little increase in intracranial pressure. A persistent increase in intracranial pressure ultimately results in atrophy of the brain. This condition is due to a reduction in cerebral blood flow, which results in cerebral hypoxia.

Various animal models of hydrocephalus have been used to study the pathophysiologic sequelae of CSF obstruction. For example, in adult dogs, chronic communicating hydrocephalus was produced by injection of kaolin into the subarachnoid space [172]. Most cases of hydrocephalus are due to a mechanism of impaired absorption. They may be further grouped as intraventricular ("obstructive") or extraventricular ("communicating obstructive"). With extraventricular hydrocephalus, there is a functional block to the circulation of CSF, and this mechanism is by far the most common encountered in children.

Overproduction

The rarest cause of hydrocephalus is an increase in CSF formation rates, associated with a tumor of the choroid plexus, either benign (papilloma) or malignant (carcinoma) [173]. A specific diagnosis of this condition can be provided preoperatively, as the choroidal transport of anions can be imaged as a prominent uptake of ^{99m}Tc-pertechnetate. It can be prevented by prior treatment with potassium perchlorate, a specific inhibitor of the anion uptake mechanism [107].

Method

Tracers used for radionuclide cisternography are confined to the CSF space and are quickly eliminated through the arachnoid plexus without being metabolized. Either ^{111}In-DTPA or ^{99m}Tc-DTPA is given in the subarachnoid space. Usual administered doses for ^{99m}Tc-DTPA are 0.3–1.0 mCi (11.1–37.0 MBq) and 0.05–0.20 mCi (1.85–74.0 MBq) for ^{111}In-DTPA. For routine cisternography in children, we prefer ^{99m}Tc-DTPA for its higher photon flux and lower radiation dose. The relatively short physical half-life of ^{99m}Tc is not an obstacle to the evaluation of CSF in children because it is distributed quickly [174]. In older children and adults, ^{111}In-DTPA is preferable. The radiation dose to the spinal cord and the surface of the brain with ^{99m}Tc-DTPA is about 1.0 rad per millicurie administered. The radiation-absorbed dose with ^{111}In-DTPA is approximately 2.5 rad/ mCi.

Careful technique is essential. The tracer is usually administered into the lumbar subarachnoid space. Other sites of injection include the cisterna magna or a lateral ventricle. Reported success rates for lumbar puncture vary considerably and clearly are highest with the most experienced operator. For this reason, we routinely request that the referring staff neurosurgeon inject the radiotracer in our department, with a nuclear medicine physician in attendance.

Following the subarachnoid administration of the tracer, an image of the injection site is obtained to establish the adequacy of the injection. Epidural injections typically produce a "Christmas tree" or a "railroad" appearance on the scintigraph, resulting in an unsatisfactory examination. Routinely, a series of images with the gamma camera are obtained in the anterior, posterior, and lateral projections at 2, 6, and 24 h after administration of the tracer. Because the turnover of CSF in children is more rapid than in adults, more frequent imaging may be necessary. A high-resolution, low-energy collimator is used.

For the evaluation of CSF leaks, more frequent images are obtained soon after administration of the tracer. This point is important in order to increase the chances of localizing the leakage. It is important that the patient be studied while there is active CSF leak in the position in which the leak is most profuse; otherwise, visualization of the leak by this method may not be possible. For this purpose, the patient is maintained in the position in which he or she may be known to leak most profusely, and images are obtained sequentially in the appropriate projection in an attempt to localize any extracranial activity. If extracranial activity due to a CSF leak is detected, the patient is imaged in other projections to allow for localization in three dimensions. The timing of the lateral and the anterior views is critical, as the CSF leak may be transient [174].

Small CSF leaks may not be detectable by scintigraphy. In some instances, it may be useful to place cotton pledgets in the nasal orifices; these pledgets should be changed and carefully labeled every 2–4 h and counted for activity. In some instances, it may be necessary to place small cotton pledgets in selected locations deeper inside the nasal cavity (e.g., over the orifices of drainage of the nasal sinuses) to determine the site of the leak. A CSF leak can be stopped with cotton pledgets [174]. Placement and maintenance of nasal cotton pledgets in children is difficult and in many cases impossible. An additional problem with pledgets is that tracers used for cisternography diffuse into the blood and may appear in nasal secretions. The pledgets should be weighed and counted, and the activity in the plasma measured. This practice helps account for normal nasal activity and to facilitate recognition of differences in absorption. Nose/serum activity ratios of less than 1.5 should not be considered indicative of CSF leak [175]. In some children, cotton pledgets were placed and maintained under general anesthesia in an attempt to localize a CSF leak. General anesthesia, however, tends to decrease or stop leakage of CSF [174].

Clinical Applications

Normal Radionuclide Cisternogram

On images at 2 and 6 h, the tracer can be seen as it migrates upward into the interhemispheric fissure and the sylvian fissure. By 24 h, the tracer can be seen over the convexity (Fig. 4.35).

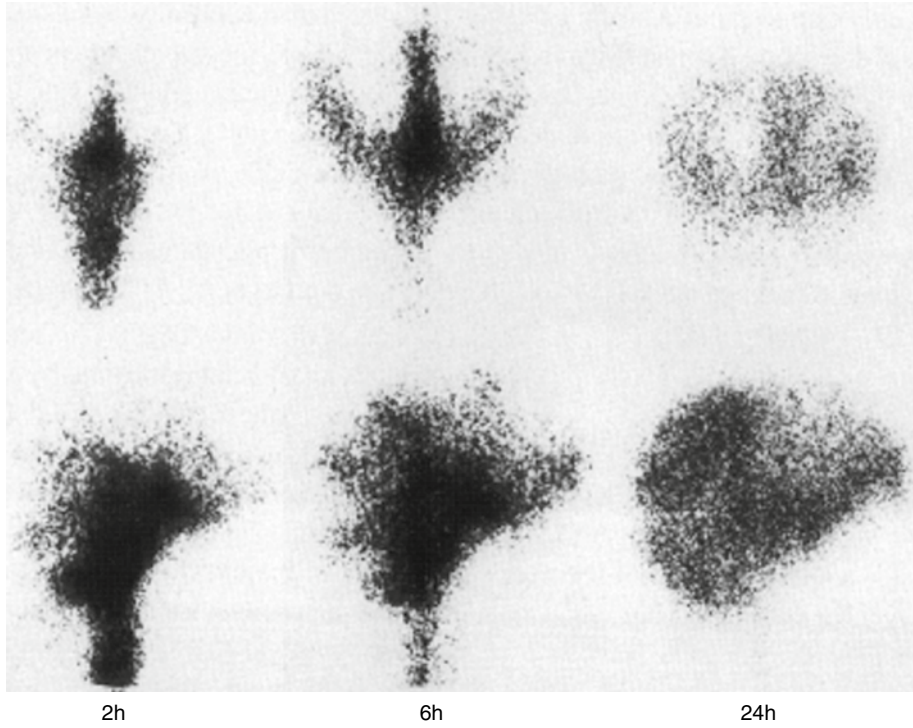

Fig. 4.35 Normal ^{111}In-diethylenetriamine pentaacetic acid (DTPA) cisternography. Anterior (*top*) and right lateral (*bottom*) images were obtained 2, 6, and 24 h after injection of the tracer into the lumbar subarachnoid space

Hydrocephalus

With communicating hydrocephalus (extraventricular obstructive hydrocephalus), the radiotracer circulates into the ventricular system and does not appear in the cerebral fissures and on the convexity. Persistence of the tracer within ventricles for more than 24 h is thought to indicate a progressive form of hydrocephalus that eventually needs shunting. In other instances of communicating hydrocephalus, a mixed pattern is seen; some tracer appears in the ventricular system and some in the fissures and over the convexity (Fig. 4.36) [157, 166, 176–178].

This pattern may indicate a partially compensated form of hydrocephalus, and these patients probably do not need CSF shunting immediately but must be followed carefully to detect any worsening. Radionuclide cisternography, however, has not been found to be a reliable test for determining the need for shunting in adults, and there is not enough experience with it in children [179–182]. It has been proposed that the pattern of turnover of tracer in CSF is a reflection of ventricular size and the increased volume of distribution of CSF [183]. This idea is in keeping with the poor correlations found by earlier investigators. In the preterm infant, Donn et al. used ^{111}In-DTPA radionuclide cisternography to delineate CSF dynamic abnormalities associated with posthemorrhagic, "ex vacuo," and postmalformational types of hydrocephalus [184]. Obstructive hydrocephalus is equated with intraventricular obstructive hydrocephalus. If intraventricular obstructive hydrocephalus is considered, the tracer is injected into a lateral ventricle. Hydrocephalus due to oversecretion of CSF is in most cases caused by a papilloma of the choroid plexus [173, 185–188]. Cerebrospinal fluid production rates of 0.75–1.45 mL/min in patients with papilloma of the choroid plexus have been measured [173, 189].

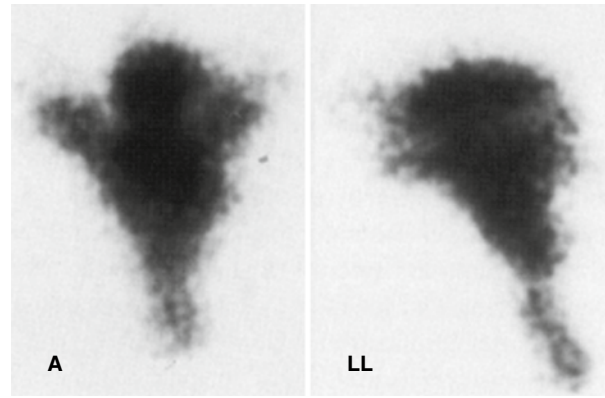

Fig. 4.36 Communicating hydrocephalus with intra- and extraventricular diffusion of tracer: ^{111}In-DTPA cisternography 2 h after injection. *A* anterior view, *LL* left lateral view

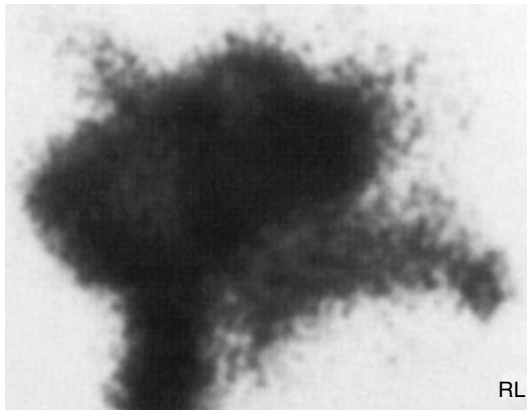

Fig. 4.37 Cerebrospinal fluid (CSF) leak, shown by ^{99m}Tc-DTPA cisternography. This right lateral view was obtained 4 h after injecting the tracer into the lumbar subarachnoid space. It is one of several images obtained every 15 min. Activity in the oropharynx due to a CSF leak is obvious. It was a posttraumatic leak through the fossa of Rosenmüller (Jaffe et al. [195], with permission)

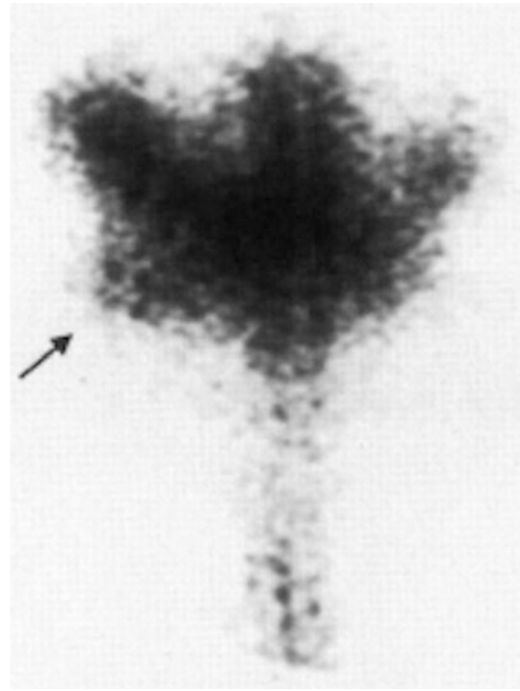

Fig. 4.38 Otorrhea, shown by ^{111}In-DTPA cisternography. This anterior view was obtained 4 h after injecting the tracer into the lumbar subarachnoid space. Extracranial tracer activity in the region of the right ear is visualized (*arrow*)

Cerebrospinal Fluid Liquorrhea

Cerebrospinal fluid liquorrhea is generally manifested by dripping from the nose or ear (Figs. 4.37 and 4.38). Profuse leakage suggests communication with a large cistern. If rhinorrhea is invariably unilateral, an opening into the nose or a paranasal sinus is suggested. If the side that drips alternates with position, a nasopharyngeal site, either directly or from the ear, is suggested. With CSF leaks, radionuclide cisternography reveals extracranial activity due to leak of the tracer outside the cranial cavity. Cerebrospinal fluid leak complicates up to one-third of fractures of the base of the skull. Most of these leaks cease spontaneously within a week. Meningitis occurs in about one-fourth of the patients if they are not treated with antibiotics [185]. Both rhinorrhea and otorrhea are amenable to investigation with radionuclide cisternography (Figs. 4.37 and 4.38) [176, 190–193].

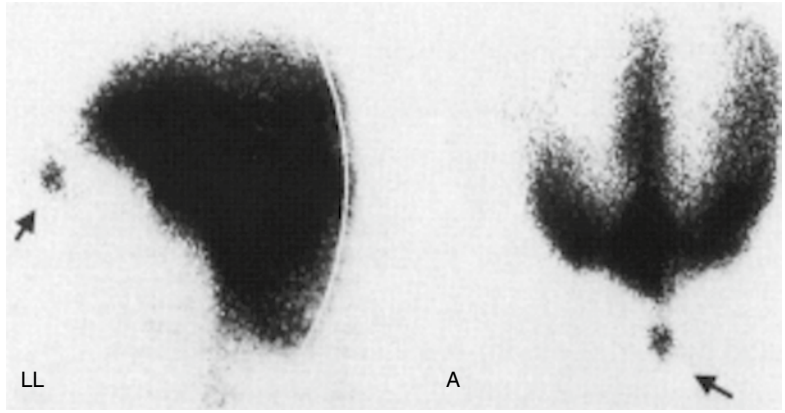

Fig. 4.39 Nasal encephalocele. ^{99m}Tc-DTPA cisternography, left lateral (*LL*) and anterior (*A*) views, obtained 4 h after injecting the tracer into the lumbar subarachnoid space. A pool of extracranial activity is visualized anteriorly, corresponding to a nasal encephalocele (*arrows*)

Contrast-enhanced CT cisternography has been found less sensitive than radionuclide cisternography for the detection of intermittent rhinoliquorrhea in children [194].

Loculations of Cerebrospinal Fluid

It is possible to have loculations of CSF in free communication with the subarachnoid pathways without loss of fluid to the external environment. Loculations of CSF appear on radionuclide cisternography as areas of accumulation and retention of the tracer over a relatively long period, for example, a nasal encephalocele or a subconjunctival loculation of CSF (Figs. 4.39 and 4.40) [195, 196].

Porencephalic Cyst

Porencephalic cysts are caused by infection, trauma, or vascular problems that result in localized atrophy of the brain. These cysts have a pia-arachnoid lining and communicate with a ventricle. Such abnormalities lead to stasis of the tracer on radionuclide cisternography, suggesting a one-way valve mechanism for the movement of CSF [197, 198].

Block of Spinal Cerebrospinal Fluid Flow

Tumors or other lesions in the spine, meninges, or spinal cord may cause blockage of CSF flow. They are seen on radionuclide cisternography as filling defects in which the radiotracer does not circulate or accumulate (Fig. 4.41) or as abrupt termination of CSF flow.

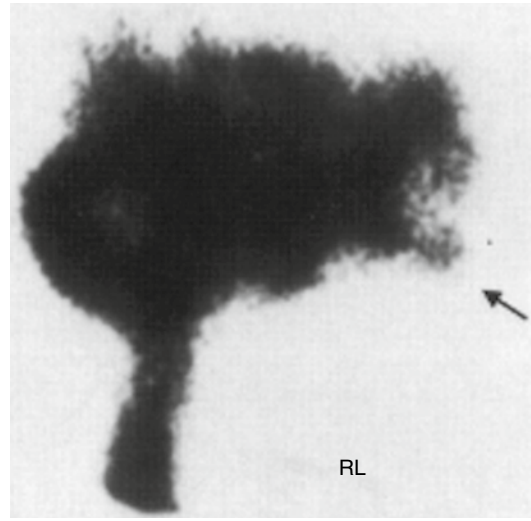

Fig. 4.40 Subconjunctival CSF loculation, shown by a right lateral view of an ^{111}In-DTPA cisternogram. There is focal extracranial tracer activity corresponding to a massive subconjunctival CSF loculation (*arrow*)

Cerebrospinal Fluid Shunts

Method of Assessment

Assessment of patency and quantitation of flow through CSF shunts can be made with radionuclide techniques in a rapid, safe, and accurate way. Technetium-99m as pertechnetate in a dose of 0.25–0.50 mCi (9.25–18.50 MBq) in a volume of 0.01–0.02 mL is used.

The patient should rest in a horizontal position for 30–60 min before the study so as to enable the measurement of shunt flow at baseline CSF pressures. The patient is positioned under the

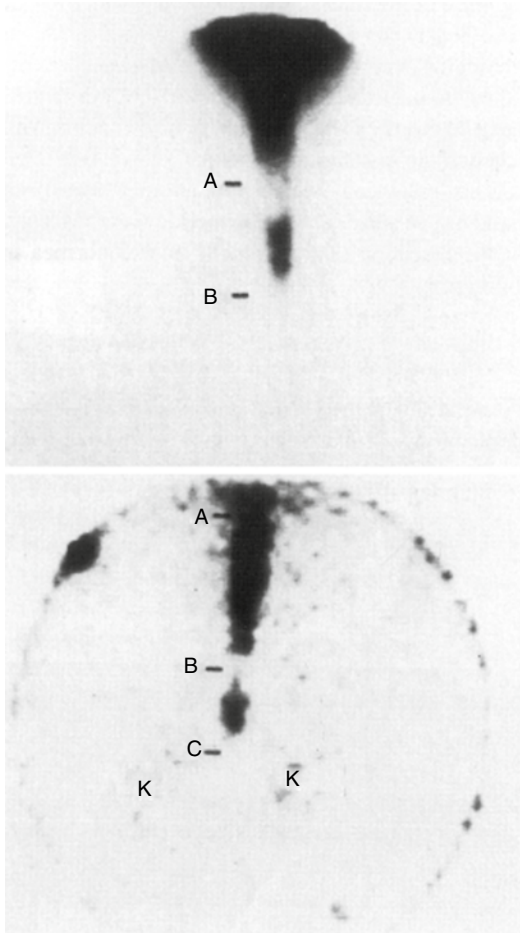

Fig. 4.41 Block of CSF diffusion due to metastatic medulloblastomas in the spine. ^{99m}Tc-DTPA was injected into a lateral ventricle. *Top*: posterior view of the cervical and thoracic spine 1 h after injection of the tracer. There are two "filling defects" corresponding to a tumor mass (*A* and *B*). *Bottom*: view of the lower thoracic and lumbar spine reveals another block of tracer movement in the CSF (*C*). Renal activity is visualized bilaterally (*K*)

gamma camera equipped with a collimator of high sensitivity. The patient must remain immobile for the duration of the study.

The radiotracer is injected into the valve reservoir of the shunt, and its disappearance is monitored with the gamma camera and the computer at a rate of one frame every 5 s for 5 min. At the end of this time, a series of images is obtained along the course of the shunt to detect any interruption of the flow of CSF. These images are evaluated visually (Figs. 4.42 and 4.43) [174].

Meticulous attention to technical detail is essential when conducting this examination. Before injecting the radiotracer, one must ensure that the needle is within the lumen of the shunt. When it is not, the tracer can be accidentally injected outside the shunt. Pertechnetate is then absorbed slowly, and it is taken up by the salivary glands, thyroid, and stomach. It is then slowly eliminated by the kidneys (Fig. 4.44).

A time-activity curve is calculated from a region over the valve of the shunt. As discussed further below, the CSF shunt flow can be calculated from this curve (Fig. 4.45) [199–201]. Alternatively, the radionuclide can be injected into the ventricle in order to follow its flow through the shunt. This method allows only qualitative estimation of shunt flow.

Clinical Applications

Ventriculoperitoneal and ventriculoatrial shunts are used in hydrocephalic patients to divert CSF into a body space so it can be absorbed. Mechanical failure, occlusion, and the development of loculated spaces around the ventricular or distal end of the shunt are causes of malfunction of a shunt. Such malfunction can usually be determined on clinical grounds, but in doubtful cases special measures may be indicated. Radionuclide studies can measure the shunt flow, determine the presence of an obstruction, and diagnose loculation of CSF at the distal end of the shunt [174, 201].

Rarely, CSF collections exist in free communication with the subarachnoid pathway, but without connecting with the exterior, as with nasoethmoidal encephaloceles [202]. With intracranial arachnoid cysts in children, radionuclide cisternography has proven useful in establishing the communication of the cyst with the ventricular or subarachnoid compartment and can aid in the assessment of associated hydrocephalus [164, 203, 204].

Quantification of Cerebrospinal Fluid Shunt Flow

Cerebrospinal fluid shunt flow may be estimated from the time-activity curve obtained from the valve of the shunt (Fig. 4.45). In one approach, the valve is modeled as a single, well-mixed

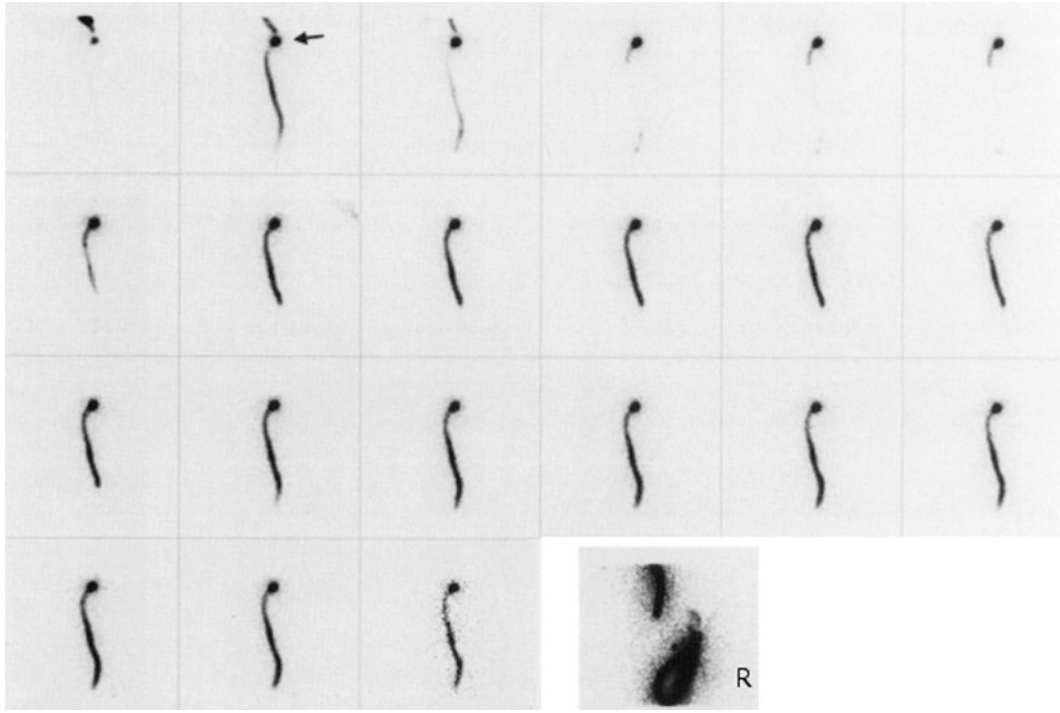

Fig. 4.42 Patent ventriculoperitoneal shunt. Series of 10-s images with the administration of 0.30 mCi of ^{99m}Tc-pertechnetate in a volume of 0.1 mL in the valve (*arrow*). The tracer can be seen as it rapidly circulated through the shunt. An image obtained at 6 min after radiotracer administration reveals tracer within the shunt loops in the abdomen (single image, *bottom right*)

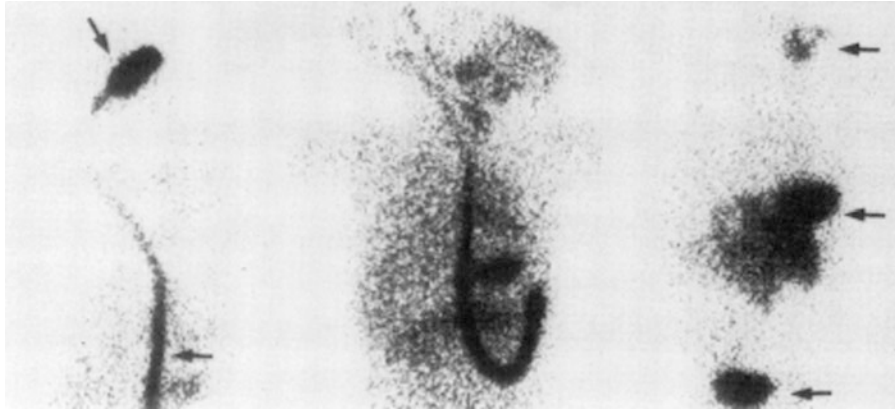

Fig. 4.43 Patent ventriculoperitoneal shunt. *Left*: image obtained almost immediately after tracer administration in the shunt. Activity in the valve and in the tubing is visualized (*arrows*). *Center*: image 5 min later shows the trajectory of the tube and the activity in the stomach, thyroid, salivary glands, and soft tissues indicating rapid absorption of the tracer. *Right*: at 2.5 h most of the activity is concentrated in the bladder, gastrointestinal tract, and thyroid (*arrows*)

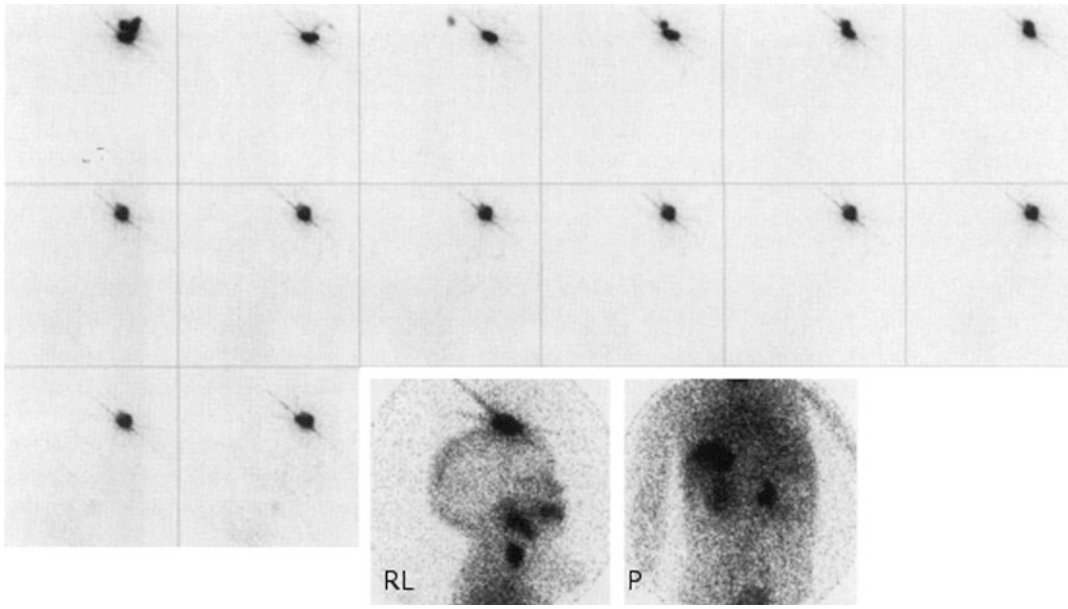

Fig. 4.44 Extravasation of pertechnetate. Serial imaging (1 frame = 20 s) reveals that the tracer remains largely at the site of injection outside the shunt. There is no tracer activity detected distally within the shunt or proximally within the ventricular system. Static planar images obtained at 10 min after injection reveal pertechnetate uptake in the salivary glands, thyroid, stomach, kidneys, and bladder, indicating systemic absorption of tracer from the injection site

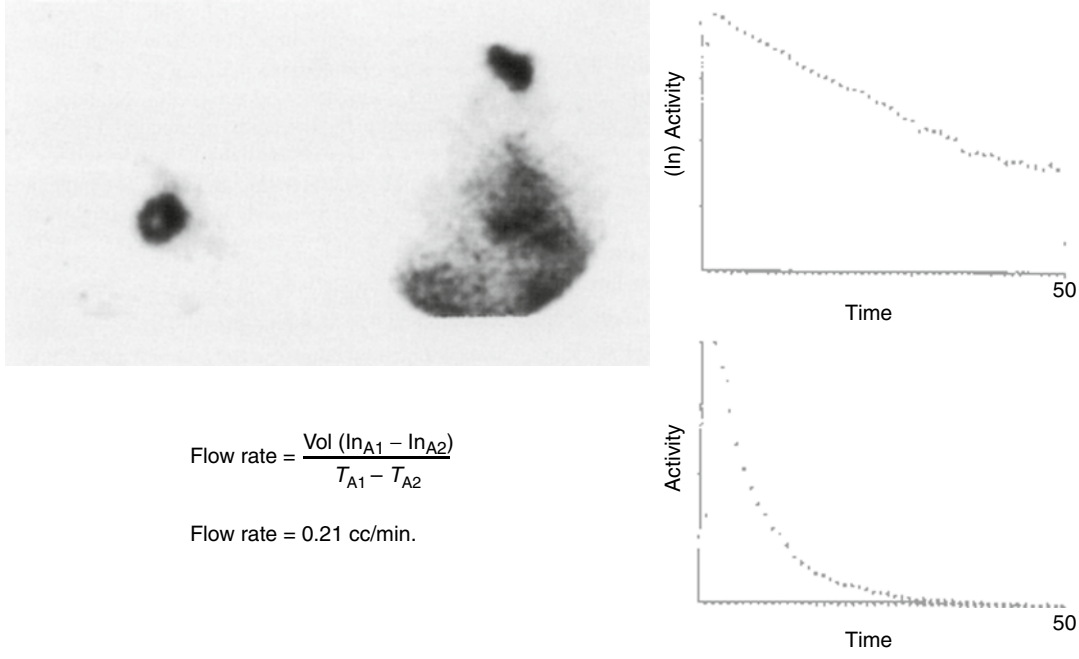

$$\text{Flow rate} = \frac{\text{Vol}\,(\ln_{A1} - \ln_{A2})}{T_{A1} - T_{A2}}$$

Flow rate = 0.21 cc/min.

Fig. 4.45 Patent ventriculoperitoneal shunt. *Top left*: anterior views of the chest and abdomen 10 min after injection of ^{99m}Tc-pertechnetate into the valve of the shunt. Both images show widespread distribution of the tracer in the body, indicating patency of the shunt. *Right*: logarithmic (*top*) and linear (*bottom*) time-activity curves from the valve obtained from images at one frame every 5 s. Calculation of CSF shunt flow is shown

compartment. The term *well mixed* means that the tracer becomes equilibrated with the entire volume of the compartment immediately after its introduction and remains so for the duration of the experiment. In such a system, the disappearance curve is of the form

$$A(t) = A(0)e^{-t/k}, \tag{4.1}$$

where t is time and k is the time constant of the system. The time constant is equal to the mean time the tracer remains in the valve. Flow (F) is calculated using the formula

$$F = V / k, \tag{4.2}$$

where V is the volume of distribution [199].

There is much experimental evidence at variance with the well-mixed compartment model. With the method described in the preceding paragraph, it was found necessary to use an experimentally determined volume of distribution rather than the physical volume of the valve to obtain quantitative results [199]. Moreover, it has been found that the observed disappearance curve differs from the exponential curve predicted by the model and depends on the injection technique [200].

As the well-mixed compartment assumption appears to be invalid, we have developed an alternative approach for estimating flow. If the radiotracer is instantaneously introduced, so the tracer is uniformly distributed across the fluid entering the compartment, one may estimate flow by calculating the mean transit time (MTT) using the formula

$$MTT = A / H, \tag{4.3}$$

where A is the total area under the disappearance curve and H is the initial height of the disappearance curve. Flow is then calculated using the formula

$$F = V / MIT. \tag{4.4}$$

This method is illustrated in Fig. 4.46. The method, which we term the *A*/*H* method, was found to be more precise than the method based on the well-mixed compartment model [200]. It has the additional advantage of working with the physical volume of the valve, obviating the need for experimentally determined volumes of distribution.

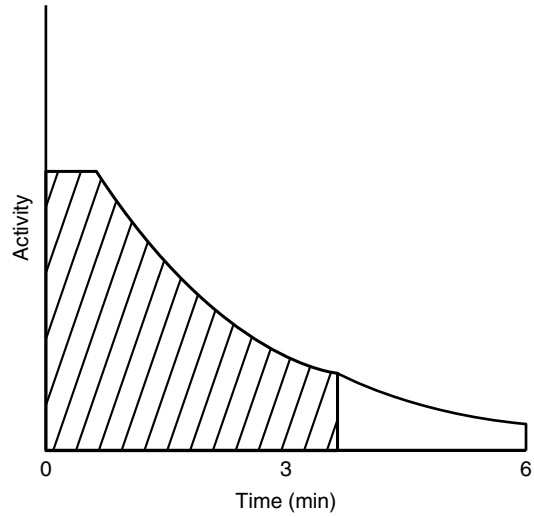

Fig. 4.46 Cerebrospinal fluid flow may be estimated from the area under the valve disappearance curve using Eq. 4.3. Because the curve may not have reached zero before the end of the recording period, the curve is extrapolated by fitting an exponential function to its final portion. The fit starts when the activity is 25 % of the maximum activity or when 75 % of the recording period has expired, whichever comes first. The total area is computed by numerically integrating the initial portion and adding the area under the exponential fit

The idea behind the *A*/*H* method is to label the fluid entering the value. Thus the best results are obtained by entering the valve at its proximal end, pointing the needle toward the proximal end of the valve, or both. If this maneuver is not feasible, the method overestimates the shunt flow to some degree. As mentioned before, the volume injected must be small in order to minimize fluid displacement from the injection. The experimental finding that the time-activity curve depends on the injection technique implies that a uniform injection technique is essential to obtain reproducible results.

References

1. Isacson O. On neuronal health. Trends Neurosci. 1993;16(8):306–8.
2. Kavdel ER, Schwartz JH. Principles of neural science. New York: Elsevier Science; 1991.
3. Gallen CC, Sobel DF, Lewine JD, et al. Neuromagnetic mapping of brain function. Radiology. 1993;187(3): 863–7.

4. Ingvar DH, Lassen NA. Quantitative determination of regional cerebral blood flow in man. Lancet. 1961; 2:806–7.
5. Habboush IH, Mitchell KD, Mulkern RV, Barnes PD, Treves ST. Registration and alignment of three-dimensional images: an interactive visual approach. Radiology. 1996;199(2):573–8.
6. Chugani HT, Phelps ME, Mazziotta JC. Positron emission tomography study of human brain functional development. Ann Neurol. 1987;22(4): 487–97.
7. Chugani HT. Metabolic imaging: a window on brain development and plasticity. Neuroscientist. 1999;5:29–40.
8. Rubinstein M, Denays R, Ham HR, et al. Functional imaging of brain maturation in humans using iodine-123 iodoamphetamine and SPECT. J Nucl Med. 1989;30(12):1982–5.
9. Chiron C, Raynaud C, Maziere B, et al. Changes in regional cerebral blood flow during brain maturation in children and adolescents. J Nucl Med. 1992;33(5):696–703.
10. Chugani HT, Phelps ME. Maturational changes in cerebral function in infants determined by 18FDG positron emission tomography. Science. 1986;231(4740):840–3.
11. Chugani HT. A critical period of brain development: studies of cerebral glucose utilization with PET. Prev Med. 1998;27(2):184–8.
12. Chugani HT, Muller RA, Chugani DC. Functional brain reorganization in children. Brain Dev. 1996;18(5):347–56.
13. Wyllie E, Rothner AD, Luders H. Partial seizures in children: clinical features, medical treatment, and surgical considerations. Pediatr Clin North Am. 1989; 36(2):343–64.
14. Vossler D, Wyler AR. Epilepsy surgery. 2004. http://www.emedicine.com/med/topic3177.htm. Accessed 21 Dec 2004.
15. National Institutes of Health Consensus Conference. Surgery for epilepsy. JAMA. 1990;264(6):729–33.
16. Koo CW, Devinsky O, Hari K, Balasny J, Noz ME, Kramer EL. Stratifying differences on ictal/interictal subtraction SPECT images. Epilepsia. 2003; 44(3):379–86.
17. Rowe CC, Berkovic SF, Austin MC, McKay WJ, Bladin PF. Patterns of postictal cerebral blood flow in temporal lobe epilepsy: qualitative and quantitative analysis. Neurology. 1991;41(7):1096–103.
18. Rowe CC, Berkovic SF, Sia ST, et al. Localization of epileptic foci with postictal single photon emission computed tomography. Ann Neurol. 1989;26(5):660–8.
19. Kuzniecky R, Mountz JM, Wheatley G, Morawetz R. Ictal single-photon emission computed tomography demonstrates localized epileptogenesis in cortical dysplasia. Ann Neurol. 1993;34(4):627–31.
20. Adams C, Hwang PA, Gilday DL, Armstrong DC, Becker LE, Hoffman HJ. Comparison of SPECT, EEG, CT, MRI, and pathology in partial epilepsy. Pediatr Neurol. 1992;8(2):97–103.
21. Chiron C, Raynaud C, Dulac O, Tzourio N, Plouin P, Tran-Dinh S. Study of the cerebral blood flow in partial epilepsy of childhood using the SPECT method. J Neuroradiol. 1989;16(4):317–24.
22. Miles D, Holmes G, Pearl P, et al. Comparison of CT, MRI, SPECT and BEAM in evaluation of pediatric epilepsy candidates in focal surgical resection. Epilepsia. 1990;31:672.
23. Uvebrant P, Bjure J, Hedstrom A, Ekholm S. Brain single photon emission computed tomography (SPECT) in neuropediatrics. Neuropediatrics. 1991; 22(1):3–9.
24. Vles JS, Demandt E, Ceulemans B, de Roo M, Casaer PJ. Single photon emission computed tomography (SPECT) in seizure disorders in childhood. Brain Dev. 1990;12(4):385–9.
25. Packard AB, Roach PJ, Davis RT. Ictal and interictal technetium-99m-bicisate brain SPECT in children with refractory epilepsy. J Nucl Med. 1996;37(7):1101–6.
26. Kaminska A, Chiron C, Ville D, et al. Ictal SPECT in children with epilepsy: comparison with intracranial EEG and relation to postsurgical outcome. Brain. 2003;126(Pt 1):248–60.
27. Davis RT, Treves ST, Zurakowski D, Bauer SB. Ictal perfusion brain SPECT in pediatric patients with intractable epilepsy: a multidisciplinary approach. J Nucl Med Technol. 1996;24:219–22.
28. O'Brien TJ, So EL, Mullan BP, et al. Subtraction peri-ictal SPECT is predictive of extratemporal epilepsy surgery outcome. Neurology. 2000;55(11):1668–77.
29. Buchhalter JR, So EL. Advances in computer-assisted single-photon emission computed tomography (SPECT) for epilepsy surgery in children. Acta Paediatr Suppl. 2004;93(445):32–5; discussion 36–7.
30. O'Brien TJ, So EL, Mullan BP, et al. Subtraction ictal SPECT co-registered to MRI improves clinical usefulness of SPECT in localizing the surgical seizure focus. Neurology. 1998;50(2):445–54.
31. Shoeb A, Edwards H, Connolly J, Bourgeois B, Treves ST, Guttag J. Patient-specific seizure onset detection. Epilepsy Behav. 2004;5(4):483–98.
32. Hrachovy RA, Frost Jr JD. Infantile spasms. Pediatr Clin North Am. 1989;36(2):311–29.
33. Chugani HT, Shewmon DA, Shields WD, et al. Surgery for intractable infantile spasms: neuroimaging perspectives. Epilepsia. 1993;34(4):764–71.
34. Chugani HT, Shields WD, Shewmon DA, Olson DM, Phelps ME, Peacock WJ. Infantile spasms: I. PET identifies focal cortical dysgenesis in cryptogenic cases for surgical treatment. Ann Neurol. 1990;27(4):406–13.
35. O'Tuama LA, Urion DK, Janicek MJ, Treves ST, Bjornson B, Moriarty JM. Regional cerebral perfusion in Landau-Kleffner syndrome and related childhood aphasias. J Nucl Med. 1992;33(10):1758–65.
36. Chiron C, Dulac O, Bulteau C, et al. Study of regional cerebral blood flow in West syndrome. Epilepsia. 1993;34(4):707–15.
37. Otsubo H, Hwang PA, Jay V, et al. Focal cortical dysplasia in children with localization-related epilepsy:

EEG, MRI, and SPECT findings. Pediatr Neurol. 1993;9(2):101–7.
38. Miyazaki M, Hashimoto T, Fujii E, Tayama M, Kuroda Y. Infantile spasms: localized cerebral lesions on SPECT. Epilepsia. 1994;35(5):988–92.
39. Haginoya K, Munakata M, Yokoyama H, et al. Mechanism of tonic spasms in West syndrome viewed from ictal SPECT findings. Brain Dev. 2001;23(7):496–501.
40. Koh S, Jayakar P, Resnick T, Alvarez L, Liit RE, Duchowny M. The localizing value of ictal SPECT in children with tuberous sclerosis complex and refractory partial epilepsy. Epileptic Disord. 1999;1(1): 41–6.
41. Chugani DC, Chugani HT, Muzik O, et al. Imaging epileptogenic tubers in children with tuberous sclerosis complex using alpha-[11C]methyl-L-tryptophan positron emission tomography. Ann Neurol. 1998;44(6):858–66.
42. Kagawa K, Chugani DC, Asano E, et al. Epilepsy surgery outcome in children with tuberous sclerosis complex evaluated with alpha-[11C]methyl-L-tryptophan positron emission tomography (PET). J Child Neurol. 2005;20(5):429–38.
43. Roach ES, Garcia JC, McLean Jr WT. Cerebrovascular disease in children. Am Fam Physician. 1984;30(5): 215–27.
44. Yamashiro Y, Takahashi H, Takahashi K. Cerebrovascular Moyamoya disease. Eur J Pediatr. 1984;142(1):44–50.
45. Feole JB, Ali A, Fordham EW, Huckman M, Shenker DM. Serial SPECT imaging in moyamoya using I-123 IMP. A method of noninvasive evaluation and follow-up. Clin Nucl Med. 1993;18(1):43–5.
46. Kobayashi H, Hayashi M, Handa Y, Kabuto M, Noguchi Y, Aradachi H. EC-IC bypass for adult patients with moyamoya disease. Neurol Res. 1991;13(2):113–6.
47. Shahar E, Gilday DL, Hwang PA, Cohen EK, Lambert R. Pediatric cerebrovascular disease. Alterations of regional cerebral blood flow detected by TC 99m-HMPAO SPECT. Arch Neurol. 1990;47(5):578–84.
48. Bourgeois M, Aicardi J, Goutieres F. Alternating hemiplegia of childhood. J Pediatr. 1993; 122(5 Pt 1):673–9.
49. Zupanc ML, Dobkin JA, Perlman SB. 123I-iodoamphetamine SPECT brain imaging in alternating hemiplegia. Pediatr Neurol. 1991;7(1):35–8.
50. Mikati MA, Maguire H, Barlow CF, et al. A syndrome of autosomal dominant alternating hemiplegia: clinical presentation mimicking intractable epilepsy; chromosomal studies; and physiologic investigations. Neurology. 1992;42(12):2251–7.
51. Clinical practice guideline: diagnosis and evaluation of the child with attention-deficit/hyperactivity disorder. American Academy of Pediatrics. Pediatrics. 2000;105(5):1158–70.
52. Lou HC, Henriksen L, Bruhn P. Focal cerebral hypoperfusion in children with dysphasia and/or attention deficit disorder. Arch Neurol. 1984;41(8):825–9.
53. Lou HC, Henriksen L, Bruhn P, Borner H, Nielsen JB. Striatal dysfunction in attention deficit and hyperkinetic disorder. Arch Neurol. 1989;46(1):48–52.
54. Zametkin AJ, Nordahl TE, Gross M, et al. Cerebral glucose metabolism in adults with hyperactivity of childhood onset. N Engl J Med. 1990;323(20): 1361–6.
55. Zametkin AJ, Liebenauer LL, Fitzgerald GA, et al. Brain metabolism in teenagers with attention-deficit hyperactivity disorder. Arch Gen Psychiatry. 1993;50(5):333–40.
56. Lorberboym M, Watemberg N, Nissenkorn A, Nir B, Lerman-Sagie T. Technetium 99m ethylcysteinate dimer single-photon emission computed tomography (SPECT) during intellectual stress test in children and adolescents with pure versus comorbid attention-deficit hyperactivity disorder (ADHD). J Child Neurol. 2004;19(2):91–6.
57. Lou HC, Henriksen L, Bruhn P. Focal cerebral dysfunction in developmental learning disabilities. Lancet. 1990;335(8680):8–11.
58. Langleben DD, Acton PD, Austin G, et al. Effects of methylphenidate discontinuation on cerebral blood flow in prepubescent boys with attention deficit hyperactivity disorder. J Nucl Med. 2002;43(12):1624–9.
59. Langleben DD, Austin G, Krikorian G, Ridlehuber HW, Goris ML, Strauss HW. Interhemispheric asymmetry of regional cerebral blood flow in prepubescent boys with attention deficit hyperactivity disorder. Nucl Med Commun. 2001;22(12):1333–40.
60. Kim BN, Lee JS, Cho SC, Lee DS. Methylphenidate increased regional cerebral blood flow in subjects with attention deficit/hyperactivity disorder. Yonsei Med J. 2001;42(1):19–29.
61. Gustafsson P, Thernlund G, Ryding E, Rosen I, Cederblad M. Associations between cerebral blood-flow measured by single photon emission computed tomography (SPECT), electro-encephalogram (EEG), behaviour symptoms, cognition and neurological soft signs in children with attention-deficit hyperactivity disorder (ADHD). Acta Paediatr. 2000;89(7): 830–5.
62. Arndt S, Cohen G, Alliger RJ, Swayze 2nd VW, Andreasen NC. Problems with ratio and proportion measures of imaged cerebral structures. Psychiatry Res. 1991;40(1):79–89.
63. Barbour RL, Graber HL, Pei Y, Zhong S, Schmitz CH. Optical tomographic imaging of dynamic features of dense-scattering media. J Opt Soc Am A Opt Image Sci Vis. 2001;18(12):3018–36.
64. Franceschini MA, Toronov V, Fillaci ME, Gratton E, Fantini S. On-line optical imaging of the human brain with 160-ms temporal resolution. Opt Express. 2000;6:49–57.
65. Volkow ND, Wang GJ, Fowler JS, et al. Effects of methylphenidate on regional brain glucose metabolism in humans: relationship to dopamine D2 receptors. Am J Psychiatry. 1997;154(1):50–5.
66. Volkow ND, Wang G, Fowler JS, et al. Therapeutic doses of oral methylphenidate significantly increase

extracellular dopamine in the human brain. J Neurosci. 2001;21(2):RC121.
67. Dougherty DD, Bonab AA, Spencer TJ, Rauch SL, Madras BK, Fischman AJ. Dopamine transporter density in patients with attention deficit hyperactivity disorder. Lancet. 1999;354(9196):2132–3.
68. Krause KH, Dresel SH, Krause J, Kung HF, Tatsch K. Increased striatal dopamine transporter in adult patients with attention deficit hyperactivity disorder: effects of methylphenidate as measured by single photon emission computed tomography. Neurosci Lett. 2000;285(2):107–10.
69. van Dyck CH, Quinlan DM, Cretella LM, et al. Unaltered dopamine transporter availability in adult attention deficit hyperactivity disorder. Am J Psychiatry. 2002;159(2):309–12.
70. Ilgin N, Senol S, Gucuyener K, Gokcora N, Sener S. Is increased D2 receptor availability associated with response to stimulant medication in ADHD. Dev Med Child Neurol. 2001;43(11):755–60.
71. Koepp MJ, Gunn RN, Lawrence AD, et al. Evidence for striatal dopamine release during a video game. Nature. 1998;393(6682):266–8.
72. Strafella AP, Paus T, Barrett J, Dagher A. Repetitive transcranial magnetic stimulation of the human prefrontal cortex induces dopamine release in the caudate nucleus. J Neurosci. 2001;21(15):RC157.
73. Volkow ND, Wang GJ, Fowler JS, et al. Relationship between blockade of dopamine transporters by oral methylphenidate and the increases in extracellular dopamine: therapeutic implications. Synapse. 2002;43(3):181–7.
74. Castellanos FX. Proceed, with caution: SPECT cerebral blood flow studies of children and adolescents with attention deficit hyperactivity disorder. J Nucl Med. 2002;43(12):1630–3.
75. Denays R, Tondeur M, Foulon M, et al. Regional brain blood flow in congenital dysphasia: studies with technetium-99m HM-PAO SPECT. J Nucl Med. 1989;30(11):1825–9.
76. Denays R, Tondeur M, Toppet V, et al. Cerebral palsy: initial experience with Tc-99m HMPAO SPECT of the brain. Radiology. 1990;175(1):111–6.
77. Mauk JE. Autism and pervasive developmental disorders. Pediatr Clin North Am. 1993;40(3):567–78.
78. Rumsey JM, Duara R, Grady C, et al. Brain metabolism in autism. Resting cerebral glucose utilization rates as measured with positron emission tomography. Arch Gen Psychiatry. 1985;42(5):448–55.
79. Heh CW, Smith R, Wu J, et al. Positron emission tomography of the cerebellum in autism. Am J Psychiatry. 1989;146(2):242–5.
80. De Volder AG, Bol A, Michel C, Cogneau M, Goffinet AM. Cerebral glucose metabolism in autistic children. Study and positron emission tomography. Acta Neurol Belg. 1988;88(2):75–90.
81. Horwitz B, Rumsey JM, Grady CL, Rapoport SI. The cerebral metabolic landscape in autism. Intercorrelations of regional glucose utilization. Arch Neurol. 1988;45(7):749–55.
82. Zilbovicius M, Garreau B, Tzourio N, et al. Regional cerebral blood flow in childhood autism: a SPECT study. Am J Psychiatry. 1992;149(7):924–30.
83. George M, Ring H, Costa D, et al. Neuroactivation and neuroimaging with SPET. London: Springer; 1991.
84. Chugani DC, Muzik O, Behen M, et al. Developmental changes in brain serotonin synthesis capacity in autistic and nonautistic children. Ann Neurol. 1999;45(3):287–95.
85. Ingvar DH. Measurements of regional cerebral blood flow and metabolism in psychopathological states. Eur Neurol. 1981;20(3):294–6.
86. Weinberger DR, Berman KF, Zec RF. Physiologic dysfunction of dorsolateral prefrontal cortex in schizophrenia. I. Regional cerebral blood flow evidence. Arch Gen Psychiatry. 1986;43(2):114–24.
87. Andreasen NC, Rezai K, Alliger R, et al. Hypofrontality in neuroleptic-naive patients and in patients with chronic schizophrenia. Assessment with xenon 133 single-photon emission computed tomography and the Tower of London. Arch Gen Psychiatry. 1992;49(12):943–58.
88. Wolkin A, Sanfilipo M, Wolf AP, Angrist B, Brodie JD, Rotrosen J. Negative symptoms and hypofrontality in chronic schizophrenia. Arch Gen Psychiatry. 1992;49(12):959–65.
89. Drevets WC, Videen TO, Price JL, Preskorn SH, Carmichael ST, Raichle ME. A functional anatomical study of unipolar depression. J Neurosci. 1992;12(9):3628–41.
90. Addario D. Developmental considerations in the concept of affective illness. J Clin Psychiatry. 1985;46(10 Pt 2):46–56.
91. Park CH, Spitzer AR, Desai HJ, Zhang JJ, Graziani LJ. Brain SPECT in neonates following extracorporeal membrane oxygenation: evaluation of technique and preliminary results. J Nucl Med. 1992;33(11):1943–8.
92. Kumar P, Bedard MP, Shankaran S, Delaney-Black V. Post extracorporeal membrane oxygenation single photon emission computed tomography (SPECT) as a predictor of neurodevelopmental outcome. Pediatrics. 1994;93(6 Pt 1):951–5.
93. Wong PC, Barlow CF, Hickey PR, et al. Factors associated with choreoathetosis after cardiopulmonary bypass in children with congenital heart disease. Circulation. 1992;86(5 Suppl):II118–26.
94. du Plessis AJ, Treves ST, Hickey PR, et al. Regional cerebral perfusion abnormalities after cardiac operations: single photon emission computed tomography (SPECT) findings in children with postoperative movement disorders. J Thorac Cardiovasc Surg. 1994;107:1036–43.
95. Bleyer WA. Epidemiologic impact of children with brain tumors. Childs Nerv Syst. 1999;15(11–12):758–63.
96. Statistical Report: Central Brain Tumor Registry of the United States (CBTRUS). 2012.
97. http://www.abta.org.
98. CBTRUS. Primary brain tumors in the United States Statistical Report 2000-2004. Hinsdale: Central Brain Tumor Registry of the United States; 2007–2008.

99. http://www.cancer.gov/cancertopics/types/brain/.
100. Kingsley DP, Kendall BE. CT of the adverse effects of therapeutic radiation of the central nervous system. AJNR Am J Neuroradiol. 1981;2(5):453–60.
101. van Dellen JR, Danziger A. Failure of computerized tomography to differentiate between radiation necrosis and cerebral tumour. S Afr Med J. 1978;53(5):171–2.
102. Julow J, Major T, Emri M, et al. The application of image fusion in stereotactic brachytherapy of brain tumours. Acta Neurochir (Wien). 2000;142(11):1253–8.
103. Kaplan WD, Takvorian T, Morris JH, Rumbaugh CL, Connolly BT, Atkins HL. Thallium-201 brain tumor imaging: a comparative study with pathologic correlation. J Nucl Med. 1987;28(1):47–52.
104. O'Tuama LA, Phillips PC, Strauss LC, et al. Two-phase [11C]L-methionine PET in childhood brain tumors. Pediatr Neurol. 1990;6(3):163–70.
105. O'Tuama LA, Treves ST, Larar JN, et al. Thallium-201 versus technetium-99m-MIBI SPECT in evaluation of childhood brain tumors: a within-subject comparison. J Nucl Med. 1993;34(7):1045–51.
106. Biersack HJ, Coenen HH, Stocklin G, et al. Imaging of brain tumors with L-3-[123I]iodo-alpha-methyl tyrosine and SPECT. J Nucl Med. 1989;30(1):110–2.
107. Kaplan WD, McComb JG, Strand RD, Treves S. Suppression of 99mTc-pertechnetate uptake in a choroid plexus papilloma. Radiology. 1973;109(2):395–6.
108. Kim KT, Black KL, Marciano D, et al. Thallium-201 SPECT imaging of brain tumors: methods and results. J Nucl Med. 1990;31(6):965–9.
109. Coleman RE, Hoffman JM, Hanson MW, Sostman HD, Schold SC. Clinical application of PET for the evaluation of brain tumors. J Nucl Med. 1991;32(4):616–22.
110. Maria BL, Drane WE, Mastin ST, Jimenez LA. Comparative value of thallium and glucose SPECT imaging in childhood brain tumors. Pediatr Neurol. 1998;19(5):351–7.
111. Di Chiro G, DeLaPaz RL, Brooks RA, et al. Glucose utilization of cerebral gliomas measured by [18F] fluorodeoxyglucose and positron emission tomography. Neurology. 1982;32(12):1323–9.
112. Delbeke D, Meyerowitz C, Lapidus RL, et al. Optimal cutoff levels of F-18 fluorodeoxyglucose uptake in the differentiation of low-grade from high-grade brain tumors with PET. Radiology. 1995;195(1):47–52.
113. Spence AM, Muzi M, Mankoff DA, et al. 18F-FDG PET of gliomas at delayed intervals: improved distinction between tumor and normal gray matter. J Nucl Med. 2004;45(10):1653–9.
114. Horky LL, Hsiao EM, Weiss SE, Drappatz J, Gerbaudo VH. Dual phase FDG-PET imaging of brain metastases provides superior assessment of recurrence versus post-treatment necrosis. J Neurooncol. 2011;103(1):137–46.
115. Horky LL, Treves ST. PET and SPECT in brain tumors and epilepsy. Neurosurg Clin N Am. 2011;22(2):169–84, viii.
116. Chen W, Delaloye S, Silverman DH, et al. Predicting treatment response of malignant gliomas to bevacizumab and irinotecan by imaging proliferation with [18F] fluorothymidine positron emission tomography: a pilot study. J Clin Oncol. 2007;25(30):4714–21.
117. van Waarde A, Cobben DC, Suurmeijer AJ, et al. Selectivity of 18F-FLT and 18F-FDG for differentiating tumor from inflammation in a rodent model. J Nucl Med. 2004;45(4):695–700.
118. Rachinger W, Goetz C, Popperl G, et al. Positron emission tomography with O-(2-[18F]fluoroethyl)-l-tyrosine versus magnetic resonance imaging in the diagnosis of recurrent gliomas. Neurosurgery. 2005;57(3):505–11; discussion 505–11.
119. Chen W, Silverman DH, Delaloye S, et al. 18F-FDOPA PET imaging of brain tumors: comparison study with 18F-FDG PET and evaluation of diagnostic accuracy. J Nucl Med. 2006;47(6):904–11.
120. Pirotte B, Goldman S, Massager N, et al. Comparison of 18F-FDG and 11C-methionine for PET-guided stereotactic brain biopsy of gliomas. J Nucl Med. 2004;45(8):1293–8.
121. Levivier M, Massager N, Wikler D, et al. Use of stereotactic PET images in dosimetry planning of radiosurgery for brain tumors: clinical experience and proposed classification. J Nucl Med. 2004;45(7):1146–54.
122. Gupta T, Beriwal S. PET/CT-guided radiation therapy planning: from present to the future. Indian J Cancer. 2010;47(2):126–33.
123. International Atomic Energy Agency. The role of PET/CT in radiation treatment planning for cancer patient treatment. Vienna: IAEA-TECDOC-1603; 2008.
124. http://www.ebroc.com/html/zoom/p_imagefusion.htm.
125. Galaske RG, Schober O, Heyer R. Determination of brain death in children with 123I-IMP and Tc-99m HMPAO. Psychiatry Res. 1989;29(3):343–5.
126. Donohoe KJ, Frey KA, Gerbaudo VH, Mariani G, Nagel JS, Shulkin B. Procedure guideline for brain death scintigraphy. J Nucl Med. 2003;44(5):846–51.
127. Spieth M, Abella E, Sutter C, Vasinrapee P, Wall L, Ortiz M. Importance of the lateral view in the evaluation of suspected brain death. Clin Nucl Med. 1995;20(11):965–8.
128. Spieth ME, Ansari AN, Kawada TK, Kimura RL, Siegel ME. Direct comparison of Tc-99m DTPA and Tc-99m HMPAO for evaluating brain death. Clin Nucl Med. 1994;19(10):867–72.
129. Jacobs AH, Dittmar C, Winkeler A, Garlip G, Heiss WD. Molecular imaging of gliomas. Mol Imaging. 2002;1(4):309–35.

130. Camargo EE. Brain SPECT in neurology and psychiatry. J Nucl Med. 2001;42(4):611–23.
131. Del Sole A, Falini A, Ravasi L, et al. Anatomical and biochemical investigation of primary brain tumours. Eur J Nucl Med. 2001;28(12):1851–72.
132. Leveille J, Demonceau G, De Roo M, et al. Characterization of technetium-99m-L, L-ECD for brain perfusion imaging, part 2: biodistribution and brain imaging in humans. J Nucl Med. 1989;30(11):1902–10.
133. Hertz-Pannier L, Chiron C, Vera P, et al. Functional imaging in the work-up of childhood epilepsy. Childs Nerv Syst. 2001;17(4–5):223–8.
134. Van Paesschen W. Ictal SPECT. Epilepsia. 2004;45 Suppl 4:35–40.
135. Sharp PF, Smith FW, Gemmell HG, et al. Technetium-99m HM-PAO stereoisomers as potential agents for imaging regional cerebral blood flow: human volunteer studies. J Nucl Med. 1986;27:171–7.
136. Tubergen K, Corlija M, Volkert WA, Holmes RA. Sensitivity of technetium-99m-d,1-HMPAO to radiolysis in aqueous solutions. J Nucl Med. 1991;32(1):111–5.
137. Weisner PS, Bower GR, Dollimore LA, Forster AM, Higley B, Storey AE. A method for stabilising technetium-99m exametazime prepared from a commercial kit. Eur J Nucl Med. 1993;20(8):661–6.
138. Greenberg JH, Kushner M, Rango M, Alavi A, Reivich M. Validation studies of iodine-123-iodoamphetamine as a cerebral blood flow tracer using emission tomography. J Nucl Med. 1990;31(8):1364–9.
139. Devous Sr MD, Payne JK, Lowe JL, Leroy RF. Comparison of technetium-99m-ECD to Xenon-133 SPECT in normal controls and in patients with mild to moderate regional cerebral blood flow abnormalities. J Nucl Med. 1993;34(5):754–61.
140. Saha GB, MacIntyre WJ, Go RT. Radiopharmaceuticals for brain imaging. Semin Nucl Med. 1994;24(4):324–49.
141. Payne JK, Trivedi MH, Devous Sr MD. Comparison of technetium-99m-HMPAO and xenon-133 measurements of regional cerebral blood flow by SPECT. J Nucl Med. 1996;37(10):1735–40.
142. Leskinen-Kallio S. Positron emission tomography in oncology. Clin Physiol. 1994;14(3):329–35.
143. Black KL, Hawkins RA, Kim KT, Becker DP, Lerner C, Marciano D. Use of thallium-201 SPECT to quantitate malignancy grade of glioma. J Neurosurg. 1989;71:342.
144. Sasaki M, Kuwabara Y, Yoshida T, et al. A comparative study of thallium-201 SPET, carbon-11 methionine PET and fluorine-18 fluorodeoxyglucose PET for the differentiation of astrocytic tumours. Eur J Nucl Med. 1998;25(9):1261–9.
145. Krishna L, Slizofski WJ, Katsetos CD, et al. Abnormal intracerebral thallium localization in a bacterial brain abscess. J Nucl Med. 1992;33(11):2017–9.
146. O'Tuama LA, Packard AB, Treves ST. SPECT imaging of pediatric brain tumor with hexakis (methoxyisobutylisonitrile) technetium (I). J Nucl Med. 1990;31(12):2040–1.
147. Soricelli A, Cuocolo A, Varrone A, et al. Technetium-99m-tetrofosmin uptake in brain tumors by SPECT: comparison with thallium-201 imaging. J Nucl Med. 1998;39(5):802–6.
148. Choi JY, Kim SE, Shin HJ, Kim BT, Kim JH. Brain tumor imaging with 99mTc-tetrofosmin: comparison with 201Tl, 99mTc-MIBI, and 18F-fluorodeoxyglucose. J Neurooncol. 2000;46(1):63–70.
149. Kung HF, Kung MP, Choi SR. Radiopharmaceuticals for single-photon emission computed tomography brain imaging. Semin Nucl Med. 2003;33(1):2–13.
150. Meegalla SK, Plossl K, Kung MP, et al. Synthesis and characterization of technetium-99m-labeled tropanes as dopamine transporter-imaging agents. J Med Chem. 1997;40(1):9–17.
151. Dresel S, Krause J, Krause KH, et al. Attention deficit hyperactivity disorder: binding of [99mTc] TRODAT-1 to the dopamine transporter before and after methylphenidate treatment. Eur J Nucl Med. 2000;27(10):1518–24.
152. Woods SW, Hegeman IM, Zubal IG, et al. Visual stimulation increases technetium-99m-HMPAO distribution in human visual cortex. J Nucl Med. 1991;32(2):210–5.
153. Stehling MK, Firth JL, Worthington BS, et al. Observation of cerebrospinal fluid flow with echo-planar magnetic resonance imaging. Br J Radiol. 1991;64(758):89–97.
154. Lorenzo AV, Page LK, Watters GV. Relationship between cerebrospinal fluid formation, absorption and pressure in human hydrocephalus. Brain. 1970;93(4):679–92.
155. Davson H, Welch K, Segal MB, Davson H. Physiology and pathophysiology of the cerebrospinal fluid. Edinburgh/New York: Churchill Livingstone; 1987.
156. Jackson RT, Tigges J, Arnold W. Subarachnoid space of the CNS, nasal mucosa, and lymphatic system. Arch Otolaryngol. 1979;105(4):180–4.
157. McComb JG, Hyman S, Weiss MH. Lymphatic drainage of cerebrospinal fluid in the cat. In: Shapiro K, Marmarou A, Portnoy H, editors. Hydrocephalus. New York: Raven Press; 1984, xiii, 401 p.
158. Winston K, Hall J, Johnson D, Micheli L. Acute elevation of intracranial pressure following transection of non-functional spinal cord. Clin Orthop Relat Res. 1977;128:41–4.
159. Rubin RC, Henderson ES, Ommaya AK, Walker MD, Rall DP. The production of cerebrospinal fluid in man and its modification by acetazolamide. J Neurosurg. 1966;25(4):430–6.
160. Cutler RW, Page L, Galicich J, Watters GV. Formation and absorption of cerebrospinal fluid in man. Brain. 1968;91(4):707–20.
161. Page LK, Bresnan MJ, Lorenzo AV. Cerebrospinal fluid perfusion studies in childhood hydrocephalus. Surg Neurol. 1973;1(6):317–20.

162. Welch K. Secretion of cerebrospinal fluid by choroid plexus of the rabbit. Am J Physiol. 1963;205: 617–24.
163. de Rougemont J, Ames AI, Nesbett FB, Hofmann HF. Fluid formed by choroid plexus; a technique for its collection and a comparison of its electrolyte composition with serum and cisternal fluids. J Neurophysiol. 1960;23:485–95.
164. Bonting SL, Simon KA, Hawkins NM. Studies on sodium-potassium-activated adenosine triphosphatase. I. Quantitative distribution in several tissues of the cat. Arch Biochem Biophys. 1961;95:416–23.
165. Vates Jr TS, Bonting SL, Oppelt WW. Na-K activated adenosine triphosphatase formation of cerebrospinal fluid in the cat. Am J Physiol. 1964;206: 1165–72.
166. Johanson CE. The choroid plexus-arachnoid membrane-cerebrospinal fluid system. In: Boulton AA, Baker GB, Walz W, editors. Neuromethods: the neuronal microenvironment. Clifton: Humana Press; 1988, xxvi, 732 p.
167. Cserr HF. Physiology of the choroid plexus. Physiol Rev. 1971;51(2):273–311.
168. Netsky MG, Samruay S. The choroid plexus in health and disease. Charlottesville: University Press of Virginia; 1975.
169. Milhorat TH. Structure and function of the choroid plexus and other sites of cerebrospinal fluid formation. Int Rev Cytol. 1976;47:225–88.
170. Wright EM. Transport processes in the formation of the cerebrospinal fluid. Rev Physiol Biochem Pharmacol. 1978;83:3–34.
171. Spector R, Johanson CE. The mammalian choroid plexus. Sci Am. 1989;261(5):68–74.
172. Price DL, James Jr AE, Sperber E, Strecker EP. Communicating hydrocephalus. Cisternographic and neuropathologic studies. Arch Neurol. 1976; 33(1):15–20.
173. Eisenberg HM, McComb JG, Lorenzo AV. Cerebrospinal fluid overproduction and hydrocephalus associated with choroid plexus papilloma. J Neurosurg. 1974;40(3):381–5.
174. Treves ST, Welch K, Kuruc A. Cerebrospinal fluid. In: Treves ST, editor. Pediatric nuclear medicine. New York: Springer; 1985. p. 223–31.
175. Dichiro G. Movement of the cerebrospinal fluid in human beings. Nature. 1964;204:290–1.
176. Bannister R, Gilford E, Kocen R. Isotope encephalography in the diagnosis of dementia due to communicating hydrocephalus. Lancet. 1967;2(7524):1014–7.
177. Benson DF, LeMay M, Patten DH, Rubens AB. Diagnosis of normal-pressure hydrocephalus. N Engl J Med. 1970;283(12):609–15.
178. Glasauer FE, Alker GJ, Leslie EV, Nicol CF. Isotope cisternography in hydrocephalus with normal pressure: case report and technical note. J Neurosurg. 1968;29:555–61.
179. Greitz T, Grepe A. Encephalography in the diagnosis of convexity block hydrocephalus. Acta Radiol Diagn. 1971;11(3):232–42.
180. Rau H, Fas A, Horst W, Baumgartner G. Clinical observations on communicating hydrocephalus of unknown etiology (author's transl). J Neurol. 1974;207(4):279–87.
181. Shenkin HA, Crowley JN. Hydrocephalus complicating pituitary adenoma. J Neurol Neurosurg Psychiatry. 1973;36(6):1063–8.
182. Tator CH, Murray S. A clinical, pneumoencephalographic and radioisotopic study of normal-pressure communicating hydrocephalus. Can Med Assoc J. 1971;105(6):573–9.
183. O'Brien MD, Haggith JW, Appleton D. Cerebrospinal fluid dynamics in dementia. Exp Brain Res. 1982;(Suppl 5):196–200. PMID: 7151909.
184. Donn SM, Roloff DW, Keyes Jr JW. Lumbar cisternography in evaluation of hydrocephalus in the preterm infant. Pediatrics. 1983;72(5):670–6.
185. Khan EA, Luros JT. Hydrocephalus from overproduction of cerebrospinal fluid. J Neurosurg. 1952;9:59–67.
186. Matson DD. Hydrocephalus in a premature infant caused by papilloma of the choroid plexus; with report of surgical treatment. J Neurosurg. 1953;10(4):416–20.
187. Matson DD, Crofton FD. Papilloma of the choroid plexus in childhood. J Neurosurg. 1960;17: 1002–27.
188. Ray BS, Peck Jr FC. Papilloma of the choroid plexus of the lateral ventricles causing hydrocephalus in an infant. J Neurosurg. 1956;13(4):317–22.
189. Johnson RT. Clinicopathological aspects of the cerebrospinal fluid circulation. Paper presented at: Ciba Foundation symposium on the cerebrospinal fluid: production, circulation and absorption, Boston, 1958.
190. Caldicott WJ, North JB, Simpson DA. Traumatic cerebrospinal fluid fistulas in children. J Neurosurg. 1973;38(1):1–9.
191. Cowan RJ, Maynard CD. Trauma to the brain and extracranial structures. Semin Nucl Med. 1974;4(4): 319–38.
192. Harwood-Nash DC. Fractures of the petrous and tympanic parts of the temporal bone in children: a tomographic study of 35 cases. Am J Roentgenol Radium Ther Nucl Med. 1970;110(3):598–607.
193. Lantz EJ, Forbes GS, Brown ML, Laws Jr ER. Radiology of cerebrospinal fluid rhinorrhea. AJR Am J Roentgenol. 1980;135(5):1023–30.
194. Wocjan J, Klisiewicz R, Krolicki L. Overpressure radionuclide cisternography and metrizamide computed tomographic cisternography in the detection of intermittent rhinoliquorrheas in children. Childs Nerv Syst. 1989;5(4):238–40.
195. Jaffe B, Welch K, Strand R, Treves S. Cerebrospinal fluid rhinorrhea via the fossa of Rosenmuller. Laryngoscope. 1976;86(7):903–7.

196. McLennan JE, Mickle JP, Treves S. Radionuclide cisternographic evaluation and follow-up of post-traumatic subconjunctival CSF loculation. Case report. J Neurosurg. 1976;44(4):496–9.
197. Ferreira S, Jhingran SG, Johnson PC. Radionuclide cisternography for the study of arachnoid cysts: a case report. Neuroradiology. 1980;19(3):167–9.
198. Front D, Minderhoud JM, Beks JW, Penning L. Leptomeningeal cysts diagnosed by isotope cisternography. J Neurol Neurosurg Psychiatry. 1973; 36(6):1018–23.
199. Harbert J, Haddad D, McCullough D. Quantitation of cerebrospinal fluid shunt flow. Radiology. 1974;112(2):379–87.
200. Kuruc A, Treves S, Welch K, Merlino D. Radionuclide estimation of cerebrospinal fluid shunt flow. Evidence supporting an alternative theoretical model. J Neurosurg. 1984;60(2):361–4.
201. Rudd TG, Shurtleff DB, Loeser JD, Nelp WB. Radionuclide assessment of cerebrospinal fluid shunt function in children. J Nucl Med. 1973;14(9):683–6.
202. Gelfand MJ, Walus M, Tomsick T, Benton C, McLaurin R. Nasoethmoidal encephalomeningocele demonstrated by cisternography: case report. J Nucl Med. 1977;18(7):706–8.
203. Lusins J, Nakagawa H, Sorek M, Goldsmith S. Cisternography and CT scanning with 111In-DTPA in evaluation of posterior fossa arachnoid cysts. Clin Nucl Med. 1979;4(4):161–3.
204. Marinov M, Undjian S, Wetzka P. An evaluation of the surgical treatment of intracranial arachnoid cysts in children. Childs Nerv Syst. 1989;5(3):177–83.

Thyroid

5

Frederick D. Grant and S. Ted Treves

Nuclear medicine techniques to diagnose and treat thyroid diseases have been in routine use for many decades [1, 2]. Most of these methods depend upon the iodine avidity (and related pertechnetate avidity) of thyroid tissues. The radioiodine isotopes (^{123}I and ^{131}I) and ^{99m}Tc (as pertechnetate) are the most commonly used radiopharmaceuticals for thyroid imaging. Both ^{123}I and ^{131}I have been used to determine thyroid iodine uptake as a measure of thyroid function. In patients with thyroid cancer, these radioiodine isotopes can be used to detect sites of remnant thyroid tissue and metastatic disease. In addition to imaging, ^{131}I is used for specific radiotherapy of hyperactive thyroid tissue and thyroid cancer. With the introduction of positron emission tomography, ^{18}F-FDG has acquired a limited role in the evaluation of thyroid cancer. Some centers also use ^{124}I PET to evaluate thyroid cancer.

F.D. Grant, MD (✉)
Joint Program in Nuclear Medicine,
Department of Radiology,
Harvard Medical School,
Boston, MA, USA

Division of Nuclear Medicine and Molecular Imaging,
Department of Radiology,
Boston Children's Hospital,
Boston, MA, USA

Department of Radiology,
Brigham and Women's Hospital,
Boston, MA, USA
e-mail: frederick.grant@childrens.harvard.edu

S.T. Treves, MD (✉)
Joint Program in Nuclear Medicine,
Department of Radiology, Harvard Medical School,
Boston, MA, USA

Division of Nuclear Medicine and Molecular
Imaging, Department of Radiology,
Boston Children's Hospital,
Boston, MA, USA

Division of Nuclear Medicine and Molecular
Imaging, Department of Radiology,
Brigham and Women's Hospital, Boston, MA, USA
e-mail: ted_treves@HMS.harvard.edu

Methods

Radiopharmaceuticals

Thyroid follicular cells have mechanisms for both the *trapping* (uptake) and the *organification* of iodine. These mechanisms provide targets for assessing thyroid function, imaging the thyroid gland, and treating hyperthyroidism and thyroid cancer. *Trapping* of iodine depends on the sodium-iodide (NaI) symporter (Fig. 5.1), a sodium-ATPase-linked transmembrane anion transporter [3, 4]. The symporter mediates energy-dependent transport of univalent anions from the extracellular to intracellular space. Although it has greatest avidity for iodide (I^-), the symporter has avidity for other univalent anions, including thiocyanate (SCN^-), perchlorate (ClO_3^-), pertechnetate (TcO_4^-), and nitrate (NO_3^-). Thus, thyroid imaging is performed with radioactive isotopes of

S.T. Treves (ed.), *Pediatric Nuclear Medicine and Molecular Imaging*,
DOI 10.1007/978-1-4614-9551-2_5, © Springer Science+Business Media New York 2014

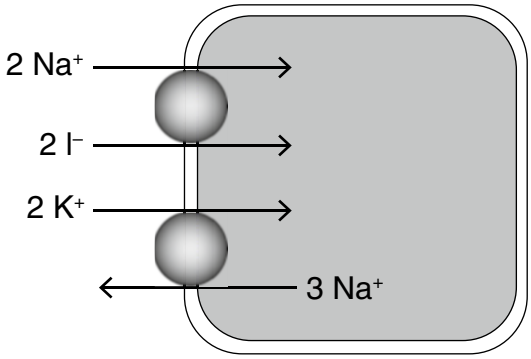

Fig. 5.1 Sodium-iodide symporter. The sodium-iodide symporter is a transmembrane glycopeptide that is the primary cellular mechanism for iodine uptake. In an energy-dependent process, the symporter actively transports two sodium cations for every iodide anion transported into the cell. It is linked to the sodium-potassium ATPase pump, which transports three sodium cations out of the cell for every two potassium cations transported into the cell and provides energy for the active symporter transport. The symporter has avidity for other univalent anions, including pertechnetate (TcO_4^-) [3]

either iodine or technetium, usually in the form of sodium salts of iodide (^{123}I, ^{131}I) or pertechnetate (^{99m}Tc). Thiocyanate or perchlorate uptake can compete with and diminish thyroid uptake of either iodine or pertechnetate.

Organification of iodine occurs in the normal thyroid, but not other tissues of the body. In thyroid follicular cells, iodine is incorporated into thyroglobulin, the tyrosine-rich peptide precursor of active thyroid hormones [5, 6]. Although the iodine symporter is expressed and can trap iodide in a wide range of organs and tissues, in most tissues, trapped iodide is washed out and returned to the extracellular space. Organification limits iodine washout, which amplifies the accumulation of radioiodine within thyroid tissue. Other anions, including pertechnetate, are not organified and are susceptible to washout from all tissues, including the thyroid. These processes of trapping and organification allow the use of iodine radioisotopes (^{123}I, ^{124}I, and ^{131}I) and ^{99m}Tc-pertechnetate to assess thyroid function, image the thyroid gland, and treat thyroid diseases.

For thyroid studies, iodine isotopes are prepared as the sodium salt ([^{131}I]NaI or [^{123}I]NaI) and administered by mouth. Usually, ^{131}I and ^{123}I are administered as a solid capsule, but a liquid formulation is available. The liquid formulation can be particularly useful in pediatrics as it can facilitate titration of a weight-based dose and may be easier for younger patients to swallow. In unusual circumstances, sodium iodide can be custom formulated for intravenous administration. Sodium pertechnetate ([^{99m}Tc]$NaTcO_4$) typically is administered by intravenous injection but also can be administered orally.

Iodine-131

Iodine-131 (physical half-life 8.1 days) has both gamma-emission (predominately 364 keV) and beta-particle emission. As a product of nuclear fission reactors, it has been widely available, and for many decades it served as the routine iodine radiopharmaceutical for both thyroid imaging and therapy. Iodine-131 is an ideal therapeutic radiopharmaceutical for both benign and malignant thyroid diseases as it has a relatively high absorbed radiation dose due to its half-life and beta-particle emission. However, this high radiation dose and the high energy of its gamma-emission make ^{131}I less satisfactory for thyroid imaging or assessing radioiodine uptake.

Iodine-123

Iodine-123 decays (physical half-life of 13.2 h) principally by electron capture and subsequent gamma-emission (159 keV). Unlike ^{131}I, ^{123}I has no beta-emission. The absence of beta-emission and the energy of the gamma-emission make ^{123}I the radiopharmaceutical of choice for thyroid imaging with a gamma-camera. However, ^{123}I decay also produces a low abundance of other higher-energy gamma-emissions (248–784 keV) that occasionally can affect image quality [7].

Iodine-123 is a cyclotron product produced from a ^{124}Xe target. Iodine-123 is produced by two different nuclear reactions with subsequent rapid decay to ^{123}I. The primary nuclear reaction is

$$^{124}\mathrm{Xe}(\mathrm{p},2\mathrm{n})^{123}\mathrm{Cs} >^{123}\mathrm{Xe} >^{123}\mathrm{I}$$

and the secondary nuclear reaction is

$$^{124}\mathrm{Xe}(\mathrm{p,pn})^{123}\mathrm{Xe} > ^{123}\mathrm{I}.$$

Compared to ^{131}I, ^{123}I has more limited commercial availability and is more expensive, but its superior imaging characteristics have made it the preferred choice for diagnostic thyroid imaging [8, 9]. The lower effective radiation dose provided by ^{123}I, compared to ^{131}I, is another reason for its use in pediatric patients.

Iodine-124

Iodine-124 is a positron emitter with a physical half-life of 4.18 days (100.3 h). It also has gamma-emission, which is predominately 603 keV. Like ^{123}I, it is a cyclotron product, which typically is produced by the nuclear reaction ^{124}Te (p,n) ^{124}I. With the widespread availability of PET scanners, some medical centers have investigated the use of ^{124}I-PET for imaging thyroid cancer [10]. Despite the excellent imaging characteristics of PET, the use of ^{124}I as a PET radiopharmaceutical has a number of disadvantages. Due to its limited commercial availability, most users must manufacture ^{124}I in an onsite cyclotron. The emitted positron has a higher energy, and thus higher range than many other PET tracers, which slightly decreases PET resolution. In addition to the predominate 603 keV gamma-emission, ^{124}I also has numerous higher-energy gamma-emissions, including 723 keV and 1,691 keV. Thus, due to its relatively higher radiation dose compared to ^{123}I, ^{124}I is not appropriate for evaluation of benign thyroid disease or for use in children, and it has not entered widespread use.

Technetium-99m Sodium Pertechnetate

Technetium-99m (physical half-life 6.0 h, 140 keV gamma-emission) is readily available in all nuclear medicine departments as a generator product (^{99}Mo > ^{99m}Tc). It also is inexpensive, provides short imaging times, and results in a low radiation dose. For these reasons, ^{99m}Tc-sodium pertechnetate sometimes is preferred for thyroid imaging [11]. After intravenous administration of pertechnetate, there is rapid thyroid uptake of pertechnetate, but, unlike iodine, pertechnetate is not organified within the thyroid cell. In the absence of organification, there is rapid washout, so that thyroid imaging must be performed soon after administration of ^{99m}Tc-pertechnetate. As a result, physiological uptake in other tissues, such as salivary glands, is more prominent on thyroid scans performed with pertechnetate than on scans performed with iodine isotopes.

Thyroid Scintigraphy

Thyroid scintigraphy can be performed with ^{99m}Tc-pertechnetate, ^{123}I, or rarely ^{131}I (Fig. 5.2). The choice of radiopharmaceutical depends upon a number of factors, including tracer availability. Overall image quality will be best with ^{123}I. Concurrent quantitative assessment of uptake requires the use of either ^{131}I or ^{123}I, but ^{131}I should rarely, if ever, be used for thyroid scintigraphy in children. The practice guidelines published by professional societies recommend a range of radiopharmaceutical doses for thyroid scintigraphy [12–14]. At our institution, the administered ^{123}I dose is 0.2 MBq/kg (0.006 mCi/kg) with a minimum dose of 0.925 MBq (0.025 mCi) and maximum dose of 14.8 MBq (0.4 mCi). To ensure rapid and complete absorption of the tracer, patients are asked to fast (except for sips of water) for 2 h before and 1 h after radioiodine administration. For children, an adequate administered dose of ^{99m}Tc-pertechnetate is 1 MBq/kg (0.03 mCi/kg) with a minimum dose of 7.4 MBq (0.2 mCi) and maximum dose of 74 MBq (2 mCi).

Imaging typically is performed 4–6 h after oral administration of ^{123}I or is started 20–30 min after intravenous administration of ^{99m}Tc-pertechnetate. Delayed images are rarely helpful, but if a concurrent thyroid uptake is being performed, then this can be determined 24 h after oral administration of ^{123}I. As a small amount of tracer is excreted with saliva, salivary accumulation in the mouth, pharynx, or even the esophagus occasionally will interfere with imaging. Usually, this can be cleared by having the patient “swish and

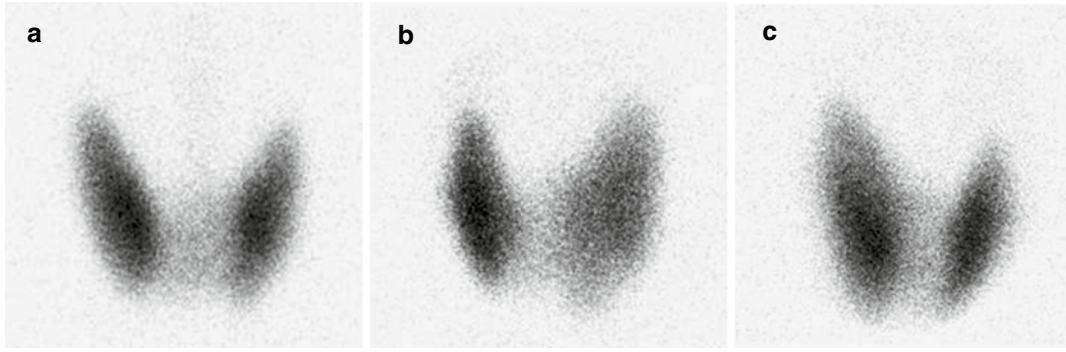

Fig. 5.2 Normal thyroid scan performed with ^{123}I. Images obtained with a pinhole collimator in the anterior (**a**), left oblique (**b**), and right oblique (**c**) projections demonstrate that the normal thyroid gland has homogeneous iodine uptake in both lobes, which should be similar in size and have smooth contours. A small amount of tracer may be seen in the thyroid isthmus, located between the two lobes of the thyroid gland. Normal thyroid uptake of the administered radioiodine dose is approximately 5–15 % at 4 h and 10–35 % at 24 h

swallow" a few sips of water before the start of imaging.

A pinhole collimator with an aperture less than 3 mm produces satisfactory image quality. A pinhole collimator is preferable to a planar collimator, as it will produce images with the fine detail necessary to evaluate thyroid structure. When positioning the pinhole collimator, the thyroid image should fit within the central two-thirds of the field of view to prevent distortion of thyroid anatomy. Images should be acquired in the anterior and two anterior oblique views. An additional "bird's-eye view" acquired with the pinhole collimator approximately 10–20 cm from the neck provides a wider field of view that can demonstrate the location and position of the thyroid gland in relation to other structures in the neck, such as salivary glands. Each image should be acquired for 50,000–100,000 counts with ^{123}I and 100,000–200,000 counts with ^{99m}Tc-pertechnetate.

Images typically are acquired with the neck extended. In some cases, such as localization of an ectopic thyroid gland, it may be helpful to acquire an image in a lateral projection. For example, this may be helpful in discriminating physiological salivary gland uptake from uptake in ectopic thyroid tissue. Anatomical correlation, either with transmission images to outline body margins or with radioactive markers, may be helpful for some studies. Radioactive markers can be placed on a palpable thyroid nodule or on anatomic landmarks, such as the chin and suprasternal notch.

Thyroid Uptake

Quantitative assessment of radioiodine uptake is useful for assessing thyroid function. When thyroid uptake is determined concurrently with ^{123}I thyroid scintigraphy, then the same dose of ^{123}I is used for both studies, and no additional radioiodine is administered for the uptake determination. When performed without concurrent ^{123}I thyroid scintigraphy, then determination of a radioiodine uptake requires a small dose of either ^{123}I or ^{131}I. Most professional guidelines [13, 15] recommend a pediatric dose of 3.7–7.4 MBq (0.1–0.2 mCi) of ^{123}I or 0.15–0.37 MBq (0.004–0.01 mCi) of ^{131}I for thyroid uptake determination without imaging. Iodine-123 is preferable, as it can provide an approximately 100-fold smaller effective radiation dose than ^{131}I at these recommended administered doses [15]. At our institution, we successfully use weight-based administration of ^{123}I for both thyroid scintigraphy and radioiodine uptake with an administered ^{123}I dose of 0.2 MBq/kg (0.006 mCi/kg) with a minimum dose of 0.925 MBq (0.025 mCi) and maximum dose of 14.8 MBq (0.4 mCi). No more than 0.4 mCi as a maximum dose should be necessary for a thyroid uptake

determination. Some clinicians have advocated ^{99m}Tc-pertechnetate for determination of thyroid uptake. However, the rapid washout of pertechnetate means that uptake must be determined within a few minutes of tracer administration, and this may not be a precise reflection of thyroid activity. Also, quantitation with ^{99m}Tc is more difficult than with radioiodine.

Thyroid radioiodine uptake can be calculated using a probe detector or by quantitative assessment of a planar scintigraphy. A radioiodine uptake calculation may be most informative when performed in conjunction with thyroid scintigraphy. Therefore, in most cases, thyroid scintigraphy, typically with a pinhole collimator, still should be performed even when a probe detector is used to determine thyroid uptake. An accurate uptake measurement requires the use of a standard, typically a second dose of radioiodine with activity similar to the dose administered to the patient. Thyroid uptake can then be determined by calculating the ratio of activity in the thyroid to the activity in the standard. This allows for accurate correction for probe sensitivity and for radioactive decay. It is not ideal practice to rely on a calculated standard activity. Some departments will place the standard dose in a neck phantom to more accurately correct for soft tissue attenuation and geometry. However, these effects are probably small, particularly in children, and not routinely used for pediatric studies.

The standard time for determining thyroid uptake is 24 h after radioiodine administration. Many departments find it useful to perform an uptake measurement at an earlier time, typically 4 or 6 h. If iodine uptake is absent or nearly absent at an early time point, then there may be little reason to have the patient return for another uptake measurement the following day. In other cases, a drop in measured uptake between early and later time points can indicate a state of high-iodine turnover in the thyroid. The typical uptake is 6–18 % at 4–6 h and 10–35 % at 24 h [15]. However, these must not be considered absolute values and must be interpreted within the context of the biochemical thyroid function tests.

Factors Affecting Thyroid Studies

Radioiodine uptake by the thyroid gland can be affected by iodine levels in the thyroid and body. For example, in populations with lower levels of dietary iodine intake, typical thyroid uptake of a radioiodine dose will be higher [16]. Recent iodine intake, whether in diet, dietary supplements, medications, or intravenous iodinated radiographic contrast, will inhibit and lower subsequent radioiodine uptake [15]. This can impair thyroid imaging, reduce the diagnostic value of a radioiodine uptake determination, decrease detection of thyroid cancer metastases, and limit the effectiveness of radioiodine therapy. Therefore, a careful medical and dietary history must be performed with each patient before performing these nuclear medicine procedures.

If feasible, thyroid imaging or uptake determination should be delayed until excess nonradioactive iodine can be cleared (Table 5.1). After administration of iodinated radiographic contrast, thyroid studies should be delayed for at least 1 month [17], although some clinicians may wish to wait up to 3 months before evaluating and treating thyroid cancer. Occasionally, it may be helpful to assess iodine economy by measuring the urinary excretion of iodine. This can be measured most accurately in a 24-h urine collection. Alternatively, iodine excretion can be estimated with the simultaneous measurement of iodine and creatinine in a random urine sample [18]. If urinary iodine excretion exceeds 50 mcg/day, it may be appropriate to delay the thyroid study, if feasible and clinically appropriate [19].

Patients should not be advised to discontinue any prescribed drug without involving the prescribing clinician and the physician managing the patient's thyroid condition. In some clinical situations, the study may need to be performed despite recent iodine intake or drug administration while recognizing that the diagnostic certainty of the study could be limited. The cardiac drug amiodarone deserves special mention. Amiodarone is 37 % iodine by weight, and the drug is cleared very slowly from the body. In some cases, amiodarone may be associated with the onset of thyroid disease. However, in

Table 5.1 Sources of iodine and ideal withholding time period before thyroid imaging

Source	Time period
I. Iodine-rich foods and supplements	
1. Seaweed, kelp, sushi	1 week
II. Medications	
A. Thyroid hormones[a]	
1. Levothyroxine (T4)	6 weeks
2. Triiodothyronine (T3, Cytomel ®)	2 weeks
3. Others (liotrix, Thyrolar ®, Armour Thyroid ®)	6 weeks
B. Antithyroid drugs (methimazole, propylthiouracil)	3 days
C. Iodine supplements[b]	
1. Iodine solutions (SSKI, Lugol's Purepac, Isostat)	1 week
2. Potassium Iodine (KI) tablets	1 week
3. Vitamin or mineral tablets with iodine	1 week
D. Medications that contain iodine	
1. Cough medications (Tussi-Organidin®, Pima syrup®)[c]	6 weeks
2. Skin cleansers and antiseptics (Betadine®)[d]	6 weeks
3. Amiodarone (Coranone®)[e]	1 year
E. Other medications that affect thyroid function	
1. Lithium carbonate[e]	1 year
III. Imaging studies	
A. Tests requiring intravenous iodinated contrast	6 weeks (arteriogram, intravenous pyelogram)
B. Contrast-enhanced CT scan[f]	4–12 weeks
C. Cardiac catheterization	6 weeks

[a]Typically, withdrawal of thyroid hormone is a concern only before performing whole body imaging or radioiodine therapy in a patient with differentiated thyroid cancer.
[b]Whole body iodine content can be confirmed with urinary iodine assay if there is clinical concern about recent iodine supplementation.
[c]Limited availability in the USA.
[d]Primarily a concern in neonates, individuals with impaired skin integrity, and after mucosal application.
[e]Rarely it is clinically appropriate to discontinue these medications, and thyroid function tests and imaging must be interpreted in the context of continued medication administration.
[f]For most thyroid studies, a 1 month period is sufficient. Some clinicians prefer to wait up to 3 months after a contrast-enhanced CT scan before a diagnostic whole body scan or radioiodine therapy in a patient with thyroid cancer

most cases, it is not clinically appropriate to discontinue amiodarone. Although amiodarone is rarely used in children, evaluation and treatment of thyroid disease can be difficult in patients treated with this drug [20].

Drugs that directly affect thyroid function, such as thionamides (e.g., propylthiouracil, methimazole), should be discontinued for a short period of time (typically 3 days) before performing thyroid scintigraphy or a radioiodine uptake study [12, 13, 15]. This is best arranged with collaboration between the referring clinician and the nuclear medicine physician. Lithium carbonate suppresses thyroid function, and in patients treated with lithium-containing drugs, any thyroid tests must be interpreted within the context of lithium therapy. It is not necessary to discontinue other drugs, such as beta-blockers used for symptomatic relief of hyperthyroidism, before performing a thyroid scan or radioiodine uptake determination.

Body Scans Using Radioiodine

Whole body scans are performed for detection of metastatic thyroid cancer [19, 21–23]. They may be performed as a diagnostic scan or may be performed as a post-therapy scan shortly after treatment with ^{131}I. Diagnostic whole body scans are

performed approximately 16–48 h (typically 24 h) after administration of a small diagnostic dose of radioiodine. They may be performed with either ^{131}I or ^{123}I, but ^{123}I has become the preferred agent due to lower radiation dose and improved image quality [9]. For a diagnostic whole body scan in a child, the usual dose of ^{123}I is 3–5 mCi. The sensitivity of a whole body scan for detecting functioning thyroid cancer metastases likely increases with increasing radioiodine dose [19]. Iodine-123 also is preferred because of concerns that diagnostic doses of ^{131}I may "stun" thyroid cancer cells [24]. Stunning potentially may lead to decreased uptake and a diminished therapeutic effect of the subsequent treatment dose of ^{131}I [25]. Iodine-131 is used for a diagnostic whole body scans when ^{123}I is not available or if the whole body scan will be used for formal dosimetry planning before treatment with ^{131}I. To minimize stunning, the administered ^{131}I dose should be limited to less than 3 mCi [26], and the usual diagnostic dose of ^{131}I is 1–2 mCi.

Patient preparation is important to ensure accurate results from a diagnostic whole body radioiodine scan [19]. The scan should be performed only under conditions of TSH stimulation and iodine depletion. Patients should maintain a low-iodine diet for 7–14 days before the diagnostic dose of radioiodine is administered and should be screened for other sources of iodine intake (see "Factors affecting thyroid studies," Table 5.1). Patients with renal failure or on dialysis will need special planning. TSH stimulation could be accomplished with either withdrawal of thyroid hormone replacement therapy or administration of recombinant TSH [23]. However, the use of recombinant TSH in preparation for either whole body scans or radioiodine therapy has not been validated for outcome in children.

Post-therapy whole body scans are performed 3–7 days after administration of ^{131}I therapy. Despite the poorer imaging characteristics of ^{131}I, the post-therapy scan can be highly sensitive for sites of disease not identified with whole body imaging after a diagnostic dose of radioiodine [23, 27, 28]. This increased sensitivity probably reflects both the much higher administered dose of radioiodine and the altered biodistribution of ^{131}I that is seen many days after administration [28]. With increased time after administration, there will be washout of radioiodine from tissues that trap, but do not organify iodine, such as salivary and lacrimal glands and gastric mucosa. With increased soft tissue clearance, there can be improved target-to-background ratio, so that sites of disease that have small size or limited radioiodine avidity may become detectable. After a few days, little radioiodine accumulation is seen in the genitourinary system, but persistent accumulation of radioiodine is seen in bowel. This may be exacerbated by the slowed colonic transit resulting from hypothyroidism due to thyroid hormone withdrawal. Physiological radioiodine uptake in breast and thymus may be more apparent on post-therapy scans. Diffuse liver uptake reflects accumulation and metabolism of thyroglobulin and thyroid hormone. Thus, diffuse liver uptake is an indicator of functional thyroid tissue (either benign or malignant) that can synthesize thyroglobulin, but should not be interpreted to represent diffuse liver involvement with metastatic disease [29].

Whole body scans are acquired with a high-energy collimator in place for ^{131}I and a medium-energy collimator in place for ^{123}I [7]. Whole body imaging is usually performed as a whole body sweep, but in younger children, it may be easier to acquire multiple planar images rather than to attempt a single whole body sweep. Typically, the whole body scan sweep rate is adjusted to take 40 min to image the entire body. If static planar images are to be used, images should be planned to acquire 300,000–500,000 counts. To assist in image comparison and interpretation, all planar images should be acquired for the same period of time. Some institutions routinely image the thyroid bed and neck with a pinhole collimator and may calculate thyroid bed radioiodine uptake as part of pre-therapy diagnostic imaging [22]. If formal dosimetry is planned, then the whole body ^{131}I images should include a standard, typically 0.05–0.1 mCi ^{131}I diluted in water or saline in a small, well-sealed flask. SPECT and SPECT/CT may be useful in some patients for detecting low-avidity lesions and for localizing sites of abnormal radioiodine uptake [30, 31].

Clinical Applications

Congenital Hypothyroidism

Nuclear medicine has little role in the evaluation of hypothyroidism but with one exception, the evaluation of congenital hypothyroidism. Congenital hypothyroidism is not common, with an incidence of approximately 1 in 3,000 live births in North America [32]. However, it is an important public health concern because of the devastating neurocognitive impairment that results from untreated congenital hypothyroidism. Thyroid hormone is critical to normal brain development, and the absence of thyroid hormone during early life results in severe and irreversible neurological damage. Congenital hypothyroidism (endemic cretinism) is the leading cause of preventable mental retardation worldwide. Because of this, all US states and Canadian provinces mandate newborn screening of all infants for congenital hypothyroidism. In much of the world, the primary cause of congenital hypothyroidism is endemic iodine deficiency. In iodine-replete populations, such as in North America, congenital hypothyroidism typically is sporadic but rarely may reflect maternal iodine deficiency.

Treatment with early replacement of thyroid hormone is effective in allowing normal neurological development and has been shown to prevent the neurocognitive damage associated with hypothyroidism. The underlying cause of congenital hypothyroidism does not determine the treatment and rarely influences the neurological outcome of congenital hypothyroidism. Therefore, in these patients, the priority is to provide adequate thyroid hormone replacement before any attempt is made to determine the etiology of the congenital hypothyroidism.

Characterizing the underlying defect in thyroid function may help in predicting the need for lifelong therapy. Most sporadic cases of congenital hypothyroidism are associated with thyroid dysgenesis or thyroid ectopia. Thyroid dysgenesis is twice as common in female as male newborns [33]. Approximately 15 % of cases are familial, typically with autosomal recessive inheritance of a syndrome of thyroid dyshormonogenesis. Other cases may represent transient hypothyroidism due to transplacental passage of maternal blocking antibodies that inhibit the function of the TSH receptor [34]. Rarely, congenital hypothyroidism is the result of a pituitary or hypothalamic abnormality. Rare cases may be caused by thyroid hypoplasia due to congenital TSH deficiency or abnormal binding or signaling of the TSH receptor located on thyroid follicular cells.

The appropriate role for imaging in the management of congenital hypothyroidism is unclear [32, 35]. Some clinicians will treat congenital hypothyroidism presumptively with thyroid hormone replacement therapy for the first 3 years of life, the critical period of neurological development. Once the child reaches age three, thyroid hormone is discontinued or decreased in dose, and an elevation in TSH level interpreted as a sign of persistent congenital hypothyroidism. In some cases, measurement of a serum thyroglobulin level can be helpful in determining the presence of functional thyroid tissue. Some clinicians find it useful to demonstrate the location and function of thyroid tissue. Identification of thyroid absence or ectopia (a majority of cases in North America) will indicate a need for lifelong thyroid hormone replacement [36].

A thyroid scan with either ^{123}I (Fig. 5.3) or ^{99m}Tc-pertechnetate (Fig. 5.4) can be useful both to demonstrate the presence and location of any functional thyroid tissue, as well as providing an indication of thyroid function. For example, rapid washout of ^{123}I between 4 and 24-h images suggests an error in iodine organification. Thus, ^{123}I may be the preferable radiopharmaceutical for assessing congenital hypothyroidism. However, thyroid hormone replacement therapy should not be discontinued with the purpose of assessing thyroid function in an infant [32, 35]. Thyroid ultrasound can be helpful in confirming that the thyroid has normal morphology and location, but ultrasound is less sensitive for localizing ectopic thyroid tissue and does not provide information about

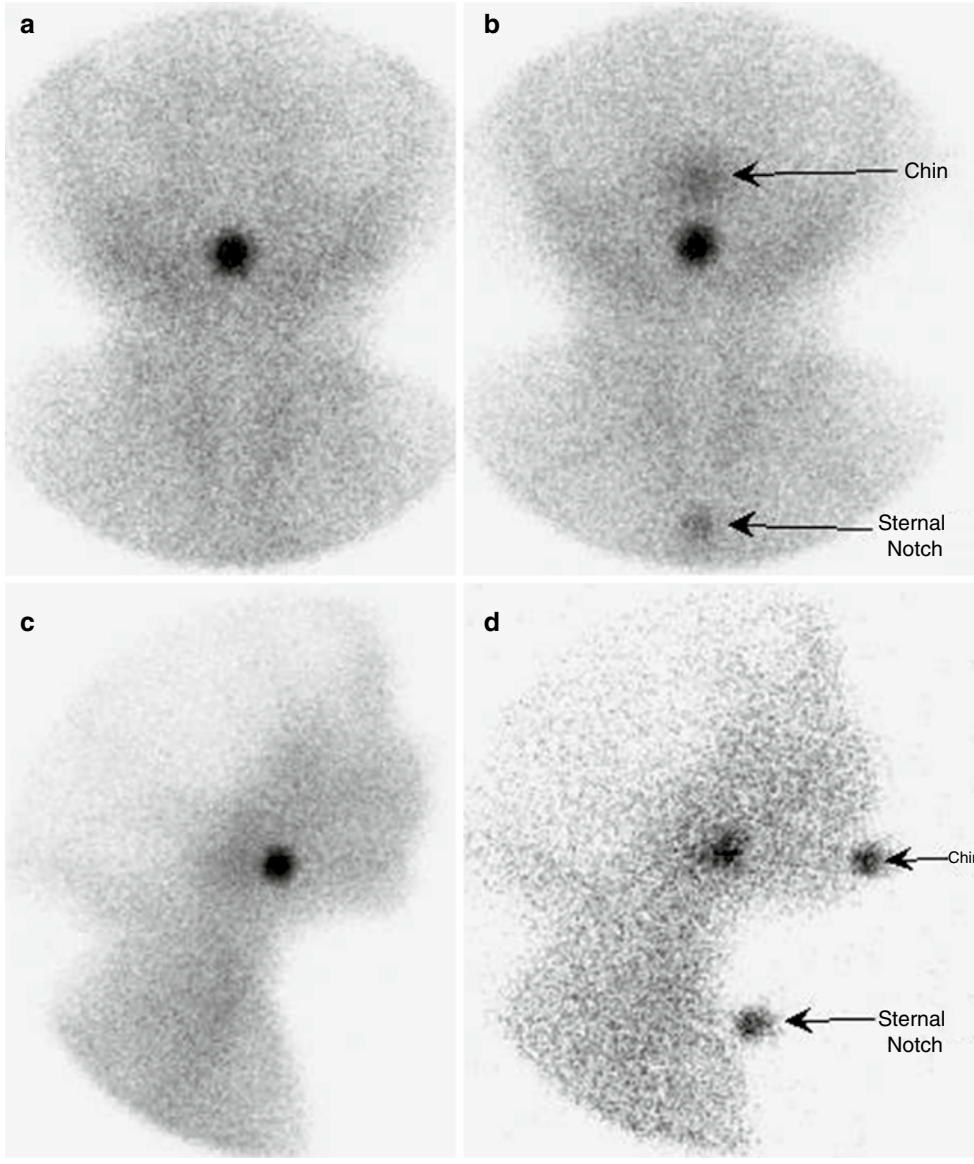

Fig. 5.3 Lingual thyroid gland detected with an ^{123}I scan. (**a**) In a patient with congenital hypothyroidism, a planar ^{123}I scan of the head and neck in the anterior projection demonstrates no thyroidal uptake in the expected location of the thyroid gland. A focus of intense radioiodine is located in the midline and superior to the neck. (**b**) External markers on the chin and at the upper sternal notch can be helpful for localization. (**c**) A planar image in a lateral projection demonstrates focal uptake in the region of the oropharynx. (**d**) External markers help confirm the likely location of the ectopic thyroid tissue to the base of the tongue

function. Infants with absent uptake on a thyroid scan should be evaluated by thyroid ultrasound. Other imaging tests, such as CT and MRI rarely, if ever, have a role in the evaluation of congenital hypothyroidism.

A young patient with no prior history of hypothyroidism may present with an ectopic thyroid gland. Ectopic thyroid tissue can be found anywhere along the usual embryological migration pathway from the foramen cecum at the base

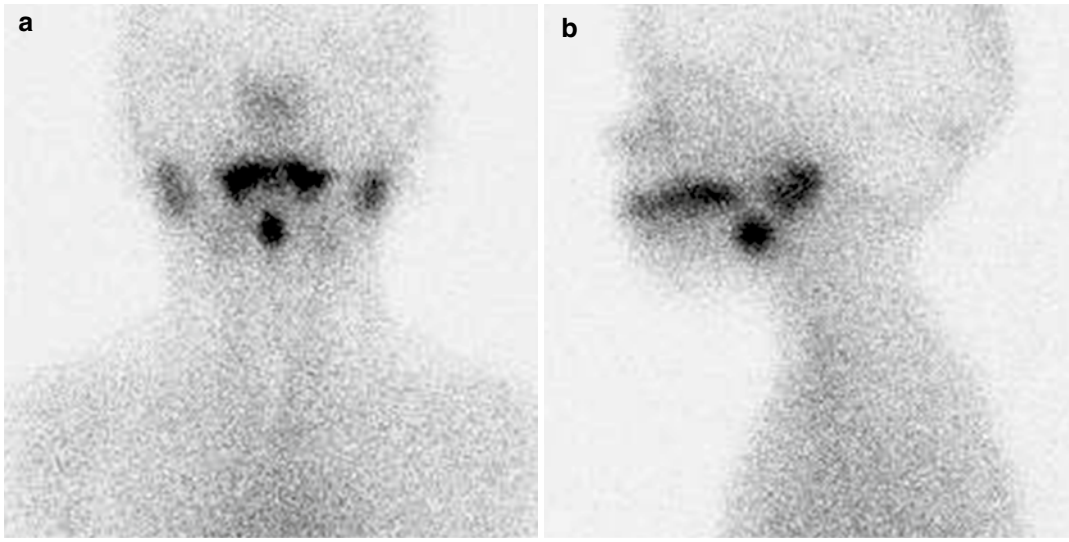

Fig. 5.4 Lingual thyroid gland detected with thyroid scan performed with [^{99m}Tc] sodium pertechnetate. (**a**) In a 3-year-old boy with congenital hypothyroidism, a planar scan performed with [^{99m}Tc] sodium pertechnetate. A planar image acquired in the anterior projection demonstrates no thyroidal uptake in the expected location of the thyroid gland. Extensive and expected uptake is seen in salivary glands and in secretions in the oral and nasal cavities. Above the neck, a midline focus of uptake is at a typical location for a lingual thyroid gland. (**b**) A planar image acquired in a lateral projection confirms the location of an ectopic lingual thyroid gland

of the tongue to the mediastinum, but development of clinically identifiable thyroid tissue is rare. Occasionally, ectopic thyroid tissue rarely is discovered elsewhere in the neck. Rarely, multiple sites of ectopic thyroid tissue can be identified [37]. At least two-thirds of patients with a clinically apparent ectopic thyroid mass have no thyroid gland in the expected location in the thyroid bed. The most common presenting symptom is new awareness of a mass in the anterior neck or at the base of the tongue. Other presenting symptoms can include dysphagia, dysphonia, or hemorrhage from a lingual thyroid gland. Almost always, the growing thyroid tissue represents histologically benign thyroid tissue, but thyroid carcinoma has been reported in ectopic thyroid tissue.

Unusual sites of ectopic thyroid tissue in the ovary (struma ovarii) and elsewhere in the abdomen and pelvis likely reflect ectopic development of thyroid tissue and not abnormal migration from the foramen cecum [37]. These sites of abnormal thyroid tissue have a higher incidence of hyperfunction and malignancy. In cases of suspected ectopic thyroid, thyroid scintigraphy can be helpful confirming that the mass represents functional thyroid tissue and at the same time can help determine if a normal thyroid gland is present [38].

Evaluation of Hyperthyroidism

Thyroid hormone contributes to the regulation of metabolic activity throughout the body. Excess levels of thyroid hormone produce symptoms of hypermetabolism, such as heat intolerance and weight loss, and symptoms of adrenergic excess, such as tremor, hyperactivity, tachycardia, palpitations, increased frequency of bowel movements, and sleep disturbance. In children, other symptoms can include behavioral disturbance, impaired school performance, and growth disturbance [39–41]. The term thyrotoxicosis refers to the clinical syndrome resulting from excess circulating levels of thyroid hormone.

Thyroid hormone excess can result from a variety of disorders (Table 5.2). With the exception of rare cases of secondary hyperthyroidism,

Table 5.2 Thyrotoxicosis in children

Cause	Typical thyroid radioiodine uptake
Graves' disease	Autonomous (usually elevated)
Toxic ("hot") nodule	Autonomous uptake in the nodule (with suppression of normal thyroid tissue)
Toxic multinodular goiter	Autonomous uptake in overactive nodules (with suppression of normal thyroid tissue)
Subacute thyroiditis	Decreased
Chronic thyroiditis ("hashitoxicosis")	Decreased
Factitious thyrotoxicosis (excess thyroxine intake)	Suppressed
Secondary thyrotoxicosis (elevated TSG, hCG)	Elevated
Ectopic thyroid tissue	Suppressed

elevated levels of thyroid hormone suppress secretion of thyroid-stimulating hormone (TSH) through the process of negative feedback on the hypothalamic-pituitary-thyroid axis. Strictly speaking, the term hyperthyroidism refers only to the overproduction of thyroid hormone by thyroid tissue, but any inappropriate elevation of circulating thyroid hormone sometimes is referred to as hyperthyroidism. The diagnoses of thyrotoxicosis and hyperthyroidism are based on clinical findings and blood tests (plasma T4, T3, and TSH). Determination of radioiodine uptake and thyroid scintigraphy can further characterize the underlying cause of the thyrotoxicosis, which is useful in guiding appropriate therapy.

Thyrotoxicosis can result from hyperthyroidism due to overproduction of thyroid hormone by a toxic goiter (Graves' disease), a toxic thyroid nodule, or a toxic multinodular goiter. These conditions are characterized by increased thyroid uptake of iodine in the overactive thyroid tissue. Graves' disease represents autonomous thyroid hyperfunction due to circulating stimulating antibodies directed against the TSH receptor on the cell surface of thyroid follicular cells. The resulting hyperthyroidism produces hyperthyroxinemia with subsequent suppression of TSH levels. Most cases of Graves' disease are characterized by elevated circulating levels of both levothyroxine (T4) and triiodothyronine (T3). However, occasional patients with Graves' disease may have elevated T3 levels without T4 elevation [39], which sometimes is referred to as "T3 toxicosis."

In patients with Graves' disease, autonomous thyroid function almost always is associated with increased radioiodine uptake. While assessing thyroid radioiodine uptake, most institutions will perform thyroid scintigraphy to assess the functional structure of the thyroid gland (Figs. 5.5 and 5.6). Occasional mild cases of Graves' disease may be associated with "normal" radioiodine uptake (Fig. 5.7). However, in the absence of circulating TSH, a normal radioiodine uptake is inappropriately normal and still consistent with Graves' disease. Other causes of a normal radioiodine uptake in Graves' disease include recent iodine intake (Table 5.1) or administration of radiographic contrast. Thyrotropin receptor antibodies (TRAb) or thyroid-stimulating antibodies (TSAb) may be assayed in patients with suspected Graves' disease, but these assays may have a false-negative rate of 10–20 %. These antibody assays are rarely necessary as the combination of thyrotoxicosis and an elevated (or inappropriately normal) radioiodine uptake is virtually diagnostic of Graves' disease [42]. While assessing thyroid radioiodine uptake, most institutions will perform thyroid scintigraphy to exclude either an autonomous or a hypofunctioning thyroid nodule (Fig. 5.8). Although cold nodules are an infrequent finding in the setting of Graves' disease, some reports have suggested that they may have an increased likelihood of malignancy or aggressive clinical features [39].

Autonomous thyroid nodules [39–41], whether solitary or within a multinodular goiter, produce elevated thyroid hormone levels that will suppress TSH levels. With the absence of TSH stimulation, the function of the remaining nonautonomous thyroid tissue is suppressed, and it will demonstrate decreased radioiodine uptake on thyroid scintigraphy. The resulting pattern of autonomous radioiodine uptake in the

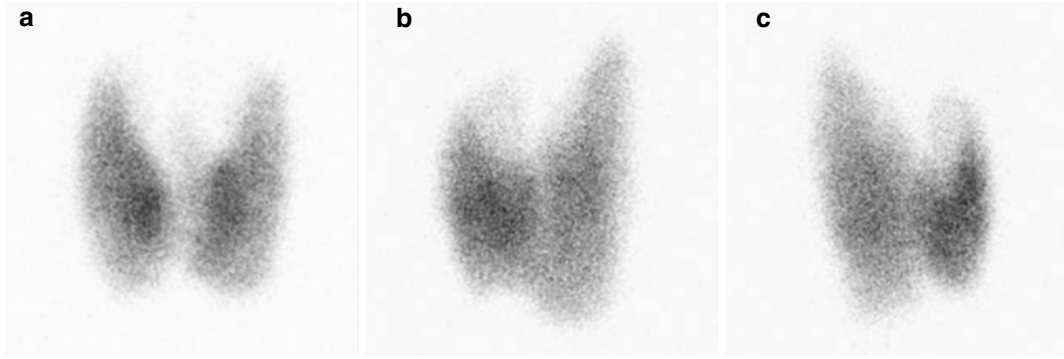

Fig. 5.5 Thyroid scintigraphy in Graves' disease. In a 15-year-old female with Graves' disease of 2 years duration, thyroid scintigraphy was performed with ^{123}I. Pinhole images acquired in the anterior (**a**), left anterior oblique (**b**), and right anterior oblique (**c**) projections demonstrate a symmetrically enlarged thyroid gland with diffuse or mildly heterogenous iodide uptake. The thyroid isthmus and a small pyramidal lobe can be identified. Radioiodine uptake was 85 % at 4 h and 83 % at 24 h. The patient was treated successfully with 15 mCi ^{131}I

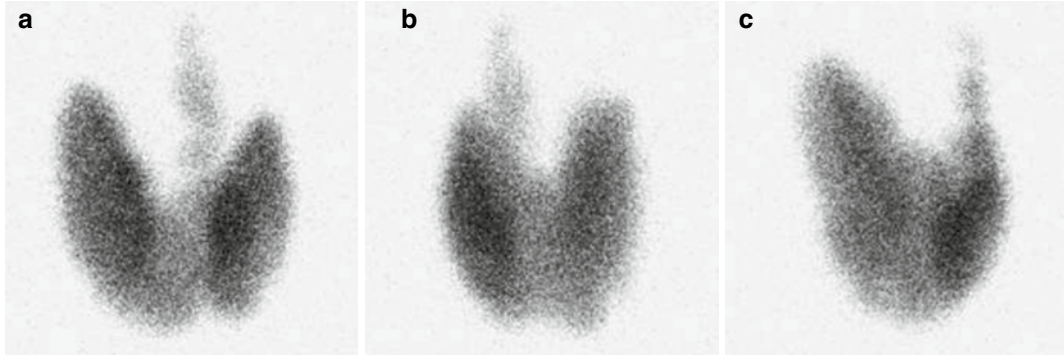

Fig. 5.6 Thyroid scintigraphy in Graves' disease. A 15-year-old male developed palpitations and heat intolerance and was diagnosed with hyperthyroidism (TSH <0.001 mU/l, free T4 >7.5 ng/dl). Iodine-123 scintigraphy was performed with pinhole images of the thyroid gland acquired in the anterior (**a**), left anterior oblique (**b**), and right anterior oblique (**c**) projections. There is diffuse or mildly heterogenous uptake in both enlarged thyroid lobes and in a long pyramidal lobe that extends along the anterior neck. Radioiodine uptake was 79 % at 4 h and 82 % at 24 h. He was treated successfully with 18 mCi ^{131}I

nodule with suppression of uptake in the remaining thyroid tissue is that of a "hot nodule" (Fig. 5.9). Other thyroid nodules may have mild autonomous overactivity, but, without suppression of TSH levels, the radioiodine uptake in the nodule will be similar to the surrounding thyroid tissue; these are "warm" thyroid nodules (Fig. 5.10)

Other causes of thyrotoxicosis [39–41] typically are associated with decreased iodine uptake throughout the thyroid gland. The combination of thyrotoxicosis with suppressed thyroid

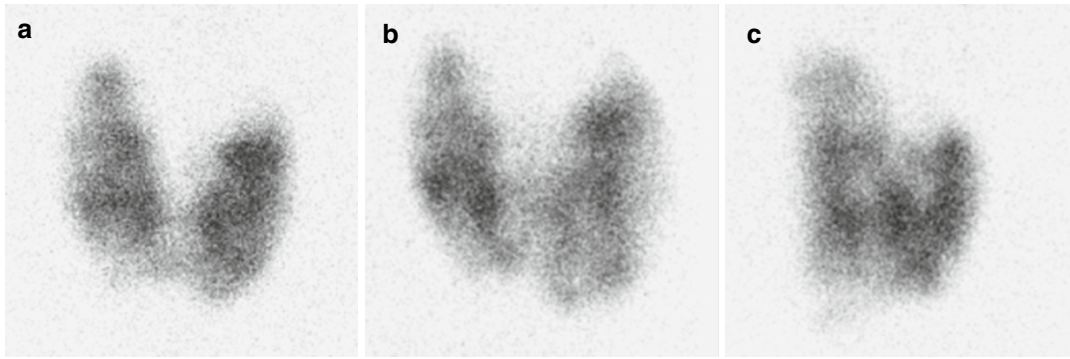

Fig. 5.7 Thyroid scintigraphy in Graves' disease with inhibited radioiodine uptake. An 11-year-old girl with Graves disease previously had been treated with oral antithyroid medications and then had been in remission without therapy for 2 years. After recurrence of Graves' disease (TSH 0.009 mU/l, free T4 1.95 ng/dl), thyroid scintigraphy was performed with ^{123}I. Pinhole images acquired in the anterior (**a**), left anterior oblique (**b**), and right anterior oblique (**c**) projections demonstrate patchy uptake throughout an enlarged thyroid gland. Radioiodine uptake was only 14 % at 4 h and 24 % at 24 h. The uptake was inappropriately normal in the absence of circulating TSH. The differential includes thyroid hormone ingestion, recurrent Graves' disease complicated by self-treatment with antithyroid medication, iodine ingestion, and mild Graves' disease. Further investigation revealed that the patient was taking an unreported dietary supplement that contained an unexpectedly high level of iodine. Three months after discontinuation of the supplement, radioiodine uptake increased to 53 % at 4 h and 61 % at 24 h, the patient was treated with 20 mCi ^{131}I

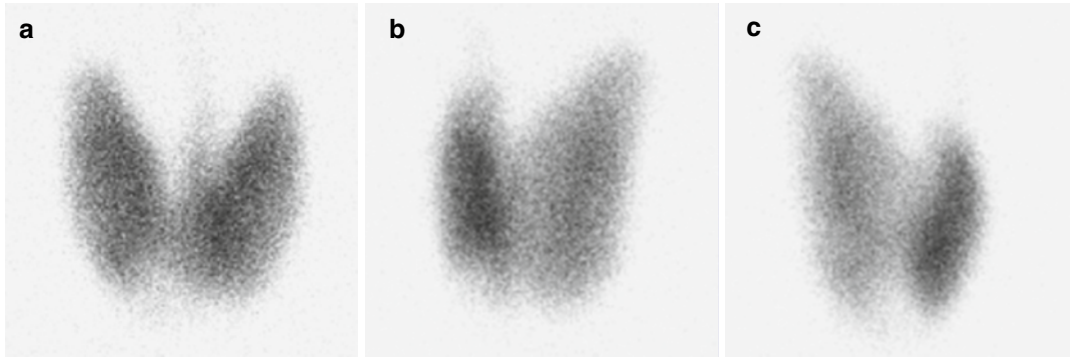

Fig. 5.8 Thyroid scintigraphy of papillary thyroid cancer in a patient with Graves' disease. An 12-year-old girl with a sore throat was found to have an enlarged thyroid gland and thyrotoxicosis (TSH <0.001 mU/l, free T4 2.8 ng/dl). Physical examination by an endocrinologist revealed an enlarged thyroid with a palpable nodule in the lower pole of the right lobe. Iodine-123 scintigraphy with pinhole images of the thyroid gland acquired in the anterior (**a**), left anterior oblique (**b**), and right anterior oblique (**c**) projections showed a bilaterally enlarged and symmetrical thyroid gland, with slightly patchy tracer uptake and prominent uptake in a pyramidal lobe. There is minimal uptake in the palpable nodule at the lower pole of the right lobe of the gland. The nodule was evaluated by fine-needle aspiration under ultrasound guidance, and cytology was suspicious for papillary carcinoma. After treatment with methimazole and SSKI, a total surgical thyroidectomy was performed, and pathology showed a 1.2 cm papillary thyroid carcinoma

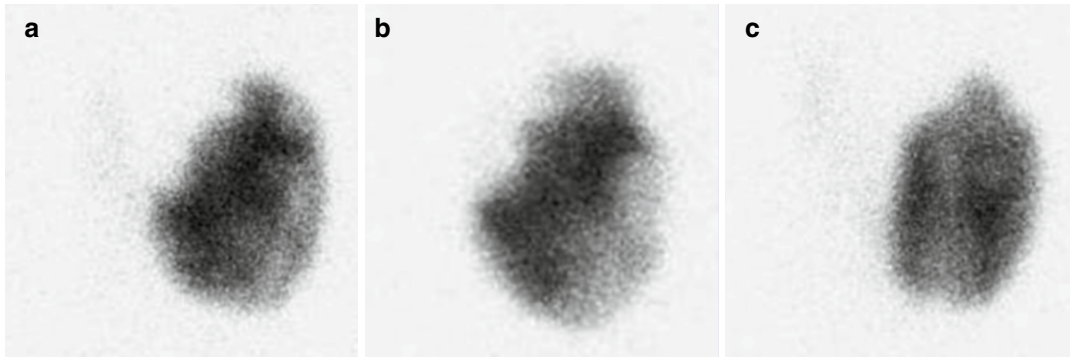

Fig. 5.9 Thyroid scintigraphy of an autonomous ("hot") thyroid nodule. A 13-year-old girl with an enlarged left thyroid lobe was found to have hyperthyroidism (TSH <0.005 mU/l, free T4 1.7 ng/dl). Iodine-123 scintigraphy was performed with pinhole images of the thyroid gland acquired in the anterior (**a**), left anterior oblique (**b**) and right anterior oblique (**c**) projections. There is mildly heterogenous and intense uptake in a large nodule in the left lobe of the thyroid gland. There is minimal uptake in the normal thyroid gland. Radioiodine uptake was 30 % at 4 h and 51 % at 24 h. Surgical thyroidectomy was performed and pathology showed benign nodular hyperplasia

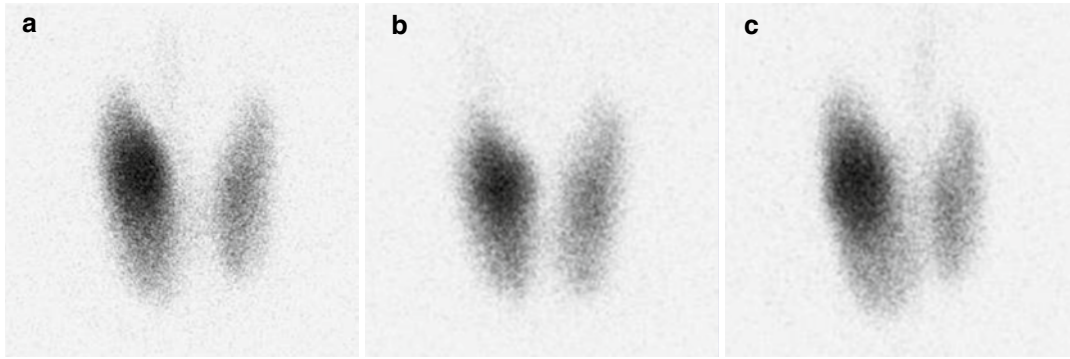

Fig. 5.10 Thyroid scintigraphy of a "warm" thyroid nodule. In a 14-year-old girl with a palpable thyroid nodule and subclinical hyperthyroidism with free T4 1.24 ng/dl (reference 0.8–1.9 ng/dl) and TSH 0.3 mU/l (reference 0.7–5.0 mU/l), ultrasound demonstrated a 3 cm nodule in the upper pole of the right lobe of the thyroid gland. Iodine-123 scintigraphy was performed with pinhole images of the thyroid gland acquired in the anterior (**a**), left anterior oblique (**b**), and right anterior oblique (**c**) projections. There is increased uptake within the nodule in the upper region of the right lobe of the thyroid, but there is no suppression of the rest of the normal appearing thyroid gland. Fine-needle aspiration revealed benign cytology, and the patient and her family have opted for close clinical follow-up

uptake most commonly represents either a subacute or chronic thyroiditis (Fig. 5.11). *Subacute* thyroiditis represents an autoimmune-mediated inflammation, and possible destruction, of the thyroid gland. There are various subgroupings and categorizations of subacute thyroiditis, such as painless or painful and lymphocytic or granulomatous, but all appear similar on thyroid scintigraphy. Postpartum thyroiditis is a common cause of painless thyroiditis. *Chronic* thyroiditis, also called Hashimoto's thyroiditis, is characterized by autoimmune inflammation and destruction of the thyroid gland that usually results in hypothyroidism, but a subset of patients

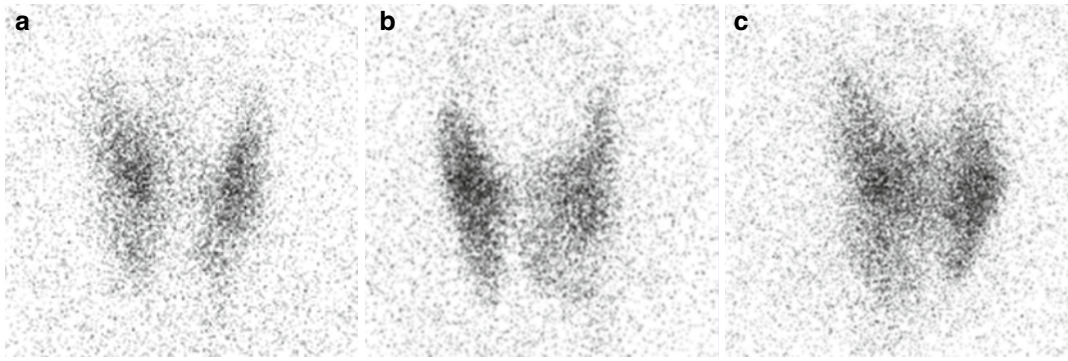

Fig. 5.11 Thyroid scintigraphy of subacute thyroiditis. A 14-year-old girl with sweating and hot flashes was found to have a suppressed TSH (0.2 mU/l) and elevated total T4 level (14.7 mcg/dl). There was no thyroid tenderness. After administration of ^{123}I, radioiodine uptake was 5 % at 4 h and 3 % at 24 h. Scintigraphy performed with pinhole images of the thyroid gland acquired in the anterior (**a**), left anterior oblique (**b**), and right anterior oblique (**c**) projections showed minimal uptake in a symmetrical thyroid gland. Symptoms of sweating and hot flashes responded to symptomatic therapy, and the patient eventually developed chronic hypothyroidism

developed transient thyrotoxicosis (sometimes called "hashitoxicosis") characterized by decreased radioiodine uptake. *Acute* thyroiditis, by comparison, refers to a suppurative infection of the thyroid, an extremely rare condition that is associated with a heterogeneous pattern of radioiodine uptake.

Suppressed radioiodine uptake has a broad differential beyond thyroiditis (Table 5.3). Other causes of thyrotoxicosis with suppressed radioiodine uptake include excess intake of thyroid hormone (*thyrotoxicosis factitia*) and ectopic thyroid tissue. Factitious thyrotoxicosis has been reported with inappropriate intake of thyroid hormone in misguided attempts at weight loss or energy stimulation, unintentional intake in non-traditional diet supplements containing thyroid hormone or the result of contamination of meat products with bovine or porcine thyroid tissue ("hamburger thyrotoxicosis"), and, in children, surreptitious ingestion of thyroid medications prescribed for family members. Ectopic thyroid tissue, such as *struma ovarii* or functional metastatic thyroid cancer, is rare but can demonstrate TSH-independent autonomy with suppression of a normal thyroid gland. Decreased or absent radioiodine uptake is seen with hypothyroidism and in patients with thyroid tissue absent due to surgery or radioiodine ablation. Antithyroid medications will decrease radioiodine uptake, so that these medications must be discontinued (typically for 3 days) before thyroid scintigraphy or determination of radioiodine uptake. Prior to performing thyroid scintigraphy, it is important to obtain a thorough dietary and medical history and to delay the study if appropriate (Table 5.1).

Table 5.3 Causes of decreased thyroid radioiodine uptake

Thyrotoxicosis
Subacute thyroiditis (lymphocytic)
Subacute thyroiditis (granulomatous)
Subacute phase of chronic thyroiditis
Factitious thyrotoxicosis
Ectopic thyrotoxicosis
Increased iodine intake/administration
Iodine-rich diet
Iodine-containing medications/supplements
Intravenous iodinated radiological contrast
Hypothyroidism
Autoimmune hypothyroidism
Athyreosis/ectopic thyroid gland
Prior thyroidectomy
Prior thyroid ablation
Antithyroid medications

Treatment of Hyperthyroidism

Treatment of thyrotoxicosis depends upon the underlying mechanism of thyroid hormone excess. No definitive therapy is available for thyroiditis, and possible medical therapy includes symptomatic therapy, such as beta-blockers, to decreased cardiac awareness and palpitations. On the other hand, the options for treatment of hyperthyroidism [39–42] include medical therapy, radioiodine therapy [43], and surgery [44]. The treatment plan must be developed in consultation with the patient and family, and usually is made in collaboration with the referring physician.

For most patients with hyperthyroidism due to Graves' disease or an autonomous thyroid nodule, medical therapy is the preferred first choice for therapy. The thionamides (propylthiouracil, methimazole) have an antithyroid effect and can be highly effective for the treatment of hyperthyroidism. In children with Graves' disease, up to one-third of patients may obtain disease remission within 2 years of starting antithyroid medications. Other patients can use these medications for long-term control of the hyperthyroidism, and some may achieve long-term remission. However, up to a third of children that go into remission may relapse [45]. Due to recent reports of hepatotoxicity associated with the use of propylthiouracil (PTU) in pediatric patients, methimazole has become the antithyroid medication of choice for children. PTU should not be the first drug of choice, and long-term PTU therapy should never be used in children [46]. However, PTU may have a very limited short-term role during the first trimester of pregnancy and in the treatment of thyroid storm [47]. Other supportive therapies, such as beta-blockers to lessen cardiac symptoms, also may be helpful early in treatment [40, 47].

Many patients experience good clinical results with medical treatment of hyperthyroidism. However, patients can have difficulty with the strict regimen of taking medication two to four times a day, and poor compliance can result in suboptimal control or treatment failure. Up to one-quarter of patients may develop minor side effects, such as pruritus, hives, myalgias, arthralgias, mild increases in liver enzymes, or mild decreases in white blood cell count [40]. Severe or life-threatening side effects of antithyroid medications are rare (probably less than 5 %) but include severe hepatotoxicity and bone marrow suppression [48, 49]. Unlike the hepatocellular injury and liver failure associated with PTU, cholestasis is more likely to be associated with methimazole [50]. Patients who do not achieve adequate long-term disease control or have medication side effects usually seek definitive therapy. Definitive therapy, with either surgery or radioiodine therapy, likely will result in permanent hypothyroidism requiring lifelong thyroid hormone replacement therapy.

Although surgical thyroidectomy was the first definitive therapy developed for hyperthyroidism, it is now rarely the first treatment of choice. Possible risks of thyroidectomy include anesthesia complications, damage to the recurrent laryngeal nerve, hypoparathyroidism due to inadvertent injury or removal of the parathyroid glands, and bleeding necessitating reoperation. These risks should be extremely low with an experienced thyroid surgeon. Surgical thyroidectomy may be the choice for definitive therapy in selected circumstances, including failed radioiodine therapy, pregnancy with intolerance or allergy to antithyroid medications, or for women planning a pregnancy in less than 4–6 months. Surgical therapy also will be the first choice for treatment of Graves' disease when concurrent thyroid malignancy is documented by cytopathology or suspected in a concurrent nonfunctioning thyroid nodule (Fig. 5.8) [47]. Surgical therapy may be an appropriate first choice for treatment of an autonomous ("hot") thyroid nodule (Fig. 5.9), particularly if the nodule is large enough to cause compressive symptoms, if there are concomitant nonfunctioning thyroid nodules, or for cosmetic reasons.

Radioiodine Therapy for Hyperthyroidism

Radioiodine therapy has been used for over 65 years for the treatment of hyperthyroidism [1, 2, 51, 52]. Iodine-131, administered as [^{131}I]

sodium iodide, is effective for treatment of both Graves' disease and toxic thyroid nodules [53]. After administration of adequate ^{131}I radioiodine therapy, approximately three-quarters of patients with Graves' disease will be euthyroid within 2 months, and over 90 % eventually will achieve hypothyroidism. Although some attempts have been made to carefully titrate the radioiodine dose in an effort to achieve post-therapy euthyroidism, this approach had an increased risk of disease recurrence, and the current consensus is to aim for thyroid ablation as definitive therapy of Graves' disease.

Although rare in young children (less than 5 years of age), Graves' disease can occur in this age group. Some clinicians advocate against radioiodine therapy in these very young children due to concerns about radiation risk, but the complication rate of surgical thyroidectomy also is greater in children than adults. Young children provide a challenge for radiation safety, as they require closer involvement with caretakers and may not yet be toilet trained. Therefore, it is preferable that the few young children requiring treatment for Graves' disease be treated with antithyroid medications until old enough for definitive therapy. However, when indicated, radioiodine therapy can be used in young children [42, 47].

For treatment of hyperactive thyroid nodules, radioiodine therapy may be the preferred therapy for a small nodule or in a patient with a higher surgical risk [53, 54]. Ablation of hyperactive thyroid tissue allows TSH levels return to normal with subsequent return of normal thyroid function [55]. The response to radioiodine therapy is more rapid with a single toxic nodule. Three-quarters of patients will reach euthyroidism within 3 months after treatment for a single nodule and within 6 months after treatment for a toxic multinodular goiter. A small number of patients will develop hypothyroidism within the first year, but nearly two-thirds of patients treated as children may develop hypothyroidism by two decades [56, 57]. Some clinicians prefer to not use radioiodine for treatment of thyroid nodules due to concerns about the theoretical risks of radiation exposure to the rim of normal thyroid tissue adjacent to the treated nodule.

Many approaches have been advocated for choosing the appropriate administered dose of ^{131}I for the treatment of hyperthyroidism [53, 58–60]. Some practitioners have administered the same empiric dose of ^{131}I, typically ranging between 5 and 29 mCi, to every patient. Another approach has been to correct an empiric dose for the measured uptake of radioiodine as determined by a prior radioiodine uptake measurement. For example, the intended goal may be to achieve delivery of 8 or 12 mCi of ^{131}I to the thyroid gland. However, both of these approaches seem less appropriate for pediatric patients, and ideally, the administered dose of ^{131}I is adjusted for both thyroid size and radioiodine uptake. The effectiveness of radioiodine therapy depends upon an adequate radiation dose to the thyroid gland. Usually, this can be achieved with an administered dose of 0.08–0.22 mCi per gram of thyroid, corrected for thyroid uptake [51, 53].

$$\text{I-131 Dose}(\text{mCi}) = \frac{(0.08 - 0.22\,\text{mCi/g}) \times \text{estimated thyroid weight}(\text{g})}{\text{iodine uptake at 24 h}}$$

Thyroid radioiodine uptake (ranging between 0.00 and 1.00) is determined 24 h after oral administration of a small dose of ^{123}I (see section "Thyroid Uptake"). Estimated thyroid size is determined by physical examination of the neck by an experienced clinician. Imaging studies, such as ultrasound or CT, are not reliable methods for estimating thyroid gland size. A dose at the higher range (0.2 mCi/g) is used for younger patients (i.e., most pediatric patients), if the gland is relatively large, or when there has been prior failure of radioiodine therapy. The higher dose also is used when the thyroid has a high iodine turnover, demonstrated by 24 h radioiodine uptake less than the 4-h radioiodine uptake. In

children, the administered dose of ^{131}I should not be decreased solely based on age, as this risks undertreatment and the need for additional doses of radioiodine therapy [47, 53].

Most guidelines recommend a low-iodine diet for at least 2 weeks before administration of radioiodine. This should include maintaining a low-salt diet, as salt may be supplemented with iodine. Although there is little evidence that a strict low-iodine diet improves outcome, substantial prior iodine intake will decrease radioiodine uptake, even in a thyroid gland with Graves' disease. As this can decrease uptake of the therapeutic dose and could require administration of a larger dose of ^{131}I to achieve adequate thyroid uptake of the therapeutic dose, it is most important to avoid sources of large doses of iodine, such as iodine-containing medications and iodinated radiological contrast. Unless contraindicated, most patients will have received treatment with antithyroid medications prior to radioiodine therapy. These medications should be discontinued 3–5 days before administration of radioiodine [47, 53]. Typically, patients will discontinue antithyroid medications at least 3 days before the pretreatment thyroid scintigraphy and uptake. In some patients, antithyroid medications will be restarted 3–7 days after radioiodine administration.

Radioiodine therapy has a number of side effects and risks [53] that should be discussed with the patient and family before making a decision to use radioiodine therapy. Transient worsening of hyperthyroidism may occur due to withdrawal of antithyroid medications or due to a potential unregulated release of thyroxine during the inflammatory response to ^{131}I. Persistent or recurrent hyperthyroidism occurs in less than 10 % of patients. Patients must understand that the goal of ^{131}I therapy is permanent hypothyroidism, which will require lifelong thyroid hormone replacement therapy. Another potential short-term complication is thyroid or salivary gland pain, which usually responds to over-the-counter anti-inflammatory agents. Long-term salivary damage is possible but very unlikely at the radioiodine doses used to treat Graves' disease. Many authorities recommend sour candies or tart juice to increase salivary flow with the goal of decreasing ^{131}I residence time in the salivary glands. Typically, this is started soon after administration of the radioiodine dose, but some studies suggest that the start of these agents be delayed for 24 h after ^{131}I administration. Antiemetics may be useful in children. As the mass of administered iodine is less than 1 microgram, allergy to iodine is not a contraindication to radioiodine therapy. There has been concern that radioiodine therapy may lead to a worsening of thyroid ophthalmopathy. More recent findings suggest that the incidence of new eye disease or worsening of know eye disease is no greater with radioiodine than other forms of therapy and that early post-therapy thyroid hormone replacement is important in limiting Graves' ophthalmopathy [61]. As a general rule, definitive therapy of Graves' disease should not be delayed due to concerns about thyroid ophthalmopathy. However, it is important that patients with eye findings receive appropriate ophthalmological care.

The potential risk of carcinogenesis after radioiodine therapy should be discussed with a patient and family. Long-term studies of large medical registries, mostly in the USA and Scandinavia, have produced conflicting results about the risk of cancer after ^{131}I therapy [62–66]. Although an increase in overall risk of cancer has not been clearly demonstrated, there may be a small increase in the risk of solid tumors in tissues that may have the greatest iodine accumulation, such as stomach, kidney, and breast. A possible increased risk of thyroid cancer reported by some early studies probably reflects the use of relatively low doses of ^{131}I resulting in incomplete thyroid ablation [47]. Prior concerns regarding leukemia risk after radioiodine therapy for hyperthyroidism have not been confirmed with any of these more recent studies. In patients receiving radioiodine for treatment of an autonomous thyroid nodule, there is concern about the theoretical risk of radiation exposure to the rim of normal thyroid adjacent to the nodule. Because of this, it may be appropriate to delay radioiodine therapy of a thyroid nodule, possibly until the patient reaches adulthood.

Pregnancy is an absolute contraindication to radioiodine therapy, and pregnancy must

be excluded before a therapeutic dose of ^{131}I is administered to a female patient. Most hospitals have clear policies regarding the timing of pregnancy testing in female children before radioiodine therapy. Gonadal radiation dose is enhanced with accumulation of ^{131}I in the bladder, so patients should be encouraged to drink copiously during the first few days after radioiodine administration. There is no evidence of teratogenesis or other adverse outcomes in future offspring conceived after administration of radioiodine therapy. Many guidelines recommend that pregnancy be delayed for a period of time, typically 3–6 months, after therapy with ^{131}I [53]. Similarly, breastfeeding must be discontinued prior to radioiodine therapy. There is no contraindication to breastfeeding children that are born of subsequent pregnancies.

Radioiodine is not indicated for some forms of thyrotoxicosis. Radioiodine is not effective in the treatment of any form of thyroiditis. The minimal iodine uptake associated with thyroiditis means that little of the administered radioiodine would be taken up in the thyroid gland. More importantly, subacute thyroiditis and chronic thyroiditis are self-limited processes of thyroid inflammation, and treatment with ^{131}I will have little effect on the course of the disease.

Radioiodine therapy should never be used for acute treatment of thyroid storm. The beneficial effects of radioiodine therapy occur over months, which is not rapid enough to serve as a useful treatment of thyroid storm. The inflammatory response to radioiodine may cause release of additional thyroid hormone, which potentially could worsen the thyrotoxicosis. Many patients with thyroid storm will have received large doses of nonradioactive iodine in an attempt to transiently decrease thyroid hormone secretion (the Wolf-Chaikoff effect), which will limit thyroid uptake of administered radioiodine. Finally, administration of a therapeutic dose of radioiodine will necessitate radiation safety precautions, which may interfere with the intensive medical and nursing care needed by a patient with thyroid storm. Thus, requests for radioiodine therapy should be strongly resisted, and ^{131}I should never used for the acute treatment of thyroid storm.

Thyroid Nodules

Thyroid nodules, and their appropriate evaluation, are important because of the concern that they may represent thyroid cancer. Thyroid nodules are a frequent finding on physical examination. Incidental thyroid nodules can be identified on any study that includes the thyroid gland in the field of view, including neck ultrasound and chest CT. Up to one-third of all women in North America may have an identifiable thyroid nodule at some time in their lives. However, thyroid cancer is rare, with approximately 40,000 new cases per year diagnosed in the USA [67]. A thyroid nodule is more likely to represent thyroid cancer in the elderly and in children. Other risk factors that increase the likelihood of thyroid cancer include a hard, fixed nodule, lymphadenopathy, hoarseness, and dysphagia, but even most of these thyroid nodules will not be cancerous. Prior neck irradiation is a risk factor for thyroid cancer, but even with prior radiation therapy, there is only a 50 % likelihood that a thyroid nodule represents cancer. Therefore, the challenge is the effective and efficient evaluation of a large number of thyroid nodules to identify the small fraction that do represent thyroid cancer. Incidental thyroid nodules may be identified on FDG-PET [68, 69]. Little data is available for children, but for all ages, focal FDG uptake in the thyroid gland is quite likely to represent thyroid cancer and deserves further evaluation.

Thyroid scintigraphy has little role in the evaluation of most thyroid nodules [21, 70]. In the past, characterizing thyroid nodule activity by scintigraphy was an important part of determining the risk that the nodule represented thyroid cancer. An autonomous ("hot") nodule (Fig. 5.9) almost never represents thyroid cancer, while cancer cannot be excluded in a thyroid nodule with any other pattern ("not hot") of uptake. Thus, thyroid nodules with uptake that is less than ("cold", Fig. 5.12) or similar to ("warm," Fig. 5.10) normal thyroid tissue must undergo further evaluation to exclude cancer. Rarely, a hypofunctioning thyroid nodule may represent a parathyroid adenoma or metastases of a nonthyroidal cancer. Therefore, thyroid scintigraphy

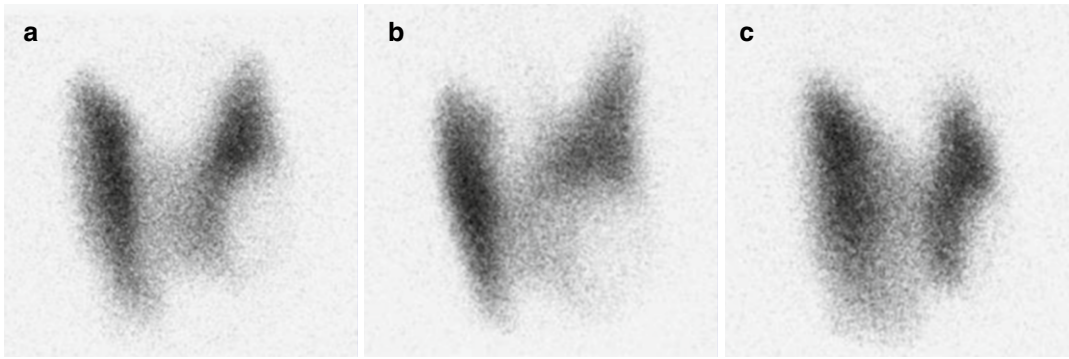

Fig. 5.12 Thyroid scintigraphy of a "cold" thyroid nodule. A 15-year-old female was found to have a thyroid nodule during a preoperative evaluation, and ultrasound confirmed a 2 cm nodule with mixed solid and cystic components in the lower pole of the left lobe of the thyroid gland. Thyroid function tests showed a TSH level of 0.95 mU/l (reference 0.7–5.0 mU/l). Iodine-123 scintigraphy was performed with pinhole images of the thyroid gland acquired in the anterior (**a**), left anterior oblique (**b**), and right anterior oblique (**c**) projection. The thyroid gland has a normal size and shape, with an ovoid region of photopenia corresponding to the palpable thyroid nodule in the lower pole of the left lobe. Radioiodine uptake was 11 % at 4 h and 28 % at 24 h. A surgical hemithyroidectomy was performed and the nodule had benign pathology

will be useful for excluding cancer in only the small fraction (<10 %) of thyroid nodules that have autonomous function. With hot nodules, the autonomous secretion of thyroid hormone from the nodule suppresses normal thyroid function by suppressing TSH secretion. Therefore, thyroid scintigraphy can be useful for thyroid nodule evaluation only in those patients with a suppressed TSH level. In all other cases, thyroid scintigraphy usually should not be performed, and a thyroid nodule should be evaluated by fine-needle aspiration, typically under ultrasound guidance. In the absence of a suppressed TSH level, thyroid scintigraphy should be considered only in unusual circumstances, such as a patient with a medical contraindication to fine-needle aspiration.

Thyroid Cancer

Nearly all thyroid cancer is categorized as differentiated thyroid cancer. Anaplastic thyroid cancer is exceedingly rare in children, but other uncommon forms of thyroid cancer, such as medullary thyroid cancer, can occur in children and young adults. The two major histological types of differentiated thyroid cancer are papillary thyroid cancer and follicular thyroid cancer. Most differentiated thyroid cancer is iodine avid and so can be imaged with radioiodine imaging and treated with ^{131}I.

Thyroid cancer is the most common endocrine malignancy in children and young adults. It represents over 3 % of all cancers diagnosed before the age of 20 years [67]. It is more common in teenagers than younger children, and it is five times more common in females than males. As in adults, the incidence of pediatric thyroid cancer has increased over the past few decades. Compared to adults, children with thyroid cancer are more likely to have widespread disease [71]. Although less common in children under the age of 10 years, thyroid cancer appears to be particularly aggressive in younger children, with higher rates of recurrence and mortality. Children are more likely than adults to have multifocal disease (up to 40 %) and disease spread to lymph nodes (greater than 50 %). Up to 30 % of all children with differentiated thyroid cancer will have distant metastatic disease, with half having metastases at the time of diagnosis. The most common site for distant metastases is the lungs. More than half the cases of lung metastases will

be micrometastases that are not evident of chest CT, but are detectable by radioiodine whole body scans [72]. Up to a third of thyroid cancer patients develop recurrent disease, and two-thirds of those will recur in the thyroid bed or cervical lymph nodes. However, one-third will recur with distant metastases, which is a risk factor for decreased survival [73].

Therapy of Thyroid Cancer

The primary treatment for thyroid cancer is surgical resection. Ideally, a near-total thyroidectomy will be performed. Compared to unilateral hemithyroidectomy, a bilateral thyroidectomy is associated with a lower rate of disease recurrence and an improved tumor-free survival rate [74, 75]. In some centers, patients with a lower risk of cancer may have surgical resection of the primary nodule and a hemithyroidectomy, with a completion thyroidectomy performed only if histology demonstrates cancer. Adjuvant chemotherapy or external beam radiation has little benefit for the treatment of differentiated thyroid cancer. Effective post-thyroidectomy treatments include TSH suppression with levothyroxine, surgical re-exploration of the neck, and ^{131}I therapy. Iodine-131 therapy increases recurrence-free survival and may increase overall survival. Iodine-131 is used for three indications: ablation of a thyroid remnant, treatment of residual disease, and treatment of metastatic disease.

Radioiodine ablation of postsurgical remnant thyroid tissue decreases recurrence of differentiated thyroid cancer [71, 76, 77], probably by treating microscopic sites of disease. Remnant ablation also facilitates post-therapy scanning for detecting disease and permits serum thyroglobulin to be used as a noninvasive marker to assess for disease recurrence [26]. Most guidelines recommend radioiodine remnant ablation in all except the very lowest-risk patients. These very low-risk patients are those who had a complete thyroidectomy with favorable histology, a single small (e.g., less than 1 cm) tumor, no local invasion, and no lymph node involvement. The typical adult ^{131}I dose for remnant ablation is 30–100 mCi, which can be scaled by patient size for younger patients [78]. However, treatment with less than 30 mCi is associated with a high failure rate, which results in the patient requiring a second dose of ^{131}I for remnant ablation [73]. In patients with known locoregional disease, remnant ablation can be combined with the first radioiodine therapy administered with therapeutic intent.

For treatment of residual neck disease or metastatic disease, the administered dose of ^{131}I is a clinical and dosimetric decision. The administered dose may depend on histology, extent of disease, location of metastases (lymph nodes, lung, or bone), and any prior therapy. There are multiple empiric approaches for determining the dose of ^{131}I [79], but most approaches typically use an adult dose of between 100 and 300 mCi per administration, which can be scaled based on patient size [78]. There is a wide variation in the frequency of ^{131}I treatment, but, for most patients, repeated radioiodine therapy is performed as long as iodine-avid disease is present. For physicians with limited experience in treating thyroid cancer, particularly in children, the most appropriate approach may be to provide treatment in collaboration with a more experienced physician or by referral to an institution with expertise in pediatric thyroid cancer.

An elevated circulating TSH level (typically greater than 30 mIU/ml) is needed to ensure adequate uptake of a therapeutic ^{131}I dose. This can be accomplished by withdrawing thyroid hormone replacement therapy for approximately 2–6 weeks prior to the anticipated treatment date. Although some adults may require up to 6 weeks to reach an adequate TSH level, young children may require as little as 1–2 weeks. Typically, thyroid hormone withdrawal is managed by the referring or treating physician. Patients and families should be advised that the patient will develop some symptoms of hypothyroidism during this time. If thyroid hormone will be withdrawn for a long period of time, some clinicians will treat with triiodothyronine (T3) for the first few weeks of thyroid hormone withdrawal [23]. As T3 has a shorter half-life than T4, it can be withdrawn 2 weeks before the planned therapy.

However, this rarely needs to be done in children. Adequate elevation of the circulating TSH level to greater than 30 mIU/l can be confirmed with a TSH blood level measured a day or two before pre-therapy imaging or administration of radioiodine. When recombinant TSH was available, some clinicians used it for preparation for radioiodine therapy in children, although the efficacy of this approach was never fully validated in this age group [19, 80].

Achieving a low-iodine state is important for ensuring that there is optimal uptake of radioiodine by thyroid cancer cells. Therefore, patients should avoid iodine intake (Table 5.1) and be placed on a low-iodine diet for 7–14 days before imaging or therapy. If there is any doubt about the success of iodine restriction, iodine economy can be assessed by measuring urinary excretion of iodine. This can be most accurately measured in a 24-h collection. Alternatively, iodine excretion can be estimated with the simultaneous measurement of iodine and creatinine in a random urine sample [18]. If urinary iodine excretion exceeds 50 mcg/day, then the patient probably has not reached an optimal low-iodine state [19].

Pregnancy is an absolute contraindication to radioiodine therapy, and a quantitative serum hCG level should be measured within 24–48 h before administration of radioiodine to any female patient at risk for pregnancy. Most institutions have established policies for determining which female patients must have a pregnancy test prior to radioiodine administration. For example, the policy may require pregnancy testing in all female patients determined to be post-menarchal by history or in all female patients older than age 10 years. Breastfeeding must be discontinued, preferably with adequate lead-time to allow involution of breast tissue, which will limit radioiodine uptake by the breasts. Breastfeeding cannot be resumed for the same child but can be done after any subsequent deliveries [19].

Many of the potential complications and long-term risks of radioiodine therapy for thyroid cancer are similar to those for treatment of hyperthyroidism. Patients should understand the lifelong need to take thyroid hormone replacement, usually at doses that will suppress TSH. Antiemetics can be useful, particularly with higher doses of radioiodine, which may be associated with nausea and vomiting [19]. Determinant (dose-dependent) risks of higher dose ^{131}I therapy include sialadenitis, xerophthalmia, and bone marrow suppression. Occasionally, there may be increased local radiation dose near sites of metastatic uptake, for example, brain and lungs, or near sites of a thyroid remnant or locoregional disease in the neck, and this may cause local tissue swelling [81]. The critical organs for radiation dose are bone marrow and sites of metastatic disease. The aim is to provide the largest effective radiation dose to sites of disease while avoiding bone marrow suppression or pulmonary fibrosis. Formal dosimetry may be useful in some cases, particularly in patients with extensive lung metastases [82, 83]. Although formal dosimetry typically has been performed with ^{131}I whole body scans, PET or PET/CT with ^{124}I may become an alternative for pre-therapy planning [10, 84].

In females, high-dose radioiodine therapy may be associated with earlier menopause [85]. In males, repeated administration of radioiodine may be associated with impaired spermatogenesis [86], leading some clinicians to suggest sperm banking if the cumulative dose of ^{131}I is likely to exceed 14 GBq (378 mCi) [71, 87]. There is no evidence of increased malformations or malignancy in offspring of males or females treated with radioiodine [71, 81]. Many guidelines recommend that pregnancy be delayed for at least 6 months after radioiodine therapy, but there is little data to support concerns that residual ^{131}I could harm a fetus conceived after radioiodine administration. However, due to normal alterations in thyroid hormone replacement needs during pregnancy [88], it may be prudent to delay pregnancy until the thyroid hormone replacement dose has been stabilized [81].

In patients treated with radioiodine for thyroid cancer, the risk of second primary malignancy is a concern. However, this is complicated by an increased risk of malignancy in patients with thyroid cancer, independent of therapy, and ascertainment bias [71, 89]. The few long-term

studies that specifically address the risk to individuals treated as children have not documented an increased risk [90]. In larger studies, including patients of all ages, radiation-related leukemia is rare but has been reported after high-dose (typically greater than a cumulative dose of 500 mCi) radioiodine therapy in a small number of cases [81]. Overall, there may be a slightly increased risk of tumors of the salivary glands, gastrointestinal tract, and soft tissue in adults receiving radioiodine for treatment of thyroid cancer [71, 81, 89].

Whole Body Scans in the Management of Thyroid Cancer

The utility of a diagnostic whole body scan (Fig. 5.13) in the management of thyroid cancer remains controversial [19, 21, 22]. A diagnostic whole body scan may be most useful in two circumstances (1) before planned therapy, when the amount of remnant thyroid tissue cannot be determined by the surgical report or ultrasound or (2) for surveillance, when the results will clearly affect the decision to administer radioiodine or the dose of radioiodine. Diagnostic

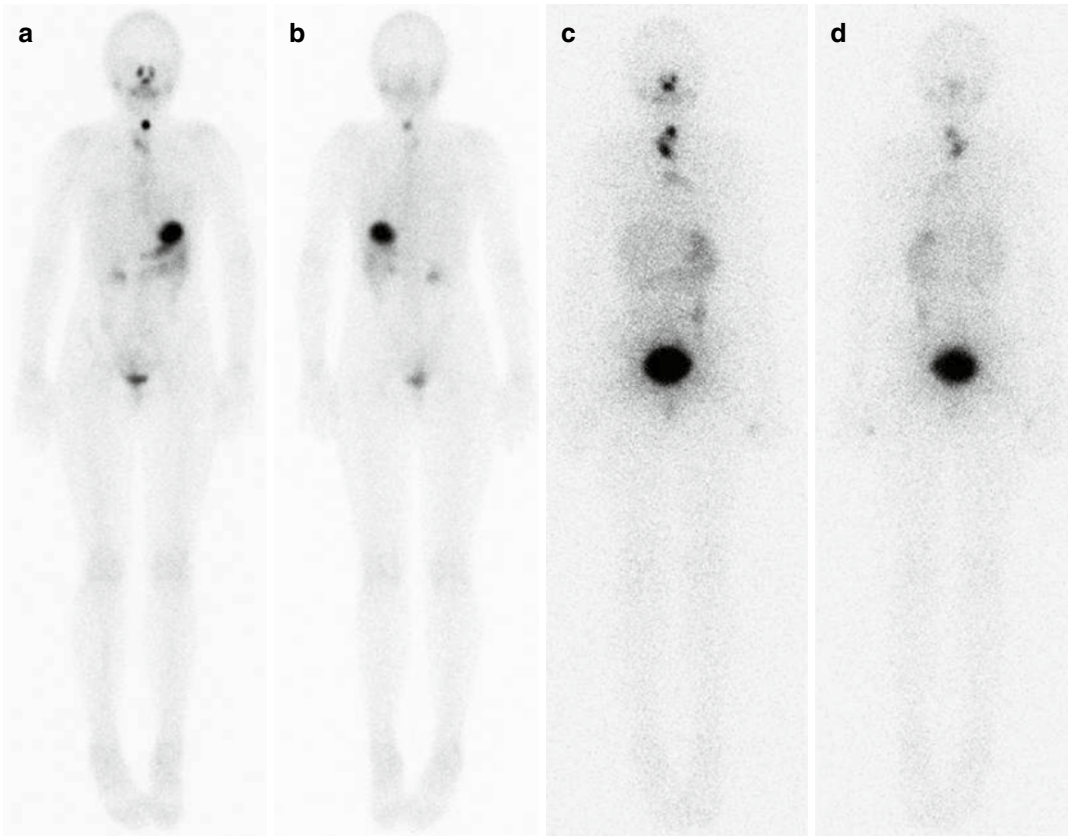

Fig. 5.13 Diagnostic and post-therapy whole body scintigraphy for thyroid cancer. A 14-year-old female with papillary thyroid cancer underwent near-total surgical thyroidectomy. Three months later, diagnostic whole body scintigraphy was performed with ^{123}I. Images acquired in the anterior (**a**) and posterior (**b**) projections demonstrate a poorly defined region of uptake in the lower right thyroid bed and an intense focus of uptake in the upper midline of the neck. Localization was confirmed with a marker at the suprasternal notch. Normal physiological accumulation of ^{123}I is seen in the lacrimal glands and nasal secretions, salivary glands and mouth, stomach, bowel, and bladder. Five days after treatment with 64 mCi ^{131}I, a post-therapy whole body scan was performed. Images acquired in the anterior (**c**) and posterior (**d**) projections demonstrate intense uptake in the remnant thyroid tissue in the neck. Physiological accumulation of ^{131}I is seen in lacrimal glands and nasal secretions, salivary glands and mouth, thymus, liver, and bowel. Intense uptake in the pelvis is in the sigmoid colon and rectum

whole body scans are not recommended for routine use in all patients by current guidelines of the American Thyroid Association [21]. However, advocates argue that pre-therapy whole body scans have the potential to provide unexpected information that may change care for many patients [22]. Primarily, this has included patients in whom identification of unexpected distant metastases leads to a decision to appropriately increase the ^{131}I dose. Pre-therapy diagnostic scans also may benefit patients found to have large thyroid remnants or unanticipated cervical lymph node metastases, as they may be advised to undergo repeat surgery before radioiodine therapy. Rarely, diagnostic scans can identify unexpected metastatic disease in the brain or spinal cord, which may require pretreatment with corticosteroids to limit post-therapy swelling [19].

Post-therapy scans will demonstrate uptake of radioiodine at sites of iodine-avid disease [21, 23, 26–28]. Approximately 10 % of patients will have iodine-avid disease identified on post-therapy whole body scan that was not apparent on the pre-therapy whole body scan [23, 26]. The post-therapy scan may be most useful in patients with elevated thyroglobulin levels and a negative diagnostic whole body scan [27]. Up to half of these individuals may be shown to have iodine-avid metastases to lung (Fig. 5.14) or bone [26, 28]. Therefore, a post-therapy whole body scan is recommended by the clinical guidelines of the American Thyroid Association [21] and American Association of Clinical Endocrinology [26].

Evaluation and Follow-Up of Patients with Thyroid Cancer

The risk of recurrence of thyroid cancer has been reported to be between 15 % [91] and 30 % [92], with the wide range likely reflecting differences in the aggressiveness of primary therapy. Age also is a risk factor for recurrence, with younger age associated with a higher risk of recurrence [73]. A third of all patients with recurrent thyroid cancer will have distant metastatic disease. Therefore, the evaluation and surveillance of patients with thyroid cancer depends on being able to detect recurrence and to localize sites of distant disease. The appropriate strategy for following patients with thyroid cancer can vary among institutions and treating physicians and is best guided by clinical guidelines developed by professional organizations, including the Society of Nuclear Medicine and Molecular Imaging [19], the American Thyroid Association [21], and the American Association of Clinical Endocrinologists and American College of Endocrinology [26]. Although there may be some variations among these guidelines, they represent the consensus opinions of clinical experts guided by the current medical literature. These guidelines recommend post-therapy surveillance with some combination of serum thyroglobulin and whole body radioiodine imaging (Figs. 5.13, 5.14, and 5.15), with the addition of neck ultrasound and chest CT when needed. The appropriate approach to long-term surveillance depends upon the risk of having persistent or recurrent disease [21].

Thyroglobulin is produced only by thyroid tissue, so serum thyroglobulin serves as a sensitive indicator of the presence of thyroid tissue. Therefore, after radioiodine ablation of normal thyroid tissue, serum thyroglobulin level can be used as a tool to follow thyroid cancer. In a patient with prior thyroid remnant ablation, serum thyroglobulin should be undetectable (<2 ng/ml) after TSH stimulation, and a rising serum thyroglobulin level is a sign of persistent or recurrent thyroid cancer [21, 93, 94]. The appropriate approach to evaluating a patient with a rising thyroglobulin level depends on the prior history of the patient but could include neck ultrasound, chest radiograph/CT, or whole body radioiodine scintigraphy.

Management of Non-iodine-avid Thyroid Cancer

Some patients with a rising serum thyroglobulin will have no iodine-avid disease identified with whole body radioiodine scanning. This so-called Thyroglobulin Elevation, Non-Iodine-avid Syndrome (TENIS) [94] is a management challenge. One approach is therapeutic administration of a relatively large dose of ^{131}I with the goal of treating disease that was not apparent on whole

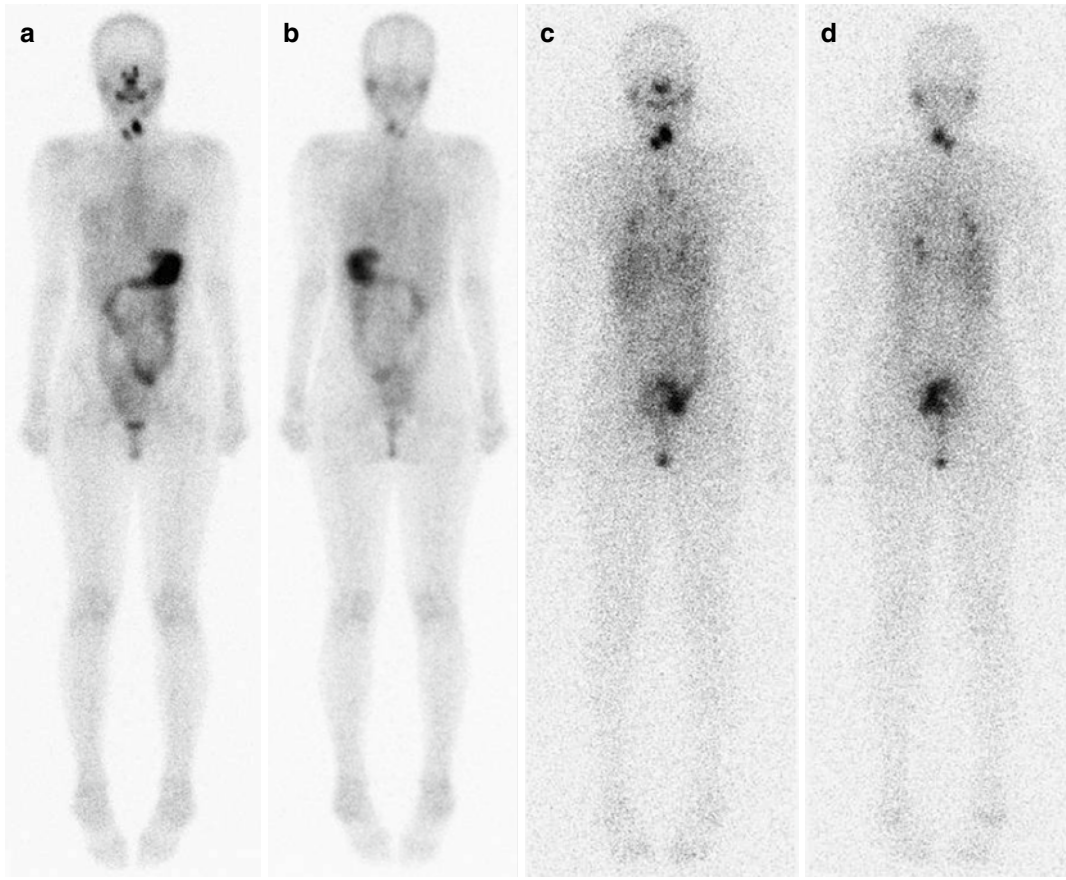

Fig. 5.14 Diagnostic and post-therapy whole body scintigraphy for metastatic thyroid cancer. A 15-year-old girl with papillary thyroid cancer underwent near-total surgical thyroidectomy, which showed disease involvement in multiple cervical lymph nodes. Six weeks later, diagnostic whole body scintigraphy was performed with ^{123}I. Images acquired in the anterior (**a**) and posterior (**b**) projections show physiological tracer accumulation is seen in the lacrimal glands and nasal secretions, salivary glands and oral secretions, breasts, stomach, bowel, and bladder. Focal uptake on each side of the thyroid bed could represent remnant thyroid tissue or metastatic disease in cervical lymph nodes, but ultrasound identified no abnormal cervical lymph nodes, and the patient was treated with 100 mCi ^{131}I. Six days later, a post-therapy whole body scan in anterior (**c**) and posterior (**d**) projections shows expected uptake in the neck. Multiple foci of uptake in the chest are consistent with multiple lung metastases. Physiological accumulation of ^{131}I is seen in nasal secretions, salivary glands and oral secretions, liver, and bowel. These findings demonstrate visualization of metastatic sites of iodine-avid disease on the post-therapy whole body scan that could not be detected on the pre-therapy diagnostic whole body scan

body scan due to either small size or diminished (but not absent) iodine avidity. The post-therapy whole body scan may detect sites of disease not detected on the pre-therapy diagnostic scan [23, 27, 28]. Imaging with neck ultrasound and chest CT may identify sites of non-iodine-avid disease, and surgical resection may be a good option for non-iodine-avid disease in cervical lymph nodes. More recently, FDG-PET has been used to evaluate patients with TENIS. FDG-PET also may be helpful when anatomic imaging, such as chest CT, indicates progressive disease, despite diminished uptake on whole body radioiodine scan (Figs. 5.15 and 5.16). In general, as iodine avidity decreases, FDG avidity increases, probably reflecting de-differentiation of tumor cells and loss of sodium-iodide symporter expression. Patients with FDG-avid thyroid cancer have decreased

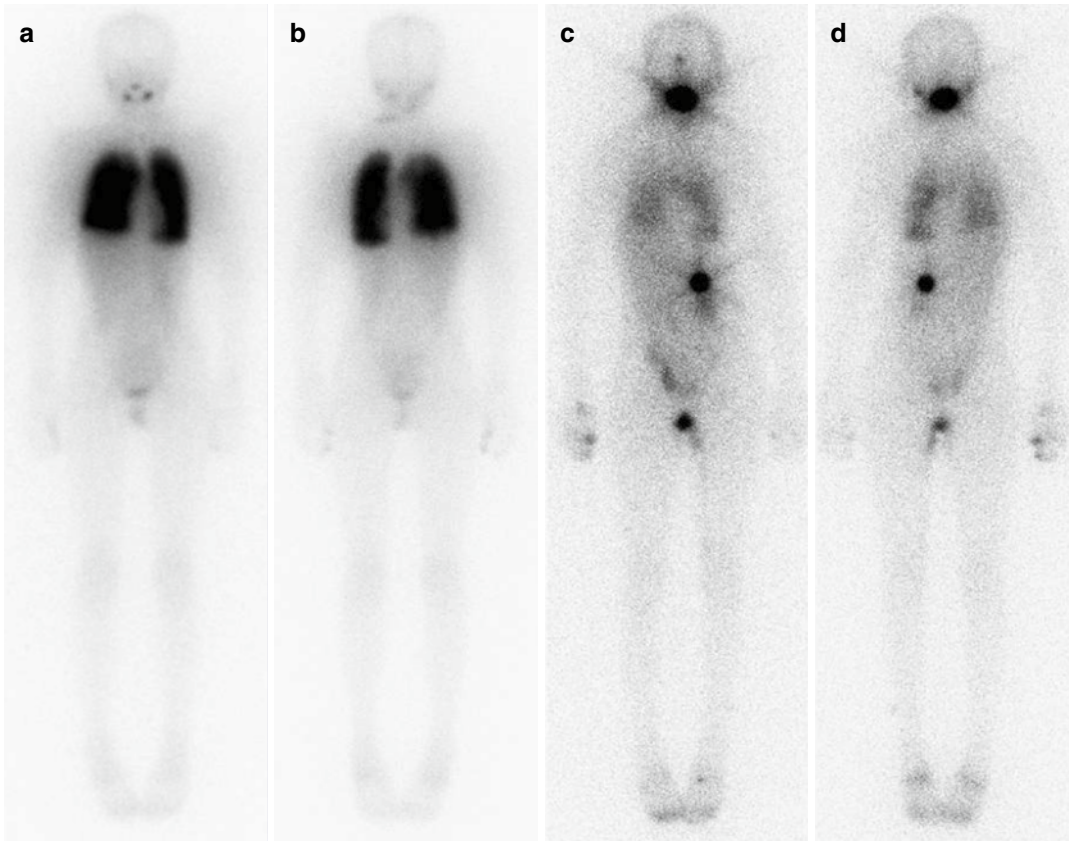

Fig. 5.15 Post-therapy whole body scintigraphy demonstrating loss of iodine avidity in metastatic thyroid cancer. A 12-year-old girl with metastatic thyroid cancer previously had been treated with 50 mCi ^{131}I and then was referred for further management and therapy. A post-therapy whole body scan performed in anterior (**a**) and posterior (**b**) projections 6 days after administration of 203 mCi ^{131}I shows intense uptake throughout both lungs, consistent with extensive metastatic disease seen on chest CT. Little uptake is identified elsewhere in the body. Because of persistent elevation in serum thyroglobulin and progression of lung disease demonstrated on chest CT 11 months later, whole body dosimetry was performed and the patient was again treated with radioiodine. Seven days after oral administration of 327 mCi, a post-therapy whole body scan was performed in anterior (**c**) and posterior (**d**) projections. Physiological accumulation of radioiodine is seen in the nasal secretions, mouth, liver, and bowel. A percutaneous gastrostomy had been placed due to frequent vomiting, and intense radioiodine accumulation is present in the mouth and on the gastrostomy. Uptake in the lungs is more heterogeneous and less intense than on the prior post-therapy scan, despite progression of disease identified by chest CT. These findings suggested that, since the previous radioiodine therapy, papillary thyroid carcinoma metastatic to the lungs had lost iodine avidity

survival compared to patients with iodine-avid disease [95]. This reflects the loss of effective therapy with radioiodine, but also likely reflects the poorer prognosis of de-differentiated disease.

Incidental Findings on FDG-PET

Large screening studies in apparently healthy adults have reported a prevalence of incidental thyroid uptake of up to 3 % [68, 69]. About half of these (1.5 %) will have focal uptake, of which 15–50 % will be found to represent thyroid cancer. Rarely, focal thyroid uptake may represent metastatic disease [96]. Diffuse ^{18}F-FDG uptake typically represents autoimmune thyroiditis, and uptake may not be affected by thyroid hormone replacement therapy [97]. Postradiation thyroiditis may be common among the patients undergoing imaging with FDG-PET.

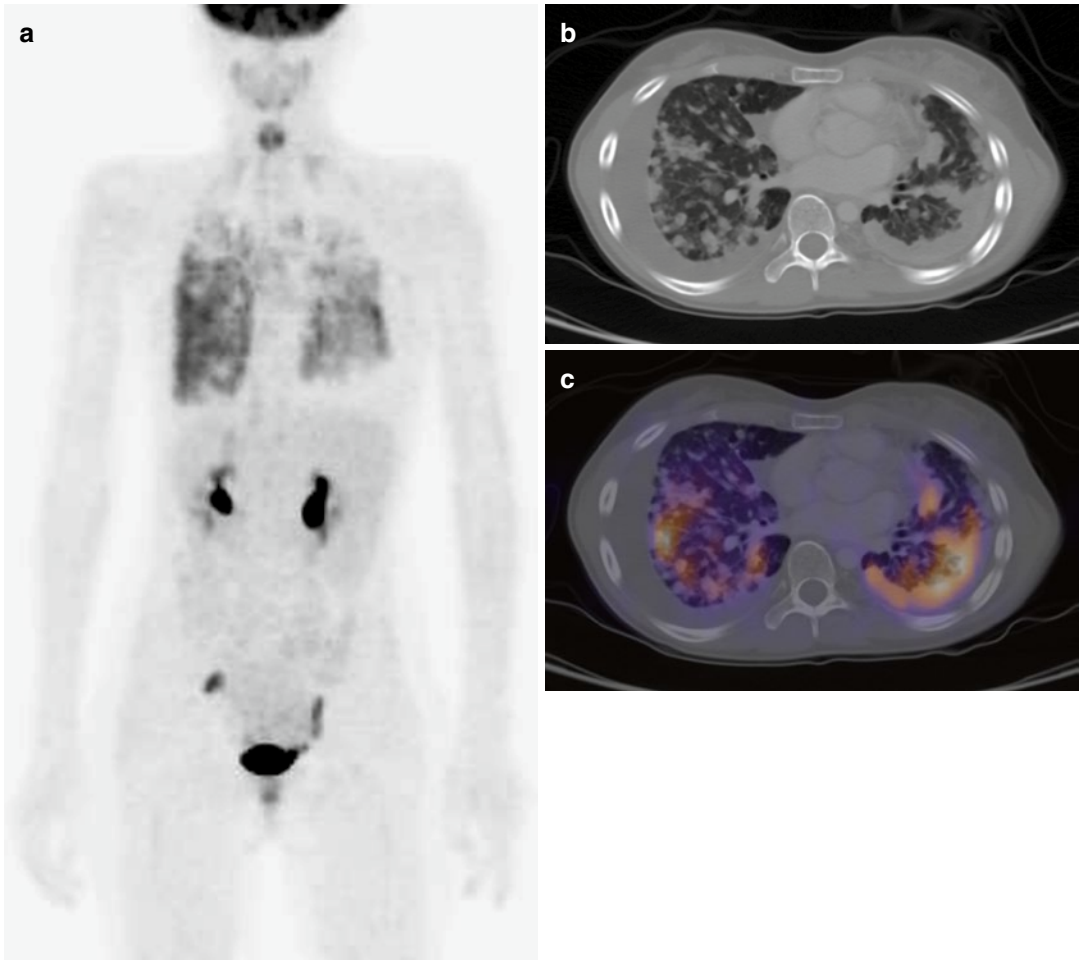

Fig. 5.16 ^{18}F-FDG PET of metastatic thyroid cancer. In a 13-year-old girl with metastatic thyroid cancer (see Fig. 5.15), decreasing radioiodine uptake in lung metastases despite progression of disease suggested that the metastases were losing iodine avidity. An ^{18}F-FDG PET was performed. A maximum intensity projection of the PET (**a**) demonstrated abnormal moderate heterogeneous uptake in both lungs. This corresponds to widespread metastatic disease identified by CT scan (**b**) in both lungs. Co-registration of PET and CT images (c) confirms abnormal uptake in widespread metastases. Note absent FDG uptake in bilateral pleural effusions. These findings in Figs. 5.15 and 5.16 demonstrate FDG avidity in metastatic thyroid carcinoma that had developed decreasing iodine avidity

Less commonly, diffuse ^{18}F-FDG uptake may reflect Graves' disease or malignancy [98]. Therefore, thyroid uptake of FDG frequently represents significant thyroid disease, and referring clinicians should be made aware of this potentially important finding. Although it may not the first clinical priority in all patients imaged with FDG-PET, the patient may benefit from further diagnostic evaluation and therapy [99].

References

1. Hertz S, Roberts A. Radioactive iodine in the study of thyroid physiology VII: the use of radioactive iodine therapy in hyperthyroidism. J Am Med Assoc. 1946;131:81–6.
2. Chapman EM, Evans RD. The treatment of hyperthyroidism with radioactive iodine. J Am Med Assoc. 1946;131:86–91.
3. Chung J-K. Sodium iodide symporter: its role in nuclear medicine. J Nucl Med. 2002;43:1188–200.

4. Bizhanova A, Koop P. Minireview: the sodium-iodide symporter NIS and pendrin in iodide homeostasis of the thyroid. Endocrinology. 2009;150:1084–90.
5. van de Graaf SAR, Ris-Stalpers C, Pauws E, Mendive FM, Targovnik HM, Vijlder JJM. Up to date with human thyroglobulin. J Endocrinol. 2001;170:307–21.
6. de Vijlder JJ. Primary congenital hypothyroidism: defects in iodine pathways. Eur J Endocrinol. 2003;149:247–56.
7. Snay ER, Treves ST, Fahey FH. Improved quality of pediatric ^{123}I-MIBG images with medium-energy collimators. J Nucl Med Technol. 2011;39:100–4.
8. Paltiel HJ, Summerville DA, Treves ST. Iodine-123 scintigraphy in the evaluation of pediatric thyroid disorders: a ten year experience. Pediatr Radiol. 1992;22:251–6.
9. Mandel SJ, Shankar LK, Benard F, Yamamoto A, Alavi A. Superiority of iodine-123 compared with iodine-131 scanning for thyroid remnants in patients with differentiated thyroid cancer. Clin Nucl Med. 2001;26:6–9.
10. Freudenberg LS, Jentzen W, Stahl A, Bockisch A, Rosenbaum-Krumme SJ. Clinical applications of ^{124}I-PET/CT in patients with differentiated cancer. Eur J Nucl Med Mol Imaging. 2011;38:S48–56.
11. Intenzo CM, Hung QD, Manzone TA, Kim SM. Imaging of the thyroid in benign and malignant disease. Semin Nucl Med. 2012;42:49–61.
12. Balon HR, Silberstein EB, Meier DA, et al. Society of Nuclear Medicine procedure guideline for thyroid scintigraphy v3.0. 2006. http://interactive.snm.org/docs/Thyroid_Scintigraphy_V3.pdf.
13. Scheff AM, Spies WG, McDougall IR, et al. ACR-SNM-SPR practice guideline for the performance of thyroid scintigraphy and uptake measurements. 2009. www.acr.org/~/media/ACR/Documents/PGTS/guidelines/Thyroid_Scintigraphy.pdf.
14. Lassmann M, Biassoni L, Monsieurs M, Franzius C, Jacobs F, EANM Dosimetry and Paediatrics Committees. The new EANM paediatric dosage card. Eur J Nucl Med Mol Imaging. 2007;34:796–8.
15. Balon HR, Silberstein EB, Meier DA, et al. Society of Nuclear Medicine procedure guideline for thyroid uptake measurement v3.0. 2006. http://interactive.snm.org/docs/Thyroid Uptake Measure v3.0.pdf.
16. Milakovic M, Berg G, Eggertssen R, Nystrom E. Effect of lifelong iodine supplementation on thyroid 131-I uptake: a decrease in uptake in euthyroid but not hyperthyroid individuals compared to observations 50 years ago. Eur J Clin Nutr. 2006;60:210–3.
17. Padovani RP, Kasamatsu TS, Nakabashi CC, et al. One month is sufficient for urinary iodine to return to its baseline value after the use of water-soluble iodinated contrast agents in post-thyroidectomy patients requiring radioiodine therapy. Thyroid. 2012;22:926–30.
18. Vejberg P, Knudsen N, Perrild H, et al. Estimation of iodine intake from various urinary iodine measurements in population studies. Thyroid. 2009;19:1281–6.
19. Silberstein EB, Alavi A, Balon HR, et al. Society of Nuclear Medicine procedure guideline for scintigraphy for differentiated papillary and follicular thyroid cancer. 2006. http://interactive.snm.org/docs/Scintigraphy for Differentiated Thyroid Cancer V3.0 (9-25-06).pdf.
20. Toubert ME, Dib-Deperrest A, Houzé P, Parquet N, Hindie E, Moretti JL. Plasma exchanges overcome persistent iodine overload to enable ^{131}I ablation of differentiated thyroid carcinoma. Thyroid. 2008;18:469–72.
21. Cooper DS, Dohery GM, Haugen BR, et al. Revised American Thyroid Association management guidelines for patients with thyroid nodules and differentiated thyroid cancer. Thyroid. 2009;19:1167–214.
22. Van Nostrand D, Aiken M, Atkins F, et al. The utility of radioiodine scans prior to iodine 131 ablation in patients with well-differentiated thyroid cancer. Thyroid. 2009;19:849–55.
23. Mazzaferri EL, Massoll N. Management of papillary and follicular (differentiated) thyroid cancer: new paradigms using recombinant human thyrotropin. Endocr Relat Cancer. 2002;9:227–47.
24. Woolfenden JM. Thyroid stunning revisited. J Nucl Med. 2006;47:1403–5.
25. Park HM, Perkins OW, Edmondson JW, Schnute RB, Manatunga A. Influence of diagnostic radioiodines on the uptake of ablative dose of iodine-131. Thyroid. 1994;4:49–54.
26. Cobin RH, Gharib H, Bergman DA, et al. AACE/AAES medical/surgical guidelines for clinical practice: management of thyroid carcinoma. Endocr Pract. 2001;7:203–20.
27. Sherman SI, Tielens ET, Sostre S, Wharam Jr MD, Ladenson PW. Clinical utility of posttreatment radioiodine scans in the management of patients with thyroid cancer. J Clin Endocrinol Metab. 1994;78:629–34.
28. Schlumberger M, Mancusi R, Baudin E, Pacini F. ^{131}I therapy for elevated thyroglobulin levels. Thyroid. 1997;7:273–6.
29. Chung JK, Lee YJ, Jeong JM, et al. Clinical significance of hepatic visualization on iodine-131 whole-body scan in patients with thyroid carcinoma. J Nucl Med. 1997;38:1191–5.
30. Avram AM. Radioiodine scintigraphy with SPECT/CT: an important diagnostic tool for thyroid cancer staging and risk stratification. J Nucl Med. 2012;53:754–64.
31. Maruoka Y, Abe K, Baba S, et al. Incremental diagnostic value of SPECT/CT with ^{131}I scintigraphy after radioiodine therapy in patients with well-differentiated thyroid carcinoma. Radiology. 2012;265:902–9.
32. LaFranchi SH. Approach to the diagnosis and treatment of neonatal hypothyroidism. J Clin Endocrinol Metab. 2011;96:2959–67.
33. LaFranchi S. Congenital hypothyroidism: etiologies, diagnosis, and management. Thyroid. 1999;9:735–40.
34. Brown RS, Bellisaro RL, Botero D, et al. Incidence of transient congenital hypothyroidism due to

maternal thyrotropin receptor-blocking antibodies in over one million babies. J Clin Endocrinol Metab. 1996;81: 1147–51.
35. Rose SR, Brown RS. Update of newborn screening and therapy for congenital hypothyroidism. Pediatrics. 2006;117:2290–303.
36. Schoen EJ, Clapp W, To TT, Fireman BH. The key role of newborn thyroid scintigraphy with isotopic iodide (^{123}I) in defining and managing congenital hypothyroidism. Pediatrics. 2004;114:e683–8.
37. Noussios G, Anagnostis P, Goulis DG, Lappas D, Natsis K. Ectopic thyroid tissue: anatomical, clinical, and surgical implications of a rare entity. Eur J Endocrinol. 2011;165:375–82.
38. Rabhar R, Yoon MJ, Connolly LP, et al. Lingual thyroid in children: a rare clinical entity. Laryngoscope. 2008;118:1174–9.
39. Bauer AJ. Approach to the pediatric patient with Graves' disease: when is definitive therapy warranted? J Clin Endocrinol Metab. 2011;96:580–8.
40. McDermott MT. Hyperthyroidism. Ann Intern Med. 2012;157:ITC1-1-16.
41. Seigel SC, Hodak SP. Thyrotoxicosis. Med Clin North Am. 2012;96:175–201.
42. Huang SA, Larsen PR. Autoimmune thyroid disease. In: Radovick S, MacGillivray MH, editors. Pediatric endocrinology: a practical guide. Totowa: Humana Press; 2003. p. 291–307.
43. Rivkees SA, Dinauer C. An optimal treatment for pediatric Graves' disease is radioiodine. J Clin Endocrinol Metab. 2007;92:797–800.
44. Lee JA, Grumbach MM, Clark OH. The optimal treatment for pediatric Graves' disease is surgery. J Clin Endocrinol Metab. 2007;92:801–3.
45. Hamburger JI. Management of hyperthyroidism in children and adolescents. J Clin Endocrinol Metab. 1985;60:1019–24.
46. Rivkees SA, Mattison DR. Ending propylthiouracil-induced liver failure in children. N Engl J Med. 2009;360:1574–5.
47. Bahn RS, Burch HB, Cooper DS, et al. Hyperthyroidism and other causes of thyrotoxicosis: management guidelines of the American Thyroid Association and American Association of Clinical Endocrinologists. Thyroid. 2011;21:593–646.
48. Zimmerman D, Lteif AN. Thyrotoxicosis in children. Endocrinol Metab Clin North Am. 1998;27:109–26.
49. Rivkees SA, Stephenson K, Dinauer C. Adverse events associated with methimazole therapy of Graves' disease in children. Int J Pediatr Endocrinol. 2010;2010:176970. doi:10.1155/2010/176970.
50. Rivkees SA, Szarfman A. Dissimilar hepatotoxicity profiles of propylthiouracil and methimazole in children. J Clin Endocrinol Metab. 2010;95:3260–7.
51. Haines SF, Keating Jr FR, Power MH, Williams MMD, Kelsey MP. The use of radioiodine in the treatment of exophthalmic goiter. J Clin Endocrinol Metab. 1948;8:813–25.
52. Soley MH, Foreman N. Radioiodine therapy in Graves' disease. J Clin Invest. 1949;28:1367–74.
53. Silberstein EB, Alavi A, Balon HR, et al. The SNMMI practice guideline for therapy of thyroid disease with ^{131}I 3.0. J Nucl Med. 2012;53:1633–51.
54. Sosa JA, Tuggle CT, Wang TS, et al. Clinical and economic outcomes of thyroid and parathyroid surgery in children. J Clin Endocrinol Metab. 2008;93: 3058–65.
55. Ratcliffe GE, Coke S, Fogelman I, Maisey MN. Radioiodine treatment of solitary functioning nodules. Br J Radiol. 1986;59:385–7.
56. Holm LE, Hall P, Wiklund K, et al. Cancer risk after iodine-131 therapy for hyperthyroidism. Clin Endocrinol (Oxf). 2004;61:641–8.
57. Ceccarelli C, Bencivelli W, Vitti P, Grasso L, Pinchera A. Outcome of radioiodine-131 therapy in hyperfunctioning thyroid nodules: a 20 years retrospective study. Clin Endocrinol (Oxf). 2005;62:331–5.
58. Alexander EK, Larsen PR. Radioiodine for thyroid cancer – is less more? N Engl J Med. 2012;366: 1732–3.
59. Reinhardt MJ, Brink I, Joe AY, et al. Radioiodine therapy in Graves' disease based on tissue-absorbed dose calculations: effect of pre-treatment thyroid volume on clinical outcome. Eur J Nucl Med Mol Imaging. 2002;29:1118–24.
60. Leslie WD, Ward L, Salamon EA, Ludwig S, Rowe RC, Cowden EA. A randomized comparison of radioiodine dose in Graves' hyperthyroidism. J Clin Endocrinol Metab. 2003;88:978–83.
61. Perros P, Kendall-Taylor P, Neoh C, Frewin S, Dickinson J. A prospective study of the effects of radioiodine therapy for hyperthyroidism in patients with minimally active Graves' ophthalmopathy. J Clin Endocrinol Metab. 2005;90:5321–3.
62. Hoffman DA, McConahey WM, Fraumeni JF, Kurland LT. Cancer incidence following treatment of hyperthyroidism. Int J Epidemiol. 1982;11: 218–24.
63. Goldman MB, Maloof F, Monson RR, Aschengrau A, Cooper DS, Ridgeway EC. Radioactive iodine therapy and breast cancer. A follow-up study of hyperthyroid women. Am J Epidemiol. 1988;127:969–80.
64. Holm L-E, Lundell G, Israelsson A, Dahlqvist I. Incidence of hypothyroidism occurring long after iodine-131 therapy for hyperthyroidism. J Nucl Med. 1982;23:103–7.
65. Franklyn JA, Masonneuve P, Sheppard M, Betteridge J, Boyle P. Cancer incidence and mortality after radioiodine treatment for hyperthyroidism: a population-based cohort study. Lancet. 1999;353:2111–5.
66. Metso S, Auvinen A, Heini H, Salmi J, Oksala H, Jaatinen P. Increased cancer incidence after radioiodine treatment for hyperthyroidism. Cancer. 2007;109: 1972–9.
67. Bernstein L, Gurney JG. Carcinomas and other malignant epithelial neoplasms. In: Ries LAG, Smith MA, Gurney JG, Linet M, Tamra T, Young JL, Bunin GR, editors. Cancer incidence and survival among children and adolescents: United States SEER program 1975-1995, SEER program. NIH

Pub. No. 99-4649. Bethesda: National Cancer Institute; 1999.
68. Shie P, Cardarelli Sprawls K, Fulda KG, Taur A. Systematic review: prevalence of malignant incidental thyroid nodules identified on fluorine-18 fluorodeoxyglucose positron emission tomography. Nucl Med Commun. 2009;30:742–8.
69. Salvatori M, Melis L, Castaldi P, et al. Clinical significance of focal and diffuse thyroid diseases identified by ^{18}F-fluorodeoxyglucose positron emission tomography. Biomed Pharmacother. 2007;61:488–93.
70. Levine RA. Current guidelines for the management of thyroid nodules. Endocr Pract. 2012;18:596–9.
71. Rivkees SA, Mazzaferri EL, Verburg FA, et al. The treatment of differentiated thyroid cancer in children: emphasis on surgical approach and radioactive iodine therapy. Endocr Rev. 2011;32:798–826.
72. Hung W, Sarlis NJ. Current controversies in the management of pediatric patients with well-differentiated non-medullary thyroid cancer: a review. Thyroid. 2002;12:683–702.
73. Sklar CA, LaQuaglia MP. Thyroid cancer in children and adolescents. In: Radovick S, Macgillivary MH, editors. Contemporary endocrinology: pediatric endocrinology: a practical clinical guide. Totawa: Humana Press; 2003. p. 327–39.
74. Grebe SK, Hay ID. The role of surgery in the management of differentiated thyroid cancer. J Endocrinol Invest. 1997;20:32–5.
75. Udelsman R, Lakatos E, Ladenson P. Optimal surgery for papillary thyroid carcinoma. World J Surg. 1996; 20:88–93.
76. Sawka AM, Kullathorn T, Brouwers M, Thabane L, Browman G, Gerstein HC. A systematic review and metaanalysis of the effectiveness of radioactive iodine remnant ablation for well-differentiated thyroid cancer. J Clin Endocrinol Metabol. 2004;89:3668–76.
77. Handkiewicz-Junak D, Wloch J, Roskosz J, et al. Total thyroidectomy and adjuvant radioiodine treatment independently decrease locoregional recurrence risk in childhood and adolescent differentiated thyroid cancer. J Nucl Med. 2007;48:879–88.
78. Verberg FA, Biko J, Diessl S, et al. I-131 activities as high as safely administrable (AHASA) for the treatment of children and adolescents with advanced differentiated thyroid cancer. J Clin Endocrinol Metab. 2011;96:E1268–71.
79. Van Nostrand D, Wartofsky L. Radioiodine in the treatment of thyroid cancer. Endocrinol Metab Clin North Am. 2007;36:807–22.
80. Schlumberger M, Catargi B, Borget I, et al. Strategies of radioiodine ablation in patients with low-risk thyroid cancer. N Engl J Med. 2012;366:1663–73.
81. Robbins RJ, Schlumberger MJ. The evolving role of ^{131}I for the treatment of differentiated thyroid carcinoma. J Nucl Med. 2005;46:28S–37.
82. Sgouros G, Song H, Ladenson PW, Wahl RL. Lung toxicity in radioiodine therapy of thyroid carcinoma: development of a dose-rate method and dosimetric implications of the 80-mCi rule. J Nucl Med. 2006;47:1977–84.
83. Song H, He B, Prideaux A, Du Y, et al. Lung dosimetry for radioiodine treatment planning in the case of diffuse lung metastases. J Nucl Med. 2006;47:1985–94.
84. Sgouros G, Hobbs RF, Atkins FB, Van Nostrand D, Ladenson PW, Wahl RL. Three-dimensional radiobiological dosimetry (3D-RD) with ^{124}I PET for ^{131}I therapy of thyroid cancer. Eur J Nucl Med Mol Imaging. 2011;38:S41–7.
85. Ceccarelli C, Bencivelli W, Morciano D, Pinchera A, Pacini R. ^{131}I therapy for differentiated thyroid cancer leads to an earlier onset of menopause: results of a retrospective study. J Clin Endocrinol Metab. 2001;86:3512–5.
86. Pacini F, Gasperi M, Fugazzola L, et al. Testicular function in patients with differentiated thyroid carcinoma treated with radioiodine. J Nucl Med. 1994;35:1418–22.
87. Krassas GE, Pontikides N. Gonadal effect of radiation from ^{131}I in male patients with thyroid carcinoma. Arch Androl. 2005;51:171–5.
88. Mandel SJ, Larsen PR, Seely EW, Brent GA. Increased need for thyroxine during pregnancy in women with primary hypothyroidism. N Engl J Med. 1990;323:91–6.
89. de Vathaire F. The carcinogenic effects of radioiodine therapy for thyroid carcinoma. Nat Clin Pract Endocrinol Metab. 2008;4:180–1.
90. Read CH Jr, Tansey MJ, Menda Y. A 36-year retrospective analysis of the efficacy and safety of radioactive iodine in treating young Graves' patients. J Clin Endocrinol Metab. 2004;89:4229–33.
91. Hay ID, Thompson GB, Gant CS, et al. Papillary thyroid carcinoma managed at the Mayo Clinic during six decades (1940-1999): temporal trends in initial therapy and long-term outcome in 2444 consecutively treated patients. World J Surg. 2002;26:879–85.
92. Mazzaferri EL, Jhiang SM. Long-term impact of initial surgical and medical therapy on papillary and follicular thyroid cancer. Am J Med. 1994;97:418–28.
93. Mazzaferri EL, Robbins RJ, Spencer CA, et al. A consensus report on the role of serum thyroglobulin as a monitoring method for low-risk patients with papillary thyroid carcinoma. J Clin Endocrinol Metab. 2003;88:1433–41.
94. Silberstein EB. The problem of the patient with thyroglobulin elevation but negative iodine scintigraphy: the TENIS syndrome. Semin Nucl Med. 2011;41:113–20.
95. Robbins RJ, Wan Q, Grewal RK, et al. Real-time prognosis for metastatic thyroid carcinoma based on 2-[^{18}F]fluoro-2-deoxy-D-glucose-positron emission tomography scanning. J Clin Endocrinol Metab. 2006;91:498–505.
96. Chen W, Parsons M, Torigian DA, Zhuang H, Alavi A. Evaluation of thyroid FDG uptake incidentally identified on FDG-PET/CT imaging. Nucl Med Commun. 2009;30:240244.

97. Karantanis D, Bogsrud RV, Wiseman GA, et al. Clinical significance of diffusely increased ^{18}F-FDG uptake in the thyroid gland. J Nucl Med. 2007;48: 896–901.
98. Soelberg KK, Bonnema SJ, Brix TH, Hegedüs L. Risk of malignancy in thyroid incidentalomas detected by (18)F-fluorodeoxyglucose positron emission tomography: a systematic review. Thyroid. 2012;22:918–25.
99. Nilsson IL, Arnberg F, Zedenius J, Sundin A. Thyroid incidentaloma detected by fluorodeoxyglucose positron emission tomography/computed tomography: practical management algorithm. World J Surg. 2001;35:2691–7.

Lung Imaging

6

Frederick D. Grant and S. Ted Treves

Nuclear medicine provides physiological and sensitive methods for assessing regional lung perfusion and ventilation. In adults, the most established indication for these studies has been suspected pulmonary embolism. In children, both perfusion and ventilation imaging have been used for a broader range of indications. In children with congenital heart disease, perfusion scintigraphy is used to assess differential (left vs. right) and regional lung perfusion. Perfusion scintigraphy also is useful for demonstrating shunts between the right (pulmonary) and left (systemic) circulation. In children with parenchymal and airway diseases, static or dynamic ventilation scintigraphy can be used to assess lung ventilation and differential lung volumes. Ventilation/perfusion (V/Q) uses both ventilation (V) and perfusion (Q) scans for the evaluation of pulmonary embolism or to demonstrate ventilation/perfusion mismatches in developmental or acquired lung diseases.

F.D. Grant, MD (✉)
Joint Program in Nuclear Medicine,
Department of Radiology, Harvard Medical School,
Boston, MA, USA

Division of Nuclear Medicine and Molecular Imaging,
Department of Radiology,
Boston Children's Hospital,
Boston, MA, USA

Department of Radiology,
Brigham and Women's Hospital, Boston, MA, USA
e-mail: frederick.grant@childrens.harvard.edu

S.T. Treves, MD (✉)
Joint Program in Nuclear Medicine,
Department of Radiology, Harvard Medical School,
Boston, MA, USA

Division of Nuclear Medicine and Molecular Imaging, Department of Radiology,
Boston Children's Hospital,
Boston, MA, USA

Division of Nuclear Medicine and Molecular Imaging,
Department of Radiology, Brigham and Women's Hospital, Boston, MA, USA
e-mail: ted_treves@HMS.harvard.edu

Methods

Little or no patient preparation is needed before performing lung scintigraphy. It may be helpful to confirm at the time of scheduling the study that a patient's respiratory status will not preclude cooperation with the study. Some guidelines suggest treating a patient to optimize control of chronic lung disease before performing a nonurgent lung scan. Although this preparation might decrease the likelihood that regional airway obstruction will interfere with study interpretation, it is not a part of routine clinical practice.

Assessment of Pulmonary Blood Flow

Regional pulmonary blood flow typically is determined with ^{99m}Tc-labeled macroaggregated albumin (MAA). After administration into the peripheral venous circulation, MAA particles

S.T. Treves (ed.), *Pediatric Nuclear Medicine and Molecular Imaging*,
DOI 10.1007/978-1-4614-9551-2_6,

circulate through the right heart and into the pulmonary circulation where they are trapped within the capillaries of the lungs. The distribution of ^{99m}Tc-MAA within the lungs reflects regional and differential pulmonary blood flow. An alternative, and now rarely used, method to demonstrate pulmonary blood flow is the intravenous administration of ^{133}Xe dissolved in saline [1].

Macroaggregated albumin (MAA) particles are created by the acid aggregation of human albumin to produce aggregated particles with diameters between 10 and 100 μm, with most between 10 and 40 μm [2]. This is greater than the diameter of pulmonary capillaries, so that MAA particles in the pulmonary circulation will be trapped at the transition from arteriole to alveolar-capillary. Macroaggregated albumin particles are labeled with ^{99m}Tc for lung perfusion scintigraphy. In an adult, the typical dose of 500,000 particles of ^{99m}Tc-labeled MAA temporarily will occlude approximately 1 in 1,000 pulmonary arterioles and have essentially no effect on normal adult lung function. The MAA particles have a biological half-life of only a few hours as they are degraded to smaller particles and polypeptides, which reenter the circulation and are cleared by the liver.

A smaller number of MAA particles are recommended for infants and young children, as their pulmonary vasculature is immature [3]. The number of pulmonary capillary beds increases during the first years of life, but reaches only one-half of the adult number by 3 years of age [4]. This suggests that the number of administered particles should not exceed 50,000 in a newborn or 165,000 in a 1-year-old child [5]. The smallest number of particles necessary should be used for all perfusion lung scans, and the number of MAA particles necessary for an adequate study will depend on the indication for lung scintigraphy and patient characteristics. When the indication for the lung scan is to assess differential or regional pulmonary perfusion (and not pulmonary embolus), nearly all pediatric lung scans can be performed with only 10,000 MAA particles. A similar number of MAA particles should be used in patients of all ages with pulmonary hypertension or with a known (or suspected) right-to-left cardiac shunt. There have been unpublished anecdotal reports of transient cerebral ischemia following administration of an adult dose of MAA particles to a pediatric patient with a pulmonary-to-systemic shunt. When higher quality lung images are needed for the evaluation of possible pulmonary embolism, a greater number of MAA particles may be required to ensure uniform particle distribution within the microcirculation of the lungs.

Image quality also will depend on the administered dose of ^{99m}Tc. The typical radiopharmaceutical preparation of MAA particles provides approximately 1 mCi per 100,000 particles (so the typical dose is 0.1 mCi or 10,000 particles). Administration of a limited number of MAA particles with this specific activity rarely provides sufficient counts for routine gamma camera imaging. Therefore, for pediatric lung scintigraphy, special preparation of ^{99m}Tc-labeled MAA particles may be needed to provide MAA particles with a higher specific activity.

Typically, ^{99m}Tc-MAA is administered by intravenous injection while the patient is supine, so that differential regional blood flow between the apex and base of the lungs is reduced. Extreme care must be taken to avoid drawing blood into the injection syringe, as this will result in formation of clots containing blood and MAA particles. If injected into the circulation, these clots will heterogeneously distribute within the pulmonary circulation. This will limit the diagnostic utility of the imaging study and could be dangerous to the patient.

Image acquisition depends on the clinical indication for lung perfusion scintigraphy. As MAA particles are trapped within the lung with a distribution reflecting pulmonary perfusion, there is no reason to perform dynamic lung imaging. Planar images are acquired with a high-resolution collimator with each view collected for 300,000–500,000 counts. Differential lung perfusion usually can be assessed with images acquired in the anterior and posterior projections. Region-of-interest analysis is used to quantitatively assess differential or regional lung perfusion. For evaluation of pulmonary embolism, planar images are acquired in multiple projections, typically anterior, posterior, and four oblique projections. Some institutions also will acquire images in the two lateral projections. Recent studies have suggested a role for lung SPECT or SPECT/CT in

the assessment of functional lung volume or evaluation for pulmonary embolism [6].

Lung Ventilation Scintigraphy

The airspaces of the lungs can be assessed by imaging the lungs after the patient inhales either radiolabeled aerosols or radioactive gases. Inhaled aerosolized nanoparticles are distributed and trapped in the pulmonary airspace in proportion to regional ventilation. Once the radiolabeled nanoparticles are trapped in the lungs, static images of the lungs can be acquired in multiple projections. The most commonly used radioactive gas for lung ventilation scintigraphy is ^{133}Xe, although other inert gases, such as ^{81m}Kr, also have been used. As inhaled gases are not trapped within the lungs, dynamic imaging of lung ventilation can be performed. With rebreathing, inhaled gases can redistribute throughout the pulmonary airspace, which permits imaging and volume assessment of the entire aerated lung volume.

^{133}Xe for Inhalation

Xenon-133 (physical half-life 5.2 days) is an inert gas at room temperature and normal pressure. Xenon-133 decays with a principal gamma emission of 87 kEv (37 % abundance). There are many commercially available systems for administration of inhaled ^{133}Xe gas for lung scintigraphy. Many require some degree of patient cooperation, but ^{133}Xe gas can be administered successfully to children with limited cooperation. Xenon-133 gas also can be administered through the endotracheal tube of intubated patients. During a rebreathing study, care must be taken to ensure that the patient is provided with adequate oxygen. One disadvantage to the use of ^{133}Xe gas for lung ventilation scintigraphy is the requirement to trap and exhaust the exhaled ^{133}Xe gas.

Dynamic ventilation studies can be performed with the patient supine over a camera equipped with a low-energy collimator [7]. Dynamic images typically are acquired in the posterior projection at a rate of one frame every five seconds. After inhalation of a single breath, the distribution of ^{133}Xe gas corresponds to regional ventilation within the lungs. After multiple breaths through a rebreathing inhalation system, the ^{133}Xe gas reaches equilibrium within the airways. ^{133}Xe distribution will reflect the distribution of aerated airspace volumes. After ^{133}Xe inhalation is stopped, continued dynamic imaging during the washout phase can be used to measure regional ventilation and to determine if there is regional air trapping within the lungs. Region-of-interest analysis is used for quantitative assessment of regional ventilation, lung volume, and air trapping.

Lung Ventilation with ^{99m}Tc-Labeled Aerosols

A variety of ^{99m}Tc-labeled aerosolized particles can be used for lung ventilation imaging. Aerosolized particles are administered through a face mask connected to an ultrasonic or jet nebulizer. In the USA, the most commonly used is aerosolized ^{99m}Tc-labeled diethylenetriamine pentaacetic acid (^{99m}Tc-DTPA). Less commonly used is aerosolized ^{99m}Tc-labeled sulfur colloid. Technetium-99m-labeled carbon nanoparticles (Technigas ®) have been used widely throughout the world [8], but this radiopharmaceutical is not approved for use in the USA. After aerosolized particles are inhaled and deposited within the small airways, planar images can be acquired in multiple projections. Because particles persist within the airways, dynamic ventilation imaging cannot be performed. Some studies have described the use of SPECT or SPECT/CT with ^{99m}Tc-labeled carbon nanoparticles to assess lung ventilation [6].

Once deposited in the alveolar space, ^{99m}Tc-DTPA is slowly absorbed through the alveolar-capillary membrane with a clearance half-time of approximately one hour in adults [9]. Technetium-99m-DTPA clearance is increased with exercise [10] and can be affected by conditions that alter alveolar membrane permeability, such as hyaline membrane disease [11]. Once absorbed into the circulation, ^{99m}Tc-DTPA is excreted by the kidneys, and a renogram pattern can be seen with delayed imaging. Inappropriate aerosolization technique can produce larger size nanoparticles which will deposit in the inhalation apparatus, oropharynx, and large airways. This results in inadequate aerosol delivery to the small airways and poor image quality. Normal mucociliary

action will clear tracer from the large airways to the oropharynx, where particles can then be swallowed and accumulate in the esophagus and stomach. These patterns of extrapulmonary tracer accumulation can interfere with study interpretation.

Clinical Applications

Lung scintigraphy can be used in the evaluation of a wide range of pulmonary, cardiac, and systemic diseases. For many indications, either a perfusion lung scan or a ventilation lung scan may be sufficient. For other indications, such as pulmonary embolism, congenital diaphragmatic hernia, and some complex congenital heart problems, a ventilation/perfusion ("V/Q") scan can be used to compare patterns of ventilation and perfusion.

Congenital Heart Disease

In most pediatric institutions, congenital heart disease is the most common indication for lung scintigraphy. A perfusion lung scan is a rapid and noninvasive method for quantitative assessment of differential (left vs. right) and regional pulmonary blood flow. As many of these patients will have a pulmonary-to-systemic (right-to-left) shunt, lung perfusion scans should be performed with the smallest possible number of MAA particles. In our experience, patients with congenital heart disease are evaluated successfully with perfusion lung scans using only 10,000 MAA particles. Although image quality can be limited and particle distribution within the lungs may appear slightly heterogeneous, this number of particles is sufficient to assess regional and differential pulmonary blood flow.

Many forms of congenital heart disease are associated with altered pulmonary perfusion (Fig. 6.1). Pulmonary artery atresia or stenosis of a main or branch pulmonary artery commonly is associated with tetralogy of Fallot. Differential lung perfusion can be used for initial evaluation and for postsurgical assessment of pulmonary blood flow after pulmonary arterioplasty or conduit placement [12]. Pulmonary vein stenosis or anomalous pulmonary venous return can affect differential lung perfusion, and a lung perfusion scan can be used to assess the severity of venous disease. In patients undergoing cardiac catheterization with balloon dilation or stenting of a pulmonary vessel or conduit, a lung perfusion scan can be performed after the procedure to assess for improved differential pulmonary perfusion and to confirm that instrumentation did not result in occlusion of the vessel. Differential lung perfusion can occur in patients with pulmonic valve stenosis. The jet of blood flow through the stenotic pulmonic valve can be preferentially directed to the left, so that the differential pulmonary blood flow will be greater in the left lung [13].

Anomalous pulmonary blood flow also can occur after corrective surgery performed for congenital heart disease. Alterations in the normal pattern of blood flow will depend on both the underlying cardiopulmonary anatomy and the surgical procedures [14]. For example, in patients with a classic Glenn shunt (end-to-end anastomosis), blood return from the superior vena cava is directed to the right lung, while the inferior vena cava blood return is to the left lung. In these patients, ^{99m}Tc-MAA intravenously administered in an upper extremity will travel only to the right lung, while tracer administered in a lower extremity vein will travel to the left lung. In patients treated with a bidirectional Glenn shunt (end-to-side anastomosis), venous return from the upper extremities is directed to both lungs, while venous return from the inferior vena cava is returned directly to the systemic circulation. In this situation, when ^{99m}Tc-MAA is administered in an upper extremity vein, it should accumulate in the pulmonary circulation of both lungs, while tracer administered intravenously in a lower extremity will bypass the pulmonary circulation and enter the systemic circulation. Thus, the pulmonary perfusion pattern depends on the pattern of cardiopulmonary circulation and the site of intravenous administration of ^{99m}Tc-MAA, and it is important to confirm the original and presumed

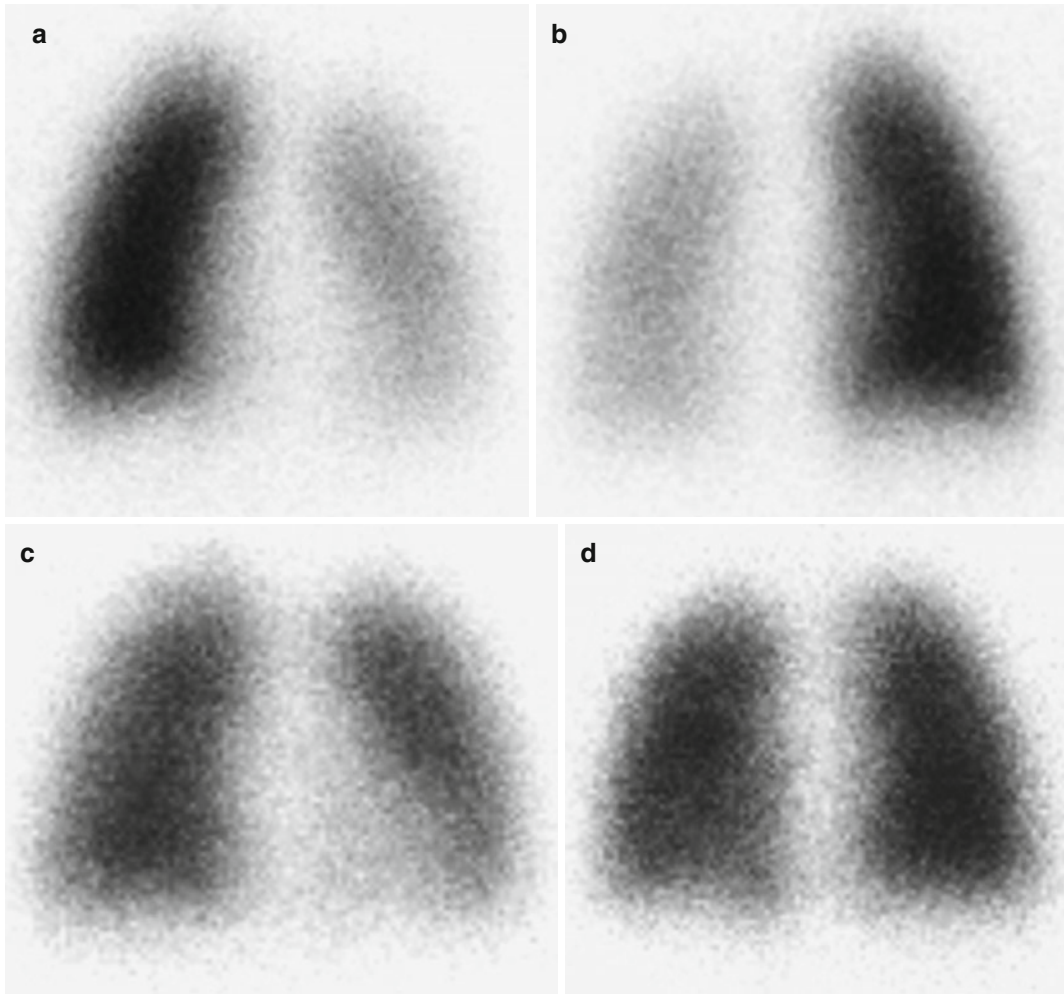

Fig. 6.1 Correction of persistent pulmonary artery stenosis in tetralogy of Fallot. In a 3-year-old girl with surgically corrected tetralogy of Fallot, a perfusion lung scan imaged in anterior (**a**) and posterior (**b**) projections shows asymmetric pulmonary perfusion (21 % left lung, 79 % right lung). Cardiac catheterization showed stenosis of the proximal left pulmonary artery, and a stent was placed at this location. A follow-up perfusion lung scan imaged in anterior (**c**) and posterior (**d**) projections demonstrates improved differential perfusion to the left lung (46 % left lung, 54 % right lung)

postoperative circulatory anatomy before performing a lung perfusion scan.

Pulmonary Shunting

A pulmonary-to-systemic (right-to-left) shunt will result in systemic penetration of intravenously administered ^{99m}Tc-MAA [15]. Tracer that has been shunted into the systemic circulation will be trapped within precapillary arterioles of organs other than the lungs. As MAA trapping will reflect relative blood flow, the largest amount of MAA accumulation is seen within the organs receiving the greatest fraction of cardiac output, such as brain and kidneys. Quantitative assessment of a right-to-left shunt may be somewhat limited by overlap between tissues with systemic circulation and the lungs, but the degree of right-to-left shunt can be evaluated qualitatively or assessed semiquantitatively using region-of-interest analysis (Fig. 6.2).

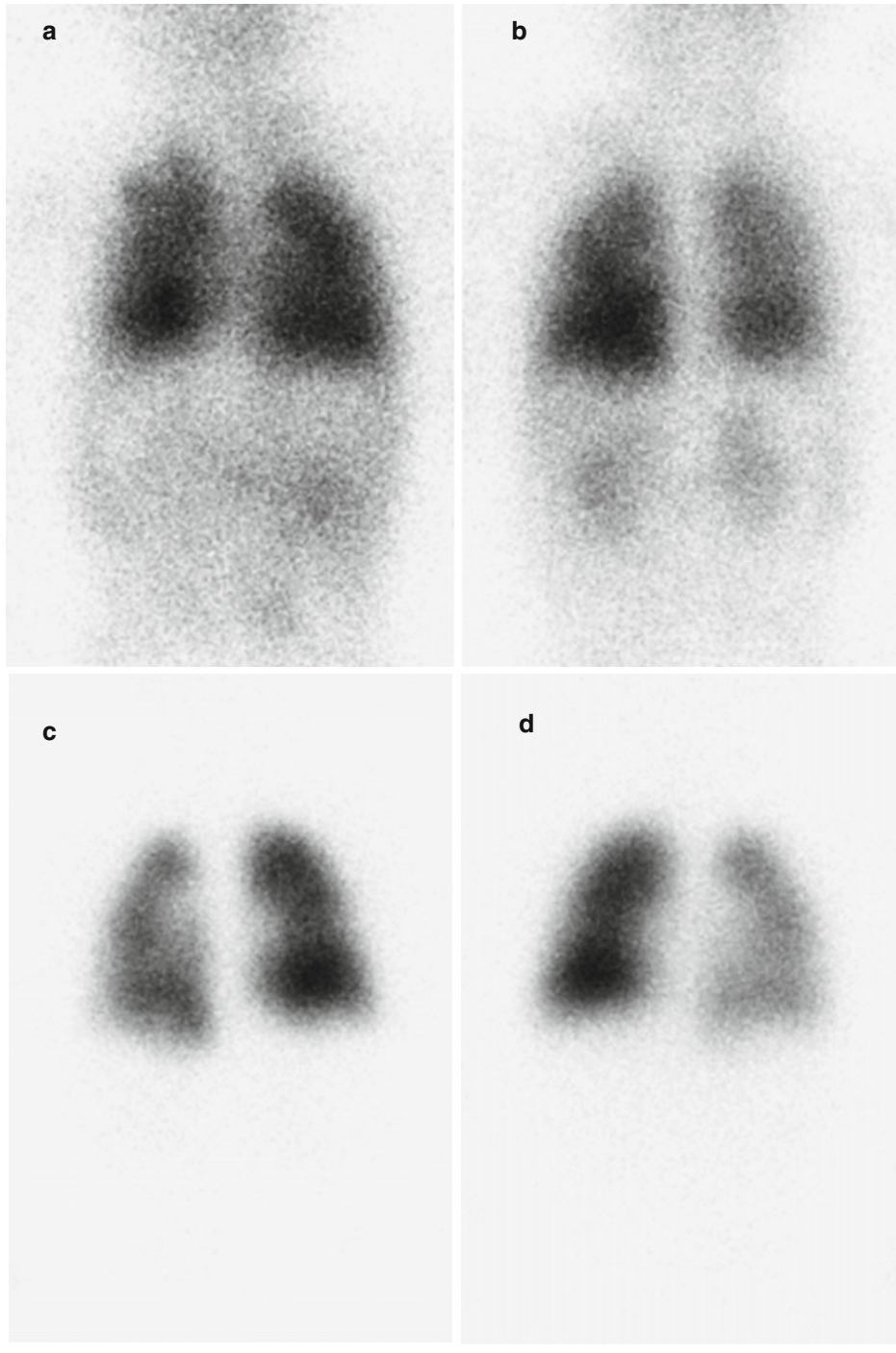

Fig. 6.2 Cardiac right-to-left shunt. In a 1-year-old girl with tetralogy of Fallot and pulmonary atresia corrected with a pulmonary artery conduit, a perfusion scan was performed with ^{99m}Tc-MAA. Anterior (**a**) and posterior (**b**) images show systemic penetration of tracer indicative of a severe intracardiac right-to-left shunt. After corrective surgery, a perfusion scan imaged in anterior (**c**) and posterior (**d**) projections shows resolution of the right-to-left shunt

Typically, right-to-left shunts are identified in patients with an atrial or ventricular septal defect. In these patients, the degree of shunting may correspond to the severity of pulmonary hypertension, with increased shunting into the systemic circulation as arterial pressures increase in the pulmonary circulation and right heart. Shunting also can occur in patients with more complex congenital heart disease that permits communication or mixing between the right and left heart circulations, such as a common ventricular outflow tract or patent ductus arteriosus.

Patients treated with a surgical cavopulmonary anastomosis, such as a Glenn shunt, also can develop intrapulmonary arteriovenous shunts, possibly reflecting dysregulated pulmonary vasodilation [14]. In a patient with a classic Glenn shunt, the degree of right-to-left shunt may be different for the superior and inferior vena cavae, so that it may be necessary to perform two lung perfusion studies and to calculate the shunt after ^{99m}Tc-MAA administration into either the upper or lower systemic venous circulation [16].

Intrapulmonary arteriovenous shunting also may develop in patients with chronic liver disease. These shunts produce systemic penetration of tracer on a perfusion lung scan [17]. Lung scan may be more sensitive than other techniques, such as contrast-enhanced echocardiography, for detecting physiologically significant intrapulmonary shunts in children with chronic liver disease [18].

Parenchymal and Bronchial Lung Disease

Ventilation lung scans can be used to evaluate parenchymal and bronchial lung disease. Ventilation scans can be helpful to assess differential and regional pulmonary function in patients with primary lung diseases, such as cystic fibrosis lung disease, bronchiectasis, and pulmonary fibrosis [19, 20]. Dynamic ventilation scans performed with ^{133}Xe can be used to identify functional airway obstruction or air trapping in patients with obstructive lung diseases, such as congenital lobar emphysema (Fig. 6.3) [21]. Ventilation/perfusion scans can be used to compare relative ventilation and perfusion or to identify a regional ventilation/perfusion mismatch that can result from obstruction of a segmental pulmonary artery. However, these studies must be interpreted with care. In patients with primary lung disease, airway obstruction will produce local hypoxia and lead to vasoconstriction and shunting of pulmonary blood flow away from the affected lung region. Therefore, airway obstruction may produce matched ventilation and perfusion defects [22].

Airway Obstruction

Lung scintigraphy can help in the functional evaluation of suspected upper airway obstruction. Airway obstruction can result from intrinsic obstruction of the lumen, such as by a foreign body or mucous plug, or by extrinsic compression of the tracheal or bronchial from an adjacent tumor or dilated vessel. A radionuclide ventilation scan can provide information about differential or regional ventilation that cannot be obtained with pulmonary function testing or other imaging. Combined ventilation and perfusion imaging has been used to evaluate children with a unilateral hyperlucent lung [23, 24]. Bronchiolitis obliterans (Swyer-James syndrome) demonstrates markedly diminished ventilation and perfusion. Airway obstruction will demonstrate absent ventilation, with a variable alteration in perfusion in response to local hypoventilation [25, 26]. In cases of partial airway obstruction, a dynamic ventilation scan performed with ^{133}Xe can be helpful in assessing the degree and extent of airway obstruction. Lung regions beyond a partial airway obstruction will demonstrate delayed tracer wash-in and delayed washout suggestive of air trapping.

Structural Abnormalities of the Chest

Ventilation/perfusion lung scans are used to assess lung function in patients with structural abnormalities of the chest, such as congenital diaphragmatic hernia, pectus excavatum, and spinal scoliosis.

Congenital diaphragmatic hernia classically presents with the triad of diaphragmatic defect,

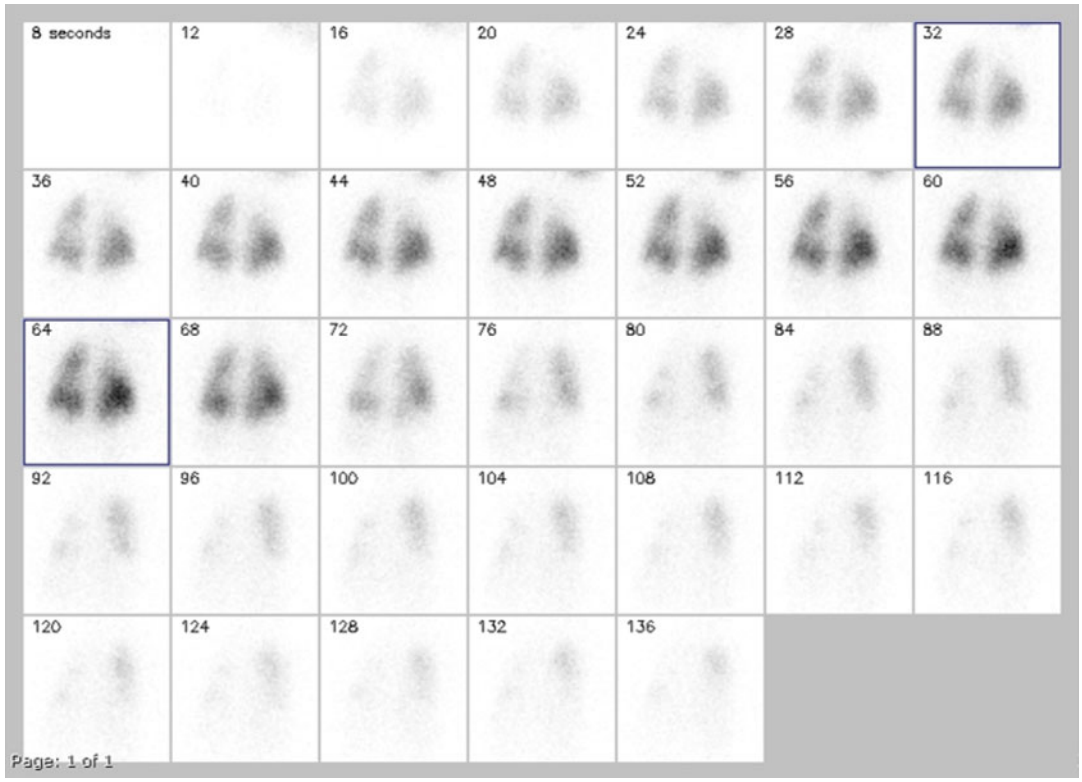

Fig. 6.3 Air trapping in congenital lobar emphysema. In a 10-month-old boy with congenital lobar emphysema of the upper right lung, a dynamic ventilation lung scan performed with ^{133}Xe gas shows both marked delay in ventilation and delayed washout consistent with air trapping in the upper right lung. Recurrent hypercapnia improved after surgical resection of the upper and middle lobes of the right lung

pulmonary hypoplasia, and pulmonary hypertension. Diagnosis now frequently is made prenatally. CDH most frequently occurs on the left (85 %), less frequently on the right (13 %), and rarely bilaterally (2 %) [27]. With surgical repair of the diaphragmatic hernia, the pulmonary sequelae become the long-term clinical effects of CDH [28]. After repair of the diaphragm, the affected lung expands to fill the affected lung cavity. Thus, the ventilation volume of the lung will increase, but the recovery of relative pulmonary perfusion is uncertain and may depend on patient age [29]. In most patients, there may be little postsurgical increase in lung perfusion. However, if the diaphragmatic hernia is corrected early in life, there may be further maturation of pulmonary circulation, so that lung perfusion will increase to nearly match lung volume [30]. In an individual patient, the degree of lung maturation is unpredictable, and ventilation/perfusion scans can be used to assess the degree of ventilation/perfusion mismatch [28] and to follow these patients after surgery (Fig. 6.4).

In patients with severe spinal scoliosis or pectus excavatum, differential compression of the pulmonary vessels and airways can produce regional or whole-lung ventilation/perfusion mismatches. For example, patients with pectus excavatum most typically have a mild reduction in ventilation and a greater reduction in perfusion in the left lung. The severity and progression of ventilation and perfusion abnormalities may help determine the need for surgery [31]. The effect of surgery, one goal of which is improvement of these ventilation and perfusion abnormalities, can be assessed with postoperative lung scintigraphy.

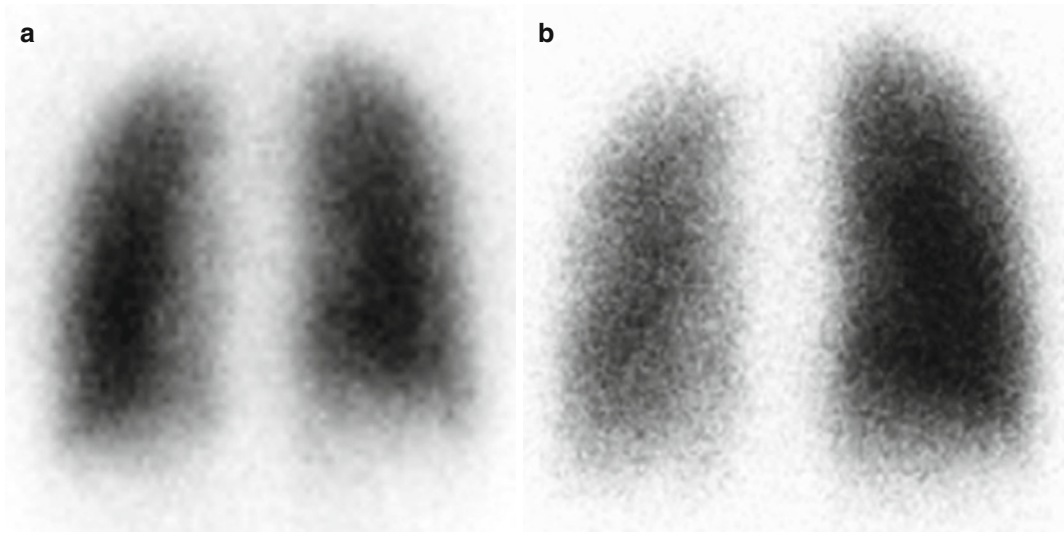

Fig. 6.4 Persistent lung hypoperfusion after repair of a congenital diaphragmatic hernia. A ventilation/perfusion scan was performed in an 8-year who had undergone repair of a left congenital diaphragmatic hernia as an infant. A lung ventilation scan shows ventilation of both lungs with no air trapping. At respiratory equilibrium, merged posterior images (**a**) show differential lung volumes of 49 % left lung and 51 % right lung. However, a lung perfusion scan imaged in the posterior projection (**b**) shows persistent hypoperfusion of the left lung with differential lung perfusion of 30 % left lung and 70 % right lung

Pulmonary Embolism

Pulmonary embolism occurs less frequently in children than adults, but over the past few decades, the reported incidence has increased. This increased frequency of diagnosis has been attributed to a heightened awareness and an increased likelihood of evaluation of pulmonary embolism [32]. However, it also likely represents a true increase in the occurrence of pulmonary embolism in children. This increased incidence has been attributed to increased long-term therapy and prolonged survival of children with predisposing diseases, such as cancer, and the increased use of indwelling venous catheters to provide the therapy for these diseases. The incidence of pediatric pulmonary embolism has a bimodal distribution, with incidence peaks in children less than 1 year of age and in teenagers [33, 34].

While up to one-third of adults with pulmonary embolism have no apparent risk factor, nearly all children have at least one identifiable risk factor [35]. More than one risk factor can be identified in over half of all children with pulmonary embolism [33, 35]. In children, most risk factors relate to an underlying medical condition or a medical intervention [33, 34]. In children, the most common risk factor for pulmonary embolism is an indwelling central venous catheter, which can serve as a nidus for a deep venous thrombosis [34, 36]. This may be related to venous obstruction, abrasion of the vessel wall caused by the catheter, or damage to the vessel wall by medications infused through the venous catheter. Venous thrombosis is more likely when an indwelling catheter becomes infected [37]. However, even in the apparent absence of these factors, venous thrombosis related to indwelling catheters can embolize to the lungs [38]. Deep venous thrombosis, and thus pulmonary embolism, is more common with central venous catheters in an upper extremity [39], and possibly more prevalent when the catheter has been placed in the left upper extremity [40].

The clinical risk factors for pulmonary embolism are different in different age groups. In infants, more than three-quarters of patients diagnosed with pulmonary embolism may have an indwelling venous catheter [34, 36]. Other less

common risk factors in this age group are congenital heart disease and recent surgery [35]. In older children, indwelling venous catheters remain a common cause of pulmonary embolism, but older patients are more likely to have other, possibly concurrent risk factors. These risk factors include immobility or recent surgery [35], malignancy [35], or an underlying clotting disorder [34]. Some clotting disorders represent a previously undiagnosed inherited thrombophilia, while others represent an acquired clotting disorder associated with a wide range of conditions, including malignancy, autoimmune disorders, and nephrotic syndrome. Birth control pills and pregnancy increase the risk of pulmonary embolism [41, 42].

The diagnosis of pulmonary embolism can be more difficult in children than adults. One autopsy study suggested that half of all children with pulmonary embolism did not have clinical findings to suggest the diagnosis [43]. Young children may be unable to express subtle symptoms. Children typically have a higher cardiopulmonary reserve and so may have milder symptoms than in an older patient [34]. Some investigators have suggested that, in most children, few symptoms will be apparent if less than 50 % of the pulmonary circulation is obstructed. However, the sensitivity to pulmonary arterial obstruction may depend on the presence of other cardiopulmonary disease and levels of circulating vasoactive molecules [42].

Pulmonary arterial obstruction creates a ventilation/perfusion mismatch and a right-to-left intrapulmonary shunt, which together result in systemic hypoxemia [44, 45]. If a significant portion of the pulmonary circulation is obstructed, then the right ventricle dilates in response to the increased afterload. Leftward shift of the interventricular septum can decrease left ventricle filling, which results in decreased cardiac output [32].

The identification of a patient with a pulmonary embolism begins with clinical assessment. Although the clinical prediction rules and D-dimer testing used in adults have not been validated in children [32], clinical risk assessment still has an important role in determining which patients should undergo further evaluation for pulmonary embolism. The diagnosis of pulmonary embolism is based on an identifiable perfusion defect within the pulmonary circulation. The traditional approach to the diagnosis of pulmonary embolism has been with a lung ventilation/perfusion (V/Q) scan. A perfusion scan may be sufficient to make the diagnosis in some patients. However, the addition of a ventilation lung scan increases the accuracy and confidence of the study.

A variety of protocols have been used for performing a V/Q scan. The ventilation study can precede or follow the perfusion scan. If the perfusion scan is performed first, then the subsequent ventilation scan must be performed with a higher radiopharmaceutical dose to overcome interference from the perfusion scan. The ventilation scan can be performed with either ^{133}Xe gas or inhaled aerosol. One advantage of assessing perfusion first is that a normal perfusion scan may eliminate the need for a subsequent ventilation study. If the ventilation scan is performed first with an inhaled aerosol, then the perfusion scan must be performed with a higher dose of ^{99m}Tc-MAA. If the ventilation scan is performed first with ^{133}Xe gas, the rapid washout of gas limits the number of views that can be acquired, but as there is little interference with the subsequent perfusion scan, the perfusion scan can be performed with a lower administered dose of ^{99m}Tc-MAA. A recent chest radiograph is essential to the correct interpretation of many V/Q scans. If a chest radiograph has not been performed as part the evaluation of the patient's presenting symptoms, then one should be obtained before performing the V/Q scan. As in adults, the diagnosis of pulmonary embolism in children is based on diagnostic criteria used for lung scintigraphy in PIOPED II (Prospective Evaluation of Pulmonary Embolism Diagnosis), but neither the original [46] nor modified [47] PIOPED II criteria have been fully validated in pediatric patients.

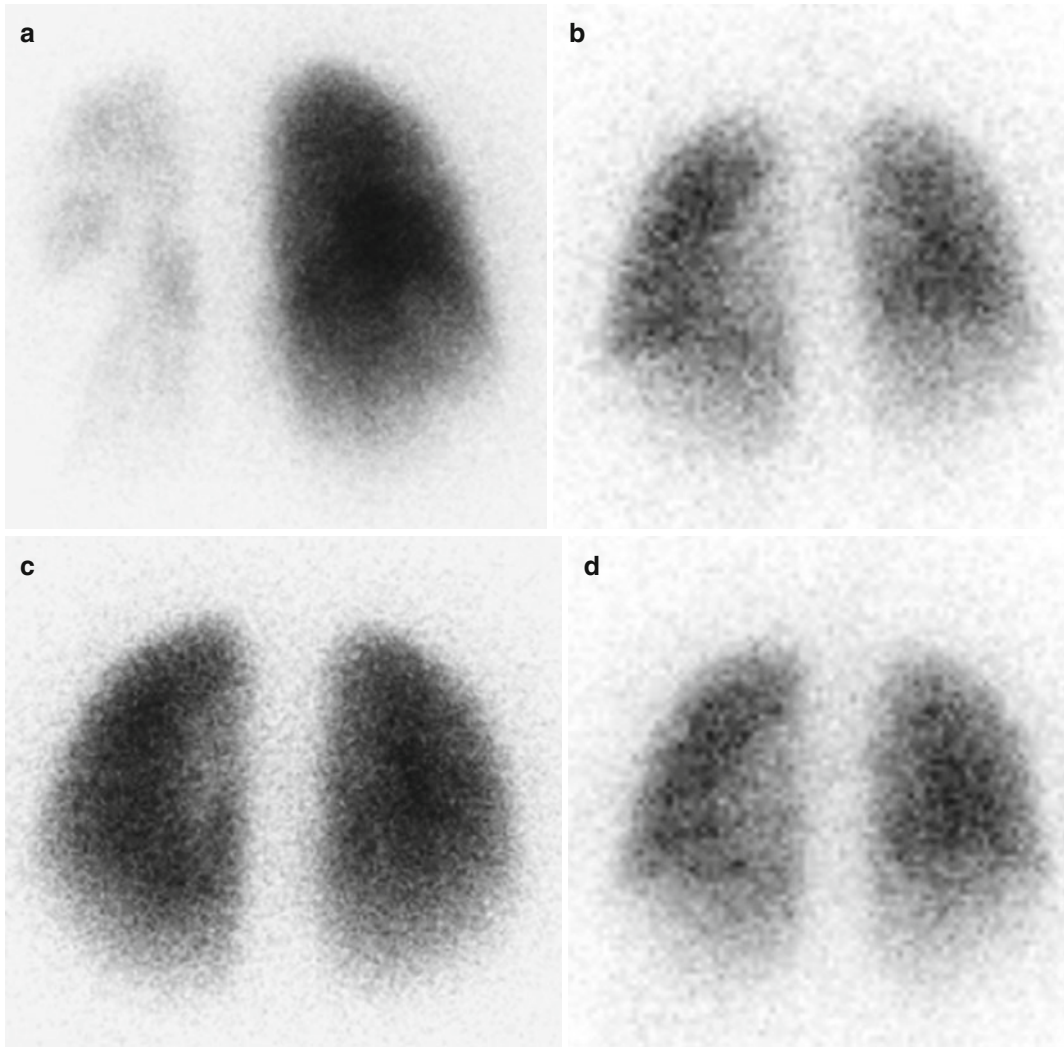

Fig. 6.5 Massive pulmonary embolism identified by ventilation/perfusion scan. A 13-year-old girl with Cushing's disease developed a postoperative deep venous thrombosis and shortness of breath. A perfusion study (**a**, posterior projection) performed with ^{99m}Tc-MAA shows markedly decreased perfusion to the left lung, while a ventilation study (**b**, posterior projection) performed with ^{133}Xe shows a normal ventilation pattern in both lungs. A follow-up study performed 6 weeks later shows resolution of the pulmonary embolism, with normal perfusion (**c**) and ventilation (**d**) in both lungs

Resolution of pulmonary embolism typically occurs spontaneously by fibrinolysis within a few days after the embolic event. However, normal pulmonary blood flow may not return for weeks. Restoration of pulmonary blood flow may be faster in younger patients [48]. Follow-up ventilation/perfusion imaging may be helpful to assess resolution of perfusion defects in patients with pulmonary embolism (Fig. 6.5). This can be particularly helpful in establishing a new baseline for patients at risk for recurrent pulmonary emboli. Ventilation/perfusion imaging also can be helpful in detecting chronic thromboembolic disease in patients with pulmonary hypertension [49].

Ventilation/perfusion scans have been replaced largely by computed tomographic (CT) angiography for evaluation of possible pulmonary embolism in both adults [50] and children [51–53], although there has been a recent resurgence in the use of lung scintigraphy. Ventilation/perfusion scans may be used in patients with contraindications to CT angiography, such as an allergy to iodinated contrast, renal insufficiency, or concerns about radiation dose [54]. In pregnant or lactating patients with suspected pulmonary embolism, the breast radiation dose is less with ventilation/perfusion scan than with CT angiography [54]. Recently, increased concern about radiation exposure, especially in children, has led to a reassessment of the role of ventilation/perfusion scans in the diagnosis of pulmonary embolus. Despite the higher radiation dose with CT angiography, the higher anatomic detail led to its widespread adoption for evaluating possible pulmonary embolism. However, with the adoption of CTA, there has been increased diagnosis of pulmonary embolism, without a clear benefit in patient mortality. This has led some investigators to question if detection of small, subsegmental emboli leads to overdiagnosis of pulmonary emboli [55, 56].

Magnetic resonance imaging techniques have been proposed as alternatives for the diagnosis of pulmonary embolism. The three most common techniques are magnetic resonance angiography (MRA), real-time MR, and MR perfusion. The sensitivity and specificity of each technique may be different, and overall, MR may be slightly less sensitive than CTA [57]. Magnetic resonance techniques have yet to be validated as a reliable method for excluding pulmonary embolism. Other current disadvantages include longer acquisition time, the need for greater patient cooperation with a prolonged breathhold, and less emergent access to MR scanners.

Notwithstanding concerns about the clinical significance of some small angiographic findings, another reason for the widespread adoption of CT angiography has been the perception of higher diagnostic certainty. However, children may have a low rate of indeterminate studies [58]. Use of single-photon emission computed tomography (SPECT) or SPECT/CT for acquiring both the ventilation and perfusion scans may increase diagnostic accuracy and, with fewer indeterminate studies, increase confidence in the interpretation of ventilation/perfusion scan [6, 59]. New diagnostic criteria, similar to PIOPED, may be needed for diagnosing pulmonary embolism by lung SPECT [60]. There has been little reported experience with using SPECT or SPECT/CT for the diagnosis of pulmonary embolism in children.

Other Causes of Pulmonary Perfusion Defects

Every pulmonary embolus does not represent a venous thromboembolism. Pulmonary embolism also can occur with tumor emboli, which may be associated with more extensive obstruction of pulmonary circulation and with systemic hypotension [61, 62]. Other causes of pulmonary emboli include foreign bodies, such as catheter fragments, and posttraumatic fat emboli [61]. Occlusion of a main or branch pulmonary artery or pulmonary vein can occur with extrinsic compression due to tumors at the hilum or in the lung parenchyma [63]. Intrinsic pulmonary artery diseases, including collagen vascular diseases and arteritis, can produce pulmonary artery occlusion [64, 65]. With pulmonary sequestration [66], the involved region of lung typically receives its blood supply from the systemic circulation and will not be visualized after intravenous administration of ^{99m}Tc-MAA. In most cases of pulmonary sequestration, there is no communication with the normal tracheobronchial tree resulting in a matching defect on a ventilation lung scan. Occasionally, a pulmonary sequestration will have an anomalous systemic blood supply with normal connection to the tracheobronchial tree (Fig. 6.6), which produces a ventilation/perfusion mismatch.

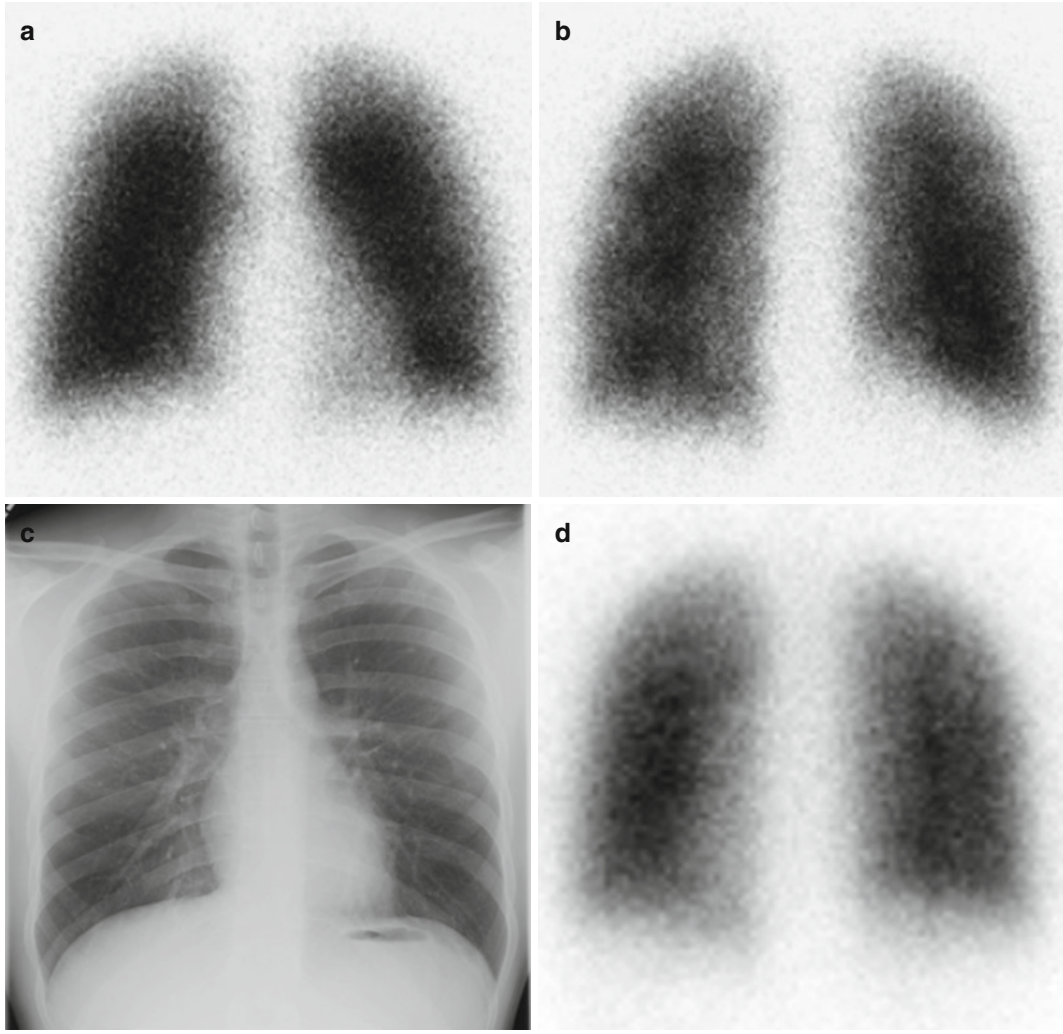

Fig. 6.6 Anomalous blood supply to a lower segment of the right lower lung. A 19-year-old male was found to have an aortopulmonary collateral supplying a segment of the lower lobe of the right lung. After surgical ligation, a ventilation/perfusion scan was performed. A perfusion lung scan in the anterior (**a**) and posterior (**b**) projections shows decreased perfusion at the posterior base of the right lung and confirms the absence of pulmonary perfusion to this region of lung. A postoperative chest radiograph (**c**) shows no abnormalities. A ventilation lung scan was performed with ^{133}Xe and, at respiratory equilibrium, merged posterior images (**d**) demonstrate normal ventilation at the site of the perfusion abnormality. These findings indicate pulmonary sequestration with anomalous systemic perfusion, but an intact tracheobronchial tree

References

1. Ball Jr WC, Stewart PB, Newsham GS, Bates DV. Regional pulmonary function studied with xenon^{133}. J Clin Invest. 1962;19:519–31.
2. Tappin GV, MacDonald NS. Radiochemistry of macroaggregated albumin and newer lung scanning agents. Semin Nucl Med. 1971;1:132–52.
3. Davies G, Reid L. Growth of the alveoli and pulmonary arteries in childhood. Thorax. 1970;25:669–81.
4. Emery JL, Mithal A. The number of alveoli in the terminal respiratory unit of man during late intrauterine life and childhood. Arch Dis Child. 1960;35:54–7.
5. Heyman S. Toxicity and safety factors associated with lung perfusion studies with radiolabeled particles. J Nucl Med. 1979;20:1098–9.

6. Roach PJ, Gradinscak DJ, Schembri GP, Bailey EA, Willowson KP, Bailey DL. SPECT/CT in V/Q scanning. Semin Nucl Med. 2010;40:455–66.
7. Treves S, Ahnberg DS, Laguarda R, Strieder DJ. Radionuclide evaluation of regional lung function in children. J Nucl Med. 1974;15:582–7.
8. James JM, Testa JH. The use of ^{99m}Tc-technegas in the investigation of patients with pulmonary embolism. Nucl Med Commun. 1995;16:802–10.
9. Coates G, O'Brodovich H. Extrapulmonary radioactivity in lung permeability measurements. J Nucl Med. 1987;28:903–6.
10. Meignan M, Russo J, Leveau J, et al. Exercise increases the lung clearance of inhaled technetium-99m DTPA. J Nucl Med. 1986;27:274–80.
11. Jeffries AL, Coates G, O'Brodovich H. Pulmonary epithelial permeability in hyaline-membrane disease. N Engl J Med. 1984;311:1075–80.
12. Dae MW. Pediatric nuclear cardiology. Semin Nucl Med. 2007;37:382–90.
13. Chen JT, Robinson AE, Goodrich JK, Lester RG. Uneven distribution of pulmonary blood flow between left and right lungs in isolated valvular pulmonary stenosis. Am J Roentgenol Radium Ther Nucl Med. 1969;107:343–50.
14. Vettukattil JJ, Slavik Z, Lamb RK, et al. Intrapulmonary arteriovenous shunting may be a universal phenomenon in patients with the superior cavopulmonary anastomosis: a radionuclide study. Heart. 2000;83:425–8.
15. Mishken F, Knote J. Radioisotope scanning of the lungs in patients with systemic-pulmonary anastomoses. Am J Roentgenol Radium Ther Nucl Med. 1968;102:267–9.
16. Pruckmayer M, Zacherl S, Ulrike SM, et al. Scintigraphic assessment of pulmonary and whole-body blood flow patterns after surgical intervention in congenital heart disease. J Nucl Med. 1999;40:1477–83.
17. Grimon G, Andre L, Bernard O, et al. Early radionuclide detection of intrapulmonary shunts in children with liver disease. J Nucl Med. 1994;35:1328–32.
18. El-shabrawi MH, Omran S, Wageeh S, et al. ^{99m}Technetium-macroaggregated albumin perfusion lung scan versus contrast enhanced echocardiography in the diagnosis of the hepatopulmonary syndrome in children with chronic liver disease. Eur J Gastroenterol Hepatol. 2010;22:1006–12.
19. Johnson K. Ventilation and perfusion scanning in children. Paediatr Respir Rev. 2000;1:347–53.
20. Navalkissoor S, Easty M, Biassoni L. Functional lung assessment with radionuclides in paediatric respiratory diseases: a useful, underutilized test in nuclear medicine? Nucl Med Commun. 2010;31:896–902.
21. Komori K, Kamagata S, Hirobe S, et al. Radionuclide imaging study of long-term pulmonary function after lobectomy in children with congenital cystic lung disease. J Pediatr Surg. 2009;44:2096–100.
22. Ciofetta G, Piepsz A, Roca I, et al. Guidelines for lung scintigraphy in children. Eur J Nucl Med Mol Imaging. 2007;34:1518–26.
23. Chen IC, Chen YW, Lin SH, Hsu JH, Wu JR, Dai ZK. Usefulness of combination of pulmonary ventilation and perfusion scintigraphy on the diagnosis of children with unilateral hyperlucent lung. Nucl Med Commun. 2011;32:1052–9.
24. Balink H, Collins J, Korsten-Meijer AG, Rotier BL. Unilateral hyperlucent lung in a child caused by a foreign body identified by V/Q scintigraphy. Clin Nucl Med. 2012;37:916–7.
25. Stinnet RG, Hietala S, Fratkin MJ. Reversible unilateral pulmonary hypoperfusion secondary to mucous plugs. Clin Nucl Med. 1977;2:157–9.
26. Makler PT, Malmud LS, Charkes ND. Diminished perfusion to an entire lung due to mucous plugging. Clin Nucl Med. 1997;2:160–2.
27. Veema DCM, de Klein A, Tibboel D. Developmental and genetic aspects of congenital diaphragmatic hernia. Pediatr Pulmonol. 2012;47:534–45.
28. Hayward MJ, Kharasch V, Sheils C, et al. Predicting inadequate long-term lung development in children with congenital diaphragmatic hernia: an analysis of longitudinal changes in ventilation and perfusion. J Pediatr Surg. 2007;42:112–6.
29. Jeandot R, Lambert B, Brendel AJ, Guyot M, Demarquez JL. Lung ventilation and perfusion scintigraphy in the follow-up of repaired congenital diaphragmatic hernia. Eur J Nucl Med. 1989;15:591–6.
30. Pal K, Gupta DK. Serial perfusion study depicts pulmonary vascular growth in the survivors of non-extracorporeal membrane oxygenation-treated congenital diaphragmatic hernia. Neonatology. 2010;98:254–9.
31. Blickman JG, Rosen JG, Welch KJ, et al. Pectus excavatum in children: pulmonary scintigraphy before and after corrective surgery. Eur J Cardiothorac Surg. 2006;30:637–43.
32. Potocka C, Nemeth J. Pulmonary embolism in pediatrics. J Emerg Med. 2012;42:105–16.
33. Andrew M, David M, Adams M, et al. Venous thromboembolic complications (VTE) in children: first analysis of the Canadian registry of VTE. Blood. 1994;83:1251–7.
34. Van Ommen CH, Peter M. Acute pulmonary embolism in childhood. Thromb Res. 2006;118:13–25.
35. Biss TT, Branda LR, Kahr WH, et al. Clinical features and outcome of pulmonary embolism in children. Br J Haematol. 2008;142:808–18.
36. Schmidt B, Andrew M. Neonatal thrombosis: report of a prospective Canadian and international registry. Pediatrics. 1995;96:939–43.
37. van Rooden CJ, Schippers EF, Barge RM, et al. Infectious complications of central venous catheters increase the risk of catheter-related thrombosis in hematology patients: a prospective study. J Clin Oncol. 2005;23:2655–60.
38. Kuter DJ. Thrombotic complications of central venous catheters in cancer patients. Oncologist. 2004;9:207–16.
39. Monagle P, Adams M, Mahoney M, et al. Outcome of pediatric thromboembolic disease: a report from the Canadian Childhood Thrombophilia Registry. Pediatr Res. 2000;47:763–6.

40. Male C, Julian JA, Massicotte P, et al. Significant association with location of central venous line placement and risk of venous thrombosis in children. Thromb Haemost. 2005;94:516–21.
41. Doll R, Crombie DL, Duncan AS, Hill AB, Inman WHW, Vessey MP. Risk of thromboembolic disease in women taking oral contraceptives: a preliminary communication to the Medical Research Council by a Subcommittee. Br Med J. 1967;2:355–9.
42. Goldhaber SZ. Epidemiology of pulmonary embolism. Semin Vasc Med. 2001;1:139–46.
43. Buck JR, Connors RH, Coon WW, Weintraub WH, Wesley JR, Coran AG. Pulmonary embolism in children. J Pediatr Surg. 1981;16:385–91.
44. Reidel M. Acute pulmonary embolism I: pathophysiology, clinical presentation, and diagnosis. Heart. 2001;85:229–40.
45. Goldhaber SZ, Elliott CG. Acute pulmonary embolism, part I: epidemiology, pathophysiology, and diagnosis. Circulation. 2003;108:2726–9.
46. Gottschalk A, Stein PD, Goodman LR, Sostman HD. Overview of prospective investigation of pulmonary embolism diagnosis II. Semin Nucl Med. 2002;32:173–82.
47. Sostman HD, Massimo M, Gottshalk A, Matta F, Stein PD, Pistolesi M. Sensitivity and specificity of perfusion scintigraphy combined with chest radiography for acute pulmonary embolism in PIOPED II. J Nucl Med. 2008;49:1741–8.
48. McGoldrick PJ, Rudd TJ, Figley MW, Wilhelm JP. What becomes of pulmonary infarcts? AJR Am J Roentgenol. 1979;133:1039–45.
49. Tunariu N, Gibbs SJ, Win Z, et al. Ventilation-perfusion scintigraphy is more sensitive than multidetector CTPA in detecting chronic thromboembolic disease as a treatable cause of pulmonary hypertension. J Nucl Med. 2007;48:680–4.
50. Pesavento R, de Conti G, Minotto I, et al. The value of 64-detector row computed tomography for the exclusion of pulmonary embolism. Thromb Haemost. 2001;8:105.
51. Kristaneepaiboon S, Lee EY, Zurakowski D, et al. MDCT pulmonary angiography evaluation of pulmonary embolism in children. AJR Am J Roentgenol. 2009;192:1246–52.
52. Prabhu SP, Majmood S, Sena L, et al. MDCT evaluation of pulmonary embolism in children and young adults following a lateral tunnel Fontan procedure: optimizing contrast-enhancement techniques. Pediatr Radiol. 2009;39:938–44.
53. Lee EY, Zurakowski D, Boiselle PM. Pulmonary embolism in pediatric patients: survey of CT pulmonary angiography practices and policies. Acad Radiol. 2010;17:1543–9.
54. Schembri GP, Miller AE, Smart R. Radiation dosimetry and safety issues in the investigation of pulmonary embolism. Semin Nucl Med. 2010;40:442–54.
55. Henry JW, Stein PD, Gottschalk A, Raskob GE. Pulmonary embolism among patients with a nearly normal ventilation/perfusion lung scan. Chest. 1996;110:395–8.
56. Sheh SH, Bellin E, Freeman KD, Haramati LB. Pulmonary embolism diagnosis and mortality with pulmonary CT angiography versus ventilation-perfusion scintigraphy: evidence of overdiagnosis with CT? AJR Am J Roentgenol. 2012;198:1340–5.
57. Clemens S, Leeper KV. New modalities for detection of pulmonary emboli. Am J Med. 2007;120:S2–12.
58. Gelfand MJ, Gruppo RA, Nasser MP. Ventilation-perfusion scintigraphy in children and adolescents is associated with a low rate of indeterminate studies. Clin Nucl Med. 2008;33:606–9.
59. Bajc M, Neilly JB, Miniatti M, et al. EANM guidelines for ventilation/perfusion scintigraphy: part 2. Eur J Nucl Med Mol Imaging. 2009;36:1528–38.
60. Bajc M, Jonson B. Ventilation/perfusion SPECT – an essential but underrated method for the diagnosis of pulmonary embolism and other diseases. Eur J Nucl Med Mol Imaging. 2009;36:875–8.
61. Babyn PS, Gahunia HK, Massicotte P. Pulmonary thromboembolism in children. Pediatr Radiol. 2005;35:258–74.
62. Baird JS, Killinger JS, Kalkbrenner KJ, Bye MR, Schleien CL. Massive pulmonary embolism in children. J Pediatr. 2010;156:148–51.
63. Mendelson DS, Train JS, Goldsmith SJ, Efremidis SC. Ventilation-perfusion mismatch due to obstruction of pulmonary vein. J Nucl Med. 1981;22:1062–3.
64. Suzuki K, Kamata N, Inokuma S, et al. Clinical significance of ventilation/perfusion scans in collagen disease patients. Ann Nucl Med. 2000;14:405–13.
65. Castellani M, Vanoli M, Cali G, et al. Ventilation-perfusion lung scan for the detection of pulmonary involvement in Takayasu's arteritis. Eur J Nucl Med. 2001;28:1801–5.
66. Sade RM, Clouse M, Ellis Jr FH. The spectrum of pulmonary sequestration. Ann Thorac Surg. 1974;18:644–58.

Cardiovascular System

7

S. Ted Treves and Heinrich Schelbert

The application of radionuclides to study the cardiovascular system was first investigated by Blumgart and Yens and Blumgart and Weiss in 1927 [1, 2]. These investigators used radium C and a primitive radiation detector to study blood-flow velocity. In 1948 and 1949, Prinzmetal et al. described radiocardiograms of three patients with congenital heart disease using ^{131}I, sodium iodine, and a Geiger-Mueller counter [3, 4].

Congenital heart disease affects 0.8 per 100 live births. Approximately one-third of these children require treatment by interventional catheterization or surgery during the first year of life [5]. Significant advances in these therapeutic methods as well as cardiac intensive care during the past decades have enabled corrective and palliative interventions to be performed in even the smallest neonates [6, 7].

Advances in imaging techniques such as echocardiography, computed tomography (CT), magnetic resonance imaging (MRI), and angiography have helped in the evaluation of anatomy and the understanding of physiology in children with heart disease in ways not possible before. With dramatic improvements in technology (radiopharmaceuticals and imaging instrumentation), nuclear medicine offers several methods applicable to the diagnosis and assessment of pediatric cardiovascular disorders. These include single photon emission computed tomography (SPECT), positron emission tomography (PET) and hybrid positron emission tomography/computer tomography (PET/CT), first-pass radionuclide angiocardiography, radionuclide ventriculography (gated blood pool scan), and venography.

Imaging of the Myocardium

Radionuclide imaging of the myocardium can be carried out with SPECT, PET or PET/CT, which can image myocardial perfusion, metabolism, neuronal innervation, and inflammation/infection. This section focuses on myocardial perfusion imaging with SPECT, as most of the experience in children has been obtained with this imaging modality. Because of its higher spatial resolution, PET/CT imaging is now also being used in pediatric patients [8, 9]. Myocardial perfusion imaging is useful in the assessment of

S.T. Treves, MD (✉)
Joint Program in Nuclear Medicine,
Department of Radiology, Harvard Medical School,
Boston, MA, USA

Division of Nuclear Medicine and
Molecular Imaging, Department of Radiology,
Boston Children's Hospital, Boston, MA, USA

Division of Nuclear Medicine and
Molecular Imaging, Department of Radiology,
Brigham and Women's Hospital, Boston, MA, USA
e-mail: ted_treves@hms.harvard.edu

H. Schelbert, MD
Division of Nuclear Medicine,
Department of Molecular and Medical Pharmacology,
Ronald Reagan UCLA Medical Center, Los Angeles,
CA, USA
e-mail: hschelbert@mednet.ucla.edu

S.T. Treves (ed.), *Pediatric Nuclear Medicine and Molecular Imaging*,
DOI 10.1007/978-1-4614-9551-2_7,

Table 7.1 Indications for myocardial perfusion scintigraphy in children

Postoperative evaluation of arterial switch operation for TGA
Takayasu arteritis
Tetralogy of Fallot repair
Mustard/Senning operation
Mucocutaneous lymph node syndrome (Kawasaki)
Anomalous left coronary artery
Cardiomyopathies (thalassemia)
Chest pain
Chest trauma

several cardiovascular disorders including Kawasaki disease, transposition of the great arteries following arterial switch operation, cardiac transplantation, cardiomyopathy, chest pain, chest trauma, and anomalous left coronary artery arising from the pulmonary artery. Other less frequent indications include hyperlipidemia, supravalvular aortic stenosis, syncope, coarctation of the aorta, Takayasu disease, and pulmonary atresia with intact ventricular septum (Table 7.1).

Clinical Applications

Kawasaki Disease

Kawasaki disease, also known as mucocutaneous lymph node syndrome, was first described in l967 by Tomisaku Kawasaki [10]. Kawasaki disease is an acute, self-limited vasculitis of unknown etiology that occurs predominantly in infants and young children of all races. The disease is characterized by fever, bilateral nonexudative conjunctivitis, erythema of the lips and oral mucosa, changes in the extremities, rash, and cervical lymphadenopathy. Coronary artery aneurysms or ectasia develops in 15–25 % of untreated children with the disease and may lead to ischemic heart disease, myocardial infarction, or even sudden death [11, 12]. In the USA, Kawasaki disease has surpassed acute rheumatic fever as the leading cause of acquired heart disease in children. The cause of Kawasaki disease is unknown, although an infectious agent seems likely, as there is a seasonal incidence with peaks during the winter and spring, and cases are usually clustered geographically. The peak incidence of Kawasaki disease is in the toddler and preschool age group (75 % of cases in children under 5 years in the USA); it is rare in adults [13]. The case fatality ratio of Kawasaki disease is approximately 0.08 %, with virtually all deaths caused by the cardiac complications of this disease [14].

Histopathologic examination findings at 0–9 days are characterized by acute perivasculitis and vasculitis of the microvessels and small arteries throughout the body [15]. At 12–25 days there is panvasculitis of the coronary arteries with aneurysm and thrombosis. Aneurysms with internal diameters greater than 8 mm carry a disproportionately high risk of myocardial infarction. Myocarditis, pericarditis, and endocarditis may be present during this phase as well. Disappearance of inflammation in the microvessels, marked intimal thickening, and granulation of the coronary arteries are present between 28 and 31 days. Subsequently, coronary artery aneurysms either regress by myointimal proliferation to normal lumen diameter, or stenosis may develop at either end of the aneurysm. Among patients with persistent coronary artery aneurysms, the prevalence and severity of stenoses increase steadily over many years and are most highly predicted by the original size of the aneurysm [16].

The risk of coronary artery thrombosis is greatest after the acute phase subsides (beyond 12 days), when coronary vasculitis occurs concomitantly with marked elevation of the platelet count and a hypercoagulable state. Standard treatment involves intravenous immunoglobulin (IVIG), other anti-inflammatory agents, and oral anticoagulant therapy. Intravenous anticoagulant therapy or thrombolytic therapy may be necessary, and in rare cases coronary artery bypass grafting is required [17].

Echocardiography is helpful for delineating aneurysms and assessing ventricular function. Myocardial perfusion imaging with SPECT and PET has been widely used in the assessment of these patients. The presence of aneurysm may or may not be correlated with abnormalities in regional myocardial perfusion. Perfusion imaging, with exercise or pharmacologic stress, may demonstrate regionally reduced myocardial perfusion or an improvement in perfusion after medical therapy. In patients with Kawasaki disease and clinical signs of myocardial ischemia, regionally abnormal wall motion is frequently associated

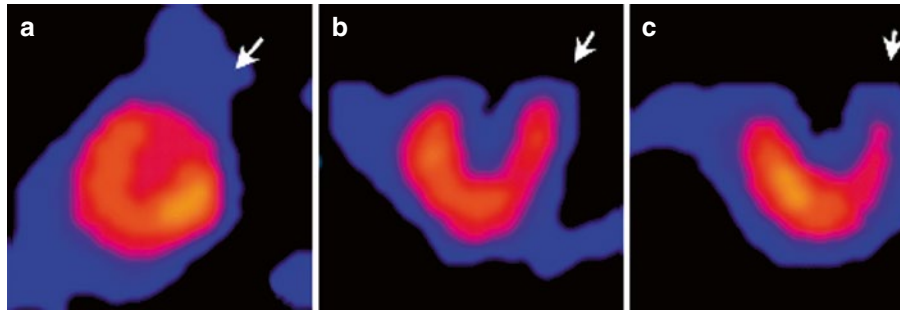

Fig. 7.1 A 6-year-old boy with Kawasaki disease and severe aneurysms in the left anterior descending and the right coronary arteries. Short axis (**a**), horizontal long axis (**b**), and vertical long axis (**c**) slices reveal a perfusion defect in the anterior wall of the left ventricle (*arrows*)

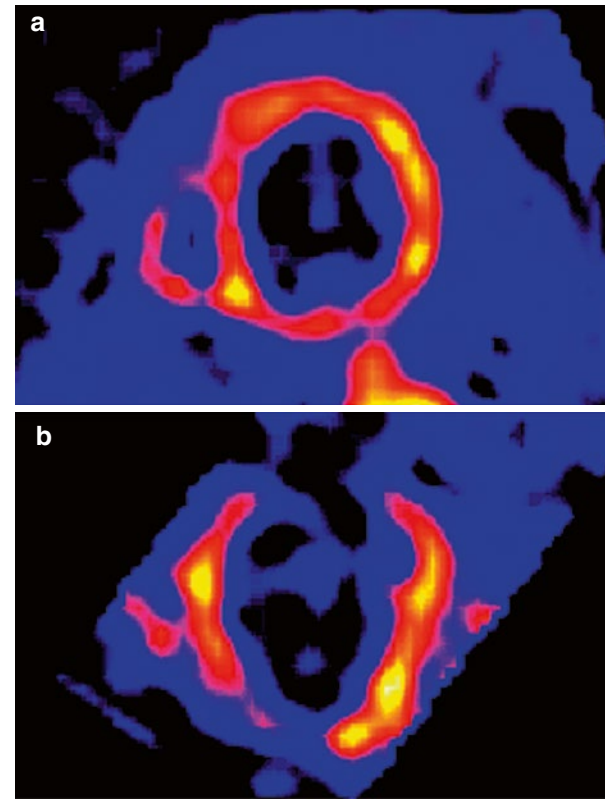

Fig. 7.2 Kawasaki disease. Dilated cardiomyopathy with focal myocardial defects and poor function. (**a**) Short axis. (**b**) Transverse long axis. *RVEF*: Right Ventricular Ejection Fraction, *LVEF*; Left Ventricular Ejection Fraction

with perfusion defects and, based on PET metabolic imaging, with increased glucose utilization as an index of myocardial viability [18, 19]. Moreover, flow responses to pharmacologic vasodilation and, thus, flow reserves have been reported to remain attenuated long after the acute phase of Kawasaki disease [20, 21]. Examples of myocardial perfusion SPECT in Kawasaki disease are illustrated in Figs. 7.1, 7.2 and 7.3.

Takayasu Disease

Takayasu disease, an inflammatory disorder of the great vessels, was described first in 1908 [22]. It is a rare disease with an estimated occurrence in the USA of 2.6 cases per one million people. It is most prevalent among individuals of Asian origin but affects individuals of all ethnic backgrounds. Women are eight to nine times more often affected than

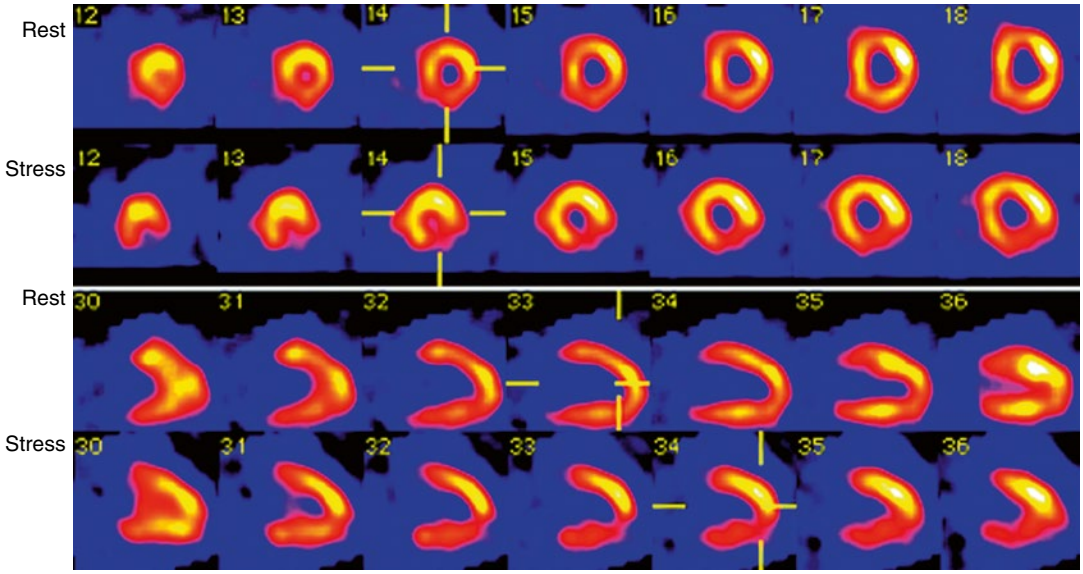

Fig. 7.3 Patient with Kawasaki disease with severe ischemia of the inferior wall of the left ventricle, most pronounced during stress

men; the disease usually occurs in the second and third decades of life [23]. However, cases in children as young as 24 months have been reported [24–29].

The pathogenesis of Takayasu disease has not been fully established. It is believed to involve cell-mediated autoimmune mechanisms, triggered by still unknown stimuli [30]. The disease preferentially targets the large brachiocephalic arterial vessels including the aortic root, the thoracic and abdominal aortas, and the proximal brachial and iliac vessels. Histology of the acutely affected arterial wall reveals concentric intimal hyperplasia with infiltration of macrophages, T cells, and natural killer cells, resembling to some extent histomorphologic features of giant cell arteritis. The disease usually progresses in three phases, beginning with an acute phase with ill-defined symptoms like fever, malaise, weight loss, and fatigue, followed by a vascular inflammatory phase and a late quiescent vascular occlusion phase. Due to frequent relapses, the three disease phases frequently coexist. Cardiovascular manifestations include hypertension, dilation of the aortic root, and coronary stenoses. Vascular alterations as seen on angiography typically include smooth, concentrically stenosed vessel segments alternating with normal vessel segments. Vascular aneurysms are frequently present. Treatment includes corticosteroids and other immunosuppressive agents as well as endoscopic or surgical revascularization of stenosed or occluded vessels.

Myocardial perfusion imaging, especially during stress, can identify obstructive coronary stenoses or, when combined with metabolic imaging, viability and dysfunctional myocardial regions. Because of the absence of disease-specific clinical manifestations during the acute phase, imaging approaches are essential for establishing the diagnosis. Ultrasound, CT, and cardiac MRI are being used for detecting inflammation-related increases in arterial wall thickness as well as the presence of vascular stenosis [31]. Also, as several investigations have indicated, the acute vascular inflammatory phase can be directly identified with FDG and PET imaging [32–36]. FDG accumulates in inflammatory neutrophils and macrophages. Increases in vascular FDG uptake thus serve as indicators of vascular inflammation. Vascular uptake is highest during the acute inflammatory phase and declines during the late quiescent phase [37–40]. Changes in vascular FDG uptake also serve as a measure of the response to

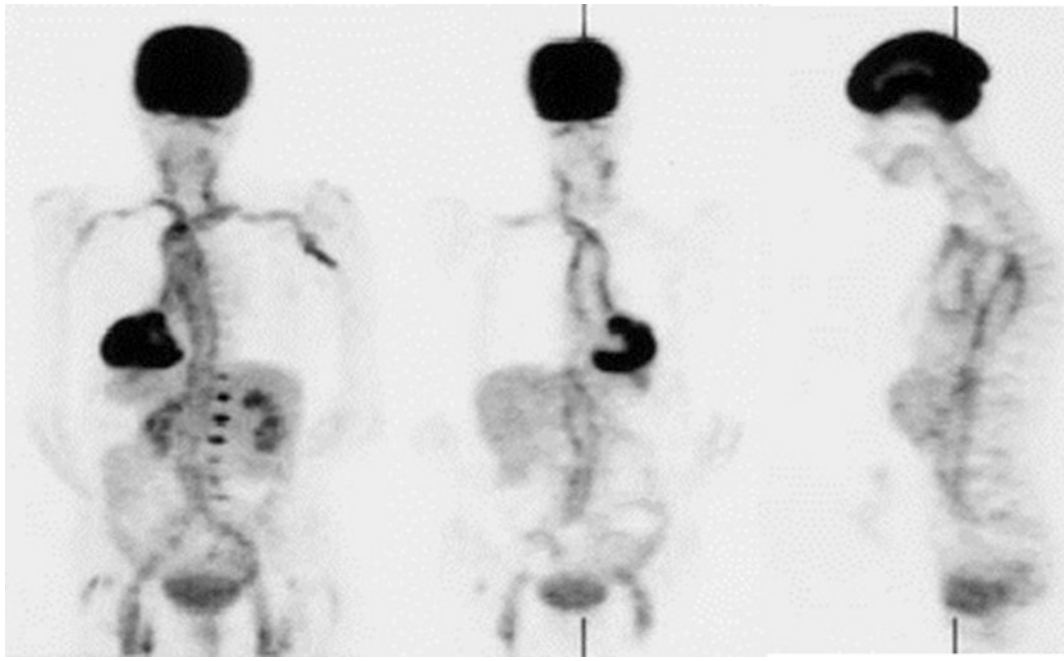

Fig. 7.4 Example of increased ^{18}F-FDG uptake in the great vessels in a patient with giant cell arteritis. Similar ^{18}F-FDG uptake is seen in patients with Takayasu arteritis, though usually less extensive (Adopted from Meller et al. [175], Figure 2)

corticosteroid or immunosuppressive treatment (Fig. 7.4) [36, 37, 41, 42].

Transposition of the Great Arteries: Arterial Switch Operation

In dextro-transposition of the great arteries (d-TGA), the aorta arises anterior from the anatomic right ventricle and the pulmonary artery arises from the anatomic left ventricle. This defect accounts for 5–7 % of all congenital cardiac malformations [43]. Without treatment, approximately 30 % of these infants die in the first week of life, 50 % within the first month, and more than 90 % within the first year [44]. Current medical and surgical treatment, which includes the arterial switch operation (ASO), provides greater than 95 % early and midterm survival. The most technically challenging portion of the ASO surgery involves the transfer of the coronary arteries from the anterior semilunar root to the reconstructed neoaorta. The short- and long-term success of this operative approach depends principally on the continued patency and adequate functioning of the coronary arteries [45–49]. Vogel et al. have previously reported areas of myocardial hypoperfusion after the ASO [50, 51]. Using ^{201}Tl perfusion scintigraphy with isoproterenol stress, we investigated the prevalence of myocardial perfusion abnormalities in children after the arterial switch operation at rest and with the physiologic stress of exercise using ^{99m}Tc-sestamibi myocardial perfusion SPECT. Abnormalities of myocardial perfusion were present in nearly all patients. These perfusion abnormalities did not correlate with echocardiographic indices of wall motion abnormalities and most likely were related to small areas of hypoperfusion resulting from aortic cross-clamping at surgery (Fig. 7.5).

Combined imaging of myocardial perfusion and glucose metabolism with positron emission tomography can identify the presence of viable myocardium and, thus, the possibility of an improvement in myocardial function after revascularization (Fig. 7.6).

The long-term patency of surgically reimplanted coronary vessels has also been assessed with ^{13}N-ammonia PET perfusion imaging

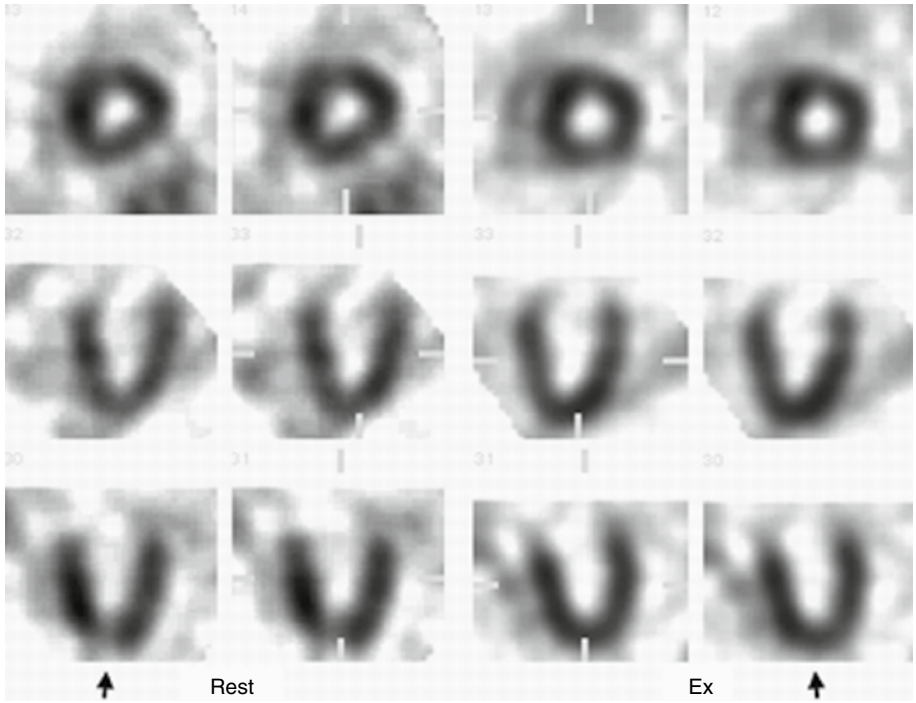

Fig. 7.5 Arterial switch operation for transposition of the great arteries. At rest, there is an apparent apical defect that is not present at exercise (*arrows*)

employing pharmacologic vasodilation or physical exercise as stressors [52, 53]. Myocardial blood flows measured quantitatively in these studies were found to be diminished during adenosine-stimulated hyperemia, despite patency of the reimplanted coronary arteries. While the reason for the attenuated hyperemic flow response and the reduced flow reserve remains uncertain, they have been attributed to impairments in coronary vasomotor function.

Anomalous Left Coronary Artery

Anomalous origin of the left coronary artery from the pulmonary artery (ALCAPA) results in severe myocardial dysfunction and ischemia during early infancy [54, 55]. Following birth, the left ventricle becomes perfused with desaturated blood at pressures that rapidly fall below systemic pressures. Classic findings include infarction of the anterolateral left ventricular free wall followed by mitral valve incompetence secondary to an infarcted anterior papillary muscle. This leads to symptomatic congestive heart failure in the first year of life. A number of surgical techniques have been utilized to transfer the anomalous coronary artery back to the aortic cusp [56–58]. The diagnosis can usually be made by history, physical examination, electrocardiogram, and echocardiogram with color Doppler. Myocardial perfusion scintigraphy may be helpful for assessing the severity of hypoperfusion and for the serial evaluation during recovery of function following repair (Figs. 7.7 and 7.8) [59].

Cardiac Transplantation

Pediatric cardiac transplantation has become a viable treatment option for neonates, infants, and children with end-stage cardiomyopathy or congenital heart disease not amenable to conventional surgical repair or palliation. Although early mortality generally results from acute rejection or infectious complications, accelerated coronary vasculopathy has become the major cause of late morbidity and mortality following transplantation [60, 61]. The specific pathogenesis of transplant coronary disease is unknown, but it is presumed to involve some form of vascular immunologic injury. In severe cases, coronary

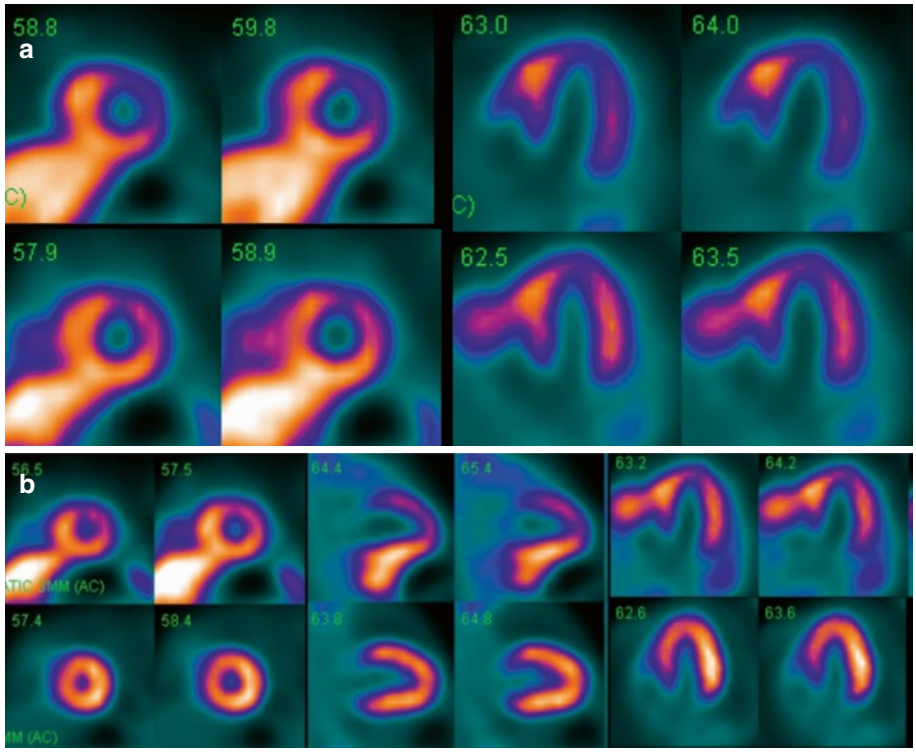

Fig. 7.6 PET stress and rest myocardial perfusion images and ^{18}F-deoxyglucose uptake images in a 22-day-old child after an arterial switch operation (ASO) for D-transposition of the great arteries. (**a**) The perfusion images obtained with ^{13}N-ammonia show a mild perfusion deficit in the anterior and lateral wall that largely normalizes on the stress images. (**b**) Comparison of the FDG uptake images to the myocardial perfusion images at rest shows increased FDG uptake in the slightly hypoperfused anterior and lateral wall, consistent with a perfusion metabolism mismatch and the presence of myocardial viability

arteriography shows progressive distal obliterative disease in the absence of collateral vessel development [62]. Myocardial perfusion imaging has been used to evaluate these patients on a regular basis. Along with coronary angiography, it helps in the diagnosis of coronary artery disease and myocardial viability. In cases showing perfusion defects associated with diminished wall motion, ^{18}F-FDG-PET can determine the presence of myocardial viability (i.e., of a potentially reversible contractile dysfunction). Examples of ^{99m}Tc-sestamibi SPECT in patients following heart transplant can be seen on Figs. 7.9, 7.10 and 7.11.

Cardiac allograft vasculopathy diffusely affects the coronary circulation. Even when discreet obstructive coronary stenoses are absent, the vasculopathy leads to concentric intimal thickening of the proximal and distal coronary arteries that is associated with coronary vasomotor abnormalities. Myocardial perfusion then remains homogeneous even during stress despite a diffuse impairment of the vasodilator function and the absence of stress-induced flow defects. Severe impairments in the coronary flow reserve appear to be correlated with decreases in left ventricular function so that increases in end-systolic and end-diastolic volumes as assessed by gated SPECT or PET perfusion imaging can contribute to the diagnosis of cardiac allograft vasculopathy [63]. Alternatively, impairments in vasodilator function can be identified directly through quantitative PET-based measurements of myocardial blood flow at rest and during pharmacologic vasodilation [64, 65]. In children with cardiac allograft vasculopathy, the coronary flow reserve as the ratio of hyperemic to rest blood

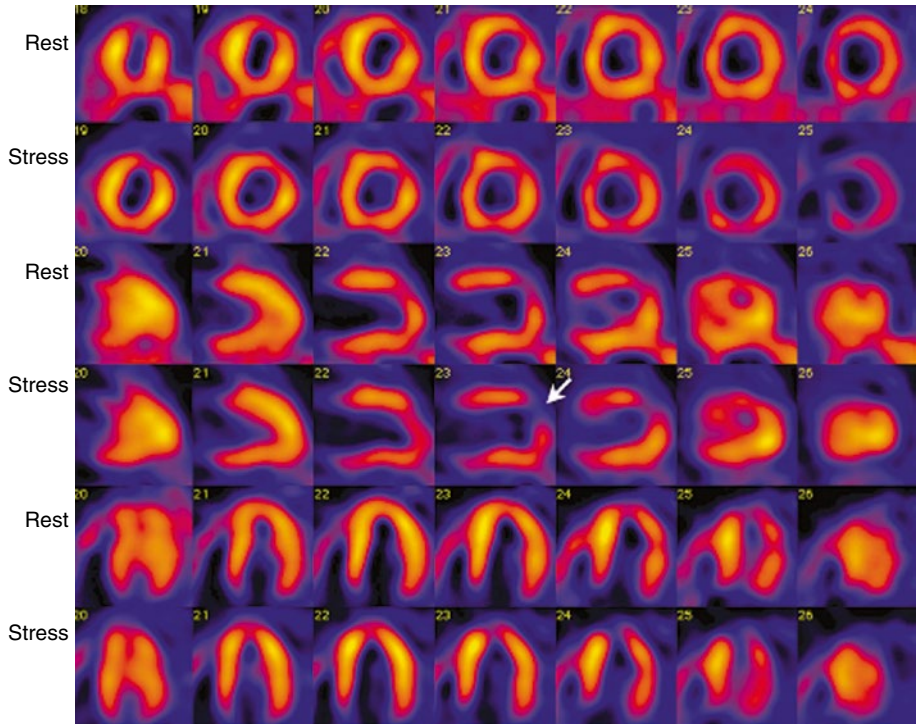

Fig. 7.7 A 5-year-old boy with anomalous coronary artery departing from the pulmonary artery. A perfusion defect gets worse with stress (*arrow*)

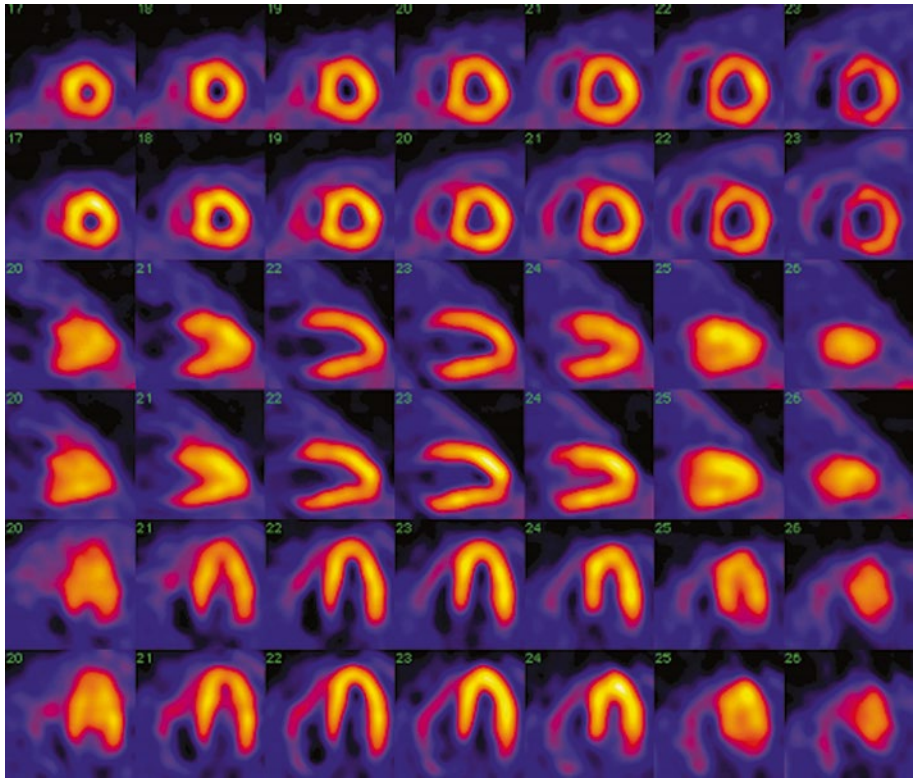

Fig. 7.8 Anomalous origin of the left anterior descending coronary artery from the right coronary artery. Successful repair

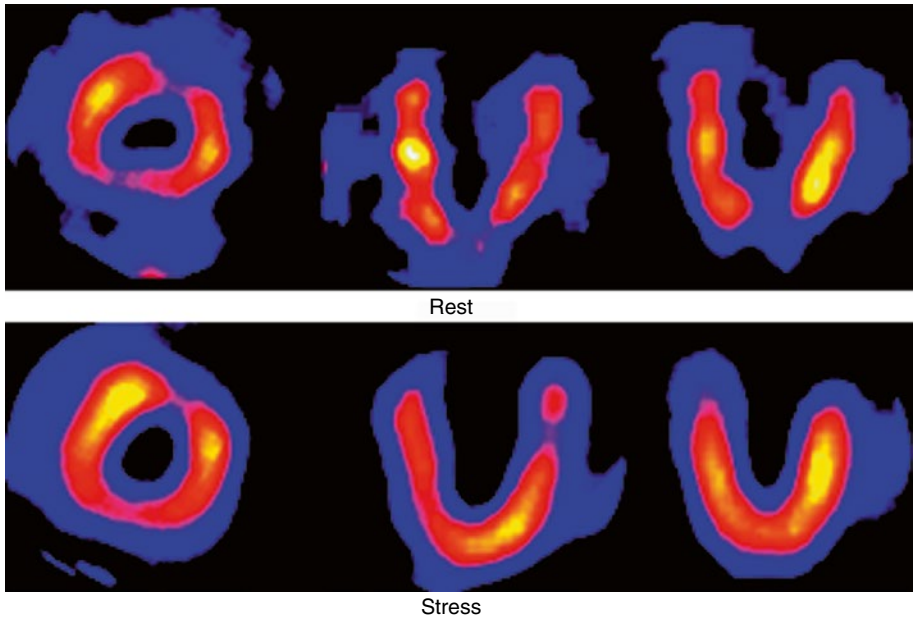

Fig. 7.9 Cardiac transplant. Images at rest reveal irregular distribution of myocardial perfusion. This pattern changes during stress. The defect in the anterior wall remains, while the apical defect improves with stress. A coronary angiogram revealed collateral circulation feeding the apex

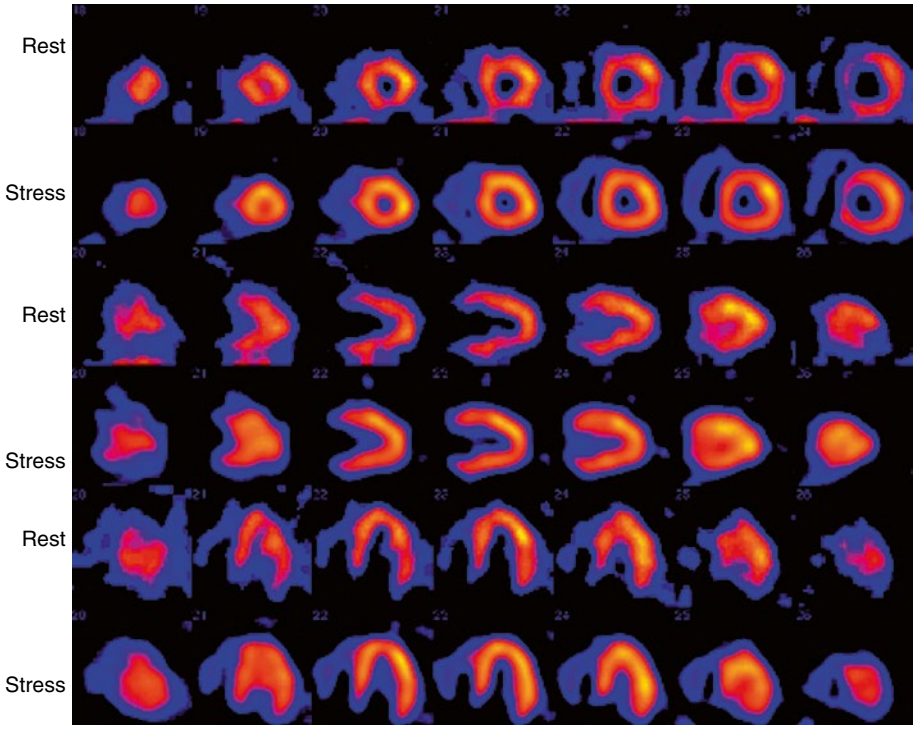

Fig. 7.10 Cardiac transplant. Images at rest reveal irregular distribution of myocardial perfusion with defects in the mid-anterior, mid-septal, and mid-inferior wall of the left ventricle. The images at stress show a more normal distribution of myocardial blood flow. There were collaterals that were recruited during the stress

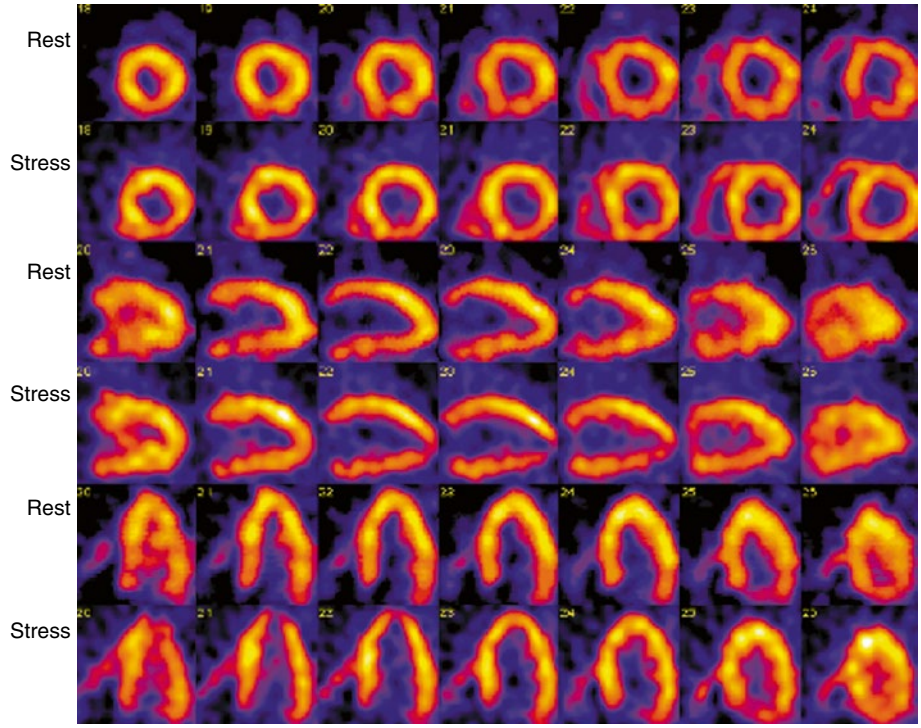

Fig. 7.11 Cardiac transplant. ^{99m}Tc-sestamibi single photon emission computed tomography (SPECT) demonstrates an apical perfusion defect that is seen at stress

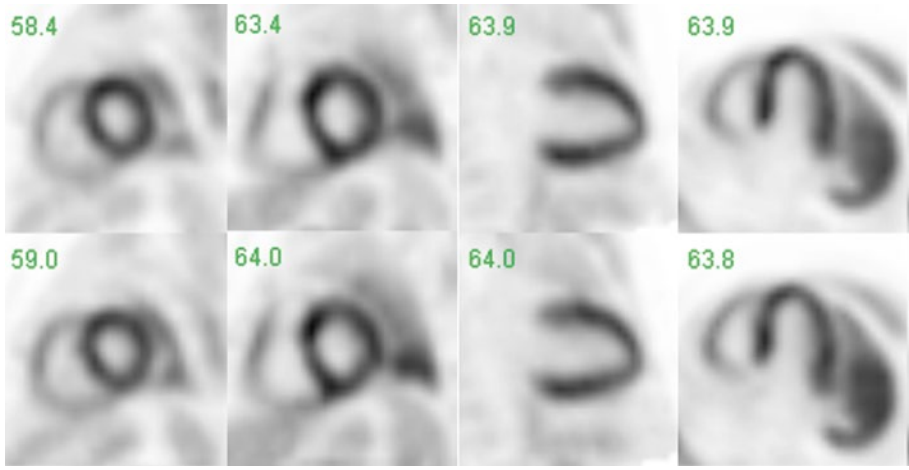

Fig. 7.12 Stress-rest myocardial perfusion images obtained with ^{13}N-ammonia and PET in a 16-year-old patient with a cardiac transplant and suspected transplant vasculopathy causing a progressive increase in left ventricular volumes. Global left ventricular blood flow at rest was 1.19 ml/mm/g and increased with adenosine stress to 1.92 ml/min/g. Accordingly, the myocardial perfusion reserve was only 1.65

flows is typically diminished. The decrease in the flow reserve occurs in an inverse proportion to the extent and severity of intimal thickening of the coronary vessels (Fig. 7.12).

Cardiomyopathy

Primary cardiomyopathies (CMs) include a diverse group of diseases affecting the heart muscle itself. There are three types of CM

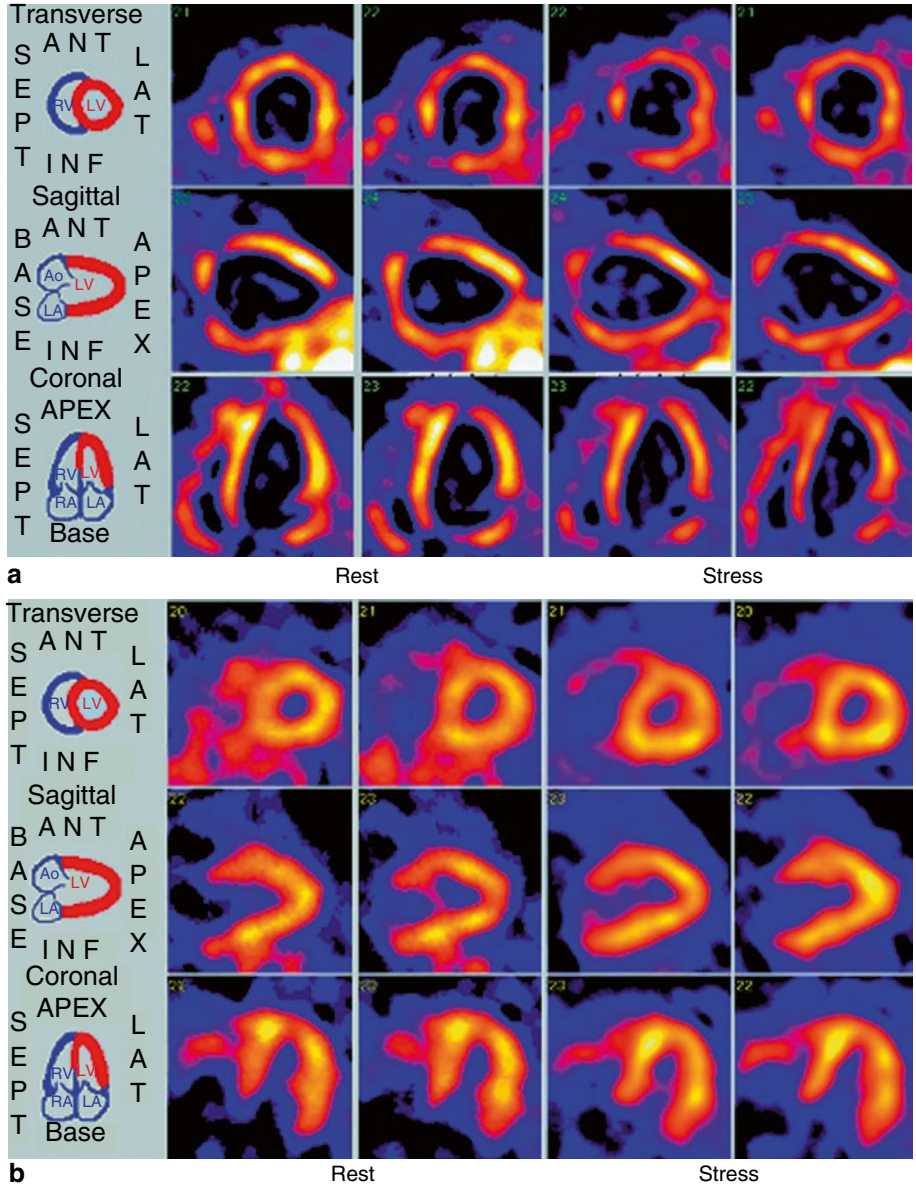

Fig. 7.13 (**a**) Patient with severe dilated cardiomyopathy. (**b**) Same patient following successful cardiac transplantation

based on anatomic and functional features: hypertrophic (HCM), dilated (DCM), and restrictive (RCM). Each type of CM is distinct in its set of etiologies, functional characteristics, clinical features, and therapeutic approach. Based on the form of cardiomyopathy, the ventricle may become hypertrophied or dilated with increasingly diminished diastolic or systolic function, ultimately leading to heart failure, arrhythmia, or sudden death. Severe reductions in the coronary flow reserve in the hypertrophied septum in children with HCM, as observed with ^{13}N-ammonia PET, may be the cause of regional myocardial ischemia [66]. Depending on the type and severity of the disease, myocardial imaging can diagnose left ventricular dilatation, myocardial thinning, focal ischemia, or infarction as well as abnormalities in regional and global left ventricular function (Fig. 7.13).

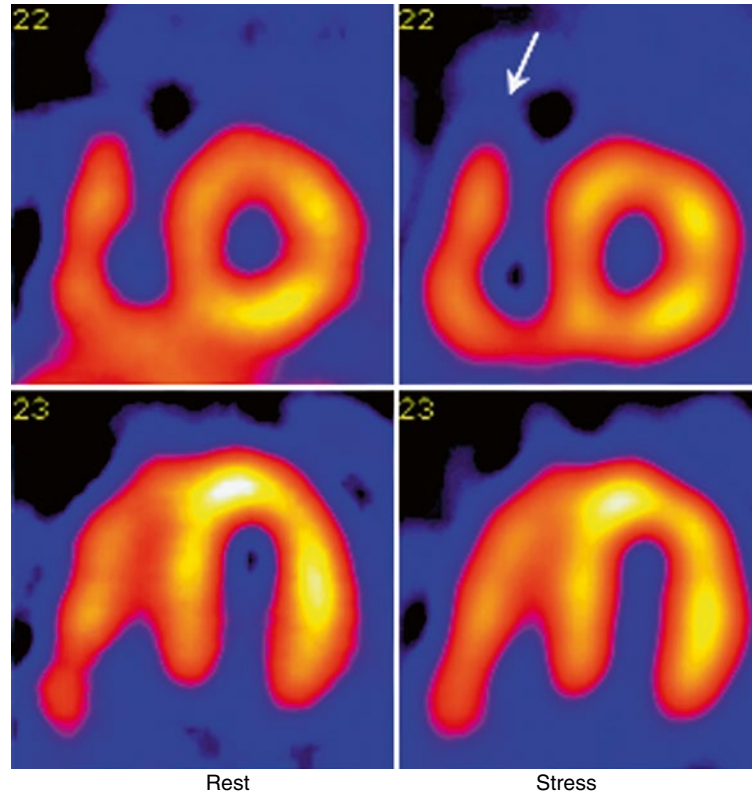

Fig. 7.14 An 11-year-old girl with truncus arteriosus. The ^{99m}Tc-sestamibi SPECT reveals increased right ventricular tracer uptake due to hypertrophy (*arrow*). Post-repair magnetic resonance imaging (MRI) shows mild narrowing of the distal conduit, a left pulmonary artery of small caliber, and regurgitant fraction of 43 %. Pulmonary hypertension and mild to moderate right ventricular dilatation are present

Chest Pain and Trauma

Chest pain is a common complaint in children, often idiopathic, commonly chronic, and most often benign. Cardiac causes of chest pain account for a small minority of potential etiologies including idiopathic (12–85 %), musculoskeletal (15–31 %), pulmonary (12–21 %), psychiatric (5–17 %), gastrointestinal (4–7 %), other (4–21 %), and cardiac (4–6 %) [67]. Cardiac-related causes of chest pain include anatomic lesions (such as aortic stenosis, anomalous coronary artery from the pulmonary artery, and coarctation), acquired lesions (cardiomyopathies, Kawasaki disease, dissecting aortic aneurysm, and pericarditis), and tachyarrhythmias. Chest pain is not a frequent referral diagnosis for myocardial perfusion imaging in children. However, in our practice we have observed that this method has been utilized to help rule out cardiac ischemia as a cause of chest pain.

Right Ventricular Hypertrophy and Hypertension

In normal individuals, the myocardium of the right ventricle has much lower tracer uptake than that of the left ventricle and therefore may not be clearly visible on myocardial perfusion imaging. The right ventricular wall can be seen in the normal individual if the injection is made during or just after exercise. High radiotracer uptake in the right ventricular myocardium at rest is seen in patients with right ventricular hypertrophy (Figs. 7.14, 7.15 and 7.16) [68, 69]. As, for example, in patients with congenital heart disease, such as tetralogy of Fallot (pre- and postoperatively), transposition of the great arteries (following Senning or Mustard repair when the right ventricle is at systemic pressure) (Table 7.2), after an arterial switch operation (ASO) with residual supravalvular pulmonary stenosis and secondary right ventricular hypertrophy, or in pulmonary artery hypertension [53, 70].

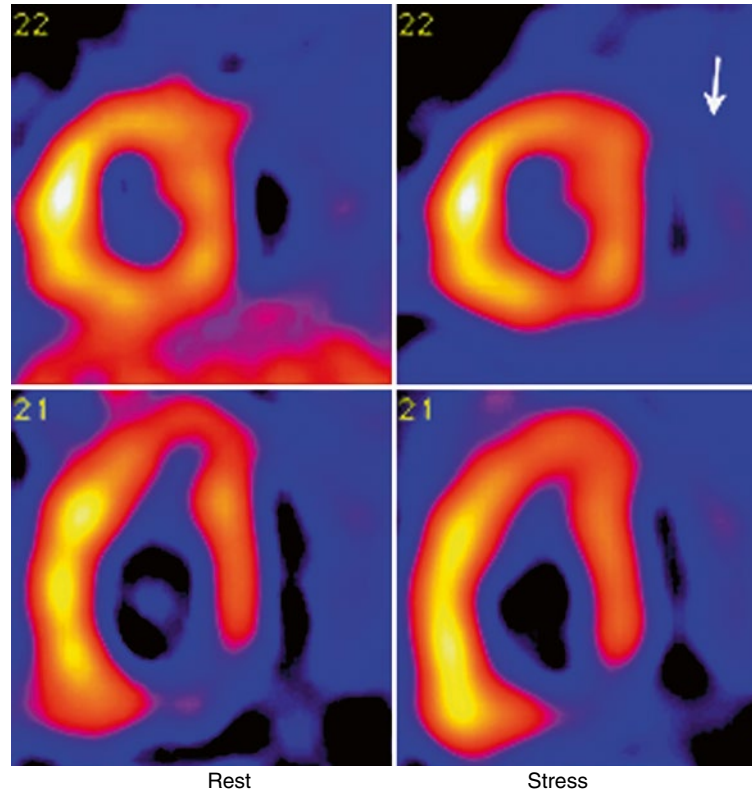

Fig. 7.15 A 28-year-old man who had a Mustard operation for transposition of the great arteries. The patient had a dilated and hypertrophic right (systemic) ventricle with depressed function, mild to moderate TR, chest pain with exertion, and systemic hypertension. The left ventricle (pulmonary) is small and takes relatively much lower amount of tracer. *Arrow* points to the Right Ventricle

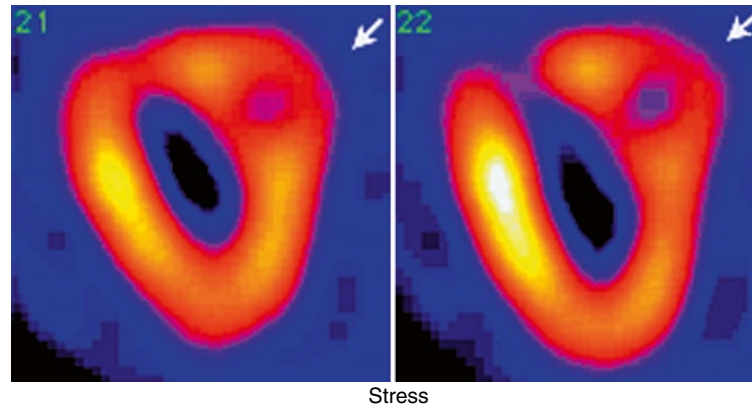

Fig. 7.16 A 13-year-old boy with double-outlet right ventricle, hypoplastic left heart syndrome, multiple septal defects, mitral atresia, and moderate RV dysfunction. Ventricular ejection fraction was 36 %

We have studied the effect of right ventricular hypertrophy on the myocardial distribution of ^{201}Tl in a small group of rats maintained in a hypobaric chamber (air at 380 mmHg) for 2 weeks to cause pulmonary arterial hypertension [71]. The hypoxic rats showed significant right ventricular hypertrophy, and the ratio between left ventricle (LV) mass and right ventricle (RV) mass decreased from 4.2 ± 0.2 (SD) in controls to 2.4 ± 0.1 in hypoxic animals. The LV/RV activity ratios in both the hypoxic and control rats were nearly identical to the respective mass ratios ($r = -0.97$). Radiographic and microscopic studies confirmed the changes of pulmonary arterial

Table 7.2 Uses of radionuclide angiography for quantitative assessment of ventricular function

Ventricle morphology	Physiology	Location	Clinical examples
Right	Pulmonary ventricle	Anterior/rightward	Tetralogy of Fallot
			Truncus arteriosus
			Valvar pulmonary stenosis
			Cystic fibrosis
Right	Systemic ventricle	Anterior/rightward	D-TGA
		Posterior/leftward	L-TGA
Left	Systemic ventricle	Posterior/leftward	Kawasaki disease
			s/p chemotherapy
			s/p transplantation
			s/p corrective cardiac surgery
Left	Pulmonary ventricle	Anterior/rightward	L-TGA
Variable	Systemic ventricle	Variable	s/p Fontan surgery

s/p, status post; TGA, transposition of the great arteries

hypertension in the lungs of hypoxic rats. The right ventricle hypertrophied in response to the increased pressure load, whereas the left ventricle remained the same in weight-adjusted comparisons of the two groups [72]. In another study, ^{201}Tl myocardial scintigraphy was performed in patients with congenital heart defects to determine if quantitative right ventricular uptake correlated with the degree of right ventricular hypertrophy and therefore the degrees of right ventricular pressure [73]. A total of 24 patients ranging from 7 months to 30 years were studied; 18 were studied before corrective surgery and six postoperatively. All but three had congenital heart defects that had resulted in pressure or volume overload (or both) of the right ventricle. During routine cardiac catheterization, ^{201}Tl was injected through the venous catheter and myocardial images were recorded in anterior and left anterior oblique projections.

Insignificant right ventricular ^{201}Tl counts were present in six patients, all with a right ventricular peak systolic pressure of less than 30 mmHg. In the remaining 18 patients, there was a good correlation between the right ventricular/left ventricular peak-systolic pressure ratio and the right ventricular/left ventricular ^{201}Tl counts ratio. All patients with right ventricular/left ventricular peak systolic pressure of less than 0.5 mmHg had a right ventricular/left ventricular ^{201}Tl count ratio of less than 0.4. Qualitative evaluation of right ventricular uptake was able to distinguish patients with right ventricular pressure at or above systemic levels. Similarly, SPECT myocardial perfusion imaging with ^{99m}Tc-sestamibi can be used to estimate right ventricular pressure and right ventricular overload in children with congenital heart disease [74]. External quantitation of right myocardial uptake of perfusion tracers could be used as an index of right ventricular mass, and this correlates with increased pressure in the right ventricle, especially in patients with echocardiographic parameters inadequate for estimating right ventricular pressure [73, 75, 76]. Such information may be useful for right-sided obstructive lesions, septal defects altering the pulmonary vasculature, and primary pulmonary disorders such as cystic fibrosis.

Pulmonary Atresia with Intact Ventricular Septum

Pulmonary atresia with intact ventricular septum represents a heterogeneous group of patients with a spectrum of disease ranging from a nearly normal-sized right ventricle and tricuspid valve to an extremely hypoplastic right ventricle and tricuspid valve with coronary sinusoids [77–80]. In many of these patients, the combination of right ventricle to coronary sinusoids and proximal coronary artery stenoses creates a right ventricle-dependent coronary circulation in which a significant portion of coronary blood supply arises from the hypertensive

right ventricle. Decompression of the right ventricle at surgical repair may thus result in significant areas of myocardial ischemia. Myocardial perfusion imaging is helpful for evaluating infarcted areas.

Radionuclide imaging procedures also contribute to the assessment of responses to corrective or palliative surgical interventions in children with congenital cardiac malformations. For example, in children after a Fontan-like operation, diminished function of the single ventricle driving the entire circulation may lower the long-term clinical outcome. Possible reasons for this diminished function include an increased ventricular mass, the morphologic type of the systemic ventricle, and an impairment in coronary blood flow [81]. In a study in 10 adolescents at 5.9 years after a Fontan-like operation, myocardial blood flow measured with ^{13}N-ammonia and PET was found to be increased at rest but significantly diminished during maximum pharmacologic vasodilation [81]. In particular, the hyperemic flows were reduced in systemic ventricles with a right morphology and in individuals with ejection fractions of less than 45 %.

Approaches to Imaging the Myocardium

Imaging of the myocardium can be performed with two modalities, the widely available single photon emission computer tomography (SPECT) and the dual-modality positron emission tomography and computed tomography (PET/CT).

Single Photon Emission Computed Tomography (SPECT)

Myocardial perfusion imaging with SPECT in children can be carried out using one of the following radiotracers: ^{99m}Tc-sestamibi (Cardiolite), ^{99m}Tc-tetrofosmin (Myoview), or ^{201}Tl. In our laboratory, the radiopharmaceutical of choice for myocardial perfusion SPECT is ^{99m}Tc-sestamibi.

Radiopharmaceuticals

Technetium-99m-Sestamibi

Technetium-99m-sestamibi is one of several ^{99m}Tc-labeled radiotracers of myocardial blood flow. It is a cationic complex that accumulates in the myocardium in proportion to regional myocardial blood flow. After intravenous administration, the agent distributes throughout the body and concentrates in several organs including the thyroid, myocardium, kidneys, and striated muscle. The agent clears rapidly from the blood with a fast initial component with a half-time of 4.3 min. There is less, approximately 8 %, of the administered tracer activity in blood by 5 min, and less than 1 % of the tracer is protein-bound in the plasma. The major route of elimination of ^{99m}Tc-sestamibi is the hepatobiliary system. Tracer activity appears within the intestine within the first hour after injection. The cumulative excretion of this agent in 48 h is 27 % of the amount administered in urine and 33 % in the feces. The biologic half-lives of ^{99m}Tc-sestamibi in the myocardium and liver are 6 h and 30 min, respectively. The effective half-lives in the same organs are 3 h and 28 min, respectively. At rest, approximately 1.5 % of the injected dose is taken up in the myocardium where it remains fixed there and shows no significant washout or redistribution over time.

Technetium-99-Tetrofosmin

This agent is taken up in the myocardium to a maximum of 1.2 % of the injected dose at 5 min and 1 % at 2 h, respectively. Activity in the blood, liver, and lung is less than 5 % of the administered activity at 10 min and less than 2 % at 30 min. Tracer activity is eliminated in the urine (approximately 40 %) and in the feces (26 %) within 48 h.

With both ^{99m}Tc-labeled radiotracers, both resting and stress evaluations can be performed; physiologic stress evaluations may be performed in patients old enough to cooperate with exercise testing (usually 7 years or older), whereas the pharmacologic stress can be used in all age groups.

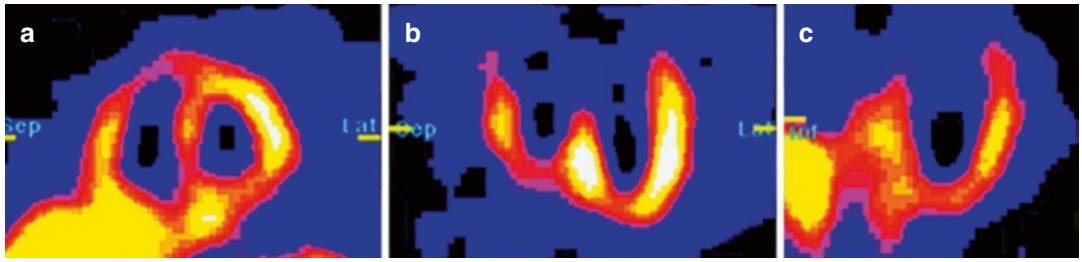

Fig. 7.17 ^{123}I-MIBG SPECT in a 10-year-old boy who was followed for neuroblastoma. (**a**) Short axis, (**b**) transverse long axis, and (**c**) vertical long axis

Thallium-201

Thallium-201 is cyclotron produced; it has a physical half-life of 73 h and decays by electron capture. During its decay, it produces mercury K x-rays of 69–83 keV (98 % abundance) and gamma rays of 135 and 167 keV (10 % abundance) [82]. A minimum dose of 0.150 mCi (5.55 MBq) and a maximum dose of 2.0 mCi (74 MBq) are suggested dose guidelines. See the chapter on Radiation Exposures for absorbed dose estimates.

Thallium-201 is considered a potassium analogue [82, 83]. Clearance of potassium from the myocardium is faster than that of thallium, however [84, 85]. After intravenous injection, the blood disappearance half-time of ^{201}Tl is less than 1 min. The peak myocardial uptake, about 3–4 % of the injected dose, occurs at approximately 10 min. At this time, the distribution of radiothallium in the heart appears to correlate with myocardial perfusion [85]. Thallium-201 is not fixed to the myocardium; it redistributes with time, exercise, drugs, and ischemia.

Neuronal Single Photon Emission Computed Tomography Tracer (^{123}I-MIBG)

Iodine-123-metaiodobenzylguanidine (^{123}I-MIBG) is a norepinephrine analogue (^{123}I has a physical half-life of 13.3 h and decays with the emission of a 159-kEV photon in 85 % abundance.) As such, this agent allows noninvasive assessment of cardiac adrenergic innervation and function. Metaiodobenzylguanidine shares the same uptake and storage mechanisms as norepinephrine. It is actively transported into the presynaptic nerve terminals by the uptake 1 system and it is stored within vesicles [86–93]. Single photon emission computed tomography can be obtained at 2–4 h (or even later) following the intravenous administration of the agent. The images reflect neuronal uptake. There are a number of drugs that interfere with MIBG uptake. MIBG imaging has been used to evaluate patients with cardiomyopathy, chronic heart failure, heart transplantation, and ventricular arrhythmias (Fig. 7.17).

Technique for Myocardial Perfusion Imaging

Usual Administered Doses of ^{99m}Tc-Sestamibi or ^{99m}Tc-Tetrofosmin

The patient should fast for 2 h prior to administration of the tracer. An intravenous needle or a short catheter is placed and secured to the skin with tape, and the line is kept open with normal saline. The intravenous line is kept in place so it can be used to inject the tracer during exercise studies. Because ^{99m}Tc-sestamibi has no significant redistribution over a 4- to 6-h period, two injections of the radiopharmaceutical are necessary to obtain resting and peak exercise during myocardial perfusion imaging [94, 95].

Single SPECT Perfusion Imaging

For a single study (rest or exercise) done alone, a dose of 0.25 mCi (9.25 MBq)/kg is used with a minimum total dose of 2 mCi (74 MBq) and a maximum dose of 10 mCi (370 MBq). If rest and exercise studies are done on separate days, the same dose of ^{99m}Tc-sestamibi can be used. In a two day protocol, it is recommended to perform

the stress test first. If the stress test is normal, there is no need to perform the resting test. In this way, radiation exposure is limited to one study and the total radiation exposure will therefore be lower than with two tests.

Rest and Exercise ^{99m}Tc-Sestamibi SPECT Studies (Same-Day Protocol)

For rest and exercise studies performed on the same day, the following dose schedule is suggested:

Rest: ^{99m}Tc-sestamibi SPECT study: 0.15 mCi (5.55 MBq)/kg, with a minimum dose of 2.0 mCi (74 MBq) and a maximum dose of 10 mCi (370 MBq).

Exercise: ^{99m}Tc-sestamibi SPECT study: At 2–4 h after the rest study, the exercise study is performed using a dose of 0.35 mCi (12.95 MBq)/kg, with a minimum dose of 4 mCi (148 MBq) and a maximum dose of 20 mCi (740 MBq), given at peak exercise. After this injection, the child is encouraged to run for an additional 30–60 s.

Patient Preparation and Procedure

The patient should fast for 4 h prior to rest and stress studies. Depending on local policies, female adolescents given a relatively high dose of tracer should undergo a pregnancy test before proceeding. An intravenous needle or short catheter is inserted and secured to the skin. A slow intravenous drip of saline runs throughout the procedure in order to maintain a viable IV line. Non-attenuating electrocardiographic electrodes are placed on the patient, two on either side of the chest superiorly and another over the left ribcage. Radiopaque objects in the area of the thorax should be removed before imaging; implanted radiopaque objects (metal, silicone, etc.) should be noted as potential attenuators of cardiac activity.

Most acquisition protocols for pediatric myocardial perfusion SPECT utilize a gamma camera with two detectors positioned at 90° from each other imaging the cardiac region for 180° for better spatial resolution, higher contrast, and less attenuation than a 360° acquisition. Either a high-resolution collimator or an ultra-high-resolution collimator set is used, and the images are recorded in a 128×128 matrix format. Either a step-and-shoot acquisition with 32 or 64 stops separated by 3° or continuous acquisition may be used. Typically each image is recorded for 25 s. Electrocardiogram electrodes are placed on the patient so that the study is triggered by the ECG signal. Typically 200–300 heartbeats are recorded and the study is completed in 20–30 min. For both the rest and the stress studies, imaging begins at 15–30 min post-tracer administration. The patient is placed in the supine position on the SPECT table with his or her left arm over the head. After the rest study is completed, the patient is taken to the stress laboratory. The radiopharmaceutical is prepared in the appropriate dose in advance and is taken with the patient to the exercise laboratory. The exercise test (treadmill or bicycle) is obtained under the supervision of a cardiologist. The tracer is injected at peak exercise or at the point where the patient states he/she is about to stop or has chest pain.

New Dedicated Detector Systems

The developments of novel dedicated detector systems are revolutionizing the acquisition and analysis of ECG-gated myocardial perfusion SPECT. These systems include the use of new detector technology including the use of materials such as CsI(Tl), CZT, and NaI(Tl) crystals. System's designs include triple planar detectors, detectors arranged in an arc design, vertical detector columns placed at 90°, multiple pinhole collimator, and astigmatic collimators.

Advanced reconstruction methods include ordered subset expectation maximization (OSEM) 3D with resolution recovery. Image quality and spatial resolution are improved. With the increased sensitivity, these systems allow imaging times that are reduced to 2–5 min from the traditional 15–30 min per study. In addition, patient comfort is improved and motion artifacts are reduced. These developments promise improved imaging protocols with improved patient comfort, higher patient throughput, and reduced radiation exposure [96, 97].

Positron Emission Tomography (PET)

Stand-alone PET systems have now been largely replaced by hybrid PET/CT imaging systems so that PET/CT imaging is the current standard.

Radiopharmaceuticals

Rubidium-82, ^{13}N-ammonia, and ^{15}O-water can be used for evaluating myocardial perfusion with PET and for measurements of myocardial blood flow.

Rubidium-82

Rubidium-82 is a generator-produced radionuclide with a half-life of 75 s. The parent radioisotope is ^{82}Sr with a physical half-life of 25.5 days. The generator eluant is injected intravenously into the patient as a 10–20 s bolus. Rubidium-82 is extracted rapidly in the myocardium; the radiotracer extraction fraction depends inversely on flow so that the myocardial radiotracer myocardial net uptake increases with higher flows in a curvilinear fashion. The short half-life of ^{82}Rb permits studies to be performed in rapid succession. The ^{82}Rb generator system can be used for approximately 1 month.

Nitrogen-13 Ammonia

Nitrogen-13 and ^{15}O require a medical cyclotron in proximity to a PET/CT scanner. Nitrogen-13 has a physical half-life of 10 min; in the form of ^{13}N-ammonia, it is rapidly extracted by the myocardium. It is trapped primarily by the glutamic-acid-glutamine reaction and accumulates in the myocardium in proportion to blood flow, though not in a linear but in a curvilinear relationship where increases of coronary flow are associated with progressively smaller increases in radiotracer uptake [98].

Oxygen-15 Water

Oxygen-15 has a physical half-life of 2 min, and as ^{15}O-water, it is taken up by the myocardium with an extraction fraction of almost 100 %. However, intravenously injected ^{15}O-H_2O also resides within the blood pool, and special processing techniques are needed to outline the myocardial image separate from the blood pool.

Quantification of regional myocardial blood flow has become available in the clinical setting. Such quantification requires serial image acquisition beginning immediately prior to injection of the radiotracer and continues for about 15–20 min and for 8–10 min for ^{13}N-ammonia and ^{82}Rb, respectively. Software routines are available for extracting time-activity curves from the serially acquired images and for computing estimates of myocardial blood flow in ml/min/g.

Fluorine-18-Labeled Myocardial Perfusion Agents

Several ^{18}F-labeled PET myocardial perfusion agents are currently under investigation. These include rhodamines, fluorobenzyl triphenyl phosphonium, flurpiridaz, and others [99–104]. Potential advantages of these radiotracers include the short physical half-life of the tracer, the higher spatial resolution, the easy availability, and the potential for quantitation of myocardial blood flow.

Perfusion Imaging

Dose Schedules for Myocardial Perfusion Tracers for PET

Nitrogen-13 Ammonia

The standard dose is 0.3 mCi/kg (11.1 MBq/kg) with a maximum dose of 30 mCi (1,110 MBq). Allowing 20 min to 25 min from the end of the first to the beginning of the repeat study (about 5 half-times between radiotracer administrations with more than 95 % of the radioactivity decayed), the same dose of ^{13}N-ammonia is administered for the stress study.

Rubidium-82

The standard dose is approximately 0.71 mCi/kg (27 MBq/kg) with a maximum dose of 60 mCi (2,200 MBq). The time interval between studies is shorter than for ^{13}N-ammonia because of the ultrashort 75-s physical half-time.

Imaging of perfusion at rest delineates abnormalities in regional myocardial blood flow

caused by an obstruction or severe constriction of a coronary vessel or due to scar tissue. When combined with stress perfusion imaging, it aids in the detection of anomalous coronary vessels, of inflammatory alterations of the coronary vessels, and of obstructive coronary lesions as, for example, associated with congenital abnormalities or after surgical reimplantation of arterial vessels.

Stress-rest perfusion imaging with PET is performed analogous to that with SPECT but distinct differences exist: First, the short physical half-time of PET perfusion tracers as, for example, 10 min for ^{13}N-ammonia and 75 s for ^{82}Rb allows repeat imaging at only 20–40 min intervals. Hence, no dose adjustments are needed for repeat studies as is done with SPECT perfusion imaging. The same dose of radiotracer activity is given for the second imaging study. Second, treadmill or bicycle exercise can be employed as stress. However, the short physical half-life of the PET perfusion radiotracers poses formidable logistic challenges so that pharmacologic vasodilation has become the widely accepted form of stress.

Patient Preparation and Procedures

Patient preparation for myocardial perfusion imaging with PET largely follows that for SPECT perfusion imaging. Patients should fast for 4–6 h prior to study and refrain from caffeine- and theophylline-containing beverages or medications as they may attenuate or abolish the hyperemic response to vasodilator agents. Female patients, if appropriate, might undergo pregnancy testing in view of the radiation exposure due to the radiotracer and computed tomographic imaging. An intravenous line is inserted and secured for administration of the radiotracer and the vasodilator stress agent. A manometer cuff is attached to the opposite arm for monitoring arterial blood pressure during the vasodilator stress. Electrocardiographic leads are attached, two on either side of the chest and a third one to the left lower rib cage.

The patient is placed supine on the imaging table with both arms extended and resting comfortably on a pillow or arm support above the head. Prior to the study, a test run of the imaging table with the patient through the imaging gantry should be done in order to assure free access to the intravenous line and to ascertain that infusion lines, electrode wires, and blood pressure lines do not become entangled between the imaging table and imaging gantry. Wrapping the patient's torso with sheets on the imaging table aids in reducing patient motion during the image acquisition.

Sedation of infants for the imaging study should be considered to ensure adequate image quality but usually is not needed in children 10 years or older. For adequate positioning of the heart in the imaging field, a low dose computed tomographic topogram is recorded during free breathing.

State-of-the-art positron emission tomographic imaging systems acquire image data in list mode, where each emission event together with its precise timing and position is recorded sequentially, together with a physiologic signal like the electrocardiogram or respiratory motion. Compared to the standard frame acquisition, list mode acquisition offers several advantages: The image data can be re-sorted into static image frames for assessing the relative radiotracer distribution throughout the myocardium, into a set of image frames throughout the cardiac cycle for evaluating regional wall motion and left ventricular volumes, or into a sequence of 5- to 10-s frames during the initial 2–3 min post injection, which like radionuclide angiocardiogram depicts the initial transit of the radiotracer bolus through the central circulation and its uptake in the myocardium. From these "dynamic image sets," time-activity curves for the left ventricular myocardium and the left ventricular blood pool are generated, and myocardial blood flow is obtained in ml/min/g.

For standard clinical assessment of the myocardial distribution of blood flow, list mode image data acquisition usually begins at 3 min after tracer administration and continues for 11 min. For ^{82}Rb, image acquisition begins at 90 s after the radiotracer injection and continues for 6–7 min. For the assessment of ventricular

volumes and wall motion, the list mode data are rebinned into 8 frames per cardiac cycle. Quantification of myocardial blood flow requires the image acquisition to start immediately before the radiotracer injection so that the initial radiotracer kinetics including the arterial input function and its rate of accumulation in the myocardium are captured.

An important aspect of the reconstruction of the image data and the correction for photon attenuation is the adequate co-registration of the CT attenuation and the PET images. In order to ascertain adequate alignment or to correct for possible patient motion between the CT and PET images, a "scout PET image" is reconstructed and its position compared against the CT images. If necessary, the CT images can be realigned with the PET images followed by reconstruction and attenuation correction of the PET images.

Technical Aspects of Pharmacologic Vasodilator Stress

For maximum coronary vasodilation and stimulation of hyperemic flows, dipyridamole, adenosine, and selective A_{2A} adenosine receptor agonists are available.

Dipyridamole at dose of 0.56 mg/kg is infused intravenously over a 4-min period. Maximum hyperemic flows are reached at 4 min after the end of the dipyridamole infusion, at which time the flow tracer is given intravenously.

Adenosine is infused intravenously at a rate of 0.14 mg/kg/min for a 6-min period. Coronary flow promptly increases within the first minute of vasodilator administration. Three minutes into the adenosine infusion, the flow tracer is administered while the adenosine infusion continues for another 3 min in order to fully maintain hyperemic blood flows.

Regadenoson (Lexiscan, Gilead Sciences, Inc.), a selective A_{2A} adenosine receptor agonist, is administered at a dose of 0.4 mg (diluted in a 5 ml solution) over 10–20 s, followed by a 5 ml saline flush. The hyperemic flow response peaks within the first minute, at which time the radiotracer is administered.

Imaging Metabolism with Positron Emission Tomography

Imaging myocardial glucose metabolism with FDG requires additional patient preparation in order to optimize the radiotracer uptake in the myocardium. Patients should fast for 6 h prior to the study. After determining the blood glucose level, dextrose is given orally or, if indicated, intravenously in order to stimulate insulin secretion and to suppress circulating free fatty acid levels. Our own approach is to administer 0.3 g/kg intravenously 1 h before the FDG injection, whereas, in another laboratory, infants and children less than 10 years of age are given 2 g of glucose orally followed by continuous IV infusion of 10 % dextrose in water at a rate of 4 ml/kg/min [9, 105]. In children older than 10 years of age, 10 % dextrose in water is infused at a rate of 1.3 ml/kg/h. FDG is administered intravenously 1 h later and acquisition of 15-min images commences at 60 min. For imaging the FDG uptake in the great arteries as, for example, in instances of suspected vascular inflammation, the time from radiotracer administration to the start of imaging is at least 90 min or even as long as 3 h in order to maximally reduce background activity.

FDG is a glucose analogue. Fluorine-18 has a physical half-life of 111 min. The radiotracer competes with glucose for hexokinase-mediated phosphorylation. Because FDG-6-phosphate is a poor substrate for glycolysis and glycogen synthesis, it becomes trapped in the myocardium. Its accumulation in the myocardium as depicted on the PET images corresponds to the rate of glucose utilization. In pediatric patients, FDG is used for the assessment of myocardial viability and for the detection of inflammatory vascular disease. Increased FDG uptake relative to blood flow in dysfunctional myocardial regions identifies the myocardium as viable, i.e., wall motion can potentially recover upon restoration of myocardial blood flow (see also Fig. 7.6). Conversely, proportional decreases in glucose uptake and in blood flow identify the myocardium as scarred.

Dose Schedules for Metabolic Imaging with FDG and PET

Imaging of the myocardial glucose utilization with FDG can detect regional metabolic abnormalities as, for example, associated with certain types of cardiomyopathies (i.e., Duchenne or Becker muscular dystrophy) or with myocardial viability as a potentially reversible form of contractile dysfunction that is associated with a regional increase in FDG uptake relative to blood flow. PET imaging with FDG also aids in identifying inflammatory disorders of the great vessels as for example in Takayasu disease.

FDG is administered at a dose of 0.14 mCi/kg (5.3 MBq/kg) with a minimum dose of 1–2 mCi (37–74 MBq).

Current Developments in Positron Emission Tomographic Imaging

PET/MRI hybrid imaging devices have now become available. Some of these devices entail separate PET and MR components, while others are fully integrated PET/MRI systems that enable simultaneous dual-modality imaging. Although the clinical role of these dual-modality devices remains to be established, it is clear that they offer advantages in cardiac imaging of pediatric patients. Besides assessment of the cardiac anatomy and contractile function, regional myocardial blood flows and metabolism can be evaluated at the same time. Moreover, use of the PET/MRI instead of PET/CT will reduce the radiation burden to children.

Assessment of Ventricular Function

Clinical Applications

Several nuclear medicine methods for the assessment of ventricular function in children are available. These include electrocardiogram (ECG)-gated myocardial perfusion SPECT (Fig. 7.18), gated metabolic PET (^{18}F-FDG), gated blood pool scintigraphy, and first-pass radionuclide angiography. Radionuclide assessments of ventricular function include right and left ejection fractions, detection of wall motion abnormalities, ventricular volume, cardiac output, and regurgitant fraction. Clinical applications of radionuclide studies to assess ventricular function have been applied to Kawasaki disease, anomalous origin of the coronary artery, cardiomyopathies, cardiac transplants, atrial and ventricular septal defects, cystic fibrosis, cardiac tumors, and certain congenital heart diseases, before and after catheter intervention or corrective surgery.

Gated Blood Pool

Gated blood pool scintigraphy is a means of imaging the cardiac blood pool by synchronizing the recording of scintillation data with the ECG [106, 107]. This technique permits repetitive sampling of the cardiac cycle from many cycles until an image of appropriate count density is recorded. Certain conditions must be met for the gated scan to be performed adequately: regular heart rate and rhythm, limited beat-to-beat variability during the study, no patient motion, minimal diaphragmatic motion, largely intravascular location of the tracer, and sufficient count density (Fig. 7.19).

Gated cardiac studies permit an evaluation of both global and regional ventricular function. Generally, no patient preparation is needed for this study, but patients under 3 years of age may require sedation in order to keep them still for the 20–30 min required for the recording.

In Vitro Labeling of Red Blood Cells

A 1- to 3-mL sample of the patient's blood is obtained and treated with heparin or acid-citrate-dextrose (ACD). Ethylenediaminetetraacetic acid (EDTA) or oxalate should not be used as an anticoagulant. The red blood cells (RBCs) are labeled with ^{99m}Tc using a commercial preparation (Ultratag RBC, Mallinckrodt, St. Louis, MO). The labeled RBCs are reinjected slowly into the patient. *Caution*: *The labeled blood cells must be reinjected only into the patient from whom the blood was drawn*. Technetium-99m-

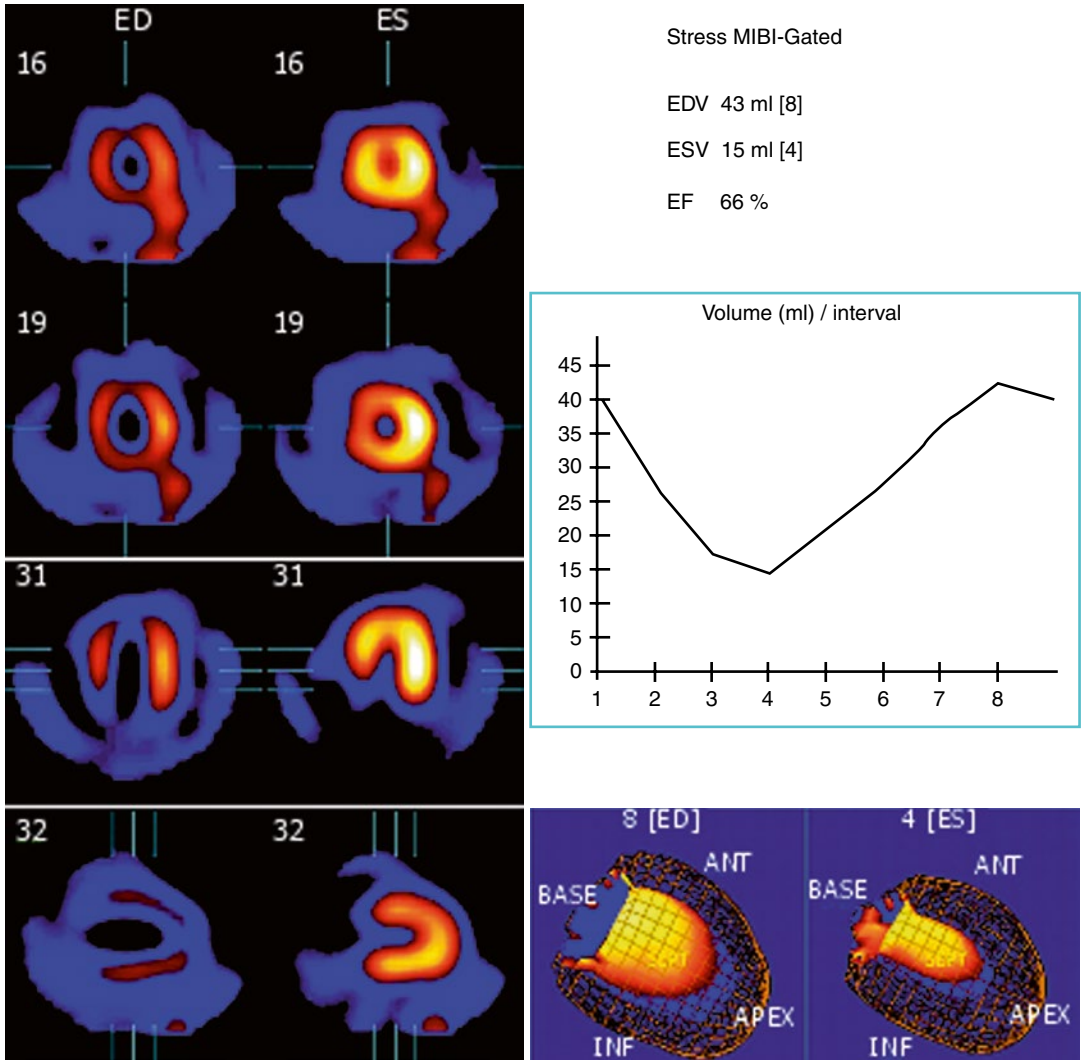

Fig. 7.18 Gated myocardial perfusion SPECT. Selected end-diastolic and end-systolic slices in the short axis and horizontal and vertical long axes are shown. Ventricular time-activity curve of a cardiac cycle is represented in the right upper quadrant

labeled RBCs are used in a dose of 0.2 mCi (8.4 MBq)/kg, with a minimum dose of 2.0 mCi (74 MBq) and a maximum of 20 mCi (740 MBq).

Technique for Gated Blood Pool Imaging

The patient is usually studied in the supine position. Sitting or upright positions are also possible. An intravenous needle (butterfly type, 23 or 25 gauge) or a short IV catheter is inserted and used to obtain blood for radiopharmaceutical labeling and re-injection. Once one is certain that the needle/catheter is properly placed and that there is no possibility of extravasation, it should be secured with tape to the patient's skin. The patient's arm should be free of any object that could interfere with venous return. Venous access is kept patent with normal saline while the patient is being readied for the angiogram. EEG electrodes are placed on both shoulders and on the patient's right costal margin. After intravenous injection of the ^{99m}Tc-RBCs, recording proceeds almost immediately. The gamma camera is usually equipped with a high-resolution parallel-hole

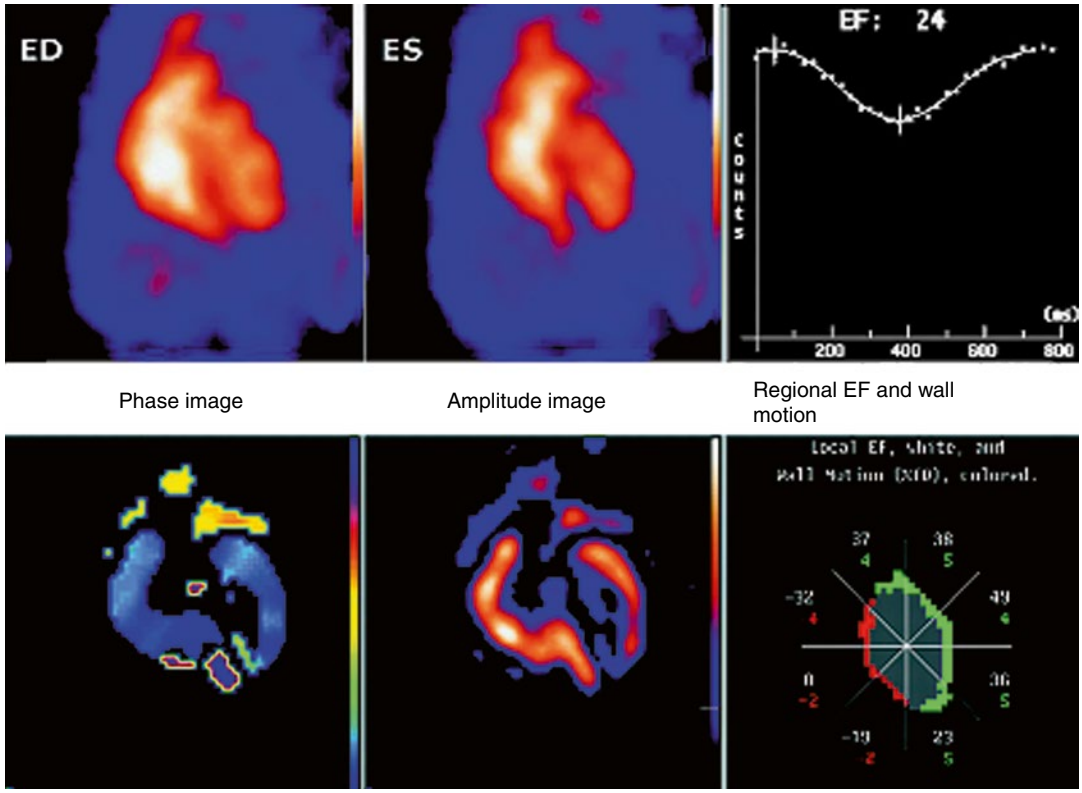

Fig. 7.19 Gated blood pool scan showing end-diastolic (*ED*) and end-systolic (*ES*) frames and a ventricular time-activity curve of an average cardiac cycle. The ejection fraction is 24 %. On the bottom of the image, a phase image, an amplitude image, and an image of regional ejection fraction are shown

collimator in the left anterior oblique projection in order to obtain maximal separation between the right and the left sides of the heart and tilted caudally so there is a separation between the aria and the ventricles. If available, a 30° slanted parallel-hole collimator positioned on contact with the patient's chest on a left anterior oblique projection and tilted caudally is preferred. Adjustments for abnormal cardiac positions may be necessary. Typically, recording consists of 32 frames per heartbeat on a 128 × 128 matrix for an appropriate amount of counts.

Data Recording

Data recording programs allow tailoring studies to each individual patient. The recording rate should be adjusted depending on the patient's heart rate. If aberrant beats occur frequently (more than 10 % of the beats) or if other arrhythmias are present (e.g., atrial fibrillation), this method may not be effective. Alternatively, it is possible to record all scintigraphic events and the electrocardiogram in list mode and then evaluate various R-R intervals after the study is recorded. The end of the study can be determined by a preset number of cardiac cycles or a preset amount of time.

Analysis

Before analyzing the gated study, it is important to assess its technical adequacy. The following items should be evaluated: adequate tracer labeling, patient motion, positioning, sharpness of the image, and adequate gating.

The study is viewed to assess global cardiac function and chamber sizes and to detect abnormal wall motion. Analysis of the study can be performed manually or by several commercially available automated methods. Time-activity curves of ventricular activity are calculated. Maps of regional ejection fraction and stroke volume are also displayed for analysis.

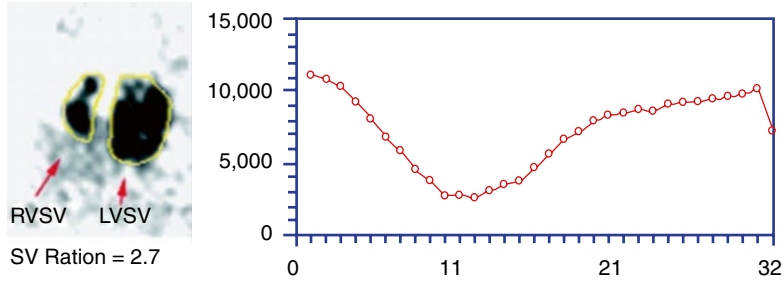

Fig. 7.20 Regurgitant fraction estimated by gated blood pool scanning. The stroke volume ratio (SV ratio) is 2.7

There are two parts to the analysis of gated scans: visual evaluation of the study on a series of images or on a movie mode display of the heart cycle and measurement of ventricular function and volumes. Ventricular volume changes can be quantitated by analyzing time-activity curves from regions of interest (ROIs) over the ventricles. Global ventricular ejection fraction, ejection rate, filling rates, and ventricular volumes can be estimated.

Valvular Regurgitation

This technique is useful for quantitating mitral valve or aortic valve regurgitation, both prospectively following the natural history and assessing the results of surgical or catheter interventions. In gated blood pool studies, a ratio of the change in count rates in the left ventricle between end diastole and end systole divided by the change in count rates in the right ventricle between end systole and end diastole (regurgitation volume index, stroke-volume ratio) provides a simple and unique way to quantitate left-sided valvular regurgitation [108–113]. Rigo et al. developed the method based on cardiac blood pool scintigraphy [111]. In the left anterior oblique projection, this study permits simultaneous assessment of the left and right ventricles. The mean left ventricular/right ventricular stroke ratio (LV/RV) in normal patients is 1.19. In patients with aortic or mitral regurgitation, this ratio is elevated. These authors found good agreement between the LV/RV stroke volume ratio and angiographic grading of valvular regurgitation. The technique is simple and does not require elaborate data processing.

Hurwitz et al., in our laboratory, evaluated this method to quantitate aortic or mitral regurgitation in children and young adults at rest and during isometric exercise [114]. There was good correlation with cineangiographic results in 47 of 48 patients. The stroke volume ratio was used to classify severity. The group with equivocal regurgitation differed from the group with mild regurgitation ($p<.02$); patients with mild regurgitation differed from those with moderate regurgitation ($p<.001$); and those with moderate regurgitation differed from those with severe regurgitation ($p<.01$). The stroke volume ratio was responsive to isometric exercise, remaining constant or increasing in 16 of 18 patients. After corrective surgery in seven patients, the stroke volume ratio significantly decreased from preoperative measurements in all patients. As in adult patients, the stroke volume ratio in normals varied between 1.0 and 1.3. This study suggested that a stroke volume ratio of more than 2.0 is compatible with moderate to severe regurgitation and that a ratio greater than 3.0 indicates severe regurgitation (Fig. 7.20).

Diagnosis and Quantitation of Left-to-Right Shunts and Ventricular Function with First-Pass Radionuclide Angiocardiography

Clinical Applications

First-pass radionuclide angiocardiography (Fig. 7.21) is a rapid, accurate, and noninvasive method that is useful in the diagnosis and measurement of left-to-right shunts in certain congenital lesions (Table 7.3). This method is useful for assessing the magnitude of the shunt in

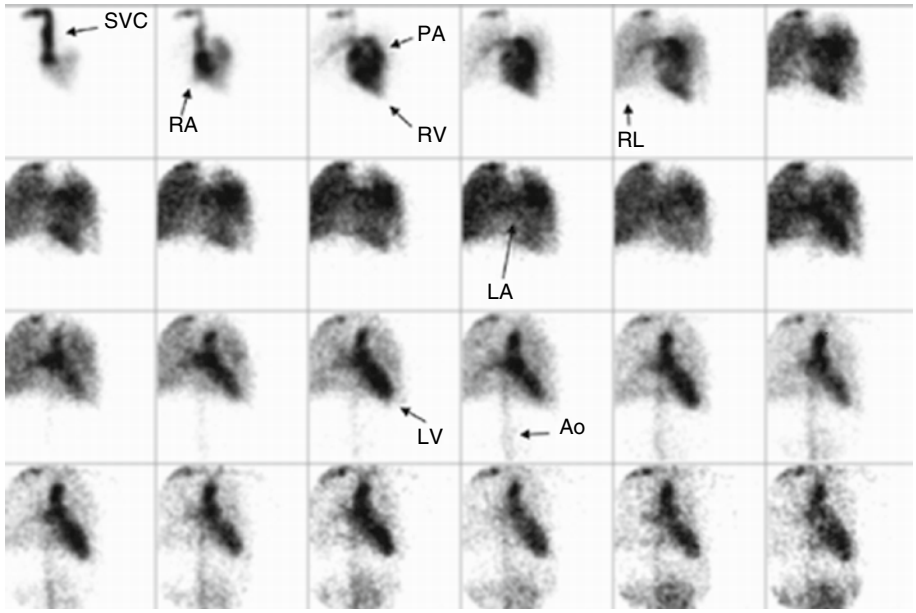

Fig. 7.21 Normal radionuclide angiocardiogram. Tracer circulates in the superior vena cava (*SVC*), right atrium (*RA*), right ventricle (*RV*), pulmonary artery (*PA*), right lung (*RL*), left atrium (*LA*), left ventricle (*LV*), and aorta (*Ao*)

Table 7.3 Indications for first-pass radionuclide angiocardiography in children

Atrial septal defect
Ventricular septal defect
Truncus arteriosus
Patent ductus arteriosus
Complete atrioventricular canal
Aortopulmonary collaterals

patients before and after repair. Determination of ventricular function with first-pass radionuclide angiocardiography is also possible in patients with most of the indications described earlier (see section "Assessment of Ventricular Function").

Detection and Quantitation of Left-to-Right Shunts

Radiopharmaceuticals

Technetium-99m as pertechnetate is the most commonly used radiopharmaceutical for first-pass radionuclide angiocardiography. Other radiopharmaceuticals labeled with ^{99m}Tc can be used so long as they remain largely within the blood during the time required for the angiocardiogram [e.g., ^{99m}Tc-methylene diphosphonate (^{99m}Tc-MDP), ^{99m}Tc-diethylenetriamine pentaacetic acid (^{99m}Tc-DTPA), and ^{99m}Tc-disodium [*N*-[*N*-*N*-(mercaptoacetyl) glycyl]-glycinato(2-)-N,N′,N″,S]oxotechnetate (2-) (^{99m}Tc-MAG3)]. Clearly agents such as ^{99m}Tc-macroaggregated albumin (^{99m}Tc-MAA) are not adequate for this purpose. Radiopharmaceuticals with rapid blood disappearance rate (^{99m}Tc-MAG3 or ^{99m}Tc-DTPA) enable repeated angiocardiograms with lower residual background than pertechnetate.

When using ^{99m}Tc-pertechnetate, the patient should be premedicated with sodium (intravenous) or potassium (oral) perchlorate to reduce thyroid uptake of the tracer. When other ^{99m}Tc-labeled radiopharmaceuticals are used, perchlorate premedication is not necessary. Recommended administered dose of ^{99m}Tc is 0.2 mCi (7.4 MBq)/kg, with a minimum total dose of 2 mCi (74 MBq) and a maximum of 20 mCi (740 MBq). The total volume of radiopharmaceutical should be less than 0.2 mL so that a small rapid bolus can be administered.

Imaging Technique

In expert hands the majority of patients do not need sedation for this short procedure. If sedation is needed, it should be prescribed for each patient individually. Prior to positioning the patient under the gamma camera for the angiocardiogram, an intravenous needle (butterfly type, 23–25 gauge) or a short IV catheter is inserted. Once one is assured that the needle/catheter is properly placed and that there is no possibility of extravasation, it should be secured with tape to the patient's skin. If possible, an antecubital vein is selected for the injection. In instances when the bolus of tracer is fragmented, the application of deconvolution analysis ensures a high percentage of successful studies.

The patient is placed supine on the imaging table. The gamma camera, equipped with a parallel-hole, high-sensitivity collimator, is positioned anteriorly over the patient's chest. The field of view should extend from the suprasternal notch to just below the xiphoid and should cover both pulmonary fields.

Data Recording

Radionuclide angiocardiography for the assessment of left-to-right shunting is recorded at two or four frames per second for 25 s on a 128×128 matrix. Alternatively, a list mode acquisition is used.

Injection Technique

For the evaluation of left-to-right shunts, the technique of injection is of utmost importance in order to obtain a good-quality angiogram with high temporal resolution. Qualitative and quantitative analyses of radionuclide angiocardiography are best done when the radiotracer is delivered as a single, small, rapid intravenous bolus injection, a point that cannot be overemphasized. The volume of saline flush varies from approximately 0.5 mL in infants to 15.0 mL in young adults. Before the tracer is injected, a trial flush with saline alone should be made to ensure against the possibility of accidental tracer extravasation. If there is no free flow into the vein or there are any doubts about the adequacy of venous access, the tracer must not be injected and another site for the injection should be selected. The tracer should not be injected while the patient is crying or producing Valsalva maneuvers. Increased or widely variable changes of intrathoracic changes will most likely cause bolus fragmentation and render the study inadequate. Injecting the tracer with the saline simultaneously allows rapid, uniform delivery of the tracer with uninterrupted saline flushing. The injection should be given in one continuous motion, and recording should begin simultaneously with tracer injection.

Quality Control

Without moving the patient, the angiocardiogram is reviewed on a cine display. Then a small ROI is placed over the superior vena cava, and a time-activity curve is generated. This curve serves to determine the adequacy of the bolus. Acceptable bolus injections reveal a single peak with an FWHM (full width at half maximum) of less than 3 s. As mentioned, some fragmented boluses can be corrected by deconvolution analysis. If the study still appears inadequate for analysis, a second study may be performed using approximately twice the amount of the initial dose. Recording for the second angiogram is begun 3–5 s after the injection to allow background correction. If both injections fail, the study should be rescheduled for another day.

Analysis

ROIs are marked over the lung fields. These regions should be placed carefully so they do not overlap the heart and great vessels. A series of images at 0.5–1.0 frames per second should be displayed. Superior vena cava time-activity curves are used to select the input for deconvolution analysis. Pulmonary time-activity curves are used for left-to-right detection and quantitation.

In a normal radionuclide angiocardiogram, tracer is seen as it circulates sequentially through the superior vena cava, right atrium, right ventricle, pulmonary artery, lungs, left atrium, left ventricle, and aorta. The left ventricle and the aorta are clearly visualized with only minimal pulmonary activity. The relative sizes of the heart chambers can be appreciated on the angiocardiogram (Fig. 7.21). A normal pulmonary time-activity curve is characteristic. Following an

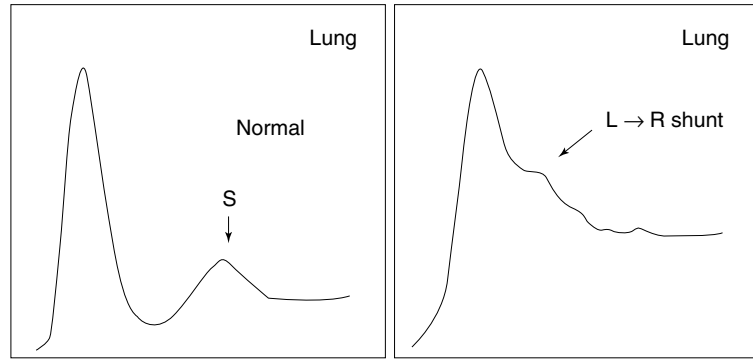

Fig. 7.22 Pulmonary time-activity curves. *Left* normal, *S* systemic peak, *Right* left-to-right shunt

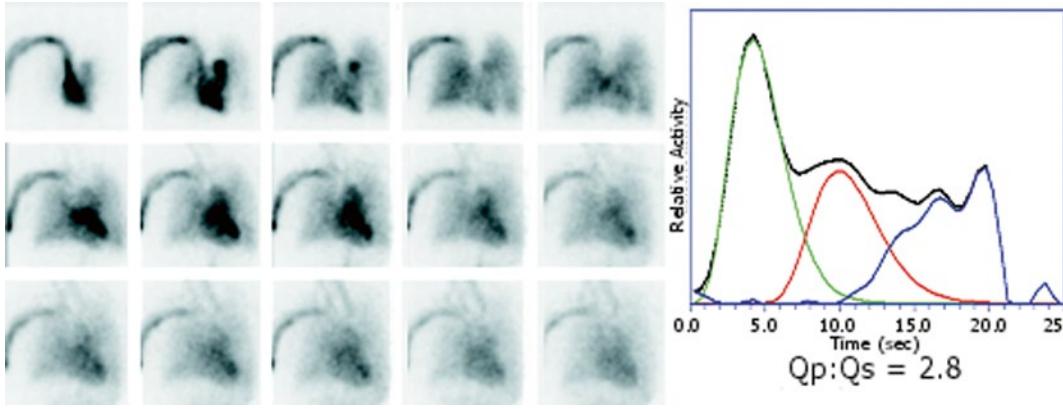

Fig. 7.23 Left-to-right shunt. Radionuclide angiocardiogram from a patient with a moderate left-to-right shunt (Q_p:Q_s = 2.8). The angiocardiogram reveals premature pulmonary recirculation

initial almost flat segment, the curve rapidly rises to a single peak and descends less rapidly to a "valley," almost reaching the baseline. This first peak represents the initial passage of the bolus through the pulmonary circulation and is followed by a second peak of less amplitude and broader than the first one. The second peak represents the portion of the initial bolus returning to the lungs after it circulates through the systemic circuit (Fig. 7.22).

With left-to-right shunting, the radionuclide angiocardiogram reveals a persistence of tracer activity in the lungs caused by premature pulmonary recirculation of the tracer through the intracardiac shunt (Figs. 7.23 and 7.24). The amount of persistent tracer activity in the lungs is directly related to the magnitude of shunt flow. In addition, in moderate to severe left-to-right shunting, the left side of the heart and the aorta are not well visualized on the angiogram. These two radionuclide angiocardiographic

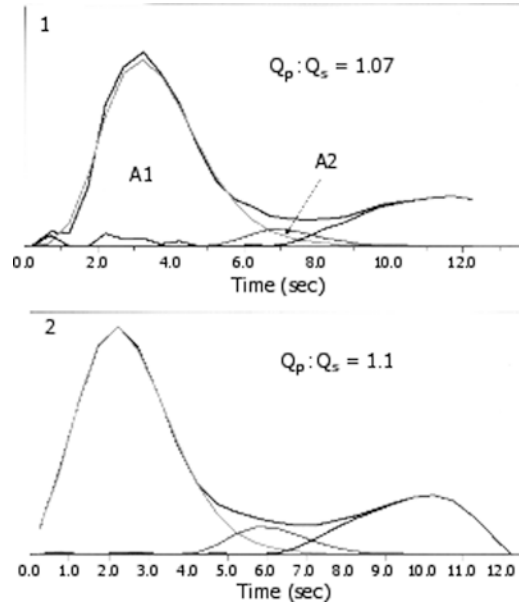

Fig. 7.24 Pulmonary time-activity curves for two patients without intracardiac shunting

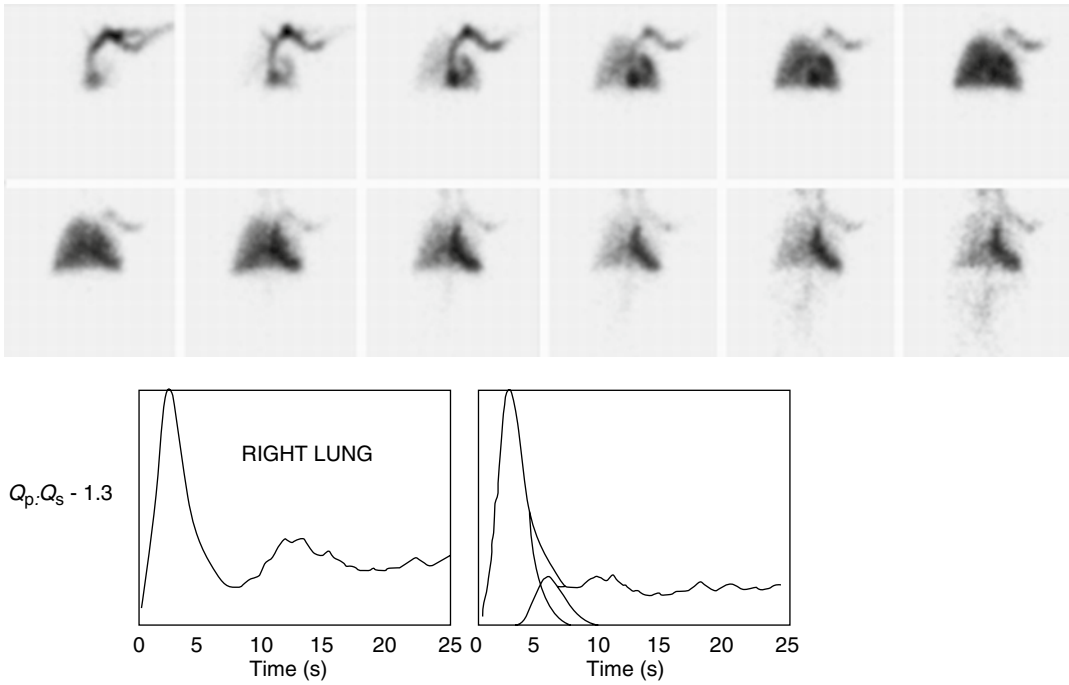

Fig. 7.25 Small left-to-right shunt. The radionuclide angiocardiogram reveals a small amount of early pulmonary recirculation accompanied by a rather clear visualization of the left side of the heart and the aorta. This is consistent with a small left-to-right shunt (Q_p:Q_s = 1.3)

features—persistent pulmonary tracer activity and poor visualization of the left side of the heart and aorta—are diagnostic for left-to-right shunting. The pulmonary time-activity curve in left-to-right shunting characteristically reveals an early secondary peak that interrupts the initial downslope of the curve. This premature secondary peak is due to premature reentry of tracer into the pulmonary circulation through the left-to-right shunt and is diagnostic. The pulmonary time-activity curve can be used to calculate the pulmonary-to-systemic flow ratio (Qp/Qs) (Figs. 7.25 and 7.26).

Assessment of Right and Left Ventricular Ejection Fraction

For determination of right and left ventricular ejection fraction, radionuclide angiocardiography should be recorded at a minimum recording rate of 25 frames per second. The study is recorded for 25 s on a 128 × 128 matrix. Alternatively, the study can be recorded on a list mode. For assessment of ventricular ejection fraction, the radionuclide angiocardiogram should be first evaluated on a cinematic mode. This provides an overall view of the study. Regions of interest are drawn over the left and right ventricles, and time-activity curves are calculated (see below). These curves are used to identify the frames in the study corresponding to end diastole and end systole. An adaptive low-pass filter is applied to eliminate high-frequency noise. Consecutive end-diastolic and end-systolic frames are selected over several cardiac cycles during the first pass of radionuclide through the right and left ventricles. Composite images of each ventricle at end diastole and end systole are formed by adding the selected frames. Subtracting the end-systolic image from the end-diastolic image results in a "stroke volume" image, which is useful for identifying the atrioventricular plane. Regions of interest are then marked over the summed right and left diastolic and systolic frames.

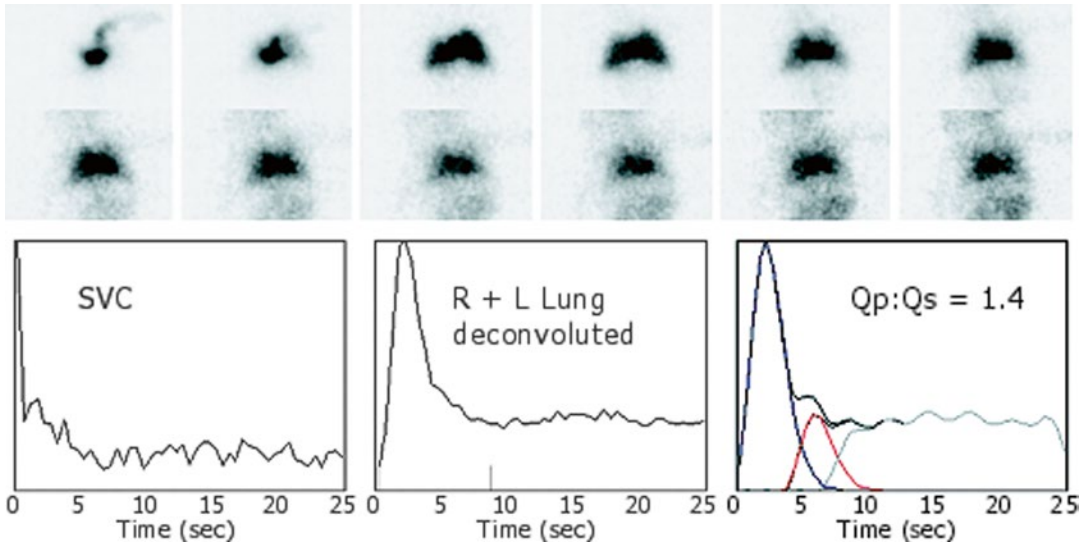

Fig. 7.26 Radionuclide angiocardiogram from a 4-month-old girl after repair of tetralogy of Fallot 8 weeks prior to this examination. *SVC* superior vena cava

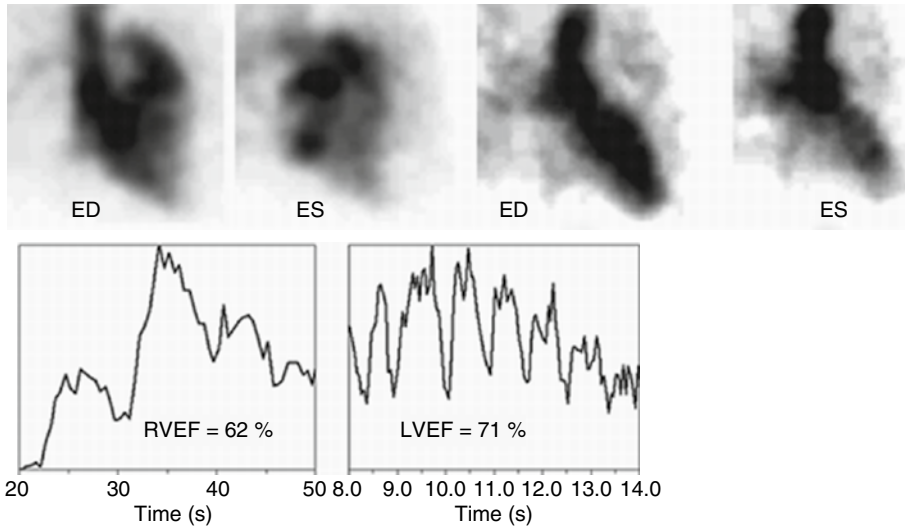

Fig. 7.27 Determination of right and left ventricular ejection fractions (*RVEF*, *LVEF*) by first-pass radionuclide angiocardiography. *Upper left*: right ventricle. *ED* end-diastolic image, *ES* end-systolic image. *Upper right*: left ventricle. *Lower quadrants*: right and left ventricular time-activity curves

Ejection fractions are calculated by the formula

$$EF = \frac{EDC - ESC}{EDC},$$

where *EF* is the right (RV) or left (LV) ventricular ejection fraction, *EDC* is the end-diastolic counts, and *ESC* is the end-systolic counts. This method is accurate and ideally suited for children because it can be performed in just a few seconds, with no need for prolonged immobilization or sedation. First-pass radionuclide angiocardiography (FPRA) has been compared in our laboratory with biplane angiocardiography, and a good correlation was found (Figs. 7.27 and 7.28) [115].

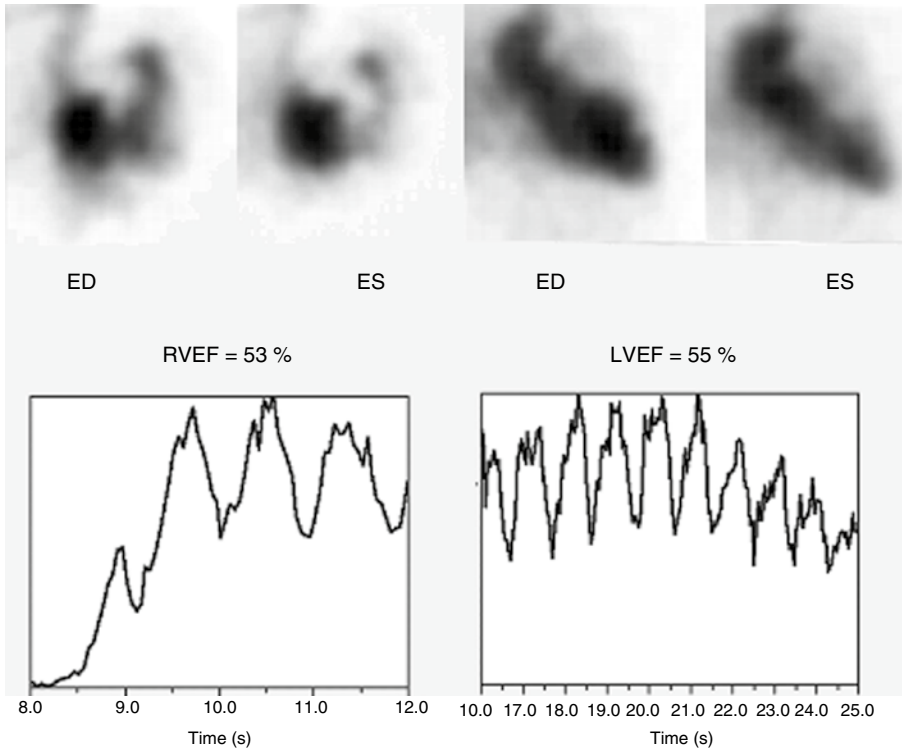

Fig. 7.28 Determination of RVEF and LVEF by first-pass radionuclide angiocardiography

To determine normal pediatric values of EF, we measured right and left ventricular ejection fractions in 74 children with normal cardiovascular function who were referred for skeletal scintigraphy [116]. These normal values are listed in Table 7.4. First-pass radionuclide angiocardiography requires meticulous attention to detail in the delineation of the edges of the ventricular margins and careful injection technique.

Table 7.4 Right and left ventricular ejection fractions in children

	Right ventricle		Left ventricle	
Age (years)	No. of patients	RVEF	No. of patients	LVEF
<1	5	0.54 ± 0.09	5	0.68 ± 0.13
1–5	12	0.53 ± 0.07	11	0.62 ± 0.09
6–10	16	0.52 ± 0.05	15	0.69 ± 0.08
11–15	19	0.54 ± 0.03	18	0.65 ± 0.09
16–20	22	0.53 ± 0.06	23	0.70 ± 0.08
Totals/mean	74	0.53 ± 0.06	72	0.68 ± 0.09

RVEF right ventricular ejection fraction, *LVEF* left ventricular ejection fraction

Right-to-Left Shunts

With right-to-left shunting, the first-pass radionuclide angiogram reveals passage of the radiotracer within the superior (or inferior) vena cava, the right atrium, and the right ventricle. There is, depending on the level of the shunt, rapid appearance of the tracer within the left atrium or the left ventricle and the aorta (or both), which on the angiogram appears to occur at the same time or before the tracer reaches the lungs. For example, with tricuspid atresia, the tracer is seen to circulate from the right atrium into the left ventricle via the left atrium, presenting a rather unique angiographic pattern. Some examples of congenital lesions where radionuclide angiocardiography may be used to detect and quantify right-to-left shunts include tetralogy of Fallot,

tricuspid atresia, pulmonary atresia/intact ventricular septum, and tetralogy of Fallot with pulmonary atresia.

Two approaches to the detection and quantitation of right-to-left shunts are available. The angiocardiographic technique is the same as that described for left-to-right shunting except that the patient (with levocardia) should be imaged in the left anterior oblique projection to obtain maximum separation between the right and left ventricles. The ROIs are marked over the superior vena cava, right ventricle, left ventricle, and lungs. The time-activity curve from a small ROI over the left ventricle is analyzed. Care must be taken to avoid contamination of counts from the right side of the heart in the ROI selected. A first peak of activity, due to blood shunted from the right to the left side of the heart, is followed by a second peak of activity due to the radioactive blood that has circulated through the lungs. Using an exponential extrapolation of the downslope following these peaks, shunt flow can be estimated as the ratio of the area under the first peak to the whole area under both peaks [117–120].

Another technique uses radioactive particles (^{99m}Tc-MAA) (Fig. 7.29). The principle of this method is that following IV injection the particles are completely extracted from the circulation in one pass through the pulmonary and systemic capillary beds. This condition is largely met for particles larger than 10 μm in diameter. It is also assumed that the particles are mixed uniformly in the blood, that the particles themselves do not affect the blood flow, and that the particles traverse the system in the same manner as the blood. After intravenous administration of radioactive particles to a patient with a right-to-left shunt, the ratio of particles that enter the pulmonary and systemic circulations equals the pulmonary blood flow/systemic blood flow ratio.

The activity in the whole body is measured and compared with that in the lungs. Gates et al., using posterior images, and Lin, using a whole-body profile device, employed this method [121, 122]. The theoretic difficulty is that the pulmonary and systemic circulations may be detected with different sensitivities owing to counting geometry and self-absorption. Good clinical results have been reported with this method. Although no adverse reactions have been reported from the intravenous administration of particles in patients with right-to-left shunting, one should be reminded that these particles produce microembolization in the systemic vascular bed, including the brain and kidneys. In patients with right-to-left shunts, we empirically employ a small number of particles (<10,000) in order to reduce systemic embolization. Assessment of right-to-left shunting with ^{99m}Tc-MAA may be particularly useful in cyanotic patients with congenital heart disease to

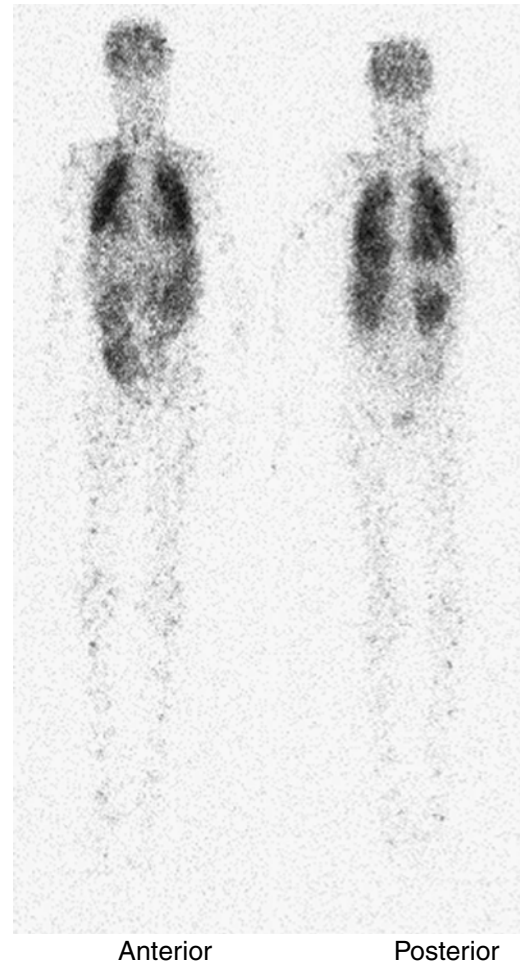

Fig. 7.29 Right-to-left shunt. The patient received ^{99m}Tc-macroaggregated albumin intravenously. The whole-body scan reveals systemic penetration of the particles. This extrapulmonary activity is noted in the brain, thyroid, myocardium, spleen, kidneys, intestine, and muscles

differentiate intrapulmonary versus intracardiac or extracardiac shunting. For example, in patients who have had either a Glenn or Fontan operation for a single ventricle, a number of "decompressing" or "shortcut" venous collaterals may develop, diverting blood from the high-pressure venous circuit in the superior vena cava to the lower-pressure left atrium. Injections in the upper extremities with visualization of the particles in territories such as the brain and the kidneys suggest an extracardiac connection between the upper venous system and the left atrium.

Right-to-left shunting can also be detected by angiocardiography with an inert gas. An inert gas is almost completely removed from the blood in one transit through the lungs. The appearance of systemic activity after intravenous injection of an inert gas (dissolved in saline) indicates a right-to-left shunt. Prior to high-resolution echocardiography and cine-MRI, some investigators used both an inert gas and a nondiffusable indicator to define the nature of the cardiac defect, especially in complicated cases [123–127].

Venography and Evaluation of Central Venous Lines

Radionuclide venography can be used to evaluate venous drainage in patients who have had multiple venous lines to determine venous patency and to help decide a site for placement of a new line. Also, this technique is indicated to evaluate venous drainage in patients with suspected superior vena cava syndrome. Another indication is the assessment of patency of central venous lines. Finally, the presence of a left superior vena cava is common in certain complex congenital heart diseases and may not be visible on the transthoracic echocardiogram. In these cases, a left-hand injection is helpful for determining the venous route to the heart. Radionuclide venography employs small volumes of material and can be done using simple intravenous needles. Radionuclide venography is a sensitive technique, as well as being safe and effective.

Radionuclide Venography

Radiopharmaceuticals

Technetium-99m pertechnetate is commonly used, although other radiopharmaceuticals, including ^{99m}Tc-DTPA and ^{99m}Tc-MAG3, may be used as well.

Imaging Technique

When evaluating venous drainage from a single extremity, the imaging method is simple. Once venous access has been gained as described above, the gamma camera equipped with a high-resolution collimator is positioned anteriorly over the patient, covering an area including the injection site, the extremity, and the heart. The tracer is injected as a bolus, as described above. The venogram is recorded beginning at the time of injection at a rate of two frames per second for 60 s on a 64×64 or 128×128 matrix. Recommended administered dose for a single study is 0.03 mCi (11.1 MBq)/kg, with a minimum of 1 mCi (37 MBq) and a maximum of 2 mCi (74 MBq) (Fig. 7.30).

Patients with central venous lines are best evaluated using three injections: one in the right arm, one in the left arm, and one in the central line itself. Three injections may be necessary, as clotting and other complications may occur in the proximal veins and not the central venous line itself. The venography technique is essentially the same as above, except it is modified by using three consecutive injections of graded amounts of radiotracer. The three sites for injection are prepared, and butterfly-type needles are placed in veins of both arms and secured with tape to the skin. The entry port of the central venous line is identified. Three syringes containing the radiopharmaceutical are prepared. The recommended administered doses for three sequential doses are as follows:

First injection: 0.03 mCi (1.11 MBq)/kg; minimum 1 mCi (37 MBq), maximum 2 mCi (74 MBq)

Second injection: 0.06 mCi (2.22 MBq)/kg; minimum 2 mCi (74 MBq), maximum 4 mCi (148 MBq)

Third injection: 0.12 mCi (4.44 MBq)/kg; minimum 4 mCi (148 MBq), maximum 8 mCi (296 MBq)

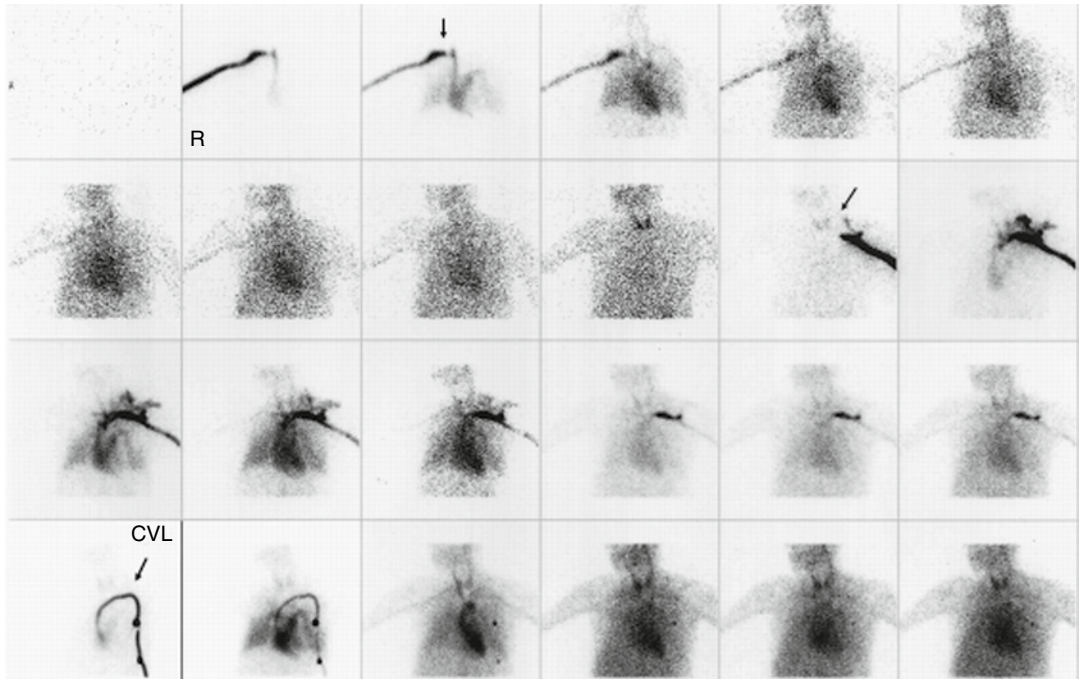

Fig. 7.30 Radionuclide venography. This patient had had several central venous lines (*CVLs*) in the past and now has a left one. Technetium-99m pertechnetate was injected first into a right antecubital vein, which shows some impediment of flow at the junction of the innominate vein and the superior vena cava (*arrow in top row*). The second injection was in a left antecubital vein, which shows obstruction (*arrow in second row*) with collaterals. The third injection in the CVL demonstrates its patency

The computer is set to record at a rate of two frames per second for 5 min, and the recording is interrupted as soon as the last venography phase is completed. Alternatively, three sequential recording phases are preset, each at a rate of two frames per second for 60 s. First the arms are injected in sequence (the right and then the left or vice versa), and the central line is injected last.

Assessment of Pulmonary Blood Flow

Abnormalities of pulmonary artery blood flow and distribution are common with complex congenital heart disease. A number of complex lesions require the combined surgical catheter and intervention approaches [128–136]. Quantitative pulmonary-perfusion scintigraphy has assumed an important role in the assessment of these repairs (see Chap. 6).

Appendix A

Quantitation of Left-to-Right Shunts

Analytic Model

The pulmonary time-activity curve recorded from a normal subject is composed of several sequential components. The first component, appearing at time t_p, is due to detection of radiotracer passing through the pulmonary vascular bed for the first time. We term this component $P(t)$. The second component, appearing at time tr_1, is due to detection of radiotracer passing through the pulmonary vascular bed for the second time, after one circuit through the systemic vascular bed. We term this component $R1(t)$. The third and later components are due to detection of radiotracer passing through the pulmonary vascular bed for the third or later time, after two or more circuits of the systemic vascular bed. The

observed normal pulmonary curve, $O(t)$, may therefore be decomposed according to the following formula:

$$O(t) = P(t) + R1(t) + \ldots.$$

In the case of a subject with a *left-to-right shunt*, a fraction (K) of radiotracer leaving the pulmonary vascular bed bypasses the systemic vascular bed by traveling through the shunt. The remaining fraction $(1-K)$ of radiotracer passes through the systemic vascular bed. Assuming the radiotracer is well mixed with the blood in the pulmonary vascular bed, these fractions are equal to the relative blood flows through the shunt and systemic vascular beds. It follows that

$$Q_p / Q_s = 1/(1-K)$$

As in a normal subject, the first component of the observed pulmonary curve, $P(t)$, is due to radiotracer passing through the pulmonary vascular bed for the first time. The minimum transit time for the radiotracer passing through the shunt and back to the pulmonary system is generally less than that for the radiotracer passing through the systemic vascular bed before returning to the pulmonary system. Therefore, the second component of $O(t)$, appearing at time t_{s1}, represents radiotracer that is passing through the pulmonary vascular bed for the second time, after one circuit through the shunt. We term this component $S1(t)$. The area under $S1(t)$ is equal to K times the area under $P(t)$. The next two components of $O(t)$, appearing at times t_{r1} and t_{s2}, are due to detection of radiotracer passing through the pulmonary vascular bed after one circuit of the systemic vascular bed and two circuits of the shunt, respectively. We term these components $R1(t)$ and $S2(t)$. The remaining components of $O(t)$ are due to radiotracer passing through the pulmonary vascular bed following multiple circuits of the shunt or systemic vascular bed (or both). The observed pulmonary curve may therefore be decomposed as

$$O(t) = P(t) + S1(t) + R1(t) + S2(t) + \ldots.$$

Shunt quantification is the problem of determining K. From the above,

$$K = \text{area under } S1(t) / \text{area under } P(t)$$

Thus, we can compute K by recovering $P(t)$ and $S1(t)$ from $O(t)$.

Gamma-Variate Analysis

We now describe the gamma-variate method for recovering $P(t)$ and $S1(t)$ from the observed pulmonary curve, $O(t)$. Consider the $O(t)$ obtained from a normal subject. The portion of $O(t)$ for t between t_p and t_{r1} is due solely to the component $P(t)$. At time t_{r1}, the component $R1(t)$ appears. In most cases, almost the entire area of $P(t)$ is to the left of t_{r1}. It is therefore possible to recover $P(t)$ almost perfectly.

It has been found empirically that the $P(t)$ obtained after a compact bolus injection of radiotracer can be closely approximated by a gamma-variate function of the form

$$P(t) = C(t - t_p)^A e_p^{-(t-t)/B}$$

where t_p is the time at which activity first appears and C, A, and B are variable parameters. The gamma-variate function can be fitted to a portion of an observed data curve by a weighted least-squares technique [137]. Thus, it is possible to estimate $P(t)$ by fitting the gamma-variate function to $O(t)$ for t between t_p and t_{r1} and extrapolating.

Consider the $O(t)$ obtained from a subject with a left-to-right shunt. The initial portion of the curve is again solely due to the component $P(t)$. At time t_{s1}, the component $S1(t)$ begins to appear. Because t_{s1} is smaller than t_{r1}, a substantial portion of the area under $P(t)$ may be to the right of t_{s1}. However, it is usually still possible to recover $P(t)$ approximately by fitting a gamma variate to $O(t)$ for t between t_p and t_{s1} and extrapolating. We denote the area under $P(t)$ by $A1$. Note that, in practice, it is necessary to infer the limits of the gamma-variate fit from $O(t)$. It can be done by visually interpreting the curve and manually choosing the points or by using a computer algorithm that automatically chooses the points [138].

We now need to recover the component $S1(t)$. Subtracting the gamma-variate fit for $P(t)$ from $O(t)$ yields the recirculation curve

$$RC(t) = S1(t) + R1(t) + S2(t) + \ldots.$$

which is equal to $S1\ (t)$ for t between t_{s1} and min (t_{s2}, t_{r1}). We denote min (t_{s2}, t_{r1}) by t_{rc}. A gamma-variate function is fit to this portion of the recirculation curve and extrapolated to recover $S1(t)$. We denote the area under $S1(t)$ by $A2$. Again it is necessary to manually or automatically infer the limits of the fit from $RC(t)$.

K is equal to the ratio $A2/A1$. Substituting $A2/A1$ for K in Eq. (1), we obtain the formula

$$\begin{aligned} Q_p / Q_s &= 1/(1 - A2/A1) \\ &= A1/(A1 - A2). \end{aligned}$$

This method provides accurate determinations of Q_p/Q_s when Q_p/Q_s is between 1.0 and 3.0, the range most important to the clinician. Q_p/Q_s values of greater than 3.0 are difficult to quantify precisely. However, large shunts (Q_p/Q_s <3.0) are usually clinically apparent, and more precise quantitation is unimportant [114]. Q_p/Q_s values between 1.0 and 1.2 may be obtained in patients with no shunt [139–144]. When the flow ratio is Q_p/Q_s <1.5, the shunt may not be recognized by visual inspection of the angiogram alone.

A number of alternative methods to estimate Q_p/Q_s from pulmonary time-activity curves have been suggested. We refer the interested reader to the available literature [145–150].

Correction for Radiotracer Delivery

Shunt quantitation by the gamma-variate method assumes that $P(t)$ and $S1(t)$ can be described by gamma-variate functions. In addition, the method assumes that sufficiently large portions of $P(t)$ and $S1(t)$ occur before t_{s1} and t_{rc}, respectively, to allow accurate extrapolation. The validity of both of these assumptions depends on the time course of delivery of the radiotracer to the cardiopulmonary system. This delivery can be monitored using an ROI over the superior vena cava.

Ideally, one would like to deliver the radiotracer to the cardiopulmonary system as an instantaneous pulse because it would maximize the separation of the components of the pulmonary curve and thus facilitate shunt quantitation. In practice, it is impossible to attain this goal by peripheral intravenous injection. It is possible, however, to estimate the pulmonary curve that would be produced from an instantaneous pulse of radiotracer from the observed superior vena cava and pulmonary curves by using a mathematical technique known as deconvolution [71, 151, 152]. Studies on dogs and humans have shown that deconvolution may improve the accuracy of shunt quantification by radionuclide angiocardiography [108, 153, 154].

Appendix B

Ultrashort-Lived Radionuclides

Although commonly used, ^{99m}Tc has limitations as a tracer for first-pass radionuclide angiography: (1) Radiation-dose constraints limit the injected dose, which, in turn, limits the number of counts present in the study and thus the statistical accuracy. (2) It is difficult to perform repeated studies within a short time (as would be required to assess the effects of an intervention such as a pharmacologic intervention or exercise) because of background interference from the previous study. (3) In small children the temporal and spatial resolution of the study may be limited because of absorbed dose considerations. These limitations are primarily a consequence of the 6-h half-life of ^{99m}Tc compared to the short time required to perform the study (<30 s).

The most obvious way to eliminate these problems is to use a tracer with a shorter half-life [155]. This group of tracers is collectively known as ultrashort-lived radionuclides and includes ^{195m}Au ($t_{1/2}$ = 30.5 s), ^{191m}Ir ($t_{1/2}$ = 5 s) [156], and ^{178}Ta ($t_{1/2}$ = 9.3 min). Because of their short half-lives, these tracers are produced at the bedside using radionuclide generators analogous to the

molybdenum ($^{99}Mo \rightarrow {}^{99m}Tc$) generator. Gold-195m was the subject of several clinical studies during the 1980s when the mercury-195m ($^{195m}Hg \rightarrow {}^{195m}Au$) generator was produced commercially, but it is no longer available [157–162].

We and others have found that ^{191m}Ir is well suited for first-pass radionuclide angiography despite its short half-life (4.96 s) [163–169]. Iridium-191m emits 65- and 129-keV photons (65 and 26 % abundance, respectively), both of which can be imaged with modern scintillation cameras [165]. In addition, the 65-keV x-rays can be imaged with the multiwire proportional camera [170]. The short half-life of ^{191m}Ir allows much larger amounts of ^{191m}Ir to be administered with an absorbed radiation dose to the patient lower than would be experienced with the normal dose of ^{99m}Tc. The resulting high photon flux permits images with high count density and thus greater statistical accuracy. The short half-life and low-radiation dose allow multiple studies to be performed within a short time to assess the cardiovascular changes that result from exercise, drugs, or catheter interventions.

Iridium-191m is the product of beta decay of ^{191m}Os, which has a physical half-life of 15.4 days. An ^{191}Os-^{191m}Ir generator system, which can deliver multiple doses of ^{191m}Ir for rapid intravenous injection, has been developed in our laboratory and used in humans [165]. If ^{191m}Ir is used, the time-activity curve from the angiogram is corrected for radioactive decay and count losses due to gamma camera dead time before analysis.

Tantalum-178 has a somewhat longer half-life than ^{195m}Au or ^{191m}Ir but is still a significant improvement over ^{99m}Tc for first-pass radionuclide angiocardiography (FPRA). Lacy et al. have described an automated generator that facilitates clinical use of ^{178}Ta [171–174].

References

1. Blumgart HL, Yens OC. Studies on the velocity of blood flow. I. The method utilized. J Clin Invest. 1927;4:1–13.
2. Blumgart HL, Weiss S. Studies on the velocity of blood flow. VII. The pulmonary circulation time in normal resting individuals. J Clin Invest. 1927;4:399–425.
3. Prinzmetal M, Corday E, Bergman HC, Schwartz L, Spritzler RJ. Radiocardiography: a new method for studying the blood flow through the chambers of the heart in human beings. Science. 1948;108:340–1.
4. Prinzmetal M, Corday E, Spritzler RJ, Flieg W. Radiocardiography and its clinical applications. JAMA. 1949;149:617–22.
5. Fyler DC. Report of the New England regional infant cardiac program. J Pediatr. 1980;65(Supp):377.
6. Castaneda AR, Mayer Jr JE, Jonas RA, Lock JE, Wessel DL, Hickey PR. The neonate with critical congenital heart disease: repair–a surgical challenge. J Thorac Cardiovasc Surg. 1989;98(5 Pt 2):869–75.
7. Chang AC, Hanley FL, Lock JE, Castaneda AR, Wessel DL. Management and outcome of low birth weight neonates with congenital heart disease. J Pediatr. 1994;124(3):461–6.
8. Chhatriwalla AK, Prieto LR, Brunken RC, Cerqueira MD, Younoszai A, Jaber WA. Preliminary data on the diagnostic accuracy of rubidium-82 cardiac PET perfusion imaging for the evaluation of ischemia in a pediatric population. Pediatr Cardiol. 2008;29(4):732–8.
9. Hernandez-Pampaloni M, Allada V, Fishbein MC, Schelbert HR. Myocardial perfusion and viability by positron emission tomography in infants and children with coronary abnormalities: correlation with echocardiography, coronary angiography, and histopathology. J Am Coll Cardiol. 2003;41(4):618–26.
10. Kawasaki T. Acute febrile mucocutaneous syndrome with lymphoid involvement with specific desquamation of the fingers and toes in children. Arerugi. 1967;16(3):178–222.
11. Kato H, Sugimura T, Akagi T, et al. Long-term consequences of Kawasaki disease. A 10- to 21-year follow-up study of 594 patients. Circulation. 1996;94(6):1379–85.
12. Dajani AS, Taubert KA, Gerber MA, et al. Diagnosis and therapy of Kawasaki disease in children. Circulation. 1993;87(5):1776–80.
13. Holman RC, Curns AT, Belay ED, Steiner CA, Schonberger LB. Kawasaki syndrome hospitalizations in the United States, 1997 and 2000. Pediatrics. 2003;112(3 Pt 1):495–501.
14. Yanagawa H, Nakamura Y, Yashiro M, et al. Results of the nationwide epidemiologic survey of Kawasaki disease in 1995 and 1996 in Japan. Pediatrics. 1998;102(6):E65.
15. Fujiwara H, Hamashima Y. Pathology of the heart in Kawasaki disease. Pediatrics. 1978;61(1):100–7.
16. Tsuda E, Kamiya T, Ono Y, Kimura K, Kurosaki K, Echigo S. Incidence of stenotic lesions predicted by acute phase changes in coronary arterial diameter during Kawasaki disease. Pediatr Cardiol. 2005;26(1):73–9.
17. Suzuki A, Kamiya T, Ono Y, Okuno M, Yagihara T. Aortocoronary bypass surgery for coronary arterial lesions resulting from Kawasaki disease. J Pediatr. 1990;116(4):567–73.

18. Hwang B, Liu RS, Chu LS, Lee PC, Lu JH, Meng LC. Positron emission tomography for the assessment of myocardial viability in Kawasaki disease using different therapies. Nucl Med Commun. 2000;21(7): 631–6.
19. Yoshibayashi M, Tamaki N, Nishioka K, et al. Regional myocardial perfusion and metabolism assessed by positron emission tomography in children with Kawasaki disease and significance of abnormal Q waves and their disappearance. Am J Cardiol. 1991;68(17):1638–45.
20. Hauser M, Bengel F, Kuehn A, et al. Myocardial blood flow and coronary flow reserve in children with "normal" epicardial coronary arteries after the onset of Kawasaki disease assessed by positron emission tomography. Pediatr Cardiol. 2004;25(2): 108–12.
21. Muzik O, Paridon SM, Singh TP, Morrow WR, Dayanikli F, Di Carli MF. Quantification of myocardial blood flow and flow reserve in children with a history of Kawasaki disease and normal coronary arteries using positron emission tomography. J Am Coll Cardiol. 1996;28(3):757–62.
22. Takayasu M. A case with unusual changes of the central vessels of the retina. Acta Soc Opthalmol Jpn. 1908;12:554–5.
23. Johnston SL, Lock RJ, Gompels MM. Takayasu arteritis: a review. J Clin Pathol. 2002;55(7):481–6.
24. Al Abrawi S, Fouillet-Desjonqueres M, David L, Barral X, Cochat P, Cimaz R. Takayasu arteritis in children. Pediatr Rheumatol Online J. 2008;6:17.
25. Brunner J, Feldman BM, Tyrrell PN, et al. Takayasu arteritis in children and adolescents. Rheumatology (Oxford). 2010;49(10):1806–14.
26. Cakar N, Yalcinkaya F, Duzova A, et al. Takayasu arteritis in children. J Rheumatol. 2008;35(5):913–9.
27. Kalangos A, Christenson JT, Cikirikcioglu M, et al. Long-term outcome after surgical intervention and interventional procedures for the management of Takayasu's arteritis in children. J Thorac Cardiovasc Surg. 2006;132(3):656–64.
28. Nascif AK, Lemos MD, Oliveira NS, Perim PC, Cordeiro AC, Quintino M. Takayasu's arteritis in children and adolescents: report of three cases. Rev Bras Reumatol. 2011;51(5):527–30.
29. Stanley P, Roebuck D, Barboza A. Takayasu's arteritis in children. Tech Vasc Interv Radiol. 2003;6(4):158–68.
30. Arnaud L, Haroche J, Mathian A, Gorochov G, Amoura Z. Pathogenesis of Takayasu's arteritis: a 2011 update. Autoimmun Rev. 2011;11(1):61–7.
31. Ginde S, Cava JR, Southern JF, Saudek DE. Delayed contrast-enhanced magnetic resonance imaging in the evaluation of Takayasu arteritis. J Am Coll Cardiol. 2012;59(12):e23.
32. Fuchs M, Briel M, Daikeler T, et al. The impact of 18F-FDG PET on the management of patients with suspected large vessel vasculitis. Eur J Nucl Med Mol Imaging. 2012;39(2):344–53.
33. Henes JC, Muller M, Krieger J, et al. [18F] FDG-PET/CT as a new and sensitive imaging method for the diagnosis of large vessel vasculitis. Clin Exp Rheumatol. 2008;26(3 Suppl 49):S47–52.
34. Jones DA, Goddard I, Wragg A. 18F-FDG positron emission tomography CT and assessment of aortitis. Heart. 2010;96(23):1952.
35. Kobayashi Y, Ishii K, Oda K, et al. Aortic wall inflammation due to Takayasu arteritis imaged with 18F-FDG PET coregistered with enhanced CT. J Nucl Med. 2005;46(6):917–22.
36. Umekita K, Takajo I, Miyauchi S, et al. [18F]fluorodeoxyglucose positron emission tomography is a useful tool to diagnose the early stage of Takayasu's arteritis and to evaluate the activity of the disease. Mod Rheumatol. 2006;16(4):243–7.
37. Direskeneli H, Aydin SZ, Merkel PA. Assessment of disease activity and progression in Takayasu's arteritis. Clin Exp Rheumatol. 2011;29(1 Suppl 64):S86–91.
38. Tezuka D, Haraguchi G, Ishihara T, et al. Role of FDG PET-CT in Takayasu arteritis: sensitive detection of recurrences. JACC Cardiovasc Imaging. 2012;5(4): 422–9.
39. Vista EG, Santos Estrella PV, Lichauco JJ. Flourine-18 fluorodeoxyglucose positron emission tomography as a non-invasive test of disease activity in Takayasu's arteritis – a report of four cases. Autoimmun Rev. 2010;9(7):503–6.
40. Walter MA. [(18)F]fluorodeoxyglucose PET in large vessel vasculitis. Radiol Clin North Am. 2007;45(4): 735–44. viii.
41. Iwabu M, Yamamoto Y, Dobashi H, Kameda T, Kittaka K, Nishiyama Y. F-18 FDG PET findings of Takayasu arteritis before and after immunosuppressive therapy. Clin Nucl Med. 2008;33(12):872–3.
42. Lee KH, Cho A, Choi YJ, et al. The role of (18) F-fluorodeoxyglucose-positron emission tomography in the assessment of disease activity in patients with takayasu arteritis. Arthritis Rheum. 2012;64(3): 866–75.
43. Fyler DC. Report of the New England regional infant cardiac program. Pediatrics. 1980;65(2 Pt 2):377.
44. Liebman J, Cullum L, Belloc NB. Natural history of transposition of the great arteries. Anatomy and birth and death characteristics. Circulation. 1969;40(2):237–62.
45. Arensman FW, Sievers HH, Lange P, et al. Assessment of coronary and aortic anastomoses after anatomic correction of transposition of the great arteries. J Thorac Cardiovasc Surg. 1985;90(4): 597–604.
46. Day RW, Laks H, Drinkwater DC. The influence of coronary anatomy on the arterial switch operation in neonates. J Thorac Cardiovasc Surg. 1992;104(3):706–12.
47. Goor DA, Shem-Tov A, Neufeld HN. Impeded coronary flow in anatomic correction of transposition of the great arteries: prevention, detection, and management. J Thorac Cardiovasc Surg. 1982; 83(5):747–54.
48. Mayer Jr JE, Jonas RA, Castaneda AR. Arterial switch operation for transposition of the great arteries with intact ventricular septum. J Card Surg. 1986;1(2):97–104.

49. Tsuda E, Imakita M, Yagihara T, et al. Late death after arterial switch operation for transposition of the great arteries. Am Heart J. 1992;124(6):1551–7.
50. Vogel M, Smallhorn JF, Gilday D, et al. Assessment of myocardial perfusion in patients after the arterial switch operation. J Nucl Med. 1991;32(2):237–41.
51. Vogel M, Smallhorn JF, Trusler GA, Freedom RM. Echocardiographic analysis of regional left ventricular wall motion in children after the arterial switch operation for complete transposition of the great arteries. J Am Coll Cardiol. 1990;15(6):1417–23.
52. Bengel FM, Hauser M, Duvernoy CS, et al. Myocardial blood flow and coronary flow reserve late after anatomical correction of transposition of the great arteries. J Am Coll Cardiol. 1998;32(7):1955–61.
53. Singh TP, Humes RA, Muzik O, Kottamasu S, Karpawich PP, Di Carli MF. Myocardial flow reserve in patients with a systemic right ventricle after atrial switch repair. J Am Coll Cardiol. 2001;37(8):2120–5.
54. Rein AJ, Colan SD, Parness IA, Sanders SP. Regional and global left ventricular function in infants with anomalous origin of the left coronary artery from the pulmonary trunk: preoperative and postoperative assessment. Circulation. 1987;75(1):115–23.
55. Sauer U, Stern H, Meisner H, Buhlmeyer K, Sebening F. Risk factors for perioperative mortality in children with anomalous origin of the left coronary artery from the pulmonary artery. J Thorac Cardiovasc Surg. 1992;104(3):696–705.
56. Bunton R, Jonas RA, Lang P, Rein AJ, Castaneda AR. Anomalous origin of left coronary artery from pulmonary artery. Ligation versus establishment of a two coronary artery system. J Thorac Cardiovasc Surg. 1987;93(1):103–8.
57. Montigny M, Stanley P, Chartrand C, Selman E, Fournier A, Davignon A. Postoperative evaluation after end-to-end subclavian-left coronary artery anastomosis in anomalous left coronary artery. J Thorac Cardiovasc Surg. 1990;100(2):270–3.
58. Vouhe PR, Tamisier D, Sidi D, et al. Anomalous left coronary artery from the pulmonary artery: results of isolated aortic reimplantation. Ann Thorac Surg. 1992;54(4):621–6. discussion 627.
59. Hurwitz RA, Caldwell RL, Girod DA, Brown J, King H. Clinical and hemodynamic course of infants and children with anomalous left coronary artery. Am Heart J. 1989;118(6):1176–81.
60. Hunt SA. Complications of heart transplantation. J Heart Transplant. 1983;3:70–4.
61. Pahl E, Naftel DC, Kuhn M, et al. The incidence and impact of transplant coronary artery disease in pediatric recipients: a 9 year multi-institutional study. Circulation. 2002;106:II-396 [abstract].
62. Gao SZ, Alderman EL, Schroeder JS, Silverman JF, Hunt SA. Accelerated coronary vascular disease in the heart transplant patient: coronary arteriographic findings. J Am Coll Cardiol. 1988;12(2):334–40.
63. Wenning C, Stypmann J, Papavassilis P, et al. Left ventricular dilation and functional impairment assessed by gated SPECT are indicators of cardiac allograft vasculopathy in heart transplant recipients. J Heart Lung Transplant. 2012;31(7):719–28.
64. Kofoed KF, Czernin J, Johnson J, et al. Effects of cardiac allograft vasculopathy on myocardial blood flow, vasodilatory capacity, and coronary vasomotion. Circulation. 1997;95(3):600–6.
65. Wu YW, Chen YH, Wang SS, et al. PET assessment of myocardial perfusion reserve inversely correlates with intravascular ultrasound findings in angiographically normal cardiac transplant recipients. J Nucl Med. 2010;51(6):906–12.
66. Tadamura E, Yoshibayashi M, Yonemura T, et al. Significant regional heterogeneity of coronary flow reserve in paediatric hypertrophic cardiomyopathy. Eur J Nucl Med. 2000;27(9):1340–8.
67. Kocis KC. Chest pain in pediatrics. Pediatr Clin North Am. 1999;46(2):189–203.
68. Kondo M. Thallium-201 myocardial imaging in patients with various heart diseases (author's transl). Nippon Igaku Hoshasen Gakkai Zasshi. 1979; 39(9):942–54.
69. Kondo M, Kubo A, Yamazaki H, et al. Thallium-201 myocardial imaging for evaluation of right ventricular overloading. J Nucl Med. 1978;19:1197–203.
70. Hauser M, Bengel FM, Hager A, et al. Impaired myocardial blood flow and coronary flow reserve of the anatomical right systemic ventricle in patients with congenitally corrected transposition of the great arteries. Heart. 2003;89(10):1231–5.
71. Bassingthwaighte JB. Circulatory transport and the convolution integral. Mayo Clin Proc. 1967; 42(3):137–54.
72. Rabinovitch M, Fisher K, Gamble W, Reid L, Treves S. Thallium-201: quantitation of right ventricular hypertrophy in chronically hypoxic rats. Radiology. 1979;130(1):223–5.
73. Rabinovitch M, Fischer KC, Treves S. Quantitative thallium-201 myocardial imaging in assessing right ventricular pressure in patients with congenital heart defects. Br Heart J. 1981;45(2):198–205.
74. Nakajima K, Taki J, Taniguchi M, Tonami N, Hisida K. Comparison of 99Tcm-sestamibi and 201Tl-chloride to estimate right ventricular overload in children. Nucl Med Commun. 1995;16(11):936–41.
75. Cohen HA, Baird MG, Rouleau JR, et al. Thallium 201 myocardial imaging in patients with pulmonary hypertension. Circulation. 1976;54(5):790–5.
76. Strauer BE, Burger S, Bull U. Multifactorial determination of 201thallium uptake of the heart: an experimental study concerning the influence of ventricular mass, perfusion and oxygen consumption. Basic Res Cardiol. 1978;73(3):298–306.
77. Bull C, de Leval MR, Mercanti C, Macartney FJ, Anderson RH. Pulmonary atresia and intact ventricular septum: a revised classification. Circulation. 1982;66(2):266–72.
78. Gentles TL, Colan SD, Giglia TM, Mandell VS, Mayer Jr JE, Sanders SP. Right ventricular decompression and left ventricular function in pulmonary atresia with intact ventricular septum. The influence

of less extensive coronary anomalies. Circulation. 1993;88(5 Pt 2):II183–8.
79. Giglia TM, Mandell VS, Connor AR, Mayer Jr JE, Lock JE. Diagnosis and management of right ventricle-dependent coronary circulation in pulmonary atresia with intact ventricular septum. Circulation. 1992;86(5):1516–28.
80. Hanley FL, Sade RM, Blackstone EH, Kirklin JW, Freedom RM, Nanda NC. Outcomes in neonatal pulmonary atresia with intact ventricular septum. A multiinstitutional study. J Thorac Cardiovasc Surg. 1993;105(3):406–23. 424-407; discussion 423-404.
81. Hauser M, Bengel FM, Kuhn A, et al. Myocardial perfusion and coronary flow reserve assessed by positron emission tomography in patients after Fontan-like operations. Pediatr Cardiol. 2003;24(4): 386–92.
82. Lebowitz E, Greene MW, Fairchild R, et al. Thallium-201 for medical use. Indian J Nucl Med. 1975;16(2):151–5.
83. Kawana N, Krizeh H, Porter J, et al. Use of Tl-201 as a potassium analog in scanning [abstract]. J Nucl Med. 1970;11:333.
84. Gehring PJ, Hammond PB. The interrelationship between thallium and potassium in animals. J Pharmacol Exp Ther. 1967;155(1):187–201.
85. Strauss HW, Harrison K, Langan JK, Lebowitz E, Pitt B. Thallium-201 for myocardial imaging. Relation of thallium-201 to regional myocardial perfusion. Circulation. 1975;51(4):641–5.
86. Karasawa K, Ayusawa M, Noto N, Sumitomo N, Okada T, Harada K. Assessment of cardiac sympathetic nerve activity in children with chronic heart failure using quantitative iodine-123 metaiodobenzylguanidine imaging. J Cardiol. 2000;36(6): 387–95.
87. Acar P, Merlet P, Iserin L, et al. Impaired cardiac adrenergic innervation assessed by MIBG imaging as a predictor of treatment response in childhood dilated cardiomyopathy. Heart. 2001;85(6):692–6.
88. Sakurai H, Maeda M, Miyahara K, et al. Evaluation of cardiac autonomic nerves by iodine-123 metaiodobenzylguanidine scintigraphy and ambulatory electrocardiography in patients after arterial switch operations. J Cardiol. 2000;35(5):353–62.
89. Maunoury C, Agostini D, Acar P, et al. Impairment of cardiac neuronal function in childhood dilated cardiomyopathy: an 123I-MIBG scintigraphic study. J Nucl Med. 2000;41(3):400–4.
90. Momose M, Kobayashi H, Kasanuki H, et al. Evaluation of regional cardiac sympathetic innervation in congenital long QT syndrome using 123I-MIBG scintigraphy. Nucl Med Commun. 1998;19(10):943–51.
91. Acar P, Merlet P, Iserin L, et al. Cardiac MIBG imaging: a new marker for myocardial function in children? Arch Mal Coeur Vaiss. 1996;89(5):599–604.
92. Olgunturk R, Turan L, Tunaoglu FS, et al. Abnormality of the left ventricular sympathetic nervous function assessed by I-123 metaiodobenzylguanidine imaging in pediatric patients with neurocardiogenic syncope. Pacing Clin Electrophysiol. 2003;26(10):1926–30.
93. Muller KD, Jakob H, Neuzner J, Grebe SF, Schlepper M, Pitschner HF. 123I-metaiodobenzylguanidine scintigraphy in the detection of irregular regional sympathetic innervation in long QT syndrome. Eur Heart J. 1993;14(3):316–25.
94. Stirner H, Buell U, Kleinhans E, Bares R, Grosse W. Myocardial kinetics of 99Tcm hexakis-(2-methoxy-isobutyl-isonitrile) (HMIBI) in patients with coronary heart disease: a comparative study versus 201Tl with SPECT. Nucl Med Commun. 1988;9(1): 15–23.
95. Magrina J, Bosch X, Garcia A, et al. Diagnostic value of technetium-99m-MIBI as a myocardial perfusion imaging agent: comparison of long and short intervals between rest and stress injections. Clin Cardiol. 1992;15(7):497–503.
96. Garcia EV. Quantitative nuclear cardiology: we are almost there! J Nucl Cardiol. 2012;19(3):424–37.
97. Slomka PJ, Patton JA, Berman DS, Germano G. Advances in technical aspects of myocardial perfusion SPECT imaging. J Nucl Cardiol. 2009;16(2): 255–76.
98. Schelbert HR, Phelps ME, Huang SC, et al. N-13 ammonia as an indicator of myocardial blood flow. Circulation. 1981;63(6):1259–72.
99. Gottumukkala V, Heinrich TK, Baker A, et al. Biodistribution and stability studies of [18F]fluoroethylrhodamine B, a potential PET myocardial perfusion agent. Nucl Med Biol. 2010;37(3):365–70.
100. Higuchi T, Bengel FM. Cardiovascular nuclear imaging: from perfusion to molecular function: noninvasive imaging. Heart. 2008;94(6):809–16.
101. Anderson CJ, Bulte JW, Chen K, et al. Design of targeted cardiovascular molecular imaging probes. J Nucl Med. 2010;51 Suppl 1:3S–17.
102. Yu M, Nekolla SG, Schwaiger M, Robinson SP. The next generation of cardiac positron emission tomography imaging agents: discovery of flurpiridaz F-18 for detection of coronary disease. Semin Nucl Med. 2011;41(4):305–13.
103. Maddahi J. Properties of an ideal PET perfusion tracer: new PET tracer cases and data. J Nucl Cardiol. 2012;19 Suppl 1:S30–7.
104. Sherif HM, Nekolla SG, Saraste A, et al. Simplified quantification of myocardial flow reserve with flurpiridaz F 18: validation with microspheres in a pig model. J Nucl Med. 2011;52(4):617–24.
105. Rickers C, Sasse K, Buchert R, et al. Myocardial viability assessed by positron emission tomography in infants and children after the arterial switch operation and suspected infarction. J Am Coll Cardiol. 2000;36(5):1676–83.
106. Berman DS, Salel AF, DeNardo GL, Bogren HG, Mason DT. Clinical assessment of left ventricular regional contraction patterns and ejection fraction by high-resolution gated scintigraphy. J Nucl Med. 1975;16(10):865–74.

107. Strauss HW, Zaret BL, Hurley PJ, Natarajan TK, Pitt B. A scintiphotographic method for measuring left ventricular ejection fraction in man without cardiac catheterization. Am J Cardiol. 1971;28(5):575–80.
108. Alderson PO, Douglass KH, Mendenhall KG, et al. Deconvolution analysis in radionuclide quantitation of left-to-right cardiac shunts. J Nucl Med. 1979; 20(6):502–6.
109. Bough EW, Gandsman EJ, North DL, Shulman RS. Gated radionuclide angiographic evaluation of valve regurgitation. Am J Cardiol. 1980;46(3):423–8.
110. Lam W, Pavel D, Byrom E, Sheikh A, Best D, Rosen K. Radionuclide regurgitant index: value and limitations. Am J Cardiol. 1981;47(2):292–8.
111. Rigo P, Alderson PO, Robertson RM, Becker LC, Wagner Jr HN. Measurement of aortic and mitral regurgitation by gated cardiac blood pool scans. Circulation. 1979;60(2):306–12.
112. Sorensen SG, O'Rourke RA, Chaudhuri TK. Noninvasive quantitation of valvular regurgitation by gated equilibrium radionuclide angiography. Circulation. 1980;62(5):1089–98.
113. Urquhart J, Patterson RE, Packer M, et al. Quantification of valve regurgitation by radionuclide angiography before and after valve replacement surgery. Am J Cardiol. 1981;47(2):287–91.
114. Hurwitz RA, Treves S, Keane JF, Girod DA, Caldwell RL. Current value of radionuclide angiocardiography for shunt quantification and management in patients with secundum atrial septal defect. Am Heart J. 1982;103(3):421–5.
115. Kurtz D, Ahnberg DS, Freed M, LaFarge CG, Treves S. Quantitative radionuclide angiocardiography. Determination of left ventricular ejection fraction in children. Br Heart J. 1976;38(9):966–73.
116. Hurwitz RA, Treves S, Kuruc A. Right ventricular and left ventricular ejection fraction in pediatric patients with normal hearts: first-pass radionuclide angiocardiography. Am Heart J. 1984;107(4):726–32.
117. Hurley PJ, Poulose KP, Wagner Jr HN. Radionuclide angiocardiography for detecting right-to-left intracardiac shunts [abstract]. J Nucl Med. 1969;10:344.
118. Riihimaki E, Heiskanen A, Tahti E. Theory of quantitative determination of intracardiac shunts by external detection. Ann Clin Res. 1974;6(1):45–9.
119. Treves S. Detection and quantitation of cardiovascular shunts with commonly available radionuclides. Semin Nucl Med. 1980;10(1):16–26.
120. Weber PM, Dos Remedios LV, Jasko IA. Quantitative radioisotopic angiocardiography. J Nucl Med. 1972; 13(11):815–22.
121. Gates GF, Orme HW, Dore EK. Measurement of cardiac shunting with technetium-labeled albumin aggregates. J Nucl Med. 1971;12(11):746–9.
122. Lin CY. Lung scan in cardiopulmonary disease. I. Tetralogy of Fallot. J Thorac Cardiovasc Surg. 1971; 61(3):370–9.
123. Bosnjakovic VB, Bennett LR. Dynamic isotope studies in cardiology. AEC Symp Series. 1972;27:562.
124. Braunwald E, Long RTL, Morrow AG. Injections of radioactive krypton (KR^{85}) solutions in the detection of cardiac shunts. J Clin Invest. 1959;38:990.
125. Long RT, Braunwald E, Morrow AG. Intracardiac injection of radioactive krypton. Clinical applications of new methods for characterization of circulatory shunts. Circulation. 1960;21:1126–33.
126. Long RT, Waldhausen JA, Cornell WP, Sanders RJ. Detection of right-to-left circulatory shunts: a new method utilizing injections of krypton. Proc Soc Exp Biol Med. 1959;102:456–8.
127. Parker JA, Secker-Walker R, Hill R, Siegel BA, Potchen EJ. A new technique for the calculation of left ventricular ejection fraction. J Nucl Med. 1972;13(8):649–51.
128. Driscoll DJ, Hesslein PS, Mullins CE. Congenital stenosis of individual pulmonary veins: clinical spectrum and unsuccessful treatment by transvenous balloon dilation. Am J Cardiol. 1982;49(7):1767–72.
129. Gentles TL, Lock JE, Perry SB. High pressure balloon angioplasty for branch pulmonary artery stenosis: early experience. J Am Coll Cardiol. 1993;22(3): 867–72.
130. O'Laughlin MP, Perry SB, Lock JE, Mullins CE. Use of endovascular stents in congenital heart disease. Circulation. 1991;83(6):1923–39.
131. O'Laughlin MP, Slack MC, Grifka RG, Perry SB, Lock JE, Mullins CE. Implantation and intermediate-term follow-up of stents in congenital heart disease. Circulation. 1993;88(2):605–14.
132. Rothman A, Perry SB, Keane JF, Lock JE. Balloon dilation of branch pulmonary artery stenosis. Semin Thorac Cardiovasc Surg. 1990;2(1):46–54.
133. Rothman A, Perry SB, Keane JF, Lock JE. Early results and follow-up of balloon angioplasty for branch pulmonary artery stenoses. J Am Coll Cardiol. 1990;15(5):1109–17.
134. Stewart JA, Silimperi D, Harris P, Wise NK, Fraker Jr TD, Kisslo JA. Echocardiographic documentation of vegetative lesions in infective endocarditis: clinical implications. Circulation. 1980;61(2):374–80.
135. Tamir A, Melloul M, Berant M, et al. Lung perfusion scans in patients with congenital heart defects. J Am Coll Cardiol. 1992;19(2):383–8.
136. Vogel M, Ash J, Rowe RD, Trusler GA, Rabinovitch M. Congenital unilateral pulmonary vein stenosis complicating transposition of the great arteries. Am J Cardiol. 1984;54(1):166–71.
137. Starmer CF, Clark DO. Computer computations of cardiac output using the gamma function. J Appl Physiol. 1970;28(2):219–20.
138. Kuruc A, Treves S, Smith W, Fujii A. An automated algorithm for radionuclide angiocardiographic quantitation of circulatory shunting. Comput Biomed Res. 1984;17(5):481–93.
139. Alderson PO, Gaudiani VA, Watson DC, Mendenhall KG, Donovan RC. Quantitative radionuclide angiocardiography in animals with experimental atrial septal defects. J Nucl Med. 1978;19(4):364–9.

140. Alderson PO, Jost RG, Strauss AW, Boonvisut S, Markham J. Detection and quantitation of left-to-right cardiac shunts in children: a clinical comparison of count ratio and area ratio techniques. J Nucl Med. 1975;16:511.
141. Askenazi J, Ahnberg DS, Korngold E, LaFarge CG, Maltz DL, Treves S. Quantitative radionuclide angiocardiography: detection and quantitation of left to right shunts. Am J Cardiol. 1976;37(3):382–7.
142. Maltz DL, Treves S. Quantitative radionuclide angiocardiography: determination of Qp: Qs in children. Circulation. 1973;47(5):1049–56.
143. Treves S, Maltz DL. Radionuclide angiocardiography. Postgrad Med. 1974;56(1):99–107.
144. Treves S, Maltz DL, Adelstein SJ. Intracardiac shunts. In: James AE, Wagner Jr HN, Cooke RE, editors. Pediatric nuclear medicine. Philadelphia: Saunders; 1974.
145. Bourguignon MH, Links JM, Douglass KH, Alderson PO, Roland JM, Wagner Jr HN. Quantification of left to right cardiac shunts by multiple deconvolution analysis. Am J Cardiol. 1981;48(6):1086–90.
146. Kveder M, Bajzer Z, Nosil J. A mathematical model for the quantitative study of left to right cardiac shunt. Phys Med Biol. 1985;30(3):207–15.
147. Kveder M, Bajzer Z, Zadro M. Theoretical aspects of multiple deconvolution analysis for quantification of left to right cardiac shunts. Phys Med Biol. 1987;32(10):1237–43.
148. Madsen MT, Argenyi E, Preslar J, Grover-McKay M, Kirchner PT. An improved method for the quantification of left-to-right cardiac shunts. J Nucl Med. 1991;32(9):1808–12.
149. Nakamura M, Suzuki Y, Nagasawa T, Sugihara M, Takahashi T. Detection and quantitation of left-to-right shunts from radionuclide angiocardiography using the homomorphic deconvolution technique. IEEE Trans Biomed Eng. 1982;29(3):192–201.
150. Parker JA, Treves S. Radionuclide detection, localization, and quantitation of intracardiac shunts and shunts between the great arteries. Prog Cardiovasc Dis. 1977;20(2):121–50.
151. Gamel J, Rousseau WF, Katholi CR, Mesel E. Pitfalls in digital computation of the impulse response of vascular beds from indicator-dilution curves. Circ Res. 1973;32(4):516–23.
152. Kuruc A, Treves S, Parker JA. Accuracy of deconvolution algorithms assessed by simulation studies: concise communication. J Nucl Med. 1983;24(3):258–63.
153. Ham HR, Dobbeleir A, Virat P, Piepsz A, Lenaers A. Radionuclide quantitation of left-to right cardiac shunts using deconvolution analysis: concise communication. J Nucl Med. 1981;22(8):688–92.
154. Kuruc A, Treves S, Parker JA, Cheng C, Sawan A. Radionuclide angiocardiography: an improved deconvolution technique for improvement after suboptimal bolus injection. Radiology. 1983;148(1):233–8.
155. Yano Y, Anger HO. Ultrashort-lived radioisotopes for visualizing blood vessels and organs. J Nucl Med. 1968;9(1):2–6.
156. Paras T, Thiessen JW. Single-photon ultrashort-lived radionuclides. Paper presented at: USDOE Symp Ser. 1985.
157. Caplin JL, Dymond DS, O'Keefe JC, et al. Relation between exercise: a study using first-pass radionuclide angiography with gold-195m. Br Heart J. 1986;55:120–8.
158. Kipper SL, Ashburn WL, Norris SL, Rimkus DS, Dillon WA. Gold-195m first-pass radionuclide ventriculography, thallium-201 single-photon emission CT, and 12-lead ECG stress testing as a combined procedure. Radiology. 1985;156(3):817–21.
159. Lahiri A, Zanelli GD, O'Hara MJ, et al. Simultaneous measurement of left ventricular function and myocardial perfusion during a single exercise test: dual isotope imaging with gold-195m and thallium-201. Eur Heart J. 1986;7(6):493–500.
160. Miller DD, Gill JB, Fischman AJ, et al. New radionuclides for cardiac imaging. Prog Cardiovasc Dis. 1986;28(6):419–34.
161. Stone DL, Barber RW, Ormerod OJ, Petch MC, Wraight EP. Quantification of intracardiac shunts by gold-195m, a new radionuclide with a short half life. Br Heart J. 1985;54(5):495–500.
162. Van der Wall EE, van Lingen A, den Hollander W, et al. Short-lived 195mAu for evaluation of left ventricular function by first-pass radionuclide angiography. Nuklearmedizin. 1985;24(4):191–2.
163. Heller GV, Treves ST, Parker JA, et al. Comparison of ultrashort-lived iridium-191m with technetium-99m for first pass radionuclide angiocardiographic evaluation of right and left ventricular function in adults. J Am Coll Cardiol. 1986;7(6):1295–302.
164. Treves S, Cheng C, Samuel A, Fujii A, Lambrecht R. Detection and quantitation of left-right shunting by iridium-191m angiography. In: Medical radionuclide imaging. 2nd ed. Vienna: IAEA; 1981. p. 231–41.
165. Treves S, Cheng C, Samuel A, et al. Iridium- 191 angiocardiography for the detection and quantitation of left-to-right shunting. J Nucl Med. 1980;21(12):1151–7.
166. Treves S, Fyler D, Fujii A, Kuruc A. Low radiation iridium 191m radionuclide angiography: detection and quantitation of left-to-right shunts in infants. J Pediatr. 1982;101(2):210–3.
167. Verani MS, Lacy JL, Ball ME, et al. Simultaneous assessment of regional ventricular function and perfusion utilizing iridium-191m and thallium-201 during a single exercise test. Am J Cardiol Imag. 1988;2:206–13.
168. Franken PR, Dobbeleir AA, Ham HR, et al. Clinical usefulness of ultrashort-lived iridium-191m from a carbon-based generator system for the evaluation of the left ventricular function. J Nucl Med. 1989;30(6):1025–31.

169. Hellman C, Zafrir N, Shimoni A, et al. Evaluation of ventricular function with first-pass iridium-191m radionuclide angiocardiography. J Nucl Med. 1989; 30(4):450–7.
170. Lacy JL, Verani MS, Ball ME, Roberts R. Clinical applications of a pressurized xenon wire chamber gamma camera utilizing the short lived agent 178Ta. Nucl Inst Meth. 1988;A269:369–76.
171. Lacy JL, Layne WW, Guidry GW, Verani MS, Roberts R. Development and clinical performance of an automated, portable tungsten-178/tantalum-178 generator. J Nucl Med. 1991;32(11):2158–61.
172. Lacy JL, Verani MS, Ball ME, Boyce TM, Gibson RW, Roberts R. First-pass radionuclide angiography using a multiwire gamma camera and tantalum-178. J Nucl Med. 1988;29(3):293–301.
173. Verani MS, Guidry GW, Mahmarian JJ, et al. Effects of acute, transient coronary occlusion on global and regional right ventricular function in humans. J Am Coll Cardiol. 1992;20(7):1490–7.
174. Verani MS, Lacy JL, Guidry GW, et al. Quantification of left ventricular performance during transient coronary occlusion at various anatomic sites in humans: a study using tantalum-178 and a multiwire gamma camera. J Am Coll Cardiol. 1992;19(2):297–306.
175. Meller J, et al. Early diagnosis and follow-up of aortitis with [18F]FDG PET and MRI. Eur J Nucl Med Mol Imaging. 2003;30:730–6.

Lymphoscintigraphy

8

Frederick D. Grant, Reid A. Maclellan, and Arin K. Greene

Radionuclide lymphoscintigraphy is the first-line test to assess lymphatic function [1–3]. It is used to diagnose lymphedema, a disease caused by either anomalous development of the lymphatic system or injury to lymphatic vasculature. Lymphoscintigraphy also can be used as a method of sentinel lymph node localization to aid in the staging of some cancers. In children and young adults, sentinel lymph node localization has been used for a variety of tumors [4–9], including melanoma, rhabdomyosarcoma, and non-rhabdomyosarcoma soft tissue sarcomas, such as synovial cell sarcoma.

F.D. Grant, MD (✉)
Joint Program in Nuclear Medicine,
Department of Radiology,
Harvard Medical School,
Boston, MA, USA

Division of Nuclear Medicine and Molecular Imaging,
Department of Radiology,
Boston Children's Hospital,
Boston, MA, USA

Department of Radiology,
Brigham and Women's Hospital,
Boston, MA, USA
e-mail: frederick.grant@childrens.harvard.edu

R.A. Maclellan, MD, MMSc
Department of Plastic and Oral Surgery,
Boston Children's Hospital,
Boston, MA, USA

A.K. Greene, MD, MMSc
Department of Plastic and Oral Surgery,
Boston Children's Hospital, Harvard Medical School,
Boston, MA, USA

Methods

Radiopharmaceuticals

The technique of lymphoscintigraphy relies on imaging the lymphatic transit and lymph node accumulation of radiolabeled colloidal nanoparticles. Many different radiopharmaceutical colloids have been developed for lymphoscintigraphy. Most are labeled with ^{99m}Tc (physical half-life 6.0 h, 140 keV gamma emission), which is readily available in all radiopharmacies and many nuclear medicine departments as a generator product (^{99}Mo > ^{99m}Tc). It also is inexpensive, provides short imaging times, and results in a low radiation dose. In most locations, regulatory restriction and commercially availability typically limit the choices of radiopharmaceutical for routine clinical use in lymphoscintigraphy.

^{99m}Tc-Labeled Sulfur Colloid (Filtered)

In the USA, filtered ^{99m}Tc-labeled sulfur colloid is the primary radiopharmaceutical used for lymphoscintigraphy [10]. Filtering with a 0.2 μm filter results in colloidal particle sizes ranging between 20 and 200 nm in diameter [11], while using a 0.1 μm filter results in colloidal particles smaller than 100 nm, with most smaller than

S.T. Treves (ed.), *Pediatric Nuclear Medicine and Molecular Imaging*,
DOI 10.1007/978-1-4614-9551-2_8, © Springer Science+Business Media New York 2014

55 nm [10]. For lymphoscintigraphy, filtered ^{99m}Tc-labeled sulfur colloid has been administered by a wide variety of routes, but most studies use the intradermal route, rather than subcutaneous or subfascial route, because of the faster uptake and transit that occur after intradermal administration [12, 13].

Intradermal administration of ^{99m}Tc-labeled sulfur colloid can cause transient discomfort due to its low pH [14]. For some patients this may seem only a minor inconvenience, but this is not true for all patients, especially younger children. The application of anesthetic cream before injection may decrease, but does not eliminate, this discomfort. Some investigators have studied the addition of either lidocaine or bicarbonate to the filtered ^{99m}Tc-labeled sulfur colloid preparation before it is administered. In patients undergoing sentinel node mapping for breast cancer, the addition of lidocaine (to make a 1 % solution) can significantly decrease the discomfort associated with subareolar injection [15]. However, for other patients, the transient discomfort associated with intradermal injection of lidocaine [14] may be no better than the transient discomfort associated with intradermal administration of sulfur colloid. Other nuclear medicine departments have found that adjusting the radiopharmaceutical to a neutral pH with sodium bicarbonate relieves most of the discomfort associated with intradermal injection of filtered ^{99m}Tc-labeled sulfur colloid. The addition of both lidocaine and sodium bicarbonate to produce filtered ^{99m}Tc-labeled sulfur colloid with a pH of 7.1 has been shown to maintain radiochemical purity (>92 %) and may result in more desirable particle size [14]. The typical dose of ^{99m}Tc-labeled sulfur colloid is a total administered dose of approximately 18–37 MBq (0.5–1 mCi) for patients of all ages.

^{99m}Tc-Tilmanocept

Recently, the radiopharmaceutical agent ^{99m}Tc-tilmanocept (Lymphoseek®) was approved by the US Food and Drug Administration for sentinel lymph node mapping in patients with breast cancer or melanoma [16]. There has been no reported experience using this agent in children.

Other ^{99m}Tc-Labeled Agents

Other ^{99m}Tc-labeled colloidal particles [10, 11, 13] used for lymphoscintigraphy include ^{99m}Tc-labeled human serum albumin (HSA) colloid, ^{99m}Tc-labeled rhenium sulfide [17], ^{99m}Tc-labeled antimony trisulfide, and ^{99m}Tc-labeled mannosyldextran [18]. Despite differences in particle sizes among these agents, the approach to lymphoscintigraphy is very similar with each one.

Procedures

Evaluation of Lymphatic Function

Lymphoscintigraphy [1–3] most frequently is used to diagnose lymphedema, a disease caused by the anomalous development of the lymphatic system or by injury to lymphatic vasculature. Lymphoscintigraphy also may be helpful in evaluating other abnormalities of lymphatic drainage, including thoracic duct leaks and other primary chylous disorders that may present as chylothorax or chylous ascites.

The radiopharmaceutical (typically filtered ^{99m}Tc-labeled sulfur colloid) is administered by intradermal injection. The volume of each injection should be limited to approximately 100 μl and should contain at least 100 microCi of filtered ^{99m}Tc-labeled sulfur colloid. In practice, we use a total dose of approximately 37 MBq (1 mCi) ^{99m}Tc-labeled sulfur colloid that is diluted and divided among four injections of 100 μl each. Meticulous skin preparation is important because of concern that there may be increased risk of infection in anatomic locations affected by lymphedema. For younger children, a topical anesthetic may decrease discomfort and improve patient cooperation.

The location of radiopharmaceutical injections depends upon the study indication and the involved body region. For lower extremity edema, the traditional site of intradermal injection has been the interdigital webspace. However, we have had excellent results with two intradermal injections placed in the dorsum of each foot just proximal to the toes. This location is easier to clean, and intradermal injections on the dorsum of the foot seem to cause less discomfort than injections in the webspace. Similarly, for evaluation of upper extremity

edema, intradermal injections are made on the dorsum of each hand. In general, the upper and lower extremities cannot be evaluated as part of the same procedure. Usually, foot injections are used to evaluate lymphatic leaks or chylous accumulation in the abdomen or chest [19], but occasionally an upper extremity injection may be helpful for assessing a chylous pleural effusion. Rarely, radiopharmaceutical may be injected at other locations, such as the skin of the scalp to assess scalp edema or in the mucosa of an ileostomy to evaluate gastrointestinal lymphatic function.

Images are acquired as sequential planar images, typically for 5 min each, with a high-resolution collimator. Images should include the extremities of interest and the torso. Transmission images can be acquired with a ^{57}Co flood source, or external markers can be used to outline the body. Typically, images must be acquired at multiple time points to fully characterize lymphatic transit. A standard imaging protocol helps to better define normal and abnormal lymphatic flow and helps for comparison of follow-up studies over time. Lymphatic function can be evaluated with semiquantitative and qualitative features of lymphatic flow. Images acquired during the first 20 min after tracer injection provide early images of the distal extremity lymphatic system.

Images acquired at 45–60 min should demonstrate normal transit of tracer from the feet to the pelvis with tracer accumulation in the inguinal and pelvic lymph nodes (Fig. 8.1). Delayed tracer accumulation in the pelvic lymph nodes suggests abnormal lymphatic transit in the adjacent limb (Fig. 8.2). In the upper extremities, tracer accumulation can be detected in the axillary lymph nodes within 30 min and may be seen as soon as 10 min after tracer injection (Fig. 8.3). In the lower extremities, ambulation may stimulate lymphatic transit, and if pelvic lymph nodes are not visualized by 1 h, patients can be encouraged to stroll in the department or hospital before returning for later images that can be obtained between 2 and 4 h after tracer injection. Similarly, light lifting may accelerate lymphatic transit in the upper extremities.

Lymphatic flow also can be evaluated by the patterns of tracer accumulation in the extremity. Signs of delayed lymphatic drainage include prominent and dilated lymphatic channels, the presence of collateral lymphatic channels, tracer accumulation in extensive cutaneous collaterals (dermal backflow), and a paucity of inguinal and pelvic lymph nodes showing tracer accumulation (Fig. 8.2) [10, 20].

For most regions of the body, the normal pathway of lymphatic drainage is from the periphery to the central lymphatic structures, the cisterna chyli and thoracic duct, which then drain into the left subclavian vein. Lymphatic drainage from the right side of the head and neck, the right arm, and some of the right thorax is through the right lymphatic duct, which drains into the right subclavian vein. Therefore, lymphatic transit should carry the radiolabeled nanoparticles from the injection site to the blood circulation. Subsequent accumulation of ^{99m}Tc-labeled sulfur colloid in the liver confirms that this pathway of lymphatic drainage is intact. Typically, liver accumulation is seen within the first 4 h, but in some patients with slow lymphatic drainage, delayed images may have to be acquired as late as 24 h to confirm that the central lymphatic drainage is intact.

Lymphoscintigraphy may be helpful in the evaluation of chylous ascites or chylous pleural effusion (Fig. 8.4). In some cases of chylous pleural effusion, it may be helpful to perform injection in the right arm as a separate study and compare the pattern of lymphatic drainage to the pattern seen after injection in either the left arm or the feet. For example, in a patient with a post-surgical leak in the thoracic duct, tracer injected into the feet can accumulate in the thoracic cavity, while tracer injected into the arms may enter the peripheral circulation.

Sentinel Lymph Node Localization

In children and young adults, sentinel node localization is used to assist in the staging of a wide variety of tumors, using techniques similar to those used in adults [11, 13]. Lymphoscintigraphy for sentinel node localization typically is performed as the first case of the morning to facilitate scheduling of the surgical procedure. However, in rare cases, it may be possible to perform lymphoscintigraphy up to 15 h prior to surgery.

Fig. 8.1 Normal lymphoscintigraphy. (**a**) After intradermal injection in the dorsum of the feet, filtered ^{99m}Tc-labeled sulfur colloid undergoes proximal lymphatic transit in lymphatic channels along the medial aspect of each leg. Within 45–60 min, there is a symmetrical pattern of tracer accumulation in inguinal and pelvic lymph nodes. Co-registration with a transmission image of the body is helpful for anatomic localization. (**b**) With additional time, there is further accumulation of tracer in popliteal, inguinal, and pelvic lymph nodes. Tracer accumulation within the liver should be apparent within 4 h and confirms that there is intact lymphatic transit through the thoracic duct and into the systemic circulation

Radiopharmaceutical (typically filtered ^{99m}Tc-labeled sulfur colloid) is administered by intradermal injection around the tumor site. Most guidelines [11, 13] recommend placing the injections within 0.5–1.0 cm of a cutaneous tumor or scar. For intradermal or subdermal injections, the volume of each injection should be limited to approximately 100 μl and should contain at least 100 microCi of filtered ^{99m}Tc-labeled sulfur colloid. In practice, we use a total dose of 18–37 MBq (0.5–1 mCi) ^{99m}Tc-labeled sulfur colloid that is diluted and divided among two to four injections of 100 μl each. The number and the location of the injections will be guided by the tumor type, tumor location, and prior surgery.

For a cutaneous tumor on an extremity (Fig. 8.5), radiopharmaceutical should be injected at two to four sites proximal to the tumor, as lymphatic flow should be proximal towards the torso [13]. Cutaneous tumors on the head, neck, trunk, and upper thighs have less predictable lymphatic drainage (Fig. 8.6). In these cases, at least four injections may be placed around the entire lesion or site of prior surgery [11]. However, care should

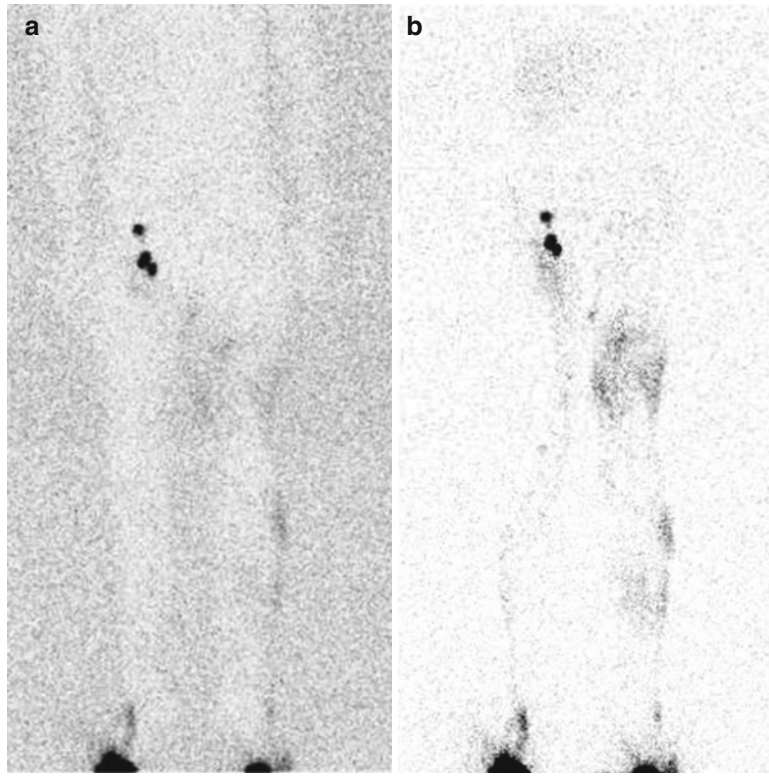

Fig. 8.2 Abnormal lymphatic function demonstrated by lymphoscintigraphy. (**a**) In a 7-year-old boy with left lower extremity edema, lymphoscintigraphy is performed after intradermal injection of filtered ^{99m}Tc-labeled sulfur colloid in the dorsum of each foot. After 50 min, tracer accumulation in numerous pelvic lymph nodes demonstrates normal lymphatic transit in the right leg. In the left leg, abnormal lymphatic transit is demonstrated by the absence of tracer accumulation in pelvic lymph nodes. Cutaneous accumulation of tracer (dermal backflow) also suggests abnormal lymphatic drainage of the left leg. Co-registration with a transmission image is helpful for anatomic localization. (**b**) After 2 h, tracer accumulation in the liver confirms lymphatic flow through an intact thoracic duct to the systemic circulation. A normal pattern of lymphatic channels is seen along the medial aspect of the right leg. In the left leg, extensive cutaneous tracer accumulation (dermal backflow) and the absence of tracer accumulation in pelvic lymph nodes confirm the diagnosis of lymphedema

be taken to limit masking the potential site of a nearby sentinel lymph node [13], and it may be appropriate to use fewer injection sites. For subcutaneous soft tissue tumors, the injection site is identified by palpation and correlation with cross-sectional imaging. Typically, two to four injections are made. One approach is to place an intradermal injection at each of the four quadrants of the tumor, determined by the diagonals of maximum transverse and longitudinal diameters of the tumor [9]. Alternatively, two of the injections may be peritumoral injections [21].

For many tumors, sentinel lymph node localization will be performed at the time that that primary tumor is resected. However, for cutaneous tumors, including melanoma, an initial excision or excisional biopsy may have been performed before the patient is referred for definitive surgical care. In these cases, radiopharmaceutical injection sites will be guided by the scar left by the prior surgery. In an extremity, drainage from the distal margin of a surgical scar may be disrupted and likely will demonstrate slower transit compared to particles injected on the proximal margin of a scar. Therefore, in the extremities, it may be appropriate to place two injections on only the proximal aspect of a transverse scar [11] or at each end of the scar. There is little information

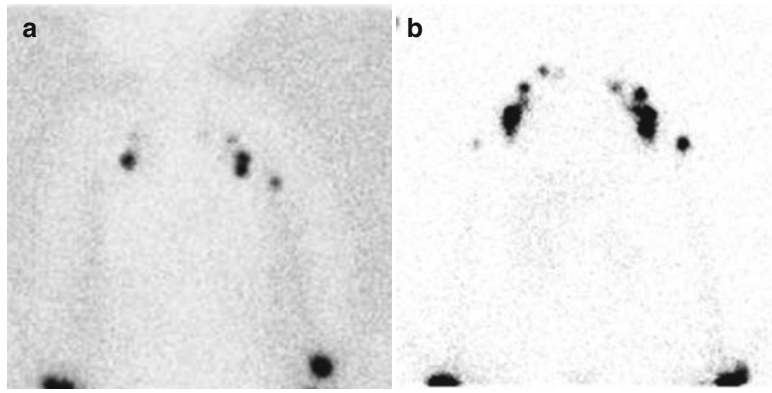

Fig. 8.3 Normal lymphoscintigraphy of the upper extremities. A 1-year-old infant with fullness of the hands was referred for evaluation of possible lymphedema. (**a**) For the upper extremities, lymphoscintigraphy was performed after intradermal injection of filtered ^{99m}Tc-labeled sulfur colloid in the dorsum of each hand. (**a**) Within 20 min, a normal pattern of tracer accumulation is seen in brachial, axillary, and infraclavicular lymph nodes. (**b**) After 2 h, additional tracer accumulation is seen in brachial, axillary, infraclavicular, and supraclavicular lymph nodes. Tracer accumulation in the liver confirms lymphatic drainage into the systemic circulation

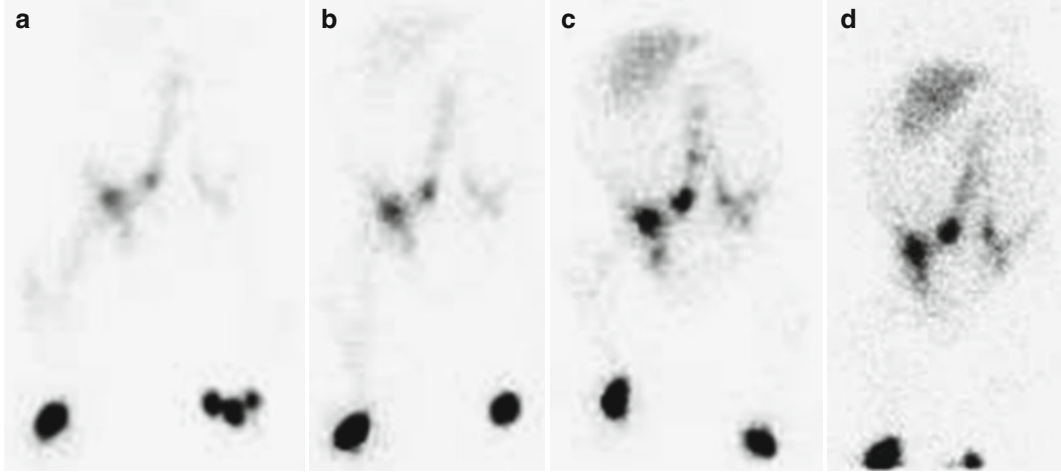

Fig. 8.4 Lymphoscintigraphy for evaluation of chylous ascites. In a 2-month-old infant with congenital chylous ascites, lymphoscintigraphy is performed after intradermal injection of filtered ^{99m}Tc-labeled sulfur colloid in the dorsum of each foot. Within 10 min (**a**), there is demonstration of normal lymphatic transit of tracer to inguinal and pelvic lymph nodes. After 30 min (**b**), there is prominent tracer accumulation in the midline of the abdomen, although tracer accumulation in the liver confirms lymphatic drainage into the systemic circulation. With additional imaging at 45 min (**c**) and 120 min (**d**), progressive diffuse accumulation of tracer within the abdominal cavity demonstrates an intra-abdominal lymphatic leak. Exploratory laparotomy demonstrated jejunal lymphangiectasis, which was treated successfully with a low-fat diet, sclerotherapy, and octreotide

about the effect of prior surgery on the accuracy of lymphoscintigraphy for sentinel node detection with pediatric solid tumors, but prior surgery does increase the rate of false-negative lymphoscintigraphy in patients with breast cancer [21]. Delayed lymphatic transit can occur if the skin injections are placed subcutaneously [12] or if the nearby tissue is inflamed or scarred [11]. Some guidelines [11, 13] suggest massaging the injection sites, but this rarely seems necessary.

Images are acquired as sequential planar images, typically for 5 min each with a high-resolution collimator. Images should include the injection site and any likely sites of sentinel

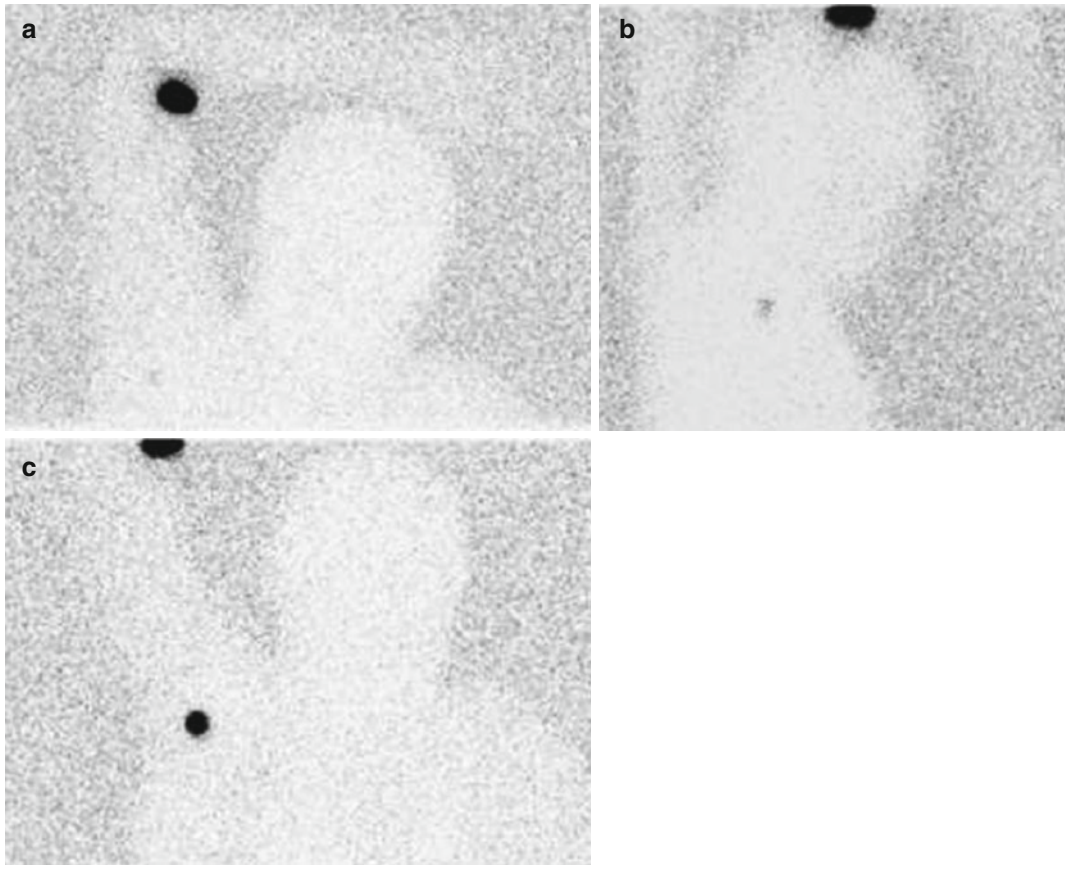

Fig. 8.5 Sentinel lymph node localization in a 13-year-old boy with synovial sarcoma in the right antecubital fossa. Lymphoscintigraphy is performed after two intradermal injections of filtered ^{99m}Tc-labeled sulfur colloid in the antecubital fossa. Planar images are co-registered with transmission images for anatomic localization. (**a**) After 25 min, a single focus of tracer accumulation is identified in the right axilla. (**b**) An image acquired in the lateral projection also demonstrates a single focus of tracer accumulation. (**c**) A small radioactive marker is used to confirm the location of the sentinel lymph node before the overlying skin is marked

node localization. For tumors located in an extremity or in the head or neck, the adjacent torso should be included. For tumors located on the torso, the entire torso should be imaged. Typically, a sentinel node is visualized between 30 and 60 min after injection. A number of techniques are helpful for localizing the sentinel node. Transmission images can be acquired with a ^{57}Co flood source, or external markers can be used to outline the body. Good localization of the sentinel node usually requires additional lateral or oblique views. Care should be taken to ensure that, in a drainage bed, the first node to be visualized is identified as the sentinel lymph node. The sentinel lymph node may not be the most intense focus of uptake identified on lymphoscintigraphy [11, 13, 22]. If necessary, additional images may be acquired at later times, although this likely will disrupt the operating room schedule.

Once the sentinel node is identified, the overlying skin is marked with a surgical pen marker. Using a handheld radioactive marker can be very helpful for confirming the exact location to be marked on the skin. Ideally, the location of the sentinel node is marked while the patient is in the same position as they will be in the operating room. For example, if the surgical procedure will be performed with arms out to the side, then the sentinel node should be localized and marked while the arms are out to the side.

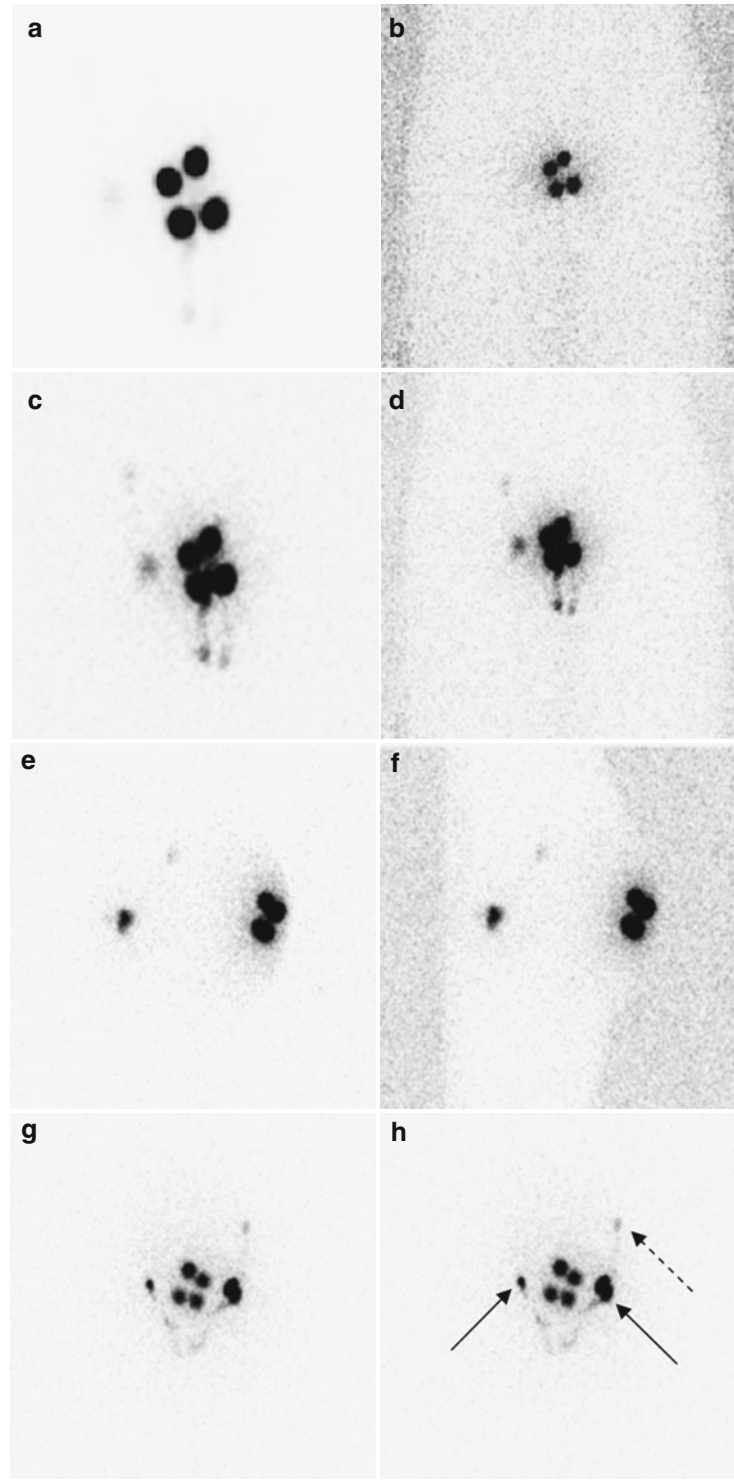

Fig. 8.6 Sentinel lymph node localization in a 16-year-old boy with a melanoma of the gluteal crease. Lymphoscintigraphy is performed after four intradermal injections of filtered ^{99m}Tc-labeled sulfur colloid around the site of prior surgical resection. By 5 min, there is a small amount of lymphatic transit of tracer from the sites of injection (**a**: posterior image, **b**: with transmission scan). By 20 min, there is lymphatic transit along the perineum and into the inguinal region (**c**: posterior image, **d**: with transmission scan). Additional imaging demonstrates lymph node accumulation in inguinal and pelvic lymph nodes (**e**: lateral image, **f**: lateral image with transmission scan, **g**: anterior image). The overlying skin was marked to indicate the location of sentinel lymph nodes in both inguinal regions (*solid arrows*). (**h**) A pelvic lymph node (*dashed arrow*) does not represent a sentinel lymph node

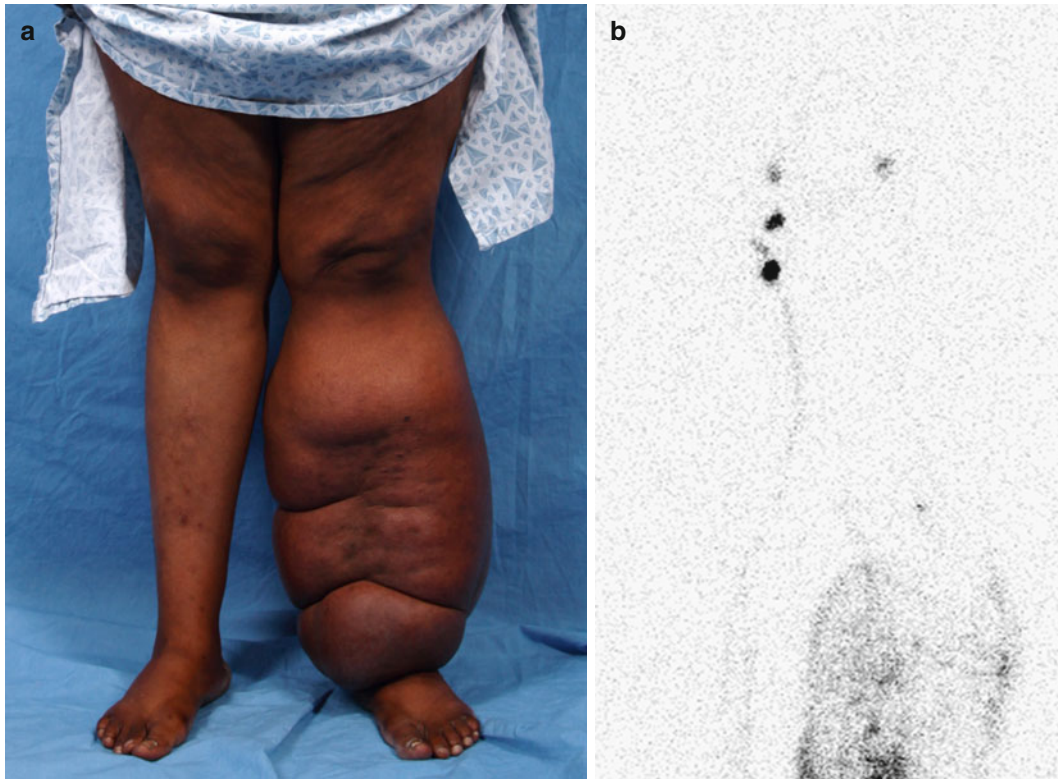

Fig. 8.7 Lymphoscintigraphy to confirm the diagnosis of lymphedema. (**a**) A 30-year-old woman had experienced swelling of the left lower extremity since adolescence. (**b**) Lymphoscintigraphy is performed after intradermal injection of filtered ^{99m}Tc-labeled sulfur colloid in the dorsum of each foot. After 45 min, normal tracer accumulation is seen in the right inguinal lymph nodes. On the left, the absence of inguinal lymph node tracer accumulation and cutaneous tracer accumulation (dermal backflow) confirms the diagnosis of adolescent-onset lymphedema in the left lower extremity

In some cases, marking in two planes may help the surgeon determine the appropriate incision site for lymph node excision (Fig. 8.5). SPECT usually is of little benefit as there are few landmarks for localization, but some nuclear medicine departments now use SPECT/CT to assist in localizing sentinel lymph nodes [23]. With tumors located in extremities, the sentinel lymph usually is located in either the inguinal or axillary region. Tumors on the head, neck, or torso may drain to multiple lymph node regions, and a sentinel lymph node should be identified and marked in each region where tracer accumulation is seen in a lymph node (Fig. 8.6). Once the patient is in the operating room, the lymph bed is surgically exposed and a portable gamma probe is used to identify and localize potential sentinel lymph nodes. One approach is to surgically resect any lymph node with a count rate 10–20 times background [11, 13]. Another approach is to remove the lymph node containing the greatest activity. Then, any other lymph nodes containing at least 10 % of the activity of the hottest lymph node are resected for histological evaluation [22].

Clinical

Lymphedema

Lymphedema is a common condition, affecting as many as 200 million people worldwide [24, 25]. In individuals with lymphedema, extracellular fluid accumulates in the interstitial space and causes progressive enlargement of the affected area; there is no cure. The extremities are most commonly involved, followed by the genitalia (Fig. 8.7).

Table 8.1 Classification of lymphedema

Primary
(Idiopathic)
Infant onset (birth–1 year)
Childhood onset (1–9 years)
Adolescent onset (10–21 years)
Adult onset (>21 years)
Secondary
(Injury to lymph nodes and/or lymphatic vessels)
Infection (e.g., cellulitis, parasite Wuchereria bancrofti)
Malignancy (e.g., lymphadenectomy, radiation, metastasis)
Trauma (e.g., penetrating, severe burns, iatrogenic postsurgical)

Complications include functional disability, psychosocial morbidity, infection, skin changes, and rarely, malignant transformation. Primary (idiopathic) lymphedema is rare; the incidence is 1.2 per 100,000 persons younger than 20 years old [26, 27]. Secondary lymphedema is the most common cause of the disease (Table 8.1). Worldwide, the most common cause of secondary lymphedema is filariasis, but in North America it typically results from injury or surgical removal of lymph nodes or lymphatic vasculature (Fig. 8.8).

A clinical diagnosis of lymphedema usually can be made by history and physical examination, but cannot be confirmed by tissue biopsy as histopathology shows only nonspecific inflammation in patients with lymphedema [1, 3]. However, 27 % of patients referred to the Children's Hospital Lymphedema Program for evaluation of "lymphedema" were found to have another condition [3]. The term "lymphedema" often has been used to describe any extremity overgrowth, regardless of the underlying cause. Many pathophysiological processes can result in extremity swelling/enlargement (Table 8.2), but lymphedema is a specific disorder that results from malfunction of the lymphatic vessels. It is important to confirm the diagnosis of lymphedema because the prognosis and management is different for lymphedema than for other causes of extremity enlargement.

Patients with suspected lymphedema undergo radionuclide lymphoscintigraphy for diagnostic confirmation and to obtain a qualitative assessment of lymphatic function. Lymphoscintigraphy serves as the definitive diagnostic study for lymphedema and can be 92 % sensitive and 100 % specific for the condition [28, 29]. Lymphoscintigraphy has replaced lymphangiography (direct injection of lymphatic channels with radiopaque contrast) for the assessment of the lymphatic vasculature. Patients undergoing lymphangiography can experience allergic reactions to the contrast, lymphangitis (19 %), or worsening lymphedema (32 %) [30], but these complications do not occur with lymphoscintigraphy. Despite concerns about an increased risk of infection after intradermal injection, this complication is not observed when appropriate technique and skin preparation are used [31]. Other imaging methods, including MRI, CT, and ultrasonography, are neither sensitive nor specific for lymphedema [1–3]. For example, ultrasonography shows nonspecific skin thickening in regions with lymphedema. MRI and CT findings in lymphedema include thickened skin and subcutaneous tissue with fluid and stranding above the muscle fascia. MR lymphangiography has been used to visualize lymphatic vessels, but does not perform as well as lymphoscintigraphy for evaluating inguinal lymph nodes [32].

The results of lymphoscintigraphy have important implications for patient management. If lymphoscintigraphy confirms delayed lymphatic transport consistent with lymphedema, then the patients are counseled that they have a progressive and incurable condition, but one that can be managed to decrease morbidity and to improve quality of life. Based on the severity of the delayed lymphatic transport, patients can be counseled about the severity of the lymphatic dysfunction and the likelihood of complications. For example, an individual with a markedly prolonged transit time of 5 h to the axillary/inguinal nodes and with dermal backflow has more severe dysfunction and may have a potentially poorer prognosis than another individual with a mildly delayed transit time of 2 h and no other signs of abnormal lymphatic flow, such as dermal backflow. Patients with

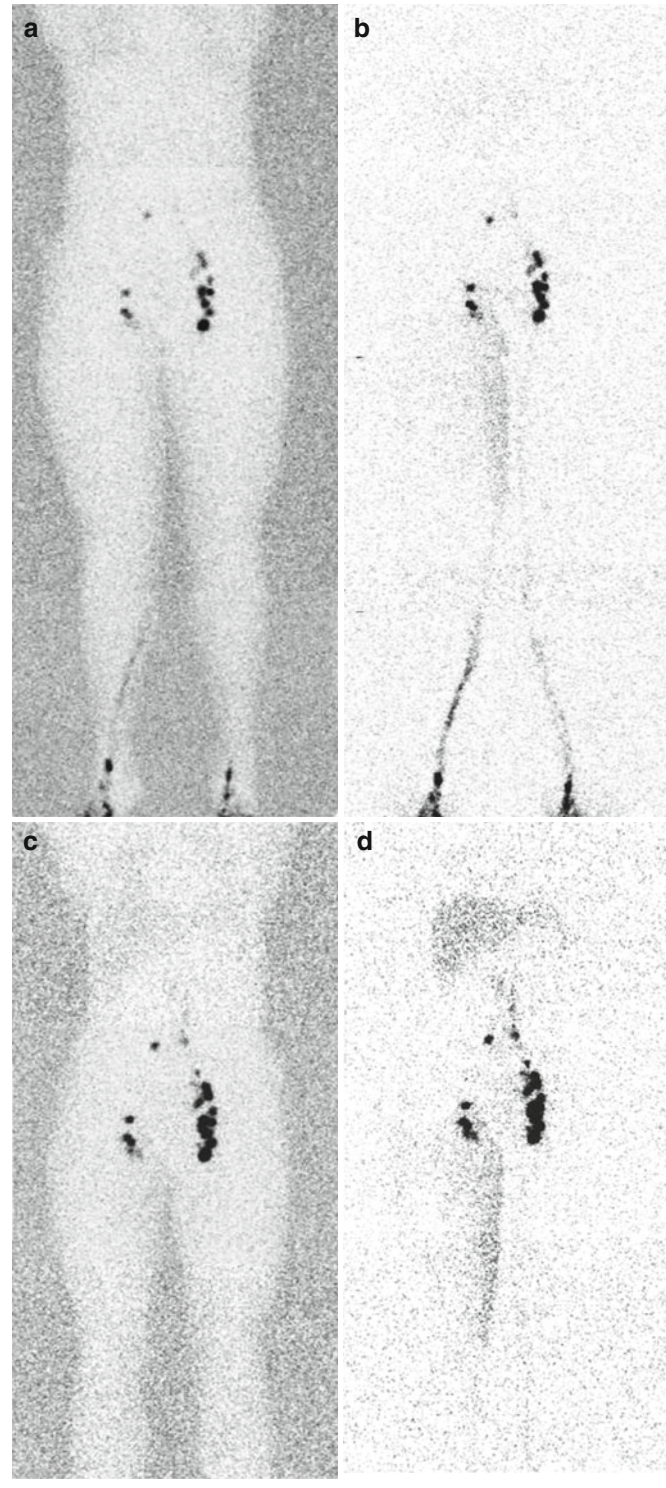

Fig. 8.8 Lymphoscintigraphy to evaluate secondary lymphedema. Two years after extensive surgical resection of a right pelvic Ewing sarcoma, an 18-year-old male had persistent right leg swelling, which was most prominent in the medial right thigh. Lymphoscintigraphy is performed after intradermal injection of filtered ^{99m}Tc-labeled sulfur colloid in the dorsum of each foot. (**a**) After 45 min, there is lymphatic transit of tracer to inguinal and pelvic lymph nodes, but fewer lymph nodes are visualized on the right compared to the left. A co-registered transmission scan is used for anatomic localization and demonstrates asymmetry (right larger than left) in leg diameter. (**b**) Without the co-registered transmission scan, a normal pattern of lymphatic channels can be seen along the medial aspect of both legs. There is diffuse tracer accumulation along the medial aspect of the right thigh. (**c**) After 3 h, there is additional accumulation of tracer in inguinal, pelvic, and retroperitoneal lymph nodes, and tracer accumulation in the liver confirms lymphatic transit of tracer to the systemic circulation. (**d**) Without the co-registered transmission scan, extensive tracer accumulation can be identified more clearly in the region of prominent lymphedema in the medial right thigh

Table 8.2 Differential diagnosis of extremity enlargement in pediatric patients referred with "lymphedema"

Capillary malformation
Hemihypertrophy
Infantile hemangioma
Kaposiform hemangioendothelioma
Klippel-Trenaunay syndrome
Lipedema
Lipofibromatosis
Lymphatic malformation
Noneponymous combined vascular malformation (e.g., capillary-venous malformation)
Obesity
Parkes Weber syndrome
Posttraumatic swelling (e.g., ligament sprain, occult fracture)
Rheumatological disease (e.g., tenosynovitis, rheumatoid arthritis)
Systemic causes of edema (cardiac, renal, hepatic disease)
Venous malformation
Venous stasis disease

lymphedema are at increased risk for infection. Skin moisturizers are used to avoid desiccation, which is another risk factor for infection. To avoid incidental cuts or injury, individuals with lymphedema are advised to wear protective clothing and to avoid walking barefoot. Compression therapy using custom-fitted garments as well as pneumatic compression can be helpful for many individuals.

If lymphoscintigraphy shows normal lymphatic transit, then alternative causes of extremity swelling must be investigated. The patient can be advised that protective clothing and compression measures are unlikely to be necessary. In patients with normal lymphatic function, the most likely causes of lower extremity edema are venous dysfunction or systemic disease, including cardiac, renal, and hepatic disease. Occasionally, MRI will be helpful to exclude other musculoskeletal disorders, such as tendonitis or ligamentous injury, before initiating a rheumatological evaluation. In North America, lymphatic filariasis is an unlikely cause of lymphedema, but lymphoscintigraphy can demonstrate abnormal lymphatic drainage in patients with this infection [33]. As lymphoscintigraphy is only 92 % sensitive for lymphedema [28, 29], some individuals with lymphedema may not be identified with lymphoscintigraphy. Individuals with clinical findings consistent with lymphedema and who have undergone a thorough evaluation revealing no other cause for extremity swelling are counseled that they may be in the latent phase of the disease that is not yet evident on radionuclide lymphoscintigraphy.

Sentinel Lymph Node Localization

The use of sentinel lymph node localization is well established for adults with certain tumors, such as breast cancer, melanoma, and some soft tissue sarcomas. Sentinel lymph node localization is used much less frequently in children and young adults, but it has been used in this age group to assist in the staging of a wide variety of tumors [4–9], including melanoma and other cutaneous tumors, rhabdomyosarcoma, and non-rhabdomyosarcoma soft tissue sarcomas, such as synovial cell sarcoma.

A sentinel lymph node refers to a lymph node that receives lymphatic drainage from a tumor [34]. Tumor spread to lymph nodes has important implications for tumor staging, and for many decades the standard practice was to look for lymph node spread by performing extensive lymph node dissection in the tumor bed likely to receive lymphatic drainage from the tumor. Problems with this approach included the absence of a method to confirm that the lymph node region received lymphatic drainage from a tumor, the low sensitivity for identifying microscopic disease among a large number of dissected lymph nodes, and the high rate of postoperative lymphedema caused by the disruption of lymphatic drainage of the affected region. More recently, the approach of sentinel lymph node mapping has been adopted for many adult and pediatric tumors [21, 35]. Successful implementation of sentinel lymph node mapping requires collaboration, coordination, and communication among surgeons, anesthesiologists, nuclear medicine physicians, and pathologists.

References

1. Schook CC, Mulliken JB, Fishman SJ, Grant FD, Zurakowski D, Greene AK. Primary lymphedema: clinical features and management in 138 pediatric patients. Plast Reconstr Surg. 2011;127:2419–31.
2. Slavin SA, Schook C, Greene AK. Lymphedema. Br Med J Point Care. www.pointofcare.bmj.com. 2011.
3. Schook CC, Mulliken JB, Fishman SJ, Alomari AI, Greene AK. Differential diagnosis of lower extremity lymphedema in pediatric patients referred with a diagnosis of lymphedema. Plast Reconstr Surg. 2011;127:1571–81.
4. Neville HL, Andrassy RJ, Lally KP, Corpron C, Ross MI. Lymphatic mapping with sentinel node biopsy in pediatric patients. J Pediatr Surg. 2000;35:961–4.
5. Kayton ML, Delgada R, Busam K, et al. Experience with 31 sentinel lymph node biopsies for sarcomas and carcinomas in pediatric patients. Cancer. 2008;112:2052–9.
6. Gow KW, Rapkin LB, Olson TA, Durham MM, Wyly B, Shehata BM. Sentinel lymph node biopsy in the pediatric population. J Pediatr Surg. 2008;43:2193–8.
7. Tunn P-U, Andreou D, Illing H, Fleige B, Dresel S, Schlag PM. Sentinel node biopsy in synovial sarcoma. Eur J Surg Oncol. 2008;34:704e–7.
8. De Corti F, Dall'Igna P, Bisogna G, et al. Sentinel node biopsy in pediatric soft tissue sarcomas of extremities. Pediatr Blood Cancer. 2009;52:51–4.
9. Parida L, Morrisson GT, Shammas A, et al. Role of lymphoscintigraphy and sentinel lymph node biopsy in the management of pediatric melanoma and sarcoma. Pediatr Surg Int. 2012;28:571–8.
10. Hung JC, Wiseman GA, Wahner HW, et al. Filtered technetium-99m-sulfur colloid evaluated for lymphoscintigraphy. J Nucl Med. 1995;36:1895–901.
11. Mariani G, Gipponi M, Moresco L, et al. Radioguided sentinel lymph node biopsy in malignant cutaneous melanoma. J Nucl Med. 2002;43:811–27.
12. Kersey TW, Van Eyk J, Lannin DR, Chua AN, Tafra L. Comparison of intradermal and subcutaneous injections in lymphatic mapping. J Surg Res. 2001;96:255–9.
13. Alazraki N, Glass EC, Castronovo F, Valdés Olmos RA, Podoloff D. Society of Nuclear Medicine procedure guideline for lymphoscintigraphy and the use of intraoperative gamma probe for sentinel lymph node localization in melanoma of intermediate thickness: version 1.0. J Nucl Med. 2002;43:1414–8.
14. Loveless VS, Surdock CP, Bhattacharjee H. Evaluation of zeta-potential and particle size of technetium ^{99m}Tc-sulfur colloid subsequent to the addition of lidocaine and sodium bicarbonate. J Nucl Med Technol. 2010;38:49–52.
15. Stojadinovic A, Peoples GE, Jurgens JS, et al. Standard versus pH-adjusted and lidocaine supplemented radiocolloid for patients undergoing sentinel-lymph-node mapping and biopsy for early breast cancer (PASSION-P trial): a double-blind, randomised controlled trial. Lancet Oncol. 2009;10:849–54.
16. Wallace AM, Han LK, Povoski SP, et al. Comparative evaluation of [^{99m}Tc]tilmanocept for sentinel lymph node mapping in breast cancer patients: Results of two phase 3 trials. Ann Surg Oncol. 2013;20:2590–9.
17. Temple CL, Scilley CG, Engel CJ, et al. Sentinel node biopsy in melanoma using technetium-99m rhenium colloid: the London experience. Ann Plast Surg. 2000;45:491–9.
18. Vera DR, Wallace AM, Hoh CK, Mattrey RF. A synthetic macromolecule for sentinel node detection: ^{99m}Tc-DTPA-mannosyl-dextran. J Nucl Med. 2001;42:951–9.
19. Bybel B, Neumann DR, Kim BY, Amin K, Rice T. Lymphoscintigraphy using ^{99m}Tc filtered sulfur colloid in chylothorax: a case report. J Nucl Med Technol. 2001;29:30–1.
20. Weissleder H, Weissleder R. Lymphedema: evaluation of qualitative and quantitative lymphoscintigraphy in 238 patients. Radiology. 1988;167:729–35.
21. Hindié E, Groheux D, Brenot-Rossi I, Rubello D, Moretti J-L, Espié M. The sentinel node procedure in breast cancer: nuclear medicine as the starting point. J Nucl Med. 2011;52:405–14.
22. Martin 2nd RC, Edwards MJ, Wong SL, et al. Practical guidelines for optimal gamma probe detection of sentinel lymph nodes in breast cancer: results of a multi-institutional study. Surgery. 2000;128:139–44.
23. Seo Y, Aparici CM, Chen CP, et al. Mapping of lymphatic drainage from the prostate using filtered ^{99}mTc-sulfur nanocolloid and SPECT/CT. J Nucl Med. 2011;52:1068–72.
24. Moffatt CJ, Franks PJ, Doherty DC, et al. Lymphoedema: an underestimated health problem. Q J Med. 2003;96:731–8.
25. Rockson SG, Rivera KK. Estimating the population burden of lymphedema. Ann N Y Acad Sci. 2008;1131:147–54.
26. Smeltzer DM, Stickler GB, Schirger A. Primary lymphedema in children and adolescents: a follow-up study and review. Pediatrics. 1985;76:206–18.
27. Greene AK, Schook CC. Primary lymphedema: definition of onset based on developmental age. Plast Reconstr Surg. 2012;129:221e–2.
28. Gloviczki P, Calcagno D, Schirger A, et al. Noninvasive evaluation of the swollen extremity: experiences with 190 lymphoscintigraphic examinations. J Vasc Surg. 1989;9:683–9.
29. Szuba A, Shin WS, Strauss HW, Rockson S. The third circulation: radionuclide lymphoscintigraphy in the evaluation of lymphedema. J Nucl Med. 2003;44:43–57.
30. O'Brien BM, Das SK, Franklin JD, Morrison WA. Effect of lymphangiography on lymphedema. Plast Reconstr Surg. 1981;68:922–6.
31. Greene AK, Borud L, Slavin SA. Blood pressure monitoring and venipuncture in the lymphedematous extremity. Plast Reconstr Surg. 2005;116:2058–9.

32. Notohamiprodjo M, Weiss M, Baumeister R, et al. MR lymphangiography at 3.0 T: correlation with lymphoscintigraphy. Radiology. 2012;264:78–87.
33. Subramanyam P, Palaniswamy SS. Lymphoscintigraphy in unilateral lower limb and scrotal lymphedema caused by filariasis. Am J Trop Med Hyg. 2012;87:963–4.
34. Mansel RE, Khonji NI, Clarke D. History, present status, and future of sentinel node biopsy in breast cancer. Acta Oncol. 2000;39:265–8.
35. Cochran AJ, Roberts AA, Saida T. The place of lymphatic mapping and sentinel node biopsy in oncology. Int J Clin Oncol. 2003;8:139–50.

9 Gastroesophageal Reflux, Gastric Emptying, Esophageal Transit, and Pulmonary Aspiration

Zvi Bar-Sever

Gastroesophageal Reflux

Definition, Pathophysiology, and Clinical Manifestations

The definition of gastroesophageal reflux (GER) is the passage of gastric contents into the esophagus. Regurgitation is defined as passage of refluxed gastric contents into the mouth. Vomiting is the expulsion of gastric contents from the mouth. Many episodes of gastroesophageal reflux occur in healthy infants and children and are considered "physiological." Such episodes are brief and either asymptomatic or cause mild regurgitation or occasional vomiting [1]. Gastroesophageal reflux disease (GERD) occurs when episodes of GER produce symptoms and complications.

The lower esophageal sphincter is the main barrier preventing retrograde passage of gastric contents into the esophagus. While the baseline tone of the lower esophageal sphincter (LES) is normal in most children with GER, transient relaxations of the sphincter, unrelated to swallowing, and inadequate adaptation of the sphincter tone to changes in abdominal pressure are the main mechanisms causing GER [2, 3]. Distention of the gastric wall can produce transient relaxations of the LES [4, 5]. Prolonged distension of the gastric walls due to delayed emptying is a proposed mechanism explaining the relationship between the two conditions. Delayed gastric emptying has been documented in adults with GERD [6–8]. In children, this relationship is controversial. Some authors found delayed gastric emptying in children with GERD while others did not [9–13]. In one study, involving 477 children, delayed gastric emptying was noted only in children with GERD that were older than 6 years [14]. According to another study, gastroesophageal reflux in children is worsened by increasing the volume and osmolality of meals that affect the LES pressure [15].

It is not well established why GER is asymptomatic in some children and produces clinical manifestations in others. Multiple factors can contribute to the pathogenesis of GERD including the frequency and duration of reflux, gastric acidity, gastric emptying, esophageal mucosal barrier, esophageal clearing mechanisms, and airway hypersensitivity. Clustering of severe GERD in families and a higher prevalence of acid reflux in monozygotic twins compared with dizygotic twins provide evidence for genetic disposition for GERD. This genetic component however only accounts for a small number of GERD cases [16, 17]. The prevalence of GER and GERD is not well established. According to some authors it ranges from 20 to 40 % in infants and 7 to 20 % in older children and adolescents [18–20]. One study found GER to be very common in preterm infants of less than 34 weeks of gestation (60–70 %) who

Z. Bar-Sever, MD
Faculty of Medicine, Tel-Aviv University, Tel-Aviv, Israel

Department of Nuclear Medicine, Schneider Children's Medical Center, Petach Tikvah, Israel
e-mail: barsever@clalit.org.il

S.T. Treves (ed.), *Pediatric Nuclear Medicine and Molecular Imaging*,
DOI 10.1007/978-1-4614-9551-2_9,

underwent gastroesophageal reflux scintigraphy. The frequency and the severity of reflux was not significantly different in symptomatic versus asymptomatic babies [21]. The prevalence of GER may be even higher when determined by clinical symptoms commonly associated with GER, especially vomiting [22]. The higher frequency of GER and GERD in infants is associated with transient immaturity of the esophagus and stomach [1].

Gastroesophageal reflux disease can affect the gastrointestinal and respiratory systems. Clinical manifestations vary with age. The main GER-related symptom in infants is recurrent vomiting. It occurs in 50 % of infants during the first 3 months of life and in 67 % of 4 months old infants. Vomiting resolves spontaneously in the majority of infants and is only encountered in 5 % of infants at the age of 10–12 months [22]. Severe symptoms of anorexia, dysphagia, painful swallowing, irritability, hematemesis, anemia, and failure to thrive occur only in a small number of infants and are related to complications of esophagitis. GER in infants has been associated with respiratory complications, including apnea and apparent life-threatening events (ALTE), recurrent pneumonia, hyperactive airway disease, chronic cough, and recurrent stridor. In preschool children, the main manifestation of GER is intermittent vomiting. In older children, common symptoms include heartburn or regurgitation with reswallowing. Rarely, esophageal pain may produce repetitive stretching and arching movements (Sandifer syndrome) commonly mistaken for atypical seizures or dystonia [23, 24]. Esophagitis in older children can manifest as dysphagia and in severe cases result in hematemesis, anemia, hypoproteinemia, and melena. Esophageal strictures and circumferential scarring can complicate untreated esophagitis.

Erosive esophagitis is encountered in less than 5 % of thriving children and is much more common in children with neurological disabilities. Chronic esophagitis may lead to replacement of the distal esophageal mucosa with Barrett's mucosa, a metaplastic, potentially malignant epithelium [25]. Barrett's esophagus is found in fewer than 2 % of children with GERD [1]. A strong association was found between gastroesophageal reflux disease and dental erosions [26]. Gastroesophageal reflux is prevalent in children with asthma. Recent research suggests that the presence of gastric acid in the esophagus alters bronchial hyperresponsiveness and that effective treatment of GERD can improve respiratory disease in selected asthma patients [27]. Aspiration pneumonia due to gastroesophageal reflux is mostly encountered in neurologically impaired children. Hoarseness also has been associated with GER in children.

Diagnosis of Gastroesophageal Reflux

Extended Esophageal pH Monitoring

Twenty-four-hour esophageal pH monitoring is the most widely accepted tool for the diagnosis of GER. This technique measures esophageal exposure to gastric acid by detecting the concentration of hydrogen ions (pH) in the distal esophagus. Values under 4 are used to indicate gastric acid exposure due to reflux (the normal esophageal pH varies from 5 to 7). The study has a sensitivity and specificity over 90 % for detection of gastroesophageal reflux disease and is considered by many as the gold standard. The electrode is placed a few centimeters above the LES, in the distal esophagus, and records the frequency and duration of reflux episodes and the accumulated exposure times. These parameters are integrated into a composite score that correlates with the degree of esophageal epithelial damage, determined histologically. The percentage of the total time that the esophageal pH is <4 is called the reflux index. Considering the fact that not all episodes of acid reflux are symptomatic or cause complications, the North American Society of Pediatric Gastroenterology and Nutrition recommended that the upper limit of normal for the reflux index is 12 % during the first year of life and 6 % thereafter [28].

Esophageal pH monitoring requires introduction of a transnasal pH catheter and is often preceded by esophageal manometry to identify the location of the LES for proper placement of the pH electrode [29]. The main strength of this technique is the 24-h observation period that provides a true estimate of the frequency of GER and cumulative residence time of acid refluxate in the

esophagus. The technique, however, cannot detect nonacidic reflux episodes. It has been shown in infants and children that reflux-associated disturbances such as bronchitis, irritability, sleep disorders, episodes of apnea, oxygen desaturation, and pulmonary aspiration can be induced by both acidic (pH<4) and nonacidic (pH>4) reflux [30]. During the postprandial period, neutralization of gastric acidity of varying duration occurs and is affected by the patient's age, volume and composition of the meal, and the frequency of feeding [31]. Reflux during these periods may occur in the physiologic esophageal pH (from 5 to 7) and will not be detected with pH monitoring. Antacid therapy for GER can also prevent detection of GER episodes with pH monitoring [32]. The invasive nature of the study and the need to hospitalize young infants for the study are additional important disadvantages. A radiotelemetric, catheter-free, pH capsule secured to the lower esophagus is under investigation as a more comfortable alternative to the pH catheter.

Multiple, Intraluminal Electrical Impedance

Multiple, intraluminal electrical impedance (IMP) is a new technique for the diagnosis of GER based on changes in electrical impedance during passage of a bolus along an esophageal segment (between two electrodes). The use of multiple segments along a catheter placed in the esophagus enables differentiation between antegrade and retrograde bolus movements in the esophagus and the detection of GER. A pH-sensitive electrode can be attached to the catheter, allowing simultaneous measurements of electrical impedance and changes in esophageal pH [32]. The dual pH-multichannel intraluminal impedance (pH-MII) is a sensitive tool for evaluating overall gastroesophageal reflux disease and particularly for permitting detection of nonacid reflux. It is considered superior to stand alone pH monitoring. It is useful in correlating symptoms with reflux and in assessment of the efficacy of anti-reflux treatment [33]. A study of infants with history of apnea, breathing irregularities, and aspiration that combined IMP with pH monitoring and overnight polysomnography showed that the majority of GER episodes (including many symptomatic episodes) were not associated with pH measurements under 4 and would probably pass undetected by esophageal pH monitoring alone [34]. Currently this promising new technique is not widely available, requires time for analysis of the recordings, and has the same disadvantage of being invasive as extended pH monitoring.

Sonography

Sonographic detection of GER has been attempted and showed encouraging results in young infants when compared with esophageal pH monitoring. In one study, sonographic detection had a sensitivity of 100 % and specificity of 87 % [35]. Despite these encouraging results, there has been very little experience with this technique, and it is not currently utilized in routine clinical practice.

Barium Contrast Radiography

Upper gastrointestinal (UGI) series are often used in the evaluation of GERD although various studies show this test is neither sensitive nor specific in comparison to 24-h pH monitoring (sensitivity ranged from 31 to 86 % and specificity from 21 to 83 %). Imaging is short and intermittent because the radiation dose of cineradiography is prohibitive [28]. The short observation period can result in false-negative studies when reflux is present, while the frequent occurrence of non-pathological reflux results in false-positive results for GERD. Upper GI series provide high-resolution images that are important in excluding anatomic abnormalities that can produce symptoms of GERD (mainly vomiting). These abnormalities include pyloric stenosis, hiatal hernia, and malrotation. The study is also useful for assessing complications of GERD such as coarse mucosal changes due to esophagitis and esophageal strictures, in more severe cases. In contrast to gastroesophageal scintigraphy, upper GI series cannot be considered a physiologic test because of the usage of barium as a contrast agent and the occasional employment of provocative measures such as abdominal compression.

Endoscopy and Biopsy

Endoscopy with biopsy can evaluate the complications of gastroesophageal reflux in GERD such

as esophagitis, strictures, and Barrett's esophagus and exclude other diseases with similar clinical symptoms such as eosinophilic or infectious esophagitis and Crohn's disease [36]. Endoscopy alone is not sufficient because a normal-appearing esophagus does not exclude microscopic esophagitis. Subtle mucosal changes such as erythema and pallor may occur in the absence of esophagitis [37]. The technique is invasive and mostly used in the evaluation of GERD-associated esophagitis.

Gastroesophageal Reflux Scintigraphy

Gastroesophageal reflux scintigraphy, also known as the "milk scan," is a radionuclide study for the detection of gastroesophageal reflux and pulmonary aspiration secondary to reflux. This section will focus on detection of gastroesophageal reflux. The ability of this study to detect pulmonary aspiration will be discussed in the section on pulmonary aspiration.

A mixture of milk or milk formula with ^{99m}Tc-sulfur colloid is introduced into the stomach by oral feeding, naso gastric tube, or gastrostomy tube. Gastroesophageal reflux episodes can be detected by showing abnormal tracer activity in the esophagus with dynamic scintigraphy of the upper abdomen and thorax over a 60-min period (Fig. 9.1). Dynamic images are followed by

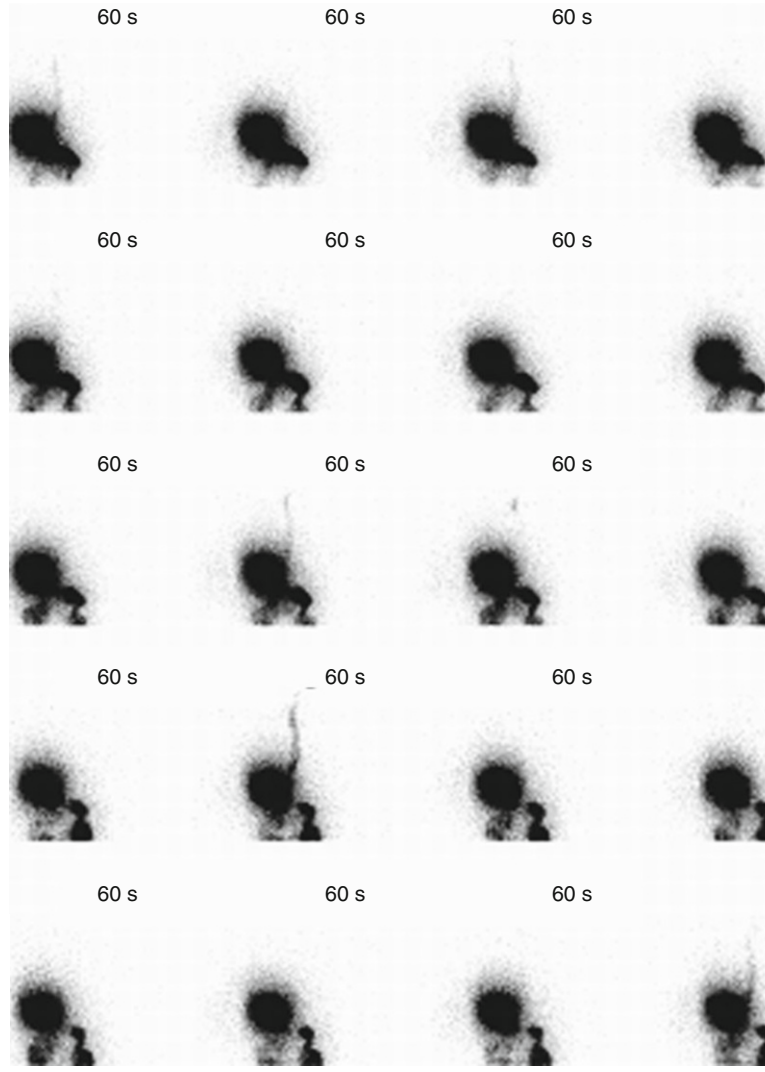

Fig. 9.1 Several episodes of gastroesophageal reflux up to the proximal esophagus in a 15-year-old girl with recurrent vomiting and rumination

anterior and posterior static images of the chest at 1 and 4 h post-feeding. Twenty-four-hour images are occasionally obtained as well. The purpose of the static images is to detect abnormal tracer activity in the lungs indicating pulmonary aspiration. They can demonstrate subtle aspiration that was not evident on the dynamic images and document aspiration that occurred after completion of the dynamic sequence. These images enhance the ability of the study to detect pulmonary aspiration.

There is no single universally accepted protocol for this study. Most techniques, however, share the same basic principles. A common protocol, used at the author's department, will be described as a general reference.

Technetium-99m-sulfur colloid is the radiopharmaceutical of choice for the study because it is not absorbed from the gastrointestinal or pulmonary mucosa and remains stable in the acidic medium of the stomach. Such absorption would increase the background activity and lower the sensitivity of the study for detection of reflux and aspiration [38]. The recommended dose range is 9.25–37 MBq (0.25–1.0 mCi). The administered activity will depend on the age of the child, the volume to be fed, and the time per frame used for imaging [39].

Older children should fast for at least 4 h prior to the exam. Young infants should replace a normal scheduled feeding with the radioactive milk or formula. The radiopharmaceutical is added to a portion of the patient's feeding (one-third or one-half of the normal milk or formula feeding volume). This volume is introduced into the stomach by oral feeding or alternatively by nasogastric tube (which should be removed after feeding) or by gastrostomy tube when used for routine feedings. A second, tracer-free volume is then given to complete the meal. The tracer-free volume has an important role of clearing residual tracer from the oropharynx and esophagus prior to imaging. The volume of the feeding varies according to the patient's age and weight. In most cases the desired volume is similar to the volume the patient is given for regular meals. It is best to wait 48 h after a barium study to avoid the possibility of inaccuracies in interpretation due the attenuating effect of residual barium in the gastrointestinal tract.

Times of the beginning and completion of feeding should be recorded. After feeding, the patient is placed supine on the imaging bed. Young infants should be burped when possible prior to imaging. Immobilization may be used to prevent motion and to secure young children on the imaging bed. Dynamic images are carried out from the posterior view with the stomach and chest in the field of view. A low-energy high-resolution collimator is used, and images are recorded on a 128×128 matrix at a rate of 30 s/frame for 60 min. The dynamic images are followed by anterior and posterior static images of the chest with the stomach out of the field of view. These images are recorded on a 256×256 matrix over 3–5 min. A second set of static images is acquired 2–4 h after completion of the meal. Delayed 24-h images are optional.

Some technical aspects of the study deserve further elaboration. Care should be taken to avoid any form of external contamination due to spillage during feeding or subsequent vomiting or regurgitation. Contamination artifacts over the lung fields could be mistaken for pulmonary aspiration or prevent detection of such aspiration. Disposable, absorbent sheets, lined on one side with plastic material, may be used to contain contamination over the neck, chest, and upper abdomen during feeding and during imaging. Residual tracer in the mouth and/or esophagus at the beginning of imaging may limit the ability to detect gastroesophageal reflux. Using a sufficient volume of non-labeled milk/formula to complete the meal will prevent this problem in most cases.

In some centers, imaging is performed in the anterior position. Anterior imaging has certain advantages. Depending on the camera and imaging table, a closer patient-to-collimator distance can be achieved with anterior imaging. In posterior imaging, counts originating from gastroesophageal reflux can be attenuated by the superimposed spine and the imaging table. Despite these considerations, we feel that posterior imaging is more practical and does not sacrifice, to any significant extent, the ability to detect reflux and aspiration. This has been

Table 9.1 Radiation dosimetry

	Dose (rads/100 μCi), by age					
Site	Newborn	1 year	5 years	10 years	15 years	Adult
Stomach	0.383	0.093	0.0507	0.0308	0.0221	0.0187
SI	0.372	0.164	0.0911	0.0583	0.0361	0.0315
ULI	0.596	0.267	0.164	0.0896	0.0539	0.0518
LLI	0.972	0.380	0.194	0.120	0.0721	0.0329
Ovaries	0.0993	0.0420	0.033	0.0722	0.00149	0.0102
Testes	0.0176	0.00717	0.00334	0.0108	0.0011	0.00029
Thyroid	0.00164	0.00062	0.000215	0.00007	0.00003	0.00002
Whole body	0.0200	0.0107	0.00633	0.00407	0.00268	0.00186

From Castronovo [45]
SI small intestine, *ULI*, *LLI* upper and lower large intestine

shown in a study that found an excellent correlation between anterior and posterior dynamic images in detection of GER [40]. Infants and young children are often intimidated by the large camera detector positioned over their head and neck for extended periods and are less likely to lie still. In posterior imaging, with the camera head positioned under the imaging table, there is an unobstructed space over the imaging bed allowing easy communication with the children and access to caregivers. The children are more relaxed and can watch an overhead television. The supine position was found to be more sensitive than prone, left lateral, and 30° right posterior oblique positions for detection of gastroesophageal reflux [41].

A more recent study, however, reported that imaging the children in multiple positions (supine, prone, right-side down, and left-side down) yielded more GER-positive studies than imaging in the traditional supine position alone [42]. It is important to perform the dynamic study over 60 min. Twenty-five percent of reflux episodes can be missed by limiting the study to 30 min [43]. Another study showed that placing the children in the upright position for a few seconds, in the middle of the examination, increased the frequency of GER episodes [44].

Recordings from pH probe monitoring show that reflux episodes may be very brief. Brief episodes of GER can be missed when using a frame time of 30–60 s during dynamic scintigraphy. Shortening the frame time to 5–10 s will usually allow detection of brief episodes and provide a more accurate estimation on the total number of reflux episodes during the study. The study could later be reformatted to 30 or 60 s per frame for more convenient display.

The dosimetry for different ages is shown in Table 9.1 [45]. The critical organ is the lower large bowel. The effective dose in this study is among the lowest for nuclear medicine studies.

Interpretation of Gastroesophageal Reflux Scintigraphy

New appearance of tracer in the esophagus indicates a reflux episode (Fig. 9.1). All recorded frames as well as the delayed static images should be inspected. Computer display allows interactive manipulation of the window as well as count truncation. These measures improve the detectability of subtle reflux episodes. Cinematic playback of the recorded frames is also helpful in detecting reflux and can easily identify patient movement that occurred during the study.

Placing markers over the suprasternal notch and over the xiphoid is helpful in determining the level of reflux in the esophagus or oropharynx and in localizing tracer activity over the lung fields. Obtaining a transmission image of the chest, with a ^{57}Co flood source, and overlaying it on the emission image is another technique that can improve localization of tracer activity in the chest.

Interpretation can be enhanced by generating time activity curves from regions of interest (ROI) placed over the esophagus. Reflux episodes are seen as a sharp spikes in the curves (Fig. 9.2). By placing one ROI over the entire esophagus and a second ROI over the upper

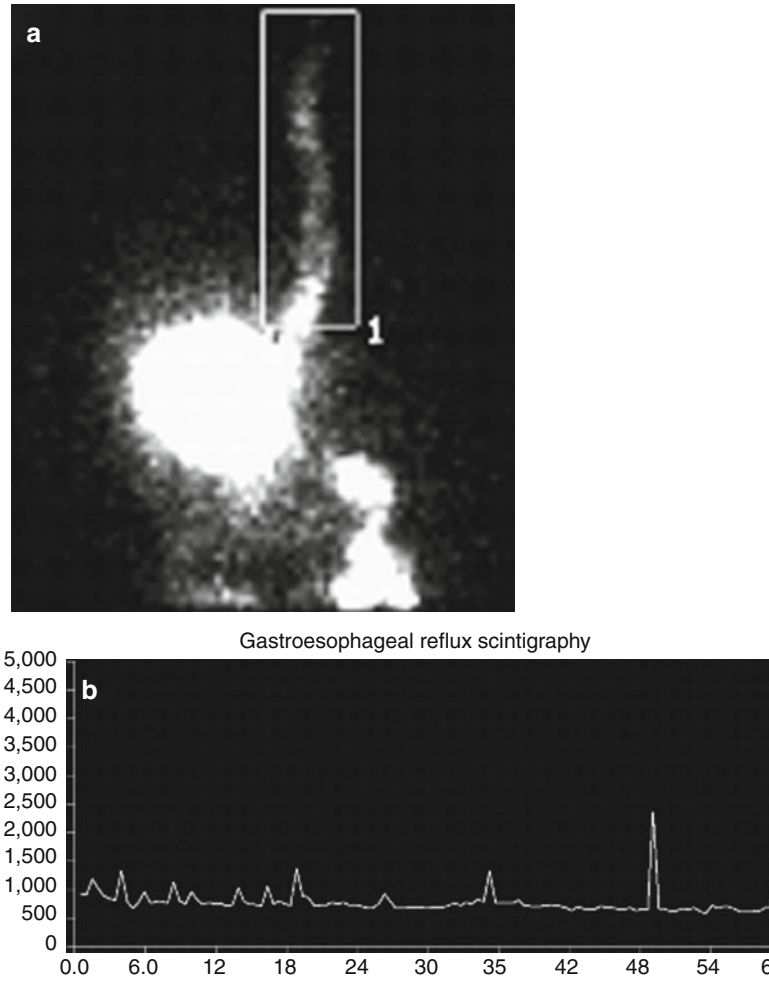

Fig. 9.2 A region of interest over the entire esophagus (**a**) is used to generate a time activity curve (**b**) shows multiple sharp peaks corresponding to episodes of gastroesophageal reflux (same study as in Fig. 7.1)

esophagus and oropharynx, the proportion of severe reflux episodes from the total number of episodes can be established. Patient motion during the study can introduce significant artifacts in the curves because motion can cause the esophageal region to overlap gastric activity, simulating the appearance of reflux. Images should always be inspected for motion prior to interpretation, and motion correction should be applied when indicated.

Visual inspection of the images in conjunction with curve interpretation is the most accurate way to read the study. The number of reflux episodes, the level of reflux (lower esophagus, upper esophagus, pharynx), and the presence of pulmonary aspiration should be documented. Dividing the number of frames showing esophageal reflux by the total number of frames provides a simple index that can roughly estimate the residence time of reflux in the esophagus during the study.

Some authors use more elaborate techniques to quantify gastroesophageal reflux. These techniques take into account the volume of reflux in each episode, the frequency of reflux, and the rate at which it clears from the esophagus. Some indices normalize esophageal activity during reflux episodes to the initial gastric activity [43, 46, 47].

Gastroesophageal reflux scintigraphy is a sensitive, noninvasive, physiologic, and direct technique to demonstrate the presence of gastroesophageal reflux. It is easy to perform and well tolerated and requires minimum patient cooperation. It also entails a relatively low radiation burden. The study can be quantified for better

intersubject comparison and for monitoring response to therapy [48]. Additional advantages of gastroesophageal reflux scintigraphy in comparison to pH monitoring and endoscopy include the ability to detect pulmonary aspiration and to evaluate gastric emptying in the same study. Scintigraphy is considered by many authors to be a safe and reliable screening test for detection of GER. It cannot distinguish, however, between physiologic reflux and reflux related to GERD.

Comparing sensitivities and specificities of the different studies for detection of gastroesophageal reflux is problematic. Techniques are often compared to extended pH monitoring as a gold standard. As mentioned earlier, pH monitoring is a sensitive and specific study for indirect detection of acid reflux, but not all symptomatic reflux episodes are acidic. Lack of uniform protocols for the various techniques is another confounding factor. Clinical signs and symptoms of GERD are used in some studies to evaluate the sensitivity and specificity of diagnostic methods. This approach is problematic because of significant overlap between signs and symptoms of GERD and those of other conditions.

According to most studies, the sensitivity of gastroesophageal scintigraphy for detection of GER in comparison to pH monitoring ranges from 60 to 90 % [46, 49–55]. Specificity is over 90 % [51, 54]. In a few studies that performed simultaneous esophageal pH monitoring and scintigraphy for 1–2 h, no correlation was found between the total number of reflux episodes detected by scintigraphy and pH monitoring. Scintigraphy, however, detected more reflux episodes than pH monitoring [56, 57]. It was concluded that the two tests measure different pathophysiologic phenomena and should be regarded as complementary. Used together they could enhance the sensitivity and specificity of the diagnostic evaluation [58]. The agreement between scintigraphy and esophageal pH monitoring depends to some extent on the acquisition and display parameters used for scintigraphy. The best correlation was achieved when images were reformatted in 60-s frames [59].

Most authors found gastroesophageal scintigraphy to be more sensitive than barium radiography for detection of GER [46, 49, 52, 55, 60]. The inherent sensitivity of scintigraphy for detection of small amounts of radioactivity in the esophagus and the longer observation period compared to barium radiography may account for these differences. A combination of diagnostic modalities may be required to diagnose GER in young children. Gastroesophageal scintigraphy is also a useful noninvasive study for assessing the outcome of anti-reflux surgery.

Treatment

According to the guidelines of the North American Society for Pediatric Gastroenterology and Nutrition, treatment options include the following categories: dietary changes, positioning, life changes in children and adolescents, acid suppressant therapy, prokinetic therapy, and surgical therapy [28].

Milk and formula thickening agents may decrease the number of vomiting episodes in infants but do not improve the reflux index score on pH monitoring. A trial of hypoallergenic formula in formula-fed infants may reduce vomiting. Twenty-four-hour pH monitoring documented a lower prevalence of GER in the prone versus the supine position. This treatment option, however, is not recommended for most infants under 1 year of age because of the increased risk for sudden infant death in the prone position compared to the supine position. Left-side positioning and elevation of the bedhead have been traditionally recommended. A systematic review of published data, however, concluded that elevation of the head of the crib in the supine position did not have any effect [61]. Lifestyle changes in older children and adolescents include recommendations to avoid caffeine, chocolate, spicy foods, tobacco, and alcohol and to treat obesity.

Acid suppressant therapy is based on histamine receptor inhibitors (H_2Ras) and on proton pump inhibitors (PPIs). Proton pump inhibitors are more effective in relieving symptoms than H_2Ras. In children requiring chronic maintenance treatment, PPIs appear to be well tolerated and effective in maintaining remission of reflux esophagitis and reflux symptoms [62]. Chronic antacid therapy is not indicated because of potential side effects

related to increased absorption of aluminum and the presence of better alternatives (H_2Ras and PPIs). Prokinetic therapy affects the LES tone, esophageal motility, and gastric emptying. Domperidone and metoclopramide have questionable efficiency and may have adverse effects on the central nervous system. The efficacy of cisapride, a mixed serotoninergic agent, in reducing the symptoms of GERD has also been questioned [63]. This drug can cause cardiac arrhythmias, however, and requires proper dosing and proper patient selection and monitoring. Surgical therapy consists of anti-reflux surgery. The most common surgery is fundoplication. It is indicated when medical therapy fails and in severe life-threatening conditions related to GERD. Surgery should be avoided, if possible, before 2 years of age [1]. Laparoscopic Nissen's fundoplication in children may be considered a safe and effective alternative to open surgery with careful case selection [64].

Gastric Emptying

Physiology

The stomach can be divided into three functional regions: proximal stomach (cardia, fundus, and proximal body), distal stomach (distal body, antrum), and the pylorus. The proximal stomach stores and accommodates food. It delivers food to the distal stomach by tonic propulsion. Smooth muscles of the proximal stomach do not exhibit rhythmic or peristaltic contractions but are rather in a state of continual partial contraction. The motor function of the proximal stomach is to regulate intragastric pressure. This is achieved by receptive relaxation (a reduction in gastric tone in response to swallowing mediated by a vago-vagal reflex) and gastric accommodation (a neural-mediated reflex triggered by mechanoreceptors in the gastric wall in response to gastric distention). Even large volumes entering the stomach do not cause significant increases in intragastric pressure due to these mechanisms [48]. Receptive relaxation is absent in newborns, which partly explains why GER is more common in newborns than in older infants [65].

Motor activity of the distal stomach is characterized by peristaltic contractions in response to rhythmic depolarization in muscle cells known as the pacesetter potential. This electrical activity originates from the interstitial cells of Cajal, a network of specialized cells extending from the corpus to the distal antrum [66]. The gastric pacesetter potential has a baseline frequency of 3 cycles per minute. The motor function of the distal stomach is to mix, grind, and triturate solid food and to propagate the chyme towards the pylorus. Chyme is formed by contact of solids with gastric juices and digestive enzymes. The antro-pyloric region prevents emptying of particles greater than 1 mm in diameter. Larger particles are repelled back, triturated, and eventually emptied with the liquid phase. During trituration no significant emptying of solids occurs, giving rise to the lag phase that may be seen on solid gastric emptying time activity curves [67]. The lag phase usually is absent with emptying of milk. The pylorus regulates the outflow of intraluminal gastric contents. The thickness of the smooth muscle layers and the abundant pyloric mucosa form a mechanical stricture preventing passage of large particles into the duodenum [48]. In general, tonic pressure in the proximal stomach is the main mechanism that regulates emptying of liquids, and the peristaltic motor activity of the distal stomach is the main mechanism that regulates emptying of solids.

Coordinated gastric motor activity in the different functional zones is the end result of complex muscular, neural, and hormonal interactions and is also affected by feedback regulation from the small bowel. Neural regulation of gastric motor activity is largely mediated through the vagus nerve. Gastric emptying rate is influenced by multiple factors. Gastrointestinal hormones such as cholecystokinin, secretin, gastrin, and gastric inhibitory peptide delay gastric emptying. Liquids empty faster than solids. Gastric emptying is delayed by high-caloric and high-osmolarity meals. High osmolarity delays emptying in adults but was shown to have a smaller influence on emptying rates in premature infants and newborns [68]. Large meals prolong emptying. This probably is due to the high-caloric content of

large meals and not as much due to the meal size [69, 70].

Varying rates of emptying are encountered with different kinds of milk and milk formulas. Human milk empties faster than cow's milk although both are isocaloric [71]. Whey-based formulas empty more rapidly than casein-based formulas despite similarities in caloric content, osmolarity, and fat content. Acidified milk, however, was found to empty more rapidly [72]. The variability in the emptying rate of different kinds of milk and milk formulas may be related to the formation of solids in the stomach by milk and formulas during digestion. Fatty acids of specific carbon chain lengths, acid solutions, and physiologic concentrations of L-tryptophan have been shown to delay gastric emptying [73, 74]. In addition to these factors, gastric emptying in children is influenced by the child's age. Longer emptying times were observed in infants [12, 75]. Gastric surgery such as antrectomy and pyloroplasty and prokinetic drugs such as metoclopramide and domperidone shorten the lag phase and can increase gastric emptying rates [48].

Clinical Manifestations and Management of Abnormal Gastric Emptying

Vomiting, abdominal pain, nausea, weight loss, early satiety, and bloating were the most common symptoms among 239 children with scintigraphic evidence of delayed solid gastric emptying. Gastroparesis was idiopathic in 70 % of the cases, drug related in 18 %, postsurgical in12.5 %, and due to diabetes in 4 %. Improvement was noted in 60 % of the children receiving various therapeutic modalities at the end of the 2-year follow-up period, regardless of age, gender, or degree of delayed emptying [76]. Delayed gastric emptying was more prevalent in children with malrotation and GERD compared to children with GERD without malrotation [77]. Delayed emptying was also prevalent among children with functional dyspepsia [78].

Therapeutic options include prokinetic therapy mainly with metoclopramide, domperidone, cisapride, and erythromycin. Neurological and cardiac side effects limit the use of metoclopramide and cisapride. Dietary treatment is especially relevant in infants with delayed gastric emptying. Mother's milk and formulas high in protein hydrolysates and carbohydrates and low in fat may enhance gastric emptying. Gastric electrical stimulation is a promising nonmedical treatment modality but is an invasive procedure currently reserved to patients refractory to medical therapy [79]. There is limited experience with this technique in children [80]. Delayed gastric emptying manifestations, however, are not specific and can be encountered in many other conditions such as anatomical obstructions (congenital and acquired), GERD, hepatobiliary disease, peptic ulcer, drug effects, and infection. Symptoms of delayed gastric emptying may be seen in systemic diseases (e.g., malignancies, diabetes) and during drug therapy.

Gastric neuromuscular disorders such as visceral hypersensitivity, gastric dysrhythmias, gastric dysrelaxation, antral hypomotility, pylorospasm, and gastroparesis are more often encountered in adults. These conditions manifest as dyspeptic symptoms with early satiety, fullness, gastric discomfort, bloating, nausea, and vomiting but could also present with ulcer-like symptoms, mainly epigastric pain [81]. Rapid gastric emptying is less frequently encountered and can manifest with signs and symptoms that are major components of the "dumping syndrome," typically seen after peptic ulcer surgery. Early symptoms include diarrhea, abdominal discomfort, and bloating, and late symptoms include tachycardia, palpitations, diaphoresis, weakness, and fainting. These late symptoms are related to reactive hypoglycemia due to exaggerated insulin release [82].

Diagnostic Evaluation of Gastric Emptying

Meaningful quantification of gastric emptying requires standardization of study techniques and standardization of the test meal. Standardization is essential for inter- and intra-subject comparisons.

Gastric emptying scintigraphy is the most widely accepted technique in clinical practice and regarded as the gold standard. Non-scintigraphic techniques will be reviewed first, followed by a detailed description of gastric emptying scintigraphy.

Upper gastrointestinal (UGI) series with barium contrast provides fine anatomical details and is important for excluding anatomical conditions that can alter gastric emptying such as pyloric stenosis or antral web. Otherwise, the emptying rate of a nonphysiologic substance such as barium does not reflect gastric emptying under native, physiologic conditions.

Gastric ultrasonography can evaluate gastric volume, emptying, and transpyloric flow. It can assess gastric contraction and distension and measure the antral cross-sectional area [83–85]. A high correlation was encountered between ultrasonographic gastric emptying parameters and scintigraphic techniques [86]. Ultrasonography was useful for detection of motor abnormalities in children with dyspeptic symptoms [87]. Ultrasonography has the advantages of being a widely available, low-cost, and a nonradioactive technique. The main limitations of this technique are a short observation period and dependency on operator skills explaining its limited use in clinical practice.

Electrogastrography measures myoelectrical activity in the gastric antrum during the fasting and postprandial states [48]. Surface recording is usually employed, using cutaneous electrodes placed over the epigastrium [88]. The normal gastric pacesetter potential range is between 2.5 and 3.75 cycles per minute. This technique can detect bradygastria (<2.5 cpm) or tachygastria (3.75–10 cpm). Gastric dysrhythmias have been associated with certain conditions such as diabetes, idiopathic gastric paresis, or motion sickness [88]. This technique, mostly utilized in adults, is not widely available in clinical practice.

Breath tests provide a simple, noninvasive, and nonradioactive technique to evaluate gastric emptying. Most tests today are based on measuring the concentration of the stable isotope ^{13}C in expired air. Carbon-13-labeled octanoic acid is used as a substrate for solid gastric emptying evaluation and ^{13}C-labeled acetate for liquid emptying. Both substrates are absorbed in the duodenum and transported to the liver. Metabolic degradation in the liver produces $^{13}CO_2$ that is excreted with exhaled air and measured with a mass spectrometer. Breath samples are measured for enrichment with ^{13}C up to 6 h. First appearance of $^{13}CO_2$ indicates the beginning of emptying. The slope of the rising time-related ^{13}C enrichment curve is related to the gastric emptying rate [89, 90]. Simultaneous performance of gastric emptying scintigraphy with a ^{13}C breath test in 29 children with dyspeptic and respiratory symptoms showed good correlation between the techniques in assessment of gastric emptying times [91]. The reliability of the breath test to accurately reflect gastric emptying can be adversely affected by certain conditions such as malabsorption and pancreatic, liver, and lung diseases and by visceral hemodynamic changes (physical exercise) that can alter the delivery of ^{13}C to the sampled breath air, irrespective of the gastric emptying rate.

Gastric MRI is an emerging technique, allowing evaluation of both gastric emptying and motility disorders without exposure to ionizing radiation or to invasive procedures (such as the barostat technique required to evaluate gastric accommodation). The technique is based on labeling a meal with Gadolinium DOTA allowing precise measurements of gastric volumes and peristalsis with dynamic protocols. Currently this technique is not widespread in routine clinical practice [92].

Gastric Emptying Scintigraphy

Gastric emptying scintigraphy is a physiologic, noninvasive, low-cost technique to evaluate gastric emptying based on imaging and quantification of a radiolabeled test meal. Several techniques are used in clinical practice for gastric emptying. The techniques vary in the meal content, volume, and imaging technique. The lack of uniformity adversely affects inter-institutional comparison of study results.

Different mechanisms regulate gastric emptying of solids and liquids. A solid test meal is considered more reliable than a liquid meal for measuring gastric emptying. Solid meals are used

in adults [48]. In the pediatric population, they are reserved for older children and adolescents. The diet of infants is milk or milk formulas, which makes them the natural and only practical choice for a test meal. This is in keeping with the physiologic nature of the study. Milk or formula is often used in young children too because it is more acceptable to them than standardized solid meals. As mentioned earlier, milk and milk formulas form solids in the stomach due to interactions with digestive enzymes and gastric acid. Their clearance does not truly represent liquid gastric emptying.

Gastric emptying evaluation with milk or formula is often performed simultaneously with evaluation of gastroesophageal reflux. We use similar preparations and acquisition parameters to those used for gastroesophageal scintigraphy (milk scan). The radiopharmaceutical of choice is ^{99m}Tc-sulfur colloid because it remains stable in an acid medium and is not absorbed from the gastrointestinal mucosa. The recommended dose range is 9.25–37 MBq (0.25–1.0 mCi). The administered activity will depend on the age of the child and the volume to be fed [39]. Preparations for the study include fasting for at least 4 h prior to the test. Young infants should miss a normal feeding just prior to the exam.

Medications that affect gastric motility should be discontinued for an appropriate period prior to the exam, depending on the pharmacokinetics of the drugs, unless the scintigraphy is used to evaluate the effect of a specific drug regimen on gastric motility. These drugs include prokinetics, narcotic analgesics, anticholinergic agents, antidepressants, gastric acid suppressants, aluminum-containing antacids, somatostatin, and calcium channel blockers [48]. Barium radiography should not be performed within 48 h prior to scintigraphy. Glycemic control is required in diabetic patients because hyperglycemia can delay gastric emptying [93]. The volume of the meal is adjusted according to the patient's age or size. For standardization purposes, the feeding period is limited to 10 min. The referring physician should indicate the volume of the meal expected to be consumed within this time frame. The radiopharmaceutical is added to the meal, and a second, tracer-free volume is added to complete the desired feeding volume. Oral feeding is preferred, but feeding through a nasogastric tube or gastrostomy tubes is occasionally required. Nasogastric tubes should be removed immediately after feeding. The volume and composition of the meal are recorded for future reference.

After completion of the feeding, the patient is placed in the supine position, and continuous dynamic images of the stomach and chest are recorded on a 128×128 matrix, 30 s per frame for 60 min. Images are obtained in the posterior projection using a low-energy, high-resolution collimator. Static images of the abdomen and chest are acquired using a 256×256 matrix at 60 min. If emptying is delayed, additional images are obtained at 2 h. Static images of the lung fields are also obtained at 4 h and occasionally at 24 h for the detection of late aspiration.

A region of interest (ROI) is placed around the stomach, as seen in the immediate post-feeding image. A time activity curve, corrected for decay, is generated from the stomach ROI. Motion correction should be applied when required. Care should be taken not to include bowel activity in the gastric ROI. An additional gastric ROI derived from the last image is often required for accurate generation of the time activity curve. Another option is to generate separate regions over the stomach every 10 or 15 min. Gastric emptying can be expressed as the percentage of the initial activity remaining at a specific time point (residual) or as the activity emptied by the stomach at these times. It can also be expressed as the half emptying time (T1/2). We use the 60-min time point for calculation of the gastric residual. Half emptying time is more commonly used in adults with solid gastric emptying. The pattern of the emptying curve, including the presence and length of the lag phase (seen in solid gastric emptying), is important because it may provide evidence on abnormalities in gastric motility. Milk usually empties in an exponential or biexponential manner. A long plateau on the time activity curve may be encountered in intermittent gastric outlet obstruction due to an antral web.

Some features of the protocol are subject to variability and deserve further discussion.

The study length is not well standardized. Gastric emptying rate may increase during the second-hour post-feeding. In a study that evaluated gastric emptying of a liquid meal for 2 h in infants and children, the 1-h measurements did not predict well the 2-h measurements. It was concluded that gastric emptying measurements in children should be continued until 2 h after feeding unless rapid emptying is observed during the first hour of the study [94, 95]. Extending dynamic acquisition for 2 h may be difficult to achieve in young children. Serial delayed static images can be used instead. The supine position is best suited for extended imaging in infants and children but can delay gastric emptying. In one study a significant number of children, 1 week to 2 years old, with delayed emptying in the supine position showed significant emptying just by changing position. It was recommended to complement gastric emptying studies with delayed views in the right lateral and upright position [96].

Physiologic movement of gastric contents from the posteriorly located fundus to the more anteriorly located antrum can produce artifacts in quantitation due to nonuniform attenuation throughout the study. Using a geometrical mean of anterior and posterior counts, acquired simultaneously with a dual detector camera, will correct this problem. It is also possible to use the left anterior oblique projection instead of anterior or posterior projections to minimize this artifact. Nonuniform attenuation is a concern mostly in adults and large or obese older children. Conjugate counting did not significantly change the results compared with anterior imaging alone in a study that evaluated gastric emptying with milk feedings in infants and young children. It was suggested that anterior imaging alone is sufficient in this patient population [97]. We prefer posterior imaging, which is much more comfortable for the patient. A recent study in children compared the effect of different imaging positions on gastric emptying calculations (60-min gastric residual) and found a high correlation between calculations from the posterior image and calculations from the geometrical mean of anterior and posterior acquisitions. The authors recommended using the posterior image for both solid and liquid gastric emptying calculations except for solid gastric emptying in children older than 8 years and heavier than 30 kg in which simultaneous acquisition from the anterior and posterior projections was advised [98].

Continuous data recording rather than serial static images is recommended and well suited for small children, who occasionally need to be restrained. Recording data only at discrete time intervals (e.g., every 10–30 min) is incapable of providing information on the lag phase and may be limited in identifying patterns of rapid gastric emptying [99].

Occasionally, significant emptying occurs during the feeding period. This emptying is not accounted for when the gastric residual is derived from a region of interest placed over the stomach in the immediate post-feeding image. Calculation of the gastric residual relative to the total dose ingested by the patient can be achieved by comparing the activity in the stomach in the final image to the activity in a ROI that includes the stomach and bowel as seen in the immediate post-feeding image. This value takes into account both the emptying that occurred during imaging and the emptying that occurred before imaging (during feeding). The two methods for calculation of the gastric residual were compared in a study that included 44 children who underwent liquid ^{99m}Tc-sulfur colloid gastric emptying. Sixty-minute gastric residuals from the total ingested dose were significantly lower by 15–16 % from gastric residuals derived only from the initial stomach activity in the first post-feeding image. It was concluded that emptying that occurs during feeding should be factored into quantitation of liquid gastric emptying in infants and young children to avoid overestimation of gastric residuals and erroneous interpretations of delayed gastric emptying [100]. Vomiting a portion of the ingested meal can result in lower gastric residual values falsely suggesting faster gastric emptying.

A major problem with gastric emptying scintigraphy in children is the lack of age-related normal values derived from large groups of normal controls. Normal children cannot be studied as control subjects due to ethical considerations.

Pooling data from different institutions to establish the normal range is problematic due to lack of standardization of the study technique and the test meal. Given these limitations, it is best for individual laboratories to establish their own normal range. The few reports concerning normal values that were published in the literature should serve as a guide. In one study, normal infants were fed with 50 ml milk labeled with ^{113m}In microcolloid. The gastric emptying time activity curve was found to be exponential, and the T1/2 was 87 ± 29 min. The 1-h normal gastric residuals extrapolated from this data were 48–70 % [101]. In another study normal emptying residuals for young children ranged between 36 and 68 % at 1 h with a sulfur colloid-labeled milk/formula. In a small number of older children, the range was between 42 and 56 % [102]. The normal range for liquid gastric emptying residuals with ^{99m}Tc-sulfur colloid-labeled dextrose at 1 h, in children less than 2 years, was 27–81 % and over 2 years 11–47 % [12]. An example of delayed gastric emptying is shown in Fig. 9.3.

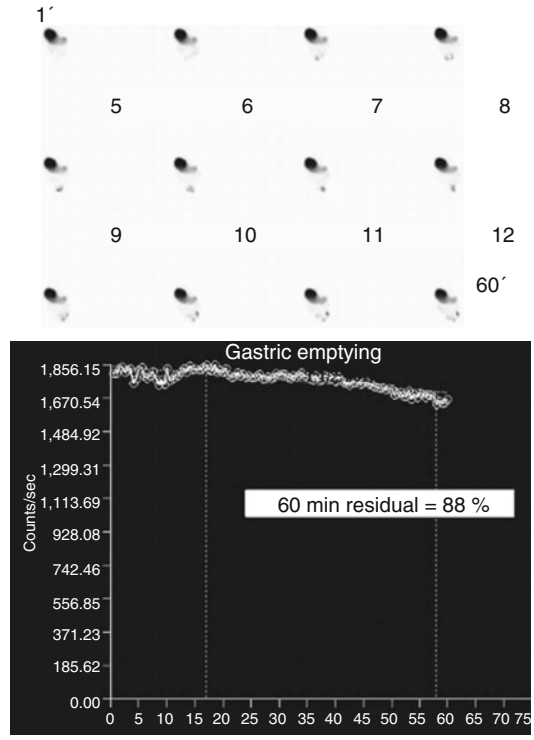

Fig. 9.3 Delayed gastric emptying in a 2-year-old boy with suspected metabolic disease, hypotonia, psychomotor retardation, and recurrent vomiting. Posterior view images, displayed at 5 min per frame, show considerable retention of labeled formula in the stomach. The 60-min gastric residual calculated from the time activity curve was 88 %

Gastric emptying with a solid test meal is the preferred method to assess gastric emptying in older children, adolescents, and adults. It is important that the radioactive label remains firmly attached to the solid phase. Since liquids affect the emptying of solids, it is common to include unlabeled liquids in the test meal. The best stability is achieved with in vivo labeling of chicken liver using ^{99m}Tc-sulfur colloid (98 % bound at 3 h in gastric juice) [103]. This method requires injecting the label into the chicken, harvesting the liver, and cooking the liver. It is therefore impractical for routine clinical use. A stable label can be achieved by mixing and cooking ^{99m}Tc-sulfur colloid with a whole egg (82 % bound at 3 h) or with the egg white (95 % bound at 3 h) [103]. A stable label can also be obtained with fat-free egg substitutes. Basing the test meal on radiolabeled eggs is convenient and widely used in clinical practice. The recommended radiopharmaceutical dose is 9.25–18.5 MBq (0.25–0.5 mCi) ^{99m}Tc-sulfur colloid [39]. Less common alternatives include ^{99m}Tc-labeled bran, pudding, or iodinated fiber [75, 104, 105]. These alternatives may be useful in cases of allergy to eggs. A solid meal consisting of a 30 g chocolate crispy cake and 100 cc of water was investigated in 24 normal children 5–10 years old. The chocolate crispy cake was labeled with a ^{99m}Tc ion exchange resin (3 MBq) to achieve a stable label. The mean gastric emptying half time in this normal cohort was 107.2 min [106]. More recently, mixing ^{99m}Tc-sulfur colloid with melted cheddar cheese was reported to produce a stable label comparable to egg white and was found to be superior to oatmeal or mashed potatoes, which had a low and variable labeling stability [107].

Simultaneous assessment of solid and liquid emptying can be achieved by labeling the solids with ^{99m}Tc-sulfur colloid and the liquid (water) with ^{111}In. Maintaining a ratio of at least 6:1 between the ^{99m}Tc and ^{111}In activities can minimize downscatter from ^{111}In into the ^{99m}Tc window. A suitable pediatric dose for this dual-isotope study is 11.1 MBq (300 microcurie) for ^{99m}Tc and

1.85 MBq (50 microcuries) for ^{111}In [67]. Preparations for solid gastric emptying in children are similar to those described for liquid emptying. Imaging duration should be at least 2 h. Continuous dynamic imaging can be used. A protocol consisting of 30-s images, acquired in the supine position every 10 min for 2 h, and keeping the patient upright between images can also be used. A gastric emptying time activity curve is constructed from the decay corrected counts in each frame.

The range of normal values for solid gastric emptying in children has not been established. In a small series of 11 normal control children, 5–11 years old, solid gastric emptying values corresponded well to those described in adults [108]. Using the anterior imaging projection, normal control values in young adult volunteers can be used as a guide. These values expressed as gastric residuals are 60–82 % at 1 h and 25–55 % at 2 h [109].

An effort has been made in recent years to standardize solid gastric emptying scintigraphy in adults resulting in joint recommendations of the American Neurogastroenterology and Motility Society and the Society of Nuclear Medicine [110]. The standard test meal is based on an egg white meal (Egg Beaters® or generic equivalent) radiolabeled with 18.5–37 MBq (0.5–1.0 mCi) ^{99m}Tc-sulfur colloid. One hundred twenty grams of liquid egg white (approximately the equivalent of two large eggs) is cooked with the radiotracer and served with 2 toasted white bread slices, 30 g of strawberry jam, and 120 g of water. The meal should be consumed over 10 min. Gastric emptying measurements are based on gastric counts derived from the geometrical mean of anterior and posterior 1-min static images in the upright position. The images are acquired immediately after meal ingestion (time 0) and at 1, 2, and 4 h after meal ingestion. Normal gastric emptying values for this protocol were adapted from a large multi-institutional, multinational study [111]. The normal gastric residuals for adults in terms of gastric residuals were 37–90 % at 1 h, 30–60 % at 2 h, and 0–10 % at 4 h. The applicability of this protocol and the validity of the normal reference values have not been determined in children capable of ingesting a solid meal. It could perhaps serve as a general guideline in older children and teenagers.

Investigational Scintigraphic Techniques

Dynamic antral scintigraphy provides information on gastric motility and can be performed in conjunction with standard gastric emptying scintigraphy. A short (4–5 min) dynamic acquisition with 1- to 2-s frames is added at the end of a standard gastric emptying study. Time activity curves are generated from ROIs placed over the proximal, middle, and distal antral areas. The data is corrected for motion artifacts and for translational movement of the stomach. Finally, a refined Fourier transform is performed on the time activity curves to determine the frequency and amplitude of antral contractions. This technique has been investigated in adults [112–114]. The amplitude rather than the baseline frequency of antral contractions (3 per min) was more useful in discriminating various patient groups. Decreased amplitudes have been noted in diabetic patients and increased amplitudes in patients with functional dyspepsia [114, 115].

Gastric SPECT is a new scintigraphic technique to evaluate gastric accommodation. Impaired postprandial gastric accommodation is responsible for symptoms of bloating, distension, early satiety, and nausea. Abnormal accommodation can be detected with barostatically controlled balloon in the proximal stomach and by ultrasonography in the distal stomach. The intragastric barostat balloon study is considered the gold standard for measurements of gastric volumes. Gastric SPECT allows evaluation of the entire gastric accommodation reflex by measuring fasting and postprandial gastric volumes. Following an overnight fast, ^{99m}Tc is injected intravenously and localizes in parietal and mucous cells in the gastric mucosa. Sequential gastric SPECTs are performed starting 10 min after injection in the fasting state and after ingestion of a test meal without changing the patient's position. Dynamic tomographic acquisition (6° steps, 3 s per frame, 128×128 matrix) has been used for gastric SPECT. Total gastric volumes are measured from the SPECT data with specialized software during the fasting state and in the postprandial state (3–12 min and 12–21 min after completion of the

meal) [116]. Gastric SPECT has been investigated in adults and showed good correlation with invasive barostat balloon studies in determining gastric volumes [117]. Impaired accommodation was found in idiopathic dyspepsia and after fundoplication [116, 118]. Simultaneous measurement of gastric emptying and accommodation was reported with dual-isotope acquisition (^{111}In for solid or liquid emptying and ^{99m}Tc for accommodation) [119].

Esophageal Transit

Anatomy and Physiology of the Esophagus

The esophagus is the conduit that delivers food from the oropharynx to the stomach with coordinated muscular peristalsis aided by gravity. It begins in the neck, at the lower border of the cricoid cartilage, extends through the diaphragm, and ends at the cardia of the stomach. Circular muscle fibers form sphincters at both ends of the esophagus. The upper esophageal sphincter prevents regurgitation of food from the esophagus back into the oropharynx. The lower esophageal sphincter (LES) controls transit of food from the esophagus into the stomach and prevents retrograde reflux of food from the stomach into the esophagus. The primary peristaltic pump originates in the pharynx and produces signals that propagate through the circular and longitudinal muscles of the esophagus at about 4 cm/s [48]. Esophageal peristalsis is coordinated with the post-swallowing relaxation of the lower esophageal sphincter [120]. The striated muscles of the esophagus are innervated through the vagus and the smooth muscles through sympathetic and parasympathetic nerves.

Esophageal Transit Disorders

Esophageal motor disorders can be primary (e.g., achalasia—failure of relaxation of the LES and loss of esophageal body peristalsis) or secondary to other conditions (e.g., esophagitis, surgery). The occurrence and severity of esophagitis depends both on severity and frequency of gastroesophageal reflux and on esophageal motility. Abnormal clearance of the refluxate contributes to the pathogenesis of esophagitis and can result from decreased amplitude of distal esophageal peristaltic contractions and from an increased frequency of non-peristaltic contractions.

Functional esophageal disorders are determined on the basis of lack of any identifiable structural or metabolic damage. They are mostly encountered in adults but may also be seen in children and adolescents. They include conditions such as rumination syndrome, globus (sensation of a lump stuck in the throat), functional dysphagia, and functional chest pain [121]. Functional esophageal disorders, in adults, are the second most common functional disorder of the gastrointestinal tract after irritable bowel syndrome and are sometimes accompanied by psychological and psychiatric disorders [121, 122].

In children and adolescents, esophageal motility disorders are encountered with tracheoesophageal fistula, esophagitis, esophageal strictures, psychomotor retardation, cerebral palsy, and Down syndrome [123–126]. Prolonged esophageal transit was noted in children with familial dysautonomia [127]. Impaired esophageal motility in children is seen following injury to the esophagus from ingestion of caustic materials and following repair of esophageal atresia [128, 129]. Common clinical presentations of esophageal disorders include dysphagia and chest pain.

Evaluation of Esophageal Transit

Non-scintigraphic Techniques

Esophageal endoscopy is the mainstay of the diagnostic procedures for esophageal disorders. It allows direct visualization of the esophageal mucosa and performance of tissue biopsies. Esophagitis, esophageal metaplasia, esophageal diverticulae, and fistulae are often evaluated with this technique. Endoscopy is usually extended to evaluate the stomach and duodenum too. It is the first-line diagnostic procedure for patients with complaints of dysphagia or dyspepsia. Endoscopy

is an invasive procedure that is not well tolerated by some patients and requires anesthesia in children. It does not provide direct information on motility disorders [48].

Upper gastrointestinal (UGI) series with barium contrast provides imaging evaluation of the esophagus, stomach, and duodenum. The study is commonly used in the diagnosis of esophageal disorders. UGI series is useful for the diagnosis of intrinsic or extrinsic anatomical obstructions (e.g., strictures or pressure from mediastinal space-occupying lesions), esophageal fistulae, and diverticulae and can also suggest mucosal changes encountered in esophagitis. It also allows dynamic evaluation of esophageal motility and transit of barium boluses from the mouth to the stomach. The radiation dose during video fluoroscopy is prohibitive. Although noninvasive, the study requires cooperation. Some children refuse to swallow the barium contrast. It is also limited in providing functional data for evaluation of certain motor disorders.

Esophageal manometry is indicated in patients with dysphagia unrelated to structural abnormalities. Manometry provides dynamic pressure measurements that are useful in the diagnosis of primary motor disorders such as achalasia, diffuse esophageal spasm, nutcracker esophagus, and hypertensive LES. It can demonstrate esophageal disorders secondary to systemic diseases such as scleroderma and dermatomyositis [48]. Multichannel intraluminal impedance is a new technique that allows evaluation of bolus movement in the esophagus. The technique was described in the section on GER. When combined with esophageal manometry, simultaneous information on esophageal pressure and bolus movement is recorded. This information is helpful in the diagnosis of motility disorders.

Esophageal Transit Scintigraphy

The study was first introduced in the early 1970s by Kazem and has been adapted for use in children [130–132]. Esophageal transit scintigraphy provides imaging and quantitative data on the transit of a labeled bolus through the esophagus. There are several protocols for the study. The following will be described as a general guide.

Study Protocol

Preparations: A 4-h fasting is recommended for most cases. In infants, the study should replace a normal scheduled feeding.

Radiopharmaceutical: ^{99m}Tc-sulfur colloid mixed with 30 ml of liquid (milk, formula, or 5 % dextrose water). The dose range is 7.4–37 MBq (200 μCi to 1 mCi). Larger volumes may be used for older patients. Labeled semisolids and solids are used infrequently.

Study technique: Infants can lie directly on the slightly inclined collimator or be supported on a secured apparatus. Older children can sit up with their back to the collimator. It is important to turn the head of bottle-fed infants to the side to prevent superimposition of the radioactivity in the bottle over the upper esophagus. Older children can be fed with a cup or, preferably, through a straw. Imaging begins at the onset of swallowing. The camera is equipped with a low-energy high-resolution collimator. Images are recorded on a 128×128 matrix, 2 s per frame for 100 s. Static images are taken after completion of the dynamic sequence. If a large residual remains in the esophagus, delayed static images are obtained at 30 and 60 min. A ^{57}Co transmission image may be taken immediately or at 10 min following completion of the dynamic sequence, when anatomical location (e.g., gastric fundus vs. esophagus) of the tracer is uncertain.

Image Processing and Interpretation

Recorded images are played back in cine mode for visual evaluation of the bolus transit. Oral or pharyngeal retention, esophageal retention, bolus fragmentation, premature swallows (resulting in deglutition inhibition), tracheobronchial aspiration, and GER can be identified by visual inspection. Slow progression or even stopping of the bolus with the cranio-caudal direction maintained can be seen in scleroderma and achalasia. Presenting the dynamic data in a single image can enhance visual inspection. The condensed dynamic image shows the profiles of the swallowing event side by side on the y-axis along with time on the x-axis [133]. The condensed image may aid identification of abnormal motility patterns.

Esophageal transit can be measured quantitatively with time and retention parameters. The esophagus is divided into upper, middle, and lower zones. Equal ROIs are placed on each zone, and a fourth ROI is placed over the stomach. Time activity curves are generated from each ROI. The curves allow qualitative and quantitative assessment of the bolus transit. The data from the 3 zones can be summed for a total esophageal measurement. Normal transit presents as a sharp peak in the upper esophageal zone followed by sequential sharp peaks in the middle and lower zone and early buildup of activity in the stomach (Fig. 9.4). Deviation from this pattern can suggest esophageal dysmotility (Fig. 9.5). Multiple peaks in the three esophageal time activity curves can be seen in diffuse esophageal spasm.

Esophageal transit time (for a single swallow) is defined as the time from initial entry of activity into the esophagus to the time activity drops to less than 10 % from the peak. It was found useful in differentiating between diffuse esophageal motility disorders, low esophageal motility disorders, and achalasia [134]. Esophageal transit time is affected by the patient's position and the consistency of the test meal. In adults, transit time for liquids was less than 5 s in the erect position

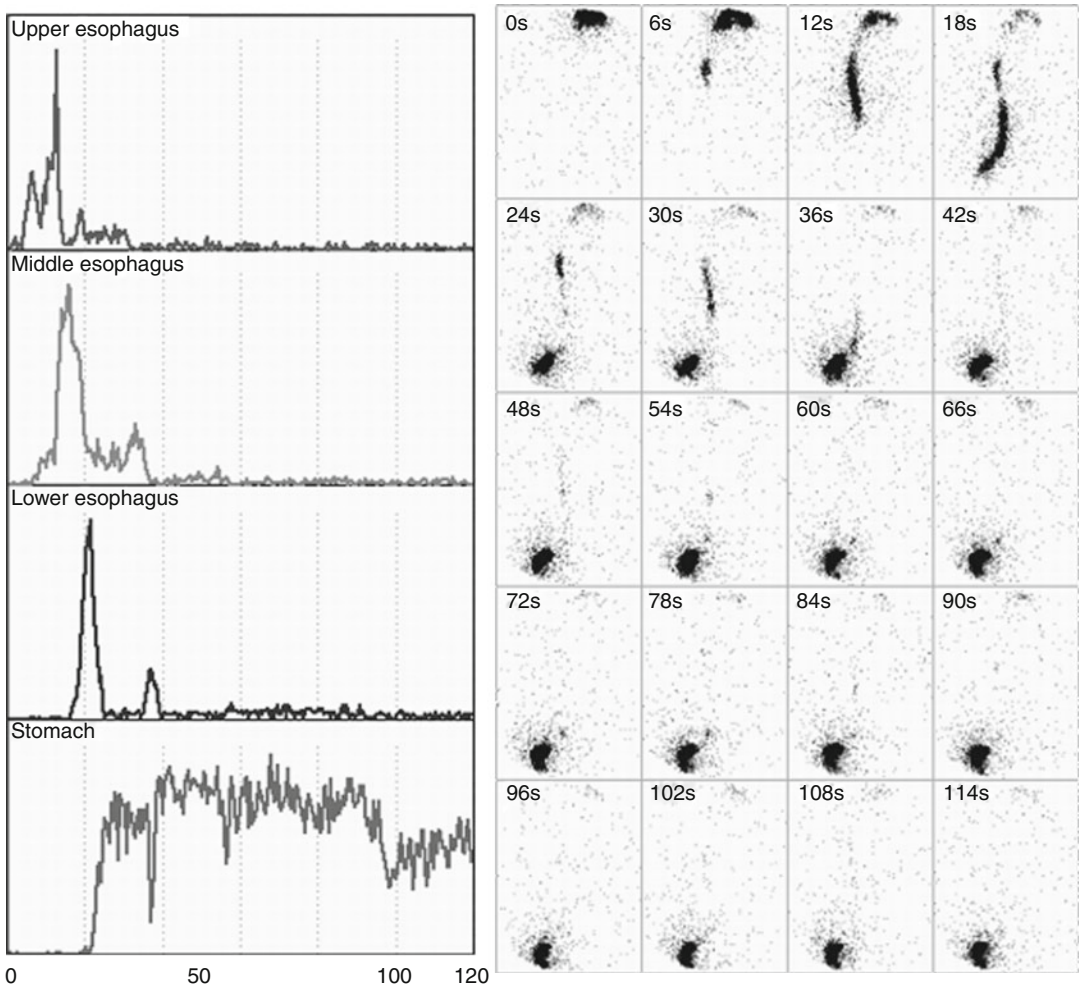

Fig. 9.4 A normal esophageal motility study. Note the sequential coordinated peaks of the time activity curves derived from the *upper*, *middle*, and *lower* esophagus and the complete clearance of activity from the esophagus at the end of the dynamic sequence

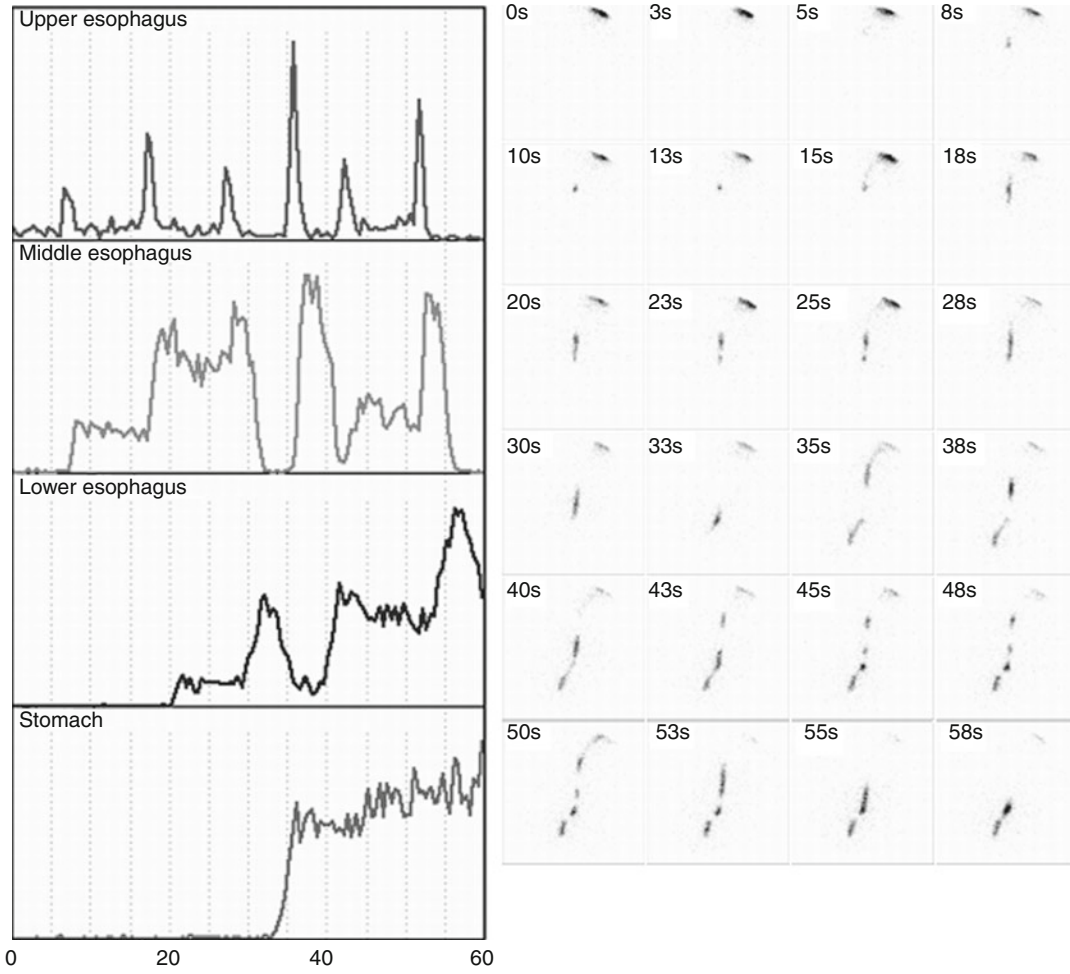

Fig. 9.5 An esophageal transit study of a young woman with history of renal transplantation and fundoplication surgery for gastroesophageal reflux. The woman presented with complaints of dysphagia and heartburn. Time activity curves obtained from regions of interest placed over the *upper*, *middle*, and *lower* esophagus show multiple uncoordinated spikes and some tracer accumulation in the distal esophagus that clears away on a delayed 10-min image (not shown). These findings suggest esophageal dysmotility

and approximately 8 s in the supine position [135]. More complex parameters such as mean transit time and mean time and retention parameters such as esophageal emptying (10 or 12 s after swallowing) as a fraction of the peak activity have been used, mostly in adults [136–138]. Normal quantitative parameters require standardization of techniques and processing algorithms. Such parameters have not been established in children. Characteristic dysmotility patterns can be elicited with esophageal scintigraphy studies in nutcracker esophagus (high-amplitude waves in the lower esophagus), diffuse esophageal spasm (multiple simultaneous contractions at different levels induced by wet swallows), scleroderma (retention in the lower esophagus in the supine position that clears after the patient is upright), and achalasia (significant retention in the lower esophagus in the absence of anatomical obstruction that does not clear in the upright position or following a drink of water) [48].

Some aspects of esophageal transit scintigraphy deserve further elaboration. Technetium-99m-sulfur colloid is the most commonly used radiopharmaceutical. Technetium-99m-nanocolloid and ^{99m}Tc-diethylenetriaminepentaacetic acid (DTPA) also

have been used. Radiopharmaceuticals used in transit scintigraphy should not be absorbed by the gastrointestinal mucosa. Esophageal transit scintigraphy has also been performed with krypton-81m (^{81m}Kr)-labeled glucose. Glucose 5 % in water is infused through a ^{81}Rb/^{81m}Kr generator producing several millicuries of ^{81m}Kr solution. In children the solution is delivered into the mouth by syringe [135]. This technique is easy to perform and provides a quantitative assessment of esophageal transit under physiologic conditions. The radiation dose to the patient from ^{81m}Kr is very low compared with other isotopes. High doses can be given to ensure good quality images, and the study can be repeated as often as necessary. Rubidium-81/krypton-81m generators are not widely available and are more expensive than ^{99m}Tc-based radiopharmaceuticals limiting the availability of this technique for routine clinical practice.

The patient's position during the study can affect results due to the effect of gravity. Performing the study in an upright position appears to be more physiologic. Eliminating the force of gravity, however, by performing the study in the supine position may be more efficient in exposing motility disorders [139]. In infants and young children, the supine or semi-recumbent positions are more practical. Most esophageal studies employ a labeled liquid meal. A semisolid bolus requires more intense peristalsis to complete the transport over the distal half of the esophagus and can increase the sensitivity of the test [140]. There is no consensus on the desired viscosity and type of the semisolid. Solids such as radiolabeled gelatin capsules or labeled chicken liver cubes have been used but can remain in the esophagus up to 2 h even in normal individuals [141, 142]. The volume of a liquid bolus may also affect transit rate. Ten-ml boluses were shown to travel faster than 20-ml boluses in the upright but not in the supine position [135]. It is obviously difficult to control the volume of the swallowed bolus in children and infants. The number and type of swallows is subject to variability. According to one approach, one wet swallow followed by three dry swallows is sufficient for estimation of esophageal residual fraction [136]. According to another approach, the patient is required to perform six independent, wet swallows 30 s apart; a summed image of the six swallows is used to analyze time and retention parameters [138]. The number and frequency of swallows in infants and young children in a given time frame is hard to control.

Sensitivity and specificity of esophageal transit scintigraphy are hard to establish given the lack of technique standardization. They may also differ for different esophageal disorders. Some studies reported sensitivities and specificities of up to 95 and 96 %, respectively, compared with the gold standard of esophageal manometry [138, 143]. Other studies found esophageal scintigraphy to be more sensitive than esophageal manometry or barium radiography [141, 144]. Common indications for esophageal transit scintigraphy in adults include evaluation of dysphagia in patients who cannot tolerate manometry or who have equivocal manometry results, repeat measurements after intervention or therapy, evaluation of ongoing esophageal symptoms in patients with esophageal cancer after esophageal patency has been achieved with stenting, and follow-up of patients with scleroderma [145]. Esophageal transit scintigraphy was found useful in detecting symptomatic and asymptomatic esophageal dysmotility in the midterm follow-up of children who underwent primary repair of esophageal atresia [146].

Dosimetry of esophageal transit scintigraphy was calculated for children assuming an ingested dose of 7.4–18.5 MBq (200–500 μCi). The critical organ was the proximal small bowel. In neonates the proximal small bowel received a dose of 2–3 mSv (200–300 mRem), and the total body dose was 0.30 mSv (30 mRem) [131].

In summary, esophageal transit scintigraphy is a noninvasive study with low radiation exposure that is well tolerated and easy to perform. It provides quantitative parameters that reflect pathophysiologic processes. It can be used for the diagnosis of organic and functional esophageal disorders and is especially valuable when performed serially to evaluate the effect of medical or surgical therapy.

^{99m}Tc-Sucralfate Scintigraphy

Sucralfate is an aluminum salt of a sulfated disaccharide that binds to proteins exposed in ulcerated mucosal surfaces. Sucralfate has protective

and healing properties and has been used therapeutically. Technetium-99m-labeled-sucralfate adheres to damaged, ulcerated surfaces in the gastrointestinal mucosa [147–149]. In children it was shown to adhere to esophageal mucosal surfaces injured by caustic ingestion. It correlated well with endoscopic findings, providing a simple noninvasive technique to assess esophageal injury after ingestion of caustic substances [150].

Pulmonary Aspiration

Aspiration is a common cause of pulmonary disease [151]. Risk factors for aspiration include neurological impairments, congenital malformations of the head and neck (e.g., cleft palate), and surgery of the upper aerodigestive tracts. Children with severe neurodisabilities often experience respiratory problems that may lead to premature death. Pulmonary aspiration has a significant role in the deterioration of respiratory function [152]. Pulmonary aspiration can occur from "above" (direct aspiration of food and saliva) or from below (aspiration of gastric contents due to gastroesophageal reflux). Investigators emphasize the role of aspiration during feeding or from gastroesophageal reflux (GER) as an important cause of acute, recurrent, and chronic pulmonary disease in children [151, 153, 154] . GERD was found in 78 % of children and adolescents with brain damage, mainly cerebral palsy [126]. Children with GERD and swallowing dysfunction have the highest risk for recurrent respiratory tract infections [155]. Imaging studies most frequently requested to evaluate children with suspected aspiration include barium swallows, upper gastrointestinal (UGI) series, and gastroesophageal scintigraphy ("milk scan"). The barium swallow shows aspiration that occurs during the voluntary ingestion of liquids or, with modified techniques, solids. Aspiration secondary to gastroesophageal reflux is demonstrated with radionuclide GER studies or with UGI series. The yield for detecting aspiration from GER has been low in most published series, even with the more sensitive radionuclide GER study [38, 156–160]. Aspiration of saliva is not evaluated with any of the studies mentioned.

Gastroesophageal Reflux Scintigraphy for Detection of Pulmonary Aspiration

Recurrent pulmonary infections have been associated with gastroesophageal reflux. Repeated aspiration of gastric contents following GER has been proposed as a pathogenic mechanism [153, 154, 161]. Gastroesophageal reflux scintigraphy ("milk scan"), developed in the late seventies, can detect pulmonary aspiration secondary to GER [38, 162]. The study technique was discussed earlier in the section on gastroesophageal reflux scintigraphy. The percent of milk scans positive for aspiration ranges from 1 to 25 % in different series [38, 157, 159, 160, 162–166]. Higher aspiration rates were found in a study on 51 children with unexplained respiratory symptoms including pneumonia, cough, asthma, apnea, and laryngitis that underwent a gastroesophageal reflux study with a test meal based on milk or formula in young children or scrambled eggs with toast in older children labeled with ^{99m}Tc-sulfur colloid. These studies included overnight planar images of the chest performed 20 h after ingestion of the test meal. An exceptionally high rate (49 %) of pulmonary aspiration was found in this cohort. Interestingly, 19 of 25 children with aspiration on scintigraphy had negative esophageal pH monitoring studies. Pulmonary aspiration was demonstrated in all children with apnea [167].

Nevertheless, the ability of milk scans to detect pulmonary aspiration continues to be a subject of considerable debate [157, 158, 164]. Some authors report a very low yield in detection of pulmonary aspiration [157, 164]. This has been the general experience of many pediatric radiology departments in the United States [158]. It was argued that milk scans are insensitive for detection of pulmonary aspiration. The success of anti-reflux treatment in lowering the incidence of pulmonary disease in children who failed to demonstrate aspiration on GER scintigraphy was used to support this argument [157].

One study found a higher incidence of aspiration in children with pulmonary disease than in children referred for gastrointestinal symptoms of GER, indicating that detection rates depend on patient selection [160]. The number of children with predisposing risk factors for aspiration such

as neurological impairment, congenital malformations, and surgery of the head and neck varied in different series as well. Differences in study technique may also play a role. Low concentration of radioactivity in the aspirate and rapid clearance of activity from the upper airway by the coughing reflex and the mucociliary transport mechanism could account for low detection rates as well [168]. A phantom study designed to estimate the detectability of different volumes of aspirated gastric contents found a minimal detectable volume of 0.025 ml using a standard concentration of ^{99m}Tc-sulfur colloid (5 μCi/ml) [38]. Low detection rates may result from the intermittent nature of pulmonary aspiration even in patients with risk factors for aspiration and recurrent lung infections [158]. Finally, the possibility that infrequent demonstration of aspiration on milk scans indicates that aspiration of gastric contents is not a common mechanism for recurrent pulmonary infections (as traditionally assumed) should also be considered. Figure 9.6 demonstrates pulmonary aspiration secondary to gastroesophageal reflux.

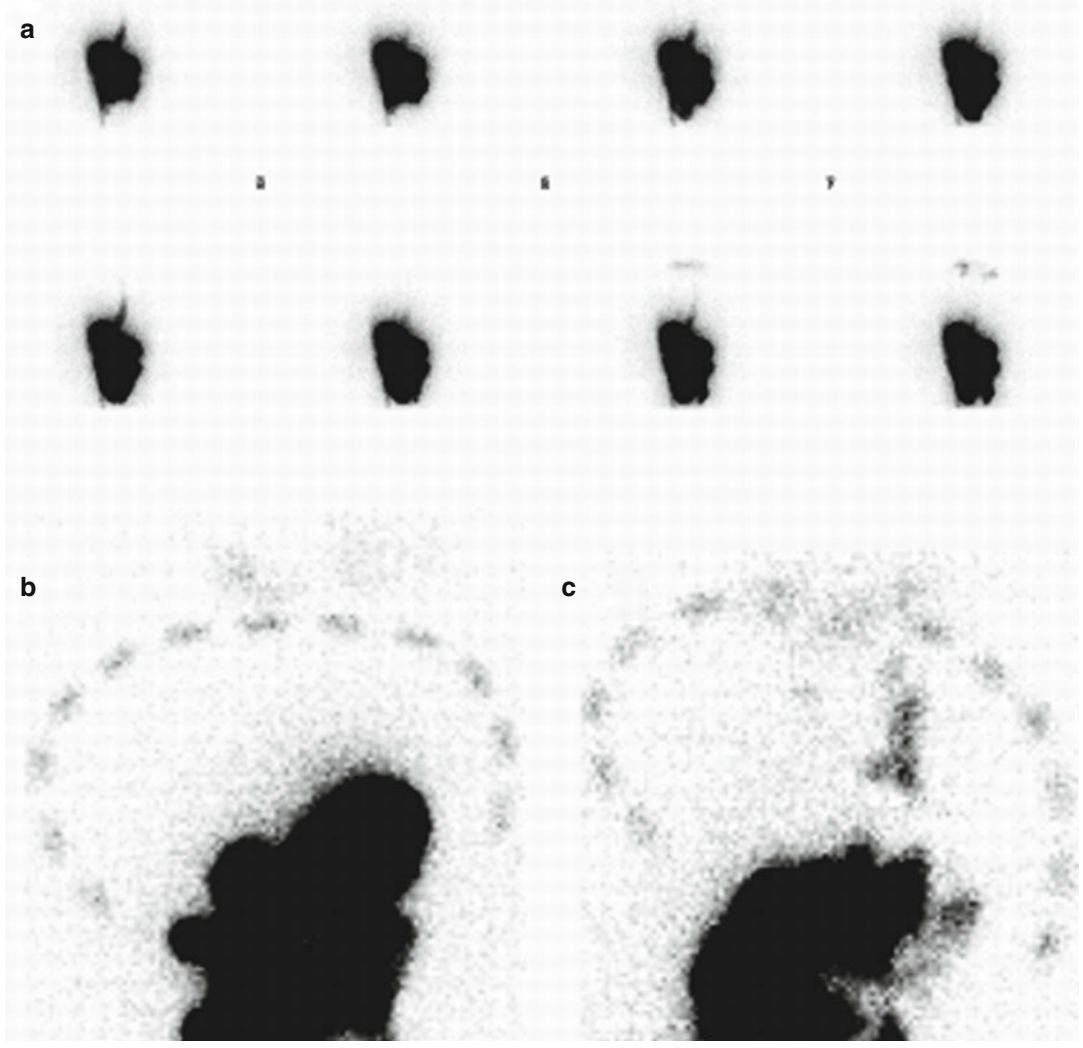

Fig. 9.6 A "milk scan" of a 1-year-old boy with neurological impairment due to thiamine deficiency and recurrent pneumonia was obtained due to suspected aspirations. Dynamic images (**a**) show multiple episodes of GER up to the oral cavity. An anterior static image (**b**) of the chest obtained at 1 h, immediately after the dynamic sequence, shows clear lung fields. A delayed anterior image of the upper abdomen and thorax (**c**) shows tracer localization in the trachea and right and left main bronchi (*arrow*), indicating late aspiration of gastric contents. The dotted line, seen on images (**b**, **c**), is a radioactive marker outlining the chest boundaries

The radionuclide gastroesophageal reflux study (milk scan) was found to be more sensitive than upper GI series for demonstrating aspiration of gastric contents [38, 163]. This observation was also noted in a study on 120 children referred for scintigraphy and UGI series due to respiratory disorders, gastroesophageal reflux, and near-miss sudden infant death syndrome [160].

Aspiration of Saliva and the Radionuclide Salivagram

Aspiration of saliva is less well recognized as a potential etiology for pulmonary disease probably due to the lack of methods that could demonstrate aspiration of saliva. Repeated aspiration of oral secretions and failure to adequately clear the aspirate from the respiratory tract have been proposed as pathogenic mechanisms leading to recurrent pulmonary infections. Bacteriologic studies showing that organisms isolated from the lower respiratory tract in aspiration pneumonia reflect the oropharyngeal flora, with a predominance of anaerobes, support this etiology [169, 170]. Aspiration of oral secretions is likely to occur in patients with abnormal laryngeal closure [171]. Aspiration of saliva accounts for ongoing pulmonary infections in neurologically impaired patients despite corrective measures to prevent aspiration such as anti-reflux surgery and discontinuation of oral feedings with gastrostomy tube feeding [172–175]. It deserves consideration and should be evaluated in the context of recurrent lung infections.

The radionuclide salivagram is a technique designed to detect aspiration of saliva. A drop of ^{99m}Tc-sulfur colloid is placed in the oral cavity, mixes with saliva, and is swallowed. Using dynamic scintigraphy, the course of the tracer-saliva mixture is followed as it passes through the esophagus into the stomach. When aspiration occurs, tracer is seen within the tracheobronchial tree (Fig. 9.7) [176].

Study Technique and Interpretation

No specific preparations are required for the test. The patient is placed supine with the camera positioned under the imaging table and centered under the patient's chest. A small drop (100 μl) containing 11.1 MBq (300 μCi) ^{99m}Tc-sulfur colloid is placed on the back of the patient's tongue.

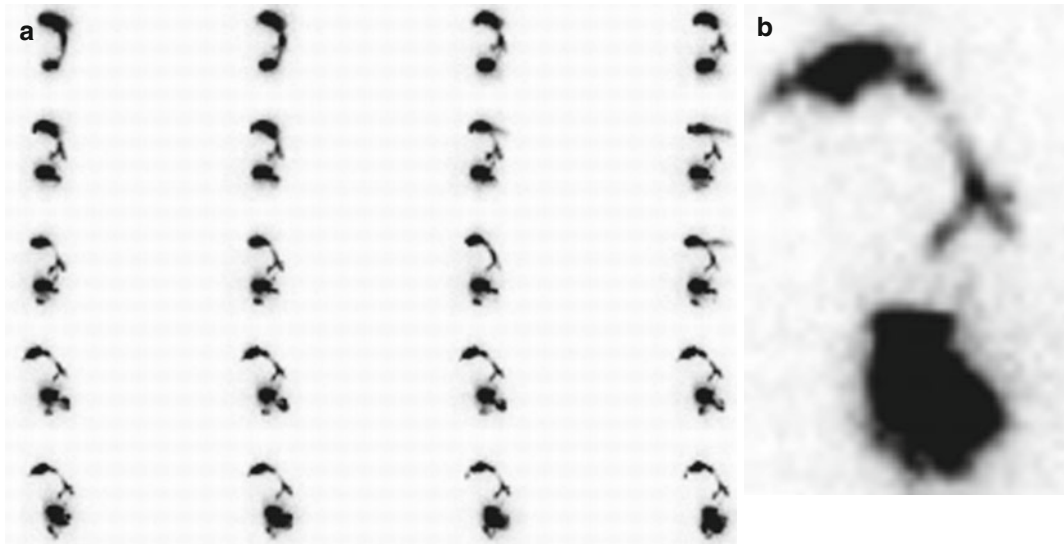

Fig. 9.7 A radionuclide salivagram was performed on a 7-week-old infant with choking episodes and suspected laryngeal cleft. (**a**) shows the dynamic study displayed at 60 s per frame. Sequential posterior images (*left to right*, *top to bottom*) demonstrate transit of tracer from the oral cavity down the esophagus into the stomach. Ectopic activity in the airways, indicating aspiration of saliva, is first noted on the second frame from the left in the top row and becomes more evident as the study progresses. (**b**) is an enlarged frame showing more clearly localization of tracer in the left and right main bronchi

Imaging commences immediately after administration. A camera equipped with a low-energy high-resolution collimator records posterior view dynamic images on a 128×128 matrix, 30 s per frame, for 60 min. Static anterior and posterior images of the chest are recorded on a 256×256 matrix immediately after the dynamic sequence. If a significant amount of tracer remains in the oral cavity, additional delayed images are obtained at 120 min. A ^{57}Co transmission image of the chest can improve localization of tracer in the lung fields. Care should be taken to avoid external contamination of cloths by labeled saliva because contamination could be mistaken for aspiration when positioned over the lung fields.

Images are inspected for evidence of tracer penetration into the tracheobronchial tree or into the lung parenchyma. The level of tracer localization in the proximal or distal airways and the persistence or clearance of aspirated tracer are noted. Cinematic display of the dynamic images is helpful. The effectiveness of this study in demonstrating aspiration of saliva has been reported in several studies. We demonstrated aspiration of saliva in 8 of 31 children (26 %) with pulmonary disease and risk factors for aspiration, especially neurological disorders and birth defects involving the head and neck [177]. Other studies, performed on children with similar risk factors, yielded similar results [166, 176].

The ability of the radionuclide salivagram to determine the level of aspiration and to determine the clearance of the aspirate from the tracheobronchial tree is important in assessing the severity of aspiration. In an animal experiment, ^{99m}Tc-sulfur colloid instilled into proximal airways cleared rapidly, but the same tracer instilled into distal airways was retained [38]. It is therefore likely that distal aspiration is more ominous than proximal aspiration. In addition, by assessing a patient's ability to clear aspirated secretions, the radionuclide salivagram evaluates the functional integrity of airway protective mechanisms such as the cough reflex and mucociliary transport (Fig. 9.8). Impairment of these protective mechanisms is a significant factor contributing to the development of lung disease in patients who aspirate [169, 178–180].

It should be emphasized that the radionuclide salivagram is not a scintigraphic counterpart of the radiographic barium swallow. The salivagram is a physiologic technique, simple to perform and requiring little patient cooperation. It involves the oral administration of only a tiny

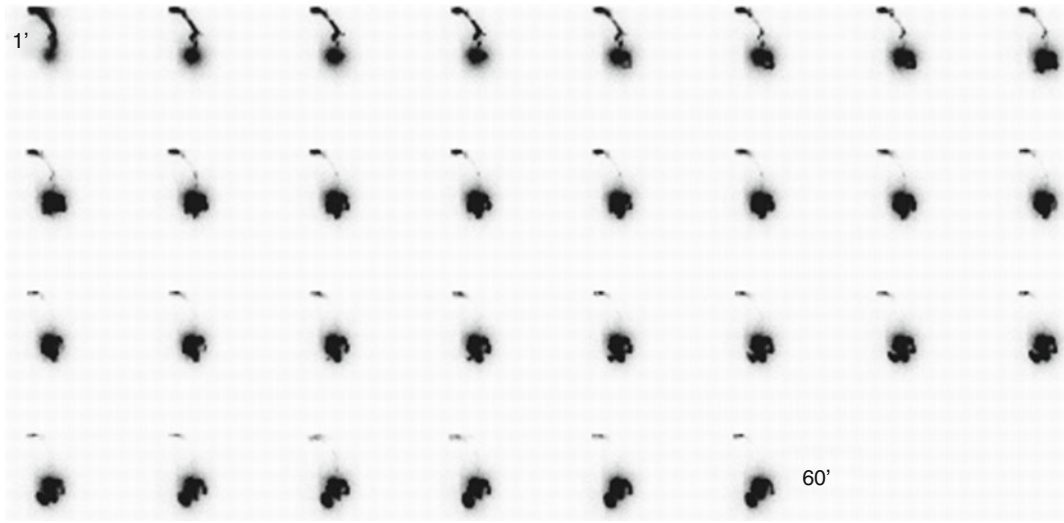

Fig. 9.8 A radionuclide salivagram of a 4-year-old girl with recurrent lung infections, macrocephalus, psychomotor retardation, and seizure disorder was obtained due to suspected aspiration. Sequential dynamic images show aspiration of saliva into the right and left main stem bronchi (*top row*) with complete clearance of tracer from the airways as the study progresses

volume of saline, often unnoticed by the patient. It provides information on aspiration of oral secretions, unrelated to the conscious ingestion of liquids and solids during feeding. It exposes the patient to minimal radiation (in the order of 0.05 mSv total body dose) [181]. By comparison, a barium swallow delivers a much higher radiation dose to the patient (up to 13 mSv for a modified barium swallow in adults), necessitates the ingestion of a larger volume of liquid, the taste of which is unpleasant to some patients, and requires a higher degree of patient cooperation [182]. It provides information on aspiration that occurs during feeding. Barium swallows provide valuable dynamic anatomical information that is used to assess the integrity of the swallowing mechanism [183].

Information provided by both techniques should be regarded as complementary. Aspiration of oral secretions, detected by salivagrams, was more commonly encountered than aspiration of barium in a study involving 46 children with lung disease, recurrent vomiting, or apnea who underwent scintigraphic and radiographic evaluations for detection of GER and aspiration [163]. In 63 children with cerebral palsy, aspiration was most commonly found with salivagrams (56 %) followed by barium videofluoroscopy (39 %) and milk scans (6 %). The authors concluded that the agreement between the tests was poor [184]. It should be kept in mind, however, that these studies detect different types of aspirations. Radionuclide salivagrams were more sensitive than barium studies in detecting aspiration in 78 patients with head and neck pathologies and neurological disorders [185].

Other Techniques for Detection of Aspiration

Scintigraphic Swallowing Studies

Scintigraphic swallowing techniques are based on swallowing of 10–15 ml boluses of liquids labeled with ^{99m}Tc-sulfur colloid. They are designed to detect aspiration that occurs during drinking, unlike the radionuclide salivagram which is designed to detect aspiration of saliva by using a very small volume of radiotracer (one drop). The majority of such studies were performed in adults with dysphagia [186, 187]. The techniques vary in protocols. Some protocols are similar to esophageal transit scintigraphy described in the previous section [159, 188, 189]. In a modified salivagram study, in which 20 ml of ^{99m}Tc-sulfur colloid were instilled into the pharynx over an hour, a pulmonary aspiration was seen in 56 % of children with cerebral palsy as opposed to 0 % in healthy young adult volunteers [190]. Aspiration of a swallowed tracer can be volume dependent. This has been shown in a 7-year-old girl with respiratory failure and suspected aspirations. Her radionuclide salivagram was normal; however, when challenged with a 10-ml-labeled water bolus, bilateral pulmonary aspiration occurred. It was hypothesized that the swallowing mechanism may be capable of handling small volumes of saliva but malfunctions when challenged with larger volumes. It was recommended to perform a labeled bolus study on patients with suspected aspiration and a normal salivagram [189].

Non-imaging Techniques for Evaluation of Pulmonary Aspiration

The lipid-laden alveolar macrophage study is a non-imaging technique used as an indicator for recurrent pulmonary aspiration by demonstrating increased lipid content in alveolar macrophages isolated from bronchoalveolar lavage (BAL) fluid. The invasive nature of this study is a disadvantage compared with imaging techniques. Studies assessing the utility of this technique in children yielded conflicting results. Significantly higher lipid-laden alveolar macrophage (LLAM) scores were found in children with lung disease due to suspected aspirations than in children without lung disease or in children with lung disease from other etiologies [191–194]. Others found elevated LLAM scores in a variety of pulmonary diseases in which there was no clinical evidence of aspiration [195].

In another study, the mean LLAM index of a subgroup of children with both reflux and respiratory symptoms was not significantly different from that of a subgroup that was negative for

both conditions [196]. These authors concluded that the low sensitivity and specificity of this test preclude it from becoming a useful indicator of silent pulmonary aspiration in children. Pepsin is a proteolytic enzyme derived from pepsinogen that is produced by the chief cells in the gastric mucosa. It has been suggested as a biomarker for the detection of aspiration secondary to GER. Pepsin can be isolated from tracheal aspirates and even from salivary secretions [152]. Pepsin enzymatic activity was found in 31/37 tracheal aspirates of children with GERD compared with 0/26 healthy controls [197]. Assays for measuring pepsin activity vary significantly in their sensitivity. The more sensitive assays have shown low pepsin activity in healthy pediatric control patients [198]. Lack of assay standardization and establishment of normal values limits the usefulness of this test [152].

Prevention of Pulmonary Aspiration

Discontinuing oral feedings, substituting gastrostomy tube feedings, and performing anti-reflux surgeries are effective means to control aspiration that occurs during feeding and aspiration secondary to gastroesophageal reflux. In contrast, therapy options for children who aspirate saliva are limited, require surgical intervention, and are associated with significant morbidity. Radical surgery is justified in some patients (mostly with severe neurological impairment and inability to handle oral secretions) in whom intractable aspiration of saliva results in life-threatening respiratory conditions. Tracheotomy is often performed in such patients to allow better respiratory control and the ability to manage secretions, but this does not solve the underlying condition of salivary aspirations.

Laryngotracheal separation is a radical, but potentially reversible, surgery that prevents aspiration of oral secretions. Phonation is sacrificed with this procedure. Using this technique, complete control of aspiration was achieved in 19 children with severe neurological impairment and chronic salivary aspiration [199]. Radionuclide salivagrams proved useful in selecting neurologically impaired children with recurrent respiratory infections and frequent hospitalizations for laryngotracheal separation [200].

Laryngeal diversion is another radical surgery that achieved stabilization or improvement of pulmonary function in a group of children with life-threatening aspiration [201]. Bilateral submandibular gland excision and parotid duct ligation is a voice-sparing procedure that reduced the incidence of aspiration pneumonia and hospitalization in a select group of neurologically impaired children [202]. A simpler procedure involving bilateral submandibular gland and parotid duct ligation achieved control of salivary aspiration in five children with severe neuromuscular impairment and recurrent aspiration pneumonia [203].

References

1. Cezard JP. Managing gastro-oesophageal reflux disease in children. Digestion. 2004;69 Suppl 1:3–8.
2. Werlin SL, Dodds WJ, Hogan WJ, et al. Mechanisms of gastroesophageal reflux in children. J Pediatr. 1980;97:244–2499.
3. Kawahara H, Dent J, Davidson G. Mechanisms responsible for gastroesophageal reflux in children. Gastroenterology. 1997;113:399–408.
4. Omari TI, Barnett CP, Benninga MA, et al. Mechanisms of gastro-oesophageal reflux in preterm and term infants with reflux disease. Gut. 2002;51:475–7.
5. Holloway R, Hongo M, Berger K, McCallum R. Gastric distention: a mechanism for postprandial gastroesophageal reflux. Gastroenterology. 1985;89:779–84.
6. Velasco N, Hill L, Gannan R, Pope C. Gastric emptying and gastroesophageal reflux. Am J Surg. 1982;144:58–62.
7. Fink SM, Barwick KW, DeLuca V, Sanders FJ, Kandathil M, McCallum RW. The association of histologic gastritis with gastroesophageal reflux and delayed gastric emptying. J Clin Gastroenterol. 1984;6:301–9.
8. Buckles DC, Sarosiek I, McMillin C, McCallum RW. Delayed gastric emptying in gastroesophageal reflux disease: reassessment with new methods and symptomatic correlations. Am J Med Sci. 2004;327:1–4.
9. Hillemeier AC, Lange R, McCallum R, Seashore J, Grybosky J. Delayed gastric emptying in infants with gastroesophageal reflux. J Pediatr. 1981;98:190–3.
10. Hillemeier AC, Grill BB, McCallum R, Grybosky J. Esophageal and gastric motor abnormalities in gastroesophageal reflux during infancy. Gastroenterology. 1983;84:742–6.

11. Cucchiara S, Salvia G, Borrelli O, et al. Gastric electrical dysrhythmias and delayed gastric emptying in gastroesophageal reflux disease. Am J Gastroenterol. 1997;92:1077–8.
12. Rosen PR, Treves S. The relationship of gastroesophageal reflux and gastric emptying in infants and children: concise communication. J Nucl Med. 1984;25:571–4.
13. Jolley SG, Leonard JC, Tunell WP. Gastric emptying in children with gastroesophageal reflux. An estimate of effective gastric emptying. J Pediatr Surg. 1987;22:923–6.
14. Di Lorenzo C, Piepsz A, Ham H, Cadranel S. Gastric emptying with gastroesophageal reflux. Arch Dis Child. 1987;2:449–53.
15. Salvia G, De Vizia B, Manguso F, et al. Effect of intragastric volume and osmolality on mechanisms of gastroesophageal reflux in children with gastroesophageal reflux disease. Am J Gastroenterol. 2001;96:1725–32.
16. Cameron AJ, Lagergren J, Henriksson C, Nyren O, Locke GR, Pedersen NL. Gastroesophageal reflux disease in monozygotic and dizygotic twins. Gastroenterology. 2002;122:55–9.
17. Orenstein SR, Shalaby TM, Barmada MM, Whitcomb DC. Genetics of gastroesophageal reflux disease: a review. J Pediatr Gastroenterol Nutr. 2002;34:506–10.
18. Shepherd RW, Wren J, Evans S, Lander M, Ong TH. Gastroesophageal reflux in children. Clinical profile, course and outcome with active therapy in 126 cases. Clin Pediatr (Phila). 1987;26:55–60.
19. Treem WR, Davis PM, Hyams JS. Gastroesophageal reflux in the older child: presentation, response to treatment and long-term follow-up. Clin Pediatr (Phila). 1991;30:435–40.
20. Vandenplas Y. Hiatal hernia and gastroesophageal reflux. In: Buts JP, Sokal EM, editors. Management of digestive and liver disorders in infants and children, Elsevier science, vol. 9. 1993. p. 103–16.
21. Morigeri C, Bhattacharya A, Mukhopadhyay K, Narang A, Mittal BR. Radionuclide scintigraphy in the evaluation of gastroesophageal reflux in symptomatic and asymptomatic pre-term infants. Eur J Nucl Med Mol Imaging. 2008;35:1659–65.
22. Nelson SP, Chen EH, Syniar GM, et al. Prevalence of symptoms of gastroesophageal reflux during infancy. A pediatric practice based survey. Pediatric Practice Research Group. Arch Pediatr Adolesc Med. 1997;151:569–72.
23. Werlin SL, D'Souza BJ, Hogan WJ, et al. Sandifer syndrome: an unappreciated clinical entity. Dev Med Child Neurol. 1980;22:374–8.
24. Gorrotxategi P, Reguilon MJ, Arana J, et al. Gastroesophageal reflux in association with the Sandifer syndrome. Eur J Pediatr Surg. 1995;5:203–5.
25. Hassall E. Barrett's esophagus: new definitions and approaches in children. J Pediatr Gastroenterol Nutr. 1993;16:345–64.
26. Ranjitkar S, Smales RJ, Kaidonis JA. Oral manifestations of gastroesophageal reflux disease. J Gastroenterol Hepatol. 2012;27:21–7.
27. Harding SM. Recent clinical investigations examining the association of asthma and gastroesophageal reflux. Am J Med. 2003;18:39S–44.
28. Rudolph CD, Mazur LJ, Liptak GS, et al. Guidelines for the evaluation and treatment of gastroesophageal reflux in infants and children. Recommendations of the North American Society for Pediatric Gastroenterology and Nutrition. J Pediatr Gastroenterol Nutr. 2001;32 suppl 2:S1–31.
29. Streets CG, DeMeester TR. Ambulatory 24-hour esophageal pH monitoring: why, when, and what to do. J Clin Gastroenterol. 2003;37:14–22.
30. Thomson M. The pediatric esophagus comes of age. J Pediatr Gastroenterol Nutr. 2002;34 suppl 1:S40–5.
31. Mitchell DJ, McClure BG, Tubman TRJ. Simultaneous monitoring of gastric and oesophageal pH reveals limitations of conventional oesophageal pH monitoring in milk fed infants. Arch Dis Child. 2001;84:273–6.
32. Wenzl TG. Evaluation of gastroesophageal reflux events in children using multichannel intraluminal electrical impedance. Am J Med. 2003;18(115 Suppl 3A):161S–5.
33. Mousa HM, Rosen R, Woodley FW, et al. Esophageal impedance monitoring for gastroesophageal reflux. J Pediatr Gastroenterol Nutr. 2011;52:129–39.
34. Wenzl TG, Silny J, Schenke S, et al. Gastroesophageal reflux and respiratory phenomena in infants: status of the intraluminal impedance technique. J Pediatr Gastroenterol Nutr. 1999;28:423–8.
35. Riccabona M, Maurer U, Lackner H, Uray E, Ring E. The role of sonography in the evaluation of gastro-oesophageal reflux-correlation to pH-metry. Eur J Pediatr. 1992;151:655–7.
36. Fornari F, Wagner R. Update on endoscopic diagnosis, management and surveillance strategies of esophageal diseases. World J Gastrointest Endosc. 2012;4:117–22.
37. Biller JA, Winter HS, Grand RJ, et al. Are endoscopic changes predictive of histologic esophagitis in children? J Pediatr. 1983;103:215–8.
38. Heyman S, Kirkpatrick JA, Winter HS, Treves S. An improved radionuclide method for the diagnosis of gastroesophageal reflux and aspiration in children (milk scan). Radiology. 1979;131:479–82.
39. Gelfand MJ, Parisi MT, Treves ST. Pediatric radiopharmaceutical administered doses: 2010 North American consensus guidelines. Pediatric Nuclear Medicine Dose Reduction Workgroup. J Nucl Med. 2011;52:318–22.
40. Reyhan M, Yapar AF, Aydin M, Sukan A. Gastroesophageal scintigraphy in children: a comparison of posterior and anterior imaging. Ann Nucl Med. 2005;19:17–21.
41. Piepsz A, Georges B, Rodesch P, Cadranel S. Gastroesophageal scintiscanning in children. J Nucl Med. 1982;23:631–2.

42. Othman S. Gastroesophageal reflux studies using milk in infants and children-the need for multiple views. Nucl Med Commun. 2011;32:967–71.
43. Piepsz A, Georges B, Perlmutter N, Rodesch P, Cadranel S. Gastro-oesophageal scintiscanning in children. Pediatr Radiol. 1981;11:71–4.
44. Braga FJ, De Miranda JR, Arbex MA, et al. A physiological manoeuvre to improve the positivity of the gastro-oesophageal reflux scintigraphic test. Nucl Med Commun. 2001;22:521–4.
45. Castronovo FP. Gastroesophageal scintigraphy in a pediatric population: dosimetry. J Nucl Med. 1986;27:1212–4.
46. Fisher RS, Malmud LS, Roberts GS, Lobis IF. Gastroesophageal (GE) scintiscanning to detect and quantitate GE reflux. Gastroenterology. 1976;70:301–8.
47. Devos PG, Forget P, DeRoo M, Eggermont E. Scintigraphic evaluation of gastrointestinal reflux (GER). J Nucl Med. 1979;20:636 (abstract).
48. Mariani G, Boni G, Barreca M, et al. Radionuclide gastroesophageal motor studies. J Nucl Med. 2004;45:1004–28.
49. Arasu TS, Wyllie R, Fitzgerald JF, et al. Gastroesophageal reflux in infants and children: comparative accuracy of diagnostic methods. J Pediatr. 1980;96:798–803.
50. Blumhagen JD, Rudd TG, Christie DL. Gastroesophageal reflux in children: radionuclide gastroesophagography. AJR Am J Roentgenol. 1980;135:1001–4.
51. Seibert JJ, Byrne WJ, Euler AR, Latture T, Leach M, Campbell M. Gastroesophageal reflux–the acid test: scintigraphy or the pH probe? Am J Roentgenol. 1983;140:1087–90.
52. Laudizi L, Zaniol P, Venuta A, Pantusa M, Sturloni N, Laudizi Z. Gastroesophageal reflux in children. A combined radiologic and scintigraphic study. Radiol Med. 1990;79:381–3.
53. Kashyap R, Sharma R, Madan N, Sachdev G, Chopra MK, Chopra K. Evaluation of radionuclide gastroesophagography as a suitable screening test for detection of gastroesophageal reflux. Indian Pediatr. 1993;30:625–8.
54. Patwari AK, Bajaj P, Kashyp R, et al. Diagnostic modalities for gastroesophageal reflux. Indian J Pediatr. 2002;69:133–6.
55. Ozcan Z, Ozcan C, Erinc R, Dirlik A, Mutaf O. Scintigraphy in the detection of gastro-oesophageal reflux in children with caustic oesophageal burns: a comparative study with radiography and 24-h pH monitoring. Pediatr Radiol. 2001;31:737–41.
56. Tolia V, Kuhns L, Kauffman RE. Comparison of simultaneous esophageal pH monitoring and scintigraphy in infants with gastroesophageal reflux. Am J Gastroenterol. 1993;88:661–4.
57. Vandenplas Y, Derde MP, Piepsz A. Evaluation of reflux episodes during simultaneous esophageal pH monitoring and gastroesophageal reflux scintigraphy in children. J Pediatr Gastroenterol Nutr. 1992;14:256–60.
58. Tolia V, Calhoun JA, Kuhns LR, Kauffman RE. Lack of correlation between extended pH monitoring and scintigraphy in the evaluation of infants with gastroesophageal reflux. J Lab Clin Med. 1990;115:559–63.
59. Orenstein SR, Klein HA, Rosenthal MS. Scintigraphy versus pH probe for quantification of pediatric gastroesophageal reflux: a study using concurrent multiplexed data and acid feedings. J Nucl Med. 1993;34:1228–34.
60. Jona JZ, Sty JR, Glicklich M. Simplified radioisotope technique for assessing gastroesophageal reflux in children. J Pediatr Surg. 1981;16:114–7.
61. Craig WR, Hanlon-Dearman A, Sinclair C, Taback SP, Moffatt M. Withdrawn: Metoclopramide, thickened feedings, and positioning for gastro-oesophageal reflux in children under two years. Cochrane Database Syst Rev. 2010;12, CD003502.
62. Illueca M, Wernersson B, Henderson C, Lundborg PJ. Maintenance treatment with proton pump inhibitors for reflux esophagitis in pediatric patients: a systematic literature analysis. J Pediatr Gastroenterol Nutr. 2010;51:733–40.
63. Maclennan S, Augood C, Cash-Gibson L, Logan S, Gilbert RE. Cisapride treatment for gastro-oesophageal reflux in children. Cochrane Database Syst Rev. 2010;14, CD002300.
64. Siddiqui MR, Abdulaal Y, Nisar A, Ali H, Hasan F. A meta-analysis of outcomes after open and laparoscopic Nissen's fundoplication for gastro-oesophageal reflux disease in children. Pediatr Surg Int. 2011;27:359–66.
65. DiLorenzo C, Mertz H, Alvarez S, Mori C, Mayer E, Hyman PE. Gastric receptive relaxation is absent in newborn infants. Gastroenterology. 1993;104:A498 (abstract).
66. Huisinga JD. Physiology and pathophysiology of interstitial cells of Cajal: from bench to bedside. II. Gastric motility lessons from mutant mice on slow waves and innervation. Am J Physiol. 2001;281:G1129–34.
67. Heyman S. Gastric emptying in children. J Nucl Med. 1998;39:865–9.
68. Siegel M, Lebenthal E, Topper W, Krantz B, Li PK. Gastric emptying in prematures of isocaloric feedings with differing osmolalities. Pediatr Res. 1982;16:141–7.
69. Christian PE, Moore JG, Brown F, et al. Effect of caloric content and meal size in gastric emptying. J Nucl Med. 1982;23(suppl):P20 [abstract].
70. Maes BD, Ghoos YF, Geypens BJ, Hiele MI, Rutgeerts PJ. Relation between gastric emptying rate and energy intake in children compared with adults. Gut. 1995;36:183–8.
71. Cavell B. Gastric emptying in infants fed human milk or infant formula. Acta Paediatr Scand. 1981;70:639–41.
72. Billeaud C, Guillet J, Sandler B. Gastric emptying in infants with or without gastro-oesophageal reflux according to the type of milk. Eur J Clin Nutr. 1990;44:577–83.
73. Hunt JN, Knox MT. A relation between the chain length of fatty acids and the slowing of gastric emptying. J Physiol. 1968;194:327–36.

74. Cooke AR, Moulang J. Control of gastric emptying by amino acids. Gastroenterology. 1972;62: 528–32.
75. Di Lorenzo C, Piepsz A, Ham H, Cadranel S. Gastric emptying with gastro-oesophageal reflux. Arch Dis Child. 1987;62:449–53.
76. Waseem S, Islam S, Kahn G, Moshiree B, Talley NJ. Spectrum of gastroparesis in children. J Pediatr Gastroenterol Nutr. 2012;55(2):166–72.
77. Demirbilek S, Karaman A, Gürünlüoğlu K, Akin M, Taş E, Aksoy RT, et al. Delayed gastric emptying in gastroesophageal reflux disease: the role of malrotation. Pediatr Surg Int. 2005;21:423–7.
78. Friesen CA, Lin Z, Hyman PE, Andre L, Welchert E, Schurman JV, et al. Electrogastrography in pediatric functional dyspepsia: relationship to gastric emptying and symptom severity. J Pediatr Gastroenterol Nutr. 2006;42:265–9.
79. Vandenplas Y, Hauser B, Salvatore S. Current pharmacological treatment of gastroparesis. Expert Opin Pharmacother. 2004;5:2251–4.
80. Islam S, Vick LR, Runnels MJ, Gosche JR, Abell T. Gastric electrical stimulation for children with intractable nausea and gastroparesis. J Pediatr Surg. 2008;43:437–42.
81. Koch KL. Diagnosis and treatment of neuromuscular disorders of the stomach. Curr Gastroenterol Rep. 2003;5:323–30.
82. Rostas 3rd JW, Mai TT, Richards WO. Gastric motility physiology and surgical intervention. Surg Clin North Am. 2011;91:983–99.
83. Portincasa P, Colecchia A, Di Ciaula A, et al. Standards for diagnosis of gastrointestinal motility disorders. Section: ultrasonography. A position statement from the Gruppo Italiano di Studio Motilita` Apparato Digerente (GISMAD). Dig Liver Dis. 2000;32:160–72.
84. Bolondi L, Bortolotti M, Santi V, Caletti T, Gaiani S, Labo G. Measurement of gastric emptying time by real-time ultrasonography. Gastroenterology. 1985; 89:752–9.
85. Berstad A, Hausken T, Gilja OH, Hveem K, Nesje LB, Odegaard S. Ultrasonography of the human stomach. Scand J Gastroenterol. 1996;220:75–82.
86. Benini L, Sembenini C, Heading RC, et al. Simultaneous measurement of gastric emptying of a solid meal by ultrasound and by scintigraphy. Am J Gastroenterol. 1999;94:2861–5.
87. Cucchiara S, Minella R, Iorio R, et al. Real-time ultrasound reveals gastric motor abnormalities in children investigated for dyspeptic symptoms. J Pediatr Gastroenterol Nutr. 1995;21:446–53.
88. Kock KL. Electrogastrography. In: Schuster M, Crowell MD, Koch KL, editors. Schuster atlas of gastrointestinal motility in health and disease. Hamilton: BC Decker; 2002. p. 185–201.
89. Ghoos YF, Maes BD, Geypens BJ, et al. Measurement of gastric emptying rate of solids by means of a carbon-labeled octanoic acid breath test. Gastroenterology. 1993;104:1640–7.
90. Kim DY, Camilleri M. Stable isotope breath test and gastric emptying. In: Schuster M, Crowell MD, Koch KL, editors. Schuster atlas of gastrointestinal motility in health and disease. Hamilton: Decker, Inc; 2002. p. 203–18.
91. Braden B, Peterknecht A, Piepho T, et al. Measuring gastric emptying of semisolids in children using the 13C-acetate breath test: a validation study. Dig Liver Dis. 2004;36:260–4.
92. de Zwart IM, de Roos A. MRI for the evaluation of gastric physiology. Eur Radiol. 2010;20:2609–16.
93. Fraser R, Horowitz M, Maddox A, Harding PE, Chatterton BE, Dent J. Hyperglycaemia slows gastric emptying in type 1 diabetes mellitus. Diabetologia. 1990;30:675–80.
94. Gelfand MJ, Wagner GG. Gastric emptying in infants and children: limited utility of 1-hour measurement. Radiology. 1991;178:379–81.
95. Heyman S. Radionuclide transit studies. In: Hyman PE, DiLorenzo CD, editors. Pediatric gastrointestinal motility disorders. 1st ed. New York: Academy Professional Information Services; 1994. p. 291–304.
96. Villanueva-Meyer J, Swischuk LE, Cesani F, Ali SA, Briscoe E. Pediatric gastric emptying: value of right lateral and upright positioning. J Nucl Med. 1996; 37:1356–8.
97. Heyman S, Reich H. Gastric emptying of milk feedings in infants and young children: anterior vs conjugate counting [abstract]. J Nucl Med. 1995; 36(suppl):259P.
98. Drubach LA, Kourmouzi V, Cao X, Zurakowski D, Fahey FH. Gastric Emptying in Children: What is the Best Acquisition Method? J Pediatr Gastroenterol Nutr. 2012;55(2):191–3.
99. Halkar KR, Paszkowski A, Jones M. Two point, timesaving method for measurement of gastric emptying with diagnostic accuracy comparable to that of the conventional method. Radiology. 1999;213: 599–602.
100. Lin E, Connolly LP, Drubach L, et al. Effect of early emptying on quantitation and interpretation of liquid gastric emptying studies of infants and young children. J Nucl Med. 2000;41:596–9.
101. Signer E. Gastric emptying in newborns and young infants. Measurement of the rate of emptying using indium-113m-microcolloid. Acta Paediatr Scand. 1975;64:525–30.
102. Seibert JJ, Byrne WJ, Euler AR. Gastric emptying in children: unusual patterns detected by scintigraphy. Am J Roentgenol. 1983;141:49–51.
103. Knight LC. Radiopharmacy aspects of gastrointestinal imaging. In: Henkin RE, Boles MA, Dillehay GL, et al., editors. Nuclear medicine, vol. 2. St. Louis: Mosby; 1996. p. 922–32.
104. Sagar S, Grime JS, Little W, et al. 99mTc labelled bran: a new agent for measuring gastric emptying. Clin Radiol. 1983;34:275–8.
105. Malagelada JR, Carter SE, Brown ML, Carlson GL. Radiolabeled fiber: a physiologic marker for gastric

emptying and intestinal transit of solids. Dig Dis Sci. 1980;25:81–7.
106. Singh SJ, Gibbons NJ, Blackshaw PE, Vincent M, Wakefield J, Perkins AC. Gastric emptying of solids in normal children–a preliminary report. J Pediatr Surg. 2006;41:413–7.
107. Drubach LA, Kourmouzi V, Fahey FH. Cheese is a reliable alternative meal for solid-phase gastric emptying study. Nucl Med Commun. 2010;31:430–3.
108. Montgomery M, Escobar-Billing R, Hellstrom PM, Karlsson KA, Frenckner B. Impaired gastric emptying in children with repaired esophageal atresia: a controlled study. J Pediatr Surg. 1998;33:476–80.
109. Malmud LS, Fisher RS, Knight LC, Rock E. Scintigraphic evaluation of gastric emptying. Semin Nucl Med. 1982;12:116–25.
110. Abell TL, Camilleri M, Donohoe K, Hasler WL, Lin HC, Maurer AH, et al. Consensus recommendations for gastric emptying scintigraphy: a joint report of the American neurogastroenterology and Motility Society and the Society of Nuclear Medicine. J Nucl Med Technol. 2008;36:44–54.
111. Tougas G, Eaker EY, Abell TL, Abrahamsson H, Boivin M, Chen J. Assessment of gastric emptying using a low fat meal: establishment of international control values. Am J Gastroenterol. 2000;95:1456–62.
112. Urbain JLC, Van Custem E, Sirgel JA, et al. Visualization and characterization of gastric contractions using a radionuclide technique. Am J Physiol. 1990;259:G1062–7.
113. Ham HR, Muls V, Cadiere G-B, et al. Radionuclide study of regional gastric motility. Nucl Med Commun. 1995;16:827–33.
114. Urbain JLC, Vekemans MC, Bouillon R, et al. Characterization of gastric antral motility disturbances in diabetes using the scintigraphic technique. J Nucl Med. 1993;34:576–81.
115. Urbain JLC, Vekemans MC, Parkman H, et al. Dynamic antral scintigraphy to characterize antral motility in functional dyspepsia. J Nucl Med. 1995;36:1579–86.
116. Kuiken SD, Samson M, Camilleri M, et al. Development of a test to measure gastric accommodation in humans. Am J Physiol. 1999;277:G1217–21.
117. Bouras EP, Delgado-Aros S, Camilleri M, et al. SPECT imaging of the stomach: comparison with barostat, and effects of sex, age, body mass index, and fundoplication. Single photon emission computed tomography. Gut. 2002;51:781–6.
118. Kim D-Y, Delgado-Aros S, Camilleri M, et al. Noninvasive measurement of gastric accommodation in patients with idiopathic nonulcer dyspepsia. Am J Gastroenterol. 2001;96:3099–105.
119. Simonian HP, Maurer AH, Knight LC, et al. Simultaneous assessment of gastric accommodation and emptying: studies with liquid and solid meals. J Nucl Med. 2004;45:1155–60.
120. Bonapace ES, Parkman HP. Normal esophageal physiology. In: Brandt LJ, editor. Clinical practice of gastroenterology. Philadelphia: Churchill Livingstone; 1999. p. 2–12.
121. Clouse RE, Richter JE, Heading RC, Janssens J, Wilson JA. Functional esophageal disorders. Gut. 1999;45:31–6.
122. Dekel R, Fass R. Current perspectives on the diagnosis and treatment of functional esophageal disorders. Curr Gastroenterol Rep. 2003;5:314–22.
123. Hillemeir C, Buchin P, Gryboski J. Esophageal dysfunction in Down's syndrome. J Pediatr Gastroenterol Nutr. 1983;1:101–4.
124. Staiano A, Cucchiara S, Del Giudice E, Andreotti MR, Minella R. Disorders of oesophageal motility in children with psychomotor retardation and gastro-oesophageal reflux. Eur J Pediatr. 1991;150:638–41.
125. Del Giudice E, Staiano A, Capano G, et al. Gastrointestinal manifestations in children with cerebral palsy. Brain Dev. 1999;21:307–11.
126. Gustafsson PM, Tibbling L. Gastroesophageal reflux and esophageal dysfunction in children and adolescents with brain damage. Acta Paediatr. 1994;83:1081–5.
127. Krausz Y, Maayan C, Faber J, Marciano R, Mogle P, Wynchank S. Scintigraphic evaluation of esophageal transit and gastric emptying in familial dysautonomia. Eur J Radiol. 1994;18(1):52–6.
128. Genc A, Mutaf O. Esophageal motility changes in acute and late periods of caustic esophageal burns and their relation to prognosis in children. J Pediatr Surg. 2002;37:1526–8.
129. Engum SA, Grosfeld JL, West KW, Rescorla FJ, Scherer 3rd LR. Analysis of morbidity and mortality in 227 cases of esophageal atresia and/or tracheoesophageal fistula over two decades. Arch Surg. 1995;130:502–8.
130. Kazem I. A new scintigraphic technique for the study of the esophagus. Am J Roentgenol Radium Ther Nucl Med. 1972;115:681–8.
131. Guillet J, Wynchank S, Basse-Cathalinat B, Christophe E, Ducassou D, Blanquet P. Pediatric esophageal scintigraphy. Results of 200 studies. Clin Nucl Med. 1983;8:427–33.
132. Heyman S. Esophageal scintigraphy (milk scans) in infants and children with gastroesophageal reflux. Radiology. 1982;144:891–3.
133. Svedberg JB. The bolus transport diagram: a functional display method applied to esophageal studies. Clin Phys Physiol Meas. 1982;3:267–72.
134. Khan SH, Rather TA, ul Rehman B, Gulzar GM, Mir TA, Zargar SA. Radionuclide esophageal transit time in patients of suspected esophageal motility disorders. Indian J Gastroenterol. 2009;28:74–5.
135. Ham HR, Piepsz A, Georges B, Verelst J, Guillaume M, Cadranel S. Quantitation of esophageal transit by means of 81mKr. Eur J Nucl Med. 1984;9:362–5.
136. Klein HA, Wald A. Computer analysis of radionuclide esophageal transit studies. J Nucl Med. 1984;25:957–64.
137. Tatsch K. Multiple swallow test for quantitative and qualitative evaluation of esophageal motility disorders. J Nucl Med. 1991;32:1365–70.
138. Tatsch K, Voderholzer WA, Weiss MJ, Schrottle W, Hahn K. Reappraisal of quantitative esophageal

scintigraphy by optimizing results with ROC analyses. J Nucl Med. 1996;37:1799–805.
139. Lamki L. Radionuclide esophageal transit study: the effect of body posture. Clin Nucl Med. 1985;10: 108–10.
140. Buthpitiya AG, Stroud D, Russell CO. Pharyngeal pump and esophageal transit. Dig Dis Sci. 1987;32: 1244–8.
141. Kjellen G, Svedberg JB, Tibbling L. Solid bolus transit by esophageal scintigraphy in patients with dysphagia and normal manometry and radiology. Dig Dis Sci. 1984;29:1–5.
142. Fisher RS, Malmud LS, Applegate G, Rock E, Lorber SH. Effect of bolus composition on esophageal transit: concise communication. J Nucl Med. 1982;23:878–82.
143. Mughal MM, Marples M, Bancewicz J. Scintigraphic assessment of esophageal motility: what does it show and how reliable is it? Gut. 1986;27: 946–53.
144. Russell CO, Hill LD, Holmes 3rd ER, Hull DA, Gannon R, Pope 2nd CE. Radionuclide transit: a sensitive screening test for esophageal dysfunction. Gastroenterology. 1981;80:887–92.
145. Odunsi ST, Camilleri M. Selected interventions in nuclear medicine: gastrointestinal motor functions. Semin Nucl Med. 2009;39:186–94.
146. Lopes MF, Botelho MF. Midterm follow-up of esophageal anastomosis for esophageal atresia repair: long-gap versus non-long-gap. Dis Esophagus. 2007;20:428–35.
147. Van Zyl JH, Nel MG, Otto AC, et al. Evaluation of reflux oesophagitis with technetium-99m labelled sucralfate. S Afr Med J. 1996;86:1422–4.
148. Mearns AJ, Hart GC, Cox JA. Dynamic radionuclide imaging with 99 m Tc-sucralfate in the detection of oesophageal ulceration. Gut. 1989;30:1256–9.
149. Dawson DJ, Khan AN, Nuttall P, Shreeve DR. Technetium 99m-labelled-sucralphate isotope scanning in the detection of peptic ulceration. Nucl Med Commun. 1985;6:319–25.
150. Millar AJ, Numanoglu A, Mann M, Marven S, Rode H. Detection of caustic oesophageal injury with technetium 99m-labelled sucralfate. J Pediatr Surg. 2001;36:262–5.
151. Cameron JL, Zuidema GD. Aspiration pneumonia: magnitude and frequency of the problem. JAMA. 1972;219:1194–6.
152. Trinick R, Johnston N, Dalzell AM, McNamara PS. Reflux aspiration in children with neurodisability-a significant problem, but can we measure it? J Pediatr Surg. 2012;47:291–8.
153. Euler AR, Byrne WJ, Ament ME, et al. Recurrent pulmonary disease in children: a complication of gastroesophageal reflux. Pediatrics. 1979;63:47–51.
154. Berquist WE, Rachelefsky GS, Kadden M, et al. Gastroesophageal reflux associated recurrent pneumonia and chronic asthma in children. Pediatrics. 1981;68:29–35.
155. Morton RE, Wheatley R, Minford J. Respiratory tract infections due to direct and reflux aspiration in children with severe neurodisability. Dev Med Child Neurol. 1999;41:329–34.
156. Heyman S. Evaluation of gastroesophageal reflux and gastrointestinal bleeding. In: Freeman LM, Weissmann HS, editors. Nuclear medicine annual. New-York: Raven Press; 1985. p. 133–69.
157. Fawcett HD, Hayden CK, Adams JC, et al. How useful is gastroesophageal reflux scintigraphy in suspected childhood aspiration? Pediatr Radiol. 1988;18:311–3.
158. Berdon WE, Mellins RB, Levy J. Commentary: on the following paper by H.D. Fawcett, C.K. Hayden, J.C. Adams and L.E. Swischuk: How useful is gastroesophageal reflux scintigraphy in suspected childhood aspiration? Pediatr Radiol. 1988;18:309–10.
159. Miller JH. How useful is gastroesophageal reflux scintigraphy in suspected childhood aspiration? Letter to the editor. Pediatr Radiol. 1988;19:70.
160. McVeagh P, Howman-Giles R, Kemp A. Pulmonary aspiration studies by radionuclide milk scanning and barium swallow roentgenography. Am J Dis Child. 1987;141:917–21.
161. Christie DL, O'Grady LR, Mack DV. Incompetent lower esophageal sphincter and gastroesophageal reflux in recurrent acute pulmonary disease of infancy and childhood. J Pediatr. 1978;93:23–7.
162. Boonyaprapa S, Alderson PO, Garfinkel DJ, Chipps BE, Wagner Jr HN. Detection of pulmonary aspiration in infants and children with respiratory disease: concise communication. J Nucl Med. 1980;21: 314–8.
163. Bar-Sever Z, Steinberg T, Connolly LP, et al. Scintigraphic and radiographic imaging of aspiration and gastroesophageal reflux in young children. J Nucl Med. 1999;40:13P [abstract].
164. MacFadyen UM, Hendry GM, Simpson H. Gastro-oesophageal reflux in near-miss sudden infant death syndrome or suspected recurrent aspiration. Arch Dis Child. 1983;58:87–91.
165. Berger D, Bischof-Delaloye A, Reinberg O, Roulet M. Esophageal and pulmonary scintiscanning in gastroesophageal reflux in children. Prog Pediatr Surg. 1985;18:68–77.
166. Levin K, Colon A, DiPalma J, Fitzpatrick S. Using the radionuclide salivagram to detect pulmonary aspiration and esophageal dysmotility. Clin Nucl Med. 1993;18:110–4.
167. Ravelli AM, Panarotto MB, Verdoni L, Consolati V, Bolognini S. Pulmonary aspiration shown by scintigraphy in gastroesophageal reflux-related respiratory disease. Chest. 2006;130:1520–6.
168. Heyman S, Eicher PS, Alavi A. Radionuclide studies of the upper gastrointestinal tract in children with feeding disorders. J Nucl Med. 1995;36:351–4.
169. Lorber B, Swenson RM. Bacteriology of aspiration pneumonia: a prospective study of community and hospital acquired cases. Ann Intern Med. 1974;81:329–31.
170. Bartlett JG, Gorbach SL, Finegold SM. The bacteriology of aspiration pneumonia. Am J Med. 1974;56:202–7.

171. Russin SJ, Adler AG. Pulmonary aspiration: the three syndromes. Postgrad Med. 1989;85:155–61.
172. Heyman S. The radionuclide salivagram for detecting the pulmonary aspiration of saliva in an infant. Pediatr Radiol. 1989;19:208–9.
173. Martinez DA, Ginn-Pease ME, Caniano DA. Sequelae of antireflux surgery in profoundly disabled children. J Pediatr Surg. 1992;27:267–71.
174. Bauer ML, Figueroa-Colon R, Georgeson K, Young DW. Chronic pulmonary aspiration in children. South Med J. 1993;86:789–95.
175. Bui HD, Dang CV, Chaney RH, Vergara LM. Does gastrostomy and fundoplication prevent aspiration pneumonia in mentally retarded persons? Am J Ment Retard. 1989;94:16–9.
176. Heyman S, Respondek M. Detection of pulmonary aspiration in children by radionuclide "salivagram". J Nucl Med. 1989;30:697–9.
177. Bar-Sever Z, Connolly LP, Treves ST. The radionuclide salivagram in children with pulmonary disease and a high risk of aspiration. Pediatr Radiol. 1995;25 Suppl 1:S180–3.
178. Huxley EJ, Viroslav J, Gray WR, et al. Pharyngeal aspiration in normal adults and patients with depressed consciousness. Am J Med. 1978;64:565–7.
179. Green GM. Pulmonary clearance of infectious agents. Annu Rev Med. 1968;19:315–36.
180. Green GM. Lung defense mechanisms. Med Clin North Am. 1973;57:547–62.
181. Siegel JA, Wu RK, Knight LC, Zelac RE, Stern HS, Malmud LS. Radiation dose estimates for oral agents used in upper gastrointestinal disease. J Nucl Med. 1983;24:835–7.
182. Crawley MT, Savage P, Oakley F. Patient and operator dose during fluoroscopic examination of swallow mechanism. Br J Radiol. 2004;77:654–6.
183. Dodds WJ, Stewart ET, Logemann JA. Physiology and radiology of the normal oral and pharyngeal phases of swallowing. Am J Roentgenol. 1990;154: 953–63.
184. Baikie G, South MJ, Reddihough DS, Cook DJ, Cameron DJ, Olinsky A, et al. Agreement of aspiration tests using barium videofluoroscopy, salivagram, and milk scan in children with cerebral palsy. Dev Med Child Neurol. 2005;47:86–93.
185. Muz J, Mathog RH, Miller PR, Rosen R, Borrero G. Detection and quantification of laryngotracheopulmonary aspiration with scintigraphy. Laryngoscope. 1987;97:1180–5.
186. Silver KH, Van Nostrand D. The use of scintigraphy in the management of patients with pulmonary aspiration. Dysphagia. 1994;9:107–15.
187. Shaw DW, Williams RB, Cook IJ, et al. Oropharyngeal scintigraphy: a reliable technique for the quantitative evaluation of oral-pharyngeal swallowing. Dysphagia. 2004;19:36–42.
188. Miller JH. Upper gastrointestinal tract evaluation with radionuclides in infants. Radiology. 1991;178:326–7.
189. Heyman S. Volume-dependent pulmonary aspiration of a swallowed radionuclide bolus. J Nucl Med. 1997;38:103–4.
190. Baikie G, Reddihough DS, South M, Cook DJ. The salivagram in severe cerebral palsy and able-bodied adults. J Paediatr Child Health. 2009;45:342–5.
191. Bauer ML, Lyrene RK. Chronic aspiration in children: evaluation of the lipid-laden macrophage index. Pediatr Pulmonol. 1999;28:94–100.
192. Ahrens P, Noll C, Kitz R, Willigens P, Zielen S, Hofmann D. Lipid-laden alveolar macrophages (LLAM): a useful marker of silent aspiration in children. Pediatr Pulmonol. 1999;28:83–8.
193. Nussbaum E, Maggi JC, Mathis R, Galant SP. Association of lipid-laden alveolar macrophages and gastroesophageal reflux in children. J Pediatr. 1987;110:190–4.
194. Colombo JL, Hallberg TK. Recurrent aspiration in children: lipid-laden alveolar macrophage quantitation. Pediatr Pulmonol. 1987;3:86–9.
195. Knauer-Fischer S, Ratjen F. Lipid-laden macrophages in bronchoalveolar lavage fluid as a marker for pulmonary aspiration. Pediatr Pulmonol. 1999;27:419–22.
196. Krishnan U, Mitchell JD, Tobias V, Day AS, Bohane TD. Fat laden macrophages in tracheal aspirates as a marker of reflux aspiration: a negative report. J Pediatr Gastroenterol Nutr. 2002;35:309–13.
197. Krishnan U, Mitchell JD, Messina I, et al. Assay of tracheal pepsin as a marker of reflux aspiration. J Pediatr Gastroenterol Nutr. 2002;35:303–8.
198. McNally P, Ervine E, Shields MD, Dimitrov BD, El Nazir B, Taggart CC, et al. High concentrations of pepsin in bronchoalveolar lavage fluid from children with cystic fibrosis are associated with high interleukin-8 concentrations. Thorax. 2011;66: 140–3.
199. Cook SP, Lawless ST, Kettrick R. Patient selection for primary laryngotracheal separation as treatment of chronic aspiration in the impaired child. Int J Pediatr Otorhinolaryngol. 1996;38:103–13.
200. Cook SP, Lawless S, Mandell GA, Reilly JS. The use of the salivagram in the evaluation of severe and chronic aspiration. Int J Pediatr Otorhinolaryngol. 1997;41:353–61.
201. De Vito MA, Wetmore RF, Pransky SM. Laryngeal diversion in the treatment of chronic aspiration in children. Int J Pediatr Otorhinolaryngol. 1989;18: 139–45.
202. Gerber ME, Gaugler MD, Myer 3rd CM, Cotton RT. Chronic aspiration in children. When are bilateral submandibular gland excision and parotid duct ligation indicated? Arch Otolaryngol Head Neck Surg. 1996;122:1368–71.
203. Klem C, Mair EA. Four-duct ligation: a simple and effective treatment for chronic aspiration from sialorrhea. Arch Otolaryngol Head Neck Surg. 1999;125:796–800.

Liver and Spleen

10

S. Ted Treves and Alun G. Jones†

This chapter focuses principally on hepatobiliary scintigraphy, as it is by far the most frequently indicated nuclear medicine method for the evaluation of the liver in pediatric patients. Later in this chapter, we will discuss splenic scintigraphy using heat-denatured red blood cells. Lastly we will briefly discuss reticuloendothelial system (RES) scintigraphy of the liver and spleen, which is currently very rarely used in children. Indications for hepatic and splenic scintigraphy in pediatrics are listed in Tables 10.1 and 10.2.

Methods

Hepatobiliary Scintigraphy

Patient Preparation

All intravenous lipids should be stopped 4 h prior to study. In infants, the principal indication is determination of the patency of the biliary tract and not the visualization of the gallbladder. Therefore, fasting prior to hepatobiliary scintigraphy is not absolutely necessary in most infants. In jaundiced neonates pretreatment with phenobarbital is frequently used to increase bile secretion and, therefore, to help improve differentiation of neonatal hepatitis and biliary atresia. Older children should fast for at least 4 h prior to the study. If a barium study has been done recently, a plain x-ray may be indicated before the scan to make sure the bowel is clear.

Pharmacologic Interventions

Phenobarbital premedication: In infants, premedication with phenobarbital is recommended. Phenobarbital dose: 5 mg/kg/day in two equal doses for 3–5 days prior to the test.

Ursodeoxycholic acid (UDCA): Oral UDCA is also thought to improve the specificity of hepatobiliary scintigraphy in ruling out extrahepatic biliary atresia in patients with neonatal jaundice. The recommended dose is 20 mg/kg every 12 h for 48–72 h. An accuracy of just over 90 % has been reported [1].

Sincalide: A cholecystokinin analogue (Kinevac, sincalide; Bracco Diagnostics, Princeton, NJ) [2] may be given to stimulate gallbladder contraction. Most pediatric institutions have adopted this method. Kinevac (Sincalide for injection) is a cholecystopancreatic-gastrointestinal hormone peptide for parenteral administration.

S.T. Treves, MD (✉)
Joint Program in Nuclear Medicine,
Department of Radiology, Harvard Medical School,
Boston, MA, USA

Division of Nuclear Medicine and Molecular Imaging,
Department of Radiology, Boston Children's Hospital,
Boston, MA, USA

Division of Nuclear Medicine and Molecular
Imaging, Department of Radiology, Brigham and
Women's Hospital, Boston, MA, USA
e-mail: ted_treves@HMS.harvard.edu

A.G. Jones, PhD
Department of Radiology,
Harvard Medical School, Boston, MA, USA

†Author was deceased at the time of publication.

S.T. Treves (ed.), *Pediatric Nuclear Medicine and Molecular Imaging*,
DOI 10.1007/978-1-4614-9551-2_10, © Springer Science+Business Media New York 2014

Table 10.1 Indications for hepatobiliary scintigraphy in pediatric patients

Biliary atresia versus neonatal hepatitis
Right upper quadrant pain/cholecystitis
Postoperative/Kasai operation
Choledochal cyst
Liver transplantation
Right upper quadrant mass
Trauma
Congenital malformations

Table 10.2 Indications for splenic scintigraphy in pediatric patients

Heterotaxia (polysplenia, asplenia)
Functional asplenia
Abdominal trauma
Accessory spleen(s)
Splenosis
Infarction

Each vial of sincalide provides a sterile non-pyrogenic lyophilized white powder consisting of 5 μg sincalide with 45 mg sodium chloride to provide tonicity; sodium hydroxide or hydrochloric acid may have been added prior to lyophilization for pH adjustment (5.5–6.5). During the manufacturing process, the air in the vial is replaced with nitrogen. The administered dose is 0.02 μg/kg CCK diluted with saline to 30 ml with a maximum dose: 1.4 μg/70 kg. The drug is reconstituted with 5 ml of sterile water. The solution then contains 5 μg of sincalide in 5 ml of water or 1 μg/ml. The individual dose is calculated according to body weight in kilograms. For example, to calculate the dose for a 10 kg patient, multiply 0.02 × 10=0.2 μg or 0.2 ml of solution. Draw 0.2 ml into a 1 ml syringe. Transfer the solution that is in the 1 ml (or 3 ml) syringe containing the sincalide into a 30 ml syringe containing saline solution. This should be mixed thoroughly. The 30 ml syringe should be appropriately labeled (date, time, patient name, etc.). The infusion tubing is attached and primed with the solution from the 30 ml syringe. The solution with sincalide is administered intravenously into the patient using a medication infusion pump at a rate of 1 ml/min for 30 min.

Fatty meal: A standard fatty meal or a milk shake will also provoke a powerful gallbladder contraction and will work in these patients.

Radiopharmaceuticals

Hepatobiliary scintigraphy employs intravenously injected radiopharmaceuticals that are rapidly taken up by the parenchymal cells of the liver and eliminated through the biliary system into the intestine. The knowledge that organic dyes are localized in the liver led to the first successful hepatobiliary imaging agent, ^{131}I-rose bengal, introduced by Taplin et al. [3] in 1955. Modern hepatobiliary agents are labeled with ^{99m}Tc (Fig. 10.1).

Administered Doses

Currently accepted minimum administered dose for hepatobiliary radiopharmaceutical is 18.5 MBq (0.5 mCi). This study evaluates if the administered radiopharmaceutical doses can be significantly reduced below the minimum in the youngest children while maintaining image quality using the Enhanced Planar Processing (EPP) (Siemens Medical Solutions USA).

Technetium-99m mebrofenin (Choletec® is available through Bracco Diagnostic Inc) or disofenin (Hepatolite, CIS-US, Bedford, MA) is given in a dose of 0.02 mCi/kg (0.74 MBq) with a minimum total dose of 0.25 mCi (9.25 MBq) and a maximum total dose of 1.4 mCi (52 MBq).

Imaging Method

Patients are studied in the supine position with the gamma camera equipped with high-resolution, parallel-hole collimator viewing the entire abdomen including the liver. Intravenous access is gained using a butterfly-type needle that is securely fastened to the skin with tape and kept patent with normal saline until the time of radiopharmaceutical administration. After the patient is positioned under the gamma camera, the radiopharmaceutical is injected as a bolus and flushed with normal saline. Recording begins simultaneously with the start of the injection.

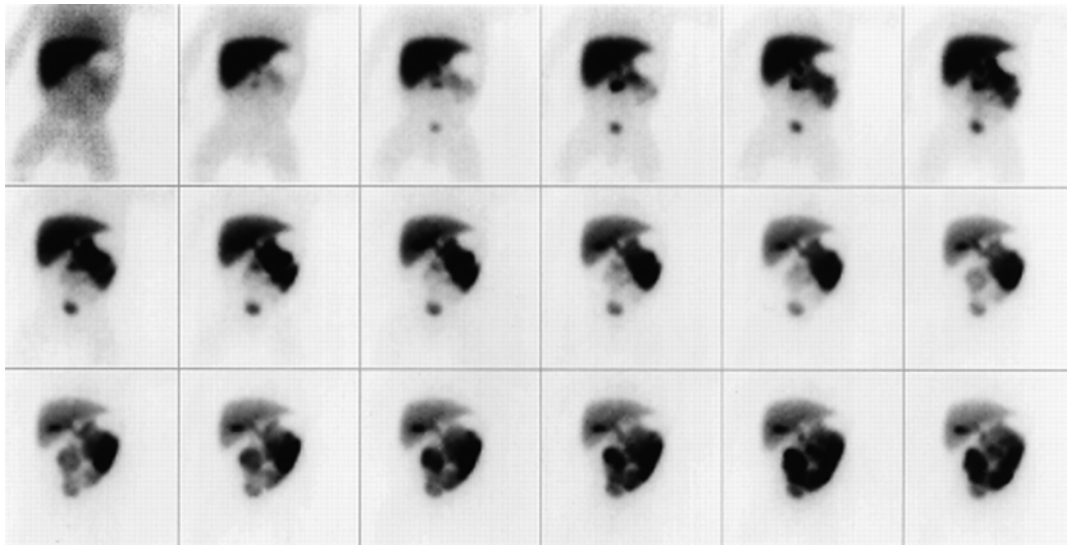

Fig. 10.1 Normal ^{99m}Tc-disofenin hepatobiliary scintigraphy in a young infant. There is normal blood clearance and hepatic uptake of the tracer. Tracer appears in the bowel within 10 min. The gallbladder is visualized at approximately 30 min. Each image represents 3 min, anterior projection

The hepatobiliary study is recorded with serial 1.0-min frames for 60 min using a 128×128 matrix with zooming determined by the patient size (Fig. 10.1). Additional images are obtained at later intervals (i.e., 2, 4, 6, and 24 h) or until radiotracer appears in the bowel. If the gallbladder fails to empty significantly during the initial 60-min period, an additional series of images (one frame per minute for 60 min) is obtained following the administration of a cholecystokinin analogue or a standard fatty meal. If a biliary leak is suspected, additional images in various projections are obtained in order to identify any abnormal collection of tracer.

Evaluation

The physician should evaluate the study on a computer monitor in a cinematic mode. Varying the playback speed, intensity, and contrast is helpful for assessment of bile flow. Evaluation of the later static images directly on the computer monitor is useful to ascertain the presence and nature of any extrahepatic tracer activity. Evaluation of time-activity curves from regions of interest over the cardiac blood pool, liver, and abdomen complements assessment of the images.

Splenic Scintigraphy (^{99m}Tc-Denatured RBCs)

Splenic scintigraphy is done using ^{99m}Tc-labeled denatured RBCs. A specimen (1–3 ml) of the patient's blood is drawn and anticoagulated with heparin or acid-citrate dextrose (ACD). Do not use ethylenediaminetetraacetic acid (EDTA) or oxalate as an anticoagulant. Red blood cells are labeled using a commercial preparation (Ultratag RBC, Mallinckrodt, Maryland Heights, MO). After the labeling procedure, the RBCs are denatured by incubating the tube containing the blood in a constant temperature bath at 49.5 °C for 12–15 min. The denatured RBCs are reinjected slowly into the patient. *The labeled blood cells must be reinjected only into the patient from whom the blood was drawn*. Splenic imaging can begin 15 min after injection.

Anterior, posterior, left and right posterior obliques, and left lateral projections are obtained using the high- or ultrahigh-resolution collimator. Images are recorded for 300,000–500,000

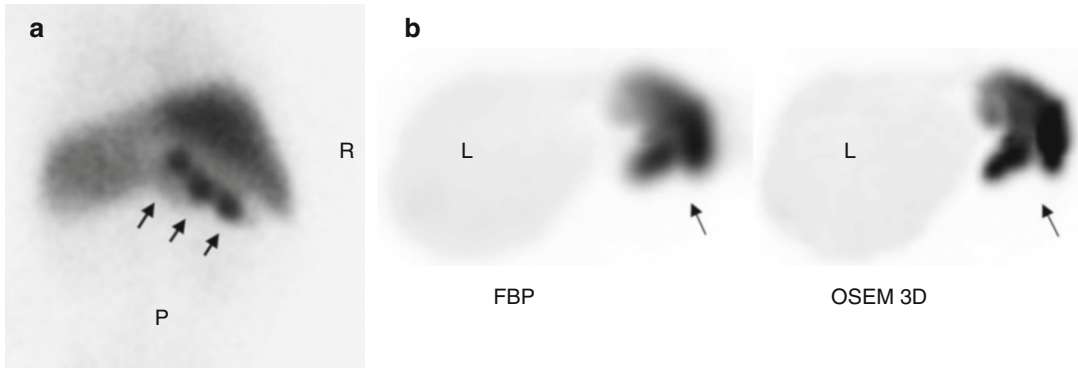

Fig. 10.2 (**a**) Two-day-old male infant with heterotaxia syndrome and polysplenia. The ^{99m}Tc-heat-denatured red cell SPECT reveals three splenules located in the right upper quadrant posterior to the liver (*arrows*), *P* Posterior, *R* Right. (**b**) Infant with heterotaxia syndrome and polysplenia. SPECT obtained with ^{99m}Tc-heat-denatured red blood cells shows the splenic mass in the right lower quadrant. On the *left* of the figure, SPECT was reconstructed using filtered back projection while on the *right* of the figure, the same study was reconstructed with OSEM-3D. Note the finer detail on the *right image* when OSEM is applied

counts each on a 256×256 matrix. The pinhole collimator (2 mm) or SPECT is helpful in some patients for obtaining more detailed assessment (Fig. 10.2).

Reticuloendothelial System Scintigraphy

Although rarely used at present, RES scintigraphy is discussed for the sake of completeness. All metallic and other photon-absorbing objects are removed from the patient's clothing before imaging. It should be noted that barium in the abdomen from previous radiographic procedures causes artifacts on ^{99m}Tc-sulfur colloid imaging.

Radiopharmaceutical

Technetium-99m–sulfur colloid in a dose of 0.05 mCi/kg (1.85 MBq), with a minimal total dose of 0.1 mCi (3.7 MBq) and a maximum total dose of 3.0 mCi (111 MBq), is administered intravenously 10–15 min prior to imaging. After intravenous injection, ^{99m}Tc–sulfur colloid is rapidly absorbed by cells of the RES in the liver (Kupffer cells), spleen, and bone marrow. The normal circulating half-time of this radiotracer in adults is approximately 2.5 min. The size of colloidal particles is 0.01–1.0 μm. Approximately 80–90 % of the radiocolloid is taken up by the liver, 5–10 % by the spleen, and the remainder by the bone marrow. Once absorbed, the colloidal particles have an effective half-life equal to the physical half-life of ^{99m}Tc [4].

Imaging Method

Patients are imaged in the supine position. For planar studies, imaging is carried out using a parallel-hole, high- or ultrahigh-resolution collimator. Electronic magnification (zoom) is used for small children. Images of 500,000 counts are obtained in the anterior, posterior, right and left lateral, right and left posterior oblique, and right and left anterior oblique projections (256×256 matrix). Magnification scintigraphy with the pinhole collimator (2 mm) is useful for evaluating small children's organs and questionable areas on planar scintigraphy. Single-photon emission computed tomography is carried out with the patient in the supine position. The same dose of ^{99m}Tc–sulfur colloid as above is given. SPECT recording consists of images 360° around the body on a 128×128 matrix format. It is evaluated using volume- and surface-rendered images, as well as through transverse, coronal, and sagittal slices (Fig. 10.3).

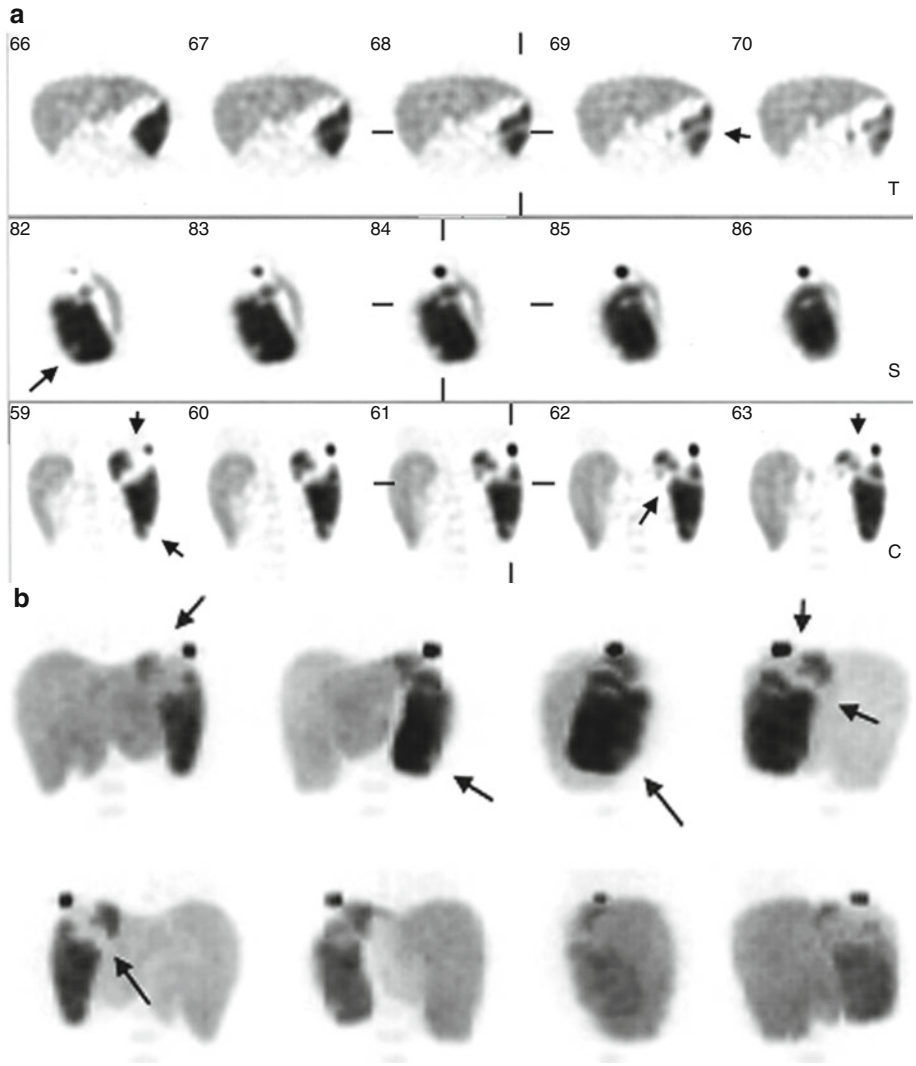

Fig. 10.3 Splenic infarction. Technetium-99m–sulfur colloid study in a 12-year-old boy with subbacterial endocarditis and recent episode of septic emboli to the brain, kidneys, and spleen. (**a**) Single-photon emission computed tomography (SPECT) reveals splenomegaly with several splenic defects (*arrows*) presumably due to infarcts (*arrows*), (*T*) Transverse, (*S*) Sagittal, (*C*) Coronal. (**b**) Volume rendered images from the same study

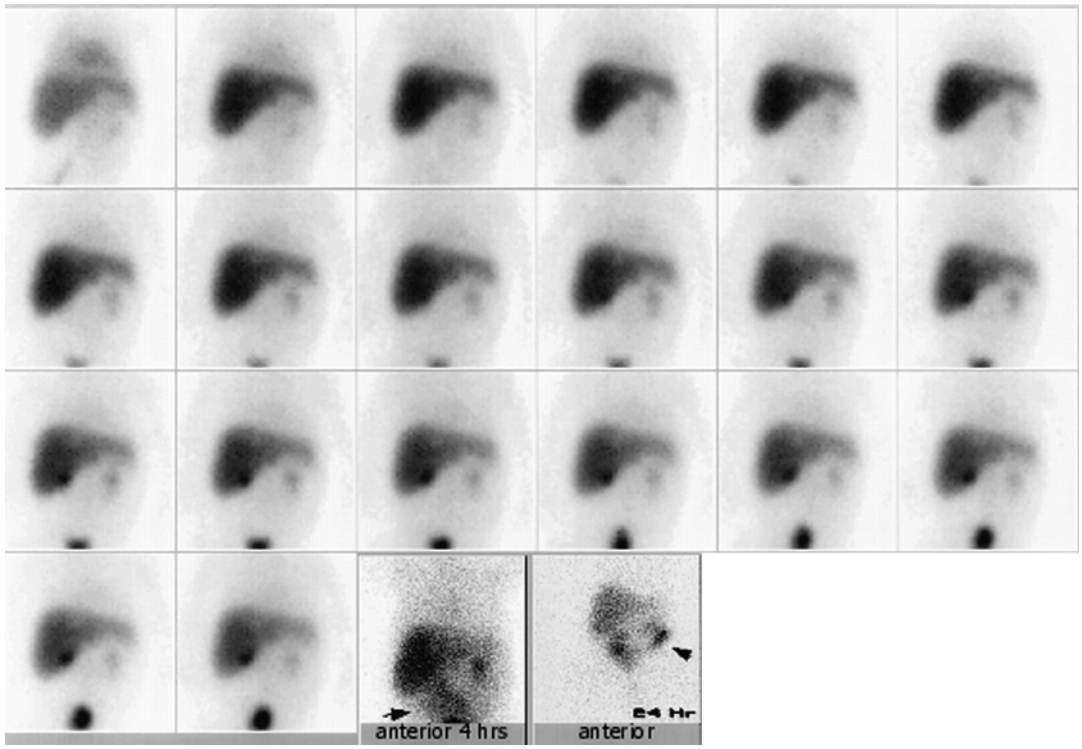

Fig. 10.4 Hepatocellular disease in a 2-week-old boy with jaundice (^{99m}Tc-disofenin 60-min dynamic study, each image represents 3 min). Hepatic uptake of the tracer is lower than normal, and renal excretion (9–12 min) of the radiopharmaceutical into the bladder (15 min) is evident. The gallbladder is visible at approximately 25 min; however, no evidence of intestinal tracer activity is detected at 1 h. Images at 4 and 24 h demonstrate tracer in the bowel (*arrows*)

Clinical Applications

Neonatal Jaundice

Neonatal hepatitis is difficult to differentiate from biliary atresia because these two conditions have similar clinical, biochemical, and histologic features (Figs. 10.4, 10.5, 10.6, 10.7, and 10.8). Early diagnosis of biliary atresia is important because the results of surgical intervention are most successful during the first 2 weeks of life. In contrast, surgery is not indicated in patients with neonatal hepatitis [5].

Clinical Characteristics

Neonatal hepatitis is almost four times more common in male infants, and biliary atresia is encountered twice as often in females. A wide variation and overlap of these two diseases must be kept in mind. Clinical criteria provide some help in differentiation of neonatal hepatitis from biliary atresia. Biliary atresia is accompanied by familial incidence, low birth weight for gestational age, associated anomalies, hemolytic anemia, and splenomegaly. These factors are not usually encountered in patients with neonatal hepatitis, which tends to occur in otherwise healthy infants between 1 and 4 weeks of age [6]. Patients with hepatitis have splenomegaly and jaundice, and with time they may develop cirrhosis. The pathologic findings vary, but in general multinucleated giant cells are present (as they are in some other liver diseases). The canaliculi are free of bile, and there is parenchymal disorganization.

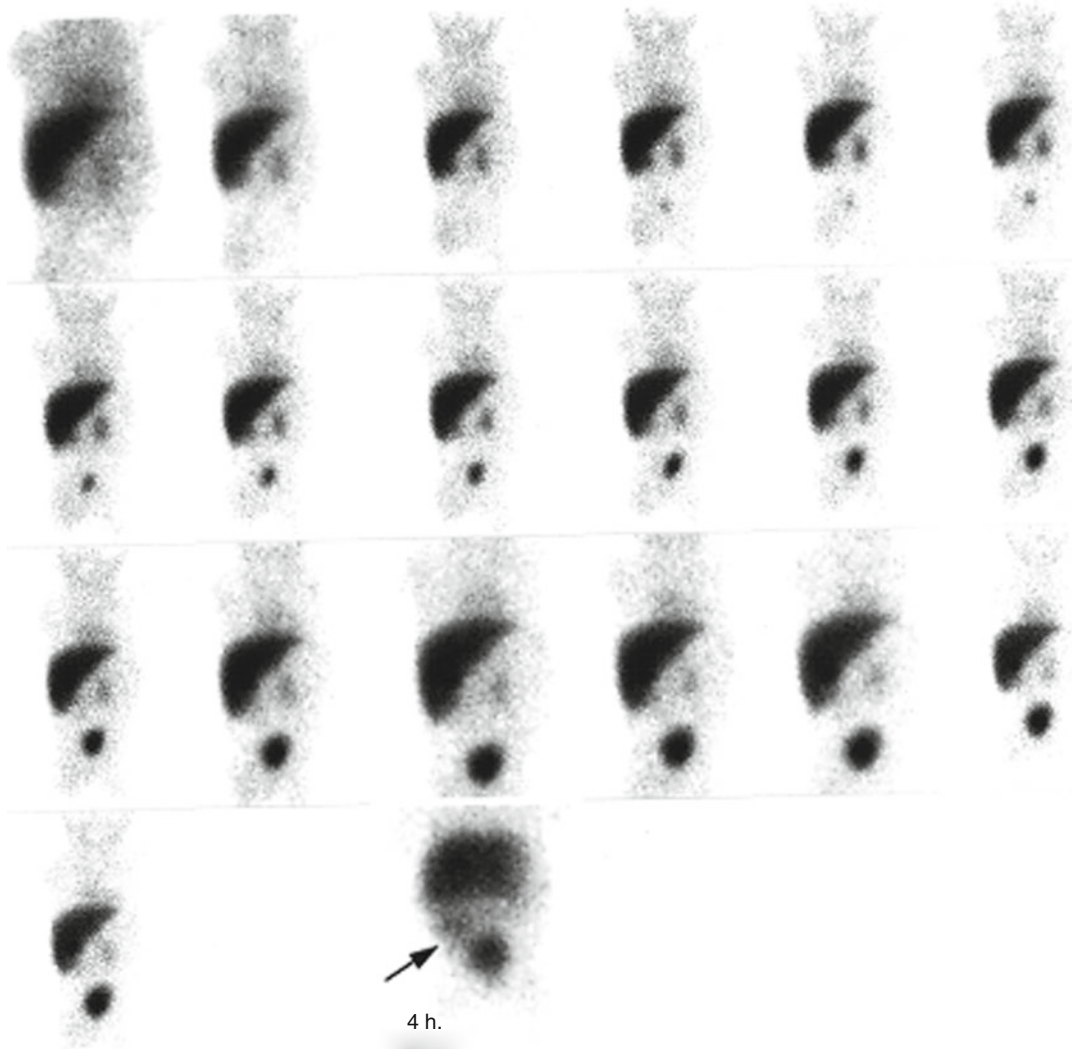

Fig. 10.5 Hepatocellular disease in a 3-month-old boy with jaundice (^{99m}Tc-disofenin, 60-min dynamic study, each image represents 3 min). Hepatic uptake of the radiopharmaceutical appears adequate. Renal excretion of the tracer into the bladder is visible early (12 min) in the study. The image at 4 h reveals tracer in the bowel (*arrow*)

Etiology

Neonatal hepatitis has been associated with a number of entities affecting the liver during the neonatal period: infectious agents (cytomegalovirus, hepatitis A and B, rubella, toxoplasma, spirochetes) and metabolic factors (α_1-antitrypsin deficiency, inborn errors of metabolism). With neonatal hepatitis the intrahepatic and extrahepatic biliary system is patent but small. Biliary atresia and neonatal hepatitis are most likely variations of the same process [7]. With biliary atresia there is sclerosing cholangitis of the extrahepatic biliary system and sometimes progressive occlusion of bile ducts after birth. In patients with biliary atresia, the major biliary ducts are partially or totally absent. Periportal fibrosis and intrahepatic proliferation of small bile ducts are characteristic, but there is no dilation of these intrahepatic ducts. Cirrhosis of the liver ultimately develops unless surgical correction is successful.

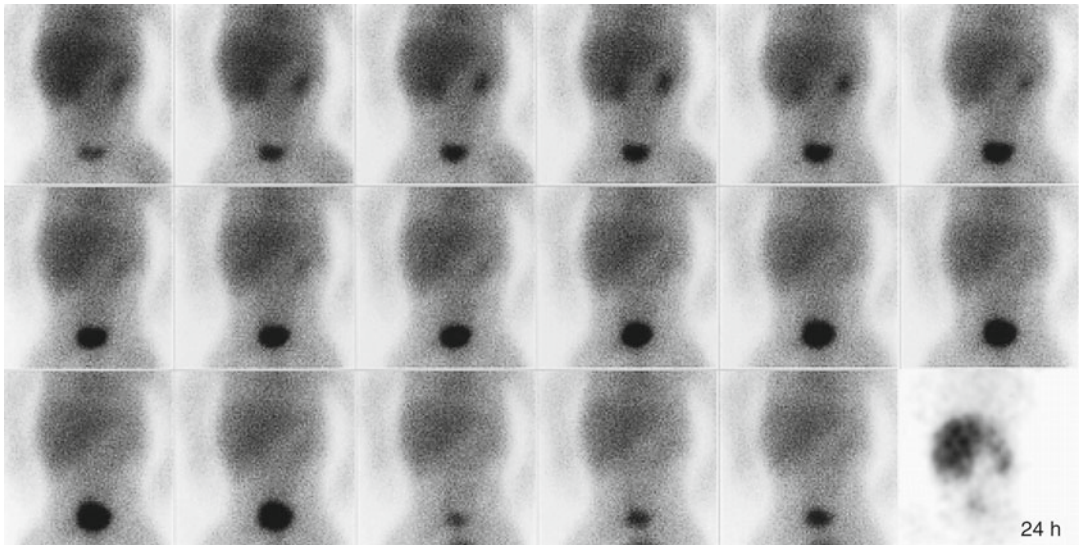

Fig. 10.6 Severe hepatocellular disease in a 1-month-old boy with severe jaundice and high bilirubin level. The ^{99m}Tc-disofenin study reveals poor extraction by the liver, high blood level, and significant urinary excretion of the tracer. An anterior image at 24 h reveals tracer in the liver, kidneys, and bladder without evidence of tracer in the bowel

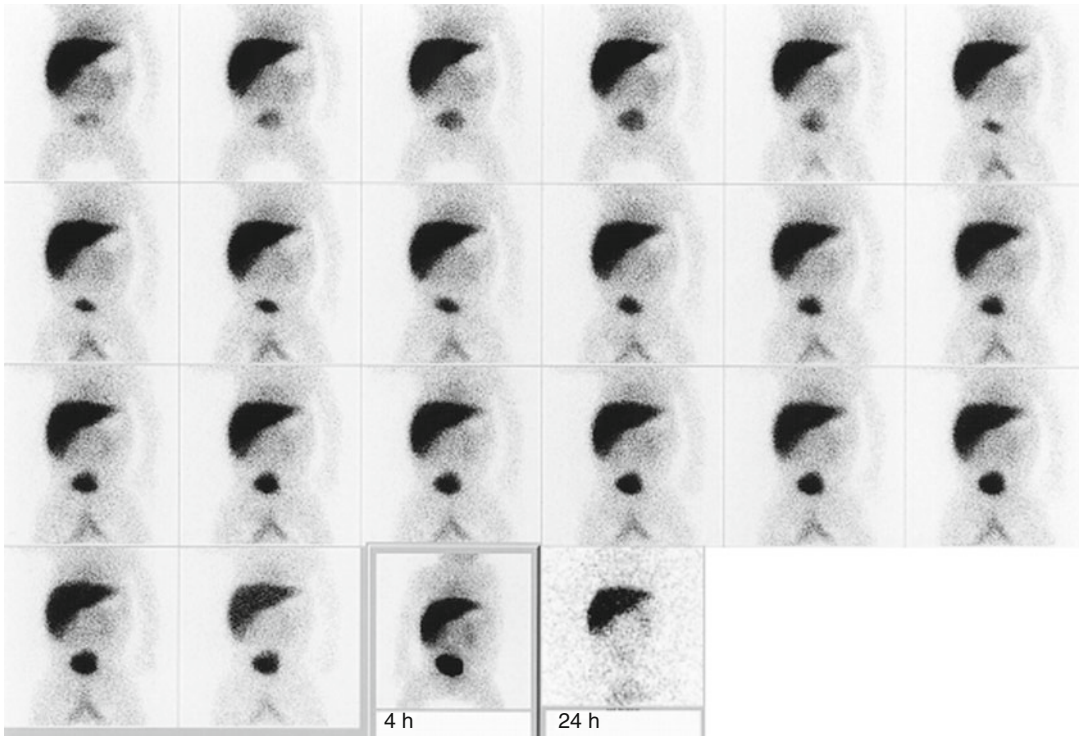

Fig. 10.7 Biliary atresia. A ^{99m}Tc-disofenin study in a 1-month-old boy with conjugated hyperbilirubinemia. Tracer is rapidly taken up by the liver. Renal excretion of the radiotracer is high. However, there is no evidence of tracer in the intestine during the initial hour of the study nor at 4 or 24 h

Fig. 10.8 Biliary atresia. (**a**) ^{99m}Tc-disofenin study in a 2-month-old boy with jaundice. The study reveals hepatomegaly, renal excretion of the tracer, and no evidence of bowel activity up to 24 h (image not shown). (**b**) Same patient after surgery for a choledochojejunal anastomosis (Kasai procedure). There is greater initial ^{99m}Tc-disofenin uptake by the liver, less renal excretion of the tracer, and passage of radiolabeled bile though the anastomosis into the bowel

Differential Diagnosis

Clinical and laboratory diagnosis of biliary atresia is difficult and often impossible. Morphologic imaging can be useful if it demonstrates a patent biliary tree, and hepatobiliary scintigraphy can rule out biliary atresia when it demonstrates passage of the radiotracer into the bowel. If passage of tracer into the bowel cannot be demonstrated, scintigraphic distinction between biliary atresia and severe hepatocellular disease cannot be made with certainty [8–11]. Repeat hepatobiliary scintigraphy after a few days may be helpful in those patients in whom excretion of tracer in the bowel is not demonstrated in a single examination.

A definitive diagnosis can be made by percutaneous transhepatic cholangiography, laparotomy, laparoscopy, or analysis of duodenal fluids [12–15].

Gerhold et al. [16] have demonstrated the accuracy (91 %), sensitivity (97 %), and specificity (82 %) of hepatobiliary imaging in the diagnosis of biliary atresia. They proposed a visual grading that includes the assessment of hepatocyte clearance and timing of radiotracer appearance in the intestine or extrahepatic biliary system. Hepatocyte clearance was graded by visually comparing hepatic activity with cardiac blood pool activity on the 5-min image. The studies were categorized as normal when hepatocyte clearance was normal and radiotracer appeared in the biliary tract or intestine (or both) within 15 min after injection. The scintigraphic diagnosis of biliary atresia was made when there was no intestinal activity through 24 h and hepatocyte clearance was relatively preserved. Studies were interpreted as compatible with neonatal hepatitis when there was impairment in hepatocyte clearance and hepatobiliary transit time and the radiotracer reached the intestine. The interpretation was intrahepatic cholestasis when hepatocyte clearance was relatively preserved compared with hepatobiliary transit time but radiotracer eventually reached the intestine. Indeterminate studies were classified as those in which there was no intestinal radiotracer and hepatocellular function was severely impaired [16]. In another study of neonatal jaundice, Majd et al. [17] concluded that hepatobiliary scintigraphy after 3–7 days of phenobarbital therapy is highly accurate for differentiating biliary atresia from other causes of neonatal jaundice.

Arteriohepatic dysplasia (Alagille syndrome) is an uncommon cause of neonatal jaundice. This syndrome is characterized by typical facial features, pulmonary artery stenosis, and a liver disorder that presents as neonatal jaundice. We have obtained hepatobiliary scintigraphy in two neonates who were later found to have Alagille syndrome. In both cases the initial scintigraphic patterns were similar to those found in biliary atresia, and both patients required surgical exploration. Bile plug syndrome in patients with cystic fibrosis, dehydration, sepsis, or on total parenteral nutrition may also appear similar to biliary atresia on scintigraphy.

Biliary Obstruction and Cholecystitis

Obstruction of the cystic duct is a major factor in the development of acute cholecystitis. The obstruction may be partial or complete and may or may not be associated with cholelithiasis. Scintigraphic visualization of the gallbladder rules out the diagnosis of acute cholecystitis with a high degree of accuracy in adults. Among 296 patients, Weissmann et al. [18–20] found an accuracy of 98 %, a specificity of 100 %, a false-negative rate of 5 %, and a false-positive rate of 0 % for hepatobiliary scintigraphy in the diagnosis of acute cholecystitis.

In children, however, visualization of the gallbladder on hepatobiliary scintigraphy does not exclude cholecystitis (Fig. 10.9). The gallbladder can be visualized in acalculous cholecystitis or toxic cholecystitis. Some patients affected by these conditions may have only partial obstruction of the cystic duct, and the gallbladder may not be visualized because of edema of the cystic duct. When acalculous cholecystitis is present, a fatty meal or injection of cholecystokinin usually results in failure of the gallbladder to contract effectively. This failure suggests partial cystic duct obstruction, chronic cholecystitis, or acalculous cholecystitis. With chronic cholecystitis there may be a delay in gallbladder filling in the presence of normal liver function.

Cholecystitis in pediatric patients is infrequently associated with cholelithiasis and is usually a complication of another infection (e.g., scarlet fever, other streptococcal infections, Kawasaki disease) [21–23].

Children with acute cholecystitis generally present with abdominal pain localized to the right upper quadrant several days after a systemic infection or a streptococcal pharyngitis. The gallbladder may be enlarged and palpable, and jaundice may be present.

Cholelithiasis can be observed in patients with cystic fibrosis who may be asymptomatic or

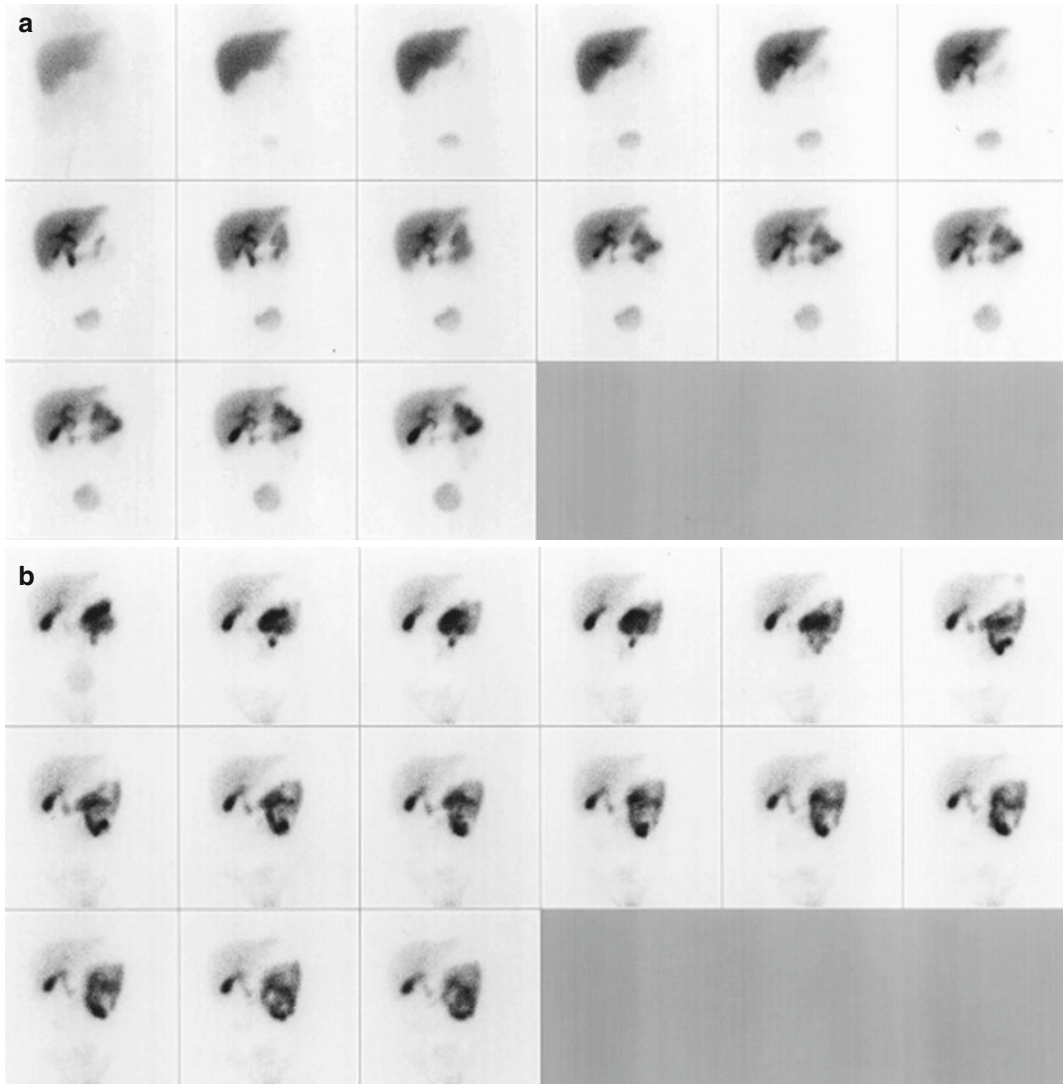

Fig. 10.9 Acalculous cholecystitis. A hepatobiliary study (^{99m}Tc-disofenin, 3-min frames) was done in a 14-year-old girl with a 3-week history of right upper quadrant pain and intermittent chills. (**a**) Initial 60-min study reveals adequate hepatic uptake of the tracer and transhepatic transit time. Tracer is visualized in the gallbladder at 15 min into the study and reveals ever-increasing concentration. Some tracer is seen in the bladder beginning at 6 min. (**b**) Gallbladder fails to contract adequately after intravenous administration of cholecystokinin analogue

present with symptoms of cholecystitis or obstruction (Fig. 10.10). Ultrasonography is an essential diagnostic modality for evaluating the biliary tract and should be performed in conjunction with hepatobiliary imaging. A large gallbladder with a thickened wall may be apparent on ultrasonography in patients with cholecystitis, although this is a nonspecific finding. Usually, there is no concomitant dilatation of the biliary tree.

Choledochal Cyst

Choledochal cyst is a congenital dilatation of the extrahepatic biliary tree. There are three types of choledochal cyst. The most common one is a dilatation of the common bile duct, which may be accompanied by dilatation of the hepatic ducts. With this type of cyst, the cystic duct and the gallbladder are usually not dilated. Approximately 15 % of these patients also have biliary atresia.

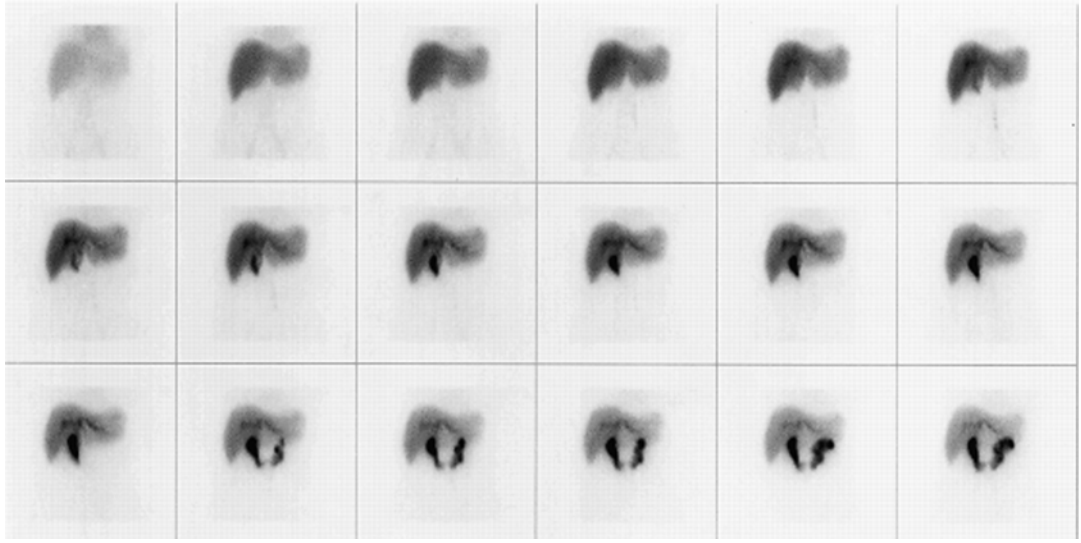

Fig. 10.10 Cholelithiasis. Hepatobiliary study in a 19-year-old woman with cystic fibrosis and gallstones. Adequate hepatic uptake of the ^{99m}Tc-disofenin without tracer entering the gallbladder. Bile flow is patent but sluggish

In a review by Kim [24], dilatation of the common bile duct accounted for 93 % of 188 cases of choledochal cyst reviewed. The second type of choledochal cyst is a diverticulum of the common bile duct, with the biliary tree being otherwise normal (diverticulum). The third type is a dilatation of the duodenal intramural portion of the common bile duct (choledochocele).

Ninety percent of the patients with choledochal cyst present before 12 years of age, 70 % before age 6, and approximately 40 % before age 1. The lesion occurs two to three times more frequently in female than in male children. The symptoms at presentation, in order of decreasing frequency, include jaundice (70 %), abdominal pain (55 %), dark urine (50 %), hepatomegaly (45 %), acholic stools (45 %), abdominal mass (40 %), and fever (35 %). Other symptoms include splenomegaly, anemia, cholecystitis, and vomiting. Ultrasonography and hepatobiliary scintigraphy (with cholecystokinin or fatty meal) can make the diagnosis of choledochal cyst in most cases (Figs. 10.11, 10.12, and 10.13).

Caroli's Disease

Caroli's disease is characterized by a saccular dilatation of the intrahepatic biliary ducts without biliary obstruction [25, 26]. This rare disease is sometimes associated with congenital hepatic fibrosis [27]. Infection of the dilated ducts may result in cholangitis, calculi, and cirrhosis. Ultrasonography and transhepatic cholangiography play a major part in the diagnosis of this rare disease by demonstrating widespread dilatation of the biliary ducts. Hepatobiliary scintigraphy demonstrates dilatation of the biliary ducts, normal transhepatocyte transit time, and, sometimes, delay in transit of tracer into the intestine without obstruction.

Biliary Leak

Biliary leak secondary to trauma or as a surgical complication can be readily demonstrated with hepatobiliary scintigraphy. This technique demonstrates leakage of radiotracer into the peritoneal cavity (Fig. 10.14). Resultant bile collections are usually contained by the hepatic capsule or localized adjacent to the liver, although free bile ascites may also occur. Advantages of the tracer method include its inherent high contrast and lack of interference from adjacent structures or bowel gas. Ultrasonography and CT can define biliary collections, but cannot easily determine if there is an active leak. A radiotracer study can establish the integrity of the capsule and determine the presence of an active leak [28].

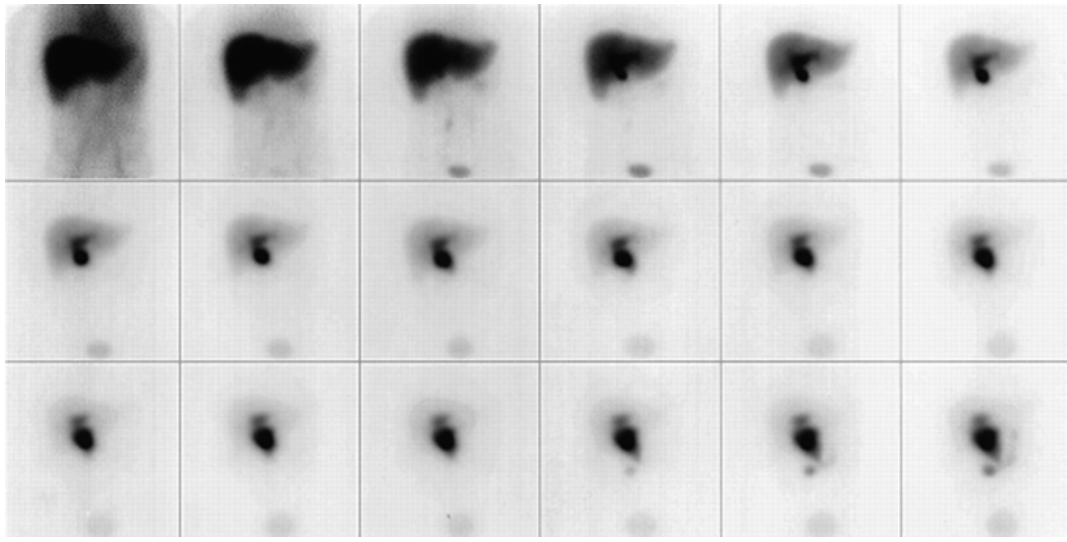

Fig. 10.11 Choledochal cyst in a 6-year-old girl with right upper quadrant pain. There is adequate uptake of tracer by the liver, with normal parenchymal transit time. ^{99m}Tc-disofenin is held in a localized dilatation of the hepatic duct (choledochal cyst)

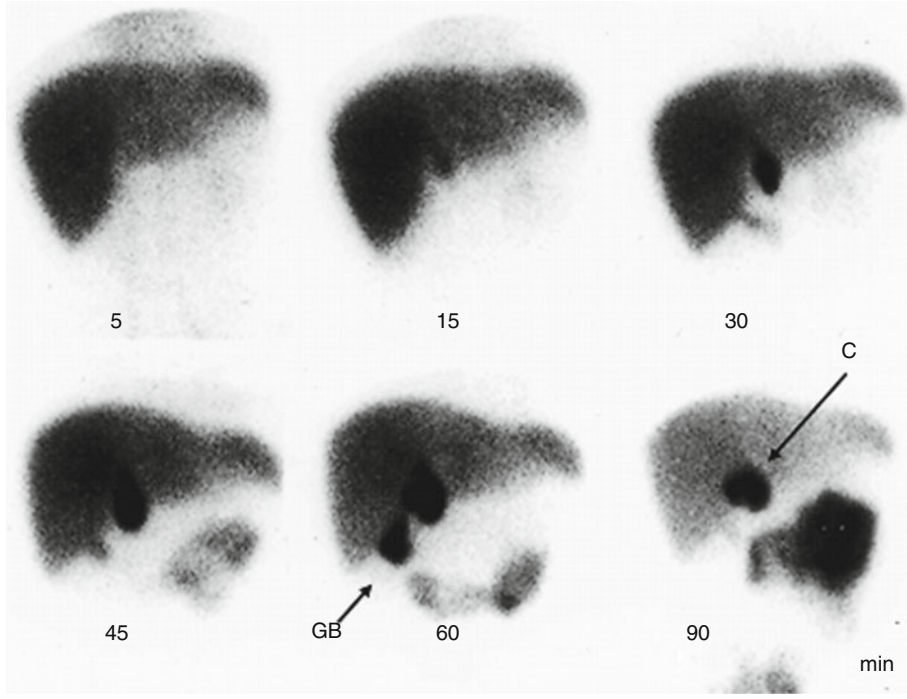

Fig. 10.12 Choledochal cyst in a 12-year-old patient. The liver takes up the tracer adequately, and it delineates a dilated common duct on the images at 15, 30, and 45 min. At 60 min tracer is seen in the gallbladder (*GB*). The image at 90 min demonstrates complete drainage of the gallbladder while the tracer is retained in the cyst (*C*)

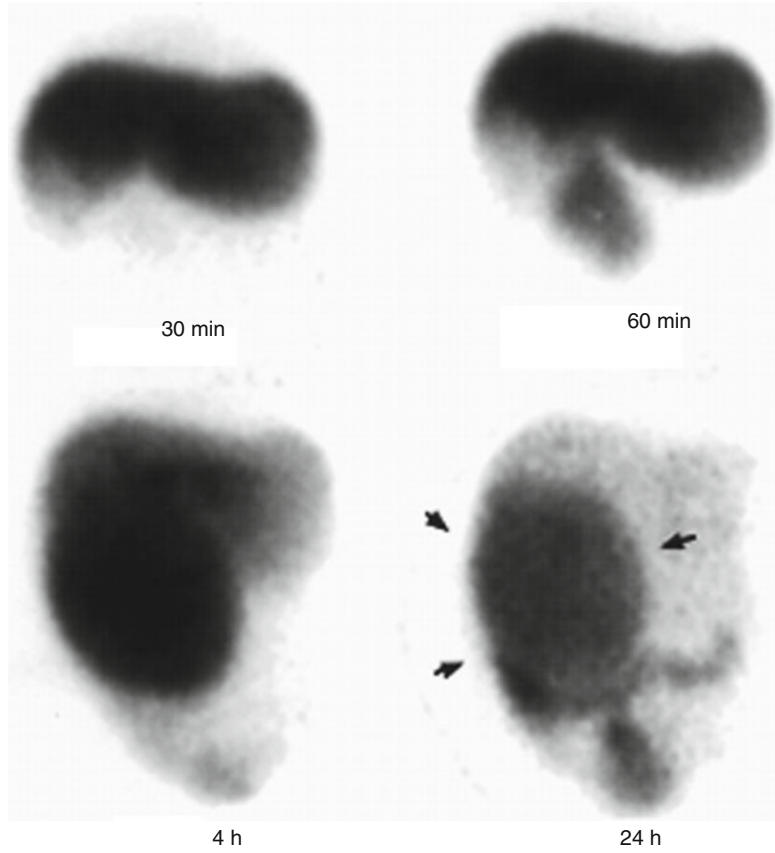

Fig. 10.13 Choledochal cyst (*arrow*). Hepatobiliary scintigraphy shows a large defect in the posterior margin of the hepatic silhouette (30 min), which corresponds to a large choledochal cyst that slowly fills with the tracer

Congenital Anomalies

Congenital abnormalities, such as organ malposition, symmetric liver, asplenia, polysplenia, and accessory spleens, can be diagnosed by ^{99m}Tc-denatured RBCs or radiocolloid scintigraphy. Hepatobiliary agents are useful in identifying an abnormal position of the gallbladder.

The heterotaxia syndrome includes complex congenital heart disease, visceral heterotaxia, bronchopulmonary abnormalities, a common gastrointestinal mesentery (often with malrotation), nonretroperitoneal location of the pancreas, and often asplenia or polysplenia. This syndrome may be accompanied by abnormalities, such as double inferior vena cava or absence of the hepatic portion of the inferior vena cava. The liver may have a symmetric or "horizontal" appearance, or it may be located in the left upper quadrant. In this syndrome the spleen may be normal or abnormal; asplenia, polysplenia, or malposition may be present [29, 30] (Figs. 10.15, 10.16, 10.17, and 10.18).

Asplenia is usually associated with other congenital abnormalities, including complex cardiac anomalies, isomerism of the liver and lungs, bowel malrotation, and dextroposition of the stomach (Fig. 10.19) [29, 31–34]. Most patients with asplenia have Howell–Jolly bodies, Heinz bodies, and siderocytes on the peripheral blood smear. Occasionally, the erythrocytes of a normal premature or term infant also demonstrate these abnormalities, possibly because of splenic immaturity. Documentation of splenic hypofunction in patients with congenital cyanotic heart disease by hematologic findings is highly suggestive of the congenital asplenia syndrome and the associated cardiac anomalies.

The specific diagnosis of polysplenia with normal splenic function can be made by scintigraphic demonstration of multiple spleens. Associated abnormalities include absence of the proximal portion of the inferior vena cava and bilateral hyperarterial bronchi. Polysplenia can also occur without significant heart disease.

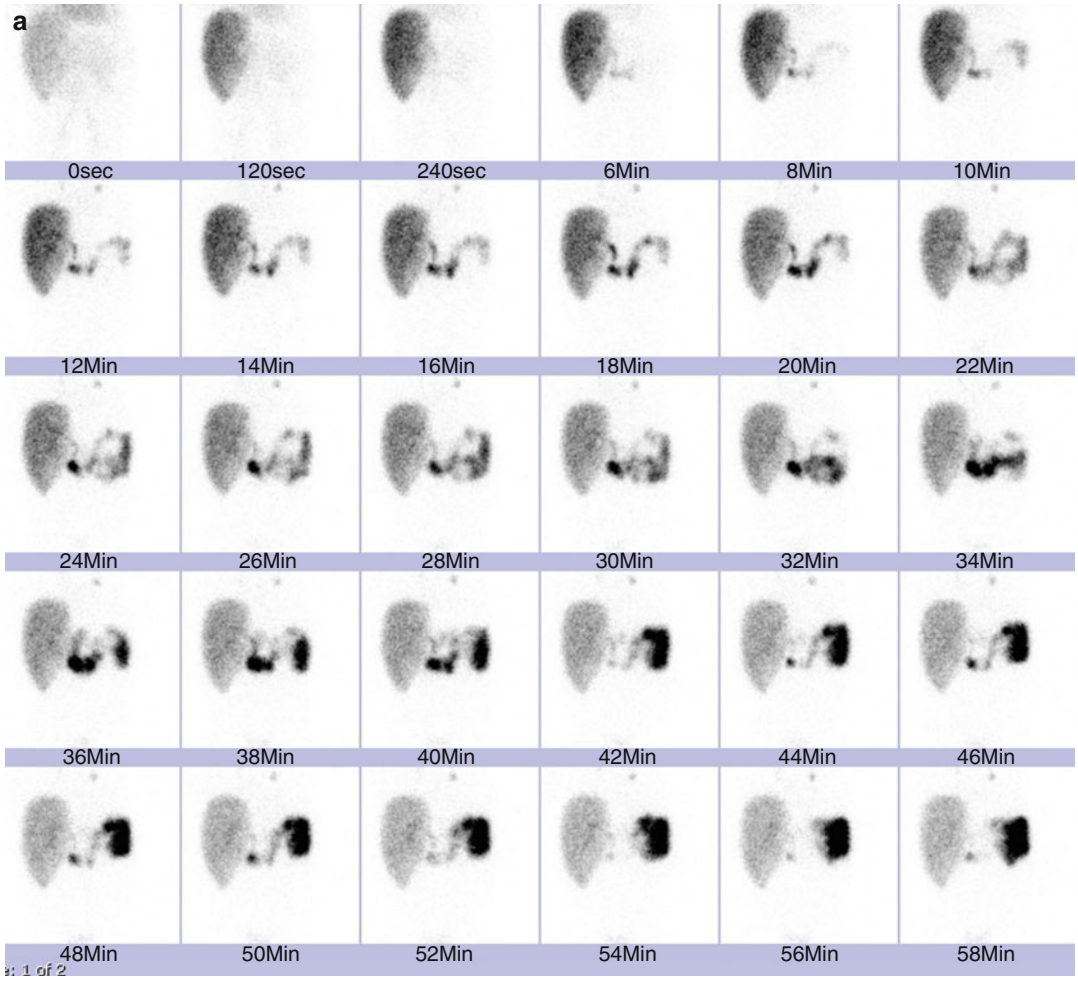

Fig. 10.14 Two-year-old male with hepatoblastoma after an exploratory laparotomy with L trisegmentectomy, en bloc splenectomy, and post-op bile leak. (**a**) Initial 60 min shows absent tracer uptake in the region of the left lobe of the liver with rapid transit into the bowel. (**b**) Images obtained 2 h later reveal tracer that has leaked into the peritoneal cavity (*arrows*)

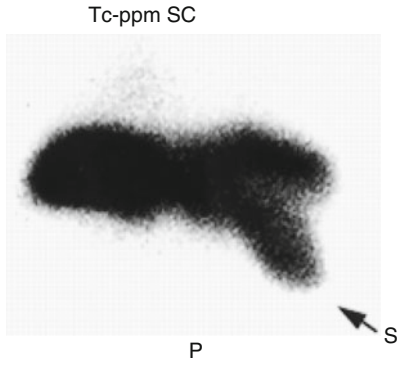

Fig. 10.15 Symmetric ("horizontal") liver and right-sided spleen. A posterior (*P*) ^{99m}Tc–sulfur colloid image reveals the spleen in the right upper quadrant (*S*). The liver has a symmetric appearance

Absence of the renal-to-hepatic portion of the inferior vena cava is accompanied by azygos or hemiazygos extension. In some cases patients also may have a persistent left superior vena cava. Radionuclide venography can detect patency of the inferior vena cava and facilitate cardiac catheterization [29].

Diffuse and Focal Liver Disease

Enlargement of the liver can be due to homogeneous involvement, such as in glycogen storage disease, biliary obstruction, congestive heart failure, infection, leukemia, Hodgkin's disease, or

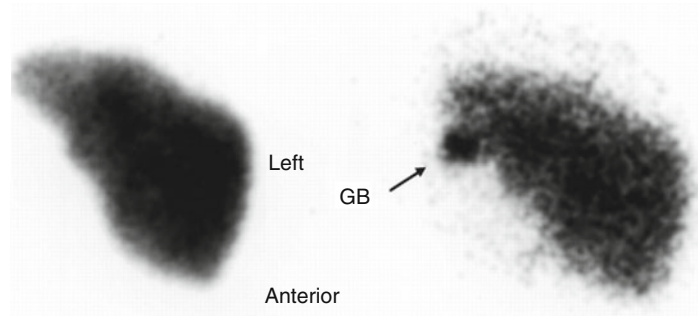

Fig. 10.16 Heterotaxia. Anterior image of the abdomen using ^{99m}Tc–sulfur colloid shows the liver in the left upper quadrant (*left*). ^{131}I-rose bengal imaging demonstrates the abnormal location of the gallbladder (*GB*, *right*)

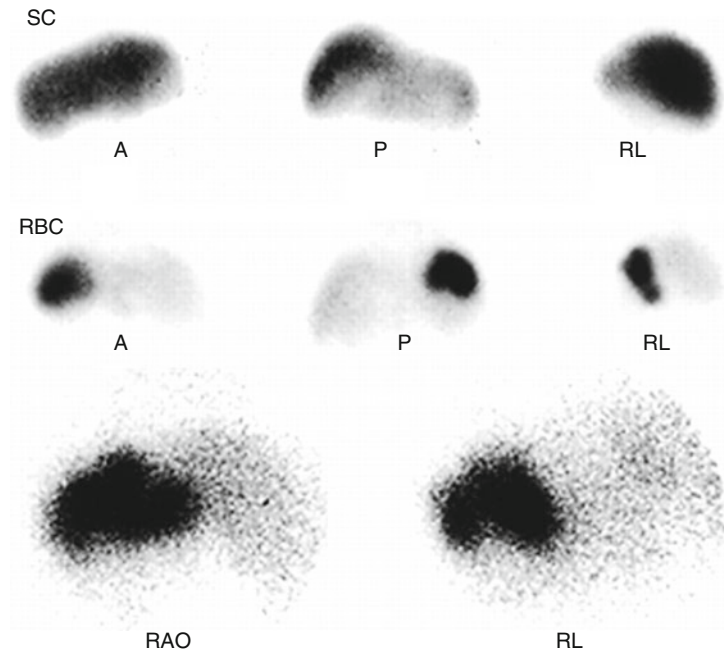

Fig. 10.17 Polysplenia in the heterotaxia syndrome. *Top*: ^{99m}Tc–sulfur colloid images (*SC*) reveal a rather uniform distribution of the tracer. *Bottom*: The same patient imaged with ^{99m}Tc–denatured red blood cells (*RBCs*) demonstrates the spleen in the right upper quadrant. Magnification (pinhole) scintigraphy in the right anterior oblique (*RAO*) and right lateral (*RL*) projections with ^{99m}Tc-denatured RBCs reveals polysplenia, *A* Anterior, *P* Posterior

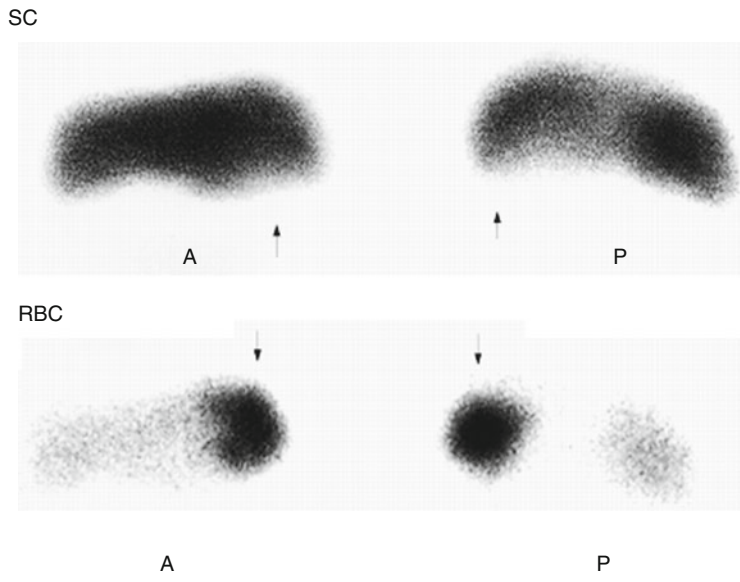

Fig. 10.18 Heterotaxia. *Top*: Anterior (*A*) and posterior (*P*) images obtained with ^{99m}Tc–sulfur colloid reveal uniform distribution of the tracer. The spleen cannot be identified. *Bottom*: Images obtained with ^{99m}Tc-denatured *RBCs* demonstrate the location of the spleen in the left upper quadrant
SC Sulfur Colloid,
RBC Red Blood Cells

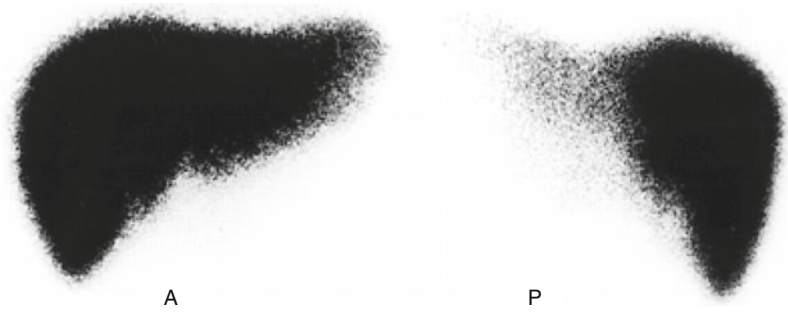

Fig. 10.19 Asplenia. Anterior (*A*) and posterior (*P*) ^{99m}Tc–sulfur colloid images reveal no evidence of functioning splenic tissue in the left upper quadrant. The hepatic silhouette appears normal

diffuse tumor. The usual appearance in glycogen storage disease is a diffuse reduction in the concentration of tracer within the liver. Diffuse parenchymal processes, such as cirrhosis (α_1-antitrypsin deficiency, congenital hepatic fibrosis, cystic fibrosis), may reveal hepatomegaly or reduction of liver size depending on the stage of the disease. Often these patients have increased uptake of radiocolloid in the spleen and vertebral marrow. With diffuse lung disease (cystic fibrosis, asthma), the hepatic silhouette may be depressed inferiorly by the expanded lungs.

Single or multiple space-occupying lesions of the liver, for example, hematoma (Fig. 10.20), abscess, cyst, tumors (hepatoma, hepatoblastoma, metastatic Wilms' tumor, neuroblastoma, hemangioma, lymphoma), can occur with or without hepatomegaly. In cirrhosis (primary, cystic fibrosis, α_1-antitrypsin deficiency) multiple hepatic defects can be seen. Liver metastases from lymphoma, leukemia, or neuroblastoma can be diffuse and infiltrative and can cause

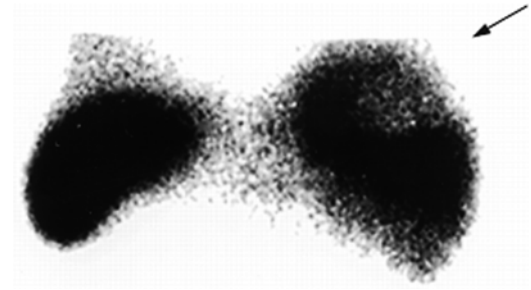

Fig. 10.20 Posttraumatic hepatic hematoma. Posterior ^{99m}Tc–sulfur colloid scintigraphy reveals a well-defined area of decreased to absent uptake posteriorly and superiorly (*arrow*) corresponding to a subcapsular hematoma

hepatomegaly with or without defects. Focal space-occupying lesions usually appear on hepatic scintigraphy as areas of reduced to absent radiocolloid uptake. A scintiscan using a ^{99m}Tc-labeled hepatobiliary agent can occasionally demonstrate uptake in a hepatoma. Hepatic adenomas and focal nodular hyperplasia may contain a sufficient concentration of Kupffer cells to allow for colloidal uptake. Areas of increased normal or decreased radiocolloid uptake within the liver may be detected in patients with focal nodular hyperplasia [35, 36].

Enlargement, tumors, or abscesses of neighboring structures can produce abnormal scintiscans. For example, a gallbladder cyst, renal mass or renal hypertrophy, pancreatic tumor or cyst, gastric or mesenteric tumors or cysts, the diaphragm, the aorta, the para-aortic nodes, and pulmonary pathology may cause impressions on the hepatic or splenic image that can be indistinguishable from intrahepatic or intrasplenic disease [37, 38].

The course of hepatic regeneration after partial hepatectomy or radiation therapy can be followed by means of hepatic scintigraphy. Radiation directed to an area of normal hepatic tissue produces a defect with well-defined margins corresponding to the radiotherapy port. Sometimes radiation injury to the liver is reversible, and the liver scan returns to normal. In other cases fibrosis leads to atrophy of the involved area of the liver. The intact portion of the liver hypertrophies in these patients and the normal portion of the liver rapidly become hyperplastic and assume a globular shape. Portions of the liver within a radiation therapy portal may not be visible by ^{99m}Tc–sulfur colloid scintigraphy or with ^{99m}Tc-labeled hepatobiliary agents. After partial hepatectomy, the liver usually undergoes rapid regeneration and resumes a normal size and shape.

Focal liver defects can also be seen with intrahepatic gallbladder, choledochal cysts, and Caroli's disease. Hepatobiliary scintigraphy confirms the biliary nature of these lesions. Reticuloendothelial system scintigraphy can easily assist with the diagnosis of eventration or herniation of the liver (Fig. 10.21). In the presence of a mass in the left lower lung field, splenic scintigraphy with ^{99m}Tc-denatured RBCs rapidly and effectively identifies misplaced splenic tissue.

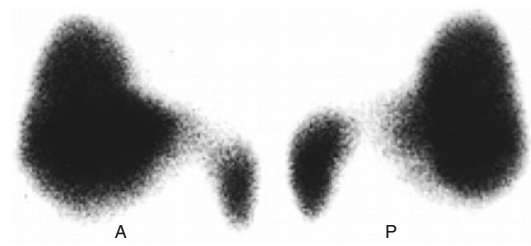

Fig. 10.21 Hepatic eventration. Anterior (*A*) and posterior (*P*) ^{99m}Tc–sulfur colloid images demonstrate part of the hepatic substance within the right lower hemithorax

Multiple intrahepatic defects can be found with polycystic liver disease, which is associated with renal cysts. Single or multiple focal defects may be seen in patients with hydatid cysts. Primary tumors of the liver may be solitary or multifocal, avascular or hypervascular, but scintigraphy does not permit differentiation of malignant and benign lesions of the liver. Tumors with high blood flow within the liver show an arterial blush on radionuclide angiography. Conventional hepatic scintigraphy reveals those tumors as areas of decreased to absent radiotracer uptake. Liver abscesses are uncommon in children, but when they occur they are usually a complication of an underlying process. For example, abscesses can be seen in chronic granulomatous disease, leukemia, and other diseases. These lesions show no radiocolloid concentration and can be seen on ^{201}Tl scintigraphy or ^{18}F-FDG-PET as areas of increased uptake.

Patients with superior vena caval obstruction and the Budd–Chiari syndrome [39] may exhibit increased focal uptake of radiocolloid within the liver. With superior vena caval obstruction, systemic-to-portal venous shunting occurs through the internal thoracic and periumbilical venous channels. After intravenous injection (within a vein of an upper extremity), part of the radiotracer reaches the liver in high concentrations, bypassing the systemic circulation. It results in an area of increased radiocolloid concentration in the medial segment of the left lobe

of the liver. If tracer is injected in a vein of the lower extremities, it reaches the liver through the normal pathways, and the distribution of colloid in the liver is normal. With inferior vena caval obstruction, the reverse is true [40]. The typical pattern of Budd–Chiari is preserved ^{99m}Tc–sulfur colloid uptake in the caudate lobe with diminished uptake by the remainder of the liver.

Hepatic scintigraphy in patients with lymphoma or leukemia usually reveals hepatosplenomegaly without focal defects, although sometimes defects are found. Hepatotoxicity due to chemotherapy in leukemia and other disorders may result in hepatomegaly with or without uniform distribution of tracer within the liver with or without splenomegaly. If severe hepatocellular damage occurs, a shift of colloid uptake to the spleen may be apparent. In other cases, when chemotherapeutic agents are given together with radiation therapy, multiple focal defects can be detected within the liver. These defects are not always metastatic tumors, and they may represent local congestion, atrophy, or necrosis.

Children with Wilms' tumor treated with radiation therapy and chemotherapy may develop sudden enlargement of the liver with intrahepatic defects resembling metastases. Temporary withdrawal of chemotherapy may result in resolution of the intrahepatic abnormalities and normalization of the liver size. Awareness of this effect of chemotherapy and radiation on the liver may prevent the erroneous diagnosis of metastatic disease.

Splenomegaly can be seen with a variety of conditions, including portal hypertension (cirrhosis, cystic fibrosis, α_1-antitrypsin deficiency), Gaucher's disease, leukemia, lymphoma, anemia, congestive heart failure, bacterial endocarditis, pyelonephritis, metastatic disease, hepatitis, granulomatous disease, hemolytic disease, glycogen storage disease, and systemic infections. Increased uptake of ^{99m}Tc–sulfur colloid in the spleen without an increase in the size of the organ can be found in children suffering from any of a large variety of infectious diseases or in children with splenic congestion following trauma. Relatively increased ^{99m}Tc–sulfur colloid uptake in the spleen with or without splenomegaly is found with severe liver dysfunction, including hepatic cirrhosis, chemotoxicity, trauma with edema of the liver, and storage disease of the liver.

Focal splenic defects can be found with splenic rupture, subcapsular hematoma, tumor, lymphoma, abscess, cyst, leukemia, infarction, and histiocytosis [41] (Treves ST, 1984, unpublished data). Positional changes may affect the shape of the spleen or simulate focal splenic defects. Likewise, gastric dilation caused by food or carbonated liquids may change the shape of the spleen. Sometimes it is difficult to distinguish the left lobe of the liver from the spleen. In these cases one may consider using oral carbonated beverages to induce gastric dilatation for better separation of these organs [42, 43]. Single-photon emission computed tomography using ^{99m}Tc–sulfur colloid improves assessment of hepatic disease [44].

Trauma

With blunt abdominal trauma, both liver and spleen may be damaged, with other abdominal organs involved as well. In large medical centers, blunt abdominal trauma is usually evaluated initially with CT, which enables the diagnosis of multiple organ involvement in one examination.

Hepatic trauma can be effectively detected by RES scintigraphy. Multiple projections (or preferably SPECT) and awareness of anatomic variants are essential for correct interpretation. Hematoma or rupture of the liver appears as an area of reduced or absent uptake of variable size or shape within the organ (Fig. 10.20) [45].

The spleen comprises 25 % of the total lymphoid mass of the body and functions to clear the body of particulate antigens. An increased risk of septicemia, often fatal in children, after splenectomy has been reported. The risk of overwhelming lethal infection following splenectomy is approximately 0.1 % in otherwise normal individuals [23, 46–50]. The risk of overwhelming sepsis is greatest in patients who require splenectomy as part of the therapy for an underlying debilitating disease, such as portal hypertension

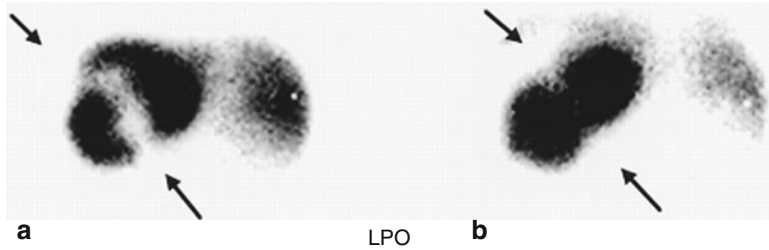

Fig. 10.22 Splenic injury. Two ^{99m}Tc–sulfur colloid images in the left posterior oblique projection (*LPO*) obtained 20 months apart. The first image (**a**), obtained shortly after blunt abdominal trauma, reveals a discrete defect extending across the spleen. The second image (**b**), obtained 20 months later, reveals significant reduction of the defect. *Arrows* point to splenic defects

or thalassemia. This risk appears to be greatest in children, especially those under age 1. Approximately 75 % of infections occur within 2 years after surgery [50]. Fifty percent of these infections are due to *Diplococcus pneumoniae* and the remainder to *Haemophilus influenzae*, *Staphylococcus aureus*, group A streptococci, and *Neisseria meningitidis*. The explanation for the increased incidence of infection is not known. One theory attributes the susceptibility to the low serum opsonin levels and defective production of immunoglobulin M (IgM) [51]. The total incidence of postsplenectomy mortality from sepsis in all groups is estimated to range from 0.25 to 0.58 % [23, 48]. Nonoperative management of patients with splenic injury has become the treatment of choice. If surgery is required, alternatives to total splenectomy include oversuturing splenic lacerations or partial splenectomy [52, 53]. Potential risks or complications associated with the failure to excise a damaged spleen include delayed rupture and the development of a splenic pseudocyst. Delayed rupture of the spleen is a controversial subject [54–56]. We have not seen a single case of delayed rupture among our patients. Splenic pseudocysts are non-epithelium-lined cystic structures that contain bloody material [57, 58]. They can present as an abdominal mass at a time when the episode of trauma may not even be remembered.

With ^{99m}Tc–sulfur colloid and multiple projections (or preferably SPECT), splenic scintigraphy

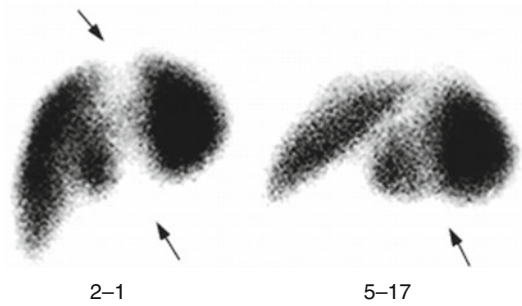

Fig. 10.23 Splenic injury. Two consecutive ^{99m}Tc–sulfur colloid images obtained 3 months apart reveal resolution of a splenic defect (*arrows*) after blunt abdominal trauma

is a reliable, simple, safe, and convenient method for diagnosing splenic injury and, if necessary, following its resolution [59–62] (Figs. 10.22 and 10.23). Splenic injury may be seen on scintigraphy as a focal defect, a band of decreased to absent activity, apparent amputation of a portion of the spleen, a T- or Y-shaped defect or band, or a very small or absent spleen. After the diagnosis of splenic trauma has been made, scintigraphy can show that the laceration or hematoma is resolving and that a posttraumatic cyst is not developing. Scintigraphic follow-up should be done if pain develops or a left upper quadrant mass appears. Fischer et al. [60] at our institution followed 20 patients with splenic trauma for 2 months to 1 year. Most of these patients showed persistent defects that became smaller with time. In no case did the scan defect enlarge with time. Only three of the 20 patients examined showed

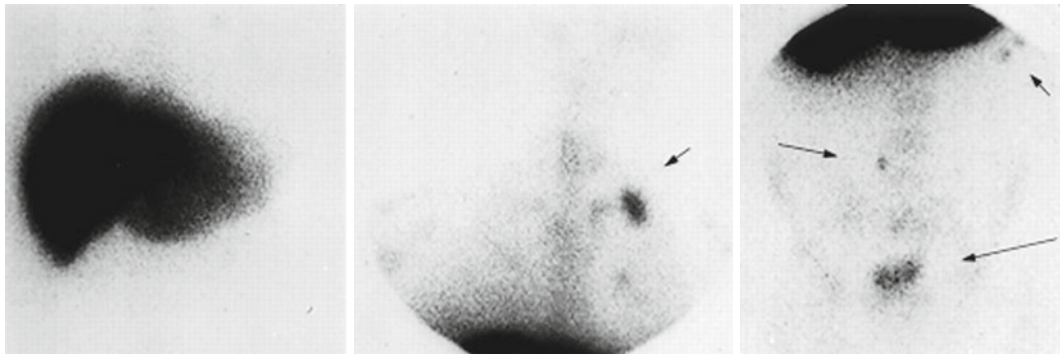

Fig. 10.24 Splenosis. A conventional anterior image of the liver using ^{99m}Tc–sulfur colloid is normal, and the spleen is not visible (*left*). There are three foci of selective radiocolloid concentration in the left hemithorax (*center*). In addition, there are three or more foci of colloid uptake in the abdomen (*right*). *Arrows* point to accessory spleens

scintigraphic healing or total disappearance of the scan defect. The presence of a residual defect on follow-up scintigraphy is probably not sufficient reason for keeping the patient on restricted activity.

Splenosis

Splenosis is autotransplantation of splenic tissue after splenic trauma [63–66]. It does not have a characteristic clinical picture and is not commonly encountered. Splenic scintigraphy using either ^{99m}Tc–sulfur colloid or ^{99m}Tc-denatured RBCs makes the specific diagnosis of splenosis. When evaluating liver and spleen scans in patients with previous abdominal trauma who may or may not be splenectomized, the possibility of splenosis should be kept in mind. Splenosis can also occur in the thorax [63] (Ehrlich CP, Treves ST, 1981, unpublished data). Radionuclide scintigraphy is useful for making the diagnosis of splenosis in any pediatric patient with an unexplained thoracic mass who has a prior history of splenic trauma and should be performed before considering thoracotomy. The uptake of radiocolloid by splenic tissue in patients with splenosis may be minimal in relation to liver uptake. To recognize splenosis, it may be necessary to shield the hepatic image or use contrast enhancement (Fig. 10.24).

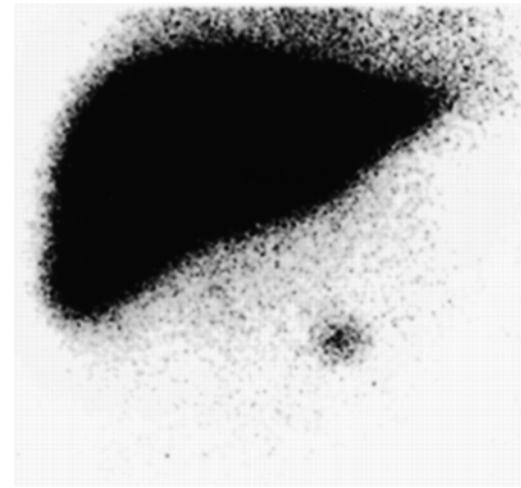

Fig. 10.25 Accessory spleen. Abnormal concentration of ^{99m}Tc–sulfur colloid below the hepatic silhouette corresponds to an accessory spleen seen after splenectomy

Accessory Spleen

Accessory spleens (one or more) are found in approximately 10–15 % of autopsies in children [65, 67]. They can be found anywhere in the abdomen but are most frequently seen in the left upper quadrant. Usually, accessory spleens are not visible on routine imaging with ^{99m}Tc–sulfur colloid or ^{99m}Tc-denatured RBCs. Accessory spleens are more likely to be seen by scintigraphy after splenectomy (Ehrlich CP, Treves ST, 1981, unpublished data) (Figs. 10.25 and 10.26).

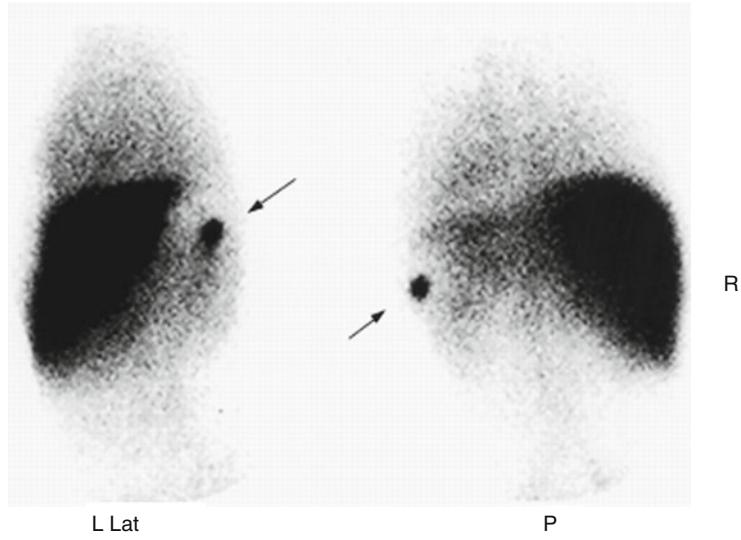

Fig. 10.26 Accessory spleen. Images obtained with ^{99m}Tc-denatured RBCs demonstrate accessory splenic tissue (*arrows*), *L Lat* Left Lateral; *P* Posterior; *R* Right

Splenic Torsion and Wandering Spleen

The main support of the spleen is provided by its various ligaments and vessels. The surrounding organs and the intra-abdominal pressure also help keep the spleen in its normal position and limit its mobility.

Torsion of the spleen, which is a rare condition, can present with a varied clinical picture, such as acute intestinal obstruction [68]. Radiographically, torsion of the spleen may not be apparent or may appear as a mass lesion on plain films. Scintigraphically, splenic torsion can cause nonvisualization of the spleen. Acute torsion of the spleen reportedly has caused gastric varices that subsequently bleed [69]. In this instance chronic splenic vein occlusion probably leads to retrograde filling of the short gastric and gastroepiploic veins, which rupture in response to the increased pressure.

Wandering spleen is a rare condition characterized by unusual mobility of this organ and is usually discovered when torsion of the splenic pedicle occurs. The patient usually presents with an acute abdomen. On scintigraphy, the spleen may appear in its normal position or be displaced inferiorly or medially. Repeated views with the patient in various positions may help diagnose the unusual mobility of the spleen [70].

Nonvisualization of the Spleen ("Functional Asplenia")

Nonvisualization of the spleen on ^{99m}Tc–sulfur colloid images was first described in patients with sickle-cell disease [71–73]. The spleen in these patients can be identified with a ^{99m}Tc bone-seeking radiopharmaceutical [74] (Fig. 10.27). Dhawan et al. [75] published a tentative classification of disorders associated with reversible functional asplenia, including certain cyanotic congenital heart diseases (treated), sickle-cell disease, hemoglobin sickle-cell disease, and combined immunodeficiency. Functional asplenia of patients with sickle-cell disease can be reversed by transfusion of normal RBCs, with the circulating level of normal RBCs required for visualization of the spleen being approximately 50 %. Functional asplenia can be observed in some patients with no circulating Howell–Jolly bodies

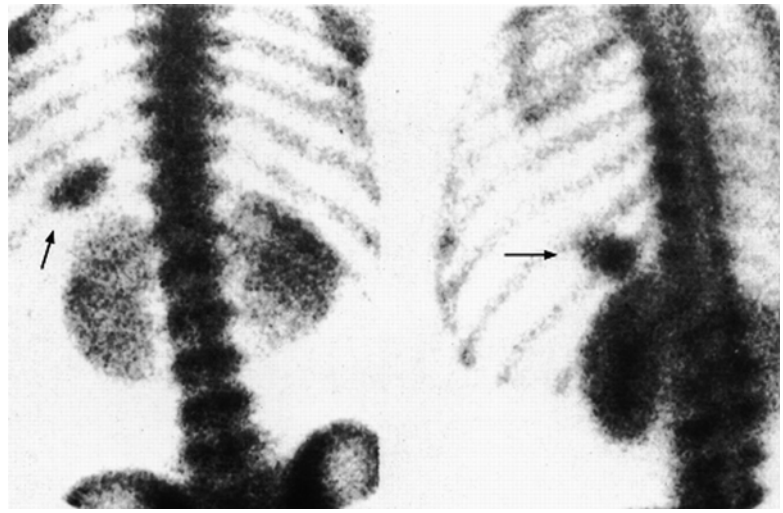

Fig. 10.27 Sickle-cell disease. The spleen (*arrows*) is visualized after administration of ^{99m}Tc–methylene diphosphonate (^{99m}Tc-MDP) for skeletal scintigraphy in a patient suffering from sickle-cell disease. ^{99m}Tc–sulfur colloid scintigraphy (not shown) did not reveal splenic uptake

[76]. Kevy et al. [77] reported a small number of children with hereditary splenic hypoplasia who had extraordinary susceptibility to infection and showed little or no evidence of significant splenic function by scintigraphy.

Splenic Abscess

Abscesses of the spleen are rare. They are most often found in patients with a preexisting hematologic disorder, primary infection elsewhere, or trauma to the spleen. Trauma is responsible for approximately 15 % of cases of splenic abscess. Brown et al. [78] reported a *Salmonella* splenic abscess detected on a ^{99m}Tc–sulfur colloid study that also appeared as a defect surrounded with a halo of increased uptake on gallium-67 (67Ga) scintigraphy [78].

Liver Transplantation

Hepatobiliary scintigraphy is useful for evaluating recipients of liver transplants [44, 79–82]. This technique provides an overall view of the transplant's functional parenchyma and of bile drainage. Typically, and unless there is a suspicion of surgical complication, a baseline study is obtained within 24 h of the transplant. This study is useful for detecting regional hepatic flow, global hepatic function, and biliary drainage. The presence of focal defects caused by vascular damage that may have occurred during harvesting can be detected early. In addition to the initial evaluation, hepatobiliary scintigraphy is useful at any time after transplantation when clinical or laboratory findings indicate that a complication may be present (Figs. 10.28 and 10.29). Bile leaks can be detected with remarkable sensitivity (Fig. 10.30).

Liver and Spleen Size

In practice, the size of the liver and spleen are estimated by the physician after physical examination with consideration of the patient's overall size and body proportions and sometimes with the aid of imaging. Comments on the size of the liver and spleen on diagnostic images must be evaluated with caution because these organs grow and change size relatively rapidly in children. Furthermore, it is difficult to establish

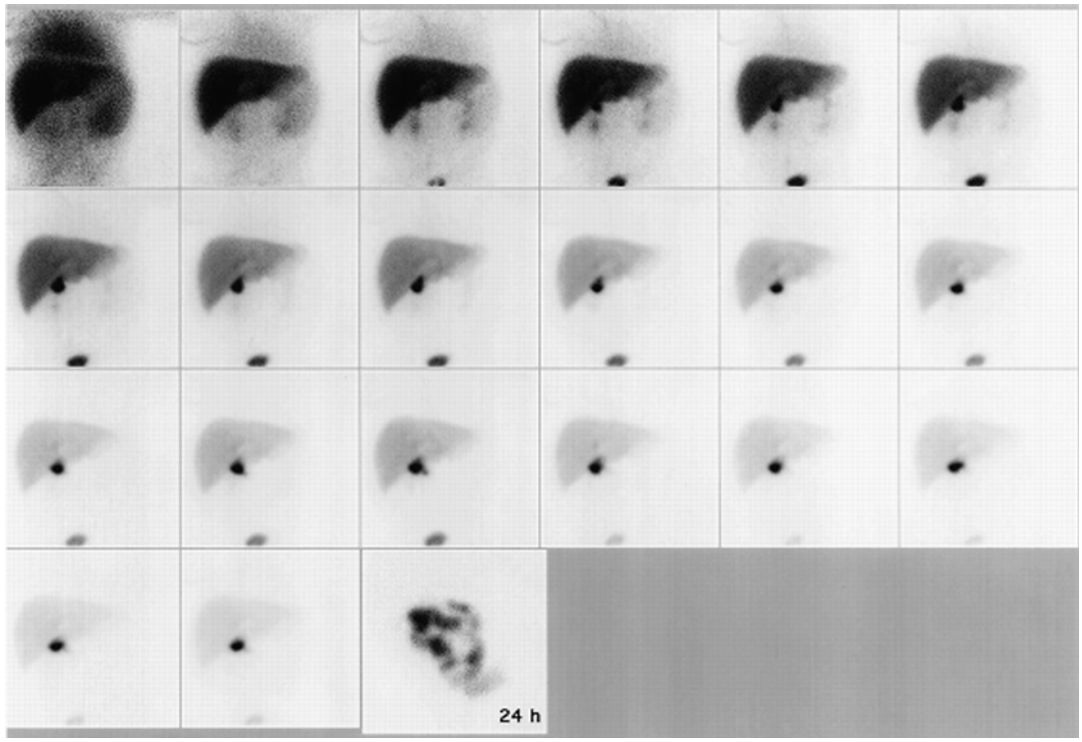

Fig. 10.28 Liver transplant. Hepatobiliary scintigraphy 1 day after liver transplantation. There is rapid uptake of the radiotracer (^{99m}Tc-disofenin) by the liver with adequate blood clearance. Minimal tracer activity is visualized in the kidneys and bladder. Throughout the 60-min study, the tracer appears to be retained in a region just below the inferior margin of the hepatic silhouette, presumably corresponding to the biliary anastomosis. An image obtained at 24 h demonstrates hepatic clearance and tracer within several bowel loops

precise normal hepatic and splenic sizes in children. Information on these sizes by scintigraphy must be refined in terms of distribution by sex, weight percentile, age, body surface area, nutritional status, and other factors.

The maximum vertical dimension (MVD) in centimeters of the hepatic silhouette on hepatic scintigrams has been related to age in years (A) in 66 children from 0 to 19 years of age by the formula: $\mathrm{MVD} = 8.8 + 0.46A$. The correlation coefficient was 0.89. Similarly, the maximum splenic dimension (MSD) on posterior splenic scintigraphy was related to age in 45 children by the formula: $\mathrm{MSD} = 5.7 + 0.31A$. The liver/spleen ratio of lengths was found to be independent of age: 1.55 at birth, 1.52 at 10 years of age, and 1.52 at 18 years of age [83, 84]. It may be possible to compare the calculated weights or dimensions of the liver or spleen (from height, weight, body surface area, or other measurements) with that suggested by the scans [38, 85]. Markisz and associates [86] from our institution found a reasonably good correlation between the maximum vertical dimension on the liver scan and the age and body weight in children with normal liver function. Good correlation was also found between estimated liver volume and patient weight. In addition, they found a good correlation of spleen measurements and age and weight in normal children (Figs. 10.31 and 10.32).

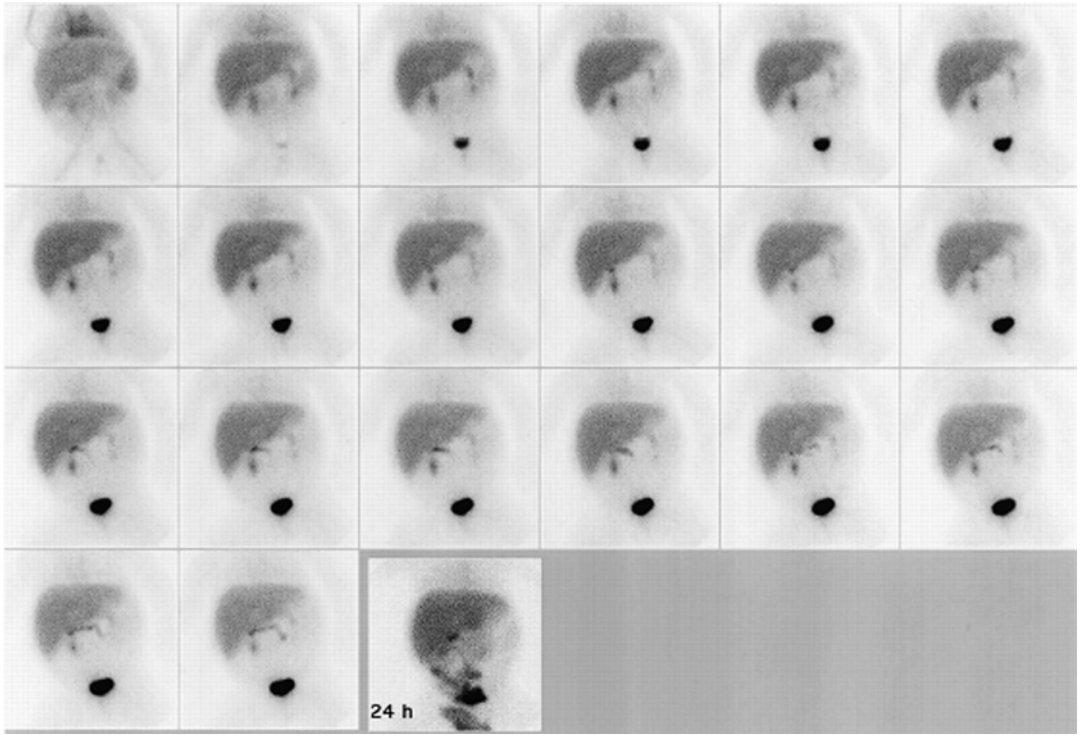

Fig. 10.29 Liver transplant with failure. Hepatobiliary study reveals poor blood clearance and poor liver uptake of the tracer. A large proportion of the tracer is excreted by the kidneys. There is no evidence of biliary obstruction as the tracer slowly appears in the bowel, and at 24 h it can be seen within several bowel loops

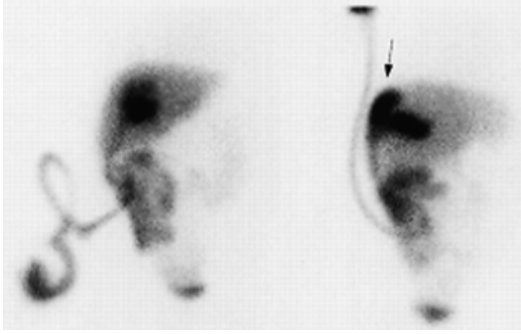

Fig. 10.30 Bile leak. Anterior (*left*) and right lateral (*right*) images demonstrating a bile leak over the posterior and superior aspects of the liver seen best on the lateral projection (*arrow*). This study is from a recipient of a liver transplant

Normal Variants

Scintigraphic recognition of normal anatomic variants of the liver and spleen is difficult at times. Prominent notches or separation of the left and right lobes of the liver or impressions by surrounding organs or the costal margins may produce irregularities in the hepatic or splenic image. An accentuated porta hepatis may simulate intrahepatic disease. A kidney situated in a high position can produce impressions on either the liver or the spleen. Gastric dilatation may produce an impression on the splenic silhouette or the left lobe of the liver that mimics a lesion [87, 88].

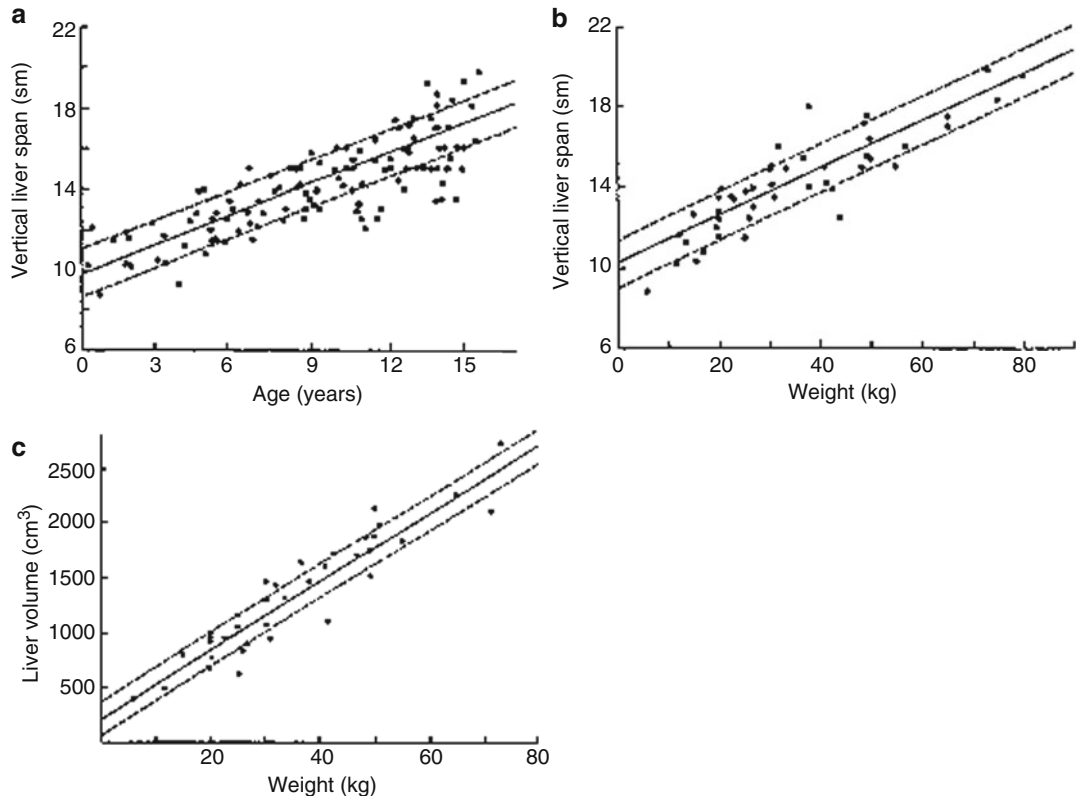

Fig. 10.31 Normal hepatic sizes in children. (**a**) Vertical liver span as a function of age. (**b**) Vertical liver span as a function of weight. (**c**) Liver volume as a function of weight.

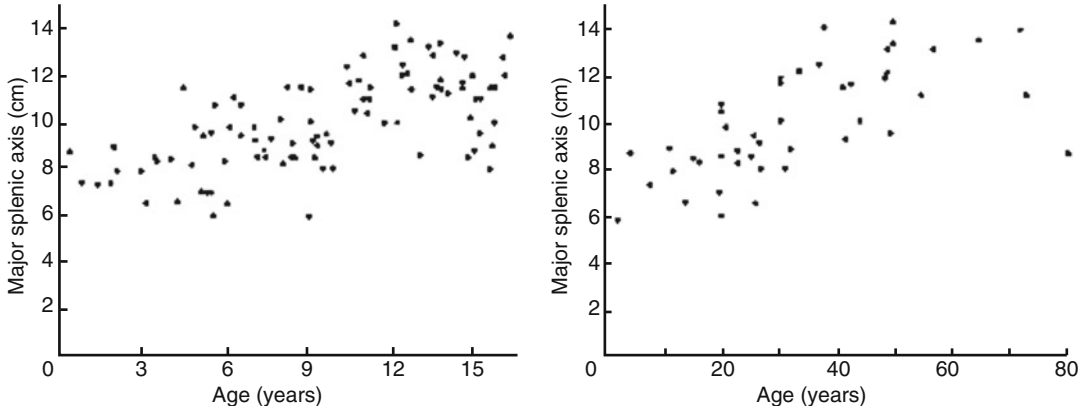

Fig. 10.32 Normal splenic sizes in children. *Left panel* shows major splenic axis as a function of age 0 to 15 years of age. *Right panel* shows major splenic axis as a function of age extending to age 80

References

1. Poddar U, Bhattacharya A, Thapa BR, Mittal BR, Singh K. Ursodeoxycholic acid-augmented hepatobiliary scintigraphy in the evaluation of neonatal jaundice. J Nucl Med. 2004;45(9):1488–92.
2. Ziessman HA, Fahey FH, Hixson DJ. Calculation of a gallbladder ejection fraction: advantage of continuous sincalide infusion over the three-minute infusion method. J Nucl Med. 1992;33(4):537–41.
3. Taplin GV, Meredith Jr OM, Kade H. The radioactive (I131 tagged) rose bengal uptake-excretion test for liver function using external gamma-ray scintillation counting techniques. J Lab Clin Med. 1955;45(5): 665–78.
4. Atkins HL, Richards P, Schiffer L. Scanning of the liver, spleen, and bone marrow with colloidal Tc-99m. Nucl Appl. 1966;2:27.
5. Kasai M, Watanabe I, Ohi R. Follow-up studies of long term survivors after hepatic portoenterostomy for "noncorrectible" biliary atresia. J Pediatr Surg. 1975;10(2):173–82.
6. Odell GBN, Boitnott JK. Evaluation of jaundice. In: James AE, Wagner HN, Cooke RE, editors. Pediatric nuclear medicine. Philadelphia: Saunders; 1974. xvi, 544 p.
7. Hays DM, Woolley MM, Snyder Jr WH, Reed GGJ, Landing BH. Diagnosis of biliary atresia: relative accuracy of percutaneous liver biopsy, open liver biopsy, and operative cholangiography. J Pediatr. 1967;71(4):598–607.
8. Johnston GS, Rosenbaum RC, Hill JL, Diaconis JN. Differentiation of jaundice in infancy: an application of radionuclide biliary studies. J Surg Oncol. 1985;30(4):206–8.
9. Majd M, Reba RC, Altman RP. Hepatobiliary scintigraphy with 99mTc-PIPIDA in the evaluation of neonatal jaundice. Pediatrics. 1981;67(1):140–5.
10. Picozzi R, Bossi MC, Arosio M, et al. Value of hepatobiliary scintigraphy and ultrasonography in the differential diagnosis of jaundice. Nucl Med Commun. 1985;6(2):97–108.
11. Spivak W, Sarkar S, Winter D, Glassman M, Donlon E, Tucker KJ. Diagnostic utility of hepatobiliary scintigraphy with 99mTc-DISIDA in neonatal cholestasis. J Pediatr. 1987;110(6):855–61.
12. Franken Jr EA, Smith WL, Smith JA, Fitzgerald JF. Percutaneous cholangiography in infants. AJR Am J Roentgenol. 1978;130(6):1057–8.
13. Greene HL, Helinek GL, Moran R, O'Neill J. A diagnostic approach to prolonged obstructive jaundice by 24-hour collection of duodenal fluid. J Pediatr. 1979;95(3):412–4.
14. Hashimoto T, Yura J. Percutaneous transhepatic cholangiography (PTC) in biliary atresia with special reference to the structure of the intrahepatic bile ducts. J Pediatr Surg. 1981;16(1):22–5.
15. Hirsig J, Rickham PP. Early differential diagnosis between neonatal hepatitis and biliary atresia. J Pediatr Surg. 1980;15(1):13–5.
16. Gerhold JP, Klingensmith 3rd WC, Kuni CC, et al. Diagnosis of biliary atresia with radionuclide hepatobiliary imaging. Radiology. 1983;146(2):499–504.
17. Majd M, Reba RC, Altman RP. Effect of phenobarbital on 99mTc-IDA scintigraphy in the evaluation of neonatal jaundice. Semin Nucl Med. 1981;11(3): 194–204.
18. Weissmann HS, Frank MS, Bernstein LH, Freeman LM. Rapid and accurate diagnosis of acute cholecystitis with 99mTc-HIDA cholescintigraphy. AJR Am J Roentgenol. 1979;132(4):523–8.
19. Weissmann HS, Rosenblatt R, Sugarman LA, Freeman LM. The role of nuclear imaging in evaluating the patient with cholestasis. Semin Ultrasound CT MR. 1980;1:134–42.
20. Weissmann HS, Sugarman LA, Freeman LM. The clinical role of technetium-99m iminodiacetic acid cholescintigraphy. In: Freeman LM, Weissmann HS, editors. Nuclear medicine annual. New York: Raven Press; 1981. p. v.
21. Crystal RF, Fink RL. Acute acalculous cholecystitis in childhood. Clin Pediatr (Phila). 1971;10(7): 423–6.
22. Dickinson SJ, Corley G, Santulli TV. Acute cholecystitis as a sequel of scarlet fever. Am J Dis Child. 1971;121(4):331–3.
23. Walker W. Splenectomy in childhood: a review in England and Wales, 1960–4. Br J Surg. 1976;63(1): 36–43.
24. Kim SH. Choledochal cyst: survey by the surgical section of the American Academy of Pediatrics. J Pediatr Surg. 1981;16(3):402–7.
25. Caroli J. Diseases of intrahepatic bile ducts. Isr J Med Sci. 1968;4(1):21–35.
26. Caroli J, Soupault R, Kossakowski J, Plocker L, Paradowska. [Congenital polycystic dilation of the intrahepatic bile ducts; attempt at classification]. Sem Hop. 1958;34(8/2):488–495/SP.
27. Wechsler RL, Thiel DV. Fibropolycystic disease of the hepatobiliary system and kidneys. Am J Dig Dis. 1976;21(12):1058–69.
28. Weissmann HS, Chun KJ, Frank M, Koenigsberg M, Milstein DM, Freeman LM. Demonstration of traumatic bile leakage with cholescintigraphy and ultrasonography. AJR Am J Roentgenol. 1979;133(5): 843–7.
29. Freedom RM, Treves S. Splenic scintigraphy and radionuclide venography in the heterotaxy syndrome. Radiology. 1973;107(2):381–6.
30. Treves ST. Spleen. In: Treves ST, editor. Pediatric nuclear medicine. New York: Springer; 1985. p. 141–56.
31. Chandra RS. Biliary atresia and other structural anomalies in the congenital polysplenia syndrome. J Pediatr. 1974;85(5):649–55.
32. Ivemark BI. Implications of agenesis of the spleen on the pathogenesis of conotruncus anomalies in childhood; an analysis of the heart malformations in the splenic agenesis syndrome, with fourteen new cases. Acta Paediatr. 1955;44 Suppl 104:7–110.

33. Roberts WC, Berry WB, Morrow AG. The significance of asplenia in the recognition of inoperable congenital heart disease. Circulation. 1962;26:1251–3.
34. Rose V, Izukawa T, Moes CA. Syndromes of asplenia and polysplenia. A review of cardiac and non-cardiac malformations in 60 cases with special reference to diagnosis and prognosis. Br Heart J. 1975;37(8): 840–52.
35. Atkinson Jr GO, Kodroff M, Sones PJ, Gay Jr BB. Focal nodular hyperplasia of the liver in children: a report of three new cases. Radiology. 1980;137(1 Pt 1): 171–4.
36. Rosenthall L. Gastrointestinal imaging: imaging the liver in pediatrics. In: James AE, Wagner HN, Cooke RE, editors. Pediatric nuclear medicine. Philadelphia: Saunders; 1974. xvi, 544 p.
37. Freeman LM, Meng CH, Johnson PM, Bernstein RG, Bosniak MA. False positive liver scans caused by disease processes in adjacent organs and structures. Br J Radiol. 1969;42(501):651–6.
38. Rollo FD, DeLand FH. The determination of liver mass from radionuclide images. Radiology. 1968; 91(6):1191–4.
39. Meindok H, Langer B. Liver scan in Budd-Chiari syndrome. J Nucl Med. 1976;17(5):365–8.
40. Gooneratne NS, Buse MG, Quinn 3rd JL, Selby JB. "Hot spot" on hepatic scintigraphy and radionuclide venacavography. AJR Am J Roentgenol. 1977;129(3):447–50.
41. Freeman MH, Tonkin AK. Focal splenic defects. Radiology. 1976;121(3 Pt. 1):689–92.
42. Landgarten S, Spencer RP. Splenic displacement due to gastric dilatation. J Nucl Med. 1972;13(3):223.
43. Parker JD, Bennett LR. Effect of water ingestion on spleen size as determined by radioisotope scans. Acta Radiol Diagn (Stockh). 1971;11(4):385–92.
44. Van Heertum RL, Yudd AP, Brunetti JC, Pennington MR, Gualtieri NM. Hepatic SPECT imaging in the detection and clinical assessment of hepatocellular disease. Clin Nucl Med. 1992;17(12):948–53.
45. Froelich JW, Simeone JF, McKusick KA, Winzelberg GG, Strauss HW. Radionuclide imaging and ultrasound in liver/spleen trauma: a prospective comparison. Radiology. 1982;145(2):457–61.
46. Eraklis AJ, Kevy SV, Diamond LK, Gross RE. Hazard of overwhelming infection after splenectomy in childhood. N Engl J Med. 1967;276(22):1225–9.
47. King H, Shumacker Jr HB. Splenic studies. I. Susceptibility to infection after splenectomy performed in infancy. Ann Surg. 1952;136(2):239–42.
48. Singer DB. Postsplenectomy sepsis. In: Rosenberg HS, Bolande RP, editors. Perspectives in pediatric pathology. Chicago: Year Book; 1973.
49. Smith CH, Erlandson M, Schulman I, Stern G. Hazard of severe infections in splenectomized infants and children. Am J Med. 1957;22(3):390–404.
50. Winter ST. Editorial: trauma, splenectomy and the risk of infection. Clin Pediatr (Phila). 1974;13(12):1011–2.
51. Likhite VV. Immunological impairment and susceptibility to infection after splenectomy. JAMA. 1976;236(12):1376–7.
52. Douglas GJ, Simpson JS. The conservative management of splenic trauma. J Pediatr Surg. 1971;6(5): 565–70.
53. Mishalany H. Repair of the ruptured spleen. J Pediatr Surg. 1974;9(2):175–8.
54. Ayala LA, Williams LF, Widrich WC. Occult rupture of the spleen: the chronic form of splenic rupture. Ann Surg. 1974;179(4):472–8.
55. Benjamin CI, Engrav LH, Perry Jr JF. Delayed rupture or delayed diagnosis of rupture of the spleen. Surg Gynecol Obstet. 1976;142(2):171–2.
56. Olsen WR. Editorial: delayed rupture of the spleen as an index of diagnostic accuracy. Surg Gynecol Obstet. 1974;138(1):82.
57. Topilow AA, Steinhoff NG. Splenic pseudocyst: a late complication of trauma. J Trauma. 1975;15(3): 260–3.
58. Wright FW, Williams EW. Large post-traumatic splenic cyst diagnosed by radiology, isotope scintigraphy and ultrasound. Br J Radiol. 1974;47(560):454–6.
59. Bethel CA, Touloukian RJ, Seashore JH, Rosenfield NS. Outcome of nonoperative management of splenic injury with nuclear scanning. Clinical significance of persistent abnormalities. Am J Dis Child. 1992;146(2):198–200.
60. Fischer KC, Eraklis A, Rossello P, Treves S. Scintigraphy in the followup of pediatric splenic trauma treated without surgery. J Nucl Med. 1978;19(1):3–9.
61. Gilday DL, Alderson PO. Scintigraphic evaluation of liver and spleen injury. Semin Nucl Med. 1974;4(4):357–70.
62. Solheim K, Nerdrum HJ. Radionuclide imaging of splenic laceration and trauma. Clin Nucl Med. 1979;4(12):528–33.
63. Ahmadi A, Faber LP, Milloy F, Jensik RJ. Intrathoracic splenosis. J Thorac Cardiovasc Surg. 1968;55(5):677–81.
64. Albrecht H. Ein Fall von sehr Zahlreichen uber ganze Peritoneum versprentgen nebenmilzen. Beitr Pathol Anat. 1918;20:513–27.
65. Buchbinder JH, Lipkoff CJ. Splenosis: multiple peritoneal splenic implants following abdominal injury. Surgery. 1939;6:927–34.
66. Jacobson SJ, De Nardo GL. Splenosis demonstrated by splenic scan. J Nucl Med. 1971;12(8):570–2.
67. Eraklis AJ, Filler RM. Splenectomy in childhood: a review of 1413 cases. J Pediatr Surg. 1972;7(4):382–8.
68. Broker FH, Khettry J, Filler RM, Treves S. Splenic torsion and accessory spleen: a scintigraphic demonstration. J Pediatr Surg. 1975;10(6):913–5.
69. Sorgen RA, Robbins DI. Bleeding gastric varices secondary to wandering spleen. Gastrointest Radiol. 1980;5(1):25–7.
70. Broker FH, Fellows K, Treves S. Wandering spleen in three children. Pediatr Radiol. 1978;6(4):211–4.
71. Pearson HA, Cornelius EA, Schwartz AD, Zelson JH, Wolfson SL, Spencer RP. Transfusion-reversible functional asplenia in young children with sickle-cell anemia. N Engl J Med. 1970;283(7):334–7.
72. Pearson HA, Schiebler GL, Spencer RP. Functional hyposplenia in cyanotic congenital heart disease. Pediatrics. 1971;48(2):277–80.

73. Pearson HA, Spencer RP, Cornelius EA. Functional asplenia in sickle-cell anemia. N Engl J Med. 1969;281(17):923–6.
74. Fischer KC, Shapiro S, Treves S. Visualization of the spleen with a bone-seeking radionuclide in a child with sickle-cell anemia. Radiology. 1977; 122(2):398.
75. Dhawan VM, Spencer RP, Sziklas JJ. Reversible functional asplenia in chronic aggressive hepatitis. J Nucl Med. 1979;20(1):34–6.
76. Dhawan VM, Spencer RP, Pearson HA, Sziklas JJ. Functional splenia in the absence of circulating Howell-Jolly bodies. Clin Nucl Med. 1977;2: 395–6.
77. Kevy SV, Tefft M, Vawier GF, Rosen FS. Hereditary splenic hypoplasia. Pediatrics. 1968;42(5):752–7.
78. Brown JJ, Sumner TE, Crowe JE, Shaffner LD. Preoperative diagnosis of splenic abscess by ultrasonography and radionuclide scanning. South Med J. 1979;72(5):575–7, 580.
79. Gelfand MJ, Smith HS, Ryckman FC, et al. Hepatobiliary scintigraphy in pediatric liver transplant recipients. Clin Nucl Med. 1992;17(7):542–9.
80. Hawkins RA, Hall T, Gambhir SS, et al. Radionuclide evaluation of liver transplants. Semin Nucl Med. 1988;18(3):199–212.
81. Klingensmith 3rd WC, Fritzberg AR, Koep LJ, Ronai PM. A clinical comparison of 99mTc-diethyl-iminodiacetic acid, 99mTc-pyridoxylideneglutamate, and 131I-rose bengal in liver transplant patients. Radiology. 1979;130(2):435–41.
82. Scott-Smith W, Raftery AT, Wraight EP, Calne RY. Tc-99m labeled HIDA imaging in suspected biliary leaks after liver transplantation. Clin Nucl Med. 1983;8(10):478–9.
83. Salvo AF, Schiller A, Athanasoulis C, Galdabini J, McKusick KA. Hepatoadenoma and focal nodular hyperplasia: pitfalls in radiocolloid imaging. Radiology. 1977;125(2):451–5.
84. Spencer RP, Banever C. Growth of the human liver: a preliminary scan study. J Nucl Med. 1970;11(11): 660–2.
85. DeLand FH, North WA. Relationship between liver size and body size. Radiology. 1968;91(6):1195–8.
86. Markisz JA, Treves ST, Davis RT. Normal hepatic and splenic size in children: scintigraphic determination. Pediatr Radiol. 1987;17(4):273–6.
87. Treves S, Spencer RP. Liver and spleen scintigraphy in children. Semin Nucl Med. 1973;3(1):55–68.
88. Treves ST, Markisz JA. Liver. In: Treves ST, editor. Pediatric nuclear medicine. New York: Springer; 1985. p. 129–40.

Gastrointestinal Bleeding

11

S. Ted Treves and Michael Manfredi

Gastrointestinal (GI) bleeding is a life-threatening presentation that the physician must recognize and manage appropriately. The annual incidence rate of upper GI bleeding in adults in the USA is 100–200 cases per 100,000 [1]. The lower GI bleeding incidence rate in US adults is lower at 20.5–27 cases per 100,000 [2]. The incidence of GI bleeding in children is not well established in the general population. For upper GI bleeds most large, prospective studies have assessed the incidence in pediatric critical care settings. In one prospective study of 984 patients, upper GI bleeds occurred in 6.4 % of admissions [3, 4]. In a study of lower GI bleeding based on 40,000 admissions to a tertiary-care pediatric emergency department, lower GI bleeding was seen in 0.3 % of all admissions [5].

S.T. Treves, MD (✉)
Division of Nuclear Medicine
and Molecular Imaging, Department of Radiology,
Boston Children's Hospital,
Boston, MA, USA

Division of Nuclear Medicine and Molecular Imaging,
Department of Radiology, Brigham and Women's Hospital,
Boston, MA, USA

Joint Program in Nuclear Medicine,
Department of Radiology,
Harvard Medical School, Boston, MA, USA
e-mail: ted_treves@HMS.harvard.edu

M. Manfredi, MD
Gastrointestinal Procedure Unit,
Division of Gastroenterology, Hepatology and Nutrition,
Boston Children's Hospital, Boston, MA, USA

Etiology

In order to better identify, manage, and treat GI bleeding, it typically is classified as upper and lower GI bleeding. This is based on the origin of bleeding being either proximal or distal to the ligament of Treitz. With the improvement in endoscopic visualization of the small intestine with newer technologies such as capsule endoscopy and single- and double-balloon enteroscopy, some experts have proposed reclassifying GI bleeding into three categories (upper, mid-, and lower GI bleeding) [6]. This new classification of GI bleeding may be more useful in improving our understanding of the problem. In this classification, mid-GI bleeding is defined as bleeding that occurs between the ligament of Treitz and the ileocecal valve. Mid-GI bleeding is especially important in the case of obscure GI bleeding which accounts for approximately 5 % of all gastrointestinal hemorrhage [6].

The classic clinical symptom of upper GI bleeding (UGIB) is hematemesis which is emesis of bright red blood or coffee grounds. Other symptoms include melena, occult blood loss, and, in the case of severe UGIB, hematochezia [7]. Table 11.1 lists common causes of UGIB in pediatrics. The classic clinical symptoms of lower GI bleeding (LGIB) are hematochezia and bright red blood mixed or coating normal stool. LGIB can also be associated with melena and occult blood loss [8]. Table 11.2 lists common causes of LGIB in pediatrics. Mid-GI bleeding (MGIB) is most commonly associated with

S.T. Treves (ed.), *Pediatric Nuclear Medicine and Molecular Imaging*,
DOI 10.1007/978-1-4614-9551-2_11, © Springer Science+Business Media New York 2014

Table 11.1 Principal causes of lower gastrointestinal bleeding in relation to age

Newborn (birth–1 month)	Infant (1 month–2 years)	Preschool age (2–5 years)	School age (>5 years)
Necrotizing enterocolitis	Anal fissure	Anal fissure	Anal fissure
Malrotation with volvulus	Infectious colitis	Infectious colitis	Infectious colitis
Allergic proctocolitis	Allergic proctocolitis	Polyp	Polyp
Hirschsprung's disease enterocolitis	Intussusception	Meckel's diverticulum	Henoch–Schönlein purpura
Hemorrhagic disease of the newborn	Meckel's diverticulum	Henoch–Schönlein purpura	Inflammatory bowel disease
	Lymphonodular hyperplasia	Hemolytic uremic syndrome	
	Malrotation with volvulus	Lymphonodular hyperplasia	
	Hirschsprung's disease enterocolitis		
	Intestinal duplication		

Table 11.2 Etiologies of upper gastrointestinal bleeding in children by age group, in relative order of frequency

Newborn	Infant	Child–adolescent
Swallowed maternal blood	Stress gastritis or ulcer	Mallory–Weiss tear
Vitamin K deficiency	Acid–peptic disease	Acid–peptic disease
Stress gastritis or ulcer	Mallory–Weiss tear	Varices
Acid–peptic disease	Vascular anomaly	Caustic ingestion
Vascular anomaly	Gastrointestinal duplications	Vasculitis (Henoch–Schönlein purpura)
Coagulopathy	Gastric/esophageal varices	Crohn's disease
Milk-protein sensitivity	Duodenal/gastric webs	Bowel obstruction
	Bowel obstruction	Dieulafoy lesion, hemobilia

Table 11.3 Etiologies of mid-GI bleeding in both children and adults

Causes of bleeding in the small intestine	
Angioectasia or vascular anomaly	NSAID enteropathy
Small bowel tumors	Dieulafoy lesion
Crohn's disease	Ectopic varices
Celiac disease	Portal hypertension enteropathy
Meckel's diverticulum	Radiation enteritis

occult blood loss; however, melena and hematochezia can also occur. Please see Table 11.3 for common causes of MGIB.

Evaluation and Management

The initial evaluation of patients presenting with GI bleeding focuses on assessment of vital signs, history of present illness, focused medical history, physical examination, and lab testing. Interpreting all of the above factors allows for early diagnosis, aggressive intervention, and timely management. In cases of acute-onset hematochezia or melena, the placement of a nasogastric (NG) tube with aspiration of contents may help diagnose the origin of bleeding [9]. In addition, nasogastric aspiration with lavage may be used to quantify active bleeding. Initial management of patients largely focuses on fluid replacement. This is accomplished first with crystalloid infusion and then blood transfusions if necessary.

The indications for early endoscopy in bleeding children are not standardized, and no pediatric studies have directly compared the outcomes of early endoscopy versus supportive, medical management. In 1996 a position statement by the North American Society of Pediatric Gastroenterology, Hepatology, and Nutrition supported therapeutic endoscopy for management of gastrointestinal bleeding under the following circumstances: [10]

- Active, persistent, or recurrent bleeding unresponsive to medical therapy
- Hemodynamically significant hemorrhage
- Management of esophageal variceal bleeding during or after a first bleeding episode

- Evaluation of unexplained gastrointestinal bleeding
- Treatment of bleeding vascular anomalies, ulcers, or a post-polypectomy site

Upper endoscopy and colonoscopy has become the prime diagnostic and therapeutic tools for UGIB and LGIB. Endoscopy will accurately delineate the bleeding site and determine the specific cause [11]. Capsule endoscopy has become a first-line treatment in adults and children to diagnose obscure causes of GI bleeding in the small intestine [12, 13]. The limiting step in capsule endoscopy is the ability of the patient to swallow the capsule. However, the capsule can be placed endoscopically into the small intestine in younger children. In cases where endoscopy fails to make the diagnosis of GI bleeding and continued bleeding is suspected, then additional imaging is indicated. The one major exception to this strategy is when there is a high clinical suspicion for a Meckel's diverticulum. In this case, scintigraphy can precede endoscopy if the patient is clinically stable.

Meckel's Diverticulum

The first recorded observation of an ileal diverticulum has been attributed to Fabricius Hildamus in 1650 [14], and the first comprehensive embryologic and pathologic description of the lesion was made by Johann Friedrich Meckel, the younger, in 1809. Ileal (Meckel's) diverticulum is a noninherited congenital abnormality of the antimesenteric side of the small intestine, resulting from incomplete closure of the embryonic vitelline or omphalomesenteric duct. Meckel's diverticula may measure from 1 to 56 cm in length and 1 to 50 cm in diameter. Most Meckel's diverticula are found within the ileum approximately 90 cm proximal to the ileocecal valve [15].

A Meckel's diverticulum usually contains ileal mucosa but may contain gastric, duodenal, jejunal, colonic mucosa, or pancreatic tissue. Heterotopic tissue in a diverticulum of the pancreatic type was reported by Zonkel in 1861 and of the gastric type by Tillmans in 1882. The relationship of aberrant gastric mucosa to the ulcer of a diverticulum was considered by Deetz in 1907. Gastric mucosa is present in Meckel's diverticulum in approximately 50 % of cases [16, 17].

Meckel's diverticulum is the most common cause of lower gastrointestinal hemorrhage in previously healthy infants, and more than 50 % of infants with the remnant have symptoms before the second year of life [18]. Clinical symptoms occur in 25–30 % of all the patients. Estimates of the probable incidence of Meckel's diverticulum in the general population range from approximately 1 to 3 %, with a frequency three times greater in males than females [16]. The most common symptom of Meckel's diverticulum is gross rectal bleeding with or without associated abdominal complaints. The bleeding apparently results from mucosal ulceration in the diverticulum or adjacent ileum caused by hydrochloric acid secreted by the ectopic gastric mucosa. Nearly all diverticula of patients with symptoms of gastrointestinal bleeding contain ectopic gastric mucosa [16, 18–21]. Other pathologic conditions associated with Meckel's diverticulum include intestinal obstruction caused by bands, knots, volvulus, inflammation, or intussusception; regional enteritis; hernia; enterolith; calcification; diverticulitis; tuberculosis; and foreign body [18, 22].

Several years ago, we reviewed the records of all patients with Meckel's diverticulum less than 2 years of age undergoing surgery at Children's Hospital Boston between 1951 and 1972. Among 60 infants less than age 2, 32 had painless rectal bleeding. Of these 32, 56 % presented before 1 year of age and the remaining 44 % before age 2. Among those symptomatic patients, 91 % (29 of 32 patients) had ectopic gastric mucosa in their Meckel's diverticula [23]. The differential diagnosis of rectal bleeding in infants less than age 2 years includes Meckel's diverticulum, anal fissure, volvulus, intussusception, peptic ulcer, and colonic polyp. Of these disorders, only colonic polyp and Meckel's diverticulum usually cause painless bleeding.

Technetium-99m Pertechnetate (^{99m}Tc-O_4^-) Abdominal Scintigraphy

Technetium-99m pertechnetate abdominal scintigraphy was initially proposed by Harden and Alexander [24] in 1967 and was subsequently introduced into clinical practice by Jewett et al.

[25] in 1970. Since then, many reports have demonstrated the safety and effectiveness of this examination in the detection of functioning ectopic gastric mucosa in a Meckel's diverticulum, as well as other sites [26–33]. A comprehensive review of the topic has been written by Sfakianakis and Conway [31, 34]. Meckel's diverticulum cannot be diagnosed as simply and reliably by other imaging modalities [23, 35–37], and at present pertechnetate abdominal scintigraphy is the best nonoperative method of definite diagnosis of this condition. It is easy to perform, and the radiation exposure to the patient is equivalent to only 20 s of fluoroscopy [38].

Indications

Asymptomatic gross rectal bleeding (bright red stools) in a young child is a frequent indication for pertechnetate scintigraphy. A pediatric patient presenting with rectal bleeding suspected to be caused by ulceration of a Meckel's diverticulum requires a complete physical examination, which may include a careful examination of the anal area, rectoscopy, or sigmoidoscopy to exclude distal colonic disease and, when indicated, a hematologic examination to exclude a systemic bleeding disorder. Pertechnetate abdominal scintigraphy should then be performed.

Radiopharmaceutical

For the detection of Meckel's diverticulum, $^{99m}Tc\text{-}O_4^-$ is injected intravenously in a dose of 0.1 mCi (3.7 MBq)/kg of body weight [minimum dose 0.2 mCi (7.4 MBq), maximum dose 10 mCi (370 MBq)]. It should be obvious that abdominal scintigraphy ($^{99m}Tc\text{-}O_4^-$) does not detect a Meckel's diverticulum per se but reveals uptake of radiopertechnetate by functioning ectopic gastric mucosa in the diverticulum or elsewhere. To give a sense of the intensity of pertechnetate uptake in gastric mucosa, normally, approximately 25 % of the intravenously administered dose of $^{99m}Tc\text{-}O_4^-$ localizes in the wall of the stomach. The gastric uptake of pertechnetate is rapid and increases in intensity over time.

A number of authors have investigated the cellular localization of pertechnetate in the stomach. Keramidas et al. [39] found no significant differences in the concentration of pertechnetate in the body and antrum of the stomach in dogs. Using microautoradiography, Meier-Ruge and Fridrich [40] demonstrated that pertechnetate is selectively taken up by the parietal cells of the stomach, whereas ^{131}I as sodium iodide is absorbed and secreted by the gastric chief and mucosal cells [40, 41]. Wine et al. [41, 42], using Heidenhain pouches and denervated antral pouches in dogs, suggested that parietal cells are not essential for $^{99m}Tc\text{-}O_4^-$ concentration and that both acid output and volume output relate to the amount of $^{99m}Tc\text{-}O_4^-$ output. Priebe et al. [43], using contact autoradiographs of canine gastric mucosa, demonstrated that $^{99m}Tc\text{-}O_4^-$ concentrated in surface mucous cells of the gastric pits but not in the gastric glands. Using autoradiography, Berquist et al. [16] showed pertechnetate concentration in the superficial cells only. These authors also had six cases of histologically proven Barrett's esophagus, all with abnormal scintigraphy. Biopsy material revealed complete absence of parietal cells in all but one [44, 45]. In contrast, the gastric type of surface epithelial cells was present in every case. The pertechnetate anion is believed to be accumulated selectively by surface cells of gastric mucosa and then secreted into the bowel lumen [46–49]. Approximately 20 % of the injected dose of $^{99m}Tc\text{-}O_4^-$ is rapidly eliminated by the kidneys. Organs that also normally concentrate radiopertechnetate include the choroid plexus, the thyroid, and the salivary glands [50–53]. The blood disappearance rate of $^{99m}Tc\text{-}O_4^-$ may be prolonged in infants because of renal immaturity, a normally low gastric mucosal uptake, or both. Slow blood disappearance and low gastric uptake of pertechnetate in older children with normal renal function may be caused by hormonal, vascular, or stress-related factors.

A variety of drugs and hormones affect the gastric uptake of pertechnetate. Perchlorate suppresses uptake of pertechnetate by the gastric mucosa two- to fourfold [41, 54–57]. Although administration of perchlorate has not been known to result in failure to identify a Meckel's diverticulum, this is theoretically possible. Consequently, premedication with perchlorate in patients undergoing radiopertechnetate abdominal scintigraphy is not recommended. Pentagastrin increases

gastric mucosal uptake of pertechnetate, and it has been used to enhance imaging on patients and animals [54, 58–61]. Cimetidine, a histamine H_2-receptor antagonist, inhibits release of pertechnetate by the intraluminal cells [62–64]. Glucagon slightly reduces gastric activity of pertechnetate and suppresses peristaltic activity [65]. Other agents that have been investigated include histamine, which has a lesser effect than pentagastrin and secretin. Secretin has little effect on pertechnetate localization [43, 54].

Imaging

As mentioned above, the patient should not be premedicated with perchlorate. Barium in the abdomen can cause false-negative results, so one must ensure that scintigraphy is performed in the absence of barium in the abdomen. All metallic and other radiation-absorbing objects (belt buckles, coins, etc.) must be removed from the patient prior to imaging. The patient should fast for approximately 4 h before the examination to reduce the size of the gastric silhouette. When available, we routinely use subcutaneous pentagastrin (6 μg/kg) a half hour prior to the administration of pertechnetate to increase its uptake by the gastric mucosa. During imaging, the patient lies supine with the gamma camera viewing the entire abdomen. A high-resolution or ultrahigh-resolution parallel-hole collimator should be used. First, a radionuclide angiogram (1- to 5-s frames for 60 s, 128 × 128 matrix format) is obtained to diagnose vascular malformations and attempt to localize a site of rapid bleeding. Second, a series of 1-min images is obtained in the anterior projection for 30 min (Figs. 11.1, 11.2, 11.3, 11.4, and 11.5). The study should be monitored on the display as it progresses. In cases of strong clinical suspicion, prolonged imaging (images at 1 and/or 2 h postinjection) may be necessary if the study appears normal.

A lateral image is helpful in determining the anterior position of uptake in a Meckel's diverticulum and to exclude uptake in the genitourinary system. This image should be obtained as

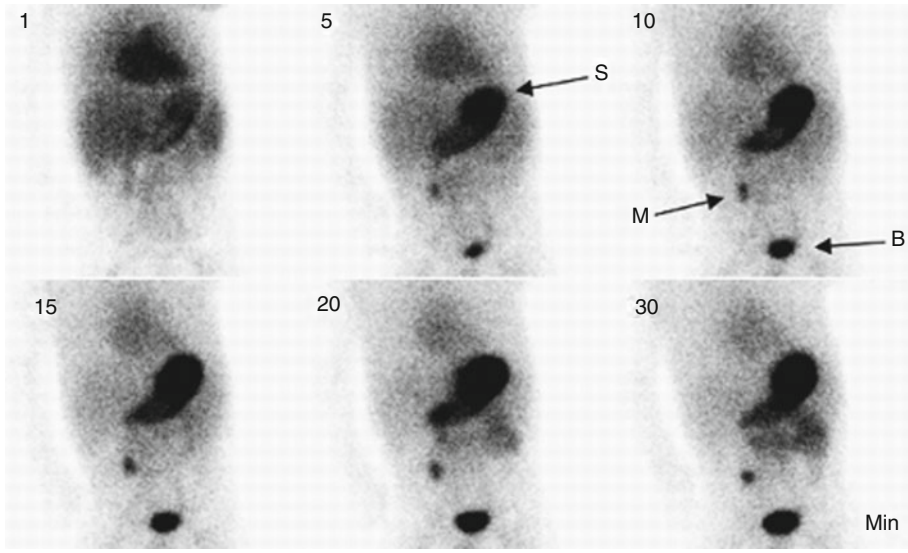

Fig. 11.1 Meckel's diverticulum. Study from a 21-month-old boy with a recent history of abdominal cramps and large blood clots in the stool 5 days prior to this examination. The patient had an air enema and a barium enema, which were both negative. Selected anterior images taken at 5-min intervals are shown. In the first image, tracer is seen in the cardiac blood pool, liver, spleen, stomach, and in the vascular and extravascular compartment. Sequential images reveal increasing concentration of tracer in the stomach (*S*) and decreasing blood pool and background activity. Beginning on the second image, there is a small, intense, and well-defined region (*M*) in the right lower quadrant that concentrates pertechnetate. This area reveals gradual increase of tracer uptake with time that is characteristic of ectopic gastric mucosa in a Meckel's diverticulum. Note tracer accumulating in the bladder (*B*) and in the small bowel. A Meckel's diverticulum containing gastric mucosa was removed at surgery

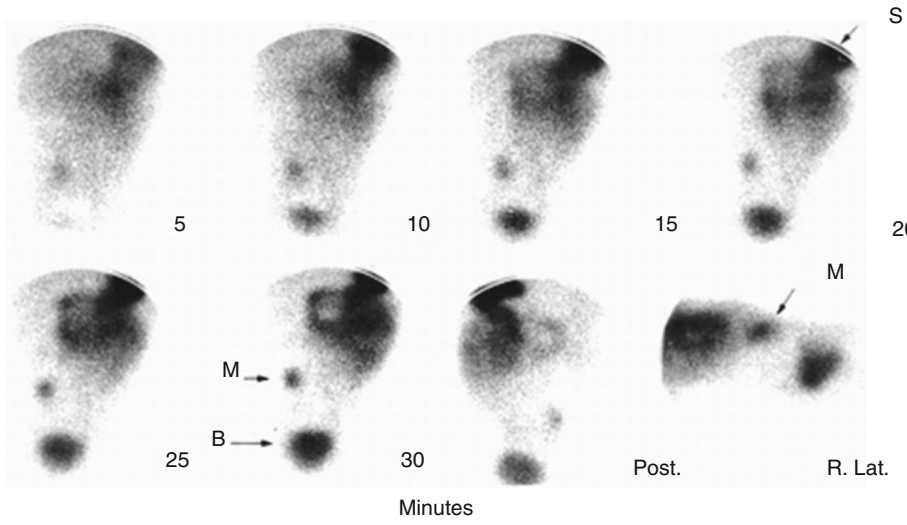

Fig. 11.2 Meckel's diverticulum. Study from a 4-year-old boy who presented with lower abdominal cramps and guaiac-positive stools. A barium enema demonstrated no evidence of intussusception or polyp. An abnormal accumulation of pertechnetate can be seen in the right lower quadrant (*M*) that appears at the same time as the gastric activity (*S*) and increases in intensity with time. The urinary bladder (*B*) is visible at 10 min and increased in intensity during the observation period. A cross-table image reveals the abnormal tracer accumulation to be located anteriorly in the abdomen. At surgery, a Meckel's diverticulum containing gastric mucosa was removed. *Post* Posterior, *R Lat* Right Lateral

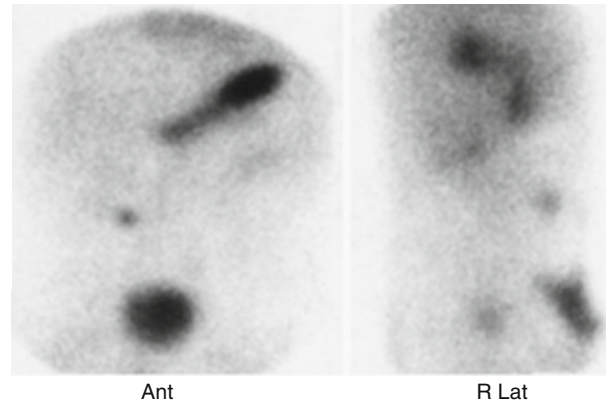

Fig. 11.3 Meckel's diverticulum. This 2-year-old boy presented with a 3-month history of bloody stools. Selected images at 10 (*Ant.*) and 15 (*R. Lat.*) minutes postinjection reveal a small, well-localized area of increased pertechnetate uptake in the right lower quadrant anteriorly

soon as a suspicious area of increased activity is visualized on the anterior view to avoid the possibility of being unable to define the abnormal uptake in three dimensions at a later time, because of the possibility of overlap with radiopertechnetate within the intestine. Laterals or posterior images should be obtained at any time after the injection to help localize abnormal tracer uptake. This may confuse untrained observers, especially if the left renal pelvis is obscured by the gastric outline, as it often is. Similarly, tracer in the right renal pelvis should be recognized. Later images, hydration, moving the patient to the upright position to help empty the renal pelvis, posterior and lateral images, and diuretic administration are often helpful maneuvers to help identify potentially confusing concentration of the tracer. Some Meckel's diverticula lie very close to the urinary bladder, preventing detection. Obtaining images with an empty bladder or even after bladder catheterization should be considered part of the routine practice. Single- photon emission computed tomography (SPECT) has been used to help identify tracer uptake in Meckel's diverticulum

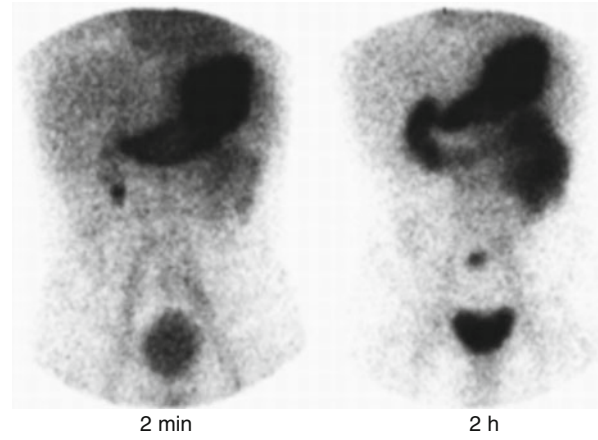

Fig. 11.4 Meckel's diverticulum. Two selected images from a 2.5-year-old boy with a history of rectal bleeding. The image at 2 min did not reveal a clear abnormality. Tracer in the right upper quadrant could have been the duodenum or a highly placed Meckel's diverticulum. The image at 2 h postinjection reveals a well-defined and focal region of increased pertechnetate concentration that suggests a Meckel's diverticulum containing gastric mucosa

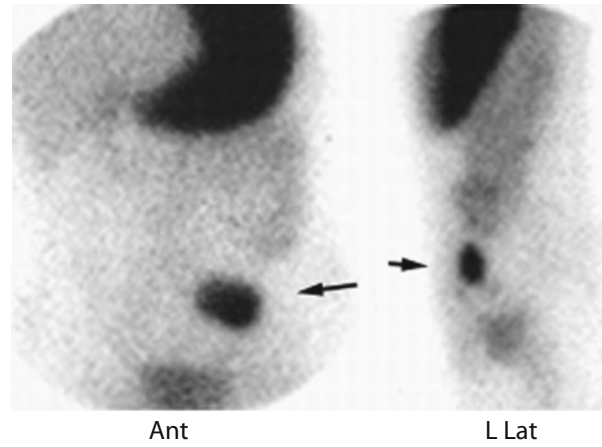

Fig. 11.5 Meckel's diverticulum, left lower quadrant. Selected anterior (*Ant*.) and left lateral (*L. Lat*.) pertechnetate images revealing a rather large and well-defined area of intense pertechnetate concentration in the left lower quadrant anteriorly

obscured by the bladder. Upright anterior and oblique images may assist in differentiating duodenal activity, which will not change position, from ectopic gastric mucosa, which may move more in response to the altered direction of gravitational pull [31, 34, 66].

Background activity in the abdomen reflecting blood levels of pertechnetate usually decreases with time and in most cases allows for identification of ectopic gastric mucosa within 30 min after injection of pertechnetate. If blood disappearance and gastric uptake of the tracer are slow, as in infants or anemic patients, the scanning time should be prolonged in order to increase the chance for identification of a lesion not visible early in the study.

Prior Bleeding Study

Yen and Lanoie [67] warned that a pertechnetate study should not be performed after a bleeding study with in vivo-labeled red blood cells using ^{99m}Tc and stannous pyrophosphate. These authors reported a case showing blood pool distribution of pertechnetate with absent gastric uptake in a 1-week-old patient who had a recent bleeding study with in vivo stannous pyrophosphate. The scan was considered uninterpretable.

However, Kwok et al. [68] reported a successful Meckel's scan done 26 h after a labeled RBC study using a commercial in vitro labeling kit, UltraTag (Mallinckrodt Medical, Inc., St. Louis, MO). Normal distribution of ^{99m}Tc was observed. This case demonstrates that it is feasible to perform an in vitro-labeled RBC study and to follow up with a Meckel's scan if necessary. However, the reverse sequence is preferred.

In the in vivo labeling method, the amount of stannous ion in the pyrophosphate kit injected into the patient is quite large (0.4–0.9 mg). If

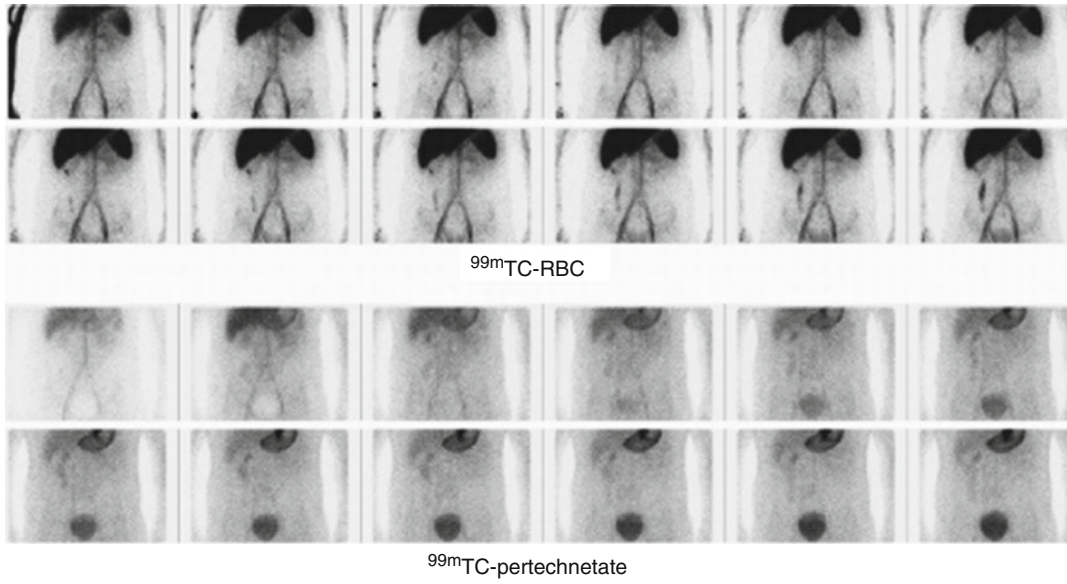

Fig. 11.6 Pertechnetate scan following ^{99m}Tc-red blood cell (RBC) study for the detection of bleeding using an in vitro labeling technique. A 15-year-old boy presented with rectal bleeding. A blood pool scan using an in vitro technique demonstrates gastrointestinal bleeding along the ascending colon (*upper panel*). A pertechnetate scan performed a day later reveals normal distribution of the tracer (*lower panel*)

pertechnetate is injected afterward, it will be rapidly and efficiently attached to the red blood cells and render a blood pool scan. This effect may last for days. In contrast, the in vitro kit has a very small amount of tin (50–96 μg of tin), and this factor may explain the differences reported.

In our practice, we have confirmed that a pertechnetate scan can be performed effectively following a bleeding study using the commercially available kit for in vitro RBC labeling. The pertechnetate biodistribution appears to not be affected by the prior blood pool study (Fig. 11.6).

Clinical Applications

Normal Pertechnetate Abdominal Scintigraphy

A normal ^{99m}Tc-O_4^- abdominal series reveals rapid gastric uptake followed by a gradual increase of tracer in the wall of the stomach. Some pertechnetate is eliminated into the gastric cavity and transported into the lumen of the duodenum and small intestine. The speed of this transit is variable. In some patients with rapid gastric emptying, tracer in the duodenum and intestine could interfere with interpretation, but this is rare. The intense gastric outline usually shows a central area of relatively lower concentration of pertechnetate corresponding to the gastric cavity. This area of decreased uptake can be quite large if the patient has eaten before the examination. The bladder (if full) initially contains less tracer activity than background. As radiopertechnetate is eliminated by the kidneys, progressively increasing levels of tracer are evident in the bladder.

Meckel's Diverticulum

A scintigraphic abdominal survey revealing ectopic gastric mucosa is almost unmistakable; in addition to the normal uptake pattern, one can observe a well-defined area of increased radiopertechnetate uptake anteriorly, usually in the right lower quadrant. This abnormal uptake of tracer in the ectopic gastric mucosa appears at the same time as the stomach and persists with increasing intensity as the study progresses (Figs. 11.1, 11.2, 11.3, 11.4, and 11.5).

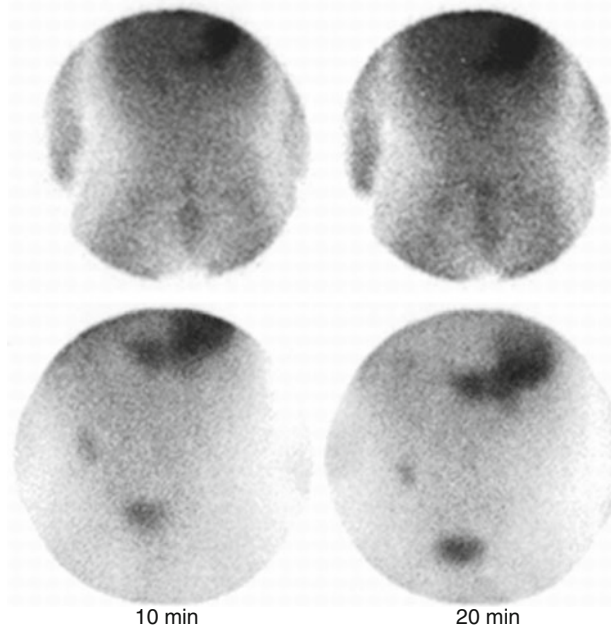

Fig. 11.7 Meckel's diverticulum, use of pentagastrin. Selected images at 10 and 20 min of two consecutive pertechnetate studies on the same patient. The study in the *upper panel* reveals no abnormality. The study following administration of pentagastrin reveals a clearly defined abnormality of pertechnetate uptake in the right lower quadrant corresponding to Meckel's diverticulum containing gastric mucosa (*lower panel*)

Rarely, tracer activity in the lesion may fluctuate if intestinal secretions or hemorrhage carries the radiotracer away from the diverticulum [31]. Observation for 30 min after injection of the radiopertechnetate is usually sufficient to detect most cases of Meckel's diverticulum containing functioning gastric mucosa.

In questionable cases or cases in which the gastric uptake or the gastric-to-background ratio is low, one should delay the imaging by 1 h or longer. A potential problem with delayed images is migration of radioactive gastric contents into the duodenum, small bowel, and even large bowel, obscuring uptake within the ectopic gastric mucosa. An alternative is to restudy the patient on another day using pentagastrin (Fig. 11.7).

A Meckel's diverticulum may appear to shift in position caudally if the patient is raised or has voided. Only rarely does more than one area of ectopic gastric mucosa occur in the intestine or does the ectopic mucosa extend beyond the diverticulum, producing a larger area of uptake [34, 45].

Abnormal Uptake Due to Other Causes

Other conditions in the abdomen that accumulate pertechnetate include intestinal obstruction or intussusception [69], inflammation [69–71], vascular malformations [72], ulcers [70], some tumors [73, 74], and various urinary tract abnormalities that interrupt urinary excretion of the pertechnetate. Certain drugs, such as ethosuximide (Zarontin) or laxatives, may also cause variable uptake of tracer in the intestine. The nature of these findings should be recognized during evaluation of the images and such findings not be considered falsely positive. They are true abnormalities in the distribution of radiopertechnetate in the abdomen, and experienced physicians will recognize their appearance as different from that of Meckel's diverticulum.

Blood pool tracer activity, as in vascular malformations or hemangiomas, should be apparent on the radionuclide angiogram and initial images and may or may not fade with time [31, 34]. However, these lesions do not exhibit a response to pentagastrin.

Other abnormalities that may contain ectopic gastric mucosa include otherwise normal bowel [45], enteric duplication [70, 75], duplication cysts [70, 76, 77], and gastrogenic cysts [78]. As in Meckel's diverticulum, the complications and symptoms in these conditions are due to hydrochloric acid secretion by the gastric mucosal cells, and the treatment is surgical excision.

In Barrett's esophagus, the esophageal mucosa may be lined with gastric epithelium rather than normal squamous epithelium and it takes up pertechnetate, yielding scans with uptake above the stomach [79]. Gastric mucosa that has been moved surgically to an ectopic site in the body will also take up pertechnetate (Fig. 11.8).

Accuracy

Among the surgically proven cases of Meckel's diverticulum in the literature, the accuracy of ^{99m}Tc-O_4^- scintigraphy is 90 %. The overall sensitivity among published accounts is 85 %, and the specificity is 95 % [34]. With meticulous attention to technique and in the appropriate clinical setting, pertechnetate scintigraphy is an effective method for the detection of Meckel's diverticulum containing functioning gastric mucosa. Prior to use of pertechnetate scintigraphy for Meckel's diverticulum, the lesion was diagnosed at laparotomy in approximately 60 % of the symptomatic patients [80, 81].

A normal pertechnetate study does not rule out the presence of a Meckel's diverticulum, however, as ectopic gastric mucosa must be functioning in order to take up pertechnetate. Hypofunction, necrosis, fibrosis, ischemia, or other causes can reduce or even prevent scintigraphic detection [42, 54]. Low pertechnetate uptake by gastric mucosa in infants may be a cause of false-negative examinations. As the child matures, normal ^{99m}Tc-O_4^- uptake should allow detection of ectopic gastric mucosa. Drug effects and normal structures may obscure ^{99m}Tc-O_4^- uptake by the gastric mucosa in the diverticulum. Because peptic ulceration of the intestinal mucosa is usually responsible for the bleeding, most of the Meckel's diverticula that bleed contain ectopic gastric mucosa. Experiments on animals show that at least 1–2 cm^2 of such tissue may be required for the lesion to be visible on scintigraphy [34, 43, 82, 83]. One reported patient whose scan was negative had considerable scarring of the diverticulum and little intact gastric mucosa [45]. In one of our patients, the pertechnetate survey was normal in the presence of a cystic Meckel's diverticulum with fluid within the cyst and necrotic gastric mucosa.

Technetium-99m-RBC Scintigraphy

Diagnosis of gastrointestinal bleeding from any cause (including bleeding from a Meckel's diverticulum) can be detected and often localized using ^{99m}Tc-labeled RBC scintigraphy. Following intravenous injection, this radiopharmaceutical remains largely within the blood pool and can be visualized with scintigraphy. Because of their long residence time in the blood pool, ^{99m}Tc-RBCs allow the possibility of localizing intermittent bleeding, as the observation period can be extended for several hours. Bleeding rates detected with ^{99m}Tc-RBC are lower than those detectable by angiography. The

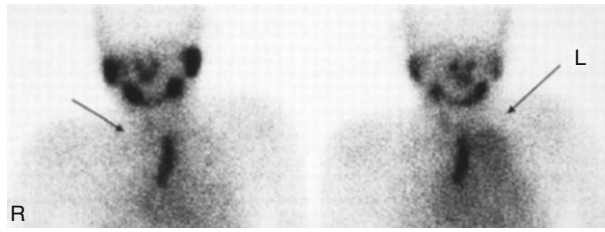

Fig. 11.8 Gastric mucosal remnant in the mediastinum. These unusual pertechnetate images are from a 12-year-old boy who swallowed caustic material at 2 years of age, damaging his esophagus. He had an esophagectomy and a gastric pull-through at that age. More recently, he underwent a colonic interposition, complicated by mediastinal fluid collection that eventually drained through the neck causing severe local pain. In addition, there was fluid collection in the left chest. The patient had multiple imaging examinations in an attempt to elucidate the problem, without much success. The image obtained at 5 min following intravenous administration of pertechnetate reveals exquisite tracer uptake in the region of the mediastinum (*left panel*, *arrow*). This was a residual gastric remnant from the surgery to place the colonic interposition. The image on the right panel reveals, in addition, tracer in the left hemithorax, due to gastric secretion from the remnant. The gastric remnant was removed surgically

bleeding rates detectable with ^{99m}Tc-RBC are 0.4 mL/min in areas of high background and 0.1 mL/min in areas of low background [84]. The sensitivity of this technique, however, depends not only on bleeding rate but also on bowel motility [85]. Another approach to the detection of bleeding employs ^{99m}Tc–sulfur colloid. The advantages of ^{99m}Tc-RBC over ^{99m}Tc–sulfur colloid have been recognized [86].

Radiopharmaceutical

Red blood cells can be labeled with ^{99m}Tc using an in vivo or an in vitro method. We routinely employ the in vitro method, in which 1–3 mL of the patient's blood is drawn and anticoagulated with heparin or acid-citrate dextrose (ACD). Ethylenediaminetetraacetic acid (EDTA) or oxalate must not be used as an anticoagulant. The red blood cells are labeled using a commercial preparation (Ultratag®RBC, Mallinckrodt, St. Louis, Mo.). Technetium-99m-labeled RBCs are given in a dose of 0.2 mCi (7.4 MBq)/kg of body weight with a minimum dose of 1.0 mCi (37 MBq) and a maximum dose of 20 mCi (740 MBq). *The labeled red blood cells are reinjected slowly into the patient and only the patient from whom the blood was drawn.*

Imaging

For this method to be most effective, it must be performed while the patient is actually bleeding. Barium within the abdomen as well as photon-absorbing objects on the patient can cause false-negative results, and their presence should be avoided. The patient is positioned supine with the gamma camera equipped with a high-resolution collimator viewing the entire abdomen. The tracer is injected, and a radionuclide angiogram is obtained at a rate of one frame per second for 60 s (128×128 matrix). The angiogram is immediately followed by serial imaging of the abdomen at one frame per minute for 60–90 min (128×128 matrix). Additional images are obtained at various intervals as needed, up to approximately 24 h. The radionuclide angiogram and the following serial imaging should be evaluated using a cinematic mode. This is more effective than reviewing a series of static images.

Clinical Application

A normal ^{99m}Tc-RBC study will demonstrate tracer within the blood pools of the aorta, inferior vena cava, and other vessels (iliac, portal, mesenteric, renal). Tracer activity can also be seen in the blood pool of the kidneys and penile blood pool. If present in sufficient amount, free pertechnetate can be seen in the kidneys, ureters, and urinary bladder. The observer should be aware of these normal scintigraphic features and not confuse them with bleeding (Fig. 11.9). None of the areas mentioned above changes in location with time, while abnormal tracer concentration associated with bleeding usually shows changes in location.

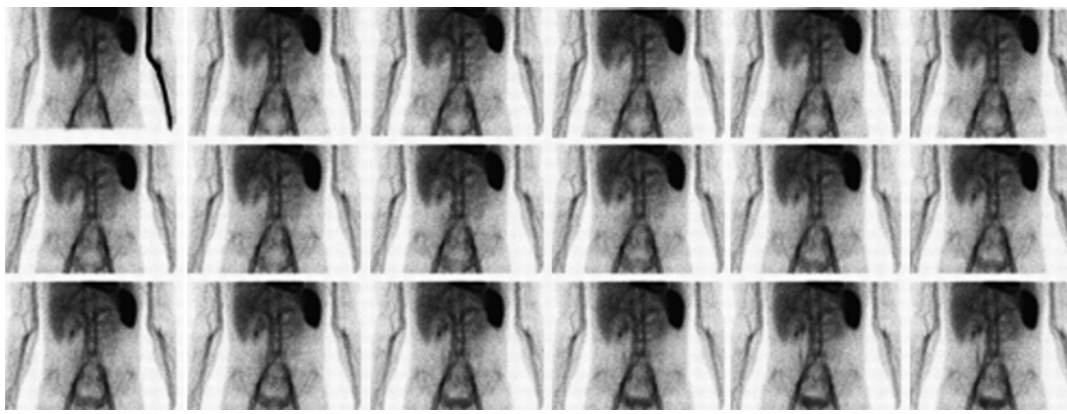

Fig. 11.9 Normal ^{99m}Tc-RBC blood pool scan. The study reveals no evidence of gastrointestinal bleeding. The patient had hemophilia; the spleen is visualized

Bleeding sites are detected by a focal intraluminal accumulation of the radiotracer with a characteristic pattern of increasing tracer in bowel. Blood entering the bowel causes altered motility, and blood may be seen moving forward and backward in the intestine [87, 88]. Even massive bleeding can be intermittent. Sometimes bleeding occurs after the initial hour of continuous observation and can only be detected on delayed images. Bleeding in these cases may have occurred during the interval while the patient was not being imaged. If bleeding is detected on delayed imaging and the clinical impression is of active bleeding, a second tracer injection may be of value [89]. Administration of heparin has been suggested as a method of enhancing detection of bleeding sites [90, 91]. Reported correct localization of bleeding sites varies from 40 to 90 % [92–96]. In most cases, surgery should not be based on scintigraphic appearance alone. There is a need for randomized studies comparing scintigraphy and angiography performed within close proximity of each other [97]. Examples of gastrointestinal bleeding detected with radiolabeled RBCs are illustrated in Figs. 11.10, 11.11, 11.12, 11.13, and 11.14.

Indium-111-RBC scintigraphy has also been proposed for the detection of gastrointestinal bleeding [98]. The potential advantage of

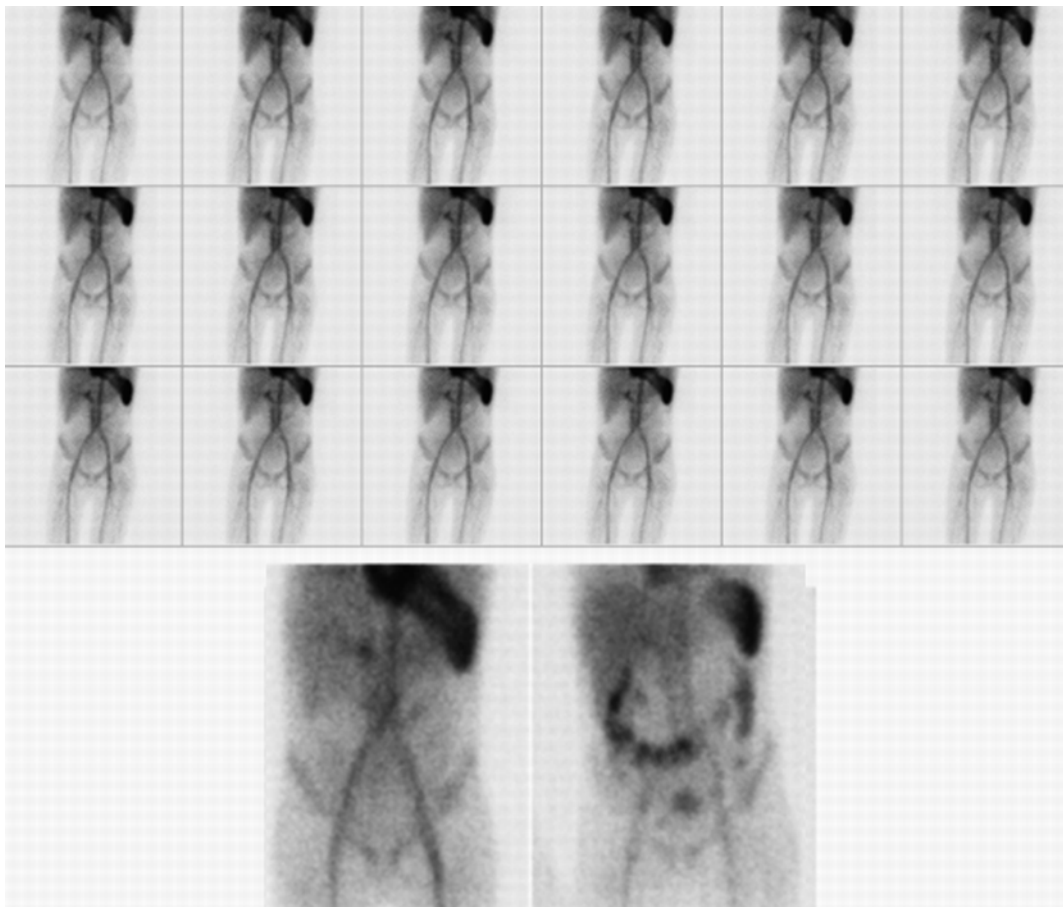

Fig. 11.10 A 10-year-old with rectal bleeding. Compressed display of initial 60-min recording (*upper panel*) reveals no evidence of bleeding. An image at 1.5 h (*lower left*) doesn't show bleeding. Bleeding into the large bowel is visible; the actual site of bleeding could not be pinpointed, however

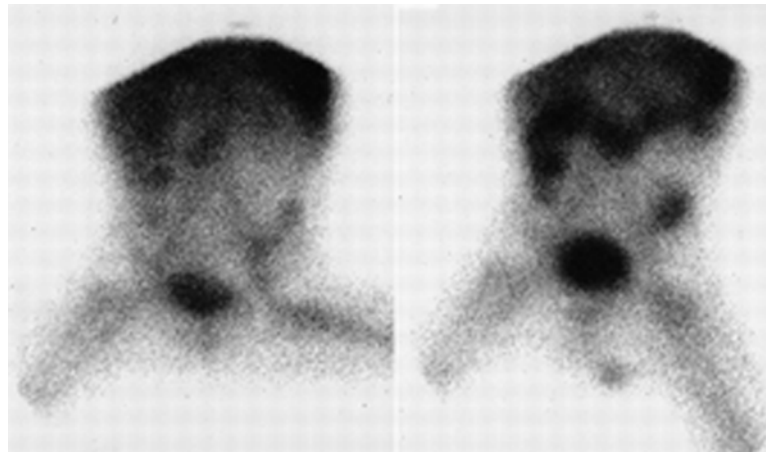

Fig. 11.11 Massive lower gastrointestinal bleeding. Technetium-99m-RBC scintigraphy from an 18-month-old boy with acute leukemia on treatment presenting with a falling hematocrit and increasingly severe gastrointestinal bleeding. The sequential anterior images reveal abnormal tracer accumulation first at the level of the epigastrium followed by tracer migrating into both the proximal and distal colon. The bleeding was thought to be secondary to chemotherapy-induced enterocolitis. The patient underwent surgery for the removal of part of his colon. At surgery, a swollen colon with marked inflammation with multiple deep linear mucosal ulcerations was noted

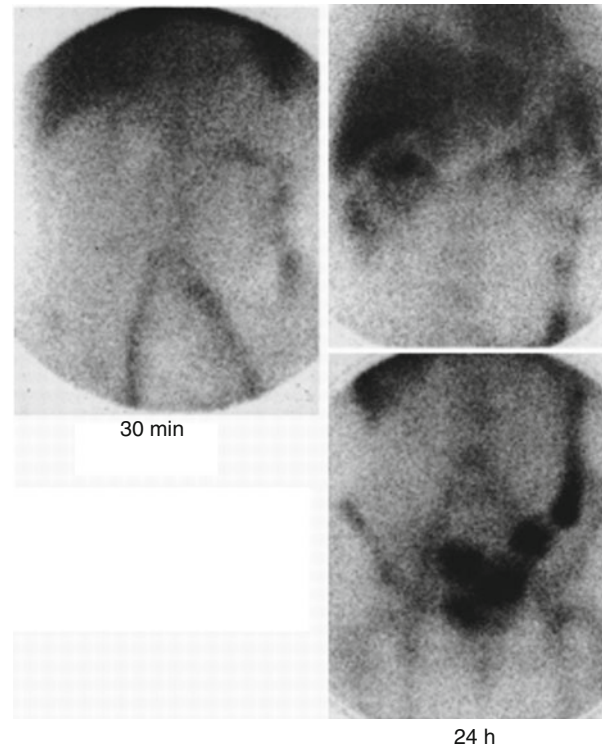

Fig. 11.12 Massive gastrointestinal bleeding. Technetium-99m-RBC scintigraphy from a teenage girl with uncontrollable gastrointestinal bleeding for several years. The image on the *left* (30 min postinjection) reveals bleeding in a portion of the small bowel. Images 24 h later (*right panel*) reveal tracer within the entire course of the colon. The patient had a small bowel resection in which a cluster of veins was found

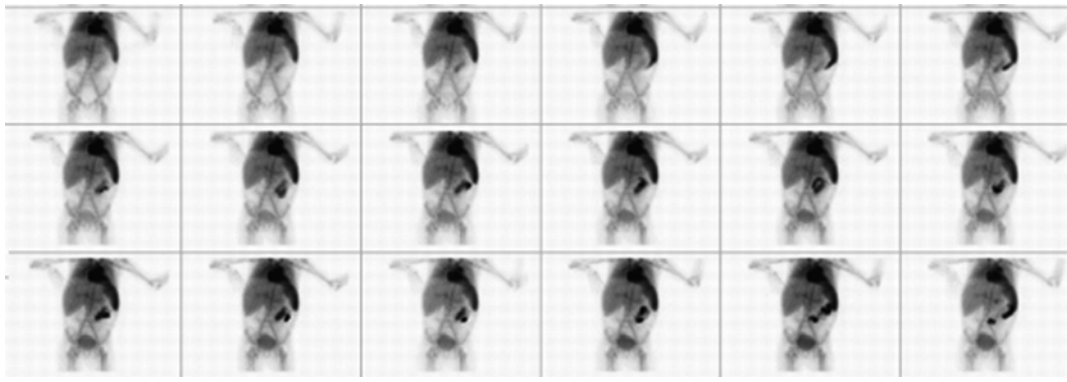

Fig. 11.13 A ^{99m}Tc-RBC scan from a 6-year-old girl with leukemia and melena. There is rapid accumulation of RBCs in the spleen, and tracer appears in the small bowel in the left upper quadrant near the midline

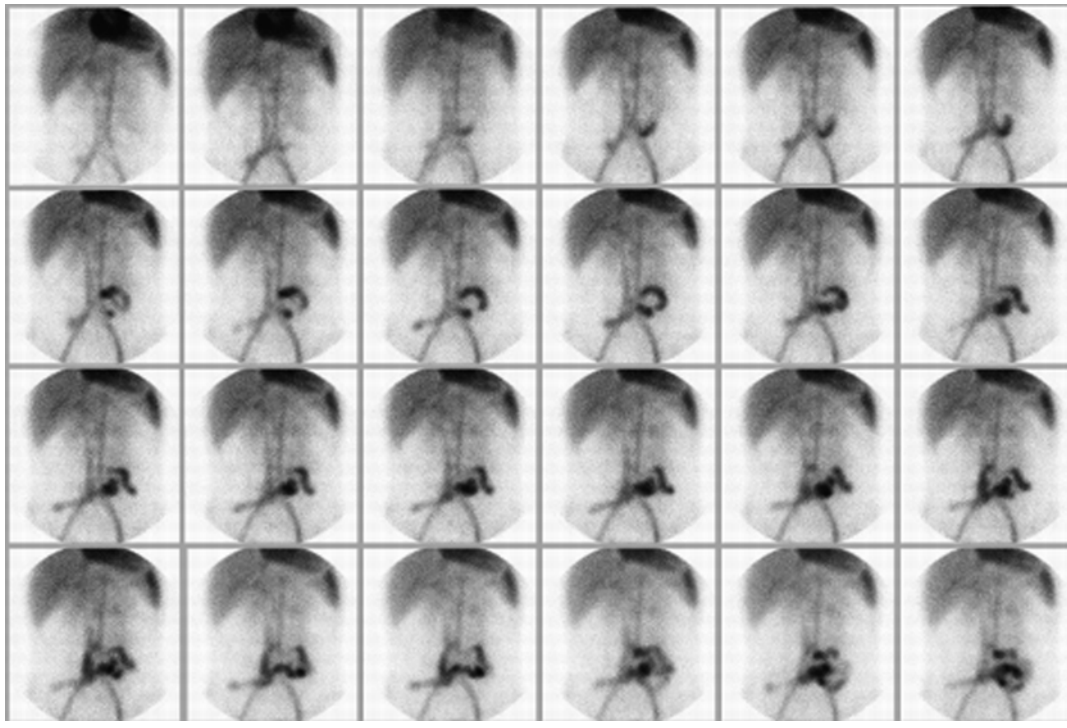

Fig. 11.14 A ^{99m}Tc-RBC scan from a 16-year-old with severe pulmonary hypertension and a hypercoagulable state treated with anticoagulants. The patient presented with a second episode of massive gastrointestinal bleeding with a hematocrit decrease from 42 to 26 during 1 day. Bleeding is detected in the small bowel in the left lower quadrant

this method is that it permits evaluation beyond 24 h. The disadvantages are the relatively lower photon flux of ^{111}In than of ^{99m}Tc and the relatively high radiation exposure for the patient.

Technetium-99m-Sulfur Colloid Scintigraphy

Another scintigraphic method to localize bleeding employs ^{99m}Tc–sulfur colloid. After intrave-

nous injection, ^{99m}Tc–sulfur colloid is extracted rapidly from the blood by cells of the reticuloendothelial system with a normal half-time in blood of 2.5–3.5 min.

The patient is examined supine with the gamma camera, which is equipped with a high-resolution collimator viewing the entire abdomen. Technetium-99m–sulfur colloid is given in a dose of 0.05 mCi/kg (1.85 MBq/kg) with a minimum total dose of 0.1 mCi (3.7 MBq) and a maximum total dose of 3.0 mCi (111 MBq). The study is recorded at 1 frame per minute for 30 min on a 128 × 128 matrix format.

If bleeding occurs during the tracer's presence in the blood pool, it extravasates, and this can be detected scintigraphically. Because of the high bleeding-to-background activity ratio achievable with this tracer, small amounts of bleeding may be detected. In the gastrointestinal tract, this technique has detected bleeding at rates as low as 0.05–0.1 mL/min [99–101]. Bleeding rates of 0.1–0.2 mL/min have been detected in dogs [102]. In patients who have intermittent bleeding, the "window of opportunity" for the detection of bleeding with colloid is very small. Another disadvantage of this method is the intense accumulation of sulfur colloid in the liver and spleen, which may obscure bleeding in this region.

References

1. Longstreth GF. Epidemiology of hospitalization for acute upper gastrointestinal hemorrhage: a population-based study. Am J Gastroenterol. 1995;90(2):206–10.
2. Longstreth GF. Epidemiology and outcome of patients hospitalized with acute lower gastrointestinal hemorrhage: a population-based study. Am J Gastroenterol. 1997;92(3):419–24.
3. Lacroix J, Nadeau D, Laberge S, Gauthier M, Lapierre G, Farrell CA. Frequency of upper gastrointestinal bleeding in a pediatric intensive care unit. Crit Care Med. 1992;20(1):35–42.
4. Lopez-Herce J, Dorao P, Elola P, Delgado MA, Ruza F, Madero R. Frequency and prophylaxis of upper gastrointestinal hemorrhage in critically ill children: a prospective study comparing the efficacy of almagate, ranitidine, and sucralfate. The Gastrointestinal Hemorrhage Study Group. Crit Care Med. 1992;20(8):1082–9.
5. Teach SJ, Fleisher GR. Rectal bleeding in the pediatric emergency department. Ann Emerg Med. 1994; 23(6):1252–8.
6. Raju GS, Gerson L, Das A, Lewis B. American Gastroenterological Association (AGA) Institute technical review on obscure gastrointestinal bleeding. Gastroenterology. 2007;133(5):1697–717.
7. Chawla S, Seth D, Mahajan P, Kamat D. Upper gastrointestinal bleeding in children. Clin Pediatr (Phila). 2007;46(1):16–21.
8. Leung AK, Wong AL. Lower gastrointestinal bleeding in children. Pediatr Emerg Care. 2002;18(4):319–23.
9. Kay MH, Wyllie R. Therapeutic endoscopy for nonvariceal gastrointestinal bleeding. J Pediatr Gastroenterol Nutr. 2007;45(2):157–71.
10. Squires Jr RH, Colletti RB. Indications for pediatric gastrointestinal endoscopy: a medical position statement of the North American Society for Pediatric Gastroenterology and Nutrition. J Pediatr Gastroenterol Nutr. 1996;23(2):107–10.
11. Cappell MS, Friedel D. Acute nonvariceal upper gastrointestinal bleeding: endoscopic diagnosis and therapy. Med Clin North Am. 2008;92(3):511–50, vii–viii.
12. Cohen SA, Klevens AI. Use of capsule endoscopy in diagnosis and management of pediatric patients, based on meta-analysis. Clin Gastroenterol Hepatol. 2011;9(6):490–6.
13. Liu K, Kaffes AJ. Review article: the diagnosis and investigation of obscure gastrointestinal bleeding. Aliment Pharmacol Ther. 2011;34(4):416–23.
14. Neff G. Sas Meckelsche Divertikel. Ergeb Chir Orthop. 1937;30:227–315.
15. DeBartolo Jr HM, van Heerden JA. Meckel's diverticulum. Ann Surg. 1976;183(1):30–3.
16. Berquist TH, Nolan NG, Carlson HC, Stephens DH. Diagnosis of Barrett's esophagus by pertechnetate scintigraphy. Mayo Clin Proc. 1973;48(4):276–9.
17. Rosenthall L, Henry JN, Murphy DA, Freeman LM. Radiopertechnetate imaging of the Meckel's diverticulum. Radiology. 1972;105(2):371–3.
18. Rutherford RB, Akers DR. Meckel's diverticulum: a review of 148 pediatric patients, with special reference to the pattern of bleeding and to mesodiverticular vascular bands. Surgery. 1966;59(4):618–26.
19. Kilpatrick JM. Scanning in diagnosis of Meckel's diverticulum. Hosp Pract. 1974;9:131–8.
20. Kilpatrick ZM, Aseron Jr CA. Radioisotope detection of Meckel's diverticulum causing acute rectal hemorrhage. N Engl J Med. 1972;287(13):653–4.
21. Martin GI, Kutner FR, Moser L. Diagnosis of Meckel's diverticulum by radioisotope scanning. Pediatrics. 1976;57(1):11–2.
22. Canty T, Meguid MM, Eraklis AJ. Perforation of Meckel's diverticulum scan (letter to the editor). Surgery. 1972;71:313.
23. Meguid MM, Wilkinson RH, Canty T, Eraklis AJ, Treves S. Futility of barium sulfate in diagnosis of bleeding meckel diverticulum. Arch Surg. 1974; 108(3):361–2.

24. Harden R, Alexander WD. Isotope uptake and scanning of stomach in man with 99mTc-pertechnetate. Lancet. 1967;1(7503):1305–7.
25. Jewett Jr TC, Duszynski DO, Allen JE. The visualization of Meckel's diverticulum with 99mTc-pertechnetate. Surgery. 1970;68(3):567–70.
26. Bauer R, van de Flierdt E, Schroter G. Holscher M [Scintigraphic detection of gastrointestinal hemorrhage and ectopic mucosa]. Z Gastroenterol Verh. 1991;26:117–24.
27. Datz FL, Christian PE, Hutson WR, Moore JG, Morton KA. Physiological and pharmacological interventions in radionuclide imaging of the tubular gastrointestinal tract. Semin Nucl Med. 1991;21(2): 140–52.
28. Giorgetti R, Dottorini M, Cazzani M, Giorgetti V. [Meckel's diverticulum: the usefulness of 99m Tc pertechnetate scintigraphy]. Minerva Pediatr. 1990; 42(9):349–50.
29. Joseph K. [Nuclear medicine methods for the detection of gastrointestinal hemorrhages]. Dtsch Med Wochenschr. 1993;118(4):109–12.
30. Sfakianakis GN, Conway JJ. Detection of ectopic gastric mucosa in Meckel's diverticulum and in other aberrations by scintigraphy: I. Pathophysiology and 10-year clinical experience. J Nucl Med. 1981;22(7): 647–54.
31. Sfakianakis GN, Conway JJ. Detection of ectopic gastric mucosa in Meckel's diverticulum and in other aberrations by scintigraphy: ii. indications and methods–a 10-year experience. J Nucl Med. 1981;22(8): 732–8.
32. Tauscher JW, Bryant DR, Gruenther RC. False positive scan for Meckel diverticulum. J Pediatr. 1978;92(6):1022–3.
33. Valenza V, Salvatori M, Calisti A, Manzoni C, Focacci C. [Scintigraphic diagnosis of Meckel's diverticulum using Tc-99m-pertechnetate]. Minerva Dietol Gastroenterol. 1990;36(3):139–43.
34. Sfakianakis GN, Anderson GF, King DR, Boles Jr ET. The effect of gastrointestinal hormones on the pertechnetate imaging of ectopic gastric mucosa in experimental Meckel's diverticulum. J Nucl Med. 1981;22(8):678–83.
35. Bree RL, Reuter SR. Angiographic demonstration of a bleeding Meckel's diverticulum. Radiology. 1973;108(2):287–8.
36. Dalinka MK, Wunder JF. Meckel's diverticulum and its complications, with emphasis on roentgenologic demonstration. Radiology. 1973;106(2):295–8.
37. Faris HC, Whitley JE. Angiographic demonstration of Meckel's diverticulum. Case report and review of the literature. Radiology. 1973;108(2):285–6.
38. Conway JJ. Radionuclide diagnosis of Meckel's diverticulum. Gastrointest Radiol. 1980;5(3):209–13.
39. Keramidas DC, Coran AG, Zaleska RW. An experimental model for assessing the radiopertechnetate diagnosis of gastric mucosa in Meckel's diverticulum. J Pediatr Surg. 1974;9(6):879–83.
40. Meier-Ruge W, Fridrich R. Distribution of technetium-99m and iodine-131 in the gastric mucosa. Microhistoautoradiography method using water-soluble isotopes. Histochemie. 1969;19(2):147–54.
41. Wine CR, Nahrwold DL, Waldhausen JA. Role of the technetium scan in the diagnosis of Meckel's diverticulum. J Pediatr Surg. 1974;9(6):885–8.
42. Wine CR, Nahrwold DL, Rose RC, Miller KL. Effect of histamine on technetium-99m excretion by gastric mucosa. Surgery. 1976;80(5):591–4.
43. Priebe Jr CJ, Marsden DS, Lazarevic B. The use of 99m technetium pertechnetate to detect transplanted gastric mucosa in the dog. J Pediatr Surg. 1974;9(5):605–13.
44. Berquist TH, Nolan NG, Stephens DH, Carlson HC. Radioisotope scintigraphy in diagnosis of Barrett's esophagus. Am J Roentgenol Radium Ther Nucl Med. 1975;123(2):401–11.
45. Berquist TH, Nolan NG, Stephens DH, Carlson HC. Specificity of 99mTc-pertechnetate in scintigraphic diagnosis of Meckel's diverticulum: review of 100 cases. J Nucl Med. 1976;17(6):465–9.
46. Chaudhuri TK. Letter: Cellular site of secretion of 99mTcO4 in the stomach–a controversial point. J Nucl Med. 1975;16(12):1204–5.
47. Chaudhuri T, Polak JJ. Autoradiographic studies of distribution in the stomach of 99mTc-pertechnetate. Radiology. 1977;123(1):223–4.
48. Taylor Jr AT, Alazraki N, Henry JE. Intestinal concentration of 99mTc-pertechnetate into isolated loops of rat bowel. J Nucl Med. 1976;17(6):470–2.
49. Winter PF. Letter: Cellular site of 99mTcO4 secretion in the stomach. J Nucl Med. 1976;17(8):756–7.
50. Harper PV, Andros G, Lathrop K. Preliminary observations on the use of six hour Tc-99m as a tracer in biology and medicine. Argonne Cancer Res Hosp. 1962;18:76–87.
51. Harper PV, Lathrop KA, Jiminez F, Fink R, Gottschalk A. Technetium 99m as a Scanning Agent. Radiology. 1965;85:101–9.
52. Lathrop KA, Harper PV. Biologic behavior of 99m Tc from 99m Tc-pertechnetate ion. Prog Nucl Med. 1972;1:145–62.
53. Loken MK, Telander GT, Salmon RJ. Technetium 99m compounds for visualization of body organs. JAMA. 1965;194(2):152–6.
54. Khettery J, Effmann E, Grand RJ, Treves S. Effect of pentagastrin, histalog, glucagon, secretin, and perchlorate on the gastric handling of 99mTc pertechnetate in mice. Radiology. 1976;120(3):629–31.
55. Marsden DS, Priebe Jr CJ. Preliminary appraisal of present 99mTc-pertechnetate techniques for detecting ectopic gastric mucosa. Radiology. 1974;113(2):459–60.
56. Oldendorf WH, Sisson WB, Lisaka Y. Compartmental redistribution of 99mTc-pertechnetate in the presence of perchlorate ion and its relation to plasma protein binding. J Nucl Med. 1970;11(2):85–8.
57. Seltzer MH, Conte Jr PJ, Rickert RR, Singer M. Diagnosis of a bleeding Meckel's diverticulum using radiopertechnetate. Am J Gastroenterol. 1977;67(3):235–9.

58. Holder LE, Ashare AB, Smith W, Saenger E. Pentagastrin: a new drug for stimulating gastric secretion of pertechnetate (abstract). J Nucl Med. 1975;16:535–6.
59. Jewett TJ, Lebowitz R, Treves S. Search for Meckel's diverticulum (letter to the editor and response). Surgery. 1972;72:492–3.
60. Johnson LR. The trophic action of gastrointestinal hormones. Gastroenterology. 1976;70(2):278–88.
61. Treves S, Grand RJ, Eraklis AJ. Pentagastrin stimulation of technetium-99m uptake by ectopic gastric mucosa in a Meckel's diverticulum. Radiology. 1978;128(3):711–2.
62. Diamond RH, Rothstein RD, Alavi A. The role of cimetidine-enhanced technetium-99m-pertechnetate imaging for visualizing Meckel's diverticulum. J Nucl Med. 1991;32(7):1422–4.
63. Petrokubi RJ, Baum S, Rohrer GV. Cimetidine administration resulting in improved pertechnetate imaging of Meckel's diverticulum. Clin Nucl Med. 1978;3(10):385–8.
64. Sagar VV, Piccone JM. The gastric uptake and secretion of Tc-99m pertechnetate after H2 receptor blockage in dogs (abstract). J Nucl Med. 1980; 21:67.
65. Necheles H, Sporn J, Walker L. Effect of glucagon on gastrointestinal motility. Am J Gastroenterol. 1966; 45(1):34–9.
66. Singh PR, Russell CD, Dubovsky EV, Bridger WM. Technique of scanning for Meckel's diverticulum. Clin Nucl Med. 1978;3(5):188–92.
67. Yen CK, Lanoie Y. Effect of stannous pyrophosphate red blood cell gastrointestinal bleeding scan on subsequent Meckel's scan. Clin Nucl Med. 1992;17(6): 454–6.
68. Kwok CG, Lull RJ, Yen CK, Lim AD. Feasibility of Meckel's scan after RBC gastrointestinal bleeding study using in-vitro labeling technique. Clin Nucl Med. 1995;20(11):959–61.
69. Duszynski DO, Jewett TC, Allen JE. Tc 99m Na pertechnetate scanning of the abdomen with particular reference to small bowel pathology. Am J Roentgenol Radium Ther Nucl Med. 1971;113(2): 258–62.
70. Ho JE, Gleason WA, Thompson JS. The expanding spectrum of disease demonstrable by Tc-99m pertechnetate (abstract). J Nucl Med. 1978;19:691.
71. Lunia S, Lunia C, Chandramouly B, Chodos RB. Radionuclide Meckelogram with particular reference to false-positive results. Clin Nucl Med. 1979;4(7): 285–8.
72. Chaudhuri TK, Christie JH. False positive Meckel's diverticulum scan. Surgery. 1972;71(2):313.
73. Polga JP. Nasogastric suction to improve gastrointestinal scanning. J Nucl Med. 1974;15(5):374.
74. Smith RK, Arterburn G. Detection and localization of gastrointestinal bleeding using Tc-99m-pyrophosphate in vivo labeled red blood cells. Clin Nucl Med. 1980;5(2):55–60.
75. Wilson JP, Wenzel WW, Campbell JB. Technetium scans in the detection of gastrointestinal hemorrhage. Preoperative diagnosis of enteric duplication in an infant. JAMA. 1977;237(3):265–6.
76. Rodgers BM, Youssef S. "False positive" scan for Meckel diverticulum. J Pediatr. 1975;87(2): 239–40.
77. Winter PF. Sodium pertechnetate Tc 99m scanning of the abdomen. Diagnosis of an ileal duplication cyst. JAMA. 1977;237(13):1352–3.
78. Mark R, Young L, Ferguson C, Sutherland JB. Diagnosis of an intrathoracic gastrogenic cyst using 99mTc-pertechnetate. Radiology. 1973;109(1): 137–8.
79. Berquist TH, Nolan NG, Adson MA, Schutt AJ. Diagnosis of Meckel's diverticulum by radioisotope scanning. Mayo Clin Proc. 1973;48(2):98–102.
80. Jaros R, Schussheim A, Levy LM. Preoperative diagnosis of bleeding Meckel's diverticulum utilizing 99m technetium pertechnetate scinti-imaging. J Pediatr. 1973;82(1):45–9.
81. Seitz W, Keim HJ, Hahn K. Abdominal scintigraphy for diagnosis of intestinal bleeding. World J Surg. 1978;2(5):613–8.
82. Anderson GF, Sfakianakis G, King DR, Boles Jr ET. Hormonal enhancement of technetium-99m pertechnetate uptake in experimental Meckel's diverticulum. J Pediatr Surg. 1980;15(6):900–5.
83. Conway JJ. The sensitivity, specificity and accuracy of radionuclide imaging of Meckel's diverticulum (abstract). J Nucl Med. 1976;17:553.
84. Chandeysson PD, Hanson RJ, Watson CE, Henery GT. Minimum gastrointestinal bleeding detectable by abdominal scintigraphy (abstract). J Nucl Med. 1983;24:97.
85. Smith RK, Arterburn JG. The advantages of delayed imaging and radiographic correlation in scintigraphic localization of gastrointestinal bleeding. Radiology. 1981;139(2):471–2.
86. Bunker SR, Lull RJ, Tanasescu DE, et al. Scintigraphy of gastrointestinal hemorrhage: superiority of 99mTc red blood cells over 99mTc sulfur colloid. AJR Am J Roentgenol. 1984;143(3): 543–8.
87. Starshak RJ, Sty JR. Trends in physiologic and pharmacologic interventions in pediatric nuclear medicine. Pediatr Ann. 1992;21(2):101–9.
88. Wise PA, Saga W. Retrograde flow pattern on a gastrointestinal bleeding scan. Clin Nucl Med. 1982;23:315–8.
89. Jacobson AF, Cerqueira MD. Prognostic significance of late imaging results in technetium-99m-labeled red blood cell gastrointestinal bleeding studies with early negative images. J Nucl Med. 1992;33(2):202–7.
90. Chaudhuri TK, Brantly M. Heparin as a pharmacologic intervention to induce positive scintiscan in occult gastrointestinal bleeding. Clin Nucl Med. 1984;9(4):187–8.

91. Murphy WD, Di Simone RN, Wolf BH, Smith GE. The use of heparin to facilitate bleeding in technetium-99m RBC imaging. J Nucl Med. 1988;29(5):725–6.
92. Bentley DE, Richardson JD. The role of tagged red blood cell imaging in the localization of gastrointestinal bleeding. Arch Surg. 1991;126(7):821–4.
93. Gupta S, Luna E, Kingsley S, Prince M, Herrera N. Detection of gastrointestinal bleeding by radionuclide scintigraphy. Am J Gastroenterol. 1984;79(1):26–31.
94. Nicholson ML, Neoptolemos JP, Sharp JF, Watkin EM, Fossard DP. Localization of lower gastrointestinal bleeding using in vivo technetium-99m-labelled red blood cell scintigraphy. Br J Surg. 1989;76(4):358–61.
95. Orecchia PM, Hensley EK, McDonald PT, Lull RJ. Localization of lower gastrointestinal hemorrhage. Experience with red blood cells labeled in vitro with technetium Tc 99m. Arch Surg. 1985;120(5):621–4.
96. Winzelberg GG, McKusick KA, Strauss HW, Waltman AC, Greenfield AJ. Evaluation of gastrointestinal bleeding by red blood cells labeled in vivo with technetium-99m. J Nucl Med. 1979;20(10):1080–6.
97. Zuckerman DA, Bocchini TP, Birnbaum EH. Massive hemorrhage in the lower gastrointestinal tract in adults: diagnostic imaging and intervention. AJR Am J Roentgenol. 1993;161(4):703–11.
98. Ferrant A, Dehasque N, Leners N, Meunier H. Scintigraphy with In-111-labeled red cells in intermittent gastrointestinal bleeding. J Nucl Med. 1980;21(9):844–5.
99. Alavi A. Scintigraphic demonstration of acute gastrointestinal bleeding. Gastrointest Radiol. 1980;5(3):205–8.
100. Alavi A. Detection of gastrointestinal bleeding with 99mTc-sulfur colloid. Semin Nucl Med. 1982;12(2):126–38.
101. Alavi A, Dann RW, Baum S, Biery DN. Scintigraphic detection of acute gastrointestinal bleeding. Radiology. 1977;124(3):753–6.
102. Barry J, Alazraki NP, Heaphy JH. Scintigraphic detection of intrapulmonary bleeding using technetium-99m sulfur colloid: concise communication. J Nucl Med. 1981;22(9):777–80.

Kidneys

12

S. Ted Treves, Alan B. Packard,
and Frederick D. Grant

Nuclear medicine techniques play a very important role in the initial diagnosis and follow-up of many renal diseases in children. These techniques are physiological, minimally invasive, and highly sensitive. They enable early detection of renal disease, even before structural changes become apparent on anatomic imaging. Nuclear medicine provides unique functional and anatomic information with minimal risk to the patient. Radionuclide techniques can be used safely in all pediatric age groups and in severely ill patients, including those with renal insufficiency or other renal impairment. These techniques require only a very small amount of tracer material (0.02–0.08 mg) in a very small volume of solution delivered by intravenous injection (0.1–0.5 mL). Radiopharmaceuticals administered in renal studies do not produce pharmacologic, osmotic, hemodynamic, or toxic effects. Renal radiotracers can be administered safely even in patients allergic to iodinated contrast agents. The radiation exposures to the patients are very low. Indications for these studies in children are listed in Table 12.1. For the vast majority of pediatric patients, sedation is not required for these studies. If motion occurs, motion correction techniques can be applied effectively [1].

The extensive use of ultrasonography has provided a clear indication of the incidence of renal disease during the prenatal and neonatal periods [2]. The complementary nature of nuclear medicine and other diagnostic imaging methods for the pediatric urinary tract, especially ultrasonography, should be emphasized. In many instances, a combined approach allows the determination of anatomic-functional relationships, which often provide additional insight into the nature and severity of the problem under investigation.

S.T. Treves, MD
Joint Program in Nuclear Medicine,
Department of Radiology, Harvard Medical School,
Boston, MA, USA

Division of Nuclear Medicine and Molecular Imaging,
Department of Radiology, Boston Children's Hospital,
Boston, MA, USA

Division of Nuclear Medicine and Molecular Imaging,
Department of Radiology,
Brigham and Women's Hospital,
Boston, MA, USA
e-mail: ted_treves@hms.harvard.edu

A.B. Packard
Joint Program in Nuclear Medicine,
Department of Radiology, Harvard Medical School,
Boston, MA, USA

Division of Nuclear Medicine and Molecular Imaging,
Department of Radiology,
Boston Children's Hospital,
Boston, MA, USA
e-mail: alan.packard@childrens.harvard.edu

F.D. Grant
Joint Program in Nuclear Medicine,
Department of Radiology, Harvard Medical School,
Boston, MA, USA

Division of Nuclear Medicine and Molecular Imaging,
Department of Radiology,
Boston Children's Hospital,
Boston, MA, USA

Department of Radiology,
Brigham and Women's Hospital, Boston, MA, USA
e-mail: frederick.grant@childrens.harvard.edu

S.T. Treves (ed.), *Pediatric Nuclear Medicine and Molecular Imaging*,
DOI 10.1007/978-1-4614-9551-2_12, © Springer Science+Business Media New York 2014

Table 12.1 Indications of nuclear medicine renal studies in children

Hydronephrosis and obstruction
Pre- and post-surgery/interventions
Pyelonephritis
Vesicoureteral reflux
Renal function. Split renal function
Cortical integrity. Scarring
Hypertension
Duplication
MCDK
Ectopia, cross fused renal ectopia
Congenital anomalies. Horseshoe kidney
Renal transplants
Urinary leak
Trauma
GFR

Collectively, congenital abnormalities account for approximately 42 % of cases of chronic renal failure [3]. The incidence of end-stage renal disease in children in the USA is approximately 11 new cases per one million total population per year [4]. Koenigsberg et al. reported that the incidence of preexisting lesions is 15–23 % in children showing serious renal injury following relatively minor trauma [5]. Associated anomalies of other organs are not uncommon. For example, infections of the urinary tract affect 3–5 % of all children. During the neonatal period, male infants are more commonly affected, but after 3 months of age, female children are affected approximately three times more often than males [6]. Approximately 10 % of the population is affected by renal anomalies, but many of these problems are minor and of no clinical significance. Excluding polycystic kidneys, the incidence of major malformations has been estimated at 4–7 per 1,000 [7]. A screening study using ultrasonography on more than 132,000 school children of both sexes revealed renal abnormalities in approximately 0.5 % of the subjects [8]. Early diagnosis and treatment of abnormalities of the urinary tract in children can reduce morbidity and mortality [9]. The high-sensitivity, noninvasive, and physiologic nature of diagnostic nuclear medicine places it in a central role in the diagnosis of renal disorders and the evaluation of renal function in pediatric patients. This chapter will review dynamic and static renal scintigraphy and its clinical applications.

Radiopharmaceuticals used in the evaluation of the kidneys may be classified into two groups. The first group includes radiopharmaceuticals that are rapidly eliminated by the kidneys and thus enable evaluation of both renal function and urine drainage. This group includes ^{99m}Tc-mercaptoacetyltriglycine (^{99m}Tc-MAG3) and ^{99m}Tc-diethylenetriaminepentaacetic acid (^{99m}Tc-DTPA), as well as ^{99m}Tc-glucoheptonate and ^{123}I-orthoiodohippurate (^{123}I-OIH).

The second group includes radiopharmaceuticals that concentrate in the renal parenchyma for a sufficiently long period so that detailed scintigraphic mapping of regional functioning renal parenchyma is possible. The current agent of choice for static renal cortical imaging is ^{99m}Tc-dimercaptosuccinic acid (^{99m}Tc-DMSA). Selection of the renal agent depends largely on the diagnostic problem to be investigated and on the practitioner's experience and preference. In general, it is best to become familiar with one agent for dynamic renal scintigraphy and one for static renal scintigraphy and to use them consistently. Many pediatric patients affected with renal disease require follow-up evaluations, and the use of the same radiopharmaceutical and technique facilitates assessment of change.

Dynamic Renal Scintigraphy

Procedure

Whenever possible, it can be useful to provide the patient and the caregiver(s) detailed explanations about the procedure in advance so that they know what to expect when they arrive in the nuclear medicine department. Parents may have questions and concerns about the need for an intravenous injection, bladder catheterization, study duration, radiation exposure, and other

risks. Information brochures can be given to the patient by the referring physician's office. Additionally, such information brochures can be placed on an appropriate website for easy access by the patient and families. The nuclear medicine physician reviews the indications for the study and determines if there are any special procedural considerations or if the use of a diuretic should be anticipated. Upon arrival to the department, the patient is greeted by a nuclear medicine technologist or a child life specialist who will review the procedure further and answer any questions. Recent administration of intravenous contrast agents may affect the renogram by reducing renal uptake or clearance of radiopharmaceutical for up to 24 h. Therefore, dynamic radionuclide studies of the kidneys should be performed either before or 24 h after the administration of radiographic contrast agents.

Patients should be encouraged to drink fluids approximately 1 h prior to the study. In pediatric practice, however, it is difficult to implement a standard pre-study hydration method; therefore, many children end up being examined in their normal state of hydration. When possible, patients are encouraged to empty their bladder before the examination begins. A catheter should be inserted into the bladder if the patient cannot or will not void. The bladder should be allowed to drain through the catheter during the entire duration of the study. Intravenous access is established using a butterfly needle (23–25 gauge) or a short intravenous catheter that is securely fastened to the skin with tape. Before proceeding, one must ensure that intravenous access is reliable and stable. Next, an intravenous infusion of normal saline (10–15 mL/kg) is begun and should be maintained during the first 20 min of the study and continued as necessary to include diuretic renography when this is indicated. Extravasation of the tracer can ruin the examination and must be avoided at by ensuring patency of the intravenous access. Partial extravasation can severely compromise the quality of the study and, if not recognized, may yield to erroneous interpretation.

Radiopharmaceuticals and Administered Doses

^{99m}Tc-MAG3

Technetium-99m-MAG3 (Mallinckrodt, St Louis, MO) is the current agent of choice for dynamic renal scintigraphy [10–15]. The agent is excreted principally through active renal tubular transport. Because ^{99m}Tc-MAG3 is eliminated by tubular secretion and has a high initial renal uptake, it produces high kidney/background ratios, which provide good images of the renal cortex. Its rapid excretion provides good temporal resolution. The usual administered dose of ^{99m}Tc-MAG3 for radionuclide angiography is 5.55 MBq/kg of body weight (0.15 mCi/kg) with a minimum of 37 MBq (1.0 mCi) and a maximum of 148 MBq (4.0 mCi). When radionuclide angiography is not needed, the usual dose of this agent is lower: 3.7 MBq/kg (0.1 mCi/kg) with a minimum of 37 MBq (1.0 mCi) and a maximum of 148 MBq (4 mCi) [16].

The use of noise reduction software may facilitate even further reductions in the administered dose [17].

^{99m}Tc-DTPA

Technetium-99m-DTPA has been used for dynamic renal scintigraphy for several decades, but largely has been replaced by ^{99m}Tc-MAG3. Technetium-99m-DTPA is excreted primarily by glomerular filtration, although with a lower renal clearance rate than ^{99m}Tc-MAG3 [18–29]. A lower rate of glomerular filtration compared with inulin is probably due to protein binding, the amount of which varies with the formulation [30]. A maximum concentration of 5 % in each kidney is achieved 2–3 min after injection [31].

^{99m}Tc-Glucoheptonate

Technetium-99m-glucoheptonate is promptly taken up by the kidneys and rapidly eliminated in the urine. By 1 h after injection, 8–10 % of the initial tracer activity is present in the kidneys and almost 40 % of the administered dose has been eliminated in the urine [32]. Therefore, this

radiopharmaceutical offers the opportunity for both a dynamic renogram and renal cortical scintigraphy, but this rarely is done [33].

^{123}I-Orthoiodohippurate (OIH)

Iodine-123-OIH is useful for dynamic renal scintigraphy because of its high uptake by the renal tubules and rapid excretion into the urine. Iodine-123-OIH has been used extensively in Europe, but the use of this agent in the USA has been limited. This radiopharmaceutical is excreted by the kidneys similarly to para-aminohippuric acid (PAH), the standard for the measurement of effective renal plasma flow [34]. Approximately 80 % of PAH is eliminated by tubular secretion and 20 % by glomerular filtration, with an extraction ratio of approximately 0.9 [35], which is approximately 85 % that of PAH [36].

The Renogram: Procedure

Dynamic renal scintigraphy or renogram consists of serial imaging following the intravenous injection of the radiotracer. Dynamic renal scintigraphy can include three phases: (1) radionuclide angiography, (2) dynamic renal scintigraphy, and (3) diuretic renography. The diuretic of choice for diuretic renography is the loop diuretic furosemide. There are three approaches to the administration of furosemide for diuretic renography. In North America, most practitioners administer furosemide after the completion of the initial 20-min dynamic renal study, usually within 30 min after the administration of ^{99m}Tc-MAG3. This has been referred as the F+20 diuretic renogram. Another approach is to administer furosemide simultaneously with ^{99m}Tc-MAG3 (F-0). This shortens overall imaging time, but results in diuretic administration to all patients. A third approach is to administer diuretic approximately 15 minutes (F-15) before administration of ^{99m}Tc-MAG3.

Children typically are examined in the supine position with the gamma camera placed underneath the examining table, viewing the area of the kidneys and bladder. In the supine position, the distance from the skin to each of the kidneys is approximately the same, and for the calculation of the left-to-right renal uptake ratio, depth correction is not done. Recipients of renal transplants located in the pelvis are examined in the supine position with the gamma camera viewing the kidney and the bladder from the anterior projection. Appropriate immobilization equipment should be employed to reduce patient motion. Sedation for this test is used very exceptionally, if ever. The gamma camera is equipped with a parallel-hole, low-energy, high-resolution collimator. Electronic magnification is employed according to the patient's size. After the patient is positioned, the tracer is administrered as a rapid intravenous bolus injection, and recording of the study is begun simultaneously with the injection.

Imaging: Radionuclide Angiography

Radionuclide angiography consists of rapid imaging of the initial minute of the renogram following the rapid intravenous injection of the tracer. Radionuclide angiography is almost never used alone and it is typically recorded during the first minute of a dynamic renogram. If the study includes a radionuclide angiogram, recording is begun at 0.25 s per frame for 60 s, immediately followed by dynamic renal scintigraphy. As few pediatric renograms are performed to evaluate the vascular supply to the kidney, images from the angiographic phase of the renogram are rarely acquired in children. The high frame rate needed for angiography requires administration of higher doses of ^{99m}Tc-MAG3. Therefore, radiation exposure can be decreased by eliminating this phase of the renogram. However, for special indications, such as evaluation of possible aortic or renal artery stenosis, the angiographic phase may be a useful part of the renogram. In practice, however, most of the relevant information about renal perfusion can be obtained from the 20-min dynamic scintigraphy phase.

Imaging: Dynamic Renal Scintigraphy

The dynamic phase of the renogram is acquired at a slower frame rate than the angiographic

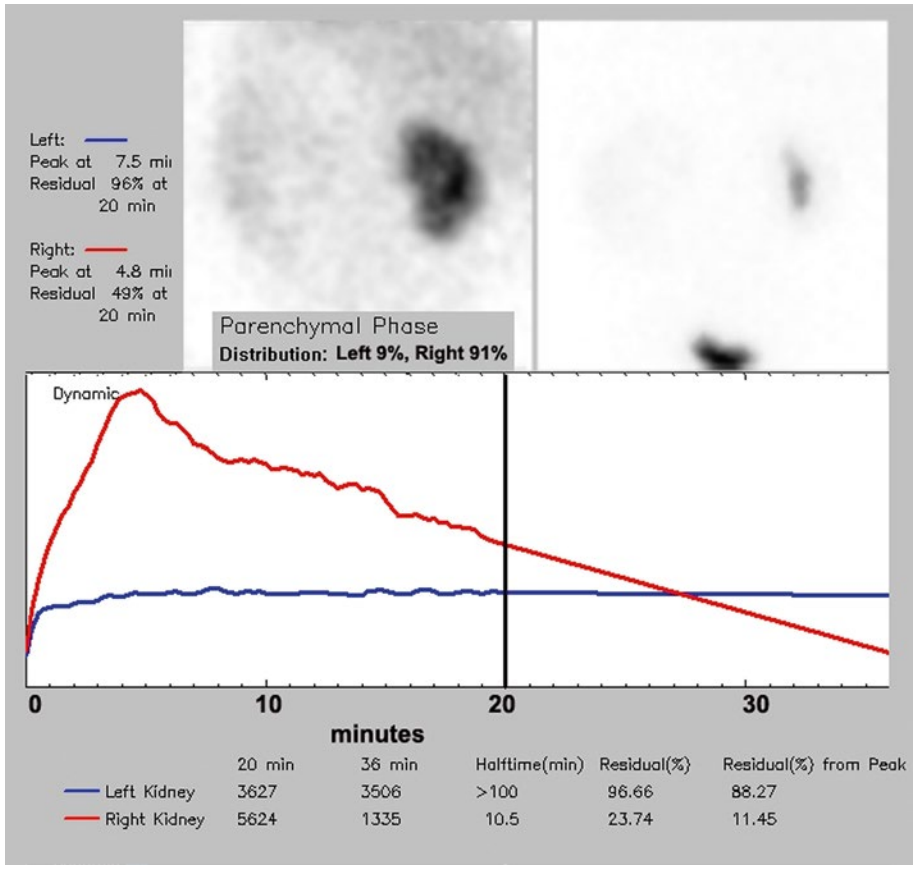

Fig. 12.1 Dynamic renography in a 4-month-old male with left multicystic dysplastic kidney and with grade 3 vesicoureteral reflux into the right kidney. Differential function is 9 % left kindey and 91 % right kidney as assessed during the second minute of imaging (*top left panel*). After twenty minutes (*top right panel*), the dysplastic left kidney shows no tracer uptake. The right kidney has 49% residual tracer in the collecting system. After postural drainage (*bottom panel*), a repeat image at 36 minutes demonstrates additional collecting system drainage with a residual of 11% of peak activity

phase. For our protocol, images are acquired at 15 seconds per frame for twenty minutes (128 x 128 matrix). At the end of the 20-min renogram, the nuclear medicine physician reviews the study and determines if there is enough information to answer the diagnostic question or if additional images and/or a diuretic renogram is needed.

If there is spontaneous, but slow, drainage of tracer, the patient can be instructed to get up (if possible), void in the bathroom, and walk around for a few minutes in order to promote postural drainage before another image of the kidneys is obtained. In a small child or a baby, the patient should be picked up and held by a caregiver for a few minutes before taking additional images (Fig. 12.1). If adequate postural drainage is not seen, the nuclear medicine physician may decide to proceed with a diuretic renogram. If postural drainage occurs, then administration of furosemide may not be necessary.

Imaging: MRI Urography

MRI urography provides exquisite detail of the kidneys, ureters, and bladder with no radiation exposure. However, there are many differences between MRI urography and dynamic radionuclide scintigraphy. Dynamic renal scintigraphy,

including diuretic renography when indicated, takes approximately 50 min to complete, while MRI urography requires approximately 1.5 h and typically requires sedation to acquire satisfactory images. For MRI urography, Ga-DTPA (0.2 mL/kg) is infused intravenously for approximately 30 s, while less than 1 nmol of ^{99m}Tc-MAG3 is given as a rapid bolus of <0.2 mL. Furosemide is given approximately 30 min before the administration of the MRI contrast agent in all patients, while in dynamic scintigraphy, furosemide is given only as needed.

Imaging: Diuretic Renography

Prior to administration of the diuretic, it is important to ensure that radiotracer has filled the renal pelvis. In a poorly functioning and severely hydronephrotic kidney, tracer may not be detected by 20 min within a very dilated renal pelvis. If this is the case, it is prudent to wait a few minutes to allow the renal pelvis to fill in with tracer and then proceed with the administration of furosemide. This may or may not resolve the diagnosis. Forced hydration has been suggested as a means to improve the diagnosis of obstruction versus non-obstruction by diuretic renography [37–39]. A compliant and dilated renal pelvis of a poorly functioning kidney leads to one of the pitfalls of diuretic renography: it may not be possible to differentiate a dilated compliant pelvis from obstruction.

The computer is set to record at a rate of 15 seconds per frame for 30 minutes in a 128 x 128 matrix format. The dose of furosemide (1.0 mg/kg, maximum dose 40 mg) is prepared and readied for intravenous injection. Image acquisition is begun 1 min prior to the administration of the diuretic; the initial images can serve as a baseline. The furosemide then is slowly injected over 2 min through the intravenous line. The diuretic effect is very rapid and it is usually seen on the renal time-activity curve by 1–2 min after administration of the furosemide.

In some patients, the forced diuresis causes or reproduces flank pain, especially in those with hydronephrosis who complain of intermittent pain. In some cases, rapid overdistention of the renal pelvis may disrupt the status of a system in which urine flow and drainage are otherwise balanced. In most cases, even with collecting system dilation, rapidly increased diuresis causes no pain or discomfort.

Processing and Display

An integrated display of the entire renogram is useful for interpreting the study as well as helpful in providing the referring physicians with a simple, intuitive, and consistent way to communicate the results (Fig. 12.2).

The Renogram: Interpretation

Interpretation of Renal Radionuclide Angiography

The radionuclide angiogram can be viewed as a series of sequential images or in a cinematic mode. The series of images depict tracer activity as it initially circulates within the aorta and the arterial-arterio territories of the kidneys. However, once tracer reaches the kidneys, dilution will make it difficult or impossible to differentiate the arterial, capillary, and venous phases. Rapid changes in renal blood flow secondary to sudden increases in pressure in the renal pelvis can be detected by radionuclide angiography. This suggests that there can be reversible changes in renal blood flow responding to acute changes in pelvic pressure (Fig. 12.3) [40, 41].

Interpretation of the Renogram

When interpreting a dynamic renal study such as the renogram, it is important to evaluate all the available information including both the images and the time-activity curves derived from appropriate regions of interest (ROI). Cinematic display of the images can be helpful for interpretation by the nuclear medicine physician and the referring physicians. Appropriate

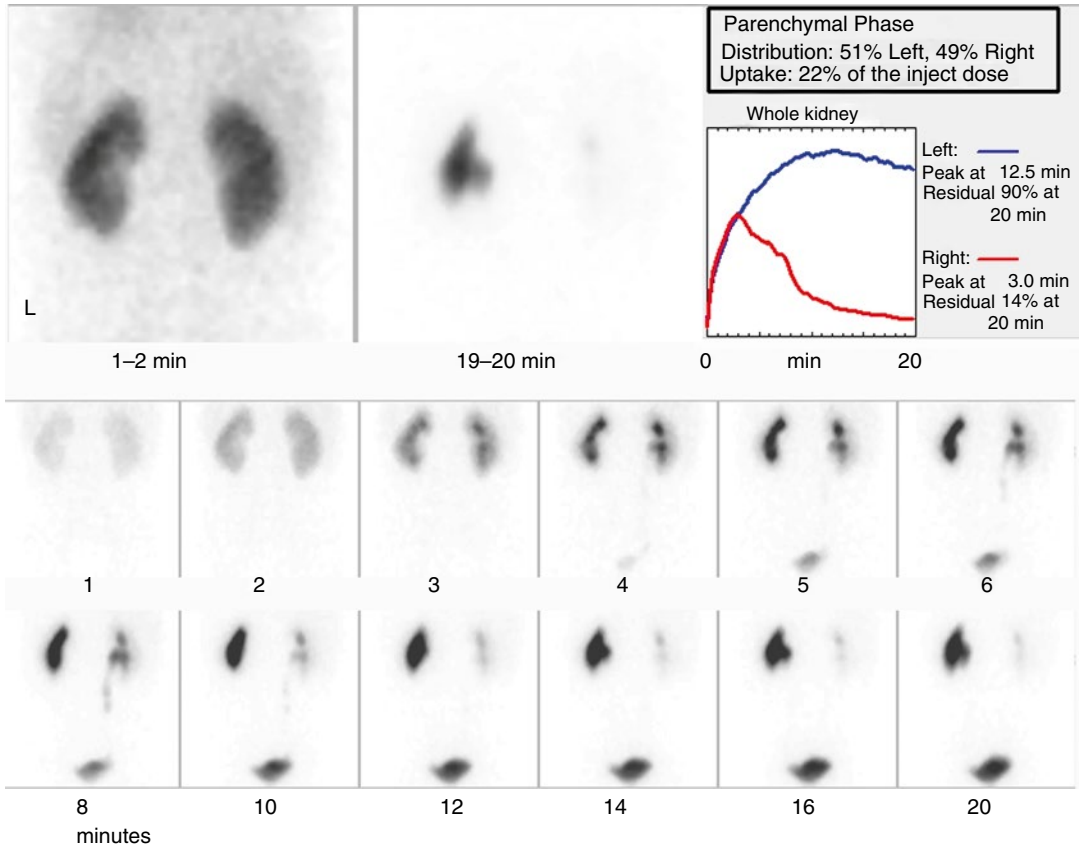

Fig. 12.2 Simplified display developed at Boston Children's Hospital. All information from the parenchymal phase of the renogram can be reviewed on a single screen. Summed dynamic images acquired over twenty minutes are displayed in the *bottom panel*. The are no segmental perfusion defects and cortical transit is identified by three minutes in both kidneys. The right kidney has normal uptake, cortical clearance, and collecting system drainage. The left kidney has normal uptake and cortical clearance, but markedly delayed collecting system drainage. Differential function determined during the second minute of imaging (*top left panel*) is 51 % left kidney and 49 % right kidney. The time activity curve and summary data are displayed in the *upper right panel*

interpretation of the renogram should include a systematic evaluation of three phases of the study. These include:

1. Parenchymal or cortical phase
2. Cortical transit time
3. Urine drainage phase

Parenchymal Phase

The parenchymal or cortical phase occurs after the initial vascular distribution of the tracer and before the first appearance of tracer in the renal collecting system. During this period, tracer concentrates in the renal cortical parenchyma while the blood level of tracer is decreasing. The parenchymal phase provides information about (a) total renal function, (b) split or differential renal function, (c) size and position of the functional renal parenchyma, and (d) renal morphology of functioning renal parenchyma. The parenchymal phase image usually is acquired during the second minute (60–120 s) following the intravenous administration of the tracer (Fig. 12.4).

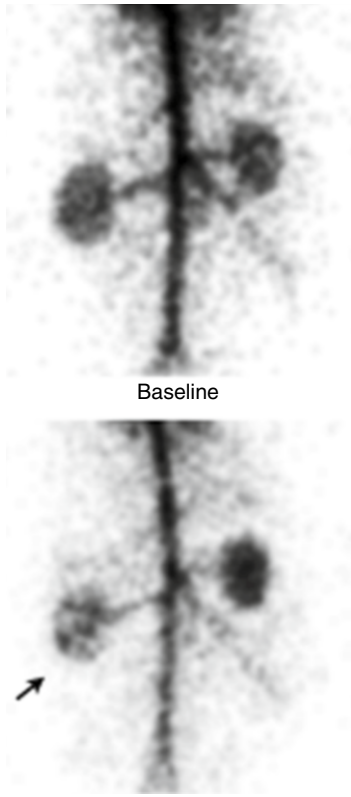

Fig. 12.3 Effect of acute increases in hydrostatic pelvic pressure on renal blood flow. Iridium-191m radionuclide angiograms, 2-s frames. *Top*: Baseline study reveals symmetric renal blood flow. *Bottom*: Decreased left renal blood flow (*arrow*) during acute increase of hydrostatic pressure in the left renal pelvis

Total Renal Function

Evaluating the ratio of the total renal uptake of ^{99m}Tc-MAG3 and the body background activity, one can obtain a qualitative estimate of *total renal function*.

A quantitative estimate of the total renal uptake of the injected dose complements this visual assessment. This can be useful in the serial evaluation of individual patients as the analog images may vary in intensity.

Total renal uptake can be estimated using the following procedure. The syringe containing the tracer to be injected is placed at 15 cm from the face of the collimator using a specially made plastic holder and the activity is recorded as the initial dose. All materials used for the injection of the tracer (e.g., syringe, butterfly needle) are saved for later counting. The dynamic study is recorded as described above. At the end of the dynamic study, the saved materials are placed in front of the collimator using the same holder, and another image (residual dose) is recorded. The total renal counts are determined in regions of interest (ROIs) drawn around the kidneys on the parenchymal phase (60–120 s). All measurements are corrected for background and radioactive decay. Results are expressed as percentage of the administered dose (initial minus residual) in the kidney(s) during the parenchymal phase.

As this approach does not correct for tissue attenuation and depth, only an estimate of the total renal uptake is obtained, not an absolute value. Meticulous attention to detail and study-to-study consistency are essential to avoiding errors that may lead to inadequate assessment of renal function. We evaluated the normal values of estimated percentages of the injected dose in the kidneys using our method in children. The estimated percentage of the total renal uptake of the injected dose in children younger than 5 years of age (range 1–60 months) with normal total renal function ranged from 8 to 23 % with an average of 15.4 % (median 15.0 %, range 8–23 %). These children's weights averaged 10.1 kg (median 8.0 kg, range 5–23 kg), serum creatinine levels averaged 0.3 mg/dL (median 0.2 mg/dL, range 0.2–0.4 mg/dL), and serum BUN levels averaged 11.7 mg/dL (median 10 mg/dL, range 5–18 mg/dL).

Split or Differential Renal Function

The parenchymal phase provides information about *differential renal function (split renal function)*. The differential renal function can be calculated in the parenchymal phase from the ratio of counts from the corresponding ROI from each kidney. This ratio is consistent with a differential

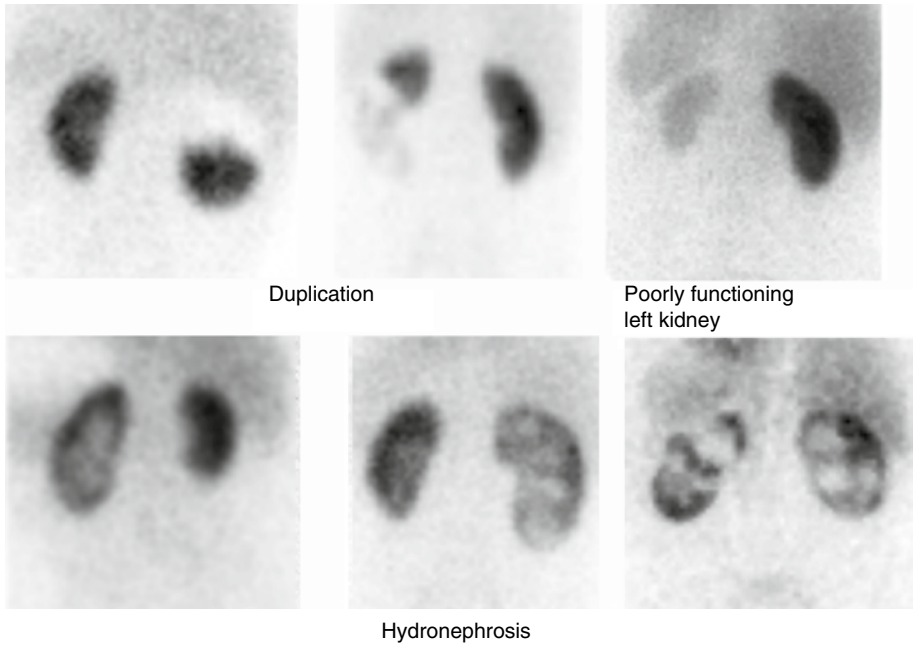

Fig. 12.4 Examples of ^{99m}Tc-MAG3 parenchymal phase images. *Top left* and *middle*: Two examples of renal duplication. *Top right*: Poorly functioning left kidney. *Bottom left*: Left hydronephrosis. *Bottom middle*: Right hydronephrosis. *Bottom right*: Bilateral hydronephrosis

renal function calculation that can be obtained from renal ^{99m}Tc-DMSA scintigraphy when the function in each kidney is greater than 10–15 % of the total renal uptake. If the renal function from an individual kidney estimated by ^{99m}Tc-MAG3 is less than 10–15 %, then this method likely will underestimate of the kidney's contribution to the total renal function. This likely is due to slow accumulation of tracer over many minutes in a kidney with markedly impaired function, as well as difficulty discriminating low levels of renal uptake from background. In these cases, ^{99m}Tc-DMSA scintigraphy will provide a more reliable determination of differential renal function.

Placement of ROIs over the kidneys without including extraparenchymal sources of activity may be difficult, especially in cases of poor renal function and in hydronephrosis. Careful attention to detail and consistency during selection of background ROIs is essential as different sizes and positions of background regions can produce different results. This can be most problematic when the renal function is low or hydronephrosis is present. Thus, it is crucial to verify any semiquantitative results with visual assessment.

Kidney Size and Position

The *relative renal size* can be estimated by simple visual observation of the parenchymal image. The maximum renal dimensions in the longitudinal and transverse planes can be measured with a calibrated system or by imaging a radioactive ruler placed to the side of the patient. In addition, the *functional size of the kidneys* can be estimated by comparing the kidneys with the body outline and relative proportions of visible organs on early images. However, this assessment is not as accurate as can be obtained with renal cortical scintigraphy. The parenchymal phase also shows the *position of the kidneys*. If a pelvic kidney is

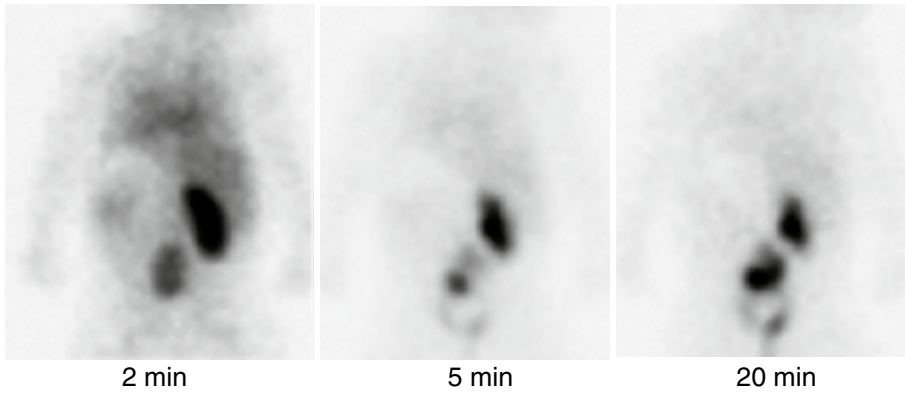

Fig. 12.5 Ectopic left kidney. ^{99m}Tc-MAG3 renogram demonstrates tracer uptake renal parenchyma of a normally positioned right kidney and ectopic pelvic right kidney on the 2-min image. By 5 min, tracer appears in the renal pelvis of both kidneys. The right kidney demonstrates persistent tracer accumulation in the collecting system, concerning for mild ureteropelvic junction obstruction

suspected, it is important to include the pelvic area within the field of view of the camera (Fig. 12.5).

Morphology of Functioning

Renal Parenchyma

The parenchymal phase provides information about *overall morphology of the kidneys* and intrarenal distribution of radiotracer. In kidneys with pelvicaliectasis or hydronephrosis the funtional cortex appears as a rim of uptake around the dilated renal pelvis. Larger cortical defects and some renal scars also can be identified, such as a malfunctioning upper pole in a duplex kidney, trauma, tumor, or cyst. The parenchymal phase does not allow detection of small cortical defects, however.

Cortical Transit Time

A very useful parameter that can be measured from the dynamic renal study is the *cortical transit time*. The cortical transit time can be defined as the time between the intravenous administration of the tracer and the first appearance of tracer within the renal collecting system. With normal renal function radiotracer should appear within the renal collecting system 2–5 min after intravenous injection. With impaired renal function, the cortical transit time will be prolonged. In the presence of pelvicalyceal dilation, a normal cortical transit time can be reassuring that there has been little loss of renal cortical function. As the tracer is excreted from the renal cortex into the renal pelvis, parenchymal renal activity should decrease gradually. Even if the cortical transit time appears to be within the normal range, it is important to confirm that it is associated with a decrease of parenchymal activity. Cortical transit time may be prolonged in several conditions that affect renal function, including renal immaturity, ureteral obstruction, hydronephrosis, renal insufficiency, acute tubular necrosis, renal artery stenosis, renal vein thrombosis, acute and chronic pyelonephritis, transplant rejection, nephrotoxicity, and trauma.

Urine Drainage Phase. As the renogram progresses to the *drainage phase*, tracer gradually is eliminated through the pelvicaliceal system and the ureters into the bladder. By the end of the 20 min renogram, nearly all of the tracer should have cleared from the renal parenchyma and most should be drained from the renal collecting system. Time-activity curves generated from regions of interest over an entire kidney usually reveal peak activity at 4–6 min with subsequent decrease by 20 min. With normal renal function and drainage, the twenty-minute residual should be less than 50 % and usually is less than 35 %. Time-activity curves must not be interpreted alone, but along with careful evaluation of the images of the parenchymal phase, cortical transit,

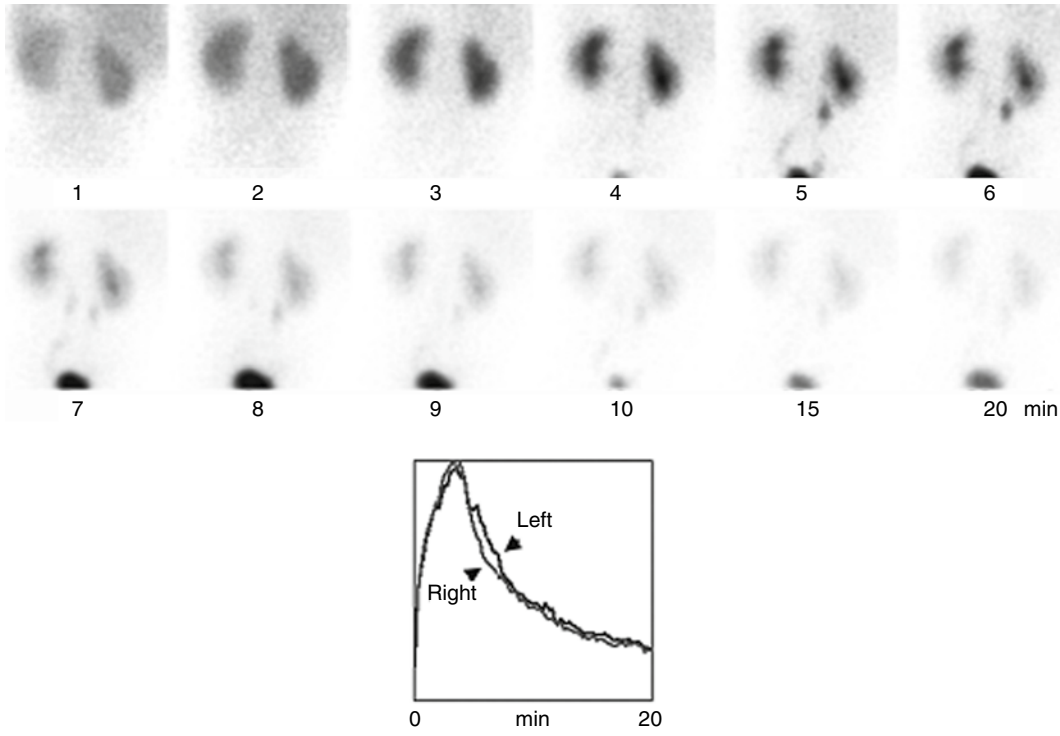

Fig. 12.6 Normal ^{99m}Tc-MAG3 renogram in a 4-week-old girl with a question of renal obstruction. Dynamic images acquired for twenty minutes after tracer administration demonstrate symmetric tracer accumulation in both kidneys. By four minutes, there has been cortical transit of tracer and tracer accumulation is seen in both ureters and the bladder. The is rapid drainage of the collecting system. The time activity curve (*bottom panel*) confirms these findings. Maximal activity is at 4 minutes in both kidney, and the curves demonstrate a normal concave appearance during the drainage phase. By twenty minutes, residual tracer in each kidney is 20–25 %

and the drainage phase. A normal cortical transit time with nearly complete cortical clearance of the tracer from the cortex at 20 min accompanied with a renal time-activity curve that reveals a delayed peak and high residual value indicates delayed urine drainage without parenchymal dysfunction. The most accurate interpretation requires examination of both serial images and time-activity curves.

A *normal dynamic renal study* reveals relatively rapid and intense concentration of the tracer in the renal parenchyma at 1–2 min after administration (Fig. 12.6). Passage of the tracer into the renal calyces and the renal pelvis occurs at 3–5 min. In the absence of ureteral dilation or obstruction, visualization of tracer in the ureters is variable. The ureter may be visualized in some normal patients and those with slow ureteral transit time. Ureteral dilatation or very slow transit time, with or without obstruction, usually shows as ureteral visualization in the renogram. By 20 min after injection, the radiotracer usually has cleared almost completely from the renal parenchyma. Small residual amounts of tracer persisting in the pelvicaliceal system at 20 min may be normal and are usually of no clinical significance. Minimal residual tracer tends to clear spontaneously, with a change in the patient's position or after voiding. Tracer appears within the bladder 3–6 min after injection, and its level increases with time as more of it is excreted by the kidneys. In a patient with normal renal function, soft-tissue background, which reflects blood clearance of the tracer and therefore total renal function, rapidly decreases with time.

If there is no retention of tracer within the pelvicaliceal system or the ureter(s), the study is terminated at 20 min. If, at the end of the initial 20 min, tracer is retained within the pelvicaliceal system, the patient should be encouraged to get up, void in the bathroom, and walk around for a few minutes if possible (a small child should be picked up for a few minutes) to promote postural drainage. An additional image is then obtained to determine if drainage has occurred. Kidneys that drain with a change in patient position should not be considered obstructed [42]. If urinary obstruction is suspected, a diuretic renogram may be indicated (see below).

Interpretation of the Diuretic Renogram

Intravenous administration of furosemide is followed by a rapid diuretic response that displaces tracer from dilated unobstructed systems. If there is significantly obstruction of the collecting system, then tracer in the renal area decreases slowly, fails to decrease, or even increases in response to the induced diuresis.

In diuretic renography, drainage is directly proportional to urine flow and inversely proportional to the volume of the renal pelvis and ureter. Urine flow depends on the level of renal function and amount of renal parenchyma present, as well as the ability of the parenchyma to respond to the diuretic. There are a set of factors that, when present, limit the ability of diuretic renography to determine if there is obstruction or not. These pitfalls include poor renal function; parenchymal loss; large, flaccid, and compliant renal pelvis and/or ureter; infiltration of the diuretic; bladder overdistention; prune-belly syndrome; and complex surgeries [43–45].

Interpretation of the diuretic study must include the evaluation of both the initial 20-min dynamic renal study and the diuretic phase.

In the absence of obstruction, rapid and almost complete washout of radiotracer from the pelvicaliceal system occurs. If a kidney drains satisfactorily during the initial dynamic renal study, half-time ($t_{1/2}$) is not calculated. As there is not much tracer remaining, a calculated $t_{1/2}$ will be prolonged and potentially misleading. In obstructed systems, drainage of tracer following administration of the diuretic is slow and there is tracer retention at the end of the study. Interpretation of intermediate diuretic renographic patterns can be more difficult.

A comparison is made of images obtained prior to the administration of the diuretic and at the end of the 30-min diuretic study. The diuretic washout $t_{1/2}$ is determined using a mono-exponential interpolation between a point on the initial descent of the time-activity curve and another point on the downslope while the curve is decaying monotonically. A rapid initial $t_{1/2}$ can be followed by significant retention of tracer in the renal pelvis. Therefore, it is important to report both the initial washout $t_{1/2}$ and the residual activity in the renal pelvis at 30 min.

Estimation of the diuretic half-time is a useful adjunct to the assessment of urinary obstruction. Washout half-time has been overemphasized as the only factor in the assessment of possible kidney obstruction. This approach can lead to oversimplification of a rather complex condition as diuretic half-time is only one of several factors considered when assessing urinary obstruction.

At least three different methods have been used to calculate the diuretic washout half-time. Therefore, diuretic half-time values vary from method to method and from observer to observer (Fig. 12.7). Despite these variations in technique, the overall sensitivity of diuretic renography for the detection of obstruction in children remains high [46].

Advanced Image Processing

Advanced planar processing software provides opportunities to decrease administered radiopharmaceutical dose while maintaining or improving the quality of planar images. Research in our laboratory has shown that the administered dose of ^{99m}Tc-MAG3 can be reduced to 2.2 MBq/kg (0.06 mCi/kg) without compromising image quality when images are viewed at 1 frame per minute. With noise reduction software, the administered dose can be reduced further to 1.5 MBq/kg (0.04 mCi/kg). Denoising software may permit a significant reduction in administered radiopharmaceutical dose and patient radiation

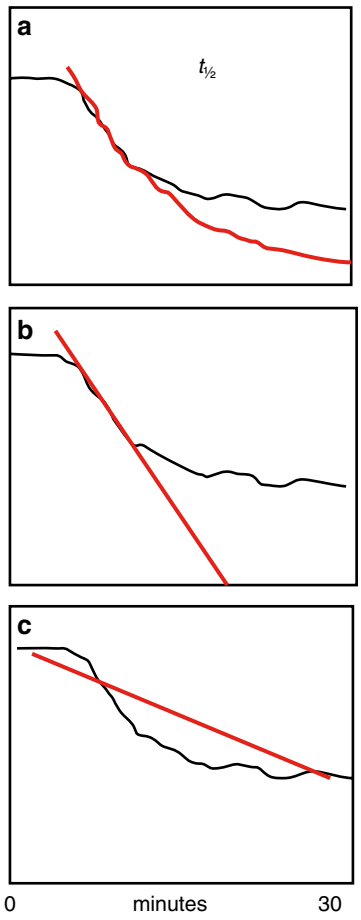

Fig. 12.7 Different ways of calculating diuretic-phase half-time from the diuresis time-activity curve: (**a**) Exponential interpolation of the washout curve in the region of fastest collecting system drainage may provide the most accurate assessment of collecting system obstruction, (**b**) Linear interpolation in the region of fastest collecting system drainage, (**c**) Linear interpolation from time 0 to the end of imaging at 30 minutes may be the least accurate

exposures without loss of diagnostic information. (Fig. 12.13) [17].

Renal Cortical Scintigraphy

Patient Preparation

There is no need for special patient preparation for this method other than informing the patient and caregivers of what to expect in terms of the method and the several hours of time commitment from arrival, tracer injection, and imaging. In our experience, sedation is used rarely, if ever, for this procedure.

Radiopharmaceutical and Administered Doses

^{99m}Tc-DMSA

Technetium-99m-DMSA is the agent of choice for renal cortical imaging by planar scintigraphy, by pinhole magnification, or by single photon emission computed tomography (SPECT). Technetium-99m-DMSA is administered intravenously with a usual dose of 0.05 mCi/kg (1.85 MBq/kg) [minimum 0.3 mCi (11.1 MBq); maximum 3.0 mCi (111 MBq)]. After intravenous injection, this agent is 90 % bound to plasma proteins, and a small amount (0–5 %) is associated with red cells [47]. In normal individuals, the blood disappearance of ^{99m}Tc-DMSA follows a single exponential with a mean half-time of 56 min and with 6–9 % of the administered dose present in the blood at 14 h after injection. The renal uptake of ^{99m}Tc-DMSA is approximately 40–50 % of the injected dose at 4 h and 70 % at 24 h, [47, 48]. Most accumulated tracer is found in the proximal convoluted tubules, with small amounts elsewhere in the kidney (Fig. 12.8) [49]. Although most ^{99m}Tc-DMSA is retained in the renal parenchyma, cumulative urinary excretion has been reported to be 6 % at one hour, 1–12 % at two hours, and 25 % at 14 hours.

The distribution of ^{99m}Tc-DMSA uptake between kidneys reflects regional renal blood flow and functional renal parenchymal mass [50, 51, 52]. There is an autoregulation phenomenon that maintains total renal function at normal levels even in an increase in the number of nephrons and apparent renal mass. For example, in experimental rats receiving a renal transplant, the animal ends up with three kidneys (two native and one transplant), and the total renal uptake of DMSA remains the same as before transplantation. The tracer is evenly distributed among the three renal units. There appears that there is a feedback signal to enable the aggregate renal

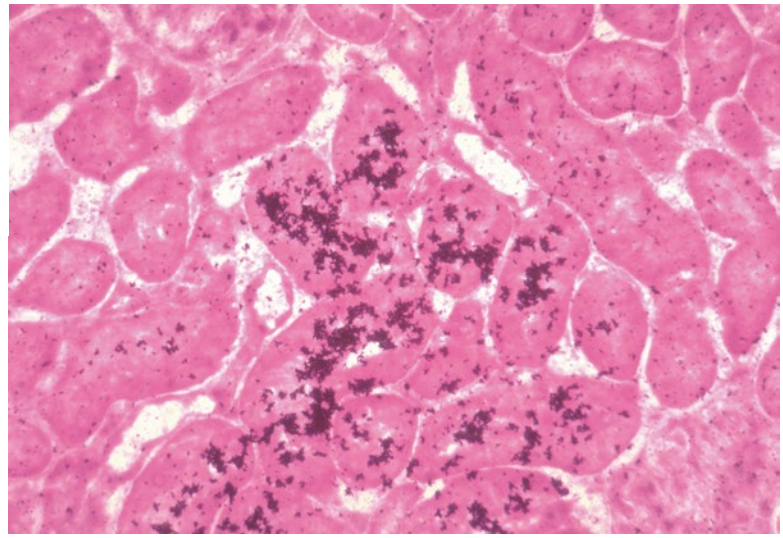

Fig. 12.8 ^{99m}Tc-DMSA. Frozen section autoradiography from a rat kidney 1 h after intravenous injection of ^{99m}Tc-DMSA. Tracer concentrates principally in the proximal convoluted tubules. Minimal or no tracer activity is seen elsewhere

Fig. 12.9 Three-kidney rat 16 h after injection of DMSA. The transplanted third kidney (T) lies below the other two [53]

glomerular and tubular clearance to remain a constant linear function of body weight even in the presence of an additional kidney (Fig. 12.9) [53].

In patients, excellent images of renal cortex can be obtained approximately 3–4 h after administration of ^{99m}Tc-DMSA. In patients with obstruction, tracer retained within the pelvicaliceal system can interfere with mapping of functioning renal parenchyma and may lead to the wrong estimate of differential renal function. It is important to evaluate carefully the images acquired at 4 h to confirm that there is no tracer in the pelvicaliceal system. If tracer is retained, later imaging (up to 24 h after injection) may allow tracer in the urine to be eliminated and permit a better assessment of renal cortices and differential renal function (Fig. 12.10).

Renal Scintigraphy: Imaging

Three to four hours after administration of ^{99m}Tc-DMSA, the kidneys may be imaged using planar scintigraphy, pinhole magnification, or SPECT.

Planar Renal Scintigraphy

Planar renal scintigraphy can provide information about: (1) number, position, size, and overall morphology of the functioning kidneys; (2) differential renal function; and (3) regional parenchymal function. For conventional planar renal scintigraphy the patient is examined in the supine position, and a posterior image containing 300,000–500,000 counts is recorded using a high-resolution or, preferably, ultrahigh-resolution

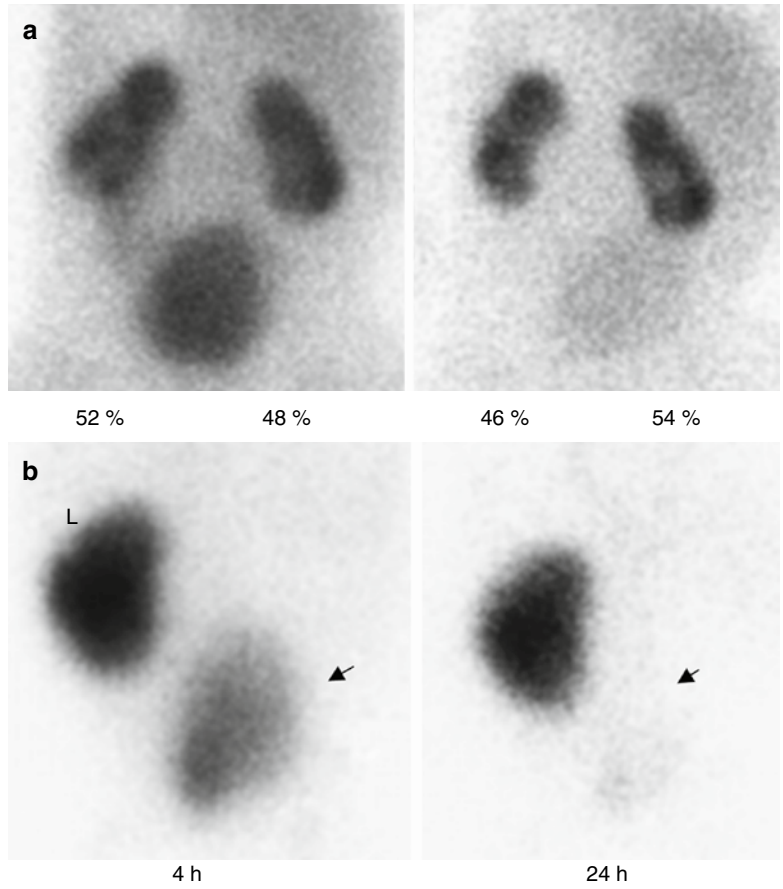

Fig. 12.10 (**a**) 4-day-old infant with bilateral hydronephrosis, hydroureters, and severe bilateral reflux. *Left*: The 4-h image estimates a 52 %–48 % differential ^{99m}Tc-DMSA uptake. However, high levels of tracer in the pelvis and ureters interfere with assessment. *Right*: An image at 24 h is clear of excreted urinary activity and best represents the differential renal function as 46 %/54 %. (**b**): ^{99m}Tc-DMSA cortical scintigraphy in a 3-month-old boy with nonvisualization of the right kidney by ultrasonography. This study was performed to look for any evidence of right renal function. *Left*: Scintigraphy at 4 h revealed normal tracer accumulation in the left kidney (*L*). Tracer accumulation in the right side could correspond to an ectopic right kidney or tracer in the bladder (*arrow*). *Right*: Image at 24 h shows clearance of tracer from the pelvis, which clearly demonstrates that tracer had accumulated in the bladder (*arrow*) with, no evidence of an ectopic pelvic right kidney

collimator on a 256 × 256 matrix format. Left and right posterior oblique projections may be useful for identifying cortical defects. A calibrated system enables measurement of the size of the functional renal parenchyma. Semi-quantitative assessment is performed with regions of interest of each kidney and background areas. The differential split renal uptake corrected for body background is then calculated. The normal differential renal uptake is nominally 50 %/50 % (+/–5 %), so it can range from 45 %/55 % to 55 %/45 %. In renal duplication, separate regions of interest of the upper and lower poles can be used to estimate the distribution of functioning renal parenchyma with in the duplicated kidney. A more detailed assessment of regional parenchymal function (e.g., scar, inflammation, infarct, duplex) is best done with SPECT or with pinhole magnification.

Magnification Renal Scintigraphy

Pinhole magnification is very effective for detailed imaging of the kidneys in both infants (in whom magnification is essential) as well as older children and adolescents. A pinhole

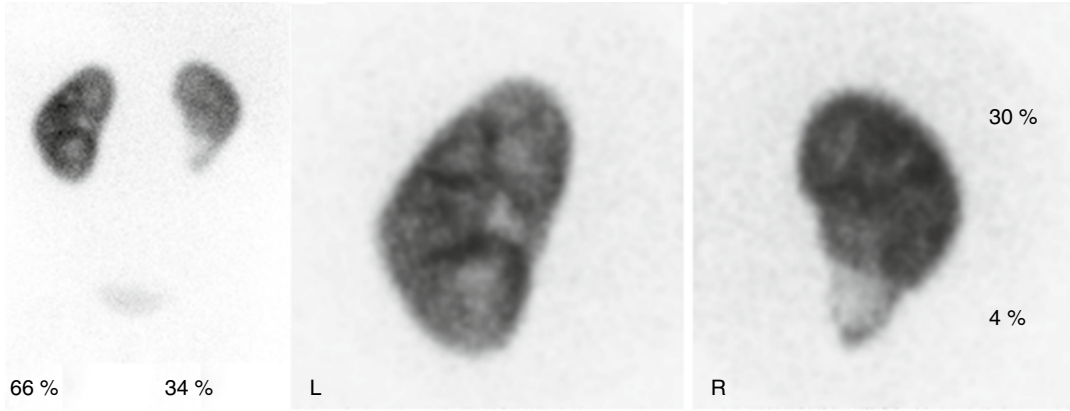

Fig. 12.11 ^{99m}Tc-DMSA pinhole scintigraphy in a 2-year-old girl with repeated urinary tract infections, a double right collecting system, and moderate vesicoureteric reflux in the right lower pole. Posterior images reveal reduced relative function of the right kidney. There is a large cortical in the lower moiety of the right kidney (*left panel*). Pinhole images (*right panel*) reveal greater detail with a clear delineation of the focal reduction of tracer uptake in the right (R) lower moiety. Region of interest analysis showed that the upper moiety contributes 30 % of total renal function, while the lower moiety contributes only 4 % of total renal function

collimator with an internal diameter of 2–3 mm provides images of high spatial resolution (2–3-mm range). Posterior and posterior oblique projections are useful to detect and outline cortical abnormalities. Each pinhole image is obtained for approximately 150,000 counts using a 256×256 matrix (Figs. 12.11 and 12.12). Cortical functional defects in pyelonephritis, infarction, scarring, duplication and fetal lobations can be discerned better with pinhole magnification than with parallel-hole, high resolution collimators.

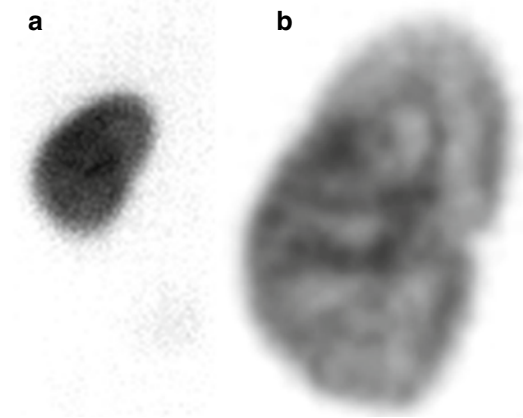

Fig. 12.12 Right multicystic dysplastic kidney. The right kidney is not visualized. Planar (**a**) and magnified pinhole images (**b**) are shown. Note the detailed visualization of renal cortex on the pinhole image

Advanced Image Processing

Advanced planar processing software provides opportunities to decrease administered radiopharmaceutical dose while maintaining or improving the quality of planar images. Denoising software may permit a significant reduction in administered radiopharmaceutical dose and patient radiation exposures without loss of diagnostic information. (Fig. 12.13) [17].

Single Photon Emission Computed Tomography (SPECT)

Technetium-99m-DMSA single photon emission computed tomography (SPECT) is superior to conventional planar or pinhole scintigraphy for mapping regional functioning renal parenchyma. By definition, SPECT permits simultaneous evaluation of images in the transverse, coronal, or sagittal plane, or in any plane. Evaluating rotating volume-rendered images permits a superior overall view of the functional anatomy of the kidneys. Using modern systems, renal SPECT

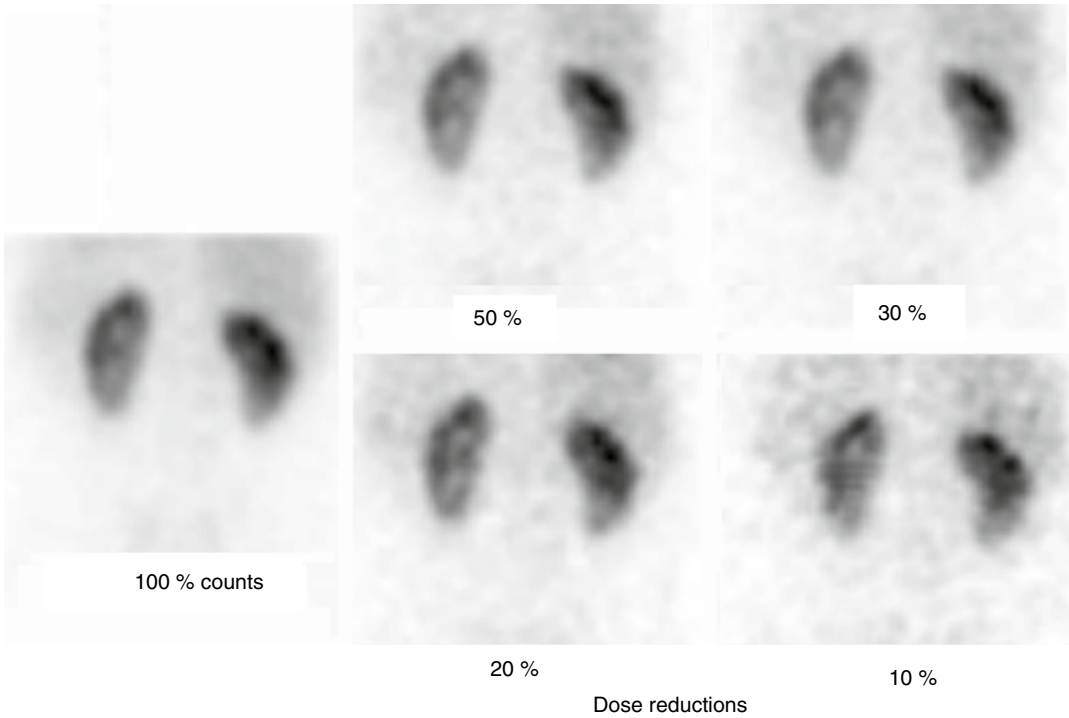

Fig. 12.13 Dose reduction using advanced image processing. Simulated noise was added to simulate fewer counts/activity. Then, spatially variant filtering was used for noise reduction, demonstrating that advanced image processing may permit high image quality with lower radiopharmaceutical doses [183]

acquisition requires 15–20 min (Figs. 12.14, 12.15, and 12.16). SPECT may be less suitable for small patients less than 1 year of age. With currently available SPECT cameras, the detectors cannot easily be positioned close to a small patient and the distance between the cameras and kidneys limits detailed renal imaging.

Iterative Reconstruction

Until recently, most renal SPECT studies have been processed using the technique of filtered back projection. The application of 3-D Ordered Subset Expectation Maximization (OSEM) with resolution recovery (for example, OSEM 3D, Flash 3D, Siemens) can result in a significant improvement in DMSA image quality compared to filtered back projection. The improved image quality can facilitate a reduction of radiopharmaceutical administered doses and, therefore, reduction in radiation exposure. Alternatively, utilization of OSEM may permit a substantial reduction in acquisition time without loss of image quality (Figs. 12.17 and 12.18) [54].

Measurement of Renal Volumes with SPECT

Measurement of individual renal volumes in children can be elegantly performed with an automated method of SPECT analysis. With this method, we measured renal volumes in 310 children without renal disease with a median age of 8.8 years (range 1–21 years of age). This automated approach showed a high level of reproducibility and reliability compared to other methods. Normal ranges of renal volumes in children were determined with this method. These volumes were determined as a function of body weight in males and females (Fig. 12.19) [55].

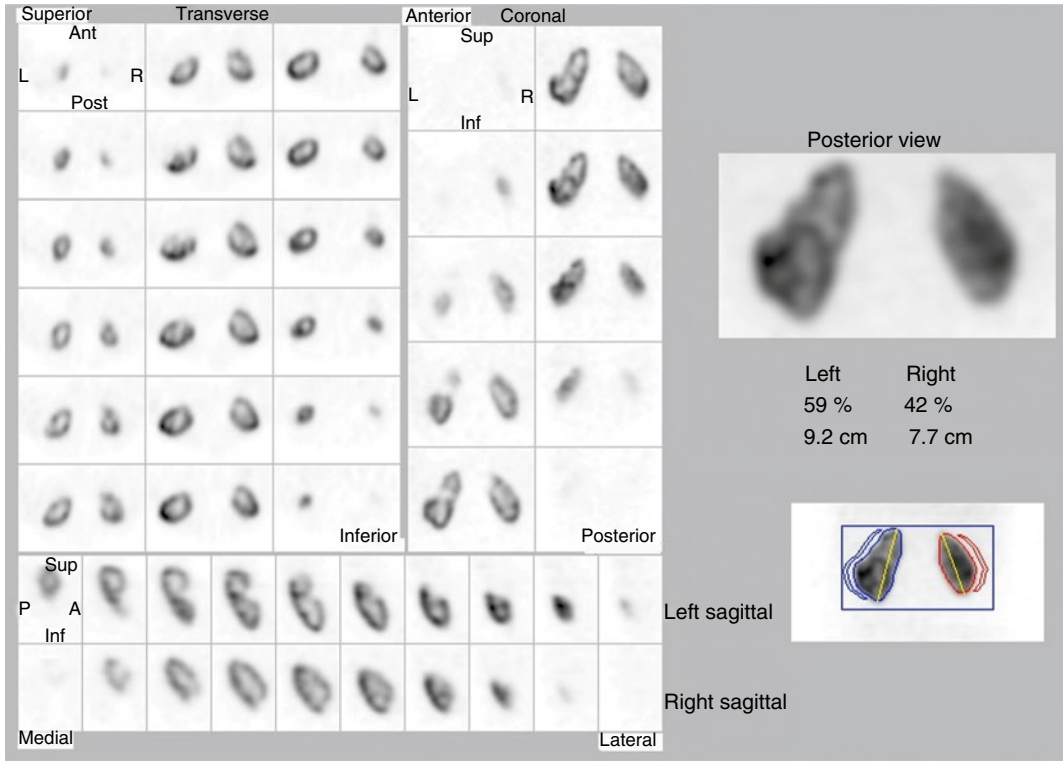

Fig. 12.14 ^{99m}Tc-DMSA SPECT in a 9-year-old female with hypertension and with normal ultrasonography with Doppler. Summed projection images are used to determine that differential renal function is left 59 % and right 42 %. The left kidney has an irregular contour and the right kidney is smaller than the left. In the *left panel*, slices in the transverse, coronal, and sagittal projections more clearly delineate cortical defects the in the lateral mid and superior aspect of the left kidney

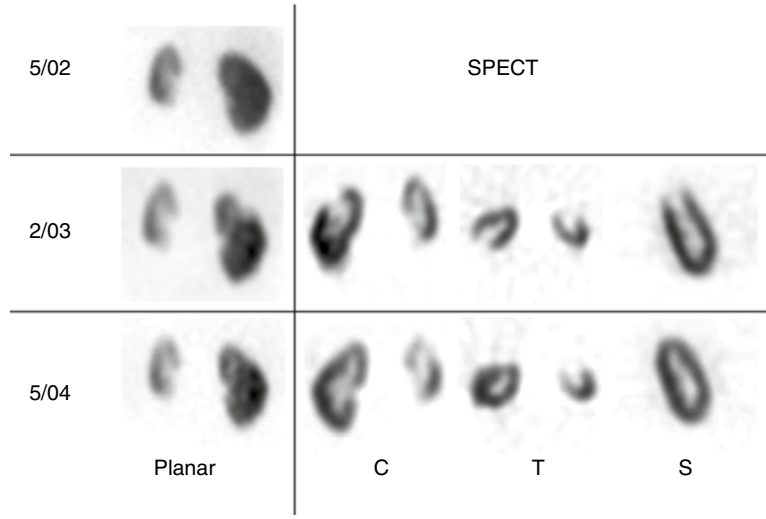

Fig. 12.15 Pyelonephritis and recovery. Planar and SPECT ^{99m}Tc-DMSA images of a 7-year-old girl with bilateral vesicoureteral reflux. Planar images reveal the left kidney has lower renal function and that on 2/03 a cortical defect was present in the right upper pole. SPECT reveals the defect more clearly. Following a course of intravenous antibiotics, the defect has largely resolved. This recovery is more clearly seen on SPECT. *C* coronal, *T* transverse, *S* sagittal

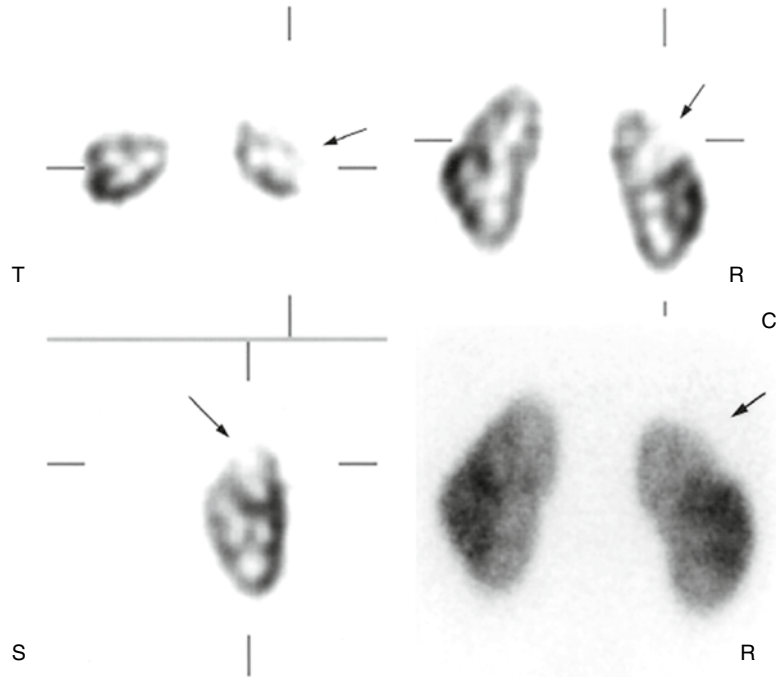

Fig. 12.16 Single photon emission computed tomography (SPECT) and conventional planar scintigraphy in pyelonephritis. This 16-year-old girl with a history of repeated urinary tract infections and vesicoureteric reflux presented with acute onset of right flank pain and fever. Selected transverse (*T*), coronal (*C*), and sagittal (*S*) slices reveal a focal cortical defect in the right upper pole (*arrows*). Conventional planar scintigraphy does not show the defect (*arrow*) as clearly as SPECT

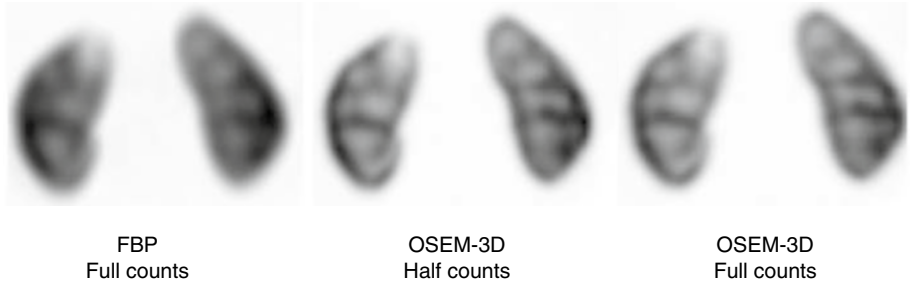

Fig. 12.17 OSEM 3D (Ordered Subset Expectation Maximization) with resolution recovery [54]. *Left*: DMSA SPECT reconstructed with Filtered Back Projection (FBP). *Middle*: Same image with 50 % counts reconstructed with OSEM 3D. *Right*: Same image with 3D OSEM containing full counts

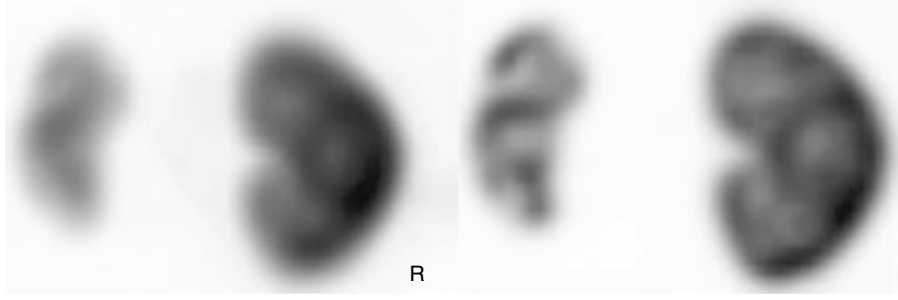

Fig. 12.18 Effect of OSEM 3D and resolution recovery on DMSA SPECT [54]. *Left*: DMSA SPECT reconstructed with Filter Back Projection. *Right*: DMSA SPECT reconstructed with OSEM 3D with resolution recovery

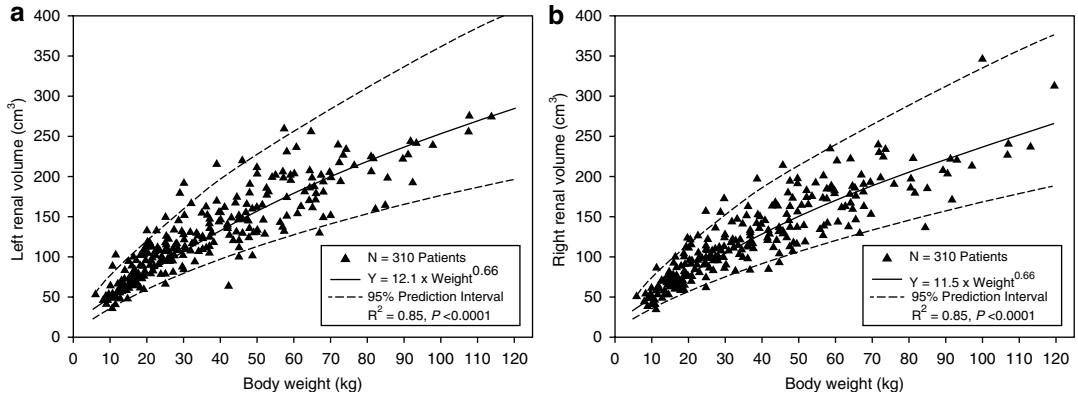

Fig. 12.19 Nonlinear relationship (*solid lines*) between renal volume and body weight for left (**a**) and right (**b**) kidneys with 95 % confidence intervals representing the normal ranges (*dashed lines*). The power models fit the empirical data closely. Male and female patients are pooled together because no gender differences were detected for left or right renal volumes [55]

Clinical Applications

Renal Immaturity/Neonatal Period

When evaluating newborn infants, nuclear medicine clinicians should recognize normal renal immaturity and its effect on the renal handling of radiotracers [56]. The glomerular filtration rate (GFR) per unit of surface area in the newborn is approximately 30 % of the adult rate. During the first few days of life, there is a dramatic rise in the renal function, followed by a more gradual increase with adult levels (normalized to BSA) reached at 6 months to 1 year of age. Studies of very low birth weight (VLBW) premature infants have revealed dramatically lower renal function with a much slower rise to normal levels [57].

Most newborns are able to urinate within 24 h from birth. In problem cases, radionuclide imaging is useful to assess renal function, even in the absence of diuresis. The combination of ultrasonography and scintigraphy has proved useful for evaluating renal function in this group of patients.

Depending on renal maturation, renal uptake of dynamic tracers may be lower in newborns than in older children and adults. In addition, intrarenal transit time and excretion of these tracers may be slow at this age. During the first or second week of life, a dynamic renogram may demonstrate faint, delayed renal uptake of the tracer with or without bladder activity at the expected times. If tracer is seen in the bladder within 2–5 min, the amount present may be lower than in older children. Background may be high throughout the study, reflecting low plasma clearance of the tracer. As the child matures and renal function increases, renal uptake, intrarenal transit time, and excretion of tracers reach normal values. Some normal newborns, however, show apparently normal handling of dynamic renal tracers (Fig. 12.7).

Renal function immaturity also may be reflected on ^{99m}Tc-DMSA studies. In normal newborns, there may be relatively low kidney/background ratio. Intravenous urography is not the initial method of choice in this age group because of the poor concentration of contrast agents by the kidneys and the relatively high doses of contrast agents that must be used [58–60].

Hydronephrosis/Obstruction

Hydronephrosis is one of the most common indications for radionuclide evaluation of the kidneys in pediatric patients. Findings on renal scintigraphy vary depending on hydration, age, type, and severity of the disease, site of obstruction, unilateral or bilateral pathology, presence

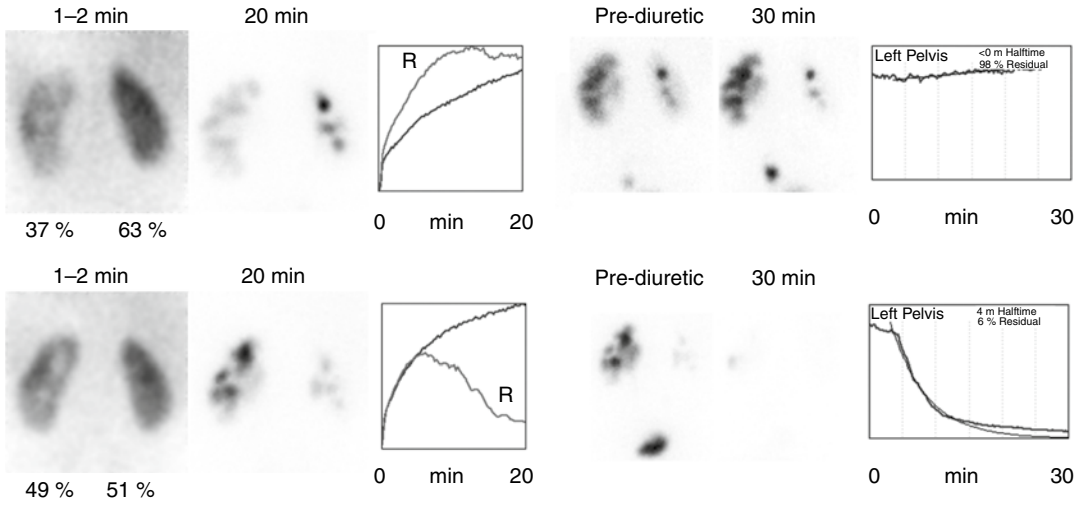

Fig. 12.20 Left hydronephrosis with ureteropelvic junction obstruction in a 2-month-old boy. *Top row*: Preoperative study reveals differential function 37 % left and 63 % right. Both kidneys have mild cortical retention, consistent with immaturity, and markedly delayed spontaneous collecting system drainage. During diuresis, there is prolonged retention of tracer in the left renal pelvis with a clearly obstructive pattern. *Bottom row*: Following left pyeloplasty, differential renal function is 49 % left and 51 % right. With maturation, the right kidney demonstrates a nearly normal time-activity curve. The left kidney still has markedly delayed spontaneous drainage, but during diuresis, there no longer are findings of obstruction (*left*, 49 %; *right*, 51 %)

or absence of reflux, and recent surgery. In cases of hydronephrosis caused by obstruction at the ureteropelvic junction or ureterovesical junction, dynamic renal scintigraphy demonstrates abnormalities in structure and function on the involved side. With posterior urethral valves, there is bilateral renal involvement, and patients who present during early infancy may have severe obstruction with impaired renal function. In young children, the evaluation of function in the presence of obstruction does not give a reliable indication of the potential for recovery. It does indicate, however, the minimal function that may be expected.

In the young, even poor renal function caused by chronic obstruction is potentially reversible [61]. In these patients, ultrasonography should be obtained to search for surgically correctable lesions. Serial renal scintigraphy can be used to assess recovery as renal function may improve once the obstruction has been relieved. In newborn hydronephrosis without obvious obstruction, the hydronephrosis may resolve spontaneously, suggesting that some hydronephrosis in neonates and infants is a manifestation of physiologic change during development [62–66]. Thus, in a young child with hydronephrosis, one should not arrive at the diagnosis of obstruction or prognosis based on a single examination. A single study provides only a "snapshot" of a changing situation. Serial studies over time provide a better indication of the natural progression of the hydronephrosis and help determine the presence of an obstruction (Figs. 12.20, 12.21, 12.22, 12.23, and 12.24).

With dynamic renography a hydronephrotic kidney initially will appear as a rim of tracer accumulating in the renal parenchyma surrounding a dilated collecting system. As dynamic imaging continues, the pelvicaliceal system slowly will fill with tracer. The rate of appearance and the amount of the tracer in the pelvicaliceal system will depend on the cortical function of the hydronephrotic kidney and the degree of collecting system obstruction. Depending on the severity and duration of the obstruction, tracer may begin to accumulate in the renal pelvis within 3–6 min despite severe dilatation; with prolonged severe obstruction, however, tracer accumulation in the dilated renal pelvis is much slower.

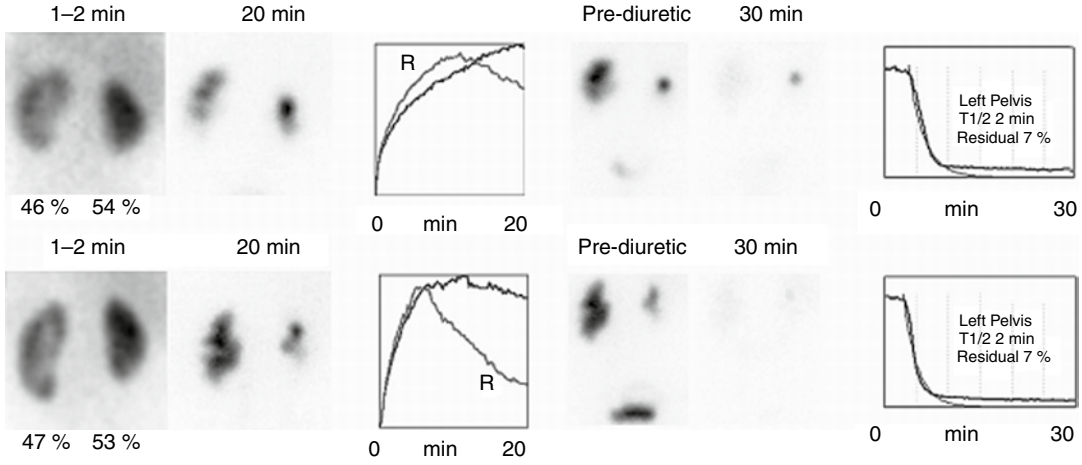

Fig. 12.21 Prenatal diagnosis of left hydronephrosis in a 2-month-old with mild ureteropelvic junction obstruction by intravenous urography. *Top row*: Preoperative ^{99m}Tc-MAG3 study reveals lack of spontaneous drainage from the left kidney. However, there was rapid washout of tracer following diuretic challenge with a washout half-time ($t_{1/2}$) of 2 min and a 30-min residual of 7 %. *Bottom row*: ^{99m}Tc-MAG3 study 3 months after left pyeloplasty. Differential renal function is stable with improved spontaneous drainage from the maturing right kidney. The diuretic phase is unchanged from the preoperative study. Ultrasonography and intravenous urogram revealed mild postoperative improvement

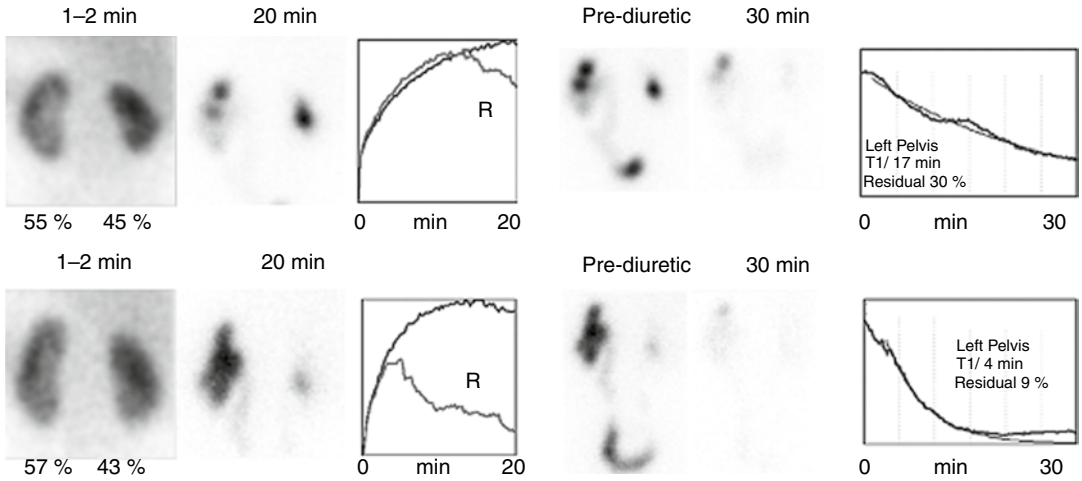

Fig. 12.22 A 1-month-old girl with prenatal diagnosis of left hydronephrosis and no treatment. *Top row*: ^{99m}Tc-MAG3 study shows lack of significant spontaneous drainage from the left kidney. The washout half-time is 17 min with a 30-min residual of 30 %. *Bottom row*: Approximately 1 year later, there is an improvement in spontaneous drainage from the left kidney, a post-diuretic washout half-time of 4 min, and a 30-min residual of 9 %

The apparent function of the hydronephrotic kidney will be affected by the severity of urinary obstruction. High pressure in the pelvicaliceal system can result in reduced renal blood flow and decreased cortical function. In the young, this can be reversed after relief of the urinary obstruction. A more accurate assessment of renal function can be attained after the obstruction is relieved (Fig. 12.25) [67, 68].

The amount of tracer uptake in the renal parenchyma is directly related to the functional capacity of the kidney. Renal blood flow decreases rapidly with increased pressure in the pelvicaliceal system (Fig. 12.3). This can be reversible for

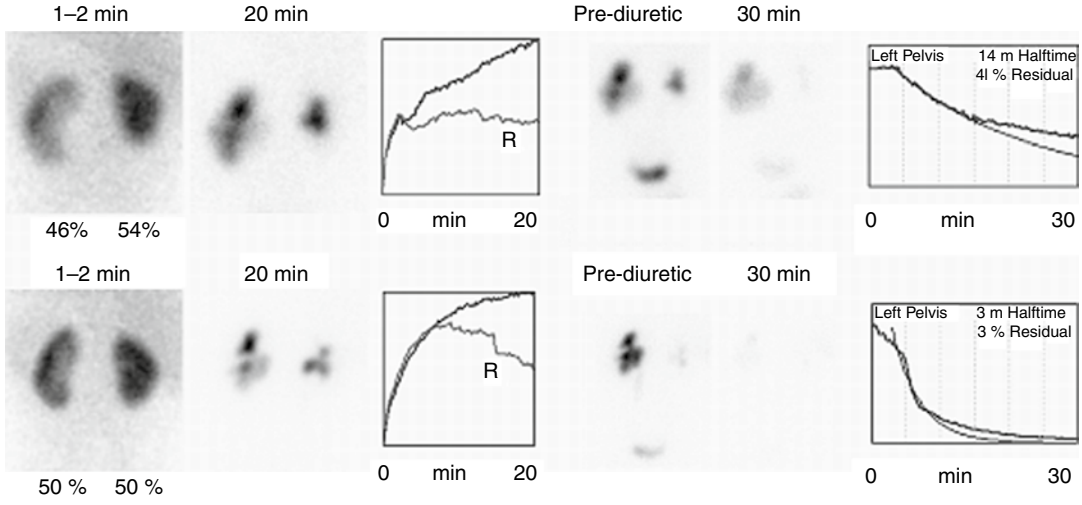

Fig. 12.23 A 2-month-old boy with congenital left hydronephrosis ^{99m}Tc-MAG3 study. *Top row*: Lack of significant spontaneous drainage from the left kidney. Following diuretic challenge, there was a washout halftime of 14 min with a high (41 %) 30-min residual. *Bottom row*: Following left pyeloplasty, there is an improvement on the split renal function to 50 % and a rapid washout following diuretic challenge ($t_{1/2}$ = 3 min, 30-min residual = 3 %)

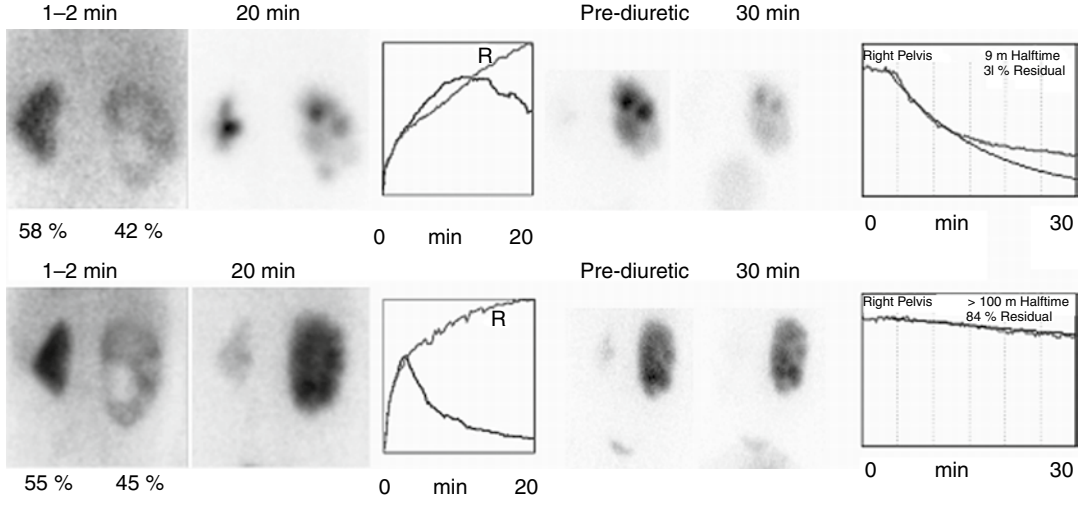

Fig. 12.24 Worsening ureteropelvic junction obstruction. A 6-month-old boy with prenatal diagnosis of right hydronephrosis. *Top row*: Baseline ^{99m}Tc-MAG3 study showing right hydronephrosis, lack of spontaneous drainage from the right kidney, and washout following diuretic challenge (washout $t_{1/2}$ = 9 min and 31 % residual). *Bottom row*: 6 months later, there is no significant spontaneous drainage from the right kidney and the diuretic renogram is grossly abnormal ($t_{1/2}$ > 100 min with a 30-min residual of 84 %). There is an apparent slight increase in right renal function. The patient underwent right pyeloplasty to relieve the obstruction

a period of time, but if increased pressure is persistent, reduction in blood flow and function can become permanent. In studies of hydronephrosis due to obstruction, the obstructed kidney may take up more tracer than the contralateral side. It has been thought that the stressed, obstructed kidney develops transiently increased blood flow.

Over time, renal function in an obstructed kidney will be reduced. It has been suggested that in preoperative patients in whom the cortical

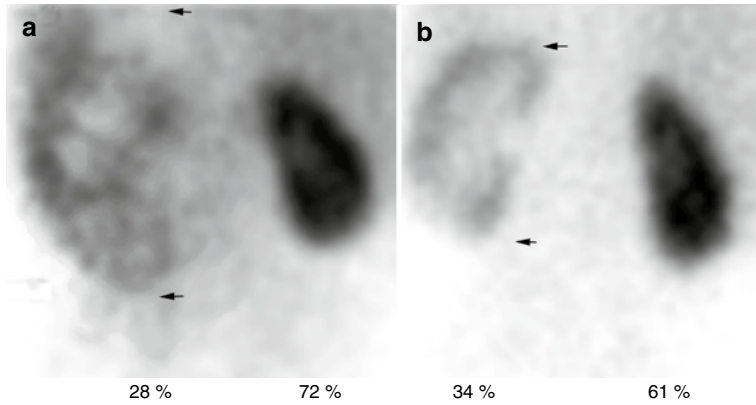

Fig. 12.25 Left ureteropelvic junction obstruction, preoperative and postoperative ^{99m}Tc-MAG3 parenchymal phase images. A 2-year-old patient with left ureteropelvic junction obstruction, before and after left pyeloplasty. (**a**) The preoperative image reveals a large left kidney with low cortical uptake and severe pelvicaliectasis. The cortical transit time of the tracer was prolonged. (**b**) The postoperative study shows a smaller left kidney with improved tracer uptake and normal cortical transit time. *Arrows* indicate upper and lower limits of the left kidney

time-activity curves appear more nearly normal than the total kidney curve, there is a strong likelihood of improvement after the obstruction is relieved. Conversely, abnormal cortical curves may be associated with a poor prognosis for functional improvement [69]. It usually is possible to identify a single site of obstruction at the ureterovesical or the pelvicaliceal junction, but obstruction at both the pelvicaliceal and ureterovesical junctions may be difficult to detect. Detection of the level of obstruction depends on adequate renal function and the presence or absence of dilatation of the pelvicaliceal system and ureter [70]. Differentiating obstructed from dilated nonobstructed systems can be achieved by serial imaging after intravenous administration of furosemide (diuretic renography).

Pyelonephritis

Clinical Features

Urinary tract infection (UTI) is a common problem in children. Presenting signs and symptoms of children with UTI are varied and sometimes confusing. Infection may be confined to the bladder (cystitis); it may involve the upper collecting systems (ureteritis, pyelitis) or the renal parenchyma (pyelonephritis). This differentiation can be difficult to make on clinical grounds alone [71]. Patients may present with fever, flank pain or tenderness, malaise, irritability, leukocytosis, and bacteriuria, but there may be no clear indication that there is renal parenchymal infection. Occasionally, patients with pyelonephritis may present with fevers of unknown origin, particularly in neonates and infants. Prospective clinical studies have shown that commonly used clinical and laboratory findings are unreliable in differentiating acute pyelonephritis from lower UTI in children [72]. Acute pyelonephritis can result in irreversible renal damage (scarring), which in the long term leads to hypertension and/or chronic renal failure [73]. Experimental and clinical studies have shown that renal scarring can be prevented or reduced by early effective antimicrobial therapy of pyelonephritis [74–76].

Vesicoureteral Reflux and Pyelonephritis

Although the coexistence of vesicoureteral reflux and pyelonephritis is well documented (see Chap. 13), many cases of pyelonephritis occur in the absence of documented vesicoureteral reflux. Once acute pyelonephritis occurs, the subsequent development of renal scarring may be independent of vesicoureteric reflux [39, 77–83]. That is,

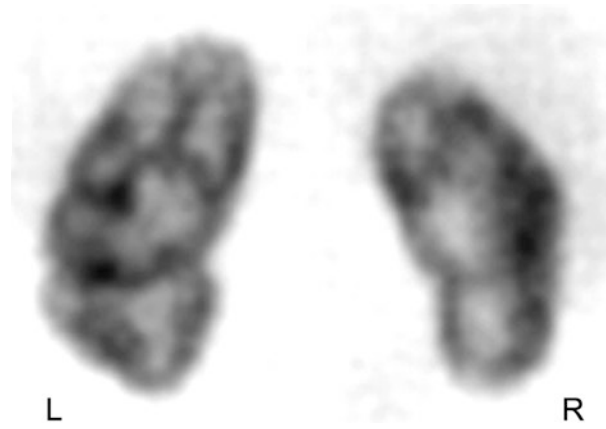

Fig. 12.26 Fetal lobation demonstrated on a ^{99m}Tc-DMSA cortical scan in a 1 month-old infant with vesicoureteral reflux. There is decreased relative function in the right kidney, but no focal cortical defects are identified. Normal fetal lobation is seen in both kidneys

some patients presenting with febrile UTI in the absence of documented vesicoureteral reflux can develop renal scaring. Therefore, it may be prudent to assess renal cortical integrity in all patients with a febrile UTI. It would seem unwise to limit evaluation of cortical integrity in UTI only to those patients who present with a history of vesicoureteral reflux. Diminished ^{99m}Tc-DMSA uptake at the site of acute pyelonephritis probably reflects both tubular dysfunction and focal ischemia related to microvascular changes [93, 94, 95].

Cortical Scintigraphy of Pyelonephritis

Renal cortical scintigraphy with ^{99m}Tc-DMSA can be a reliable, simple, and practical imaging technique for routine use in the initial evaluation and follow-up of children with febrile UTI. It is useful to identify the degree of renal damage and to assess recovery or residual renal damage. The high sensitivity of ^{99m}Tc-DMSA scintigraphy for the early diagnosis and localization of acute pyelonephritis is well established [50, 51, 84–86]. The sensitivity of ^{99m}Tc-DMSA scintigraphy for pyelonephritis is 96 % and the specificity is 98 % [87]. Imaging strategies in patients suspected of pyelonephritis or patients with sudden onset of fever, flank pain, and pyuria or bacteriuria should include ^{99m}Tc-DMSA scintigraphy [88–90].

Images should be obtained in the posterior and posterior oblique projections using a parallel-hole, high or ultrahigh-resolution collimator. Pinhole magnification provides greater diagnostic sensitivity than the parallel-hole collimator for the detection of small focal cortical defects. Technetium-99m-DMSA SPECT provides additional sensitivity and specificity over planar imaging in the evaluation of patients suspected of having pyelonephritis (Figs. 12.15 and 12.16) [85, 91, 92].

In normal kidneys, ^{99m}Tc-DMSA scintigraphy shows a pattern of tracer distribution reflecting the morphology of the renal cortex. No tracer uptake is seen in the medulla or in the collecting system. Flattening of the superolateral aspect of the left cortex may be due to splenic impression. Irregularities in the contour of the renal image may be due to fetal lobations (Fig. 12.26). In these instances, cortical thickness and tracer uptake are normal. Acute pyelonephritis usually appears as a single or as multiple focal areas of reduced or absent uptake with a soft edge, without deformity of the renal outline or apparent loss of volume (Figs. 12.27, 12.28, 12.29, and 12.30).

In some cases, reduced uptake may be accompanied by an acute increase in volume of the affected area. Although the majority of lesions occur in the upper or lower poles, the mid-zone is not protected, and cortical defects can be seen in this area, also. By comparison, renal scars typically show loss of cortical volume with relatively sharp edges to the cortical defect. A less common scintigraphic pattern is one of diffusely decreased tracer uptake throughout an enlarged kidney. If treated appropriately within 48 hours, acute

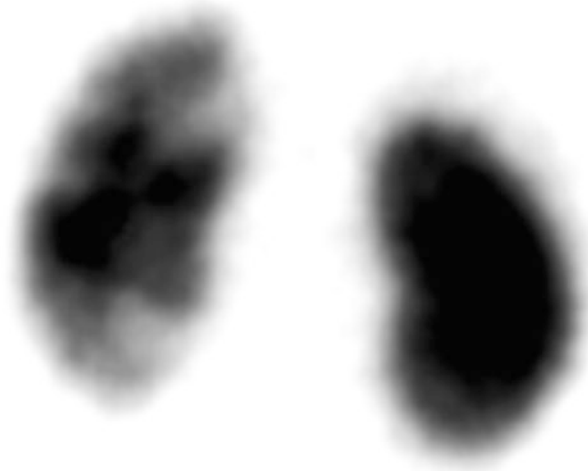

Fig. 12.27 Acute multifocal pyelonephritis in a 2-year-old boy who presented with recurrent fever and left flank pain. The patient had no documented vesicoureteric reflux. ^{99m}Tc-DMSA planar scintigraphy reveals several cortical defects in the left kidney

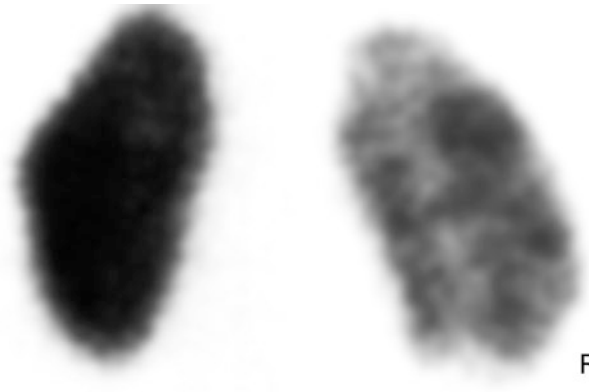

Fig. 12.28 Diffuse acute pyelonephritis. Diffuse and focal pattern of decreased ^{99m}Tc-DMSA uptake in an enlarged (swollen) right kidney

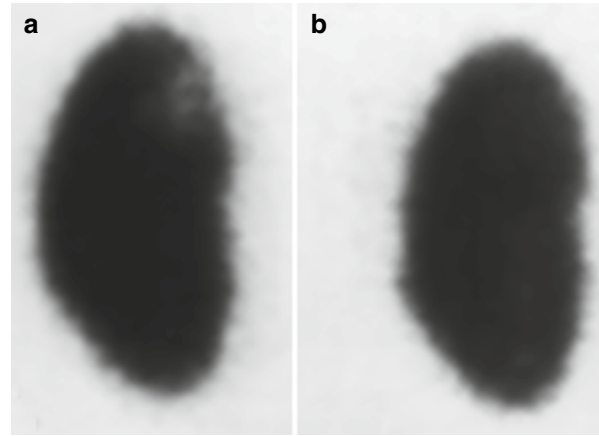

Fig. 12.29 Resolution of acute pyelonephritis. (**a**) Magnified image of a 3-month-old infant at the time of acute febrile urinary tract infection shows focal decreased uptake of ^{99m}Tc-DMSA in the medial aspect of the left upper pole. (**b**) Corresponding image 6 months later shows complete resolution

pyelonephritis may resolve completely and scintigraphic images typically would become normal within 4–6 months (Fig. 12.31).

Alternatively, without adequate and early antibiotic treatment, a permanent cortical scar may develop. A mature cortical scar is usually associated with contraction and apparent loss of volume of the involved cortex. This may manifest as cortical thinning, flattening of the renal contour, or a wedge-shaped defect. The

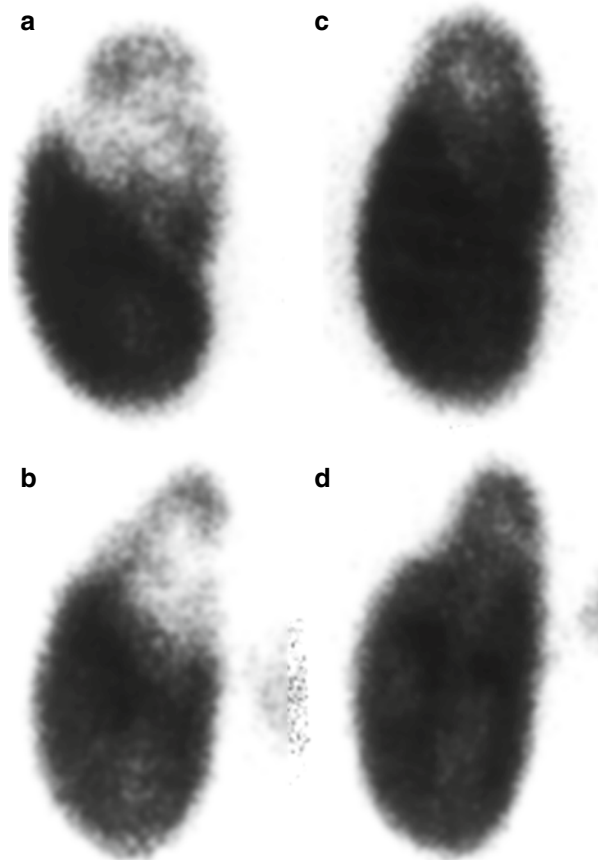

Fig. 12.30 Progression of acute pyelonephritis to cortical scar. Posterior (**a**) and posterior oblique (**b**) images of the left kidney from a 5-year-old child at the time of acute febrile urinary tract infection demonstrate focally decreased ^{99m}Tc-DMSA uptake in the upper pole with preserved renal outline and without evidence of volume loss. Corresponding images obtained 1 year later (**c**, **d**) show contraction and apparent loss of volume of the upper pole, consistent with cortical scarring

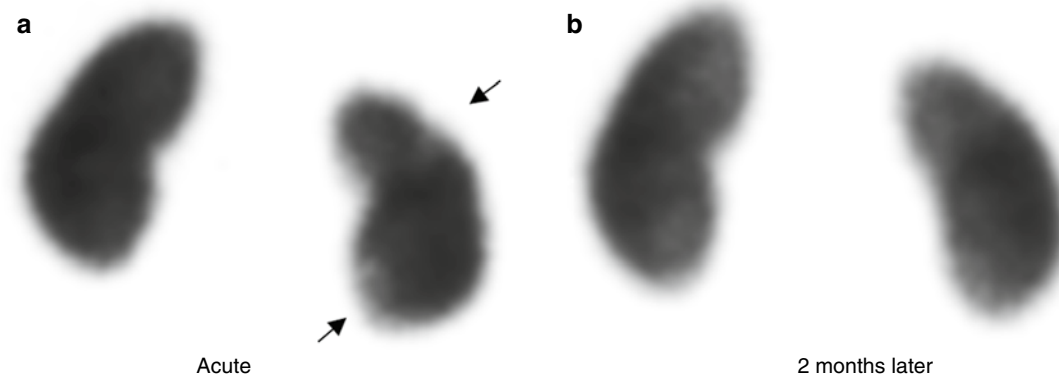

Fig. 12.31 Recovery of cortical function with rapid antibiotic therapy of a febrile urinary tract infection. The 9-year-old girl presented with right flank pain and fever. A urinary infection was diagnosed. (**a**) ^{99m}Tc-DMSA demonstrates focal cortical defects (*arrows*) in the right kidney. Ultrasonography was normal. (**b**) Two months later, a follow-up ^{99m}Tc-DMSA cortical renal scan shows complete resolution of cortical defects. With rapid antibiotic therapy of pyelonephritis, cortical scarring can be avoided

scintigraphic pattern of a maturing scar varies according to the severity, age, and location of the lesion as well as the rate of growth of surrounding normal tissue.

The diminished uptake of ^{99m}Tc-DMSA in areas of acute inflammation probably reflects both focal tubular cell dysfunction and ischemia [81, 93, 94, 95].

Intravenous Urography and Renal Ultrasonography

The limited sensitivities of intravenous urography and ultrasonography for identifying early renal infection have been well-studied [87, 88, 96–98]. Ultrasonography is very useful in diagnosing renal or perirenal abscesses, but less valuable in acute pyelonephritis in which renal enlargement may be the only abnormal finding. Intravenous urograms are abnormal in only 24–26 % of patients with acute pyelonephritis [96, 98]. Possible abnormal urographic findings include a renal pelvis of small volume, dilated and distorted pelvicaliceal structures, renal enlargement, delayed pyelogram, reduced concentration of urographic material, and dilatation of the ureter without obstruction. In contrast to urography, cortical scintigraphy can detect cortical defects that do not deform the renal outline or the collecting system [97, 99]. Computed tomography is an effective technique for documenting the nature of parenchymal involvement, particularly for the evaluation of the perinephric space. Concern about CT radiation exposures limits its use; therefore, routine use in the initial and follow-up evaluation of children with UTI is not practical, and CT should be reserved for complicated cases [100, 101]. The role of magnetic resonance imaging (MRI) in the diagnosis of acute pyelonephritis remains to be defined [102].

In the diagnosis of pyelonephritis, the combination of ultrasonography and cortical scintigraphy is useful. Changes secondary to pyelonephritis may be recognized on ultrasonography as hyperechoic or hypoechoic foci, loss of corticomedullary differentiation, focal or diffuse renal enlargement, and mild or moderate dilatation of the renal pelvis. However, renal ultrasonography has proved to have a low sensitivity for the detection of acute focal inflammatory changes of the renal cortex. In a prospective study, ultrasonographic changes consistent with acute pyelonephritis were found in only 39 % of the children with scintigraphically documented acute pyelonephritis. When abnormal, ultrasonography underestimated the number and extent of the pyelonephritic lesions [77]. Ultrasonography should not, therefore, be regarded as the primary imaging technique for the diagnosis of acute pyelonephritis. Ultrasonography is, however, highly reliable for the detection of hydronephrosis and of the congenital abnormalities that may be associated with UTI in some patients.

Renal Vein Thrombosis

Most types of acquired renal disease in newborns are due to circulatory disturbances, such as renal arterial or venous thrombosis. Approximately two-thirds of all cases of renal vein thrombosis occur in the pediatric age group, with most seen during the neonatal period. In older children, renal vein thrombosis may develop as a consequence of nephrotic syndrome or severe illness. Nephrotic syndrome is a very frequent cause of large-vessel thrombosis because of urinary losses of antithrombin III, protein C, protein S, and other factors. In infants renal vein thrombosis usually is related to venous stasis secondary to shock, septicemia, or dehydration. The diagnosis of renal vein thrombosis may be suggested by the presence of oliguria, mild hematuria, and proteinuria. Renal vein thrombosis also is seen in infants of diabetic mothers and children with congenital heart disease. Consumptive coagulopathy or intravascular coagulation may be present in some of these patients [78, 103–109].

Renal vein thrombosis has been described as a bilateral disease, with asymmetric involvement. Because of this characteristic, a minor lesion in the apparently noninvolved kidney may be missed. Most frequently, the thrombus originates in the interlobar or arcuate veins and less commonly in the main renal vein. The thrombus may extend into the main renal vein and the inferior vena cava, or in a retrograde fashion, it may involve the renal cortex. The venous obstruction then leads to infarction and hemorrhage. Blood leaking into the interstitium and renal tubules may ultimately result in fibrosis. Most patients with renal vein thrombosis are treated medically with maintenance of normal fluid and electrolyte balance [107].

There is considerable variability in the urographic identification of renal vein thrombosis. In

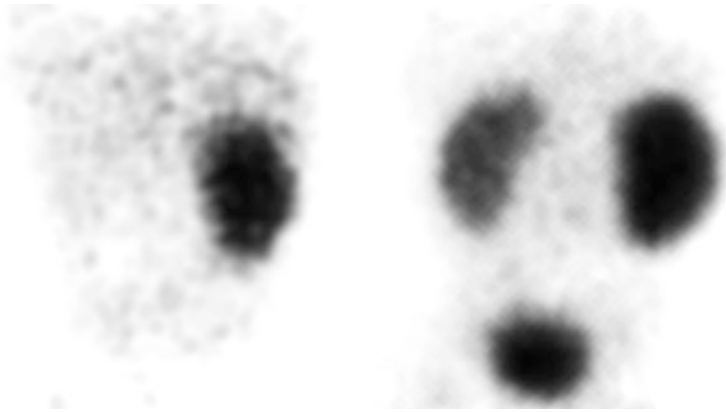

Fig. 12.32 Renal vein thrombosis. This ^{99m}Tc-DMSA study was performed in a premature, 1,400-g female infant who developed hypertension after withdrawal of an umbilical artery catheter. Ultrasonography showed two kidneys of normal size. On the initial study (*left panel*), the kidney is not visualized. After treatment with hydralazine, the patient became normotensive, and another study 3 weeks later showed return of left renal function (*right panel*)

most patients with this condition, the kidney involved is not visualized by intravenous urography. Before modern nuclear medicine techniques were widely employed, it was thought that affected renal units not visible on initial urographic examination virtually ensured an atrophic, functionless kidney later [110]. Doppler ultrasonography typically shows decreased or absent flow in the affected kidney or renal vein.

Renal scintigraphy using ^{99m}Tc-MAG3 or ^{99m}Tc-DMSA is a sensitive method for screening patients with renal vein thrombosis because the findings on serial renal scintigraphy that show the evolution of renal function correlate well with the ultimate outcome [111].

In severe cases, there may be no perfusion or apparent function in the involved side. A follow-up study may be useful to demonstrate the residual renal function after recovery. Radionuclide studies may reveal information of prognostic significance, with a normal study predicting a rapid and complete recovery (Figs. 12.32 and 12.33).

Renal Infarction

Renal infarction can occur in patients with cyanotic congenital heart disease, polycythemia, atrial fibrillation, dehydration, or trauma. Aortic thrombosis and renal infarction are also well-recognized complications of prolonged umbilical artery catheterization. Treatment with thrombolytic agents has produced resolution of the clot and recovery of renal function in some cases. Technetium-99m-DMSA scintigraphy demonstrates focal perfusion defect(s) in the affected kidney(s) (Fig. 12.34).

Hypertension

The prevalance of hypertension in children is less than 2.5 % [112], but the reported prevalance of secondary hypertension varies with the source of patients [113–115]. The younger the patient, the more likely that hypertension has a secondary cause, and the most common cause of secondary hypertension in children is renal disease. Renal disease associated with hypertension can be caused by diseases that involve the renal arteries or the renal parenchyma. In a study of 563 pediatric patients with secondary hypertension, 78 % had a renal abnormality and 12 % were diagnosed with renal artery disease [114]. Less frequently, secondary hypertension may be caused by disorders of the endocrine, cardiovascular, or nervous systems. Radionuclide renal studies play an important role in the evaluation and treatment of hypertension in infants and children.

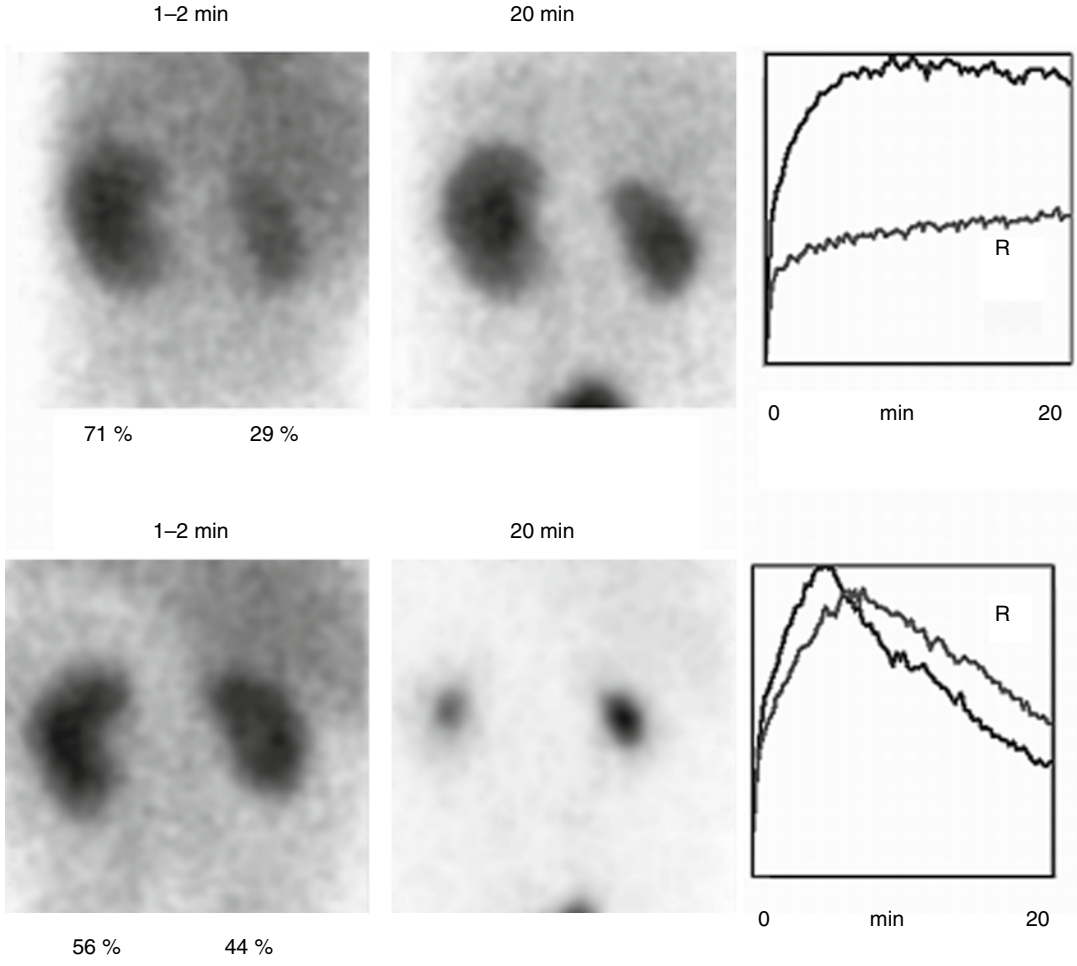

Fig. 12.33 Renal vein thrombosis demonstrated by a ^{99m}Tc-MAG3 renogram in a 1-week-old girl presenting with oliguria, cardiomegaly, and hypertension. *Top row*: First study shows asymmetric renal function (L>R) with bilateral delay in transit time. There is marked cortical retention of tracer. *Bottom row*: 1 month later, there is more symmetric renal function (L=56 %, R=44 %) and a normalization of cortical transit. There is minimally delayed drainage of tracer from the right pelvis. The time activity curve demonstrates a longer time to peak and slower drainage of the collecting system on the right

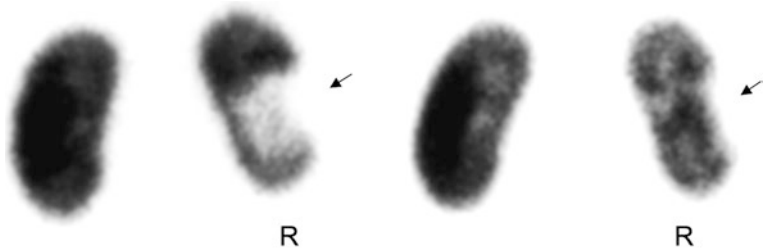

Fig. 12.34 Renal infarct. A 16-year-old boy with cyanotic congenital heart disease had undergone several surgical interventions and presented with acute right flank pain. *Left*: Initial ^{99m}Tc-DMSA scintigraphy shows a well-defined defect in the right kidney due to ischemia. *Right*: A follow-up study 1.5 months later shows considerable resolution of the defect (*arrow*), but there is a persistent scar

Some of the renal causes of hypertension, such as infarction, postpyelonephritic scarring, and posttraumatic lesions, are easily diagnosed by conventional renal scintigraphy. Both dynamic and static renal scintigrapy are very sensitive for the identification of renovascular hypertension [95, 109, 116]. On dynamic scintigraphy, the affected kidney is usually smaller and shows less uptake than the contralateral kidney. With mild renal artery stenosis, a renogram may appear normal. When stenosis is severe, however, excretion of tracer in the collecting system is delayed or even absent during the 20-min observation period. Parenchymal retention of the tracer increases with severity of stenosis. Technetium-99m-DMSA scintigraphy in patients with renovascular hypertension typically reveals renal asymmetry; the affected kidney is smaller, has decreased relative function, and may demontrate cortical defects.

A kidney with a stenotic artery may remain adequately perfused due to the renal autoregulation mechanism. The radionuclide renal study therefore may appear normal in many patients with renal artery stenosis. The efficacy of renal scintigraphy for the diagnosis of renovascular hypertension, however, can be improved by the use of angiotensin-converting enzyme (ACE) inhibitors, such as captopril. These block the formation of angiotensin II, resulting in dilatation of the efferent arterioles and a decrease in the transcapillary pressure gradient. This can lead to a marked decrease in glomerular filtration in a kidney with significant renal artery stenosis. This stimulated loss of renal function can be detected by renal scintigraphy and renography [117–121].

The choices of radiopharmaceutical, ACE inhibitor, and examination technique vary among institutions. In the original studies in pediatric patients, ^{99m}Tc-DTPA was used [118]. Subsequent experience has shown that either glomerular or tubular agents can be used. Technetium-99m-MAG3 captopril renography appears to be effective. The radiopharmaceutical of choice for detecting focal parenchymal abnormalities such as infarcts and pyelonephritic scars is ^{99m}Tc-DMSA [52, 88, 116, 122]. Administration of captopril may cause a decrease in the renal ^{99m}Tc-DMSA uptake in patients with renovascular hypertension [123].

Either captopril (1 mg/kg, up to 50 mg) or enalaprilat can be used as the ACE inhibitor. To ensure better absorption of captopril, the patient should not eat solids for approximately 4 h before the study. The advantage of enalaprilat is that it is administered intravenously and, unlike oral captopril, its effect does not depend on variable rate of absorption through the gastrointestinal tract.

A significant fall in blood pressure can be observed even after a single dose of captopril. Therefore, the patient should be well hydrated, well monitored, and an intravenous access maintained throughout the study. The blood pressure should be monitored every 5–15 min. The probability of severe hypotensive crisis is even higher with intravenous enalaprilat, so that its routine use is not recommended. Diuretics may exaggerate the hypotensive effect of ACE inhibitors and should not be used in conjunction with captopril renography.

Ideally, both a baseline and stimulated study should be performed. An alternative approach is to obtain the initial study with an ACE inhibitor and then, if the first study is abnormal, repeat the study without the use of ACE inhibitor.

The scintigraphic manifestations of decreased renal function induced by ACE inhibition in the presence of hemodynamically significant renal artery stenosis depend on which radiopharmaceutical is used. The primary effect of ACE inhibitors is decreased GFR. Therefore, the effect of an ACE inhibitor on a ^{99m}Tc-DTPA study will be observed as a varying degree of decreased extraction of tracer and delayed visualization of the collecting system, whereas with the use of tubular agents, prolonged cortical retention of the tracer is seen. Therefore, detection of focal cortical changes is easier with ^{99m}Tc-MAG3 (Figs. 12.35a–c and 12.36).

The typical findings of a positive captopril study include an decrease in the differential renal uptake, an increase in cortical transit time, a prolongation of time to peak, and retention of tracer in the renal parenchyma. Scintigraphic abnormalities in unilateral renal artery stenosis can be appreciated visually by inspection of the images and the renal time-activity curves. Numerical or

semiquantitative evaluation of time-activity curves has been utilized. In the presence of bilateral renal artery stenosis, narrowing is usually asymmetrical, as is the effect of captopril on each kidney. In this case, evaluation of the time-activity curves may be most revealing.

In hypertensive adult patients, scintigraphic abnormalities induced by the administration of captopril appear to be strongly associated with cure or improvement in blood pressure control following revascularization or nephrectomy. Cases in which captopril does not induce scintigraphic changes are associated with failure of revascularization or nephrectomy [124–127]. Such failure may be due to a high prevalence of coexisting essential hypertension. Angiographic demonstration of renal artery narrowing in older patients does not, therefore, necessarily indicate renovascular hypertension, and revascularization may fail to cure hypertension. In hypertensive children, however, a negative captopril renogram rarely is associated with angiographic evidence of renal artery stenosis.

Congenital Anomalies

Ectopic Kidney and Solitary Kidney

One or both kidneys may be displaced in association with, or independent of, other renal malformations. Ectopic kidneys situated in the pelvis may be difficult to visualize on intravenous urography, partly because of interference by surrounding bony structures. Scintigraphy with ^{99m}Tc-DMSA or ^{99m}Tc-MAG3 is helpful for diagnosing renal ectopia or a solitary kidney (Figs. 12.6 and 12.37).

Horseshoe Kidney

With horseshoe-shaped kidneys, fusion is between the two lower poles. Radionuclide studies are useful for assessing functional abnormalities when there are symptoms referable

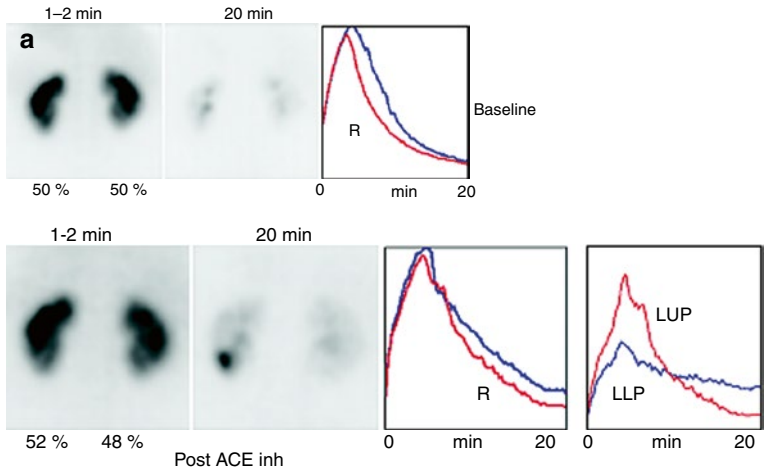

Fig. 12.35 (**a**) Hypertension. Baseline and post-angiotensin-converting enzyme (*ACE*) inhibitor ^{99m}Tc-MAG3 studies. On the baseline study (*top*), renal function is symmetric, and there is no retention of tracer in the renal parenchyma. The time activity curve shows a slightly delayed time to peak in the left kidney. On the post-ACE inhibitor study (*bottom*), relative renal function appears normal. However, there is focal parenchymal retention of tracer in the left lower pole. The time-activity curve of the left lower pole (*LLP*) shows lower peak amplitude and higher residual at 20 min than the left upper pole (*LUP*). (**b**) Baseline study (*top*): 1- to 2-min and 20-min images of the left kidney reveal normal intrarenal distribution of tracer. Similar images of the left kidney (*bottom*) after administration of ACE inhibitor reveal decreased tracer uptake in the left lower pole (1–2 min) and focal parenchymal tracer retention in the same region after 20 min. (**c**) Renal angiography reveals arterial stenosis to the involved segment of the left lower pole. Following selective balloon angioplasty, the patient's blood pressure dropped from 170/110 to 120/60 mmHg

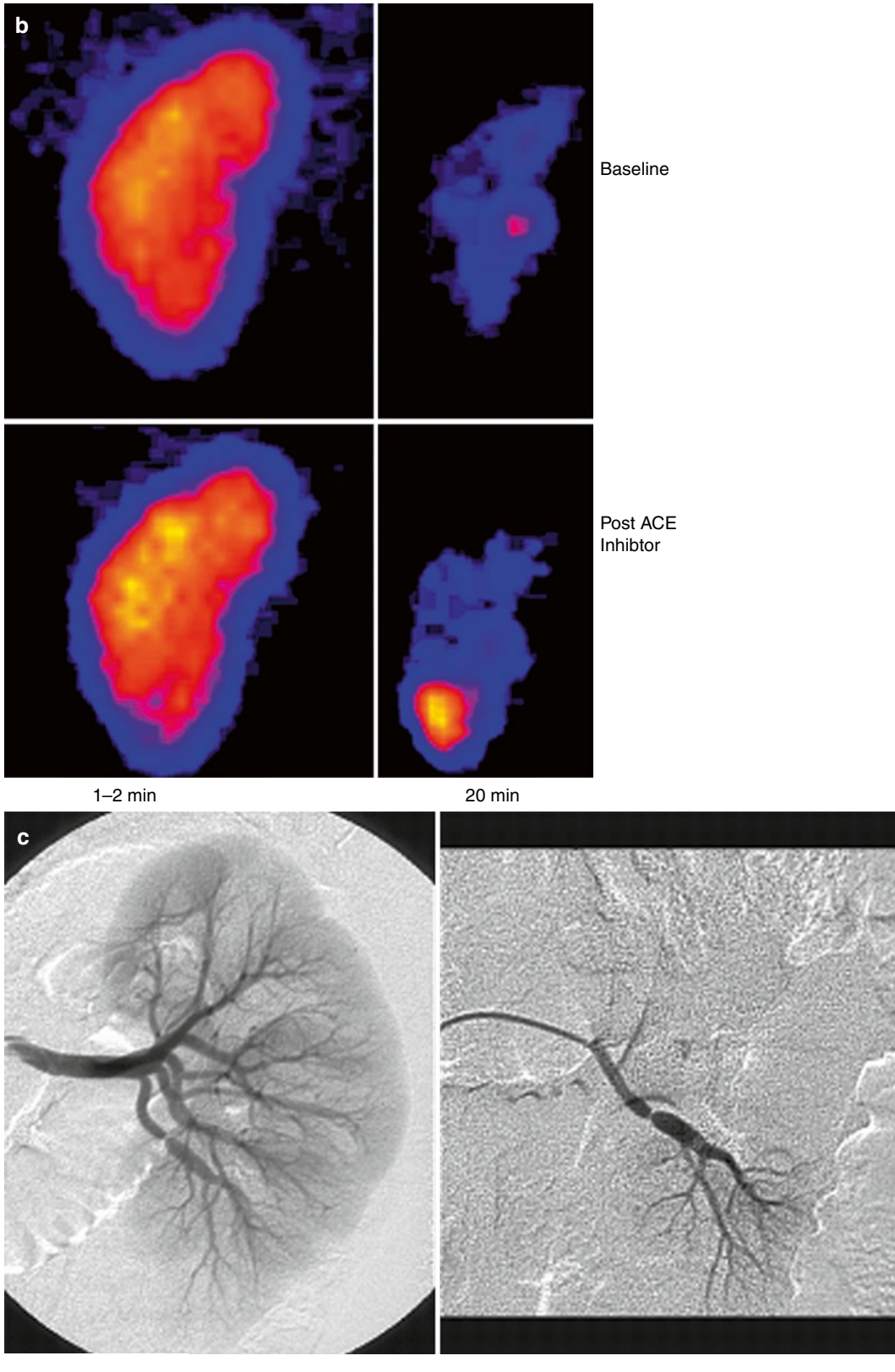

Fig. 12.35 (continued)

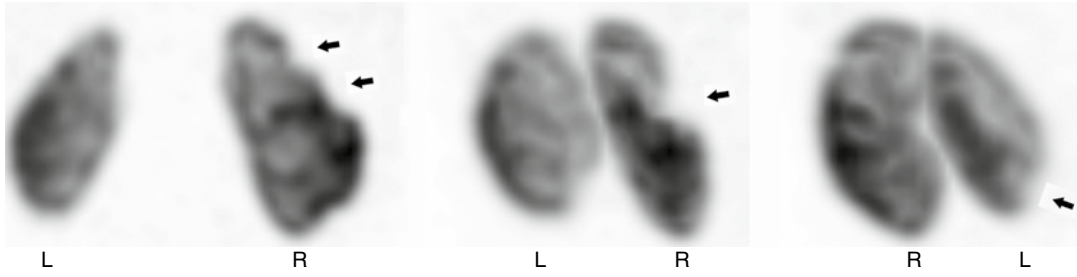

Fig. 12.36 Patient with renovascular hypertension and DMSA SPECT revealing well-defined cortical defects caused by renal artery stenosis. *Arrows* show well-defined cortical defects in the right kidney

Fig. 12.37 Ectopic right kidney. ^{99m}Tc-DMSA renal scan of a 2.5-month-old female showing an ectopic right kidney in the right flank and pelvis

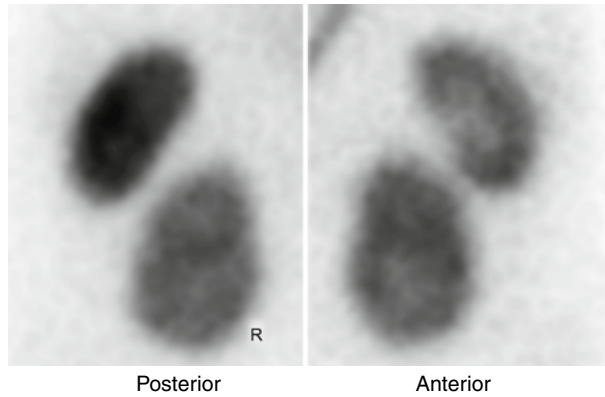

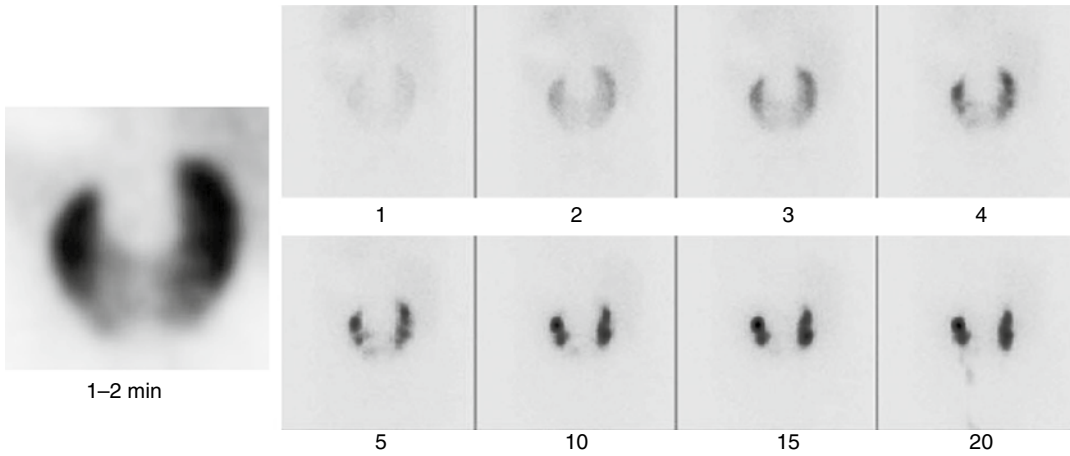

Fig. 12.38 Horseshoe-shaped kidney imaged with ^{99m}Tc-MAG3 dynamic renography

to the kidney, such as infection, hypertension, and hematuria. Technetium-99m-DMSA images (including anterior views) show whether the kidneys are joined by functioning renal tissue or by a fibrous band (Fig. 12.38).

Duplication

Duplication of the ureter and renal pelvis is one of the most common abnormalities of the urinary tract. It occurs bilaterally in 25–30 % of affected patients. The upper pole ureter tends to insert

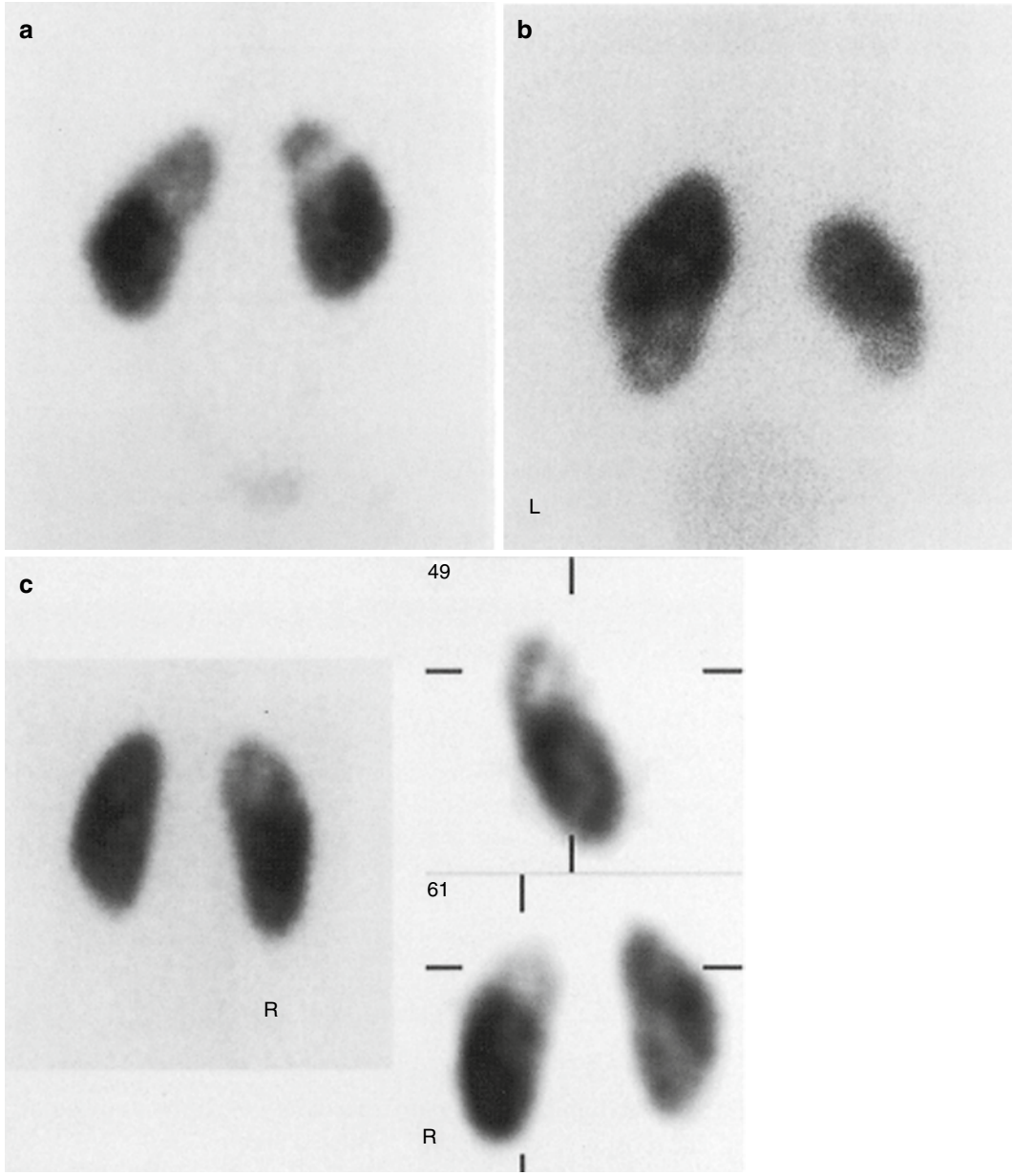

Fig. 12.39 Renal duplication. Three examples of ^{99m}Tc-DMSA scintigraphy in kidneys with duplication. (**a**) Bilateral duplication with relatively poor function in both upper moieties. (**b**) Bilateral duplication with less function in the smaller right kidney and in both lower moieties. (**c**) Conventional planar scintigraphy (*left*) and selected sagittal and transverse SPECT slices (*right*) in unilateral duplication with relatively poor function of the right upper moiety, anteriorly

more caudally and medially than the normally placed lower pole ureter. The ureter from the lower pole is more often affected by vesicoureteral reflux, whereas the upper ureter is more often obstructed. When surgery is contemplated, ^{99m}Tc-DMSA can be used to evaluate the relative function of the upper and lower renal moieties (Figs. 12.12 and 12.39).

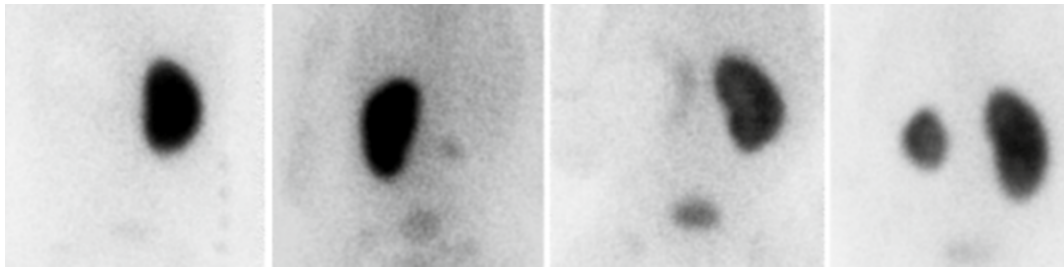

Fig. 12.40 Multicystic dysplastic kidneys (MCDK) imaged with ^{99m}Tc-DMSA scintigraphy. Different appearances illustrating the degree of severity. *0* no evidence of tracer uptake, *1* minimal tracer uptake detected after image enhancement, *2* minimal uptake without image enhancement, *3* substantial uptake in a small kidney

Polycystic Kidney Disease

There are two types of polycystic kidney disease. Autosomal dominant polycystic kidney disease is the more common type, but usually does not present until adulthood. Autosomal recessive polycystic kidney disease usually presents during infancy and is an inherited cystic disorder affecting both kidneys. It is twice as frequent in male infants as in female infants. Scintigraphy with ^{99m}Tc-DMSA often reveals large renal silhouettes and outlines of renal parenchymal uptake surrounding the cysts. The appearance of the scan in polycystic kidney disease depends on the degree of renal involvement. In more severe cases, no functional cortex may be identified by ^{99m}Tc-DMSA.

Multicystic Dysplastic Kidneys

Multicystic dysplasia of the kidney (MCDK) is the most frequent cystic disorder of infants and children [128]. There is marked variation in the size of the lesions and extent of involvement. Classically, MCDK has been described as a mass of noncommunicating cysts with no discernible renal parenchyma or pelvis [129, 130]. Urogenital abnormalities are frequently associated with MCDK. In approximately 75 % of the cases, scintigraphy with ^{99m}Tc-DMSA does not demonstrate tracer uptake in the involved kidney. In some instances, however, some tracer uptake can be seen in small regions of distorted renal parenchyma. Sometimes scintigraphic images of newborns with MCDK will appear similar to the images seen with hydronephrosis (Fig. 12.40).

Prune-Belly Syndrome

Prune-belly syndrome occurs in male infants and manifests as dilatation of the urinary bladder and ureters with a bizarre, wrinkled, flabby abdominal wall [131–134]. The cause of the abdominal muscular deficiency is not known. The most severely affected patients die soon after birth or may be stillborn. Abnormalities associated with this syndrome include pulmonary hypoplasia, renal dysplasia, urethral obstruction, weak chest wall muscles, vesicoureteric reflux, and undescended testes. Dynamic renal scintigraphy reveals a spectrum of findings. Scintigraphy may show dilatation of the pelvicaliceal systems without obstruction; yet others reveal dilatation with apparent obstruction. Technetium-99m-DMSA scintigraphy can help assess regional distribution of functioning renal parenchyma, detect renal scarring, and evaluate the course of the renal disease. Frequently, ^{99m}Tc-DMSA imaging may be delayed until 24 h to allow drainage of the tracer activity from the dilated ureters.

Renal Trauma

Radionuclide imaging is used infrequently in these patients. In some cases, ^{99m}Tc-DMSA scintigraphy can be helpful for detecting nonobvious functional or structural damage to the kidney. Renal scintigraphy can be used to assess recovery or residual damage. Studies using ^{99m}Tc-MAG3 or ^{99m}Tc-DTPA can effectively detect urinary leaks following trauma (Figs. 12.41 and 12.42).

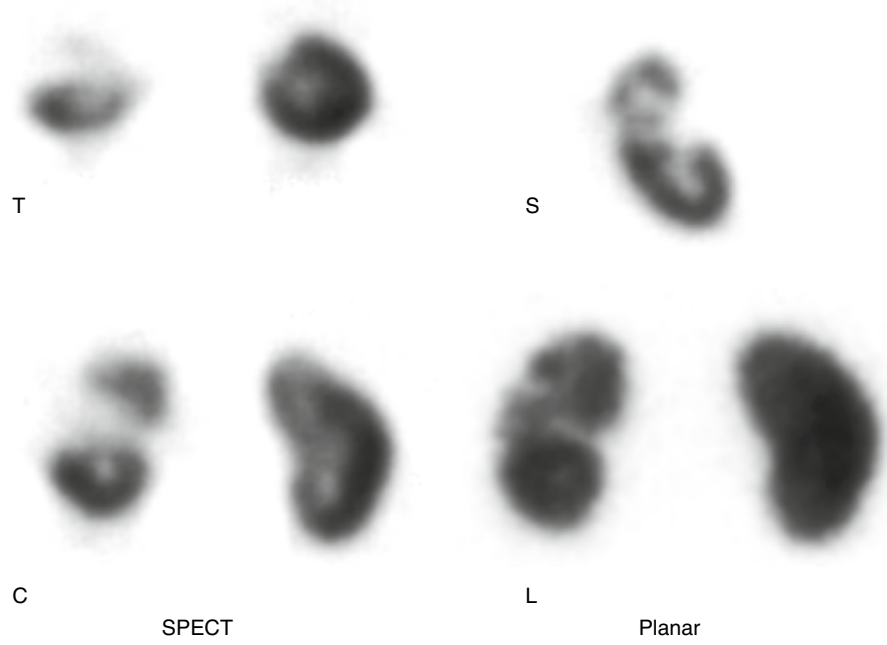

Fig. 12.41 Trauma. Selected transverse, sagittal, and coronal ^{99m}Tc-DMSA SPECT slices as well as planar scintigraphy reveal cortical damage of the left kidney after trauma. These images are from a follow-up study to assess recovery. *T* Transverse; *C* Coronal; *S* sagittal; *L* Left

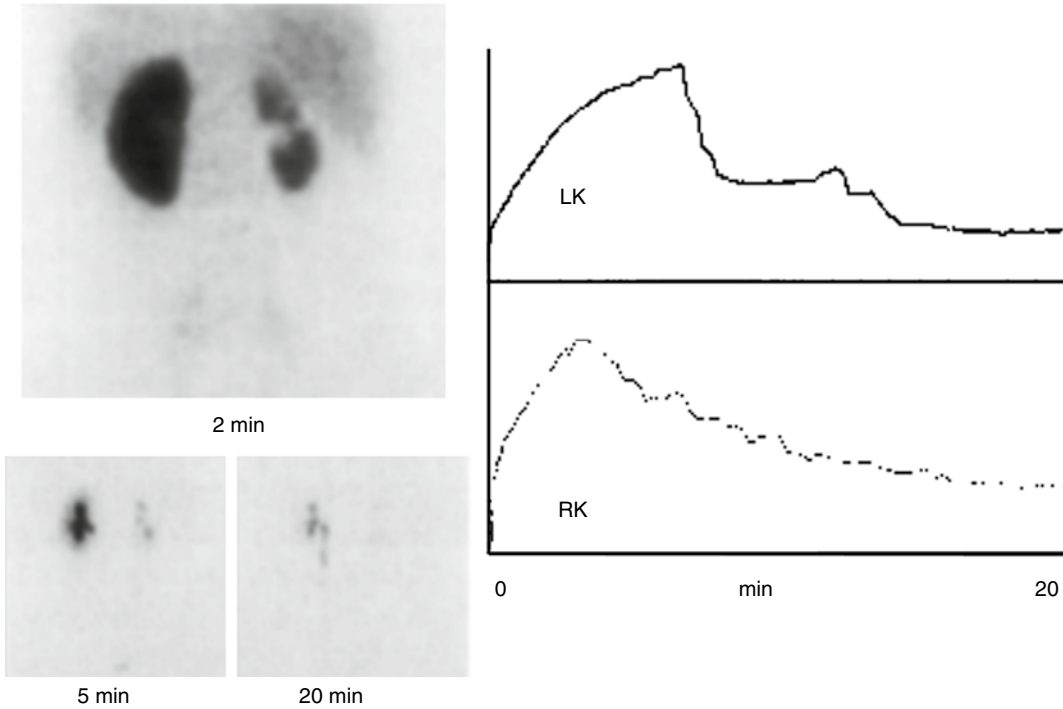

Fig. 12.42 Trauma. Example of a ^{99m}Tc-MAG3 study from a patient who had sustained previous renal trauma. The parenchymal phase (*top left*) reveals a hypertrophic left kidney and a small right kidney with a cortical defect in its midportion at the site of prior traumatic injury. Cortical transit time and drainage are normal bilaterally. *LK* left Kidney; *RK* Right Kidney

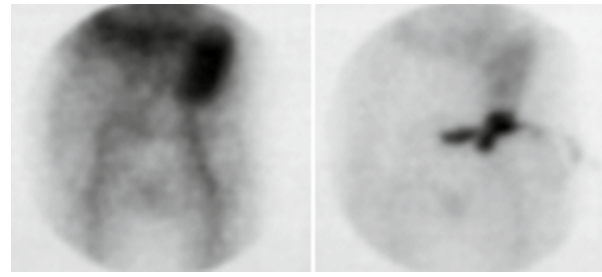

Fig. 12.43 Urinary leak. Postoperatively, this recipient of a renal transplant developed a urinary leak. Selected images of a ^{99m}Tc-MAG3 study (left to right: 2, 20 min) reveal an abnormal accumulation of radiotracer inferior to the left-sided transplant, which corresponded to a urine leak through the transplanted ureter

Acute Renal Failure

With acute renal failure, dynamic renography with ^{99m}Tc-MAG3 will show delayed cortical clearance of tracer. Cortical transit of tracer and appearance of tracer in the renal collecting system is delayed. The typical finding is cortical retention of tracer, but with severe renal insufficiency or renal damage, there may be absent or significantly diminished cortical uptake of tracer. Improvements in function detected on such studies usually precede biochemical changes by 1–2 days. In patients with known urinary obstruction, dynamic renography may be used to exclude concurrent parenchymal disease as a cause of acute renal failure.

Tumors

Renal scintigraphy is very infrequently used in the investigation of renal tumors. Diagnosis and further evaluation of renal and perirenal masses and tumors are carried out with ultrasonography, MRI, and CT. Hypertrophy of a renal column of Bertin may appear as a mass that at times is difficult to distinguish from neoplasm or cyst on urography. Cortical radionuclide imaging can firmly establish the diagnosis of normal renal cortex and absence of tumor [135–137].

Effect of Radiotherapy

Radiation therapy can cause transient or permanent functional defect(s) in the irradiated kidney. This effect can be seen as one or more regions in the kidney with reduced to absent uptake of ^{99m}Tc-DMSA and ^{99m}Tc-MAG3. Prior radiation therapy also can cause cortical retention of ^{99m}Tc-MAG3. Radiation therapy can cause delayed uptake and retention of dynamic renal tracers.

Renal Transplantation

Living Renal Donors

Living donors comprise approximately 60 % of all donors for renal transplants in children [3]. Renal scintigraphy is useful for assessing both renal function and anatomy in living donors. For example, if previously undetected renal abnormalities are seen, a donor may be considered unsuitable. If a radionuclide study on a living donor reveals renal function asymmetry, the surgeon may elect to transplant the kidney showing less function.

Recipients of Renal Transplants

Radionuclide studies are useful during the early and late periods after renal transplantation to assess surgical results and detect complications [138–144]. As radiopharmaceuticals produce no osmotic load and no pharmacologic effects they can be used safely even in the presence of severe renal transplant dysfunction. It is possible with scintigraphic methods to assess perfusion of the transplant during the early and late postoperative periods and assist in the differential diagnosis of diminished graft function, which includes rejection, obstruction, and urinary leak (Fig. 12.43).

If there are no suspected surgical complications, a baseline evaluation of the transplant is often obtained during the first 24 h following transplantation. Subsequent studies are performed depending on the patient's progress. Renal transplants from living donors that have had short periods of

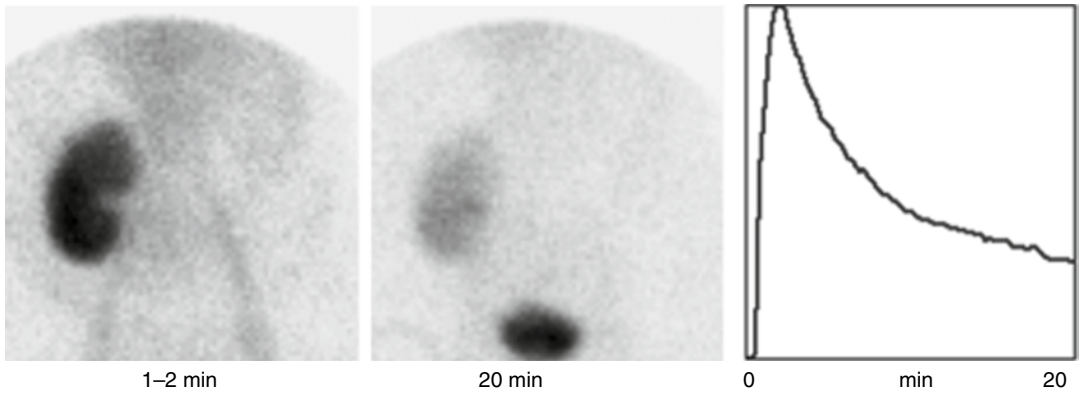

Fig. 12.44 Kidney from a living donor. The recipient was imaged with ^{99m}Tc-MAG3 renography a few hours post-transplantation. Tracer uptake is brisk at 1–2 min, and there is minimal parenchymal or urinary retention at 20 min. The renal time-activity curve shows a time to peak of only 2 min and less than 35 % residual at 20 min. Therefore, there is little post-transplant ATN

cold and warm ischemia often will function immediately after transplantation. The initial uptake of the tracers in these transplants is normal and occasionally more intense than in a normally functioning kidney. In addition, the intrarenal transit time is normal or even faster than normal (Fig. 12.44). After a few days, in the absence of complications, the handling of tracers by the transplant becomes nearly identical to that of normal kidneys.

As many as one-third of grafts, particularly those from deceased donors, are affected by acute tubular necrosis (ATN), which can persist for just a few days or for as long as 2 months after the transplant procedure. In patients with ATN, delayed images obtained with ^{99m}Tc-MAG3 several hours after administration of the tracer reveal retention of the radionuclide within the renal parenchyma with little, if any, accumulation or passage of activity into the renal pelvis, ureter, or bladder. If tracer activity within the transplant is similar to background on radionuclide angiography and later images, it indicates severe depression of renal function. However, the kidney should not be assumed nonviable, as most transplanted kidneys will recover from ATN unless rejection or other complications occur.

Thrombosis

Renal graft thrombosis and infarction is the third most frequent cause of graft loss in pediatric renal transplantation [145]. The apparent lack of perfusion of a renal transplant, seen on radionuclide angiography, does not always signify occlusion of the main renal artery leading to the transplant. Lack of blood flow to a transplanted kidney also may be due to hyperacute rejection. Correlative ultrasonography can be helpful to distinguish thrombosis from renal causes of decreased renal perfusion. Renal graft thrombosis in a living-related donor transplant is most frequently seen when the recipient is less than 5 years of age. On the other hand, thrombosis following cadaveric renal transplant is most common when the donor is young usually less than 5 years of age. All these conditions present as a lack of renal blood flow to the transplant on a radionuclide angiogram and failure to visualize the kidney on subsequent serial images. Chances of recovery of renal function in these patients are remote, and unfortunately, surgical removal of the graft may be indicated.

Rejection

The most common cause of renal graft dysfunction during the first several months following transplantation is an acute rejection episode. As many as 25 % of deceased transplants and 15 % of living-related donor transplant recipients have acute rejection episodes during the first year after transplantation. Rejection is often suspected on the basis of nonspecific clinical findings (fever, tenderness over the graft site) or specific clinical findings (decreased urine output, increased serum

urea nitrogen and creatinine). A renal biopsy is frequently obtained to confirm the diagnosis of rejection. Treatment for acute rejection episodes includes high-dose "pulse" corticosteroid treatment or the use of antilymphocyte preparations. Complications associated with these therapies, particularly opportunistic infections, are sometimes severe.

Renal scintigraphy is generally performed during the evaluation of an apparent acute rejection episode. The scintigraphic findings during acute rejection episodes include diminished perfusion of the graft, poor uptake of ^{99m}Tc-MAG3, and, occasionally, increased size of the renal silhouette. There are no specific findings in renal scintigraphy to confirm renal transplant rejection. The major value of the study is to rule out other conditions (e.g., renal obstruction, vascular comprise, or urinary leak) that could cause diminished graft function. These studies are particularly important, as they provide the basis for avoiding unnecessary therapy when processes other than rejection account for the diminished graft function.

Virtually all acute rejection episodes are reversible with treatment. With many episodes, however, return of graft function to prerejection levels may be delayed for up to several weeks, possibly related to renal interstitial edema secondary to the infiltrating lymphocytes and their subsequent destruction. Serial follow-up radionuclide studies may be helpful for assessing the returning renal function, as these studies often predict the recovery of function 24–48 h before the blood chemistry values improve.

Obstruction

Urinary obstruction is a very rare complication following renal transplantation. It can be difficult to diagnose in the presence of depressed renal function, such as occurs in acute tubular necrosis or after a rejection episode. Obstruction soon after surgery may be due to edema and/or inflammation in the region of the ureterovesical junction, which may be temporary. Later, obstruction may be due to external compression, which may be caused by (1) a lymphocele or scarring secondary to previous surgery or (2) internal obstruction, such as that caused by a ureteral stone or stenosis at the ureteral anastomosis site. In most cases, the transplant ureter is implanted directly into the bladder. In some cases, however, the native ureter may be used as a ureterostomy or, by anastomosis, connected directly to the pelvis of the graft. Because the transplant ureter obtains its blood supply only from the graft, the distal ureter may be poorly perfused, which may result in distal ureteral scarring and obstruction. Partial or even total obstruction of a transplant kidney may be relatively asymptomatic, as the graft is not innervated. Diagnosis of partial obstruction is sometimes difficult, and the use of furosemide after injection of the tracer may aid in the diagnosis. In cases of diminished graft function, ^{99m}Tc-MAG3 sometimes can demonstrates urinary obstruction, even in the presence of severe renal failure.

Urinary Leak

Urinary leak usually occurs in the first few months following transplantation. It can occur at the site of anastomosis of the transplant ureter or through necrosis of the distal transplant ureter related to diminished perfusion. The presence of urinary leak is detected with serial scintigraphy, usually as part of a ^{99m}Tc-MAG3 renogram, with greater sensitivity than other methods because of the high contrast of the radiotracer technique [146]. Multiple images at several minutes to several hours after the injection tracer may be necessary to detect urinary leakage. On the series of scintigrams, the leakage appears as a focal or diffuse area of increasing tracer accumulation outside the confines of the transplant, the ureter, or the bladder. In patients with a post-surgical drain in the abdominal cavity, leaked urine may cleared by the drain and little extravasated tracer may be seen in the abdomina cavity. The drain collection container must be imaged to exclude this possibility. Urinoma usually appears as a photon-deficient area on early images (5–10 min) with subsequent tracer accumulates on later images. If the area that is photon-deficient on early images does not concentrate radiotracer on later images, this region may represent a hematoma or a lymphocele (Fig. 12.43).

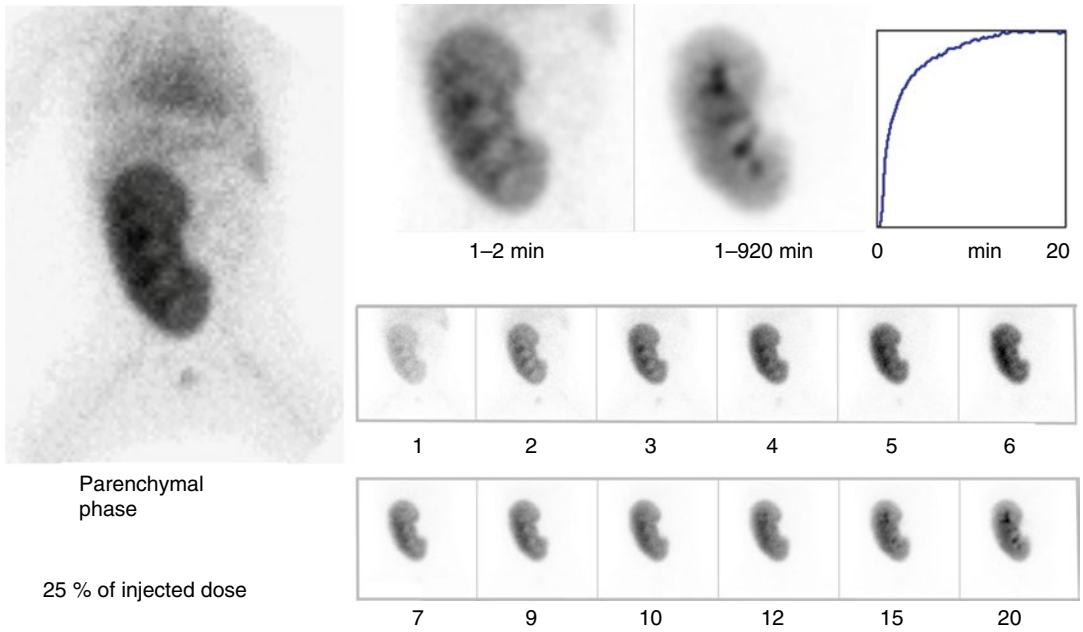

Fig. 12.45 A 9-month-old recipient of a living-related donor kidney transplant who was studied with a ^{99m}Tc-MAG3 renogram 1 day following transplantation. The parenchymal phase reveals a relatively large renal transplant (see the proportion to the baby's whole body). There is prompt and adequate tracer uptake in the viable transplant with delayed transit time and marked cortical retention, consistent with post-transplant ATN. With minimal tracer excretion into the collecting system, no determination can be made about urinary obstruction or leak

Transplantation of Adult Kidneys into Babies

When a kidney from an adult donor is transplanted into a baby, the large disproportion between the size of the transplant and the patient's body may interfere with drainage of the renal collecting system (Fig. 12.45).

Appendix: Quantitative Analysis of Renal Function

Nuclear medicine is unique among medical imaging modalities in that it is capable of providing detailed quantitative physiologic information about the kidneys. In large part, this is due to the availability of radiotracers whose properties approximate those of the classic tracers PAH and inulin.

Although quantitative physiologic information is useful in monitoring patients, producing it in a consistent and accurate way requires close attention to detail. In what follows, we have tried to emphasize the assumptions that are made in some common approaches to the quantitative analysis of the renogram.

Correction for Tissue Attenuation and Detection of Extrarenal Activity

In quantitative analysis of dynamic renal scintigraphy, one is attempting to measure the amount of activity in each kidney as a function of time. These functions are approximated by time-activity curves obtained from ROIs over the kidneys. The resulting time-activity curves have components that are due to the detection of extrarenal (i.e., background) activity. In addition, there is attenuation of photons from the kidney due to the intervening tissue. Thus, in order to estimate the activity in each kidney, it is desirable to attempt to correct for background activity and attenuation.

Background and attenuation correction for renography is a somewhat controversial subject

that is an area of ongoing research. We limit ourselves here to describing some simple first-order corrections that illustrate the general ideas involved and that are adequate except in the case of extremely poor renal function. For more sophisticated approaches, we refer the reader to the literature.

Background correction is usually based on the time-activity curve obtained from an ROI adjacent to the kidneys. This ROI is termed the background region. Various background regions have been proposed: an area between the kidneys, an area around the kidneys, an area superior to the kidneys, and an area inferolateral to the kidney have been used [147–149].

A simple approach to *background correction* is as follows: Let $K(t)$ and $B(t)$ denote the kidney and background time-activity curves, respectively. Let A_K and A_B denote the area in pixels of the renal and background ROIs, respectively. The background-corrected kidney time-activity curve, $K_c(t)$, is computed using the formula

$$K_c(t) = K(t) - S(A_K / A_B) B(t),$$

where S is a scaling factor (usually equal to 1) [147].

More sophisticated techniques for background correction take into account such factors as kidney volume and differences in kinetics between the kidney and background curves [150, 151]. The use of such techniques reportedly results in more accurate quantification of renal function [151].

A simple approach to *attenuation correction* is based on the mean distance of the kidney from the surface of the body. This distance may be measured by the gamma camera using a lateral view or by ultrasonography. Alternatively, this distance may be estimated from the patient's height and weight using a nomogram [152]. Attenuation correction is done by multiplying the background-corrected renal time-activity curve by e^{ux}, where u is the linear attenuation coefficient of the radiotracer in soft tissues and x is the mean distance of the kidney from the surface of the body [149, 153]. A more sophisticated approach may be found in the paper by Takaki et al. [151].

Deconvolution Analysis

After background and attenuation correction, the renal time-activity curve approximates the amount of tracer in the kidney as a function of time. It is intuitively clear that this time-activity curve depends on how much radiotracer enters the kidney from the bloodstream as a function of time, which we refer to as the input function, as well as the handling of the radiotracer by the kidney. The input function and hence the observed renal time-activity curve are affected by factors that have no bearing on the function of a particular kidney, such as the function of the other kidney, loss of radiotracer from the intravascular space, and, occasionally, continued input of radiotracer from a partially extravasated injection [154]. The purpose of deconvolution analysis is to describe the handling of the tracer by the kidney in a way that is independent of the input function.

One way to describe the handling of radiotracer by the kidney is to construct a curve showing the fraction of radiotracer entering the kidney at time 0, and the fraction that remains in the kidney at time t. We call this curve the retention function. The retention function is of direct clinical significance. For example, prolonged retention of radiotracer suggests obstruction. It is intuitively clear that the observed renal curve is determined by the input function and the retention function. To make this statement mathematically precise, the kidney is modeled as a linear, time-invariant system whose input is the input function discussed above and whose unit impulse response is equal to the retention function. With this model, the observed renal curve is given by the mathematical operation of convolution of the input function and the retention function. Denoting the input, retention, and kidney functions by $I(t)$, $R(t)$, and $K(t)$, respectively, we can write it as

$$K(t) = I(t) * R(t),$$

where * denotes the mathematical operation of convolution. Given $I(t)$ and $K(t)$, one can solve this equation for $R(t)$. This is known as deconvolution. The concepts of linear, time-invariant

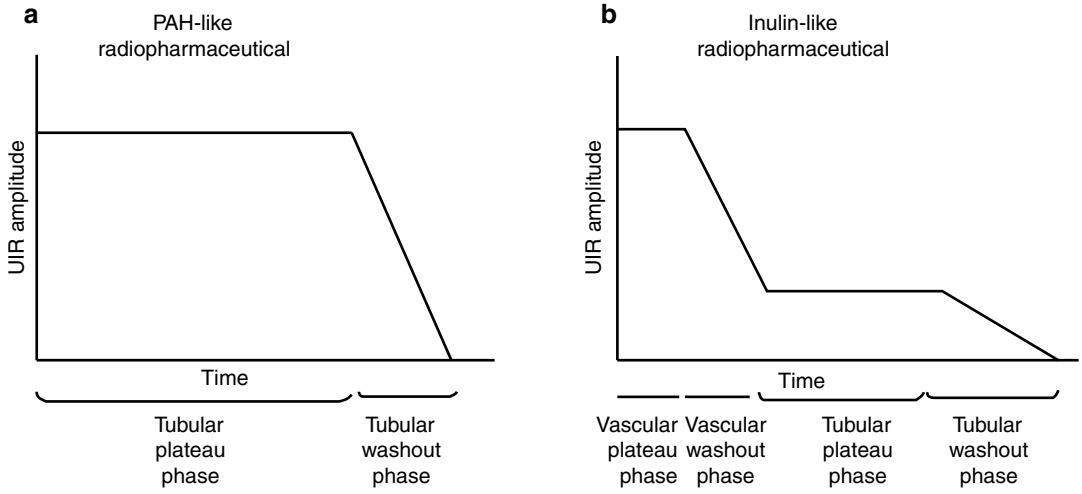

Fig. 12.46 (**a**) Deconvoluted renal time-activity histogram from a substance behaving like para-aminohippuric acid (*PAH*). (**b**) Deconvoluted renal time-activity curve from a substance behaving like inulin

system, unit impulse response, convolution, and so forth are discussed in more detail by Oppenheim et al. [155].

The input function is commonly assumed to be proportional to the plasma tracer concentration in the blood entering the kidney. This function is difficult to measure directly. In practice, the input function may be approximated as being proportional to a time-activity curve obtained from the abdominal aorta, heart, liver, or brain [154, 156]. There are two possible sources of error in this approximation: temporal differences in tracer concentration between the plasma in the pool being monitored and the renal artery and possible contamination of the observed blood-pool curve by detection of extravascular activity. However, this approximation of the input function by externally detected time-activity curves has been found to work well in practice [157].

Several investigators have reported using deconvolution to estimate the renal retention function [57, 147, 154, 158]. One difficulty with deconvolution is that small observation errors may lead to physiologically unrealistic negative values and high-frequency oscillations in the computed retention function [159]. To prevent this, we have found it useful to introduce constraints derived from physiologic considerations of the renal system into the deconvolution process. Specifically, the computed retention function is constrained to be nonnegative and nonincreasing. Retention functions computed using this technique have been shown to be relatively insensitive to random data errors [160].

Interpretation of the Renal Retention Function

The computed retention function is an estimate of the renal time-activity curve that would be obtained after an instantaneous intra-arterial injection of a radiotracer without recirculation. Consider such a curve obtained with a PAH-like substance that is handled primarily by tubular secretion (e.g., ^{123}I-OIH). All of the tracer arriving in the kidney subsequently enters the tubular space by either glomerular filtration or tubular secretion and leaves via the ureter. The corresponding retention function, shown in Fig. 12.46a, consists of a tubular plateau phase (from time 0 to the minimal tubular transit time) followed by a tubular washout phase. In contrast, consider such a curve obtained with a substance like inulin that is handled primarily by glomerular filtration (e.g., ^{99m}Tc-DTPA). A fraction of the tracer, equal to the filtration fraction, enters the tubular space by

glomerular filtration and leaves via the ureter. The remainder of tracer stays in the vascular space and leaves the kidney via the renal vein. The corresponding retention function, shown in Fig. 12.46b, consists of a vascular plateau phase (from time 0 until the minimal vascular transit time), a vascular washout phase (until the maximal vascular transit time), a tubular plateau phase (until the minimal tubular transit time), and a tubular washout phase. The amplitude of the tubular plateau divided by the amplitude of the vascular plateau is equal to the filtration fraction. The vascular phase occurs quite rapidly, however, and is difficult to delineate at the frame rates commonly used for dynamic renal imaging. It is sometimes useful for interpretation to eliminate the vascular phase of the retention function by setting the retention function values prior to a set time (chosen to be greater than the maximal vascular transit time and less than the minimal tubular transit time) equal to the retention function value at that time. The resulting curve is termed the tubular retention function.

Computed retention functions may be used to calculate indices of relative renal function (i.e., left versus right). Relative effective renal plasma flow (ERPF) may be estimated from the relative initial amplitudes of the retention functions obtained using a tracer that is handled like PAH [147, 158]. Relative GFR may be estimated from the relative initial amplitudes of the tubular retention functions obtained using a tracer that is handled like inulin [154]. Relative GFR calculated by this method has been shown to correlate well with individual kidney creatinine clearance [161]. Computed retention functions are also useful for quantifying transit times of radiotracer through the kidney. The mean tubular transit time (MTTT) (i.e., the mean time that filtered or secreted radiotracer remains in the kidney) has been shown to be of value for distinguishing obstructive from nonobstructive renal disease [156]. The MTTT may be computed using the formula

$$\mathrm{MTTT} = \int_0^\infty t\left(-dR\left(t\right)/\,\mathrm{dt}\right)\mathrm{dt},$$

where $R(t)$ is the tubular retention function [151].

Glomerular Filtration Rate

The GFR may be estimated following intravenous injection of a radiotracer that is handled like inulin (see Chap. 13). The substance most commonly used for this purpose is ^{99m}Tc-DTPA. There are two basic approaches to the estimation of GFR. The first approach is based on clearance of the radiotracer from the plasma, and the second approach is based on the rate of tracer uptake by the kidney. Both approaches are reasonable, and the choice between them is a matter of convenience.

With the plasma clearance method, it is assumed that the radiotracer leaves the body solely through the urine. Single-injection techniques have largely replaced the classic, but tedious, constant-infusion techniques and have been shown to correlate well with results obtained using the constant-infusion technique [162, 163]. The concentration of the tracer in the plasma as a function of time may be monitored by counting a series of blood samples. Alternatively, plasma concentration of the tracer may be recorded by an external detector over the heart or head. The resulting time-activity curve must be calibrated by one or more blood samples. External detection introduces a possible source of error because activity outside of the intravascular space may be detected [164]. But has the advantage of reducing the number of blood samples needed [165, 166].

Equations for calculating the clearance of a radiotracer after a single injection are derived from either a single- or multiple-compartment model [167, 168]. The parameters of the model are estimated by fitting a single or multiple exponential curve to the plasma concentration curve [162, 163, 166, 169, 170, 171].

The other approach to estimation of GFR, based on the uptake of the tracer by the kidney, assumes that the radiotracer remains in the kidney for at least some fixed period of time after it enters (typically 2–3 min) [172, 173].

One goal has been to eliminate the need for blood sampling. As with the plasma clearance approach, this is done, in essence, by using an empirically derived approximation for the effective volume of distribution of the radiotracer.

Gates reported using such a method to estimate GFR from the percentage of the ^{99m}Tc-DTPA dose taken up by the kidneys during the 2- to 3-min interval after injection [149]. More recently, Gordon et al. have reported using such a method in children [174].

The percent uptake of ^{99m}Tc-DTPA during the 1- to 2-min interval after injection can be used to estimate differential renal function. With this method, it is possible to monitor changes in renal function in patients undergoing surgical or medical treatment for a variety of renal diseases. It is also possible to estimate differential GFR from the relative percentage of uptake by the two kidneys [175].

Effective Renal Plasma Flow

The effective renal plasma flow (ERPF) may be estimated in the same manner as GFR if a radiotracer is used that is handled as PAH rather than as inulin. The most commonly used radiotracers for this purpose are ^{99m}Tc-MAG3 and ^{123}I-OIH [171]. In practice, ERPF measured with tracers such as these are always slightly lower than the actual renal plasma flow because no substance is completely extracted in a single pass [176]. The plasma clearance and renal uptake approaches have both been used. The techniques used are essentially the same as those used for estimating GFR from inulin-like radiopharmaceuticals.

As with estimation of GFR, the concentration of the tracer in plasma may be followed by either multiple blood samples or external detection. The two methods have been found to produce similar results. Blaufox et al. found a good correlation in the measurement of ERPF using ^{131}I-OIH with serial blood sampling and external detection using a scintillation probe over the patient's head [167]. Similarly, Ram et al. and Razzak et al. found good agreement in the values of ERPF calculated by serial blood sampling and external detection over the precordium [177, 178]. Ram et al. reported a strong correlation between ERPF estimates obtained by single-exponential extrapolation of ^{125}I-OIH time-activity curves obtained from over the precordium and PAH clearance. Mackay et al. reported the estimation of ERPF from a ^{123}I-OIH time-activity curve obtained over the abdomen and a single blood sample using single-exponential extrapolation [179]. The ERPF estimates were found to correlate closely with PAH clearances but tended to be slightly lower. The average value was 89 % of the PAH clearance values. Heidenreich et al. reported their clinical experience in the estimation of ERPF from the clearance of ^{123}I-OIH in 153 children [180].

As in the case of estimating GFR, there has been much interest in procedures for estimating ERPF that require no external counting and only a single blood sample. Again, these procedures work by using an empirically derived approximation for the effective volume of distribution of the radiotracer. Such simplified techniques have been shown to produce reasonable estimates of ERPF in children [30].

The renal uptake approach to ERPF estimation has also been used [152]. Thompson et al. reported the renal uptake of ^{131}I-OIH in the 1- to 2-min interval after injection correlated with PAH clearances [181].

Relative ERPF may also be estimated from the relative percentage of uptake of the two kidneys [153, 180, 182]. Relative uptake of ^{123}I-OIH in the 0.5- to 2.5-min interval following injection has been shown to correlate with separate kidney PAH clearance values obtained by ureteral catheterization [121].

References

1. Cao X, Tetrault T, Fahey F, Treves T. Automated motion correction based on target tracking for dynamic nuclear medicine studies. Proc SPIE. 2008;6914(1):69142B.
2. Moretti M, Magnani C, Calzolari E, Roncarati E. Genitourinary tract anomalies: neonatal medical problems. Fetal Ther. 1986;1(2–3):114–5.
3. Seikaly M, Ho PL, Emmett L, Tejani A. The 12th Annual Report of the North American Pediatric Renal Transplant Cooperative Study: renal transplantation from 1987 through 1998. Pediatr Transplant. 2001;5(3):215–31.
4. National Institute of Diabetes and Digestive and Kidney Diseases (U.S.). Division of Kidney Urologic and Hematologic Diseases: United States renal data system …1993 annual data report. Bethesda, MD:

National Institutes of Health, National Institute of Diabetes and Digestive and Kidney Diseases, Division of Kidney, Urologic, and Hematologic Diseases; Urban Institute. Renal Research Program, University of Michigan, USRDS Coordinating Center; 1993. p. v.
5. Koenigsberg M, Blaufox MD, Freeman LM. Traumatic injuries of the renal vasculature and parenchyma. In: Freeman LM, Blaufox MD, editors. Radionuclide studies of the genitourinary system. New York: Grune & Stratton; 1975. ix, 220 p.
6. Burko H, Rhamy RK. Lower urinary tract problems related to infection: diagnosis and treatment. Pediatr Clin North Am. 1970;17(2):233–53.
7. Bois E, Feingold J, Benmaiz H, Briard ML. Congenital urinary tract malformations: epidemiologic and genetic aspects. Clin Genet. 1975;8(1):37–47.
8. Sheih CP, Liu MB, Hung CS, Yang KH, Chen WY, Lin CY. Renal abnormalities in schoolchildren. Pediatrics. 1989;84(6):1086–90.
9. Barakat AJ, Drougas JG. Occurrence of congenital abnormalities of kidney and urinary tract in 13,775 autopsies. Urology. 1991;38(4):347–50.
10. Taylor Jr A, Eshima D, Fritzberg AR, Christian PE, Kasina S. Comparison of iodine-131 OIH and technetium-99m MAG3 renal imaging in volunteers. J Nucl Med. 1986;27(6):795–803.
11. Bubeck B, Brandau W, Steinbacher M, et al. Technetium-99m labeled renal function and imaging agents: II. Clinical evaluation of ^{99m}Tc MAG3 (99mTc mercaptoacetylglycylglycylglycine). Int J Rad Appl Instrum B. 1988;15(1):109–18.
12. Jafri RA, Britton KE, Nimmon CC, et al. Technetium-99m MAG3, a comparison with iodine-123 and iodine-131 orthoiodohippurate, in patients with renal disorders. J Nucl Med. 1988;29(2):147–58.
13. Russell CD, Thorstad B, Yester MV, Stutzman M, Baker T, Dubovsky EV. Comparison of technetium-99m MAG3 with iodine-131 hippuran by a simultaneous dual channel technique. J Nucl Med. 1988;29(7):1189–93.
14. Russell CD, Thorstad BL, Yester MV, Stutzman M, Dubovsky EV. Quantitation of renal function with technetium-99m MAG3. J Nucl Med. 1988; 29(12):1931–3.
15. Taylor Jr A, Eshima D, Alazraki N. ^{99m}Tc-MAG3, a new renal imaging agent: preliminary results in patients. Eur J Nucl Med. 1987;12(10):510–4.
16. Gelfand MJ, Parisi MT, Treves ST. Pediatric radiopharmaceutical administered doses: 2010 North American consensus guidelines. J Nucl Med. 2011; 52(2):318–22.
17. Hsiao EM, Cao X, Zurakowski D, et al. Reduction in radiation dose in mercaptoacetyltriglycerine renography with enhanced planar processing. Radiology. 2011;261(3):907–15.
18. Atkins HL, Cardinale KG, Eckelman WC, Hauser W, Klopper JF, Richards P. Evaluation of 99mTc-DTPA prepared by three different methods. Radiology. 1971;98(3):674–7.
19. Cohen ML, Smith Jr FG, Mindell RS, Vernier RL. A simple, reliable method of measuring glomerular filtration rate using single, low dose sodium iothalamate I-131. Pediatrics. 1969;43(3):407–15.
20. Elwood CM, Sigman EM. The measurement of glomerular filtration rate and effective renal plasma flow in man by iothalamate 125-I and iodopyracet 131-I. Circulation. 1967;36(3):441–8.
21. Elwood CM, Sigman EM, Treger C. The measurement of glomerular filtration rate with ^{125}I-sodium iothalamate (Conray). Br J Radiol. 1967;40(476):581–3.
22. Gagnon JA, Schrier RW, Weis TP, Kokotis W, Mailloux LU. Clearance of iothalamate-125 I as a measure of glomerular filtration rate in the dog. J Appl Physiol. 1971;30(5):774–8.
23. Hauser W, Atkins HL, Nelson KG, Richards P. Technetium-99m DTPA: a new radiopharmaceutical for brain and kidney scanning. Radiology. 1970; 94(3):679–84.
24. Houwen B, Donker A, Woldring MG. Simultaneous determination of glomerular filtration rate with ^{125}I-iothalamate and effective renal plasma flow with ^{131}I-hippuran. Paper presented at: Dynamic studies with radioisotopes in medicine. Proceedings of the symposium … organized by the International Atomic Energy Agency, and held in Rotterdam, Vienna, 31 Aug–4 Sept 1970–1971.
25. Klopper JF, Hauser W, Atkins HL, Eckelman WC, Richards P. Evaluation of 99m Tc-DTPA for the measurement of glomerular filtration rate. J Nucl Med. 1972;13(1):107–10.
26. Kountz SL, Yeh SH, Wood J, Cohn R, Kriss JP. Technetium-99m(V)-citrate complex for estimation of glomerular filtration rate. Nature. 1967;215(108): 1397–9.
27. Maher FT, Nolan NG, Elveback LR. Comparison of simultaneous clearances of 125-I-labeled sodium iothalamate (Glofil) and of inulin. Mayo Clin Proc. 1971;46(10):690–1.
28. Oester A, Wolf H, Madsen PO. Double isotope technique in renal function testing in dogs. Invest Urol. 1969;6(4):387–92.
29. Sigman EM, Elwood C, Reagan ME, Morris AM, Catanzaro A. The renal clearance of I-131 labelled sodium iothalamate in man. Invest Urol. 1965;15: 432–8.
30. Russell CD, Bischoff PG, Rowell KL, et al. Quality control of Tc-99m DTPA for measurement of glomerular filtration: concise communication. J Nucl Med. 1983;24(8):722–7.
31. McAfee JG, Gagne G, Atkins HL, et al. Biological distribution and excretion of DTPA labeled with Tc-99m and In-111. J Nucl Med. 1979;20(12):1273–8.
32. Arnold RW, Subramanian G, McAfee JG, Blair RJ, Thomas FD. Comparison of 99mTc complexes for renal imaging. J Nucl Med. 1975;16(5):357–67.
33. Lee HB, Blaufox MD. Mechanism of renal concentration of technetium-99m glucoheptonate. J Nucl Med. 1985;26(11):1308–13.
34. Tubis M, Posnick E, Nordyke RA. Preparation and use of I 131 labeled sodium iodohippurate in kidney function tests. Proc Soc Exp Biol Med. 1960;103:497–8.

35. Chervu LR, Freeman LM, Blaufox MD. Radiopharmaceuticals for renal studies. Semin Nucl Med. 1974;4(1):3–22.
36. Mailloux LU, Gagnon JA. Measurement of effective renal plasma flow. In: Blaufox MD, editor. *Progress in Nuclear Medicine*. Baltimore: University Park Press; 1972. xiv, 315 p.
37. Howman-Giles R, Uren R, Roy LP, Filmer RB. Volume expansion diuretic renal scan in urinary tract obstruction. J Nucl Med. 1987;28(5):824–8.
38. Nauta J, Pot DJ, Kooij PP, Nijman JM, Wolff ED. Forced hydration prior to renography in children with hydronephrosis. An evaluation. Br J Urol. 1991;68(1): 93–7.
39. Sukhai RN, Kooy PP, Wolff ED, Scholtmeijer RJ. Predictive value of ^{99m}Tc-DTPA renography studies under conditions of maximal diuresis for the functional outcome of reconstructive surgery in children with obstructive uropathy. Br J Urol. 1986;58(6):596–600.
40. Treves ST, Packard AB, Fung LC. Assessment of rapid changes in renal blood flow with (^{191m})Ir, an ultra-short-lived radionuclide. J Nucl Med. 2004; 45(3):508–11.
41. Treves ST, Fung L, Packard AB. Rapid renal single-photon emission tomography by continuous infusion of iridium-191m. Eur J Nucl Med. 1999;26(5): 489–93.
42. Shore RM, Uehling DT, Bruskewitz R, Polcyn RE. Evaluation of obstructive uropathy with diuretic renography. Am J Dis Child. 1983;137(3):236–40.
43. Koff SA, Thrall JH, Keyes Jr JW. Assessment of hydroureteronephrosis in children using diuretic radionuclide urography. J Urol. 1980;123(4):531–4.
44. Mesrobian HG, Perry JR. Radionuclide diuresis pyelography. J Urol. 1991;146(2 Pt 2):601–4.
45. Thrall JH, Koff SA, Keyes Jr JW. Diuretic radionuclide renography and scintigraphy in the differential diagnosis of hydroureteronephrosis. Semin Nucl Med. 1981;11(2):89–104.
46. Meller ST, Eckstein HB. Renal scintigraphy: quantitative assessment of upper urinary tract dilatation in children. J Pediatr Surg. 1981;16(2):126–33.
47. Enlander D, Weber PM, dos Remedios LV. Renal cortical imaging in 35 patients: superior quality with 99mTc-DMSA. J Nucl Med. 1974;15(9):743–9.
48. Kawamura J, Hosokawa S, Yoshida O. Renal function studies using ^{99m}Tc-dimercaptosuccinic acid. Clin Nucl Med. 1979;4(1):39–46.
49. Willis KW, Martinez DA, Hedley-Whyte ET, Davis MA, Judy PF, Treves S. Renal localization of ^{99m}Tc-stannous glucophetonate and ^{99m}Tc-stannous dimercaptosuccinate in the rat by frozen section autoradiography. The efficiency and resolution of technetium-99m. Radiat Res. 1977;69(3):475–88.
50. Daly MJ, Jones WA, Rudd TG, Tremann JA. Differential ^{99m}Tc dimercaptosuccinic acid (DMSA) renal localization: correlation with renal function. J Nucl Med. 1977;18:594–5.
51. Daly MJ, Jones W, Rudd TG, Tremann J. Differential renal function using technetium-99m dimercaptosuccinic acid (DMSA): in vitro correlation. J Nucl Med. 1979;20(1):63–6.
52. Taylor Jr A. Quantitation of renal function with static imaging agents. Semin Nucl Med. 1982;12(4):330–44.
53. Gittes RF, Rist M, Treves S, Biewiner A. Autoregulation in rats with transplanted supernumerary kidneys. Nature. 1980;284(5757):618–20.
54. Sheehy N, Tetrault TA, Zurakowski D, Vija AH, Fahey FH, Treves ST. Pediatric 99mTc-DMSA SPECT performed by using iterative reconstruction with isotropic resolution recovery: improved image quality and reduced radiopharmaceutical activity. Radiology. 2009;251(2):511–6.
55. Cao X, Zurakowski D, Diamond DA, Treves ST. Automatic measurement of renal volume in children using ^{99m}Tc dimercaptosuccinic acid SPECT: normal ranges with body weight. Clin Nucl Med. 2012;37(4):356–61.
56. Treves ST, Baker A, Fahey FH, et al. Nuclear medicine in the first year of life. J Nucl Med. 2011; 52(6):905–25.
57. Vanpee M, Blennow M, Linne T, Herin P, Aperia A. Renal function in very low birth weight infants: normal maturity reached during early childhood. J Pediatr. 1992;121(5 Pt 1):784–8.
58. Dunbar JS, Nogrady B. Excretory urography in the first year of life. Radiol Clin North Am. 1972; 10(2):367–91.
59. Martin DJ, Gilday DL, Reilly BJ. Evaluation of the urinary tract in the neonatal period. Radiol Clin North Am. 1975;13(2):359–68.
60. Slutsky LJ, Golimbu M, Braunstein P, Al-Askari S, Genieser N, Golimbu C. Urographic imaging in neonatal period: radionuclide scan and x-ray. Urology. 1977;10(2):169–72.
61. Sherman RA, Blaufox MD. Obstructive uropathy in patients with nonvisualization on renal scan. Nephron. 1980;25(2):82–6.
62. Chung YK, Chang PY, Lin CJ, Wang NL, Sheu JC, Shih BF. Conservative treatment of neonatal hydronephrosis. J Formos Med Assoc. 1992;91(1):75–80.
63. Gordon I, Dhillon HK, Peters AM. Antenatal diagnosis of renal pelvic dilatation–the natural history of conservative management. Pediatr Radiol. 1991;21(4): 272–3.
64. Homsy YL, Saad F, Laberge I, Williot P, Pison C. Transitional hydronephrosis of the newborn and infant. J Urol. 1990;144(2 Pt 2):579–83; discussion 593–4.
65. Ransley PG, Dhillon HK, Gordon I, Duffy PG, Dillon MJ, Barratt TM. The postnatal management of hydronephrosis diagnosed by prenatal ultrasound. J Urol. 1990;144(2 Pt 2):584–7; discussion 593–84.
66. Samuelson U, Granerus G, Bjures J, Hagberg S, Hjalmas K. Renal function in idiopathic hydronephrosis in children. Follow-up after conservative and surgical treatment. Scand J Urol Nephrol. 1984;18(2): 135–41.
67. Djurhuus JC, Dorph S, Christiansen L, Ladefoged J, Nerstrom B. Predictive value of renography and i.v.

urography for the outcome of reconstructive surgery in patients with hydronephrosis. Acta Chir Scand Suppl. 1976;472:37–41.
68. McAfee JG, Singh A, O'Callaghan JP. Nuclear imaging supplementary to urography in obstructive uropathy. Radiology. 1980;137(2):487–96.
69. Kalika V, Bard RH, Iloreta A, Freeman LM, Heller S, Blaufox MD. Prediction of renal functional recovery after relief of upper urinary tract obstruction. J Urol. 1981;126(3):301–5.
70. Jamar F, Piret L, Wese FX, Beckers C. Influence of ureteral status on kidney washout during technetium-99m-DTPA diuresis renography in children. J Nucl Med. 1992;33(1):73–8.
71. Busch R, Huland H. Correlation of symptoms and results of direct bacterial localization in patients with urinary tract infections. J Urol. 1984;132(2):282–5.
72. Majd M, Rushton HG, Jantausch B, Wiedermann BL. Relationship among vesicoureteral reflux, P-fimbriated Escherichia coli, and acute pyelonephritis in children with febrile urinary tract infection. J Pediatr. 1991;119(4):578–85.
73. Jacobson SH, Eklof O, Eriksson CG, Lins LE, Tidgren B, Winberg J. Development of hypertension and uraemia after pyelonephritis in childhood: 27 year follow up. BMJ. 1989;299(6701):703–6.
74. Glauser MP, Lyons JM, Braude AI. Prevention of chronic experimental pyelonephritis by suppression of acute suppuration. J Clin Invest. 1978;61(2):403–7.
75. Miller T, Phillips S. Pyelonephritis: the relationship between infection, renal scarring, and antimicrobial therapy. Kidney Int. 1981;19(5):654–62.
76. Slotki IN, Asscher AW. Prevention of scarring in experimental pyelonephritis in the rat by early antibiotic therapy. Nephron. 1982;30(3):262–8.
77. Bjorgvinsson E, Majd M, Eggli KD. Diagnosis of acute pyelonephritis in children: comparison of sonography and ^{99m}Tc-DMSA scintigraphy. AJR Am J Roentgenol. 1991;157(3):539–43.
78. Farnsworth RH, Rossleigh MA, Leighton DM, Bass SJ, Rosenberg AR. The detection of reflux nephropathy in infants by ^{99m}technetium dimercaptosuccinic acid studies. J Urol. 1991;145(3):542–6.
79. Jantausch BA, Wiedermann BL, Hull SI, et al. Escherichia coli virulence factors and ^{99m}Tc-dimercaptosuccinic acid renal scan in children with febrile urinary tract infection. Pediatr Infect Dis J. 1992;11(5):343–9.
80. Kass EJ, Fink-Bennett D, Cacciarelli AA, Balon H, Pavlock S. The sensitivity of renal scintigraphy and sonography in detecting nonobstructive acute pyelonephritis. J Urol. 1992;148(2 Pt 2):606–8.
81. Majd M, Rushton HG. Renal cortical scintigraphy in the diagnosis of acute pyelonephritis. Semin Nucl Med. 1992;22(2):98–111.
82. Rushton HG, Majd M, Jantausch B, Wiedermann BL, Belman AB. Renal scarring following reflux and nonreflux pyelonephritis in children: evaluation with ^{99m}technetium-dimercaptosuccinic acid scintigraphy. J Urol. 1992;147(5):1327–32.
83. Verber IG, Meller ST. Serial ^{99m}Tc dimercaptosuccinic acid (DMSA) scans after urinary infections presenting before the age of 5 years. Arch Dis Child. 1989;64(11):1533–7.
84. Goldraich NP, Ramos OL, Goldraich IH. Urography versus DMSA scan in children with vesicoureteric reflux. Pediatr Nephrol. 1989;3(1):1–5.
85. Itoh K, Asano Y, Tsukamoto E, et al. Single photon emission computed tomography with Tc-99m-dimercaptosuccinic acid in patients with upper urinary tract infection and/or vesicoureteral reflux. Ann Nucl Med. 1991;5(1):29–34.
86. Verboven M, Ingels M, Delree M, Piepsz A. ^{99m}Tc-DMSA scintigraphy in acute urinary tract infection in children. Pediatr Radiol. 1990;20(7):540–2.
87. Merrick MV, Uttley WS, Wild SR. The detection of pyelonephritic scarring in children by radioisotope imaging. Br J Radiol. 1980;53(630):544–56.
88. Handmaker H. Nuclear renal imaging in acute pyelonephritis. Semin Nucl Med. 1982;12(3):246–53.
89. Jakobsson B, Nolstedt L, Svensson L, Soderlundh S, Berg U. ^{99m}Technetium-dimercaptosuccinic acid scan in the diagnosis of acute pyelonephritis in children: relation to clinical and radiological findings. Pediatr Nephrol. 1992;6(4):328–34.
90. Tappin DM, Murphy AV, Mocan H, et al. A prospective study of children with first acute symptomatic E. coli urinary tract infection. Early ^{99m}technetium dimercaptosuccinic acid scan appearances. Acta Paediatr Scand. 1989;78(6):923–9.
91. Applegate KE, Connolly LP, Davis RT, Zurakowski D, Treves ST. A prospective comparison of high-resolution planar, pinhole, and triple-detector SPECT for the detection of renal cortical defects. Clin Nucl Med. 1997;22(10):673–8.
92. Joseph DB, Young DW, Jordon SP. Renal cortical scintigraphy and single proton emission computerized tomography (SPECT) in the assessment of renal defects in children. J Urol. 1990;144(2 Pt 2):595–7; discussion 606.
93. Roberts JA, Roth Jr JK, Domingue G, Lewis RW, Kaack B, Baskin G. Immunology of pyelonephritis in the primate model. V. Effect of superoxide dismutase. J Urol. 1982;128(6):1394–400.
94. Kaack MB, Dowling KJ, Patterson GM, Roberts JA. Immunology of pyelonephritis. VIII. E. coli causes granulocytic aggregation and renal ischemia. J Urol. 1986;136(5):1117–22.
95. Androulakakis PA, Ransley PG, Risdon RA, Sorger K, Hohenfellner R. Microvascular changes in the early stage of reflux pyelonephritis. An experimental study in the pig kidney. Eur Urol. 1987;13(4):219–23.
96. Elink M. Emergency uroradiology for the nontraumatized patient. Radiol Clin North Am. 1978;16(1):135–46.
97. Handmaker H, Young BW, Lowenstein JM. Clinical experience with ^{99m}Tc-DMSA (dimercaptosuccinic acid), a new renal-imaging agent. J Nucl Med. 1975;16(1):28–32.

98. Silver TM, Kass EJ, Thornbury JR, Konnak JW, Wolfman MG. The radiological spectrum of acute pyelonephritis in adults and adolescents. Radiology. 1976;118(1):65–71.
99. Kahn PC. Renal imaging with radionuclides, ultrasound, and computed tomography. Semin Nucl Med. 1979;9(1):43–57.
100. June CH, Browning MD, Smith LP, et al. Ultrasonography and computed tomography in severe urinary tract infection. Arch Intern Med. 1985;145(5):841–5.
101. Montgomery P, Kuhn JP, Afshani E. CT evaluation of severe renal inflammatory disease in children. Pediatr Radiol. 1987;17(3):216–22.
102. Raynaud C, Tran-Dinh S, Bourguignon M, et al. Acute pyelonephritis in children. Preliminary results obtained with NMR imaging. Contrib Nephrol. 1987;56:129–34.
103. Arneil GC, MacDonald AM, Sweet EM. Renal venous thrombosis. Clin Nephrol. 1973;1(3):119–31.
104. Avery ME, Oppenheimer EH, Gordon HH. Renal-vein thrombosis in newborn infants of diabetic mothers; report of 2 cases. N Engl J Med. 1957;256(24):1134–8.
105. Kaufmann HJ. Renal vein thrombosis. 1. Age incidence in infancy and childhood. 2. Sex incidence. 3. Incidence of unilateral and bilateral involvement. AMA J Dis Child. 1958;95(4):377–84.
106. Rasoulpour M, McLean RH. Renal venous thrombosis in neonates. Initial and follow-up abnormalities. Am J Dis Child. 1980;134(3):276–9.
107. Stark H. Renal vein thrombosis in infancy. Recovery without nephrectomy. Am J Dis Child. 1964;108:430–5.
108. Takeuchi A, Benirschke K. Renal venous thrombosis of the newborn and its relation to maternal diabetes. Report of 16 cases. Biol Neonat. 1961;3:237–56.
109. Verhagen AD, Hamilton JP, Genel M. Renal vein thrombosis in infants. Arch Dis Child. 1965;40:214–7.
110. Duncan RE, Evans AT, Martin LW. Natural history and treatment of renal vein thrombosis in children. J Pediatr Surg. 1977;12(5):639–45.
111. Quigley JM, Druy EM, Rich JI. Acute renal vein thrombosis with a diagnostic renal scintigram. AJR Am J Roentgenol. 1981;137(5):1066–8.
112. Blaufox MD. Systemic arterial hypertension in pediatric practice. Pediatr Clin North Am. 1971;18(2):577–93.
113. Ingelfinger JR. Pediatric hypertension. Philadelphia: Saunders; 1982.
114. Londe S. Causes of hypertension in the young. Pediatr Clin North Am. 1978;25(1):55–65.
115. Olson DL, Lieberman E. Renal hypertension in children. Pediatr Clin North Am. 1976;23(4):795–805.
116. Rosen PR, Treves S. The efficacy of ^{99m}Tc screening of pediatric patients for renal etiologies in hypertension. J Nucl Med. 1983;24(5):22.
117. Geyskes GG, Oei HY, Puylaert CB, Dorhout Mees EJ. Renography with captopril. Changes in a patient with hypertension and unilateral renal artery stenosis. Arch Intern Med. 1986;146(9):1705–8.
118. Majd M, Potter BN, Guzzeta PC, Ruley EJ. Effect of captopril on efficacy of renal scintigraphy in detection of renal artery stenosis [abstract]. J Nucl Med. 1983;24:23.
119. Sfakianakis GN, Sfakianaki E, Bourgoignie J. Lasix captopril renography in the diagnosis of renovascular hypertension. Contrib Nephrol. 1990;79:219–27.
120. Siegel MJ, St Amour TE, Siegel BA. Imaging techniques in the evaluation of pediatric hypertension. Pediatr Nephrol. 1987;1(1):76–88.
121. Wenting GJ, Tan-Tjiong HL, Derkx FH, de Bruyn JH, Man in't Veld AJ, Schalekamp MA. Splint renal function after captopril in unilateral renal artery stenosis. Br Med J (Clin Res Ed). 1984;288(6421):886–90.
122. Vivan G, Stringer D, DeBruyn R, et al. ^{99m}Tc DMSA in renovascular hypertension in children. Paper presented at: Nuclear medicine and biology advances: proceedings of the Third World Congress of Nuclear Medicine and Biology, August 29 to September 2, 1982, Paris, France. Oxford [Oxfordshire]/New York, 1983.
123. Minty I, Lythgoe MF, Gordon I. Hypertension in paediatrics: can pre- and post-captopril technetium-99m dimercaptosuccinic acid renal scans exclude renovascular disease? Eur J Nucl Med. 1993;20(8):699–702.
124. Dondi M. Captopril renal scintigraphy with ^{99m}Tc-mercaptoacetyltriglycine (^{99m}Tc-MAG3) for detecting renal artery stenosis. Am J Hypertens. 1991;4(12 Pt 2):737S–40.
125. Dondi M, Fanti S, De Fabritiis A, et al. Prognostic value of captopril renal scintigraphy in renovascular hypertension. J Nucl Med. 1992;33(11):2040–4.
126. Oei HY. Captopril renography. Early observations and diagnostic criteria. Am J Hypertens. 1991;4(12 Pt 2):678S–84.
127. Setaro JF, Chen CC, Hoffer PB, Black HR. Captopril renography in the diagnosis of renal artery stenosis and the prediction of improvement with revascularization. The Yale Vascular Center experience. Am J Hypertens. 1991;4(12 Pt 2):698S–705.
128. Hildebrandt O. Anatomie der Nierengeschwulste. Arch Klin Chir. 1894;48:343.
129. Bernstein J. The morphogenesis of renal parenchymal maldevelopment (renal dysplasia). Pediatr Clin North Am. 1971;18(2):395–407.
130. Zerres K, Volpel MC, Weiss H. Cystic kidneys. Genetics, pathologic anatomy, clinical picture, and prenatal diagnosis. Hum Genet. 1984;68(2):104–35.
131. Berdon WE, Baker DH, Wigger HJ, Blanc WA. The radiologic and pathologic spectrum of the prune belly syndrome. The importance of urethral obstruction in prognosis. Radiol Clin North Am. 1977;15(1):83–92.
132. Guthrie L. Case of congenital deficiency of the abdominal muscles with dilatation and hypertrophy of the bladder ureters. Trans Pathol Soc Lond. 1918;47:139–45.
133. Parker RW. Case of an infant in whom some of the abdominal muscles were absent. Trans Clin Soc Lond. 1895;28:201–3.

134. Williams DI, Burkholder GV. The prune belly syndrome. J Urol. 1967;98(2):244–51.
135. Leonard JC, Allen EW, Goin J, Smith CW. Renal cortical imaging and the detection of renal mass lesions. J Nucl Med. 1979;20(10):1018–22.
136. Older RA, Korobkin M, Workman J, et al. Accuracy of radionuclide imaging in distinguishing renal masses from normal variants. Radiology. 1980;136(2):443–8.
137. Parker JA, Lebowitz R, Mascatello V, Treves S. Magnification renal scintigraphy in the differential diagnosis of septa of Bertin. Pediatr Radiol. 1976;4(3):157–60.
138. Awad W, Bennett LR, Martin DC. Detection of renal homograft rejection reaction with a single dose of radiohippuran. J Urol. 1968;100(3):233–7.
139. Awad W, Boake RC, Bennett LR, Martin DC. Double isotope scan in kidney transplantation. Am Surg. 1968;34(11):768–74.
140. Figueroa JE, Maxfield WS, Batson HM, Birchall R. Radioisotope renal function studies in human renal allografts: value in the differential diagnosis of oliguria in the presence of obstructive disease with and without urinary extravasation. J Urol. 1968;100(2): 104–8.
141. Lubin E, Lewitus Z, Rosenfield J, Levi N. Kidney scanning with hippuran, a necessary complement for correct interpretation of renography in the transplanted kidney. Paper presented at: Medical radioisotope scintigraphy. Proceedings of a symposium … held by the International Atomic Energy Agency in Salzburg, Vienna, 6–15 Aug 1968–1969.
142. Magnusson G, Collste L, Franksson C, Lundgren G. Radiorenography in clinical transplantation. Scand J Urol Nephrol. 1967;1:132–51.
143. Treves ST, Lebowitz R, Kuruc A, Heyman S, Rose P. Kidneys. In: Treves S, editor. Pediatric nuclear medicine. New York: Springer; 1985. p. 63–103.
144. Zum Winkel K, Harbst H, Schenck P, et al. Sequential scintigraphy in renal transplantation. Paper presented at: Medical radioisotope scintigraphy. Proceedings of a symposium … held by the International Atomic Energy Agency in Salzburg, Vienna, 6–15 Aug 1968–1969.
145. Harmon WE, Stablein D, Alexander SR, Tejani A. Graft thrombosis in pediatric renal transplant recipients. A report of the North American Pediatric Renal Transplant Cooperative Study. Transplantation. 1991;51(2):406–12.
146. Spigos DG, Tan W, Pavel DG, Mozes M, Jonasson O, Capek V. Diagnosis of urine extravasation after renal transplantation. AJR Am J Roentgenol. 1977; 129(3):409–13.
147. Kenny RW, Ackery DM, Fleming JS, Goddard BA, Grant RW. Deconvolution analysis of the scintillation camera renogram. Br J Radiol. 1975;48(570): 481–6.
148. Short MD, Glass HI, Chisholm GD, Vernon P, Silvester DJ. Gamma-camera renography using ^{123}I-hippuran. Br J Radiol. 1973;46(544):289–94.
149. Gates GF. Glomerular filtration rate: estimation from fractional renal accumulation of ^{99m}Tc-DTPA (stannous). AJR Am J Roentgenol. 1982;138(3):565–70.
150. Decostre PL, Salmon Y. Temporal behavior of peripheral organ distribution volume in mammillary systems. II. Application to background correction in separate glomerular filtration rate estimation in man. J Nucl Med. 1990;31(10):1710–6.
151. Takaki Y, Kojima A, Tsuji A, Nakashima R, Tomiguchi S, Takahashi M. Quantification of renal uptake of technetium-99m-DTPA using planar scintigraphy: a technique that considers organ volume. J Nucl Med. 1993;34(7):1184–9.
152. Schlegel JU, Hamway SA. Individual renal plasma flow determination in 2 minutes. J Urol. 1976; 116(3):282–5.
153. Moser E, Jocham D, Beer M, Bull U. Effects of obstruction on single-kidney function: clinical and experimental results with ^{131}I-hippurate and ^{99m}Tc-DMSA. Nuklearmedizin. 1980;19(6):257–62.
154. Diffey BL, Hall FM, Corfield JR. The ^{99m}Tc-DTPA dynamic renal scan with deconvolution analysis. J Nucl Med. 1976;17(5):352–5.
155. Oppenheim AV, Willsky AS, Young IT. Signals and systems. Englewood Cliffs, N.J.: Prentice-Hall; 1983.
156. Piepsz A, Ham HR, Erbsmann F, et al. A co-operative study on the clinical value of dynamic renal scanning with deconvolution analysis. Br J Radiol. 1982;55(654):419–33.
157. Erbsmann F, Strugven J, Ham H, Piepsz A. Analysis of errors and systemic biases in the calculation of the renal retention function. Paper presented at: Information Processing in Medical Imaging (Proceedings of the Vth International Conference), Nashville, 1978.
158. Fleming JS, Goddard BA. A technique for the deconvolution of the renogram. Phys Med Biol. 1974;19(4): 546–9.
159. Gamel J, Rousseau WF, Katholi CR, Mesel E. Pitfalls in digital computation of the impulse response of vascular beds from indicator-dilution curves. Circ Res. 1973;32(4):516–23.
160. Kuruc A, Caldicott WJ, Treves S. An improved deconvolution technique for the calculation of renal retention functions. Comput Biomed Res. 1982;15(1):46–56.
161. Kainer G, McIlveen B, Hoschl R, Rosenberg AR. Assessment of individual renal function in children using ^{99m}Tc-DTPA. Arch Dis Child. 1979;54(12): 931–6.
162. Huttunen K, Huttunen NP, Koivula A, Ahonen A, Puukka R. ^{99m}Tc-DTPA–a useful clinical tool for the measurement of glomerular filtration rate. Scand J Urol Nephrol. 1982;16(3):237–41.
163. Powers TA, Stone WJ, Grove RB, et al. Radionuclide measurement of differential glomerular filtration rate. Invest Radiol. 1981;16(1):59–64.
164. Kuruc A, Treves ST, Rosen PR, Greenberg D. Estimating the plasma time-activity curve during

radionuclide renography. J Nucl Med. 1987;28(8): 1338–40.
165. Owen JE, Walker RG, Willems D, Guignard PA, d'Apice AJ. Cadmium telluride detectors in the external measurement of glomerular filtration rate using ^{99m}Tc-DTPA (Sn): comparison with ^{51}Cr-EDTA and ^{99m}Tc-DTPA (Sn) plasma sample methods. Clin Nephrol. 1982;18(4):200–3.
166. Rossing N, Bojsen J, Frederiksen PL. The glomerular filtration rate determined with ^{99m}Tc-DTPA and a portable cadmium telluride detector. Scand J Clin Lab Invest. 1978;38(1):23–8.
167. Blaufox MD, Potchen EJ, Merrill JP. Measurement of effective renal plasma flow in man by external counting methods. J Nucl Med. 1967;8(2):77–85.
168. Sapirstein LA, Vidt DG, Mandel MJ, Hanusek G. Volumes of distribution and clearances of intravenously injected creatinine in the dog. Am J Physiol. 1955;181(2):330–6.
169. Rootwelt K, Falch D, Sjokvist R. Determination of glomerular filtration rate (GFR) by analysis of capillary blood after single shot injection of ^{99m}Tc-DTPA. A comparison with simultaneous 125I-iothalamate GFR estimation showing equal GFR but difference in distribution volume. Eur J Nucl Med. 1980;5(2):97–102.
170. Hall JE, Guyton AC, Farr BM. A single-injection method for measuring glomerular filtration rate. Am J Physiol. 1977;232(1):F72–6.
171. Ham HR, Piepsz A. Estimation of glomerular filtration rate in infants and in children using a single-plasma sample method. J Nucl Med. 1991;32(6):1294–7.
172. Piepsz A, Dobbeleir A, Erbsmann F. Measurement of separate kidney clearance by means of ^{99m}Tc-DTPA complex and a scintillation camera. Eur J Nucl Med. 1977;2(3):173–7.
173. Piepsz A, Denis R, Ham HR, Dobbeleir A, Schulman C, Erbsmann F. A simple method for measuring separate glomerular filtration rate using a single injection of ^{99m}Tc-DTPA and the scintillation camera. J Pediatr. 1978;93(5):769–74.
174. Gordon I, Anderson PJ, Orton M, Evans K. Estimation of technetium-99m-MAG3 renal clearance in children: two gamma camera techniques compared with multiple plasma samples. J Nucl Med. 1991;32(9):1704–8.
175. Bailey SM, Evans DW, Fleming HA. Intravenous urography in investigation of hypertension. Lancet. 1975;2(7924):57–8.
176. Chervu LR, Blaufox MD. Renal radiopharmaceuticals–an update. Semin Nucl Med. 1982;12(3): 224–45.
177. Ram MD, Evans K, Chisholm GD. A single injection method for measurement of effective renal plasma flow. Br J Urol. 1968;40(4):425–8.
178. Razzak MA, Botti RE, MacIntyre WJ, Pritchard WH. External monitoring of ^{113}1-hippuran disappearance as a measure for renal blood flow. Int J Appl Radiat Isot. 1967;18(12):825–8.
179. Mackay A, Eadie AS, Cumming AM, Graham AG, Adams FG, Horton PW. Assessment of total and divided renal plasma flow by ^{123}I-hippuran renography. Kidney Int. 1981;19(1):49–57.
180. Heidenreich P, Lauer O, Fendel H, Oberdorfer M, Pabst HW. Determination of total and individual kidney function in children by means of 123-I-hippuran whole body clearance and scintillation camera. Pediatr Radiol. 1981;11(1):17–27.
181. Thompson Jr IM, Boineau FG, Evans BB, Schlegel JU. The renal quantitative scintillation camera study for determination of renal function. J Urol. 1983;129(3):461–5.
182. Tauxe WN, Tobin M, Dubovsky EV, Bueschen AJ, Kontzen F. A macrofunction for computer processing of comprehensive renal function studies. Eur J Nucl Med. 1980;5(2):103–8.
183. Edward Hsiao, Xinhua Cao, Katherine Zukotynski, Laura Drubach, David Zurakowski, Royal T. Davis, Frederic H. Fahey and S. Ted Treves A. Hans Vija, Amos Yahil. Dose reduction in pediatric MAG-3 renal scans J Nucl Med. 2009;50 (Suppl 2): 253.

Vesicoureteral Reflux and Radionuclide Cystography

13

S. Ted Treves and Frederick D. Grant

Vesicoureteric reflux (VUR) is the retrograde transit of urine from the urinary bladder to the ureters and kidneys. VUR is caused by a failure of the ureterovesical valve mechanism. This failure may be due to a congenital variation, immaturity, or a pathologic process, such as an infection that distorts the anatomy or function (or both) of the ureterovesical junction. The clinical importance of VUR is its association with pyelonephritis and its contribution to reflux-related nephropathy. Although an evolving field, identification of VUR remains an important part of the evaluation of patients with febrile urinary tract infections, especially those with documented involvement of the kidney as a site of infection [1–5]. VUR also can contribute to nephropathy resulting from the reflux of urine into the renal collecting system without a concurrent infection. Radionuclide cystography (RNC) is a sensitive and easy method for the diagnosis and follow-up of VUR. In conjunction with ^{99m}Tc-DMSA, ultrasonography, and voiding cystourethrography, RNC can be an important part of the evaluation of recurrent febrile urinary tract infections in children.

S.T. Treves, MD (✉)
Joint Program in Nuclear Medicine,
Department of Radiology, Harvard Medical School,
Boston, MA, USA

Division of Nuclear Medicine and Molecular Imaging,
Department of Radiology,
Boston Children's Hospital,
Boston, MA, USA

Division of Nuclear Medicine and Molecular
Imaging, Department of Radiology,
Brigham and Women's Hospital,
Boston, MA, USA
e-mail: ted_treves@HMS.harvard.edu

F.D. Grant, MD
Joint Program in Nuclear Medicine,
Department of Radiology, Harvard Medical School,
Boston, MA, USA

Division of Nuclear Medicine and Molecular Imaging,
Department of Radiology,
Boston Children's Hospital, Boston, MA, USA

Department of Radiology,
Brigham and Women's Hospital, Boston, MA, USA
e-mail: frederick.grant@childrens.harvard.edu

The Ureterovesical Junction

Passive and active factors characterize the normal valve mechanism of the ureterovesical junction. Passive factors include the obliquity of entry of the ureter into the bladder; the length of the intramural ureter, particularly of its submucosal segment; and the ratio of the length of the submucosal tunnel to the diameter of the ureter. The active factors include the contraction of the ureterotrigonal muscles, which close the ureteral meatus and the submucosal tunnel, and active ureteral peristalsis, as seen during diuresis [6]. The intramural ureter becomes longer with age, often producing sufficient length to convert a refluxing ureterovesical junction into a nonrefluxing one. The principal long-term consequence of VUR, particularly when associated with infection, is the development of pyelonephritis, which in turn

S.T. Treves (ed.), *Pediatric Nuclear Medicine and Molecular Imaging*,
DOI 10.1007/978-1-4614-9551-2_13, © Springer Science+Business Media New York 2014

may lead to scarring, hypertension, and chronic renal failure.

Incidence

The incidence of VUR in the general population is not well-defined. Approximately 1 % (7 of 535) of apparently normal neonates, infants, and children have been found to have VUR [6]. The incidence of VUR in siblings of children with reflux is much greater than in the general population and may be as high as 45 % [7–11]. In a study at Boston Children's Hospital six of 16 refluxing-symptom-free siblings of children with VUR had evidence of cortical renal damage as assessed by technetium-99m-dimercaptosuccinic acid (^{99m}Tc-DMSA) scintigraphy [12–15]. ^{99m}Tc-DMSA cortical scintigraphy provides an early indicator of renal damage, and it can be considered in the assessment of symptomatic and asymptomatic siblings of refluxing children. Using radionuclide cystography, we also have found previously undiagnosed asymptomatic reflux in parents of index children with VUR.

Diagnosis

The imaging method most frequently used for the detection of VUR has been radiographic voiding cystourethrography (VCUG). It provides fine anatomic detail of the bladder and the urethra. In patients with reflux, it clearly outlines the anatomy of the pelvicaliceal systems, the ureters, and their insertion into the bladder. It has some limitations, however, including gonadal radiation exposure and low temporal resolution, which prevents diagnosis of intermittent VUR. In the past decades, radionuclide cystography (RNC) gained increasing acceptance for both the initial diagnosis and follow-up of VUR (Fig. 13.1). Advantages

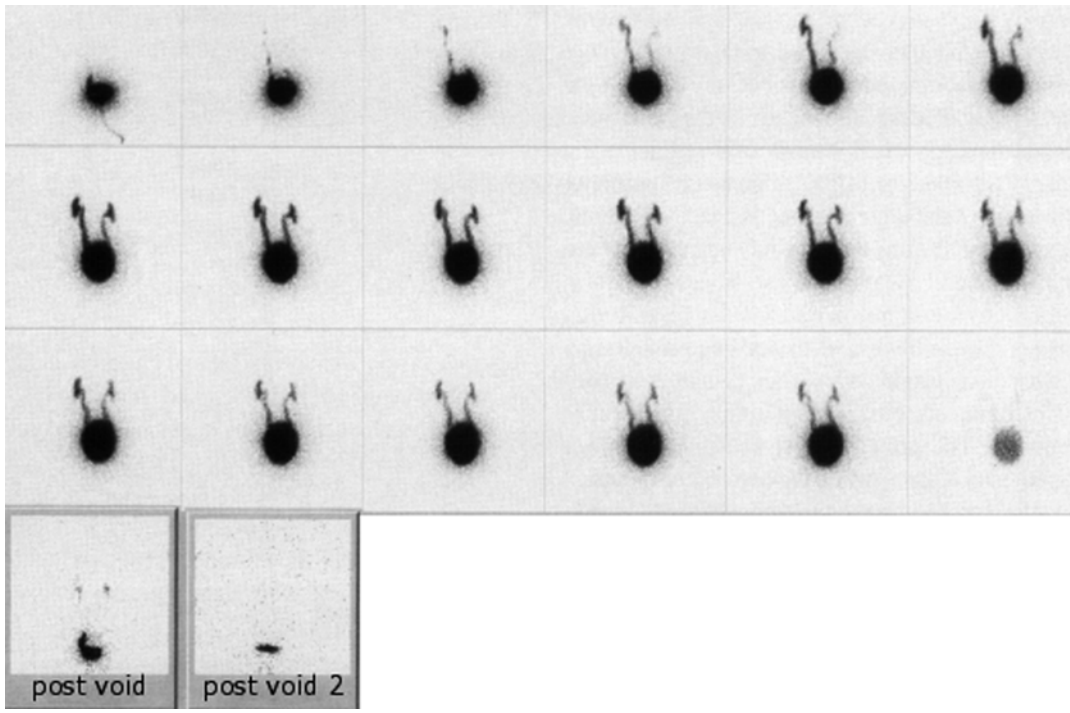

Fig. 13.1 Bilateral vesicoureteric reflux, as shown by radionuclide cystography. Initial left reflux followed by right reflux reaching the renal pelves. Reflux appears early and persists during the entire voiding phase. The patient could not void while on the examination table. Postvoid images reveal complete drainage of tracer from the ureteropelvicaliceal systems

of RNC include lower gonadal radiation exposure, high temporal resolution, and higher sensitivity for the detection of mild VUR. Also RNC may be less expensive to perform than VCUG [16]. However, RNC cannot delineate the anatomy of the bladder and urethra. Therefore, one approach is to to use VCUG for the initial diagnosis of VUR, and then to follow patients with RNC. RNC may be appropriate for the initial diagnosis of VUR in sibling studies and in older girls, in whom excluding urethral valves is not important [17–19].

Grading the Severity of Vesicoureteric Reflux

The severity of VUR has been classified by its morphologic appearance on VCUG or RNC. A report by an international group studying VUR adopted a VCUG classification of reflux illustrated in Fig. 13.2 [20]. This grading system is convenient for communication but need not be applied rigidly in an individual case [6]. Moreover, this classification is not exact, as VUR appearances vary over a continuum and often some VURs do not fall precisely within one of the five grades. For example, the same patient may be classified with a grade II reflux during one examination and a grade I or III at another.

With RNC it is possible to recognize at least three degrees of reflux severity (Fig. 13.3) [21]. The least severe degree shows reflux limited to the

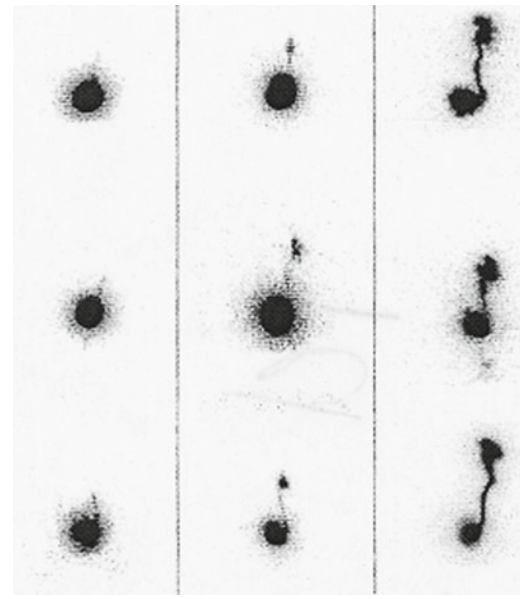

Fig. 13.3 Reflux severity in radionuclide cystography (RNC)

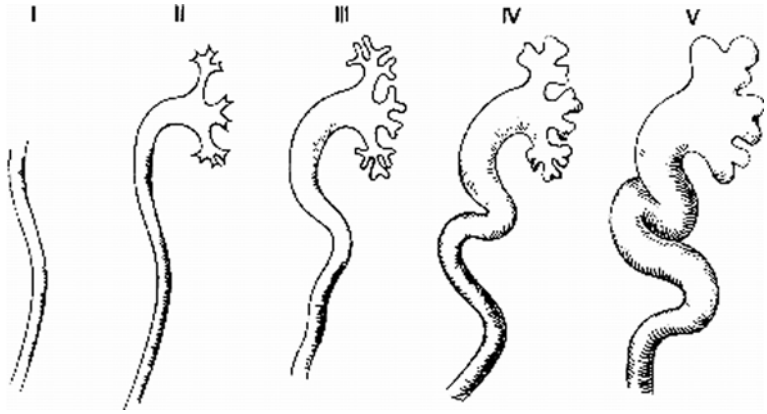

Fig. 13.2 Grading of vesicoureteral reflux by voiding cystourethrography, international study classification. Grade *I*: ureter only. Grade *II*: ureter, pelvis, and calyces; no dilatation, normal caliceal fornices. Grade *III*: mild or moderate dilatation or tortuosity of ureter (or both) and mild or moderate dilatation of renal pelvis but no or slight blunting of fornices. Grade *IV*: moderate dilatation or tortuosity of ureter (or both) and moderate dilatation of renal pelvis and calyces. Complete obliteration of sharp angles of fornices but maintenance of papillary impressions in majority of calyces. Grade *V*: gross dilatation and tortuosity of ureter; gross dilatation of renal pelvis and calyces; papillary impressions are no longer visible in most calyces

distal ureter without reaching the renal pelvis (Fig. 13.4). This corresponds to grade I reflux and can be called RNC-grade 1. Another appearance is that of a small volume of VUR reaching the renal pelvis with minimal or no visualization of the ureter (Fig. 13.5). This appearance corresponds to radiographic grades II or III, as it is not possible by the radionuclide technique to assess finely the diameter of the ureter and the anatomy of the pelvicaliceal system (RNC-grade 2). Finally, the radionuclide cystogram may reveal a large volume of reflux reaching a dilated pelvicaliceal system with definite or marked dilatation and even elongation and tortuosity of the ureter corresponding in appearance to radiographic grades IV and V (RNC-grade 3) (Figs. 13.6 and 13.7). Comparing the five VCUG grades of reflux with the three grade of reflux severity on RNC can be difficult, because of the technical differences between these two methods. This may be of particular concern when trying to compare the VCUG and RNC findings in the same patient to determine if reflux severity has changed over time.

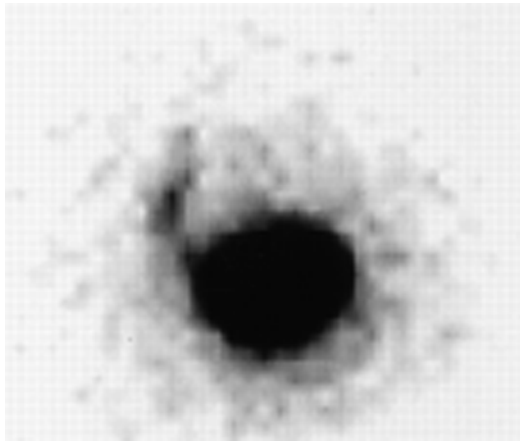

Fig. 13.4 Distal left vesicoureteric reflux, RNC severity grade 1. Reflux is limited to the left distal ureter without reaching the renal pelvis

Variability of Low-Grade Vesicoureteric Reflux

Vesicoureteric reflux is not a constant phenomenon. Low-grade VUR may vary from examination to examination. In our observation, using RNC, VUR varies also with bladder volume, voiding or filling, patient position, and level of anxiety. Reflux may be present during most of the filling and voiding phases of the radionuclide cystogram, or it may be intermittent (Fig. 13.8) [21, 22]. Therefore, it is

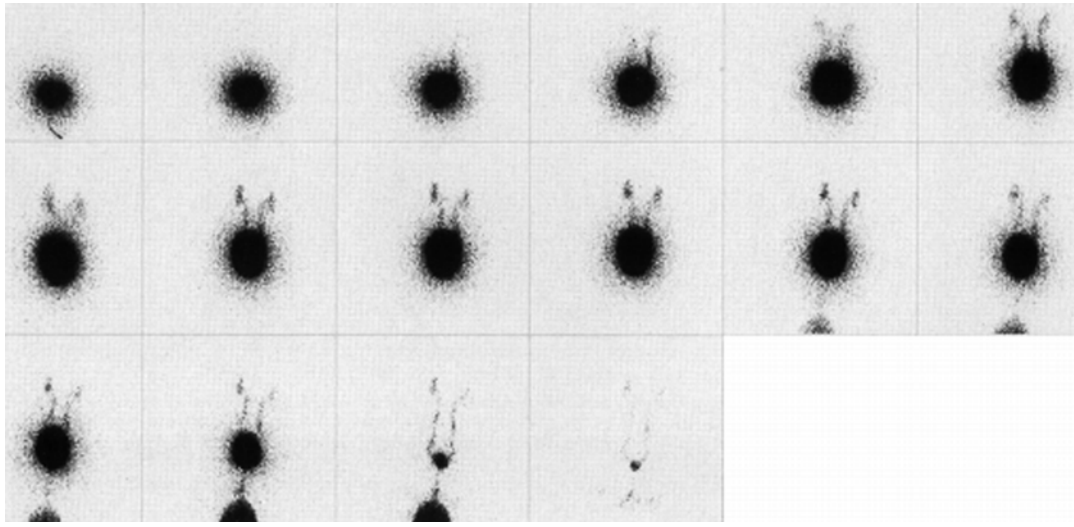

Fig. 13.5 Bilateral vesicoureteric reflux, RNC severity grade 2. Reflux reaches both renal pelves and persists during the filling and voiding phases of the RNC. At the end of voiding, a significant amount of tracer has drained out of the renal pelves, ureters, and bladder

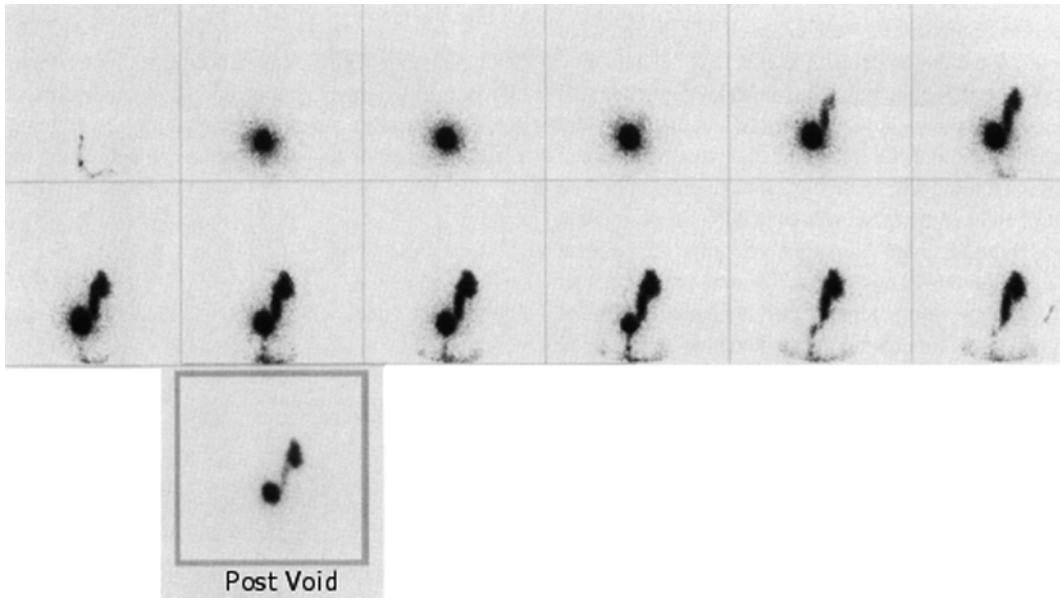

Fig. 13.6 Severe unilateral vesicoureteric reflux, RNC severity grade 3. Reflux is visualized in a dilated right ureter and renal pelvis. A postvoid image reveals significant retention of tracer in the renal pelvicaliceal system and ureter with secondary filling of the bladder

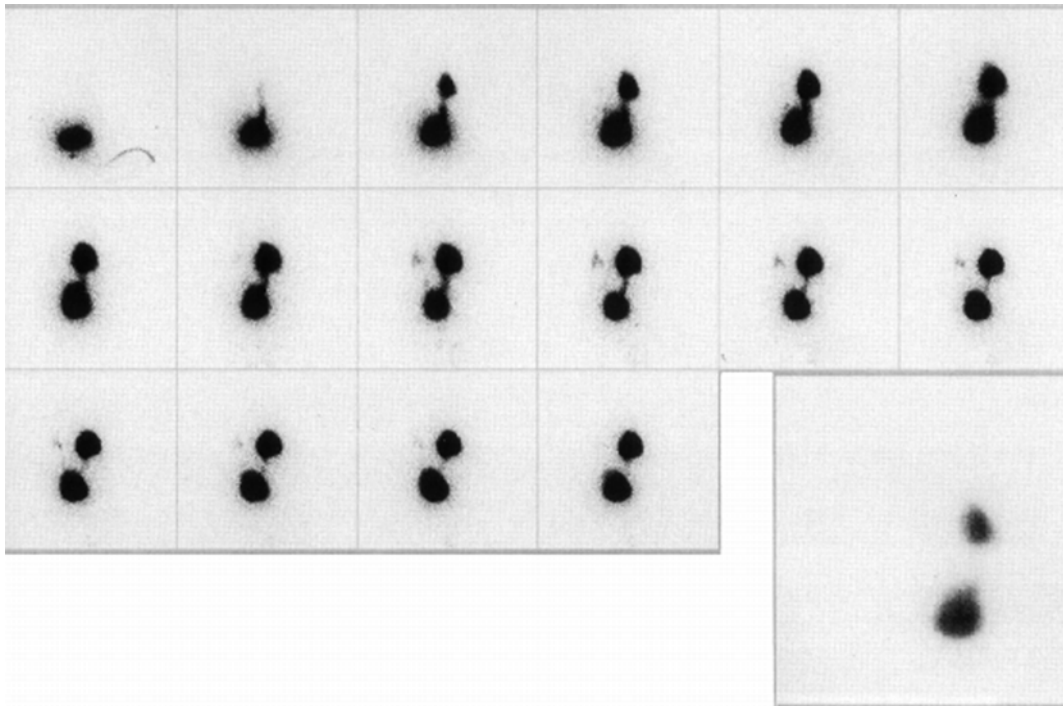

Fig. 13.7 Severe right vesicoureteric reflux (RNC severity grade 3) and mild to moderate left vesicoureteric reflux (RNC grade 2). Right reflux appears early at low bladder volume and persists during the entire examination. A postvoid image (*bottom right*) reveals secondary bladder filling and significant retention of tracer in the right renal pelvis. In addition, there is mild to moderate left vesicoureteric reflux reaching the renal pelvis. Left reflux occurs at higher bladder volumes, is intermittent, and drains rather rapidly even during bladder filling

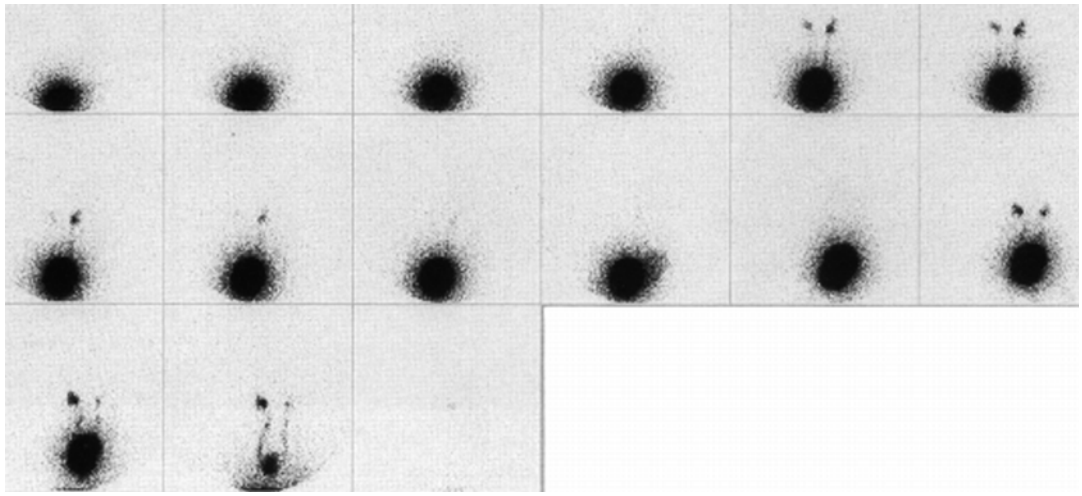

Fig. 13.8 Intermittent bilateral vesicoureteric reflux. Mild to moderate reflux appears almost simultaneously during the mid-filling phase in both ureters and renal pelves. During the mid- to late filling phase, reflux subsides temporarily in both sides and reappears during the late filling and voiding phases

clear that a single normal examination may not sufficient to ensure that VUR has resolved. Serial cystograms over several (6–12) months should provide greater assurance of complete cessation of reflux [23]. We have evaluated 480 ureters from 240 patients on two separate occasions when patients underwent RNC. The period between observations averaged 13 months (3 months to 3.7 years). None of the patients had prior surgery, neurogenic bladder, or other anatomic abnormality. This study revealed that 85 % of the ureters showed either no change (55 %) or decrease (30 %) in reflux severity. However, 15 % revealed an apparent worsening in reflux severity (9 %), or reflux was detected only on the second RNC (6 %). Two-stage RNC has also shown the variable nature of VUR [24, 25]. Treatment programs for VUR, therefore, should take into account the variability of low-grade reflux.

Spontaneous Cessation of Reflux

VUR frequently resolves with growth and maturation of the urinary tract. Spontaneous cessation of reflux was reported in approximately 71 % of children and 79 % of ureters studied by Normand and Smellie [26] in 1979. The most important factor in the resolution of VUR seemed to be the apparent diameter of the ureter at the time of diagnosis. Resolution of VUR took place in 85 % of ureters of normal caliber but in only 41 % of dilated ureters. In addition, these authors reported that 65 % of ureters associated with scarred kidneys also ceased to reflux spontaneously.

Treatment

Traditionally, patients with low-grade reflux have been treated with a regimen of long-term antibiotic prophylaxis. With severe reflux, spontaneous resolution of reflux can occur but is less likely. Continuous antibiotic therapy may be given to these patients provided their urine remains sterile, frequent urine cultures are performed, and that serial evaluation for reflux is carried out. This routine requires careful compliance by the patient and parents. Patients with peristent reflux, requiring prolonged antibiotic prophylaxis, febrile urinary infection despite prophylaxis, or severe reflux may be offered surgical correction of the vesicoureteral reflux.

Surgical treatment of VUR has a high degree of success in experienced hands [27, 28], offers an immediate correction of the anatomic problem,

and reduces the risk of pyelonephritis. Neither medical nor surgical treatment, however, seems to offer a clear advantage related to subsequent development of hypertension or impairment of renal growth. Whichever form of therapy is chosen, long-term follow-up and observation are essential to assess the patient's progress and the presence of complicating factors, such as residual VUR, pyelonephritis, new scarring, hypertension, or renal dysfunction.

Radionuclide Cystography

Indications

Radionuclide cystography has four principal indications (Table 13.1) [1]. Because of its safety, high sensitivity, and minimal radiation exposure, RNC can be an ideal method for the initial diagnosis of VUR in some patients. For example, RNC can be an appropriate test in an older girl in whom there is less concern for urethral obstruction or anatomic abnormalities of the urinary tract. However, for younger children, most clinicians prefer to use VCUG for the first evaluation of the urinary tract, as it will provide more anatomic detail and better visualization of the urethra. Radionuclide cystography is indicated for the follow-up of patients who have been diagnosed previously with VUR and are receiving long-term prophylactic antibiotic therapy. Patients undergoing this type of treatment are typically monitored for reflux every 12–24 months. RNC also can be used for follow-up evaluation of patients found to have VUR during the evaluation of persistent prenatal hydronephrosis [29]. Radionuclide cystography is an effective technique for evaluating the results of surgical repair of VUR. In addition, and because of the low radiation dose and high sensitivity, RNC is a useful method for the evaluation of siblings for familial reflux [7–12].

Table 13.1 Indications for radionuclide cystography

Initial diagnosis of vesicoureteric reflux (VUR)
Follow-up of previously diagnosed VUR to assess for spontaneous resolution
Assessment of antireflux surgery
Diagnosis of familial VUR

Methods

There are two principal nuclear medicine methods to diagnose VUR: direct RNC and indirect radionuclide cystography (IRC). The direct method, which is by far the most common approach, requires bladder catheterization to introduce the radionuclide into the bladder in a retrograde fashion. Indirect radionuclide cystography does not require catheterization. Studies comparing RNC with IRC have suggested that RNC is more sensitive than IRC [30–32]. However, RNC is an invasive technique, so IRC may still have a role in the diagnosis of VUR in cooperative patients and in those who refuse catheterization [33]. Indirect radionuclide cystography requires that the patient refrain from voiding until the time of examination. Increased urinary output caused by recent administration of a diuretic (e.g., furosemide) or an intravenous contrast agent for urography or overhydration can interfere with the detection of VUR. Therefore, cystography should be performed first, or one should wait 1 day after administration of these agents.

Patient Preparation

The same patient preparation applies for both direct RNC and IRC. A complete explanation of the procedure should be given to the patient and parents. When done with patience and understanding, such a conversation can reduce anxiety before the examination. In addition, we find it helpful to hand out or mail a brochure with information and instructions for the RNC [21, 34]. We do not use sedation for RNC in the vast majority of the patients. The patient is instructed to void in the bathroom before the examination if possible and then to lie supine on the examination table for the study (see below).

Direct Radionuclide Cystography

Radionuclide cystography can detect small volumes of reflux, as little as 0.2 mL at 2 cm from the projected edge of the bladder [22]. RNC is indeed a stress test of the ureterovesical junction, with the bladder being filled in a retrograde fashion with a fluid at a higher rate than is natural. The radiation exposure to the patient with RNC is low, with a gonadal absorbed radiation dose of less than 0.03 mGy (3 mrad). Radionuclide cystography is highly sensitive, and the operator has greater control of the procedure than with IRC. Patients of all ages can be examined. As part of the procedure, a urine sample under aseptic conditions is obtained for culture.

Radiopharmaceutical

Technetium-99m (^{99m}Tc) as pertechnetate is used. The usual administered dose is 1 mCi (37 MBq). Alternative radiopharmaceuticals include ^{99m}Tc-labeled sulfur colloid and ^{99m}Tc-DTPA. Technetium-99m as pertechnetate should not be used in patients who have undergone bladder augmentation with gastric or intestinal mucosa. In these patients, ^{99m}Tc-pertechnetate may be absorbed into the circulation and interfere with detection of mild vesicoureteral reflux [35].

Equipment and Recording

The examination table is covered with plastic-lined absorbent paper to contain any spilled tracer and to reduce contamination of the table. A gamma scintillation camera system equipped with a high-resolution collimator is used. In our practice, the RNC is recorded as a series of 10-s frames in a 128 × 128 matrix format for the duration of the filling and voiding phases of the study. Postvoid images are obtained if the patient is not able to empty the bladder while on the imaging table.

Catheterization

Sterile urethral catheterization trays prepared for each study contain the following items: three small containers, cotton, and a sterile towel with a central opening. Other materials needed include antiseptic solution (PROVON Antimicrobial Lotion Soap, GOJO Industries, Inc., Akron, OH), sterile water, lidocaine anesthetic jelly, and a 10-mL syringe with a blunt, tapered adapter ("fistula tip"). Catheters of two sizes are used: a 2.6-mm-diameter catheter (French 8) for most patients and a 1.5-mm-diameter catheter (French 5) for infants.

The success of the examination depends to a great extent on careful catheterization technique. If necessary, a parent or aide assists in immobilizing the patient, who lies supine and is encouraged to relax. The so-called frog position is useful in catheterizing females. The periurethral area in females and the glans penis in males is carefully cleansed with antiseptic solution and sterile water warmed to body temperature before use. The catheter is lubricated with the anesthetic jelly to facilitate a smooth insertion. Using a bright spotlight, the female urethral orifice must be clearly identified before attempting catheterization. The catheter should be introduced easily in one motion, without hesitation. Any additional contact with the area surrounding the urethral orifice should be avoided because it causes discomfort. This point cannot be emphasized enough, because a child who has had a bad first experience with this procedure is not likely to cooperate in the future.

In boys, the urethra is anesthetized. The penis is held with one hand, while lidocaine jelly (5–10 mL) is slowly injected into the urethra using the blunt adapter. Slow and deep breathing helps to relax the sphincter and allows anesthesia of the entire urethra. Slightly squeezing the anterior portion of the penis for a minute or so prevents the lidocaine from draining out. The catheter is then gently and continuously introduced into the bladder. Encourage the patient to breathe deeply and attempt to void, which may relax the sphincter. If the sphincter remains closed, the catheter should be kept under continuous and mild pressure against it. In most cases, the catheter eventually glides through the sphincter.

Do not try to overcome a closed or spastic sphincter by repeated back-and-forth motions of the catheter as it may result in urethral injury. In the rare instance when it is necessary to repeat

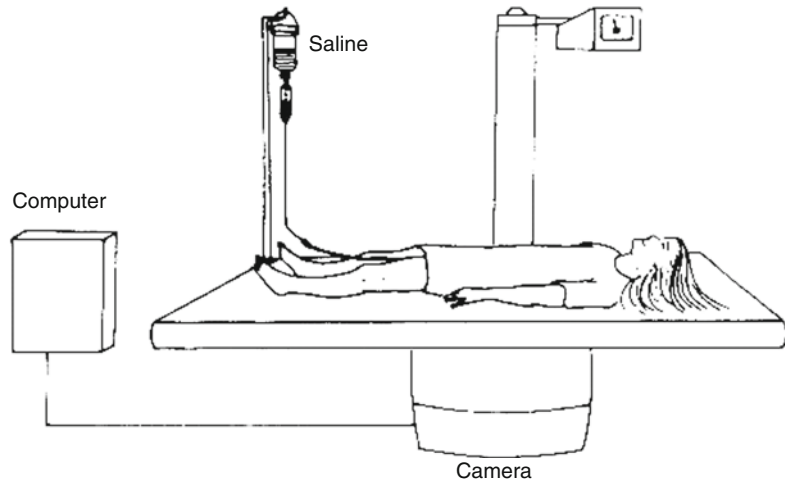

Fig. 13.9 Method of direct radionuclide cystography

the urethral anesthesia, a second attempt at catheterization is almost always successful.

Once the catheter has been advanced beyond the sphincter, most children cooperate. The residual bladder volume is then measured. The catheter is fixed with adhesive surgical tape to the inner thigh in girls and to the dorsal shaft of the penis in boys. Leaving the catheter in place until the end of the study allows for a repeat examination in case of failure, as well as for additional filling of the bladder if needed. In most cases, however, the catheter is removed gently before the patient voids. Some investigators have suggested direct RNC by direct percutaneous administration rather than bladder catheterization [36]. We have not employed this approach.

Filling and Voiding

The child is encouraged to lie quietly on the table. A calm environment and dim room lighting during the procedure often have a quieting effect. Many patients (and parents) find that watching a small ceiling-mounted TV while the study is in progress greatly helps reduce anxiety and makes the time pass more quickly.

The tracer is administered directly into the patient's bladder via the catheter (For computerized radionuclide cystography (CRVC), the radiopharmaceutical is mixed with the saline in the bottle and infused into the bladder [see section "Computerized Radionuclide Cystography", following]). A bag of 500 mL of normal saline (or irrigating solution) is suspended 70–90 cm above the bladder and connected to the catheter (Fig. 13.9). Gravity allows the saline solution to drain freely into the bladder. In our practice, we examine most patients in the supine position to more easily control the examination. However, the RNC can be performed in the sitting or semi-recumbent position if so desired.

While the bladder is filling, the operator monitors the entire examination on the computer monitor. The end of the filling phase is usually indicated by a bladder volume appropriate for the patient's age (see below) or a reduction or cessation of the infusate's rate of flow. When the bladder is filled to its capacity, voiding is usually initiated without delay. Careful and complete collection of the voided fluid is necessary for quantitation (see "Computerized Radionuclide Cystography" section below). We use a plastic urinal for both girls and boys. In girls its lower border is gently pressed against the perineum and inner thighs. If patients cannot void in the supine position, they are asked to try voiding in the sitting position.

The technologist or physician conducting the study should record the following: residual bladder volume, the fact that a urine sample was obtained under aseptic conditions for culture, any problems during the catheterization or the procedure, and voided volume. The data can be entered

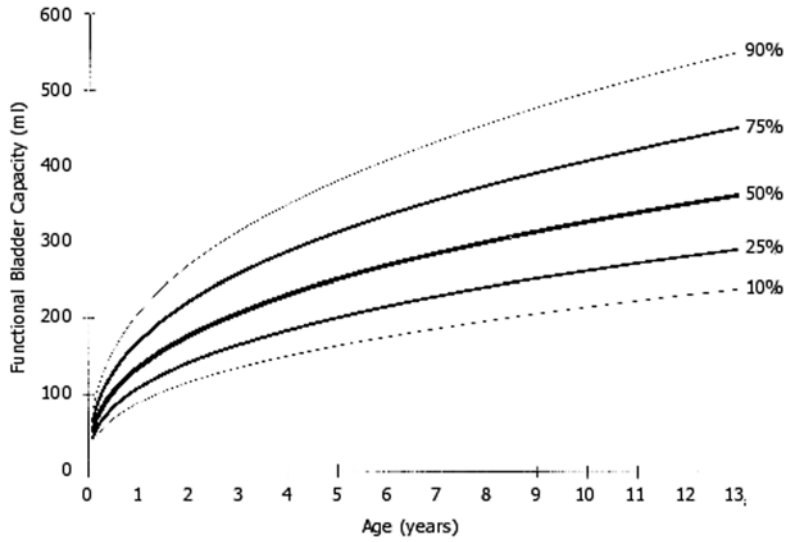

Fig. 13.10 Functional bladder capacity as a function of age in children less than 13 years of age

directly on the computer to be included within the diagnostic report.

Functional Bladder Capacity

Knowledge of the expected functional bladder capacity is useful for evaluation of VUR in children. However, a priori prediction of bladder capacity in children is difficult. Subjective criteria of complete bladder filling produced by the patient (toes curling upward, jiggling leg movements, complaints of urgency) should be noted, but their value may be unreliable.

Although bladder capacity generally increases with age and maturation, its variability at a given age or in a given patient may correspond to 100 % or more of the mean volume. Influences operating at the time of examination may cause the functional bladder capacity to be different from the actual capacity. Mechanical factors, such as rapid filling of the bladder, irritation from the catheter, or low temperature of the instilled fluid, can induce high bladder tonus and thus lower bladder capacity. Apprehension may provoke the same response. Uninhibited bladder contractions related to irritability from severe inflammation characteristically cause intermittent pain and urgency and tend to keep bladder capacity low. In most of the children with urinary tract infection (UTI) bladder capacity does not seem to be affected [21].

Information about bladder capacity on previous studies, mean values, and observation of the infusion flow rate should aid the operator in filling the patient's bladder to its approximate functional capacity. Several studies have addressed bladder capacity as a function of age in children, but published studies have included fewer than 250 observations [22, 37–40]. Those reports have indicated a linear relationship between age and functional bladder capacity. The following formula has been suggested: [37] bladder capacity (ounces) = age (years) plus 2. In addition, for children up to 1 year of age, a linear regression has been suggested: [38] capacity (mL) = [7.0 × weight (kg)] − 1.2. However, our experience using direct RNC suggests that this relationship is not linear [22].

We have reviewed the functional bladder capacities for more than 4,000 RNC examinations in children under 13 years of age. The relationship of functional bladder capacity and age seems to be nonlinear, and it can be described by a power model: $Y = \beta_0 X^{\beta 1}$, where Y is the estimated bladder capacity, β_o is the volume (constant), X is the age, and $^{\beta 1}$ is the slope power (Fig. 13.10) [41].

Analysis of Radionuclide Cystography

In routine practice, analysis of RNC is visual. The RNC should be viewed whenever possible on cinematic display, and the interpreter should be able to vary the playback speed and the contrast of the dynamic image set. With most low-grade reflux, the volume and amount of activity of refluxed tracer is much smaller than the activity within the bladder, so reflux could be missed if no contrast enhancement is used. No single approach covers all cases. Generally, it is useful to vary the upper threshold in the range between 5 and 15 % of the maximum level of activity in the image. Evaluation of the RNC with a series of static images is generally effective; however, evaluation on cinematic display is strongly recommended to achieve a higher diagnostic yield. Even with patient motion, dynamic evaluation enables the operator to distinguish scatter from minimal reflux better than on serial static images. Motion correction helps in the assessment of RNC where the patient has moved during the examination.

On occasion, time-activity curves from regions of interest over the renal, ureteral, and vesical regions may be utilized for quantitative evaluation of reflux, bladder volumes, and voiding flow rates with RNC (See following discussion of computerized voiding cystography). Meticulous attention to technique and complete avoidance of patient motion are mandatory for this approach [21].

Reporting Results

The RNC report should address at least the following information: voiding prior to the examination, residual bladder volume, the fact that a urine sample obtained under aseptic conditions was collected and sent to the laboratory for culture, problems with catheterization or the procedure, volume infused in the bladder, volume voided, presence and severity of reflux, and comparison with previous examinations (same, better, or worse). Most of our patients see a urologist after completion of RNC study; in our practice, the RNC report and images are immediately transmitted to the referring urologist.

Vesicoureteric Reflux in Radionuclide Cystography

An analysis of 135 consecutive radionuclide studies in our hospital revealed a 32 % incidence of VUR, usually RNC grades 1 or 2. Reflux was present in 47 % of the nonsurgical patients and in 11 % of the patients evaluated after surgery. It was unilateral in 60 % and bilateral in 40 %. Unilateral reflux occurred in the right and left ureters with equal frequency. In the 59 refluxing renal units, reflux occurred during filling and voiding in 80 %, whereas reflux present during voiding only was seen in 17 % of the ureters. These findings underscore the importance of examining the patient during voiding as well as during filling. The remaining 3 % of ureters refluxed during bladder filling only. Almost 80 % of those patients with reflux during filling and voiding refluxed 2–34 mL (average 7 mL) [21].

Patterns of Reflux

The ability to continuously monitor during RNC permits observation of several dynamic patterns of reflux. Continuously increasing reflux characteristically occurs during the early or mid-filling phase, supposedly through a patulous ureteral orifice that allows the bladder and ureter(s) to behave as a single chamber. This is the most severe reflux. Occurrence of reflux in this condition appears to be independent of intravesical pressure, which is usually low during the beginning of bladder filling [42].

Most commonly, VUR does not start until a certain bladder volume has been reached and then either continues to increase until the end of the filling phase or shows intermittent increases and decreases in volume. In some patients, however, there may be only one or few transient episodes of reflux during the filling or voiding phase (Figs. 13.11, 13.12 and 13.13). Some children who are unwilling or unable to void during the cystogram are asked to urinate in the bathroom, and a postvoid image is obtained. In some cases, the postvoid image shows the only evidence of VUR. Therefore, a postvoid image must be considered a routine part of the examination. In certain cases of bilateral reflux, one ureter can be

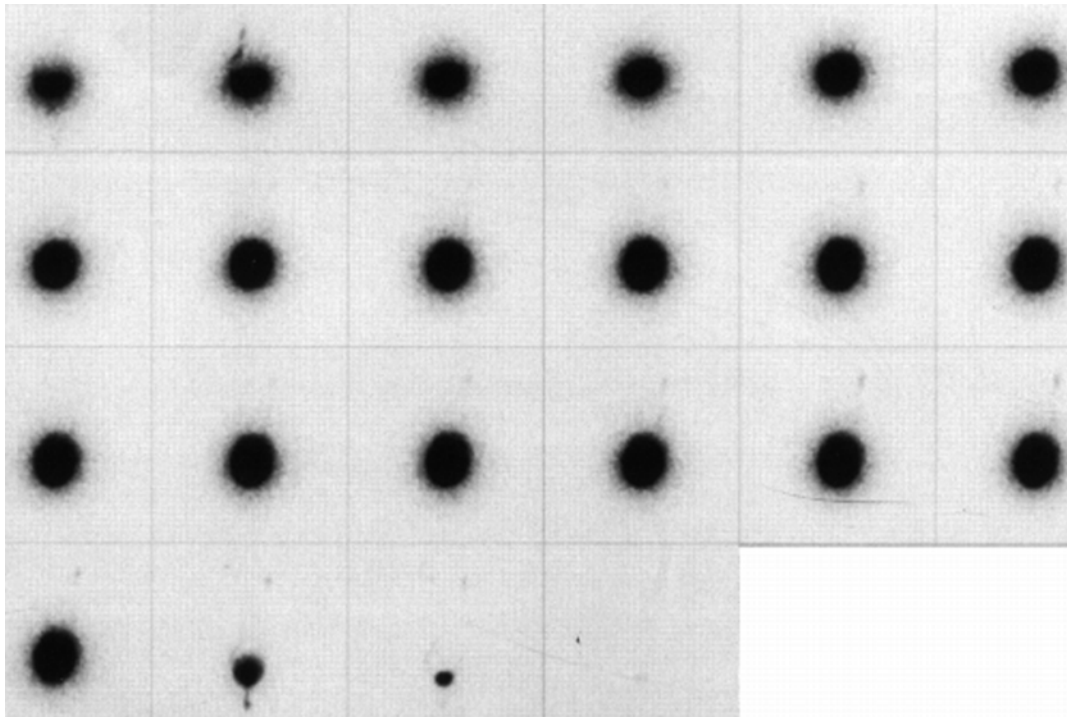

Fig. 13.11 Intermittent mild bilateral vesicoureteric reflux. Early (low bladder volume) left vesicoureteric reflux (VUR) subsides rapidly. As the RNC progresses toward the end of filling, there is mild bilateral VUR. An image obtained following the completion voiding reveals complete drainage of both ureteropelvicaliceal systems and the bladder

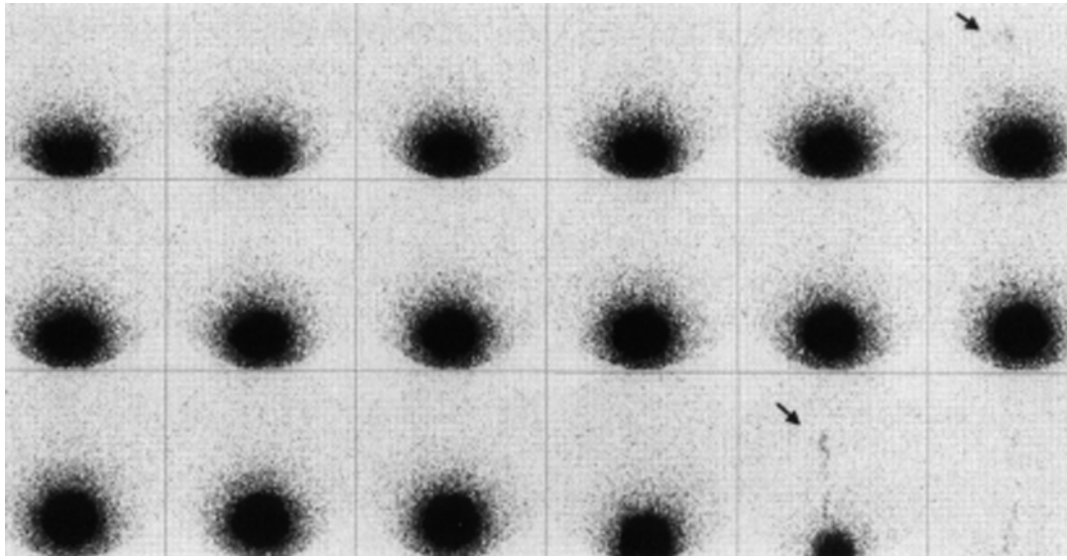

Fig. 13.12 Mild intermittent left vesicoureteric reflux. Left VUR is visualized briefly during the mid-filling phase; it then disappears completely and returns during the voiding phase (*arrows*)

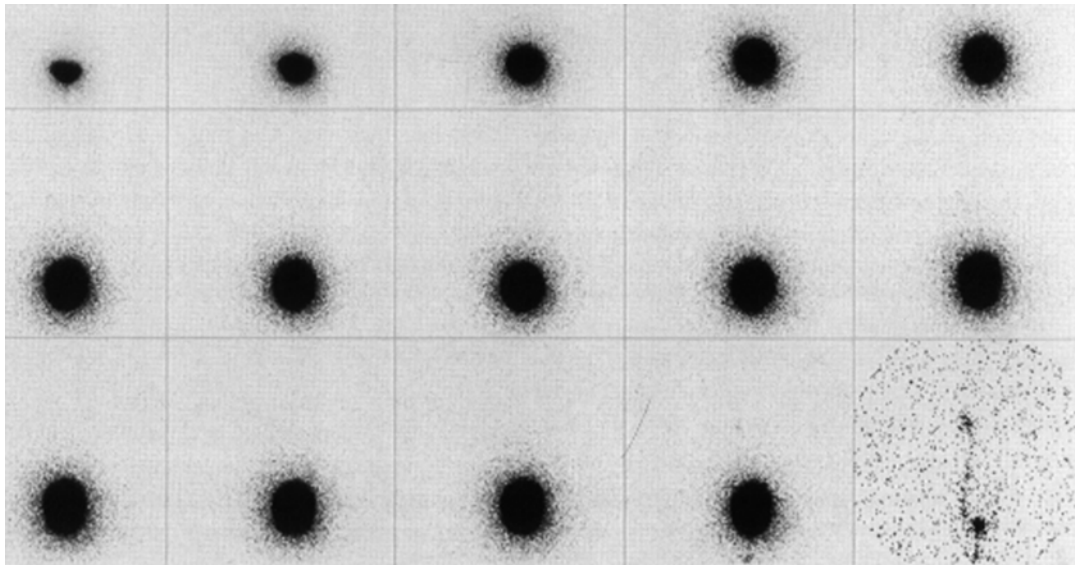

Fig. 13.13 Mild left vesicoureteric reflux. Reflux is seen only during voiding

seen to begin refluxing at a certain bladder volume, with reflux beginning in the contralateral ureter at a greater bladder volume.

If reflux has occurred during the filling phase, it may or may not increase in volume during the voiding phase, and in certain instances, it may decrease or disappear altogether during voiding. Refluxed fluid may continuously drain into the bladder immediately after completion of voiding, despite the fact that at this time intravesical pressure frequently reaches its maximum. Reflux, therefore, may have little to do with intravesical pressure and be more related to the degree of bladder filling and contraction.

Bladder Emptying and Voiding Flow Rate

The urine flow rate can be easily calculated with RNC [43, 44]. We calculated the voiding flow rates in 75 patients [21]. The average rate in 26 normal children was 10.2 mL/s [range 2.0–21.0 mL/s ± 4.5 standard deviation (SD)]. In 49 abnormal patients (reflux with or without infection or previous surgery), the voiding flow rates averaged 10.5 mL/s (range 1.4–31.0 mL/s ± 5.7 SD). In all 75 patients, the average voiding flow rate was 10.4 mL/s (range 1.4–31.0 mL/s ± 5.3 SD). The average voiding flow rate seemed to relate to the initial bladder volume and thus to age. The greater the initial bladder volume, the higher was the voiding flow rate. The presence of an indwelling catheter did not seem to reduce the voiding flow rate significantly. In patients with an indwelling catheter, it averaged 10.7 mL/s (range 2.0–31.0 mL/s), whereas in those without a catheter the average flow rate was 9.8 mL/s (range 1.4–25.0 mL/s). The voiding time was 10–116 s (average 35 s). With the exception of a few extreme values, the voiding time in normal patients is comparable to that in patients with reflux.

Children typically do not use abdominal straining during voiding [45]. When they do, the urinary flow either increases or decreases, probably reflecting whether the external sphincter is contracted along with the abdominal muscles [46]. Thus urging the child to strain in order to void may be counterproductive.

Residual Bladder Volume

Residual volumes measured by catheterization and RNC may or may not be the same, and in many instances, there is gross discrepancy between these two measurements for any number of

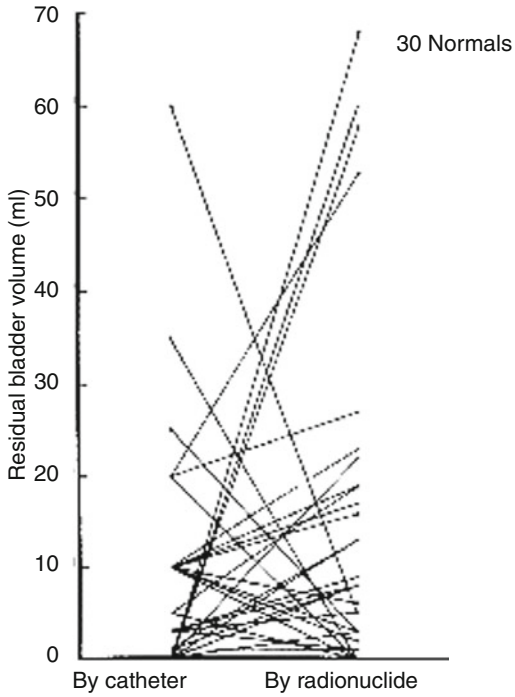

Fig. 13.14 Residual bladder volumes measured in the same patients by catheterization and by radionuclide cystography in 30 normal children

reasons (Fig. 13.14). For example, the patient may not adequately empty the bladder because of some underlying abnormality such as aberrant micturition, as in some cases of reflux or dysuria [47]. The bladder may not be properly drained because the tip of the catheter abuts the bladder wall, or the patient may simply be unwilling or unable to void because of the unnatural situation [48].

We have observed more complete emptying of the bladder in patients whose bladders were filled to a maximum or optimal volume during cystography. Apparently, high tonicity of the bladder wall induced adequate contraction and more complete emptying. A large residual volume in children at the beginning or end of the study does not necessarily mean that the patient has a significant abnormality. On the other hand, demonstration of an empty bladder is useful.

Urine Culture

We reviewed the results of urine culture in 113 consecutive children referred for radionuclide cystography. Urinary infection with *Escherichia coli* or *Streptococcus faecalis* was found in 11 % despite their history of continuous antibiotic treatment and careful follow-up by their physicians. Patients on antibiotic treatment and those who had undergone surgery showed a nearly equal incidence of urinary infection. Our experience agrees with that of other workers, suggesting that reflux and infection are independent of one another [49–53].

Dosimetry

For children undergoing RNC between ages 1 and 10, the absorbed radiation dose estimates for the bladder wall are 0.18–0.27 mGy and for ovaries 10–20 mGy. The testicular dose is less than the dose to the ovaries. The dose to the kidneys is estimated to be 0.02–0.04 mrad/mL of reflux per minute of residence in the collecting system. The estimated dose to the ureter in reflux is 13 mGy/min (1.3 mrad/min) [21, 54–56]. The dose to the ovaries is 100–200 times less with RNC than with conventional VCUG and 20–40 times less than pulsed fluoroscopy [21, 57, 58]. For these dose calculations, the residence time for the activity in the bladder is determined from the duration of the study in patients of various age groups and the empty bladder mass is estimated by extrapolation from data in adults, using growth curves [59].

Indirect Radionuclide Cystography

The principal advantages of IRC are that it can demonstrate reflux under physiologic conditions. It uses radiopharmaceuticals that, after intravenous injection, are rapidly eliminated in the urine and not retained in the renal parenchyma. Vesicoureteric reflux can be detected during voiding only. This technique has the advantage that it permits evaluation of renal function and urine drainage as well as detection of VUR. Indirect radionuclide cystography is less traumatic for the patient than RNC, physically and emotionally. It does not require catheterization and allows the bladder to be filled and emptied physiologically (Fig. 13.15). The minimal risk of induced infection is eliminated with IRC.

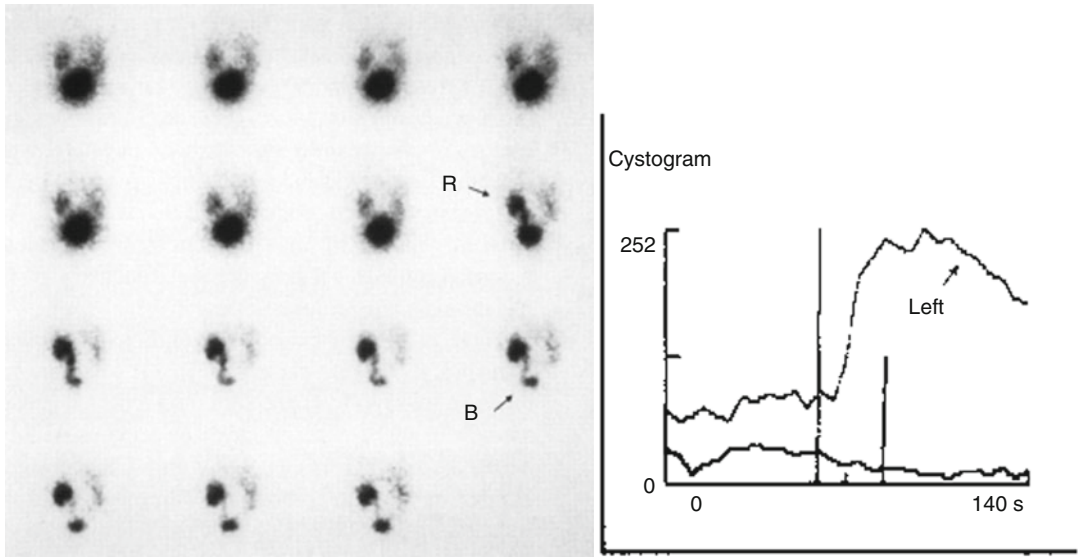

Fig. 13.15 Indirect radionuclide cystography (^{99m}Tc-MAG_3). *Left panel*: The bladder is filled with radiotracer. As the patient voids, there is left vesicoureteric reflux (*R*) and secondary bladder (*B*) filling. *Right panel*: The time-activity curve from a region of interest over the left kidney reveals a sharp increase coinciding with the reflux seen on the images (Courtesy of Dr. Isky Gordon, London, England)

However, IRC cannot detect VUR that occurs during the filling period only.

The patient can void in the usual position, so the competence of the vesicoureteral mechanism is tested under normal voiding pressures [33]. A relative disadvantage of IRC is that it requires complete patient cooperation. Clearly, IRC is not meant for newborns, infants, and those patients who cannot or will not cooperate. Another disadvantage of IRC is that it requires that the imaging room be available when the patient is ready to void.

Radiopharmaceuticals

The radiopharmaceuticals ^{99m}Tc-mercaptoacetyltriglycine (^{99m}Tc-MAG3) or ^{99m}Tc-diethylenetriamine pentaacetic acid (^{99m}Tc-DTPA) are suitable agents for IRC. Technetium-99m-MAG3 is a better choice, as it has a higher extraction fraction with less soft-tissue background. The intravenous administered dose should be the same used as for dynamic renal scintigraphy.

Recording

Indirect radionuclide cystography should be preceded by a conventional dynamic renal scan in order to evaluate renal function and assess complete drainage of tracer from the kidneys. Ideally, no significant amount of tracer should be present in the renal regions prior to the start of the IRC, as VUR may be difficult to detect in the presence of residual tracer in the pelvicaliceal system. For the voiding phase, the patient is positioned in the sitting position with the gamma camera centered over the region of the bladder and kidneys. The patient voids into a urinal, a bedpan, or a specially made commode. Precautions to reduce contamination of the equipment and the room must be taken. Recording is begun when the patient is ready to void and continues until the end of voiding. Additional images may have to be obtained following voiding. The IRC is recorded using the same camera and computer acquisition parameters described under RNC (see above).

Analysis

Analysis of IRC is identical to that described above for RNC. The physician should review the IRC in a dynamic mode, varying the display rate and the image contrast.

Computerized Radionuclide Cystography

Computerized radionuclide voiding cystography (CRVC) is a refinement of RNC. It is a quantitative method and enables simultaneous measurement of bladder volumes and pressures. When using CRVC, the following parameters are obtained:

1. Volume of the bladder at the first occurrence of reflux and at the time of maximum reflux during filling and/or voiding
2. Maximum bladder volume (end of filling)
3. Volumes of reflux (initial, maximum, residual)
4. Residual bladder volume
5. Average voiding flow rate
6. Bladder pressures

Intravesical Pressure

With CRVC, it is possible to simultaneously record the radionuclide cystogram and the intravesical pressures. Using a double-lumen catheter, one channel is used for infusion and the other is connected to a pressure transducer. We use a 3-mm-diameter double-lumen catheter (French 9). The pressure transducer output is connected through an analog-to-digital converter to the computer. Time-activity and time-pressure curves can then be displayed simultaneously [21, 60, 61].

In a study in our institution aimed at establishing normal and abnormal ranges of intravesical pressure, measurements during RNC were obtained for 40 patients. There were 16 normal children, 15 with reflux, and nine who had previous surgery. In the normal children maximum intravesical pressures during filling were 15–80 cm H_2O (average 42 cm H_2O) and during voiding or postvoiding 24–136 cm H_2O (average 78 cm H_2O). There was no significant difference between the normal children, patients with reflux, and those who had prior reimplants. In all these groups, the initial voiding pressure was always slightly higher than the maximum filling pressure. Intravesical pressures decreased with increasing bladder volume. During filling of the bladder, the intravesical pressure showed a continuous increase until full bladder capacity was reached. Toward the end of voiding, a pressure peak that occurred after contraction characterized the pressure curve. In most instances, the highest recorded intravesical pressure was reached during this moment after contraction.

There is no clear evidence that intravesical pressure causes VUR [62]. A relationship between intravesical pressure and cortical renal damage in the absence of infection remains widely debated [63], although in patients with VUR there are alterations in renal blood flow during voiding [64]. Renal damage from pyelotubular backflow has also been considered [65]. It has been clearly demonstrated in children under 6 years of age, but mainly in infants, that massive reflux in the presence of urinary tract infection leads to renal damage [49, 62, 66–69].

Studies in rabbits reveal that renal blood flow decreases with acute increase of pressures in the pelvicaliceal system. This is reversible [70]. Intrarenal reflux seems to play an important role in the etiology of renal damage [71]. Because intravesical pressure is higher in younger than older children, it follows that intravesical pressure decreases with increasing bladder capacity. With renal damage occurring mainly in younger children, perhaps there is some relationship between intravesical pressure and reflux nephropathy. In the absence of a barrier at the ureterovesical junction, the upper urinary system and the bladder act as a single chamber. Studies in our laboratory seem to indicate that intravesical pressure is probably least important in terms of etiology, management, and prognosis of reflux provided that distal obstruction or neurogenic dysfunction is not present. Most of our patients exhibited reflux during filling at a relatively large bladder volume. The increasing bladder volume during the cystogram probably influences the anatomy and competence of the ureterovesical junction more than the increase in pressure.

In the growing child, maturation of the ureterovesical junction probably implies not only lengthening of the intravesical ureter but also strengthening of the specific musculature related to the ureterovesical junction. Therefore decreasing occurrence of reflux with age is to be expected [72–74]. Controversy still exists about maturation of the ureterovesical junction [53, 75]. Reflux only during voiding may be related to the changing anatomic condition of the ureterovesical

junction during bladder contraction. The intravesical pressure at the initiation of voiding is not significantly higher than at the end of filling. Reflux that occurs at low bladder volume is more damaging [76].

Analysis

With CRVC, the sequential images of the cystogram are displayed on the computer monitor and evaluated visually (see above). If reflux is present, regions of interest (ROIs) are drawn over the kidneys and bladder. In addition, another region near the bladder is selected to correct for background scatter.

It is important to determine if patient motion occurred during the study because it invalidates any attempts at quantitation. Motion correction should be applied. Time-activity curves are calculated for each ROI.

To obtain and estimate the volumes of reflux, bladder capacity, and residual capacity, a relation between activity and volume is obtained. Assuming that attenuation of the gamma rays is constant, that the radioisotope is well mixed with the solution of saline, and that a negligible amount of urine is produced by the kidneys during the study, the counts recorded are proportional to the volume(s):

$$V = RC \tag{13.1}$$

where V is volume, R is a constant, and C is counts. Note that 0 counts represents zero volume. The constant R is calculated by relating the voided volume to the drop in total vesical counts during the voiding phase of the study. At the beginning of the voiding phase, the volume is V_0 and the counts are C_0. At the end of the voiding phase, the volume is V_e and the counts C_e. Substituting these values into Eq. 13.1 yields:

$$V_0 = RC_0 \tag{13.2}$$

$$V_e = RC_e \tag{13.3}$$

Subtracting Eq. 13.3 from Eq. 13.2 yields:

$$R = \frac{V_0 - V_e}{C_0 - C_e} = \frac{V}{C} = \frac{\text{Change in volume}}{\text{Change in counts}} \tag{13.4}$$

Once the ratios are calculated, it is easy to obtain any volume of interest for any particular time of the study (e.g., maximum volume of reflux). One simply has to multiply the ratio R by the number of counts over a particular region at a given frame. After the counts in each region are converted to volumes, it is possible to calculate rates of flow. To obtain the average voiding flow rate, the count loss during voiding must be divided by the time of voiding and multiplied by the constant R.

$$\text{Average flow rate} = R = \frac{\square V}{AT} \tag{13.5}$$

References

1. Subcommittee on urinary tract infection, Steering Committee for the diagnosis and management of the initial UTI in febrile infants and children 2 to 24 months. Pediatrics. 2011;128:595–610
2. Finnell SME, Carroll AE. Downs SM and the subcommittee on urinary tract infection. Diagnosis and management of an initial UTI in febrile infants and young children. Pediatrics. 2011;128:e749–e770.
3. Wan J, Skoog SJ, Hulbert WC, et al. Section of urology response to the new guidelines fo the diagnosis and management of UTI. Pediatrics. 2012;129: e1054–e1056.
4. Juliano TM, Stephany HA, Clayton DB, et al. Incidence of abnormal imaging and recurrent pyelonephritis after first febrile urinary tract infection in children 2-24 months. J Urol. 2013;190:1505–1510.
5. Suson KD, Matthews R. Evaluation of children with urinary tract infection – impact of the 2011 AAP guidelines o the diagnosis of vesicoureteral reflux using a historical series. J Pediatr Urol. 2014;10: 182–185.
6. Ransley PG. Vesicoureteric reflux. In: Williams DI, Johnston JH, editors. Pediatric urology. London: Butterworth; 1982.
7. Noe HN. The long-term results of prospective sibling reflux screening. J Urol. 1992;148(5 Pt 2):1739–42.
8. Van den Abbeele AD, Treves ST, Lebowitz RL, et al. Vesicoureteral reflux in asymptomatic siblings of patients with known reflux: radionuclide cystography. Pediatrics. 1987;79(1):147–53.
9. Kenda RB, Fettich JJ. Vesicoureteric reflux and renal scars in asymptomatic siblings of children with reflux. Arch Dis Child. 1992;67(4):506–8.
10. Ataei N, Madani A, Esfahani ST, et al. Screening for vesicoureteral reflux and renal scars in siblings of children with known reflux. Pediatr Nephrol. 2004; 19(10):1127–31.
11. Houle AM, Cheikhelard A, Barrieras D, Rivest MC, Gaudreault V. Impact of early screening for reflux in

siblings on the detection of renal damage. BJU Int. 2004;94(1):123–5.
12. Buonomo C, Treves ST, Jones B, Summerville D, Bauer S, Retik A. Silent renal damage in symptom-free siblings of children with vesicoureteral reflux: assessment with technetium Tc 99m dimercaptosuccinic acid scintigraphy. J Pediatr. 1993;122(5 Pt 1):721–3.
13. Sukan A, Bayazit AK, Kibar M, et al. Comparison of direct radionuclide cystography and voiding direct cystography in the detection of vesicoureteral reflux. Ann Nucl Med. 2003;17(7):549–53.
14. Gordon I, Barkovics M, Pindoria S, Cole TJ, Woolf AS. Primary vesicoureteric reflux as a predictor of renal damage in children hospitalized with urinary tract infection: a systematic review and meta-analysis. J Am Soc Nephrol. 2003;14(3):739–44.
15. McLaren CJ, Simpson ET. Vesico-ureteric reflux in the young infant with follow-up direct radionuclide cystograms: the medical and surgical outcome at 5 years old. BJU Int. 2002;90(7):721–4.
16. Medina LS, Aguirre E, Altman NR. Vesicoureteral reflux imaging in children: comparative cost analysis. Acad Radiol. 2003;10(2):139–44.
17. Polito C, Rambaldi PF, La Manna A, Mansi L, Di Toro R. Enhanced detection of vesicoureteric reflux with isotopic cystography. Pediatr Nephrol. 2000; 14(8–9):827–30.
18. Poli-Merol ML, Francois S, Pfliger F, et al. Interest of direct radionuclide cystography in repeated urinary tract infection exploration in childhood. Eur J Pediatr Surg. 1998;8(6):339–42.
19. Saraga M, Stanicic A, Markovic V. The role of direct radionuclide cystography in evaluation of vesicoureteral reflux. Scand J Urol Nephrol. 1996;30(5):367–71.
20. Medical versus surgical treatment of primary vesicoureteral reflux: report of the International Reflux Study Committee. Pediatrics. 1981;67(3):392–400.
21. Willi U, Treves ST. Radionuclide voiding cystography. In: Treves ST, editor. Pediatric nuclear medicine. New York: Springer; 1985. p. 105–20.
22. Willi U, Treves S. Radionuclide voiding cystography. Urol Radiol. 1983;5(3):161–73. 175.
23. Grmek M, Fettich J. The importance of follow-up of children with vesicoureteral reflux grade 1. Acta Paediatr. 2003;92(4):435–8.
24. Pozderac RV, Becker CJ, Reitelman C, Kuhns LR. Comparison of single and two stage radionuclide cystography (RNC) for evaluation of reflux. J Nucl Med. 1990;31:893 [abstract].
25. Neel KF, Shillinger JF. The prevalence of persistent vesicoureteral reflux after 1 negative nuclear medicine cystogram. J Urol. 2000;164(3 Pt 2):1067–9.
26. Normand LCS, Smellie J. Vesicoureteric reflux: the case for conservative management. In: Hodson J, Kincaid-Smith P, editors. Reflux nephropathy. New York: Masson Pub; 1979. p. 352.
27. Hubert KC, Kokorowski PJ, Hunag L, et al. Clinical outcomes and long-term resolution in patients with persistent vesciouretral relux after open ureteral reimplantation. J Urol. 2012;188:1474–1479.
28. Sung J, Skoog S. Surgical management of vesicoureteral reflux in children. Pediatr Nephrol. 2012;27:551–561.
29. Estrada CR Jr. Prenatal hydronephrosis: early evaluation. Curr Opin Urol. 2008;18:401–403.
30. Bower G, Lovegrove FT, Geijsel H, Van der Schaff A, Guelfi G. Comparison of "direct" and "indirect" radionuclide cystography. J Nucl Med. 1985;26(5): 465–8.
31. Conway JJ, Belman AB, King LR. Direct and indirect radionuclide cystography. Semin Nucl Med. 1974; 4(2):197–211.
32. Majd M, Kass EJ, Belman AB. Radionuclide cystography in children: comparison of direct (retrograde) and indirect (intravenous) techniques. Ann Radiol (Paris). 1985;28(3-4):322–8.
33. Gordon I, Peters AM, Morony S. Indirect radionuclide cystography: a sensitive technique for the detection of vesico-ureteral reflux. Pediatr Nephrol. 1990; 4(6):604–6.
34. Hass EA, Solomon DJ. Telling children about diagnostic radiology procedures. Radiology. 1977; 124(2):521.
35. Palestro CJ, Gelfand MJ, Majd M et al. ACR-SPR-SNM practice guideline for the performance of radionuclide cystography. www.acr.org/~/media/ACR/Documents/PGTS/guidelines/Radionuclide_Cystography.org.
36. Wilkinson AG. Percutaneous direct radionuclide cystography in children: description of technique and early experience. Pediatr Radiol. 2002;32(7):511–7.
37. Berger RM, Maizels M, Moran GC, Conway JJ, Firlit CF. Bladder capacity (ounces) equals age (years) plus 2 predicts normal bladder capacity and aids in diagnosis of abnormal voiding patterns. J Urol. 1983;129(2): 347–9.
38. Fairhurst JJ, Rubin CM, Hyde I, Freeman NV, Williams JD. Bladder capacity in infants. J Pediatr Surg. 1991;26(1):55–7.
39. Koff SA. Estimating bladder capacity in children. Urology. 1983;21(3):248.
40. Starfield B. Functional bladder capacity in enuretic and nonenuretic children. J Pediatr. 1974;111:167–72.
41. Treves ST, Zurakowski D, Bauer SB, Mitchell KD, Nichols DP. Functional bladder capacity measured during radionuclide cystography in children. Radiology. 1996;198(1):269–72.
42. Lattimer JK, Apperson JW, Gleason DM, Baker D, Flemming SS. The pressure at which reflux occurs, an important indicator of prognosis and treatment. J Urol. 1963;89:395–404.
43. Spencer RP, Treves S. Bladder emptying flow rate as a function of bladder volume. Yale J Biol Med. 1971;44(2):199–205.
44. Strauss BS, Blaufox MD. Estimation of residual urine and urine flow rates without urethral catheterization. J Nucl Med. 1970;11(2):81–4.
45. Gierup J. Micturition studies in infants and children. Normal urinary flow. Scand J Urol Nephrol. 1970;4(3): 191–7.

46. Whitaker J, Johnston GS. Urinary flow rate with two techniques of bladder pressure measurement. Invest Urol. 1966;4(3):235–8.
47. Hutch JA. Aberrant micturition. J Urol. 1966;96(5): 743–5.
48. Poznanski E, Poznanski AK. Psychogenic influences on voiding: observations from voiding cystourethrography. Psychosomatics. 1969;10(6):339–42.
49. Cremin BJ. Observations on vesico-ureteric reflux and intrarenal reflux: a review and survey of material. Clin Radiol. 1979;30(6):607–21.
50. Faure C. Le reflux vesico-ureteral. In: Lefebvre J, editor. Traite de radiodiagnostic. Paris: Masson et Cie; 1973.
51. Friedland GW. Recurrent urinary tract infections in infants and children. Radiol Clin North Am. 1977; 15(1):19–35.
52. Stephens FD. Urologic aspects of recurrent urinary tract infection in children. J Pediatr. 1972;80(5):725–37.
53. Stephens FD, Lenaghan D. The anatomical basis and dynamics of vesicoureteral reflux. J Urol. 1962;87: 669–80.
54. Dilman LD, Van der Lage FC. Radionuclide decay schemes and nuclear parameters for use in radiation dose estimation. In: Society of Nuclear Medicine, editor. NM/Medical Internal Radiation Dose Committee. Pamphlet No. 10. New York: Society of Nuclear Medicine; 1975.
55. Loevinger R, Berman M. A revised schema for calculating the absorbed dose from biologically distributed radionuclides. In: Society of Nuclear Medicine, editor. NM/Medical Internal Radiation Dose Committee. Pamphlet No. 1. New York: Society of Nuclear Medicine; 1975.
56. Snyder WS, Ford MR, Warner GG. Estimates of specific absorbed fractions for photon sources uniformly distributed in various organs of heterogeneous phantom. In: Society of Nuclear Medicine, editor. NM/Medical Internal Radiation Dose Committee. Pamphlet No. 5. New York: Society of Nuclear Medicine; 1978.
57. Fendel H. Radiation exposure due to urinary tract disease. In: Kaufmann HJ, editor. Progress in pediatric radiology. Basel/New York: S. Karger; 1970. p. 116–35.
58. Leibovic SJ, Lebowitz RL. Reducing patient dose in voiding cystourethrography. Urol Radiol. 1980;2: 103–7.
59. Snyder WS, Cook MJ, Nasset ES. Report of the task group on reference man: a report. In: International commission on radiological protection. Oxford/New York: Pergamon Press; 1975. xix, 480 p.
60. Papachristou F, Printza N, Doumas A, Koliakos G. Urinary bladder volume and pressure at reflux as prognostic factors of vesicoureteral reflux outcome. Pediatr Radiol. 2004;34(7):556–9.
61. Cooper CS, Madsen MT, Austin JC, Hawtrey CE, Gerard LL, Graham MM. Bladder pressure at the onset of vesicoureteral reflux determined by nuclear cystometrogram. J Urol. 2003;170(4 Pt 2):1537–40; discussion 1540.
62. Smith JC. Urethral resistance to micturition. Br J Urol. 1968;40(2):125–56.
63. Bailey RR. Sterile reflux: is it harmless? In: Hodson J, Kincaid-Smith P, editors. Reflux nephropathy. New York: Masson Pub; 1979. p. 352.
64. Orr WA, Kimbrough H, Gillenwater JY. Alterations in renal blood flow with voiding in the presence of vesicoureteral reflux. J Urol. 1971;106(2):214–9.
65. King LR. Vesicoureteral reflux: history, etiology, and conservative management. In: Kelalis PP, King LR, Belman AB, editors. Clinical pediatric urology. Philadelphia: Saunders; 1976. 2 v. (xiii, 1107 p., xxix).
66. Hodson CJ, Edwards D. Chronic pyelonephritis and vesico-ureteric reflex. Clin Radiol. 1960;11:219–31.
67. Rolleston GL, Shannon FT, Utley WL. Follow-up of vesico-ureteric reflux in the newborn. Kidney Int Suppl. 1975;4:S59–64.
68. Rolleston GL, Shannon FT, Utley WL. Relationship of infantile vesicoureteric reflux to renal damage. Br Med J. 1970;1(694):460–3.
69. Smellie J, Edwards D, Hunter N, Normand IC, Prescod N. Vesico-ureteric reflux and renal scarring. Kidney Int Suppl. 1975;4:S65–72.
70. Treves ST, Packard AB, Fung LC. Assessment of rapid changes in renal blood flow with (191m)Ir, an ultra-short-lived radionuclide. J Nucl Med. 2004; 45(3):508–11.
71. Rolleston GL, Maling TM, Hodson CJ. Intrarenal reflux and the scarred kidney. Arch Dis Child. 1974; 49(7):531–9.
72. Hutch JA. Theory of maturation of the intravesical ureter. J Urol. 1961;86:534–8.
73. Tanagho EA, Meyers FH, Smith DR. Urethral resistance: its components and implications. I. Smooth muscle component. Invest Urol. 1969;7(2):136–49.
74. Tanagho EA, Meyers FH, Smith DR. Urethral resistance: its components and implications. II. Striated muscle component. Invest Urol. 1969;7(3): 195–205.
75. Lyon RP, Marshall S, Tanagho EA. Theory of maturation: a critique. J Urol. 1970;103(6):795–800.
76. Tepmongkol S, Chotipanich C, Sirisalipoch S, Chaiwatanarat T, Vilaichon AO, Wattana D. Relationship between vesicoureteral reflux and renal cortical scar development in Thai children: the significance of renal cortical scintigraphy and direct radionuclide cystography. J Med Assoc Thai. 2002;85 Suppl 1:S203–9.

Radionuclide Determination of Glomerular Filtration Rate

14

Frederick D. Grant, Frederic H. Fahey, and S. Ted Treves

Glomerular filtration rate (GFR) provides a quantitative measure of renal function and can be used as an indicator of renal dysfunction. The clinical indications for the radionuclide determination of GFR in pediatrics are broad [1]. A quantitative direct determination of GFR can be helpful in the evaluation and management of renal disease. Radionuclide GFR determination may be especially useful when GFR estimation based on creatinine may be unreliable or in the setting of systemic disease, such as diabetes mellitus or recovering hemolytic uremic syndrome. Radionuclide GFR can be used to monitor the renal effects of nephrotoxic drugs and for individual dose adjustment of chemotherapy in patients with potentially impaired renal function. A radionuclide GFR determination also can be used to confirm the suitability of a potential renal transplant donor.

All methods of determining GFR rely on estimating the plasma clearance or renal excretion of a substance that is excreted by the mechanism of glomerular filtration. In many clinical cases, endogenous serum creatinine level, or at most creatinine clearance, can provide reasonable estimates of GFR. A variety of mathematical methods have been proposed to estimate GFR based on serum creatinine, body size, and patient characteristics such as age, gender, and race [2]. Plasma creatinine levels are not sensitive to small changes in glomerular function [1] and changes in serum creatinine levels may lag deterioration in renal function. These methods assume that creatinine is cleared almost entirely by glomerular filtration, but up to 5 % of creatinine clearance is through other mechanisms of renal clearance. This fraction of non-glomerular clearance can increase to as high as 50 % in the setting of renal failure. Therefore, GFR estimations based on

F.D. Grant, MD (✉)
Joint Program in Nuclear Medicine,
Department of Radiology, Harvard Medical School,
Boston, MA, USA

Division of Nuclear Medicine and Molecular Imaging,
Department of Radiology,
Boston Children's Hospital,
Boston, MA, USA

Department of Radiology,
Brigham and Women's Hospital,
Boston, MA, USA
e-mail: frederick.grant@childrens.harvard.edu

F.H. Fahey, DSc
Joint Program in Nuclear Medicine,
Department of Radiology, Harvard Medical School,
Boston, MA, USA

Division of Nuclear Medicine and Molecular
Imaging, Department of Radiology,
Boston Children's Hospital, Boston, MA, USA

S.T. Treves, MD (✉)
Joint Program in Nuclear Medicine,
Department of Radiology, Harvard Medical School,
Boston, MA, USA

Division of Nuclear Medicine and Molecular Imaging,
Department of Radiology, Boston Children's Hospital,
Boston, MA, USA

Division of Nuclear Medicine and Molecular
Imaging, Department of Radiology,
Brigham and Women's Hospital, Boston, MA, USA
e-mail: ted_treves@HMS.harvard.edu

S.T. Treves (ed.), *Pediatric Nuclear Medicine and Molecular Imaging*,
DOI 10.1007/978-1-4614-9551-2_14,

serum creatinine and creatinine clearance can be much less reliable in patients with renal impairment [3, 4]. These estimates also may be inaccurate in patients with low creatinine levels, such as those who are fasting, have low muscle mass, or are in a catabolic metabolic state related to critical illness or a genetic disorder of metabolism. With all methods that use serum creatinine to estimate GFR, precision can be poor, and variability may be as high as 40 %, especially in children [5, 6]. Thus, these methods of estimating GFR are not satisfactory when an accurate determination of GFR is needed.

Although there is no perfect substrate for determining GFR, the gold standard for many decades has been inulin. Inulin is a small (average molecular weight ~5,000) non-charged polymeric molecule that is cleared rapidly from the circulation by filtration through the renal glomeruli. As inulin has a high rate of renal extraction, a continuous intravenous infusion of inulin is required for determination of GFR. Therefore, this approach may not be feasible for clinical studies. Methods more practical for routine clinical applications have been developed using radiopharmaceuticals. These techniques require only a single intravenous administration of radiopharmaceutical, which can be assayed easily and accurately in blood or urine.

Methods

Radionuclide determination of GFR can be performed using one of four different general methods. One method is to administer the radiopharmaceutical with a continuous intravenous infusion and then determine renal excretion of radiopharmaceutical with blood and urine assays performed at steady state. The more common method is to administer the radiopharmaceutical as a single intravenous injection. Then, either a single blood sample or multiple blood samples are used to calculate plasma clearance of the radiopharmaceutical. An alternative method uses an image-based approach to estimate the renal clearance of a radiopharmaceutical administered with a single intravenous injection.

Radiopharmaceuticals

Many different radiopharmaceuticals have been used for the radionuclide determination of GFR. Radiopharmaceuticals less than 60 kilodaltons in size are ultrafiltrated by glomeruli in proportion to the GFR and the free (nonprotein-bound) fraction in the plasma [7]. Therefore, any radiolabeled agent that has minimal protein binding and is excreted solely by glomerular filtration could be used to determine GFR. That is, the agent should not undergo renal tubular secretion or reabsorption, should not be excreted through a nonrenal route, and must not be metabolized before excretion [1]. In practice, one of three radiopharmaceuticals, ^{51}Cr-EDTA, ^{125}I iothalamate, or ^{99m}Tc-DTPA, is commonly used, and, in general, all will give similar results [4]. However, with each radiopharmaceutical, there is some systematic variance in GFR determination compared to the true GFR. This may be due to clearance by non-glomerular mechanisms, binding to plasma proteins, or the rate of renal extraction from plasma. The choice of radiopharmaceutical typically depends on commercial availability and local convention. In Europe, ^{51}Cr-EDTA has been the usual agent of choice [4]. In North America, some institutions continue to use ^{125}I-iothalamate, but in most pediatric hospitals, the current choice of agent is ^{99m}Tc-DTPA, due to its commercial availability, relatively short half-life, and lower radiation dose compared to other radiopharmaceuticals.

^{99m}Tc-DTPA

Diethylenetriamine pentaacetic acid (DTPA) can be labeled with a number of radioisotopes, but most commonly is labeled with ^{99m}Tc (physical half-life 6 h, primary gamma emission 140 keV), because of its ready availability in most radiopharmacies and nuclear medicine departments. Technetium-99m-DTPA is cleared essentially only by glomerular filtration. Renal clearance of ^{99m}Tc-DTPA appears to be slightly slower than inulin, probably due to a small amount of protein binding in the circulation. However, this may be less of an issue with current commercial preparations of

^{99m}Tc-DTPA [8]. There is no binding of ^{99m}Tc-DTPA to red blood cells [9]. Technetium-99m-DTPA can be used with both in vitro assay and in vivo imaging techniques for determining GFR. For in vitro assay methods of determining GFR, the usual pediatric dose of ^{99m}Tc-DTPA is 1.85 MBq/kg (0.05 mCi/kg) with a minimum dose of 11.1 MBq (0.3 mCi) and a maximum dose of 111 MBq (3 mCi).

^{51}Cr-EDTA

Ethylenediaminetetraacetic acid (EDTA) labeled with ^{51}Cr (physical half-life of 27.8 days) can been used for in vitro determination of GFR. Chromium-51 decays by electron capture with emission of 5 keV x-rays, Auger electrons, and a low abundance (9 %) of a high-energy (323 keV) gamma emission. There is minimal protein binding of ^{51}Cr-EDTA, but a number of factors make it less attractive than ^{99m}Tc-DTPA. Some studies [10] have demonstrated that there is a small amount of nonrenal plasma clearance of ^{51}Cr-EDTA. With ^{51}Cr as the radiolabel, both the radiation dose will be greater and the counting time will be longer than with ^{99m}Tc-DTPA [9]. One potential advantage of ^{51}Cr-EDTA is that, due to the longer half-life of ^{51}Cr, samples do not need to be assayed on the same day as the study is performed. However, with clinical expectations of rapid results turnaround, this characteristic of ^{51}Cr-EDTA seems of little practical benefit.

^{125}I-Iothalamate

Iothalamate can be radioiodinated, usually with ^{125}I to produce ^{125}I-iothalamate (Glofil®), which is a commercially available radiopharmaceutical. Iodine-125 has a physical half-life of 60.14 days and decays by electron capture with emission of a low-abundance (7 %), low-energy (35.5 keV) gamma emission and high abundance of low-energy x-rays. The use of ^{125}I complicates radioactive counting due to the low count rate and the low-energy gamma emission, so that each plasma sample may require a long period of counting to obtain adequate reproducibility. The long physical half-life of ^{125}I also means that samples may need to be stored for long periods to allow decay onsite before disposal. Before administration of ^{125}I-iothalamate, patients must receive iodine supplementation to limit thyroid uptake of unincorporated ^{125}I (approximately 1 % free iodine). As indicated in the package insert, ^{125}I-iothalamate should not be administered by central line. Commercial preparations of ^{125}I-iothalamate can contain 0.9 % benzyl alcohol, which limits its use in infants.

Either a continuous intravenous infusion [11] or the single intravenous injection method [12] can be used to determine GFR with ^{125}I-iothalamate. The recommended adult dose is 0.74–3.7 mBq (0.02–0.1 mCi) for the continuous infusion method and 0.37–1.11 MBq (0.01–0.03 mCi) for the single injection method. Some studies have suggested that a substantial fraction of ^{125}I-iothalamate can be excreted by tubular secretion and not glomerular filtration [13]. Therefore, ^{125}I-iothalamate may overestimate GFR, particularly in patients with renal dysfunction.

Radionuclide GFR Methods

Continuous Infusion

The most accurate determination of GFR can be obtained with continuous infusion of a pharmaceutical and intermittent sampling of both blood, to determine plasma clearance, and urine, to determine renal excretion of the pharmaceutical. This method typically has been used with nonradioactive tracers, but also can be used with radiolabeled tracers. For example, this method is necessary when using inulin, which has served as the gold standard method for GFR determination. Inulin has a rapid rate of clearance, which means that a single bolus administration of inulin will be filtered before it can reach equilibrium throughout the plasma volume. Therefore, when used to determine GFR, inulin must be administered by constant intravenous infusion until a steady-state plasma inulin level has been reached. Then, blood and

urine samples are collected to determine GFR. A similar approach has been used to determine GFR with nonradioactive iothalamate. Some professional guidelines [4] recommend that this method be used when GFR is being determined for physiological research or clinical investigation. However, the continuous infusion method is not feasible for clinical use, and methods that utilize a single injection of radiopharmaceutical usually are adequate for clinical applications [4].

Single Administration with Serial Blood Sampling

An alternative to the continuous infusion method is the administration of the radiopharmaceutical as a single intravenous injection followed by one of several methods of sampling: single blood sample, multiple blood samples, or image-based analysis. Plasma clearance of each of the GFR radiopharmaceuticals is sufficiently slow that each is assumed to reach compartmental equilibrium before blood samples are obtained. This clearance can be described with a two-compartment exponential curve, with a fast component of about 20 min and a slow component of several hours. Often the fast component (which is the component typically characterized in a dynamic renogram) is ignored so that the number of blood samples can be decreased [14], although this approach will slightly overestimate the GFR value [4]. The slow component of clearance can be analyzed with one to four blood samples over several hours, with increasing accuracy as the number of blood samples is increased. The range of sampling times depends somewhat on the expected rate of clearance of the tracer. If the samples are taken over a short period of time or all of the samples are drawn too early or too late, they will not adequately characterize the clearance time (Fig. 14.1). Utilizing several samples drawn over a period of hours makes it more likely that at least two of the samples will define the clearance. In addition, if one of the samples is compromised, the adequacy of the method still may be maintained. For most clinical needs, this method of radionuclide GFR determination provides the best balance between feasibility, robustness, and accuracy.

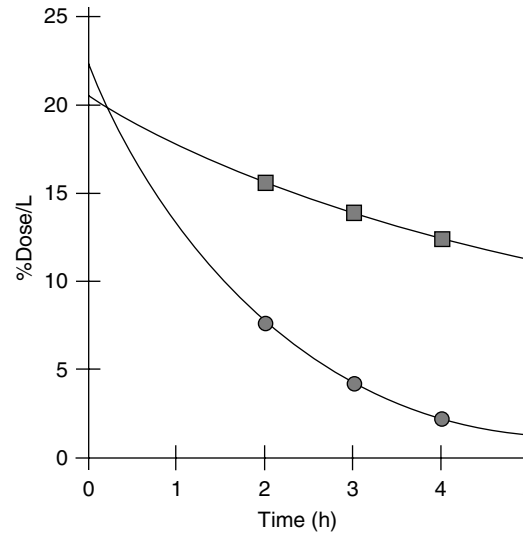

Fig. 14.1 Determination of glomerular filtration rate after a single administration of ^{99m}Tc-DTPA. Blood samples were obtained at 2, 3, and 4 h after tracer administration in two patients. In a 2-year-old patient (○), there is rapid clearance of tracer, with a calculated GFR of 39 ml/min (131 ml/min/1.73 m^2), within the reference range (67–231 ml/min/1.73 m^2) for a patient of this age. In a patient with chronic kidney disease (□), there is slow clearance of tracer from the blood, and the calculated GFR is only 11 ml/min (28 ml/min/1.73 m^2)

Single Administration with a Single Blood Sample

The single blood sample method assumes that a single blood sample drawn at an appropriate time, typically 2 h after tracer administration, can describe the plasma clearance of tracer. However, the sampling time must match the expected clearance time of the tracer. Cristensen and Groth [15] were among the first to develop a single-sample method. The inaccuracy associated with the single-sample method may be higher than with multiple samples [4], particularly in children, who may need different equations to express variations in body size. However, some investigators have demonstrated reasonable accuracy even in children [16, 17]. One additional concern with the

single-sample method is that quality control is more difficult with only one blood sample [18].

In Vivo Image-Based Determination of GFR

Most methods of radionuclide GFR determination require blood samples to be obtained by venipuncture or through an indwelling intravenous catheter. This requirement led to the development of noninvasive imaging-based methods for determining GFR. After administration of radiopharmaceutical, a gamma camera is used to acquire dynamic images of the kidneys. Renal clearance of the tracer is determined by region-of-interest analysis of the acquired dynamic images.

Different approaches have been used to analyze the renal images. Some require calibration with a single blood sample, so that they are not entirely noninvasive [19]. The most commonly used approach depends entirely on image analysis to estimate GFR [20]. One advantage of this approach is that differential GFR can be estimated based on differential renal uptake of tracer within the first few minutes of imaging [21]. However, camera-based methods have some technical limitations. Assumptions must be made for renal depth, and therefore results may vary depending on body habitus, which may be particularly problematic in children. Also, the need for background correction remains unresolved [4]. Most comparative studies have demonstrated that camera-based methods provide GFR estimates that generally correlate with other methods, but are not as precise or as reproducible as the methods utilizing serial blood samples [4, 22–25].

Serial Blood Sampling Method: Procedure

The serial blood sampling method published by Rodman et al. [26] provides an easily implemented, accurate, and reproducible procedure for determining GFR by measuring clearance of a dose of ^{99m}Tc-DTPA administered by a single intravenous injection. In our pediatric nuclear medicine department, we use this method with three blood samples obtained at 2, 3, and 4 h (Fig. 14.1). An accurate result depends on adequate patient preparation, well-trained staff, and very careful attention to technique.

Before the study, all current medications should be recorded, as many of them may have an effect on renal blood flow or glomerular filtration rate. Medications may not be a contraindication to GFR determination, but the results must be interpreted and reported in the context of medication use. For example, angiotensin-converting enzyme inhibitors, such as captopril, will dilate the efferent glomerular capillary, which can decrease GFR. Chronic diuretic use can decrease intravascular volume. Any substantial decrease in renal blood flow can decrease glomerular filtration and lead to an inaccurately decreased determination of GFR. Ideally, patients should discontinue diuretics for a few days before the study, but this usually is not clinically possible. Similarly, patients should be well hydrated, and hydration status should be noted, particularly in ill children. Patients should be allowed ad lib access to fluids or receive maintenance intravenous fluids until all blood samples have been obtained. A GFR determination should not be performed in children who are fasting or restricting oral intake in preparation for other medical procedures. If necessary, and clinically allowed, a volume-depleted patient may have volume repletion with oral or intravenous administration of fluids (e.g., 10 ml/kg). Patients also should be encouraged to avoid vigorous exercise on the day of the study.

Accurate height and weight must be obtained before the study. We prefer to perform these measurements in our department to minimize error and to maintain clear accountability for the results. An estimated or previously recorded height should not be used, except in unusual circumstances, such as when the clinical status prevents measurement of height. As a high-protein diet will increase GFR, some clinical guidelines [18] recommend instructing the patient to limit protein intake before the study, in order to improve reproducibility of serial studies. However, in clinical practice, excess protein intake does not appear to be a major consideration, but protein deficiency related to underlying illness or nephrotic syndrome may have an effect on GFR. Serial plasma sample methods may not

be accurate in patients with substantial third spacing, e.g., ascites, and it may be appropriate to consider a method that uses urinary assay to determine renal clearance of tracer in these individuals [18].

There should be no opportunity for cross-contamination between the site of radiopharmaceutical administration and the site where blood samples are drawn. The smallest amount of contamination of one or more blood samples will produce a spurious result for the GFR determination. Therefore, the best practice is to use different sites for radiopharmaceutical administration and blood draws. These should never be at the same site and, if at all possible, should be in different extremities. Many patients find it easier to have an indwelling intravenous catheter placed for blood draws. A central venous line can be used for either radiopharmaceutical administration or blood draws. When a central line has more than one lumen, we successfully have used separate lumens for administration and blood draws, but this requires clear and careful communication, so that the appropriate lumens are used by all caregivers involved in the procedure. Central lines should be accessed only by appropriately trained and credentialed healthcare professionals.

For administration of radiopharmaceuticals, the injection technique is critical. An indwelling or central catheter should be thoroughly flushed multiple times with an adequate volume of flush solution to ensure that the entire administered dose enters the circulation. Similarly, extravascular infiltration of tracer must be avoided. Ideally, the injection site is imaged to confirm that there is no substantial infiltration of the administered dose. Extravasation with subcutaneous infiltration of radiopharmaceutical at the time of intravenous injection both decreases the dose administered into the circulation with the injection and produces a reservoir of tracer that will enter the circulation in an unpredictable manner. Either of these can result in a spurious GFR determination. A planar image of the injection site is an effective method of confirming that there was no infiltration. Infiltration is unusual, but if infiltration is detected, then region-of-interest analysis of whole-body imaging can be used to determine the fraction of the dose at the infiltration site. In practice, the GFR determination remains clinically valid if less than 5 % of the administered dose has infiltrated. In the rare circumstance that greater than 5 % of the dose infiltrates, then the GFR procedure must be discontinued and rescheduled. In our department, we limit the incidence of infiltration by injecting only through an indwelling catheter or central line, and not using a "butterfly" or a straight needle for the radiopharmaceutical injection.

Blood samples should be obtained as close as possible to the scheduled times (2, 3, and 4 h), but it is most important that the times be precisely recorded, even if the samples are not obtained at the scheduled times. The time between samples is not crucial, as long as the exact times are recorded. In our department, all times are determined with small portable timers, with one timer kept with the same patient during the entire 4-h procedure. This avoids any error related to differences in the time recorded by clocks in different rooms or different departments. Additional blood samples may increase accuracy, although this has not been fully established. Obtaining one of the blood samples up to 5 h after radiopharmaceutical administration does not seem to adversely affect the GFR determination. Some guidelines [1] have suggested that blood samples may be obtained later (5–24 h) in patients with severely impaired renal function.

When using an indwelling catheter, the line should be flushed with saline, and then approximately 2 ml of blood withdrawn and discarded before the sample is drawn. For central lines, similar procedures should be used, as appropriate for the line, to ensure that the blood sample is not contaminated by residual blood or flush solution. Blood samples are drawn into tubes (typically "red top") that do not contain an anticoagulant or a serum separator device. The blood is allowed to clot at room temperature, centrifuged at 3,500 rpm for 5 min, and then aliquoted in duplicate for assay in a well counter. Aliquots typically are measured with an automatic pipette, and careful pipetting technique must be used. Some published procedures [24, 27] have recommended ultrafiltration of blood samples to limit

protein-bound tracer, but careful evaluation in our department has shown that this step is not necessary, unless the patient has a known hyperviscosity/hyperproteinemia syndrome.

Serial Blood Sampling Method: Analysis

The calculations necessary to determine GFR can be performed with a spreadsheet application on a personal computer or may be programmed into the radiopharmaceutical management or image acquisition computers available in a nuclear medicine department. In the serial-sampling approach, blood samples are obtained at several sampling times over several hours. The exponential curve fitting method assumes one compartment and requires at least two blood samples, typically drawn between 2 and 4 h after intravenous injection of radiopharmaceutical.

Prior to administration, a dose calibrator is used to determine the activity (MBq) of the administered dose and of a second sample that is used to make a standard. The standard is made by using a set, known level of dilution of the assayed sample. Typically, the assay standard is made by diluting a known amount of activity (9–10 MBq, 0.24–0.27 mCi assayed in the dose calibrator) in 250 ml water in a volumetric flask. Dilution is necessary so that the specific activity of the standard solution is similar to that of the blood samples, which allows the standard samples to be counted in the well counter. This provides a comparison between the efficiencies of the dose calibrator and the well counter and provides a conversion factor for the administered dose, which can be counted only in the dose calibrator.

After all samples have been collected, the samples and the standard are counted in a well counter. The well counter should be windowed with the appropriate energy peak (typically 140 keV for ^{99m}Tc) and window. All samples and standards are counted at the same time so that a single correction for radioactive decay of ^{99m}Tc can be applied. The counting efficiency of the well counter is estimated from the count rate of the standard since both the activity concentration and volume of the standard are known.

$$\text{Counting Efficiency} = \text{Counts (cpm)}/\text{Volume (ml)}/\text{Standard Activity (kBq/ml)}$$

For the blood samples, a one-component exponential rate of clearance is assumed, and thus a least squares fit is applied to estimate the biological half-life and, thereby, characterize the clearance rate. The sample counts, decay corrected to the time of administration, are fit to the following equation:

$$SC = e^{B(1-t/A)}$$

where t is the time after administration. A and B are the fitting parameters for the exponential fit. The ratio of B/A is the clearance coefficient in units of reciprocal time (min^{-1}) (analogous to the radioactive decay coefficient, λ), and it represents the fraction of the tracer cleared per unit time. The clearance curve is extrapolated back to the time of injection and corrected by the counting efficiency to estimate the distribution volume (DV) in ml. The gross clearance is thus estimated by scaling the fractional clearance coefficient (B/A) by the distribution volume.

$$\text{Gross Clearance (ml/min)} = (\text{B/A}) * \text{DV} = (0.693/\text{T1/2}) * (\text{DV})$$

This value may be scaled by the body surface area or to a standardized adult value for body surface area.

Serial Blood Sampling Technique: Quality Control

An important component of the radionuclide GFR determination is using quality control procedures to maintain the accuracy and validity of the procedure. As with other nuclear medicine procedures, confirming the performance of equipment, such as the well counter and dose calibrator, is a necessary component of a quality control program. However, quality control procedures should cover many other aspects of an in vitro procedure and can be performed with every radionuclide GFR determination [1].

During the analysis procedure, all samples should be assayed in duplicate, and there should be minimum variation between duplicate samples. Visual confirmation of the curve fit to the data points is useful as another quality control.

Table 14.1 Pediatric reference ranges for glomerular filtration rate determined by a single injection of ^{99m}Tc-DTPA

Age (years)	*N*	GFR (ml/min)	GFR/BSA (ml/min/m^2)	GFR/1.73 m^2 (ml/min/1.73 m^2)	GFR/1.73 m^2 (ml/min/1.73 m^2)
		mean ± 2SD	mean ± 2SD	mean ± 2SD	Reference range
<1	18	28 ± 26	79 ± 58	137 ± 100	37–237
1–2.5	27	43 ± 28	86 ± 48	149 ± 82	67–231
2.5–5	29	72 ± 40	111 ± 58	192 ± 100	92–292
5–10	31	89 ± 60	95 ± 50	165 ± 86	79–251
10–15	38	125 ± 81	85 ± 44	147 ± 74	73–220
15–25	37	155 ± 72	84 ± 34	146 ± 60	86–206

The GFR results should be compared to prior GFR determinations for the same patient. A large change in GFR raises concern for a technical error, unless the clinical situation provides an explanation. Lastly, the samples and standards periodically should be counted on a separate well counter and cross compared to assure the integrity of the process.

Correcting GFR for Body Size

For many clinical purposes, and especially in children, it can be useful to express the GFR corrected for estimated body surface area (BSA) as ml/min/m^2 or by a standard adult body surface area (ml/min/1.73 m^2). Body surface area can be estimated by the formula of DuBois and DuBois [28]:

$$\text{BSA } (m^2) = 0.007184 \times \text{height } (cm)^{0.725} \times \text{weight } (kg)^{0.425}$$

An alternative method for estimating body surface area is the formula of Haycock [29], which has been validated in adults and children.

$$\text{BSA } (m^2) = 0.24265 \times \text{height } (cm)^{0.3964} \times \text{weight } (kg)^{0.5378}$$

This is a routine approach for standardizing results for patient size. For example, in pediatrics, the dose of many chemotherapy agents and other medications may be adjusted for the GFR corrected for body surface area (ml/min/m^2). Guidelines for intravenous administration of gadolinium-based contrast agents for MRI are based on GFR for a typical adult body size (ml/min/1.73 m^2).

Corrections for body size may not accurately reflect renal function in some groups of individuals. Children less than 1 year of age have relative renal immaturity, so that true renal function, even corrected for body size, is less than in older children. In addition, formulae for estimating body surface area may not apply to all patients. These methods may not be appropriate for calculating body surface area in infants and young children or in older children with a severely distorted body habitus, such as severe obesity or developmental delay. In some circumstances, it may be more important to report serial values for GFR over time, and standardization by body size may be less important [30], although as children grow or change in body habitus, the accuracy of BSA estimation also may change. Therefore, it is important that the absolute GFR, as well as the values normalized by body size, be reported with each GFR determination [30].

Normal Range for GFR

Normal GFR values have been determined for children of different ages (Table 14.1) [31]. Absolute GFR increases with increasing age and renal size. In children younger than age 3, lower GFR values also reflect renal immaturity. When corrected for body size, peak GFR typically is observed at approximately age 5 years. Although it can be helpful to know the expected range for GFR in a child, it may be most important to note any decrement in GFR over time. More difficult is identifying an absence of the expected increase in absolute

GFR. Correcting for body size and having age-appropriate normal GFR values can be helpful for evaluating the results of a radionuclide GFR.

References

1. Piepsz A, Colarinha P, Gordon I, et al. Guidelines for glomerular filtration rate determination in children. Published under the auspices of the Paediatric Committee of the European Association of Nuclear Medicine. 2000. www.eanm.org/publications/guidelines/gl_paed_gfrd.pdf.
2. Léger F, Bouissou F, Coulais Y, Tafani M, Chatelut E. Estimation of glomerular filtration rate in children. Pediatr Nephrol. 2002;17:903–7.
3. Seikaly MG, Browne R, Bajaj G, Arant Jr BS. Limitations to body length/serum creatinine ratio as an estimate of glomerular filtration in children. Pediatr Nephrol. 1966;10:709–11.
4. Blaufox MD, Aurell M, Bubeck B, et al. Report of the Radionuclides in Nephrourology Committee on renal clearance. J Nucl Med. 1996;37:1883–90.
5. Hjorth L, Wiebe T, Karpman D. Correct evaluation of renal glomerular filtration rate requires clearance assays. Pediatr Nephrol. 2002;17:847–51.
6. Gretz N, Schock D, Dadick M, Pill J. Bias and precision of estimated glomerular filtration rate in children. Pediatr Nephrol. 2007;22:167–9.
7. Trejtnar F, Laznicek M. Analysis of renal handling of radiopharmaceuticals. Q J Nucl Med. 2002;46:181–94.
8. Rehling M, Nielsen LE, Marqversen J. Protein binding of ^{99m}Tc-DTPA compared with other GFR tracers. Nucl Med Commun. 2001;22:617–23.
9. Rootwell K, Falch D, Sjökvist R. Determination of glomerular filtration rate (GFR) by analysis of capillary blood after single shot injection of ^{99m}Tc-DTPA. Eur J Nucl Med. 1980;5:97–102.
10. Bröchner-Mortensen J, Rödbro P. Comparison between total and renal plasma clearance of [^{51}Cr] EDTA. Scand J Clin Lab Invest. 1976;36:247–9.
11. Sigman EM, Elwood CM, Reagan ME, Morris AM, Catanzaro A. The renal clearance of ^{131}I- labeled sodium iothalamate in man. Invest Urol. 1965;2:432–8.
12. Cohen FT, Smith Jr FG, Mindell RS, Vernier RL. A simple reliable method of measuring glomerular filtration rate using single low dose sodium iothalamate ^{131}I. Pediatrics. 1969;43:407–15.
13. Odlind B, Hällgren R, Sohtell M, Lindström B. Is ^{125}I iothalamate an ideal marker for glomerular filtration? Kidney Int. 1985;27:9–16.
14. Bröchner-Mortensen J. A simple method for the determination of glomerular filtration rate. Scand J Clin Lab Invest. 1972;30:271–4.
15. Cristensen AB, Groth S. Determination of ^{99m}Tc-DTPA clearance by a single plasma sample method. Clin Physiol. 1986;6:579–88.
16. Tauxe WN, Bagchi A, Tepe PG, Krishnaiah PR. Single-sample method for the estimation of glomerular filtration rate in children. J Nucl Med. 1987;28:366–71.
17. Ham HR, Peipsz A. Estimation of glomerular filtration rate in infants and in children using a single-plasma sample method. J Nucl Med. 1991;32:1294–7.
18. Fleming JS, Zivanovic MA, Blake GM, Burniston M, Cosgriff PS. Guidelines for the measurement of glomerular filtration rate using plasma sampling. Nucl Med Commun. 2004;25:759–69.
19. Piepsz A, Denis R, Ham HR, Dobbeleir A, Schulman C, Erbsmann F. A simple method for measuring separate glomerular filtration rate using a single injection of ^{99m}Tc-DTPA and the scintillation camera. J Pediatr. 1978;93:769–74.
20. Gates GF. Glomerular filtration rate: estimation from fractional renal accumulation of ^{99m}Tc-DTPA (stannous). Am J Roentgenol. 1982;138:565–70.
21. Dubovsky EV, Russell CD. Quantitation of renal function with glomerular and tubular agents. Semin Nucl Med. 1982;12:308–29.
22. Waller DG, Keast CM, Fleming JS, Ackery DM. Measurement of glomerular filtration rate with technetium-99m DTPA: comparison of plasma clearance techniques. J Nucl Med. 1987;28:372–7.
23. Mulligan JS, Blue PW, Hasbargen JA. Methods for measuring GFR with technetium-99m-DTPA: an analysis of several common methods. J Nucl Med. 1990;31:1211–9.
24. Goates JJ, Morton KA, Whooten WW, et al. Comparison of methods for calculating glomerular filtration rate: technetium-99m-DTPA scintigraphic analysis, protein-free and whole-plasma clearance of technetium-99m-DTPA and iodine-125-iothalamate clearance. J Nucl Med. 1990;31:424–9.
25. Itoh K. Comparison of methods for determination of glomerular filtration rate: Tc-99m-DTPA renography, predicted creatinine clearance method and plasma sample method. Ann Nucl Med. 2003;17:561–5.
26. Rodman JH, Maneval DC, Magill HL, Sunderland M. Measurement of Tc-99m DTPA serum clearance for estimating glomerular filtration rate in children with cancer. Pharmacotherapy. 1993;13:10–6.
27. Treves ST, Harmon WE, Packard AB. Kidneys. In: Treves ST, editor. Pediatric nuclear medicine/PET. 3rd ed. New York: Springer; 2007. p. 239–85.
28. Dubois D, DuBois EF. A formula to estimate the approximate surface area if height and weight be known. Arch Intern Med. 1916;17:863–71.
29. Haycock GB, Schwartz GJ, Wisotsky DH. Geometric method for measuring body surface area: a height-weight formula validated in infants, children, and adults. J Pediatr. 1978;93:62–6.
30. Heilbron DC, Holiday MA, Al-Dahwi A, Kogan BA. Expressing glomerular filtration rate in children. Pediatr Nephrol. 1991;5:5–11.
31. Du L, Zukotynski K, Hsiao E, et al. Pediatric reference ranges for glomerular filtration rate determined by a single injection of Tc-99m DTPA. J Nucl Med. 2009;50:S1375.

Skeletal Scintigraphy: General Considerations

15

S. Ted Treves

Skeletal scintigraphy provides a functional image of bone. It is a highly sensitive method that depicts early changes in bone flow and turnover. Because of this high sensitivity, skeletal scintigraphy allows early diagnosis of disease often days or weeks before disease can be visualized on anatomic imaging. Therefore, skeletal scintigraphy assists in establishing early treatment and hopefully achieving better patient outcomes. However, as with other nuclear medicine imaging procedures, this high sensitivity is generally accompanied by a low level of specificity. Information about early changes in blood flow and bone turnover cannot be obtained, or not easily obtained, by other imaging methods. Although the spatial resolution of bone scintigraphy is relatively low compared to anatomic imaging, one can say that its functional resolution is very high.

Skeletal development and remodeling are integral parts of the physiology of bone. As the patient grows and develops, bone undergoes constant remodeling. Immature bone (woven bone) is replaced by mature lamellar bone. A skeletal scintigram can be considered not just as a static image but also as a "snapshot" of an ongoing dynamic process. As such, the bone scan can be thought of as a "slow dynamic" study. Approximately 10 % of the entire adult skeleton is replaced every year. Remodeling is, in great part, a functional adaptation of bone to the forces or stresses of daily life. When interpreting pediatric skeletal scintigraphy, it is important to keep in mind the characteristic patterns of pediatric skeletal growth and development and learn to recognize these patterns so they can be distinguished from actual lesions. The distribution of bone-seeking radiopharmaceuticals varies with age and with the activity of growth centers. It is necessary for growth centers to be ossifying in order for bone-seeking radiopharmaceuticals to be taken up in these regions. Otherwise, the center will appear devoid of activity. Ossification of growth centers occurs at different ages until all close by approximately 25 years of age. During the first year of life until 5 years of age, secondary ossification centers appear in the epiphysis. From 5 to 14 years of age, ossification rapidly spreads from the ossification centers, and various bones become ossified. The upper limbs and the scapula become ossified by 17–20 years. The bones of the lower limbs and the os coxae completely ossify by ages 18–23. By ages 23–25, the sternum, clavicles, and vertebrae become completely ossified. There may or may not be direct correlation between the radiographic and scintigraphic appearance of growth centers. Examples of absent-to-reduced tracer uptake in growth centers include the femoral head,

S.T. Treves, MD
Joint Program in Nuclear Medicine,
Department of Radiology, Harvard Medical School,
Boston, MA, USA

Division of Nuclear Medicine and Molecular Imaging, Department of Radiology,
Boston Children's Hospital,
Boston, MA, USA

Division of Nuclear Medicine and Molecular Imaging, Department of Radiology,
Brigham and Women's Hospital, Boston, MA, USA
e-mail: ted_treves@HMS.harvard.edu

S.T. Treves (ed.), *Pediatric Nuclear Medicine and Molecular Imaging*,
DOI 10.1007/978-1-4614-9551-2_15,

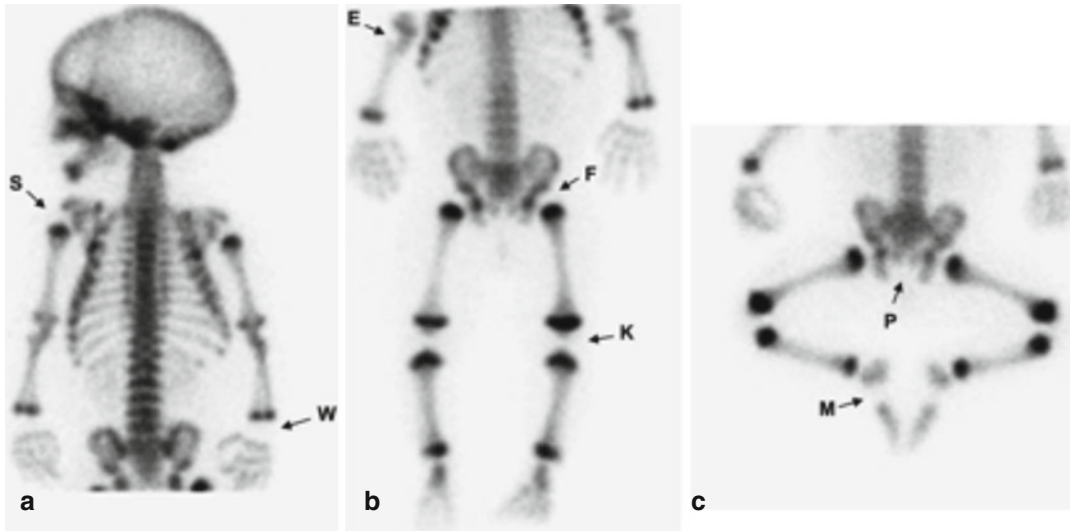

Fig. 15.1 (**a**–**c**) Absent tracer uptake in non-ossified centers. *S* shoulder, *W* wrist, *E* elbow, *F* femoral head, *K* knee, *P* pubis, *M* mid-foot

Fig. 15.2 Bilateral open ischiopubic synchondrosis (*arrows*)

Table 15.1 Indications for skeletal scintigraphy in children

Osteomyelitis
Chronic recurrent multifocal osteomyelitis (CRMO)
Sports injuries
Back pain
Avulsion fractures
The limping child. Toddler's injuries
Localization of the source of pain
Non-accidental trauma
Avascular necrosis of bone
Benign tumors (osteoid osteoma)
Bone infarction
Cysts
Fibrous dysplasia
Bone island
Hemangioma
Langerhans cell histiocytosis
Hyperostosis oncologic disorders (osteosarcoma, Ewing's sarcoma, rhabdomyosarcoma)
Radiation injury

the patella, the tarsal navicular, and the ischiopubic synchondrosis. During ossification, the ischiopubic synchondrosis can show focal increased tracer uptake which can be unilateral or bilateral, and this appearance should not be confused with a lesion (Figs. 15.1 and 15.2).

Whether a lesion is detected on conventional anatomic imaging depends on the degree of bone loss or deposition and on the stage of development of the lesion. For example, when excessive force is applied to a bone, or a lesion affects the bone, the bone reacts by forming new and stronger bone. In this early phase, anatomic imaging may not detect the abnormality unless significant bone loss has developed. Initially, the region of bone exposed to such force shows increased regional blood flow, which is part of the process of bone remodeling. During the process of bone remodeling, the bone is rather weak and vulnerable to further injury. Focal or diffuse increased blood flow can be seen on radionuclide angiography and on immediate (tissue) images as well as on skeletal images as regions of increased tracer concentration. Bone remodeling accompanied by increased tracer

uptake can go on for a period of time and depends on the progress stage of the lesion. Increased tracer uptake can persist, can become less noticeable, or can even disappear, and the bone scan may appear normal. For example, a bone scan may, at the end, appear normal in the presence of a well-established bone lesion. As an example, in an old spondylolytic lesion where the bone has become "quiescent" (doesn't show increased blood flow or high bone turnover), the bone scan may not demonstrate a focal abnormality, while anatomic imaging will likely show the fracture. Pediatric indications for skeletal scintigraphy that include benign and oncologic disorders are listed in Table 15.1. In the assessment of children with lower extremity or back pain, consider the benefit of large area imaging easily available with ^{99m}Tc-MDP scintigraphy or ^{18}F-NaF PET in the diagnosis and localization of pain of skeletal origin. This concept is applicable anywhere in the body. Children (and sometime adults) may have trouble identifying the source of pain. Pain may be referred to region distant from the site of a bone lesion. Some patients have conventional imaging focusing on a small area, which is clinically thought to be the source of pain. This approach may miss a skeletal source of pain. Therefore, one should keep in mind the benefit of skeletal scintigraphy evaluating a large area that goes beyond the reported symptom. A useful approach would be as follows: once an abnormality is identified on scintigraphy, anatomic imaging can be focused to the area of interest and help provide a higher level of diagnostic specificity (Fig. 15.3).

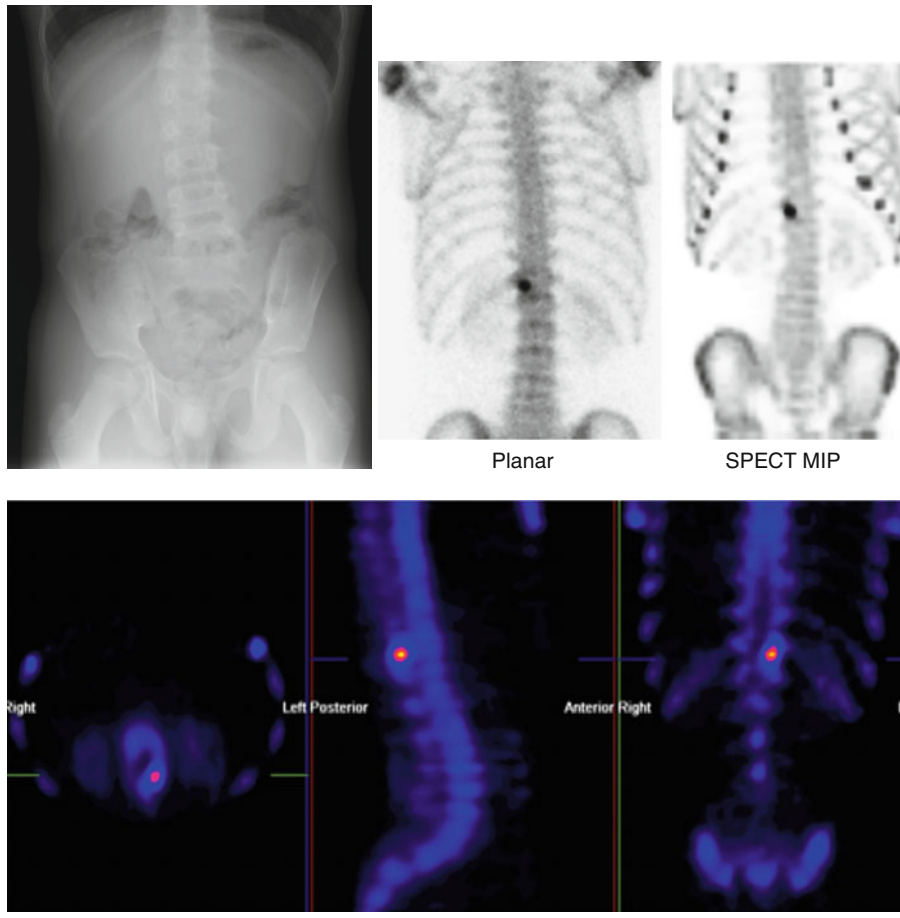

Fig. 15.3 An 11-year-old male with low back pain for several months. Relieved by Advil. X-ray suggested scoliosis. New plain x-rays suggested sclerosis of pedicle of L5. Bone SPECT showed intense and focal increased tracer uptake at T12. Finding suggested osteoid osteoma. A repeat CT showed findings compatible to an osteoid osteoma at T12

Fig. 15.3 (continued)

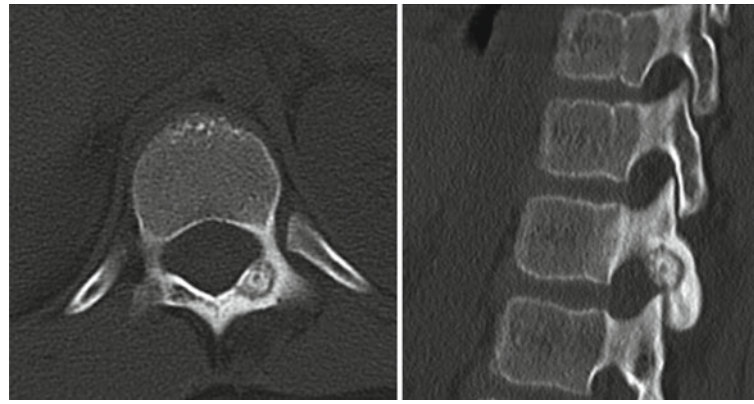

CT

Fig. 15.4 Vascular tamponade. Pinhole ^{99m}Tc-MDP images of the right hip from an 11-month-old with a tense hip effusion producing vascular tamponade of the femoral head. There is absent tracer uptake in the femoral head (*left image*). A follow-up image after the patient's effusion was drained reveals return of flow to the femoral head as evidenced by tracer uptake in it (*right image*)

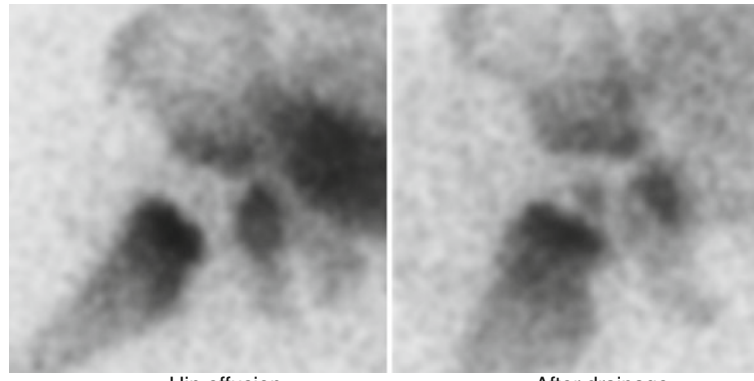

Hip effusion After drainage

Radiopharmaceuticals

Technetium-99m-MDP

Technetium-99m-MDP is the most commonly used radiopharmaceutical for skeletal scintigraphy. It is easily prepared in the nuclear medicine department from a kit, or it can be obtained already prepared and calibrated from commercial radiopharmacies. Following intravenous injection of ^{99m}Tc-MDP, skeletal distribution and uptake of this agent depend on regional blood flow and bone turnover. On skeletal scintigraphy, regions of reduced-to-absent blood flow will be seen as regions of reduced-to-absent tracer uptake (e.g., in a tense hip effusion or in the femoral head after a femoral neck fracture) (Figs. 15.4 and 15.5).

Hip effusion can occur without compromising perfusion of the femoral head (Fig. 15.6). Disuse of an extremity, for example, after a fall, can cause relatively decreased tracer uptake in the extremity not bearing weight even for a few days. Conversely, the contralateral extremity that bears weight will show relatively increased tracer uptake owing to the relatively increased blood flow to such extremity (Fig. 15.7).

In bone infarction such as in sickle cell disease, blood flow to the area involved is significantly reduced or absent. In this case, tracer delivery and bone uptake will be reduced to absent (Fig. 15.8).

Elegant autoradiography studies by Tilden et al. revealed that ^{99m}Tc-phosphates localize in lines between osteoid lining marrow cavities and the more peripheral bone (Fig. 15.9) [1]. After intravenous injection, blood activity levels fall to 4–10 % of the administered dose by 2 h and down to 3–5 % in 3 h. Less than 2 % of the activity is in the blood by 24 h after administration. Approximately 30 % of the activity is

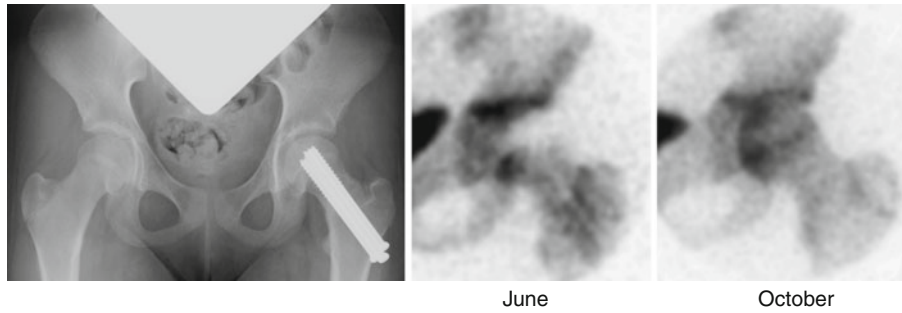

Fig. 15.5 Avascular femoral head and reperfusion after treatment. A 12-year-old girl with a left femoral neck fracture. Metallic pins (*left*) were inserted under an open reduction internal fixation (ORIF), and the initial ^{99m}Tc-MDP pinhole image (*center*) obtained soon after the surgery shows lack of vascularity in the femoral head as well as the defects corresponding to the metallic pins. A similar image obtained 4 months after surgery (*right*) reveals reperfusion of the left femoral head

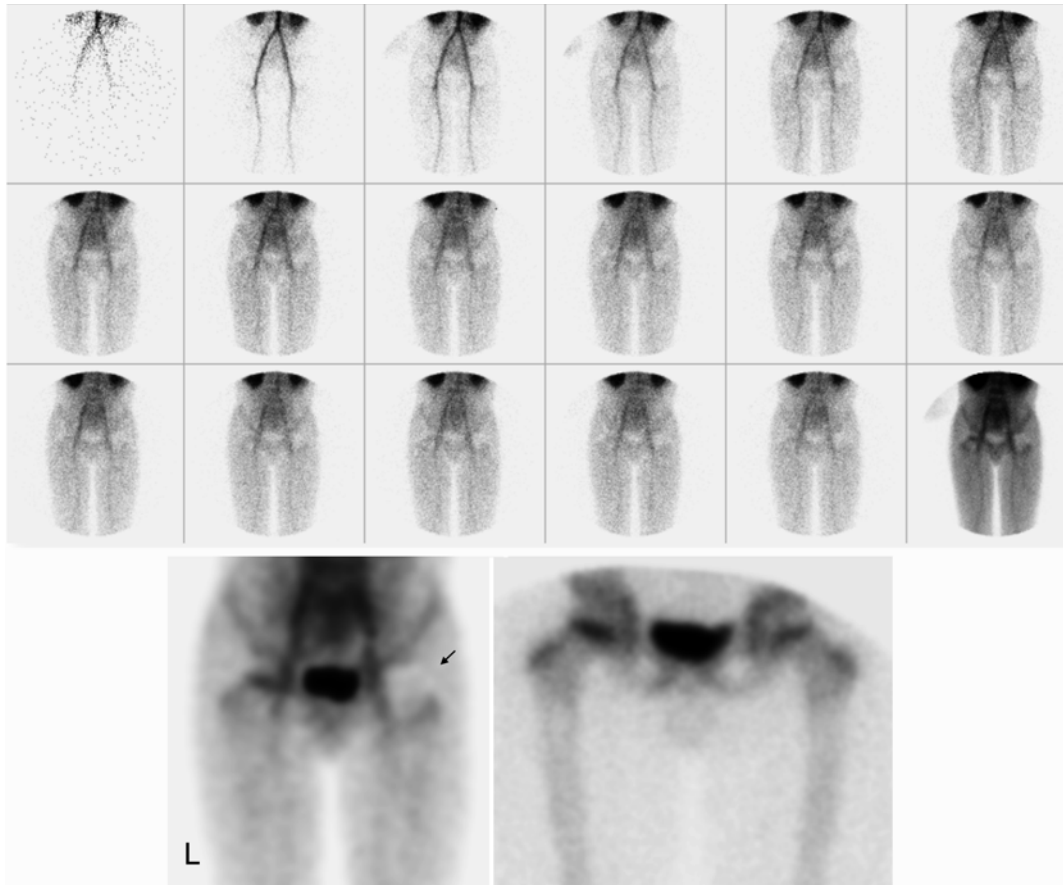

Fig. 15.6 Left hip effusion. The radionuclide angiogram reveals that left hip effusion is seen as absent tracer concentration in the region of the right hip (*top*). The tissue image (*left lower image*) shows decreased tracer concentration in the region of the left hip (*arrow*). The skeletal phase image (*right lower image*) shows that the left femoral head perfusion is preserved

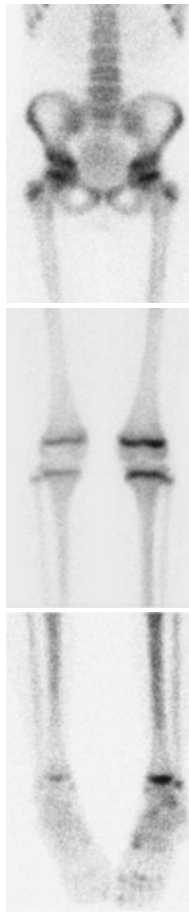

Fig. 15.7 An 8-year-old female with right leg pain for a week after a fall with twisting of her right leg. MRI revealed no hip pathology. The patient was using crutches and did not put weight on her right leg. There is diffusely decreased uptake throughout the right lower extremity due to reduced overall flow with disuse. Conversely, the left leg that was supporting the patient's weight reveals relatively increased tracer uptake

protein bound during the first hour, 45 % at 3 h and 100 % at 24 h. Approximately 40 % of the administered activity is found in the urine in one hour to 60 % and 70 % at 4 and 24 h after injection, respectively [2, 3]. Usual administered doses are 0.2 mCi (7.4 MBq)/kg of body weight with a minimum total dose of 0.5 mCi (18.5 MBq) [4].

Technetium-99m-phosphates are also known to accumulate in soft tissue lesions prone to ischemia and/or microcalcification such as in neuroblastoma, stroke, metastatic osteosarcoma, myocardial infarction, functional asplenia, muscle trauma, myositis ossificans, necrotizing enterocolitis, and hyperparathyroidism (Fig. 15.10).

Fluorine-18 Sodium Fluoride

Fluorine-18 sodium fluoride was recognized as an excellent skeletal imaging agent several decades ago [5]. Two principal factors are responsible for the increasing use of ^{18}F-NaF skeletal PET. One is due to the improved distribution of ^{18}F-labeled radiotracers that had been paved by the wide use of FDG. Therefore, commercially available ^{18}F-NaF is widely available at the present time. The other important factor is the development and wide installed base of modern PET and PET/CT scanners [6–8].

After intravenous administration, ^{18}F-NaF is rapidly cleared from the plasma by a biexponential mode. The first phase has a half-time of 0.4 h, and the second phase has a half-time of 2.6 h. Essentially all the ^{18}F-NaF that is delivered to bone by the blood is retained in the bone. One hour after administration of ^{18}F-NaF, only about 10 % of the injected dose remains in blood. Fluorine-18 sodium fluoride diffuses through capillaries into extracellular fluid space in bone, where it becomes bound by chemisorption at the surface of bone crystals, preferentially at sites of newly mineralizing bone. Deposition of ^{18}F in bone appears to be primarily a function of blood flow to, and the efficiency of the bone extracting ^{18}F-NaF. Fluorine-18 sodium fluoride does not appear to be permanently bound to serum proteins. In patients with normal renal function, 20 % or more of the fluorine ion is cleared from the body in the urine within the first 2 h after intravenous administration. A usual pediatric administered dose is 0.06 mCi (2.2 MBq)/kg to a maximum of 4 mCi (148 MBq). The usual minimum administered amount of this tracer is 0.5 mCi (18.5 MBq). Our experience with ^{18}F-NaF skeletal imaging goes back to the early 1970s, when for a period of time we used ^{18}F-NaF as a routine procedure. We obtained ^{18}F-NaF scintigraphy using a whole-body rectilinear scanner in patients of all ages (Fig. 15.11).

During the transition from ^{18}F-NaF to ^{99m}Tc-phosphates in 1974, we compared ^{18}F-NaF and pyrophosphate in children with neuroblastoma,

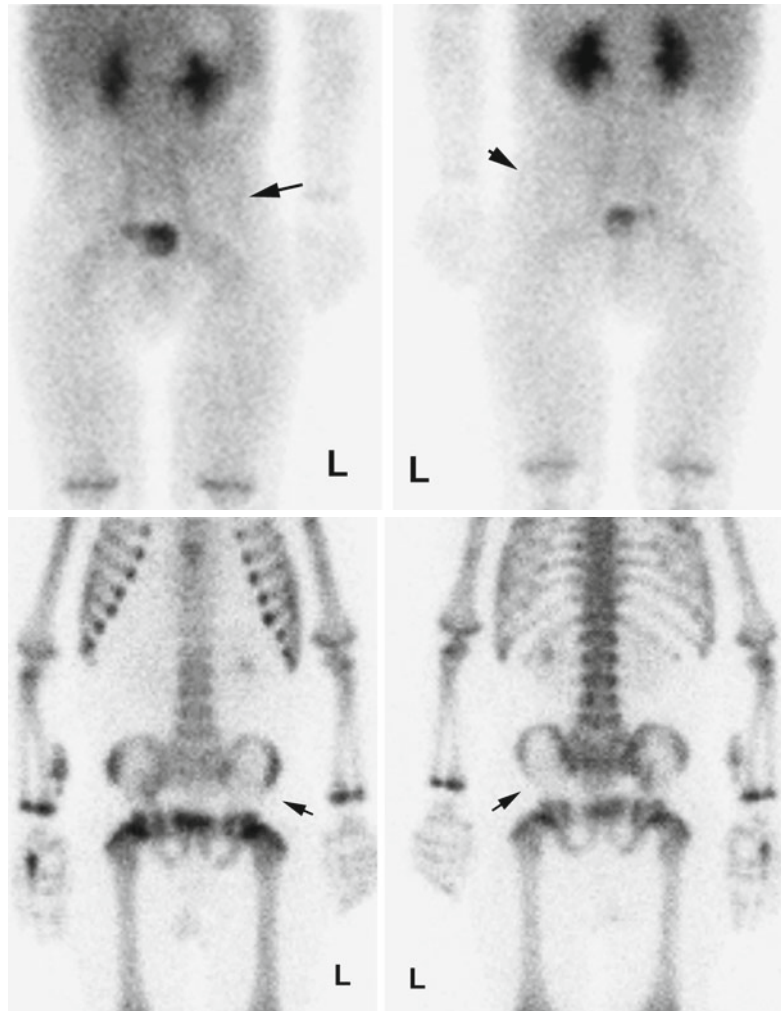

Fig. 15.8 Bone infarct. Images from a 5-year-old male with sickle cell disease. The tissue phase images show relatively reduced tracer accumulation in the region of the left hip (*top image*, *arrows*). The skeletal phase images reveal decreased-to-absent tracer uptake in the left iliac bone (*lower images*)

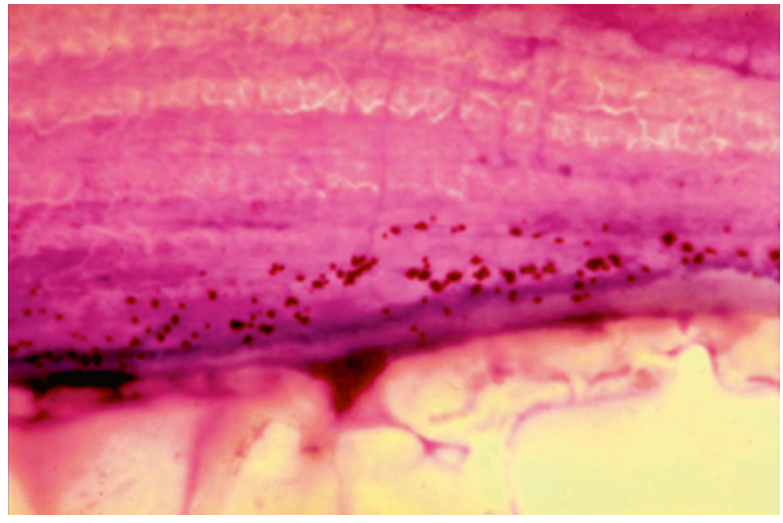

Fig. 15.9 Autoradiography of ^{99m}Tc-pyrophosphate from a human femur showing localization of silver granules just beneath osteoid

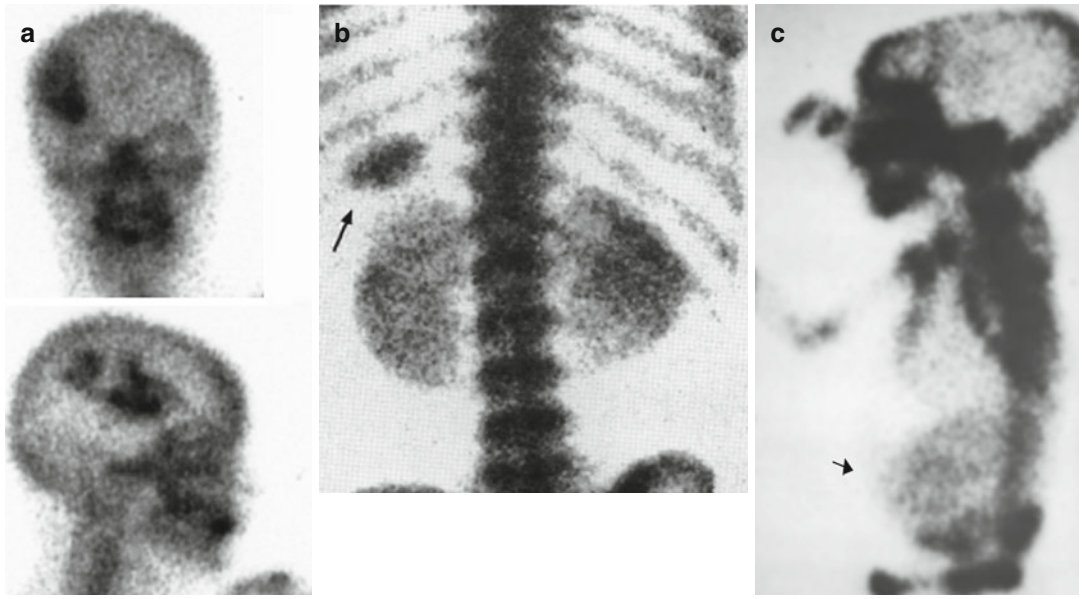

Fig. 15.10 Uptake of ^{99m}Tc-phosphates in soft tissues. (**a**) Stroke. (**b**) MDP in spleen (*arrow*) of patient with sickle cell disease. (**c**) Necrotizing enterocolitis in a newborn, intestine (*arrow*)

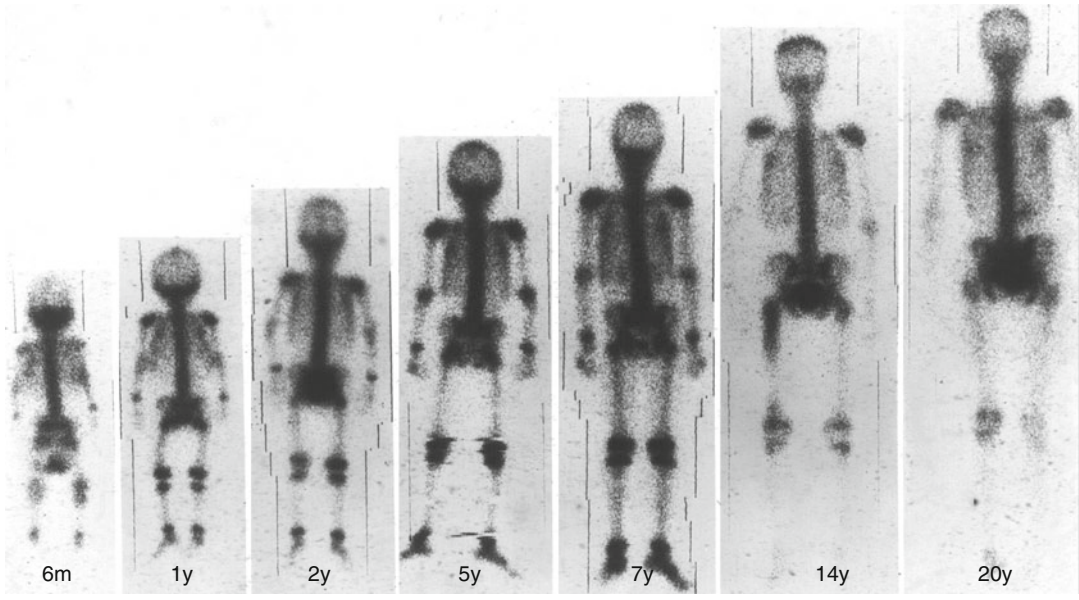

Fig. 15.11 ^{18}F-NaF whole-body scans in patients of all ages obtained with a whole-body rectilinear scanner

and the resulting patterns of distribution were similar [9]. Soon after technetium-labeled phosphates were introduced and made widely available, the use of ^{18}F-NaF decreased dramatically. The spatial resolution available with whole-body rectilinear scanners was rather poor compared with images obtained with modern PET systems (Fig. 15.12).

In addition to the agents mentioned above, other agents have been used for radionuclide skeletal imaging. These include ^{99m}Tc-sulfur colloid for bone marrow imaging, ^{18}F-FDG for tumors and infection/inflammation, ^{99m}Tc-HMPAO-labeled white blood cells for infection, and ^{201}Tl-chloride for tumor imaging.

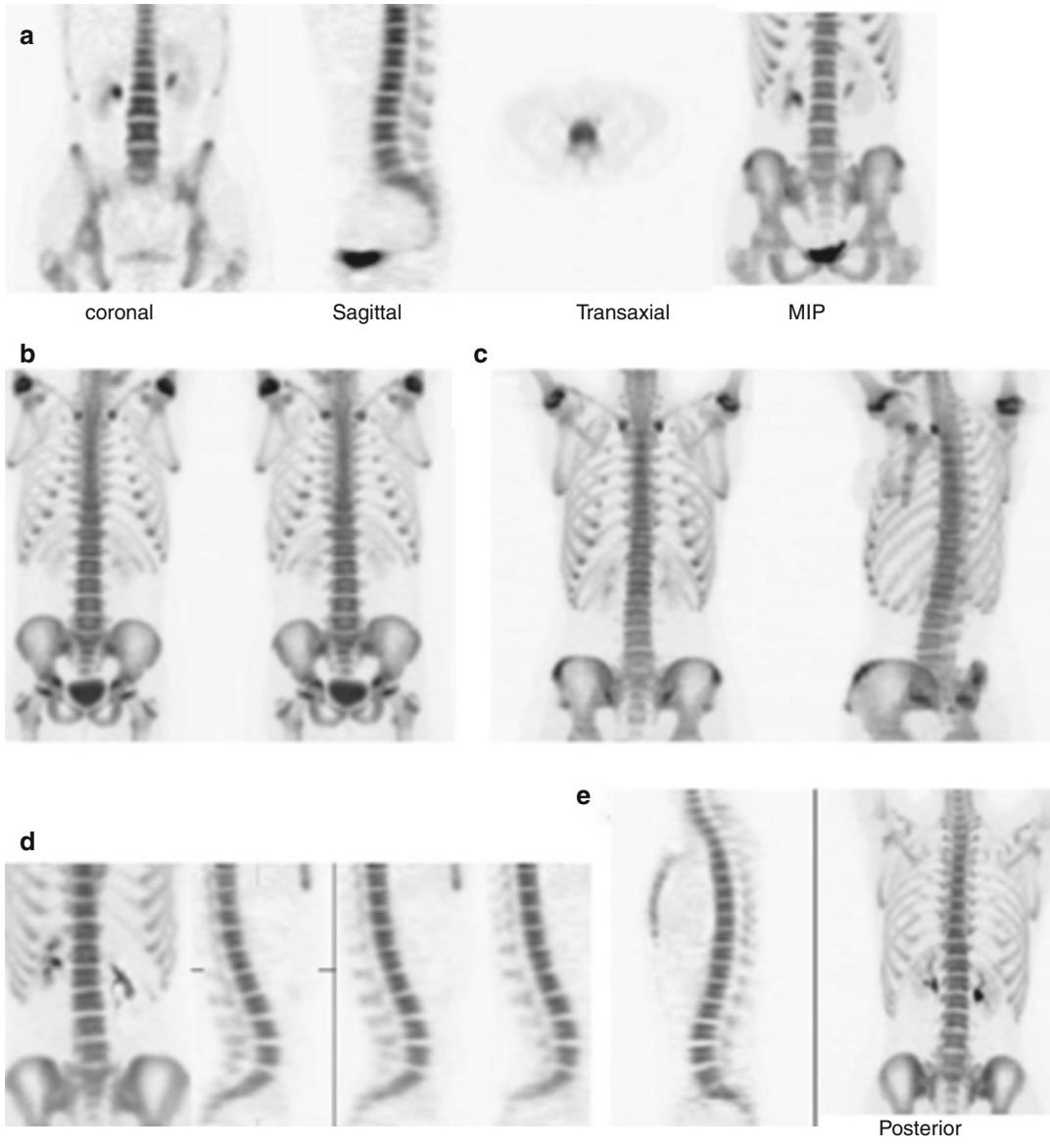

Fig. 15.12 Normal skeletal ^{18}F-NaF PET in patients aged 5 years (**a**), 11 years (**b**), 15 years (**c**), 19 years (**d**), and 30 years (**e**). Pattern of ^{18}F-NaF uptake in skeleton is similar to pattern seen with more familiar ^{99m}Tc-labeled diphosphonate bone scans and illustrates changes that occur with maturation of skeleton (Reproduced with permission by Grant et al.)

Imaging with ^{99m}Tc-MDP

Patient Preparation: The patient should be encouraged to drink plenty of fluids before scanning. No other preparation is needed, except to let the patient and caregivers know how long the entire procedure will take so that appropriate scheduling arrangements can be made. In the hands of well-trained and experienced technologists, patients do not need to be sedated for ^{99m}Tc-MDP scintigraphy. Small patients may need sedation for SPECT. If possible, patients should be asked to void before imaging. Examination of the pelvic region may be limited

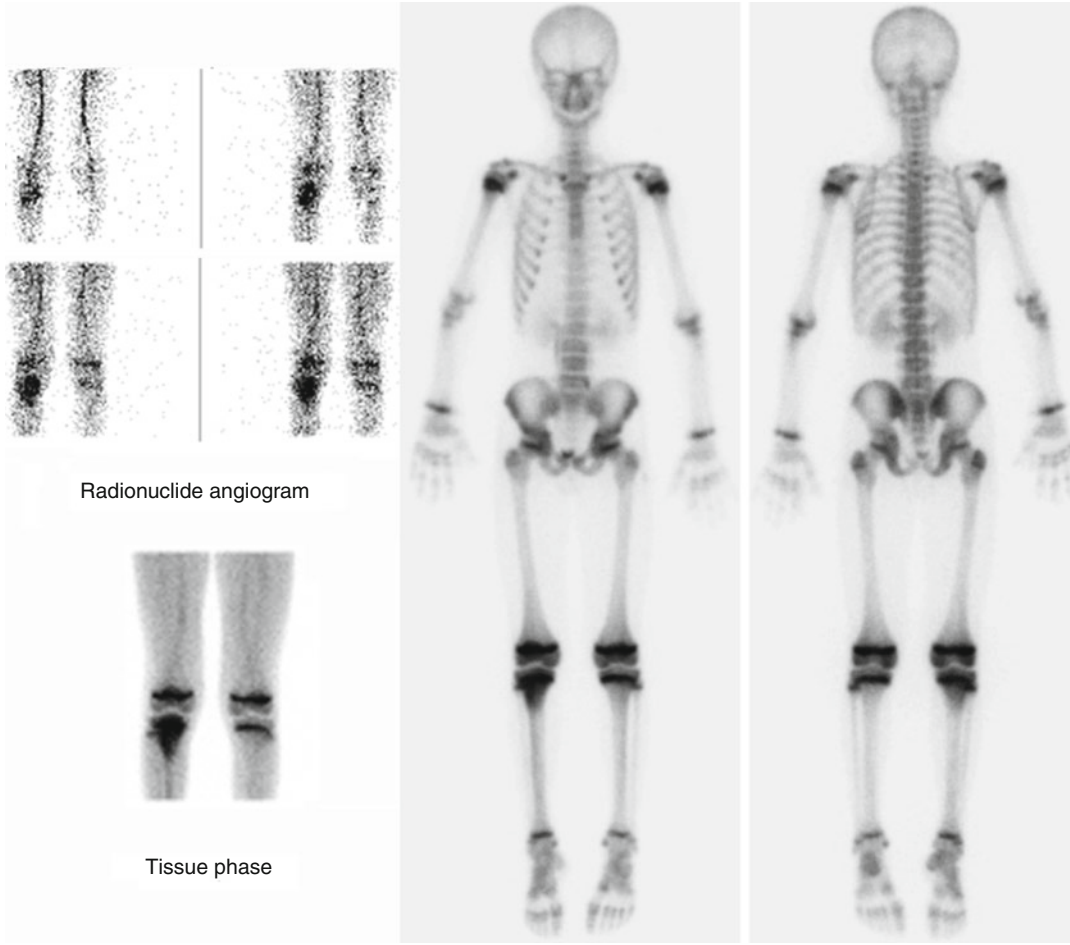

Fig. 15.13 A three-phase ^{99m}Tc-MDP bone scan in a teenager with osteomyelitis of the right proximal tibia. Increased blood flow to the area is seen on the radionuclide angiogram and increased localization in the right proximal tibia on the tissue phase image. The skeletal phase image also shows increased tracer uptake in the right proximal tibia

if the bladder is full of tracer. In some cases, bladder catheterization may be necessary in order to evaluate this region better.

Planar Imaging

Planar imaging may include one, two, or three phases (the "three-phase bone scan"): (a) radionuclide angiography, (b) immediate tissue phase images, and (c) skeletal images. The nuclear medicine physician may choose all three phases or would be satisfied by the skeletal phase only, and this will be determined by the patient condition and the diagnostic task at hand. Figure 15.13 shows a three-phase bone scan in a patient with osteomyelitis.

The three-phase approach is used when the clinical indication suggests infection, inflammation, or an aneurismal bone cyst. In cases of soft tissue inflammation without osteomyelitis, this can be revealed by radionuclide angiography and immediate phase images, but not on skeletal images if the bone itself has not been affected by increased blood flow, etc. The more time that elapses between tracer administration, the greater

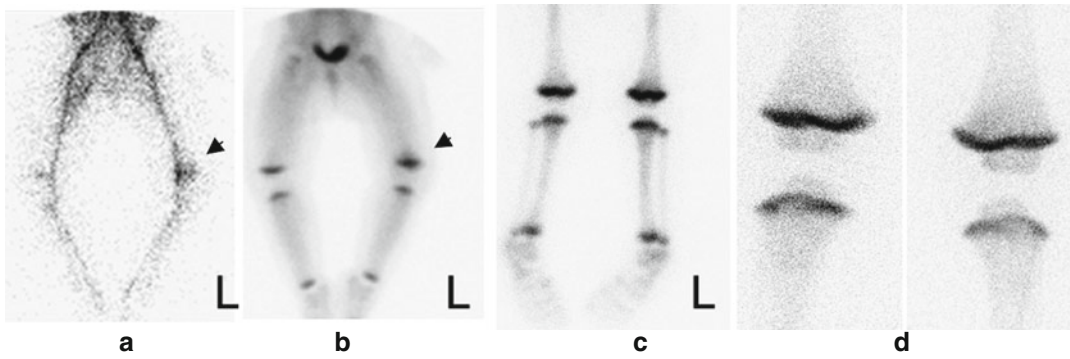

Fig. 15.14 Soft tissue inflammation, cellulitis. (**a**) Radionuclide angiogram shows increased blood flow to the region of the left knee. (**b**) Immediate tissue image shows a mild accumulation of tracer in the same region. (**c**) Skeletal phase image shows very mild increased uptake in the left distal femur and left proximal tibia. (**d**) Pinhole images do not reveal abnormal focal uptake in the bones of the left knee

the bone-to-background ratio. In some instances, images at approximately 24 h following tracer administration can be obtained and can be useful to further enhance the lesion-to-background difference ("the four-phase bone scan") [10].

Radionuclide Angiography

Radionuclide angiography is obtained immediately after the intravenous injection of the tracer as a dynamic study using a high-resolution collimator. Usual framing rates are from 1 frame per second to 1 frame per 0.5 s or on list mode with post-acquisition reframing. As the photon flux is relatively low given the amount of administered tracer, viewing is usually on summed 1.0 min images. Cinematic display is helpful for interpretation in some cases, and it should be used liberally. Images are usually acquired on a 128×128 format.

In patients with soft tissue inflammation without bone involvement, the radionuclide angiogram will show a focal region of increased tracer delivery corresponding to the region of inflammation (cellulitis). This may or may not be accompanied by bone involvement (Fig. 15.14).

The field of view for the angiogram is chosen based on the site of patient symptoms or the expected location of a lesion. However, if there is referred pain, the angiogram may miss the lesion. If this is suspected, it is useful to obtain tissue phase images of adjacent areas around the initial region of interest.

Immediate Tissue Phase Images

These images (also called "blood pool" images) are useful to assist in the detection of soft tissue lesions such as inflammation, infection, and soft tissue tumors. This information complements the radionuclide angiography and skeletal phase images allowing the differentiation of soft tissue only (cellulitis) versus a combination of soft tissue and skeletal abnormality (certain tumors). In some cases, it is useful to obtain a tissue phase image of the whole body. Since these images take a few minutes to obtain, tracer is already seen in the soft tissues and in bone, so the images are not purely reflecting the blood pool.

Skeletal Phase Images

Following the intravenous injection of ^{99m}Tc-MDP, skeletal phase images are usually obtained at 2, 3, or 4 h later. Techniques for planar skeletal

Fig. 15.15 A 2.5-year-old boy fell from bed 2 weeks ago and had normal x-rays of the ankle. The patient was treated with high-top sneakers. Patient did not improve. Skeletal scintigraphy reveals a curvi linear pattern of increased tracer uptake along the left tibia suggesting a spiral fracture. One week after the bone scan, follow-up radiographs confirmed a spiral fracture of the left tibia

phase imaging include multispot imaging, whole-body imaging, and pinhole magnification.

Multispot Imaging

Multispot imaging does not require patient sedation and can be relatively easily obtained with gentle immobilization in the hands of experienced technologists. Each image is obtained for approximately 500,000 counts on a 128×128 or 256×256 matrix format. Imaging symmetric parts of the body should be obtained based on the same imaging time so that right-left comparisons are easier to achieve. Multispot images are usually of higher spatial resolution than whole-body images (Fig. 15.15).

Whole-Body Imaging

These images give an overall view of tracer biodistribution throughout the body, which can be useful in the detection of focal lesions or help in elucidating certain systemic conditions. Some children, however, cannot or will not stay still for the duration of the whole-body scan (20–30 min) and may need to either be sedated or, alternatively, have the study done with multispot imaging. With the application of enhanced planar processing, it is possible to cut the whole-body scanning in half so that it is possible to obtain whole-body scans in some children without the need for sedation. Alternatively, with a normal scanning time, this method allows the administration of 50 % less radiopharmaceutical dose, thus reducing patient radiation exposure by half [11].

Pinhole Magnification Scintigraphy

Pinhole magnification is very useful for imaging small bones in children. The pinhole collimator provides images of very high resolution by spreading every point of the object over a larger area of the detector crystal. So, although the intrinsic spatial resolution of the gamma camera is not affected per se, the system's resolution is greatly improved so that objects in the 1–2 mm range can be imaged (see Chap. 27).

Pinhole magnification scintigraphy is useful in the evaluation of the hip (Figs. 15.4, 15.5, and 15.16), in the evaluation of small bones of the hands (Fig. 15.17) and feet, as well as in the characterization of osteoid osteoma (Figs. 15.18 and 15.19). The smaller the pinhole, the greater the system's spatial resolution. This is at the cost of sensitivity. The closer the pinhole collimator to the object, the higher the spatial resolution and the higher the sensitivity (Fig. 15.16).

In osteoid osteoma, the characteristic appearance on pinhole magnification is a focal and very intense region of tracer uptake corresponding to the area of the nidus. This is typically surrounded by an area of mild and diffuse tracer uptake. Planar imaging can detect the focal increased uptake, but the pinhole image shows a more characteristic diagnostic pattern.

Pinhole magnification scintigraphy can effectively assist before and during the surgical excision of osteoid osteomas anywhere in the body and especially in the central skeleton to ensure complete removal of the lesion. For this purpose, we use a mobile solid-state camera equipped

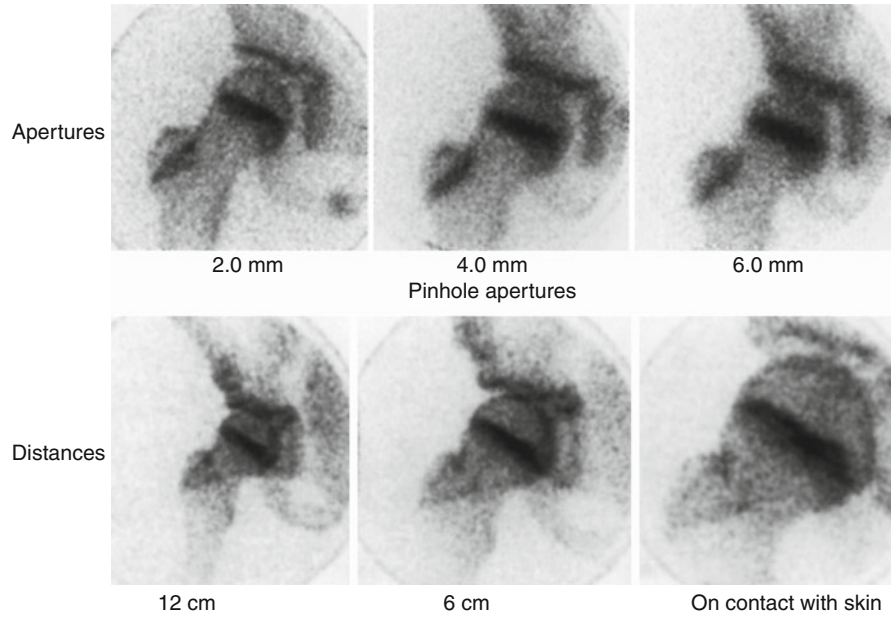

Fig. 15.16 Pinhole images of the hip showing the effects of different collimator apertures and different distances from the object

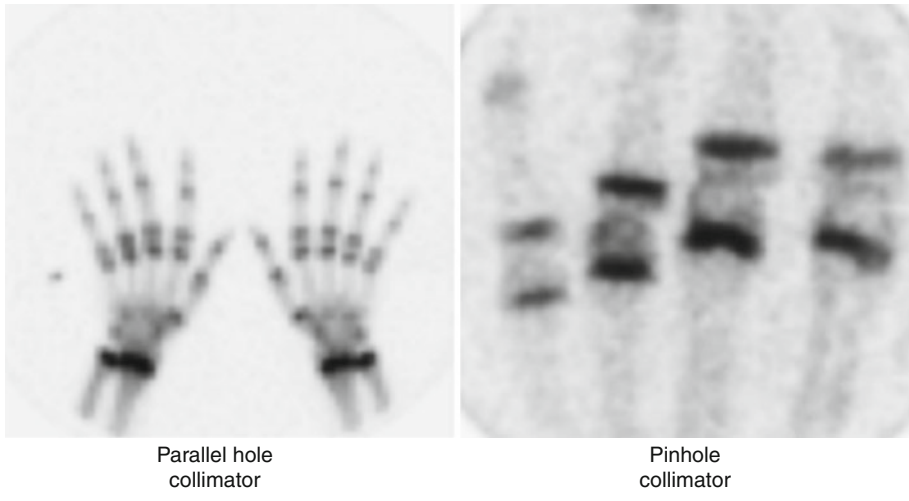

Fig. 15.17 A 10-year-old male with 2 months of pain and swelling in the region of the fourth left metacarpal phalangeal joint. The x-rays, CBC, and ESR were normal. The clinical question was osteomyelitis versus soft tissue process. The pinhole image (*right*) shows focally increased tracer uptake in the distal metacarpal bone adjacent to the joint

with a pinhole collimator, which is brought into the operating theatre. There, the camera is covered with sterile sheets, and the surgeon and the nuclear medicine physician collaborate using a series of images during the operation until there is assurance that no residual tissue corresponding to the osteoid osteoma is left behind. With this approach, the number of recurrent osteoid osteomas in our setting is virtually nonexistent (Fig. 15.19) [12–14].

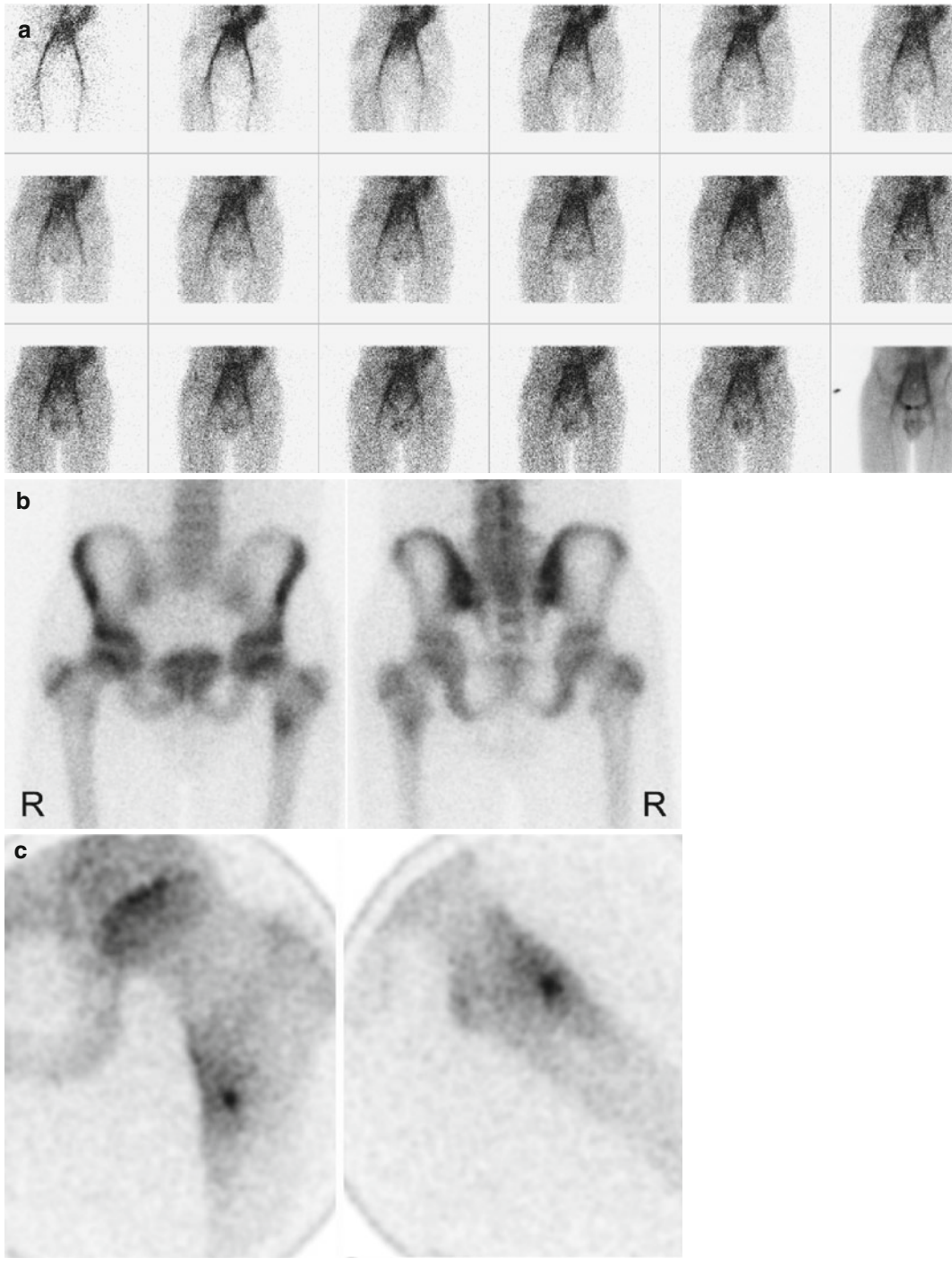

Fig. 15.18 Osteoid osteoma of the left proximal femur. Typical appearance where the radionuclide angiogram and the tissue phase image do not show an abnormality (**a**). The skeletal phase reveals focally increased tracer uptake in the region of the lesion (**b**). The pinhole image (**c**) shows the typical appearance of an osteoid osteoma: intense focal tracer uptake surrounded by a "cloud" of less intense and diffusely increased tracer uptake

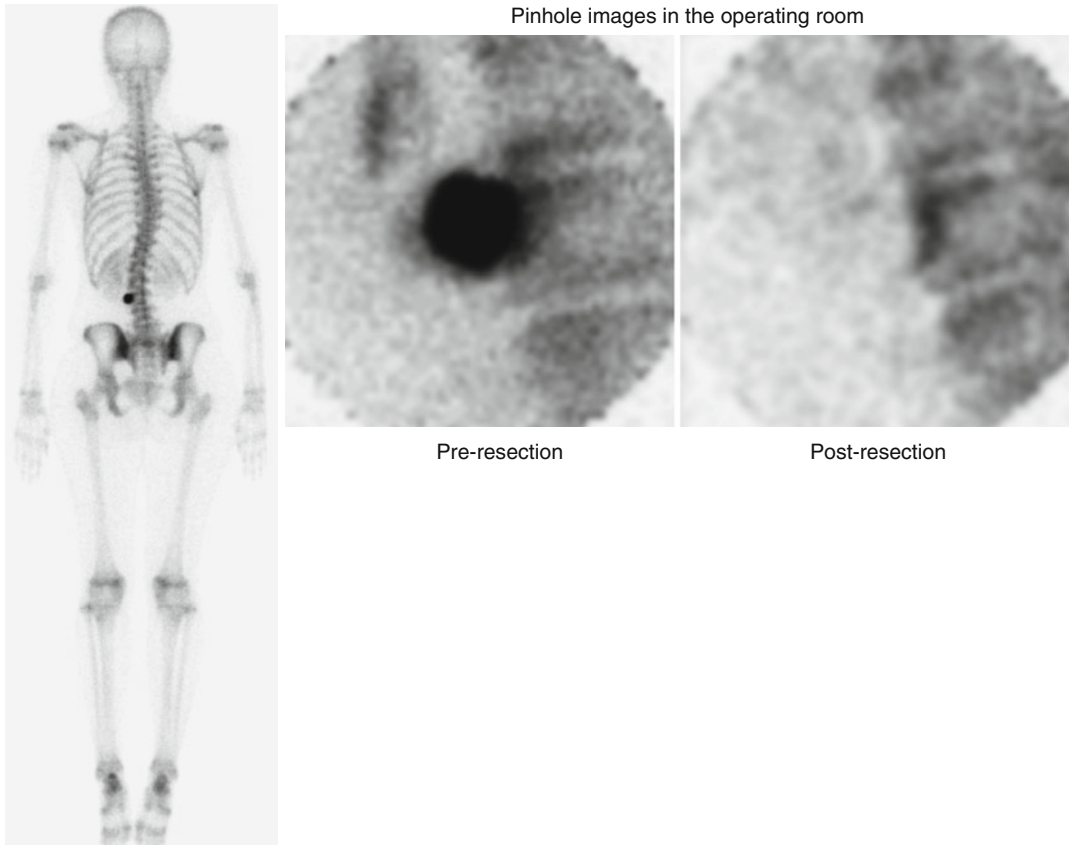

Fig. 15.19 Osteoid osteoma of the spine. The whole-body ^{99m}Tc-MDP bone scan shows an intense and well-localized region of increased uptake (*left panel*). Pinhole images obtained in the operating room show the osteoid osteoma as well as its absence after surgical resection (*right panel*)

The physical characteristics of the pinhole and pinhole magnification are discussed in greater detail in the chapter on Instrumentation and Image Processing. The closer the collimator is to the object, the greater the magnification and spatial resolution achieved.

SPECT

SPECT should be considered an integral tool in the routine evaluation of pediatric skeletal disorders including the investigation of the cause of back pain, fractures, osteoid osteoma, and tumors (Fig. 15.20). SPECT provides a three-dimensional image for improved localization and much higher contrast than planar imaging. SPECT has proven invaluable in the detection of skeletal abnormalities in young children and adolescents with back pain. SPECT is definitely superior to planar imaging for this diagnostic task, as planar imaging can frequently miss lesions that can be more readily detected on SPECT. Therefore, SPECT should be considered indispensable in the clinical setting of back pain. Most patients referred to our practice with back pain are young athletes. SPECT can detect early stress changes in the affected bones such as posterior elements, the spinous processes, and the pelvis (Fig. 15.21).

In addition to the role of SPECT in teenage athletes, we have seen stress changes in children younger than 10 years of age. In children of this age group complaining of back pain, skeletal SPECT reveals a high incidence of abnormal

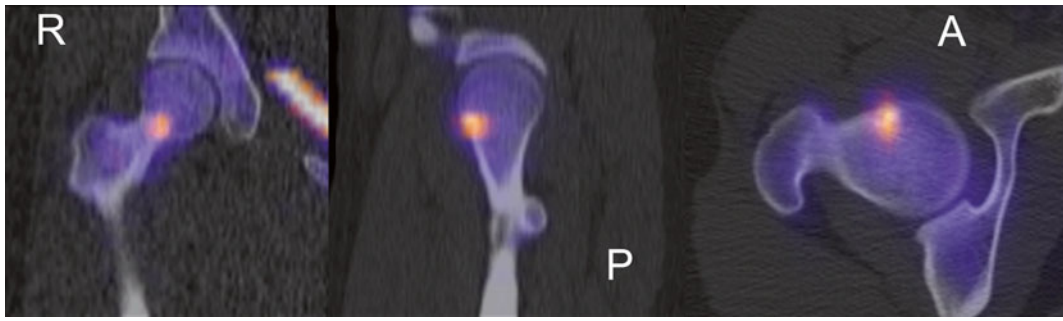

Fig. 15.20 Osteoid osteoma of the right femoral neck. ^{99m}Tc-MDP SPECT fused to a CT helps with the anatomic localization of the lesion

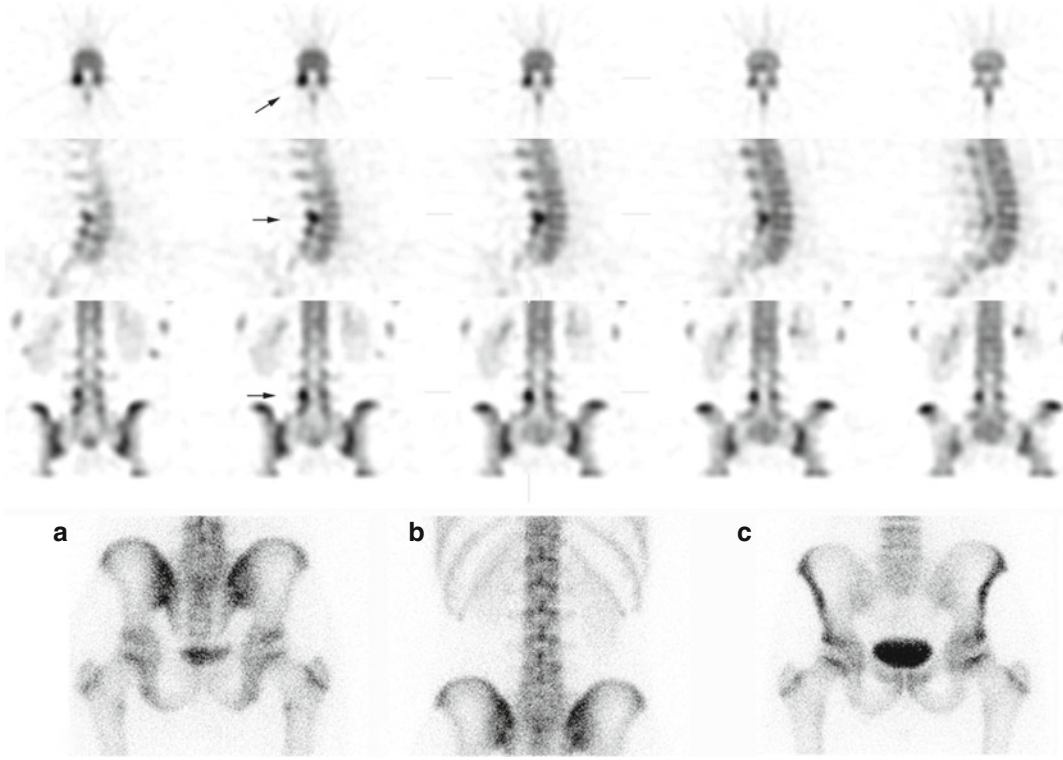

Fig. 15.21 A 17-year-old male experienced recent recurrence of back pain after high jumping, and running. Planar imaging (*bottom a–c)* does not reveal focal abnormality while the SPECT (*top*) clearly reveals focal increased tracer uptake at the level of left posterior element at L4 (*arrows*)

scintigraphic findings similar to those patterns seen in the older patients. In an early study, we found that in 50 patients younger than 10 years of age, approximately 20 % of the SPECT showed focal SPECT abnormalities in the spine (Fig. 15.22) [15].

Traditionally, pediatric SPECT is reconstructed with filtered back projection (FBP). Compared with newer reconstruction techniques, the spatial resolution and image quality with FBP are relatively low. Using advanced image processing such as *ordered subset expectation*

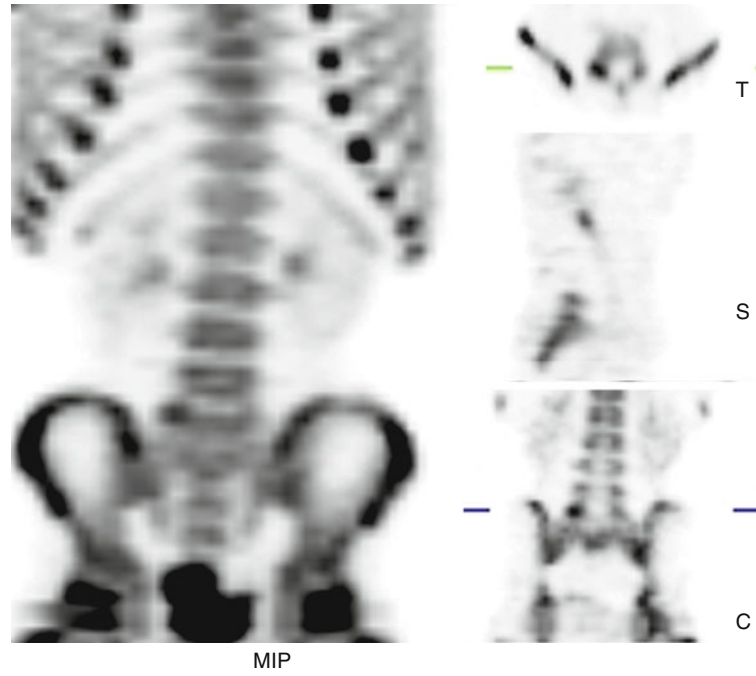

Fig. 15.22 SPECT with ^{99m}Tc-MDP. A 6-year-old male with mild levoscoliosis of the thoracolumbar spine and back pain. Radiographs at the times of the SPECT were unremarkable. SPECT shows focal intense tracer uptake in the posterior elements of the right L5. Later x-rays demonstrated grade I anterolisthesis of L5 on S1

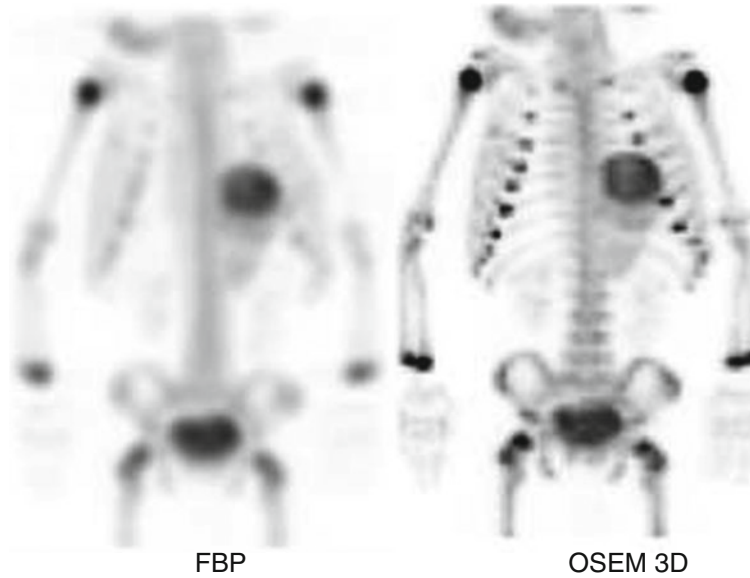

Fig. 15.23 Technetium-99m-MDP SPECT in neuroblastoma. OSEM-3D. Multiple-intensity projections (MIP) of a ^{99m}Tc-MDP SPECT from an 11-month-old boy with a right suprarenal mass later found to represent a neuroblastoma. On the left of the image is a conventional FBP reconstruction. The right image from the same acquisition was processed with OSEM-3D showing improvement in image quality

maximization iterative reconstruction with isotropic 3D resolution recovery (OSEM-3D) can significantly improve SPECT image resolution. At the same time, this method allows for a reduction of radiopharmaceutical administered dose and therefore patient radiation dose (Fig. 15.23). In addition, OSEM-3D allows for significant shorter image acquisition times, thus improving patient comfort and reducing patient motion as well. Depending on the patient's clinical need, it is possible to achieve a combination of gains in terms of improved resolution as well as in dose

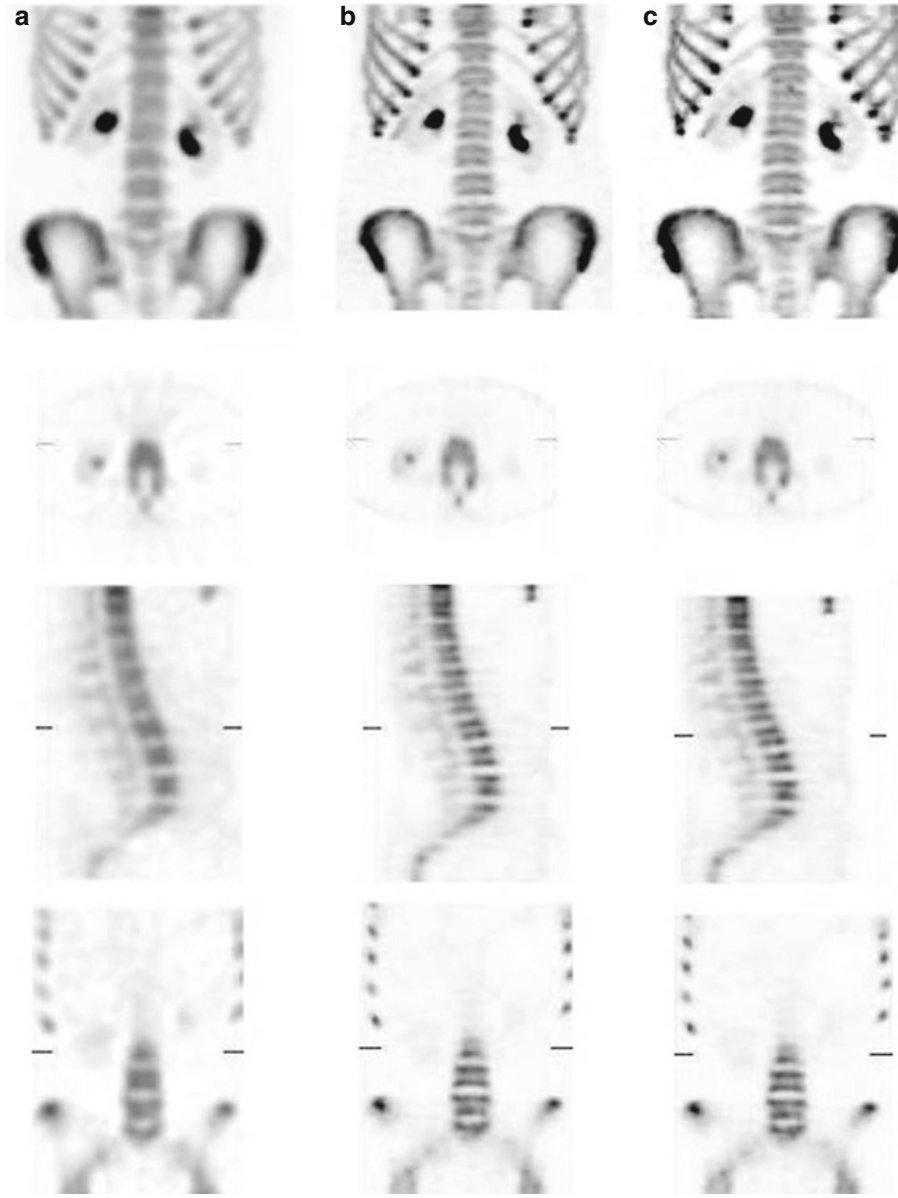

Fig. 15.24 Normal spine SPECT study reconstructed three different ways: (**a**) two-detector FBP at full tracer dose; (**b**) two-detector FBP reconstructed with OSEM-3D, also at the full tracer dose showing resolution improvement; and (**c**) one-detector FBP which corresponds to half the counts reconstructed with OSEM-3D. Observe that there is no significant difference between full dose and half dose with OSEM-3D. *Top row*: volume rendered images. *Second row*: transaxial images. *Third row*: sagittal images. Bottom row: coronal images (From Stansfield et al. [17], with permission)

reduction and scanning speed [16–18]. We have evaluated the use of OSEM-3D (Flash 3D, Siemens Medical Solutions) in patients undergoing ^{99m}Tc-MDP SPECT of the spine and found the results with OSEM-3D quite impressive compared to conventional SPECT reconstruction using filtered back projection (FBP) (Fig. 15.24).

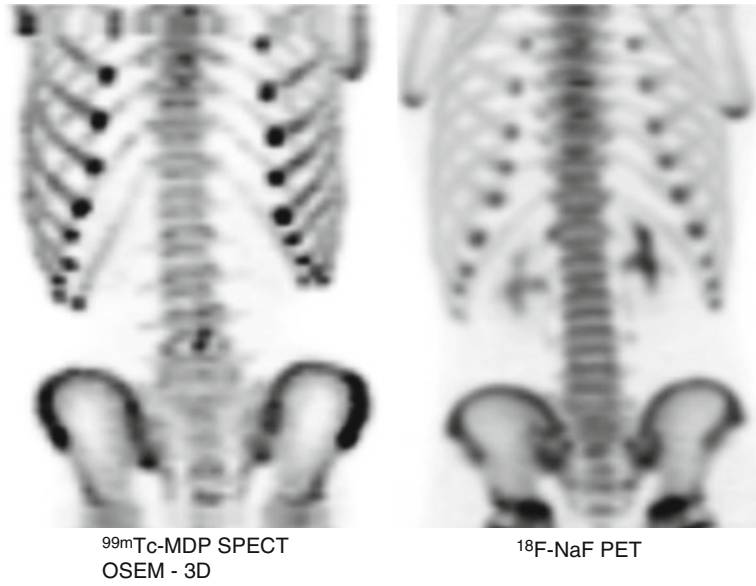

Fig. 15.25 Comparison of ^{99m}Tc-MDP SPECT reconstructed with OSEM-3D with resolution recovery (*left*) with ^{18}F-NaF PET (*right*) in two age-matched patients. The images appear very similar in terms of quality and spatial resolution

Fluorine-18 Sodium Fluoride PET

Characteristics of skeletal ^{18}F-NaF PET include the ability to obtain the images 0.5–1.0 h after the tracer administration, rather than the 15–30 min with ^{99m}Tc-MDP. Results can be available rapidly to be communicated to the referring physician. Patient schedule is more convenient, as the total time commitment for the patient is much less than with ^{99m}Tc-MDP SPECT. Also, the spatial resolution of PET is relatively high. However, total scanning time may be the same or, depending on the PET scanner and the volume imaged, longer than with SPECT. Tracer availability with ^{18}F-NaF is rather limited, while MDP is readily available at any time. With PET it is not easy to obtain a three-phase study as with single-photon studies. An equivalent to pinhole magnification is not available with ^{18}F-NaF PET. Also, one should consider advanced image processing of ^{99m}Tc-MDP SPECT such as OSEM-3D as a viable alternative (Fig. 15.25).

For ^{18}F-NaF PET, no patient preparation is required. However, if possible, the patient should be well hydrated before the injection in order to promote urinary elimination of the tracer for imaging. The patient is injected with ^{18}F-NaF intravenously. It is possible to obtain adequate skeletal PET following oral administration of ^{18}F-NaF. However, the time for imaging for the oral route should be approximately one hour after administration to allow for a slower oral absorption compared to the intravenous route. Also, it is important to note that some of the tracer may remain in the GI tract at the time of imaging. Oral administration should be considered in children that do not have easy intravenous access or when the region to be imaged is outside the abdomen. Imaging can begin at 15–30 min following intravenous tracer injection. If possible, the patient is instructed to void just before imaging. In some patients, it is necessary to use sedation for PET imaging. Our studies are acquired in 3D mode. The field of imaging depends on the clinical indication. For back pain, we image the lower thoracic, lumbar, and pelvic region, but this can be extended as needed according to the patient's symptoms. In oncology patients, imaging is from head to toes. For the assessment of non-accidental trauma, imaging is also from head to toes. Assessment of the pelvic region can be compromised if the bladder is full of tracer. In these cases, the patient should be asked to void if possible and a repeat image should be obtained. In certain cases, it may be necessary to place a bladder catheter to clear the bladder of activity before reimaging.

The skeletal PET scan is viewed as rotating MIP images and by evaluating slices in three dimensions. If the scanner has no CT, in some cases, it is useful to fuse the PET image with a preexisting CT to aid in lesion localization. In our experience, this is not frequently needed. Of course, if a PET/CT instrument is used, anatomic localization of lesions is readily available in all cases. As in the case of skeletal imaging with ^{99m}Tc-MDP, most lesions will reveal increased tracer uptake regionally or locally, depending on the diagnosis. Certain lesions such as vascular tamponade, aseptic necrosis, and infarcts may appear devoid of activity.

PET images show relatively high resolution compared to conventional SPECT reconstructed with filtered back projection (FBP). However, as mentioned earlier, recent application of iterative reconstruction with 3D resolution recovery has proven to improve skeletal SPECT at spatial resolutions closer to that of PET and with lower radiation exposure to the patient.

References

1. Tilden RL, Jackson Jr J, Enneking WF, DeLand FH, McVey JT. 99m Tc-polyphosphate: histological localization in human femurs by autoradiography. J Nucl Med. 1973;14(8):576–8.
2. Subramanian G, McAfee JG, Bell EG, Blair RJ, O'Mara RE, Ralston PH. 99m Tc-labeled polyphosphate as a skeletal imaging agent. Radiology. 1972; 102(3):701–4.
3. Subramanian G, McAfee JG, Blair RJ, Kallfelz FA, Thomas FD. Technetium-99m-methylene diphosphonate–a superior agent for skeletal imaging: comparison with other technetium complexes. J Nucl Med. 1975;16(8):744–55.
4. Gelfand MJ, Parisi MT, Treves ST. Pediatric radiopharmaceutical administered doses: 2010 North American consensus guidelines. J Nucl Med. 2011;52(2):318–22.
5. Blau M, Nagler W, Bender MA. Fluorine-18: a new isotope for bone scanning. J Nucl Med. 1962;3:332–4.
6. Grant FD, Fahey FH, Packard AB, Davis RT, Alavi A, Treves ST. Skeletal PET with 18F-fluoride: applying new technology to an old tracer. J Nucl Med. 2008; 49(1):68–78.
7. Grant FD, Drubach LA, Treves ST. 18F-Fluorodeoxyglucose PET and PET/CT in pediatric musculoskeletal malignancies. PET Clin. 2010;5(3):349–61.
8. Grant FD, Laffin SP, Davis RT, Drubach LA, Fahey FH, Treves ST. Skeletal PET with F-18 sodium fluoride as an alternative to Tc-99m bone SPECT in children. Pediatr Radiol. 2010;40(4):538.
9. Rosenfield N, Treves S. Osseous and extraosseous uptake of fluorine-18 and technetium-99m polyphosphate in children with neuroblastoma. Radiology. 1974;111(1):127–33.
10. Alazraki N, Dries D, Datz F, Lawrence P, Greenberg E, Taylor Jr A. Value of a 24-hour image (four-phase bone scan) in assessing osteomyelitis in patients with peripheral vascular disease. J Nucl Med. 1985;26(7): 711–7.
11. Mawlawi O, Yahil A, Vija H, Erwin W, Macapinlac H. Reduction in scan duration or injected dose in planar bone scintigraphy enabled by Pixon(R) postprocessing. Soc Nucl Med Annu Meet Abstr. 2007;48(Meeting Abstracts 2):13P-b.
12. Roach PJ, Connolly LP, Zurakowski D, Treves ST. Osteoid osteoma: comparative utility of high-resolution planar and pinhole magnification scintigraphy. Pediatr Radiol. 1996;26(3):222–5.
13. Taylor GA, Shea N, O'Brien T, Hall JE, Treves ST. Osteoid osteoma: localization by intraoperative magnification scintigraphy. Pediatr Radiol. 1986;16(4): 313–6.
14. Blaskiewicz DJ, Sure DR, Hedequist DJ, Emans JB, Grant F, Proctor MR. Osteoid osteomas: intraoperative bone scan-assisted resection. Clinical article. J Neurosurg Pediatr. 2009;4(3):237–44.
15. Sokol L, Zurakowski D, D'Hemecourt P, Micheli L, Treves ST. Back pain in children less than 10 years of age: high incidence of abnormalities detected on skeletal single photon emission computed tomography (SPECT). Pediatr Radiol. 2010;40(4):539.
16. Sheehy N, Tetrault TA, Zurakowski D, Vija AH, Fahey FH, Treves ST. Pediatric 99mTc-DMSA SPECT performed by using iterative reconstruction with isotropic resolution recovery: improved image quality and reduced radiopharmaceutical activity. Radiology. 2009;251(2):511–6.
17. Stansfield EC, Sheehy N, Zurakowski D, Vija AH, Fahey FH, Treves ST. Pediatric 99mTc-MDP bone SPECT with ordered subset expectation maximization iterative reconstruction with isotropic 3D resolution recovery. Radiology. 2010;257(3):793–801.
18. Vija AH, Hawman EG, Engdahl JC. Analysis of a SPECT OSEM reconstruction method with 3D beam modeling and optional attenuation correction: phantom studies. Paper presented at Nuclear Science Symposium Conference Record, IEEE; 19–25 Oct 2003.

Sports Injuries

16

Katherine A. Zukotynski

Sports injuries are commonly encountered in pediatric patients. It is estimated that over four million sports or recreational injuries occur in children and young adults each year in the United States [1]. These include elbow, shoulder, and hip disorders, back pain, and concussions, among others. In fact, it has been suggested that children are more susceptible to injury than adults due to their decreased coordination, open physes, and growing cartilage [2]. Recent results in the literature report that elbow pain is seen in 50–70 % of adolescent baseball players yearly, possibly due to skeletal immaturity and poor pitching mechanics [3, 4]. Further, children are often involved in several athletic activities as well as repetitive types of activity. It has been suggested that fatigue or stress-related injuries may be more common in 6–18-year-old children than acute injuries [5]. Proper technique, core strengthening, neuromuscular conditioning, and appropriate time for rest can be helpful protective measures [6]. For example, warm-up and sport-specific agility exercises are being developed to decrease the incidence of knee injuries, particularly in young female athletes [7, 8]. It has been recommended that at least 2 h of recovery occur between moderate to vigorous intensity training sessions and that the importance of rest be emphasized [5]. Although these are important preventative measures aimed at decreasing the risk of sports-related injury in pediatric patients, early and accurate diagnosis of injury is key to ensure appropriate therapy. Imaging with nuclear medicine techniques plays a central role in the diagnosis of sports-related injury in this patient population.

There is a wide spectrum of sports-related injuries in pediatric patients, and as a result, there are several anatomic and nuclear medicine-based imaging modalities that can be used for diagnosis. In our experience, the most common reason for referral to the division of nuclear medicine is to evaluate suspected skeletal injury with skeletal scintigraphy or positron emission tomography (PET). The remainder of this chapter will discuss technetium-99m-labeled methylene diphosphonate (^{99m}Tc-MDP) skeletal scintigraphy and Fluorine-18 sodium fluoride (^{18}F-NaF) PET in pediatric athletes.

K.A. Zukotynski, MD
Department of Medical Imaging,
Sunnybrook Health Sciences Centre,
University of Toronto, Toronto, ON, Canada

Joint Program in Nuclear Medicine,
Department of Radiology, Harvard Medical School,
Boston, MA, USA

Department of Radiology,
Brigham and Women's Hospital,
Boston, MA, USA
e-mail: katherine.zukotynski@utoronto.ca,
kzukotynski@partners.org

S.T. Treves (ed.), *Pediatric Nuclear Medicine and Molecular Imaging*,
DOI 10.1007/978-1-4614-9551-2_16,

Patient Preparation, Imaging Techniques, and Radiopharmaceuticals

There is no standard patient preparation required for ^{99m}Tc-MDP skeletal scintigraphy or ^{18}F-NaF PET. Unless contraindicated, children should be hydrated prior to the study, should void prior to imaging, and should drink plenty of fluid for at least 24 h after radiopharmaceutical administration. For ^{99m}Tc-MDP skeletal scintigraphy, the North American consensus guidelines recommend 9.3 MBq/kg ^{99m}Tc-MDP (minimum, 37 MBq) or 250 μCi/kg (minimum, 1 mCi) be administered intravenously immediately prior to image acquisition [9]. For a three-phase ^{99m}Tc-MDP skeletal scintigraphy study, angiographic (flow phase) images are acquired over the region of interest for 2 min at a frame rate of 2 s per frame following the radiopharmaceutical administration. Once these images have been obtained, tissue phase images are acquired for an additional 2 min. Skeletal phase images are obtained 3–4 h after radiotracer injection. Pinhole or converging collimators can be used to obtain magnification and are suggested for imaging small parts such as the hips or wrists. For ^{18}F-NaF PET, the North American consensus guidelines recommend 2.22 MBq/kg ^{18}F-NaF (minimum, 18.5 MBq) or 60 μCi/kg (minimum, 500 μCi) be administered intravenously [9]. Images are typically acquired approximately 30 min after radiopharmaceutical injection. For further protocol details please refer to Chap. 15 and to the Society of Nuclear Medicine and Molecular Imaging [10].

Clinical Applications

Pediatric athletes with sports injury often have radiographs at the time of initial evaluation. These are easily accessible and inexpensive and can provide rapid feedback to the physician. Depending on the clinical presentation and radiographic findings, additional imaging may be warranted.

Technetium-99m-MDP skeletal scintigraphy has several advantages for the evaluation of pediatric athletes with suspected osseous injury. Technetium-99m-MDP skeletal scintigraphy is sensitive for the detection of osseous injury and can demonstrate acute injury prior to the development of radiographic abnormalities [11, 12]. Although the optimal time for imaging has not been determined, the majority of fractures are identified within 72 h of symptom onset in pediatric patients. Further, ^{99m}Tc-MDP skeletal scintigraphy can provide whole-body images, even in very young patients, without the need for sedation. A small amount of ionizing radiation is needed to generate the images; however, this is less than would be needed for whole-body computed tomography (CT) [13]. Since pediatric athletes can have multifocal injuries including clinically occult abnormalities, ^{99m}Tc-MDP skeletal scintigraphy is often helpful to assess for additional sites of injury (Fig. 16.1). The main disadvantage of ^{99m}Tc-MDP skeletal scintigraphy is its low specificity [14]. This can be improved by correlating scintigraphic abnormalities with clinical findings, use of pinhole images for magnification, and/or the addition of single photon emission computed tomography (SPECT) to increase abnormality localization. Furthermore, the advent of hybrid imaging including SPECT/CT has improved study resolution and accuracy.

Fluorine-18-NaF PET is an alternative to ^{99m}Tc-MDP scintigraphy for skeletal imaging in pediatric athletes with suspected skeletal injury (Fig. 16.2). Fluorine-18-NaF is a sensitive bone-seeking PET tracer that can be used to produce images with improved spatial resolution and accuracy compared with ^{99m}Tc-MDP skeletal scintigraphy. Multiplanar images are automatically generated and provide accurate localization of abnormalities. Further, ^{18}F-NaF PET requires less time than ^{99m}Tc-MDP skeletal scintigraphy [15, 16]. In the past, $^{18F\text{-}NaF}$ PET has been difficult to obtain because of limited access to equipment and expense. However, in the current era of expanding access to PET technology and the tenuous availability of ^{99m}Tc, there has been a growing interest in ^{18}F-NaF PET.

Based on the clinical indication and availability of equipment, either a ^{99m}Tc-MDP skeletal scintigraphy study or ^{18}F-NaF PET is acquired.

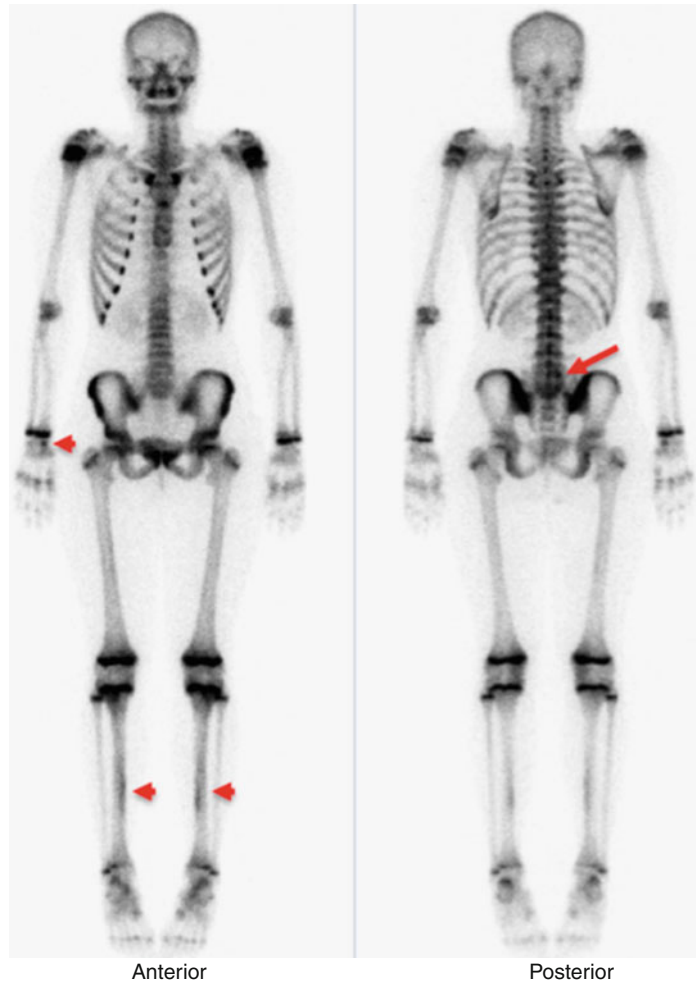

Fig. 16.1 A 14-year-old female soccer and lacrosse player with lower back pain: whole-body skeletal scintigraphy shows focal radiotracer uptake consistent with right L5 pars stress (*red arrow*), linear uptake in both tibiae consistent with stress changes (*red arrowheads*), and uptake in the right distal radius (*red arrowhead*), likely at an additional site of stress (From Zukotynski et al. [30], with permission)

Fig. 16.2 ^{18}F-NaF skeletal PET in children with sports injuries: (**a**) an 11-year-old female soccer player with back pain and bilateral L5 pars interarticularis stress; (**b**) a 17-year-old runner with multifocal osseous stress/fractures of both lower extremities (From Zukotynski et al. [30], with permission)

Typical indications for multiphase ^{99m}Tc-MDP skeletal scintigraphy in pediatric athletes include complex regional pain syndrome or a suspected osteoid osteoma, among others. Skeletal phase images may be sufficient in certain cases of traumatic injury or for follow-up of a known abnormality. SPECT is often performed in addition to planar imaging in pediatric patients with back pain in order to increase the sensitivity of ^{99m}Tc-MDP skeletal scintigraphy and allow localization of abnormalities. To date, the literature comparing the effectiveness of ^{18}F-NaF PET with ^{99m}Tc-MDP scintigraphy in pediatric athletes is limited. However, ^{18}F-NaF PET is becoming increasingly important in the evaluation of sports injury and is preferred when high spatial resolution and accuracy is needed, often in cases of pediatric athletes with back pain or traumatic injury.

The main advantage of ^{99m}Tc-MDP skeletal scintigraphy and ^{18}F-NaF PET compared with CT is the ability to obtain whole-body images with low radiation exposure. Technetium-99m-MDP skeletal scintigraphy and ^{18}F-NaF PET are recommended for pediatric athletes who are suspected to have widespread or multifocal injuries. Since CT provides excellent characterization of osseous structure and anatomy, targeted CT can be helpful to evaluate the site of abnormality once this has been identified. The main advantage of ^{99m}Tc-MDP skeletal scintigraphy and^{18}F-NaF PET compared with magnetic resonance imaging (MRI) is the ability to obtain whole-body images, even in very young children, without the need for sedation. Since MRI provides excellent soft tissue and marrow characterization, MRI can be helpful to evaluate the site of abnormality. Ultimately, the choice of imaging modality depends on the clinical indication. In the era of multimodality and hybrid imaging, this question can be a difficult one to answer and depends closely on the clinical findings.

Interpretation of pediatric ^{99m}Tc-MDP skeletal scintigraphy and ^{18}F-NaF PET is challenging because of differences in uptake related to the skeletal immaturity. There is absent uptake in non-ossified structures and high uptake in the physes and apophyses. Thus, knowledge of the ossification pattern in children and young adults is needed. The following sections illustrate specific pathology encountered in pediatric athletes on ^{99m}Tc-MDP skeletal scintigraphy and ^{18}F-NaF PET. Although we will focus our attention on ^{99m}Tc-MDP skeletal scintigraphy since this is more commonly used in routine clinical practice, the radiotracer uptake and distribution as well as the spectrum of abnormalities is similar on ^{18}F-NaF PET.

Hybrid Imaging

Hybrid imaging including the co-registration of CT with SPECT and ^{18}F-NaF PET/CT is becoming increasingly ubiquitous. Preliminary assessments suggest the addition of anatomic imaging leads to improved diagnostic accuracy compared with functional imaging alone [17]. Although, the financial and radiation exposure cost of hybrid imaging remains to be fully evaluated, this powerful new tool will likely play a central role in our approach to imaging pediatric athletes over the next few years.

Osseous Stress, Deformity, and Fractures of the Upper and Lower Extremities

One of the most common reasons for sports-related injury in pediatric athletes is stress related to overtraining or overuse [6]. This typically affects the lower extremities (Fig. 16.3) as a result of an increase in activity or repetitive exertion without sufficient rest [18]. Radiographs are often the first imaging study obtained. Although inexpensive and accessible, stress fractures and osteochondral injuries can be radiographically occult at clinical presentation [11, 19]. Either MRI or ^{99m}Tc-MDP skeletal scintigraphy can be used to detect acute fractures. There are mixed results in the literature concerning the utility of MRI and ^{99m}Tc-MDP skeletal scintigraphy for evaluating stress fractures in athletes. Several reports suggest equivalence of MRI and ^{99m}Tc-MDP skeletal scintigraphy for early detection of stress fractures and sports injury [20–22].

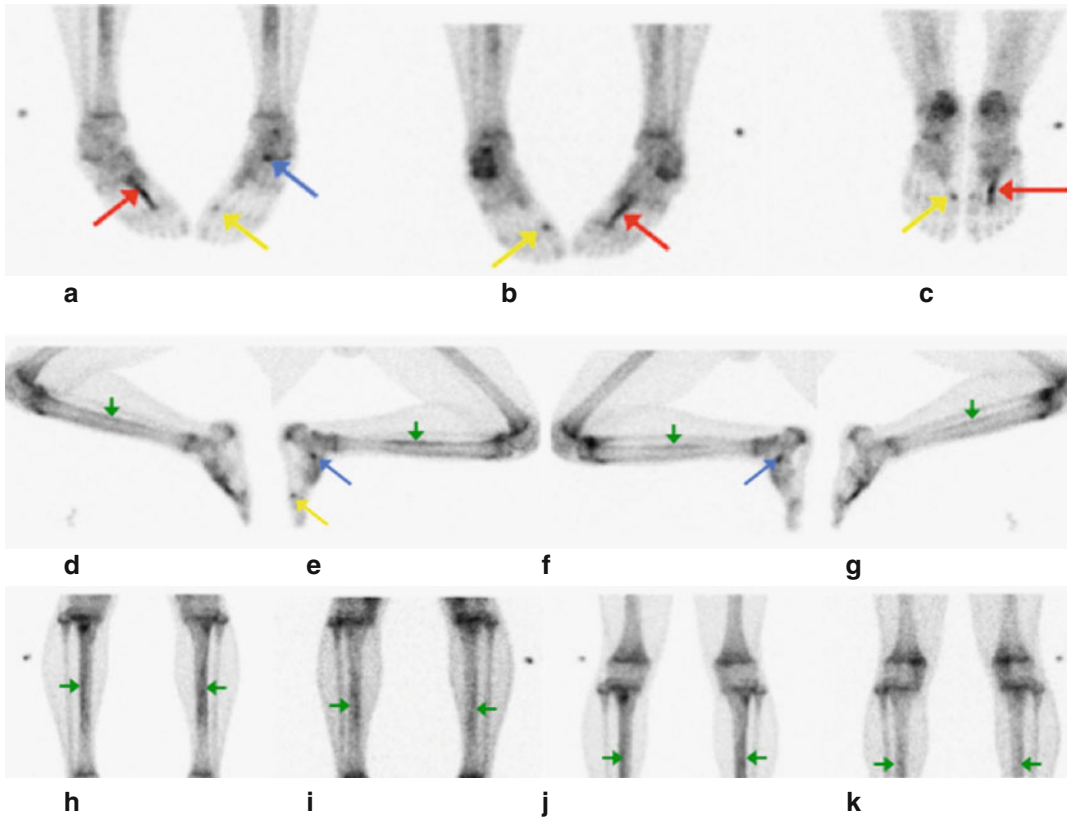

Fig. 16.3 A 16-year-old male runner with bilateral leg and foot pain referred for further evaluation with skeletal scintigraphy. Images of the feet in anterior (**a**), posterior (**b**), and plantar (**c**) projections and lower extremities in right medial (**d**), left medial (**e**), left lateral (**f**), right lateral (**g**), anterior (**h**, **j**), and posterior (**i**, **k**) projections show multiple sites of increased radiotracer uptake consistent with osseous stress and fractures. For example, intense elongated radiotracer uptake throughout the right second metatarsal bone (*red arrow*) and intense focal radiotracer uptake in the region of the left navicular bone (*blue arrow*) are concerning for stress fractures. Mild focal radiotracer uptake in the region of the sesamoid bones of the left foot (*yellow arrow*) and at the base of the left first metatarsal is likely due to bone stress. Mild diffusely increased radiotracer uptake in both tibiae is also likely due to stress (*green arrows*)

Although MRI can identify specific anatomic information such as in pathology of the knee and ankle joints, ^{99m}Tc-MDP skeletal scintigraphy has high sensitivity and can provide whole-body images. Recently, Dobrindt et al. reported that ^{99m}Tc-MDP skeletal scintigraphy was slightly more sensitive and had a higher negative predictive value compared with MRI in 28 athletes, while MRI was slightly more specific for the diagnosis of stress injury [23]. CT can be helpful for detailed characterization of osseous abnormalities, when clinically warranted.

Technetium-99m-MDP skeletal scintigraphy shows increased perfusion from inflammation and increased uptake at sites of bone turnover due to stress. Blood pool images can be helpful to demonstrate soft tissue injury and tendonitis [24]. Examples of soft tissue causes of ankle pain that are associated with radiotracer uptake include, among others, retrocalcaneal bursitis, apophysitis of the calcaneum, and calcaneal stress fracture [24]. The Achilles tendon and tibialis posterior tendon are two of the more commonly injured tendons, often in gymnasts and ballet dancers. Osseous stress at muscle insertion sites is also common. Avulsion fractures are seen in pediatric athletes, often as a result of violent contraction of a large muscle attached to bone. In pediatric

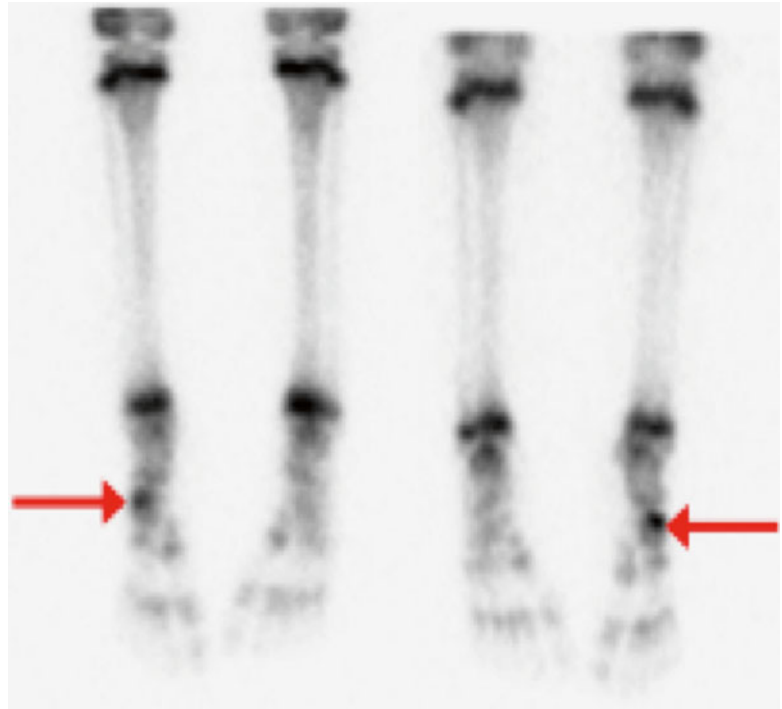

Fig. 16.4 A 3-year-old male with right limp following a fall from his parents' bed. Anterior (*left*) and posterior (*right*) images of both feet show increased bone turnover in the lateral aspect of the right mid-foot (*red arrow*) concerning for a cuboid bone fracture

athletes, stress involving the growth plate is particularly important since the physis is the weakest portion of the immature skeleton and injury to the germinal zone can lead to growth arrest. Stress in an apophysis can result in asymmetric radiotracer uptake, increased at the site of stress. Attention should be paid to the medial epicondyle (little leaguer's elbow), olecranon, coracoid, acromion, vertebrae, and pelvis, since these are among the most commonly affected apophyses. Ultimately, osseous stress can result in fracture and fragmentation.

Fractures are typically identified as sites of focal intense radiotracer uptake on ^{99m}Tc-MDP skeletal scintigraphy (Fig. 16.4). For example, in the metatarsal bones, uptake due to stress fractures can be either fusiform and vertically oriented along the metatarsal shaft (Fig. 16.3) or well defined, focal (Fig. 16.5), and/or linear and transversely oriented to the metatarsal shaft [11]. Tibial stress fractures are identified by focal or fusiform uptake involving the tibial cortex and extending transverse to the tibial shaft (Fig. 16.6). The posterior upper third of the tibial shaft is most commonly affected. By comparison, shin splints demonstrate increased uptake extending along the posterior tibial surface without significant associated focal or fusiform uptake (Fig. 16.7). Lateral blood pool imaging can provide additional insight into vascular abnormalities in athletes with suspected stress fractures of the tibia [25].

Healed fractures do not demonstrate abnormal radiotracer uptake unless associated with persistent osseous stress, although abnormalities may persist for up to 1 year. Fracture complications such as vascular compromise, osteomyelitis, hardware failure, or nonunion can demonstrate abnormal radiotracer uptake for many years.

Back Pain

Back pain in pediatric athletes is often associated with stress in the region of the pars interarticularis commonly at the level of the L5 vertebral body [26, 27]. If untreated, this stress can lead to spondylolysis, a non-displaced fracture of the

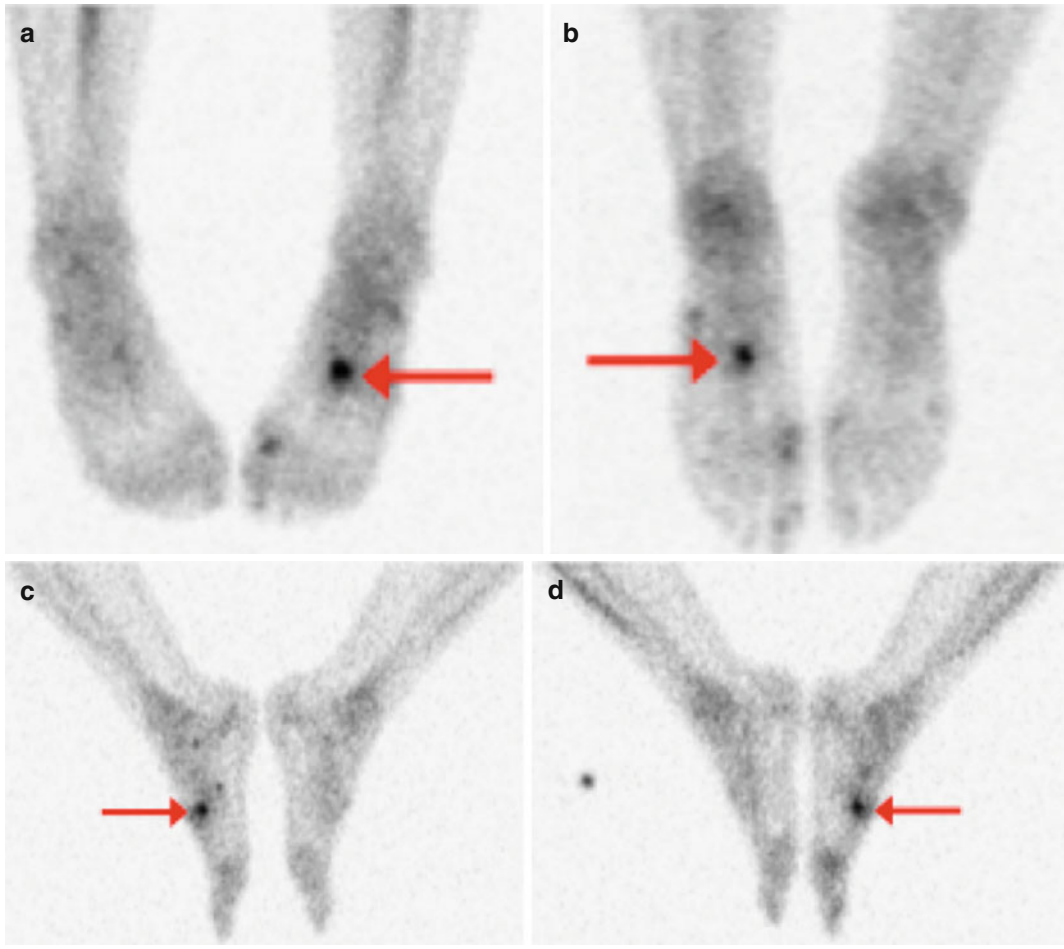

Fig. 16.5 A 23-year-old female who is a nationally competing Irish step-dancer presented with left foot pain for further evaluation. Anterior (**a**), posterior (**b**), lateral (**c**), and medial (**d**) images of both feet show focal intense radiotracer uptake at the base of the second metatarsal (*orange arrow*) concerning for a stress fracture. Elsewhere in the foot mild multifocal increased radiotracer uptake is likely due to skeletal stress

pars interarticularis, and spondylolisthesis, slippage of one vertebral body upon another.

On imaging, there is a spectrum of abnormalities associated with stress, spondylolysis, and spondylolisthesis. Spine radiographs have limited sensitivity in detecting bone stress, although they can show spondylolysis, spondylolisthesis, and chronic abnormalities of the pars interarticularis. Further, when radiographic abnormalities are detected, these may not be symptomatic. Technetium-99m-MDP skeletal scintigraphy detects stress in the region of the pars interarticularis because stress leads to bone turnover and increased uptake. Results in the literature suggest that uptake in the region of the pars interarticularis on ^{99m}Tc-MDP skeletal scintigraphy is associated with pain [28]. SPECT is often performed in addition to planar skeletal scintigraphy in pediatric athletes with back pain because SPECT increases contrast and sensitivity (Fig. 16.8). SPECT also improves anatomic localization of skeletal lesions and provides an opportunity for better correlation with anatomic imaging without exposing the patient to additional radiation. Abnormalities on ^{99m}Tc-MDP skeletal scintigraphy may be the earliest finding in athletes with back pain. CT shows detailed bone morphology and, although less sensitive than ^{99m}Tc-MDP

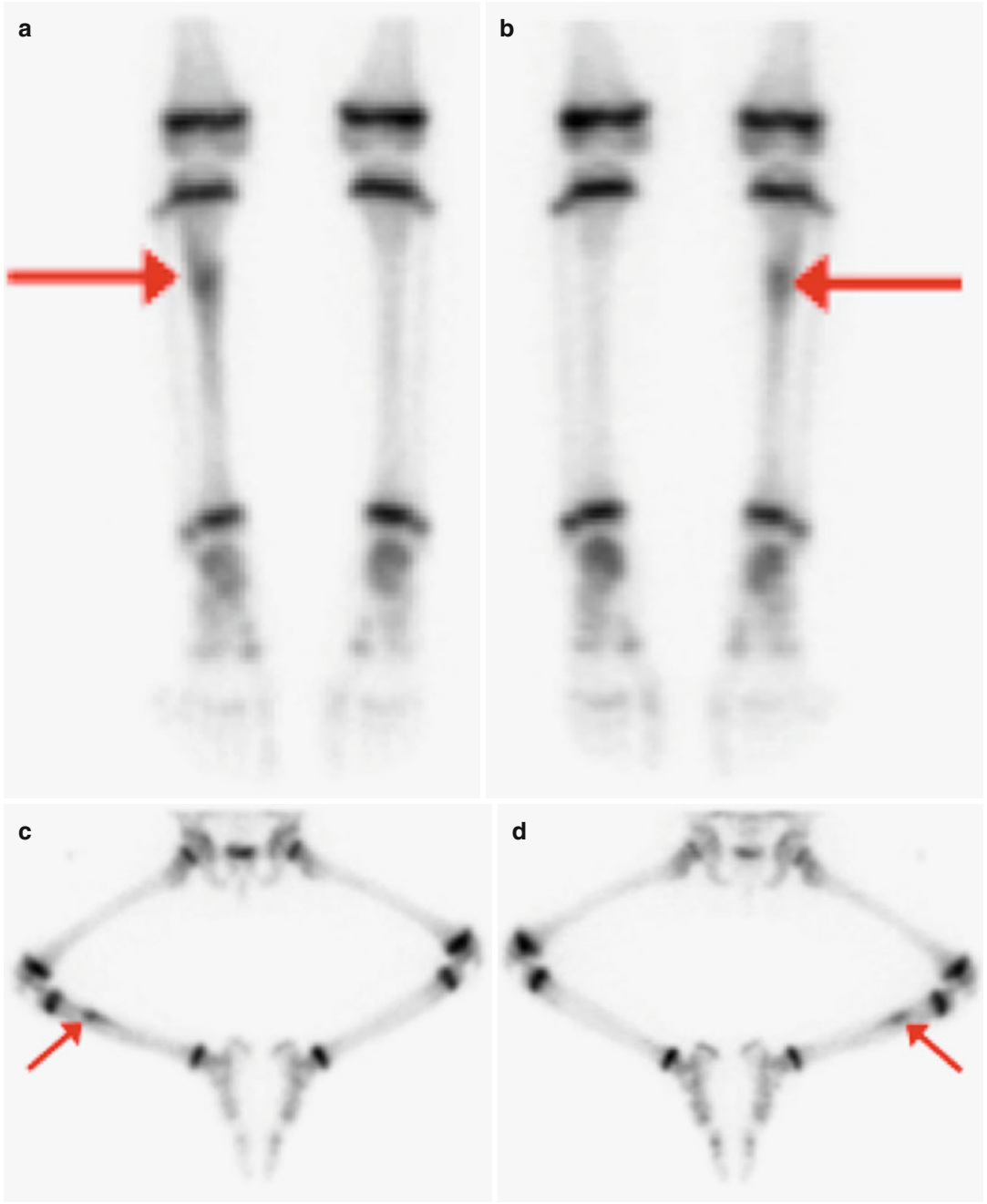

Fig. 16.6 A 3-year-old girl with limp and pain after falling from monkey bars. Intense focal radiotracer uptake in the posterior proximal diaphysis of the right tibia on anterior (**a**), posterior (**b**), medial (**c**), and lateral (**d**) images (*orange arrow*) likely represents a stress fracture

skeletal scintigraphy for the detection of stress, provides more specific abnormality characterization. CT findings may suggest the probability of bone healing. However, CT of the spine has higher radiation exposure than whole-body ^{99m}Tc-MDP skeletal scintigraphy. MRI does not require exposure to ionizing radiation and is excellent in identifying soft tissue and marrow pathology including

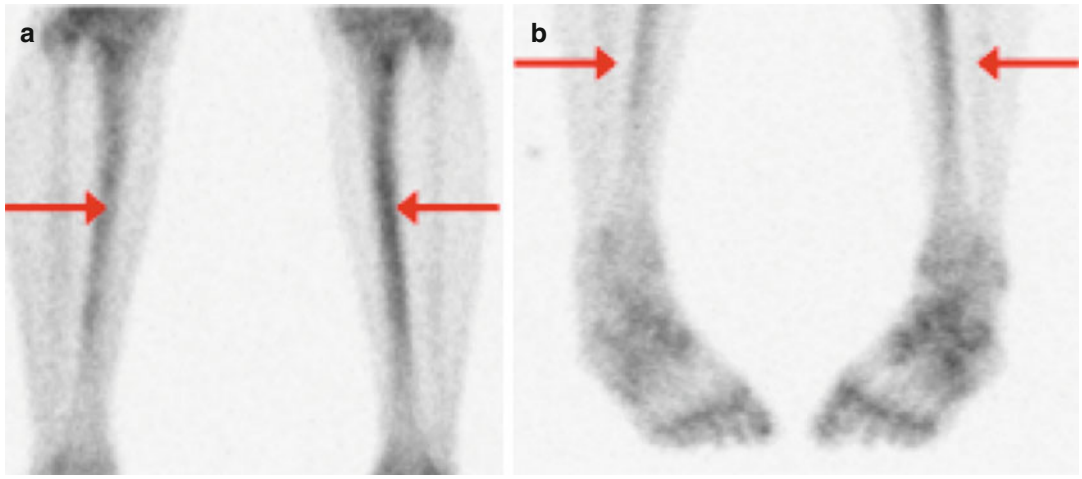

Fig. 16.7 An 18-year-old male runner with bilateral leg pain. Anterior images of both lower extremities (**a**, **b**) show diffuse moderately intense increased radiotracer uptake throughout both tibiae (*orange arrows*) consistent with bilateral tibial stress syndrome. No abnormal focal uptake is identified in either tibia to suggest a fracture

bone edema. However, MRI is not as sensitive as skeletal scintigraphy with SPECT for pars interarticularis stress and does not delineate osseous detail to the same extent as CT.

In the current era of multimodality imaging, both anatomic imaging and functional imaging play an important role in the assessment of athletes with back pain. The most appropriate imaging to perform in cases of suspected pars interarticularis injury remains controversial. Radiographs are often the initial study performed. Technetium-99m-MDP skeletal scintigraphy with SPECT is frequently the next study done in pediatric athletes with back pain from suspected injury of the pars interarticularis. Following this, CT through the area of abnormality can characterize the osseous lesion. Alternatively, MRI can be used to identify the cause of back pain [29].

Complex Regional Pain Syndrome

Complex regional pain syndrome otherwise known as reflex sympathetic dystrophy or algodystrophy is characterized by pain, swelling, skin changes, and limited range of motion. Symptoms typically develop following a traumatic injury and treatment consists of supportive care and/or the use of sympatholytic agents.

Multiphase ^{99m}Tc-MDP skeletal scintigraphy can suggest a diagnosis of complex regional pain syndrome. In adults, imaging findings typically include increased perfusion to the effected extremity on angiographic images and increased periarticular activity in the effected extremity on skeletal phase images. In children, imaging findings typically include decreased perfusion to the effected extremity on angiographic images and decreased periarticular activity in the effected extremity on skeletal images (Fig. 16.9).

Other Causes of Pain in Pediatric Athletes

There are several non-traumatic causes of pain in pediatric athletes such as arthropathy, inflammation, infection, and neoplastic disease that can be accentuated by participation in sports. For example, an osteoid osteoma is a benign osseous lesion that can be a cause for pain in pediatric athletes. Associated with a vascular nidus, an osteoid osteoma typically has significant adjacent reactive sclerosis. Commonly found in the lower extremities and spine, ^{99m}Tc-MDP skeletal scintigraphy

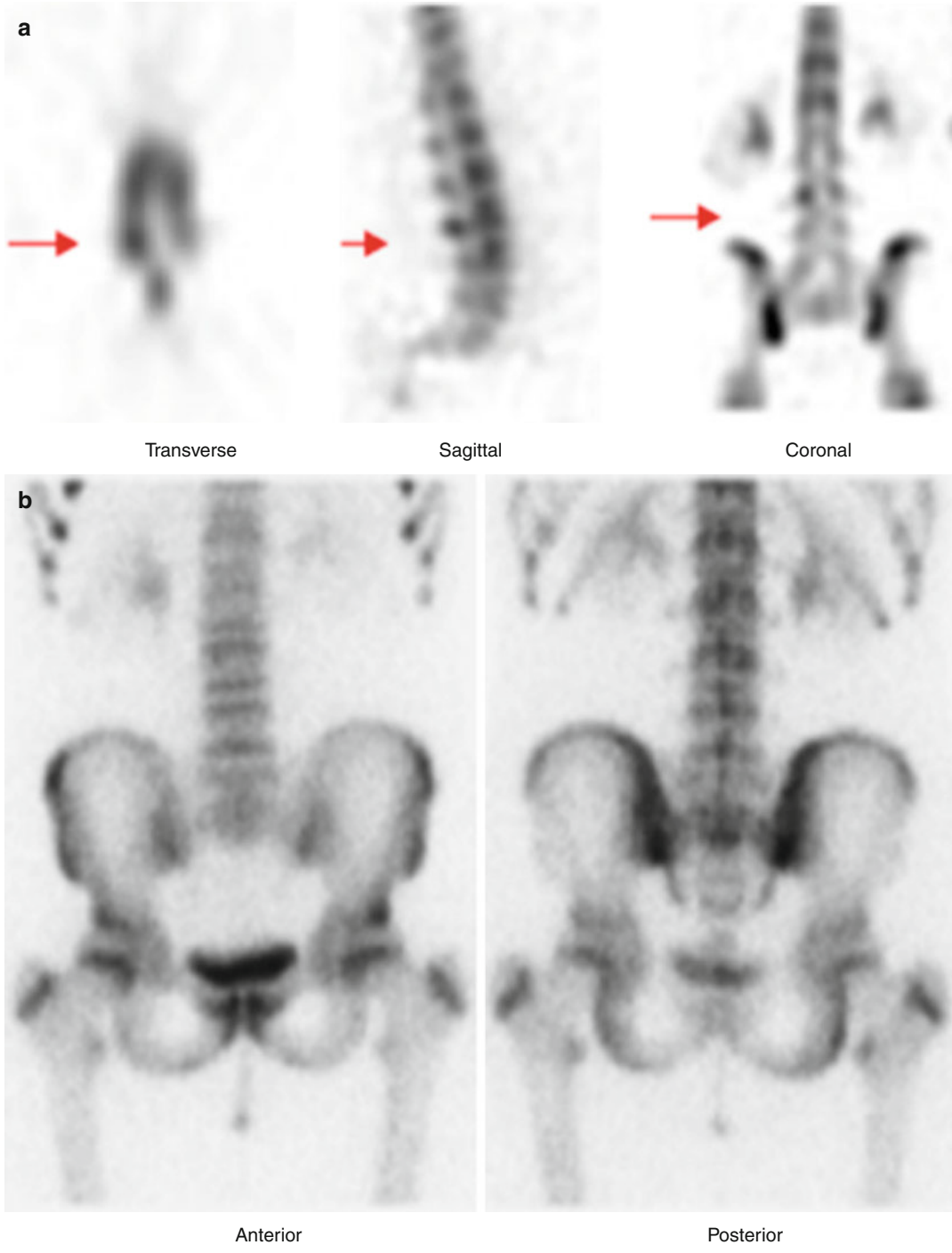

Fig. 16.8 A 15-year-old female figure skater with back pain; added value of SPECT in the detection of pars interarticularis stress: (**a**) SPECT demonstrates right pars interarticularis stress in vertebra L4 (*red arrow*), while no abnormality is detected on (**b**) planar skeletal scintigraphy (From Zukotynski et al. [30], with permission)

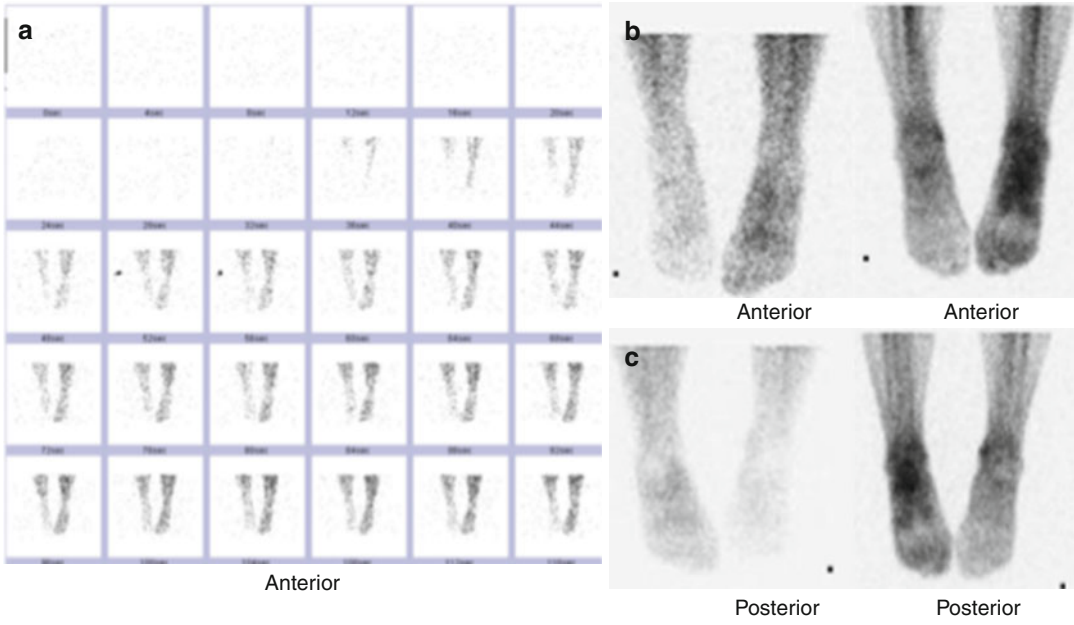

Fig. 16.9 A 15-year-old female involved in field hockey, basketball, and softball who developed complex regional pain syndrome after an ankle sprain. On skeletal scintigraphy: (**a**) angiographic images of the lower extremities show relative decreased perfusion to the right leg, (**b**) tissue phase images of the lower extremities show relative photopenia of the right leg, and (**c**) skeletal phase images of the lower extremities show relative photopenia of the right leg (From Zukotynski et al. [30], with permission)

is highly sensitive for the diagnosis. Images show increased uptake on angiographic, tissue phase, and skeletal phase images in the area of the osteoid osteoma. Pinhole images can aid in lesion detection and SPECT can improve localization. Intraoperative skeletal scintigraphy with pinhole collimation is useful to ensure complete surgical resection. Another cause of osseous pain in pediatric athletes is malignancy. For further details, please refer to Chap. 22.

Anatomic imaging, ^{99m}Tc-MDP skeletal scintigraphy, and ^{18}F-NaF PET provide complementary information in the evaluation of traumatic injury in pediatric athletes with malignancy. In particular, hybrid imaging combining ^{99m}Tc-MDP skeletal scintigraphy and CT is becoming an increasingly popular tool allowing anatomic localization of scintigraphic abnormalities.

Conclusion

Pediatric athletes with sports-related injury are often referred to the division of nuclear medicine for evaluation with ^{99m}Tc-MDP skeletal scintigraphy and ^{18}F-NaF PET. These imaging modalities may detect abnormalities prior to anatomic imaging and provide a practical tool for whole-body imaging without the need for sedation. However, study interpretation in children can be challenging and familiarity with imaging technique and interpretation can improve diagnosis. This chapter has reviewed imaging technique and findings commonly encountered in pediatric athletes with suspected skeletal injury.

References

1. Monroe KW, Thrash C, Sorrentino A. Most common sports-related injuries in a pediatric emergency department. Clin Pediatr. 2011;50:17–20.
2. Nettle H, Sprogis E. Pediatric exercise: truth and/or consequences. Sports Med Arthrosc. 2011;19:75–80.
3. Greiwe RM, Saifi C, Ahmad CS. Pediatric sports elbow injuries. Clin Sports Med. 2010;29:677–703.
4. Mariscalo MW, Saluan P. Upper extremity injuries in the adolescent athlete. Sports Med Arthrosc. 2011;19:17–26.

5. Luke A, Lazaro RM, Bergeron MF, et al. Sports-related injuries in youth athletes: is overscheduling a risk factor? Clin J Sport Med. 2011;21:307–14.
6. Franklin C, Weiss J. Stopping sports injuries in kids: an overview of the last year in publications. Curr Opin Pediatr. 2012;24:64–7.
7. Schul D, Saluan P. Anterior cruciate ligament injuries in the young athlete: evaluation and treatment. Sports Med Arthrosc. 2011;19:34–43.
8. Gilchrist J, Mandelbaum BR, Melancon H, et al. A randomized controlled trial to prevent noncontact anterior cruciate ligament injury in female collegiate soccer players. Am J Sports Med. 2008;36:1476–83.
9. Gelfand MJ, Parisi MT, Treves ST. Pediatric radiopharmaceutical administered doses: 2010 North American consensus guidelines. J Nucl Med. 2011;52:318–22.
10. Segall G, Delbeke D, Stabin M, et al. SNM practice guidelines for sodium 18F-fluoride PET/CT bone scans 1.0. J Nucl Med. 2010;51:1813–20.
11. Minoves M, Ponce A, Balius R, et al. Stress fracture of the first metatarsal in a fencer. Clin Nucl Med. 2011;36(10):e150–2.
12. Anderso IF, Crichton KJ, Grattan-Smith T, et al. Osteochondral fractures of the dome of the talus. J Bone Joint Surg. 1989;71-A:1143–52.
13. Fahey FH, Treves ST, Adelstein SJ. Minimizing and communicating radiation risk in pediatric nuclear medicine. J Nucl Med. 2011;52:1240–51.
14. Dobrindt O, Hoffmeyer B, Ruf J, et al. Blinded-read of bone scintigraphy: the impact on diagnosis and healing time for stress injuries with emphasis on the foot. Clin Nucl Med. 2011;36:186–91.
15. Lim R, Fahey FH, Drubach LA, et al. Early experience with 18F sodium fluoride bone PET in young patients with back pain. J Pediatr Orthop. 2007;27(3):277–82.
16. Grant FD, Fahey FH, Packard AB, et al. Skeletal PET with 18F-fluoride: applying new technology to an old tracer. J Nucl Med. 2008;49(1):68–78.
17. Schillaci O, Danieli R, Manni C, et al. Is SPECT/CT with a hybrid camera useful to improve scintigraphic imaging interpretation? Nucl Med Commun. 2004;25:705–10.
18. Patel D, Roth M, Kapil N. Stress fractures: diagnosis, treatment and prevention. Am Fam Physician. 2011;83(1):39–46.
19. Stroud CC, Marks RM. Imaging of osteochondral lesions of the talus. Foot Ankle Clin. 2000;5:119–33.
20. Brukner P, Bennell K. Stress fractures in female athletes. Diagnosis, management and rehabilitation. Sports Med. 1997;24:419–29.
21. Ishibashi Y, Okamura Y, Otsuka H, et al. Comparison of scintigraphy and magnetic resonance imaging for stress injuries of bone. Clin J Sport Med. 2002;12:79–84.
22. Ryan PJ, Reddy K, Fleetcroft J. A prospective comparison of clinical examination, MRI, bone SPECT, and arthroscopy to detect meniscal tears. Clin Nucl Med. 1998;23:803–6.
23. Dobrindt O, Hoffmeyer B, Ruf J, et al. MRI versus bone scintigraphy. Evaluation for diagnosis and grading of stress injuries. Nuklearmedizin. 2012;51(3):88–94.
24. Van der Wall H, Lee A, Magee M, et al. Radionuclide bone scintigraphy in sports injuries. Semin Nucl Med. 2010;40:16–30.
25. Mohan HK, Clarke SE, Centenara M, et al. Value of lateral blood pool imaging in patients with suspected stress fractures of the tibia. Clin Nucl Med. 2011;36(3):173–7.
26. Micheli LJ, Wood R. Back pain in young athletes: significant differences from adults in causes and patterns. Arch Pediatr Adolesc Med. 1995;149:15–8.
27. Lawrence JP, Green HS, Grauer JN. Back pain in athletes. J Am Acad Orthop Surg. 2006;14:726–35.
28. Sanpera Jr I, Beguiristain-Gurpide JL. Bone scan as a screening tool in children and adolescents with back pain. J Pediatr Orthop. 2006;26:221–5.
29. Kim HJ, Green DW. Spondylolysis in the adolescent athlete. Curr Opin Pediatr. 2011;23:68–72.
30. Zukotynski K, Grant FD, Curtis C, Micheli L, Treves ST. Skeletal scintigraphy in pediatric sports medicine. AJR Am J Roentgenol. 2010;195(5):1212–9.

Child Abuse

17

Laura Drubach

Child abuse continues to be a serious social problem. Based on data from the National Child Abuse and Neglect Data System, in the year 2011 there were an estimated 3.4 million referrals made to the Child Protective Agencies for suspected child abuse and neglect, involving 6.2 million children [1].

Of the children evaluated, there were 676,569 victims (9.1 victims per 1,000 children in the population). Children younger than 1 year had the highest victimization rate (21.2 per 1,000). Boys accounted for 48.6 % and girls 51.1 % of cases. More than 75 % of the victims suffered neglect, while 15 % suffered physical abuse and less than 10 % suffered sexual abuse. In the year 2011 there were a total of 1,545 fatalities reported (2.1 deaths per 100,000 children), with 81 % of these children being younger than 4 years. Boys had a higher fatality rate than girls (2.47 per 100,000 for boys and 1.77 for girls).

L. Drubach, MD
Joint Program in Nuclear Medicine,
Department of Radiology, Harvard Medical School,
Boston, MA, USA

Division of Nuclear Medicine and Molecular Imaging,
Department of Radiology, Boston Children's Hospital,
Boston, MA, USA

Department of Emergency Medicine,
Boston Children's Hospital, Boston, MA, USA
e-mail: laura.drubach@childrens.harvard.edu

The high prevalence of child abuse mandates that health-care providers be attentive to the problem and maintain a high index of suspicion when presented with injuries that may be secondary to child abuse. Prompt referrals to Child Protective Agencies can allow institution of appropriate preventive measurement that can potentially avoid further injuries and deaths. Knowledge of suspicious patterns of skeletal fracture and institution of early intervention in cases of inflicted injury is essential.

When presented with a case of possible child abuse, the first steps are to obtain a detailed history of the events leading to the injury and to conduct a thorough physical examination. There are several factors that may heighten the suspicion for abuse: if there are inconsistencies in the events that lead to the injury, if the injury is not consistent with the mechanism presented, or if the injury is not consistent with the child's developmental age [2–5].

Bone fractures are common in cases of child abuse and are second in incidence only to soft tissues injuries. Skeletal injuries are present in approximately 55 % of children that are physically abused [6]. Occasionally a fracture is the first sign that child abuse is present so early detection is important. Fractures seen in child abuse are often clinically occult, so it is important to recognize the characteristic patterns of fractures that are suspicious for abuse when presented with abnormal radiological findings [5].

S.T. Treves (ed.), *Pediatric Nuclear Medicine and Molecular Imaging*,
DOI 10.1007/978-1-4614-9551-2_17,

Fracture Patterns in Child Abuse

Bone fractures are a common finding in normal active children [7]. The ability to differentiate between fractures secondary to an accident and fractures due to child abuse requires knowledge about the types of fractures most commonly seen in child abuse and the ability to recognize specific patterns of fractures that suggest the possibility of abuse. Although any bone in the skeleton can be involved with a fracture in cases of child abuse, certain bones are more commonly involved than others. In a study performed by Kemp et al. in 2008, it was found that rib fractures were the most common fractures found in cases of child abuse and were seen in 71 % of cases [8]. Long bone fractures were less frequent than rib fractures but were also common, with humeral fractures in 48 % of cases and femoral fractures in 28 %. The incidence of skull fractures was 30 %, most commonly a linear skull fracture [8, 9]. A study by Worlock et al. found that the presence of multiple fractures was more likely to result from child abuse than from accidental injuries, especially in children younger than 18 months of age [9]. In this study, fractures of the ribs were also commonly detected in abused children and their presence was strongly associated with child abuse when major accidental trauma was ruled out [9].

Certain types of fractures, because of the mechanism of injury needed to produce them, are considered especially suspicious for child abuse, while other fractures are commonly seen in accidental injuries and do not by themselves necessarily raise the suspicion for child abuse (Table 17.1) [10].

One type of fracture that is highly specific for child abuse and that requires special consideration is the classic metaphyseal lesion or corner fracture [11–15]. These occur when the child is shaken violently, leading to a series of microfractures across the spongiosa of the bone metaphysis. Classic metaphyseal lesions (CML) occur most commonly in younger infants, often less than 2 years old. The presence of these fractures heightens the suspicion for child abuse dramatically. The presence of even a single classic metaphyseal lesion raises the possibility of child abuse and requires a thorough evaluation for the presence of other fractures.

Table 17.1 Specificity for child abuse of different types of fractures

Specificity of fractures for child abuse		
High specificity	Moderate specificity	Low specificity
Classic metaphyseal lesion	Multiple fractures	Subperiosteal new bone formation
Rib fractures	Fractures of different ages	Clavicular fractures
Scapular fractures	Epiphyseal separation	Long bone shaft fractures
Spinous process fractures	Vertebral body fracture	Linear skull fractures
Sternal fractures	Digital fractures	
	Complex skull fractures	

From Kleinman [10], with permission

Radiological Evaluation of Fractures

Skeletal Survey

Guidelines of both the American Academy of Pediatrics and the American College of Radiology indicate that the imaging method of choice for the evaluation of fractures of children younger than 2 years at the time of presentation is the radiographic skeletal survey [16, 17].

The radiographic survey includes X-rays of the entire body, especially important in young infants since localization of fractures based on clinical symptoms or signs is difficult. In older children a more focused radiological approach based on signs and symptoms may be acceptable.

The standard skeletal survey includes radiographs of the arms, forearms, hands, thighs, lower legs, feet, axial skeleton, thorax (including the thoracic spine and ribs), abdomen, lumbosacral spine and pelvis, cervical spine, and skull.

When the skeletal survey demonstrates fractures, it can be used to date the age of those fractures based on the presence of periosteal new

bone formation, callus formation, or blurring of the fracture line [18]. A repeat skeletal survey performed 2–3 weeks after the initial evaluation can be performed either if the initial survey is negative or if increased sensitivity for the detection of fractures is not initially identified. On the follow-up survey, callus formation that was not initially detectable may be visible. Although the use of follow-up imaging after several weeks can provide more sensitive detection of fractures, it may present a significant logistical problem because decisions about whether or not to place the child in foster care must be made at the time of initial investigation and therefore must be based upon initial information. Needing to wait several weeks for better diagnostic information can present a serious challenge to child welfare.

It has been shown that at least 8.5 % of children who undergo a second follow-up skeletal survey have forensically important findings that increase certainty of the diagnosis of child abuse, even if the initial survey was negative [19]. The majority of these findings are healing rib fractures (75 % of the time) that were not detected in the initial survey [19]. Even a limited follow-up skeletal survey that excludes images of the pelvis, lateral spine, hands, and skull is able to detect additional fractures [20].

One of the major drawbacks of the skeletal survey is that plain radiographs show low sensitivity for the detection of rib fractures, the most common fractures present in cases of child abuse. In a study comparing the detection rate of radiography and chest CT, it was found that radiographs detected only 60 % of the rib fractures shown by CT [21]. A study that evaluated the detection of fractures by skeletal surveys and bone scintigraphy showed that neither diagnostic modality detects as many fractures as the two combined [22].

Thus, although the radiographic skeletal survey is considered the first-line evaluation for fractures in suspected child abuse, its inability to detect all fractures shown by other modalities presents substantial logistical challenges. If results of the skeletal survey alone are used, the care provider could be at risk of making an incorrect decision about whether to allow the child to return home or be placed in foster care.

Bone Scintigraphy

Bone imaging and skeletal survey are believed to be complementary studies in the evaluation of non-accidental injury and could both be performed in cases of suspected child abuse [23, 24] (Fig. 17.1). In addition to detection of skeletal fractures, bone scintigraphy has the ability in some cases to identify soft tissue changes that lead to the detection of injuries other than bone fractures [25].

In current practice, the role of bone scintigraphy in the evaluation of child abuse is variable from institution to institution. Historically, bone scintigraphy has been performed in selected cases as a second-line evaluation following skeletal survey, serving in a complementary role. Some authors have suggested that bone scintigraphy could be used as an alternative to skeletal survey in the primary evaluation for fractures, while other authors have recommended scintigraphy only as a complementary examination [23, 26, 27].

A study performed by Wood et al. found a great variability among the hospitals in the performance of screening for occult fractures as defined by receipt of skeletal survey or radionuclide bone scan. In this group of patients, screening for occult fractures was performed in 83 % of children <2 years old [28].

Bone scintigraphy has traditionally been performed with ^{99m}Tc-MDP, obtaining planar anterior and posterior images of the whole body, without sedation (Fig. 17.1). Although this has been shown to be a useful technique in many instances, it has poor sensitivity for some common fractures, including skull fractures and classic metaphyseal lesions. More recently, ^{18}F-NaF PET bone imaging has been performed using ^{18}F-sodium fluoride (^{18}F-NaF). This radiopharmaceutical is commercially available in areas where ^{18}F-FDG is offered. The ^{18}F-NaF PET technique has several advantages over the traditional single-photon scintigraphic approach using

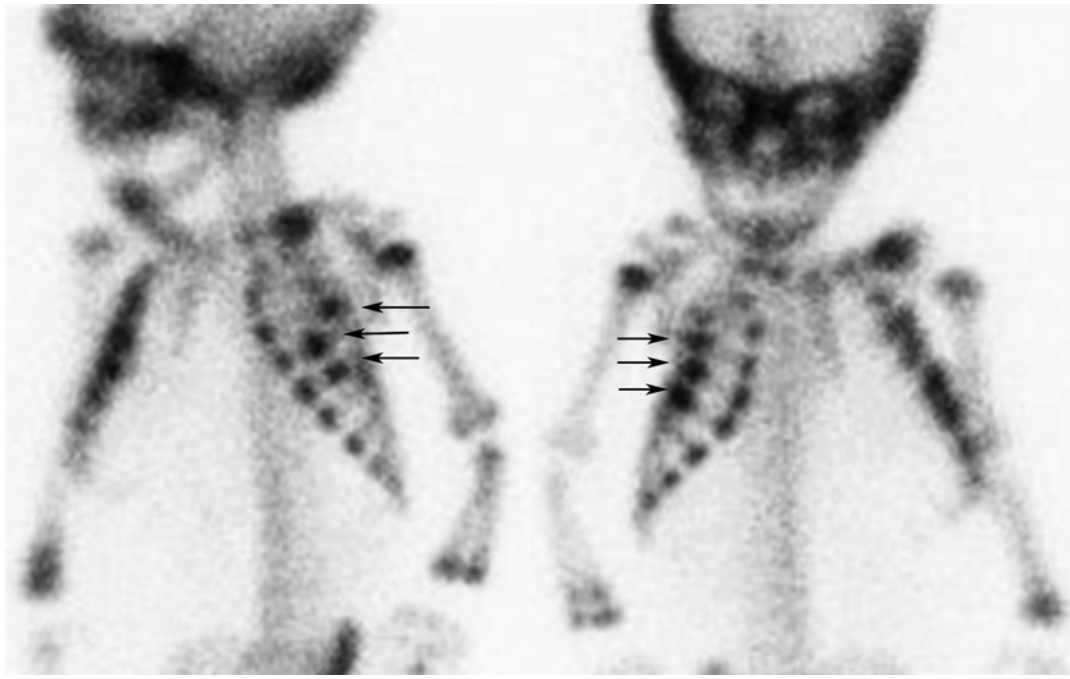

Fig. 17.1 Lateral oblique images of ^{99m}Tc-MDP in a 2-month-old boy showing multiple rib fractures (*arrows*)

diphosphonates. Fluorine-18-NaF imaging results in a higher concentration of the radiopharmaceutical in bone (approximately 2 times higher than ^{99m}Tc-MDP). The clearance of NaF from soft tissue is also faster than ^{99m}Tc-MDP, resulting in better overall image contrast with the ^{18}F-NaF PET technique. The higher spatial resolution of PET imaging devices, intrinsic tomographic acquisition, and ability to use attenuation correction all contribute to the superior imaging quality of ^{18}F-NaF images in comparison to standard ^{99m}Tc-MDP imaging and suggest that it might be possible to increase the detectability of fractures using the ^{18}F-NaF PET technique.

A direct one-to-one comparison between ^{99m}Tc-MDP and ^{18}F-NaF PET in the same patient in children would be difficult due to the double radiation exposure to the patient. In the setting of trauma related to child abuse, ^{18}F-NaF PET has been shown to be useful in the detection of skeletal fractures and, in particular, to be highly sensitive for the detection of fractures that may be difficult to identify radiographically [29, 30] (Fig. 17.2).

A study performed by Mandelstam in 2003 compared the effectiveness of skeletal survey and bone scintigraphy performed with ^{99m}Tc-MDP in the detection of bone fractures in 30 patients that were suspected victims of child abuse. In the 124 fractures identified, 64 fractures were detected on bone scan and 77 on skeletal survey. Rib fractures represented 48 % of the total fractures. Excluding rib fractures, 33 % of fractures were seen on both imaging modalities, 44 % were seen on skeletal survey only, and 25 % were seen on bone scans alone. In the same study the metaphyseal lesions typical of child abuse were present in 20 cases on the skeletal survey but were detected only in 35 % of these cases on bone scan. Standard scintigraphy with ^{99m}Tc-MDP is therefore not sensitive for detection of this important type of fracture.

A study performed by Drubach et al. in 2010 evaluated the sensitivity of ^{18}F-NaF PET for detection of fractures in infants being evaluated for child abuse. In this study ^{18}F-NaF PET had higher sensitivity than skeletal survey for detection of fractures in general (85 % for ^{18}F-NaF

Fig. 17.2 (**a**) X-ray of a 15-month-old being evaluated for child abuse shows a questionable periosteal new bone formation in the distal left ulna (*arrow*). These findings were not certain on radiography. (**b**) The patient underwent an ^{18}F-NaF PET. MIP images show increased uptake in the distal ulna confirming the diagnosis of fracture (*arrow*)

PET compared to 72 % for skeletal survey). This difference was even more striking when looking at rib fracture detection (92 % for ^{18}F-NaF PET compared to 68 % for skeletal survey). Fluorine-18-NaF PET was also more sensitive than skeletal survey in the detection of posterior costovertebral rib fractures, an important fracture in the diagnosis of child abuse (Fig. 17.3). Although ^{18}F-NaF PET was less sensitive than skeletal survey in the detection of CML (^{18}F-NaF PET detected 67 % of the lesions seen on skeletal survey), the detection rate was higher than the historically reported detection rate using ^{99m}Tc-MDP imaging.

Nuclear bone imaging therefore has advantages over skeletal survey in that it is more sensitive in the detection of rib fractures, especially posterior rib fractures. Since these are the most common fractures found in child abuse, it would be important that a sensitive technique be used in the evaluation. The early identification of additional fractures can change the outcome of child placement.

In addition to rib fractures, nuclear bone imaging is very sensitive in the detection of fractures in the shoulder, scapula and sternum, and pelvis areas that are very difficult to image with radiography. The identification of these

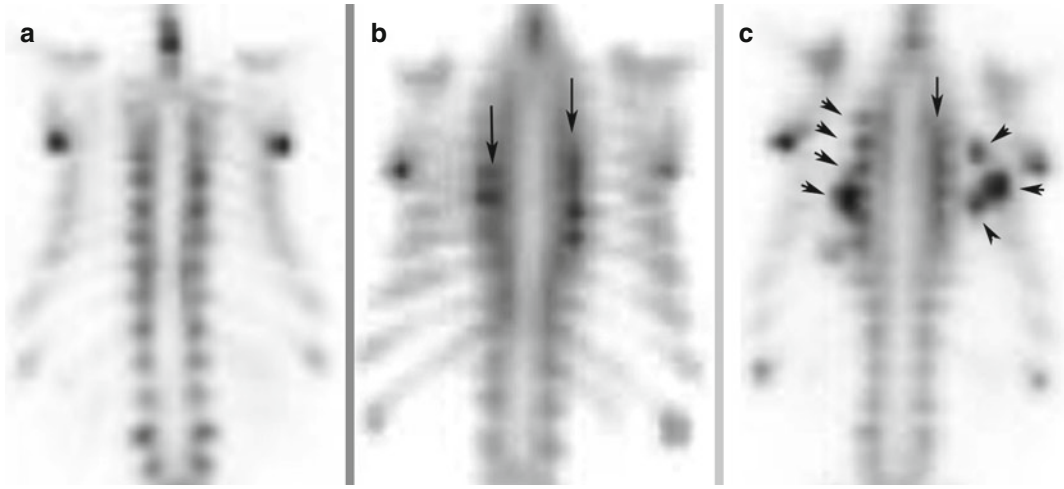

Fig. 17.3 (**a**) Fluorine-18-NaF PET coronal image of a 3-month-old girl shows multiple areas of increased uptake representing fractures in the posterior ribs (*arrows and arrowheads*). (**b**) Fluorine-18-NaF PET coronal image of a 3-month-old girl shows multiple areas of increased uptake representing fractures in the posterior ribs (*arrows*). (**c**) Fluorine-18-NaF PET coronal image of a 3-month-old boy shows multiple areas of increased uptake in the posterior and lateral ribs representing fractures

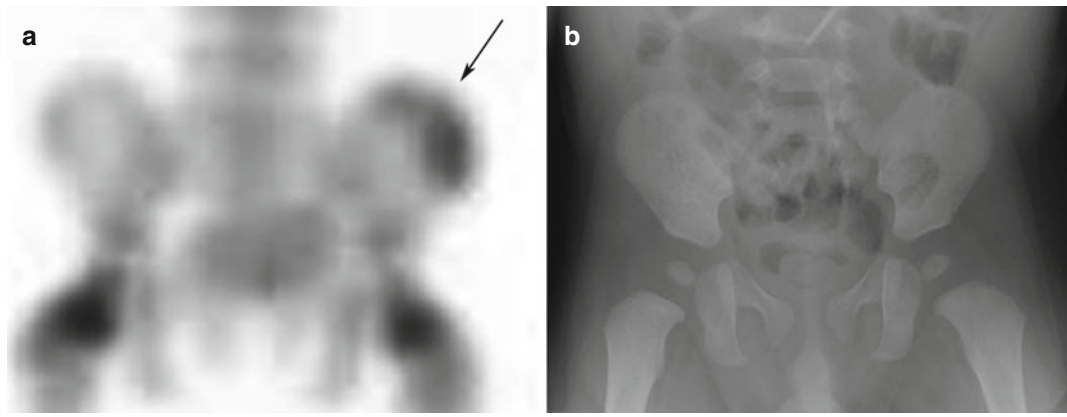

Fig. 17.4 (**a**) Fluorine-18-NaF PET MIP image of the pelvis in a 3-month-old boy showing increased uptake in the left iliac crest representing a fracture. (**b**) Corresponding image of the pelvis of the initial skeletal survey was falsely negative for fracture

fractures heightens the suspicion for child abuse (Fig. 17.4).

One of the drawbacks of scintigraphy is that there are no guidelines for the determination of the age of fractures. Another drawback is that bone scintigraphy is not very sensitive in the detection of skull fractures; therefore, radiography is needed in these circumstances.

Whole-Body MRI

The ability to evaluate young children without the use of ionizing radiation has prompted interest in whole-body MRI imaging for the evaluation of child abuse. In comparison to standard radiographic skeletal survey, MRI has low sensitivity (40 %) for detection of fractures in general.

MRI detected only 57 % of rib fractures and had very low sensitivity for detection of CML (31 %). Whole-body MRI is therefore not recommended in the evaluation of patients suspected of child abuse [31].

Rib Fractures

As previously described, rib fractures are the most common fractures found in cases of child abuse. They can be unilateral or bilateral, single or multiple. These fractures may have occurred in a single episode of trauma or may have occurred at different times. Fractures that occurred at different points in time indicate repeated episodes of trauma, heightening the suspicion for child abuse. Dating rib fractures is an important part of the evaluation of these children that is currently performed with radiography.

In the absence of a confirmed significant traumatic etiology, rib fractures have a high probability (71 %) of being caused by abuse [8].

In children younger than 3 years of age, it has been found that the positive predictive value of a rib fracture as an indicator of child abuse is 95 %. The positive predictive value increased to 100 % once historical and clinical circumstance excluded all other causes for rib fractures [32].

In a study published in the year 2000, the authors reviewed the skeletal surveys and bone scintigraphy of 18 infants under 2 years of age and found that bone scintigraphy revealed eight rib fractures undetected by skeletal survey in 4 patients. In three of these patients, the rib fractures were an isolated finding. Three of the infants with inflicted rib injuries were discharged home. In one such infant a significant reinjury occurred [33]. Nuclear bone imaging, preferably with ^{18}F-NaF PET, is the most sensitive method for detection of rib fractures [29].

Metaphyseal Fractures

Classic metaphyseal lesions are a series of microfractures across the metaphysis due to the shearing forces applied, usually a twisting motion of the extremity or violent shaking of the child [10]. They usually occur in young children, less than 2 years of age. The fracture line of the CML courses through the primary spongiosa of the metaphysis, and the metaphyseal fragment tends to be thicker peripherally than centrally. The presence of CML of the long bone is highly specific for physical abuse [10]. In infants younger than 1 year, these fractures are usually found in the distal femur, the proximal tibia, the distal tibia, or the proximal humerus. Depending on the direction of the X-ray beam projection, these fractures may appear as a corner fracture or as a bucket-handle fracture. There are no clinical signs or symptoms associated with these types of fractures so a high index of suspicion and careful radiological evaluation is necessary.

Nuclear bone imaging has lower sensitivity for detection of these fractures. Imaging with ^{18}F-NaF PET was shown to have a higher sensitivity for detection of these fractures in comparison to the standard bone scan with ^{99m}Tc-MDP [29]. Because these are a type of fractures highly specific for child abuse, the technique with higher sensitivity for detection should be performed in children younger than 2 years, that is, the skeletal survey.

Long Bone Fractures

Accidental long bone fractures are not uncommon in ambulatory young children, especially in toddlers. In contrast, if a long bone fracture occurs in a nonambulatory child or infant, child abuse is present between 60 and 80 % of the times.

A study that reviewed 80 femoral fractures in children under 4 years of age revealed that 8.5 % were due to violent trauma, 12.5 % were "pathologic" fractures, 30 % were related to child abuse, and 49 % resulted from normal trauma to normal children. In the same study child abuse as a cause of femoral fracture was more common in children under 1 year of age, in first-born

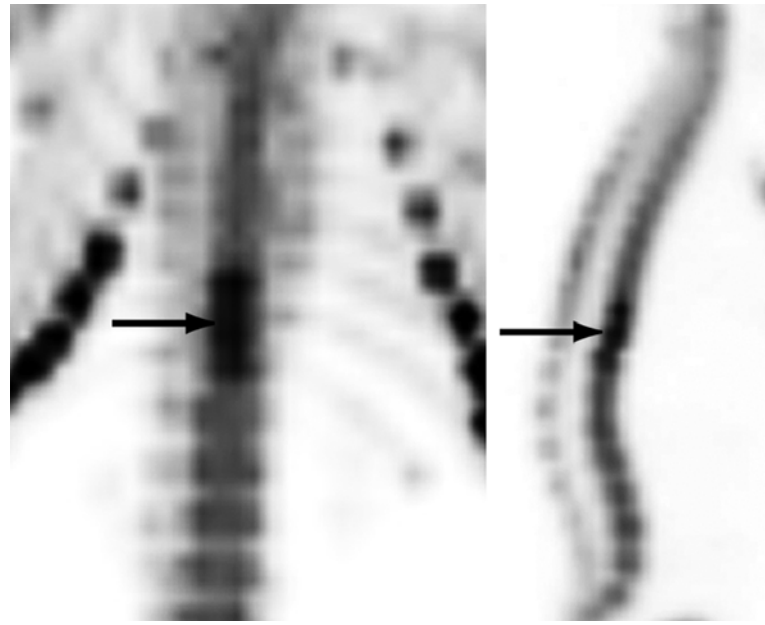

Fig. 17.5 Fluorine-18-NaF PET coronal (*left*) and sagittal (*right*) view of the spine of a 10-month-old boy showing increased uptake in several vertebral bodies (*arrows*) representing compression fractures (From Drubach et al. [29], with permission)

children, in patient with preexisting brain damage, and in cases of bilateral fractures [34]. With the exception of distal femur metaphyseal fractures, the fracture configuration was not pathognomonic of abuse [34]. In another study it was found that almost one-half of the femoral fractures sustained in children younger than 1 year were secondary to child abuse [35].

Spinal Fractures

Spinal fractures have been described as being very uncommon in cases of child abuse, with a maximum incidence of 3 % of all fractures found by skeletal survey. Compression fractures are the most common type of fracture found [36]. Nuclear bone imaging is able to detect spinal compression fractures and spinous process fractures otherwise not visible on radiography; therefore, the true incidence of spinal fractures is likely higher than has been historically thought [29] (Fig. 17.5).

Skull Fractures

Skull fractures are frequently seen in abused children, with linear, nondepressed skull fractures most commonly seen. Bone scintigraphy performed with either ^{99m}Tc-MDP or ^{18}F-NaF PET has lower sensitivity than radiography for detection of skull fractures. Radiographic evaluation with skeletal survey is needed to evaluate for this fracture.

Conclusion

Obtaining a skeletal survey at the time of presentation remains the standard of care of radiological evaluation for child abuse in children younger than 2 years. Because of the legal implication inherent in the evaluation of children for child abuse and the important decisions that must be made about allowing the child to return home or to have the child placed in foster care it is important to have all possible information at the time of the initial evaluation to be able to make the best possible informed decision. The addition of a nuclear bone imaging provides greater sensitivity for detection of fractures in areas where the skeletal survey is known to have limited sensitivity. A diagnostic approach that combines the use of both techniques is therefore optimal. Nuclear bone imaging is in addition an important tool for evaluation of questionable fractures detected on skeletal survey. The

confirmation or negation of additional fractures with nuclear bone imaging may have an implication as to the child's placement in foster care. In children older than 2 years, where the presence of CML is not prevalent, nuclear bone imaging alone may suffice for evaluation of fractures.

References

1. National Child Abuse and Neglect Data System. In: Services UDoHaH, editor. Administration for Children and Families: US. Department of Health and Human Services; 2011;1–112.
2. Sugar NF, Taylor JA, Feldman KW. Bruises in infants and toddlers: those who don't cruise rarely bruise. Puget Sound Pediatric Research Network. Arch Pediatr Adolesc Med. 1999;153:399–403.
3. Wagner GN. Crime scene investigation in child-abuse cases. Am J Forensic Med Pathol. 1986;7:94–9.
4. McMahon P, Grossman W, Gaffney M, Stanitski C. Soft-tissue injury as an indication of child abuse. J Bone Joint Surg Am. 1995;77:1179–83.
5. Cramer KE. Orthopedic aspects of child abuse. Pediatr Clin North Am. 1996;43:1035–51.
6. Loder RT, Bookout C. Fracture patterns in battered children. J Orthop Trauma. 1991;5:428–33.
7. Landin LA. Fracture patterns in children. Analysis of 8,682 fractures with special reference to incidence, etiology and secular changes in a Swedish urban population 1950–1979. Acta Orthop Scand Suppl. 1983; 202:1–109.
8. Kemp AM, Dunstan F, Harrison S, et al. Patterns of skeletal fractures in child abuse: systematic review. BMJ. 2008;337:a1518.
9. Worlock P, Stower M, Barbor P. Patterns of fractures in accidental and non-accidental injury in children: a comparative study. Br Med J (Clin Res Ed). 1986;293: 100–2.
10. Kleinman PK. Skeletal trauma: general considerations. In: Kleinman PK, editor. Diagnostic imaging of child abuse. 2nd ed. St. Louis: Mosby; 1998. p. 8–25.
11. Kleinman PK, Marks Jr SC. A regional approach to the classic metaphyseal lesion in abused infants: the proximal tibia. AJR Am J Roentgenol. 1996;166: 421–6.
12. Kleinman PK, Marks Jr SC. A regional approach to classic metaphyseal lesions in abused infants: the distal tibia. AJR Am J Roentgenol. 1996;166: 1207–12.
13. Kleinman PK, Marks Jr SC. A regional approach to the classic metaphyseal lesion in abused infants: the proximal humerus. AJR Am J Roentgenol. 1996; 167:1399–403.
14. Kleinman PK, Marks Jr SC. A regional approach to the classic metaphyseal lesion in abused infants: the distal femur. AJR Am J Roentgenol. 1998;170:43–7.
15. Kleinman PK, Marks SC, Blackbourne B. The metaphyseal lesion in abused infants: a radiologic-histopathologic study. AJR Am J Roentgenol. 1986;146:895–905.
16. American Academy of Pediatrics, Section on Radiology. Diagnostic imaging of child abuse. Pediatrics. 2009;123:1430–5.
17. American College of Radiology e.A.S.R., VA, American College of Radiology. ACT practice guideline for skeletal surveys in children. 2006:145–9.
18. Chapman S. The radiological dating of injuries. Arch Dis Child. 1992;67:1063–5.
19. Bennett BL, Chua MS, Care M, Kachelmeyer A, Mahabee-Gittens M. Retrospective review to determine the utility of follow-up skeletal surveys in child abuse evaluations when the initial skeletal survey is normal. BMC Res Notes. 2011;4:354.
20. Sonik A, Stein-Wexler R, Rogers KK, Coulter KP, Wootton-Gorges SL. Follow-up skeletal surveys for suspected non-accidental trauma: can a more limited survey be performed without compromising diagnostic information? Child Abuse Negl. 2010;34:804–6.
21. Wootton-Gorges SL, Stein-Wexler R, Walton JW, Rosas AJ, Coulter KP, Rogers KK. Comparison of computed tomography and chest radiography in the detection of rib fractures in abused infants. Child Abuse Negl. 2008;32:659–63.
22. Kemp AM, Butler A, Morris S, et al. Which radiological investigations should be performed to identify fractures in suspected child abuse? Clin Radiol. 2006;61:723–36.
23. Mandelstam SA, Cook D, Fitzgerald M, Ditchfield MR. Complementary use of radiological skeletal survey and bone scintigraphy in detection of bony injuries in suspected child abuse. Arch Dis Child. 2003;88:387–90; discussion 387–90.
24. Conway JJ, Collins M, Tanz RR, et al. The role of bone scintigraphy in detecting child abuse. Semin Nucl Med. 1993;23:321–33.
25. Howard JL, Barron BJ, Smith GG. Bone scintigraphy in the evaluation of extraskeletal injuries from child abuse. Radiographics. 1990;10:67–81.
26. Smith FW, Gilday DL, Ash JM, Green MD. Unsuspected costo-vertebral fractures demonstrated by bone scanning in the child abuse syndrome. Pediatr Radiol. 1980;10:103–6.
27. Nimkin K, Kleinman PK. Imaging of child abuse. Radiol Clin North Am. 2001;39:843–64.
28. Wood JN, Feudtner C, Medina SP, Luan X, Localio R, Rubin DM. Variation in occult injury screening for children with suspected abuse in selected US children's hospitals. Pediatrics. 2012;130:853–60.
29. Drubach LA, Johnston PR, Newton AW, Perez-Rossello JM, Grant FD, Kleinman PK. Skeletal trauma in child abuse: detection with 18F-NaF PET. Radiology. 2010;255:173–81.
30. Drubach LA, Sapp MV, Laffin S, Kleinman PK. Fluorine-18 NaF PET imaging of child abuse. Pediatr Radiol. 2008;38:776–9.

31. Perez-Rossello JM, Connolly SA, Newton AW, Zou KH, Kleinman PK. Whole-body MRI in suspected infant abuse. AJR Am J Roentgenol. 2010;195: 744–50.
32. Barsness KA, Cha ES, Bensard DD, et al. The positive predictive value of rib fractures as an indicator of nonaccidental trauma in children. J Trauma. 2003; 54:1107–10.
33. Cadzow SP, Armstrong KL. Rib fractures in infants: red alert! The clinical features, investigations and child protection outcomes. J Paediatr Child Health. 2000;36:322–6.
34. Beals RK, Tufts E. Fractured femur in infancy: the role of child abuse. J Pediatr Orthop. 1983;3: 583–6.
35. Gross RH, Stranger M. Causative factors responsible for femoral fractures in infants and young children. J Pediatr Orthop. 1983;3:341–3.
36. Kocher MS, Kasser JR. Orthopaedic aspects of child abuse. J Am Acad Orthop Surg. 2000;8:10–20.

18 The Role of Skeletal Scintigraphy in the Diagnosis and Management of Mandibular Growth Abnormalities and Asymmetry

Zachary S. Peacock, Matthew E. Lawler, Frederic H. Fahey, and Leonard B. Kaban

Abnormalities in mandibular growth can result in significant facial deformity and asymmetry. Mandibular asymmetry may be congenital or acquired and often has functional, esthetic, and social consequences [1–3]. In general, asymmetry of the mandible may be classified as overgrowth or undergrowth conditions. Unilateral condylar hyperplasia is the most common overgrowth asymmetry. Overgrowth can also occur in response to trauma (e.g., condylar fracture in children), tumors in the condylar region, or fibrous dysplasia. Undergrowth of one side may be the result of trauma, radiation, inflammatory joint disease, idiopathic condylar resorption, or congenital malformation such as hemifacial microsomia.

Z.S. Peacock, DMD, MD (✉) • M.E. Lawler, DMD
L.B. Kaban, DMD, MD
Department of Oral and Maxillofacial Surgery,
Massachusetts General Hospital,
Boston, MA, USA

Department of Oral and Maxillofacial Surgery,
Harvard School of Dental Medicine,
Boston, MA, USA
e-mail: zpeacock@partners.org; lkaban@partners.org

F.H. Fahey, DSc
Joint Program in Nuclear Medicine,
Department of Radiology, Harvard Medical School,
Boston, MA, USA

Division of Nuclear Medicine and Molecular Imaging,
Department of Radiology, Boston Children's Hospital,
Boston, MA, USA

Important diagnostic considerations for the clinician are (1) to determine which is the normal versus the abnormal side and (2) to determine if the asymmetric growth pattern is progressive (active) or stable (quiescent). Treatment of the deformity depends on the etiopathogenesis of the condition and varies based on growth activity.

Unilateral condylar hyperplasia (UCH) as with other growth abnormalities can be classified as active or quiescent [1, 4–6]. During the active growth phase in UCH, the deformity becomes progressively worse with increasing vertical elongation of the mandibular ramus (vertical pattern) or increasing convexity of the mandibular ramus and body with deviation of the chin toward the unaffected side (rotational pattern). Progression or worsening of the deformity is the hallmark of active condylar hyperplasia. Undergrowth (e.g., hemifacial microsomia) is considered progressive when there is remaining somatic growth of the non-affected side [7]. Determining the metabolic and physiologic status of an asymmetric mandible is a challenging problem, and uptake of bone-seeking radiopharmaceuticals can be utilized to help identify the abnormal side and to evaluate activity or inactivity of the condition.

The severity of the deformity and activity of the disease dictate the treatment. Serial clinical examinations with standardized photographs, although subjective in nature, remain the gold standard for assessment of the progression of facial asymmetries. Plain x-rays (i.e., lateral and anteroposterior (AP) cephalograms and panoramic radiographs) allow for measurements of

S.T. Treves (ed.), *Pediatric Nuclear Medicine and Molecular Imaging*,
DOI 10.1007/978-1-4614-9551-2_18, © Springer Science+Business Media New York 2014

bone height and position; however, multiple time points over a period of years are needed to determine disease activity [8]. These modalities measure the effects of overgrowth or undergrowth but do not provide any physiologic information.

Skeletal scintigraphy using ^{99m}Tc-labeled methylene diphosphonate (^{99m}Tc-MDP) is an effective method for evaluating the metabolic state of the mandibular condyle to determine the normal versus abnormal side and the degree of bone activity (i.e., growth or breakdown) at a particular point in time [9–12]. Bone scanning for assessment of abnormal growth centers of the mandible has evolved from planar scintigraphy [12] to single-photon emission computed tomography (SPECT) [13] and hybrids of SPECT with multi-detector computed tomography (SPECT/CT) [14].

Study Acquisition, Reconstruction and Analysis

As is typical for all bone scanning using ^{99m}Tc-MDP, 7.4 Mbq/kg (18.5 MBq minimum, 518 Mbq maximum) is typically administered intravenously, and imaging is performed 3–4 h post-injection. The reader is referred to Chapter 15 for more details regarding bone scanning.

Uptake values within the mandibular condyle may require external and internal standardization to correct for differences in image timing, reconstruction, and pharmacokinetics of tracer in each patient. The external standard consists of a culture flask containing a known amount of ^{99m}Tc between 370 and 555 kBq and is placed above the patient's head to be included in the field of view. A calibration factor is determined by dividing the activity in the flask by the total counts measured over the standard. Internal standards correct for variations in the concentration of tracer at the time of imaging due to differences in the volumes of distribution, metabolism, and renal clearance.

For planar images, a γ-camera is used with a low-energy, high-resolution or ultrahigh resolution collimator. The patients head is positioned in front of the γ-camera with the neck hyperextended to separate the mandibular ramus and the cervical spine. Images of the fourth lumbar vertebra (L4) are also obtained for use as an internal standard since it can be dependably localized and has symmetric uptake of radiotracer [16].

Regions of interest (ROIs) are traced over the mandibular condyle, ramus, and body bilaterally and L4 as described above (Fig. 18.1). The ratio of uptake (RU) of ^{99m}Tc-MDP is calculated as follows:

RU = (counts in ROI of mandible – background counts) / (counts in L4 – background counts)

SPECT images are obtained using a dual-detector γ-camera with a low-energy, high-resolution or ultrahigh-resolution collimator in a 128 × 128 matrix for 120 views per detector for 360° with 15 s/view. For SPECT, an external standard containing 370-740 kBq of ^{99m}Tc can be included in the field of view. The acquired data are typically reconstructed with filtered back projection. An iterative reconstruction algorithm such as ordered subset expectation maximization (OSEM) may also be used, but it may be necessary to develop a different set of normal range values to compensate for the enhanced contrast.

For SPECT, ROIs can also be traced over the mandibular condyle, ramus, and body bilaterally and the culture flask. The clivus can be used as an internal standard for SPECT as it is typically included within the field of view, and predictably ceases growth when the sphenooccipital synchondrosis fuses [16]. After cessation of growth, it is thought to be one of the least metabolically active bones as it has no articulations and bears no weight. Multiple slices on SPECT allow for volumetric 3-dimensional (3D) ROI (Fig. 18.2).

The maximum pixel counts within each ROI are recorded. Condyle counts are corrected with each standard as follows:

Internal standard : condyle uptake = (condyle counts) / (clivus counts)

External standard : condyle uptake = (condyle counts) x (standard activity in mCi) / standard counts

The right to left ratio of condylar, body, and ramus activity is used to compare the two sides.

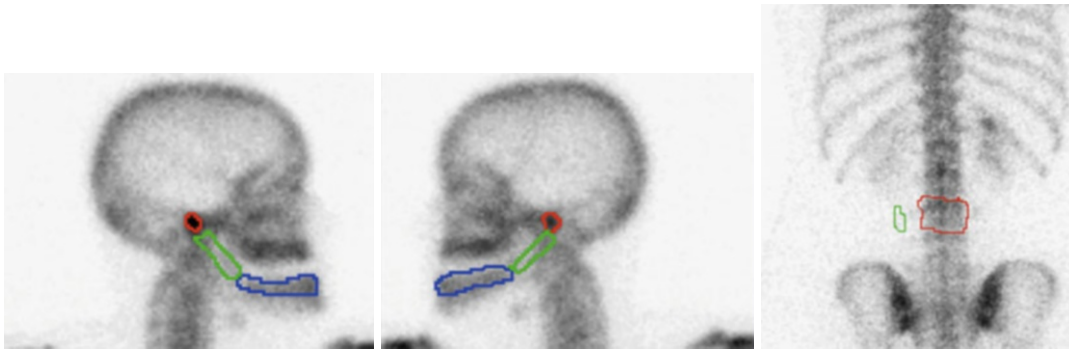

Ratio of uptake	Right	Left
Condyle (red)	7.7	5.2
Ramus (green)	2.7	2.6
Body (blue)	3.0	2.8

Fig. 18.1 Planar scintigram revealed right to left ratio of uptake (RU) of 1.48. Clinical correlation with the indicated increased uptake led to a diagnosis of active right unilateral condylar hyperplasia. The scintigram on the top right shows the L4 (*red*) and additional reference (*green*)

Clinical Applications

Unilateral Condylar Hyperplasia

Unilateral condylar hyperplasia (UCH) is the most common growth abnormality of the temporomandibular joint after birth. Clinically, it can result in facial asymmetry with deviation of the chin to one side, occlusal disturbances, and temporomandibular joint dysfunction. UCH results in disproportionate mandibular growth due to hyperactivity within the mandibular condyle. It can occur during normal growth when one condyle grows out of proportion to the contralateral condyle, it can also occur after cessation of somatic growth. Both cases result in shifting of the mandible in a direction down and away from the affected side. Although, the etiology remains uncertain, purported causes include trauma, hormonal inbalances, arthrosis, and hypervascularity [3, 17–19].

Skeletal scintigraphy allows comparison of the metabolic activity within each condyle and relative to external and internal standards. An enlarged but quiescent condyle is generally left intact provided there are no functional abnormalities such as decreased motion. The mandibular asymmetry is treated by conventional orthognathic reconstructive surgery to align the mandible (and maxilla if necessary) and to correct the occlusion. This spares the patient an open-joint operation which can have long-term consequences such as limited mouth opening and joint pain. Conversely, treatment of active or progressive condylar hyperplasia consists of a high partial condylectomy to arrest growth. The growth-arresting procedure can be done in conjunction with orthognathic surgery to correct the asymmetry. If standard osteotomies are done during a period of active overgrowth within the condyle, further deformity will occur and the patient may need additional operations.

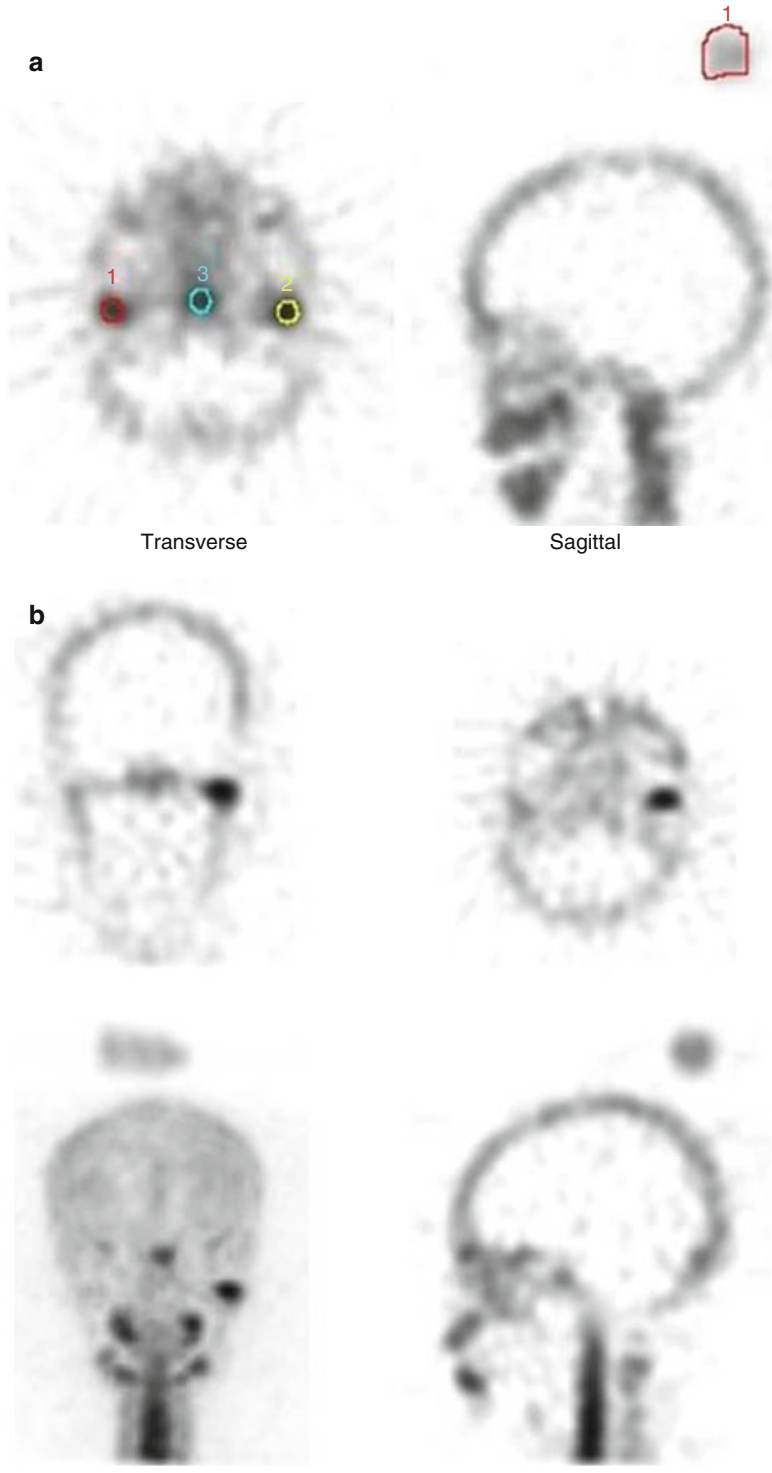

Fig. 18.2 SPECT Quantitation. (a) Circular regions of interest (ROI) (1.13 cm^2) are placed over the mandibular condyles (red and yellow) and the clivus (blue) as seen on the axial view. The slice containing the maximum pixel value is chosen. 3D ROIs consist of the 2D ROI as well as similar ROIs applied to the slices above and below the slice with the maximum pixel value, and the counts from the 3 slices combined are averaged. The outline of the external standard containing known counts (red) is seen above the sagittal view (From Fahey et al. [40], with permission). (**b**) SPECT study of an 18 year old with hyperplasia of the left condyle. The study is strikingly abnormal (right-to-left ratio of 0.333 is substantially outside the normal range). When using either the external standard or the clivus as an internal standard, the right condyle is normal whereas the left condyle has abnormally high uptake

Planar Scintigraphy

The planar method of scintigraphy allows quantification of condylar activity by assessing regions of interest (ROI) about the condyle, ramus, and body of the mandible. Activity within the condyle is quantified as a ratio of condyle uptake and is normalized by comparison to the fourth lumbar vertebrate and correlated with age (Fig. 18.2) [15, 20]. Normative data was developed by assessing condylar activity during growth [11]. Subsequent studies compared patients with mandibular asymmetries to known age-adjusted standards [15]. L4 is used as an internal standard since it has a constant low-level uptake after cessation of somatic growth. Correlation of the technique with clinical data has shown reliability, but limitations exist. First, uptake in L4 may be abnormal in patients with arthritis or other lumbar disease. Second, planar images result in superimposition of the cervical spine and the ROI of the contralateral condyle providing a potential source of inaccuracy. Planar imaging requires careful patient positioning and collimation to avoid overlapping areas of interest. The development of the SPECT technique has improved on the weakness of the planar technique and is currently the most common method used.

SPECT Imaging

SPECT studies have largely replaced planar scintigraphy in assessing mandibular asymmetry and growth. SPECT represents a more sensitive technique without the limitations of patient positioning and superimposition with the planar technique. It provides 3D representations of the radiopharmaceutical distribution within the craniofacial skeleton. Areas of increased uptake such as hyperplastic mandibular condyles are easily identified and assessed in three dimensions.

Quantitative SPECT studies for assessment of radiopharmaceutical uptake were first applied to bone scintigraphy in the late 1980s [21–24]. Subsequent assessment studies compared SPECT with planar images for condylar activity [13, 25–29]. Pogrel et al., in 1995, demonstrated that the SPECT scan is statistically correlated with the planar image condyle/L4 scintigram [13]. In the study, the clivus was introduced as a new internal standard. With its positioning at the skull base at the same axial level of the mandibular condyles, all three structures can be seen on one slice [22, 30]. The clivus has also been shown to have less variation in activity than L4 [13]. Hodder et al., in 1999, compared one mandibular condyle to the other by calculating an uptake ratio and postulated that it was a more accurate and sensitive way to detect unilateral condylar abnormalities than comparison with an internal standard such as L4 or the clivus [25]. They also confirmed that a relative percentage uptake of 55 % in the affected condyle as previously shown for planar imaging [13] also applied to SPECT imaging. Saridin et al. then showed SPECT scanning to be the preferred method of assessment over planar scintigraphy [31]. Using clinical outcomes, the group subsequently showed that condyle to condyle ratios may be superior to comparisons with an internal osseous standard [32].

Clinical Case Examples

N.C is a 23-year-old woman who presented with progressive facial asymmetry that began around the age of 10. Her lower face was obviously asymmetric (Fig. 18.3a, b) with the right mandible ramus being significantly longer than the left. She had slight deviation of the chin to the right side, but the asymmetric discrepancy was most notable in the vertical plane (Fig. 18.3c). Intraorally, she had an open bite on the right side with a mandibular occlusal cant downward on the right (Fig. 18.3d). A panoramic radiograph revealed an enlarged right condylar head and elongated right condylar neck (Fig. 18.3e–g). The differential diagnosis included unilateral condylar hyperplasia, left condylar hypoplasia, and generalized mandibular asymmetry. The clinical presentation was most consistent with right unilateral condylar hyperplasia, vertical pattern. Given the long-standing nature of the asymmetry, it was thought to be likely quiescent. However, Planar and SPECT scans were obtained which showed markedly increased uptake in the right condyle versus the left (Fig. 18.4). The ratio of the right and left condyle

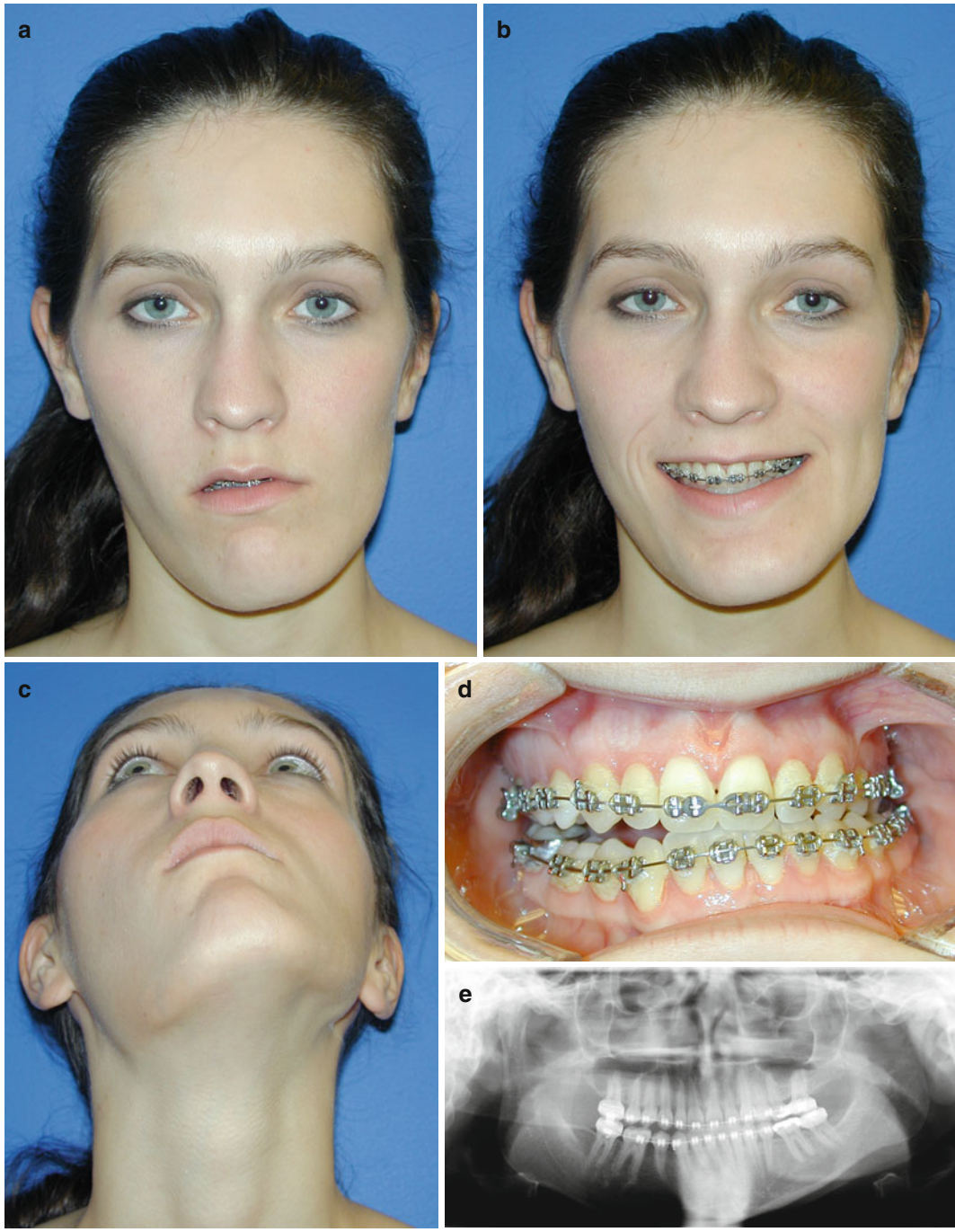

Fig. 18.3 (**a**) Frontal repose, (**b**) smiling, and (**c**) submental views of the patient with progressive facial asymmetry. The chin point is seen deviated to the left and the mandible is flatter on the right. (**d**) The mandibular occlusal plane is tilted down on the right with a right lateral open bite. (**e**) Panoramic radiograph demonstrates elongation of the right mandibular condyle-ramus unit. (**f**) AP and (**g**) lateral cephalograms demonstrate the asymmetry with tilting of the mandible down on the right and double inferior border on the lateral view

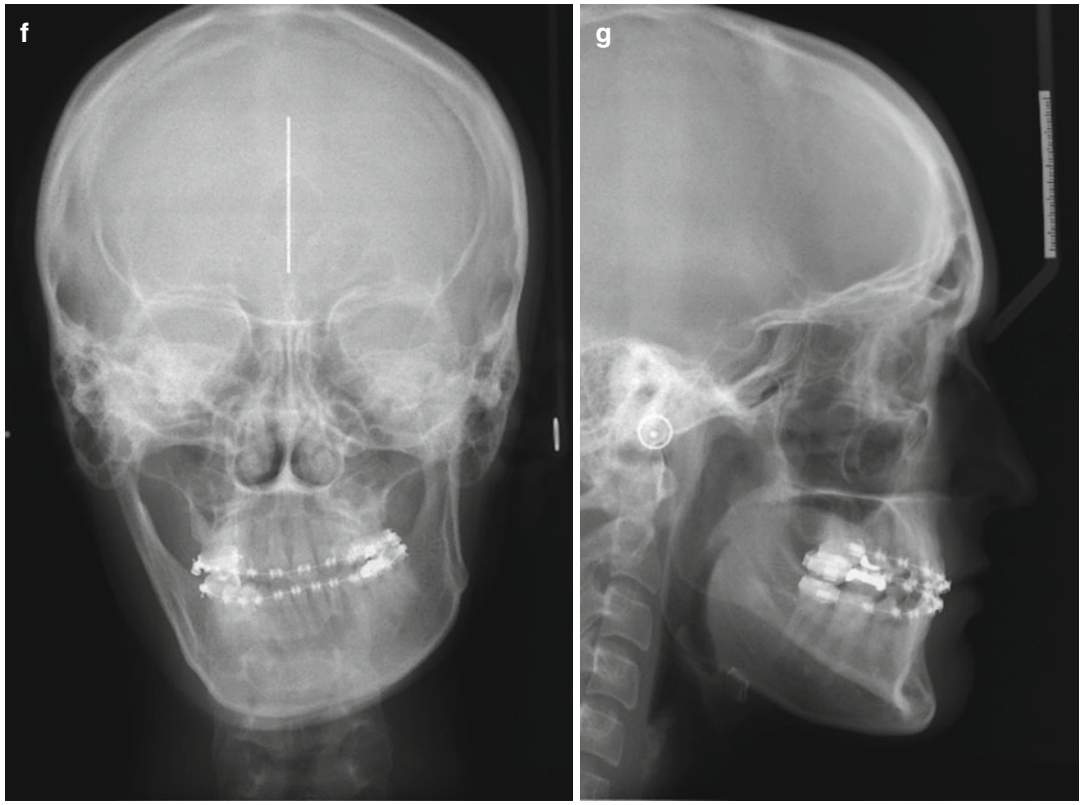

Fig. 18.3 (continued)

to L4 was 4.0 and 2.75, respectively. The ratio of the bilateral ramus and body to L4 uptake was 1.25 and 1.5, respectively. A diagnosis of active right condylar hyperplasia was made. The patient was treated with a "growth-arresting" procedure consisting of an endoscopic high condylectomy to stop the active abnormal condylar growth (Fig. 18.5a). Also, a left mandibular sagittal split osteotomy was performed to allow rotation of the occlusal plane to match the maxilla. An ostectomy of the right inferior border was performed to correct the vertical discrepancy. Postoperative radiographs showed improvement in symmetry (Fig. 18.5b–d). Three years after the correction, her skeleton and occlusion remained symmetric (Fig. 18.5e, f).

R.C., a 16-year-old girl, developed a malocclusion and mandibular asymmetry after completing orthodontia 3 years prior to presentation. Examination revealed the chin point deviated to the right with class III skeletal malocclusion (Fig. 18.6a–c). Her mandibular midline was 6 mm to the right of the maxillary midline and midsagittal plane (Fig. 18.6d). Radiographic exam showed a longer condyle-ramus unit on the left than the right (Fig. 18.6e–g). The differential diagnoses included active and quiescent left unilateral condylar hyperplasia, right condylar hypoplasia, and late asymmetric mandibular growth. A SPECT scan was obtained which showed a ratio of uptake in the left to right condyle of

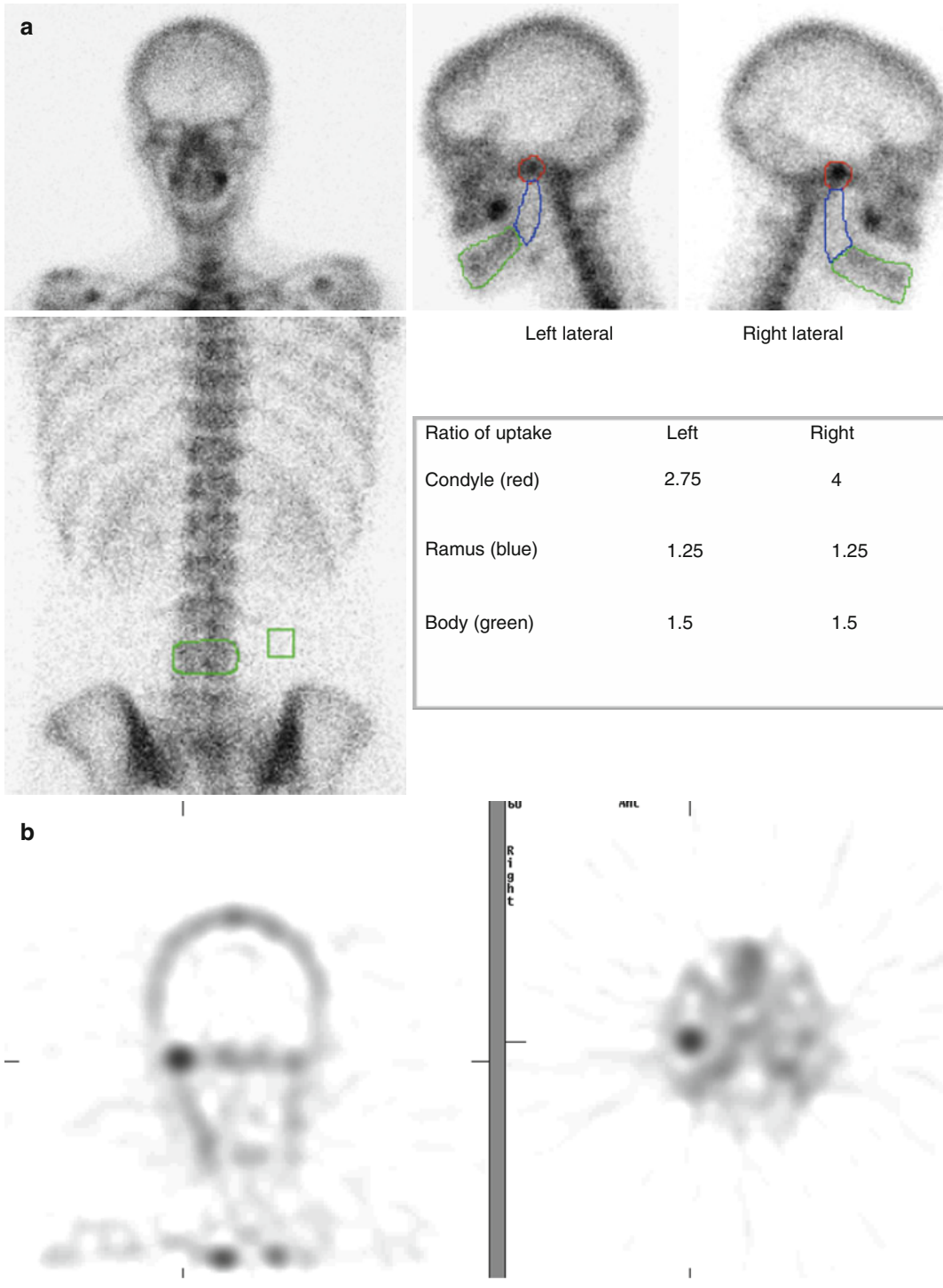

Ratio of uptake	Left	Right
Condyle (red)	2.75	4
Ramus (blue)	1.25	1.25
Body (green)	1.5	1.5

Fig. 18.4 (**a**) Planar scan using L4 as internal reference point (*green* in left bottom left picture) showed RU of 4 indicating active right unilateral condylar hyperplasia. The RU in the bilateral ramus and body were equal. (**b**) SPECT scan on same patient demonstrates abnormally high uptake in the right condyle

0.96 (Fig. 18.7). The ratio of uptake of both condyles was slightly greater than the clivus and external standard indicating some symmetric active growth in both condylar regions consistent with her remaining somatic growth potential (growth is usually complete 3 years after menses begins; she had started menses 2 years earlier). Her diagnosis was quiescent unilateral condylar hyperplasia, rotational pattern. No operation was necessary on the inactive condyle or the maxilla, which remained symmetric in this case. She was corrected with a bilateral sagittal split osteotomy and genioplasty to rotate the mandible and chin back

Fig. 18.5 Intraoperative and postoperative views of the patient from Fig. 18.3. (**a**) Intraoperative view of the elongated right mandibular condylar head marked for high condylectomy. The patient also underwent a left sagittal split osteotomy and right inferior border ostectomy. The correction and restoration of symmetry is seen on the postoperative (**b**) panoramic radiograph, (**c**) AP, and (**d**) lateral cephalogram. (**e**, **f**) The position remained stable at latest follow-up, 3 years after correction

Fig. 18.5 (continued)

to the midsagittal plane. Postoperative radiographs showed correction of the asymmetry (Fig. 18.8a–c). Two-year follow-up revealed symmetry of her mandible (Fig. 18.8d, e).

Assessment of Surgical Therapy

Skeletal scintigraphy also has a role in the assessment of treatment for active abnormal condylar growth in mandibular asymmetry. When clinical exam reveals mandibular asymmetry, and it is confirmed to be active by a SPECT scan, a high condylectomy is performed. This serves as a "growth-arresting" procedure and the abnormal growth center is excised. Postoperative SPECT scanning can confirm the lack of continued abnormal growth activity. It essentially can establish the effectiveness of the surgical excision of the abnormal mandibular condyle when indicated clinically.

Assessment of Growth

An assessment of craniofacial growth is critical in treatment planning for any patient requiring surgical or orthodontic intervention [7]. Persistent somatic growth postoperatively can result in skeletal changes requiring reoperation. Serial clinical examination is commonly employed, but the psychosocial effect of craniofacial deformities on the patient may require the surgeon to operate as soon as possible. This may not allow enough time to confirm the end of growth via serial examination [33]. Contributing to the challenge is the growth pattern of the mandible: It grows at a high rate during adolescence [34, 35],

Fig. 18.6 (**a**) Frontal repose, (**b**) smiling, (**c**) submental and (**d**) intraoral views demonstrate lower facial asymmetry with chin point and mandibular occlusion deviated to the right. Her mandibular dental midline is 6 mm to the right of the maxillary midline. (**e**) Panoramic, (**f**) AP, and (**g**) lateral radiographs show elongation of the left condyle-ramus unit and shifted to the right

Fig. 18.6 (continued)

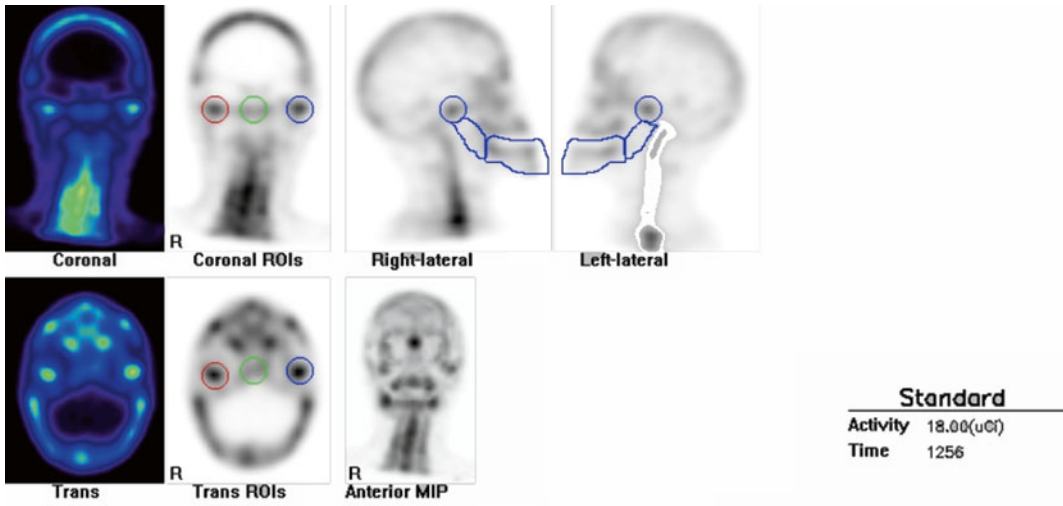

Standard

Activity	18.00(uCi)
Time	1256

Condyle

	Results	Normal Range
Right/Left	0.96	0.62 - 1.24
Right/std	10.55	3.40 – 10.00
Left/std	11.02	3.40 – 10.00
Right/Clivus	2.17	0.88 – 1.80
Left/Clivus	2.26	0.88 – 1.80

Ramus

	Results	Normal Range
Right/Left	1.50	
Right/std	14.12	
Left/std	9.41	
Right/Clivus	2.98	
Left/Clivus	1.98	

Body

	Results	Normal Range
Right/Left	1.29	
Right/std	31.50	
Left/std	24.43	
Right/Clivus	6.64	
Left/Clivus	5.15	

Fig. 18.7 SPECT scan showed right (*red*) to left (*blue*) RU of 0.96 indicating quiescent left condylar hyperplasia, rotational pattern. Compared to the external and internal (clivus, *green*) standards revealed slightly increased uptake consistent with remaining somatic growth of each condyle that was symmetric

is the last facial bone to complete growth [36, 37], and grows in a pattern that does not correlate with other bones in the axial and appendicular skeleton [38]. In addition, high individual variability in amount and timing of mandibular growth makes predicting growth potential based on age or pubertal status unreliable [39].

Many methods to assess craniofacial growth have been reported in the surgical and orthodontic literature. The gold standard remains serial clinical observation, which is subjective, takes many years to obtain necessary information, and is difficult to standardize [40]. Several imaging techniques to approximate axial skeletal growth have been used to supplement clinical examination including radiographic assessment of the hand and wrist, cervical vertebrate, or serial cephalometric analysis [41–43]. Radiographic examinations are quantitative and objective, but limitations persist due to the overall lack of correlation of mandibular and axial growth and the time required for serial cephalograms.

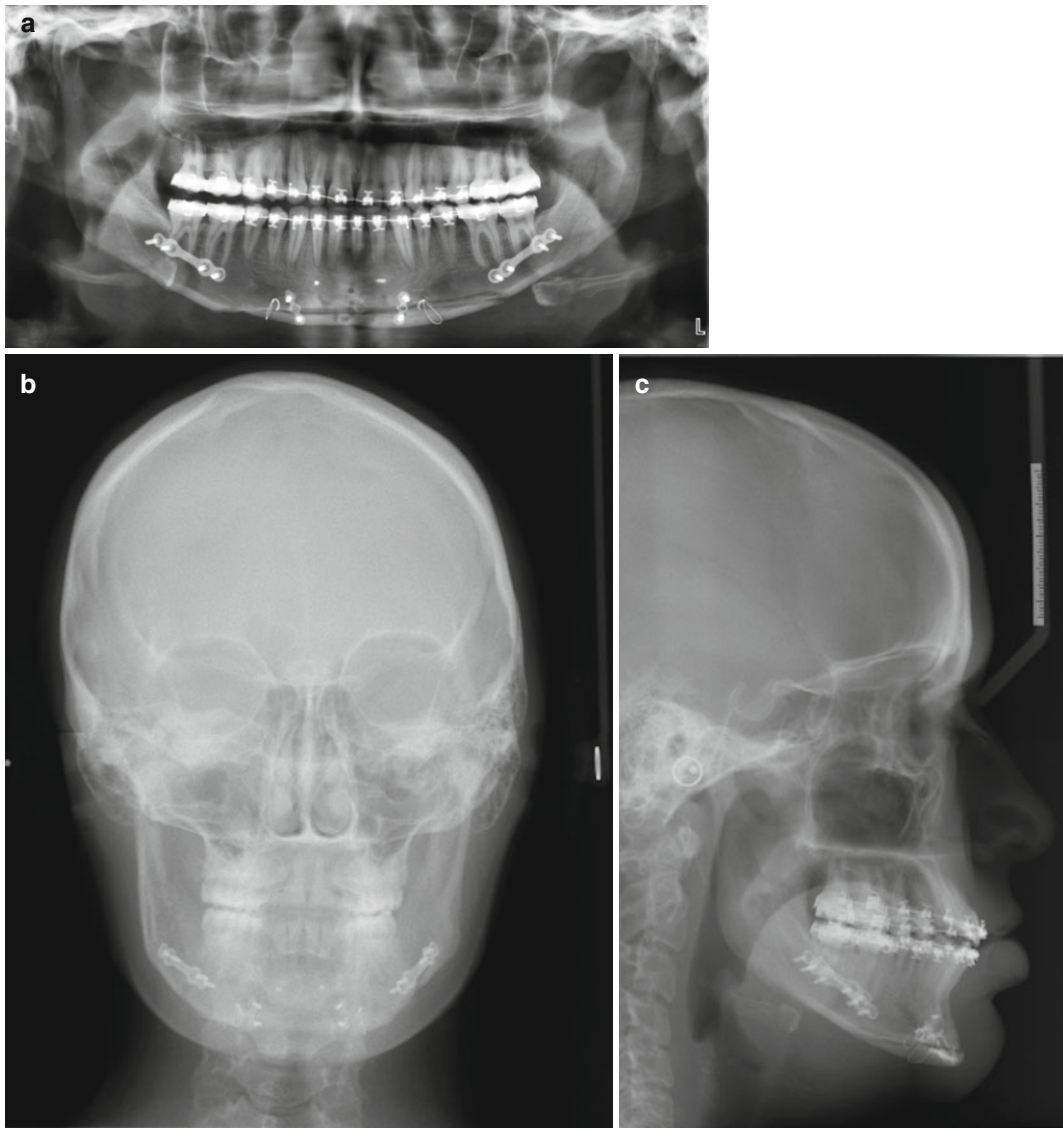

Fig. 18.8 Postoperative (**a**) panoramic radiograph, (**b**) AP, and (**c**) lateral cephalograms confirm correction of the asymmetry with leveling of the occlusal plane. (**d**, **e**) Two years follow-up demonstrated stability of the correction of the quiescent condylar hyperplasia without need for condylectomy

Fig. 18.8 (continued)

Skeletal scintigraphy with ^{99m}Tc-MDP and normalized data could potentially allow for a single time-point growth analysis. This would enable the clinician to efficiently determine the growth status of the patient and decrease the delay in operative treatment. In addition, ensuring growth cessation can decrease the need for reoperation due to postoperative growth [40]. Normative data was obtained using ^{99m}Tc-MDP planar scintigraphy utilizing the 4th lumbar vertebra as an internal standard for 90 patients with normal craniofacial growth [11, 20]. Based on a linear regression model, approximate age-matched normal RU ranges were proposed (Fig. 18.9a, b). In subsequent studies it was found that ^{99m}Tc-MDP SPECT using the clivus as an internal standard was more sensitive than planar scintigraphy [27]. In a study by Pripatnanont et al., who collected data from 29 subjects (5 normal, 26 with mandibular asymmetry), the authors found quantitative differences between patients with normal active growth when compared to those with asymmetric abnormal growth and skeletally mature patients [28]. Fahey et al. sought out to find quantitative normal values in a group of 32 normal subjects (22 females and 10 males) between the age of 8 and 25, who underwent SPECT scans for unrelated reasons. They used two-dimensional maximal counts and both an internal (clivus) and an external (beaker of known quantity of radiotracer) standard [40]. There was a significant correlation with nonstandardized and externally standardized data with age and no significant age correlation when using the internal standard. They

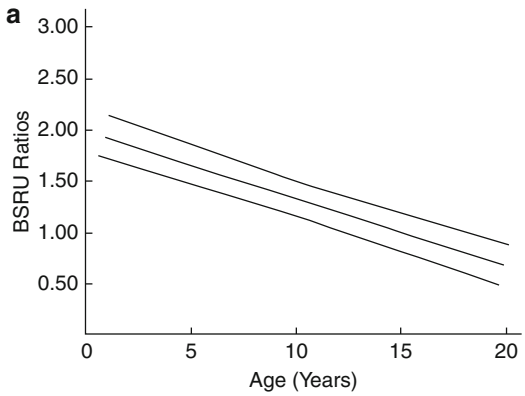

b

Age	Ratio*
0–2	2.0–1.85
2–5	1.85–1.65
5–10	1.65–1.30
10–15	1.30–1.10
15–20	1.10-0.7
20	< .70

*Approximate mean – graph shows standard deviation

Fig. 18.9 (**a**) The standard curve of bone-seeking radioisotope uptake by age for normal subjects and (**b**) normal uptake ratios based on the standard curve (From Cisneros and Kaban [15], with permission)

found that using the external standard allowed for increased sensitivity and a clear distinction between subjects who would be expected to be actively growing (under 17 years old) and those that were not. Future research aimed at standardizing the SPECT algorithm and how ROI's are analyzed and reported (2D versus 3D, maximum counts versus average counts) may improve the ability to compare individual SPECT data and increase the utility of SPECT for assessing normal growth.

Symmetric Abnormalities

Unilateral mandibular condylar abnormalities allow comparison to internal and external standards as well as the contralateral condyle. Bilaterally symmetric mandibular growth abnormalities provide additional challenge using SPECT. These abnormalities include progressive mandibular prognathism (symmetric condylar hyperplasia), idiopathic condylar resorption, and condylosis resulting from juvenile rheumatoid arthritis or other arthritides. Traditional SPECT assessment utilizing the R/L ratio would not enable the clinician to determine the activity of the disease [40]. Condylar growth is 98 % complete by the age of 15 and 18 in females and males, respectively. The average horizontal growth rate has been shown to be 1.6–2.2 mm per year [5]. Symmetric growth at a faster rate or longer duration has been proposed to represent bilateral condylar hyperplasia [5, 44]. Similarly, diagnosis of active or inactive symmetric condylar hyperplasia has relied upon serial clinical and cephalometric examination. Mandibular scintigraphy has yet to be established as an aid to diagnosis in symmetric overgrowth. This is postulated to be due to the relatively slow growth of the condyles compared to unilateral condylar hyperplasia preventing detection. Also, symmetric overgrowth often occurs during concurrent axial growth limiting comparisons to internal standards [5]. Future studies using SPECT with internal and external standardization normalized for age may increase the utility of SPECT in diagnosis and subsequent treatment of these patients.

Idiopathic condylar resorption (ICR) is a poorly understood condition affecting primarily females between the ages of 15 and 35 years [45]. It most often occurs bilaterally and typically progresses to the sigmoid notch of the mandible eliminating the entire condyle. This usually results in quiescence [46, 47]. Patients develop a progressive anterior open bite, disappearing chin, decreased mandibular range of motion, and often temporomandibular joint pain and crepitus [47–49]. Although the cause has not been elucidated, onset of disease has been associated with trauma, steroid use, autoimmune conditions, orthognathic surgery, and orthodontics [47].

Serial clinical and radiographic analysis including cephalograms and dental models are used to determine the disease activity. SPECT studies have recently been used to aid in determining the presence of active resorption [47, 50]. As with other growth abnormalities, the treatment options for ICR depend on the presence of active disease. Active resorption can be treated with (1) resection of the abnormal condyles (condylectomy) and reconstruction with a costochondral graft or (2) observation until quiescence is confirmed for at least 2 years and then treatment by orthognathic surgery if a functional joint remains [50]. The two-year period serves to reduce the possibility of reactivation of ICR and relapse of the surgical correction [47]. Current studies are investigating the use of SPECT to facilitate confirmation of activity or quiescence in ICR to reduce overall treatment time.

Fig. 18.10 (**a**) Frontal repose and (**b**) lateral views demonstrate poorly defined chin point and severely convex profile. (**c**) Panoramic radiograph and (**d**) lateral cephalogram show the shortened mandibular condyles bilaterally and the severe mandibular retrognathism

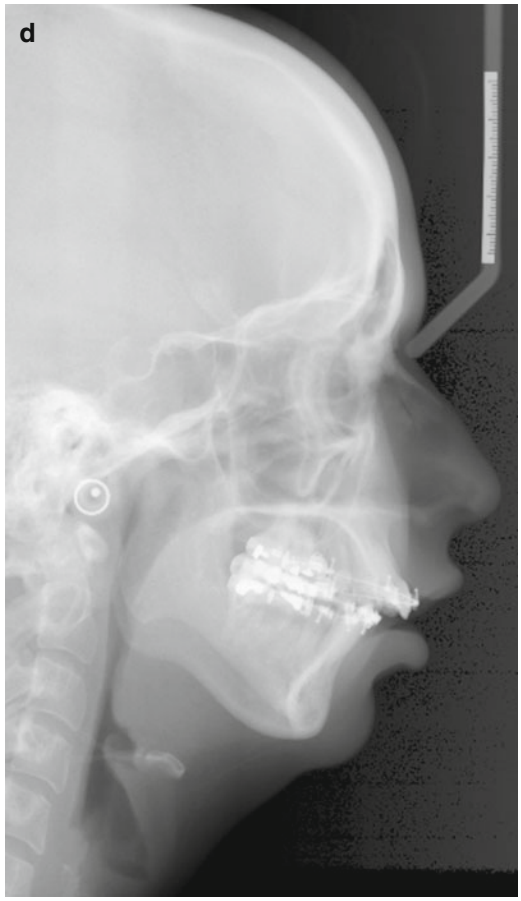

Fig. 18.10 (continued)

Clinical Case Example

MB is a 23-year-old woman with a complaint of a "disappearing chin." She had noted loss of her chin projection and pain in her bilateral temporomandibular joints. Clinical exam revealed a severely convex profile and retruded mandible (Fig. 18.10a, b). A panoramic radiograph and lateral cephalogram revealed shortened mandibular condyles bilaterally and clockwise rotation of the mandible (Fig. 18.10c–d). A negative autoimmune workup ruled out inflammatory arthropathy, and a diagnosis of idiopathic condylar resorption was made. A planar bone scan was obtained which revealed increased uptake in both mandibular condyles. The right side had higher uptake than the left which corroborated with the presence of more resorption on the right and chin deviation to the right (Fig. 18.11). The patient underwent endoscopic condylectomy bilaterally as well as Le Fort I osteotomy to correct the occlusal plane. The condyles were reconstructed using costochondral rib grafts as demonstrated by postoperative panoramic and lateral cephalometric radiographs (Fig. 18.12a, b). Two years postoperatively, the improvement in her profile remained (Fig. 18.12c).

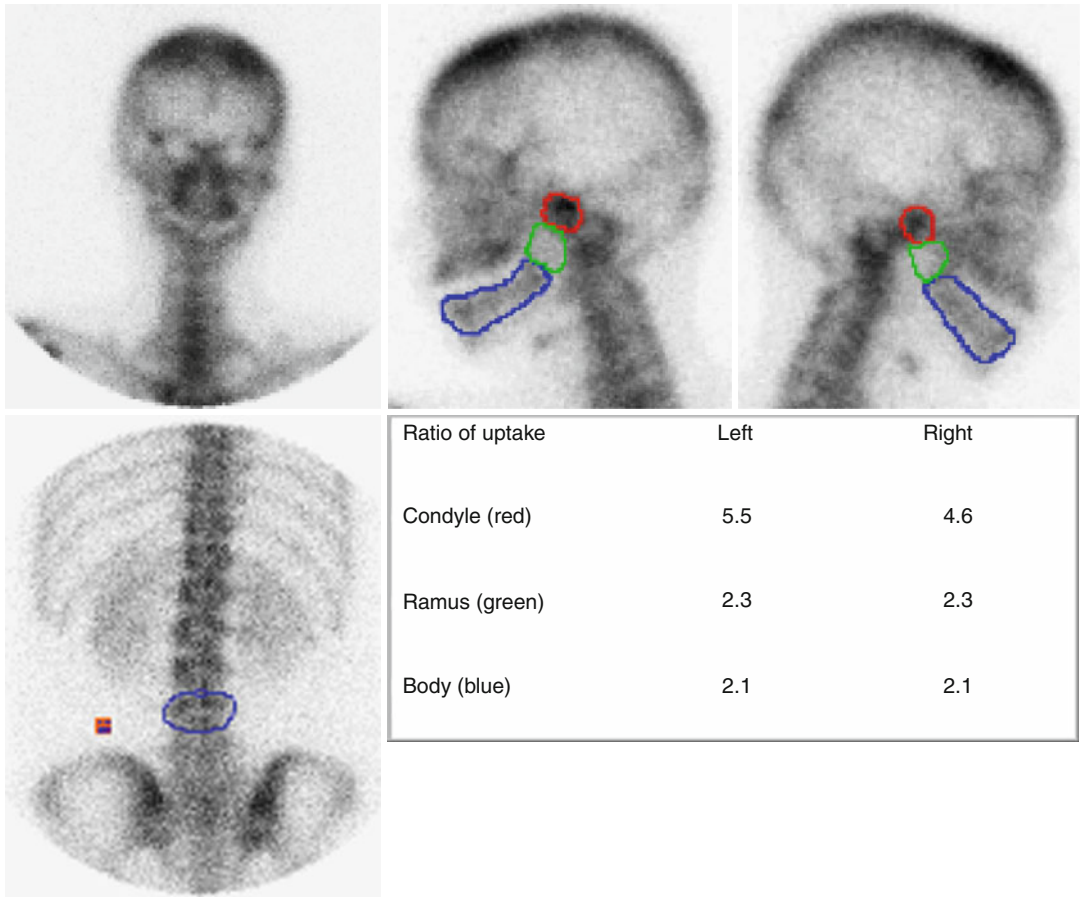

Ratio of uptake	Left	Right
Condyle (red)	5.5	4.6
Ramus (green)	2.3	2.3
Body (blue)	2.1	2.1

Fig. 18.11 Planar scan showing increased uptake in the mandibular condyles bilaterally when compared to the internal standard L4 (*blue*) in bottom left picture indicating active condylar resorption bilaterally

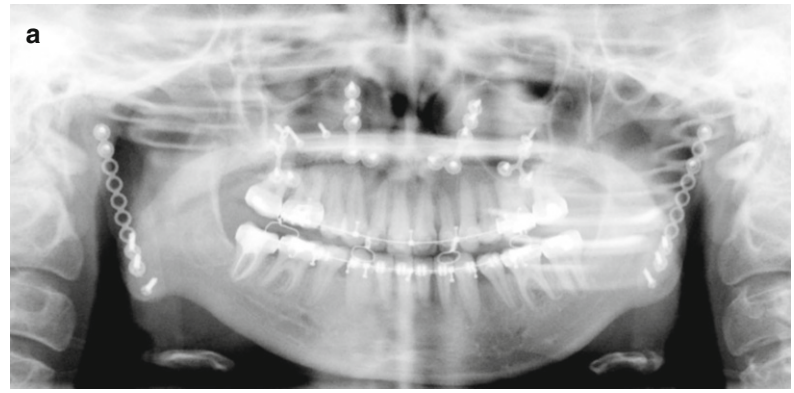

Fig. 18.12 Postoperative (**a**) panoramic radiograph after bilateral condylectomy and costochondral grafts placed to reconstruct the mandibular condyles. (**b**, **c**) Lateral cephalogram and photograph showing improvement in the sagittal projection of the mandible and improvement in facial profile

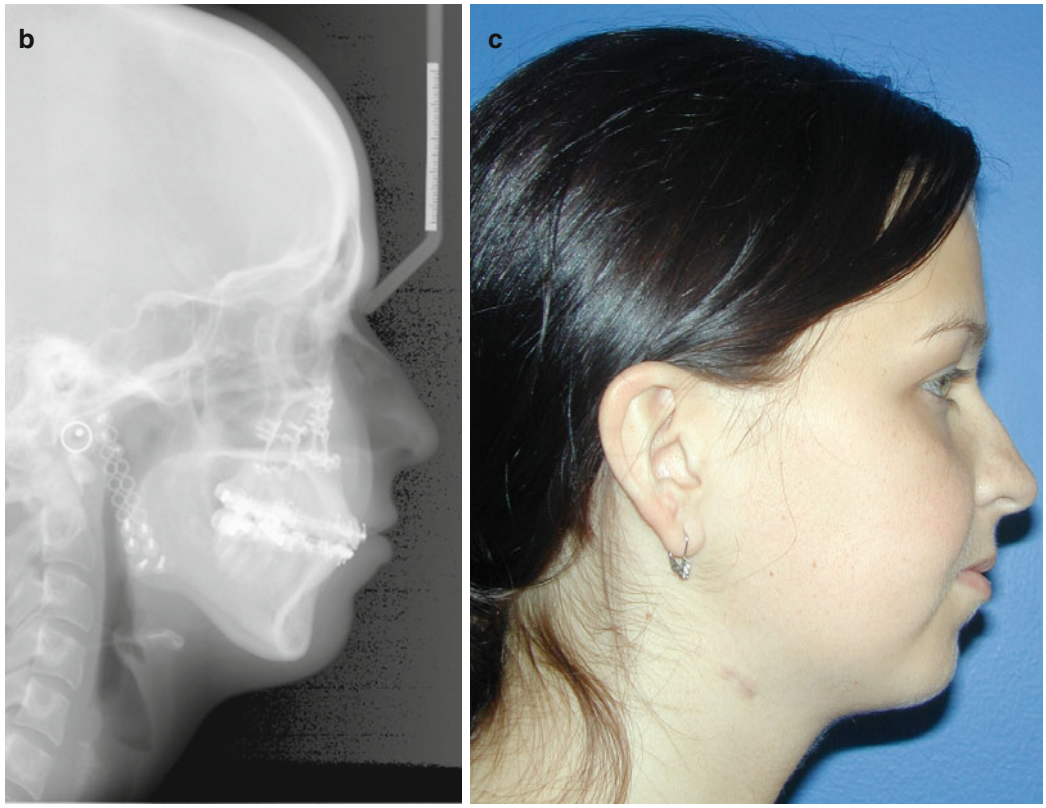

Fig. 18.12 (continued)

Conclusion

Skeletal scintigraphy is a useful tool for physiologic assessment of mandibular growth abnormalities especially that of condylar over- or undergrowth. The timing and type of operative correction is aided by the use of scintigraphy.

References

1. Kaban LB. Acquired abnormalities of the temporomandibular joint. In: Kaban LB, Troulis MJ, editors. Pediatric oral and maxillofacial surgery. New York: Elsevier; 2004. p. 340–76.
2. Gottlieb O. Hyperplasia of the mandibular condyle. J Oral Surg (Chic). 1951;9(2):118–35.
3. Obwegeser HL, Makek MS. Hemimandibular hyperplasia–hemimandibular elongation. J Maxillofac Surg. 1986;14(4):183–208.
4. Hampf G, Tasanen A, Nordling S. Surgery in mandibular condylar hyperplasia. J Maxillofac Surg. 1985;13(2):74–8.
5. Wolford LM, et al. Efficacy of high condylectomy for management of condylar hyperplasia. Am J Orthod Dentofacial Orthop. 2002;121(2):136–50; discussion 150–1.
6. Lippold C, et al. Treatment of hemimandibular hyperplasia: the biological basis of condylectomy. Br J Oral Maxillofac Surg. 2007;45(5):353–60.
7. Kaban LB. Mandibular asymmetry and the fourth dimension. J Craniofac Surg. 2009;20 Suppl 1:622–31.
8. Edler R, Wertheim D, Greenhill D. Comparison of radiographic and photographic measurement of mandibular asymmetry. Am J Orthod Dentofacial Orthop. 2003;123(2):167–74.
9. Alexander JM. Radionuclide bone scanning in the diagnosis of lesions of the maxillofacial region. J Oral Surg. 1976;34(3):249–56.
10. Beirne OR, Leake DL. Technetium 99m pyrophosphate uptake in a case of unilateral condylar hyperplasia. J Oral Surg. 1980;38(5):385–6.
11. Kaban LB, et al. Assessment of mandibular growth by skeletal scintigraphy. J Oral Maxillofac Surg. 1982;40(1):18–22.
12. Kaban LB, Treves ST, Pogrel MA, Hattner RS. Skeletal scintigraphy for assessment of mandibular asymmetry. In: Treves ST, editor. Pediatric nuclear medicine. New York: Springer; 1995.

13. Pogrel MA, et al. A comparison of single-photon emission computed tomography and planar imaging for quantitative skeletal scintigraphy of the mandibular condyle. Oral Surg Oral Med Oral Pathol Oral Radiol Endod. 1995;80(2):226–31.
14. Kao YH, Magsombol BM, Ng DC. The potential of hybrid SPECT/CT fusion imaging to improve diagnostic accuracy in the scintigraphic quantitative functional assessment of suspected unilateral mandibular hyperactivity. Oral Maxillofac Surg. 2012;16(1):89–93.
15. Cisneros GJ, Kaban LB. Computerized skeletal scintigraphy for assessment of mandibular asymmetry. J Oral Maxillofac Surg. 1984;42(8):513–20.
16. Melsen B. The cranial base. Acta Odontol Scand. 1974;32 suppl 62:86–101.
17. Egyedi P. Aetiology of condylar hyperplasia. Aust Dent J. 1969;14(1):12–7.
18. Yang J, Lignelli JL, Ruprecht A. Mirror image condylar hyperplasia in two siblings. Oral Surg Oral Med Oral Pathol Oral Radiol Endod. 2004;97(2):281–5.
19. Oberg T, et al. Unilateral hyperplasia of the mandibular condylar process. A histological, microradiographic, and autoradiographic examination of one case. Acta Odontol Scand. 1962;20:485–504.
20. Cisneros GJ. The use of bone seeking radiopharmaceutical uptake in the assessment of facial growth and development. Harvard University: Cambridge, MA; 1982.
21. Front D, et al. Quantitative bone scintigraphy using SPECT. J Nucl Med. 1989;30(2):240–5.
22. Kircos LT, Carey Jr JE, Keyes Jr JW. Quantitative organ visualization using SPECT. J Nucl Med. 1987;28(3):334–41.
23. Kircos LT, et al. Bayesean-deblurred planar and SPECT nuclear bone imaging for the demonstration of facial anatomy and craniomandibular disorders. Oral Surg Oral Med Oral Pathol. 1988;66(1):102–10.
24. Kircos LT, et al. Emission imaging of patients with craniomandibular dysfunction. Oral Surg Oral Med Oral Pathol. 1988;65(2):249–54.
25. Hodder SC, et al. SPECT bone scintigraphy in the diagnosis and management of mandibular condylar hyperplasia. Br J Oral Maxillofac Surg. 2000; 38(2):87–93.
26. Norman JE. Re: Hodder et al. SPECT bone scintigraphy in the diagnosis and management of mandibular condylar hyperplasia. Br J Oral Maxillofac Surg 2000;38:87–93. Br J Oral Maxillofac Surg. 2001;39(3):244–5.
27. Chan WL, et al. Planar versus SPET imaging in the assessment of condylar growth. Nucl Med Commun. 2000;21(3):285–90.
28. Pripatnanont P, et al. The use of SPECT to evaluate growth cessation of the mandible in unilateral condylar hyperplasia. Int J Oral Maxillofac Surg. 2005;34(4):364–8.
29. Kajan ZD, et al. Assessment of growth activity in the mandibular condyles by single-photon emission computed tomography (SPECT). Aust Orthod J. 2006;22(2):127–30.
30. Israel O, et al. Normal and abnormal single photon emission computed tomography of the skull: comparison with planar scintigraphy. J Nucl Med. 1988;29(8):1341–6.
31. Saridin CP, et al. Comparison of planar bone scintigraphy and single photon emission computed tomography in patients suspected of having unilateral condylar hyperactivity. Oral Surg Oral Med Oral Pathol Oral Radiol Endod. 2008;106(3): 426–32.
32. Saridin CP, et al. Comparison of different analytical methods used for analyzing SPECT scans of patients with unilateral condylar hyperactivity. Int J Oral Maxillofac Surg. 2009;38(9):942–6.
33. Turvey TA, Simmons KE. Orthognathic surgery before completion of growth. Oral Maxillofac Surg Clin North Am. 1994;6:121.
34. Sierra AM. Assessment of dental and skeletal maturity. A new approach. Angle Orthod. 1987;57(3): 194–208.
35. Hunter CJ. The correlation of facial growth with body height and skeletal maturation at adolescence. Angle Orthod. 1966;36(1):44–54.
36. Singh IJ, Savara BS. Norms of size and annual increments of seven anatomical measures of maxillae in girls from three to sixteen years of age. Angle Orthod. 1966;36(4):312–24.
37. Savara BS, Singh IJ. Norms of size and annual increments of seven anatomical measures of maxillae in boys from three to sixteen years of age. Angle Orthod. 1968;38(2):104–20.
38. Gomes AS, Lima EM. Mandibular growth during adolescence. Angle Orthod. 2006;76(5):786–90.
39. Moss ML. Vertical growth in the human face. Am J Orthod. 1964;50:121.
40. Fahey FH, et al. Use of (99m)Tc-MDP SPECT for assessment of mandibular growth: development of normal values. Eur J Nucl Med Mol Imaging. 2010;37(5):1002–10.
41. Greulich W, Pyle S. Radiographic atlas of skeletal development of the hand and wrist. Palo Alto: Stanford University Press; 1959.
42. Gandini P, Mancini M, Andreani F. A comparison of hand-wrist bone and cervical vertebral analyses in measuring skeletal maturation. Angle Orthod. 2006;76(6):984–9.
43. Hassel B, Farman AG. Skeletal maturation evaluation using cervical vertebrae. Am J Orthod Dentofacial Orthop. 1995;107(1):58–66.
44. Wolford LM, et al. Surgical management of mandibular condylar hyperplasia type 1. Proc (Bayl Univ Med Cent). 2009;22(4):321–9.

45. Huang YL, Pogrel MA, Kaban LB. Diagnosis and management of condylar resorption. J Oral Maxillofac Surg. 1997;55(2):114–9; discussion 119–20.
46. Rabey GP. Bilateral mandibular condylysis-a morph-analytic diagnosis. Br J Oral Surg. 1977;15(2):121–34.
47. Papadaki ME, et al. Condylar resorption. Oral Maxillofac Surg Clin North Am. 2007;19(2):223–34. vii.
48. Arnett GW, Milam SB, Gottesman L. Progressive mandibular retrusion–idiopathic condylar resorption. Part I. Am J Orthod Dentofacial Orthop. 1996; 110(1):8–15.
49. Arnett GW, Milam SB, Gottesman L. Progressive mandibular retrusion-idiopathic condylar resorption. Part II. Am J Orthod Dentofacial Orthop. 1996; 110(2):117–27.
50. Troulis MJ, et al. Condylectomy and costochondral graft reconstruction for treatment of active idiopathic condylar resorption. J Oral Maxillofac Surg. 2008;66(1):65–72.

Neuroblastoma: Functional Imaging

19

Susan E. Sharp, Michael J. Gelfand, and Barry L. Shulkin

Neuroblastoma, ganglioneuroblastoma, and ganglioneuroma are tumors derived from primitive neural crest cells of the sympathetic nervous system. Neuroblastoma and ganglioneuroblastoma are usually grouped together for clinical purposes as both contain undifferentiated neuroblasts with malignant or potentially malignant behavior. In contrast, ganglioneuroma is a benign tumor containing only mature ganglion cells and other mature tissues [1].

Neuroblastoma is the most common extracranial solid tumor of childhood, comprising approximately 8 % of pediatric cancers. Median age at diagnosis is 15 months, with the vast majority of patients presenting during infancy or early childhood [2].

S.E. Sharp, MD (✉)
Department of Radiology,
Cincinnati Children's Hospital Medical Center,
University of Cincinnati College of Medicine,
Cincinnati, OH, USA
e-mail: susan.sharp@cchmc.org

M.J. Gelfand, MD
Section of Nuclear Medicine,
Department of Radiology,
Cincinnati Children's Hospital Medical Center,
Cincinnati, OH, USA

B.L. Shulkin, MD, MBA
Division of Nuclear Medicine,
Department of Radiological Sciences,
St. Jude Children's Research Hospital,
Memphis, TN, USA
e-mail: barry.shulkin@stjude.org

Neuroblastoma can arise anywhere along the sympathetic chain. Primary tumors most commonly occur in the adrenal gland (35 %), retroperitoneum (30–35 %), or posterior mediastinum (20 %) with pelvic and cervical primary sites less frequently seen (<5 %), respectively. Neuroblastoma rarely can present with metastatic disease without an identifiable primary tumor [1].

Metastatic disease is seen in more than half of neuroblastoma patients at diagnosis. Bone marrow and cortical bone are the most frequent metastatic sites, with lymph node and hepatic metastases also commonly seen. Lung and central nervous system metastases are rare and associated with very poor outcomes [3].

Neuroblastoma is staged using the International Neuroblastoma Staging System (INSS) which was developed in 1988 and revised in 1993 as summarized in Table 19.1 [4]. Presurgical staging of localized disease cannot be performed using the INSS, as staging is based on the extent of tumor resection and surgical assessment of lymph node involvement.

In 2009, the International Neuroblastoma Risk Group Staging System (INRGSS) was described, allowing presurgical staging of localized tumors as summarized in Table 19.2 [5]. The INRGSS uses imaging-defined risk factors to help predict surgical risk and surgical outcome [5–7]. The INRGSS also raises the age cutoff for the special stage used in infants with distant metastatic involvement limited to liver, skin, and/or bone marrow. This change reflects recent literature which suggests that a cutoff of 18 months more

S.T. Treves (ed.), *Pediatric Nuclear Medicine and Molecular Imaging*,
DOI 10.1007/978-1-4614-9551-2_19,

Table 19.1 Summary of the International Neuroblastoma Staging System (INSS)

Stage	Description
1	Localized tumor with complete gross excision. Negative ipsilateral lymph nodes (unless adherent to and removed with the tumor)
2A	Localized tumor with incomplete gross excision. Negative nonadherent ipsilateral lymph nodes
2B	Localized tumor with or without complete gross excision. Positive nonadherent ipsilateral lymph nodes
3	Unresectable tumor infiltrating across the midline with or without positive regional lymph nodes, localized unilateral tumor with positive contralateral lymph nodes, or midline tumor with bilateral extension by infiltration or lymph node involvement
4	Any primary tumor with distant metastatic disease (except stage 4s)
4s	Localized primary tumor (as defined by stage 1, 2A, or 2B) with distant metastatic disease limited to the skin, liver, and/or bone marrow in patients less than 12 months of age

From Brodeur et al. [4]. Reprinted with permission. Copyright 1993 American Society of Clinical Oncology. All rights reserved

Table 19.2 Summary of the International Neuroblastoma Risk Group Staging System (INRGSS)

Stage	Description
L1	Localized tumor without image-defined risk factors[a] and confined to one body compartment[b]
L2	Locoregional tumor with one or more image-defined risk factors[a]
M	Distant metastatic disease (except stage MS)
MS	Distant metastatic disease confined to skin, liver, and/or bone marrow in patients less than 18 months of age

From Monclair et al. [5]. Reprinted with permission. Copyright 2009 American Society of Clinical Oncology. All rights reserved

[a]Imaging defined risk factors include, but are not limited to, encasement of major vascular structures and invasion of adjacent organs

[b]Body compartments include the neck, chest, abdomen, and pelvis. Contiguous disease involvement of more than one body compartment (e.g., upper abdominal tumor with positive ipsilateral inferior mediastinal lymph nodes) would make a patient stage L2

accurately predicts outcome [8–12]. The INRGSS is meant to be used in conjunction with, but not replace, the INSS [5, 6].

The prognosis of neuroblastoma is widely variable. Some neuroblastomas spontaneously regress or mature without therapy, while others progress to widespread and fatal disease in spite of intensive multimodality therapy [8, 13, 14]. Neuroblastoma patients are divided into risk groups to guide therapy and predict outcomes. Risk groups are based on stage, age, and biologic tumor factors (such as histology, DNA ploidy, and MYCN amplification) [8, 13, 15].

Low-risk disease is treated with surgery or supportive care alone with survival rates of greater than 95 % [15–21]. Intermediate-risk disease is treated with surgery and chemotherapy with survival rates of greater than 90 % [15, 16, 22–24]. In contrast, high-risk disease is treated with intensive multimodality therapy (including high-dose chemotherapy, radiation therapy, and stem cell transplantation) with long-term survival rates of approximately 30–40 % [15, 16, 25, 26].

Multiple clinical and imaging tests are used in neuroblastoma, both at diagnosis and during follow-up, to ensure accurate disease assessment. Clinical testing includes bone marrow biopsy and urine catecholamine levels. Imaging evaluation includes both anatomic and functional imaging modalities [27, 28].

CT and MRI are the anatomic imaging modalities recommended for neuroblastoma. They are used to evaluate the primary tumor and involved lymph nodes, including 3D measurements and assessment of imaging-defined risk factors [4–6, 29–34]. MRI is the preferred anatomic imaging modality for tumors which extend into the spinal canal [33–35].

Iodine-123-MIBG is the recommended first-line functional imaging agent for neuroblastoma, allowing visualization of the primary tumor and metastatic sites. Technetium-99m-MDP bone scans and/or ^{18}F-FDG PET scans are recommended for evaluation of MIBG-negative patients [4–6].

Multiple novel PET radiopharmaceuticals have been investigated for use in neuroblastoma, including ^{11}C-hydroxyephedrine (^{11}C- HED), ^{11}C-epinephrine, ^{18}F-fluorodopamine (F-18 DA), ^{18}F-dihydroxyphenylalanine (^{18}F-DOPA), ^{18}F-fluorothymidine (^{18}F-FLT),

^{68}Ga-DOTA-Tyr3-octreotide (^{68}Ga-DOTATOC), ^{18}F-fluoro-3-iodobenzylguanidine (FIBG), and P-^{18}F-fluorobenzylguanidine (PFBG) [36–50]. However, regulatory issues and the PET chemistry expertise needed for synthesis limit availability of these novel radiopharmaceuticals, making it unlikely that they will have a major role in neuroblastoma imaging in the near future. The remainder of this chapter will discuss ^{123}I-MIBG, ^{99m}Tc-MDP, and ^{18}F-FDG imaging of neuroblastoma.

Metaiodobenzylguanidine (MIBG) Scintigraphy

MIBG is related to norepinephrine, entering neural crest cells via the type I catecholamine reuptake system with concentration in the cell cytoplasm. MIBG is highly specific for neuroendocrine tumors, such as neuroblastoma and pheochromocytoma [51–55].

Iodine-131-MIBG was initially used for neuroblastoma imaging [56, 57], as ^{123}I-MIBG was not FDA approved in the USA until 2008. However, ^{123}I-MIBG is now commercially available and preferred for diagnostic imaging as it gives superior image quality at a lower patient radiation dose [58]. Administered doses of ^{131}I-MIBG are limited by its relatively long physical half-life (8 days), high-energy photon (364 keV), and beta particle emission. In contrast, ^{123}I-MIBG has a shorter physical half-life (13 h) and an ideal photon energy for gamma camera and SPECT imaging (159 keV), without beta particle emission.

Patient Preparation

Thyroid uptake of free iodide should be blocked by administration of saturated solution of potassium iodide (SSKI). The dosage and timing of SSKI administration vary with local practice. Although a single SSKI dose at the time of MIBG injection has been shown to adequately block thyroid uptake [59], many sites will administer SSKI doses for 2–3 days starting on the day before ^{123}I-MIBG administration [60–62].

Numerous medications interfere with MIBG uptake, with potential to affect the results of MIBG imaging. Some of these medications (such as phenylephrine, tricyclic antidepressants, and labetalol) are used in children. Medications should therefore be reviewed when scheduling MIBG imaging. Any interfering medications should be discussed with the referring physician with discontinuation for an appropriate time frame when possible [60].

Imaging Technique

The North American Consensus Guidelines recommend an ^{123}I-MIBG administered activity of 0.14 mCi/kg (5.2 MBq/kg) with a minimum dose of 1 mCi (37 MBq) and a maximum dose of 10 mCi (370 MBq); alternatively the European Association of Nuclear Medicine dosage card may be used for patients weighing more than 10 kg [63].

Planar and SPECT (and/or SPECT/CT) imaging typically is performed 24 h after ^{123}I-MIBG injection. Planar imaging includes anterior and posterior whole-body images, which can be performed as overlapping spot images or as a whole-body acquisition. Whole-body planar images are frequently supplemented with lateral views of the skull. Additional planar images can be performed at 48 h if needed to clarify uptake abnormalities or allow clearance of bowel activity [60–62].

SPECT generally includes the abdomen or the primary tumor site if it lies outside of the abdomen. SPECT often improves diagnostic accuracy and certainty of lesion detection, especially for small lesions or lesions near sites of physiologic uptake. SPECT also improves anatomic localization and facilitates correlation with CT and MRI [64–66]. SPECT images can be co-registered and fused to separately acquired CT and MRI studies if patient positioning is similar.

Integrated SPECT/CT (with imaging performed on the same gantry) has more recently become an important diagnostic tool in oncology patients. In comparison to SPECT alone, SPECT/CT further improves MIBG uptake localization and certainty of lesion detection [67–70].

Medium-energy collimators are preferred over low-energy high-resolution collimators for both

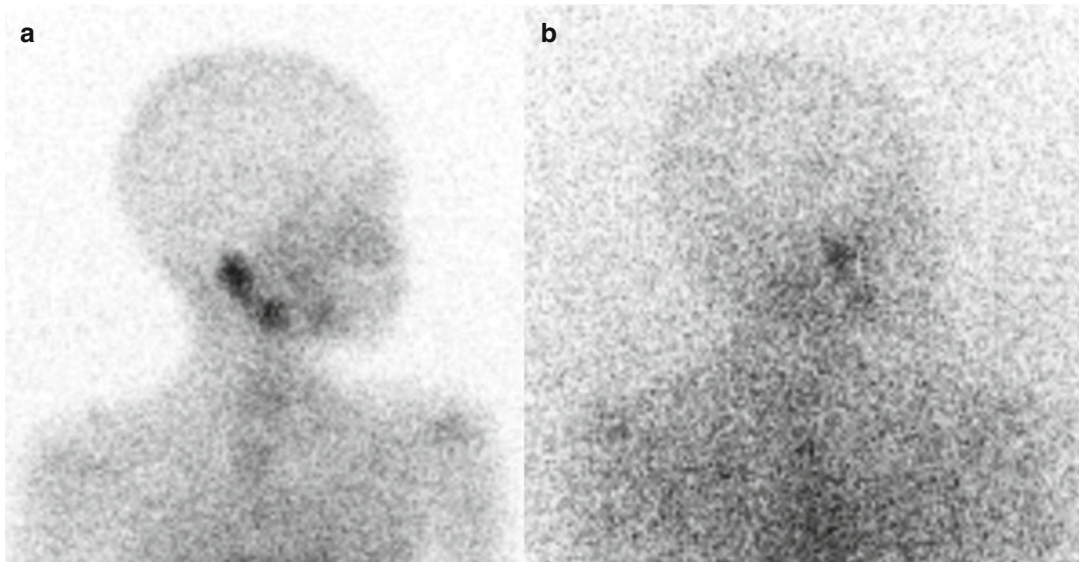

Fig. 19.1 Lateral planar ^{123}I-MIBG images of the skull obtained with (**a**) medium-energy and (**b**) low-energy high-resolution collimators. Use of medium-energy collimation gives higher image quality. Differences in image quality occur at all body masses but become more apparent as patient size increases

planar and SPECT acquisition. Approximately 3 % of photons emitted by ^{123}I-MIBG have energies above 400 keV. Medium-energy collimators significantly reduce septal penetration from these high-energy photons, improving image quality (Fig. 19.1) [71]. Sedation is required for children who are unable to remain still during planar and SPECT imaging. Toilet-trained patients should be encouraged to void prior to imaging.

Clinical Applications

Iodine-123-MIBG imaging is recommended to evaluate neuroblastoma at diagnosis and to monitor MIBG-avid disease during and after therapy (Figs. 19.2 and 19.3) [4–6, 62]. Iodine-123-MIBG imaging also is necessary to determine eligibility for ^{131}I-MIBG therapy, as documentation of MIBG-avid disease is needed prior to treatment. The International Neuroblastoma Risk Group Task Force recently developed guidelines for the evaluation of disease extent by ^{123}I-MIBG scans [62].

Iodine-123-MIBG has a sensitivity of 88–93 % and a specificity of 83–92 % in neuroblastoma [64]. More than 90 % of neuroblastomas will demonstrate MIBG uptake, allowing visualization of both the primary tumor and metastatic sites. At diagnosis, ^{123}I-MIBG imaging is a sensitive whole-body method to evaluate both soft tissue and cortical bone/bone marrow disease. It is therefore an essential tool for initial staging [62].

During therapy, ^{123}I-MIBG imaging is useful for assessing disease response. At the primary tumor site, MIBG imaging differentiates residual active tumor from post-therapy changes which may be seen on CT or MR [62]. MIBG imaging depicts response of cortical bone metastases to therapy, while bone scan and CT may give false-positive results due to continued bone healing in the absence of tumor [27, 72]. MIBG imaging also depicts response of bone marrow metastases to therapy, while interpretation of MRI and ^{18}F-FDG PET scans may be complicated by post-therapy bone marrow changes [73–76].

During surveillance, ^{123}I-MIBG has been shown to be highly sensitive for relapsed bone metastases, with a detection rate of 94 % (compared to 43 % for ^{18}F-FDG PET) [62, 77]. Iodine-123-MIBG imaging also has been shown

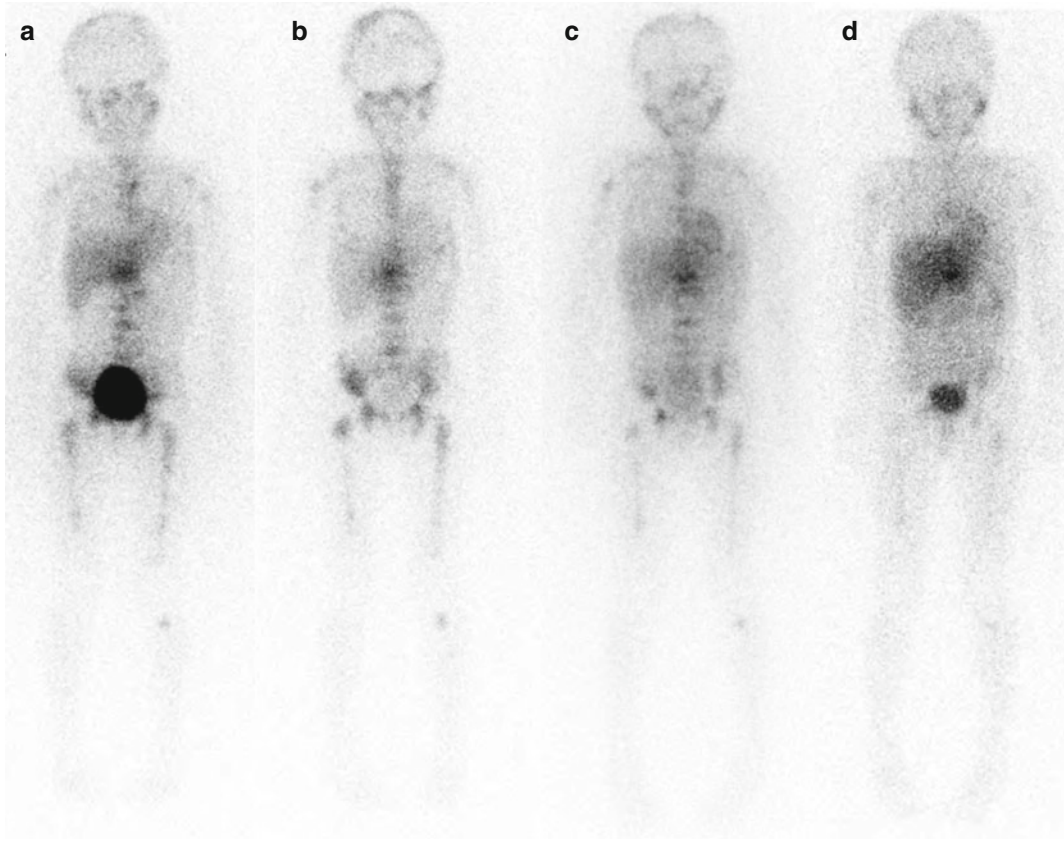

Fig. 19.2 Serial anterior planar ^{123}I-MIBG images obtained in a stage 4 patient. (**a**) At diagnosis, uptake is seen in the midline upper abdominal primary tumor and extensive metastases throughout the appendicular and axial skeleton, including the skull. (**b**) At 6 weeks and (**c**) at 6 months, persistent uptake is seen in both the primary tumor and diffuse skeletal metastases. (**d**) At 12 months, some improvement is seen in skeletal metastatic disease

to be a sensitive method to evaluate for unsuspected disease relapse, with a detection rate of 82 % (compared to 36 % for bone scan and 34 % for bone marrow biopsy) [78].

The results of ^{123}I-MIBG imaging can have prognostic implications. At diagnosis, the extent of MIBG-avid disease may predict response to chemotherapy in children over 1 year of age who have metastatic disease [79]. After initial chemotherapy, persistence of ^{123}I-MIBG uptake in cortical bone and bone marrow may be associated with poor prognosis [80–82]. During surveillance, high-risk patients with unsuspected relapses detected by ^{123}I-MIBG may have longer survival times than high-risk patients with symptomatic relapses [78].

Semiquantitative scoring systems have been described for MIBG imaging of neuroblastoma, with scores correlating with response and survival in some but not all studies [79, 83–89]. Although not yet widely used in clinical practice, scoring systems have been used in research trials to improve interobserver agreement and precision of reporting. Scoring systems divide the skeleton into 6–12 compartments, with each compartment scored for disease extent. The individual compartment scores are added together to give a cumulative score. The Children's Oncology Group (COG) and the New Approaches to Neuroblastoma Therapy (NANT) consortium use the Curie scoring system (Fig. 19.4) [62, 83].

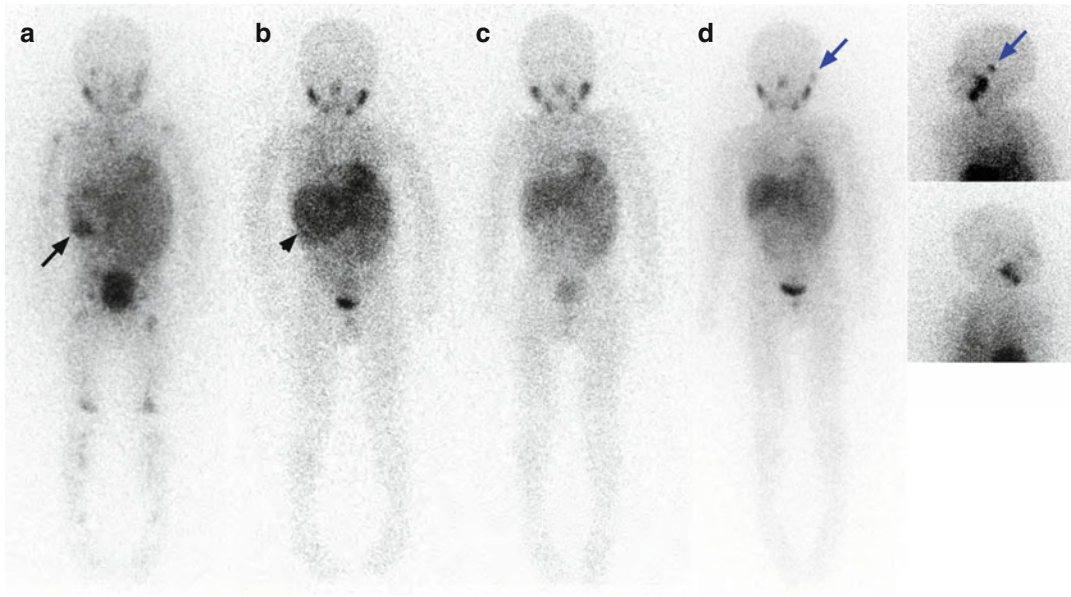

Fig. 19.3 Serial anterior planar ^{123}I-MIBG images obtained in a stage 4 patient. (**a**) At diagnosis, uptake is seen in the right upper quadrant primary tumor (*black arrow*) and scattered skeletal metastases. (**b**) At 1 month, no abnormal skeletal uptake is seen with only minimal residual uptake at the primary tumor site (*black arrowhead*), better demonstrated on SPECT imaging (not shown). (**c**) At 6 months, ^{123}I-MIBG images have normalized. (**d**) At 18 months, an unsuspected recurrence is seen in the left temporal bone (*blue arrows*)

Potential Pitfalls

False-Positive Studies

Physiologic MIBG uptake is normally seen in the salivary glands, olfactory mucosa, myocardium, liver, and bowel. Physiologic adrenal gland activity also may be demonstrated, especially after contralateral adrenalectomy. Urinary excretion of ^{123}I-MIBG results in physiologic accumulation in the kidneys and bladder. Low-level uptake also may be seen in the lungs on 24-h images [90, 91]. More focal lung uptake has been described in areas of atelectasis and pneumonia, but this is rarely seen [92, 93]. Physiologic uptake of ^{123}I-MIBG in brown adipose tissue is, most often seen in the neck and supraclavicular regions [94, 95].

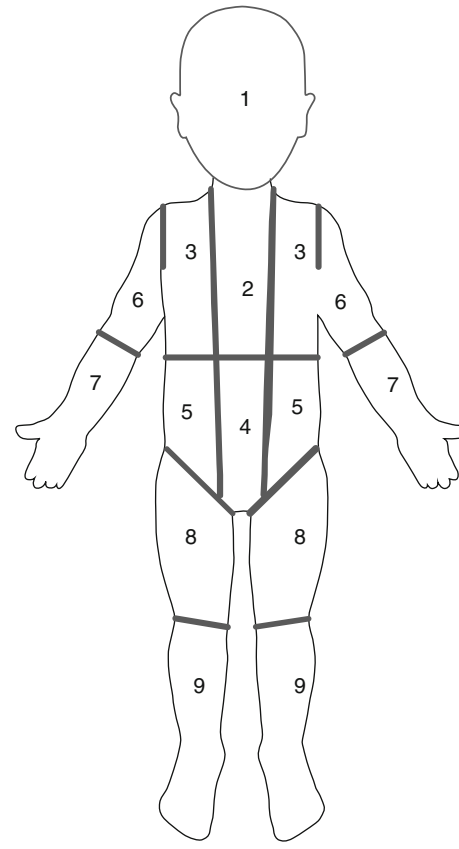

Fig. 19.4 The Curie scoring system divides the skeleton into nine compartments with a tenth compartment used for soft tissue disease. Each compartment is scored for disease extent, where *0* no disease sites, *1* one disease site, *2* more than one disease site (<50 % involvement), and *3* diffuse disease (>50 % involvement). Compartment scores are added together to give a cumulative score

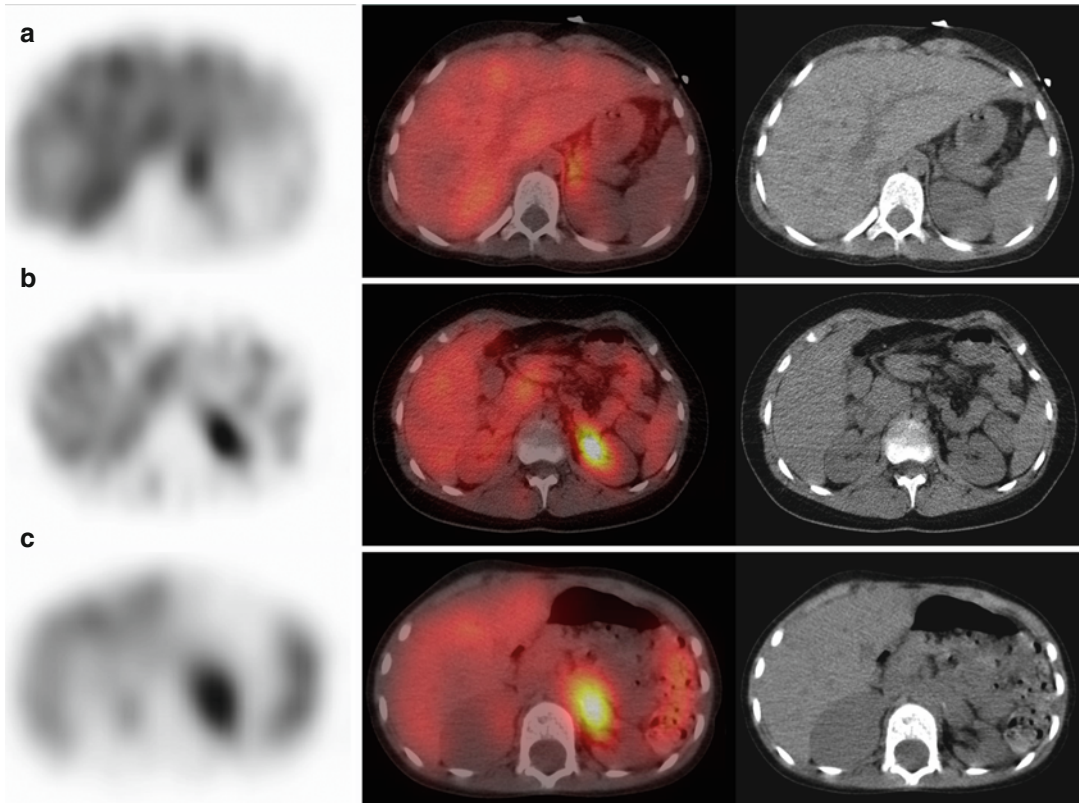

Fig. 19.5 Iodine-123-MIBG SPECT/CT images in three different patients with focal uptake in the left retroperitoneum. (**a**) Physiologic uptake in the normal left adrenal gland. (**b**) Physiologic accumuation in the left renal pelvis reflects urinary excretion of tracer. (**c**) Abnormal uptake in a residual left retroperitoneal soft tissue mass in the region of the renal vessels represents neuroblastoma; the left kidney is noted to be atrophic with compensatory hypertrophy of the right kidney

Misinterpretation of physiologic foci of uptake can result in false-positive MIBG studies [64, 96, 97]. Alternatively, areas of physiologic uptake can obscure small areas of tumor uptake [28]. SPECT and SPECT/CT can improve diagnostic accuracy in areas where physiologic uptake and tumor are both common, especially the retroperitoneum and upper abdomen (Fig. 19.5) [64–70].

The right and left hepatic lobes normally demonstrate significant differences in uptake, with relatively higher uptake in the left hepatic lobe [98]. Physiologic ^{123}I-MIBG uptake in the liver is often heterogeneous, especially on SPECT images. Liver uptake must therefore be interpreted with caution to avoid false-positive studies [66]. Hepatic metastases can be demonstrated with ^{123}I-MIBG, although small metastases may be difficult to visualize. Correlation with CT or MRI is often helpful when hepatic metastases are suspected (Fig. 19.6).

Iodine-123 MIBG uptake in mature ganglioneuromas or other neuroendocrine tumors can be falsely interpreted as uptake in neuroblastoma [64, 96].

False-Negative Studies

Less than 10 % of neuroblastomas demonstrate no MIBG uptake, resulting in false-negative studies. Some neuroblastomas will be MIBG-negative at diagnosis, while others become MIBG-negative during therapy. Patients can have both MIBG-avid and non-avid disease sites at the same time [99–101].

False-negative MIBG studies are also seen in patients with minimal residual disease after therapy [64]. Iodine-123-MIBG can fail to detect subtle bone marrow involvement, usually when

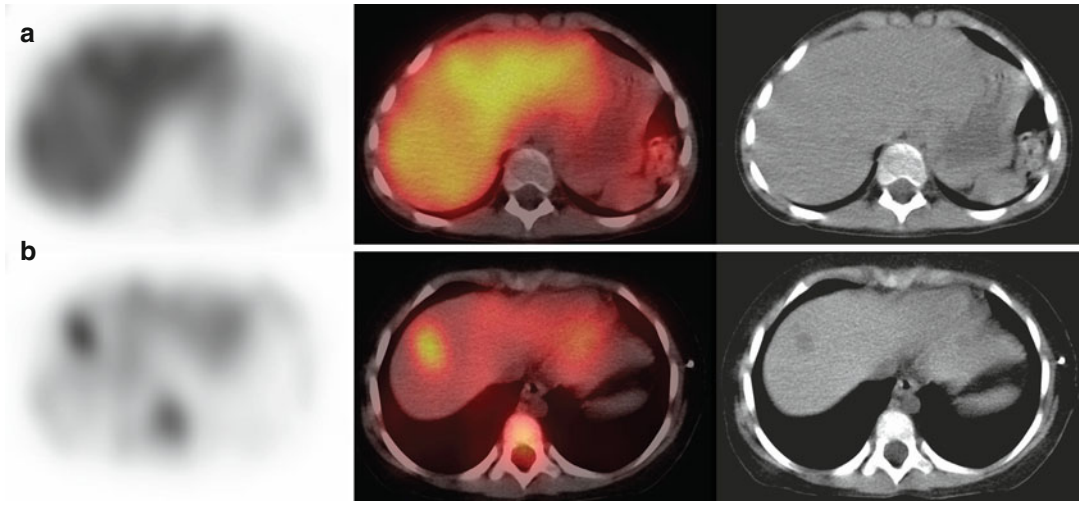

Fig. 19.6 Iodine-123-MIBG SPECT/CT images in two different patients. (**a**) Relatively increased uptake is seen within the left hepatic lobe, a common normal finding. (**b**) Focal increased uptake is seen at the hepatic dome, corresponding to a hypodense liver metastasis

involvement is less than 10 %. Bone marrow biopsy is therefore a standard part of neuroblastoma evaluation [28, 77, 82, 97, 102]. Interestingly, to be classified as a stage 4S or MS, infants must have less than 10 % bone marrow involvement with bone marrow which is ^{123}I-MIBG negative [4, 5].

The sensitivity of disease detection with MIBG increases with increasing administered activities. This is seen when ^{123}I-MIBG pre-therapy diagnostic scans are compared with immediate post-therapy ^{131}I-MIBG scans, which often demonstrate more disease sites [62, 70, 103, 104].

^{99m}Tc-Methylene Diphosphonate (^{99m}Tc-MDP) Bone Scan

Technetium-99m-MDP is taken up primarily in the mineral phase of bone, with relatively increased uptake at sites of bone formation and increased blood flow. Uptake abnormalities are demonstrated at sites of trauma, infection/inflammation, and benign or malignant bony lesions. Technetium-99m-MDP is therefore less specific for neuroblastoma than ^{123}I-MIBG, which utilizes the type I catecholamine reuptake system for uptake into neural crest cells.

Imaging Technique

The North American Consensus Guidelines recommend a ^{99m}Tc-MDP administered activity of 0.25 mCi/kg (9.3 MBq/kg) with a minimum dose of 1 mCi (37 MBq); alternatively, the European Association of Nuclear Medicine dosage card may be used [63].

Planar imaging is typically performed 2–4 h after ^{99m}Tc-MDP injection. Planar imaging includes anterior and posterior whole-body images, which can be performed as overlapping spot images or as a whole-body acquisition. Whole-body planar images are frequently supplemented with lateral views of the skull, oblique views of the torso, or lateral views of the extremities if needed to clarify uptake abnormalities. Sedation is required for children who are unable to remain still during planar imaging. Toilet-trained patients should be encouraged to void prior to imaging.

Clinical Applications

In patients with neuroblastoma, ^{99m}Tc-MDP bone scans traditionally have been used to assess for cortical bone metastases. Bone scans also can demonstrate uptake in the primary tumor, partic-

ularly in areas of calcification. In contrast to MIBG scans, bone scans do not demonstrate bone marrow metastases unless they are large enough to affect adjacent cortical bone.

A bone scan often is performed at diagnosis, as studies have shown discrepancies between MIBG and bone scans that can affect staging [81, 105, 106]. However, neuroblastoma patients usually are followed with MIBG scans alone, as bone scans provide little or no additional information during follow-up of patients with MIBG-avid disease [102, 107, 108]. Bone scans are recommended for assessment of patients with MIBG-negative tumors [4–6].

Potential Pitfalls

Physiologic ^{99m}Tc-MDP bone uptake can complicate detection of metastatic disease. Intense physiologic uptake at the growth plates can be problematic, making metaphyseal metastases difficult to visualize. Neuroblastoma often symmetrically involves the long bones, so abnormalities appear similar on side-to-side comparison (Fig. 19.7). False-positive bone scans can be seen after trauma. During and after therapy, persistent uptake at sites of prior metastases can also be seen in the absence of tumor [27, 72].

^{18}F-Fluorodeoxyglucose (FDG) PET and PET/CT

FDG is a glucose analog that is concentrated in metabolically active sites, including most tumors and areas of infection/inflammation. Fluorine-18-FDG is therefore less specific for neuroblastoma than ^{123}I-MIBG, which utilizes the type I catecholamine reuptake system for uptake into neural crest cells.

Patient Preparation

Appropriate patient preparation is important before ^{18}F-FDG PET or PET/CT (see Chap. 3). Patients should be warmed for 30–60 min prior to ^{18}F-FDG administration to limit uptake in brown adipose tissue, with premedication also used at some centers [109–113]. Patients should fast for 4 h prior to ^{18}F-FDG injection. Any glucose-containing intravenous fluids should be discontinued 4 h prior to ^{18}F-FDG administration [114]. After administration, patients should limit physical activity to avoid muscular uptake of ^{18}F-FDG [114].

Imaging Technique

The North American Consensus Guidelines recommend an ^{18}F-FDG administered activity of 0.10–0.14 mCi/kg (3.7–5.2 MBq/kg) with a minimum dose of 1.0 mCi (37 MBq); alternatively, the European Association of Nuclear Medicine dosage card may be used [63]. Appropriate pediatric CT settings should be utilized to minimize radiation dose. PET or PET/CT is performed approximately 1 h after ^{18}F-FDG injection. The lower extremities and skull should routinely be included in the scan, as disease involvement commonly occurs in these areas. Sedation is required for children who are unable to remain still during PET and PET/CT imaging. Toilet-trained patients should be encouraged to void prior to imaging.

Clinical Applications

The majority of neuroblastomas concentrate ^{18}F-FDG both before and after therapy, with uptake seen in both soft tissue and skeletal disease sites [28, 97, 115]. Findings on ^{18}F-FDG scans have been shown to correlate with disease status with serial scans accurately depicting treatment effects and disease evolution [28].

However, when compared to ^{123}I-MIBG, ^{18}F-FDG is often inferior for neuroblastoma evaluation. Fluorine-18-FDG can show lower tumor to non-tumor uptake ratios, especially after therapy [115]. Fluorine-18-FDG PET is less sensitive for neuroblastoma detection, especially in high-risk or relapsed disease. The inferiority of ^{18}F-FDG PET often is due to poorer depiction of cortical bone/bone marrow metastases, especially during therapy [76, 77, 116].

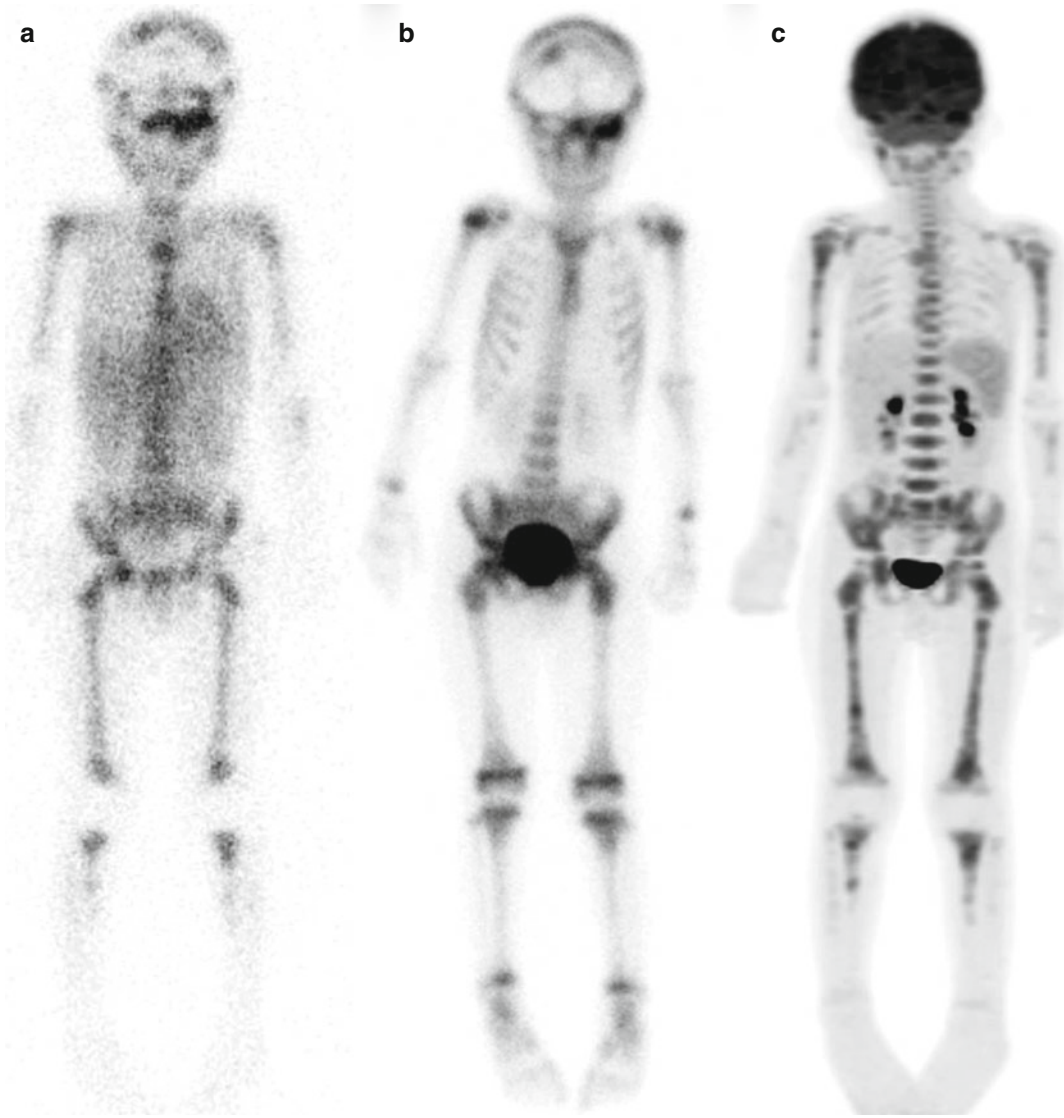

Fig. 19.7 Stage 4 patient imaged at diagnosis. (**a**) Iodine-123-MIBG anterior planar image shows diffuse metastatic disease throughout the axial and appendicular skeleton, including the skull. (**b**) Technetium-99m-MDP anterior planar image shows multiple bony metastases in the skull, pelvis, and long bones; however, extent of involvement in the spine and long bones is somewhat difficult to judge given the physiologic uptake in bone and diffuse symmetric disease involvement. (**c**) Fluorine-18-FDG PET MIP shows diffuse metastatic disease throughout the axial and appendicular skeleton; extent of skull involvement is difficult to visualize due to adjacent brain activity, although the larger skull lesions can be visualized on tomographic images (see Fig. 19.10)

Fluorine-18-FDG PET is most useful for imaging neuroblastomas that fail to or weakly accumulate ^{123}I-MIBG [76, 97, 115, 116] and is recommended as an option for evaluation of MIBG-negative tumors (Fig. 19.8) [5, 6]. Use of ^{18}F-FDG PET should be considered when CT/MR or clinical findings suggest more disease than demonstrated by ^{123}I-MIBG scans [97, 116–118]. A study of patients with MIBG-negative tumors or discrepancies between their ^{123}I-MIBG scans and CT/MRI or clinical findings showed that ^{18}F-FDG PET was more sensitive (78 %

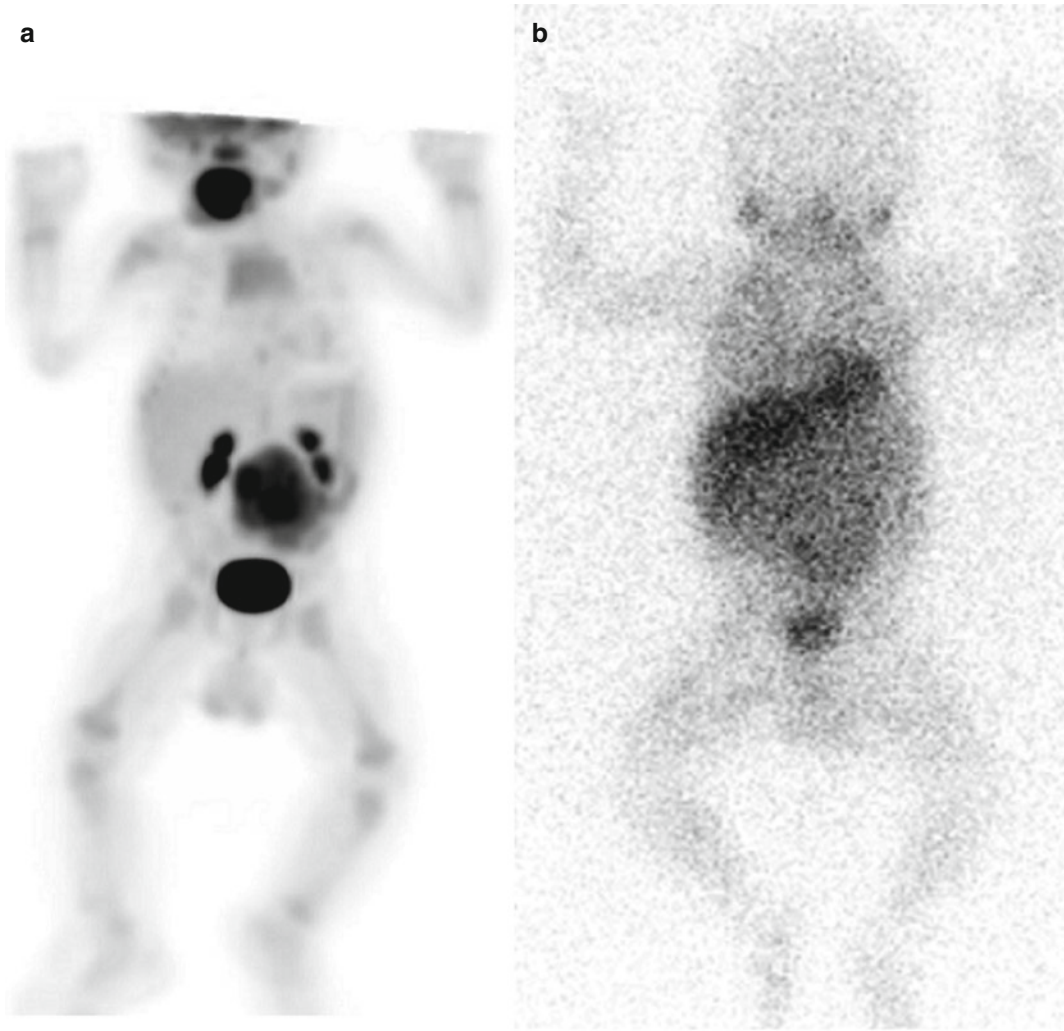

Fig. 19.8 Stage 3 patient imaged at diagnosis (**a**). FDG anterior projection MIP image demonstrates marked uptake in the large abdominal primary tumor; mild diffuse physiologic uptake in the bone marrow is also noted. (**b**) Iodine-123-MIBG anterior planar image demonstrates minimal uptake in the large abdominal primary tumor, slightly above background (This figure/research was originally published in *JNM*. Sharp et al. [76] © by the Society of Nuclear Medicine and Molecular Imaging, Inc., with permission)

versus 50 %) and specific (92 % versus 75 %) than ^{123}I-MIBG in this population, although review of both ^{123}I-MIBG scan and ^{18}F-FDG PET together gave the highest sensitivity (85 %) [97].

Fluorine-18-FDG PET and ^{123}I-MIBG scans can be complimentary, with each study sometimes demonstrating disease sites not identified with the other [28, 76, 97, 115]. Concurrent ^{123}I-MIBG scans and ^{18}F-FDG PET or PET/CT may therefore be useful to evaluate the full extent of disease involvement, especially at therapeutic decision points [76].

The intrinsic tomographic nature and higher spatial resolution of ^{18}F-FDG PET and PET/CT improves disease localization and detection of small lesion [28, 77]. Fluorine-18-FDG PET can be useful especially for identifying disease sites in the chest, abdomen, and pelvis [76].

A study including 10 patients with stage 1 and 2 neuroblastoma suggested that ^{18}F-FDG PET

may be superior to ^{123}I-MIBG in this population. In this study, 6 patients had better depiction of their primary tumor and/or regional metastases with ^{18}F-FDG PET [76]. A study including 17 soft tissue lesions suggested that ^{18}F-FDG PET may have higher sensitivity than ^{123}I-MIBG scans for soft tissue lesions. In this study, 6 lesions were seen only on ^{18}F-FDG PET [77]. However, larger studies are needed to confirm these findings.

A study reviewing neuroblastoma staging evaluations (including ^{18}F-FDG PET, ^{123}I-MIBG, ^{99m}Tc-MDP bone scans, CT/MRI, urine catecholamines, and bone marrow biopsy) suggested that ^{18}F-FDG PET and bone marrow sampling may be sufficient to monitor for progressive disease after tumor resection, as long as there were no skull lesions [28]. However, ^{123}I-MIBG remains a standard part of neuroblastoma assessment with a later study from this institution stating that ^{123}I-MIBG is essential for valid estimation of relapse-free survival in high-risk neuroblastoma patients [78].

Potential Pitfalls

Fluorine-18-FDG is a less-specific imaging agent than ^{123}I-MIBG. Physiologic uptake and uptake at sites of inflammation/infection can complicate image interpretation [28, 115]. Benign fibro-osseous lesions can also demonstrate variable ^{18}F-FDG uptake and mimic cortical bone metastases [119, 120].

Assessment of bone marrow involvement can be especially problematic. Physiologic ^{18}F-FDG uptake in bone marrow is seen in the absence of tumor [77, 115, 116]. Bone marrow metastases also sometimes produce ^{18}F-FDG uptake patterns that are indistinguishable from normal or physio-

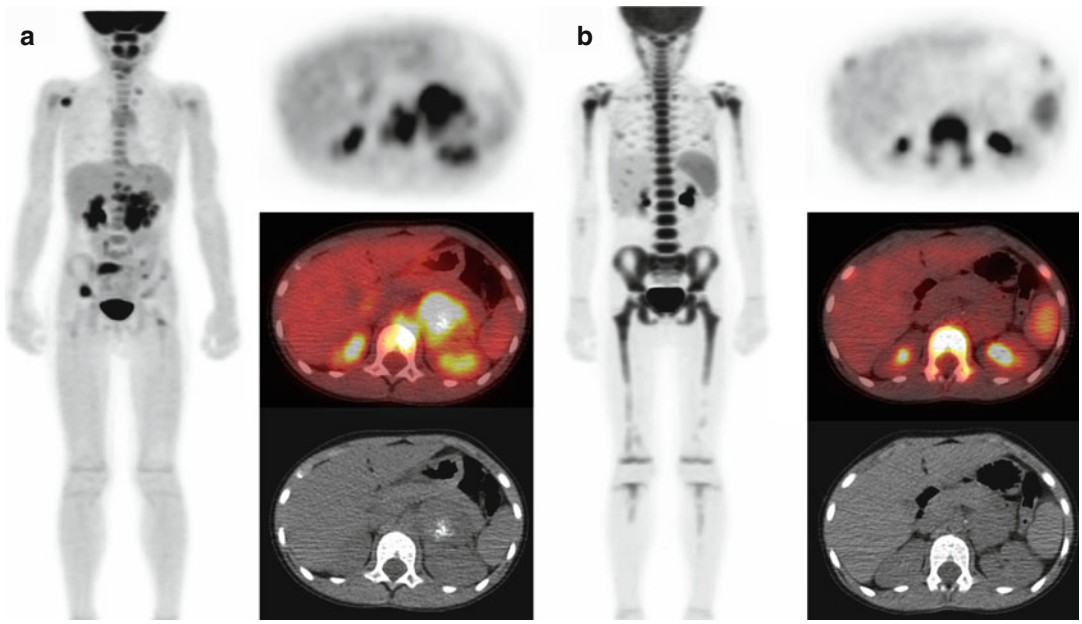

Fig. 19.9 Serial ^{18}F-FDG anterior projection MIP and axial PET/CT images in a patient with stage 4 neuroblastoma. (**a**) At diagnosis, ^{18}F-FDG uptake is seen in the primary partially calcified left retroperitoneal tumor, retroperitoneal lymphadenopathy, and multiple skeletal metastases (most notably involving the right glenoid, L1 vertebral body, right sacrum, and right iliac bone). (**b**) After chemotherapy and G-CSF therapy, intense diffuse bone marrow uptake is seen, potentially obscuring or mimicking metastatic disease; the primary left retroperitoneal tumor has decreased in size and no longer demonstrates FDG avidity (This figure/research was originally published in *JNM*. Sharp et al. [76] © by the Society of Nuclear Medicine and Molecular Imaging, Inc., with permission)

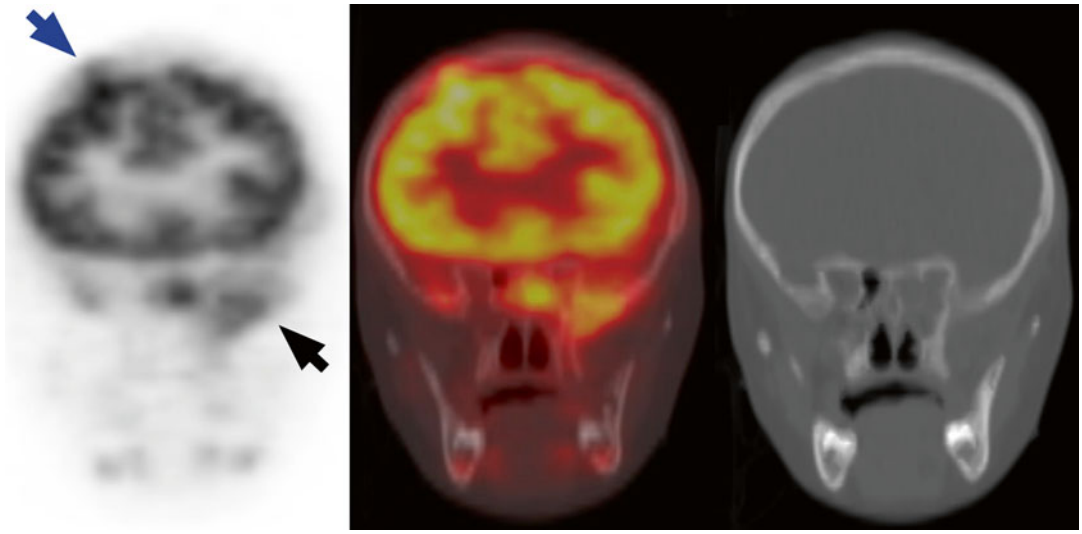

Fig. 19.10 Patient with stage 4 neuroblastoma also shown in Fig. 19.7. Coronal ^{18}F-FDG PET/CT images show abnormal uptake within the large right frontal (*blue arrow*) and left skull base (*black arrow*) lesions. Other smaller skull lesions are not as well seen

logic bone marrow activity [76]. During or after granulocyte colony-stimulating factor (G-CSF) therapy, extensive ^{18}F-FDG uptake in bone marrow can obscure or mimic metastatic disease [76, 77, 116] (Fig. 19.9). Like ^{123}I-MIBG, ^{18}F-FDG also can fail to detect minimal bone marrow disease [28, 77]. For example, cranial vault lesions can be difficult to identify near adjacent brain activity [28, 77, 115, 116], although large skull lesions usually can be identified (Figs. 19.7 and 19.10).

^{131}I-MIBG Therapy

Targeted therapy for neuroblastoma utilizing ^{131}I-MIBG is made possible by the radiosensitivity and MIBG avidity of most tumors. Clinical studies have evaluated the use of ^{131}I-MIBG in neuroblastoma therapy, both as a single agent and in combination with other agents including radiation sensitizers and cytotoxic chemotherapy [121]. Initial studies focused on use in patients with refractory or recurrent neuroblastoma, with objective responses seen in a significant minority of patients. More recent studies have investigated the use of ^{131}I-MIBG therapy in newly diagnosed high risk patients. In North America, ^{131}I-MIBG therapy currently is administered as an investigational agent at several sites in the United States and Canada. Myelosuppression is the main toxicity of ^{131}I-MIBG therapy. The maximum administered dose may depend upon the availability of autologous stem cells that can be used for bone marrow rescue.

References

1. Lonergan GJ, Schwab CM, Suarez ES, et al. Neuroblastoma, ganglioneuroblastoma, and ganglioneuroma: radiologic-pathologic correlation. Radiographics. 2002;22(4):911–34.
2. Kaatsch P. Epidemiology of childhood cancer. Cancer Treat Rev. 2010;36(4):277–85.
3. DuBois SG, Kalika Y, Lukens JN, et al. Metastatic sites in stage IV and IVS neuroblastoma correlate with age, tumor biology, and survival. J Pediatr Hematol Oncol. 1999;21(3):181–9.
4. Brodeur GM, Pritchard J, Berthold F, et al. Revisions of the international criteria for neuroblastoma diagnosis, staging, and response to treatment. J Clin Oncol. 1993;11(8):1466–77.
5. Monclair T, Brodeur GM, Ambros PF, et al. The International Neuroblastoma Risk Group (INRG) staging system: an INRG task force report. J Clin Oncol. 2009;27(2):298–303.
6. Brisse HJ, McCarville MB, Granata C, et al. Guidelines for imaging and staging of neuroblas-

tic tumors: consensus report from the International Neuroblastoma Risk Group Project. Radiology. 2011;261(1):243–57.
7. Gunther P, Holland-Cunz S, Schupp CJ, et al. Significance of image-defined risk factors for surgical complications in patients with abdominal neuroblastoma. Eur J Pediatr Surg. 2011;21(5):314–7.
8. Cohn SL, Pearson AD, London WB, et al. The International Neuroblastoma Risk Group (INRG) classification system: an INRG Task Force report. J Clin Oncol. 2009;27(2):289–97.
9. Moroz V, Machin D, Faldum A, et al. Changes over three decades in outcome and the prognostic influence of age-at-diagnosis in young patients with neuroblastoma: a report from the International Neuroblastoma Risk Group Project. Eur J Cancer. 2011;47(4):561–71.
10. London WB, Castleberry RP, Matthay KK, et al. Evidence for an age cutoff greater than 365 days for neuroblastoma risk group stratification in the Children's Oncology Group. J Clin Oncol. 2005;23(27):6459–65.
11. George RE, London WB, Cohn SL, et al. Hyperdiploidy plus nonamplified MYCN confers a favorable prognosis in children 12 to 18 months old with disseminated neuroblastoma: a Pediatric Oncology Group study. J Clin Oncol. 2005;23(27):6466–73.
12. Schmidt ML, Lal A, Seeger RC, et al. Favorable prognosis for patients 12 to 18 months of age with stage 4 nonamplified MYCN neuroblastoma: a Children's Cancer Group study. J Clin Oncol. 2005;23(27):6474–80.
13. Maris JM, Hogarty MD, Bagatell R, et al. Neuroblastoma. Lancet. 2007;369(9579):2106–20.
14. Brodeur GM. Neuroblastoma: biological insights into a clinical enigma. Nat Rev Cancer. 2003;3(3):203–16.
15. Park JR, Eggert A, Caron H. Neuroblastoma: biology, prognosis, and treatment. Hematol Oncol Clin North Am. 2010;24(1):65–86.
16. Maris JM. Recent advances in neuroblastoma. N Engl J Med. 2010;362(23):2202–11.
17. Strother DR, London WB, Schmidt ML, et al. Outcome after surgery alone or with restricted use of chemotherapy for patients with low-risk neuroblastoma: results of Children's Oncology Group study P9641. J Clin Oncol. 2012;30(15):1842–8.
18. Hero B, Simon T, Spitz R, et al. Localized infant neuroblastomas often show spontaneous regression: results of the prospective trials NB95-S and NB97. J Clin Oncol. 2008;26(9):1504–10.
19. Simon T, Spitz R, Faldum A, et al. New definition of low-risk neuroblastoma using stage, age, and 1p and MYCN status. J Pediatr Hematol Oncol. 2004;26(12):791–6.
20. Perez CA, Matthay KK, Atkinson JB, et al. Biologic variables in the outcome of stages I and II neuroblastoma treated with surgery as primary therapy: a Children's Cancer Group study. J Clin Oncol. 2000;18(1):18–26.
21. Nickerson HJ, Matthay KK, Seeger RC, et al. Favorable biology and outcome of stage IV-S neuroblastoma with supportive care or minimal therapy: a Children's Cancer Group study. J Clin Oncol. 2000;18(3):477–86.
22. Matthay KK, Perez C, Seeger RC, et al. Successful treatment of stage III neuroblastoma based on prospective biologic staging: a Children's Cancer Group study. J Clin Oncol. 1998;16(4):1256–64.
23. Schmidt ML, Lukens JN, Seeger RC, et al. Biologic factors determine prognosis in infants with stage IV neuroblastoma: a prospective Children's Cancer Group study. J Clin Oncol. 2000;18(6):1260–8.
24. Baker DL, Schmidt ML, Cohn SL, et al. Outcome after reduced chemotherapy for intermediate-risk neuroblastoma. N Engl J Med. 2010;363(14):1313–23.
25. Matthay KK, Villablanca JG, Seeger RC, et al. Treatment of high-risk neuroblastoma with intensive chemotherapy, radiotherapy, autologous bone marrow transplantation, and 13-cis-retinoic acid. Children's Cancer Group. N Engl J Med. 1999;341(16):1165–73.
26. Matthay KK, Reynolds CP, Seeger RC, et al. Long-term results for children with high-risk neuroblastoma treated on a randomized trial of myeloablative therapy followed by 13-cis-retinoic acid: a Children's Oncology Group study. J Clin Oncol. 2009;27(7):1007–13.
27. Kushner BH. Neuroblastoma: a disease requiring a multitude of imaging studies. J Nucl Med. 2004;45(7):1172–88.
28. Kushner BH, Yeung HW, Larson SM, et al. Extending positron emission tomography scan utility to high-risk neuroblastoma: fluorine-18 fluorodeoxyglucose positron emission tomography as sole imaging modality in follow-up of patients. J Clin Oncol. 2001;19(14):3397–405.
29. Stark DD, Moss AA, Brasch RC, et al. Neuroblastoma: diagnostic imaging and staging. Radiology. 1983;148(1):101–5.
30. Stark DD, Brasch RC, Moss AA, et al. Recurrent neuroblastoma: the role of CT and alternate imaging tests. Radiology. 1983;148(1):107–12.
31. Golding SJ, McElwain TJ, Husband JE. The role of computed tomography in the management of children with advanced neuroblastoma. Br J Radiol. 1984;57(680):661–6.
32. Siegel MJ, Ishwaran H, Fletcher BD, et al. Staging of neuroblastoma at imaging: report of the Radiology Diagnostic Oncology Group. Radiology. 2002;223(1):168–75.
33. Hugosson C, Nyman R, Jorulf H, et al. Imaging of abdominal neuroblastoma in children. Acta Radiol. 1999;40(5):534–42.
34. Sofka CM, Semelka RC, Kelekis NL, et al. Magnetic resonance imaging of neuroblastoma using current techniques. Magn Reson Imaging. 1999;17(2):193–8.
35. Slovis TL, Meza MP, Cushing B, et al. Thoracic neuroblastoma: what is the best imaging modality for evaluating extent of disease? Pediatr Radiol. 1997; 27(3):273–5.
36. Ilias I, Shulkin B, Pacak K. New functional imaging modalities for chromaffin tumors, neuroblastomas and ganglioneuromas. Trends Endocrinol Metab. 2005;16(2):66–72.

37. Rufini V, Calcagni ML, Baum RP. Imaging of neuroendocrine tumors. Semin Nucl Med. 2006;36(3):228–47.
38. Chen CC, Carrasquillo JA. Molecular imaging of adrenal neoplasms. J Surg Oncol. 2012;106(5):532–42.
39. Franzius C, Hermann K, Weckesser M, et al. Whole-body PET/CT with 11C-meta-hydroxyephedrine in tumors of the sympathetic nervous system: feasibility study and comparison with 123I-MIBG SPECT/CT. J Nucl Med. 2006;47(10):1635–42.
40. Shulkin BL, Wieland DM, Baro ME, et al. PET hydroxyephedrine imaging of neuroblastoma. J Nucl Med. 1996;37(1):16–21.
41. Shulkin BL, Wieland DM, Castle VP, et al. Carbon-11 epinephrine PET imaging of neuroblastoma. J Nucl Med. 1999;40s:129 [abstract].
42. Lopci E, Piccardo A, Nanni C, et al. 18F-DOPA PET/CT in neuroblastoma: comparison of conventional imaging with CT/MR. Clin Nucl Med. 2012;37(4):e73–8.
43. Piccardo A, Lopci E, Conte M, et al. Comparison of 18F-dopa PET/CT and 123I-MIBG scintigraphy in stage 3 and 4 neuroblastoma: a pilot study. Eur J Nucl Med Mol Imaging. 2012;39(1):57–71.
44. Tzen K, Wang L, Lu M. Characterization of neuroblastic tumors using F-18 DOPA PET. J Nucl Med. 2007;48s:117 [abstract].
45. Valentiner U, Haane C, Peldschus K, et al. [18F]FDG and [18F]FLT PET-CT and MR imaging of human neuroblastoma in a SCID mouse xenograft model. Anticancer Res. 2008;28(5A):2561–8.
46. Krieger-Hinck N, Gustke H, Valentiner U, et al. Visualisation of neuroblastoma growth in a Scid mouse model using [18F]FDG and [18F]FLT-PET. Anticancer Res. 2006;26(5A):3467–72.
47. Kroiss A, Putzer D, Uprimny C, et al. Functional imaging in phaeochromocytoma and neuroblastoma with 68Ga-DOTA-Tyr3-octreotide positron emission tomography and 123I-metaiodobenzylguanidine. Eur J Nucl Med Mol Imaging. 2011;38(5):865–73.
48. Vaidyanathan G, Zhao XG, Strickland DK, et al. No-carrier-added iodine-131-FIBG: evaluation of an MIBG analog. J Nucl Med. 1997;38(2):330–4.
49. Vaidyanathan G, Affleck DJ, Zalutsky MR. Validation of 4-[fluorine-18]fluoro-3-iodobenzylguanidine as a positron-emitting analog of MIBG. J Nucl Med. 1995;36(4):644–50.
50. Vaidyanathan G, Affleck DJ, Zalutsky MR. (4-[18F] fluoro-3-iodobenzyl)guanidine, a potential MIBG analogue for positron emission tomography. J Med Chem. 1994;37(21):3655–62.
51. Leung A, Shapiro B, Hattner R, et al. Specificity of radioiodinated MIBG for neural crest tumors in childhood. J Nucl Med. 1997;38(9):1352–7.
52. Sisson JC, Shulkin BL. Nuclear medicine imaging of pheochromocytoma and neuroblastoma. Q J Nucl Med. 1999;43(3):217–23.
53. Shapiro B, Gross MD. Radiochemistry, biochemistry, and kinetics of 131I-metaiodobenzylguanidine (MIBG) and 123I-MIBG: clinical implications of the use of 123I-MIBG. Med Pediatr Oncol. 1987;15(4):170–7.
54. Smets LA, Loesberg C, Janssen M, et al. Active uptake and extravesicular storage of m-iodobenzylguanidine in human neuroblastoma SK-N-SH cells. Cancer Res. 1989;49(11):2941–4.
55. Smets LA, Janssen M, Metwally E, et al. Extragranular storage of the neuron blocking agent meta-iodobenzylguanidine (MIBG) in human neuroblastoma cells. Biochem Pharmacol. 1990;39(12):1959–64.
56. Treuner J, Feine U, Niethammer D, et al. Scintigraphic imaging of neuroblastoma with 131I-iodobenzylguanidine. Lancet. 1984;1(8372):333–4.
57. Geatti O, Shapiro B, Sisson JC, et al. Iodine-131 metaiodobenzylguanidine scintigraphy for the location of neuroblastoma: preliminary experience in ten cases. J Nucl Med. 1985;26(7):736–42.
58. Gelfand MJ. I-123-MIBG and I-131-MIBG imaging in children with neuroblastoma. J Nucl Med. 1996;37s:35 [abstract].
59. Wood DE, Gilday DL, Kellan J. Stable iodine requirements for thyroid gland blockage of iodinated radiopharmaceuticals. J Can Assoc Radiol. 1974;25(4):295–6.
60. Bombardieri E, Giammarile F, Aktolun C, et al. 131I/123I-metaiodobenzylguanidine (mIBG) scintigraphy: procedure guidelines for tumour imaging. Eur J Nucl Med Mol Imaging. 2010;37(12):2436–46.
61. Olivier P, Colarinha P, Feltich J, et al. Guidelines for radioiodinated MIBG scintigraphy in children. Eur J Nucl Med Mol Imaging. 2003;30(5):B45–50.
62. Matthay KK, Shulkin B, Ladenstein R, et al. Criteria for evaluation of disease extent by (123) I-metaiodobenzylguanidine scans in neuroblastoma: a report for the International Neuroblastoma Risk Group (INRG) Task Force. Br J Cancer. 2010;102(9):1319–26.
63. Gelfand MJ, Parisi MT, Treves ST. Pediatric radiopharmaceutical administered doses: 2010 North American consensus guidelines. J Nucl Med. 2011;52(2):318–22.
64. Vik TA, Pfluger T, Kadota R, et al. (123)I-mIBG scintigraphy in patients with known or suspected neuroblastoma: results for a prospective multicenter trial. Pediatr Blood Cancer. 2009;52(7):784–90.
65. Gelfand MJ, Elgazzar AH, Kriss VM, et al. Iodine-123-MIBG SPECT versus planar imaging in children with neural crest tumors. J Nucl Med. 1994;35(11):1753–7.
66. Rufini V, Fisher GA, Shulkin BL, et al. Iodine-123-MIBG imaging of neuroblastoma: utility of SPECT and delayed imaging. J Nucl Med. 1996;37(9):1464–8.
67. Rozovsky K, Koplewitz BZ, Krausz Y, et al. Added value of SPECT/CT for correlation of MIBG scintigraphy and diagnostic CT in neuroblastoma and pheochromocytoma. Am J Roentgenol. 2008;190(4):1085–90.
68. Bar-Sever Z, Steinmetz A, Ash S, et al. The role of MIBG SPECT/CT in children with neuroblastoma. J Nucl Med. 2008;49s:84 [abstract].

69. Sharp SE, Gelfand MJ. Utility of SPECT/CT imaging in neuroblastoma. J Nucl Med. 2009;50s:52 [abstract].
70. Fukuoka M, Taki J, Mochizuki T, et al. Comparison of diagnostic value of I-123 MIBG and high-dose I-131 MIBG scintigraphy including incremental value of SPECT/CT over planar image in patients with malignant pheochromocytoma/paraganglioma and neuroblastoma. Clin Nucl Med. 2011;36(1):1–7.
71. Snay ER, Treves ST, Fahey FH. Improved quality of pediatric 123I-MIBG images with medium-energy collimators. J Nucl Med Technol. 2011;39(2):100–4.
72. Englaro DD, Gelfand MJ, Harris RE, et al. I-131 MIBG imaging after bone marrow transplantation for neuroblastoma. Radiology. 1992;182(2):515–20.
73. Tanabe M, Takahashi H, Ohnuma N, et al. Evaluation of bone marrow metastasis of neuroblastoma and changes after chemotherapy by MRI. Med Pediatr Oncol. 1993;21(1):54–9.
74. Tanabe M, Ohnuma N, Iwai J, et al. Bone marrow metastasis of neuroblastoma analyzed by MRI and its influence on prognosis. Med Pediatr Oncol. 1995;24(5):292–9.
75. Lebtahi N, Gudinchet F, Nenadov-Beck M, et al. Evaluating bone marrow metastasis of neuroblastoma with iodine-123-MIBG scintigraphy and MRI. J Nucl Med. 1997;38(9):1389–92.
76. Sharp SE, Shulkin BL, Gelfand MJ, et al. 123I-MIBG scintigraphy and 18F-FDG PET in neuroblastoma. J Nucl Med. 2009;50(8):1237–43. http://jnm.snmjournals.org/site/misc/permission.xhtml
77. Taggart DR, Han MM, Quach A, et al. Comparison of iodine-123 metaiodobenzylguanidine (MIBG) scan and [18F]fluorodeoxyglucose positron emission tomography to evaluate response after iodine-131 MIBG therapy for relapsed neuroblastoma. J Clin Oncol. 2009;27(32):5343–9.
78. Kushner BH, Kramer K, Modak S, et al. Sensitivity of surveillance studies for detecting asymptomatic and unsuspected relapse of high-risk neuroblastoma. J Clin Oncol. 2009;27(7):1041–6.
79. Suc A, Lumbroso J, Rubie H, et al. Metastatic neuroblastoma in children older than one year: prognostic significance of the initial metaiodobenzylguanidine scan and proposal for a scoring system. Cancer. 1996;77(4):805–11.
80. Ladenstein R, Philip T, Lasset C, et al. Multivariate analysis of risk factors in stage 4 neuroblastoma patients over the age of one year treated with megatherapy and stem-cell transplantation: a report from the European Bone Marrow Transplant Solid Tumor Registry. J Clin Oncol. 1998;16(3):953–65.
81. Perel Y, Conway J, Kletzel M, et al. Clinical impact and prognostic value of metaiodobenzylguanidine imaging in children with metastatic neuroblastoma. J Pediatr Hematol Oncol. 1999;21(1):13–8.
82. Schmidt M, Simon T, Hero B, et al. The prognostic impact of functional imaging with (123)I-mIBG in patients with stage 4 neuroblastoma >1 year of age on a high-risk treatment protocol: results of the German Neuroblastoma Trial NB97. Eur J Cancer. 2008;44(11):1552–8.
83. Ady N, Zucker JM, Asselain B, et al. A new 123I-MIBG whole body scan scoring method – application to the prediction of the response of metastases to induction chemotherapy in stage IV neuroblastoma. Eur J Cancer. 1995;31A(2):256–61.
84. Frappaz D, Bonneu A, Chauvot P, et al. Metaiodobenzylguanidine assessment of metastatic neuroblastoma: observer dependency and chemosensitivity evaluation. The SFOP Group. Med Pediatr Oncol. 2000;34(4):237–41.
85. Hero B, Hunneman DH, Gahr M, et al. Evaluation of catecholamine metabolites, mIBG scan, and bone marrow cytology as response markers in stage 4 neuroblastoma. Med Pediatr Oncol. 2001;36(1):220–3.
86. Matthay KK, Edeline V, Lumbroso J, et al. Correlation of early metastatic response by 123I-metaiodobenzylguanidine scintigraphy with overall response and event-free survival in stage IV neuroblastoma. J Clin Oncol. 2003;21(13):2486–91.
87. Katzenstein HM, Cohn SL, Shore RM, et al. Scintigraphic response by 123I-metaiodobenzylguanidine scan correlates with event-free survival in high-risk neuroblastoma. J Clin Oncol. 2004;22(19):3909–15.
88. Messina JA, Cheng SC, Franc BL, et al. Evaluation of semi-quantitative scoring system for metaiodobenzylguanidine (mIBG) scans in patients with relapsed neuroblastoma. Pediatr Blood Cancer. 2006;47(7):865–74.
89. Lewington V, Bar Sever Z, Lynch T, et al. Development of a new, semiquantitative I-123 mIBG reporting method in high risk neuroblastoma. Eur J Nucl Med Mol Imaging. 2009;36:334 [abstract].
90. Paltiel HJ, Gelfand MJ, Elgazzar AH, et al. Neural crest tumors: I-123 MIBG imaging in children. Radiology. 1994;190(1):117–21.
91. Bonnin F, Lumbroso J, Tenenbaum F, et al. Refining interpretation of MIBG scans in children. J Nucl Med. 1994;35(5):803–10.
92. Acharya J, Chang PT, Gerard P. Abnormal MIBG uptake in a neuroblastoma patient with right upper lobe atelectasis. Pediatr Radiol. 2012;42(10):1259–62.
93. Schindler T, Yu C, Rossleigh M, et al. False-positive MIBG uptake in pneumonia in a patient with stage IV neuroblastoma. Clin Nucl Med. 2010;35(9):743–5.
94. Okuyama C, Sakane N, Yoshida T, et al. (123)I- or (125)I-metaiodobenzylguanidine visualization of brown adipose tissue. J Nucl Med. 2002;43(9):1234–40.
95. Okuyama C, Ushijima Y, Kubota T, et al. 123I-metaiodobenzylguanidine uptake in the nape of the neck of children: likely visualization of brown adipose tissue. J Nucl Med. 2003;44(9):1421–5.
96. Pfluger T, Schmied C, Porn U, et al. Integrated imaging using MRI and 123I metaiodobenzylguanidine scintigraphy to improve sensitivity and specificity in the diagnosis of pediatric neuroblastoma. Am J Roentgenol. 2003;181(4):1115–24.
97. Melzer HI, Coppenrath E, Schmid I, et al. 123I-MIBG scintigraphy/SPECT versus 18F-FDG PET in paediatric neuroblastoma. Eur J Nucl Med Mol Imaging. 2011;38(9):1648–58.

98. Jacobsson H, Hellstrom PM, Kogner P, et al. Different concentrations of I-123 MIBG and In-111 pentetreotide in the two main liver lobes in children: persisting regional functional differences after birth? Clin Nucl Med. 2007;32(1):24–8.
99. Heyman S, Evans AE, D'Angio GJ. I-131 metaiodobenzylguanidine: diagnostic use in neuroblastoma patients in relapse. Med Pediatr Oncol. 1988;16(5):337–40.
100. Schmiegelow K, Simes MA, Agertoft L, et al. Radio-iodobenzylguanidine scintigraphy of neuroblastoma: conflicting results, when compared with standard investigations. Med Pediatr Oncol. 1989;17(2):127–30.
101. Biasotti S, Garaventa A, Villavecchia GP, et al. False-negative metaiodobenzylguanidine scintigraphy at diagnosis of neuroblastoma. Med Pediatr Oncol. 2000;35(2):153–5.
102. Kushner BH, Yeh SD, Kramer K, et al. Impact of metaiodobenzylguanidine scintigraphy on assessing response of high-risk neuroblastoma to dose-intensive induction chemotherapy. J Clin Oncol. 2003;21(6):1082–6.
103. Hickeson MP, Charron M, Maris JM, et al. Biodistribution of post-therapeutic versus diagnostic (131)I-MIBG scans in children with neuroblastoma. Pediatr Blood Cancer. 2004;42(3):268–74.
104. Parisi MT, Matthay KK, Huberty JP, et al. Neuroblastoma: dose-related sensitivity of MIBG scanning in detection. Radiology. 1992;184(2):463–7.
105. Gordon I, Peters AM, Gutman A, et al. Skeletal assessment in neuroblastoma – the pitfalls of iodine-123-MIBG scans. J Nucl Med. 1990;31(2):129–34.
106. Turba E, Fagioli G, Mancini AF, et al. Evaluation of stage 4 neuroblastoma patients by means of MIBG and 99mTc-MDP scintigraphy. J Nucl Biol Med. 1993;37(3):107–14.
107. Shulkin BL, Shapiro B, Hutchinson RJ. Iodine-131-metaiodobenzylguanidine and bone scintigraphy for the detection of neuroblastoma. J Nucl Med. 1992; 33(10):1735–40.
108. Hadj-Djilani NL, Lebtahi NE, Delaloye AB, et al. Diagnosis and follow-up of neuroblastoma by means of iodine-123 metaiodobenzylguanidine scintigraphy and bone scan, and the influence of histology. Eur J Nucl Med. 1995;22(4):322–9.
109. Zukotynski KA, Fahey FH, Laffin S, et al. Constant ambient temperature of 24 degrees C significantly reduces FDG uptake by brown adipose tissue in children scanned during the winter. Eur J Nucl Med Mol Imaging. 2009;36(4):602–6.
110. Gelfand MJ, O'Hara SM, Curtwright LA, et al. Premedication to block [(18)F]FDG uptake in the brown adipose tissue of pediatric and adolescent patients. Pediatr Radiol. 2005;35(10):984–90.
111. Parysow O, Mollerach AM, Jager V, et al. Low-dose oral propranolol could reduce brown adipose tissue F-18 FDG uptake in patients undergoing PET scans. Clin Nucl Med. 2007;32(5):351–7.
112. Soderlund V, Larsson SA, Jacobsson H. Reduction of FDG uptake in brown adipose tissue in clinical patients by a single dose of propranolol. Eur J Nucl Med Mol Imaging. 2007;34(7):1018–22.
113. Tatsumi M, Engles JM, Ishimori T, et al. Intense (18) F-FDG uptake in brown fat can be reduced pharmacologically. J Nucl Med. 2004;45(7):1189–93.
114. Delbeke D, Coleman RE, Guiberteau MJ, et al. Procedure guideline for tumor imaging with 18F-FDG PET/CT 1.0. J Nucl Med. 2006;47(5):885–95.
115. Shulkin BL, Hutchinson RJ, Castle VP, et al. Neuroblastoma: positron emission tomography with 2-[fluorine-18]-fluoro-2-deoxy-D-glucose compared with metaiodobenzylguanidine scintigraphy. Radiology. 1996;199(3):743–50.
116. Papathanasiou ND, Gaze MN, Sullivan K, et al. 18F-FDG PET/CT and 123I-metaiodobenzylguanidine imaging in high-risk neuroblastoma: diagnostic comparison and survival analysis. J Nucl Med. 2011;52(4):519–25.
117. Colavolpe C, Guedj E, Cammilleri S, et al. Utility of FDG-PET/CT in the follow-up of neuroblastoma which became MIBG-negative. Pediatr Blood Cancer. 2008;51(6):828–31.
118. McDowell H, Losty P, Barnes N, et al. Utility of FDG-PET/CT in the follow-up of neuroblastoma which became MIBG-negative. Pediatr Blood Cancer. 2009;52(4):552 [letter].
119. Goodin GS, Shulkin BL, Kaufman RA, et al. PET/CT characterization of fibroosseous defects in children: 18F-FDG uptake can mimic metastatic disease. Am J Roentgenol. 2006;187(4): 1124–8.
120. Shammas A, Lim R, Charron M. Pediatric FDG PET/CT: physiologic uptake, normal variants, and benign conditions. Radiographics. 2009;29(5): 1467–86.
121. DuBois SG and Matthay KK. ^{131}I-Metaiodobenzylguanidine therapy in children with advanced neuroblastoma. Q J Nucl Med Mol Imaging. 2013;57:53–65.

Imaging Parathyroid and Neuroendocrine Tumors

20

Frederick D. Grant

Nuclear medicine has widely variable roles in evaluating endocrine and neuroendocrine disorders. For example, thyroid imaging and therapy are a fundamental part of nuclear medicine practice (see Chap. 5). In pediatrics, nuclear medicine is indispensable in the management of neuroblastoma (see Chap. 19). Nuclear medicine studies also play a role in the evaluation and localization of the diverse group of endocrine and neuroendocrine tumors that includes tumors of the parathyroid glands, tumors originating in neural crest-derived cells in the sympathetic nervous system, and neuroendocrine tumors arising from the pancreas, thyroid gland, and the respiratory and gastrointestinal tracts. Nuclear medicine evaluation of these tumors typically has relied on single-photon emitting radiopharmaceuticals. Parathyroid imaging most commonly is performed with ^{99m}Tc-sestamibi, but [^{201}Tl] thallium chloride has been used in the past. Imaging of other neuroendocrine tumors typically has used radioiodinated (^{123}I, ^{131}I) meta-iodobenzylguanidine (MIBG) and ^{111}In-pentetreotide. There is a developing role for PET using ^{18}F-FDG, as well as newer PET radiopharmaceuticals labeled with ^{18}F, ^{11}C, and ^{68}Ga.

F.D. Grant, MD
Joint Program in Nuclear Medicine,
Department of Radiology, Harvard Medical School,
Boston, MA, USA

Division of Nuclear Medicine and Molecular Imaging,
Department of Radiology,
Boston Children's Hospital,
Boston, MA, USA

Department of Radiology,
Brigham and Women's Hospital,
Boston, MA, USA
e-mail: frederick.grant@childrens.harvard.edu

Parathyroid Imaging

The parathyroid glands, usually located adjacent to upper and lower poles of the thyroid gland, regulate blood levels of calcium and in doing so regulate the calcium economy of the body. Hyperparathyroidism is a state of parathyroid gland overactivity. *Primary hyperparathyroidism* is characterized by autonomous overproduction of parathyroid hormone (PTH), and PTH levels are inappropriately elevated despite a normal or elevated blood calcium level [1, 2]. Primary hyperparathyroidism may be caused by a parathyroid adenoma, multigland hyperplasia, or, rarely, parathyroid carcinoma. *Secondary hyperparathyroidism* reflects a physiological elevation of the blood PTH level in response to relative calcium deficiency and most commonly is associated with chronic renal failure. With prolonged secondary hyperparathyroidism, the parathyroid glands can undergo hyperplasia. Occasionally, with long-standing secondary hyperparathyroidism, one of the parathyroid glands can undergo adenomatous changes and develop autonomous function, a condition referred to as *tertiary hyperparathyroidism*. Important considerations in the appropriate management hyperparathyroidism include determining whether the hyperparathyroidism is primary

S.T. Treves (ed.), *Pediatric Nuclear Medicine and Molecular Imaging*,
DOI 10.1007/978-1-4614-9551-2_20,

or secondary and whether there is a parathyroid adenoma or parathyroid hyperplasia. Parathyroid imaging can play an essential role in answering these questions, particularly if surgical parathyroidectomy is being considered.

Method

There is no radiopharmaceutical that is specific for parathyroid tissue. Therefore, parathyroid scintigraphy depends upon nonspecific uptake and retention of a radiopharmaceutical in abnormal parathyroid tissue. Numerous approaches have been developed for parathyroid radionuclide imaging, all of which attempt to distinguish an abnormal parathyroid gland from nearby thyroid tissue [3]. *Dual-isotope* imaging uses two radiopharmaceuticals. One radiopharmaceutical has nonspecific uptake in both parathyroid and thyroid tissues, and this is compared to the thyroid-specific uptake of the second radiopharmaceutical. *Dual-phase* (washout) imaging relies on a single radiopharmaceutical, typically ^{99m}Tc-sestamibi, which has nonspecific parathyroid and thyroid uptake, but which demonstrates differential washout from thyroid tissue and retention in parathyroid adenomas [4]. In some cases, SPECT and, when available, SPECT/CT may be helpful for localization of a scintigraphic abnormality [5]. Other imaging methods, such as ultrasound, also are sensitive for identifying and localizing parathyroid adenomas [5–7]. The most accurate approach to parathyroid imaging may be the combination of scintigraphy and ultrasound [6–8]. However, with the increasing availability of SPECT and SPECT/CT, parathyroid scintigraphy may be adequate for detection and anatomic localization of abnormal parathyroid glands [5, 9].

Radiopharmaceuticals

^{99m}Tc-Sestamibi

The most commonly used radiopharmaceutical for identification and localization of parathyroid adenomas is ^{99m}Tc-sestamibi. Technetium-99m (physical half-life 6 h, 140 keV gamma emission) is readily available in all nuclear medicine departments as a generator product (^{99}Mo > ^{99m}Tc). Technetium-99m-sestamibi can be prepared easily from a kit or purchased as a unit dose from a commercial radiopharmacy. In children, a typical administered dose is 11 MBq/kg (0.3 mCi/kg) with a minimum dose of 37 MBq (1 mCi) and a maximum dose of 740 MBq (20 mCi). Abnormal parathyroid adenomas can be distinguished from normal thyroid using either dual-phase imaging with ^{99m}Tc-sestamibi or dual-isotope imaging with ^{99m}Tc-sestamibi and a thyroid-specific tracer. Cellular uptake of ^{99m}Tc-sestamibi parallels blood flow, but as a lipophilic positive ion, it is taken up in mitochondria and retained in the cell [10, 11]. Normal parathyroid and thyroid tissue also take up, but will not retain, ^{99m}Tc-sestamibi, possibly reflecting a greater expression of P-glycoprotein (multidrug resistance-associated protein) in these normal tissues [12]. Uptake of ^{99m}Tc-sestamibi may be inhibited by calcium channel blockers [13]. Technetium-99m-tetrofosmin uptake is similar to ^{99m}Tc-sestamibi, but it does not demonstrate differential thyroid and parathyroid retention [14] and is not used for dual-phase imaging.

[^{201}Tl] Thallium Chloride

Thallium-201 (physical half-life 73.1 h) decays by electron capture with release of a spectrum of x-rays (68–83 keV), as well as lower-abundance gamma (135 and 167 keV) emission. It is a cyclotron-produced radioisotope, produced with the following reaction:

$$^{203}\mathrm{Tl}\left(\mathrm{p},3\mathrm{n}\right)^{201}\mathrm{Pb} > ^{201}\mathrm{Tl}$$

Thallium-201 is a cationic analog of potassium, and cellular uptake is mediated by the sodium-potassium-ATPase transmembrane pump located in both thyroid and parathyroid cells. With no intracellular mechanism for specific concentration of thallium, there is ^{201}Tl washout from all tissues, making ^{201}Tl less suited to dual-phase imaging. Thallium-201, as [^{201}Tl] thallium chloride, was used for many years, but has been used less commonly since the introduction of ^{99m}Tc-sestamibi for parathyroid imaging

[15]. This decreased utilization may be due to both the higher radiation dose and the lower image quality provided by ^{201}Tl [16]. The lower image quality reflects both soft tissue attenuation of the low-energy x-rays and the need to limit the administered dose of ^{201}Tl due to the relatively high radiation dose. As a result, [^{201}Tl] thallium chloride has lower sensitivity than ^{99m}Tc-sestamibi for identification of abnormal parathyroid glands [16].

Iodine-123 (^{123}I)

Iodine-123 decays principally by electron capture and subsequent gamma emission with a physical half-life of 13.2 h. The most abundant gamma emission is 159 keV, but there are many other lower-abundance, higher-energy gamma emissions. Iodine-123 is a cyclotron product produced from a ^{124}Xe target. Iodine-123 is produced by two different nuclear reactions with subsequent rapid decay to ^{123}I. The primary nuclear reaction is

$$^{124}\mathrm{Xe}\left(\mathrm{p},\,2\mathrm{n}\right)^{123}\mathrm{Cs} >^{123}\mathrm{Xe} >^{123}\mathrm{I}$$

and the secondary nuclear reaction is

$$^{124}\mathrm{Xe}\left(\mathrm{p},\,\mathrm{pn}\right)^{123}\mathrm{Xe} >^{123}\mathrm{I}.$$

In the thyroid gland, the sodium-iodide symporter mediates iodine uptake (trapping) into follicular cells, where it then is organified and incorporated into thyroglobulin, the peptide precursor of the thyroid hormones. Other tissues, such as salivary glands, also may trap iodine, but, as they cannot organify iodine, it soon washes out of these tissues. Parathyroid cells do not express the sodium-iodide symporter and do not trap iodine. Therefore, ^{123}I does not localize the parathyroid glands but provides an imaging method to discriminate the thyroid gland and parathyroid tissue. The practice guidelines published by professional societies recommend a range of radiopharmaceutical doses for thyroid scintigraphy [17–19]. At our institution, the administered ^{123}I dose is 0.2 MBq/kg (0.006 mCi/kg) with a minimum dose of 0.925 MBq (0.025 mCi) and maximum dose of 14.8 MBq (0.4 mCi).

Technetium-99m Sodium Pertechnetate ([^{99m}Tc]NaTcO$_4$)

Technetium-99m (physical half-life 6.0 h, 140 keV gamma emission) is readily available in all nuclear medicine departments as a generator product (^{99}Mo > ^{99m}Tc). It is inexpensive, provides short imaging times, and provides a low radiation dose. For these reasons, [^{99m}Tc] sodium pertechnetate sometimes is preferred for thyroid imaging [20]. An adequate administered dose of ^{99m}Tc-pertechnetate is 1 MBq/kg (0.03 mCi/kg) with a minimum dose of 7.4 MBq (0.2 mCi) and maximum dose of 74 MBq (2 mCi). After intravenous administration of pertechnetate, the sodium-iodide symporter mediates rapid uptake of pertechnetate in thyroid cells, but not parathyroid cells. Unlike iodine, pertechnetate is not organified within thyroid cells, and it undergoes rapid washout, so that thyroid imaging must be performed soon after administration of [^{99m}Tc] sodium pertechnetate.

Parathyroid Scintigraphy

Parathyroid scintigraphy can be performed as *dual-phase* imaging with a single radiopharmaceutical, usually ^{99m}Tc-sestamibi [4], or as a *dual-isotope* procedure that relies on one nonspecific agent, such as ^{99m}Tc-sestamibi, and another agent with thyroid-specific uptake [3]. For most dual-isotope scintigraphy, extra care is needed with image acquisition, processing, and registration. As dual-phase scintigraphy has excellent diagnostic performance and is less complex than dual-isotope imaging, it has become the more common method for parathyroid imaging [21].

Dual-phase parathyroid scintigraphy relies on ^{99m}Tc-sestamibi retention in adenomas compared to ^{99m}Tc-sestamibi washout from normal thyroid and parathyroid tissue [3, 22]. Images are acquired at two time points (a) soon after tracer administration and (b) at a later time point (typically 1–2 h later). Comparison of the two sets of images should show washout of tracer from normal thyroid tissue and retention in parathyroid adenomas. A similar pattern of tracer retention can be seen in a thyroid adenoma or in a

carcinoma. At each time point, a planar image of the neck and mediastinum is acquired with a high-resolution collimator. Ideally, images of the neck also are acquired with a pinhole collimator in the anterior projection. Most clinical guidelines [21, 23] recommend that early image acquisition be started at 10–30 min and later image acquisition be started 1–2 h after tracer administration. Although some authors have advocated that delayed image acquisition be started as early as 1 h after tracer administration to avoid missing a small number of parathyroid lesions that may demonstrate early washout [24], this is not routine practice.

Dual-isotope scintigraphy uses two radiopharmaceuticals [3, 21]. The first, usually either ^{99m}Tc-sestamibi or [^{201}Tl] thallium chloride, demonstrates nonspecific uptake in both thyroid and parathyroid tissues. The second, usually either ^{123}I or ^{99m}Tc-pertechnetate, has thyroid-specific uptake and is used to distinguish normal thyroid tissue from an adenoma. There are many different approaches to dual-isotope imaging, each using the combination of one thyroid-specific agent (^{123}I or ^{99m}Tc-pertechnetate) and one nonspecific agent (^{99m}Tc-sestamibi, ^{99m}Tc-tetrofosmin, or [^{201}Tl] thallium chloride) [23, 25]. In nearly all facilities, the nonspecific agent of choice is ^{99m}Tc-sestamibi, but ^{99m}Tc-tetrofosmin could be used for the dual-isotope method [14]. Because of higher cost and longer uptake time (2 h) for ^{123}I, some centers prefer to use ^{99m}Tc-pertechnetate as the thyroid-specific agent. However, one potential advantage of ^{123}I is that gamma camera windowing could be adjusted for simultaneous imaging of ^{123}I and ^{99m}Tc-pertechnetate [26, 27]. Images from the two scintigraphic studies can be compared by side-by-side comparison, overlay of digital images, or digital subtraction of thyroid images from parathyroid images. If digital overlay or subtraction of separately acquired images is to be used, care must be taken to ensure that images are acquired with the same geometry and magnification. With digital subtraction, image misregistration will cause artifacts that can obscure true findings.

A site of focal ^{99m}Tc-sestamibi uptake outside the contour of the thyroid gland is assumed to represent a parathyroid adenoma. With a dual-phase ^{99m}Tc-sestamibi scan, uptake usually will be seen on both the initial and delayed images, but in 10 % of positive cases, the focus of uptake may be seen on only the initial or the delayed images [28]. If a lesion is identified within the thyroid gland, uptake of either ^{123}I or ^{99m}Tc-pertechnetate may identify a nodule as of thyroid origin, but neither dual-phase nor dual-isotope scintigraphy will clearly discriminate an intrathyroidal parathyroid adenoma (or rarely carcinoma) from a nonfunctional thyroid nodule [29, 30]. Occasionally, even after completing a dual-phase study, it might be helpful to perform a thyroid scan to help differentiate a thyroid nodule from a parathyroid adenoma [23]. A subcapsular or intrathyroidal parathyroid adenoma may produce a focal defect on the thyroid scan [31]. Intrathyroidal parathyroid adenomas may account for 1 % of all parathyroid adenomas and typically are smaller than extrathyroidal glands [30]. Uptake of ^{99m}Tc-sestamibi can occur in a variety of thyroid lesions [30], such as benign thyroid follicular adenoma, Hürthle cell neoplasm, and thyroid cancer, as well as metastatic disease to the thyroid or lymph nodes and reactive lymph nodes. Even if a lesion is characterized as thyroid tissue, further evaluation may be needed, including ultrasound and possibly fine needle aspiration.

A pinhole collimator (aperture less than 3 mm) is preferable for parathyroid scintigraphy of the neck, as it provides magnification, higher lesion conspicuity, and improved accuracy for identifying parathyroid pathology [9, 21, 23, 32, 33]. Typically, the collimator is positioned so that the thyroid region is contained within the central two-thirds of the pinhole field of view. An additional "bird's-eye" view can be acquired with the pinhole collimator positioned 15–30 cm from the neck. In addition, a high-resolution parallel-hole collimator provides a wide field of view to image from the base of the tongue to the thorax. With either planar or pinhole collimator, images are acquired for 10 min or 100,000 counts. Anatomic correlation, either with transmission images to

outline body margins or with radioactive markers on anatomic landmarks, such as chin and suprasternal notch, can be helpful.

SPECT can improve localization of ectopic parathyroid tissue in the neck or chest but may be no more sensitive for identifying parathyroid pathology than planar or pinhole imaging [3, 33]. There is no consensus on the timing of SPECT, but for a dual-phase study, many institutions perform SPECT at a time point between the early and delayed planar images [3, 33]. For a dual-isotope study, SPECT can be performed concurrent with or in place of planar imaging. When available, SPECT/CT may increase specificity of a SPECT study, but this may reflect, in part, the poor specificity of SPECT alone [27]. One group of investigators has reported that the combination of early SPECT/CT together with any delayed-phase imaging method may be superior to other approaches using SPECT or planar imaging [5]. However, other groups have shown that SPECT or SPECT/CT is less sensitive than pinhole imaging for identification of abnormal parathyroid glands in the neck [3, 33, 34]. This may reflect the loss of SPECT resolution that occurs with the increased distance from detector to target neck tissue when the shoulders must be included in the arc of the camera rotation.

SPECT/CT may be useful in some clinical circumstances. SPECT/CT may help in evaluating patients with persistent or recurrent hyperparathyroidism after surgery, when the normal anatomy of the neck has been surgically disrupted [34]. SPECT/CT may be helpful in the localization of ectopic hyperactive parathyroid glands, which may be located in the chest or in an ectopic location in the neck. The search for a potentially ectopic parathyroid gland is complicated by possible supernumerary parathyroid glands. Although the usual number of parathyroid glands is four, one in ten individuals has between five and seven parathyroid glands [35]. Finally, some investigators have reported that SPECT/CT has higher specificity than SPECT when performing dual-isotope parathyroid imaging [27]. With increasing availability of SPECT/CT, some general nuclear medicine departments use this approach routinely for all parathyroid imaging. However, in children and young adults, there has been no clear demonstration that the additional information provided by routine SPECT/CT outweighs the increased radiation exposure of this technique. One approach may be to reserve SPECT/CT for clinical situations where parathyroid imaging with planar imaging is difficult or confusing.

Clinical Parathyroid

Clinical Approach to Hyperparathyroidism

Many of the clinical signs and symptoms of primary hyperparathyroidism are those of hypercalcemia [36, 37]. *Gastrointestinal* symptoms of hypercalcemia include anorexia, constipation, and abdominal pain. *Psychiatric* symptoms can range from fatigue to severe depression or psychosis. Nearly all patients with primary hyperparathyroidism have *hypercalciuria* and may develop polyuria or kidney stones. The classic *bone* findings of hyperparathyroidism included subperiosteal bone resorption and osteopenia. A rare complication of hyperparathyroidism is osteitis fibrosa cystica (brown tumor), which occurs most commonly in cases of prolonged or uncontrolled hyperparathyroidism [38]. In the current era, these classic signs and symptoms are uncommon, and most patients with hyperparathyroidism are diagnosed when they have few, if any, symptoms. However, "asymptomatic" hyperparathyroidism still may be associated with an increased risk of hypertension, kidney stones, nonspecific neurocognitive or psychiatric symptoms, and decreased cortical bone density [37].

Most cases of primary hyperparathyroidism are due to the sporadic development of a single parathyroid adenoma in one of the four parathyroid glands. Occasionally, more than one parathyroid gland will contain an adenoma. In adults, approximately 15 % of all cases of primary hyperparathyroidism are the result of hyperplasia of all the parathyroid glands. Parathyroid hyperplasia can be either sporadic or familial. Many

familial cases of parathyroid hyperplasia represent a defined endocrine syndrome, such as multiple endocrine hyperplasia I (MEN I) or MEN IIa [39]. In children, up to half of all cases of primary hyperparathyroidism may be associated with an identifiable genetic syndrome. Therefore, children with primary hyperparathyroidism are more likely than adults to have parathyroid hyperplasia, but most cases of pediatric hyperparathyroidism remain due to parathyroid adenomas. Parathyroid carcinoma is a rare (1 %) cause of hyperparathyroidism [40].

In the evaluation of presumed hyperparathyroidism, the diagnosis of familial hypocalciuric hypercalcemia (FHH) should be excluded, usually by determining urinary calcium excretion. Further intervention, such as parathyroid scintigraphy or parathyroidectomy, is rarely necessary for this usually benign disorder [41]. However, other inherited disorders of calcium handling related to mutations in the calcium-sensing receptor may require further evaluation and, occasionally, surgery [42]. Medications that can alter calcium metabolism, such as lithium and thiazide diuretics, should be excluded as the cause of hypercalcemia or PTH stimulation [39]. Vitamin D deficiency is common in patients with hyperparathyroidism. Vitamin D deficiency can be a cause of secondary hyperparathyroidism and may worsen primary hyperparathyroidism [43].

The definitive treatment for primary hyperparathyroidism is surgical parathyroidectomy of all involved parathyroid glands. Complications of hyperparathyroidism can be corrected by successful surgery. For example, in adolescents with primary hyperparathyroidism, parathyroidectomy is associated with a rapid increase in bone density [44]. The traditional surgical approach for parathyroidectomy included exploration of the neck with identification and evaluation of all four parathyroid glands and required little preoperative imaging. In cases of a single adenoma, an experienced surgeon could achieve surgical cure in over 95 % of patients [45]. One advantage of full exploration of the neck is identification and resection of a second adenoma in a small fraction of patients. In patients with parathyroid hyperplasia, all parathyroid glands are involved, but complete four-gland parathyroidectomy is complicated by hypoparathyroidism and hypocalcemia [46]. In these patients, most surgeons have attempted to remove at least three glands, and some may try to remove part of the fourth hyperplastic gland. Thus, the surgical success rate is lower in patients with parathyroid gland hyperplasia.

In the 1970s and 1980s, with the increased use of multichannel blood chemistry analyzers and the availability of a PTH radioimmunoassay, many cases of primary hyperparathyroidism were diagnosed in asymptomatic patients with mild hypercalcemia [36, 38]. The resulting uncertainty regarding the appropriate management of asymptomatic hyperparathyroidism led to publication of a landmark consensus clinical guideline by the National Institutes of Health [47]. This most recently was updated in 2009 [43, 48]. These guidelines recommend that many asymptomatic adult patients not routinely undergo surgical parathyroidectomy. Definitive surgical therapy is recommended in patients with clearly identifiable symptoms, including kidney stones and severe osteoporosis, while patients with mild hypercalcemia and without symptoms may be managed expectantly. However, the intent of these guidelines has been to guide management of adults with hyperparathyroidism, and nearly all children with primary hyperparathyroidism should be treated with parathyroidectomy. Interestingly, with the more recent decrease in utilization of multi-test chemistry panels, fewer patients are now identified with asymptomatic hypercalcemia, and more patients with hyperparathyroidism are again presenting with symptoms of hypercalcemia.

Clinical Use of Parathyroid Imaging

As parathyroid imaging procedures, including parathyroid scintigraphy and ultrasound, have become more accepted, many surgeons now rely on preoperative imaging to guide the surgical approach. The use of preoperative imaging improves the likelihood of operative success and, by limiting the need for full neck dissection, decreases the risk of postoperative hypocalcemia [16]. For example, preoperative imaging may permit minimally invasive resection of a single parathyroid adenoma without further exploration of the neck. Many surgeons will confirm operative success by measuring a serum PTH level after

resection of the presumed parathyroid adenoma. Successful resection has been defined as a 50 % drop in parathyroid hormone levels 10 min after resection of the adenoma [49]. This approach has the advantages of lower surgical morbidity and quicker recovery time but relies on the availability of reliable preoperative imaging [22].

The sensitivity of a ^{99m}Tc-sestamibi study ranges between 80 and 90 % for a single adenoma (Fig. 20.1), but the sensitivity is lower (40–60 %) in cases of multiple adenomas or hyperplasia [5–7, 9, 22, 50]. The sensitivity of a dual-phase ^{99m}Tc-sestamibi scan may be higher for parathyroid adenomas in the lower neck, for

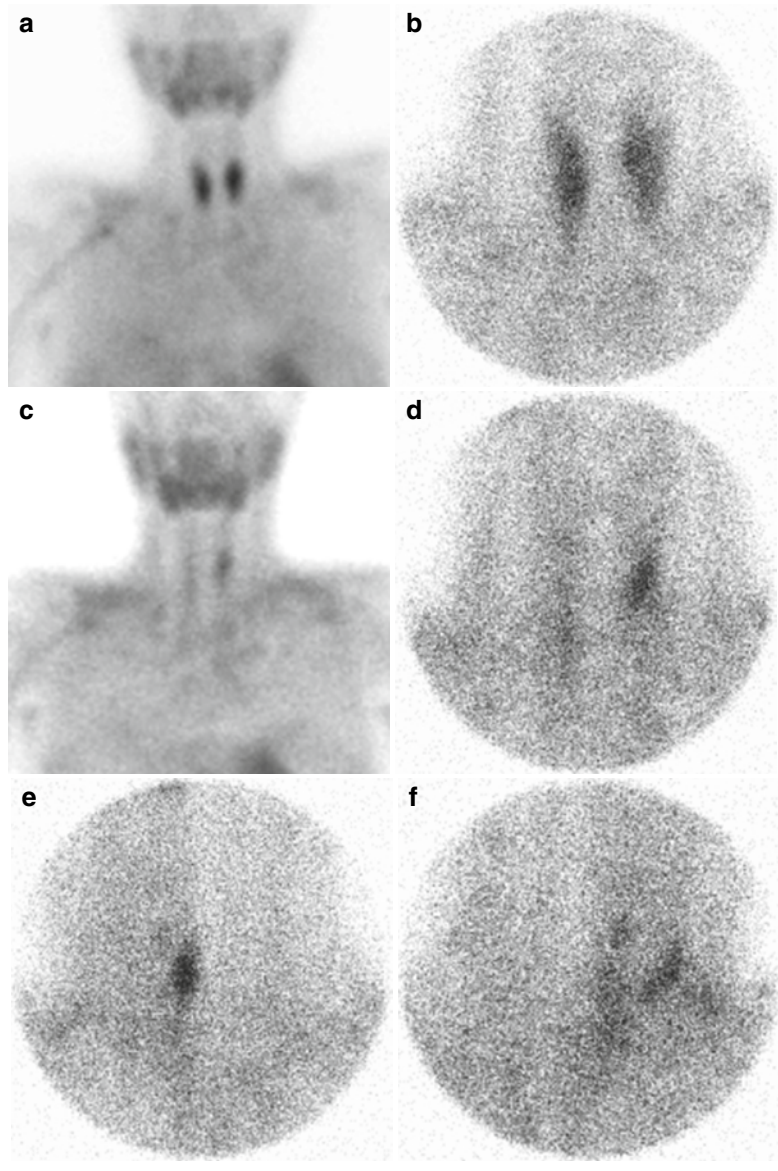

Fig. 20.1 Parathyroid adenoma localized with dual-phase ^{99m}Tc-sestamibi scintigraphy. Planar image of the upper torso and neck (**a**) and pinhole image of the neck (**b**) acquired soon after tracer administration show diffuse uptake in the thyroid gland. Two hours later, the planar image (**c**) and pinhole (**d**) images demonstrate tracer washout from the thyroid gland with persistent ^{99m}Tc-sestamibi accumulation in a single focus near the left upper pole of the thyroid gland. Additional pinhole images in (**e**) left anterior oblique and (**f**) right anterior oblique projections confirm the location of the abnormal focal uptake. No abnormality could be identified on neck ultrasound. Surgical resection revealed a single parathyroid adenoma adjacent to the upper pole of the left lobe of the thyroid gland

larger adenomas, and in patients with higher PTH levels, but the pretest PTH level cannot determine which patients should undergo presurgical imaging [51]. In a substantial minority (reported between 6 and 16 %) of patients with primary hyperparathyroidism, a hyperfunctioning parathyroid gland may be located in an ectopic location [52]. Most of these are a single adenoma, but a tenth may represent a second parathyroid adenoma. Ectopic parathyroid glands most commonly are found in the thymus, in the retroesophageal region, or within the thyroid gland. In patients who have not undergone prior surgery, the sensitivity of well-performed ^{99m}Tc-sestamibi scintigraphy is not much less for an ectopic parathyroid adenoma than for one located in the neck. SPECT or SPECT/CT may be helpful in localizing ectopic parathyroid lesions.

With an experienced operator, ultrasound may have a sensitivity in the range of 70–90 % for a single parathyroid adenoma [5–7]. Like parathyroid scintigraphy, ultrasound is less sensitive for multiple adenomas or multigland parathyroid hyperplasia [53, 54]. The sensitivity of ultrasound for identifying an abnormal parathyroid may be decreased by the presence of thyroid nodules [7]. Compared to scintigraphy, ultrasound is less sensitive for localizing ectopic adenomas [52] and may have less utility in cases of recurrent hyperparathyroidism.

For localization of a single parathyroid adenoma, the combined use of parathyroid scintigraphy and ultrasound has highest sensitivity (94–99 %) of any approach to parathyroid imaging, but even this combination is less effective for the identification of multigland hyperplasia. In a patient with clearly identified hyperparathyroidism, the lack of an identifiable adenoma on either scintigraphy or ultrasound increases the likelihood of the diagnosis of parathyroid hyperplasia [9]. One clinical approach endorsed by the European Society of Endocrine Surgeons [16] is to image first with dual-phase parathyroid scintigraphy and then to confirm the scintigraphic findings with high-frequency ultrasound [9, 16]. If the studies provide concordant results, then the patient may be candidate for minimally invasive surgery [22]. If only one test, either scintigraphy or ultrasound, is positive, then unilateral neck exploration guided by intraoperative PTH assays may be appropriate. In cases where scintigraphy and ultrasound are discordant or both are negative, then bilateral neck exploration may be the most appropriate surgical approach.

Parathyroid carcinoma is a rare (1 %) cause of hyperparathyroidism [40]. Parathyroid imaging cannot distinguish a benign adenoma from a carcinoma. In general, a parathyroid carcinoma will be larger and associated with higher serum calcium levels than a benign adenoma (Fig. 20.2).

Persistent or Recurrent Hyperparathyroidism

In some patients with hyperparathyroidism, a single surgery will not be curative. Patients with persistent or recurrent hyperparathyroidism may be the greatest diagnostic and management challenge of hyperparathyroidism. Persistent or recurrent hyperparathyroidism can be due to unrecognized hyperplasia or familial disease, an ectopic or supernumerary parathyroid gland, a second undetected adenoma, inadequate imaging, or operative failure [22, 39]. Recurrent disease is less common than persistent disease but can occur in patients with familial hyperparathyroidism [39]. An ideal approach would be to prevent the need for reoperation by having the initial evaluation performed by an integrated and experienced multidisciplinary team including an endocrinologist, endocrine surgeon, nuclear medicine physician, radiologist, and pathologist [22, 51]. When a patient has recurrent or persistent hyperparathyroidism, then repeat surgery by an experienced surgeon is indicated. In most patients with recurrent or persistent hyperparathyroidism, the abnormal parathyroid gland will be in the normal position or in an ectopic location that is accessible through a standard neck incision [39]. The preoperative imaging approach still relies on ^{99m}Tc-sestamibi scintigraphy and ultrasound [7, 16, 21]. SPECT or SPECT/CT should be considered, particularly if not

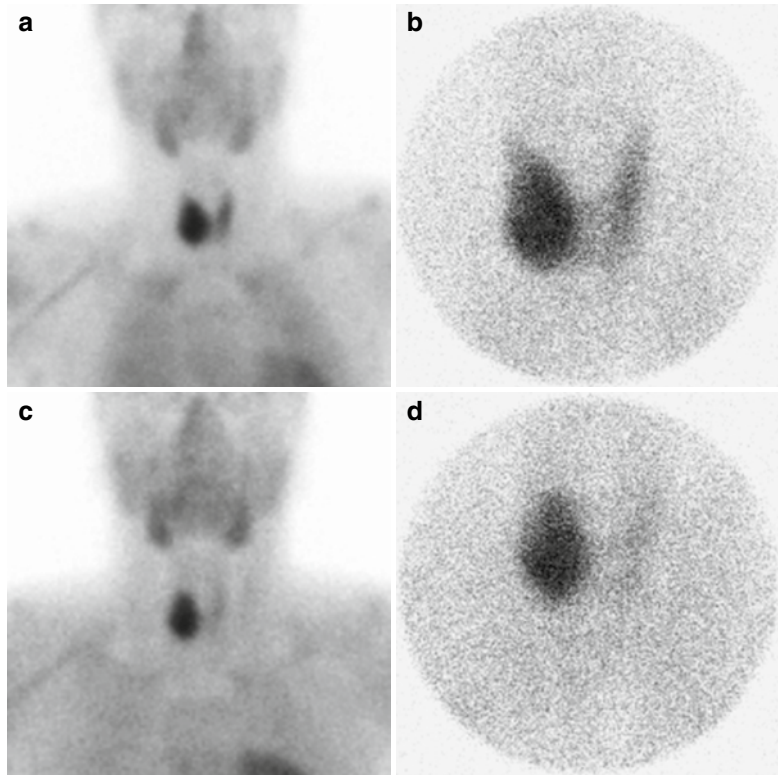

Fig. 20.2 Parathyroid carcinoma evaluated with dual-phase ^{99m}Tc-sestamibi scintigraphy. Early-phase planar image of the upper torso (**a**) and pinhole image of the neck (**b**) both show intense uptake in a large mass in the right thyroid bed and moderate uptake in the left lobe of the thyroid gland. A planar image of the torso acquired at 105 min (**c**) and pinhole image of the neck acquired at 115 min (**d**) show persistent tracer uptake in the right-side mass and tracer washout from the left lobe of the thyroid gland. The differential for this mass includes parathyroid adenoma or carcinoma, benign or malignant thyroid nodule, and metastatic lesion to the thyroid gland. Surgical exploration revealed a large parathyroid carcinoma on the surface of the right lobe of the thyroid gland

performed during the initial evaluation. Fine needle aspiration with PTH measurement may be useful to evaluate an inconclusive ultrasound finding. Although contrast-enhanced CT and MRI have low sensitivity for parathyroid adenomas, either may be helpful to confirm inconclusive imaging findings in the mediastinum of patients with persistent or recurrent hyperparathyroidism [5, 6, 55]. One disadvantage to using CT for parathyroid gland localization is radiation exposure to the thyroid gland, which may be of particular concern in children [39]. Very rarely, venous sampling for PTH may help to demonstrate laterality of an overactive gland in the neck or may demonstrate whether the abnormal gland is in the neck or mediastinum [7, 16].

Secondary and Tertiary Hyperparathyroidism

Secondary hyperparathyroidism refers to parathyroid hyperactivity in response to prolonged absolute or relative deficiency of calcium. The resulting elevation in PTH levels may be successful in maintaining blood calcium levels in normal range but at the cost of inducing calcium loss from bone and eventual osteomalacia. The most common cause of clinically apparent secondary hyperparathyroidism is chronic renal failure [34]. In the absence of normal renal function, 25-hydroxy-vitamin D is not activated to the active form, 1,25-dihydroxy-vitamin D. This results in decreased

intestinal absorption of calcium, relative calcium deficiency, and stimulation of PTH secretion. This secondary hyperparathyroidism can be an important cause of morbidity and mortality in patients with chronic renal failure, especially those on chronic dialysis [55]. Patients with vitamin D deficiency also can develop secondary hypoparathyroidism. Correction of the underlying medical or nutritional condition, if possible, should result in resolution of secondary hyperparathyroidism.

With long-standing secondary hyperparathyroidism and prolonged parathyroid gland stimulation, secondary parathyroid gland hyperplasia may develop [3]. Even with correction of the underlying problem, such as renal transplant, these patients may have persistent PTH hypersecretion. Occasionally, in an individual with chronic secondary hyperparathyroidism, usually from chronic renal failure, one or more parathyroid glands may undergo adenomatous changes and develop autonomous function and secretion of PTH, which is referred to as tertiary hyperparathyroidism. In these patients, correction of the underlying medical condition is unlikely to reverse the hyperparathyroidism, and parathyroid surgery may be required [56].

Parathyroid imaging has a limited role in the evaluation of secondary hyperparathyroidism, unless parathyroidectomy is being considered. Then, parathyroid imaging may be useful in distinguishing secondary and tertiary hyperparathyroidism (Fig. 20.3). Preoperative imaging and localization can help identify an ectopic or supernumerary gland and thus decrease the likelihood of surgical failure and reduce the extent of surgical exploration. Parathyroid scintigraphy may have limited sensitivity for hyperplastic parathyroid glands but should have higher sensitivity for an autonomous parathyroid gland causing tertiary hyperparathyroidism [34]. Some investigators have reported improved localization of secondary hyperparathyroidism with pinhole imaging [33] or dual-tracer subtraction scintigraphy (Fig. 20.4) [3], but the relative utility of different methods of parathyroid scintigraphy is not clearly defined in this group of patients [34].

Neuroendocrine Tumors: Imaging

Neuroendocrine tumors are uncommon, particularly in children and young adults. These tumors arise from cells with an embryological origin in the neural crest and can be located nearly anywhere in the body. Neuroendocrine tumors encompass a heterogeneous group of tumors that secrete a wide variety of peptides and amines and thus present with a broad range of clinical features. With the exception of neuroblastoma, they typically come to clinical attention because of the physiological effects of their secretory products, although some may be discovered as an incidental finding. Occasionally, tumor bulk or metastatic disease is the major cause of morbidity and mortality. Most neuroendocrine tumors probably have malignant potential with the possibility of metastases [57], but the frequency of malignancy varies among different cell types. At least nine different neuroendocrine cell types can undergo development into neuroendocrine tumors [58]. *Sympathochromaffin tumors* of the autonomic nervous system, including pheochromocytoma and paraganglioma, can secrete catecholamines. *Enterochromaffin tumors*, such as carcinoid tumors, can secrete a wide variety of biologically active compounds, including serotonin, but only rarely produce the carcinoid syndrome. Classic *gastro-entero-pancreatic* (*GEP*) *tumors* (also called *pancreato-gastrointestinal tumors*) include secretory and nonsecretory tumors derived from cell types typically found in the pancreatic islet but may occur throughout the gastrointestinal tract. They are categorized based on cell type and secretory products, such as gastrinoma or insulinoma. In newborns, benign hyperplasia of pancreatic islet beta cells produces a state of *congenital hyperinsulinism*, which can result in severe and life-threatening hypoglycemia. More unusual neuroendocrine tumors include *medullary thyroid cancer*. Functional imaging of neuroendocrine tumors is used for diagnosis and initial staging, to assess for recurrence, and to assess response to therapy.

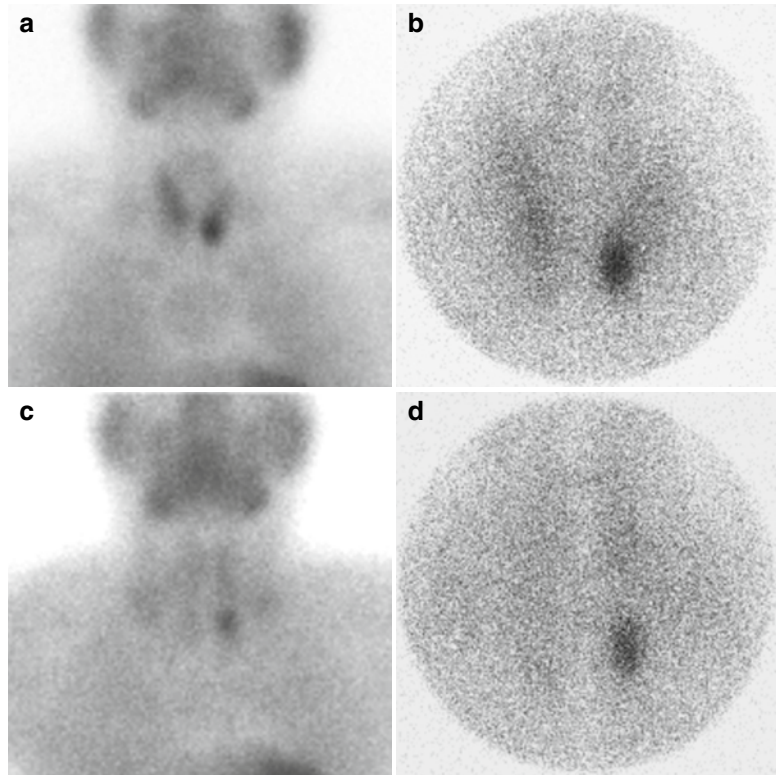

Fig. 20.3 Tertiary hyperparathyroidism as a complication of chronic renal failure evaluated by dual-phase ^{99m}Tc-sestamibi scintigraphy. Early-phase planar image of the neck and torso (**a**) and pinhole image of the neck (**b**) demonstrate diffuse uptake in the thyroid gland, with prominent tracer accumulation near the lower left pole of the thyroid gland. Late-phase (2 h) planar image of the torso (**c**) and pinhole image of the neck (**d**) show tracer washout from the thyroid with persistent focal uptake near the lower pole of the left lobe of the thyroid gland. Ultrasound identified an extrathyroidal cystic nodule, consistent with a parathyroid adenoma at this location

Methods

Nuclear medicine imaging of neuroendocrine tumors utilizes radiopharmaceuticals that recognize cell-surface or intracellular targets. Radionuclide therapy utilizes radiopharmaceuticals labeled with beta (or alpha) emitting radioisotopes (such as ^{131}I) that recognize the same cellular targets that are used for imaging. Two of these agents supported by the most clinical experience are ^{123}I-MIBG (targeting the norepinephrine transporter) and ^{111}In-pentreotide (targeting somatostatin receptors). With increasing availability of PET, ^{18}F-FDG has become more commonly used for neuroendocrine tumor imaging. The appropriate role for novel PET radiopharmaceuticals, such as ^{18}F-DOPA, ^{18}F-dopamine, and ^{11}C-labeled tracers, remains to be determined. Recently, ^{68}Ga-labeled PET radiopharmaceuticals have seen increasing use in adults and may become the agents of choice for imaging some neuroendocrine tumors in patients of all ages.

Frequently, more than one functional imaging test must be used to identify and localize a neuroendocrine tumor in any particular patient. The first choice of an imaging agent is determined by the clinical syndrome, an understanding of the biology of the likely tumor, and evolving imaging experience. Identifying the appropriate second-choice, and even third-choice, imaging study depends upon an informed nuclear medicine physician working in consultation with experienced referring clinicians, as ongoing clinical studies and the availability of new radiopharmaceuticals

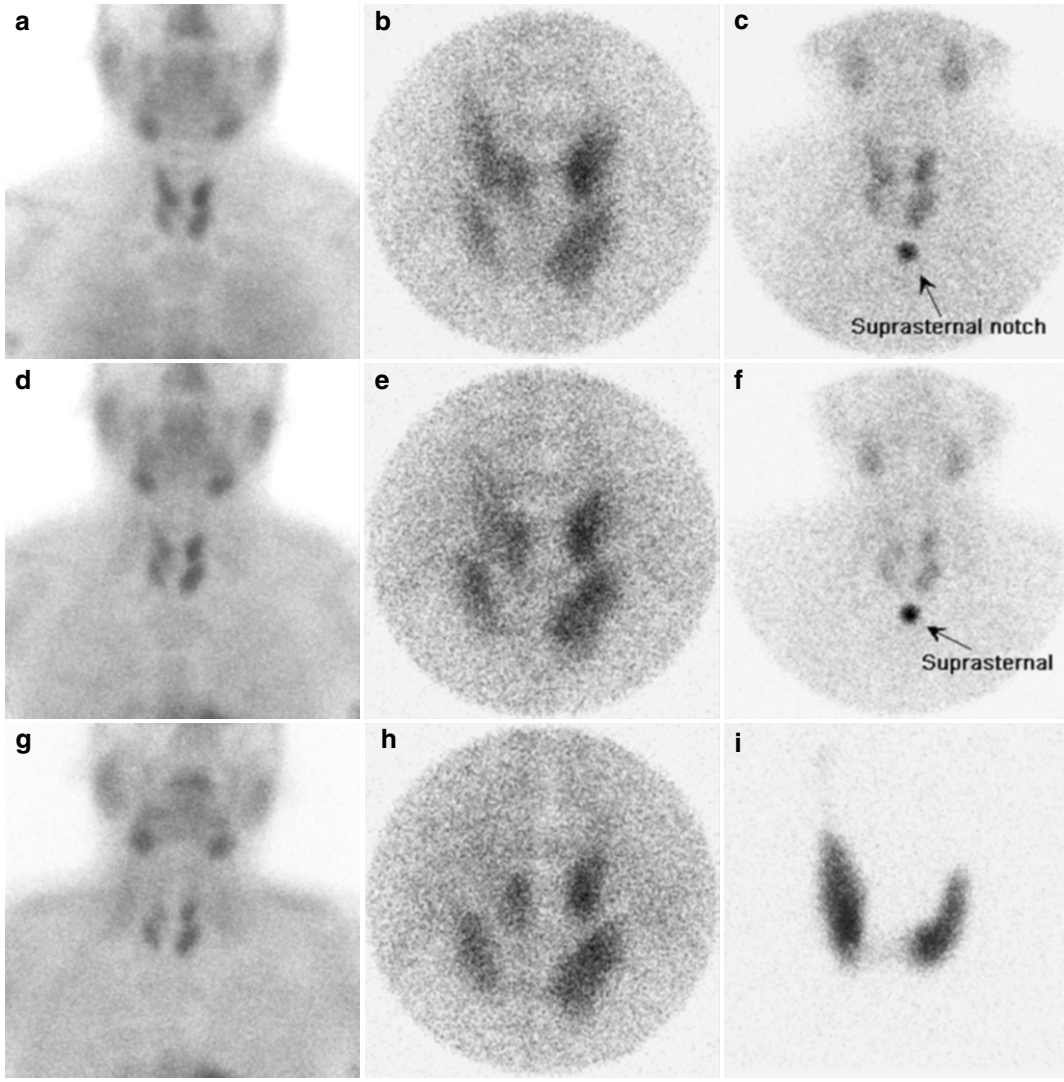

Fig. 20.4 Combined dual-phase and dual-isotope parathyroid imaging to identify four-gland parathyroid hyperplasia as a complication of chronic renal failure. After administration of ^{99m}Tc-sestamibi, a planar image of the torso and neck (**a**) shows multiple sites of abnormal uptake. A pinhole image of the neck (**b**) demonstrates at least five sites of abnormal tracer accumulation. A bird's-eye pinhole view with a marker in the suprasternal notch (**c**) demonstrates the location of abnormal uptake in the neck. Two hours later, a planar image of the torso and neck (**c**), pinhole image of the neck (**d**), and bird's-eye pinhole view with suprasternal marker (**e**, **f**) all show multiple sites of increased uptake in the neck, with partial washout at two upper sites. Four hours later, a planar view of the torso and neck (**g**) and anterior pinhole view of the neck (**h**) show persistent uptake at four sites in the neck. Delayed images can be helpful in evaluating patients with slow washout from some sites of abnormal tracer uptake. One week later, an ^{123}I thyroid scan (**i**) demonstrates intense uptake in both lobes of the thyroid gland. Demonstrating the location of the thyroid gland helps to confirm that, on the dual-phase scan, ^{99m}Tc-sestamibi washed out of the thyroid gland and was retained in four non-thyroidal lesions. Surgical exploration identified four enlarged hyperplastic parathyroid glands

will likely change the standard approach to evaluating many neuroendocrine tumors.

Radiopharmaceuticals

(^{123}I or ^{131}I)-Meta-iodobenzylguanidine (^{123}I-MIBG or ^{131}I-MIBG)

Meta-iodobenzylguanidine (MIBG) is a catecholamine analog that can be radiolabeled with either ^{123}I (physical half-life 13 h, primary gamma emission 159 keV) or ^{131}I (physical half-life 8 days, primary gamma emission 360 keV, as well as beta emission). MIBG is a ligand of the norepinephrine transporter (NET), which typically is found on autonomic nerve endings. By facilitating reuptake of catecholamines, the NET clears and thus modulates autonomic stimulation of effector tissues. As the NET also is expressed by most pheochromocytomas and by many paragangliomas, these cells will concentrate radiolabeled MIBG, which can be used to localize and image these tumors. Iodine-131-MIBG also is used for tumor-specific radiotherapy of neuroendocrine tumors expressing the norepinephrine transporter.

Many early methods of MIBG radioiodination produced a radiopharmaceutical with relatively low specific activity. When administered by rapid intravenous injection, the high levels of unlabeled or "cold" ^{127}I-MIBG could induce tachycardia and elevated blood pressure and cause adverse symptoms such as nausea, vomiting, and chest tightness. Therefore, radiolabeled MIBG typically has been administered by slow intravenous infusion over 3–5 min. Many institutions monitor and document heart rate and blood pressure during administration of ^{131}I-MIBG or ^{123}I-MIBG. With the recent commercial availability of no-carrier ^{123}I-MIBG (AdreView®, GE Healthcare), which contains minimal ^{127}I-MIBG, these concerns seem to be lessened. After administration of MIBG, a small amount of free iodine may be excreted through the kidneys, but most radiolabeled MIBG is excreted through the liver and bowel. Tracer accumulation in the bowel may obscure visualization of intra-abdominal pathology, especially on planar images.

Adequate patient preparation is necessary to ensure a technically adequate and clinically informative study. This includes blocking radioiodine uptake in the thyroid and screening the patient's medication list for drugs that may interfere with the study. Thyroid uptake is a concern for two reasons. Accumulation of ^{131}I can lead to thyroid dysfunction or ablation and increases the risk of thyroid cancer. Although current preparations are more likely to be labeled with ^{123}I and will contain less free iodine than in the past, intense tracer accumulation in the thyroid also may obscure nearby sites of disease in the neck. Pretreatment with nonradioactive iodine, as potassium iodine capsules or solution, is used to limit thyroid uptake of radioactive iodine. We routinely recommend SSKI at a dose of 1 drop three times a day, but some guidelines suggest much larger doses [59]. In preparation for an ^{123}I-MIBG study, thyroid blockade should be initiated 1 day before and continued for 3 days after the administration of ^{123}I-MIBG. Longer periods of blockage are needed with an ^{131}I-MIBG diagnostic study (6 days) or ^{131}I-MIBG therapy.

Numerous drugs have the potential to interfere with MIBG scintigraphy by interfering with MIBG uptake or vesicular storage (Table 20.1), and extensive lists of interfering drugs are available for reference [59–62]. For some of these drugs, specific interference with MIBG scintigraphy has been demonstrated. However, most drugs have been included because of similarity to the drugs with demonstrated interference. Most current clinical guidelines recommend that potentially interfering drugs be discontinued for 2–3 days before MIBG scintigraphy, but there are exceptions. For example, neuroleptic drugs administered in depot form may have an effect for up to 1 month. Ideally, any potentially interfering drug will be discontinued before the study is performed, but this may not be possible with many drugs. For example, it may not be possible to discontinue neuropsychiatric drugs or to hold antihypertensive medications necessary to control the symptoms of catecholamine excess. Any decision to discontinue prescription medications in preparation for an MIBG scan must be made in consultation with the referring or treating clinicians. In addition, patients and families should be advised to avoid over-the-counter cough and cold remedies.

Iodine-123-MIBG scintigraphy is performed 1 day after tracer administration and usually

Table 20.1 Drugs that may interfere with MIBG scintigraphy

CNS and psychiatric drugs (*many also used as antiemetics*)
Phenothiazines (e.g., chlorpromazine, fluphenazine, thioridazine, prochlorperazine, promethazine)
Butyrophenones (e.g., haloperidol, droperidol)
Atypical antipsychotics (e.g., clozapine, olanzapine, risperidone, aripiprazole, loxapine)
Tricyclic antidepressants (e.g., amitriptyline, imipramine, doxepin)
Other antidepressants (e.g., trazodone, venlafaxine, maprotiline, mirtazapine)
Stimulants (e.g., dextroamphetamine, methylphenidate, phentermine, cocaine, methamphetamine)
Other CNS-acting drugs (e.g., tramadol)
Cardiovascular medications
Calcium channel blockers (e.g., diltiazem, nifedipine, amlodipine, verapamil, felodipine)
Combined alpha-/beta-blocker (e.g., labetalol)
Inotropes and vasoconstrictors (e.g., dopamine, dobutamine, norepinephrine)
Adrenergic blockers (e.g., guanethidine, bretylium, reserpine)
Other cardiovascular drugs (e.g., amiodarone)
Other sympathomimetics
Over-the-counter decongestants and cold remedies (e.g., phenylephrine, pseudoephedrine, oxymetazoline, naphazoline)
Beta-2 sympathomimetics (except metered-dose inhaler) (e.g., albuterol/salbutamol, terbutaline, metaproterenol)
Sympathomimetics for glaucoma (e.g., brimonidine, dipivefrine)

Data from Refs. [59–62]

includes both whole-body planar imaging and SPECT or SPECT/CT. Although the primary emission of ^{123}I is a 159 keV gamma emission, 17 % of the gamma emission is greater than 159 keV. A substantial portion of this high-energy gamma emission penetrates a low-energy collimator, which will increase image noise and decrease image quality. Imaging ^{123}I-labeled radiopharmaceuticals with a medium-energy collimator improves image quality with little sacrifice in sensitivity [63]. Because of the longer half-life of ^{131}I, ^{131}I-MIBG can be imaged up to many days after administration but usually is imaged after 1 day, as there is little improvement in image quality or accuracy with delayed imaging. Iodine-131-MIBG is appropriately imaged using a high-energy collimator. However, many gamma cameras are unable to perform SPECT with the heavy high-energy collimator. Also, the radiation dose may be up to 20-fold greater with ^{131}I-MIBG than with ^{123}I-MIBG. Because of this higher radiation dose, the inability to perform SPECT, and the poorer planar image quality, ^{131}I-MIBG now is used much less frequently than ^{123}I-MIBG for diagnostic imaging. Interpretation of MIBG scintigraphy requires familiarity of the normal patterns of physiological uptake of ^{123}I/^{131}I-MIBG uptake (Fig. 20.5). This includes uptake in the liver and salivary glands and variable uptake in the heart, lungs, and brown adipose tissue. Physiological tracer accumulation in bowel and the urinary collecting system can obscure sites of abnormal uptake. For nearly all MIBG studies, SPECT will increase sensitivity and may help localize a site of abnormal uptake. Hybrid imaging (SPECT/CT) or software co-registration with CT or MR images allows improved localization and may improve specificity (Fig. 20.6).

^{111}In-Pentetreotide

Indium-111-pentetreotide is an ^{111}In-labeled peptide ligand that targets cell-surface somatostatin receptors [57, 64–66]. There are five well-characterized somatostatin receptors (SST1–SST5), for which the 14-amino acid peptide somatostatin is the native ligand and produces an inhibitory effect on neuroendocrine cell function. Somatostatin has an extremely short biological half-life, but octreotide, an 8-amino acid somatostatin analog, has a biological half-life of many hours and can be used as an effective therapeutic agent for many neuroendocrine tumors. Using DTPA as a chelator, octreotide can be labeled with ^{111}In as [^{111}In] indium chloride ($InCl_3$) to produce ^{111}In-DTPA-octreotide, also called ^{111}In-pentetreotide (OctreoScan®). Indium-111-

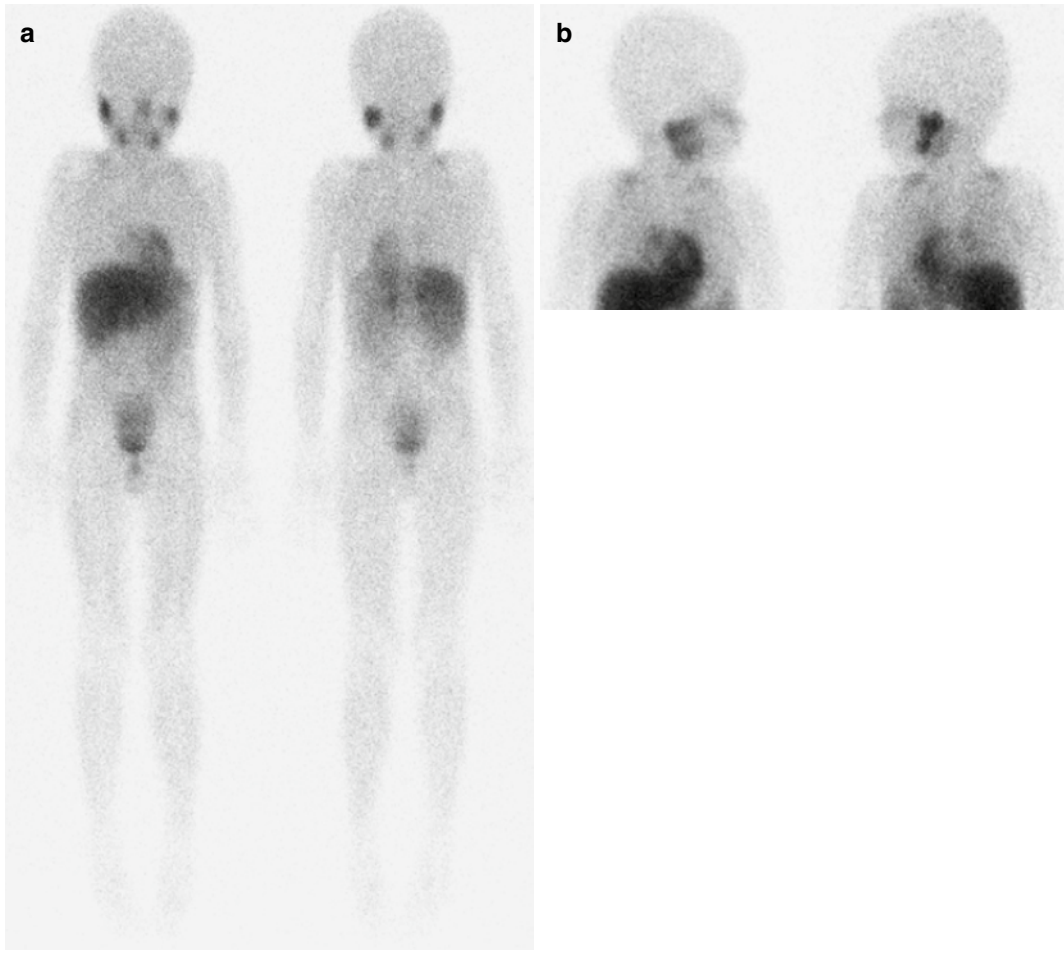

Fig. 20.5 Normal ^{123}I-MIBG scans. (**a**) The normal distribution of ^{123}I-MIBG includes uptake in the salivary glands, myocardium, and liver. Myocardial uptake can be variable and may not be seen in some children. Physiological uptake also is seen in both adrenal glands. Excreted tracer is seen in the urinary tract and gastrointestinal tract. (**b**) In another patient, lateral views of the head are routinely performed to better evaluate for involvement with MIBG-avid disease. Bilateral supraclavicular uptake reflects normal uptake at sites of brown adipose tissue. In the chest, subtle bilateral uptake throughout both lung fields represents normal physiological uptake in the lungs

pentetreotide has the highest affinity for SST2 receptors but also may bind to SST5, and possibly SST3, receptors [67]. Indium-111 is a cyclotron product produced by proton irradiation (p, 2n reaction) of a ^{112}Cd enriched target and decays (physical half-life 67 h or 2.8 days) with gamma emission of multiple energies, the most abundant with energies of 171 and 245 keV.

The recommended administered dose of ^{111}In-pentetreotide for children is 3 MBq/kg (0.08 mCi/kg) with a maximum dose of 200–220 mBq (5.4–6 mCi) [65, 66]. Therapeutic octreotide acetate (Sandostatin®) typically is discontinued before administration of ^{111}In-pentreotide. This should be done in collaboration with the treating clinician, as occasionally a patient may not be able to tolerate even short periods of withdrawal. The appropriate period of withdrawal depends on the octreotide formulation. One to three days of withdrawal have been recommended for the standard formulation of octreotide. For long-acting/sustained-release formulations of octreotide (e.g., Sandostatin-LAR®), 3–6 weeks of withdrawal may be needed. Typically, for patients being

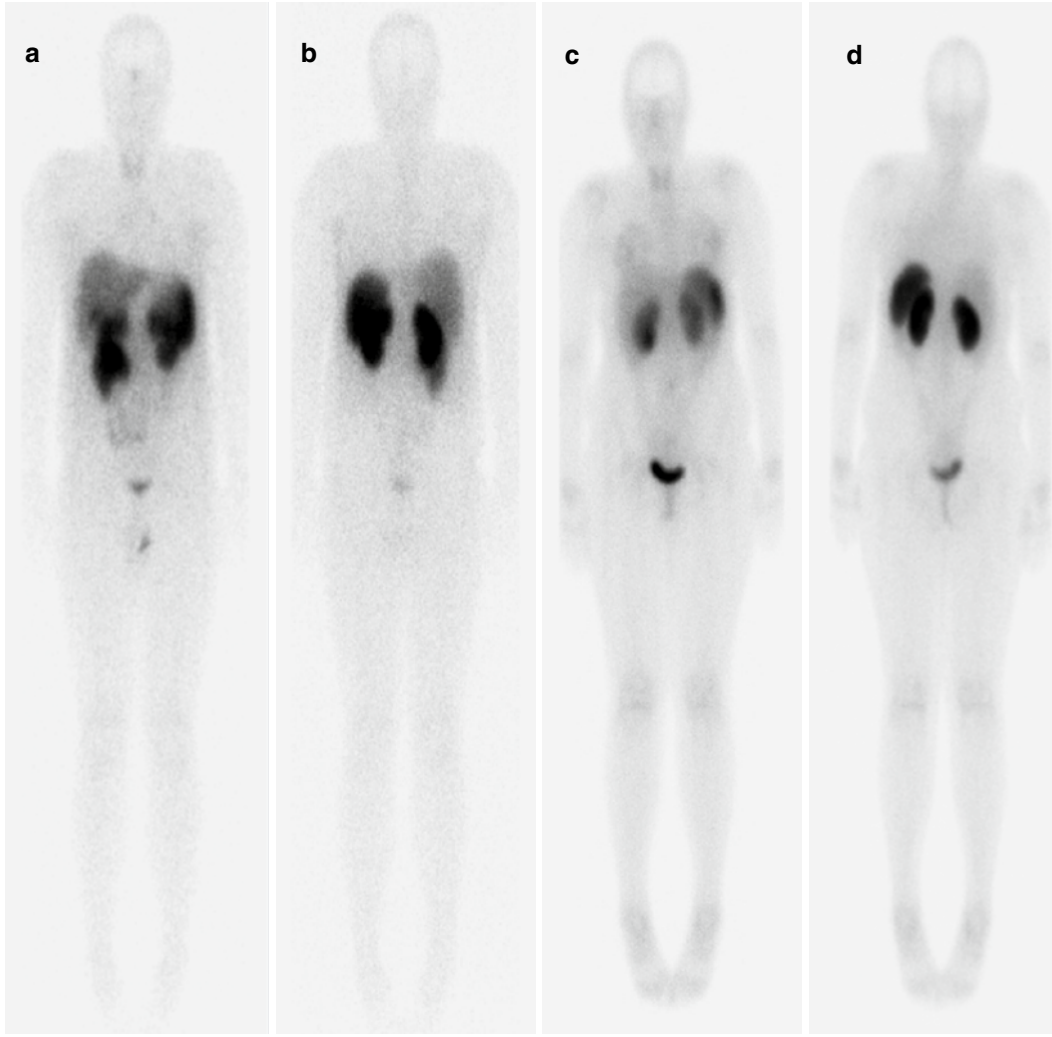

Fig. 20.6 Normal ^{111}In-pentreotide scans. Whole-body images 1 day after administration of ^{111}In-pentreotide in the anterior (**a**) and posterior (**b**) projections show intense uptake in the spleen, gallbladder, and both kidneys; moderate uptake in the liver; and mild uptake in the thyroid and pituitary glands. Accumulation of excreted tracer is seen in the bowel and urinary tract. In another patient, whole-body images in the anterior (**c**) and posterior (**d**) projections show a similar pattern of uptake with intense uptake in both kidneys and the spleen and mild uptake in the liver, breasts, and thyroid gland

treated with a monthly dose of sustained-release formulation, the imaging study is performed about 1 month after the last dose and just before the next scheduled dose of sustained-release octreotide.

Images routinely are acquired 1 day after administration of ^{111}In-pentreotide. Most tracer is excreted through the kidneys, so patients should be encouraged to maintain fluid intake and to void before imaging. A small amount of tracer is excreted through the biliary system and typically may be present in the gut for up to 48 h after administration. As this can interfere with detection of abnormal uptake, patients with suspected intra-abdominal disease will need additional imaging of the abdomen and pelvis. This is performed either at 4 h, before there is substantial bowel accumulation of tracer, or at 48 h, after clearance of tracer from the bowel. In our department, we routinely acquire images of the abdomen 4 h after administration of ^{111}In-pentetreotide.

Administration of a mild laxative may help to clear tracer from the bowel. Most clinical guidelines [65, 66] suggest that bisacodyl or lactulose be given both in the evening before radiopharmaceutical administration and in the evening before imaging. Alternatively, in our department, we have found that bowel preparation using a polyethylene glycol solution given only the evening after radiopharmaceutical administration avoids the risk of dehydration and is effective and well tolerated. Patient compliance can be improved by using a flavored clear liquid to dissolve the polyethylene powder or by using commercially available sulfate-free, flavored solutions [68].

Patients with biochemical evidence of an insulinoma require special attention when performing somatostatin-receptor scintigraphy [66]. They may be less tolerant of the withdrawal of octreotide (Sandostatin®) therapy, and the plan to delay administration of octreotide must be done in consultation with the treating endocrinologist. On the other hand, there is a theoretical possibility that acute administration of ^{111}In-pentetreotide will suppress glucagon secretion and result in hypoglycemia. Therefore, the ^{111}In-pentetreotide package insert recommends that patients with suspected insulinoma receive an intravenous infusion of dextrose at the time of ^{111}In-pentetreotide administration. Finally, any bowel preparation and dietary restrictions should be planned with care and in collaboration with the treating endocrinologist.

Images are acquired using a medium-energy collimator with energy windows centered around both major ^{111}In photopeaks (171 and 245 keV). Planar images are acquired of the whole body, including extremities if indicated. If the child can cooperate, a whole-body sweep can be performed, but additional planar images, including lateral views, of the head and neck are recommended to detect possible metastatic disease in cervical lymph nodes [66]. SPECT of the torso can improve scan sensitivity and can assist in localization of disease. SPECT/CT or software fusion of SPECT images with a prior CT or MR scan also may be helpful for disease localization [69, 70].

Interpretation of somatostatin-receptor scintigraphy requires familiarity of the normal pattern of physiological uptake of ^{111}In-pentetreotide (Fig. 20.7). This includes intense uptake in the spleen, liver, gallbladder, and kidneys. Mild uptake may be seen in the breast and occasionally in the pituitary and thyroid glands. Physiological tracer accumulation in bowel and the urinary collecting system can obscure sites of abnormal uptake.

^{18}F-Fluoro-Deoxyglucose (FDG)

Fluorine-18-labeled PET agents have become alternatives to gamma-emitting radiopharmaceuticals for imaging and detecting neuroendocrine tumors. Fluorine-18-fluoro-2-deoxyglucose (^{18}F-FDG) is a glucose analog labeled with ^{18}F. Fluorine-18-FDG is taken into cells through one of the transmembrane glucose transporters but does not enter the energy-producing metabolic pathways [71]. Insulin-mediated stimulation of expression of some glucose transporters (e.g., GLUT-4) will increase cellular uptake of ^{18}F-FDG in insulin-sensitive tissues such as skeletal muscle, liver, and myocardium [72]. Fluorine-18-FDG is phosphorylated by cellular hexokinases, but after monophosphorylation, FDG-6 phosphate cannot be phosphorylated and is trapped in the cell [73], which provides a mechanism for amplification of the ^{18}F signal. Only a few tissues, such as the liver, express sufficient phosphorylase activity to dephosphorylate a substantial fraction of FDG-6 phosphate to FDG, which can then be cleared from the cell. The North American consensus guidelines [74] recommend a pediatric dose of 3.7–5.2 MBq/kg (0.10–0.14 mCi/kg) for torso/whole-body imaging. The appropriate role of ^{18}F-FDG, compared to ^{111}In-pentreotide and ^{123}I-MIBG, is not yet resolved. Compared to these agents, ^{18}F-FDG is a nonspecific indicator of tumor metabolism but in some circumstances also may demonstrate increased sensitivity. Another benefit of ^{18}F-FDG may be the ability to quantitatively assess uptake and to follow uptake over time [75]. Fluorine-18-FDG is not well suited to imaging patients with a functional insulinoma, as the elevated insulin levels will stimulate FDG uptake into skeletal and myocardial muscle, which can obscure sites of disease and will decrease availability for tumor uptake [57].

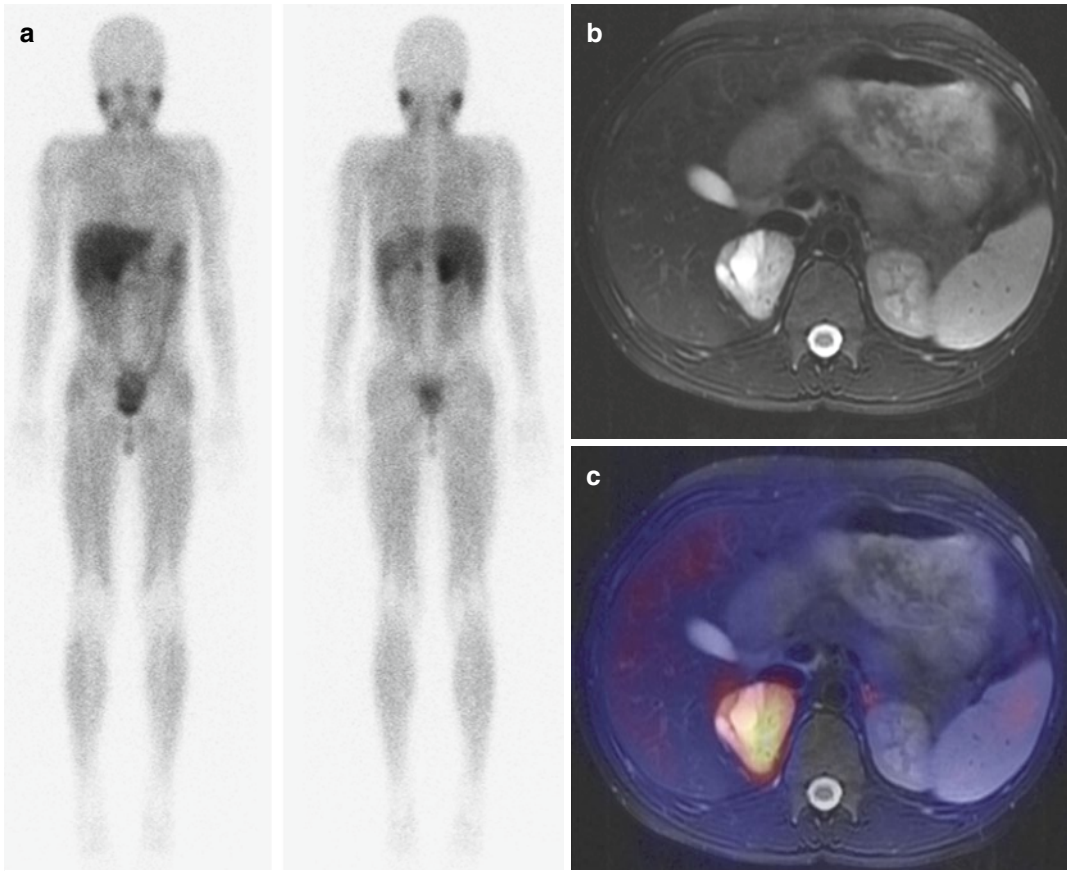

Fig. 20.7 Pheochromocytoma imaged with an ^{123}I-MIBG scan. (**a**) An ^{123}I-MIBG whole-body scan in anterior and posterior projections shows intense focal uptake in the right upper quadrant and a smaller focus of increased uptake in the left upper quadrant. (**b**) A previously acquired MR showed a T2-hyperintense heterogenous adrenal mass with both cystic and solid components in the right adrenal gland. (**c**) Software co-registration of ^{123}I-MIBG SPECT and MR images confirms that the adrenal mass has abnormal ^{123}I-MIBG avidity, which is most intense in the solid components of the mass. Physiological ^{123}I-MIBG uptake is seen in the normal left adrenal gland. Genetic testing identified no underlying genetic predisposition for neuroendocrine tumors

Other ^{18}F-Labeled PET Agents

Fluorine-18-fluoro-dihydrophenylalanine (^{18}F-DOPA) is an F-18-labeled radiopharmaceutical that may act as a radiolabeled analog of both an amino acid derivative and a catecholamine precursor. Cellular uptake of ^{18}F-DOPA is mediated by the large amino acid transporter (LAT), but once in the cell ^{18}F-DOPA can function as an indicator of catecholamine synthesis [75, 76]. The use of ^{18}F-DOPA for neuroendocrine imaging has been reported extensively [75, 76], but its role has not been defined for the evaluation of most neuroendocrine tumors. ^{18}F-DOPA also has proven useful for the evaluation of beta-cell hyperplasia in infants with congenital hypoglycemia. One limitation to the wider use of ^{18}F-DOPA has been the need for elemental ($^{18}F_2$) ^{18}F for synthesis and the poor yield of the standard ^{18}F-DOPA synthesis reactions.

Fluorine-18-dopamine is less readily available than other ^{18}F-labeled PET agents used for neuroendocrine imaging, but it may have a high level of accuracy for identifying primary sites of disease and metastases of neuroendocrine tumors. It is transported into cells by the dopamine transporter (DAT) in the brain and by the norepinephrine transporter (NET) found in autonomic nerve endings and neuroendocrine tumors [76].

^{68}Ga-Labeled Radiopharmaceuticals

Gallium-68 (physical half-life 68 h) decays by positron emission and is available as the product of a ^{68}Ge generator. Gallium-68 has seen increasing use as a PET radiotracer, particularly for labeling somatostatin-receptor-binding peptides for neuroendocrine tumor imaging [75]. Using the chelator DOTA, ^{68}Ga has been used to radiolabel several octreotide analogs, such as Tyr3-octreotide (^{68}Ga-DOTA-TOC) [67, 75, 77]. Many of these ^{68}Ga-labeled compounds have been studied as investigational neuroendocrine tumor imaging agents.

Neuroendocrine Tumors: Clinical

Sympathochromaffin Tumors

Sympathochromaffin tumors arise in cells of the autonomic nervous system [78] and have the potential to secrete sympathetic amines, typically norepinephrine, epinephrine, and dopamine, which can produce adrenergic symptoms such as hypertension, tachycardia, and anxiety. The different sympathochromaffin tumors demonstrate a range of malignant potential and a range of catecholamine secretion. *Neuroblastoma* is the most common extracranial solid malignant tumor of childhood (see Chap. 19). Neuroblastoma may secrete catecholamines at low levels that rarely are sufficient to cause adrenergic symptoms. *Pheochromocytoma* refers to sympathochromaffin tumors in the medulla of the adrenal gland, and *paraganglioma* refers to a sympathochromaffin tumor that arises from the extra-adrenal autonomic nervous system. Typical locations for a paraganglioma are the sympathetic plexi of the heart, kidneys, or urinary bladder, the inferior mesenteric sympathetic ganglion (body of Zuckerkandl), and aortopulmonary sympathetic ganglion [79]. Generally, these tumors can secrete high levels of catecholamines to produce severe, and potentially life-threatening, adrenergic symptoms, but they can be subclinical or asymptomatic. A paraganglioma arising from a parasympathetic ganglion in the head and neck (sometimes referred to as a glomus tumor) rarely secretes catecholamines. Well-differentiated sympathochromaffin tumors, such as *ganglioneuroma*, also rarely secrete catecholamines and usually present as a mass lesion or incidental finding, most commonly along the spine.

In the past, it was taught of pheochromocytomas that 10 % were bilateral, 10 % were familial, and 10 % were malignant. However, these numbers do not accurately reflect the current understanding of pheochromocytoma, particularly when it occurs in children. Although most sympathochromaffin tumors present as single tumors, pheochromocytomas can be bilateral, with involvement of both adrenal glands, and paragangliomas may occur as multifocal disease. In children, multifocal pheochromocytoma and paragangliomas occur in over one-third of cases [79]. Sympathochromaffin tumors often appear as sporadic tumors but also can occur as part of hereditary tumor syndromes. As specific genetic mutations are identified for more tumor syndromes, an increasing number of sympathochromaffin tumors are recognized to be a manifestation of a hereditary syndrome. This particularly is true in children and teenagers, in whom approximately half of pheochromocytomas may be due to an identifiable mutation. In children less than 10 years of age, up to 70 % of pheochromocytomas may be hereditary [80].

In patients with hereditary syndromes, pheochromocytoma is more likely to be bilateral, and paragangliomas are more likely to be multifocal [78]. In children, the hereditary syndromes most commonly associated with sympathochromaffin tumors are von Hippel-Lindau (VHL) syndrome and the multiple endocrine neoplasia (MEN) 2A and 2B syndromes. Familial paraganglioma (and pheochromocytoma) syndromes can be associated with mutations in genes encoding one of the subunits of succinate dehydrogenase (SDH), a mitochondrial enzyme. Mutations in three of these genes, SDHB, SDHC, and SDHD, have high penetrance in association with hereditary sympathochromaffin tumors. With identification of additional tumor susceptibility genes for sympathochromaffin tumors, the number of apparently sporadic tumors will continue to decrease [81, 82].

Approximately 10 % of pheochromocytomas will have metastases and on this basis are considered to be malignant. For sympathochromaffin tumors, no histological feature reliably defines malignancy. Malignancy is identified by the presence of metastases at sites where sympathochromaffin tissue usually is not present, such as bone, liver, lungs, and lymph nodes. Malignancy is more common with paragangliomas and in sympathochromaffin tumors with specific genetic markers, such as mutations in the succinyl dehydrogenase B (SDHB) gene [83].

Children with sympathochromaffin tumors (excluding neuroblastoma) usually present with signs and symptoms of catecholamine excess but less commonly may present with a tumor mass, as an incidental finding on an unrelated radiological study or during screening of family members with a suspected hereditary syndrome [78]. The diagnosis of secretory sympathochromaffin tumor is confirmed with biochemical testing for catecholamine and catecholamine metabolites in urine and blood. Chromogranin A is a circulating tumor marker that may correlate with tumor size and malignant potential and that is useful for long-term follow-up.

With few exceptions, imaging studies should not be performed before the clinical and biochemical diagnosis of a sympathochromaffin tumor has been established. Usually, the first imaging test is either CT or MRI of the torso. On a non-contrast CT, an adrenal lesion with an attenuation value less than 10 HU excludes pheochromocytoma [80]. Otherwise, intravenous contrast will be needed to characterize the lesion. As the use of iodinated contrast has been associated with hyperadrenergic crisis in patients with pheochromocytoma, adequate alpha-adrenergic, and possibly beta-adrenergic, blockade is recommended before a contrast-enhanced CT scan. This may be less of a concern with nonionic contrast [80]. The classic MR appearance of sympathochromaffin tumors is T2 hyperintensity. However, this is not specific, as similar hyperintensity can be seen with hemorrhage. On the other hand, larger sympathochromaffin tumors may appear inhomogeneous due to necrosis or hemorrhage.

The appropriate use of nuclear medicine studies has not been settled for patients with the biochemical diagnoses of pheochromocytoma and a solitary adrenal mass on cross-sectional imaging (Fig. 20.7). Some investigators have suggested that in adults with a solitary adrenal mass, an ^{123}I-MIBG scan will be only confirmatory and is unlikely to alter the surgical approach [84, 85]. However, others have reported that an ^{123}I-MIBG study can confirm catecholamine production in the identified tumor and may identify other sites of disease not found on cross-sectional imaging [78, 80]. This may be most important to identify or to exclude other sites of disease in patients with suspected multifocal disease, particularly those with a known hereditary syndrome or germ line mutation (Fig. 20.8) [86].

Iodine-123-MIBG typically has up to 95 % sensitivity and greater than 95 % specificity for pheochromocytoma [80, 87] but only approximately 70 % sensitivity for paragangliomas (Fig. 20.9). Iodine-131-MIBG demonstrates slightly less sensitivity for both types of tumors, possibly due to the poorer imaging characteristics of ^{131}I. The accuracy of MIBG imaging may depend, in part, on the experience of the interpreter. Both sensitivity and specificity may be improved by SPECT, SPECT/CT, or software co-registration of SPECT with a diagnostic CT or MR study (Fig. 20.10). However, not all sympathochromaffin tumors will be detected with MIBG (Fig. 20.11). One common cause of a false-negative scan is interference by other drugs, if these drugs were not discontinued appropriately prior to administration of ^{123}I-MIBG (Table 20.1).

If a patient with a biochemically confirmed sympathochromaffin tumor has a negative MIBG scan, then a second, or even third, functional imaging test will be necessary to localize the tumor or metastases. In this circumstance, the usual second agent has been ^{111}In-pentreotide. However, with the availability of ^{18}F-FDG and an increasing number of other PET agents, the most appropriate approach for diagnostic localization of sympathochromaffin tumors has not been settled,

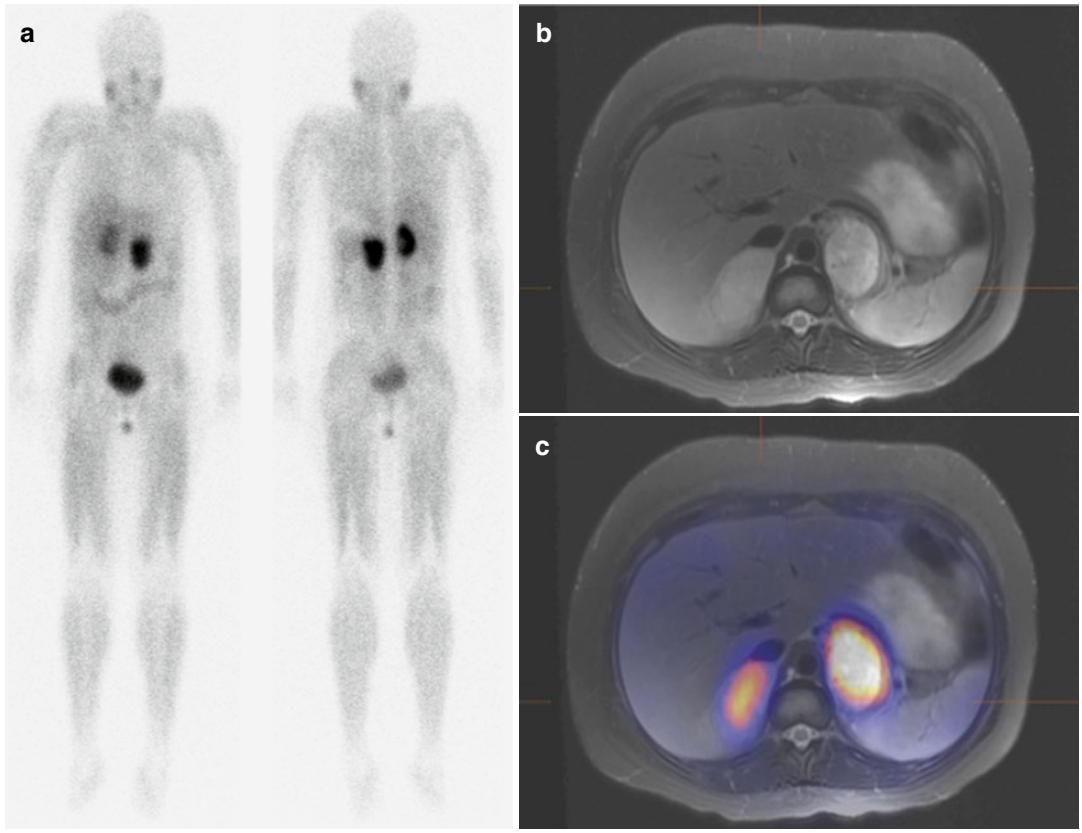

Fig. 20.8 Bilateral pheochromocytomas identified by ^{123}I-MIBG scan. (**a**) An ^{123}I-MIBG whole-body scan in anterior and posterior projections shows intense focal uptake in both upper quadrants. (**b**) Correlative MRI demonstrates bilateral adrenal masses with heterogenous T2 hyperintensity. (**c**) Software co-registration of ^{123}I-MIBG SPECT and MR images confirms bilateral MIBG-avid adrenal masses. After surgical resection of bilateral pheochromocytomas, genetic testing confirmed the diagnosis of von Hippel-Lindau syndrome

especially for children. Overall, ^{111}In-pentreotide is less sensitive than ^{123}I-MIBG for detection of sympathochromaffin tumors but may detect some MIBG-negative tumors. One exception is the higher sensitivity of ^{111}In-pentreotide for imaging head and neck paragangliomas [88]. In most institutions, the other alternative to ^{123}I-MIBG is ^{18}F-FDG-PET. Fluorine-18-FDG is highly sensitive, but not specific, for sympathochromaffin tumors. Fluorine-18-FDG may be more sensitive than ^{123}I-MIBG for detecting one subtype of sympathochromaffin tumor, those associated with mutations in the SDHB gene [89]. Some investigators have reported that other ^{18}F-labeled PET radiopharmaceuticals, such as ^{18}F-DOPA and ^{18}F-dopamine (^{18}F-DA), are highly sensitive for detecting sympathochromaffin tumors [89]. However, there have been few studies to confirm these findings or determine their widespread applicability.

Enterochromaffin (Carcinoid) Tumors

Carcinoid (*enterochromaffin*) *tumors* can develop anywhere along the respiratory or gastrointestinal tracts. The most common presentation is as a single pulmonary nodule, which may be identified during evaluation of a post-obstructive pneumonia or may come to attention as an incidental finding on chest radiograph or CT (Fig. 20.12). In the gastrointestinal tract,

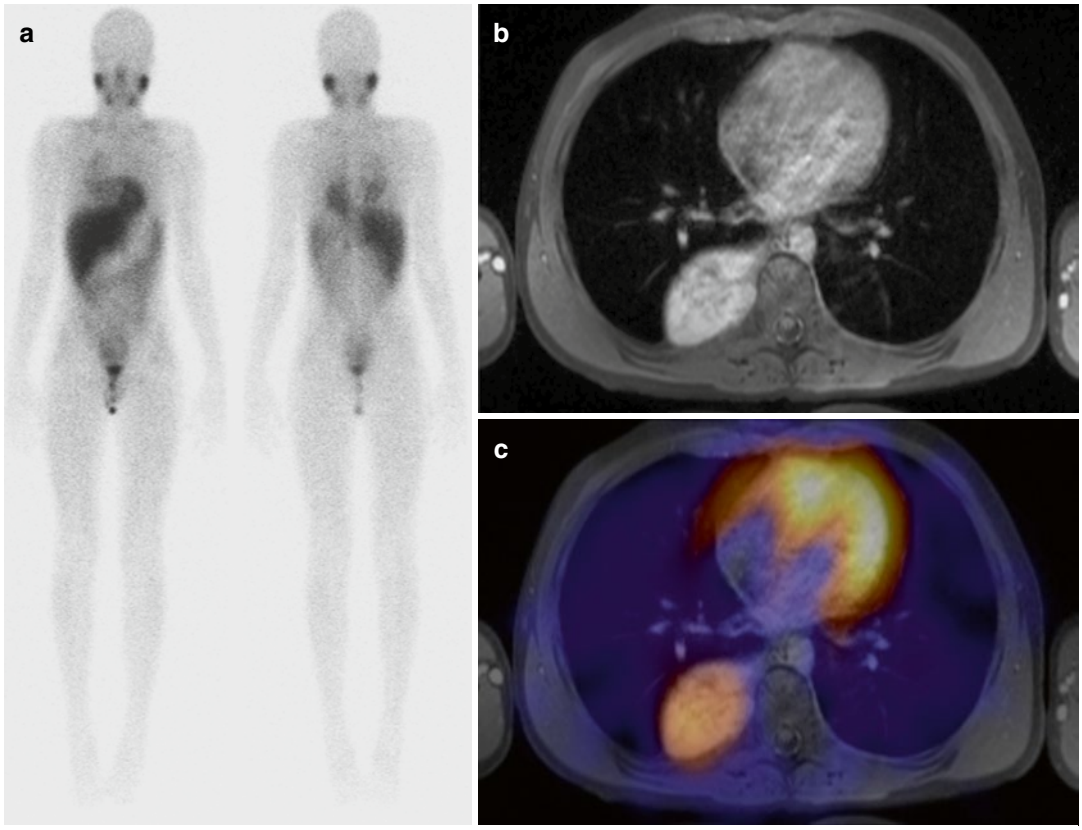

Fig. 20.9 Paravertebral paraganglioma localized with ^{123}I-MIBG scan. (**a**) An ^{123}I-MIBG whole-body scan in anterior and posterior projections shows abnormal uptake in the right hemithorax. (**b**) MR of the chest also shows a heterogeneously enhancing T2 hyperintense right paravertebral mass. (**c**) Software co-registration of ^{123}I-MIBG SPECT and MR images confirms that the paravertebral mass has abnormal ^{123}I-MIBG avidity. The diagnosis of paraganglioma was made on surgical pathology

a carcinoid tumor may be found obstructing the appendix at the time of appendectomy for acute appendicitis. Carcinoid tumors can secrete a wide range of vasoactive amines. The most common secretory product is serotonin, which can produce the classic carcinoid syndrome, with symptoms such as tachycardia, flushing, and bronchoconstriction. However, the carcinoid syndrome is extremely rare in children. Carcinoid tumors can be classified based on location (foregut, midgut, and hindgut) or histology. Typical carcinoids appear well differentiated, while atypical carcinoids are characterized by increased proliferation and nuclear atypia. Recently, there has been an attempt to provide a more detailed histological characterization of carcinoid tumors to grade tumors with proliferative index as a measure of malignant potential [90].

Imaging of carcinoid tumors depends on both anatomic and functional imaging. Nuclear medicine imaging is focused depending upon the location of the primary tumor. CT provides excellent anatomic imaging of bronchopulmonary carcinoids but may detect only half of intra-abdominal carcinoid tumors. CT and MRI have higher sensitivity for mesenteric or liver metastases [90]. In bronchopulmonary carcinoid tumors, FDG avidity may reflect malignant potential, with atypical carcinoids demonstrating higher uptake than typical carcinoid tumors (Fig. 20.13). In the abdomen, ^{18}F-FDG PET is less useful, as

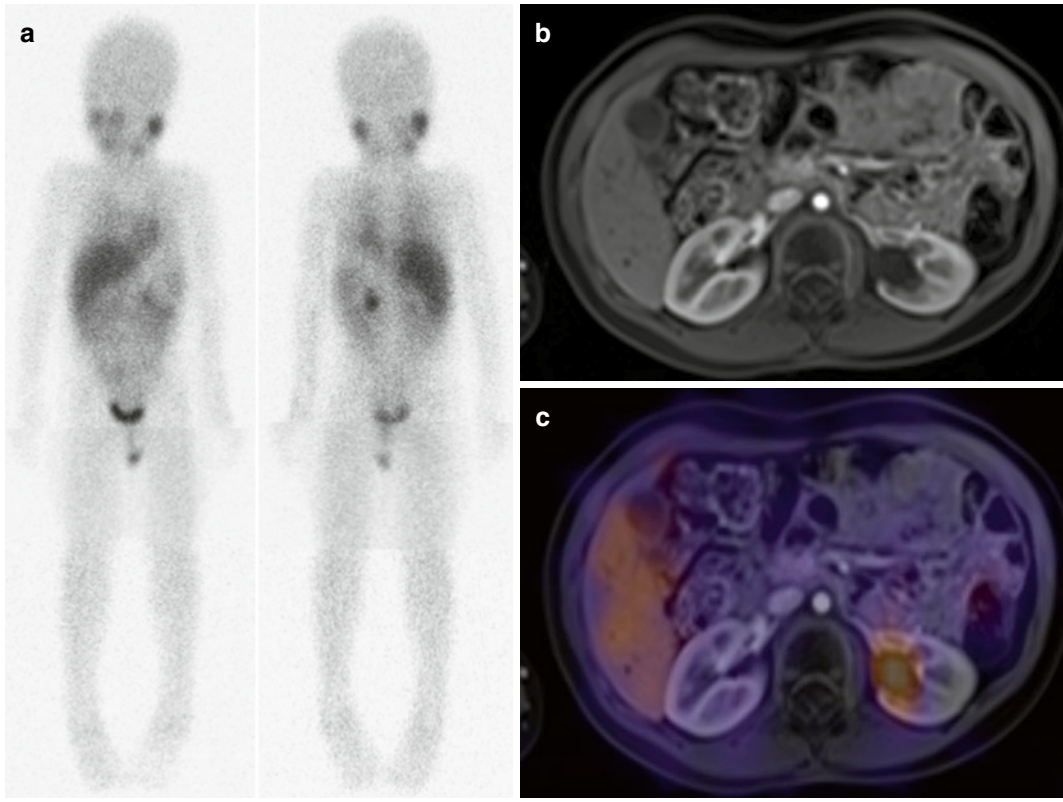

Fig. 20.10 Iodine-123-MIBG SPECT and CT co-registration are useful to exclude recurrent tumor. (**a**) After resection of a large left suprarenal neuroblastoma, a postoperative restaging ^{123}I-MIBG whole-body scan in anterior and posterior projections shows intense tracer accumulation in the left upper quadrant and a small focus of mild uptake in the right upper quadrant. (**b**) A contrast-enhanced CT of the abdomen shows a dilated left renal pelvis but no abnormal soft tissue masses to suggest residual or recurrent tumor. (**c**) Co-registration of ^{123}I-MIBG SPECT and CT images demonstrates tracer accumulation in the left renal collecting system and confirms the absence of MIBG-avid tumor. ^{123}I-MIBG SPECT/CT fusion images also confirmed physiological ^{123}I-MIBG uptake in the right adrenal gland

carcinoid tumors may have variable uptake and small tumors may be obscured by physiological ^{18}F-FDG accumulation in the intestine and liver [91]. Both ^{111}In-pentreotide and ^{123}I-MIBG have high sensitivity (60–90 %) for carcinoid tumors, and the combined use of both agents may provide higher sensitivity. Typically, ^{111}In-pentreotide is used as the first agent of choice as tumor uptake provides prognostic information about the potential tumor response to octreotide therapy [92]. Fluorine-18-DOPA and ^{68}Ga-labeled PET agents have been used to evaluate carcinoid tumors, but these agents have not yet entered routine clinical use [92, 93].

Gastro-Entero-Pancreatic (GEP) Tumors

As with other neuroendocrine tumors, the clinical presentation of GEP tumors will reflect the specific peptides that are secreted by the tumor cells. In children and young adults, the most common of these tumors are insulinoma and gastrinoma. Occasionally, a GEP tumor will produce a syndrome of ectopic hormone production. Nonsecretory GEP tumors will present first with a mass effect, for example, biliary or pancreatic duct obstruction, or as an incidental finding.

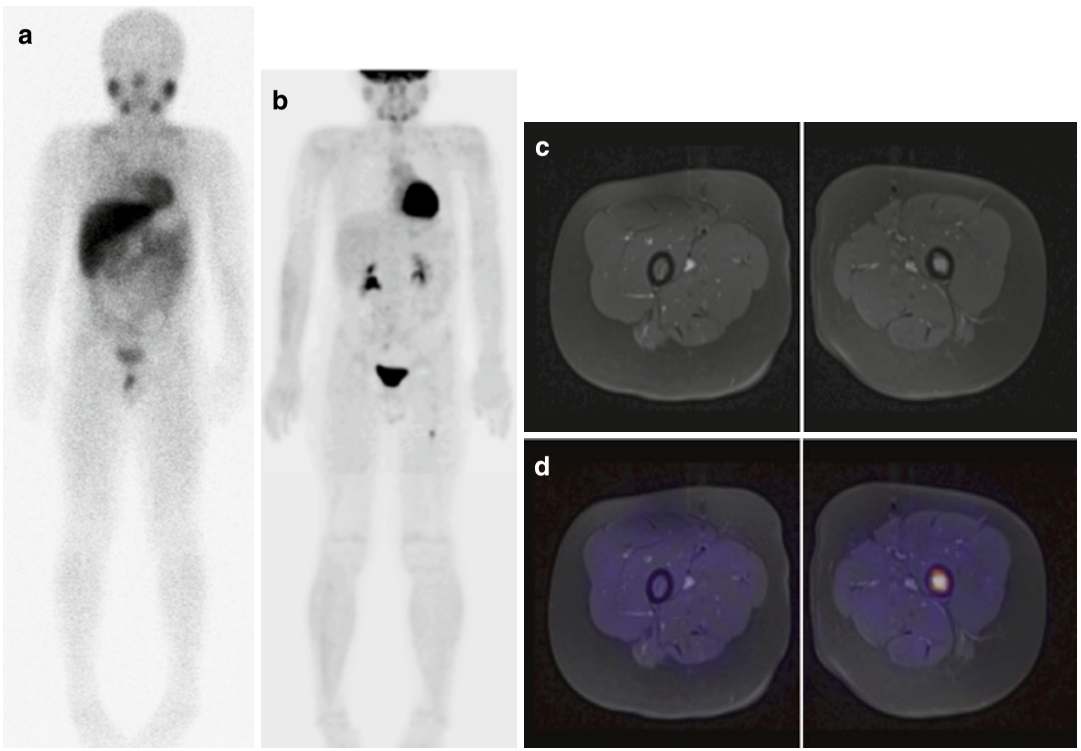

Fig. 20.11 A paraganglioma demonstrates differential avidity for ^{18}F-FDG and ^{123}I-MIBG. (**a**) After resection of an abdominal paraganglioma, a surveillance ^{123}I-MIBG scan in anterior projection shows the expected normal distribution of ^{123}I-MIBG scan. (**b**) Four months later, a surveillance ^{18}F-FDG PET shows an abnormal focal uptake in the left thigh. (**c**) MRI of the lower extremities shows an enhancing intramedullary lesion in the left femur. (**d**) Co-registration of ^{18}F-FDG PET and MR images confirms that the enhancing marrow lesion is FDG-avid, consistent with paraganglioma. Genetic testing identified a germ line mutation in the SHDB gene, and the lesion was treated with radio-frequency ablation

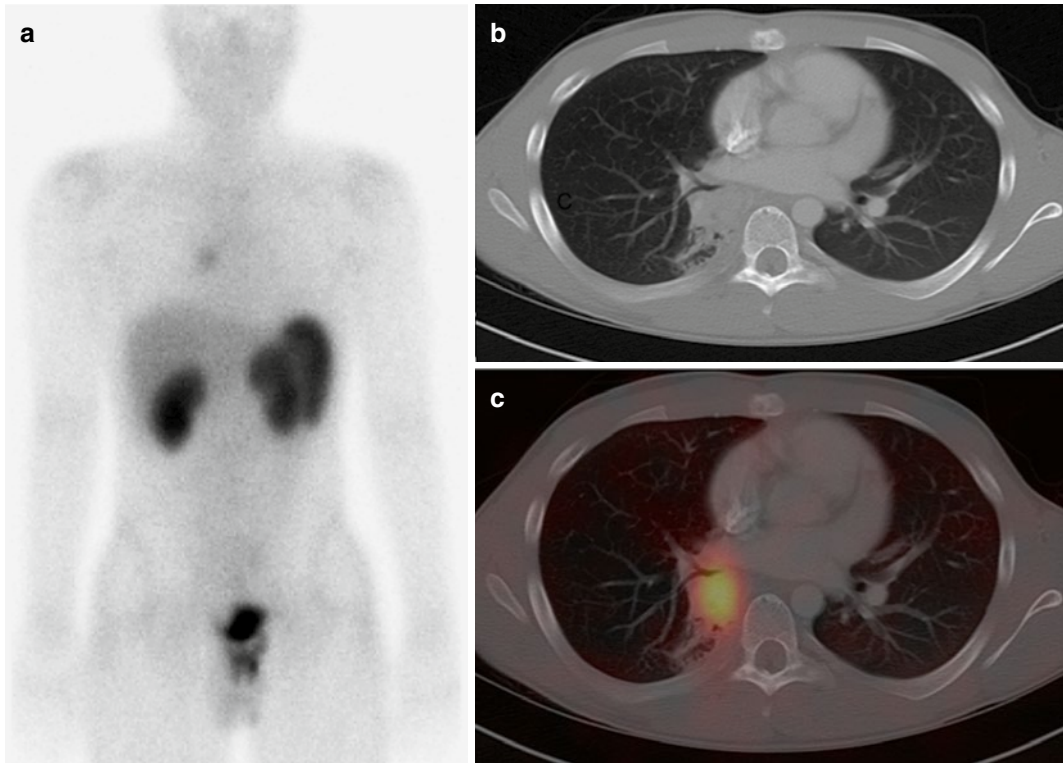

Fig. 20.12 Indium-131-pentreotide scan of an endobronchial carcinoid. (**a**) Whole-body ^{111}In-pentreotide scan in the anterior projection shows a focus of abnormal moderate uptake near the right hilum. (**b**) Chest CT shows a 2 cm mass lesion obstructing the lower right bronchus. (**c**) Co-registration of ^{111}In-pentreotide SPECT images and chest CT confirm that the abnormal pentetreotide avidity is in the endobronchial lesion, which was an endobronchial carcinoid

Insulinoma is one of the more common GEP tumors of childhood. Patients present with episodic hypoglycemia, particularly after periods of relative fasting. For example, a child may present with early-morning irritability, headaches, or hyperphagia due to hypoglycemia. Initial evaluation may be directed at the behavioral and psychosocial aspects of the disease, and recognition of hypoglycemia may be delayed. Some individuals may develop symptoms of catecholamine excess, such as tachycardia and diaphoresis, in response to hypoglycemia. More severe or prolonged hypoglycemia may cause confusion, lethargy, altered consciousness, or even seizures or coma. Documentation of hypoglycemia is required for diagnosis, which can be confirmed by demonstrating inappropriate insulin secretion despite hypoglycemia. Insulinomas typically are located in the pancreas and in 10 % of cases are multifocal. Insulinomas may occur as part of the multiple endocrine neoplasia (MEN) I syndrome, but most present as sporadic disease. Malignant insulinomas typically metastasize to local lymph nodes and the liver.

Gastrinomas secrete gastrin, which stimulates hypersecretion of gastric acid and causes the Zollinger-Ellison syndrome. The Zollinger-Ellison syndrome is characterized by gastritis, peptic ulcer disease, or esophagitis related to gastroesophageal reflux. Gastrinomas usually occur as sporadic tumors but also may be part of the MEN I syndrome. Gastrinomas frequently are multifocal and usually are located in the pancreas or duodenum but rarely may occur elsewhere in the gastrointestinal tract, liver, or lungs. Diagnosis of gastrinoma can be delayed when symptoms are treated initially with H2 blockers or proton pump inhibitors. This may explain why, by the time of

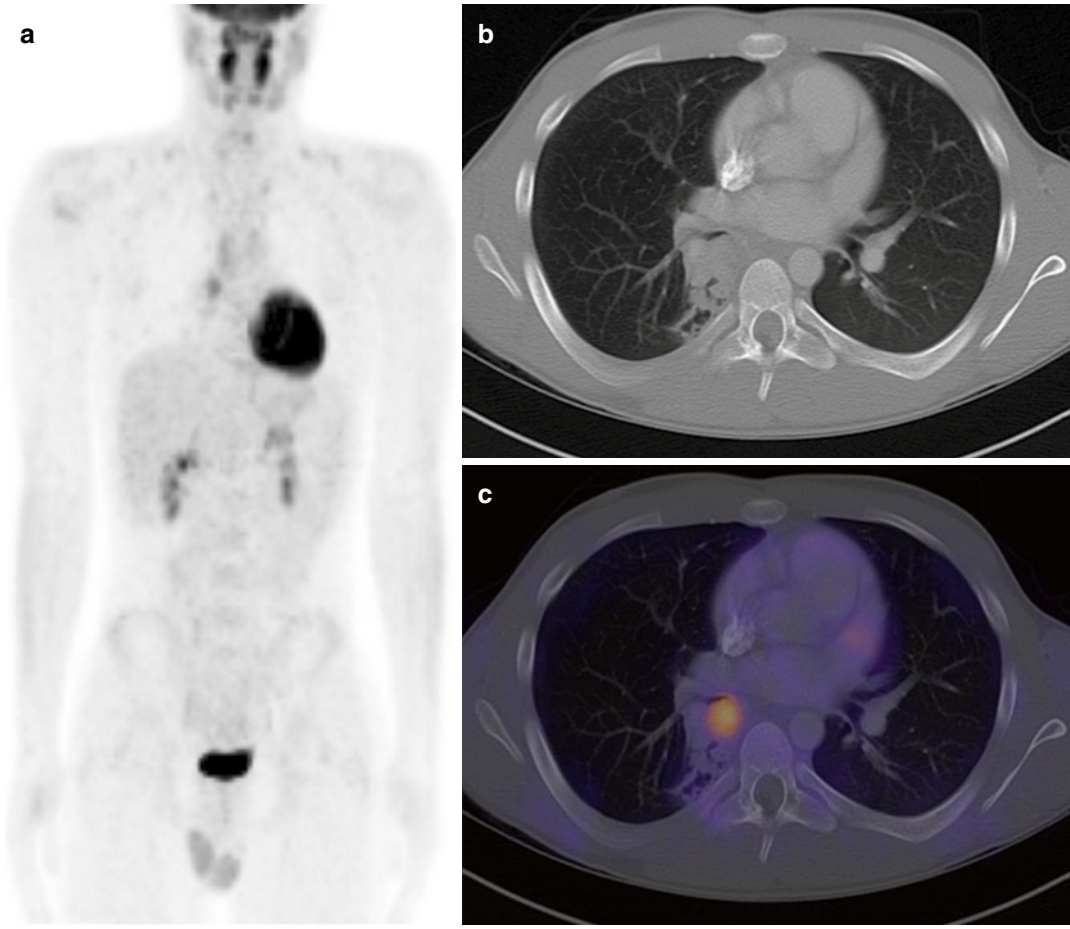

Fig. 20.13 ^{18}F-FDG PET of an endobronchial carcinoid. The patient shown in Fig. 20.12 also had an ^{18}F-FDG-PET. (**a**) The maximum intensity projection image shows mildly increased focal uptake near the right hilum. (**b**) Chest CT shows a 2 cm mass lesion obstructing the lower right bronchus. (**c**) Co-registration of PET and CT images confirms that the endobronchial lesion is FDG-avid. Therefore, in this patient, both ^{111}In-pentreotide and ^{18}F-FDG were able to detect the carcinoid tumor

diagnosis, gastrinomas may be larger and are more likely to be malignant than other neuroendocrine tumors. When malignant, gastrinomas may demonstrate local invasion and spread to local lymph nodes or distant metastases to the liver.

Other less common gastro-entero-pancreatic tumors occur very rarely in children and young adults. These include tumors that secrete vasoactive intestinal peptide (VIPoma), glucagon (glucagonoma), and somatostatin (somatostatinoma). Most of these tumors occur in the pancreas but can be found in the intestinal wall. In addition to type-specific hormone secretion, any of the neuroendocrine tumors may demonstrate ectopic hormone secretion. In children, ectopic hormone secretion by neuroendocrine tumors is unusual, but most common is ectopic secretion of ATCH, which will stimulate adrenal gland function to produce Cushing's syndrome.

Prognosis and long-term survival of patients with neuroendocrine tumors depends on both the management of the syndrome of hormone excess and the characteristics and natural history of the tumor. In the past, morbidity and mortality

occurred due to hormone excess, and long-term survival was most dependent on the control of the resulting symptoms. With the availability of drugs, such as octreotide, to suppress tumor function, the natural history of the tumor, such as likelihood of metastases, has become a more important determinant of long-term survival. Complete surgical resection of a neuroendocrine tumor can produce a cure but depends upon accurate identification and localization of all sites of disease.

Localization of neuroendocrine tumors is used to identify all sites of disease, determine if surgical resection is possible, and assess response to therapy [94]. Demonstration of functional somatostatin receptors also predicts the therapeutic response to somatostatin-receptor antagonists, such as octreotide (Sandostatin ®). Imaging studies should not be performed before the clinical diagnosis of neuroendocrine tumor has been confirmed. In the absence of a well-documented biochemical diagnosis, using imaging to explore for a suspected, but unconfirmed, neuroendocrine tumor risks incidental findings and misdiagnosis.

For a tumor that comes to attention as an incidental finding on a CT or MRI, the site of the primary tumor and possibly metastases may be clearly defined. However, for the majority of neuroendocrine tumors that come to attention because of the symptoms produced by hormone secretion, the tumors may be smaller and more difficult to detect with conventional imaging. Wide ranges of sensitivities have been reported for the different methods of imaging used to image GEP tumors. CT, MRI, or angiography typically will detect less than half of all GEP tumors. A planar ^{111}In-pentreotide scan has greater sensitivity (up to 70 %), but tumor size also affects the sensitivity of ^{111}In-pentreotide scans, with lower sensitivity for tumors less than 1 cm in size. Indium-111-pentreotide has higher specificity than other imaging methods. SPECT improves the accuracy of ^{111}In-pentreotide imaging. All imaging methods are reported to have greater sensitivity for liver metastases, but the relative performance of these different methods remains the same, with ^{111}In-pentreotide scans having higher sensitivity than other imaging methods. For most GEP tumors, multimodality imaging, using either ^{111}In-pentreotide SPECT/CT or software fusion of ^{111}In-pentreotide SPECT with either CT or MRI, may provide the most accurate approach for identifying both the primary site and the extent of disease.

When a GEP tumor is not detected by ^{111}In-pentreotide, the choice for second-line imaging agent is not clear. Compared to ^{111}In-pentreotide, ^{123}I-MIBG has much lower sensitivity for GEP tumors and is less likely to detect primary or metastatic lesions [75, 95–97]. The utility of ^{18}F-FDG PET may be limited by physiological ^{18}F-FDG uptake in the liver and an intestine, which may obscure sites of disease [98]. However, FDG avidity may be greatest in poorly differentiated tumors, so that ^{18}F-FDG PET may complement ^{111}In-pentreotide and be most useful when an aggressive, poorly differentiated GEP tumor is not detected by ^{111}In-pentreotide [75, 97]. Although not yet available for routine clinical use, PET radiopharmaceuticals labeled with ^{68}Ga such as ^{68}Ga-DOTA-TOC and ^{68}Ga-DOTATATE have high sensitivity for GEP tumors [75, 98].

Medullary Thyroid Cancer

Medullary thyroid cancer develops from parafollicular C cells found in the thyroid gland. Most cases appear to be sporadic, but there is a strong relationship between medullary thyroid cancer and the multiple endocrine neoplasia syndromes. Nearly every individual with MEN-1 will develop medullary thyroid cancer. Definitive therapy of medullary thyroid cancer is surgical resection of the thyroid. The role of functional imaging in the evaluation of medullary thyroid cancer has not been well studied, particularly in children. FDG-PET and PET/CT have been used to localize recurrent disease but do not seem to have a role in the initial evaluation of disease [99]. The use of other PET agents, such as ^{18}F-DOPA and ^{68}Ga-DOTATATE, has been reported, but the clinical role and utility of these agents have not been confirmed for medullary thyroid cancer.

Congenital Hyperinsulinism

Congenital hyperinsulinism (sometimes called nesidioblastosis or islet-cell hyperplasia) presents as recurrent or persistent hypoglycemia resulting from inappropriate pancreatic secretion of insulin. It typically presents as severe or life-threatening hypoglycemia in neonates or infants, but occasionally, the diagnosis is delayed until during the first year of life. Congenital hyperinsulinism reflects an underlying abnormality in the insulin-secreting beta cells of the pancreas. Many patients will respond to medical therapy, but others will require pancreatic surgery, which can be guided by nuclear medicine imaging. Medical therapies include diazoxide, which acts through the K_{ATP} channel to inhibit insulin secretion. Some patients are responsive to octreotide, which acts through somatostatin receptors to suppress insulin secretion. Diazoxide or octreotide can be used successfully for long-term management in about half the children with congenital hyperinsulinism [100, 101]. With age and maturation, many patients have resolution of disease and can be weaned from pharmacological therapy.

In patients unresponsive to pharmacological therapy, blood glucose levels must be maintained with glucose infusions or with frequent or continuous feedings. These patients remain at high risk for recurrent hypoglycemia with a high risk of brain damage and may be candidates for pancreatic surgery. The histological pattern of beta-cell hyperplasia affects the surgical approach to therapy [101, 102]. *Focal* congenital hyperinsulinism involves only a small region of the pancreas, and local surgical resection or partial pancreatectomy can be curative. *Diffuse* congenital hyperinsulinism involves all beta cells in the pancreas, and subtotal pancreatectomy may be required in these patients. With a loss of nearly all the pancreas, these patients can be at risk for both persistent hyperinsulinism and insulin-dependent diabetes mellitus and ideally receive surgery and postoperative care from a multidisciplinary team experienced in the treatment of congenital hyperinsulinism [100]. *Atypical* congenital hyperinsulinism is less well defined than the other two categories but has been reported to have a diffuse pattern of involvement in a large region of the pancreas.

Conventional cross-sectional imaging, such as CT or MRI, typically is not helpful in the preoperative evaluation of congenital hyperinsulinism [100]. In the past, standard surgical practice included intraoperative biopsies to determine if beta-cell abnormalities were focal or diffuse. Most centers with extensive experience in the surgical treatment of congenital hyperinsulinism now use ^{18}F-DOPA PET for routine preoperative evaluation, as it is highly accurate in differentiating focal and local disease. Although some studies using PET alone had suggested that ^{18}F-DOPA PET cannot always localize the site of focal uptake [103], this concern has been resolved with the use of hybrid imaging, such as PET/CT [104]. However, the expected pattern of abnormal ^{18}F-DOPA uptake still is not well defined in the small group of patients with a possible atypical histological pattern of disease.

References

1. Kukorka JS, Zeigler MA, Clark OH, et al. The American Association of Clinical Endocrinologists and the American Association of Endocrine Surgeons position statement on the diagnosis and management of primary hyperparathyroidism. Endocr Pract. 2005;11:49–54.
2. DeLellis RA, Mazzaglia P, Mangray S. Primary hyperparathyroidism. Arch Pathol Lab Med. 2008;132:1251–62.
3. Palestro CJ, Tomas MB, Tronco GG. Radionuclide imaging of the parathyroid glands. Semin Nucl Med. 2005;35:266–76.
4. Taillefer R, Boucher Y, Potvin C, Lambert R. Detection and localization of parathyroid adenomas in patients with hyperparathyroidism using a single radionuclide imaging procedure with technetium-99m-sestamibi (double-phase study). J Nucl Med. 1992;33:1801–7.
5. Eslamy HK, Ziessman HA. Parathyroid scintigraphy in patients with primary hyperparathyroidism: ^{99m}Tc sestamibi SPECT and SPECT/CT. Radiographics. 2008;28:1461–76.
6. Johnson NA, Tublin ME, Ogilvie JB. Parathyroid imaging: technique and role in the preoperative evaluation of primary hyperparathyroidism. AJR Am J Radiol. 2007;188:1706–15.
7. Mihai R, Simon D, Hellman P. Imaging for primary hyperparathyroidism – an evidence-based analysis. Langenbecks Arch Surg. 2009;394:765–84.

8. Bergenfelz AOJ, Hellamn P, Harrison B, Sitges-Serra A, Dralle H. Langenbecks Arch Surg. 2009;394: 761–4.
9. Nichols KJ, Tomas MB, Tronco GG, et al. Preoperative parathyroid scintigraphic lesion localization: accuracy of various types of readings. Radiology. 2008; 248:221–32.
10. O'Doherty MJ, Kettle AG, Collins REC, Coakley AJ. Parathyroid imaging with technetium-99m-sestamibi: preoperative localization and tissue uptake studies. J Nucl Med. 1992;33:313–8.
11. Hetrakul N, Civelek AC, Stagg CA, Udelsman R. In vitro accumulation of technetium-99m-sestamibi in human parathyroid mitochondria. Surgery. 2001;130: 1011–8.
12. Pons F, Torregrosa JV, Fuster D. Biological factors influencing parathyroid localization. Nucl Med Commun. 2003;24:121–4.
13. Friedman K, Somervell H, Patel P, et al. Effect of calcium channel blockers on the sensitivity of preoperative ^{99m}Tc-MIBI SPECT for hyperparathyroidism. Surgery. 2004;136:1199–204.
14. Ffeld JG, Erichson K, Pfeffer PF, Clausen OP, Rootwelt K. Technetium-99m-tetrofosmin for parathyroid scintigraphy: a comparison with sestamibi. J Nucl Med. 1997;38:831–4.
15. Coakely AJ, Kettle AG, Wells CP, O'Doherty MJ, Collins RE. ^{99m}Tc-sestamibi – a new agent for parathyroid imaging. Nucl Med Commun. 1989;10: 791–4.
16. Bergenfelz A, Tennvall J, Valdermarsson S, Lindblom P, Tibblin S. Sestamibi versus thallium subtraction scintigraphy in parathyroid localization: a prospective comparative study in patients with predominantly mild primary hyperparathyroidism. Surgery. 1997;121:601–5.
17. Balon HR, Silberstein EB, Meier DA, et al. Society of Nuclear Medicine procedure guideline for thyroid scintigraphy v3.0. 2006. http://interactive.snm.org/docs/Thyroid_Scintigraphy_V3.pdf. Accessed 28 Nov 2012.
18. Scheff AM, Spies WG, McDougall IR, et al. ACR-SNM-SPR practice guideline for the performance of thyroid scintigraphy and uptake measurements. 2009. www.acr.org/~/media/ACR/Documents/PGTS/guidelines/Thyroid_Scintigraphy.pdf. Accessed 28 Nov 2012.
19. Lassmann M, Biassoni L, Monsieurs M, Franzius C, Jacobs F; for the EANM Dosimetry and Paediatrics Committees. The new EANM paediatric dosage card. Eur J Nucl Med Mol Imaging. 2007;34:796–8.
20. Intenzo CM, Dam HQ, Manzone TA, Kim SM. Imaging of the thyroid in benign and malignant disease. Semin Nucl Med. 2012;42:49–61.
21. Greenspan BS, Dillehay G, Intenzo C, et al. SNM practice guideline for parathyroid scintigraphy 4.0. J Nucl Med Technol. 2012;40(2):111–8.
22. Judson BL, Shaha AR. Nuclear imaging and minimally invasive surgery in the management of hyperparathyroidism. J Nucl Med. 2008;49:1813–8.
23. Hindié E, Ugur Ő, Fuster D, et al. 2009 EANM parathyroid guidelines. Eur J Nucl Med Mol Imaging. 2009;36:1201–16.
24. Bénard F, Lefebvre B, Beuvon F, Langlois M-F, Bisson G. Rapid washout of technetium-99m-MIBI from a large parathyroid adenoma. J Nucl Med. 1995;36:241–3.
25. Giordano A, Rubello D, Casara D. New trends in parathyroid scintigraphy. Eur J Nucl Med. 2001;28:1409–20.
26. Hindié E, Mellière D, Jeanguillaume C, Perlemuter L, Chéhadé F, Galle P. Parathyroid imaging using simultaneous double-window recording of technetium-99m-sestamibi and iodine-123. J Nucl Med. 1998;39:1100–5.
27. Neumann DR, Obuchowski NA, DiFilipo FP. Preoperative ^{123}I/^{99m}Tc-sestamibi subtraction SPECT and SPECT/CT in primary hyperparathyroidism. J Nucl Med. 2008;49:2012–7.
28. Siegel A, Mancuso M, Seltzer M. The spectrum of positive scan patterns in parathyroid scintigraphy. Clin Nucl Med. 2007;32:770–4.
29. Foppiani L, Del Monte P, Sartini G, et al. Intrathyroidal parathyroid carcinoma as a cause of hypercalcemia and pitfall of localization techniques: clinical and biological features. Endocr Pract. 2007;13:176–81.
30. Mazeh H, Kouniavsky G, Schneider DF, Makris KI, Sippel RS, Dackiw AP, Chen H, Zeiger MA. Intrathyroidal parathyroid glands: Small, but mighty (a Napoleon phenomenon). Surgery. 2012;152(6): 1193–200.
31. Kraas J, Clark PB, Perrier ND, Morton KA. The scintigraphic appearance of subcapsular parathyroid adenomas. Clin Nucl Med. 2005;30:213–7.
32. Sarikaya A, Huseyinova G, Irfanoğlu ME, Erkmen N, Cermik TF, Berkarda S. The relationship between ^{99}Tc(m)-sestamibi uptake and ultrastructural cell types of thyroid tumors. Nucl Med Commun. 2001;22: 39–44.
33. Ali L, Loutfi I, Biswas G, Hadi N, Girgis T. Improved delineation of parathyroid lesions in patients with chronic renal failure using magnified pinhole imaging. J Nucl Med Technol. 2011;39:35–9.
34. Hindie E, Zanotti-Fregonara P, Just PA. Eur J Nucl Med Mol Imaging. 2010;37:623–34.
35. Shaha AR. Parathyroid re-exploration. Otolaryngol Clin North Am. 2004;37:833–43.
36. Khan A, Bilezikian J. Primary hyperparathyroidism: pathophysiology and impact on bone. Can Med Assoc J. 2000;163:164–87.
37. Marcocci C, Cetani F. Primary hyperparathyroidism. N Engl J Med. 2011;365:2389–97.
38. Parisien M, Silverberg SJ, Shane E, Dempster DW, Bilezikian JP. Bone disease in primary hyperparathyroidism. Endocrinol Metab Clin North Am. 1990;19:19–34.
39. Udelsman R. Approach to the patient with persistent or recurrent primary hyperparathyroidism. J Clin Endocrinol Metab. 2011;96:2950–8.
40. Delellis RA. Challenging lesions in the differential diagnosis of endocrine tumors: parathyroid carcinoma. Endocr Pathol. 2008;19:221–5.

41. Varghese J, Rich T, Jimenez C. Benign familial hypocalciuric hypercalcemia. Endocr Pract. 2011;17: S13–7.
42. Egbuna OI, Brown EM. Hypercalcaemic and hypocalcaemic conditions due to calcium-sensing receptor mutations. Best Pract Res Clin Rheumatol. 2008;22: 129–48.
43. Eastell R, Arnold A, Branid L, et al. Diagnosis of asymptomatic primary hyperparathyroidism: proceedings of the third international workshop. J Clin Endocrinol Metab. 2009;94:340–50.
44. Vanstone MB, Udelsman RD, Cheng DW, Carpenter TO. Rapid correction of bone mass after parathyroidectomy in an adolescent with primary hyperparathyroidism. J Clin Endocrinol Metab. 2011;96:E347–50.
45. Zarabczan B, Chen H. Influence of surgical volume on operative failures for hyperparathyroidism. Adv Surg. 2011;45:237–48.
46. Augustine MM, Bravo PE, Zeiger MA. Surgical treatment of primary hyperparathyroidism. Endocr Pract. 2011;17:S75–82.
47. Potts JT, Ackerman IP, Barker CF, et al. Diagnosis and management of asymptomatic primary hyperparathyroidism: consensus development conference statement. Ann Intern Med. 1991;114:593–7.
48. Bilezikian JP, Khan AA, Potts Jr JT. Guidelines for the management of asymptomatic primary hyperparathyroidism: summary statement from the Third International Workshop. J Clin Endocrinol Metab. 2009;94:335–9.
49. Carniero-Pla DM, Solorzano CC, Lew JI, Irvin 3rd GL. Long-term outcome of patients with intraoperative parathyroid level remaining above the normal range during parathyroidectomy. Surgery. 2008;144: 989–93.
50. Kettle AG, O'Doherty MJ. Parathyroid imaging: how good is it and how should it be done? Semin Nucl Med. 2006;36:206–11.
51. Siegel A, Alvarado M, Barth Jr RJ, Brady M, Lewis J. Parameters in the prediction of the sensitivity of parathyroid scanning. Clin Nucl Med. 2006;31: 679–82.
52. Roy M, Mazeh H, Chen H, Sippel RS. Incidence and localization of ectopic parathyroid adenomas in previously unexplored patients. World J Surg. 2013;37: 102–6.
53. Phillips CD, Shatzkes DR. Imaging of the parathyroid glands. Semin Ultrasound CT MR. 2012;33: 123–9.
54. Vazquez BJ, Richard ML. Imaging of the thyroid and parathyroid glands. Surg Clin North Am. 2011;91: 15–32.
55. Tentori F, Blayney MJ, Albert JM, et al. Mortality risk for dialysis patients with different levels of serum calcium, phosphorus, and PTH: the Dialysis Outcomes and Practice Patterns Study (DOPPS). Am J Kidney Dis. 2008;52:519–30.
56. Triponez F, Clark OH, Vanrenthergem Y, Evenepoel P. Surgical treatment of persistent hyperparathyroidism after renal transplantation. Ann Surg. 2008;248: 18–30.
57. Hicks RJ. Use of molecular targeted agents for the diagnosis, staging and therapy of neuroendocrine malignancy. Cancer Imaging. 2010;10:S83–91.
58. Rindl G, Klöppel G. Endocrine tumors of the gut and pancreas tumor biology and classification. Neuroendocrinology. 2004;80:S12–5.
59. Emilio Bombardieri E, Giammarile F, Aktolum C, et al. ^{131}I/^{123}I Metaiodobenzylguanidine (mIBG) scintigraphy – procedures guidelines for tumour imaging. 2010. http://interactive.snm.org/docs/EANM_Guideline_for_1131_1123. Accessed 12 Oct 2012.
60. Khafagi FA, Shapiro B, Fig LM, Mallette S. Labetalol reduces iodine-131 MIBG uptake by pheochromocytoma and normal tissues. J Nucl Med. 1989;30: 481–9.
61. Solanki KK, Bomanji J, Moyes J, Mather S, Trainer PJ, Britton KE. A pharmacological guide to medicines which interfere with biodistribution of radiolabelled meta-iodobenzylguanidine (MIBG). Nucl Med Commun. 1992;13:513–21.
62. Giammarile F, Chiti A, Lassman M, Brans B, Flux G. EANM procedure guidelines for ^{131}I-meta-ioidobenzylguanidine (^{131}I-mIBG) therapy. Eur J Nucl Med Mol Imaging. 2008;35:1039–47.
63. Snay ER, Treves ST, Fahey FH. Improved quality of pediatric 123I-MIBG images with medium-energy collimators. J Nucl Med Technol. 2011;39:100–4.
64. Intenzo CM, Jabbour S, Lin HC, et al. Scintigraphic imaging of body neuroendocrine tumors. Radiographics. 2007;27:1355–69.
65. Bombardieri E, Ambrosini V, Aktolun C, et al. ^{111}In-pentreotide scintigraphy: procedure guidelines for tumour imaging. Eur J Nucl Med Mol Imaging. 2010;37:1441–8.
66. Balon HR, Brown TLY, Goldsmith SJ, et al. The SNM practice guideline for somatostatin receptor scintigraphy 2.0. J Nucl Med Technol. 2011;39: 317–24.
67. Graham MM, Menda Y. Radiopeptide imaging and therapy in the United States. J Nucl Med. 2011;52:56S–63.
68. Atreja A, Nepal S, Lashner BA. Making the most of currently available bowel preparations for colonoscopy. Cleve Clin J Med. 2010;77:317–26.
69. Bombardieri E, Coliva A, Maccauro M, et al. Imaging of neuroendocrine tumours with gamma-emitting radiopharmaceuticals. Q J Nucl Med Mol Imaging. 2010;54:3–15.
70. Wong KK, Wynn EA, Myles J, Ackerman RJ, Frey KA, Avram AM. Comparison of single time-point [111-In] pentetreotide SPECT/CT with dual time-point imaging of neuroendocrine tumors. Clin Nucl Med. 2011;36:25–31.
71. Gatley SJ. Labeled glucose analogs in the genomic era. J Nucl Med. 2003;44:1082–6.
72. The MICAD Research Team. [^{18}F]Fluoro-2-deoxy-2-D-glucose. In: Molecular imaging and contrast agent database (MICAD). Bethesda: National Center for Biotechnology Information (US); 2004–2012. www.ncbi.nlm.nih.gov/books/NBK23335. Accessed 6 Aug 2012.

73. Fowler JS, Ido T. Initial and subsequent approach for the synthesis of ^{18}FDG. Semin Nucl Med. 2002; 32:6–12.
74. Treves ST, Parisi MT, Gelfand MJ. Pediatric radiopharmaceutical doses: new guidelines. Radiology. 2011;261:347–9.
75. Goldsmith S. Update on nuclear medicine imaging of neuroendocrine tumors. Future Oncol. 2009;5:75–84.
76. Koopmans KP, Neels ON, Kema IP, et al. Molecular imaging in neuroendocrine tumors: molecular uptake mechanisms and clinical results. Crit Rev Oncol Hematol. 2009;71:199–213.
77. Breeman WA, de Blois E, Szechan H, Konijnenberg M, Kwekkeboom DJ, Krenning EP. ^{68}Ga-labeled DOTA-peptides and ^{68}Ga-labeled radiopharmaceuticals for positron emission tomography: current status of research, clinical applications, and future perspectives. Semin Nucl Med. 2011;41:314–21.
78. Waguespack SG, Rich T, Grubbs E, et al. A current review of the etiology, diagnosis, and treatment of pediatric pheochromocytoma and paraganglioma. J Clin Endocrinol Metab. 2010;95:2023–37.
79. Timmers HJ, Taieb D, Pacek K. Current and future anatomical and functional imaging approaches to pheochromocytoma and paraganglioma. Horm Metab Res. 2012;44:367–72.
80. Ilias I, Pacak K. Current approaches and recommended algorithm for the diagnostic localization of pheochromocytoma. J Clin Endocrinol Metab. 2004;89:479–91.
81. Neumann HP, Bausch B, McWhinney SR, et al. Freiburg-Warsaw-Columbus Pheochromocytoma Study Group. Germ-line mutations in nonsyndromic pheochromocytoma. N Engl J Med. 2002;346:1459–66.
82. Eisenhofer G, Schott M, Bornstein S. Pheochromocytoma and paraganglioma: Recent progress and new vistas for improved patient care. Horm Metab Res. 2012;44:325–7.
83. Scholtz T, Eisenhofer G, Pacak K, Dralle H, Lehnert H. Current treatment of malignant pheochromocytoma. J Clin Endocrinol Metab. 2007;92:1217–25.
84. Miskulin J, Shulkin BL, Doherty GM, Sisson JC, Burney RE, Gauger PG. Is preoperative iodine 123 meta-iodobenzylguanidine scintigraphy routinely necessary before initial adrenalectomy for pheochromocytoma? Surgery. 2003;134:918–22.
85. Mihai R, Gleeson F, Roskell D, Parker A, Sadler G. Routine preoperative ^{123}I-MIBG scintigraphy for patients with phaeochromocytoma is not necessary. Langenbecks Arch Surg. 2008;393:725–7.
86. Meyer-Rochow GY, Schembri GP, Benn DE, et al. The utility of metaiodobenzylguanidine single photon emission computed tomography/computed tomography (MIBG SPECT/CT) for the diagnosis of pheochromocytoma. Ann Surg Oncol. 2010;17: 392–400.
87. Jacobson AF, Deng H, Lombard J, Lessig HJ, Black RR. ^{123}I-meta-iodobenzylguanidine scintigraphy for the detection of neuroblastoma and pheochromocytomas: Results of a meta-analysis. J Clin Endocrinol Metab. 2010;95:2596–606.
88. Koopmans KP, Jager PL, Kema IP, Kerstens MN, Albers F, Dullaart RP. ^{111}In-octreotide is superior to ^{123}I-metaiodobenzylguanidine for scintigraphic detection of head and neck paragangliomas. J Nucl Med. 2008;49:1232–7.
89. Timmers HJ, Chen CC, Carrasquillo JA, et al. Comparison of ^{18}F-fluoro-L-DOPA, ^{18}F-fluorodeoxyglucose, and ^{18}F-fluorodopamine PET and ^{123}I-MIBG scintigraphy in the localization of pheochromocytoma and paraganglioma. J Clin Endocrinol Metab. 2009;94:4757–67.
90. Pinchot SN, Holen K, Sippel RS, Chen H. Carcinoid tumors. Oncologist. 2008;13:1255–69.
91. Khan MU, Morse M, Coleman RE. Radioiodinated metaiodobenzylguanidine in the diagnosis and therapy of carcinoid tumors. Q J Nucl Med Mol Imaging. 2008;52:441–54.
92. Ilias I, Pacak K. A clinical overview of pheochromocytomas/paragangliomas and carcinoid tumors. Nucl Med Biol. 2008;35:S27–34.
93. Jager PL, Chirakal R, Marriot CJ, Brouwers AD, Koopmans KP, Gulenchyn KY. 6-L-^{18}F-fluorodihydroxyphenylalanine PET in neuroendocrine tumors: basic aspects and emerging clinical applications. J Nucl Med. 2008;49:573–86.
94. Jensen RT, Cadiot G, Brandi ML, et al. ENETS consensus guidelines for the management of patients with digestive neuroendocrine neoplasms: functional pancreatic endocrine tumor syndromes. Neuroendocrinology. 2012;95:98–119.
95. Kaltsas G, Korbonits M, Heintz E, et al. Comparison of somatostatin analog and metaiodobenzylguanidine radionuclides in the diagnosis and localization of advanced neuroendocrine tumors. J Clin Endocrinol Metab. 2001;86:895–902.
96. Ezziden S, Logvinski T, Yong-Hing C, et al. Factors predicting tracer uptake in somatostatin receptor and MIBG scintigraphy of metastatic gastroenteropancreatic neuroendocrine tumors. J Nucl Med. 2006;47:223–33.
97. Binderup T, Knigge U, Loft A, et al. Functional imaging of neuroendocrine tumors: a head-to-head comparison of somatostatin receptor scintigraphy, ^{123}I-MIBG scintigraphy, and ^{18}F-FDG PET. J Nucl Med. 2010;51:704–12.
98. Rufini V, Baum CP, Castaldi P, et al. Role of PET/CT in the functional imaging of endocrine pancreatic tumors. Abdom Imaging. 2012;37:1004–20.
99. Treglia G, Rufini V, Salvatori M, Giordano A, Giovanella L. PET imaging in recurrent medullary thyroid carcinoma. Int J Mol Imaging. 2012;2012;9. Article ID 324686, doi:10.1155/2012/324686.
100. Palladino AA, Stanley CA. A specialized team approach to diagnosis and medical versus surgical treatment of infants with congenital hyperinsulinism. Sem Pediatr Surg. 2011;20:32–7.
101. Arnoux J-B, Verkarre V, Saint-Martin C, et al. Congenital hyperinsulinism: current trends in diagnosis and therapy. Orphanet J Rare Diseases. 2011;6:63. http://www.ojrd.com/content/6/1/63.

102. Ismail D, Hussain K. Role of 18F-DOPA PET/CT imaging in congenital hyperinsulinism. Rev Endocr Metab Disord. 2010;11:165–9.
103. Zani A, Nah SA, Ron O, Totonelli G, et al. The predictive value of preoperative fluorine-18-L-3,4-dihydroxyphenylalanine positron emission tomography-computed tomography scans in children with congenital hyperinsulinism of infancy. J Pediatr Surg. 2011;46:204–8.
104. Mohnike W, Barthlen W, Mohnike K, Blankenstein O. Positron emission tomography/computed tomography diagnostics by means of fluorine-18-L-dihydroxyphenylalanine in congenital hyperinsulinism. Sem Pediatr Surg. 2011;20:23–7.

Lymphomas and Lymphoproliferative Disorders

21

Frederick D. Grant

As a group, lymphomas are the third most common malignancy in children [1] and represent more than a quarter of all new malignancies in older teenagers [2]. Two-thirds are Hodgkin disease and the remainder includes a diverse group of lymphoid malignancies, the non-Hodgkin lymphomas. Most childhood non-Hodgkin lymphomas are aggressive, and unlike in adults, indolent lymphomas are rare in children. Most lymphomas present as painless lymph node enlargement that is apparent on physical examination or on conventional imaging studies, such as chest radiograph or CT [3]. At the time of diagnosis, more than two-thirds of patients with Hodgkin's disease have a mediastinal mass apparent on chest radiograph [4].

Most traditional staging schemes relied on anatomical imaging findings, with gallium scans used as a complementary study in patients with Hodgkin's disease. In the past decade, ^{18}F-FDG PET or PET/CT has become the standard imaging procedure for pediatric and adult lymphomas. However, when access to PET/CT is limited due to regulatory policy or location, whole-body gallium scans may continue to have a role in imaging lymphomas. Accurate interpretation of ^{18}F-FDG PET/CT requires familiarity with the patterns of FDG biodistribution (see Chap 3 PET and PET/CT in Children and Young Adults), understanding of the normal biology of Hodgkin's disease and the non-Hodgkin lymphomas, and awareness of other malignant and benign diseases whose ^{18}F-FDG-PET appearance may resemble lymphoma. The appropriate utilization of ^{18}F-FDG-PET for evaluating pediatric lymphomas is a rapidly evolving topic. Ongoing clinical studies should help to better define the appropriate use of ^{18}F-FDG PET and PET/CT for staging, assessing the response to therapy, and follow-up surveillance of both Hodgkin's disease and the non-Hodgkin lymphomas.

Methods

Flourine-18-FDG PET or PET/CT has become part of the standard imaging procedures used for both Hodgkin's disease and non-Hodgkin lymphomas (see Chap 3). Gallium scans still are used to image patients with Hodgkin's disease when PET/CT is not available.

F.D. Grant, MD
Joint Program in Nuclear Medicine,
Department of Radiology, Harvard Medical School,
Boston, MA, USA

Division of Nuclear Medicine and Molecular Imaging,
Department of Radiology,
Boston Children's Hospital,
Boston, MA, USA

Department of Radiology,
Brigham and Women's Hospital,
Boston, MA, USA
e-mail: frederick.grant@childrens.harvard.edu

S.T. Treves (ed.), *Pediatric Nuclear Medicine and Molecular Imaging*,
DOI 10.1007/978-1-4614-9551-2_21,

^{67}Ga-Gallium Scan

Radiopharmaceutical

Gallium-67 (physical half-life of 78.3 h) decays by electron capture to emit gamma emission of multiple energies, of which the most abundant are 93 keV, 184 keV, and 296 keV. Gallium-67 is a cyclotron product that is produced by the nuclear reaction ^{68}Zn (p, 2n) ^{67}Ga. Gallium-67 is administered intravenously as the citrate salt ([^{67}Ga]-gallium citrate) at a typical adult dose of 74–220 mBq (2–6 mCi), but up to 330 mBq (9 mCi) may be given in larger patients. In children, the typical administered dose is 1.5–2.6 mBq/kg (0.04–0.07 mCi/kg), with a minimum dose of 9–18 MBq (0.25–0.5 mCi) and maximum dose of 220 mBq (6 mCi) [5].

Gallium Scan

For oncological imaging, whole-body imaging typically is performed 48 h after the administration of [^{67}Ga] gallium citrate. A whole-body scan can be acquired as a whole-body sweep or with multiple planar images. A whole-body sweep is acquired for a total of 1.5–2 million counts, while regional planar images of the torso typically are acquired to obtain 250,000–1,000,000 million counts. SPECT of the torso frequently will assist in localizing sites of abnormal uptake. Gallium is excreted through both the genitourinary and gastrointestinal tracts, and findings may be obscured by excreted ^{67}Ga accumulation in the gut. In this case, delayed images of the abdomen and pelvis acquired 72–96 h after tracer administration may assist image interpretation.

^{18}F-FDG PET and ^{18}F-FDG PET/CT

Radiopharmaceutical

Fluorine-18-fluoro-2-deoxyglucose (^{18}F-FDG) is a glucose analogue labeled with ^{18}F. Fluorine-18-FDG is taken into cells through one of the transmembrane glucose transporters, but does not enter the energy-producing metabolic pathways [6]. Insulin-mediated stimulation of expression of some glucose transporters (GLUT-4) will increase cellular uptake of ^{18}F-FDG in insulin-sensitive tissues such as skeletal muscle, liver, and myocardium [7]. Fluorine-18-FDG is phosphorylated by cellular hexokinases, but after monophosphorylation, FDG-6 phosphate cannot be further phosphorylated and is trapped in the cell [8], which provides a mechanism for amplification of the ^{18}F signal. The North American consensus guidelines [9] recommend a pediatric dose of 3.7–5.2 MBq/kg (0.10–90.14 mCi/kg) for torso/whole-body imaging with a minimum dose of 37 MBq (1.0 mCi).

^{18}F-FDG PET and PET/CT

Fluorine-18-FDG-PET has greater sensitivity than gallium scan for identifying sites of lymphoma [4, 10], particularly in the abdomen where bowel excretion of ^{67}Ga may obscure sites of disease [11, 12]. However, ^{18}F-FDG PET can be limited by intense ^{18}F-FDG uptake in brown adipose tissue, which is not a concern with gallium scans [13]. Fluorine-18-FDG uptake in brown adipose tissue can obscure an adjacent site of residual disease. Although uptake in brown adipose tissue may be less prominent in patients with extensive disease [14], interference from brown adipose tissue may be of most concern when looking for sites of minimal residual disease. Therefore, when imaging lymphoma, particular efforts should be made to prepare or pretreat patients to limit uptake in brown adipose tissue (see Chap 3) [15, 16].

The combination of ^{18}F-FDG PET and CT provides optimal disease localization and improved specificity for staging pediatric lymphoma, particularly Hodgkin's disease [17–19]. Although the combination of PET and CT can be accomplished with software co-registration of PET and CT studies, most PET/CT studies are acquired on hybrid PET/CT scanners.

Clinical

Hodgkin's Disease

In pediatric oncology, Hodgkin's disease is more common in teenagers and young adults but also can occur in children less than 10 years of age [1]. Hodgkin's disease can be categorized as either classic type (more common) or nonclassic type (uncommon). Classic Hodgkin's disease

includes a number of subtypes, including the nodular sclerosis subtype, which accounts for over three-quarters of pediatric Hodgkin's disease. Other classic subtypes include the lymphocyte-rich, lymphocyte-depleted, and mixed cellularity subtypes [20]. Nodular lymphocyte-predominant Hodgkin's disease is a nonclassic type of Hodgkin's disease that is much less common than the classic subtypes [21, 22]. Compared to other forms of Hodgkin's disease, nodular lymphocyte-predominant disease is less likely to involve the mediastinum [22]. The histological classification of Hodgkin's disease can affect prognosis and may influence the choice of therapy, but usually does not change the approach to imaging.

Typical therapy for Hodgkin's disease includes systemic chemotherapy and radiation therapy of involved regions. Most patients undergo remission with standard chemotherapy and involved-field radiation therapy, but a small number of patients require more aggressive chemotherapy or bone marrow transplantation [23, 24]. With adequate therapy, pediatric Hodgkin's disease has an excellent prognosis, with overall survival of approximately 95 % [25]. With this high rate of survival has come an increased recognition of drug side effects and the late effects of therapy [2, 3, 26, 27], which has encouraged attempts to minimize therapy, such as altering chemotherapy regimens or decreasing or eliminating radiation therapy [3]. As efforts are made to modify standard therapies and institute response-adapted therapy, ^{18}F-FDG PET or PET/CT will have a greater role in both staging and assessing the response to therapy [28].

The Ann Arbor staging system with Cotswolds modifications [29–32] is the standard staging system for Hodgkin's disease. It classifies Hodgkin's disease into four major stages (I–IV) based on the number and location of lymph node regions and extranodal sites with disease involvement. Additional subcategories indicate the presence of contiguous spread of disease from an involved lymph node into a single site of contiguous extranodal soft tissue (E), splenic involvement (S), and bulky disease (X) [31, 32] (Table 21.1). A single lymph node region may include lymph nodes from a number of anatomic lymph node groups as, for the most part, these lymph node regions reflect traditional radiation therapy fields and have been agreed to by convention [31].

Table 21.1 Modified Ann Arbor staging system for Hodgkin's disease

Anatomic staging	
Stage I	Involvement of a single lymphatic site (i.e., nodal region, Waldeyer's ring, thymus, or spleen) (I) or localized involvement of a single extralymphatic organ or site in the absence of any lymph node involvement (IE)
Stage II	Involvement of two or more lymph node regions on the same side of the diaphragm (II), or localized involvement of a single extralymphatic organ or site in association with regional lymph node involvement with or without involvement of other lymph node regions on the same side of the diaphragm (IIE)
Stage III	Involvement of lymph node regions on both sides of the diaphragm (III), which also may be accompanied by extralymphatic extension in association with adjacent lymph node involvement (IIIE) or by involvement of the spleen (IIIS) or both (IIIE,S)
Stage IV	Diffuse or disseminated involvement of one or more extralymphatic organs, with or without associated lymph node involvement, or isolated extralymphatic organ involvement in the absence of adjacent regional lymph node involvement, but in conjunction with disease in distant sites(s). Stage IV includes an involvement of the liver or bone marrow, lungs (other than by direct extension from another site), or cerebrospinal fluid
Designations applicable to any stage	
A	No symptoms
B	Fever (temperature >38 °C), drenching night sweats, unexplained loss of >10 % of body weight within the preceding 6 months
E	Involvement of a single extranodal site that is adjacent to a known lymph node site
S	Splenic involvement

Used with permission of the American Joint Committee on Cancer, Chicago, Illinois. The original source for this material is the *AJCC Cancer Staging Manual*, Seventh Edition (2010) published by Springer Science + Business Media LLC, www.springer.com

Patients with Hodgkin's disease also are staged on the basis of constitutional symptoms. Group A includes asymptomatic patients and group B includes patients with unexplained fever, weight loss, or night sweats. For most treatment plans and clinical trials, staging and clinical features are used to stratify patients into low-, intermediate-, and high-risk disease, but there are no

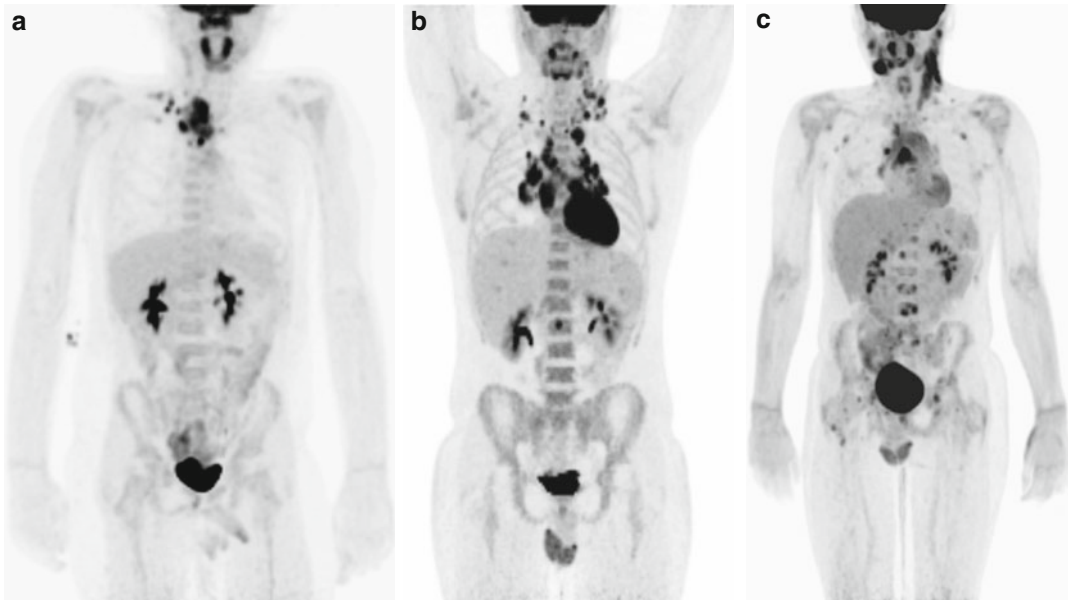

Fig. 21.1 Using ^{18}F-FDG PET and PET/CT to stage Hodgkin's disease. Fluorine-18-FDG PET has a role when using the modified Ann Arbor criteria for staging pediatric Hodgkin's disease. (**a**) Stage II: In a 16-year-old male with stage II nodular sclerosis classic Hodgkin's disease, there is FDG-avid disease in the mediastinum and right supraclavicular lymph nodes. No FDG-avid disease is identified below the diaphragm. (**b**) Stage III: In a 15-year-old male with stage III nodular sclerosis classic Hodgkin's disease, there is FDG-avid disease in the mediastinum and lymph nodes of both supraclavicular regions, as well as in a single FDG-avid para-aortic retroperitoneal lymph node (confirmed with PET/CT). Diffusely increased uptake in the expected locations of bone marrow is a frequent finding in patients with Hodgkin's disease and does not represent widespread disease involvement. (**c**) Stage III: In a 13-year-old male with stage III lymphocyte-predominant Hodgkin's disease, there is widespread FDG-avid disease in numerous lymph nodes above and below the diaphragm and focal involvement of the spleen. Typical of lymphocyte-predominant Hodgkin's disease, there is limited involvement of mediastinal lymph nodes

standardized criteria for risk assignment [3, 33]. Fluorine-18-FDG PET and PET/CT have become an important part of imaging pediatric Hodgkin's disease for staging and evaluating the response to therapy. The role of ^{18}F-FDG PET or PET/CT in follow-up imaging to assess for disease recurrence is less clear.

Staging

Most studies demonstrating a role for ^{18}F-FDG PET in staging Hodgkin's disease have been performed in adults, but ^{18}F-FDG PET also has a role in staging pediatric Hodgkin's disease (Fig. 21.1) [34, 35]. A staging ^{18}F-FDG PET or PET/CT for pediatric Hodgkin's disease may include either the whole body (head to toes) or only the torso (skull base to thighs). Some guidelines [36] recommend routine whole-body ^{18}F-FDG PET/CT for the initial staging of pediatric Hodgkin's disease. However, a whole-body study rarely will identify additional sites of Hodgkin's disease that will influence therapy [37]. If a whole-body ^{18}F-FDG PET/CT is used for initial staging and identifies no disease outside the field of view of a torso scan, then subsequent follow-up ^{18}F-FDG PET/CT can be limited to the torso [37].

Both ^{67}Ga-gallium scan and ^{18}F-FDG PET may identify pathology unrelated to Hodgkin's disease. Gallium scan may identify infection and benign skeletal abnormalities, such as fractures and benign bone lesions. Compared to gallium scan, ^{18}F-FDG PET has a different range of nonspecificity and may be more sensitive for infection, such as pneumonia, and unrelated neoplasms [11, 38]. Hodgkin's disease typically extends to contiguous lymph node sites and rarely has a

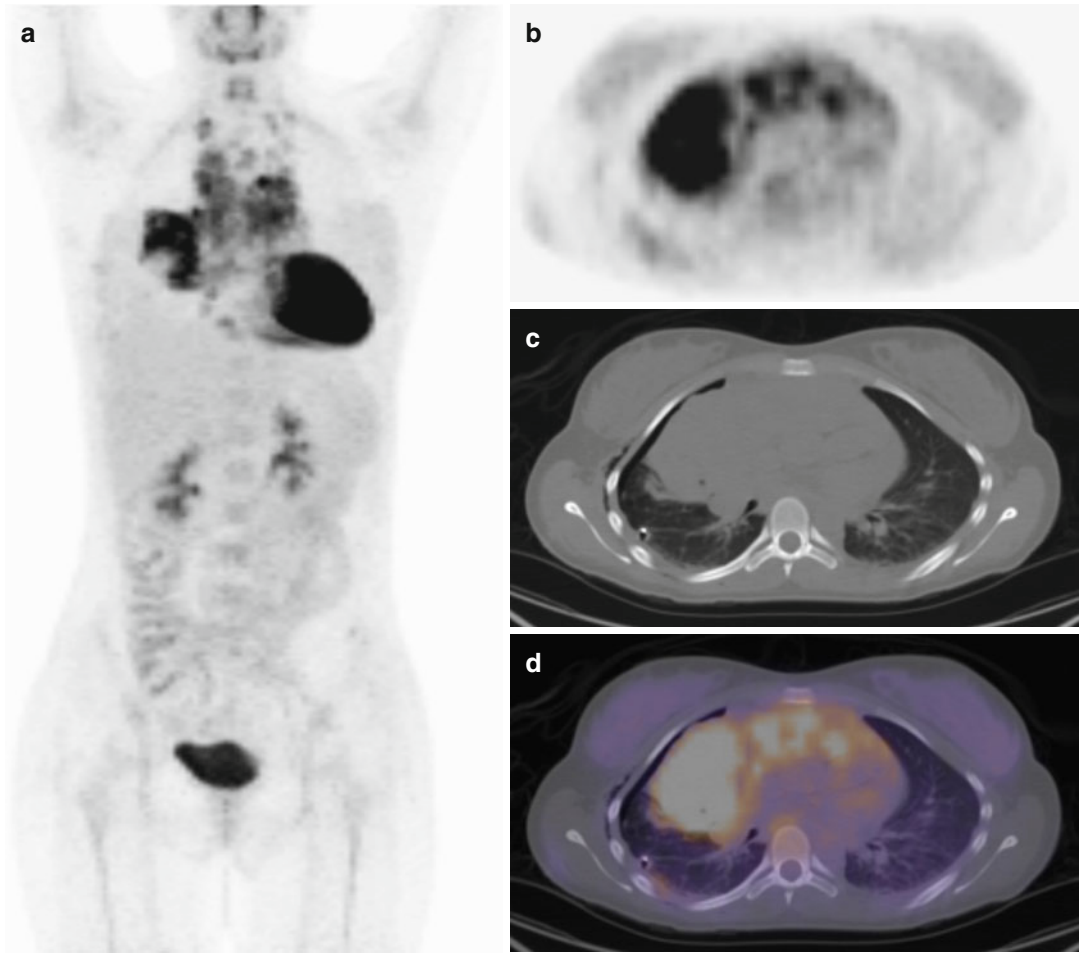

Fig. 21.2 ^{18}F-FDG PET/CT to evaluate advanced stage Hodgkin's disease. (**a**) In a 17-year-old female with stage IV nodular sclerosis classic Hodgkin's disease, the MIP of an FDG-PET shows widespread disease involvement in the chest that is further characterized with PET/CT. (**b**) Transaxial ^{18}F-FDG PET image shows extensive FDG-avid disease in the mediastinum and in the right hemithorax. (**c**) Transaxial CT image shows marked mediastinal lymphadenopathy and a large consolidative mass involving the right middle lobe (the small pneumothorax reflects a recent thoracotomy for tissue sampling). (**d**) Co-registration of PET and CT images confirms that the mediastinal lymph nodes and right lung mass both represent FDG-avid disease

single site of distant disease. An imaging abnormality, on either gallium scan or ^{18}F-FDG PET, that does not conform to this pattern requires further characterization to determine if it is another site of Hodgkin's disease or represents an unrelated pathology [38].

^{18}F-FDG PET is more accurate than conventional imaging, including CT, in identifying sites of Hodgkin's disease [39]. ^{18}F-FDG PET/CT outperforms diagnostic CT at identifying disease in small lymph nodes that do not meet CT criteria for disease, as well as finding disease in bone marrow, spleen, and liver [40]. However, in the unusual circumstance of lung involvement by Hodgkin's disease, diagnostic CT has greater sensitivity than ^{18}F-FDG PET for identifying small pulmonary nodules [41]. Thus, the combination of torso ^{18}F-FDG PET/CT and a diagnostic chest CT may provide optimal disease localization and improved specificity for staging pediatric Hodgkin's disease (Figs. 21.1 and 21.2) [17–19].

Visual assessment of ^{18}F-FDG uptake is appropriate for assessing a response to therapy. The use of standard uptake value (SUV) is not required [42]. In part, this reflects that even with well-controlled conditions, SUV values may vary by up to 20–25 % [43]. Therefore, clinically meaningful changes in uptake should be apparent by visual inspection. Ideally, uptake is compared to a standard region or background. ^{18}F-FDG accumulation in the mediastinal blood pool can provide an appropriate background for comparison [42, 44].

The appropriate use of ^{18}F-FDG PET/CT for evaluating bone marrow involvement with Hodgkin's disease is in transition. Among patients of all ages, bone marrow involvement may be identified in up to one-fourth of all cases, but the incidence of marrow disease is closer to 5 % in pediatric Hodgkin's disease [45]. Bone marrow biopsy, usually in the iliac crest, remains the standard staging study for identifying marrow involvement in patients with Hodgkin's disease. However, bone marrow biopsy may be limited by sampling error due to the focal pattern of marrow involvement [45, 46]. Recent reports [45, 47] suggest that ^{18}F-FDG PET/CT may perform better than biopsy for detecting bone marrow involvement. The pattern of abnormal ^{18}F-FDG uptake is an important characteristic, as abnormal focal FDG avidity likely represents disease, while diffusely increased FDG avidity is unlikely to be disease and much more likely to represent an inflammatory response related to Hodgkin's disease [48]. Although rare, cortical bone involvement can be detected by ^{18}F-FDG PET, and there is no role for bone scintigraphy in the staging of Hodgkin's disease [49].

The overall effect on patient outcome of using ^{18}F-FDG PET or PET/CT to stage pediatric Hodgkin's disease remains unclear. Using ^{18}F-FDG PET for staging can improve outcome by helping to better define sites of disease to be included in involved-field radiation therapy [40]. Fluorine-18-FDG PET findings may alter radiation therapy treatment planning in up to one-fifth of patients [50, 51]. On the other hand, when ^{18}F-FDG PET or PET/CT is used for staging, patients may be staged at a higher stage (upstaged) and receive more intensive therapy than if they had been staged with CT alone. As current therapies for pediatric Hodgkin's disease are associated with a high likelihood of cure, upstaging could lead to more therapy with little additional improvement in outcome. Because of this, ongoing studies are investigating the feasibility of using less intensive therapy in patients that are staged with ^{18}F-FDG PET/CT.

Response to Therapy

The response of Hodgkin's disease to therapy can be assessed at the completion of planned therapy (restaging) or at an interim time point during therapy. Until recently, the response to therapy of pediatric Hodgkin's disease was assessed similarly to other solid tumors and used anatomic imaging measurements of disease lesions. However, these techniques can underestimate the response to therapy of Hodgkin's disease. Even after cure, patients with Hodgkin's disease may have measurable lymph node enlargement and residual soft tissue masses. Therefore, the International Harmonization Project was established to develop response criteria that included both anatomic and metabolic measures in patients with lymphoma. The resulting guidelines [44, 52, 53] provide one set of consensus criteria to assess end of therapy response to therapy. These criteria define four levels of response: complete response (CR), partial response (PR), stable disease (SD), or progression/relapse (PD), in patients with Hodgkin's disease or non-Hodgkin lymphoma. Other standardized criteria have been proposed for using ^{18}F-FDG PET/CT to assess the response to therapy at an interim time before completion of planned therapy [53–55]. However, all of these guidelines were designed for adult patients and have not been validated in pediatric patients.

Using the response to therapy to guide therapy is a rapidly evolving topic. A minority of patients will have residual FDG avidity after completion of therapy. This finding indicates a poorer prognosis and is used to guide future therapy, but it is not clear that image-guided changes in therapy alter the prognosis in this group of patients. On the other hand, a patient with early resolution of FDG-avid disease may have a better prognosis

than most patients, but the appropriate changes in therapy in response to early resolution of FDG avidity remain under study.

Follow-up Surveillance

The role of ^{18}F-FDG PET or PET/CT in follow-up surveillance of patients treated for pediatric Hodgkin's disease has not been resolved. Flourine-18-FDG PET/CT frequently is used for long-term surveillance in adult Hodgkin's disease patients and may have a role for follow-up of other pediatric lymphomas. However, there has been no definitive study demonstrating a role for ^{18}F-FDG PET or PET/CT in the long-term follow-up of patients treated for pediatric Hodgkin's disease.

Non-Hodgkin Lymphoma

Non-Hodgkin lymphoma includes a wide variety of lymphoid tumors with a range of incidence and prognosis [2, 56] that account for approximately 7 % of cancers in children [1]. In children, indolent lymphoma is rare, and the most common forms of non-Hodgkin lymphoma are Burkitt's lymphoma, diffuse large B-cell lymphoma, anaplastic large cell lymphoma, and lymphoblastic lymphoma. Primary mediastinal B-cell lymphoma previously was categorized as a diffuse large B-cell lymphoma but now is considered a separate category of non-Hodgkin lymphoma [57]. The prevalence of different lymphomas depends on age. In teenagers, diffuse large B-cell lymphoma is the most common non-Hodgkin lymphoma, while sporadic Burkitt's lymphoma and lymphoblastic lymphoma are extremely rare in older children. In younger children, Burkitt's lymphoma is the most common non-Hodgkin lymphoma [2]. A common presentation of Burkitt's lymphoma is as a single lesion in the intestine, frequently accompanied by intussusception. Lymphoblastic lymphoma and primary mediastinal B-cell lymphoma nearly always present as a mediastinal mass. Lymphoblastic lymphoma typically is treated similarly to acute lymphoblastic leukemia [2]. Diffuse large B-cell lymphoma and anaplastic large cell lymphoma are more likely to present with widespread disease.

Even with current appropriate therapy, overall survival is lower in children with the non-Hodgkin lymphomas than with Hodgkin's disease [1, 2]. Overall survival for pediatric patients with non-Hodgkin lymphomas is nearly 85 %, although outcome varies and depends on the histology and extent of disease. Patients with localized diffuse large B-cell lymphoma or localized Burkitt's lymphoma may have an overall survival of greater than 95 % [2]. Widespread disease is more common with non-Hodgkin lymphoma than with Hodgkin's disease.

The most commonly used clinical staging classification system for pediatric non-Hodgkin lymphoma was first reported by Murphy [58] and frequently is referred to as the St. Jude staging system. It uses the number and location of involved lymph nodes and location of any extranodal disease to classify pediatric non-Hodgkin lymphomas into four staging groups [56, 58, 59]. In this staging system, stage I indicates disease in a single lymph node site or a single extranodal tumor but excludes primary disease in the mediastinum or abdomen. Stage II indicates two or more sites of disease (nodal or extranodal) on one side of the diaphragm, while stage III indicates disease on both sides of the diaphragm. Primary intrathoracic tumors, including disease involving the mediastinum, pleura, or thymus, and paraspinal or epidural tumors are included in stage III. In the abdomen, localized resectable gastrointestinal disease is staged as stage II, while stage III includes more extensive intra-abdominal primary disease. Stage IV indicates initial disease within the central nervous system or bone marrow.

Occasionally, non-Hodgkin lymphoma may present without apparent lymph node involvement, but this is less common in children than in adults [60]. In children, the most common subtype of primary extranodal lymphoma is diffuse large B-cell lymphoma, but all other subtypes have been reported to present with primary extranodal disease. The two most common sites of primary extranodal lymphoma in children are the skeleton and the central nervous system.

Primary lymphoma of bone can occur anywhere in the skeleton but usually occurs in bones containing active bone marrow, such as the femur

[61]. At presentation, primary lymphoma of the bone may be confused with nonmalignant osseous conditions, including osteomyelitis and primary bone lesions, such as osteoid osteoma [62, 63], and rarely will present with a pathological fracture [61]. Primary bone lymphoma typically has an excellent response to chemotherapy [64].

Primary central nervous system lymphoma can occur in either the brain or the leptomeninges [65]. Primary central nervous system lymphoma typically has been thought of as a disease of immunodeficiency, but most cases occur in immunocompetent children [66, 67]. Before a diagnosis is made, primary central nervous system lymphoma may be confused with vascular disease, infection, or primary brain tumor. Histological diagnosis of a central nervous system lymphoma may be made by tumor resection, tissue biopsy, or analysis of cerebrospinal fluid.

Staging

Initial staging of non-Hodgkin lymphoma usually is performed with CT scan, although MRI may be used to assess suspected sites of disease in the skeleton or brain. Fluorine-18-FDG PET/CT may detect additional sites of disease, but may not identify additional sites of clinically important disease for staging most types of non-Hodgkin lymphoma (Fig. 21.3) [68]. This may, in part, reflect the higher rate of widespread disease in patients with non-Hodgkin's lymphoma. In a patient being treated with systemic chemotherapy for widespread disease, finding additional sites of disease may have little impact on staging or planned therapy. As a result, ^{18}F-FDG PET/CT rarely has been used for initial staging of pediatric non-Hodgkin's lymphoma. One exception has been the use of ^{18}F-FDG PET/CT for staging Burkitt's lymphoma (Fig. 21.4).

Burkitt's lymphoma frequently occurs as a single site of disease, and ^{18}F-FDG PET/CT can help guide initial therapy by confirming that there are no other sites of disease. Burkitt's lymphoma presenting as a single site of disease has a high cure rate with surgical resection followed by limited chemotherapy. The most typical locations for Burkitt's lymphoma are the abdomen and the head and neck [35]. A common presentation of Burkitt's lymphoma is as a single lesion in the intestine, frequently accompanied by intussusception. This usually represents primary lymph node disease rather than primary involvement of the intestinal wall. Abdominal Burkitt's lymphoma

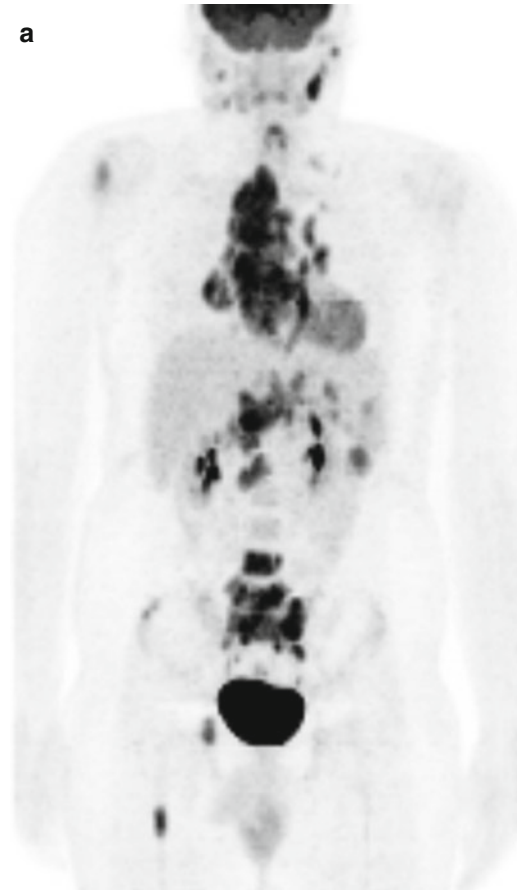

Fig. 21.3 ^{18}F-FDG PET/CT in pediatric patients with non-Hodgkin lymphoma. (**a**) In a 15-year-old male with anaplastic large cell lymphoma, the MIP of an ^{18}F-FDG PET demonstrates the typical widespread involvement of disease. FDG-avid disease is identified in cervical, mediastinal, hilar, retroperitoneal, and pelvic lymph nodes, and there is focal involvement of the spleen and bone marrow, including in the right humerus, spine, pelvis, and right femur. (**b**) In a 13-year-old girl with primary mediastinal B-cell lymphoma, the MIP of an ^{18}F-FDG PET shows a large FDG-avid mass in the chest that is evaluated with ^{18}F-FDG PET/CT. (**c**) Transaxial ^{18}F-FDG PET image shows a thick rim of FDG-avid disease in the mid-chest. (**d**) Transaxial CT shows a large anterior mediastinal mass with posterior displacement of mediastinal structures. (**e**) Co-registration of PET and CT images confirms that the large anterior mediastinal mass represents FDG-avid disease

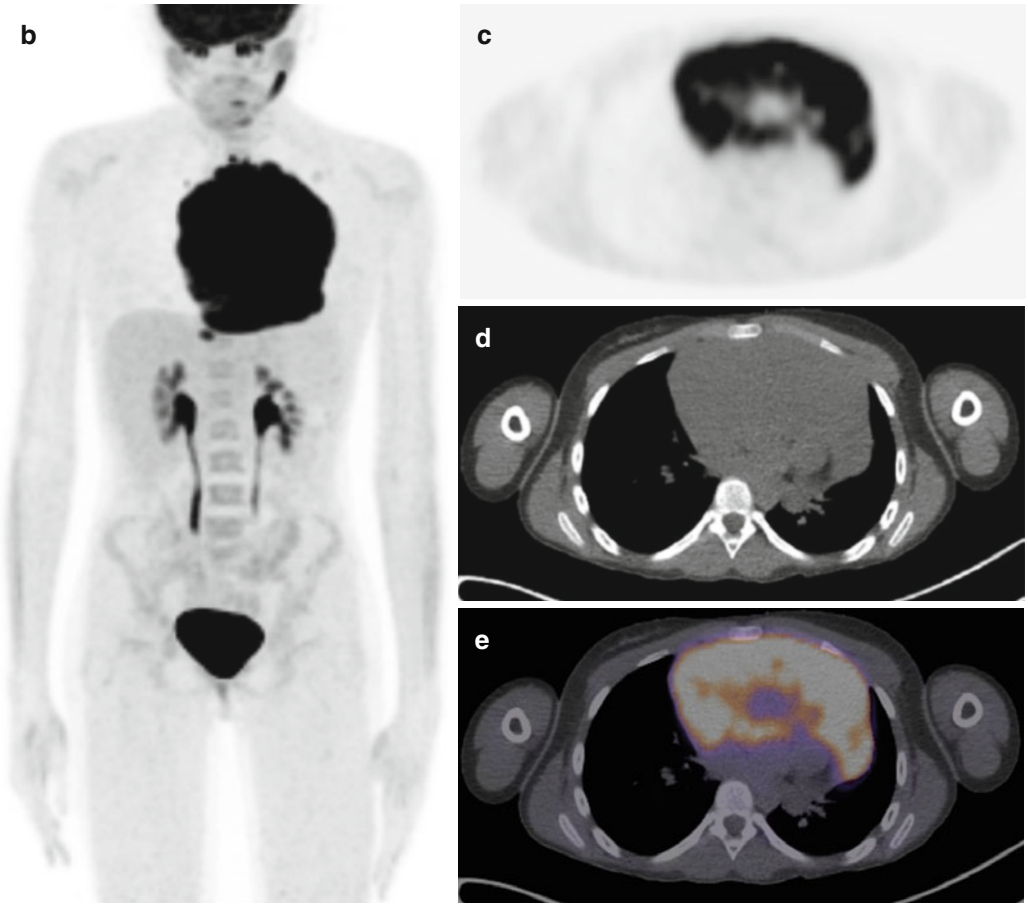

Fig. 21.3 (continued)

also may present with widespread lymph node involvement. In a patient discovered with a single site of abdominal Burkitt's lymphoma, ^{18}F-FDG PET/CT can be used to confirm that there are no other sites of disease.

Response to Therapy and Follow-Up

For pediatric patients with a non-Hodgkin lymphoma, there is limited information on the use of ^{18}F-FDG PET/CT either to assess a response to therapy or for follow-up surveillance. In adults with non-Hodgkin lymphoma, the ^{18}F-FDG PET response after two cycles of chemotherapy is correlated with outcome and is used to guide changes in therapy. However, in children, ^{18}F-FDG PET/CT may have more value for restaging non-Hodgkin lymphoma at the completion of treatment. As with Hodgkin's disease, FDG avidity may be a better indicator than CT for identifying sites of persistent non-Hodgkin lymphoma at the end of therapy [68, 69]. There is no clear role for ^{18}F-FDG PET/CT in surveillance for recurrence of non-Hodgkin lymphoma. However, when recurrent disease is detected, then ^{18}F-FDG PET/CT can be useful for restaging in anticipation of therapy.

Posttransplantation and Immunodeficiency-Related Lymphoproliferative Disorders

Children with acquired or inherited immune deficiency may develop lymphoproliferative disease and are at increased risk for lymphoma [70]. Posttransplantation lymphoproliferative disorder

(PTLD) may be the most common posttransplant malignancy in children [71, 72]. The risk of developing PTLD is greatest during the first year after transplantation [73]. PTLD occurs in up to one-quarter of children receiving a solid organ transplant [72], but the risk of PTLD depends on the type of organ transplant. The risk is highest in individuals with combined heart/lung or with bowel transplant and is lowest in recipients of a kidney transplant [74]. Other risk factors PTLD include an EBV-negative recipient (a common risk factor for children) and the intensity of immunosuppressive therapy [75]. Most PTLD is of B-cell origin and up to 90 % of cases are associated with Epstein-Barr virus infection [72, 76, 77]. PTLD can range from indolent lymphoproliferation to aggressive lymphoma and has been divided into four pathological categories: (1) reactive lymphoid proliferation; (2) polymorphic PTLD, characterized by heterogeneous populations of lymphocytes; (3) monomorphic PTLD, meeting histological criteria for non-Hodgkin's lymphoma; and (4) Hodgkin-type PTLD. Of these, polymorphic PTLD is the most common form of PTLD in pediatric transplant recipients [72]. However, many cases may not fit clearly into one of these categories [73, 75]. Although most high-grade PTLD is a non-Hodgkin lymphoma, approximately one-fourth of cases may be Hodgkin-type PTLD [75].

First-line therapy for PTLD includes a reduction in immunosuppression. This increases the risk of transplant rejection, which can be more critical with heart, lung, and liver transplants and less critical with kidney transplants. Antiviral therapy may have a role, especially in patients with high EBV titers, but the appropriate management of antiviral therapy remains controversial [75]. Patients with an inadequate response to these measures or with aggressive disease are treated with standard chemotherapy, similar to that used to treat non-Hodgkin lymphoma in immunocompetent patients. However, transplant patients may be at higher risk of chemotherapy-related infectious complications. Radiation therapy and surgery are rarely used to treat PTLD, except in cases of limited or localized disease or when the primary site is the central nervous system [78]. Immunotherapy has gained an

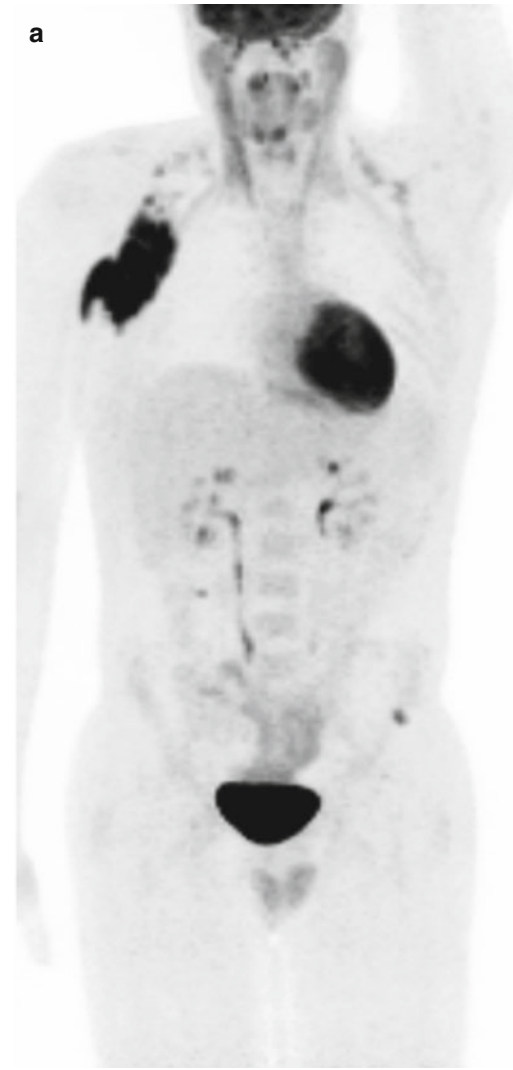

Fig. 21.4 Using ^{18}F-FDG PET/CT to evaluate Burkitt's lymphoma. (**a**) In a 14-year-old boy presenting with a large mass in the right axilla, tissue biopsy revealed Burkitt's lymphoma. The MIP of an ^{18}F-FDG PET demonstrates FDG-avid disease in the right axilla. Subcutaneous nodules on the lower anterior abdominal wall and overlying the left buttock also show intense FDG avidity. Tissue biopsy of the anterior abdominal wall nodule demonstrated Burkitt's lymphoma, indicating stage III disease. (**b**) In a 9-year-old boy with an obstructing nasopharyngeal mass, tissue biopsy revealed Burkitt's lymphoma. The MIP of an ^{18}F-FDG PET demonstrates abnormal ^{18}F-FDG uptake in the region of the nasopharynx without abnormal ^{18}F-FDG uptake elsewhere in the head and neck or torso. (**c**) A transaxial PET image shows intense uptake in the expected locations of the nasal cavity and upper pharynx. (**d**) A transaxial CT shows a soft tissue mass filling the posterior nasal cavity and nasopharynx without osseous invasion. (**e**) Co-registration of PET and CT images confirms the intense FDG avidity of the soft tissue mass

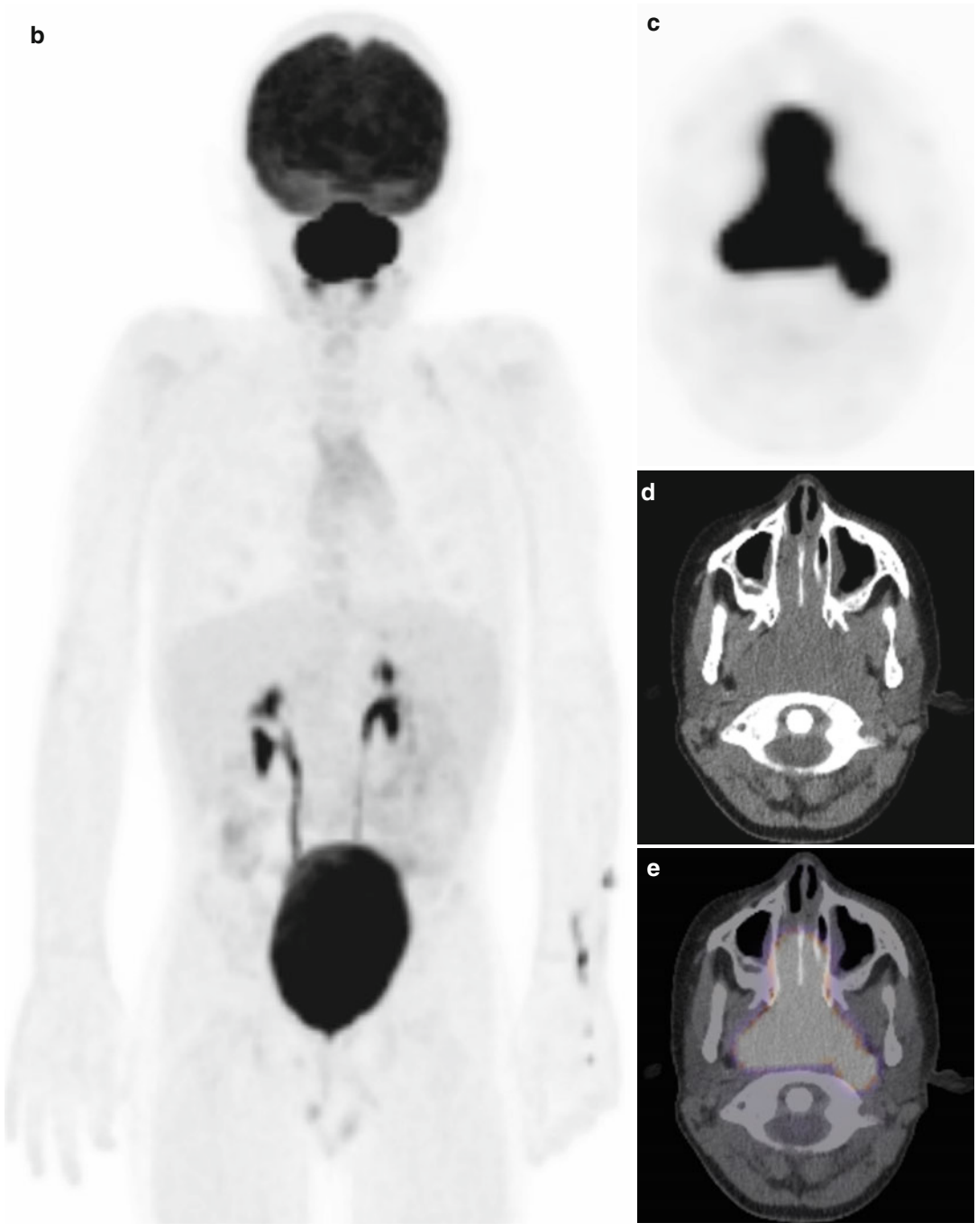

Fig. 21.4 (continued)

increasingly important role in the treatment of PTLD. This includes the use of anti-CD20 antibody therapy for B-cell PTLD. Drugs such as rituximab may be as effective as, but associated with fewer complications than, standard chemotherapy [75]. There have been no published reports describing the use of radioimmunotherapy for treatment of PTLD.

Lymphoproliferative disorders and lymphoma may be associated with other immunodeficiency syndromes. With the improved survival provided by highly active antiretroviral therapy, children with human immunodeficiency virus (HIV) are at increased risk of malignancy. This includes an increased risk for lymphomas, most commonly Burkitt's lymphoma [79]. Treatment of HIV-associated lymphoma is similar to that used in noninfected children [80]. Patients with inherited immunodeficiency syndromes also are at risk for immunodeficiency-related lymphoma. For example, immunodeficiency-related lymphoma can occur in children with the autoimmune lymphoproliferative syndrome (ALPS) [81]. Immunodeficiency-related lymphoma has been reported in children with a wide variety of rare inherited defects of the immune system, including combined variable immunodeficiency, Wiskott-Aldrich syndrome, and chromosomal breakage syndromes such as ataxia telangiectasia and Nijmegen syndrome [70].

Staging and Follow-up Imaging

Fluorine-18-FDG PET or PET/CT can have a role in the evaluation or management of patients with posttransplant or immunodeficiency-related lymphoproliferative syndromes and lymphomas. The use of ^{18}F-FDG PET/CT for evaluating patients with these disorders typically is guided by its use for imaging lymphomas in immunocompetent patients. Case reports and reports of small series of patients have demonstrated the utility in ^{18}F-FDG PET and PET/CT for staging and following patients with PTLD, although only a few of these published reports have included children [82–84]. In patients with PTLD, ^{18}F-FDG PET/CT can identify more sites of disease than other imaging modalities and can be particularly helpful for identifying sites of extranodal disease (Fig. 21.5) [84, 85]. Fluorine-18-FDG PET/CT can be useful for evaluating the response to therapy and identifying recurrent disease [82, 83].

Fluorine-18-FDG PET/CT can have a role in the management of patients with immunodeficiency-related lymphoproliferation and lymphoma. In patients with ALPS, both benign lymphoproliferation and lymphoma are FDG avid, and tissue biopsy is necessary whenever there is a change in symptoms or appearance of lymphadenopathy [86]. Fluorine-18-FDG PET/CT cannot discriminate benign and malignant lymph node enlargement, but can guide tissue biopsy to ensure that FDG-avid lymph nodes are sampled [86].

Non-neoplastic Syndromes of Lymphadenopathy

FDG avidity is not specific to malignancy, and a wide variety of non-neoplastic syndromes of lymphadenopathy can have ^{18}F-FDG PET/CT findings that may be confused with Hodgkin's disease or non-Hodgkin lymphoma (Fig. 21.6) [87]. Enlarged lymph nodes are common in childhood [88, 89], and with identification of new FDG-avid lymphadenopathy, tissue sampling may be needed to make a definite diagnosis.

Infectious causes of benign lymphadenopathy may be mistaken for lymphoma [87]. For example, patients with EBV-related mononucleosis occasionally may undergo evaluation for presumed lymphoma and can be found to have intensely FDG-avid lymphadenopathy and splenomegaly [90] (Fig. 21.6). Similarly, patients with acute CMV [91] or hepatitis B infection [92] have been reported to have FDG-avid lymphadenopathy. Patients with tuberculosis can develop enlarged, FDG-avid lymph nodes. Granulomas can form in lymph nodes of the chest, even in the absence of lung disease, and lymphadenopathy may be discovered during evaluation of fever or respiratory symptoms [93]. In some circumstances, ^{18}F-FDG PET/CT may be used to assess the response to therapy of patients with tuberculosis [94].

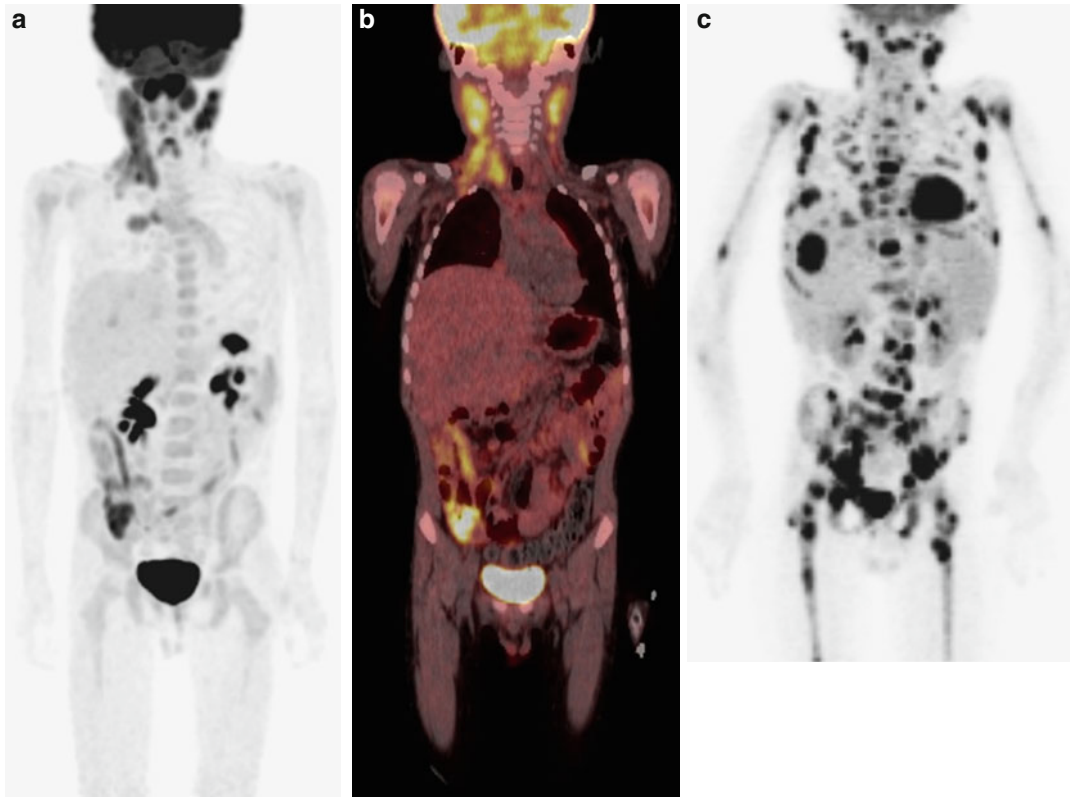

Fig. 21.5 ^{18}F-FDG PET/CT evaluation of lymphoproliferative disorders in patients with immune deficiency. (**a**) Three years after liver transplant for biliary atresia, an 8-year-old boy developed lymphadenopathy. Cervical lymph node biopsy demonstrated polyclonal posttransplant lymphoproliferative disorder. An MIP of an ^{18}F-FDG PET demonstrates FDG-avid disease involving cervical, supraclavicular, internal mammary, and cardiophrenic lymph nodes and focal FDG uptake in the right lower quadrant. (**b**) Co-registration of coronal ^{18}F-FDG PET and CT images confirms FDG-avid lymphadenopathy and abnormal FDG avidity in the terminal ileum. (**c**) A 15-year-old male with a congenital immune deficiency developed widespread adenopathy. Lymph node biopsy demonstrated lymphocyte-predominant Hodgkin's disease and ^{18}F-FDG PET/CT was used for staging. A MIP of the PET shows widespread FDG-avid disease involving innumerable lymph nodes throughout the neck and torso, numerous pulmonary nodules, the liver, and multiple sites in bone marrow in the axial and appendicular skeleton, indicating stage IV Hodgkin's disease

Lymphadenitis related to other infections, such as toxoplasmosis [95] or cat-scratch fever [96], has been reported to be FDG-avid. Dermatopathic lymphadenitis has been reported to be intensely FDG-avid [97] (Fig. 21.6).

Other unusual pediatric causes of FDG-avid lymphadenopathy can raise concern for lymphoma [87]. These include Rosai-Dorfman disease [98], Kikuchi syndrome (histiocytic necrotizing lymphadenitis) [99] (Fig. 21.6), and Castleman's disease [100, 101]. FDG-avid lymphadenopathy has been reported in children with systemic lupus erythematosus [102] and juvenile arthritis [103]. For most forms of non-neoplastic lymphadenopathy, there rarely is a role for ^{18}F-FDG PET or PET/CT in the management of disease. However, in patients with lymphadenopathy in a site not amenable to easy tissue sampling, then ^{18}F-FDG PET/CT might be helpful to search for other, more accessible, sites of disease. This may permit a less invasive approach to tissue biopsy and might help avoid an invasive and higher-risk procedure for the diagnosis of a benign condition.

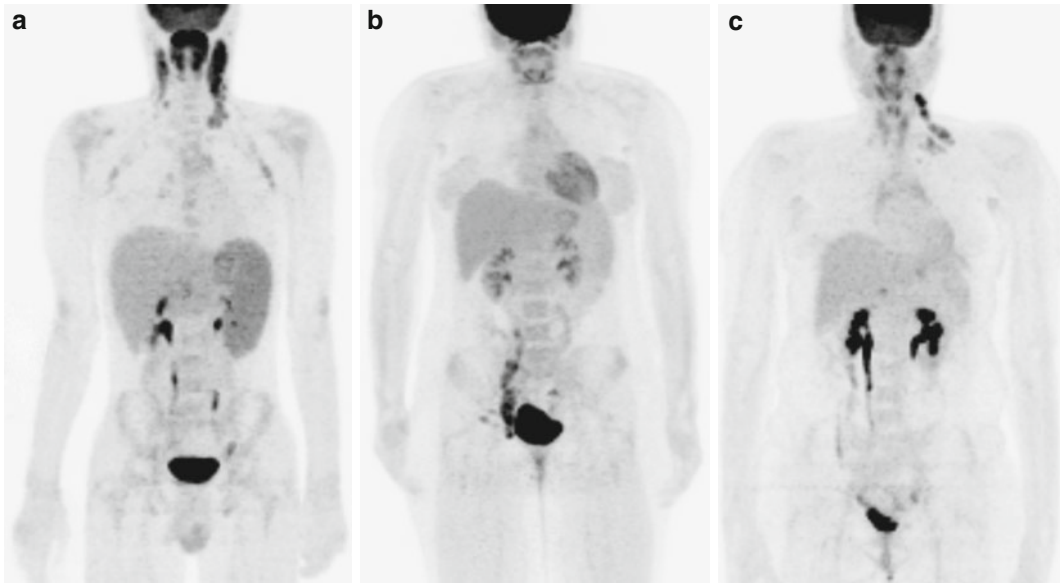

Fig. 21.6 ^{18}F-FDG PET in patients with non-neoplastic syndromes of lymphadenopathy. (**a**) A 16-year-old boy presented with fatigue, afebrile drenching night sweats, and increasing cervical lymphadenopathy. Initial viral titers were negative. A MIP of an ^{18}F-FDG PET demonstrates intense uptake in the tonsils and in cervical and supraclavicular lymph nodes and diffusely increased uptake in the enlarged spleen. Lymph node biopsy and repeat viral titers were consistent with EBV mononucleosis. (**b**) A 14-year-old female had a hip MRI for evaluation of pain and was found to have an incidental finding of extensive pelvic lymphadenopathy. ^{18}F-FDG PET/CT was performed to guide minimally invasive tissue sampling. The MIP of the PET shows FDG-avid extensive right iliac lymphadenopathy extending towards the inguinal region, with no other FDG-avid disease. Open biopsy of the inguinal lymph node demonstrated dermatopathic lymphadenopathy. (**c**) A 14-year-old female presented with persistent cervical lymphadenopathy and weight loss. A MIP of an ^{18}F-FDG PET shows abnormal FDG avidity in cervical and supraclavicular lymph nodes on the left, with no other sites of abnormal ^{18}F-FDG uptake. Cervical lymph node biopsy demonstrated histiocytic necrotizing adenitis (Kikuchi syndrome)

Although uncommon, juvenile sarcoidosis in older children can resemble the adult form of the disease, with the most common sites of disease in the lungs and thoracic lymph nodes [104, 105]. For evaluation of sarcoidosis, ^{18}F-FDG PET has better diagnostic accuracy than gallium scan [106]. Bilateral FDG-avid hilar adenopathy is the most typical pattern on ^{18}F-FDG PET, but other somewhat common sites of possible FDG-avid disease include lymph nodes in the mediastinum and elsewhere in the body, lungs, myocardium, liver, and spleen. In adults, FDG avidity has been reported at sites of disease throughout the body [104, 109]. Fluorine-18-FDG PET or PET/CT cannot distinguish sarcoidosis from lymphoma, but once the diagnosis of sarcoidosis is made, ^{18}F-FDG PET/CT can be used to determine the extent of disease, assess the response to therapy, and perform follow-up surveillance of disease [106].

The possibility of non-neoplastic lymphadenopathy can be more problematic when it is identified in a patient undergoing imaging for evaluation or follow-up surveillance of Hodgkin's disease or non-Hodgkin lymphoma. In these patients, it can be hard to distinguish persistent or recurrent lymphoma from benign lymphadenopathy. This task becomes even harder when there is an association between the malignant and benign processes. For example, patients with Hodgkin's disease may develop FDG-avid lymphadenopathy due to progressive transformation of the germinal centers (PTGC) [107] or hemophagocytic lymphohistiocytosis [108]. Conversely, some benign syndromes of adenopathy, such as systemic lupus erythematosus and monocentric Castleman's

disease, as well as progressive transformation of the germinal centers (PTGC) [109], have been associated with an increased risk of lymphoma. Finally, FDG-avid non-neoplastic lymphadenopathy may obscure sites of malignant disease and can limit the utility of ^{18}F-FDG PET/CT for evaluation or surveillance of Hodgkin's disease or non-Hodgkin lymphoma.

References

1. Wood WA, Lee SJ. Malignant hematologic diseases in adolescents and young adults. Blood. 2011;117:5803–15.
2. Hochberg J, Waxman IM, Kelly KM, Morris E, Cairo MS. Adolescent non-Hodgkin lymphoma and Hodgkin lymphoma: state of the science. Br J Haematol. 2008;144:24–40.
3. Punnett A, Tsang RW, Hodgson DC. Hodgkin lymphoma across the age spectrum: epidemiology, therapy, and late effects. Semin Radiat Oncol. 2010;20:30–44.
4. Abramson SJ, Price AP. Imaging of pediatric lymphomas. Radiol Clin North Am. 2008;46:313–38.
5. Palestro CJ, Brown ML, Forstrom LA, et al. Society of Nuclear Medicine procedure guideline for gallium scintigraphy in inflammation V3.0. http://interactive.snm.org/docs/Gallium_Scintigraphy_in_Inflammation_v3.pdf.
6. Gatley SJ. Labeled glucose analogs in the genomic era. J Nucl Med. 2003;44:1082–6.
7. The MICAD Research Team. [^{18}F]Fluoro-2-deoxy-2-D-glucose. In: Molecular imaging and contrast agent database (MICAD) [internet]. Bethesda: National Center for Biotechnology Information (US); 2004–2012. Bookshelf ID: NBK23335PMID: 20641537.
8. Fowler JS, Ido T. Initial and subsequent approach for the synthesis of ^{18}FDG. Semin Nucl Med. 2002;32:6–12.
9. Gelfand MJ, Parisi MT, Treves ST. Pediatric radiopharmaceutical administered doses: 2010 North American consensus guidelines. J Nucl Med. 2011;52:318–22.
10. Hines-Thomas M, Kaste SC, Hudson MM, et al. Comparison of gallium and PET scans at diagnosis and follow-up of pediatric patients with Hodgkin lymphoma. Pediatr Blood Cancer. 2008;51:198–203.
11. Van Den Bossche B, Lambert B, De Winter F, et al. ^{18}FDG PET versus high-dose ^{67}Ga scintigraphy for restaging and treatment follow-up of lymphoma patients. Nucl Med Commun. 2002;23:1079–83.
12. Grant F, Treves S. Comparison of Ga-67 SPECT and F-18-FDG PET in the evaluation of pediatric Hodgkin's disease. J Nucl Med. 2006;47:S87P.
13. Hong TS, Shammas A, Cheron M, Zukotynski KA, Drubach LA, Lim R. Brown adipose tissue ^{18}F-FDG uptake in pediatric PET/CT imaging. Pediatr Radiol. 2011;41:759–68.
14. Gilsanz V, Hu HH, Smith ML, et al. The depiction of brown adipose tissue is related to disease status in pediatric patients with lymphoma. AJR Am J Roentgenol. 2012;198:909–13.
15. Zukotynski KA, Fahey FH, Laffin S, et al. Constant ambient temperature of 24 degrees C significantly reduces FDG uptake by brown adipose tissue in children scanned during the winter. Eur J Nucl Med Mol Imaging. 2009;36:602–6.
16. Gelfand MJ, O'Hara SM, Curtwright LA, MacLean JR. Premedication to block [^{18}F] FDG uptake in brown adipose tissue of pediatric and adolescent patient. Pediatr Radiol. 2005;35:989–90.
17. Furth C, Denecke T, Steffen I, et al. Correlative imaging strategies implementing CT, MRI, and PET for staging of childhood Hodgkin disease. J Pediatr Hematol Oncol. 2006;28:501–12.
18. Hutchings M, Loft A, Hansen M, et al. Positron emission tomography with or without computed tomography in the primary staging of Hodgkin's lymphoma. Haematologica. 2006;91:482–9.
19. Riad R, Omar W, Kolb M, et al. Role of PET/CT in malignant pediatric lymphoma. Eur J Nucl Med Mol Imaging. 2010;37:319–29.
20. Campo E, Swerdlow SH, Harris NL, Pileri S, Stein H, Jaffe ES. The 2008 WHO classification of lymphoid neoplasms and beyond: evolving concepts and practical applications. Blood. 2011;117:5019–32.
21. Lee AI, LaCasce AS. Nodular lymphocyte predominant Hodgkin lymphoma. Oncologist. 2009;14:739–51.
22. Shankar A, Daw S. Nodular lymphocyte predominant Hodgkin lymphoma in children and adolescents – a comprehensive review of biology, clinical course and treatment options. Br J Haematol. 2012;159:288–98.
23. Mendler JH, Friedberg JW. Salvage therapy in Hodgkin's lymphoma. Oncologist. 2009;14:425–32.
24. Daw S, Wynn R, Wallace H. Management of relapsed and refractory classical Hodgkin lymphoma in children and adolescents. Br J Haematol. 2011;152:249–60.
25. Smith MA, Seibel NL, Altekruse SF, et al. Outcomes for children and adolescents with cancer: challenges for the twenty-first century. J Clin Oncol. 2010;28:2625–34.
26. Schwartz CL. Special issues in pediatric Hodgkin's disease. Eur J Haematol. 2005;75:S55–62.
27. Eichenauer DA, Borchmann P, Engert A. Adolescents with Hodgkin lymphoma: old children or young adults? Leuk Lymphoma. 2012;53:1257–62.
28. Olson MR, Donaldson SS. Treatment of pediatric Hodgkin lymphoma. Curr Treat Options Oncol. 2008;9:81–94.
29. Lister TA, Crowther SB, Sutcliffe SB, et al. Report of a committee to discuss the evaluation and staging of patients with Hodgkin's disease: Cotswolds Meeting. J Clin Onocol. 1989;7:1630–6.

30. Crowther D, Lister TA. The Cotswolds report on the investigation and staging of Hodgkin's disease. Br J Cancer. 1990;62:551–2.
31. AJCC. Hodgkin and non-Hodgkin lymphomas. In: Edge SB, Byrd DR, Compton CC, et al., editors. AJCC Cancer Staging Manual, vol. 7. New York: Springer; 2010. p. 607–11.
32. Schwartz CL. Prognostic factors in pediatric Hodgkin disease. Curr Oncol Rev. 2003;5:498–504.
33. Kelly KM. Management of children with high-risk Hodgkin lymphoma. Br J Haematol. 2012;157: 3–13.
34. Mody RJ, Bui C, Hutchinson RJ, Frey KA, Shulkin BL. Comparison of ^{18}F-fluorodeoxyglucose PET with Ga-67 scintigraphy and conventional imaging modalities in pediatric lymphoma. Leuk Lymphoma. 2007;48:699–707.
35. Guillerman RP, Voss SD, Parker BR. Leukemia and Lymphoma. Radiol Clin N Am. 2011;49:767–97.
36. Stauss J, Franzius C, Pfluger T, et al. Guidelines for ^{18}F-FDG PET and PET-CT imaging in paediatric oncology. Eur J Nucl Med Mol Imaging. 2008;35: 1581–8.
37. Sammer MB, Shulkin BL, Alessio A, Parisi MT. Role of limited whole-body PET/CT in pediatric lymphoma. AJR Am J Roentgenol. 2011;195: 1047–55.
38. Zukotynski K, Treves ST, Grant F. Atypical sites of FDG avidity are unlikely to represent lymphoma, but may reveal incidental pathology, when staging pediatric Hodgkin's disease. J Nucl Med. 2008;49: S276P.
39. London K, Cross S, Onikul E, Dalla-Pozza L, Howman-Giles R. ^{18}F-FDG PET/CT in paediatric lymphoma: comparison with conventional imaging. Eur J Nucl Med Mol Imaging. 2011;38:274–84.
40. Robertson VL, Anderson CL, Keller FG, et al. Role of FDG-PET in the definition of involved-field radiation therapy and management of pediatric Hodgkin's lymphoma. Int J Radiat Oncol Biol Phys. 2011;80:324–32.
41. Kabickova E, Sumerauer D, Cumlivska E, et al. Comparison of ^{18}F-FDG-PET and standard procedures for the pretreatment staging of children and adolescents with Hodgkin's disease. Eur J Nucl Med Mol Imaging. 2006;33:1025–31.
42. Delbeke D, Stroobants S, de Kerviler E, et al. Expert opinions on positron emission tomography and computed tomography imaging in lymphoma. Oncologist. 2009;14:S30–40.
43. Fahey FH, Kinahan PE, Doot RK, Kocak M, Thurston H, Poussaint TY. Variability in PET quantitation within a multicenter consortium. Med Phys. 2010;37:3660–6.
44. Cheson BD, Pfistner B, Juweid ME, et al. Revised response criteria for malignant lymphoma. J Clin Oncol. 2007;25:579–86.
45. Purz S, Mauz-Körholz C, Körholz D, et al. [18F] Fluorodeoxyglucose positron emission tomography for detection of bone marrow involvement in children and adolescents with Hodgkin's lymphoma. J Clin Oncol. 2011;29:3523–8.
46. Hofman MS. Fluorodeoxyglucose positron emission tomography/computed tomography for evaluation of bone marrow involvement in lymphoma: when is it superior to biopsy? Leuk Lymphoma. 2012;53: 349–51.
47. Richardson SE, Sudak J, Warbey V, et al. Routine bone marrow biospy is not necessary in the staging of patients with classical Hodgkin lymphoma in the ^{18}F-fluoro-2-deoxyglucose positron emission tomographic era. Leuk Lymphoma. 2012;53:381–5.
48. Salaun PY, Gastinne T, Bodet-Milin C, et al. Analysis of ^{18}F-FDG PET diffuse bone marrow uptake and splenic uptake in staging of Hodgkin's lymphoma: a reflection of disease infiltration or just inflammation? Eur J Nucl Med Mol Imaging. 2009;36:1813–21.
49. Shulkin BL, Goodin GS, McCarville MB, et al. Bone and [^{18}F]fluorodeoxyglucose positron-emission tomography/computed tomography scanning for the assessment of osseous involvement in Hodgkin lymphoma in children and young adults. Leuk Lymphoma. 2009;50:1794–802.
50. Pommier P, Dussart S, Girinsky T, et al. Impact of ^{18}F-fluoro-2-deoxyglucose positron emission tomography on treatment strategy and radiotherapy planning for stage I-II Hodgkin disease: a prospective multicenter study. Int J Radiat Oncol Biol Phys. 2011; 79:823–8.
51. Paulino AC, Margolin J, Dreyer Z, Teh BS, Chiang S. Impact of PET-CT on involved field radiotherapy design for pediatric Hodgkin lymphoma. Pediatr Blood Cancer. 2012;58:860–4.
52. Juweid ME, Stroobants S, Koekstra OS, et al. Use of positron emission tomography for response assessment of lymphoma: consensus of the imaging subcommittee of International Harmonization Project in Lymphoma. J Clin Oncol. 2007;25:571–8.
53. Cheson BD. The international Harmonization Project for response criteria in lymphoma clinical trials. Hematol Oncol Clin North Am. 2007;21:841–54.
54. Barrington SF, Qian W, Somer EJ, et al. Concordance between four European centres of PET reporting criteria designed for use in multicentre trials in Hodgkin lymphoma. Eur J Nucl Med Mol Imaging. 2010;37: 1824–33.
55. Meignan M, Gallamini A, Emmanuel I, Barrington S, Haioun C, Polliack A. Report on the Third International Workshop on Interim Positron Emission Tomography in Lymphoma held in Menton, France, 26–27 September 2011 and Menton 2011 consensus. Leuk Lymphoma. 2012;53:1876–81.
56. Gross TG, Termuhlen AM. Pediatric non-Hodgkin's lymphoma. Curr Oncol Rep. 2007;9:459–65.
57. Attias D, Hodgson D, Weitzman S. Primary mediastinal B-cell lymphoma in the pediatric patient: Can a rational approach to therapy be based on adult studies? Pediatr Blood Cancer. 2009;52:566–70.
58. Murphy S. Childhood non-Hodgkin's lymphoma. N Engl J Med. 1978;26:1446–8.

59. AJCC. Pediatric lymphoid malignancy. In: Edge SB, Byrd DR, Compton CC, et al., editors. AJCC Cancer Staging Manual. 7th ed. New York: Springer; 2010. p. 619–20.
60. Padhi S, Paul TR, Challa S, et al. Primary extra nodal non Hodgkin lymphoma: a 5 year retrospective analysis. Asian Pac J Cancer Prev. 2012;13:4889–95.
61. Siddiqui YS, Kan AQ, Sherwani M. Pathological fracture in primary non-Hodgkin's lymphoma of the bone: a case series with review of the literature. J Clin Diagn Res. 2013;7:513–7.
62. Mika J, Schleicher I, Gerlach U, Adler CP, Uhl M, Knoeller SM. Primary bone lymphomas thought to be osteomyelitis urgently demand a rapid diagnosis in bone pathology. Anticancer Res. 2012;32:4905–12.
63. Croteau SE, Henderson ER, Billett AL, Gebhardt MC, Voss SD. Resolving bony abnormality evolves to diffuse large B-cell lymphoma. Pediatr Blood Cancer. 2013;60:E113–5. doi:10.1002/pbc.24609.
64. Lones MA, Perkins SL, Sposto R, et al. Non-Hodgkin's lymphoma arising in bone in children and adolescents is associated with an excellent outcome: a Children's Cancer Group report. J Clin Oncol. 2002;20:2293–301.
65. Jordaan MR, Prabhu SP, Silvera VM. Primary leptomeningeal central nervous system lymphoma in an immunocompetent adolescent: an unusual presentation. Pediatr Radiol. 2010;40:S141–4.
66. Karikari IO, Thomas KK, Lagoo A, Cummings TJ, George TM. Primary cerebral ALK-1-positive anaplastic large cell lymphoma in a child: Case report and literature review. Pediatr Neurosurg. 2007;43:516–21.
67. Abla O, Weitzman S, Blay J-Y, et al. Primary CNS lymphoma in children and adolescents: A descriptive analysis from the International Primary CNS Lymphoma Collaborative Group (IPCG). Clin Cancer Res. 2011;17:346–52.
68. Shankar A, Fiumara F, Pinkerton R. Role of FDG PET in the management of childhood lymphomas - case proven or is the jury still out? Eur J Cancer. 2008;44:663–73.
69. Depas G, De Barsey C, Jerusalem G, et al. ^{18}F-FDG PET in children with lymphomas. Eur J Nucl Med Mol Imaging. 2005;32:31–8.
70. van Krieken JH. Lymphoproliferative disease associated with immune deficiency in children. Am J Clin Pathol. 2004;122:S122–7.
71. Boubenider S, Hiesse C, Goupy C, Kriaa F, Marchand S, Charpentier B. Incidence and consequences of post-transplantation lymphoproliferative disorders. J Nephrol. 1997;10:136–45.
72. Gross TG, Savoldo B, Punnett A. Posttransplant lymphoproliferative diseases. Pediatr Clin North Am. 2010;57:481–503.
73. Parker A, Bowles K, Bradley JA, et al. Management of post-transplant lymphoproliferative disorder in adult solid organ transplant recipients – BCSH and BTS Guidelines. Br J Haematol. 2010;149:693–705.
74. Tsao L, His ED. The clinicopathologic spectrum of posttransplantation lymphoproliferative disorders. Arch Pathol Lab Med. 2007;131:1209–18.
75. Dierickx D, Tousseyn T, Sagaert X, et al. Single-center analysis of biopsy-confirmed posttransplant lymphoproliferative disorder: incidence, clinicopathological characteristics and prognostic factors. Leuk Lymphoma. 2013;54:2433–40. doi:10.3109/10428194.2013.780655.
76. Allen U, Hebert D, Petric M, et al. Utility of semiquantitative polymerase chain reaction for Epstein-Barr virus to measure virus load in pediatric organ transplant recipients with and without posttransplant lymphoproliferative disease. Clin Infect Dis. 2001;33:145–50.
77. Kutok JL, Wang F. Spectrum of Epstein-Barr virus-associated diseases. Annu Rev Pathol. 2006;1:375–404.
78. Cavaliere R, Petroni G, Lopes MB, Schiff D. Primary central nervous system post-transplantation lymphoproliferative disorder: an International Primary Central Nervous System Lymphoma Collaborative Group report. Cancer. 2010;116:863–70.
79. Godat C, Patte C, Blanche S, Rohrlich P, Dollfus C, Tabone M-D. Characteristics and prognosis of B-cell lymphoma in HIV-infected children in the HAART era. J Pediatr Hematol Oncol. 2012;34:e282–8.
80. Navaro WH, Kaplan LD. AIDS-related lymphoproliferative disease. Blood. 2006;107:13–20.
81. Oliviera JB, Bleesing JJ, Dianzini U, et al. Revised diagnostic criteria and classification for the autoimmune lymphoproliferative syndrome (ALPS): report from the 2009 NIH International Workshop. Blood. 2010;116:e35–40.
82. von Falck C, Maecker B, Schirg E, et al. Post transplant lymphoproliferative disease in pediatric solid organ transplant patients: A possible role for [^{18}F]-FDG-PET(/CT) in initial staging and therapy monitoring. Eur J Radiol. 2007;63:427–35.
83. Blaes AN, Cioc AM, Froelich JW, Peterson BA, Dunitz JM. Positron emission tomography scanning in the setting of post-transplant lymphoproliferative disorders. Clin Transplant. 2009;23:794–9.
84. Panagiotidis E, Quigley A-M, Pencharz D, et al. ^{18}F-FDG PET/CT in the diagnosis of post-transplant lymphoproliferative disorders. Leuk Lymphoma. 2013; Epub ahead of print. doi:10.3109/10428194.2013.813501.
85. Marom EM, McAdams HP, Butnor KJ, Coleman RE. Positron emission tomography with fluoro-2-deoxyglucose (FDG-PET) in the staging of post transplant lymphoproliferative disorder in lung transplant recipients. J Thorac Imaging. 2004;19:74–8.
86. Rao VK, Oliveira JB. How I treat autoimmune lymphoproliferative syndrome. Blood. 2001;118:5741–51.
87. Aragon-Ching JB, Akin EA. Positron emission tomography findings in clinical mimics of lymphoma. Ann N Y Acad Sci. 2011;1228:19–28.
88. Ramsey AD. Reactive lymph nodes in pediatric patients. Am J Clin Pathol. 2004;122:S87–97.

89. Monaco SE, Khalbuss WE. Benign non-infectious causes of lymphadenopathy. Diagn Cytopathol. 2012; 40:925–38.
90. Tomas MB, Tronco GG, Karayalcin G, Palestro CJ. FDG uptake in infectious mononucleosis. Clin Positron Imaging. 2000;3:176.
91. Banzo J, Ubieto MA, Prats E, et al. ^{18}F-FDG PET-CT in cytomegalovirus-induced mononucleosis. Rev Esp Med Nucl. 2010;29:304–7.
92. Jacene HA, Stearns V, Wahl RL. Lymphadenopathy resulting from acute hepatitis C infection mimicking metastatic breast carcinoma on FDG PET/CT. Clin Nucl Med. 2006;31:379–81.
93. Martinez V, Castilla-Lievre MA, Guillet-Caruba C, et al. ^{18}F-FDG PET/CT in tuberculosis: an early non-invasive marker of therapeutic response. Int J Tuberc Lung Dis. 2012;16:1180–5.
94. Sathekge M, Maes A, D'Asseler Y, Vorster M, Gongxeha H, Van de Wiele C. Tuberculous lymphadenitis: FDG PET and CT findings in responsive and non-responsive disease. Eur J Nucl Med Mol Imaging. 2012;39:1184–90.
95. Yamazaki Y, Kitagawa Y, Hata H, Sakakibara N, Shindoh M, Tmamaki N. Cervical toxoplasmosis lymphadenitis can mimic malignant lymphoma on FDG PET. Clin Nucl Med. 2008;33:819–20.
96. Imperiale A, Blondet C, Ben-Sellem D, et al. Unusual abdominal localization of cat scratch disease mimicking malignancy on F-18 FDG PET/CT. Clin Nucl Med. 2008;33:621–3.
97. Makis W, Hickeson M, Blumenkrantz M. Dermatopathic lymphadenitis: A pitfall for lymphoma evaluation by F-18 FDG PET/CT. Clin Nucl Med. 2010;35:872–4.
98. Hock ATE, Long MTM, Sittampalam K, Eng DNC. Rosai-Dorfman disease: FDG PET/CT findings in a patient presenting with pyrexia and cervical adenopathy. Clin Nucl Med. 2010;35:576–8.
99. Kim CH, Hyun OJ, Yoo IR, Kim SH, Sohn HS, Chung SK. Kikuchi disease mimicking malignant lymphoma on FDG PET/CT. Clin Nucl Med. 2007;32:711–2.
100. Toita N, Kawamura N, Hatano N, et al. A 5-year-old boy with unicentric Castleman disease affecting the mesentery: utility of serum IL-6 level and ^{18}F-FDG PET for diagnosis. J Pediatr Hematol Oncol. 2009;31: 693–5.
101. Farrugia P, Trizzino A, Scibetta N, et al. Castleman's disease in childhood: report of three cases and review of the literature. Ital J Pediatr. 2011;37:50. www.ijponline.net/content/37/1/50.
102. Fey GL, Jolles PR, Buckley LM, Massey GV. 2-deoxy-2-[^{18}F]fluoro-D-glucose positron emission tomography uptake in systemic lupus erythematosus-associated adenopathy. Mol Imaging Biol. 2004;6: 7–11.
103. Lord M, Allaoua M, Ratib O. Positron emission tomography findings in systemic juvenile idiopathic arthritis. Rheumatology. 2011;50:1177.
104. Jain V, Hasselquist S, Delaney MD. PET scanning in sarcoidosis. Ann N Y Acad Sci. 2011;1228:46–58.
105. Fretzayas A, Moustaki M, Vougiouka O. The puzzling clinical spectrum and course of juvenile sarcoidosis. World J Pediatr. 2011;7:103–10.
106. Treglia G, Taralli S, Giordano A. Emerging role of whole-body ^{18}F-fluorodeoxyglucose positron emission tomography as a marker of disease activity in patients with sarcoidosis: a systematic review. Sarcoidosis Vasc Diffuse Lung Dis. 2011;28:87–94.
107. Levine JM, Weiner M, Kelly K. Routine use of PET scans after completion of therapy in pediatric Hodgkin disease results in a high false positive rate. Pediatr Hematol Oncol. 2006;28:711–4.
108. Corapcioglu F, Öncel S, Berberğlu K, Kiliç SÇ, Aydoğan A, Doğan S. False positivity of FDG-PET during hemophagocytic lymphohistiocytosis in a child with Hodgkin lymphoma in remission. J Pediatr Hematol Oncol. 2009;31:74–5.
109. Shaikh F, Ngan B-Y, Alexander S, Grant R. Progressive transformation of germinal centers in children and adolescents: An intriguing cause of lymphadenopathy. Pediatr Blood Cancer. 2013;60: 26–30.

Functional Imaging of Pediatric Musculoskeletal Tumors

22

Frederick D. Grant and S. Ted Treves

Musculoskeletal malignancies are among the more common solid tumors of childhood. These include osteogenic sarcoma, or osteosarcoma, the Ewing family of tumors, and rhabdomyosarcoma. Other less common pediatric tumors, including non-rhabdomyosarcoma sarcomas, frequently involve the musculoskeletal system (see Chap. 23). Pediatric lymphomas occasionally present with primary bone lymphoma (see Chap. 21). Successful treatment of primary musculoskeletal malignancies requires multiagent systemic chemotherapy and adequate local control. Local control may be either surgery or radiation therapy, except with osteosarcoma, which is relatively insensitive to radiation therapy. Many treatment regimens utilize neoadjuvant chemotherapy, which may decrease the extent and morbidity of subsequent local control. For example, neoadjuvant chemotherapy may allow for limb-sparing surgery and decrease the need for complete amputation [1]. Inadequate local control is associated with local disease recurrence and poor outcome.

Imaging studies are used for initial staging, assessing the response to therapy, and surveillance for recurrent disease. In initial staging, identification of distant metastases is a common need with all three tumor types. In addition to prognostic implications, identification of distant disease can guide therapy. For example, in patients with osteosarcoma, distant metastases may delay local control surgery, while in patients with Ewing sarcoma, each site of distant disease must receive local control therapy.

The relative utility of different imaging methods for the evaluation of pediatric musculoskeletal tumors is unsettled and requires further study. This may, in part, reflect the low prevalence of these tumors in children and the need to make extrapolations from studies involving patients of all ages. Some musculoskeletal lesions have distinctive imaging features on radiograph, computed tomography (CT), or magnetic resonance imaging (MRI). In these cases a diagnosis may

F.D. Grant, MD (✉)
Joint Program in Nuclear Medicine,
Department of Radiology, Harvard Medical School,
Boston, MA, USA

Division of Nuclear Medicine and Molecular Imaging,
Department of Radiology,
Boston Children's Hospital,
Boston, MA, USA

Department of Radiology,
Brigham and Women's Hospital,
Boston, MA, USA
e-mail: frederick.grant@childrens.harvard.edu

S.T. Treves, MD (✉)
Joint Program in Nuclear Medicine,
Department of Radiology,
Harvard Medical School,
Boston, MA, USA

Division of Nuclear Medicine and Molecular Imaging,
Department of Radiology, Boston Children's Hospital,
Boston, MA, USA

Division of Nuclear Medicine and Molecular
Imaging, Department of Radiology,
Brigham and Women's Hospital, Boston, MA, USA
e-mail: ted_treves@HMS.harvard.edu

S.T. Treves (ed.), *Pediatric Nuclear Medicine and Molecular Imaging*,
DOI 10.1007/978-1-4614-9551-2_22, © Springer Science+Business Media New York 2014

be made on imaging findings alone. However, for most tumors, additional evaluation, such as tumor biopsy, will be needed.

Many research groups have attempted to identify a role for ^{18}F-FDG PET in distinguishing benign from malignant tumors. Malignant tumors typically have greater FDG avidity than benign tumors. In both adults and children with musculoskeletal tumors, there is a strong correlation between tumor grade and FDG avidity [2, 3]. However, there is much overlap in FDG uptake between malignant and benign tumors, and FDG avidity cannot be used to reliably predict tumor characteristics. In particular, most attempts to use a specific SUV value as a "cut-off" to predict malignancy have had little success.

For most musculoskeletal malignancies, whole-body imaging is essential to identify distant sites of disease. Whether the appropriate whole-body scan is a bone scan or ^{18}F-FDG PET appears to depend on the tumor type. In many cases, these studies may be complementary, and it can be appropriate to use both. The role of whole-body MRI is evolving, and in some cases, it may be a useful addition for whole-body imaging.

Methods

Nuclear medicine studies used to evaluate musculoskeletal tumors include bone scans and ^{18}F-FDG PET. Bone scans typically are performed using a bisphosphonate labeled with ^{99m}Tc, such as ^{99m}Tc-methylene diphosphonate (^{99m}Tc-MDP) (see Chap. 15). With the wider availability of PET scanners, ^{18}F-sodium fluoride (^{18}F-NaF) PET provides an alternative bone scanning technique [4]. Fluorine-18-FDG PET and ^{18}F-FDG PET/CT have an increasing role in the evaluation of pediatric musculoskeletal malignancies (see Chap. 3) [5, 6].

Osteosarcoma

Clinical

Osteosarcoma is the most common bone tumor of young adults and children, with 80 % of osteosarcomas presenting between the ages of 5 and 25 years [7]. Nearly all of these are primary tumors. There is a second peak of incidence in older adults, which is more likely to include secondary osteosarcoma. Primary osteosarcoma typically occurs in the metaphyses of the long bones of the extremities, with less than a third of all cases occurring at other sites. Secondary cases of osteosarcoma occur at the sites of predisposing processes, such as Paget's disease, fibrous dysplasia, and multiple chondromas. Secondary osteosarcoma also occurs at sites of prior radiation for treatment of other tumors. The most common association of radiation therapy and osteosarcoma is with retinoblastoma, which may reflect an increased risk of osteosarcoma unrelated to radiation therapy in patients with retinoblastoma. However, osteosarcoma also occurs within the field of radiation therapy for other tumors, such as Ewing sarcoma. There are numerous pathological subtypes of osteosarcoma, based on histological characteristics and tumor location in the skeleton. In over half the cases of osteosarcoma, metastatic disease will be discovered at or soon after the time of diagnosis. The lungs are the most common location for metastases, while bone metastases occur in 10–20 % of cases. Lymph node metastases are unusual with osteosarcoma.

In patients with localized primary osteosarcoma, the combination of effective multi-agent chemotherapy and adequate local control leads to 65–70 % event-free survival [8]. The prognosis is not as good for patients with metastatic disease or secondary osteosarcoma [9]. Inadequate local control is associated with treatment failure and poor outcome [8, 10]. Osteosarcoma is resistant to radiation therapy [9], so the only effective local control is surgery. Frequently, limb-preserving surgery can provide adequate local control [11]. Identification of lung metastases at the time of diagnosis makes 2-year survival unlikely, but surgical resection of metastases can improve survival by up to 50 % [12]. Treatment of recurrent disease prolongs survival, so identifying and localizing recurrent disease can be an important part of follow-up imaging.

Diagnosing and Staging of Osteosarcoma

For many decades, the standard initial evaluation of osteosarcoma (Fig. 22.1) has included

Fig. 22.1 Initial presentation and imaging evaluation of osteosarcoma in a 12-year-old girl with left leg pain. Lateral (**a**) and anterior-posterior (**b**) radiographs show an aggressive mixed sclerotic and lytic expansile lesion in the distal left femur with a marked periosteal reaction. (**c**) On MRI there is a heterogeneous mass involving the distal metaphysis of the left femur that extends to the physis and is surrounded by soft tissue edema. (**d**) After gadolinium contrast, there is peripheral enhancement of the tumor, suggesting central necrosis. (**e**) A whole-body ^{99m}Tc-MDP bone scan shows intense uptake at the site of the known distal femur tumor without metastatic disease. A chest CT was obtained to exclude lung metastases

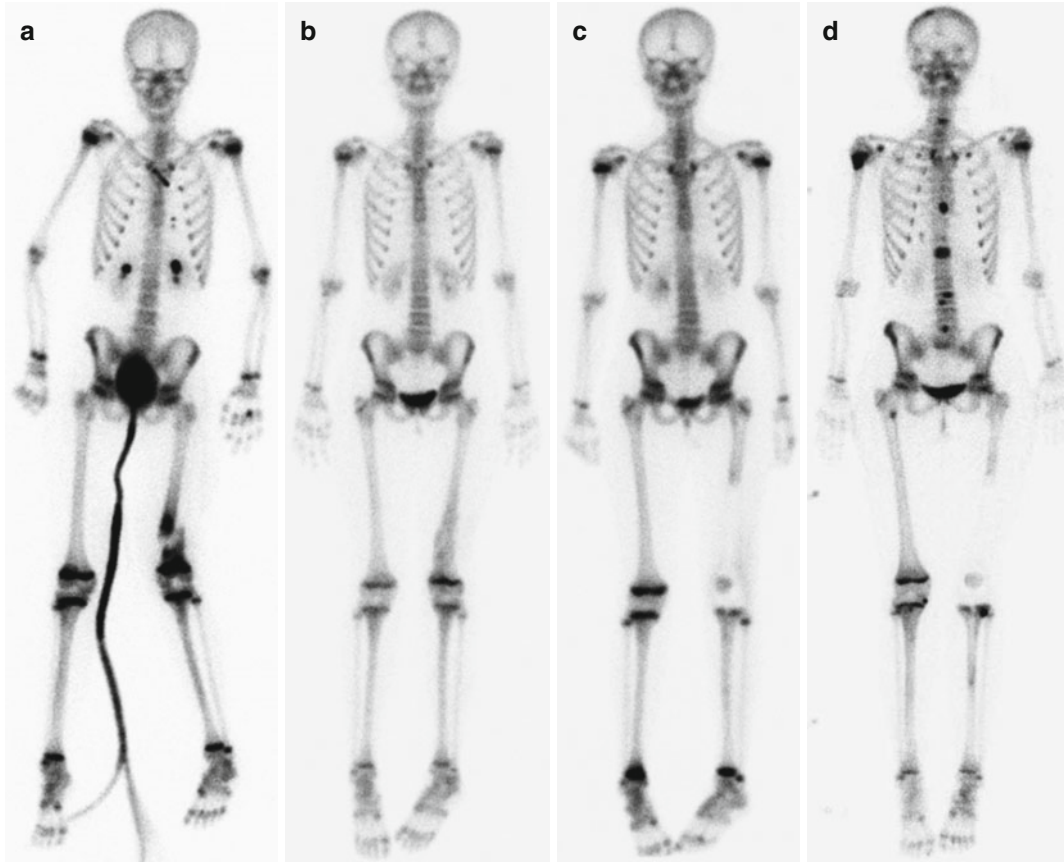

Fig. 22.2 Osteosarcoma presenting with a pathological fracture and complicated by bone metastases. An 11-year-old girl presented with a pathological fracture of the distal left femur and the diagnosis of osteosarcoma was made. ^{99m}Tc-MDP bone scans were used for staging and follow-up. (**a**) Staging bone scan shows intense uptake at the site of the fracture in the distal left femur, but no osseous metastases are identified. Note tracer accumulation in the bladder catheter and leg positioning related to immobilization of the fracture. (**b**) Ten weeks after surgical fixation of the fracture and administration of neoadjuvant chemotherapy, uptake is less intense, but there is increased bone turnover in the expansile lesion in the angulated distal left femur. (**c**) Follow-up bone scan 6 months after surgical resection of the tumor shows mildly increased cortical uptake around the intramedullary rods of the prosthesis in the proximal femur and proximal tibia. Prominent uptake in the patella is a typical finding after this reconstructive surgery. (**d**) A surveillance bone scan performed 6 months later shows widespread osseous metastatic disease involving the calvarium, inferior sternum, right scapula, multiple ribs, numerous vertebrae and the sacrum, left acetabulum, and proximal left tibia. Focal uptake in the lesser trochanter of the right femur and proximal right tibia may be additional sites of metastatic disease or may represent stress changes related to an altered gait

a whole-body bone scan using a ^{99m}Tc-labeled agent such as ^{99m}Tc-methylene diphosphonate (^{99m}Tc-MDP). More recently, some institutions have used ^{18}F-NaF PET [4]. Bone scan is sensitive and accurate for demonstrating the extent of local osteoblastic disease and for identifying metastatic bone disease (Fig. 22.2). Although ^{18}F-FDG PET can detect many osseous metastases [13], early studies demonstrated that planar bone scan with ^{99m}Tc-MDP could detect more sites of skeletal metastases than ^{18}F-FDG PET [14]. A few studies suggested that the combination of bone scan and ^{18}F-FDG PET is more accurate [15], but most multicenter studies suggest that bone scan is sufficient for the initial evaluation for skeletal metastases in patients with osteosarcoma. Some studies [16] have demonstrated the use of whole-body MRI for the initial evaluation

of osteosarcoma, but the performance of whole-body MRI has been no better than whole-body bone scan. Soft tissue metastases rarely occur in patients with osteosarcoma, and so there is little published information about identifying these sites of disease. However, osteoblastic soft tissue metastases are likely to be seen on bone scan (Fig. 22.3).

High-quality helical CT is the study of choice for identifying metastatic osteosarcoma in the lungs. Both ^{18}F-FDG PET and bone scan can detect lung metastases but have lower sensitivity for smaller metastatic lesions. Early studies comparing ^{18}F-FDG PET and single detector CT suggested the two studies had similar accuracy for detecting lung metastases [2, 17], but in later studies, spiral CT was shown to be much more sensitive than ^{18}F-FDG PET [18]. However, ^{18}F-FDG PET and helical CT have similar high levels of specificity for lung metastases [18].

Many research groups have studied the use of ^{18}F-FDG PET for the initial evaluation of osteosarcoma. FDG uptake (measured by SUV) is greater in osteosarcoma than in many other sarcomas [15] and may be related to tumor grade [2, 19]. Lower ^{18}F-FDG uptake is associated with improved survival [20], but predicting histological tumor grade has been hindered by the heterogeneous pattern of FDG uptake typical of osteosarcoma. Therefore, ^{18}F-FDG PET is not used routinely for the initial evaluation of pediatric and young adult patients with osteosarcoma.

Osteosarcoma Response to Therapy

Patients with osteosarcoma typically receive neoadjuvant chemotherapy before having local control surgery. A favorable histological response to chemotherapy, demonstrated by greater than 90 % tumor necrosis, is associated with a much lower rate of local recurrence compared to tumors with an unfavorable response to chemotherapy [17]. In addition to being a predictor of prognosis, the histological response to chemotherapy is used to guide both the surgical approach to local control [17] and the choice of subsequent chemotherapy [9]. Both bone scans and ^{18}F-FDG PET have been used for the preoperative evaluation of the histological response to chemotherapy, as this could guide the surgical approach to local control. Fluorine-18-FDG PET performs better than bone scan for this preoperative assessment [21], probably because of the slower response of bone scan to changes in the tumor in response to therapy. With ^{18}F-FDG PET, SUV_{max} can be a good predictor of the histological response to neoadjuvant chemotherapy [22, 23] but is less reliable at intermediate levels of FDG uptake [24]. Therefore, ^{18}F-FDG PET typically is not used to evaluate the response to chemotherapy before surgery.

Identifying Osteosarcoma Recurrence

The most appropriate imaging approach for identifying recurrence of osteosarcoma has not been determined. Because of the high rate of lung metastases, post-therapy imaging surveillance includes chest CT. MRI frequently is used to evaluate the primary site, but MR can be nonspecific and cannot detect metastatic recurrent disease outside the field of view of regional MRI [2], while both bone scan and ^{18}F-FDG PET provide an opportunity for whole-body imaging [25]. Based on the sensitivity of bone scan for osseous metastatic disease and the likelihood that large soft tissue and lung metastases also can be identified by bone scan, a whole-body bone scan usually is part of the follow-up imaging for osteosarcoma (Figs. 22.2 and 22.3). Evaluation for recurrent local disease can be particularly difficult when the primary site is at an amputation stump. MRI can be affected by artifacts caused by metallic implants, and some metallic prosthesis precludes the use of MRI for postoperative imaging. On bone scan, persistent uptake can occur for many years after surgery because of continued postsurgical bone remodeling and from stress changes due to weight-bearing (Fig. 22.4). Increased FDG uptake has been reported at an amputation stump for up to 18 months after surgery [26], also probably related to weight-bearing with the prosthesis [27]. Therefore, all imaging studies can be nonspecific

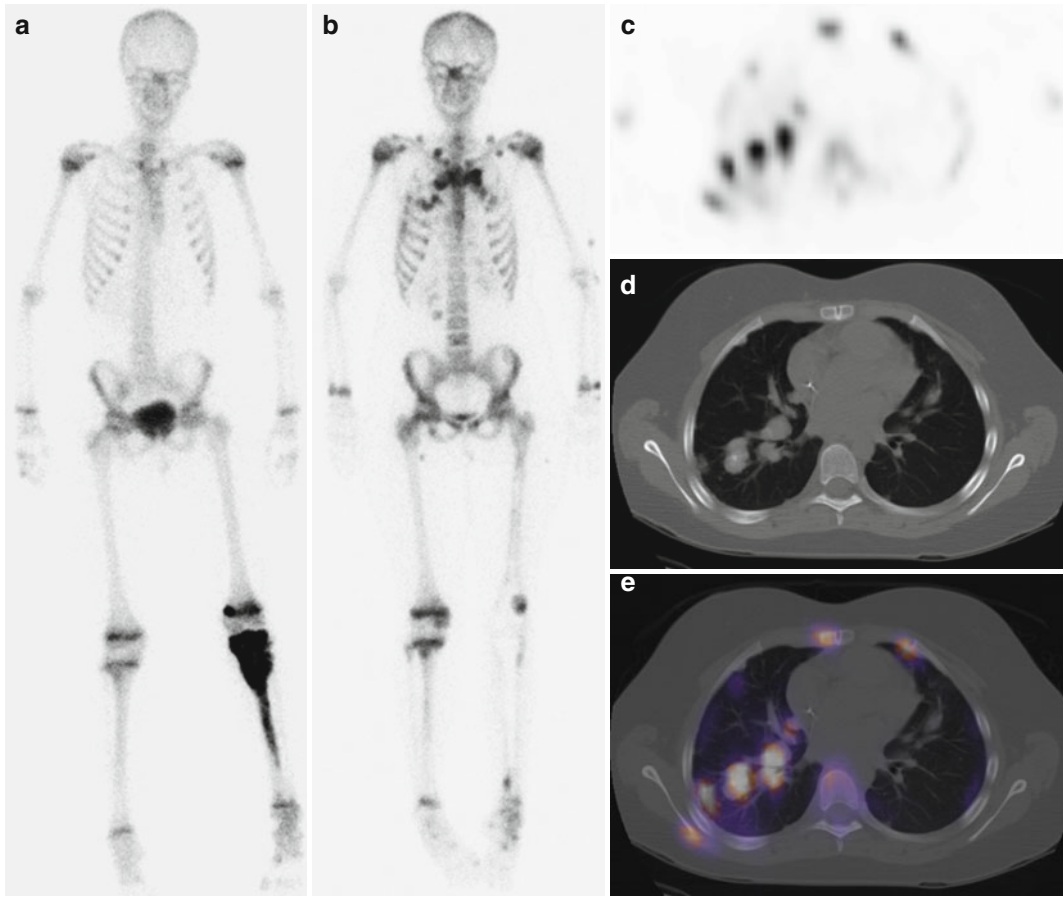

Fig. 22.3 Osteosarcoma complicated by widespread metastases demonstrates that bone scan and chest CT are complementary for finding metastases. A 14-year-old girl was diagnosed with osteosarcoma of the left tibia. (**a**) Initial ^{99m}Tc-MDP bone scan shows intense uptake in an expansile lesion of the proximal left tibia, but no metastases. (**b**) One year after chemotherapy and surgical resection with placement of a prosthesis, bone scan shows numerous sites of abnormal osseous and soft tissue uptake in the torso that are concerning for metastases. In the legs, increased cortical bone uptake adjacent to intramedullary rods in the left femur and tibia is an expected finding, but abnormal focal uptake in the distal left tibia and at multiple sites of the right leg may represent metastases or stress changes. (**c**) A single transaxial image from a SPECT bone scan demonstrates numerous sites of abnormal uptake within the chest cavity and ribs. (**d**) A single slice of a chest CT shows multiple pulmonary and pleural-based nodules. The CT also showed numerous enlarged mediastinal, hilar, and supraclavicular lymph nodes, but no skeletal abnormalities. (**e**) Co-registration of SPECT and CT images confirms abnormal uptake in pulmonary and pleural-based nodules, but skeletal metastases localized by bone scan are not identified on CT

and recurrent osteosarcoma should be diagnosed with caution. At the same time, recurrent disease can be obscured by nonspecific uptake. The most accurate approach for detecting local recurrence of osteosarcoma appears to be the complementary use of both local anatomic imaging, usually MRI, and whole-body functional imaging, usually bone scan.

Ewing Sarcoma

Clinical

Ewing sarcoma is the second most frequent bone tumor in children and young adults [28] and can occur anywhere in the body (Figs. 22.5 and 22.6). The Ewing family of sarcomas includes a

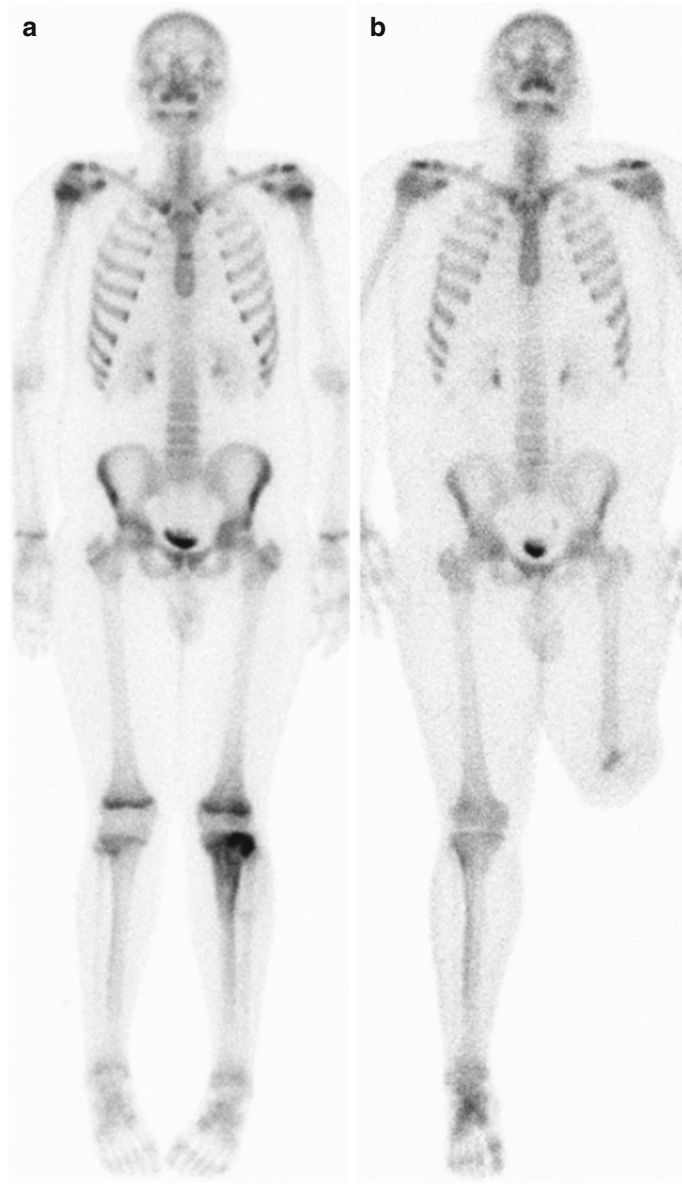

Fig. 22.4 Persistent bone turnover at the distal femur after above-the-knee amputation in a 16-year-old boy with osteosarcoma of the proximal left tibia. (**a**) Staging ^{99m}Tc-MDP bone scan shows intense uptake in the proximal tibia, including the proximal epiphysis adjacent to the knee joint space. (**b**) A follow-up bone scan obtained 5 years after an above-the-knee amputation shows persistent and stable uptake at the distal stump of the left femur. This is a stable pattern of increased bone turnover related to weight-bearing on a prosthesis and does not represent recurrent disease

histologically diverse group of tumors, including tumors of bone, soft tissue, and nerves, including primitive neuroectodermal tumors (PNET). Metastatic disease is common with these tumors. Approximately one-fourth of patients will have metastases at the time of diagnosis, and metastatic relapse will occur in a third of patients that had nonmetastatic disease at the time of diagnosis [29]. The most common sites for metastases are the lungs, bone, and bone marrow [30].

Patients with localized Ewing sarcoma that are treated with the combination of appropriate multi-agent chemotherapy and adequate local control have a 60–70 % chance of event-free survival [8]. Local control may be either radiation therapy or surgery, but inadequate local control is associated with treatment failure and poor outcome [31]. Long-term survival is only 40 % for patients with lung metastases and less than 20 % with bone or bone marrow metastases [4, 29, 32, 33].

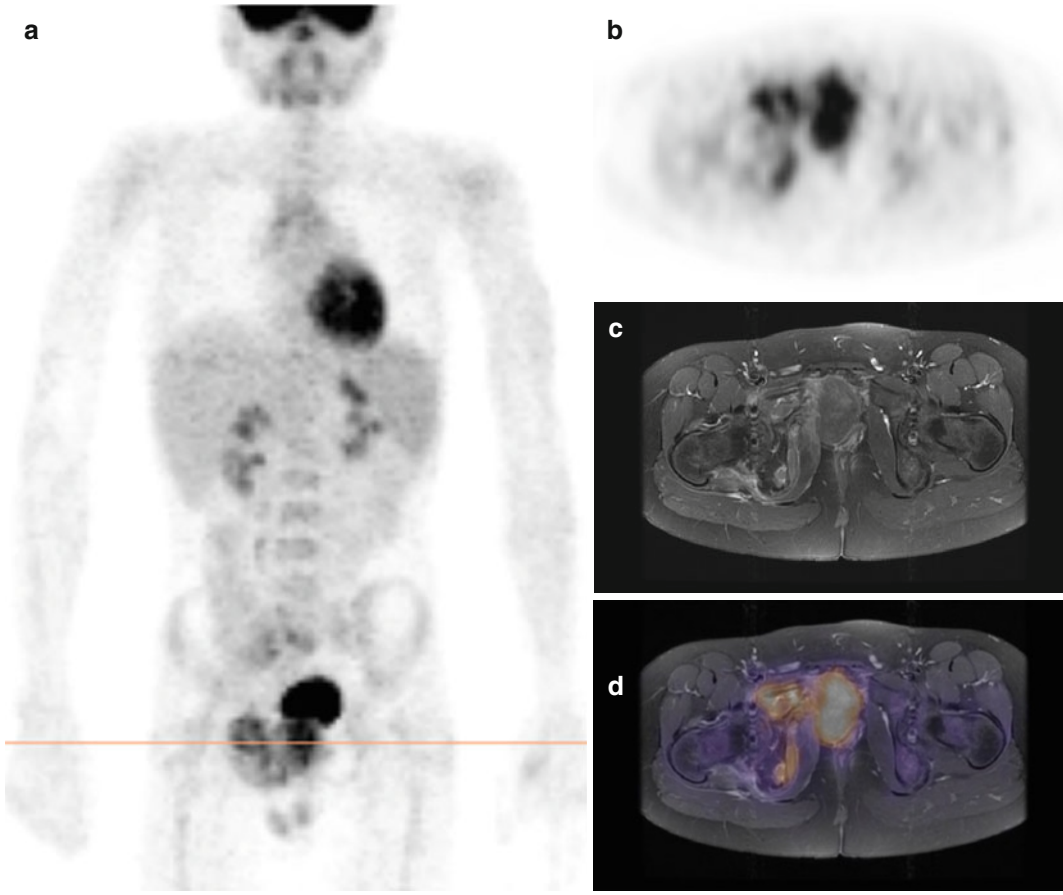

Fig. 22.5 ^{18}F-FDG PET and MRI demonstrate the extent of a Ewing sarcoma in an 11-year-old boy with hip pain. (**a**) The MIP of the ^{18}F-FDG PET shows an irregular pattern of abnormal uptake in the lower pelvis and upward displacement of the bladder. (**b**) In the transaxial plane, abnormal ^{18}F-FDG uptake is seen in the midline of the lower pelvis and in the expected locations of the right ischium and pubic ramus. (**c**) MRI shows a large heterogeneously enhancing pelvic mass. Abnormal enhancement also is seen in the pubic rectus muscle, in a soft tissue mass between the ischium and pubic rectus muscle, and in the right ischium and pubic ramus. (**d**) Co-registration of PET and MR images demonstrates FDG-avid disease in the large pelvic mass, right ischium and pubic ramus, and the soft tissue mass adjacent to the pubic rectus muscle, but not in the pubic rectus muscle

Diagnosis and Staging Ewing Sarcomas

Ewing sarcoma tumors usually are first identified during evaluation of presenting symptoms such as pain or mass. Initial evaluation usually includes radiography or MRI. Fluorine-18-FDG PET is no better than conventional imaging for evaluation of the primary site [15] and FDG avidity does not predict prognosis [34]. MRI typically is used to assess the extent of local disease. As with most tumors, identification of all sites of disease, including localization of metastases, is important for staging, but is particularly important in patients with Ewing sarcoma, as all sites of disease will receive local control therapy [28].

Whole-body imaging has a role for identifying both osseous and non-osseous distant sites of disease. Evaluation can include bone scan and bone marrow aspiration. Bone scan may have lower sensitivity for some sites of disease, as Ewing sarcoma typically involves bone marrow and can be osteolytic [21]. Whole-body imaging typically relies on ^{18}F-FDG PET, although some efforts have been made to use whole-body MRI. However, as these imaging methods have low

sensitivity for small lung metastases [18], a high-quality chest CT remains necessary for identifying lung metastases. For identification of distant skeletal disease, both MRI and ^{18}F-FDG PET are more sensitive than bone scan [21, 28, 35] and ^{18}F-FDG PET is more sensitive than whole-body MRI, particularly for detecting metastatic disease in the ribs [16], growth plates, and bone marrow [36]. However, most comparative studies compare ^{18}F-FDG PET to ^{99m}Tc-MDP planar bone scans, which may not be as sensitive as ^{99m}Tc-MDP SPECT or ^{18}F-NaF PET [4]. Reports of bone lesions seen on ^{99m}Tc-MDP bone scan that are not identified by either MRI or ^{18}F-FDG PET [37, 38] indicate that the most appropriate approach for the initial imaging of Ewing sarcoma may require both bone scan and ^{18}F-FDG PET (Fig. 22.6).

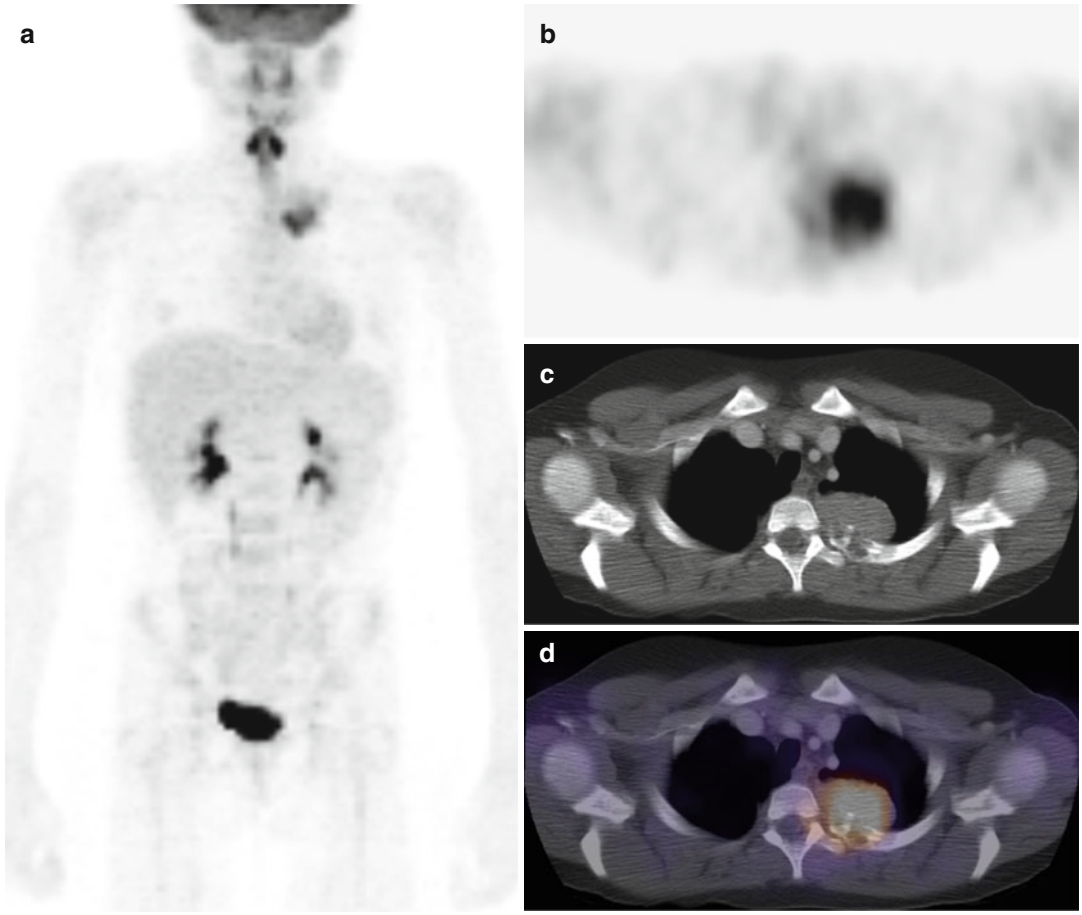

Fig. 22.6 Fluorine-18-FDG PET, bone scan, and contrast-enhanced CT for the evaluation of Ewing sarcoma of the chest in a 13-year-old girl with back pain. (**a**) The MIP of the ^{18}F-FDG PET demonstrates heterogeneous uptake in the upper left back, corresponding to the site of pain. No other sites of abnormal ^{18}F-FDG uptake are identified. (**b**) In the transaxial plane, abnormal ^{18}F-FDG uptake is seen in the posterior left chest. (**c**) A diagnostic CT shows a heterogeneously enhancing paravertebral mass that involves the left third rib and extends into the chest cavity and the spinal canal. (**d**) Co-registration of PET and CT images confirms that the chest wall mass is FDG-avid, consistent with Ewing sarcoma. (**e**) Whole-body ^{99m}Tc-MDP bone scan in anterior and posterior projections shows two foci of increased uptake along the posterior left third rib. No other osseous lesions are identified. (**f**) SPECT bone scan confirms focal uptake in the posterior left third rib. (**g**) CT shows a complex expansile and lytic lesion in the posterior left third rib that extends into the chest cavity and spinal canal. (**h**) Co-registration of SPECT and CT images demonstrates increased bone turnover in cortical bone adjacent to the destructive soft tissue mass in the posterior third rib

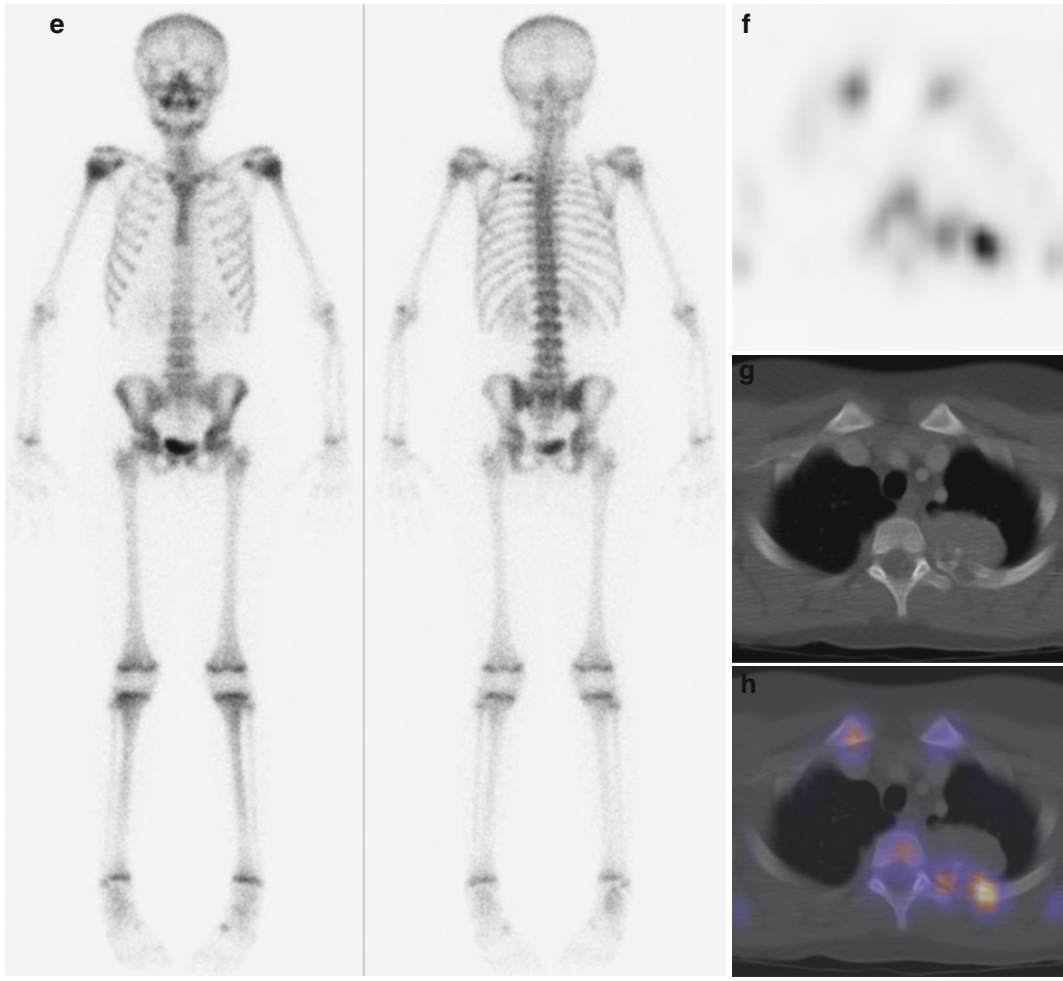

Fig. 22.6 (continued)

Response to Therapy of Ewing Sarcoma

For Ewing sarcoma, accurately assessing the response to therapy may require multimodality imaging. MRI alone may not detect minimal residual disease and may not always distinguish residual tumor from necrotic tissue. The addition of ^{18}F-FDG PET can identify sites of minimal disease and help better assess the metabolic response to therapy [21]. The European Organization for Research and Treatment of Cancer (EORTC) attempted to establish a standardized approach to assessing tumor response to therapy, but this approach has not been widely implemented [39]. Some studies [1, 33, 40] have suggested that ^{18}F-FDG PET can predict the histological response to preoperative neoadjuvant chemotherapy. Hybrid ^{18}F-FDG PET/CT may improve the accuracy of ^{18}F-FDG PET, with fewer equivocal lesions and better localization of disease [41].

Imaging Recurrence of Ewing Sarcoma

In patients with Ewing sarcoma, recurrent local disease typically is identified by MRI of known sites of disease. Chest CT remains most appropriate for detecting recurrent lung disease [2, 18], but

little has been published regarding the relative utility of different imaging studies for detecting recurrent distant disease. Both bone scan and ^{18}F-FDG PET/CT may be helpful, but care must be taken to perform whole-body imaging to avoid missing disease in the skull or lower extremities [37, 38].

Rhabdomyosarcoma

Clinical

Rhabdomyosarcoma is the most common soft tissue malignancy in children and young adults [42]. There are many different histological subtypes of rhabdomyosarcoma. More than 70 % of pediatric cases are the embryonal subtype and about 20 % are the alveolar subtype. In children with rhabdomyosarcoma, the most common primary site is in the head, skull, or neck (Fig. 22.7). The next most common primary site is the bladder or prostate (Fig. 22.8). Rarely, rhabdomyosarcoma may present as disseminated disease with an unknown primary site [43]. Regional lymph nodes are the most common site of metastatic disease, which is associated with poorer overall survival [44]. Rhabdomyosarcoma therapy includes both multiagent chemotherapy and local control, which may be either surgery or radiation therapy [45]. Inadequate local control is associated with local treatment failure and poor outcome [46, 47].

FDG PET of Rhabdomyosarcoma

Whole-body imaging with ^{18}F-FDG PET has two important roles in the initial evaluation and staging of rhabdomyosarcoma. Fluorine-18-FDG PET can demonstrate regional adenopathy that is not identified on conventional imaging and thus provide earlier identification of metastatic lymph node disease [15, 40]. Fluorine-18-FDG PET also can be helpful for excluding metabolically active disease at sites of ambiguous findings on conventional imaging [48, 49]. Fluorine-18-FDG PET may be limited in evaluating lymph nodes in close proximity to an FDG-avid primary tumor or adjacent to other sites of FDG accumulation, such as the bladder [48]. Fluorine-18-FDG PET also can identify widespread bone marrow involvement (Fig. 22.8) by rhabdomyosarcoma [49, 50]. Some patients with rhabdomyosarcoma (approximately 4 % of cases) present with widespread disseminated disease with an unknown primary. In these cases, the wide field of view and high sensitivity of ^{18}F-FDG PET/CT can help identify the primary site of disease. Identifying and localizing metastatic disease can guide decisions about the need and surgical approach for local control and also may prompt intensified chemotherapy. Fluorine-18-FDG PET/CT also can have a role in detecting local recurrence or distant metastatic rhabdomyosarcoma [37].

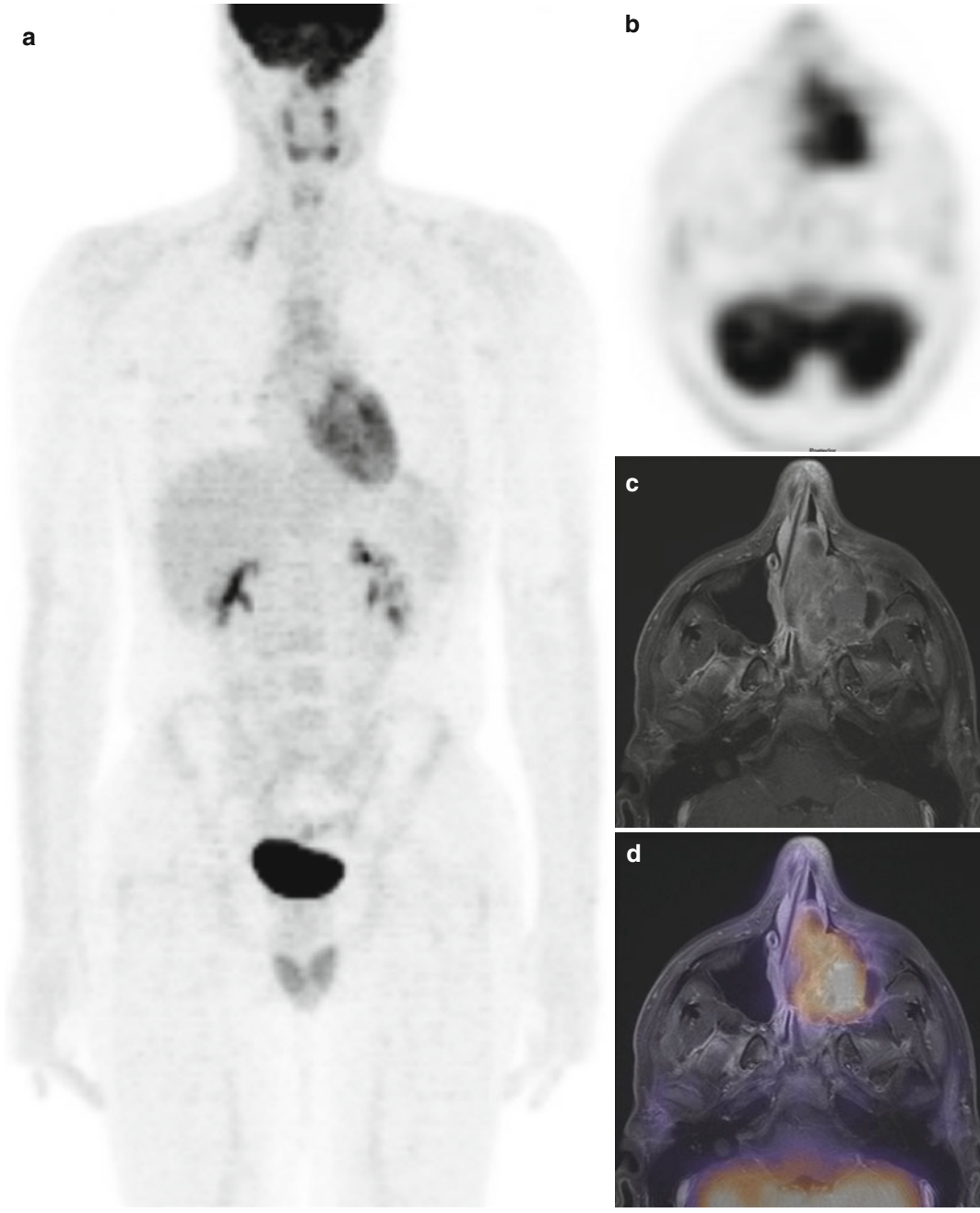

Fig. 22.7 ^{18}F-FDG PET and MRI of a sinonasal alveolar rhabdomyosarcoma in a 14-year-old boy. (**a**) The MIP of the ^{18}F-FDG PET shows a region of intense uptake at the base of the skull. No other sites of abnormal ^{18}F-FDG uptake are identified. (**b**) In the transaxial plane, the abnormal ^{18}F-FDG uptake appears to be in the expected location of the nasal cavity and left sinuses. (**c**) An axial slice of a sinus MRI demonstrates a heterogeneously enhancing soft tissue mass in the nasal cavity and left maxillary sinus. The MRI also demonstrated tumor extension into the frontal and ethmoid sinuses and into the anterior cranial fossa. (**d**) Co-registration of PET and MR images confirms intense FDG avidity of this parameningeal sinonasal alveolar rhabdomyosarcoma

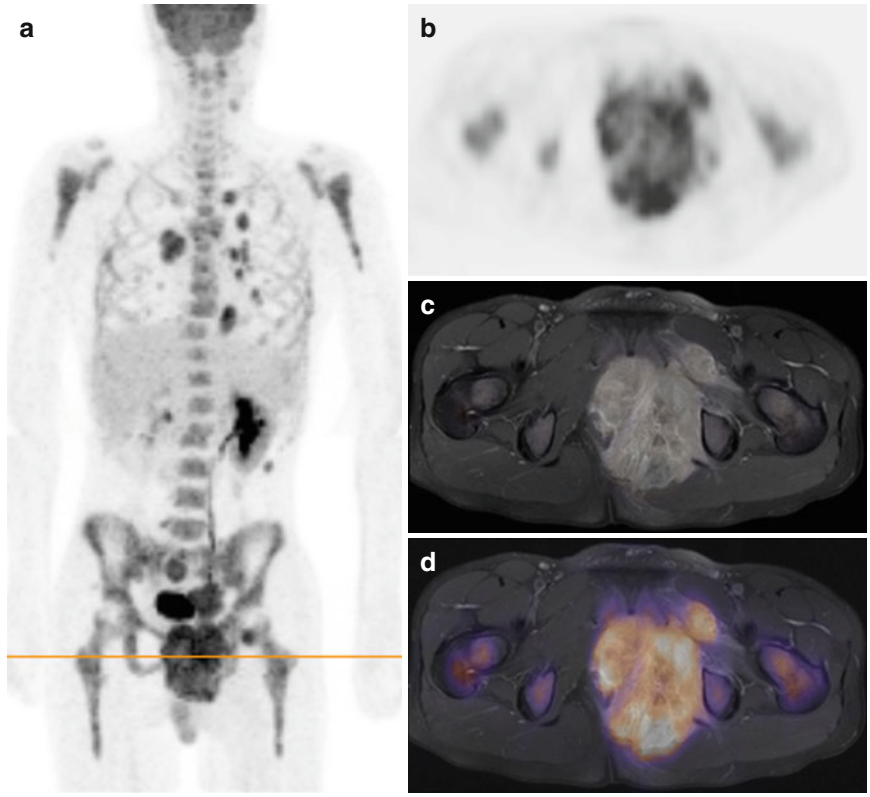

Fig. 22.8 ^{18}F-FDG PET and MRI of a pelvic rhabdomyosarcoma with lung and bone marrow metastases. A 16-year-old boy presented with a gluteal mass and radicular pain in the left leg and was diagnosed with alveolar rhabdomyosarcoma. (**a**) The MIP of the ^{18}F-FDG PET shows a large heterogeneous, lobated mass in the lower left pelvis, multiple sites of abnormal uptake in the lungs, and increased uptake throughout expected locations of bone marrow. (**b**) In the transaxial plane, a heterogeneous pattern of ^{18}F-FDG uptake is seen in the pelvic mass. Increased uptake also is seen in the bones of the pelvis and proximal femurs. (**c**) A pelvic MRI shows a large heterogeneously enhancing mass in the lower pelvis that extends through the left obturator foramen. Abnormal marrow signal suggests infiltrative bone marrow disease. (**d**) Co-registration of PET and MRI images demonstrates that the large pelvic mass is FDG-avid and confirms diffuse bone marrow involvement with FDG-avid rhabdomyosarcoma

References

1. Hawkins DS, Rajendran JG, Conrad III EU, Bruckner JD, Eary JF. Evaluation of chemotherapy response in pediatric bone sarcomas by [F-18]-fluorodeoxy-D-glucose positron emission tomography. Cancer. 2002;94:3277–84.
2. Lucas JD, O'Doherty MJ, Cronin BF, et al. Prospective evaluation of soft tissue masses and sarcomas using fluorodeoxyglucose positron emission tomography. Br J Surg. 1999;86:550–6.
3. Schuetze SM, Rubin BP, Vernon C, et al. Use of positron emission tomography in localized extremity soft tissue sarcoma treated with neoadjuvant chemotherapy. Cancer. 2005;103:339–48.
4. Grant FD, Fahey FH, Packard AB, et al. Skeletal PET with ^{18}F-fluoride: applying new technology to an old tracer. J Nucl Med. 2008;49:68–78.
5. Aoki J, Watanabe H, Shinozaki T, et al. FDG PET of primary benign and malignant bone tumors: standardized uptake value in 52 lesions. Radiology. 2001;219:774–7.
6. Bischoff M, Bischoff G, Buck A, et al. Integrated FDG-PET-CT: its role in the assessment of bone and soft tissue tumors. Arch Orthop Trauma Surg. 2009;130:819–27.
7. Gurney JG, Swensen AR, Bulterys M. Malignant bone tumors. In: Ries LA, Smith MA, Gurney JG, et al., editors. Cancer incidence and survival among children and adolescents: United States SEER Program 1975–1995. Bethesda: National Cancer Institute, SEER Program. NIH Pub. No. 99–4649; 1999.
8. Grier HE, Krailo MD, Tarbell NJ, et al. Addition of ifosfamide and etoposide to standard chemotherapy for Ewing's sarcoma and primitive neuroectodermal tumor of bone. N Engl J Med. 2003;348:694–701.

9. Brenner W, Bohuslavizki KH, Eary JF. PET imaging of osteosarcoma. J Nucl Med. 2003;44:930–42.
10. Weeden S, Grimer RJ, Cannon SR, Taminiau AHM, Uscinska BM, on behalf of the European Osteosarcoma Group. The effect of local recurrence on survival in resected osteosarcoma. Eur J Cancer. 2001;37:39–46.
11. Marina N, Gebhardt M, Teot L, Gorlick R. Biology and therapeutic advances for pediatric osteosarcoma. Oncologist. 2004;9:422–41.
12. Enneking WF. A system of staging musculoskeletal neoplasms. Clin Orthop Relat Res. 1986;204:9–24.
13. Wuisman P, Enneking WF. Prognosis for patients who have osteosarcoma with skip metastases. J Bone Joint Surg Am. 1990;72:60–8.
14. Franzius C, Sciuk J, Daldrup-Link HE, Jurgens H, Schober O. FDG-PET for detection of osseous metastases from malignant primary bone tumours: comparison with bone scintigraphy. Eur J Nucl Med. 2000;27:1305–11.
15. Völker T, Denecke T, Steffen I, et al. Positron emission tomography for staging of pediatric sarcoma patients: results of a prospective multicenter trial. J Clin Oncol. 2007;25:5435–41.
16. Daldrup-Link HE, Franzius C, Link TM, et al. Whole-body MR imaging for detection of bone metastases in children and young adults: comparison with skeletal scintigraphy and FDG PET. Am J Roentgenol. 2001;177:229–36.
17. Schulte M, Brecht-Krauss D, Werner M, et al. Evaluation of neoadjuvant therapy response of osteogenic sarcoma using FDG PET. J Nucl Med. 1999;40:1637–43.
18. Franzius C, Daldrup-Link HE, Sciuk J, et al. FDG-PET for detection of pulmonary metastases from malignant primary bone tumors: comparison with spiral CT. Ann Oncol. 2001;12:479–86.
19. Eary JF, Conrad EU, Bruckner JD, et al. Quantitative [F-18] fluorodeoxyglucose positron emission tomography in pretreatment and grading of sarcoma. Clin Cancer Res. 1998;4:1215–20.
20. Franzius C, Bielack S, Flege S, Sciuk J, Jurgens H, Schober O. Prognostic significance of ^{18}F-FDG and ^{99m}Tc-methylene diphosphonate uptake in primary osteosarcoma. J Nucl Med. 2002;43:1012–7.
21. Franzius C, Sciuk J, Brinkschmidt C, Jurgens H, Schober O. Evaluation of chemotherapy response in primary bone tumor with F-18 FDG positron emission tomography compared with histologically assessed tumor necrosis. Clin Nucl Med. 2000;25:874–81.
22. Hawkins DS, Conrad III EU, Butrynski JE, Schuetze SM, Eary JF. [F-18]-Fluorodeoxy-D-glucose positron emission tomography response is associated with outcome for extremity osteosarcoma in children and young adults. Cancer. 2009;115:3519–25.
23. Hamada K, Tomita Y, Inoue A, et al. Evaluation of chemotherapy response in osteosarcoma with FDG-PET. Ann Nucl Med. 2009;23:89095.
24. Cheon GJ, Kim MS, Lee JA, et al. Prediction model of chemotherapy response in osteosarcoma by ^{18}F-FDG PET and MRI. J Nucl Med. 2009;50:1435–40.
25. Franzius C, Daldrup-Link HE, Wagner-Bohn A, et al. FDG-PET for detection of recurrences from malignant primary bone tumors: comparison with conventional imaging. Ann Oncol. 2002;13:157–60.
26. Jadvar H, Gamie S, Ramanna L, Conti PS. Musculoskeletal system. Semin Nucl Med. 2004;34:254–61.
27. Hain SF, O'Doherty MJ, Lucas JD, Smith MA. Fluorodeoxyglucose PET in the evaluation of stumps following amputation for soft tissue sarcoma. Nucl Med Commun. 1999;20:845–8.
28. Furth C, Amthauer H, Denecke T, Ruf J, Henze G, Gutberlet M. Impact of whole-body MRI and FDG-PET on staging and assessment of therapy response in a patient with Ewing sarcoma. Pediatr Blood Cancer. 2006;47:607–11.
29. Paulussen M, Ahrens S, Dunst J, et al. Localized Ewing tumor of the bone: final results of the cooperative Ewing's sarcoma study CESS 86. J Clin Oncol. 2001;19:1818–29.
30. Marec-Bérard P, Philip T. Ewing sarcoma: the pediatrician's point of view. Pediatr Blood Cancer. 2004;42:477–80.
31. Krasin MJ, Rodriguez-Galindo C, Billups CA, et al. Definitive irradiation in multidisciplinary management of localized Ewing sarcoma family of tumors in pediatric patients: outcome and prognostic factors. Int J Radiat Oncol Biol Phys. 2004;60:830–8.
32. Cotterill SJ, Ahrens S, Paulussen M, et al. Prognostic factors in Ewing's tumor of bone: analysis of 975 patients from the European Intergroup CEwing's Sarcoma Study Group. J Clin Oncol. 2000;18:3108–14.
33. Barker LM, Pendergrass TW, Sanders JE, Hawkins DS. Survival after recurrence of Ewing's sarcoma family of tumors. J Clin Oncol. 2005;23:4354–62.
34. Hawkins DS, Schuetze SM, Butrynski JE, et al. [^{18}F] Fluorodeoxyglucose positron emission tomography predicts outcome for Ewing sarcoma family of tumors. J Clin Oncol. 2005;23:8828–34.
35. Mazumdar A, Siegel MJ, Narra V, Luchtman-Jones L. Whole-body fast inversion recovery MR imaging of small cell neoplasms in pediatric patients: a pilot study. Am J Roentgenol. 2002;179:1261–6.
36. Mentzel H-J, Kentouche K, Sauner C, et al. Comparison of whole-body STIR-MRI and ^{99m}Tc-methylene-diphosphonate scintigraphy in children with suspected multifocal bone lesions. Eur Radiol. 2004;14:2297–302.
37. Arush WM, Israel O, Postovksy S, et al. Positron emission tomography/computed tomography with 18Fluor-deoxyglucose in the detection of local recurrence and distant metastases of pediatric sarcoma. Pediatr Blood Cancer. 2007;49:901–5.
38. DeLonga D, Baker A, Treves ST, Grant FD. Utility of bone scintigraphy as an adjunct to FDG-PET in the initial evaluation of Ewing's sarcoma. Annual meeting of the Society of Nuclear Medicine, Salt Lake City. 2010. Abstract 1650.
39. Young H, Baum R, Cremerius U, et al. Measurement of clinical and subclinical tumour response using [^{18}F]-fluorodeoxyglucose and positron emission

tomography: review and 1999 EORTC recommendations. Eur J Cancer. 1999;35:1773–82.
40. McCarville MB, Christie R, Daw NJ, Spunt SL, Kaste SC. PET/CT in the evaluation of childhood sarcomas. Am J Roentgenol. 2005;184:1293–304.
41. Gerth HU, Juergens KU, Dirksen U, Gerss J, Schober O, Franzius C. Significant benefit of multimodal imaging: PET/CT compared with PEt alone in staging and follow-up of patients with Ewing tumors. J Nucl Med. 2007;48:1932–9.
42. Raney RB, Anderson JR, Barr FG, et al. Rhabdomyosarcoma and undifferentiated sarcoma in the first two decades of life: a selective review of Intergroup Rhabdomyosarcoma Study group experience and rationale for Intergroup Rhabdomyosarcoma Study V. J Pediatr Hematol Oncol. 2001;23:215–20.
43. Etcubanas E, Peiper S, Stass S, Green A. Rhabdomyosarcoma presenting as disseminated malignancy from an unknown primary site: a retrospective study of ten pediatric cases. Med Pediatr Oncol. 1989;17:39–44.
44. LaQuaglia MP. Extremity rhabdomyosarcoma : biological principals, staging, and treatment. Semin Surg Oncol. 1993;9:510–9.
45. Baker KS, Anderson JR, Link H, et al. Benefit of intensified therapy for patients with local or regional embryonal rhabdomyosarcoma: results from the Intergroup Rhabdomyosarcoma Study IV. J Clin Oncol. 2000;18:2427–34.
46. Wharam MD, Meza J, Anderson J, et al. Failure pattern and factors predictive of local failure in rhabdomyosarcoma: a report of group III patients on the third Intergroup Rhabdomyosarcoma Study. J Clin Oncol. 2004;22:1902–8.
47. Flamant F, Rodary C, Rey A, et al. Treatment of nonmetastatic rhabdomyosarcomas in childhood and adolescence. Results of the second study of the international society of paediatric oncology: MMT84. Eur J Cancer. 1998;34:1050–62.
48. Klem ML, Grewal RK, Wexler LH, Schoder H, Meyers PA, Wolden SL. PET for staging in rhabdomyosarcoma: an evaluation of PET as an adjunct to current staging tools. J Pediatr Hematol Oncol. 2007;29:9–14.
49. Tateishi U, Hosono A, Makimoto A, et al. Comparative study of FDG PET/CT and conventional imaging in the staging of rhabdomyosarcoma. Ann Nucl Med. 2009;23:155–61.
50. Seshadri N, Wright P, Balan KK. Rhabdomyosarcoma with widespread bone marrow infiltration: beneficial management role for F-18 FDG PET. Clin Nucl Med. 2007;32:787–9.

Solid Tumors in Childhood

23

Robert Howman-Giles, Kevin London,
and Roger F. Uren

This chapter examines the role of nuclear medicine in solid tumors in childhood and adolescence excluding the common malignancies that are discussed in other chapters. In this wide group of malignancies the main nuclear medicine procedures found to be most useful are total body bone scintigraphy and ^{18}F-fluorodeoxyglucose (^{18}F-FDG) PET/CT imaging [1–3]. These investigations are used at initial staging, in assessment of response to therapy, and in detection of residual, recurrent, and metastatic malignant disease [2–4].

R. Howman-Giles, MB BS, MD, FRACP, FAANMS, DDU (✉)
Discipline of Imaging and Discipline of Paediatrics and Child Health, Faculty of Medicine, University of Sydney, Sydney, Australia

Department of Nuclear Medicine, The Children's Hospital at Westmead, Sydney, Australia
e-mail: r.howmangiles@sydney.edu.au

K. London, BHB, DipSci, MBChB, DCH, MM(Clin Epi), FRACP
Discipline of Paediatrics and Child Health, Faculty of Medicine, University of Sydney, Sydney, Australia

Department of Nuclear Medicine, The Children's Hospital at Westmead, Sydney, Australia
e-mail: kevin.london@health.nsw.gov.au

R.F. Uren, MBBS, MD, FRACP, DDU
Discipline of Medicine, University of Sydney, Sydney, Australia

Department of Nuclear Medicine and Diagnostic Ultrasound, Royal Prince Alfred Hospital Medical Centre, Sydney, Australia
e-mail: ruren@usyd.edu.au

MRI and contrast CT are the recommended anatomical imaging modalities for evaluation of primary tumors, and pulmonary CT is the recommended investigation for pulmonary metastases [2, 5, 6]. Wilms' tumor and many types of sarcomas usually first metastasize to the lungs, but some of the sarcoma group will initially metastasize locally to regional lymph node basins [7–9]. In these latter malignancies, lymphoscintigraphy and sentinel lymph node biopsy also are recommended [10–12]. There is good evidence that ^{18}F-FDG PET imaging is superior to conventional imaging for the diagnosis of metastatic disease in many common pediatric and adolescent malignancies [2, 4, 5, 13, 14]. Fluorine-18-FDG PET has been shown to accurately predict overall survival and progression-free survival in many tumors [8, 13, 15]. As FDG uptake relates to the metabolic activity of tumor cells, ^{18}F-FDG PET used for staging, response to therapy, and detection of residual and recurrent and metastatic disease can be applied to the uncommon and rare forms of solid tumors as the level of metabolic activity generally relates to the aggressiveness of the particular tumor.

Tumors of Early Childhood

Wilms' Tumor

Wilms' tumor is a malignant embryonal tumor originating from kidney progenitor cells and makes up 95 % of renal cancer in children. It is the fourth most common childhood cancer. Ninety-

S.T. Treves (ed.), *Pediatric Nuclear Medicine and Molecular Imaging*,
DOI 10.1007/978-1-4614-9551-2_23, © Springer Science+Business Media New York 2014

five percent of cases are unilateral and bilateral disease presents at an earlier age [16, 17]. Wilms' tumor has been associated with genetic mutations, as well as other congenital syndromes of the urinary tract, such as WAGR syndrome and Denys-Drash syndrome. Familial germ line mutations are rare, occurring in less than 2 % of all Wilms' tumor cases [18, 19]. Most Wilms' tumors contain a mixture of blastemal, stromal, and epithelial cell components in varying proportions. Up to 10 % will demonstrate anaplasia, which is associated with a poorer prognosis [20]. Current treatment results in 90 % overall survival for children with WT. Treatment of WT is based on histopathology (favorable vs anaplastic histology) and the stage of the disease. Staging is based on surgical and imaging findings. The primary goals of surgery are nephrectomy, resection of involved lymph nodes, and avoidance of tumor spillage. Adjuvant chemotherapy and radiation therapy depend on the extent of the disease [21, 22]. Imaging studies at initial staging include CT, MRI, or ultrasound to determine the size and location of the primary tumor, involvement of locoregional lymph nodes, and vascular invasion. Bone scan is used if there is suspicion of skeletal metastases; however, skeletal metastases in WT are rare. The use of ^{18}F-FDG PET has been described in WT, but its main application has been in cases with recurrent or metastatic disease. Misch et al. [23] concluded that PET did not provide additional information to the traditional workup for staging WT, preoperative response assessment, and clinical outcome. They found PET was advantageous in ruling out residual disease after completion of first-line treatment and in pre-therapeutic staging of relapse patients. There was also a good correlation of SUVmax and histological differentiation. Begent et al. [24] showed that PET/CT findings following initial chemotherapy correlated with histologically confirmed viable tumor, presence of lung metastases, and areas of anaplasia. More recently, Hossain et al. [21] showed avid FDG uptake in 27 children, the majority with recurrent disease. PET was able to visualize bone, extra-abdominal lymph nodes, and chest wall and pancreatic metastases. Small pulmonary and hepatic metastases were better delineated on CT and MRI. The authors suggested that ^{18}F-FDG PET would be useful in the initial diagnostic workup, evaluation for recurrent disease, and as a monitor of chemotherapy response [21] (Fig. 23.1).

Non-Wilms' Renal Tumors

Non-Wilms' renal tumors in children are rare. They are a heterogeneous group of tumors that share many features on light microscopy, but molecular genetic profiling allows a more accurate diagnosis and classification. They comprise approximately 10 % of pediatric renal cancers. These tumors include mesoblastic nephroma, renal cell carcinoma, clear-cell sarcoma of the kidney, malignant rhabdoid tumor of the kidney, and renal medullary carcinoma [25]. As with Wilms' tumor, the initial imaging for staging is with ultrasound, CT, and/or MRI and bone scan to exclude bone metastases.

Mesoblastic nephroma accounts for 3–10 % of all childhood renal tumors, but in infants, is the most common and accounts for up to two-thirds of renal tumors in the first 3 months of life. Mesoblastic nephroma has a low propensity for metastasis. Nuclear medicine procedures do not usually have a role in MN. Renal cell carcinoma and clear cell sarcoma of the kidney are aggressive malignant tumors and may metastasize early. Metastases can be to the bone, brain, liver, lymph nodes, and lungs. Imaging with nuclear medicine techniques is primarily bone scan for detection of skeletal metastases. Fluorine-18-FDG PET also may have a role in management of renal cell carcinomaa. Krajewski et al. reported utility for ^{18}F-FDG PET in the diagnosis of recurrence and distant metastases in renal cell carcinoma [26]. The use of ^{18}F-FDG PET in clear cell sarcoma of the kidney has not been reported. Malignant rhabdoid tumors of the kidney are rare, and account for less than 2 % of renal malignancies in childhood. These tumors originally were thought to be an unfavorable histological subtype of WT, but now are considered a separate pathological entity [25, 27]. This very aggressive renal tumor can metastasize early with 80 % of patients having metastases involving the lungs, liver, and brain at diagnosis [28]. Concurrent malignant rhabdoid tumors of the brain may occur and are probably synchronous tumors

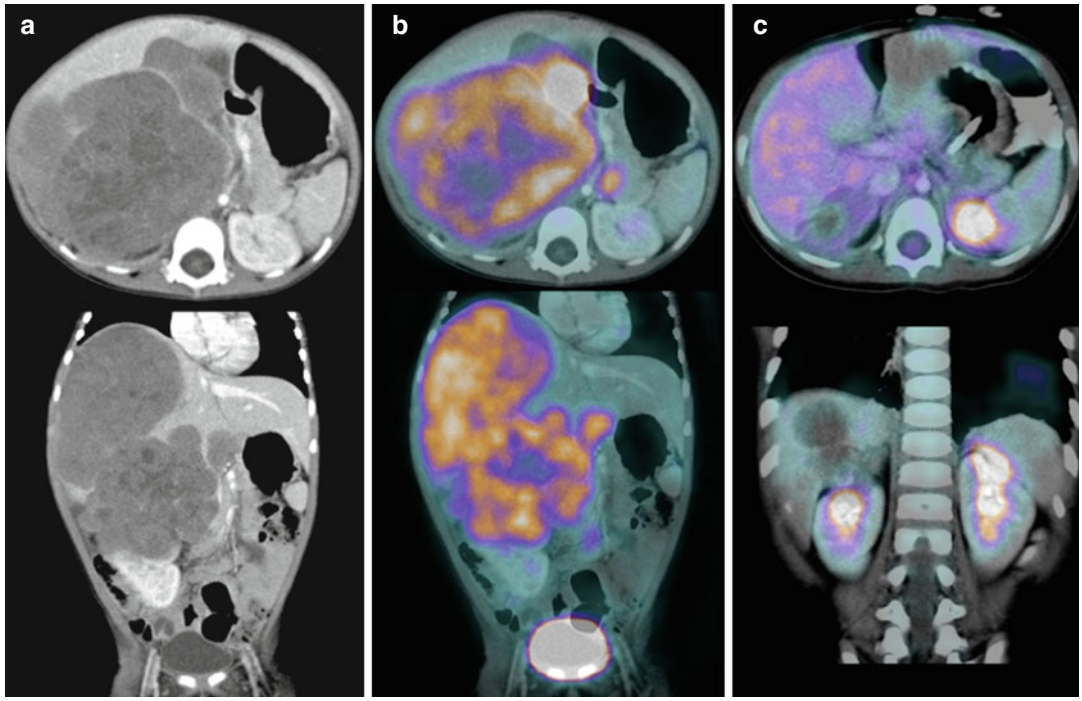

Fig. 23.1 Wilms' tumor in a 20-month-old female who presented with a large right-sided abdominal mass. Fluorine-18-FDG PET/CT scan at initial staging (**a**, **b**: *top* axial; *lower* coronal) shows a large mass arising from the right kidney with central necrosis and multiple metastases in the liver and para-aortic nodes. After chemotherapy (**c**) there is a very good response with marked shrinkage of the primary tumor and metastatic deposits. The ^{18}F-FDG PET confirmed complete response, and a surgery no viable tumor was found

rather than metastases [28, 29]. Fluorine-18-FDG PET has been shown to be useful in the identification of both recurrent metastatic renal rhabdoid tumors [30] and extrarenal rhabdoid tumors [31].

Hepatoblastoma and Hepatocellular Carcinoma

Hepatoblastoma is a rare but highly malignant embryonal liver tumor that occurs in infants and younger children. It arises from stem cells or early progenitor cells of epithelial components of the liver [32]. Hepatoblastoma is associated with an elevated serum alpha fetoprotein (AFP) in more than 90 % of patients. Surgical resection in conjunction with chemotherapy is the primary therapy, but tumors often cannot be fully resected. Imaging is predominantly US, CT, and MRI to assess the extent and vascular involvement of the primary tumor and to detect pulmonary metastases and lymph node status. Fluorine-18-FDG PET scans have been shown to be positive in 90 % of pediatric patients. Mody et al. reported that ^{18}F-FDG PET imaging was in accord with CT/MRI results, AFP levels, and postoperative findings [32, 33]. Fluorine-18-FDG PET may be useful in localizing sites of recurrence when conventional imaging has been unsuccessful. Philip et al. found if the AFP level is <1,000 U/ml, tumor size is likely to be less than 1 cc. Conventional imaging seldom detects these small sites of recurrence, particularly when the regional anatomy has been altered by previous surgery [34, 35]. Fluorine-18-FDG PET/CT also may be useful in conjunction with CT and MRI for determining appropriate surgical resection margins (Fig. 23.2a).

Hepatocellular carcinoma is the fifth most common cancer worldwide in adults and has a high mortality rate. Its global distribution is related to the prevalence of hepatitis virus infection and cirrhosis. Hepatocellular carcinoma is a very rare aggressive hepatic tumor in children and adolescents. Serum AFP will be elevated in 50–60 % of

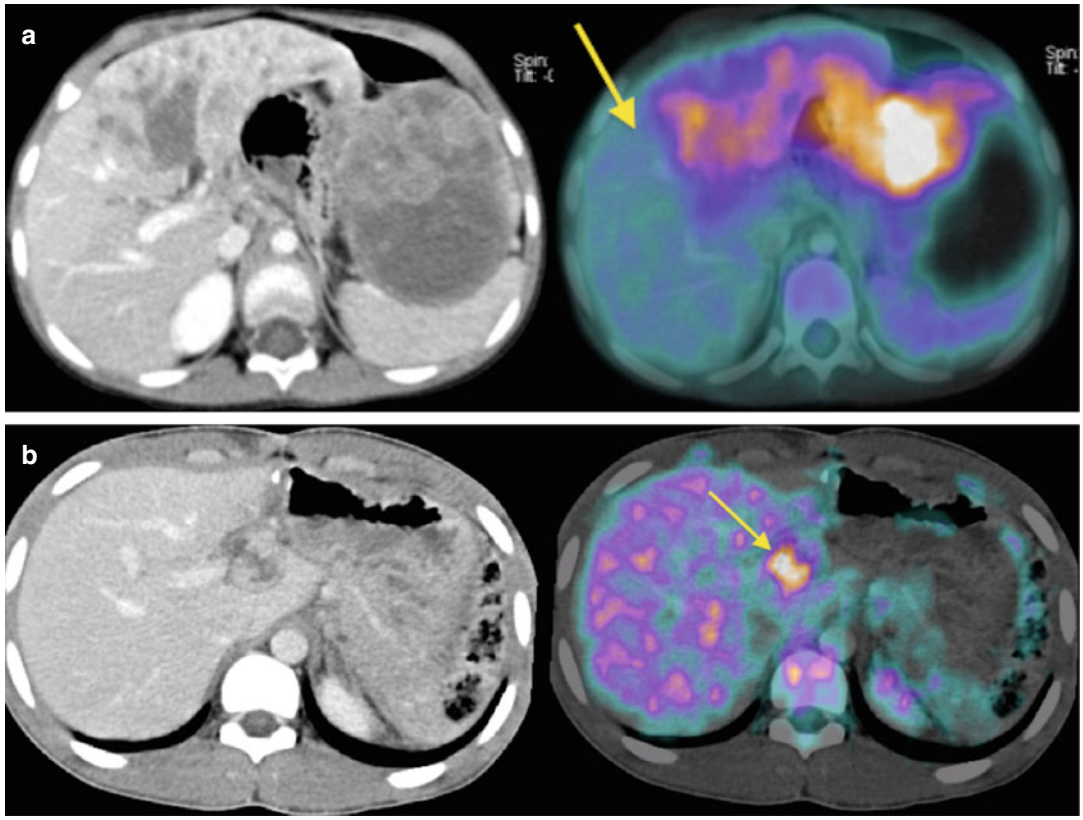

Fig. 23.2 (**a**) Primary hepatoblastoma in a 5-year-old female with axial CT (*left*) and ^{18}F-FDG PET/CT scan (*right* co-registered image) showing moderate increase in ^{18}F-FDG uptake (SUVmax 5.3) in viable tumor. There is no ^{18}F-FDG uptake in the left side of the mass, which is undergoing necrosis. The PET was considered helpful by the surgeon in defining the resection margin (*arrow*). (**b**) Recurrent hepatocellular hepatocarcinoma in a 9-year-old male who had resection of the primary tumor 12 months previously. Fluorine-18-FDG PET/CT performed because of rising AFP and an equivocal contrast CT and MRI for recurrence along the resection margin. The contrast CT (*left*) shows a possible mass or intestine near the resection margin. The ^{18}F-FDG PET/CT (*right*) shows avid ^{18}F-FDG uptake in the mass (*arrow*) on the left resection margin confirming recurrence. This was confirmed as hepatocellular carcinoma at surgery

cases. The initial imaging of these hepatic tumors usually is by US combined with CT or MRI to assess the primary tumor, identify locoregional spread, visualize the vasculature, and to detect pulmonary metastases. The use of ^{18}F-FDG PET has been reported in adults with hepatocellular carcinoma. Between 50 and 70 % of hepatocellular carcinomas accumulate ^{18}F-FDG, but uptake is variable due to variable levels of glucose-6-phosphatase activity. Fluorine-18-FDG uptake also may correlate with the degree of differentiation of these tumors, with the poorly differentiated, more aggressive cancers accumulating FDG more avidly [36, 37]. Other PET agents, e.g., ^{18}F-fluorodeoxygalactose, ^{11}C-acetate, ^{11}C or ^{18}F-F-choline, and ^{18}F-fluorothymidine, also have been used to assess metabolism, lipogenesis, cellular membrane metabolism, and proliferation, respectively, in these tumors [37]. Although the clinical role of PET is still uncertain it has been found to be useful in determining extrahepatic spread and recurrence of disease (Fig. 23.2b) [36, 38]. Fluorine-18-FDG PET also may have a role as a prognostic indictor. Higashi et al. found that post-therapeutic ^{18}F-FDG PET performed within 1 month after nonoperative therapy can be a good predictor of overall survival in unresectable hepatocellular carcinoma [39]. Surgical resection is the treatment of choice for hepatocellular carcinoma, but many tumors cannot be completely resected.

Hepatocellular carcinoma has a poor response to conventional chemotherapy [40, 41]. Other therapeutic techniques include liver transplantation and ablative therapies, e.g., radiofrequency ablation, ethanol injection, and radiopharmaceutical techniques. These have variable success for cure but are often palliative [40]. Intra-arterial injection of ^{131}I-lipiodol has had variable success in these tumors. Other methods use ^{90}Y-labelled microspheres, which requires pretreatment imaging with ^{99m}Tc-MAA scintigraphy to exclude patients with pulmonary shunting. Other labelled conjugates with ^{188}Re and ^{90}Y and radiolabelled antibodies have also been used with initial promising results.

Retinoblastoma

Retinoblastoma is the most common intraocular tumor in children, with an incidence of one case per 15,000–20,000 live births. The mean age at presentation is 2 years for unilateral disease and 1 year for bilateral disease [42, 43]. There is a germline mutation of the RB-1 gene on chromosome 13q14 in all patients with bilateral disease and 15 % of patients with unilateral disease [44]. Patients usually present with leukocoria or a squint. Management of retinoblastoma depends on the stage and is highly curable if detected early and confined to the globe with no metastatic diseases. Diagnostic imaging, mainly US and high-resolution MRI, is used to determine the local extent and associated brain abnormalities, including intracranial extension, midline primitive neuroectodermal tumors (trilateral retinoblastoma), and brain malformations. Current treatment protocols attempt to preserve the eye and may include external beam radiotherapy, chemotherapy, laser coagulation, cryotherapy, or radioactive plaque [45, 46]. Imaging plays an important role to determine the stage of disease. Retinoblastoma may spread by direct extension through the bulbar wall into the orbit or via the optic nerve and meningeal sheath or by hematogenous spread. US is used to examine the eye, and MRI is used to identify deeper lesions in the skull base and central nervous system [47]. If there are high-risk factors for local or distant spread, bone scan is indicated to exclude skeletal metastases; however, the rate of skeletal metastases is low (8–10 %) [45, 47, 48]. Fluorine-18-FDG PET use has been described in retinoblastoma. Radhakrishnan et al. reported 25 children with advanced stage III retinoblastoma [49]. Twenty-four patients had tumors that were FDG-avid at diagnosis. Fluorine-18-FDG PET was repeated after 3 cycles of neoadjuvant chemotherapy, and the reduction of extraocular tumor SUVmax was a significant predictor of both event-free survival and overall survival [49]. The role of ^{18}F-FDG PET in the management of retinoblastoma remains unclear. It may be most useful in the assessment of the metabolic response to cytoreductive chemotherapy prior to enucleation.

Germ Cell Tumors of Childhood

Germ cell tumors (GCT) are a diverse group of neoplasms that are derived from primordial germ cells, which migrate during embryogenesis from the yolk sac through the mesentery to the gonads. There are many different types of GCT due to variations from normal development (gonadal GCT) or aberrant migration (extragonadal GCT). Extragonadal GCT usually occurs in midline locations (mediastinal, retroperitoneal, sacrococcygeal, genital, and cranial areas). The histology and genetic profiles of GCT are heterogeneous and vary depending on primary tumor site, gender, and age of the patient [50, 51]. Histologically, GCT in infants and younger children has different biological characteristics than GCT in adolescents and adults. GCT represents 1–3 % of childhood tumors, and approximately 20 % are malignant [52]. There are several histological classifications; however, the National Cancer Institute categorizes them into three groups: (1) mature teratomas, (2) immature teratomas, and (3) malignant GCT [53]. Mature GCT typically is benign and is the most common GCT in childhood. Immature teratomas are graded according to the amount of immature neural tissue present. Malignant GCT contains malignant tissues arising from any of the 3 germ cell layers. In young children the histology is usually yolk sac tumor or dysgerminoma. In adolescent and young adults, the histology depends on

the anatomic site and includes seminoma or choriocarcinoma, dysgerminoma, yolk sac tumor, mixed GCT (ovarian and extragonadal), and germinoma. There are several distinguishing features between adult and childhood GCT. In children, extragonadal sites are found in 50 % of cases, whereas in adults this is 10 %. AFP elevation is seen in the presence of yolk sac tumor and is an indicator of residual or recurrent disease [50–52]. Rarely, there is malignant transformation from a benign teratoma to aggressive malignant tumors such as adenocarcinoma [54]. In older children and adolescents, mediastinal lesions predominate. These tumors typically present as a mass and secrete serum tumor markers. Elevated alpha fetoprotein (AFP), human chorionic gonadotropin (hCG), and lactate dehydrogenase levels may help in the diagnosis and are useful markers to evaluate therapy or detect recurrence. Surgery is the primary treatment, and with modern chemotherapy, there has been a significant improvement in overall survival [50]. Anatomic imaging is used to identify the extent of the primary tumor and locoregional nodal and metastatic disease. If pathology indicates malignant disease, bone scan and ^{18}F-FDG PET/CT may be used to identify metastatic disease, determine the response to treatment, and detect recurrence. Bone metastases tend to be more common in patients with mediastinal lesions with yolk sac histology [55]. Spread to draining lymph nodes in the retroperitoneal area is often the first manifestation of metastases. Hematogenous spread occurs to the lungs, and CT scans are required for diagnosis. Approximately 30 % of patients will have microscopic metastases that are not detectible with anatomical imaging such as CT, and functional imaging with ^{18}F-FDG PET may have a role [56]. If teratomas are excluded (due to low glycolytic rate and low ^{18}F-FDG uptake) many germ cell tumors will demonstrate abnormal utptake on ^{18}F-FDG PET (Fig. 23.3a, b). There is little data on the use of PET in pediatrics, and as the biological behavior of GCTs in children compared to adult disease may be different, the experience with ^{18}F-FDG PET in adults may not apply. In adults, seminomatous GCTs have higher ^{18}F-FDG uptake than non-seminomatous GCTs [57]. Fluorine-18-FDG PET as a primary staging tool for non-seminomatous GCTs may be only slightly better than CT alone and may be most useful when the CT findings are equivocal [58]. Fluorine-18-FDG PET can detect viable tumor in mass lesions seen on CT, which can reduce false-positive findings in stage II disease but does not improve staging in stage I disease [59]. PET also may have a high false-negative rate in identifying relapse after treatment and so may not have utility in this role [60]. However in seminoma, ^{18}F-FDG PET does appear to be useful to assess viability in residual tumor masses post-therapy. It was more accurate than other imaging modalities [60, 61] where it successfully identified 100 % of cases >3 cm in diameter and 95 % of those <3 cm. Detection of recurrent disease can be an important role of ^{18}F-FDG PET/CT in patients who have either masses (Fig. 23.4) or raised tumor markers with a normal CT scan [62]. However ^{18}F-FDG PET has been reported to be disappointing when used to detect retroperitoneal lymph node involvement post-chemotherapy in patients with advanced GCT of the testis [63].

Non-rhabdomyosarcoma Soft Tissue Sarcoma

Non-rhabdomyosarcoma soft tissue sarcomas in childhood and adolescents represent a subgroup of sarcomas that arise from primitive mesenchymal tissues and include over 50 different tumors. The subgroups described in this section are based on a modification of the histomorphologic classification of Spunt et al. [64]. These tumors account for 4.5 % of all childhood malignancies and are overall slightly more common than rhabdomyosarcoma [65, 66]. The most common non-rhabdomcosarcoma sarcomas of childhood are synovial sarcoma, dermatofibrosarcoma protuberans, malignant peripheral nerve sheath tumors (MPNSTs), and a malignant subset now more commonly termed by histopathology as "unclassified/undifferentiated sarcoma". The majority of these tumors are sporadic, but some may have specific chromosomal rearrangements, e.g., t(X;18) (p11;q11) with SYT-SSX fusion; and MYCN overexpression in synovial sarcoma [64, 66]. For the majority MRI and/or CT will be

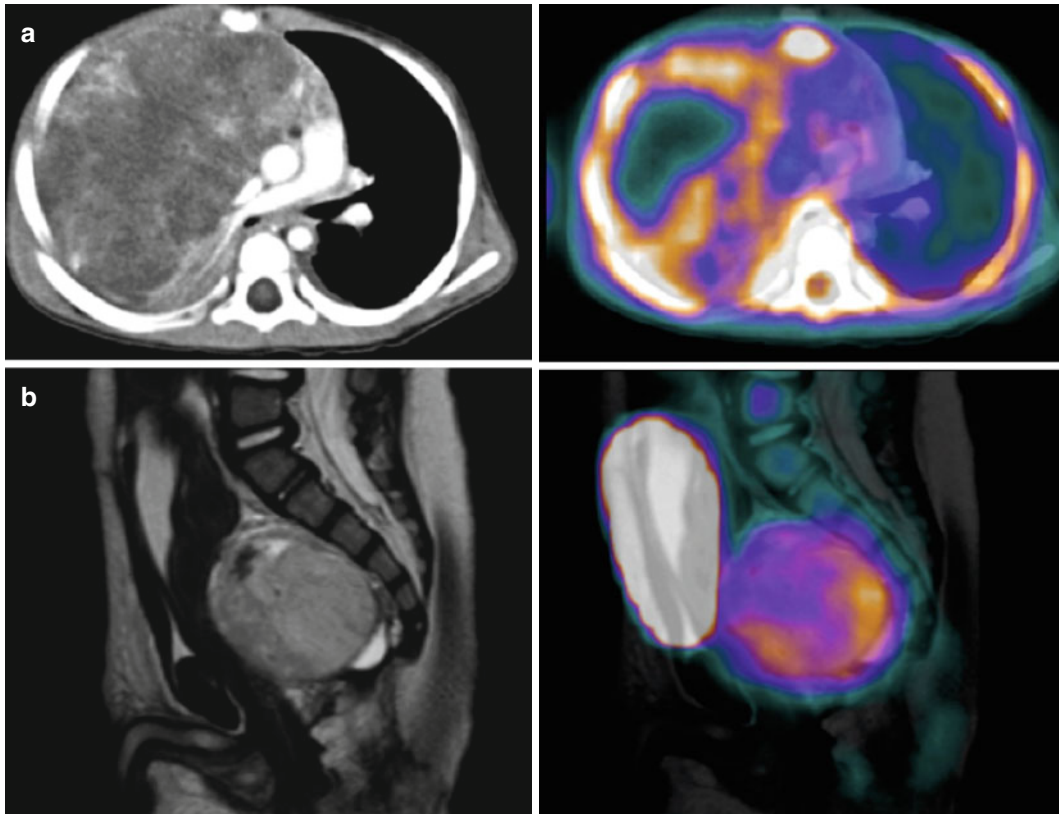

Fig. 23.3 (**a**) Mediastinal yolk sac tumor. A 2-year-old male presented with a cough and increasing respiratory distress. CXR and CT scan showed a large mediastinal mass with areas of necrosis and a pleural effusion. Biopsy showed yolk sac tumor. The ^{18}F-FDG PET/CT scan was performed after 5 days of chemotherapy. There is increased metabolic activity peripherally in the viable tumor with minimal uptake in large areas of necrosis. No metastatic disease is detected. There was very high serum AFP. (**b**) Yolk sac tumor. An 11-month-old male with a presacral tumor shown to be a yolk sac tumor on biopsy. Past history of surgical resection of a sacrococcygeal teratoma at 3 days of age. Current MRI (sagittal T2FS) and ^{18}F-FDG PET co-registered show a large mass in the pelvis, which is mildly hyper metabolic (SUVmax 2.9). There was no evidence of metastatic disease

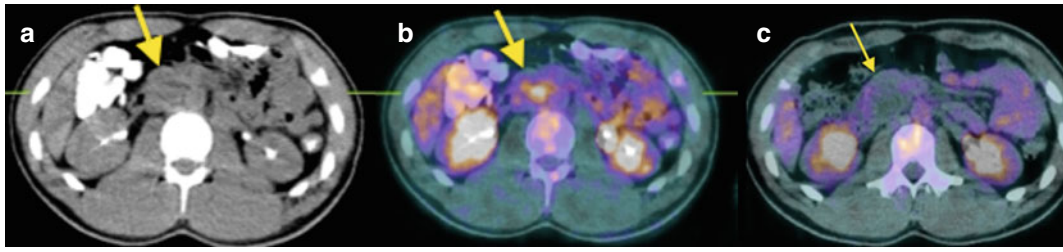

Fig. 23.4 Recurrent non-seminomatous germ cell tumor. A 10-year-old male with a past history of previous right orchidectomy for non-seminomatous germ cell tumor. Routine follow-up blood tests showed increasing hCG and AFP. (**a**) CT scan (axial slice) shows a low-density mass in right para-aortic region at the renal hila level. (**b**) Fluorine-18-FDG PET/CT shows increased metabolic activity (SUVmax 4.5) in this mass and lymph nodes below the right kidney confirming relapse. (**c**) After salvage chemotherapy the follow-up ^{18}F-FDG PET/CT shows a persistent mass but no metabolic activity. Surgical resection of the abnormal nodes showed mature teratomatous elements with no viable malignant GCT elements, (arrows indicate the mass)

used to define the primary tumor and CT of the lungs will be used to exclude pulmonary metastases. Reports of using ^{18}F-FDG PET are becoming more common as it is used for staging, assessing response to treatment, and detecting residual, recurrent, or metastatic disease.

Spindle Cell Tumors

Synovial Sarcomas

Synovial sarcomas are rare malignant tumors and represent a biologically diverse subset of soft tissue sarcomas. They account for 6–10 % of all soft tissue sarcomas and are the most common (one-third) non-rhabdomyosarcoma sarcomas that occur in childhood and adolescence [67, 68]. Most synovial sarcomas are intermediate- to high-grade tumors with an overall survival at 5 and 10 years of 85 and 78 %, respectively [9]. Fluorine-18-FDG PET can have an important role in the management of synovial sarcoma (Fig. 23.5). Lisle et al. showed good correlation of SUVmax with overall and progression-free survival. SUVmax of >4.35 was associated with decreased survival and a higher risk of local recurrence and metastatic disease [67].

Dermatofibrosarcoma Protuberans (DP)

DP is an uncommon, low-grade, fibrohistiocytic tumor that occurs usually in young adulthood but can occur in childhood. Surgery is the main treatment; however, some patients who have unresectable disease may develop recurrent or metastatic disease [9, 67]. Fluorine-18-FDG PET has been used to assess the response of this tumor to imatinib therapy [69].

Inflammatory Myofibroblastic Tumors

Inflammatory myofibroblastic tumors (IMTs) are rare. They have been reported in multiple anatomical locations, with the lung being the most common site [70]. IMTs have been seen after therapy for other malignancies, such as lymphoma [71]. These lesions are considered to be benign, but they may be locally invasive and rarely metastasize. IMTs demonstrate increased metabolic activity on ^{18}F-FDG PET. The histopathology of IMTs can vary in the degree of cellularity, but all are composed of myofibroblastic cells admixed with variable inflammatory infiltrates. This may explain the high metabolic activity seen on ^{18}F-FDG PET [71].

Malignant Peripheral Nerve Sheath Tumors

Peripheral nerve sheath tumors (PNSTs) are benign or malignant tumors that arise from peripheral nerves. They include benign forms such as schwannoma and neurofibroma (NF) and malignant variants such as malignant peripheral nerve sheath tumor (MPNST). Several hereditary syndromes are associated with the development of PNSTs in particular neurofibromatosis type 1 (NF1). MPNST accounts for 3–6 % of all soft tissue sarcomas. Favorable prognostic indicators are age <10 years, location in an extremity, tumor size <5 cm, the ability to deliver radiotherapy, a good response to chemotherapy, and complete resection of the primary tumor [72, 73]. The initial imaging is usually by MRI or CT. Differentiating benign tumors such as schwannoma and NF from MPNST is difficult, particularly in NF1 as these patients often have multiple lesions (see section on patients with NF1 [105]). MPNSTs are highly aggressive with a 5-year survival-specific mortality of 75 %. They often require radical surgical resection, radiation therapy, and chemotherapy. Fluorine-18-FDG PET has been shown to differentiate benign from malignant tumors with high specificity and sensitivity. In children and adolescents, surveillance of these tumors is usually by MRI. If there is an increase in size or symptoms, then ^{18}F-FDG PET is used to further characterize each lesion. When MPNST is diagnosed, ^{18}F-FDG PET is used for staging with assessment of locoregional involvement and distant metastatic disease. Fluorine-18-FDG PET also is used to in assess response to treatment and detect disease recurrence (Figs. 23.6 and 23.7).

Others

This subgroup includes infantile fibrosarcoma, leiomyosarcoma, and angiosrcoma. These tumors are very rare in childhood. Fluorine-18-FDG PET has been shown to be positive in these tumors, particularly in the leiomyosar-

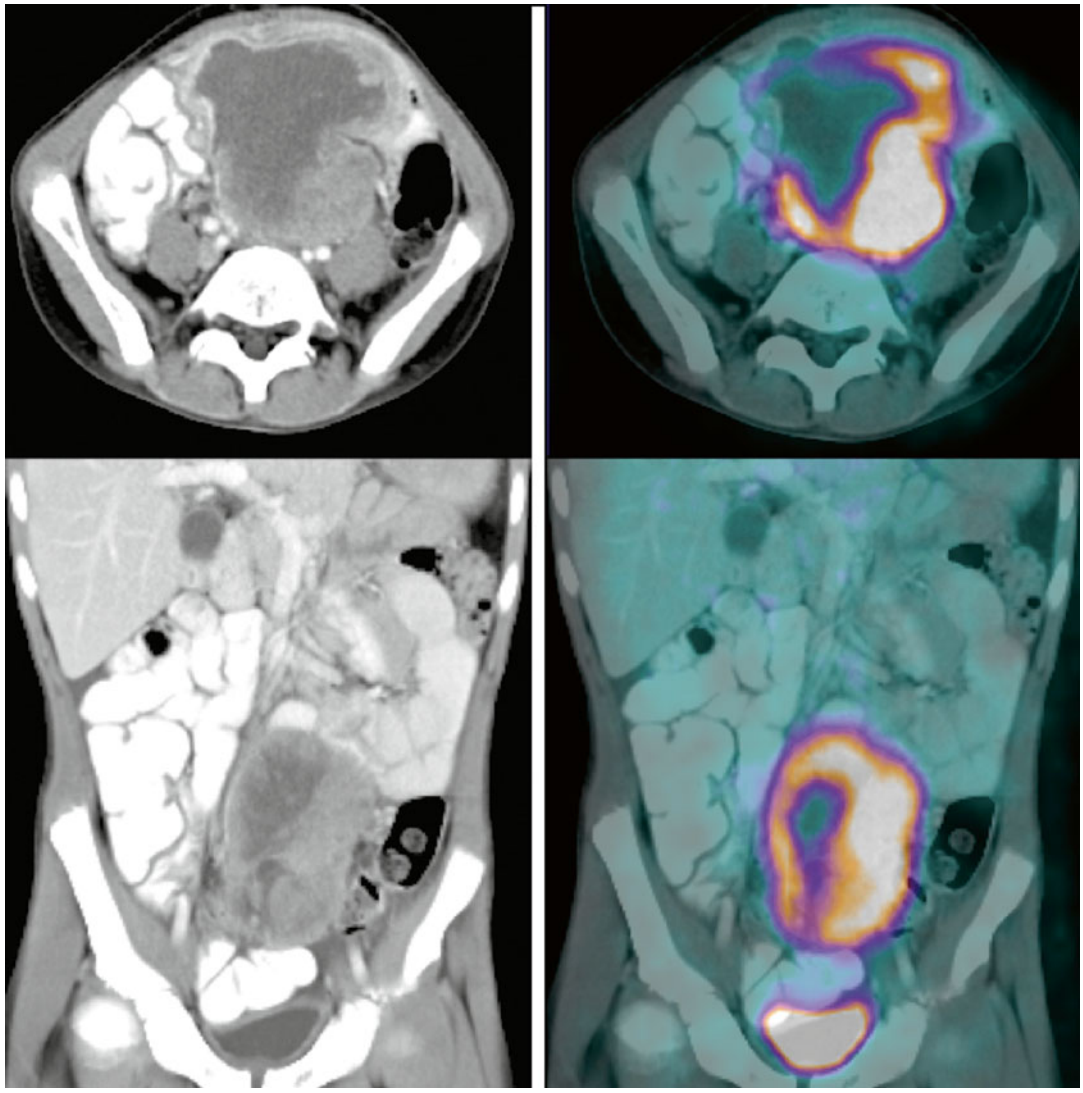

Fig. 23.5 Synovial sarcoma. A 13-year-old male with a past history of Wilms' tumor presented with an abdominal mass. Biopsy revealed high-grade synovial sarcoma. The co-registered ^{18}F-FDG PET/CT [*left side* CT (*top* axial, *bottom* coronal), *right side* PET/CT] shows a large highly metabolic abdominal and pelvic mass (SUVmax 8.2) with central necrosis. No metastases were detected

coma, which is a more malignant aggressive tumor [9, 74].

Small Round Cell Tumors

Desmoplastic Small Round Cell Tumors

Desmoplastic small round cell tumors are rare in children and mainly occur in adolescents and young male adults. The use of ^{18}F-FDG PET has been described and to show significantly increased metabolic activity with SUVmax ranging from 5.2 to 12.7. Fluorine-18-FDG PET may identify more lesions than standard radiological imaging and is useful in staging and assessing response to therapy [75–77].

Clear-Cell Sarcoma

Clear-cell sarcoma is a rare, malignant, soft tissue tumor that involves the extremities, particularly

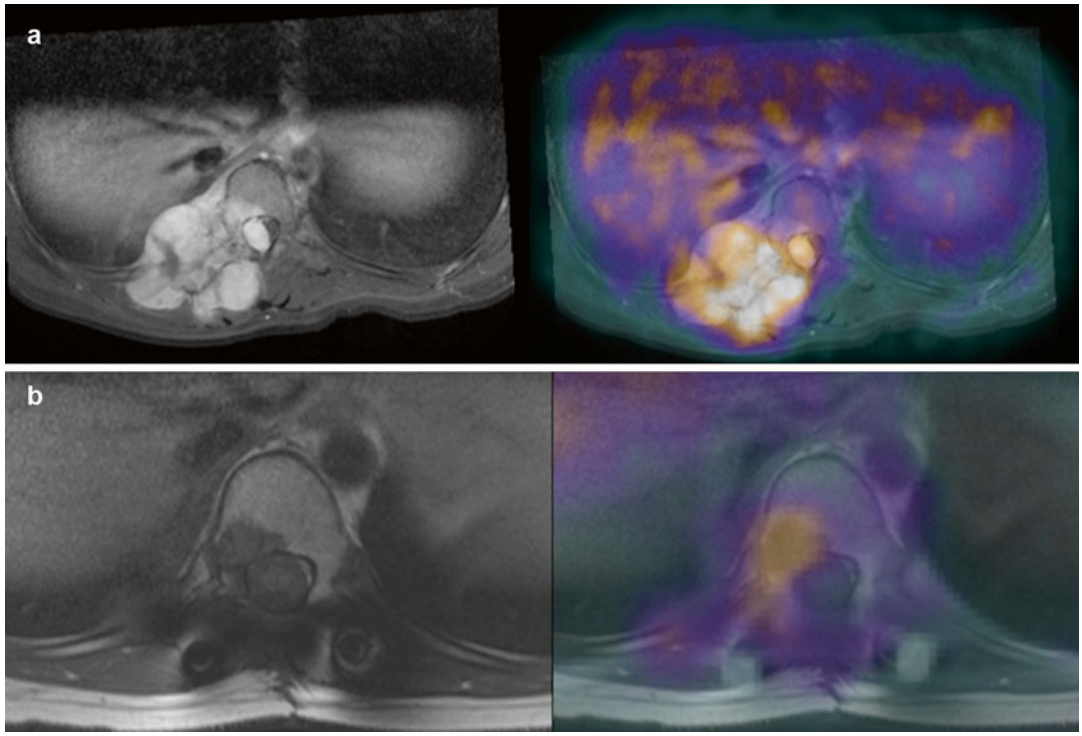

Fig. 23.6 Malignant peripheral nerve sheath tumor. A 12-year-old female presented with a painful right paraspinal mass. MRI showed tumor extension into the spinal canal and involvement of the head of the 10th right rib. Fluorine-18-FDG PET/CT was performed and co-registered with MRI (**a**: *top row* MRI (*left*) and co-registered image (*right*)). The mass has moderately increased metabolism (SUVmax 4.2) with no metastatic disease. Biopsy showed MPNST. She underwent laminectomy with post-surgery chemotherapy and radiotherapy. On a routine surveillance ^{18}F-FDG PET/CT scan 14 months later, an abnormal focus (SUVmax 2.5) was seen in the 10th thoracic vertebral body (**b**: *lower row* MRI (*left*) and co-registered image (*right*) suggestive of recurrence). The patient underwent surgical resection confirming recurrent MPNST

tendons and aponeuroses. The prognosis for this tumor is poor because of the high prevalance of lymph node metastases at diagnosis and a high frequency of recurrence and distant metastases. The use of sentinel lymph node biopsy (see Chap. 8) has been recommended to exclude regional lymph node involvement. Fluorine-18-FDG PET has been used for staging and detection of recurrence and metastatic disease in this malignancy [77–80].

Extraskeletal Myxoid Chondrosarcoma

Extraskeletal chondrosarcoma is a subset of the chondrosarcomas, but it most likely is a unique tumor entity. It is considered as low grade with a high rate of local recurrence. The use of ^{18}F-FDG PET has been described, and usually there is high metabolic activity with high SUVmax values [81].

Malignant Rhabdoid Tumors (See Malignant Rhabdoid Tumor of the Kidney)

Extrarenal malignant rhabdoid tumor is a rare aggressive malignancy in childhood and has a poor prognosis. Accurate histopathologic diagnosis and staging of the malignancy has major implications for management [82]. Fluorine-18-FDG PET/CT has been found to be useful in staging and detection of metastatic disease and recurrence [31]. There are case reports describing the use of ^{18}F-FDG PET to evaluate malignant rhabdoid tumors of the lungs and atypical teratoid rhabdoid tumor of the brain [31, 83].

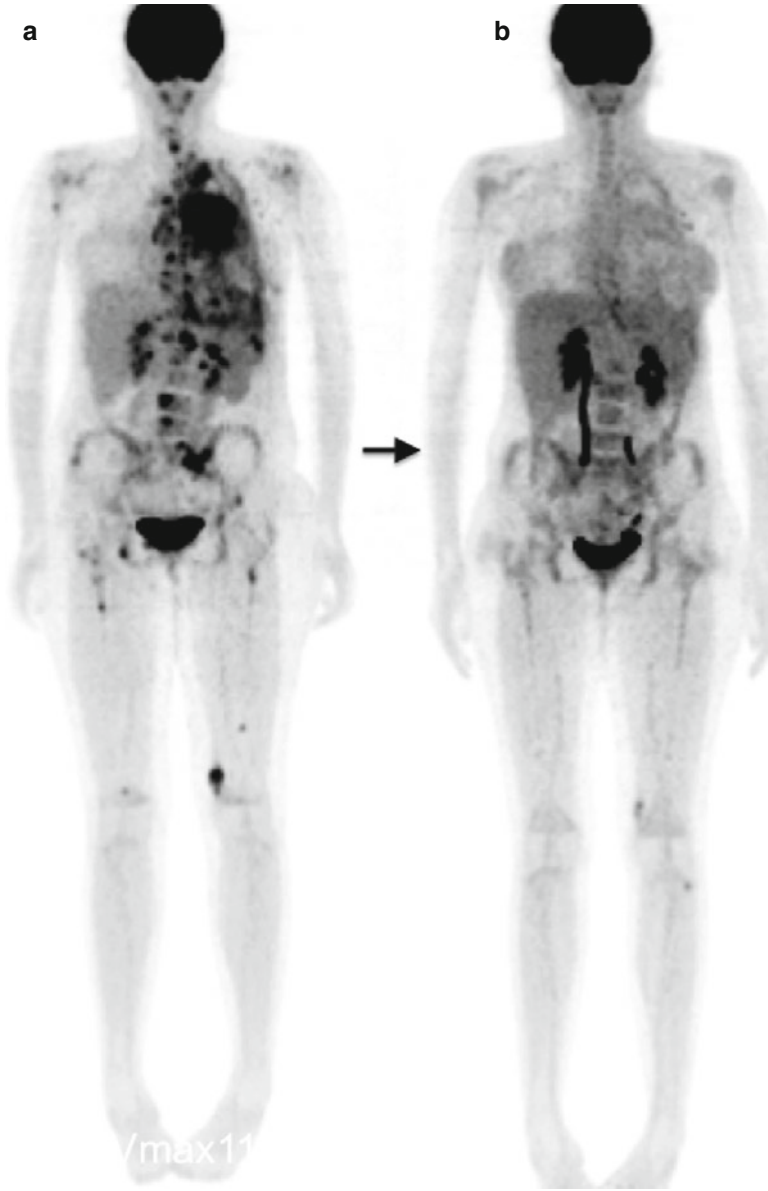

Fig. 23.7 Epithelioid variant MPNST. A 15-year-old female who presented with fevers and shortness of breath and found to have a large left-sided pleural effusion. On drainage malignant cells were found. (**a**) MIP image. Fluorine-18-FDG PET/CT showed a soft tissue mass in the left hemithorax and multiple abnormal areas consistent with metastatic disease in the skeleton, bone marrow, and lymph nodes of the neck, chest, and abdomen. Biopsy of the left pleural mass showed epithelioid variant MPNST. (**b**) MIP Image. After salvage chemotherapy and radiotherapy, there was a good response with persistent low uptake in the left pleura and in lymph nodes in the lower left neck and lower left thigh. Mild increased marrow uptake is consistent with therapy-related marrow stimulation

Epithelioid Tumors

Epithelioid Sarcoma

Epithelioid sarcoma is a rare, high-grade soft tissue sarcoma that most often develops in tissues under the skin of the hands, forearms, feet, or lower legs. They tend to occur in young adults, but have been reported in pediatric and adolescent patients. They have a propensity for local recurrence, regional lymph node involvement, and distant metastases. Sentinel lymph node biopsy (see Chap. 8) has been recommended [80]. Fluorine-18-FDG PET has been shown to be positive in a child with metastatic epitheliod sarcoma [80, 84, 85].

Alveolar Soft Part Sarcoma

Alveolar soft part sarcoma is a very rare tumor that usually affects adolescents and young adults, but it has been described in infants and children. The use of ^{18}F-FDG PET has been reported to show high metabolic activity in the primary tumor and metastases and has been used to assess the response to sunitinib therapy [86].

Myxoid Tumor

The myxoid tumors include lipoblastoma, myxoid liposarcoma, and low-grade fibromyxoid sarcoma. The majority of these rare tumors are considered low grade; however, they may recur locally and if unresectable may eventually metastasize. There are case reports describing the use of ^{18}F-FDG PET in these tumors. The low-grade malignancies such as fibromyxoid sarcoma may have mild to moderate ^{18}F-FDG uptake [81, 87] (Fig. 23.8).

Unclassified/Undifferentiated Sarcoma

Unclassified/undifferentiated sarcoma is a malignancy previously called "pleomorphic malignant fibrous histiocytoma," but the World Health Organization has changed the name to "undifferentiated high-grade pleomorphic sarcoma not otherwise specified." The most common sites are the lower extremity and head and neck. Surgery is the primary treatment as chemotherapy and radiotherapy appear to have little effect in improving outcome [9]. The use of ^{18}F-FDG PET has been described in these tumors [88]. Our experience at the Children's Hospital, Sydney with the use of ^{18}F-FDG PET/CT in these tumors has shown high metabolic activity and accurate assessment of response to therapy and detection of metastatic disease. Follow-up PET may be used to detect recurrence or metastatic disease (Figs. 23.9 and 23.10).

Gastrointestinal Stromal Tumors

Gastrointestinal stromal tumors (GIST) are the most common mesenchymal tumors of the gastrointestinal tract and typically occur in middle-aged and older patients with a median age of 60 years. GIST is 0.1–3.0 % of all cancers involving the

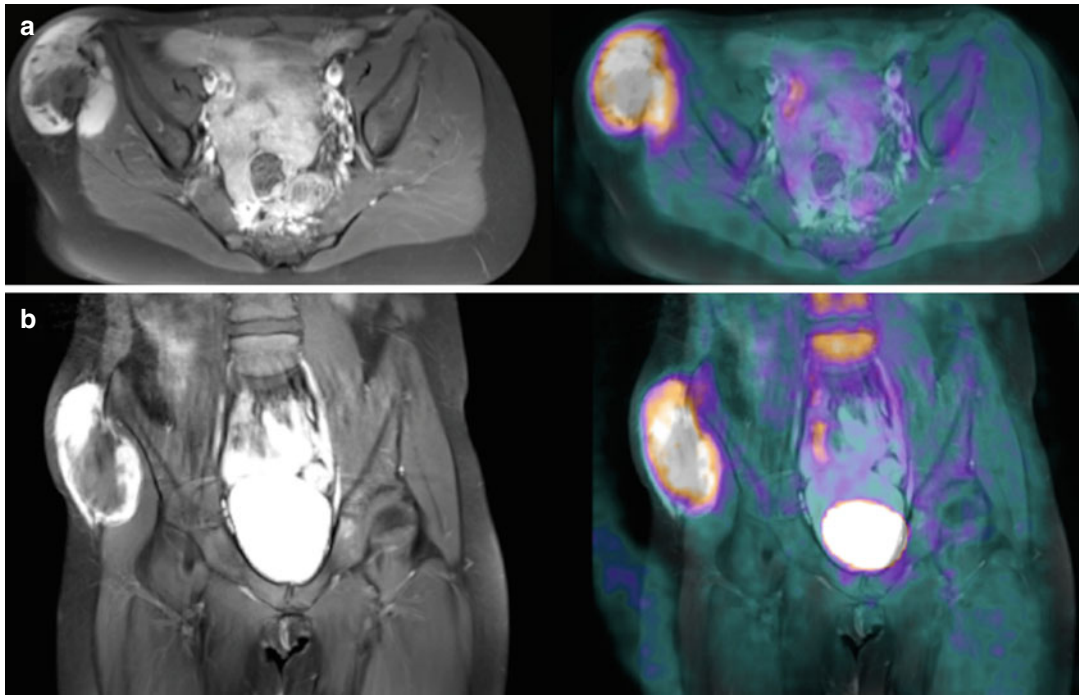

Fig. 23.8 Fibromyxoid sarcoma. A 10-year-old female presented with a slowly enlarging mass on the side of her right pelvis. MRI (*left* axial (**a**), coronal (**b**)) showed a heterogeneous mass with intermediate T1 intensity arising in the gluteus medius and having areas of central necrosis. There were prominent lymph nodes in the inguinal and right pelvic wall suggesting possible metastatic node involvement. Fluorine-18-FDG PET/CT (**a**: axial, **b**: coronal co-registered MRI and PET) confirms that the mass is metabolically active (SUVmax 5.1) with a "photopenic" central area consistent with necrosis. There is no abnormal lymph node uptake and no evidence of metastatic spread. Histopathology after surgical resection showed fibromyxoid sarcoma (low-grade)

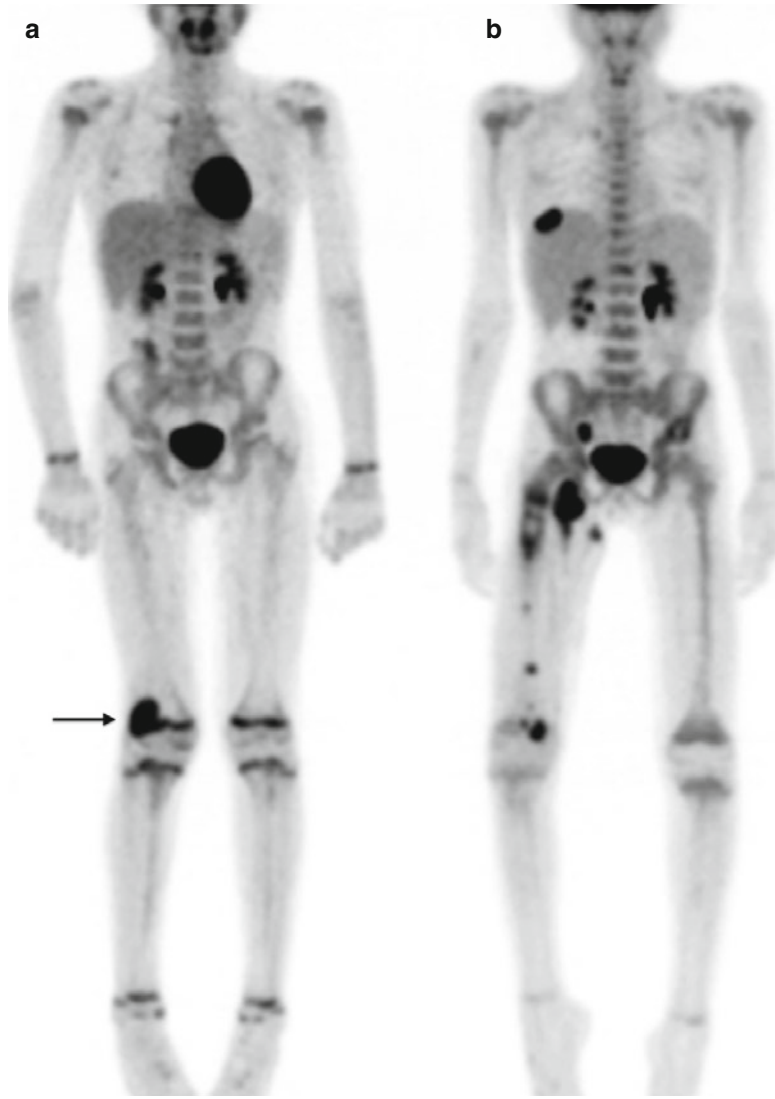

Fig. 23.9 Undifferentiated high-grade large cell sarcoma. An 11-year-old male presented with a mass in the right popliteal fossa. Biopsy showed undifferentiated sacrcoma. (**a**) MIP image. Staging with CT and ^{18}F-FDG PET/CT showed a localized mass (*arrow*) with no evidence of metastases. A sentinel lymph node biopsy of a femoral lymph node was negative. The patient underwent chemotherapy and showed an initial response on ^{18}F-FDG PET and CT. After the third cycle of chemotherapy, the patient developed a mass in the right femoral region. Biopsy showed metastatic disease. (**b**) MIP image. A repeat ^{18}F-FDG PET showed the primary tumor in the right popliteal fossa was smaller but remained metabolic. There was metastatic disease in right inguinal and external iliac nodes; multiple bone marrow metastases in the right femur, left acetabulum, and 12th thoracic vertebra; and a liver metastasis. This indicated severe disease progression on therapy and the patient was placed on palliative care

gastrointestinal tract. GIST is rare in childhood and adolescents, and accounts for 0.5–2.7 % in patients <21 year old [89]. Approximately 90 % of adult GIST have a mutation of the KIT and PDGFR proto-oncogenes, whereas these mutations are infrequent in pediatric cases (15 %). These proto-oncogenes allow successful treatment with tyrosine kinase receptor inhibitors (TKI) such as imatinib and sunitinib. GIST is more common in pediatric females and more often have the epithelioid or mixed morphology compared to the more common spindle morphology in

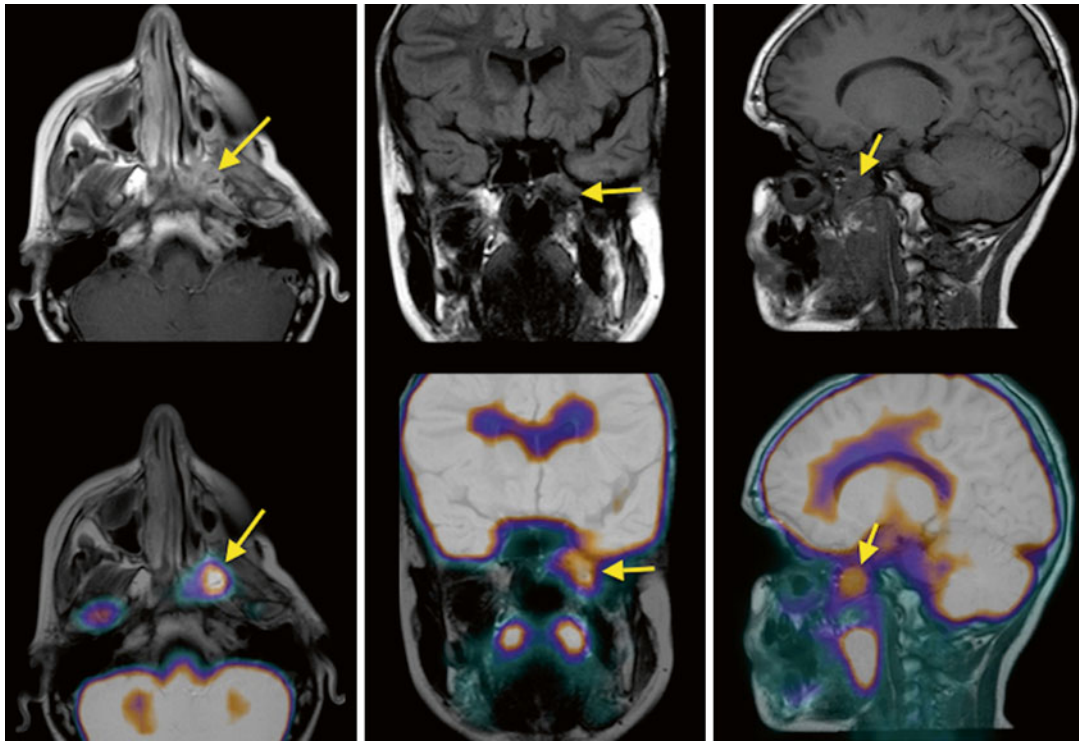

Fig. 23.10 Recurrent pleomorphic spindle cell sarcoma. A 13-year-old male with past history of bilateral familial retinoblastoma treated by chemotherapy and radiotherapy developed a second malignant neoplasm diagnosed as a pleomorphic spindle cell sarcoma. Treatment was by chemotherapy and surgery. Follow-up MRI showed mass in left lateral sphenoid region. PET/CT showed increased metabolic activity in the mass confirming recurrence (*arrows*). The mass failed to respond to salvage chemotherapy. Biopsy confirmed same histology and patient was placed on palliative care

adults. The most common localization of GIST in children and adolescents is the stomach (60 %), small intestine (30 %), large intestine (5 %), and esophagus (<1 %) [89, 90]. Multiple tumor nodules are common, and recurrence of disease occurs in approximately 20 % of cases. In children, GIST is usually sporadic but rarely may be associated with other tumor syndromes, such as neurofibromatosis Type 1 (NF1). GIST in NF1, and familial forms are most commonly multicentric and found in the small intestine. Up to half will experience recurrence, metastases, or both. Imaging techniques depend on the presenting symptoms and signs. Abdominal and pelvic CT with intravenous and enteral contrast is the usual initial investigation. This helps identify abdominal masses and metastatic disease to the liver and lymph nodes. MRI can be very useful for identifying masses in the liver and lymph nodes. The use of ^{18}F-FDG PET has been well described in adult patients and has been used for staging and assessment of response to TKR inhibitors. There is very little data on the appropriate imaging approach in pediatric patients, but several articles have reported FDG avidity in GIST (Fig. 23.11). Fluorine-18-FDG PET imaging has been successfully used to monitor the response to therapy. Surgery is the primary mode of treatment; however, even with complete resection, recurrence has been reported to occur in 40–90 % of cases in adults [89–91].

Langerhans Cell Histiocytosis

Langerhans cell histiocytosis (LCH) is a rare disorder resulting from clonal proliferation of cells resembling the epidermal dendritic cells called

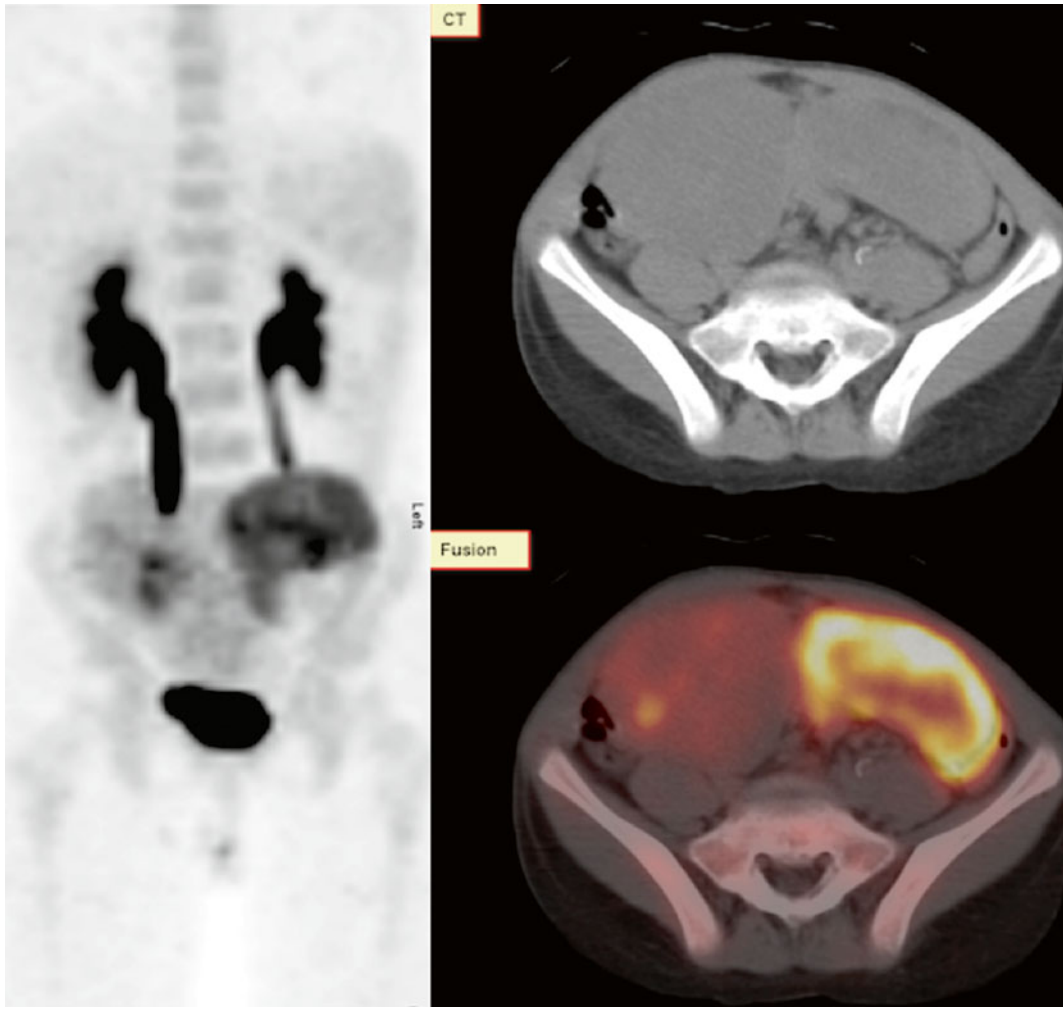

Fig. 23.11 A 9-year-old female with pelvic masses. Fluorine-18-FDG PET/CT (*left* MIP; *right upper row* low dose CT; lower co-registered PET/CT axial views) confirmed 2 solid pelvic masses with variable FDG uptake SUVmax 8.3. Surgical resection confirmed GIST (Case courtesy of Dr Barry Shulkin, St. Jude Children's Research Hospital, Memphis, Tennessee, USA)

Langerhans cells [92]. These diseases all involve abnormal histiocytes but on electron microscopy cytoplasmic "Birbeck" granules are characteristic of normal Langerhans cells found in the skin [93]. LCH now describes all of the patients previously diagnosed with histiocytosis X, eosinophilic granuloma, Letterer-Siwe disease, Hand-Schuller-Christian disease, and diffuse reticuloendotheliosis. LCH is a rare disease with 2–10 cases per million children <15 years and a median age at diagnosis of 30 months. LCH has a wide range of clinical presentations from single organ (single-system LCH) involvement such as the skin or bone to multifocal disease (multisystem LCH) of the liver, lung, bone marrow, and central nervous system. More extensive organ involvement is associated with a poorer prognosis [94]. Clinical presentation depends on the pattern of organ involvement and the course of the disease can vary from spontaneous regression to rapid progression and death. Any bone can be involved in LCH, although there is a predilection for flat bones. The skull is the most commonly involved, followed by the pelvis, spine, mandible, and ribs [95] (Fig. 23.12). In patients with bone disease one third or more have involvement of the

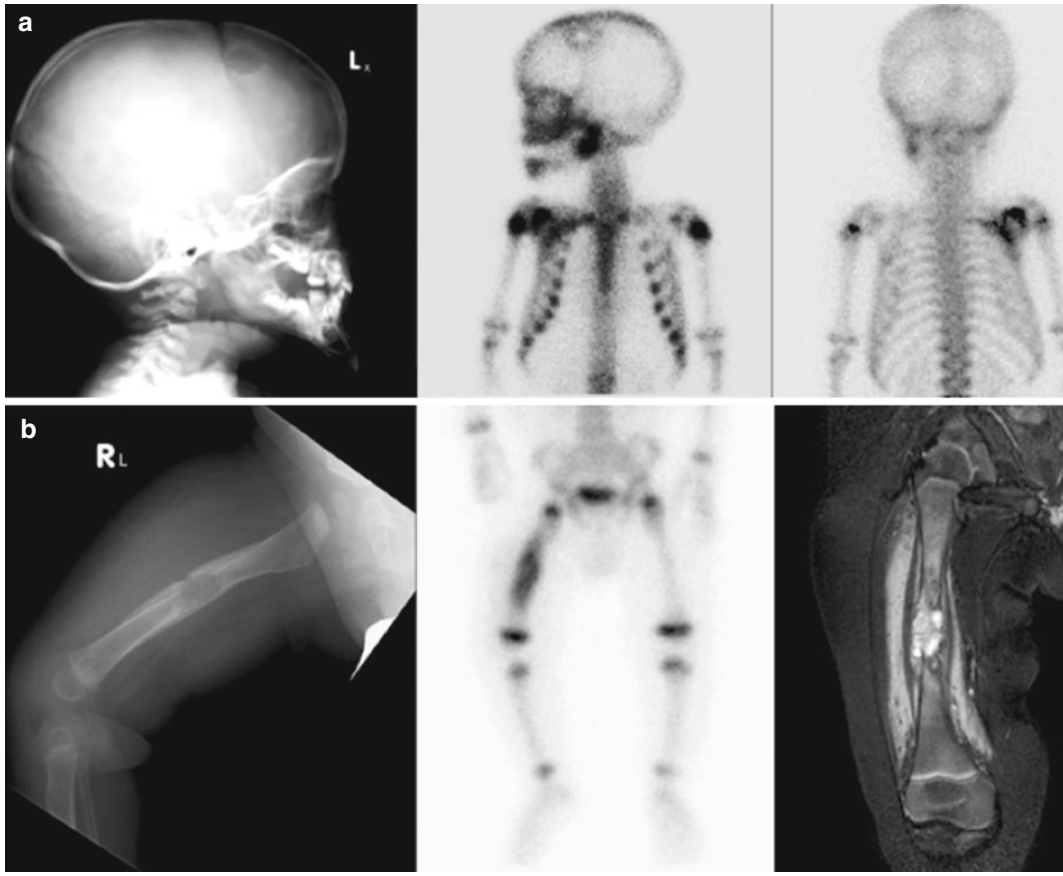

Fig. 23.12 Langerhans cell histiocytosis. (**a**) A 7-year-old male presented with a mass on the left side of his skull. Biopsy confirmed LCH. Skull radiograph shows a typical geographic lytic lesion in the left frontal bone. On bone scintigraphy this is seen as a "doughnut" lesion with a peripheral rim of increased osteoblastic activity. The bone scan also showed other lesions in the left mandible, right scapula, and right second rib consistent with multiple sites of disease. (**b**) A 7-month-old male presented with decreased movement and pain in the right femur. Radiograph (*left*) showed a diaphyseal lytic lesion with marked lamellar and periosteal reaction. Bone scan (*middle*) showed marked focal osteoblastic reaction corresponding to the periosteal reaction and a central photopenic area in the mid right femur corresponding to the lytic lesion on the radiograph. No other lesions were detected. MRI (T1FS with gadolinium) shows an expansile multicystic lesion in the mid diaphysis with loss of overlying cortex and extensive periosteal reaction (*right*). Biopsy confirmed LCH

long bones, with the femur as the most common followed by the humerus and tibia. The diaphysis is most commonly involved (Fig. 23.12). In the spine the vertebral body is usually involved with the thoracic spine as the most common, then the lumbar and cervical vertebrae [95, 96]. Lymph node involvement with LCH is most common in the cervical chain. Mediastinal lymph node disease may mimic lymphoma. The pituitary may be affected, which may cause diabetes insipidus, growth failure, or delayed or precocious puberty. Multiorgan disease may involve the liver, resulting in cholestasis and sclerosing cholangitis [97]. Bone marrow involvement tends to occur in children with diffuse disease in the liver, spleen, skin, and lymph nodes and results in low platelets and red blood cells [97, 98]. The central nervous system may be involved with mass lesions. A rare degenerative syndrome with ataxia and dysarthria has been reported. Fluorine-18-FDG PET in these patients showed an abnormality in the caudate nucleus [99]. Initial staging includes a skeletal survey and bone scan. These two modalities are complimentary, as up to one-fifth of lesions

are not seen on bone scan, and up to one-third may not be seen on plain radiograph [100–102]. Dogan et al. recommend both total body skeletal survey and bone scan to fully evaluate the skeleton. Bone scan is more sensitive than skeletal survey in detecting lesions in the ribs, spine, and pelvis and less sensitive in identifying lesions in the skull [101, 102]. CT and MRI are indicated in many patients to investigate specific symptoms of organ involvement. CT confirms the presence of bone lesions by cortical destruction and shows soft tissue involvement. MRI is very sensitive to showing bone marrow disease and soft tissue masses. In patients with skull or vertebral lesions, MRI is important to determine if there is involvement of the dura or brain and to assess for possible soft tissue impingement of the spinal cord. The typical skeletal radiological finding in LCH is a lytic lesion in the skull. On bone scan, this produces the "doughnut" sign (Fig. 23.12a) with a photopenic central region surrounded by a rim of increased uptake in the surrounding osseous reaction. In patients with bony involvement, 70 % will have a single lesion. Some lesions produce very little response in the surrounding bone and may be seen only as a photopenic "cold" lesion. These are more difficult to detect on bone scan, but SPECT/CT improves the detection of such lesions. In recent years ^{18}F-FDG PET has been reported to be useful for management and assessment of therapy. LCH lesions are usually FDG-avid as this reflects the intralesional metabolic activity (Fig. 23.13a, b). Fluorine-18-FDG PET has been reported to be more sensitive than skeletal survey and bone scan. Phillips et al. reviewed 102 ^{18}F-FDG PET scans in 44 pediatric patients with LCH. Fluorine-18-FDG PET was rated confirmatory or superior to plain radiography, bone scan, CT, and MRI in 236/256 (92 %) of lesions overall. When ^{18}F-FDG PET was compared more specifically to other modalities, it was superior finding new or recurrent lesions and as an indicator of therapy response. Fluorine-18-FDG PET was rated confirmatory or superior for 96 % of skull lesions, 86 % of vertebral lesions, 93 % of pelvic lesions, 100 % of rib lesions, 97 % of limb and other bone lesions, and 86 % of other body sites, including the brain, liver, lung, lymph nodes, and soft tissue. Fluorine-18-FDG PET was most helpful in identifying additional lesions in the skull, limbs, pelvis, scapula and clavicle, lymph nodes, lung, and spleen. This is important for management, as therapy choices for LCH depend on whether the disease is a single lesion or multifocal and whether there is involvement of "high-risk" organs, i.e., the liver, lung, spleen, and bone marrow. Response assessment is essential, particularly in those at high risk of disease reactivation and progressive disease. Lack of early response irrespective of the risk factors indicates a poor prognosis. Jurban et al. reported that in patients with multiorgan involvement, the risk of reactivation, progression, or death was significantly increased in those with poor initial response and progressive disease [94, 102, 103]. Therapeutic response is usually monitored by morphologic change on radiographs, CT, and MRI and on normalization of lesions on bone scan. These imaging modalities are limited and do not allow quantitative metabolic information on tumor viability and delayed morphologic change and have limited specificity and sensitivity. Fluorine-18-FDG PET/CT has been used to monitor disease response to chemotherapy and clarify discrepancies between clinical examination and other imaging results (Fig. 23.13a, b) [102, 103]. Therefore, nuclear medicine techniques including ^{18}F-FDG PET/CT and bone scan have important and complimentary roles in the management of LCH.

Neurofibromatosis Type 1

Neurofibromatosis type 1 (NF1) is a common autosomal dominant neurocutaneous syndrome affecting approximately 1/3,500 individuals. The manifestations of NF1 result from a mutation in or deletion of the NF1 gene. The NF1 gene (chromosome 17) codes for a protein neurofibromin, which acts as a tumor suppressor via the *ras* pathway. The diagnosis is based on the presence of 2 or more pathognomic features: café au lait spots, skinfold freckling, cutaneous or plexiform neurofibromas, Lisch nodules, optic path gliomas, skeletal dysplasia, and a positive

family history. Significant cognitive impairment and learning disabilities have been reported in up to 50–81 % of patients. NF1 is associated with an increased incidence of other tumors and malignancies. MRI is the main imaging modality to evaluate the central nervous system, plexiform neurofibromas and optic gliomas as these occur at a high frequency in children and adults with NF1. The major complication of a plexiform neurofibroma is malignant transformation to malignant peripheral nerve sheath tumors (MPNSTs). These tumors are highly malignant and have a poor prognosis. MPNSTs account for 5–10 % of soft tissue sarcomas, and approximately half of all MPNSTs are diagnosed in NF1 patients. The lifetime risk for MPNST is 8–13 %. The 5-year survival rates in MPNST range from 21 to 52 % and are poorer in NF1 patients. The symptoms of an enlarging benign neurofibroma and a MPNST are often identical, with increasing pain, growth of the lesion, and/or neurological deficits. Clinical and MRI surveillance of plexiform neurofibromas is unreliable in distinguishing benign from malignant tumors. Fluorine-18-FDG PET is accurate in detecting MPNST with a sensitivity ranging from 89 to 100 %, specificity 72–95 %, NPV 95–100 %, and PPV 50–71 %. Moharir et al. reviewed ^{18}F-FDG PET in children with NF1 and diagnosed malignant transformation with sensitivity of 100 %

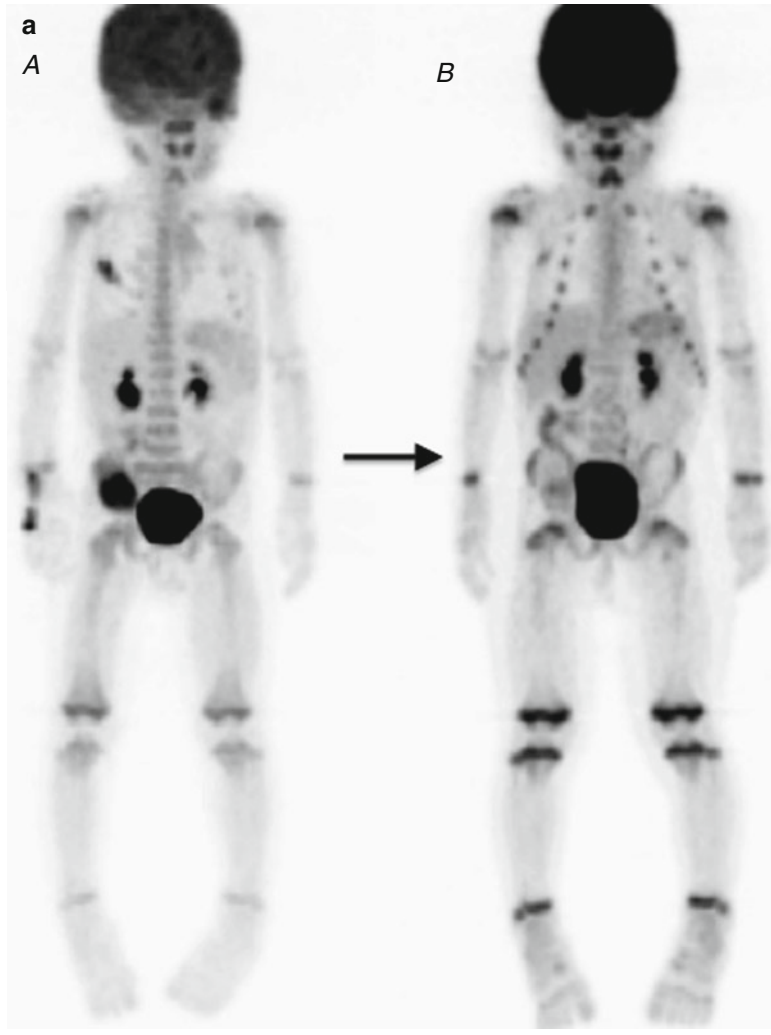

Fig. 23.13 (**a**, **b**) Multifocal Langerhans cell histiocytosis. A 2 year old male presented unable to walk with pain in the right leg and hip. Bone scan showed marked osteoblastic reaction in the right iliac bone and right 3rd rib (not shown). (**a**) Total body PET MIPS (**b**) Co-registered PET/CT images, (*A*) At diagnosis and (*B*) Post chemotherapy. The PET/CT scans at diagnosis (*aA, bA*) shows focal areas of increased uptake in the right iliac bone, third right rib and left petrous temporal bone (SUV max 6.5) with bone destruction on the CT component. Biopsy confirmed LCH. The PET/CT scans after chemotherapy (*aB, bB*) shows persisting lytic lesions on the CT but no significant metabolic activity on FDG PET with SUVmax 2.1

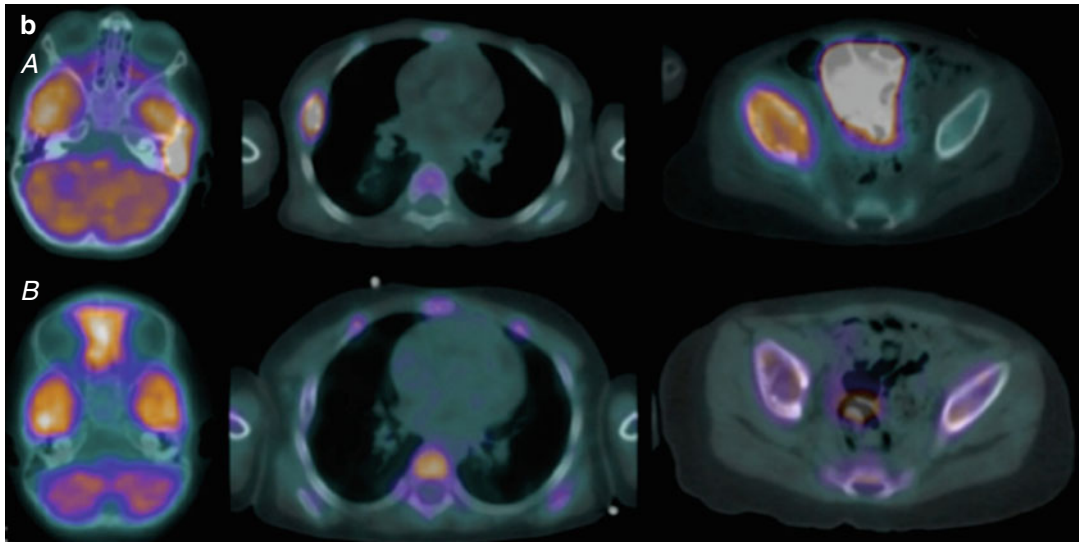

Fig. 23.13 (continued)

and specificity of 86 %. However, there can be an overlap of SUVmax values. Ferner et al. evaluated 105 adult patients with NF1 and symptomatic plexiform neurofibromas with ^{18}F-FDG PET. Twenty-eight malignant lesions were identified in 34 FDG-avid lesions. The SUVmax for all malignant lesions was >2.5. Six lesions were benign plexiform neurofibromas, and 2 were atypical plexiform neurofibromas. The mean SUVmax was 5.7 ± 2.6 in MPNST, and 1.5 ± 1.06 in plexiform neurofibromas. They recommended that symptomatic lesions with SUVmax 3.5 and above should be excised, lesions between 2.5 and 3.5 be reviewed clinically, and those with SUVmax <2.5 considered benign. Brenner et al. showed a significant differentiating ability for malignant transformation with SUVmax >3 and also correlated tumor SUV with long-term survival [104]. Warbey et al. improved the ability to differentiate benign from malignant lesions by performing imaging at 90 min and delayed imaging at 4 h post-FDG injection. They demonstrated a correlation between SUVmax and tumor grade. The sensitivity for diagnosing NF1 MPNST was 97 %, and specificity was 87 % using SUVmax >3.5 as the cutoff for surgical excision [105]. Recently Tsai et al. published data in pediatric NF1 patients, which further evaluated SUVmax in differentiating benign and malignant lesions and more specifically categorized MPNST into low-, intermediate-, and high-grade tumors. They report on 20 patients (average age 14.9 year) with 27 lesions, who had pathological and imaging correlation. The mean SUVmax of plexiform neurofibroma and MPNST were 2.49 (SD 1.50) and 7.63 (SD 2.96), respectively. When plexiform neurofibromas were separated into typical and atypical, there was no apparent difference in FDG-avidity. However, both subtypes showed a significant difference from MPNST. The sensitivity and specificity was optimal at 100 and 94 %, respectively, for distinguishing between neurofibroma and MPNST with a cutoff of SUVmax of 4.00 [106]. Fluorine-18-FDG PET/CT also may indicate the most metabolic site for biopsy. Benz et al. recommend that patients with suspected MPNST should have ^{18}F-FDG PET/CT imaging prior to surgery or biopsy (Fig. 23.14a). As many patients may require follow-up with PET, they recommend ^{18}F-FDG PET studies every six months for 2 years and then annually if the clinical status does not change [107]. Besides MPNSTs, patients with NF1 have an increased predisposition for other malignancies, which include GIST, rhabdomyosarcoma, carcinoid tumors, pheochromocytoma, and intracranial neoplasms. The most common intracranial tumors are optic

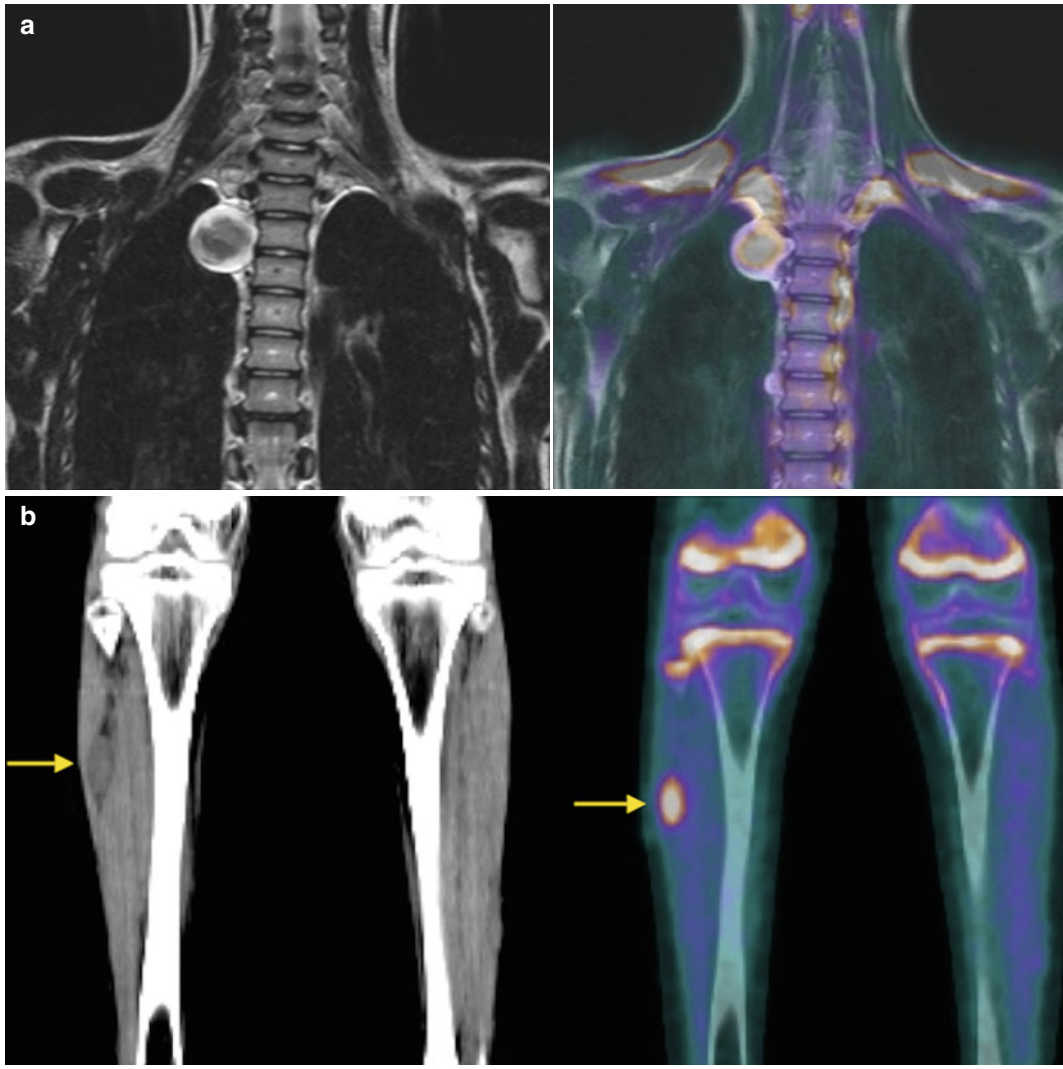

Fig. 23.14 (**a**) A 12-year-old female with NF1 showed an increasing mass in the thoracic paravertebral region T3–4 on MRI. Coronal MRI (T2FS + GAD) on left shows an enhancing lesion in the right paravertebral region. Co-registered MRI and ^{18}F-FDG PET show increased uptake (SUVmax7.8) suggesting malignant transformation. Note brown fat uptake in supraclavicular fossae and intercostal spaces. (**b**) Fluorine-18-FDG PET/CT of the lower legs with the CT (*left*) shows a plexiform neurofibroma in the lateral right calf (*arrow*) with mild FDG uptake (*right*) SUVmax 2.2. At surgery the thoracic lesion was an MPNST, and the right calf lesion was benign plexiform neurofibroma

nerve gliomas and brain stem gliomas. There is also increased risk of other tumors of the CNS including malignant astrocytomas, ependymomas, meningiomas, medulloblastomas, and MPNSTs arising from the cranial nerves. Optic nerve gliomas are histopathologically low-grade pilocytic astrocytomas. Patients <6 years of age are at greatest risk, and one-eighth will have progressive disease warranting specific treatment. This is usually by chemotherapy rather than radiation therapy [108]. Progressive optic pathway gliomas can appear metabolically active on ^{18}F-FDG PET. Fluorine-18-FDG may have a role in differentiating these

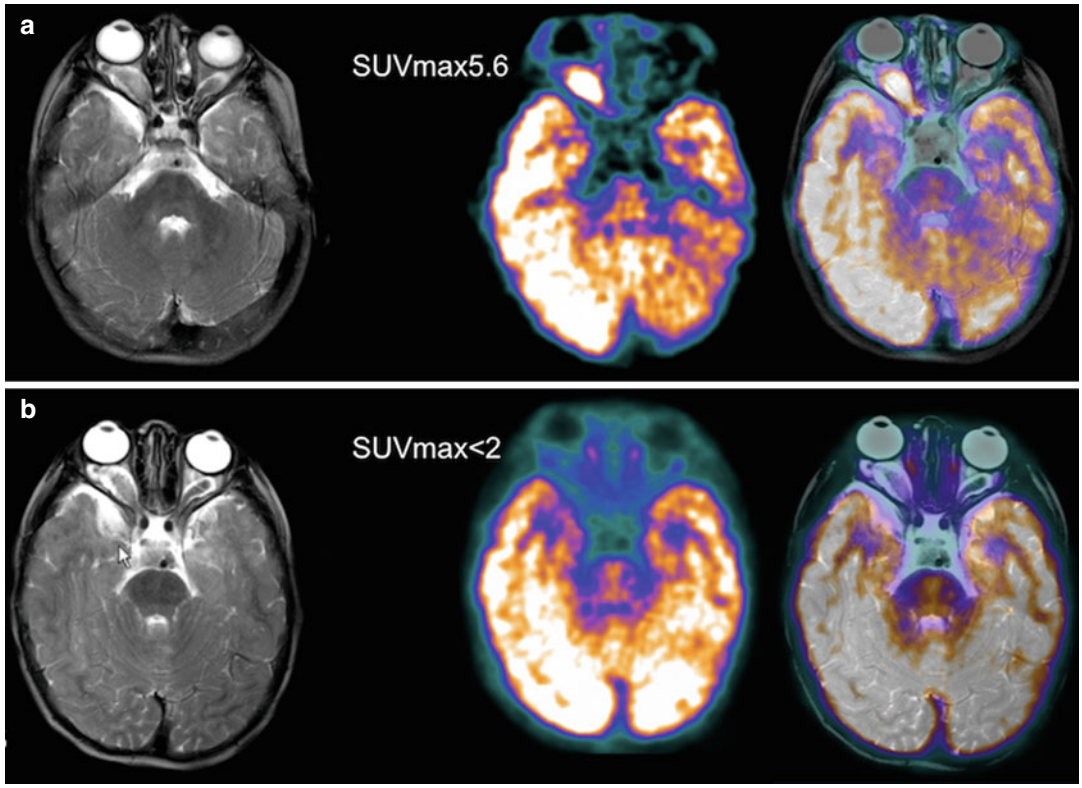

Fig. 23.15 Optic nerve gliomas. A 3-year-old male with NF1 and bilateral ONGs showed progressive proptosis and visual deterioration on the right and was treated with chemotherapy (vincristine and carboplatin). (**a**) (*top row*) MRI (T1Flair + GAD), FDG PET, co-registered MRI, and PET. The right OPG is FDG avid SUVmax 5.6 and minimal uptake in the left OPG. (**b**) (*lower row*) After chemotherapy, there is marked reduction in metabolic activity with the right OPG SUVmax <2. The patient's visual acuity improved and the proptosis stabilized

from those that are not likely to progress and/or cause morbidity. Fluorine-18-FDG PET has been shown to demonstrate the response to chemotherapy [109] (Fig. 23.15). Brain stem gliomas typically are low-grade gliomas and show an indolent clinical course compared to sporadic cases. Leonard et al. have shown that tumors outside the optic pathway, rapidly growing or arising in older children with NF1, may be more likely to be higher-grade lesions [110]. Fluorine-18-FDG PET is relatively accurate in predicting the tumor grade of CNS lesions except for pilocytic astrocytomas [109, 111]. MRI is the primary imaging technique. Areas of hyperintense signal on T2 weighted cerebral MRI scans, known as T2 hyperintensities (T2H), are seen in up to 90 % of patients with NF1. These lesions occur in the cortical and subcortical grey matter, basal ganglia, and in the deep white matter. Studies have suggested that there may be an association between discrete T2H in the thalami and cognitive impairment in children with NF1 [112, 113]. A significant challenge in children with NF1 is differentiating T2H from gliomas, especially in the setting of lesions that do not show contrast enhancement or a significant mass effect on MRI. T2H have reduced FDG uptake compared to nearby normal brain areas [114]. This is an important discriminating characteristic enabling these to be differentiated from non-optic pathway gliomas and to direct stereotactic biopsy. Application of PET agents ^{18}F-FDG and ^{18}F-ethyl-tyrosine (FET) for intracranial neoplasms also has been useful in determining residual or recurrent malignancy and differentiating recurrent disease from radiation necrosis [115,

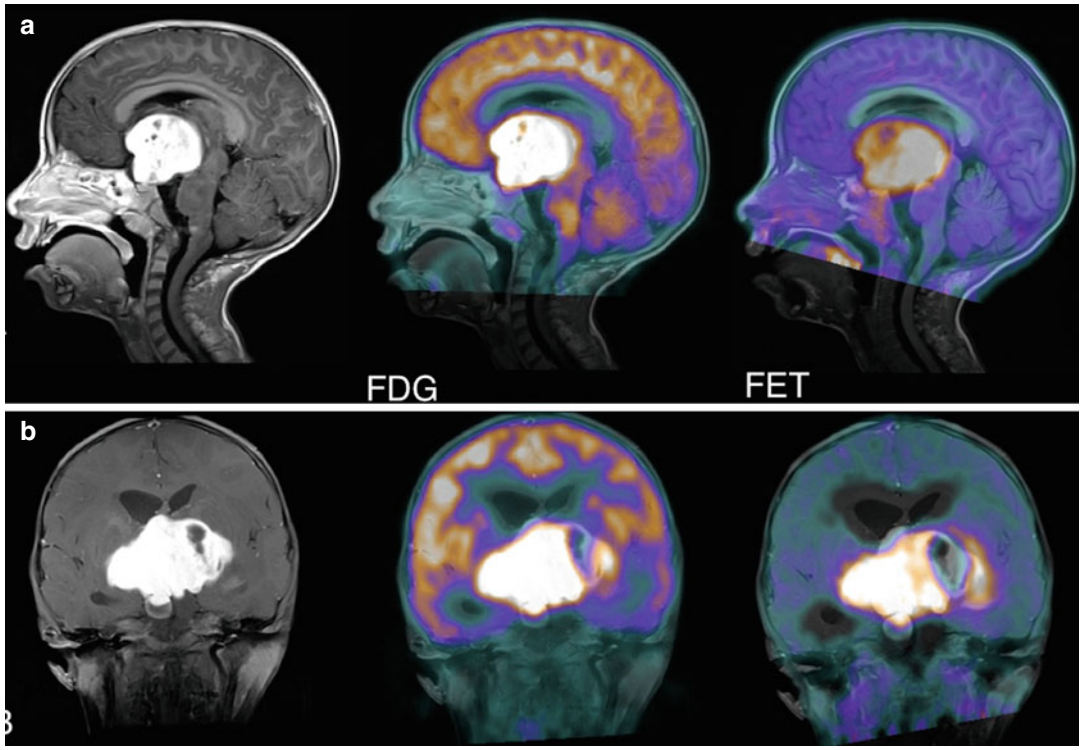

Fig. 23.16 A 3 year-old girl with NF1 presented with weight loss and lethargy. The sagittal (**a**) and coronal (**b**) MRI post-gadolinium T1 FLAIR sequences show a large hypothalamic tumor with contrast enhancement. The tumor deviates the brainstem and compresses the pituitary. Fused ^{18}F-FDG (*middle*) and ^{18}F-FET (*right*) PET images show intense uptake of both tracers in the tumor. Fluorine-18-FET images demonstrate greater target to background uptake, as there is little FET uptake in the normal cerebral cortex. Biopsy of the tumor revealed a pilocytic astrocytoma (WHO grade 1)

116]. Fluorine-18-FET PET in adults appears to be more accurate than ^{18}F-FDG in the detection of brain tumors regardless of tumor grade [115], but to date no studies have been published evaluating the performance of ^{18}F-FET PET in children with NF1. Our experience in pediatric patients at the Children's Hospital at Westmead, Sydney, parallels the adult experience (Fig. 23.16). Overall, the experience with PET radiotracers for brain tumors in adults with NF1 appears to be applicable to children with NF1 [117]. With regard to neurocognitive deficits, there is emerging evidence that children with NF1 have a different pattern of cerebral metabolism compared to children without this condition. A few small studies have suggested reduced glucose utilization in the thalamus and, less consistently, in various cortical regions [114, 118]. The significance of these changes is uncertain [119].

Epithelial Neoplasms and Malignant Melanoma

Carcinomas originate from epithelial tissues and are very rare in children and adolescents. All carcinomas combined account for less than 10 % of cancer in children. The majority of these are thyroid carcinoma, with nasopharyngeal (4.5 %), adrenocortical (1.3 %), and other skin carcinomas (0.5 %) combined being a small proportion and unspecified carcinomas 27.3 %. Approximately 75 % of carcinomas in childhood and adolescence occur between 15 and 19 years of age. Carcinomas commonly first metastasize to locoregional lymph nodes, but also may metastasize more distantly. Imaging usually includes contrast CT and MRI of the primary tumors for evaluation of the extent of the

primary tumor and determination of spread to locoregional lymph nodes. Bone scan and ^{18}F-FDG PET/CT play important roles in identifying skeletal metastases and other regional and distant metastases. The International Classification of Childhood Cancer (ICCC) classifies epithelial neoplasms and skin malignancy into six broad groups [120, 121]: adrenocortical carcinoma, thyroid carcinoma, nasopharyngeal carcinoma, malignant melanoma, skin cancer other than melanoma, and other and unspecified carcinomas.

Adrenocortical Carcinoma

Adrenocortical carcinoma is a rare malignancy with a poor prognosis in childhood. Patients may present with signs of virilization due to adrenal androgen secretion. Initial imaging is by CT scans and MRI for detection of the primary, locoregional disease and lung metastases. The initial treatment is adrenalectomy and adjuvant therapy with mitotane. Recurrence rates are high and imaging is required to detect early recurrence. Fluorine-18-FDG PET/CT has been reported for staging and for detection of recurrence and metastatic disease in adults and children [122–124].

Nasopharyngeal Carcinoma

Pediatric nasopharyngeal carcinoma is a rare disease in childhood and one of the few malignancies in childhood arising from epithelium. It accounts for <1 % of all childhood malignancies. It is distinguishable from the adult forms of disease due to a close association with Epstein-Barr virus (EBV). It usually has an undifferentiated histopathology with high incidence of locoregional nodal involvement. More than 80 % of children will have stage IV locoregional advanced disease at presentation. The early peak incidence in children and adolescents is 10–20 years of age with the adult peak at 40–60 years. The treatment guidelines have evolved from adult protocols, with current treatment usually including a combination of chemotherapy and radiotherapy [125]. Contrast-enhanced CT and MRI allow for assessment of the extent of local tumor growth, base of skull involvement, and regional lymph node involvement. CT is required for detection of pulmonary and liver metastases and bone scintigraphy for skeletal metastases. Fluorine-18-FDG PET/CT has been reported to be useful for confirming the extent of local disease, assessing regional nodal involvement, determining distant metastatic spread in adult patients [126]. Our institution routinely uses ^{18}F-FDG PET/CT at initial staging, for assessing response assessment, and for surveillance for recurrence of disease (Fig. 23.17).

Melanoma

Melanoma is reported to be rare in children and uncommon in adolescents. However, there has been an increasing incidence of melanoma in children over the last two decades with increases of 3–7 % being reported. Management of pediatric melanoma follows the principles used for adult melanoma. Sentinel lymph node biopsy (see Chap. 8) is recommended in intermediate-stage melanoma, as the status of the sentinel lymph nodee is the strongest indicator of survival in melanoma patients. If the sentinel node is positive, most centers will recommend therapeutic lymphadenectomy. Sentinel lymph node mapping can show many different patterns of lymph drainage. The technique has to be meticulous, and there must be good communication between the nuclear medicine physicians and surgeons involved [127]. Pediatric patients with melanoma generally present late and have a higher rate of positive sentinel lymph nodes than the adult population. The pediatric survival rate, however is higher than the adult rate [128]. If there is advanced melanoma with evidence of regional involvement or other distant metastatic spread, total body CT scans and ^{18}F-FDG PET/CT are recommended to accurately stage the disease. MRI of the brain may be indicated to exclude cerebral metastases [129].

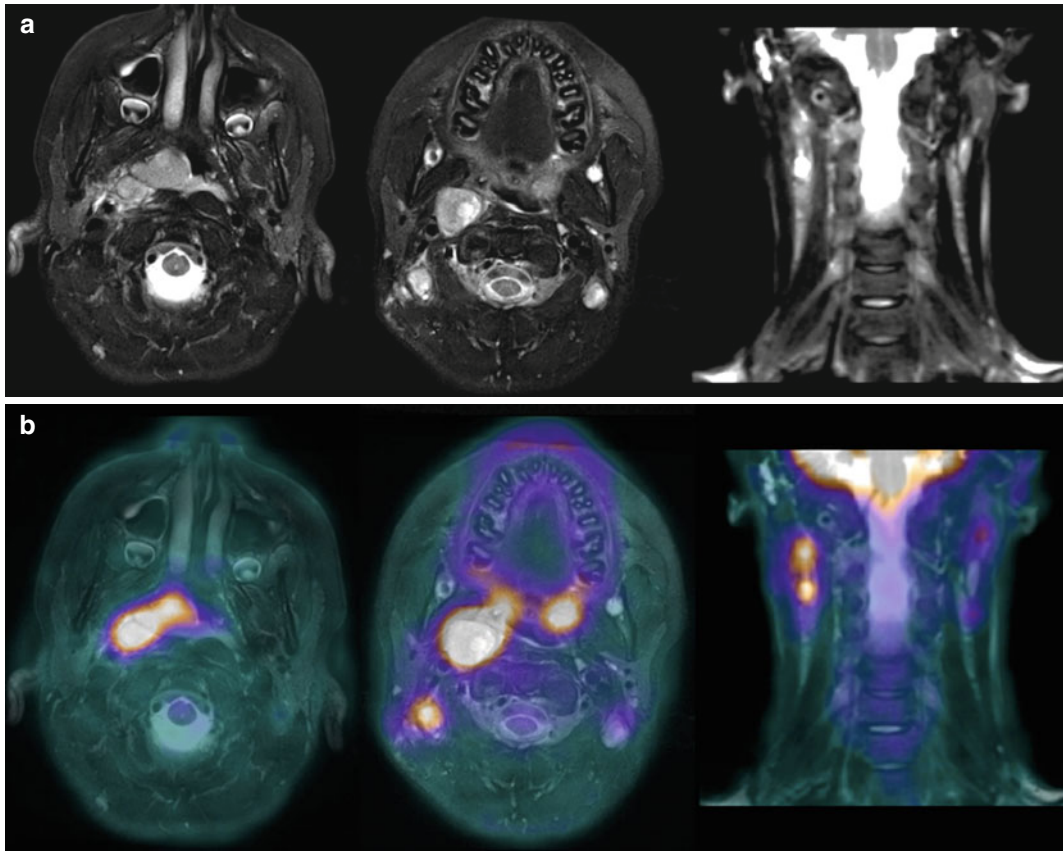

Fig. 23.17 Nasopharyngeal carcinoma. A 15-year-old female presented with enlarged lymph nodes in the right cervical region. Biopsy revealed metastatic carcinoma. CT showed a mass in the right nasopharynx (not shown). MRI T2FS axial ((**a**) *top row* left to right) showed a large enhancing mass in the right nasopharynx, abnormal lymph nodes in the right cervical chain, and probably abnormal nodes on the left side. (**b**) Fluorine-18-FDG PET/CT (co-registered MRI and PET *lower row*) confirms a hyper metabolic primary tumor (SUVmax 8.1) and abnormal lymph nodes in the right cervical chain, while the left cervical lymph nodes appear normal

References

1. Howman-Giles R, Bernard E, Uren R. Pediatric nuclear oncology. Q J Nucl Med. 1997;41(4):321–35.
2. Jadvar H, Connolly LP, Fahey FH, Shulkin BL. PET and PET/CT in pediatric oncology. Semin Nucl Med. 2007;37(5):316–31.
3. Connolly LP, Drubach LA, Ted TS. Applications of nuclear medicine in pediatric oncology. Clin Nucl Med. 2002;27(2):117–25.
4. Kleis M, Daldrup-Link H, Matthay K, et al. Diagnostic value of PET/CT for the staging and restaging of pediatric tumors. Eur J Nucl Med Mol Imaging. 2009; 36(1):23–36.
5. London K, Stege C, Cross S, et al. 18F-FDG PET/CT compared to conventional imaging modalities in pediatric primary bone tumors. Pediatr Radiol. 2012;42(4): 418–30.
6. Franzius C, Juergens KU. PET/CT in paediatric oncology: indications and pitfalls. Pediatr Radiol. 2009;39 Suppl 3:446–9.
7. Dasgupta R, Rodeberg DA. Update on rhabdomyosarcoma. Semin Pediatr Surg. 2012;21(1):68–78.
8. Baum SH, Fruhwald M, Rahbar K, Wessling J, Schober O, Weckesser M. Contribution of PET/CT to prediction of outcome in children and young adults with rhabdomyosarcoma. J Nucl Med. 2011; 52(10):1535–40.
9. Hayes-Jordan A. Recent advances in non-rhabdomyosarcoma soft-tissue sarcomas. Semin Pediatr Surg. 2012;21(1):61–7.
10. La TH, Wolden SL, Rodeberg DA, et al. Regional nodal involvement and patterns of spread along intransit pathways in children with rhabdomyosarcoma of the extremity: a report from the Children's Oncology Group. Int J Radiat Oncol Biol Phys. 2011; 80(4):1151–7.

11. Gow KW, Rapkin LB, Olson TA, Durham MM, Wyly B, Shehata BM. Sentinel lymph node biopsy in the pediatric population. J Pediatr Surg. 2008;43(12): 2193–8.
12. Kayton ML, Delgado R, Busam K, et al. Experience with 31 sentinel lymph node biopsies for sarcomas and carcinomas in pediatric patients. Cancer. 2008; 112(9):2052–9.
13. Juweid ME, Stroobants S, Hoekstra OS, et al. Use of positron emission tomography for response assessment of lymphoma: consensus of the Imaging Subcommittee of International Harmonization Project in Lymphoma. J Clin Oncol. 2007;25(5):571–8.
14. London K, Cross S, Onikul E, Dalla-Pozza L, Howman-Giles R. 18F-FDG PET/CT in paediatric lymphoma: comparison with conventional imaging. Eur J Nucl Med Mol Imaging. 2011;38(2):274–84.
15. Zinzani PL, Rigacci L, Stefoni V, et al. Early interim 18F-FDG PET in Hodgkin's lymphoma: evaluation on 304 patients. Eur J Nucl Med Mol Imaging. 2012;39(1):4–12.
16. Stiller CA, Allen MB, Eatock EM. Childhood cancer in Britain: the National Registry of Childhood Tumours and incidence rates 1978–1987. Eur J Cancer. 1995;31A(12):2028–34.
17. Rivera MN, Haber DA. Wilms' tumour: connecting tumorigenesis and organ development in the kidney. Nat Rev Cancer. 2005;5(9):699–712.
18. Little M, Wells C. A clinical overview of WT1 gene mutations. Hum Mutat. 1997;9(3):209–25.
19. Breslow NE, Olson J, Moksness J, Beckwith JB, Grundy P. Familial Wilms' tumor: a descriptive study. Med Pediatr Oncol. 1996;27(5):398–403.
20. Faria P, Beckwith JB, Mishra K, et al. Focal versus diffuse anaplasia in Wilms tumor–new definitions with prognostic significance: a report from the National Wilms Tumor Study Group. Am J Surg Pathol. 1996;20(8):909–20.
21. Moinul Hossain AK, Shulkin BL, Gelfand MJ, et al. FDG positron emission tomography/computed tomography studies of Wilms' tumor. Eur J Nucl Med Mol Imaging. 2010;37(7):1300–8.
22. Hamilton TE, Shamberger RC. Wilms tumor: recent advances in clinical care and biology. Semin Pediatr Surg. 2012;21(1):15–20.
23. Misch D, Steffen IG, Schonberger S, et al. Use of positron emission tomography for staging, preoperative response assessment and posttherapeutic evaluation in children with Wilms tumour. Eur J Nucl Med Mol Imaging. 2008;35(9):1642–50.
24. Begent J, Sebire NJ, Levitt G, et al. Pilot study of F(18)-fluorodeoxyglucose positron emission tomography/computerised tomography in Wilms' tumour: correlation with conventional imaging, pathology and immunohistochemistry. Eur J Cancer. 2011; 47(3):389–96.
25. Ahmed HU, Arya M, Levitt G, Duffy PG, Mushtaq I, Sebire NJ. Part I: primary malignant non-Wilms' renal tumours in children. Lancet Oncol. 2007;8(8):730–7.
26. Krajewski KM, Giardino AA, Zukotynski K, Van den Abbeele AD, Pedrosa I. Imaging in renal cell carcinoma. Hematol Oncol Clin North Am. 2011;25(4): 687–715.
27. Ahmed HU, Arya M, Levitt G, Duffy PG, Sebire NJ, Mushtaq I. Part II: treatment of primary malignant non-Wilms' renal tumours in children. Lancet Oncol. 2007;8(9):842–8.
28. Gonzalez-Crussi F, Baum ES. Renal sarcomas of childhood. A clinicopathologic and ultrastructural study. Cancer. 1983;51(5):898–912.
29. Smets AM, de Kraker J. Malignant tumours of the kidney: imaging strategy. Pediatr Radiol. 2010;40(6): 1010–8.
30. Pirro V, Skanjeti A, Pelosi E. 18F-fluorodeoxyglucose-positron emission tomography in the characterization of suspected rhabdoid renal tumor recurrence: a case report. J Pediatr Hematol Oncol. 2007;29(1): 69–71.
31. Howman-Giles R, McCowage G, Kellie S, Graf N. Extrarenal malignant rhabdoid tumor in childhood application of 18F-FDG PET/CT. J Pediatr Hematol Oncol. 2012;34(1):17–21.
32. von Schweinitz D. Hepatoblastoma: recent developments in research and treatment. Semin Pediatr Surg. 2012;21(1):21–30.
33. Mody RJ, Pohlen JA, Malde S, Strouse PJ, Shulkin BL. FDG PET for the study of primary hepatic malignancies in children. Pediatr Blood Cancer. 2006;47(1): 51–5.
34. Philip I, Shun A, McCowage G, Howman-Giles R. Positron emission tomography in recurrent hepatoblastoma. Pediatr Surg Int. 2005;21(5):341–5.
35. Figarola MS, McQuiston SA, Wilson F, Powell R. Recurrent hepatoblastoma with localization by PET-CT. Pediatr Radiol. 2005;35(12):1254–8.
36. Sacks A, Peller PJ, Surasi DS, Chatburn L, Mercier G, Subramaniam RM. Value of PET/CT in the management of primary hepatobiliary tumors, part 2. AJR Am J Roentgenol. 2011;197(2):W260–5.
37. Goh V, Sarker D, Osmany S, Cook GJ. Functional imaging techniques in hepatocellular carcinoma. Eur J Nucl Med Mol Imaging. 2012;39(6):1070–9.
38. Yoon KT, Kim JK, Kim do Y, et al. Role of 18F-fluorodeoxyglucose positron emission tomography in detecting extrahepatic metastasis in pretreatment staging of hepatocellular carcinoma. Oncology. 2007;72 Suppl 1:104–10.
39. Higashi T, Hatano E, Ikai I, et al. FDG PET as a prognostic predictor in the early post-therapeutic evaluation for unresectable hepatocellular carcinoma. Eur J Nucl Med Mol Imaging. 2010;37(3):468–82.
40. Blum HE. Hepatocellular carcinoma: therapy and prevention. World J Gastroenterol. 2005;11(47): 7391–400.
41. Lambert B, Van de Wiele C. Treatment of hepatocellular carcinoma by means of radiopharmaceuticals. Eur J Nucl Med Mol Imaging. 2005;32(8):980–9.
42. MacCarthy A, Draper GJ, Steliarova-Foucher E, Kingston JE. Retinoblastoma incidence and survival

in European children (1978–1997). Report from the Automated Childhood Cancer Information System project. Eur J Cancer. 2006;42(13):2092–102.
43. Abramson DH. Retinoblastoma in the 20th century: past success and future challenges the Weisenfeld lecture. Invest Ophthalmol Vis Sci. 2005;46(8):2683–91.
44. Poulaki V, Mukai S. Retinoblastoma: genetics and pathology. Int Ophthalmol Clin. 2009;49(1):155–64.
45. Karcioglu ZA, al-Mesfer SA, Abboud E, Jabak MH, Mullaney PB. Workup for metastatic retinoblastoma. A review of 261 patients. Ophthalmology. 1997;104(2):307–12.
46. Chintagumpala M, Chevez-Barrios P, Paysse EA, Plon SE, Hurwitz R. Retinoblastoma: review of current management. Oncologist. 2007;12(10):1237–46.
47. de Graaf P, Goricke S, Rodjan F, et al. Guidelines for imaging retinoblastoma: imaging principles and MRI standardization. Pediatr Radiol. 2012;42(1): 2–14.
48. Pratt CB, Crom DB, Magill L, Chenaille P, Meyer D. Skeletal scintigraphy in patients with bilateral retinoblastoma. Cancer. 1990;65(1):26–8.
49. Radhakrishnan V, Kumar R, Malhotra A, Bakhshi S. Role of PET/CT in staging and evaluation of treatment response after 3 cycles of chemotherapy in locally advanced retinoblastoma: a prospective study. J Nucl Med. 2012;53(2):191–8.
50. Rescorla FJ. Pediatric germ cell tumors. Semin Pediatr Surg. 2012;21(1):51–60.
51. Horton Z, Schlatter M, Schultz S. Pediatric germ cell tumors. Surg Oncol. 2007;16(3):205–13.
52. Poynter JN, Amatruda JF, Ross JA. Trends in incidence and survival of pediatric and adolescent patients with germ cell tumors in the United States, 1975 to 2006. Cancer. 2010;116(20):4882–91.
53. NCI: www.cancer.gov/cancertopics/pdq/treatment/extracranial-germ-cell/HealthProfessional/page2.
54. Howman-Giles R, Holland AJ, Mihm D, Montfort JM, Arbuckle S, Kellie S. Somatic malignant transformation in a sacrococcygeal teratoma in a child and the use of F18FDG PET imaging. Pediatr Surg Int. 2008;24(4):475–8.
55. Oechsle K, Hartmann M, Brenner W, et al. [18F]fluorodeoxyglucose positron emission tomography in nonseminomatous germ cell tumors after chemotherapy: the German multicenter positron emission tomography study group. J Clin Oncol. 2008;26(36):5930–5.
56. Sohaib SA, Cook G, Koh DM. Imaging studies for germ cell tumors. Hematol Oncol Clin North Am. 2011;25(3):487–502, vii.
57. Cremerius U, Effert PJ, Adam G, et al. FDG PET for detection and therapy control of metastatic germ cell tumor. J Nucl Med. 1998;39(5):815–22.
58. de Wit M, Brenner W, Hartmann M, et al. [18F]-FDG-PET in clinical stage I/II non-seminomatous germ cell tumours: results of the German multicentre trial. Ann Oncol. 2008;19(9):1619–23.
59. Albers P, Bender H, Yilmaz H, Schoeneich G, Biersack HJ, Mueller SC. Positron emission tomography in the clinical staging of patients with stage I and II testicular germ cell tumors. Urology. 1999;53(4): 808–11.
60. Huddart RA, O'Doherty MJ, Padhani A, et al. 18fluorodeoxyglucose positron emission tomography in the prediction of relapse in patients with high-risk, clinical stage I nonseminomatous germ cell tumors: preliminary report of MRC Trial TE22–the NCRI Testis Tumour Clinical Study Group. J Clin Oncol. 2007;25(21):3090–5.
61. De Santis M, Becherer A, Bokemeyer C, et al. 2-18fluoro-deoxy-D-glucose positron emission tomography is a reliable predictor for viable tumor in postchemotherapy seminoma: an update of the prospective multicentric SEMPET trial. J Clin Oncol. 2004;22(6):1034–9.
62. Hain SF, O'Doherty MJ, Timothy AR, Leslie MD, Harper PG, Huddart RA. Fluorodeoxyglucose positron emission tomography in the evaluation of germ cell tumours at relapse. Br J Cancer. 2000;83(7): 863–9.
63. Akbulut Z, Canda AE, Atmaca AF, Caglayan A, Asil E, Balbay MD. Is positron emission tomography reliable to predict post-chemotherapy retroperitoneal lymph node involvement in advanced germ cell tumors of the testis? Urol J. 2011;8(2):120–6.
64. Spunt SL, Skapek SX, Coffin CM. Pediatric nonrhabdomyosarcoma soft tissue sarcomas. Oncologist. 2008;13(6):668–78.
65. Smith MA, Seibel NL, Altekruse SF, et al. Outcomes for children and adolescents with cancer: challenges for the twenty-first century. J Clin Oncol. 2010;28(15):2625–34.
66. Linabery AM, Ross JA. Childhood and adolescent cancer survival in the US by race and ethnicity for the diagnostic period 1975–1999. Cancer. 2008;113(9): 2575–96.
67. Lisle JW, Eary JF, O'Sullivan J, Conrad EU. Risk assessment based on FDG-PET imaging in patients with synovial sarcoma. Clin Orthop Relat Res. 2009;467(6):1605–11.
68. Cheung MC, Zhuge Y, Yang R, et al. Incidence and outcomes of extremity soft-tissue sarcomas in children. J Surg Res. 2010;163(2):282–9.
69. Rubin BP, Schuetze SM, Eary JF, et al. Molecular targeting of platelet-derived growth factor B by imatinib mesylate in a patient with metastatic dermatofibrosarcoma protuberans. J Clin Oncol. 2002;20(17): 3586–91.
70. Kovach SJ, Fischer AC, Katzman PJ, et al. Inflammatory myofibroblastic tumors. J Surg Oncol. 2006;94(5):385–91.
71. Howman-Giles R, London K, McCowage G, Graf N, Harvey J. Pulmonary inflammatory myofibroblastic tumor after Hodgkin's lymphoma and application of PET imaging. Pediatr Surg Int. 2008;24(8):947–51.
72. Carli M, Ferrari A, Mattke A, et al. Pediatric malignant peripheral nerve sheath tumor: the Italian and German soft tissue sarcoma cooperative group. J Clin Oncol. 2005;23(33):8422–30.

73. Zou C, Smith KD, Liu J, et al. Clinical, pathological, and molecular variables predictive of malignant peripheral nerve sheath tumor outcome. Ann Surg. 2009;249(6):1014–22.
74. Punt SE, Eary JF, O'Sullivan J, Conrad EU. Fluorodeoxyglucose positron emission tomography in leiomyosarcoma: imaging characteristics. Nucl Med Commun. 2009;30(7):546–9.
75. Hayes-Jordan A, Anderson PM. The diagnosis and management of desmoplastic small round cell tumor: a review. Curr Opin Oncol. 2011;23(4):385–9.
76. Zhang WD, Li CX, Liu QY, Hu YY, Cao Y, Huang JH. CT, MRI, and FDG-PET/CT imaging findings of abdominopelvic desmoplastic small round cell tumors: correlation with histopathologic findings. Eur J Radiol. 2011;80(2):269–73.
77. Ben-Sellem D, Liu KL, Cimarelli S, Constantinesco A, Imperiale A. Desmoplastic small round cell tumor: impact of F-FDG PET induced treatment strategy in a patient with long-term outcome. Rare Tumors. 2009;1(1):e19.
78. Nguyen BD, Roarke MC, Ram PC. PET monitoring of clear cell sarcoma of tendons and aponeuroses. Clin Nucl Med. 2007;32(5):415–7.
79. Finley JW, Hanypsiak B, McGrath B, Kraybill W, Gibbs JF. Clear cell sarcoma: the Roswell Park experience. J Surg Oncol. 2001;77(1):16–20.
80. Maduekwe UN, Hornicek FJ, Springfield DS, et al. Role of sentinel lymph node biopsy in the staging of synovial, epithelioid, and clear cell sarcomas. Ann Surg Oncol. 2009;16(5):1356–63.
81. Brenner W, Conrad EU, Eary JF. FDG PET imaging for grading and prediction of outcome in chondrosarcoma patients. Eur J Nucl Med Mol Imaging. 2004;31(2):189–95.
82. Wu X, Dagar V, Algar E, et al. Rhabdoid tumour: a malignancy of early childhood with variable primary site, histology and clinical behaviour. Pathology. 2008;40(7):664–70.
83. Sasajima T, Oda M, Kinouchi H, Hatazawa J, Mizoi K. [Frontal atypical teratoid/rhabdoid tumor evaluated by single-photon emission computerized tomography and positron emission tomography]. No Shinkei Geka. 2002;30(6):639–45.
84. Chen YW, Huang MY, Chang CC, et al. FDG PET/CT findings of epithelioid sarcoma in a pediatric patient. Clin Nucl Med. 2007;32(11):898–901.
85. Sobanko JF, Meijer L, Nigra TP. Epithelioid sarcoma: a review and update. J Clin Aesthet Dermatol. 2009;2(5):49–54.
86. Stacchiotti S, Negri T, Zaffaroni N, et al. Sunitinib in advanced alveolar soft part sarcoma: evidence of a direct antitumor effect. Ann Oncol. 2011;22(7):1682–90.
87. Jadvar H, Fischman AJ. Evaluation of rare tumors with [F-18]fluorodeoxyglucose positron emission tomography. Clin Positron Imaging. 1999;2(3):153–8.
88. Murphy JJ, Tawfeeq M, Chang B, Nadel H. Early experience with PET/CT scan in the evaluation of pediatric abdominal neoplasms. J Pediatr Surg. 2008;43(12):2186–92.
89. Benesch M, Wardelmann E, Ferrari A, Brennan B, Verschuur A. Gastrointestinal stromal tumors (GIST) in children and adolescents: a comprehensive review of the current literature. Pediatr Blood Cancer. 2009;53(7):1171–9.
90. Janeway KA, Pappo A. Treatment guidelines for gastrointestinal stromal tumors in children and young adults. J Pediatr Hematol Oncol. 2012;34 Suppl 2:S69–72.
91. Janeway KA, Weldon CB. Pediatric gastrointestinal stromal tumor. Semin Pediatr Surg. 2012;21(1): 31–43.
92. Chikwava K, Jaffe R. Langerin (CD207) staining in normal pediatric tissues, reactive lymph nodes, and childhood histiocytic disorders. Pediatr Dev Pathol. 2004;7(6):607–14.
93. Arceci RJ, Longley BL, Emanuel PD. Atypical cellular disorders. Hematology 2002;1:297–314
94. Jubran RF, Marachelian A, Dorey F, Malogolowkin M. Predictors of outcome in children with Langerhans cell histiocytosis. Pediatr Blood Cancer. 2005;45(1):37–42.
95. Azouz EM, Saigal G, Rodriguez MM, Podda A. Langerhans' cell histiocytosis: pathology, imaging and treatment of skeletal involvement. Pediatr Radiol. 2005;35(2):103–15.
96. Porn U, Howman-Giles R, Onikul E, Uren R. Langerhans cell histiocytosis of the lumbar spine. Clin Nucl Med. 2003;28(1):52–3.
97. Braier J, Ciocca M, Latella A, de Davila MG, Drajer M, Imventarza O. Cholestasis, sclerosing cholangitis, and liver transplantation in Langerhans cell histiocytosis. Med Pediatr Oncol. 2002;38(3): 178–82.
98. McClain K, Ramsay NK, Robison L, Sundberg RD, Nesbit Jr M. Bone marrow involvement in histiocytosis X. Med Pediatr Oncol. 1983;11(3):167–71.
99. Ribeiro MJ, Idbaih A, Thomas C, et al. 18F-FDG PET in neurodegenerative Langerhans cell histiocytosis : results and potential interest for an early diagnosis of the disease. J Neurol. 2008; 255(4):575–80.
100. McCarville MB. The child with bone pain: malignancies and mimickers. Cancer Imaging. 2009;9(Spec No A):S115–21.
101. Dogan AS, Conway JJ, Miller JH, Grier D, Bhattathiry MM, Mitchell CS. Detection of bone lesions in Langerhans cell histiocytosis: complementary roles of scintigraphy and conventional radiography. J Pediatr Hematol Oncol. 1996;18(1):51–8.
102. Kaste SC, Rodriguez-Galindo C, McCarville ME, Shulkin BL. PET-CT in pediatric Langerhans cell histiocytosis. Pediatr Radiol. 2007;37(7):615–22.
103. Phillips M, Allen C, Gerson P, McClain K. Comparison of FDG-PET scans to conventional radiography and bone scans in management of Langerhans cell histiocytosis. Pediatr Blood Cancer. 2009;52(1):97–101.
104. Brenner W, Friedrich RE, Gawad KA, et al. Prognostic relevance of FDG PET in patients with

neurofibromatosis type-1 and malignant peripheral nerve sheath tumours. Eur J Nucl Med Mol Imaging. 2006;33(4):428–32.
105. Warbey VS, Ferner RE, Dunn JT, Calonje E, O'Doherty MJ. [18F]FDG PET/CT in the diagnosis of malignant peripheral nerve sheath tumours in neurofibromatosis type-1. Eur J Nucl Med Mol Imaging. 2009;36(5):751–7.
106. Tsai LL, Drubach L, Fahey F, Irons M, Voss S, Ullrich NJ. [18F]-Fluorodeoxyglucose positron emission tomography in children with neurofibromatosis type 1 and plexiform neurofibromas: correlation with malignant transformation. J Neurooncol. 2012;108(3):469–75.
107. Benz MR, Czernin J, Dry SM, et al. Quantitative F18-fluorodeoxyglucose positron emission tomography accurately characterizes peripheral nerve sheath tumors as malignant or benign. Cancer. 2010; 116(2):451–8.
108. Patil S, Chamberlain RS. Neoplasms associated with germline and somatic NF1 gene mutations. Oncologist. 2012;17(1):101–16.
109. Moharir M, London K, Howman-Giles R, North K. Utility of positron emission tomography for tumour surveillance in children with neurofibromatosis type 1. Eur J Nucl Med Mol Imaging. 2010;37(7): 1309–17.
110. Leonard JR, Perry A, Rubin JB, King AA, Chicoine MR, Gutmann DH. The role of surgical biopsy in the diagnosis of glioma in individuals with neurofibromatosis-1. Neurology. 2006;67(8):1509–12.
111. Borgwardt L, Hojgaard L, Carstensen H, et al. Increased fluorine-18 2-fluoro-2-deoxy-D-glucose (FDG) uptake in childhood CNS tumors is correlated with malignancy grade: a study with FDG positron emission tomography/magnetic resonance imaging coregistration and image fusion. J Clin Oncol. 2005;23(13):3030–7.
112. Hyman SL, Gill DS, Shores EA, Steinberg A, North KN. T2 Hyperintensities in children with neurofibromatosis type 1 and their relationship to cognitive functioning. J Neurol Neurosurg Psychiatry. 2007;78(10):1088–91.
113. Gill DS, Hyman SL, Steinberg A, North KN. Age-related findings on MRI in neurofibromatosis type 1. Pediatr Radiol. 2006;36(10):1048–56.
114. Kaplan AM, Chen K, Lawson MA, Wodrich DL, Bonstelle CT, Reiman EM. Positron emission tomography in children with neurofibromatosis-1. J Child Neurol. 1997;12(8):499–506.
115. Lau EW, Drummond KJ, Ware RE, et al. Comparative PET study using F-18 FET and F-18 FDG for the evaluation of patients with suspected brain tumour. J Clin Neurosci. 2010;17(1):43–9.
116. Dunet V, Rossier C, Buck A, Stupp R, Prior JO. Performance of 18F-fluoro-ethyl-tyrosine (18F-FET) PET for the differential diagnosis of primary brain tumor: a systematic review and metaanalysis. J Nucl Med. 2012;53(2):207–14.
117. Pirotte B, Acerbi F, Lubansu A, Goldman S, Brotchi J, Levivier M. PET imaging in the surgical management of pediatric brain tumors. Childs Nerv Syst. 2007;23(7):739–51.
118. Buchert R, von Borczyskowski D, Wilke F, et al. Reduced thalamic 18F-flurodeoxyglucose retention in adults with neurofibromatosis type 1. Nucl Med Commun. 2008;29(1):17–26.
119. Payne JM, Moharir MD, Webster R, North KN. Brain structure and function in neurofibromatosis type 1: current concepts and future directions. J Neurol Neurosurg Psychiatry. 2010;81(3):304–9.
120. Bernstein L, Gurney J. Carcinomas and other malignant epithelial neoplasms. http://seer.cancer.gov/publications/childhood/carcinomas.pdf.
121. Kramarova E, Stiller CA. The international classification of childhood cancer. Int J Cancer. 1996;68(6):759–65.
122. Binkovitz I, Henwood M, Caniano D, Ruymann F, Binkovitz L. Early detection of recurrent pediatric adrenal cortical carcinoma using FDG-PET. Clin Nucl Med. 2008;33(3):186–8.
123. Mackie GC, Shulkin BL, Ribeiro RC, et al. Use of [18F]fluorodeoxyglucose positron emission tomography in evaluating locally recurrent and metastatic adrenocortical carcinoma. J Clin Endocrinol Metab. 2006;91(7):2665–71.
124. Wong KK, Arabi M, Zerizer I, Al-Nahhas A, Rubello D, Gross MD. Role of positron emission tomography/computed tomography in adrenal and neuroendocrine tumors: fluorodeoxyglucose and nonfluorodeoxyglucose tracers. Nucl Med Commun. 2011;32(9):764–81.
125. Ayan I, Kaytan E, Ayan N. Childhood nasopharyngeal carcinoma: from biology to treatment. Lancet Oncol. 2003;4(1):13–21.
126. Gordin A, Golz A, Daitzchman M, et al. Fluorine-18 fluorodeoxyglucose positron emission tomography/computed tomography imaging in patients with carcinoma of the nasopharynx: diagnostic accuracy and impact on clinical management. Int J Radiat Oncol Biol Phys. 2007;68(2):370–6.
127. Uren RF, Howman-Giles R, Thompson JF, et al. Lymphoscintigraphy to identify sentinel lymph nodes in patients with melanoma. Melanoma Res. 1994;4(6):395–9.
128. Howman-Giles R, Shaw HM, Scolyer RA, et al. Sentinel lymph node biopsy in pediatric and adolescent cutaneous melanoma patients. Ann Surg Oncol. 2010;17(1):138–43.
129. Uren RF, Howman-Giles R, Chung D, Thompson JF. Guidelines for lymphoscintigraphy and F18 FDG PET scans in melanoma. J Surg Oncol. 2011;104(4):405–19.

Infection and Inflammation

24

Christopher J. Palestro

Despite dramatic advances in its prevention and treatment, infection remains a major cause of morbidity in children, accounting for approximately 30 % of childhood deaths worldwide [1]. The development of powerful antimicrobial agents has improved patient survival, but timely diagnosis is equally, if not more, important. In adults, most infections can be diagnosed with a thorough history, a complete physical examination, and appropriate laboratory tests. In the pediatric population, unfortunately, this is a difficult task. Children do not, or will not, verbalize their feelings, and often the history is little more than secondhand information obtained from a parent. The physical examination of an ailing child can be difficult, if not impossible. Further complicating matters is the fact that conditions such as vasculitis and other inflammatory diseases can mimic infection. Consequently, empiric treatment with antibiotics, which may be neither appropriate nor effective, often is instituted. Imaging procedures usually are reserved for those patients in whom symptoms or physical findings point to a specific region of the body. Because of concerns about radiation exposure, pediatricians tend to utilize radionuclide imaging only as a last recourse after all other resources have been exhausted. The nuclear physician often is faced with the formidable task of diagnosing and localizing infection and inflammation late in the course of an illness when an expeditious and correct diagnosis is even more critical.

C.J. Palestro, MD
Department of Radiology, Hofstra North Shore-LIJ School of Medicine, Hempstead, NY, USA

Division of Nuclear Medicine and Molecular Imaging, Department of Radiology, North Shore Long Island Jewish Health System, New Hyde Park, NY, USA
e-mail: palestro@nshs.edu

Tracers

Methylene Diphosphonate (MDP)

The uptake of ^{99m}Tc-MDP depends on blood flow and the rate of new bone formation. When performed for osteomyelitis, a three-phase study usually is performed. Three-phase bone imaging consists of a dynamic imaging sequence, the perfusion phase, followed immediately by static images of the region of interest, the blood pool or soft tissue phase. The third, or bone, phase is performed 2–4 h later. Images should be acquired on a large field of view gamma camera equipped with a low-energy, high-resolution parallel hole collimator and a 15–20 % window centered on 140 keV. The usual injected dose is 9–11 MBq (0.20–0.30 mCi)/kg of ^{99m}Tc-MDP [2]. In children, the normal distribution of this tracer, by 2 h after injection, includes the skeleton, urinary tract, and soft tissues. Intense, symmetric uptake in the physes of the long bones, which are centers of growth and hematopoietic production, is present. Intense uptake can be appreciated in the marrow-rich flat facial bones as well [3].

S.T. Treves (ed.), *Pediatric Nuclear Medicine and Molecular Imaging*,
DOI 10.1007/978-1-4614-9551-2_24,

Gallium-67

For nearly 40 years, gallium-67 citrate (^{67}Ga) has been used for localizing foci of infection and inflammation. In spite of its disadvantages, including an inherent nonspecificity, the delay between injection and imaging, poor imaging characteristics, and a variable biodistribution that can confound image interpretation, gallium imaging remains useful, providing information that is complimentary to, and at times not available from, other tests.

^{67}Ga, a group III transition metal with a half-life of 78 h, emits a broad spectrum of gamma rays between 92 and 889 keV. Energies suitable for imaging include 92 keV (38 %), 184 keV (23 %), and 300 keV (16 %). By 24 h after injection, about 10–25 % of the administered dose is excreted via the kidneys. The large bowel is the principal excretory pathway beyond 24 h. At 72 h after injection, about 75 % of the administered dose remains in the body, equally distributed among the soft tissues, bone/bone marrow, and liver [4]. The normal distribution, however, is variable. Nasopharyngeal and lacrimal gland activity can be quite prominent, even in the absence of disease. Breast uptake usually is faint and symmetric; intense uptake is associated with hyperprolactinemic conditions such as pregnancy, lactation, certain drugs, and hypothalamic lesions (Fig. 24.1) [5–8]. In patients who have undergone multiple transfusions, increased renal, bladder, and bone activity, together with decreased hepatic and colonic activity, can be observed, presumably due to iron receptor saturation by exogenous iron from the transfused cells [9]. The MRI contrast agent gadolinium can cause a similar alteration in the biodistribution of gallium [10].

Several factors govern gallium uptake in inflammation and it is not necessary that they all

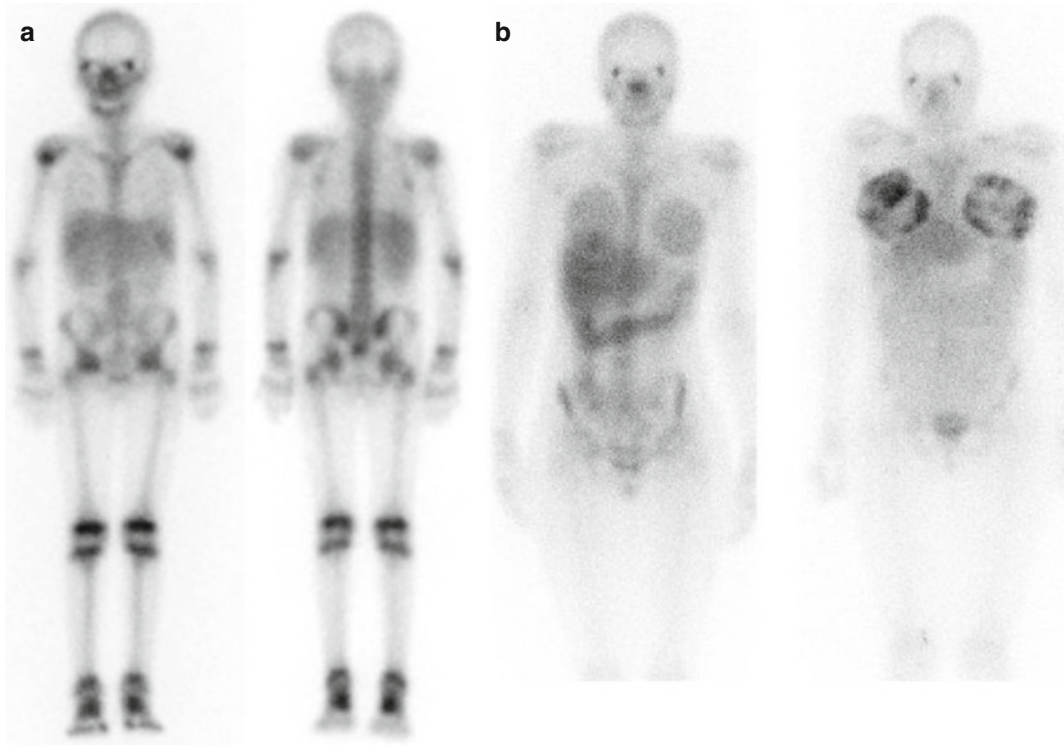

Fig. 24.1 (**a**) Normal anterior (*left*) and posterior (*right*) 72-h images from a gallium scan performed on a 10-year-old patient. Note the uniformly intense activity in the ends of the long bones that correspond to active growth plates. (**b**) Compare the mild, bilateral breast uptake of gallium in an asymptomatic 15-year-old female patient (*left*) with the intense breast uptake in a 17-year-old patient (*right*), who had given birth recently

be present for such uptake to occur. Following intravenous injection, more than 90 % of circulating gallium is in the plasma, nearly all transferrin bound. Increased blood flow and increased vascular membrane permeability result in increased delivery to, and accumulation of, the transferrin-bound gallium at inflammatory foci. Gallium also binds to lactoferrin, which is present in high concentrations in sites of inflammation. Direct uptake by certain bacteria, including *Staphylococcus aureus*, has been observed in vitro, and this too may account for gallium uptake in infection. Siderophores, which are small molecular weight chelates produced by bacteria for iron binding and transport, are gallium-avid. It has been postulated that the siderophore-gallium complex is transported into the bacterium, where it remains until phagocytosed by macrophages. Some gallium may be transported bound to leukocytes. It is important to note, however, that even in the absence of circulating leukocytes, gallium accumulates in inflammation and infection [4].

Imaging usually is performed 18–72 h after injection of 1.5–2.6 MBq (0.04–0.07 mCi)/kg ^{67}Ga-citrate [11]. A gamma camera capable of imaging multiple energy peaks and equipped with a medium-energy collimator must be used. Gallium is excreted via the large bowel and colonic activity can make image interpretation difficult. The use of SPECT, SPECT/CT, and/or delayed imaging facilitates image interpretation. Bowel preparation with laxatives prior to imaging sometimes is used, but is of questionable value [4, 12].

Labeled Leukocytes

In vitro labeling of leukocytes most often is performed using the lipophilic compounds ^{111}In-oxyquinolone and ^{99m}Tc-exametazime. The usual dose of ^{111}In-labeled leukocytes is 0.15–0.25 MBq (0.004–0.007 mCi)/kg; the usual dose of ^{99m}Tc-exametazime-labeled leukocytes is 3.7–7.4 MBq (0.1–0.2 mCi)/kg [13, 14]. A limiting factor to the use of labeled leukocyte imaging in children is the amount of blood that must be withdrawn in order to obtain a sufficiently large quantity of leukocytes to label and subsequently image. In adults and older children, 40–60 mL of whole blood can be withdrawn without fear of precipitating a hemodynamic crisis. This is not the case in younger children and infants, however, and unfortunately there are no data available on the smallest quantity of blood that can be withdrawn to satisfactorily perform the test. For safety reasons, not more than 5 % of a child's total blood volume, or about 3.5 mL/kg, should be withdrawn. Using this guideline, we have successfully imaged infants as young as 6 weeks old, after labeling leukocytes separated from as few as 7 mL of blood.

The success of labeled leukocyte imaging depends on intact chemotaxis, the number and types of cells labeled, and the cellular response to a particular inflammatory process. The conventional labeling process does not normally affect leukocyte chemotaxis. A circulating white cell count of at least $2–3 \times 10^6$/mL probably is needed to obtain satisfactory images. In most clinical settings, the majority of leukocytes labeled are neutrophils, and hence the procedure is most sensitive for identifying neutrophil-mediated inflammatory processes, such as bacterial infections. The procedure is less sensitive for detecting illnesses, such as sarcoidosis and tuberculosis, in which the predominant cellular response is not neutrophilic [12, 15].

Regardless of whether leukocytes are labeled with ^{111}In or ^{99m}Tc, intense diffuse, bilateral pulmonary activity normally is observed on images obtained shortly after injection. This activity decreases over time, reaching background levels by about 4 h after injection (Fig. 24.2). This phenomenon likely is due to several factors. Neutrophils spend more time in contact with the pulmonary endothelium than they do in the systemic vascular bed. One reason for this is that the mean pressure across the pulmonary circulation is lower than that in the systemic circulation. Cell size is another factor. In order to pass through the pulmonary capillaries, which are about 5.5 μm in diameter, neutrophils, which are about 8 μm in diameter, must undergo cytoskeletal deformation. During the labeling procedure, neutrophils are activated. Activated cells are more rigid and

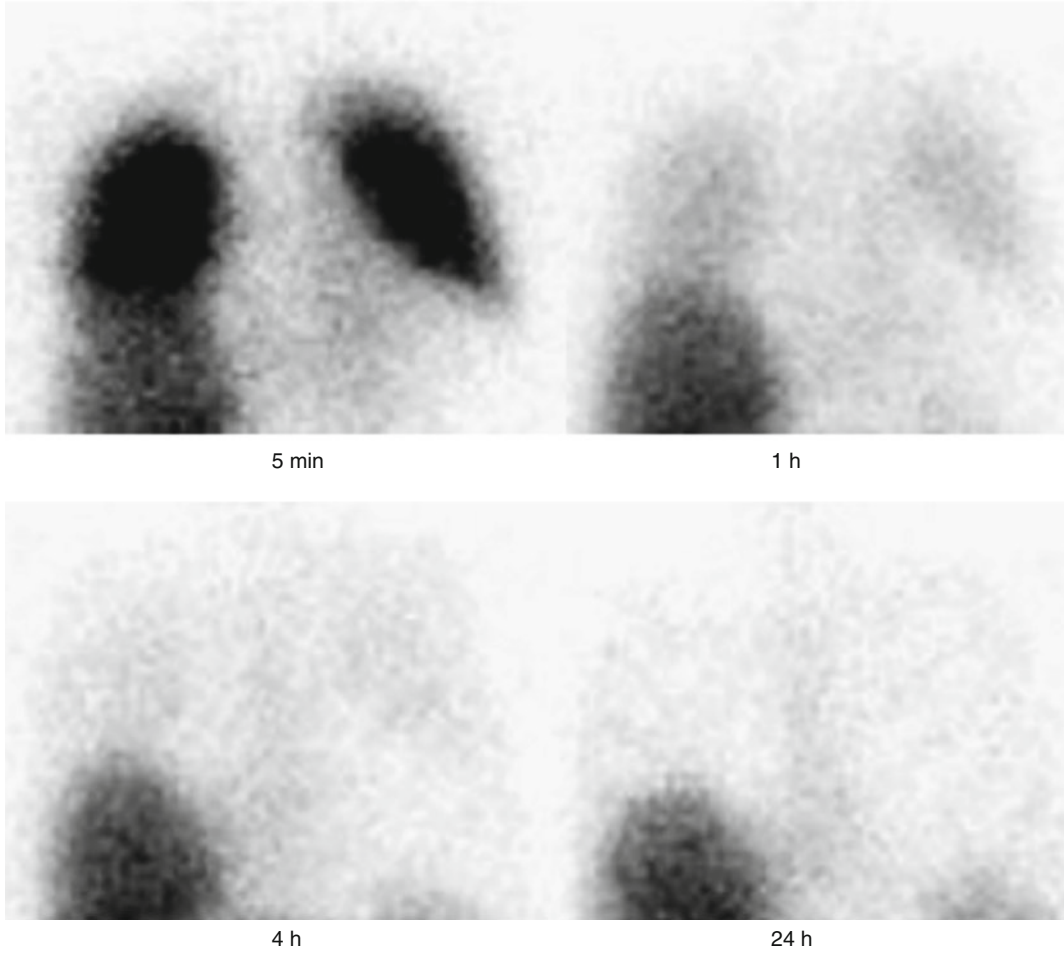

Fig. 24.2 Labeled leukocyte images are characterized by intense pulmonary activity soon after injection. The intensity of this activity rapidly decreases, approaching background within about 4 h after injection. This phenomenon is independent of the radiolabel used

less easily deformed and consequently pass more slowly through the pulmonary vessels. Activated leukocytes adhere to the pulmonary capillaries for a longer time than do non-activated cells. Finally, there is evidence that the in vitro labeling procedure itself causes prolonged pulmonary transit of leukocytes, perhaps as a result of cell trauma during the labeling process [15–18].

By 24 h after injection, the usual imaging time for ^{111}In-labeled leukocytes, the normal distribution of activity is limited to the liver, spleen, and bone marrow (Fig. 24.3). Images should be acquired on a large field of view gamma camera equipped with a medium-energy parallel hole collimator. Energy discrimination is accomplished by using 15 % windows centered on the 174-keV and 247-keV photopeaks of ^{111}In [12, 15].

The normal biodistribution of ^{99m}Tc-labeled leukocytes is more variable than that of ^{111}In-labeled leukocytes. In addition to the reticuloendothelial system, activity normally is present in the urinary tract, large bowel (within 4 h after injection), blood pool, and occasionally gall bladder. The time interval between injection of ^{99m}Tc-labeled leukocytes and imaging varies with the indication; imaging usually is performed within a few hours after injection. A high-resolution, low-energy parallel hole collimator is used with a 15 % window centered on the 140-keV photopeak of ^{99m}Tc [12, 15, 19].

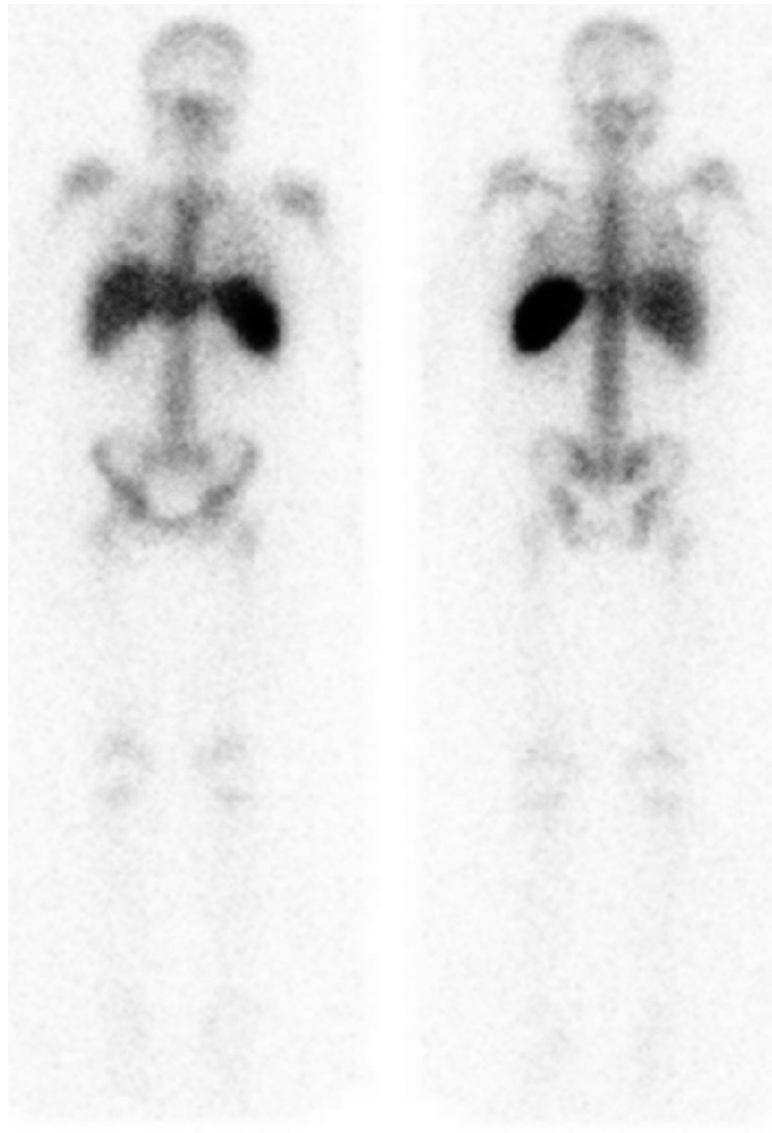

Fig. 24.3 Normal anterior (*left*) and posterior (*right*) 24-h whole-body images from an ^{111}In-labeled leukocyte study performed on a 9-year-old child. Activity is limited to the liver, spleen, and bone marrow. The distribution of hematopoietically active bone marrow varies with the age, with decreasing appendicular activity, as the child grows older. Regardless of the radiolabel used, splenic uptake normally is more intense than hepatic uptake

There are advantages and disadvantages to both ^{111}In- and ^{99m}Tc-labeled leukocytes. Advantages of the ^{111}In label are the stability of the label and a virtually constant normal distribution of activity limited to the liver, spleen, and bone marrow. The 67-h physical half-life of ^{111}In allows for delayed imaging, which is valuable for musculoskeletal infection. There is another advantage to the use of ^{111}In-labeled leukocytes in musculoskeletal infection. Many of these patients require bone or marrow scintigraphy, which can be performed while the patient's cells are being labeled, or as part of a simultaneous dual isotope acquisition, or immediately after completion of the ^{111}In-labeled leukocyte study [15].

Disadvantages of the ^{111}In label include a low photon flux, less than ideal photon energies, and the fact that a 24-h interval between injection and imaging is generally required [15].

Advantages of the ^{99m}Tc label include a photon energy that is optimal for imaging using state-of-the-art instrumentation, a high photon flux, and the ability to detect abnormalities within a few hours after injection. Disadvantages include

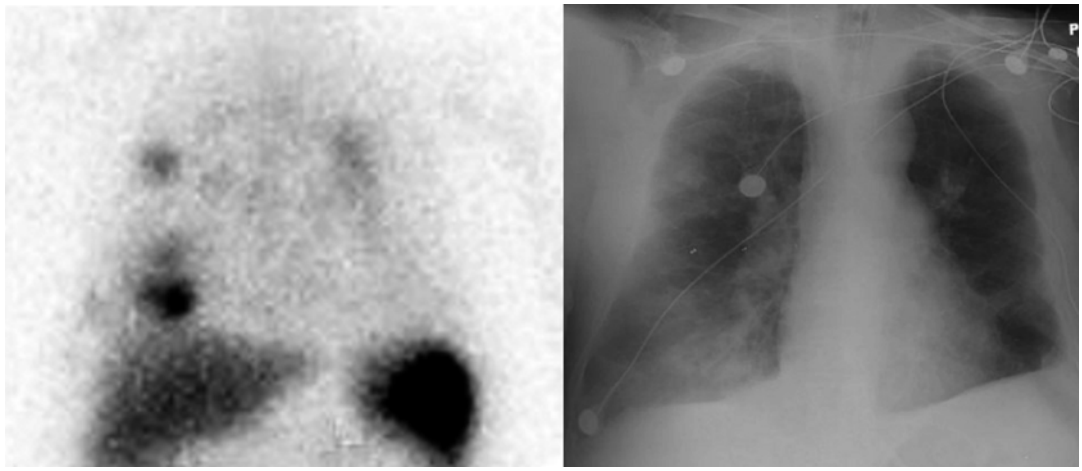

Fig. 24.4 Bilateral, multifocal areas of pulmonary activity are present on the ^{111}In-labeled leukocyte image of a patient with pneumonia (*left*). Bilateral infiltrates are present on the chest x-ray performed the same day (*right*)

urinary tract activity, which appears shortly after injection, and bowel activity, which appears by 4 h after injection. The instability of the label and the short half-life of ^{99m}Tc are disadvantages when delayed 24-h imaging is needed. This occurs in those infections that tend to be indolent in nature and for which several hours may be necessary for accumulation of a sufficient quantity of labeled leukocytes to be successfully imaged. When ^{99m}Tc-labeled leukocytes are used, an interval of least 48 h is required between the white cell and bone or marrow scans [15].

Technetium-99m-labeled leukocytes are best suited to imaging acute inflammatory conditions, such as inflammatory bowel disease, while ^{111}In-labeled leukocytes are preferred for more indolent conditions such as musculoskeletal infection.

To maximize the value of labeled leukocyte imaging, pitfalls of the technique must be recognized. Although pulmonary uptake of labeled leukocytes is a normal physiologic event during the first few hours after injection, by 24 h such uptake is abnormal. Focal pulmonary uptake that is segmental or lobar in appearance usually is associated with bacterial pneumonia (Fig. 24.4). In addition to pneumonia, segmental/lobar pulmonary uptake of labeled leukocytes can be seen in patients with cystic fibrosis. This uptake usually is intense, multifocal, and bilateral, and is due to accumulation of labeled leukocytes in pooled secretions in bronchiectatic regions of the lungs. In patients with cystic fibrosis, the presence of pulmonary activity on labeled leukocyte images cannot be equated automatically with infection (Fig. 24.5) [21].

Focal pulmonary uptake that is not segmental or lobar also may be due to technical problems during labeling or reinfusion and usually is not associated with infection [17, 20].

Diffuse pulmonary uptake on images obtained more than 4 h after reinjection of labeled cells is associated with a variety of pathologic conditions, including opportunistic infection, radiation pneumonitis, pulmonary drug toxicity, and adult respiratory distress syndrome. This pattern is almost never seen in bacterial pneumonia, however [17, 22–25].

Diffuse pulmonary uptake of labeled leukocytes also can be observed in septic patients whose chest x-rays are normal and who have no clinical evidence of respiratory tract inflammation or infection. It is believed that the circulating neutrophils are activated by cytokines, which are released peripherally in response to an infection. These activated neutrophils pool in the pulmonary circulation because it is more difficult for them to undergo the cytoskeletal deformation required to maneuver through the pulmonary circulation. The cytokines presumably also activate pulmonary vascular endothelial cells, causing increased adherence of leukocytes to the cell walls (Fig. 24.6) [17, 25–28].

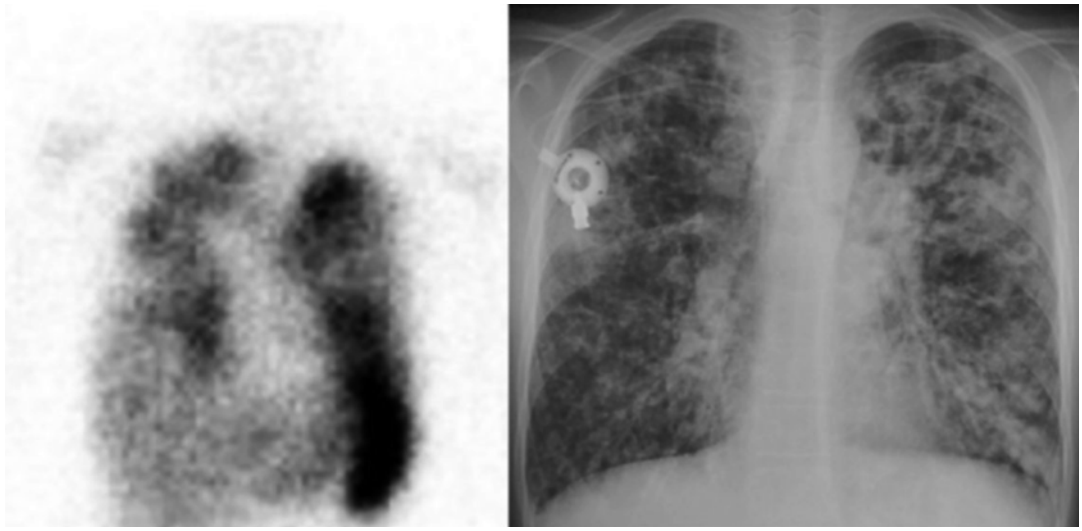

Fig. 24.5 There is intense, multifocal, bilateral pulmonary uptake of ^{111}In-labeled leukocytes (*left*) in a 15-year-old patient with cystic fibrosis. Chest radiograph (*right*), which demonstrates diffuse fibrotic changes with large bronchiectatic cavities and air space infiltrates, was unchanged from prior studies, and the patient's respiratory status was stable. In the patient with cystic fibrosis, pulmonary uptake of labeled leukocytes cannot be equated automatically with infection (From Love et al. [17], by permission of *RadioGraphics*)

Indium-111-labeled leukocytes do not accumulate in normal bowel and such activity is abnormal. In hospitalized patients, a frequent cause of this activity is antibiotic-associated, or pseudomembranous, colitis. Other etiologies include inflammatory bowel disease, ischemic colitis, and gastrointestinal bleeding (Fig. 24.7) [12, 15].

Labeled leukocytes do not accumulate in normally healing surgical wounds, and the presence of such activity indicates infection. There are, however, certain exceptions. Granulating wounds, or wounds that heal by secondary intention, can appear as areas of intense activity on leukocyte images even in the absence of infection. Examples include "ostomies" (tracheostomies, ileostomies, feeding gastrostomies, etc.) and skin grafts (Fig. 24.8) [29].

Focal uptake, especially when superficial, requires careful clinical correlation. Vascular access lines, dialysis catheters, and even lumbar punctures all can yield false-positive results in the absence of appropriate clinical history [29].

Despite its value, there are significant limitations to the in vitro-labeled leukocyte procedure, and considerable effort has been devoted to developing in vivo methods of labeling leukocytes, including peptides and antigranulocyte antibodies/antibody fragments. In the United States at the present time none of these agents are available, even on an investigational basis.

^{18}F-Fluorodeoxyglucose

Fluorine-18-Fluorodeoxyglucose (^{18}F-FDG) is readily available, exquisitely sensitive, and relatively inexpensive. Imaging is completed rapidly and the high-resolution tomographic PET images are superior to those provided by single-photon emitting tracers. It is not surprising that the potential of ^{18}F-FDG for detecting infection and inflammation has attracted considerable interest.

FDG, a glucose analogue, is transported into cells via glucose transporters. Intracellular radiolabeled ^{18}F-FDG is phosphorylated by hexokinase enzyme to ^{18}F-2′-FDG-6 phosphate, which does not pass easily through the cell membrane. Compared with glucose, this fluorinated deoxyglucose is not metabolized. Increased ^{18}F-FDG uptake in inflammation is related, at least in part, to an increased number of glucose transporters. In addition, in inflammation, the affinity of glucose transporters for deoxyglucose presumably is increased by various cytokines and growth factors [30–36].

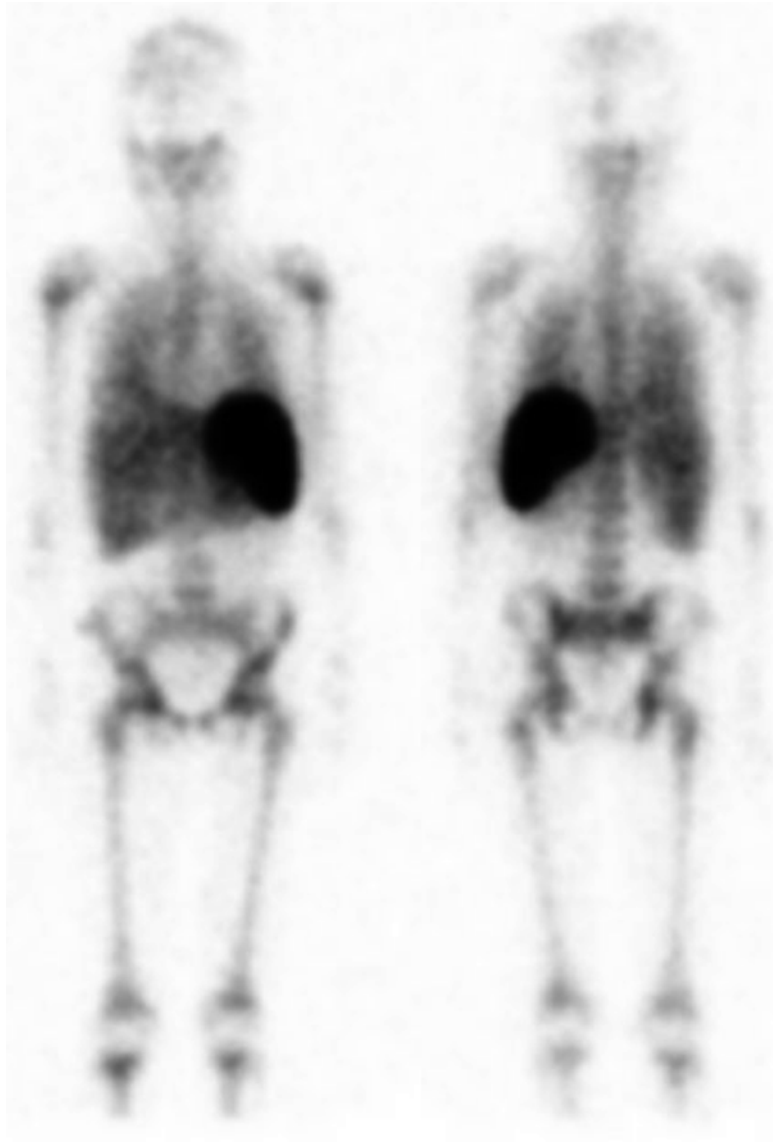

Fig. 24.6 Anterior (*left*) and posterior (*right*) 24-h whole-body images from an ^{111}In-labeled leukocyte study performed on a 9-year-old patient with septicemia, but with no respiratory tract signs or symptoms. Note the diffuse bilateral pulmonary uptake of labeled leukocytes, which has been observed in septic patients and is apparently of no clinical significance

The normal distribution of ^{18}F-FDG includes brain, myocardium, and genitourinary tract. Bone marrow, gastric, and bowel activities are variable. Thymic uptake, especially in children, can be prominent. Liver and spleen uptake generally are low grade and diffuse, although in infection, splenic uptake may be intense. The spleen is an integral part of the body's immune system. Increased splenic activity in infection likely reflects increased glucose utilization by this organ, and it is important to recognize that this increased activity cannot automatically be attributed to infection or tumor of the organ itself [30]. The usual pediatric dose is 3.7–5.2 MBq (0.10–0.14 mCi)/kg [37].

Indications

Opportunistic Infection

Nuclear medicine plays an important role in the detection of infections unique to the immunocompromised patient, and for most of them,

gallium imaging is the radionuclide procedure of choice. Many opportunistic infections affect the lungs, and a normal gallium scan of the chest excludes infection with a high degree of certainty, especially in the setting of a negative chest radiograph. In the HIV (+) patient, lymph node uptake of gallium most often is due to mycobacterial disease or lymphoma. Focal, or localized, pulmonary parenchymal gallium uptake usually is associated with bacterial pneumonia. Diffuse pulmonary gallium uptake is indicative of *Pneumocystis jirovecii* pneumonia, especially when the uptake is intense (Fig. 24.9). In addition to its value as a diagnostic test, gallium can be used for monitoring response to therapy [4, 12, 38].

Fig. 24.7 Activity within the large bowel on ^{111}In-labeled leukocyte images always is abnormal. In patients receiving antibiotics, this uptake often is indicative of antibiotic-associated colitis

Fluorine-18-FDG PET also is useful in this population, especially in the central nervous system, where it accurately distinguishes lymphoma from toxoplasmosis [30, 39, 40].

Labeled leukocyte scintigraphy is not sensitive for detecting opportunistic infections presumably because most opportunistic infections do not incite a neutrophilic response [12, 15, 22, 38].

Fever of Unknown Origin

While there is some disagreement about its precise definition, for most clinical situations, a persistent fever for at least 8 days in a child in whom a thorough history, complete physical examination, and laboratory data fail to reveal a cause is considered a fever of unknown origin or "FUO." The three most common causes of FUO in children in the United States are infections, connective tissue diseases, and neoplasm. In up

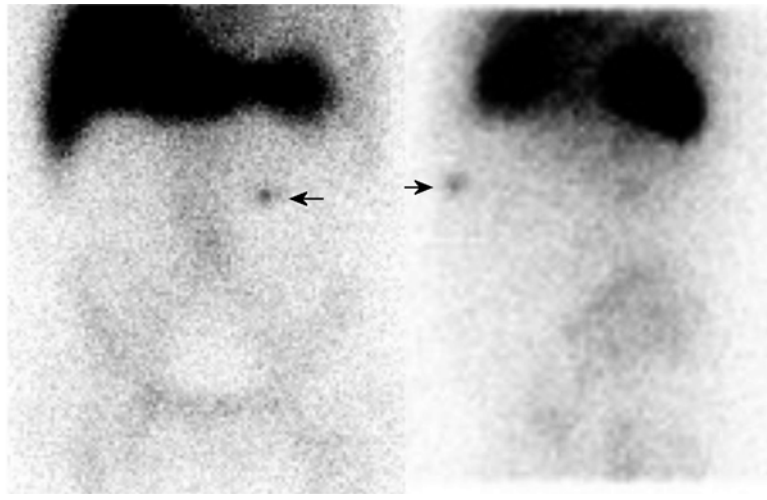

Fig. 24.8 There is a superficial focus (*arrows*) of labeled leukocyte activity in the left upper abdomen of a patient with a feeding gastrostomy. This uptake, which can be intense at times, normally is present around "ostomy" sites and does not indicate infection

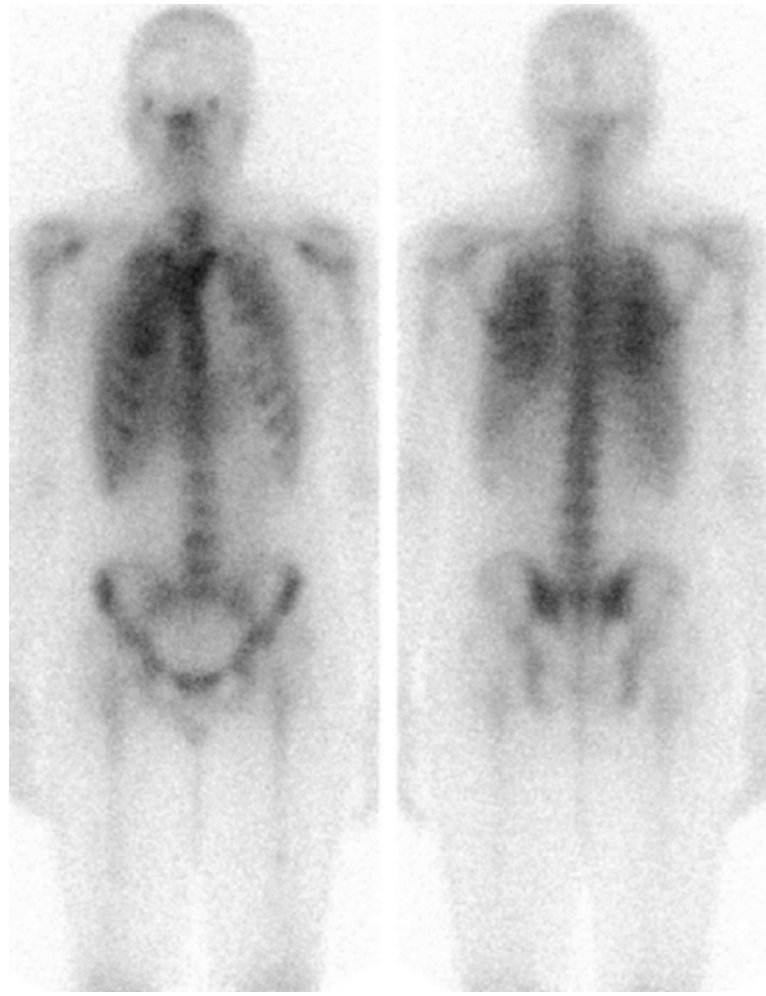

Fig. 24.9 There is intense, diffuse bilateral pulmonary uptake of ^{67}Ga in a 20-year-old patient who had recently completed treatment for non-Hodgkin's lymphoma. Although diffuse lung uptake of gallium is not specific, the more intense the uptake, the more likely the patient is to have *Pneumocystis jirovecii* pneumonia

to 20 % of cases, however, a definitive diagnosis never is established. The most frequently diagnosed systemic infections in children with FUO include tuberculosis, brucellosis, tularemia, salmonellosis, and various viruses. Focal infections include urinary tract infection, osteomyelitis, and abdominal/pelvic abscesses. The connective tissue disorders most commonly presenting as FUO are juvenile rheumatoid arthritis, systemic lupus erythematosus, and vasculitis. Leukemia and lymphoma are the malignancies most often presenting as FUO [41].

The results of conventional radionuclide studies in the evaluation of children with FUO for the most part have been disappointing. Buonomo et al. [42] found that although gallium imaging was positive in three of five children with focal signs and symptoms, the test was positive in only one of 25 children with only systemic signs or symptoms. These investigators concluded that the test is of little use in children with FUO who present only with systemic signs or symptoms.

Haentjens et al. [43] reviewed the results of labeled leukocyte imaging in 15 children and reported that false-negative results were found in five: pericarditis, osteomyelitis, hepatic abscess [2], and lung abscess. Williamson et al. [44] found that labeled leukocyte imaging was sensitive (94 %), but not specific (57 %). Steele et al. [45] found that imaging procedures, including radionuclide tests, rarely identified an unsuspected diagnosis.

Fluorine-18-FDG is an intriguing and exciting alternative to the conventional radionuclide

Fig. 24.10 Fluorine-18-FDG PET imaging performed on a 14-year-old boy with a history of 3 weeks of intermittent fevers, and a "widened mediastinum" on chest x-ray revealed hypermetabolic foci in the mediastinum. Lymph node biopsy was negative for tumor, but cultures grew out *Mycobacterium tuberculosis*

approach to the patient with FUO. Fluorine-18-FDG, though not specific, is exquisitely sensitive, making it ideally suited to the evaluation of an entity with diverse etiologies. The short half-life of ^{18}F, moreover, does not delay the performance of any additional radionuclide studies that might be contemplated. Several studies support the use of ^{18}F-FDG PET in adults with FUO [46–49]. Available data suggest that this test also may be useful in children with FUO (Fig. 24.10). Jasper et al. [50] retrospectively reviewed the results of 44 ^{18}F-FDG PET or PET/CT scans performed on children with FUO. Scans were classified as helpful or not helpful. Scans were considered "helpful" if they revealed a focus which subsequently could be evaluated by further investigations leading to a final diagnosis. Scans showing no abnormal focus also were considered helpful by directing the differential diagnosis towards autoimmune diseases and avoiding unnecessary additional investigations. Nineteen of the 44 scans were helpful by allowing targeted evaluation in nine cases and by eliminating the need for further evaluation in ten cases. The authors concluded that even though the test was helpful in only 43 % of the cases, similar to what has been reported in adults with FUO, ^{18}F-FDG imaging is useful in children with FUO, because traumatic investigations are avoided and the time to diagnosis may be shortened, allowing prompt institution of appropriate therapy.

The management of pediatric patients with terminal chronic liver failure can be complicated by FUO during the pretransplantation period. Extrahepatic infections may render the patient unsuitable for transplantation, whereas hepatic infections may necessitate organ resection for a cure. Accurate localization of the source of infection is necessary for appropriate management of children on the waiting list for liver transplantation. Sturm at al. [51] performed ^{18}F-FDG PET on 11 children with biliary cirrhosis who presented with FUO while waiting for a liver transplant. Standard imaging techniques failed to reveal evidence of infection in any of the children. Focal intrahepatic FDG hypermetabolism was present in five children. Based on the ^{18}F-FDG PET results, these patients underwent transplantation after continuous antibiotic treatment with ongoing, recurrent episodes of fever. Imaging results correlated with bacterial cultures of the excised liver and/or anatomic or histologic signs of infection. There was no abnormal intrahepatic ^{18}F-FDG accumulation in six children, and no hepatic infections were found. Transplantation in these patients was performed only after they became afebrile. These investigators concluded that ^{18}F-FDG PET may help guide decisions on therapy and transplantation suitability in children with biliary cirrhosis and FUO who are on the waiting list for liver transplantation.

Vasculitis, another cause of FUO in children, is a heterogeneous group of disorders characterized by a leukocytic infiltration of the vessel wall with reactive destruction of mural structures and surrounding tissues leading to infarction. The overall incidence of vasculitis in children is about

50 cases per 100,000 children per year. The most common method of classifying vasculitis is based on the caliber of the vessels involved: large vessel (Takayasu arteritis), medium vessel (childhood polyarteritis nodosa, cutaneous polyarteritis, Kawasaki disease), small vessel (granulomatous, non-granulomatous), and others (Behcet disease, vasculitis secondary to infection, drugs, malignancy, vasculitis associated with connective tissue disease, isolated CNS vasculitis, and Cogan syndrome) [52, 53].

With the exception of Kawasaki disease, the reference standard for diagnosis of vasculitis is histopathological demonstration of vascular injury on tissue biopsy. The discovery of specific autoantibodies characterized by immunofluorescence patterns, cytoplasmic ANCA (cANCA) and perinuclear ANCA (pANCA), and subsequently by the relevant target antigens, proteinase 3 (PR3-ANCA) and myeloperoxidase (MPO-ANCA), has been a major advance in the diagnosis of small-vessel vasculitis, especially for microscopic polyangiitis and Wegener's granulomatosis [52, 54].

Imaging studies are being increasingly used in the assessment of large-vessel vasculitis. Magnetic resonance angiography and computed tomographic angiography provide good resolution of large- and medium-sized vessels and have become the standard for evaluation of Takayasu arteritis and monitoring of established disease, although the standard for evaluation of smaller vessels remains the conventional angiogram. Among conventional radionuclide studies, gallium and labeled leukocyte imaging have met with only limited success and are not used widely for this indication [55].

Although pediatric data are scarce, there are an increasing number of studies in the literature that report the usefulness of ^{18}F-FDG PET in large-vessel arteritis in adults, especially in individuals with nonspecific presentations. The sensitivity and specificity of the test for diagnosis of large-vessel vasculitis in untreated patients with elevated inflammatory markers range from 77 to 92 % and 89 to 100 %, respectively. Fluorine-18-FDG PET also appears to be useful for monitoring response to therapy in large-vessel vasculitis [56–59].

The test is less useful for identifying individuals likely to relapse and for assessing disease activity in complicated large-vessel vasculitis [59, 60]. Although ^{18}F-FDG PET can detect the extent and activity of large-vessel vasculitis in untreated patients, data suggest that it is not reliable for diagnosis in patients on steroid treatment [61].

In contrast to its utility in large-vessel vasculitis, ^{18}F-FDG PET is less useful in medium- and small-vessel inflammation [58]. Data on the role of ^{18}F-FDG PET in other small- and medium-vessel vasculitis such as Churg-Strauss syndrome, Wegener's granulomatosis, and polyarteritis nodosa suggest that these entities are detected only when there is large-vessel involvement or there is damage to adjacent tissues [56, 57, 61].

In summary, ^{18}F-FDG is useful for diagnosing large-vessel vasculitis and for monitoring response to therapy. It is less useful for predicting relapse and for diagnosing and assessing disease activity in patients on immunosuppressive therapy. Fluorine-18-FDG is not useful for evaluation of medium- and small-vessel vasculitis, probably because of the inherent limits of resolution of the technique [55].

Inflammatory Bowel Disease

Inflammatory bowel disease (IBD) is a group of idiopathic, chronic disorders, of uncertain etiology, that include Crohn disease and ulcerative colitis. The natural course of these disorders is one of unpredictable exacerbations and remissions. Although it can begin as early as the first year of life, IBD usually develops during adolescence and young adulthood and, in developed countries, is the major cause of chronic intestinal inflammation in children beyond the first few years of life [62]. Signs and symptoms of IBD in children often are nonspecific and the diagnosis is entertained in many children who ultimately are found to have other maladies. Definitive diagnosis is made with a combination of barium contrast radiography, upper gastrointestinal endoscopy, and colonoscopy with biopsy. Barium contrast radiography is associated with

significant levels of ionizing radiation. Pediatric endoscopy requires special expertise and facilities, and sedation or general anesthesia may be necessary. Bowel evacuation regimens are a prerequisite for successful colonoscopy [63]. All of these tests are invasive, time consuming, and unpleasant for the patient. Thus, while radiological studies and endoscopy are important for making the diagnosis of IBD, they are not appropriate screening tests, nor are they well suited for routine follow-up.

Though not a substitute for conventional diagnostic methods in pediatric IBD, labeled leukocyte imaging is useful in a variety of situations. Several investigators have reported that the test is very sensitive for detecting IBD, with a high negative predictive value [63–71]. Because a negative study excludes, with a high degree of certainty, IBD as the cause of the patient's symptoms, labeled leukocyte imaging can be used as a screening test to determine which children need to undergo more invasive investigation (Fig. 24.11). In the patient thought to have ulcerative or indeterminate colitis, the presence of skip areas of activity in the colon or the presence of small bowel activity supports the diagnosis of Crohn disease (Fig. 24.12). The radionuclide study also is helpful in patients who refuse endoscopy or contrast radiography and in those individuals in whom these studies cannot be satisfactorily performed because of narrowing of the bowel lumen. The ability of the radionuclide study to differentiate active inflammation, which may respond to medical therapy, from scarring, which may require surgery, can have a significant impact on patient management [65].

Radionuclide imaging can be used to monitor patient response to therapy. Persistent bowel activity after a conventional course of therapy suggests that more intensive medical therapy, or even surgery, is in order. Similarly, decreasing bowel uptake on serial studies confirms that the patient is responding to the therapeutic regimen, while persistent or recurrent uptake is indicative of residual disease or relapse. In the asymptomatic patient with elevated laboratory markers of inflammation, an abnormal labeled leukocyte study confirms the presence of active disease and appropriate therapy can be instituted promptly. In the patient with a history of IBD and recurrent symptoms, but with a normal physical examination and normal laboratory tests, a negative labeled leukocyte study effectively excludes active IBD as the cause of the symptoms [65, 66].

Although early studies were performed with ^{111}In-labeled leukocytes, it is now agreed that ^{99m}Tc-labeled leukocytes should be used for the evaluation of IBD. Imaging at multiple time points maximizes the sensitivity of the test. In one series in which imaging was performed within 1 h and again within 3 h after injection, 12 % of patients with disease were detected only

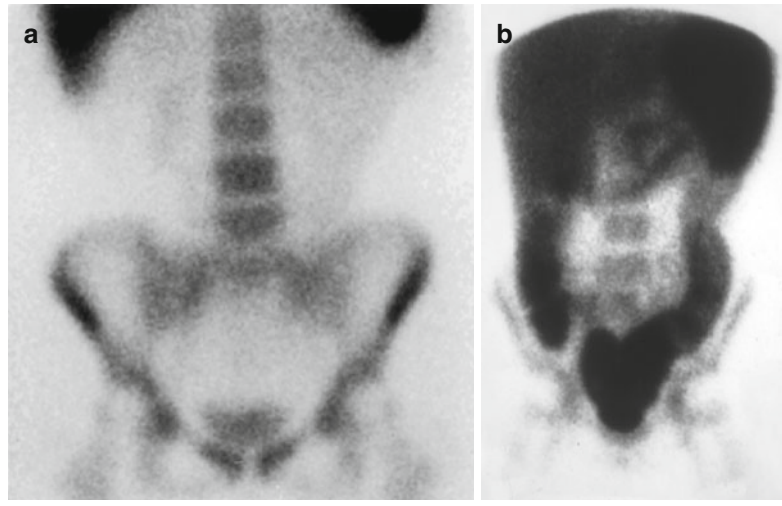

Fig. 24.11 (**a**) Normal ^{99m}Tc-labeled leukocyte image. Labeled leukocyte imaging is very sensitive for detecting IBD. Consequently, in the symptomatic individual, a negative scan excludes IBD, with a high degree of certainty, as the cause of the patient's symptoms. (**b**) There is intense labeled leukocyte activity throughout the colon in a patient with ulcerative colitis (Courtesy of Dr. Martin Charron)

Fig. 24.12 In addition to mild pancolonic activity, abnormal labeled leukocyte activity also is present in the distal jejunum/proximal ileum and distal ileum. The presence of small bowel activity in the patient with colitis supports the diagnosis of Crohn disease (Courtesy of Dr. Martin Charron)

on the later images. SPECT also increases the sensitivity of the test [67]. The caudal, or pelvic outlet, view facilitates detection of rectal disease that otherwise might be masked by urinary bladder activity. Physiologic bowel activity, probably due to hepatobiliary excretion of ^{99m}Tc-labeled hydrophilic complexes, appears on delayed images in up to 20 % of children and must be differentiated from activity secondary to inflammation. Physiologic activity appears in the distal small bowel no less than 3 h after injection, is diffuse and mild in intensity, and migrates into the cecum by 4 h. There must be no accumulation in other bowel segments [67].

There are some limitations to labeled leukocyte imaging. It cannot be the only imaging test used for IBD. It cannot define anatomic changes such as strictures, which are best delineated with endoscopy and contrast radiography. The test is less sensitive for upper, than for lower, gastrointestinal tract disease [72, 73]. The sensitivity of the test also may be affected adversely by concomitant corticosteroid administration [65]. Nevertheless, labeled leukocyte imaging is useful as an initial screening test to identify patients who need further investigation, for monitoring response to treatment, for detecting recurrent disease in patients who have completed treatment, and for determining the presence of active disease in patients whose physical presentation and laboratory test results are discordant.

Although labeled leukocyte imaging remains the nuclear medicine test of choice for IBD, there are data that indicate that ^{18}F-FDG PET may be a useful alternative (Fig. 24.13). Bicik et al. [74] reported that, in seven patients with IBD, ^{18}F-FDG uptake was high both in areas of macroscopic disease and in areas of biopsy-proven inflammation in the absence of active disease. Skehan et al. [75] compared ^{18}F-FDG PET to colonoscopy or small bowel series or both in 25 children with suspected IBD. Disease activity was recorded in five bowel segments. Fluorine-18-FDG PET was 71 % sensitive and 86 % specific in this investigation. Complete colonoscopy with ileal intubation was successful in only about one third of the patients and the authors concluded that, in children with suspected IBD, ^{18}F-FDG imaging could be a useful adjunct when conventional studies are not feasible.

Lemberg et al. [76] studied 65 children, including 55 with IBD (17 with ulcerative colitis, 38 with Crohn disease) and ten with abdominal pain who served as controls. In patients with ulcerative colitis, the sensitivity of ^{18}F-FDG, compared to colonoscopy, was 81 %. In the children with Crohn disease, ^{18}F-FDG PET identified inflammation in at least one bowel segment in 90 % of the patients; the specificity was 50 %. Correlation of colonoscopy and ^{18}F-FDG PET results in the children with Crohn disease was limited because complete colonoscopy with ileal intubation could not be performed in many of the patients. There was no significant ^{18}F-FDG activity in any of the bowel segments of the controls.

Loffler et al. [77] retrospectively evaluated the diagnostic potential of ^{18}F-FDG PET performed on 23 children, 2–16 years old, with suspected IBD. Imaging results were compared

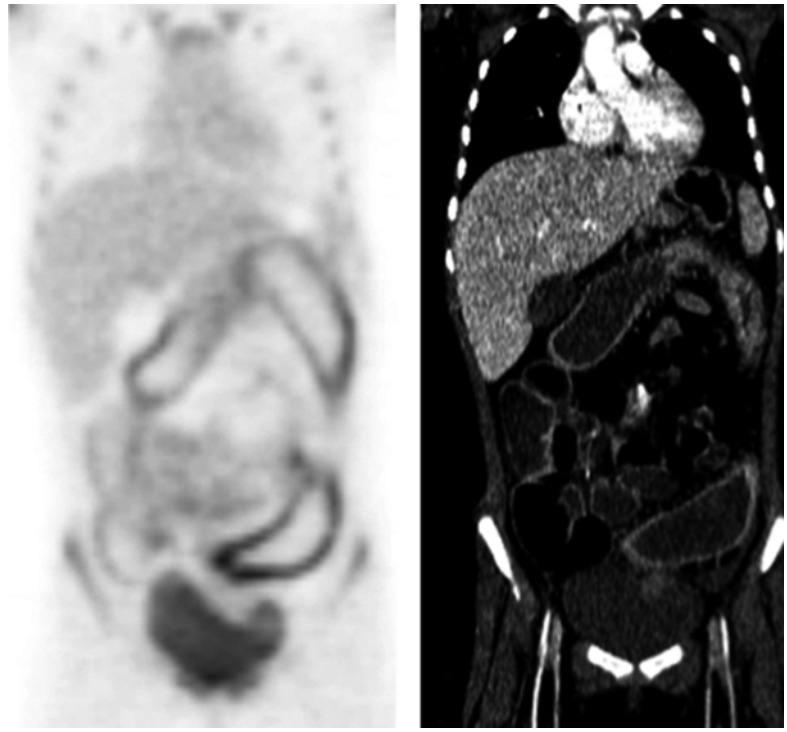

Fig. 24.13 Inflammatory bowel disease. There is intense FDG accumulation in the colon as well as small bowel in a 16-year-old child with Crohn disease (Courtesy of Dr. Helen Nadel)

to endoscopic, histologic, and abdominal ultrasound findings. Eight bowel segments were evaluated in each patient. Sensitivity, specificity, and accuracy were calculated on a segment-based analysis, using histology as the standard of reference. Fluorine-18-FDG had sensitivity, specificity, and accuracy of 98, 68 and 83 % versus 90, 75 and 82 % for endoscopy and 56, 92 and 75 % for ultrasound. In the small intestine, sensitivity, specificity, and accuracy of ^{18}F-FDG were 100, 86 and 90 %, respectively. These investigators concluded that ^{18}F-FDG PET is an excellent, noninvasive diagnostic tool for IBD and, because it is not traumatic, it is especially attractive for use in children.

Dabritz et al. [78] analyzed ^{18}F-FDG imaging in 45 children with IBD. Twenty-four studies were performed as PET studies, the remaining 21 as PET/CT studies. Imaging results were compared to conventional diagnostic procedures (endoscopy, histology, and ultrasound) using a segment-based analysis. Overall, 253 gastrointestinal tract segments were explored by endoscopy/histology and ^{18}F-FDG PET/CT. Twenty-five additional small bowel segments were assessed by abdominal ultrasound and an additional 152 segments not reached during endoscopy were evaluated by ^{18}F-FDG. Fluorine-18-FDG revealed a segment-based sensitivity, specificity, positive predictive value, negative predictive value, and accuracy for the detection of IBD of 82, 97, 96, 88 and 91 %, respectively. The patient-based sensitivity and specificity were 97 and 100 %, respectively. Co-registration of CT did not improve the results. The authors concluded that ^{18}F-FDG PET is a reliable tool for detecting inflamed gut segments in children with IBD with high sensitivity and specificity. Performing the study as PET/CT had no additional benefit.

Based on currently available data, ^{18}F-FDG PET can be used to identify areas of active inflammation in patients with IBD. Its role for monitoring response to therapy, however, has yet to be established. Similarly there are few data available about the ability of ^{18}F-FDG to differentiate fibrostenotic strictures from strictures secondary to active inflammation.

Patients with IBD are predisposed to develop irritable bowel syndrome, a condition whose presentation cam mimic that of IBD. The ability to differentiate between these two entities would have considerable clinical utility; at the present

time, however, there are no data on the ability of ^{18}F-FDG to distinguish between them [79].

Musculoskeletal Infection

Osteomyelitis

Infection of the bone, or osteomyelitis, usually is bacterial in origin, occurs most frequently in children younger than 5 years of age, and most often is hematogenous in origin [80–82]. Osteomyelitis has a predilection for the highly vascular metaphyses of the long bones. Sluggish blood flow in the distal metaphyseal vessels makes them prone to necrosis and facilitates the deposition of blood-borne bacteria [83]. The distal femora and the proximal tibiae and humeri are the most commonly involved bones [80]. *Staphylococcus aureus* is the most frequently encountered organism in pediatric osteomyelitis, except in neonates, where group A *beta-hemolytic streptococcus* is the usual culprit [84]. Because the clinical manifestations may be subtle and may mimic other medical conditions, the diagnosis of osteomyelitis cannot be established solely on clinical grounds, especially in very young children and during the early stages of the disease, when appropriate treatment is more likely to eradicate the infection and prevent complications such as osteonecrosis and growth disturbance related to damage to the physes [85]. Consequently, imaging tests play an important role in the diagnosis of this entity.

In unviolated bone, focal hyperperfusion, focal hyperemia, and focally increased bony uptake on delayed images are the classic appearance of osteomyelitis on the three-phase bone scan (Fig. 24.14) [86]. There has been some controversy over the years about the value of bone scintigraphy in children, especially in neonates. Ash et al. [87] reported a sensitivity of only about 32 % for bone scintigraphy in neonatal osteomyelitis, a marked contrast to the sensitivity of 100 % in slightly older infants. These investigators concluded that neonatal osteomyelitis is a different disease from that in older infants and children. Berkowitz et al. [88] reported similar findings in neonates. Sullivan et al. [89] reported that the appearance of childhood osteomyelitis on radionuclide bone imaging is very variable and that a normal bone image does not exclude osteomyelitis. Subsequently, Bressler et al. [90] retrospectively reviewed the results of three-phase bone scintigraphy in neonates and found that all 15 sites of infection were identified on bone scintigraphy, although 2 (13 %) of the 15 sites were photopenic.

The variable appearance of childhood osteomyelitis may be related to the evolution of the disease itself. In children, especially neonates, subperiosteal edema, effusion, or vasospasm can cause occlusion of small vessels, reducing blood flow to the infected area. Early in the course of the disease, therefore, hyperperfusion and hyperemia may be absent, and on delayed images, the abnormality may appear as decreased, rather than

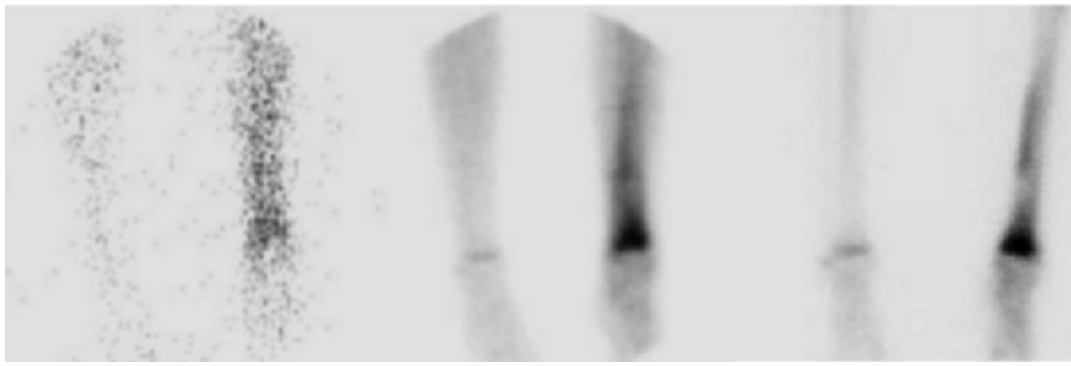

Fig. 24.14 There is focal hyperperfusion, focal hyperemia, and focally increased bony uptake on a three-phase bone scan performed on a 10-year-old child with distal left tibial osteomyelitis

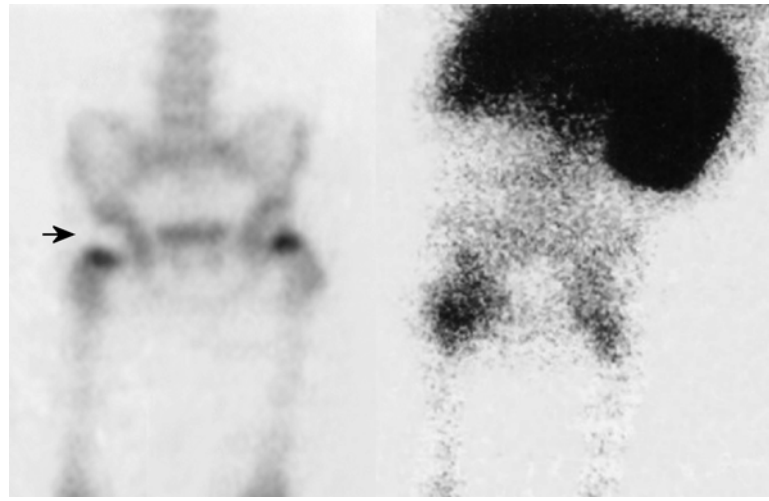

Fig. 24.15 The bone scan (*left*) performed on a 3-year-old girl with right hip pain demonstrates absent activity in the right femoral head (*arrow*), while the labeled leukocyte study (*right*) performed 24 h later demonstrates intense activity in the right femoral head and hip joint. Septic arthritis and osteomyelitis were found at surgery (From Palestro [92], with permission)

increased, bony activity (Fig. 24.15) [91]. As blood flow is restored, bony uptake of the tracer gradually increases until it exceeds that in normal bone. At some point during the scintigraphic evolution of osteomyelitis, the intensity of tracer uptake in the infected bone will be indistinguishable from that in adjacent, normal bone and therefore will not be detected. The focus of infection typically is located in the metaphysis, and the importance of meticulous technique, to facilitate the discrimination of normally increased activity in the physis from abnormally increased uptake in the juxtaposed metaphysis, cannot be overemphasized [92].

Because prompt diagnosis of osteomyelitis in the child is critical, three-phase bone scintigraphy, even with its shortcomings, usually is the first radionuclide test performed. As osteomyelitis may be multifocal in children, the ability to image the whole body is an added benefit of this test.

For those studies that are normal or inconclusive or in children with underlying bony abnormalities, gallium and labeled leukocyte imaging provide additional information. The use of combined bone/gallium scintigraphy in the diagnosis of the so-called complicating osteomyelitis was first described more than 30 years ago [93, 94]. The uptake mechanisms of gallium and bone-seeking tracers are different, and each study, therefore, provides information about different aspects of a particular disease process. Over the years standardized criteria for interpreting bone/gallium images have evolved [4, 92, 95]. The study is:

Positive for osteomyelitis when the distribution of the two tracers is spatially incongruent, *or* when the distribution is spatially congruent, *and* the relative intensity of uptake of gallium exceeds that of the diphosphonate (Fig. 24.16a)

Negative for osteomyelitis when the gallium images are normal, regardless of the bone scan findings, *or* when the distribution of the two tracers is spatially congruent, *and* the relative intensity of uptake of gallium is less than that of the diphosphonate (Fig. 24.16b)

Equivocal for osteomyelitis when the distribution of the two radiotracers is congruent, both spatially *and* in terms of intensity (Fig. 24.16c)

Although combined bone/gallium imaging is accurate when the study is positive or negative, the study frequently is equivocal and the overall accuracy ranges between about 60 and 80 % [4, 92, 95]. The less than ideal imaging characteristics of gallium and the need for two isotopes with multiple imaging sessions over several days are additional disadvantages. Bone/gallium imaging should be reserved for suspected spinal osteomyelitis and for those situations in which labeled leukocyte imaging cannot be performed.

Labeled leukocytes usually do not accumulate at sites of increased bone mineral turnover in the absence of infection and would seem to be ideally suited for diagnosing complicated osteomyelitis. The results reported have been

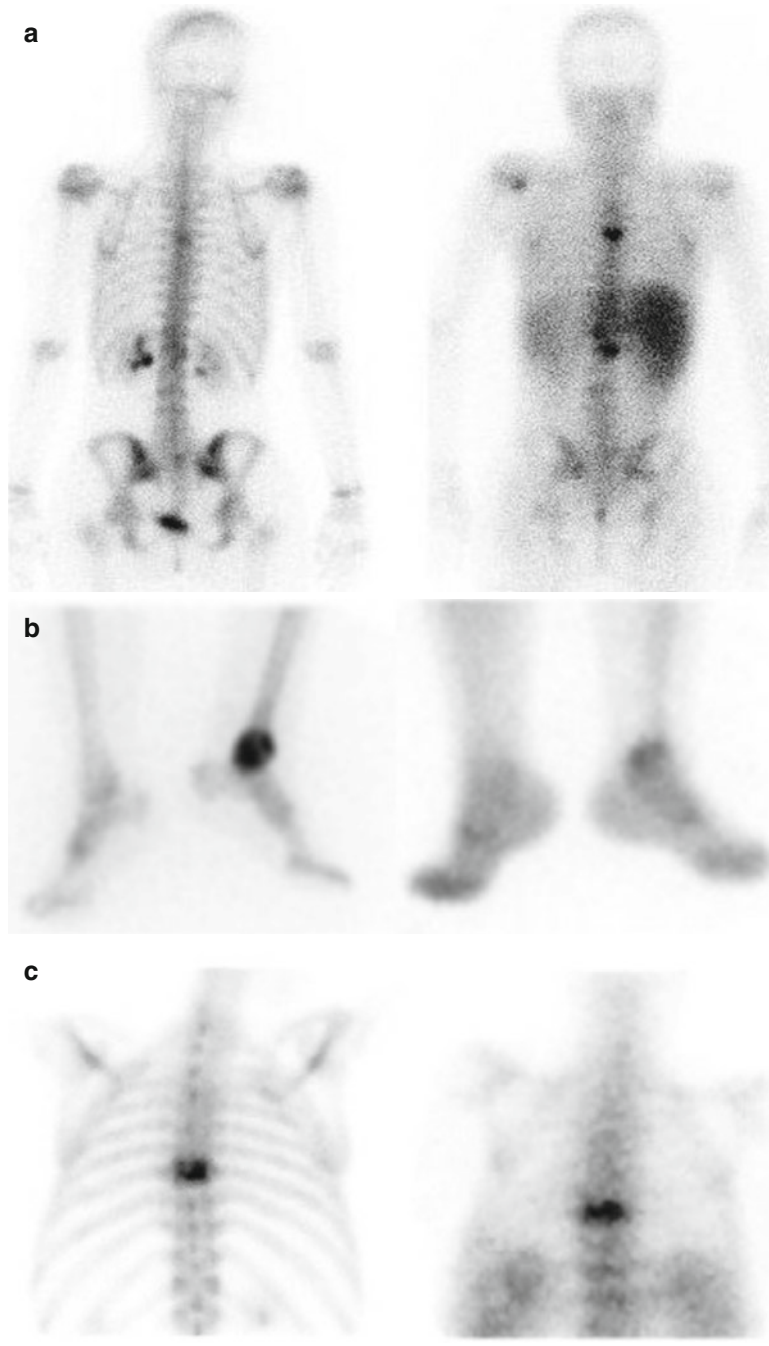

Fig. 24.16 (**a**) There is increased activity in the mid-thoracic, lower thoracic, and upper lumbar spine on both the bone (*left*) and gallium (*right*) images. Although the spatial distribution of abnormal activity is congruent on both images, the intensity of the abnormal activity on the gallium image is greater than that on the bone image, and the combined study is positive for osteomyelitis. The combined study also is positive for osteomyelitis when the spatial distribution of the two tracers is different (not shown). (**b**) Increased activity is present in the distal left tibia on both the bone (*left*) and gallium (*right*) images. The intensity of activity on the gallium image is considerably less than that on the bone image, and the combined study is negative for osteomyelitis. The combined study also is negative for osteomyelitis when the gallium scan is normal, regardless of the findings on the bone scan (not shown). (**c**) Abnormal activity in a mid-thoracic vertebra is congruent, both spatially and in terms of intensity, on the bone and gallium images, and the combined study is equivocal for infection

very variable, however. The primary difficulty in the interpretation of labeled leukocyte images is an inability to distinguish labeled leukocyte uptake in infection from uptake in bone marrow [92, 96]. The normal distribution of labeled leukocytes includes the liver, the spleen, and the bone marrow, which, in adults, is limited to the axial and proximal appendicular skeleton. Any focus outside the normal distribution of labeled leukocytes is, therefore, indicative of infection. This "normal" distribution of hematopoietically active marrow, however, is quite variable.

Systemic diseases such as sickle-cell and Gaucher disease produce generalized alterations in marrow distribution, while fractures and orthopedic hardware can cause localized alterations. In children, furthermore, the normal distribution varies with age. Consequently, it may not be possible to determine if an area of activity on a labeled leukocyte image reflects infection or marrow [92, 95, 96]. Performing complementary bone marrow imaging overcomes this problem. Leukocytes and sulfur colloid both accumulate in the bone marrow; leukocytes also accumulate in infection, but sulfur colloid does not. The combined study is positive for infection when there is uptake on the labeled leukocyte image without corresponding uptake on the sulfur colloid bone marrow image. Any other pattern is negative for infection (Fig. 24.17) [92, 96].

Combined leukocyte/marrow imaging can be performed in various ways. The protocols that follow are offered as general suggestions, albeit ones that, in our experience over several years, have yielded very satisfactory results. Patients should be injected with 4.0–5.3 MBq (0.10–0.15 mCi)/kg of freshly prepared ^{99m}Tc-sulfur colloid [13]. Using preparations more than 2 h

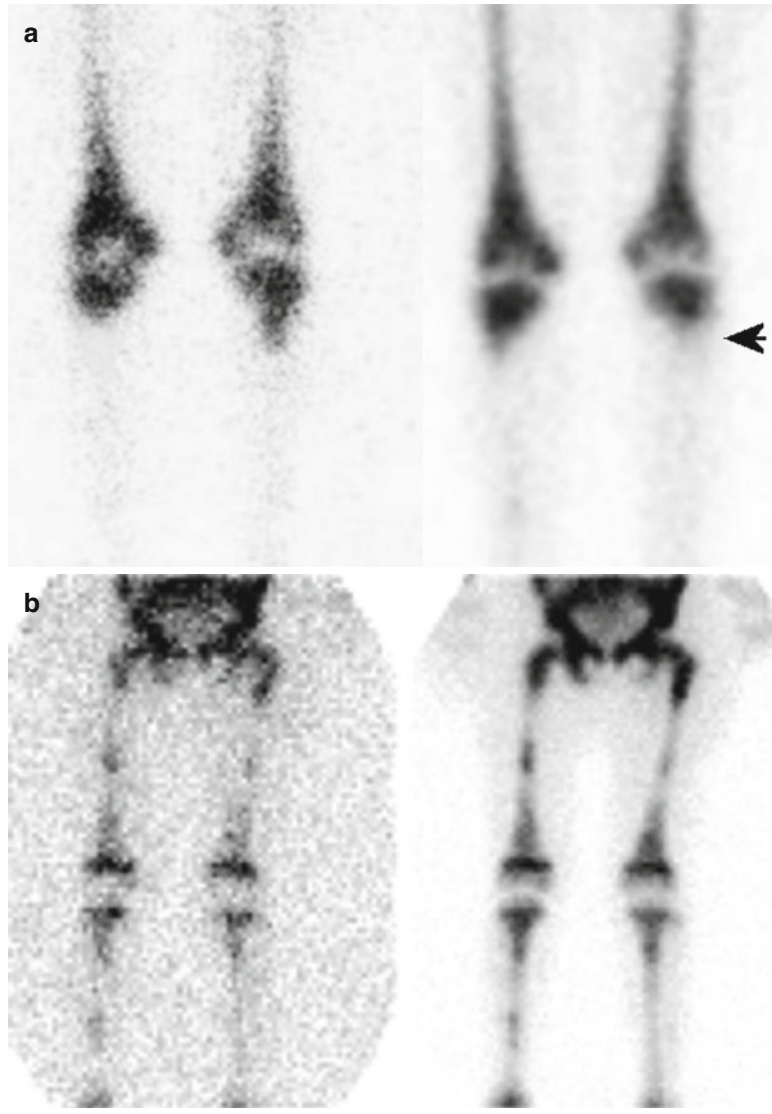

Fig. 24.17 (**a**) There is irregularly increased ^{111}In-labeled leukocyte activity around the knees of a 10-year-old patient, with sickle-cell disease and lower extremity pain (*left*). A photopenic defect in the proximal left tibia (*arrow*) is seen on the marrow image (*right*) and the combined study is consistent with osteomyelitis of the proximal left tibia. (**b**) Labeled leukocyte (*left*) and sulfur colloid (*right*) images of the pelvis and lower extremities performed on a 3-year-old girl with aplastic anemia and left thigh pain. On the labeled leukocyte image, several foci of activity can be appreciated in the mid-right femur, proximal right tibia, and proximal and mid-left femur. On the basis of the leukocyte image alone, it would be difficult to exclude osteomyelitis. The distribution of activity on the sulfur colloid image is virtually the same, however, and therefore the activity present on the leukocyte image is due to marrow, not infection

old may result in persistent blood pool and urinary bladder activity, both of which degrade image quality. The interval between injection and imaging should be at least 30 min. Ten-minute images of the region of interest are acquired on a large field of view gamma camera using a 128×128 matrix. If marrow imaging is performed prior to injection of the ^{111}In-labeled leukocytes, a low-energy, high-resolution parallel hole collimator and a 15 % window centered on 140 keV should be used. If imaging is performed after injection of labeled cells, a 10 % window centered on 140 keV should be used. If simultaneous dual isotope imaging is to be performed, a medium-energy parallel hole collimator is used, with a 10 % window centered on 140 keV, a 5 % window centered on 174 keV, and a 10 % window centered on 247 keV [12].

The overall accuracy of combined leukocyte/marrow imaging is approximately 90 %, which is superior to the 60–80 % accuracy of bone/gallium imaging [95–97]. Labeled leukocyte imaging is preferred to gallium imaging for diagnosing the so-called complicating osteomyelitis [95, 96]. The one exception, in adults, is the spine, where the results of labeled leukocyte imaging have been disappointing, and gallium or FDG imaging is preferred [12, 92, 95, 98]. Although the accuracy of labeled leukocyte imaging in pediatric spinal osteomyelitis is unknown, based on results in the adult population, we use FDG (preferably) or gallium imaging for this indication in children.

Several investigations have confirmed the value of SPECT/CT in the diagnostic workup of musculoskeletal infection. Bar-Shalom et al. [99] reviewed SPECT/CT in 32 patients suspected of having musculoskeletal infection, including 21 who underwent gallium imaging and 11 who underwent labeled leukocyte imaging. They found that SPECT/CT was helpful in about half the patients, primarily by providing precise anatomic localization and delineation of the extent of the infection (Fig. 24.18). Horger et al. [100] compared three-phase bone imaging with SPECT

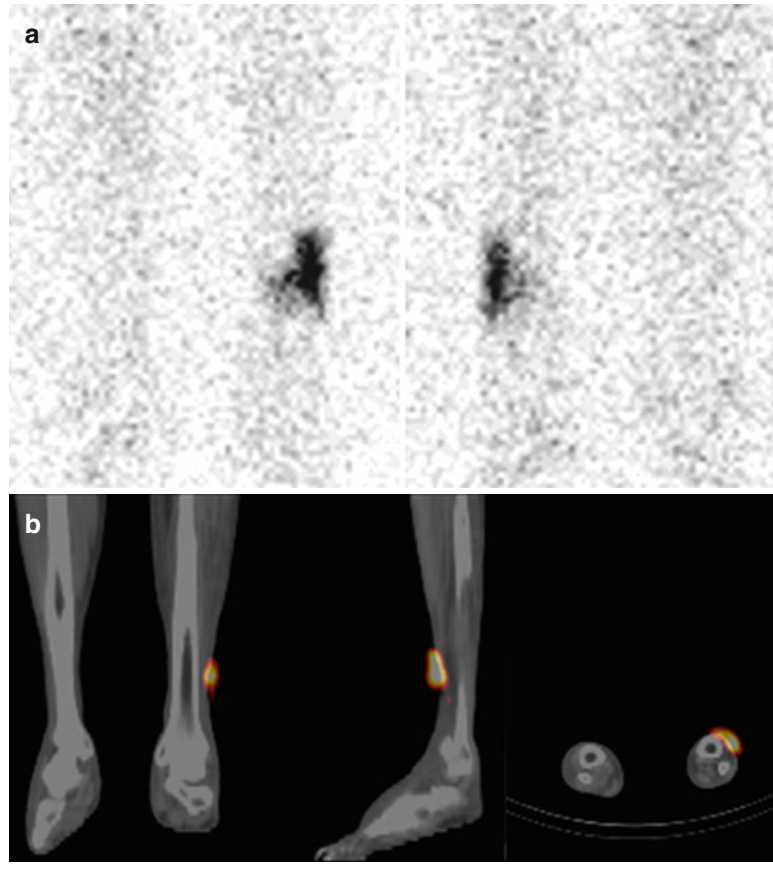

Fig. 24.18 (**a**) Soft tissue infection of the left lower leg. There is a focus of intensely increased activity on the anterior (*left*) and posterior (*right*) ^{111}In-labeled leukocyte images of a patient with a nonhealing ulcer of the lateral aspect of the left lower leg. It is not possible to determine, from these images, whether or not the infection extends into the bone. (**b**) On the coronal (*left*), sagittal (*center*), and axial (*right*) SPECT/CT images, the abnormal uptake clearly is confined to the soft tissues. The tibia and fibula are spared. SPECT/CT is especially useful for localizing labeled leukocyte accumulation in the lower extremities, where there are few or no anatomic landmarks

versus SPECT/CT in 31 patients, including nine with osteomyelitis. Although the sensitivities of the three-phase bone and SPECT/CT both were 78 %, SPECT/CT was significantly more specific than bone scintigraphy alone (86 % versus 50 %, $p<0.05$). The CT component improved specificity by excluding active bone infection and by identifying causes besides infection that were responsible for increased tracer accumulation.

Filippi et al. [101] compared ^{99m}Tc-labeled leukocyte SPECT and SPECT/CT in 28 patients with suspected musculoskeletal infection. Accuracy improved from 64 % for SPECT to 100% for SPECT/CT. The CT component of the test improved localization of labeled leukocyte activity, making it possible to exclude osteomyelitis in seven patients and to provide more precise delineation of the extent of infection in three patients.

Radionuclide imaging is used to evaluate infections in the skull and facial bones. The anatomy of these structures, however, is complex, making tracer localization difficult. Bruni et al. [102] reported that labeled leukocyte SPECT/CT was useful for discriminating between soft tissue and bone involvement and confirming the presence of osteomyelitis by providing accurate anatomic localization and precise delineation of the extent of infection. Moschilla et al. [103] found that, in focal infections involving the skull and skull base, the addition of CT overcomes the poor resolution and variable distribution associated with gallium. They concluded that SPECT/CT obviates the need to routinely perform bone scintigraphy before gallium imaging and improves both diagnostic confidence and test accuracy.

Fluorine-18-FDG PET potentially offers several advantages over conventional nuclear medicine techniques in the evaluation of musculoskeletal infection. PET intrinsically is a high-resolution tomographic technique that enables precise localization, especially when performed as PET/CT, of abnormalities. The small ^{18}F-FDG molecule enters poorly perfused regions quickly; the procedure is completed in 1–2 h and has a relatively low radiation dose. Semiquantitative analysis, readily available with PET, but less feasible with conventional gamma camera imaging, potentially could be useful for differentiating infectious from noninfectious conditions and for monitoring response to therapy. Normal bone marrow has a low glucose metabolism, which may facilitate the distinction of inflammatory cellular infiltrates from hematopoietic marrow. Degenerative bone changes usually show only faintly increased ^{18}F-FDG uptake. Fluorine-18-FDG uptake normalizes relatively rapidly, usually within 3–4 months, following trauma or surgery. Fluorine-18-FDG PET is less expensive than the combinations of leukocyte/bone and leukocyte/marrow imaging [104].

In acute and subacute bone infection, sensitivities of more than 95 % and specificities ranging from 75 to 99 % have been reported for ^{18}F-FDG PET. The test also is useful for diagnosing chronic and low-grade infection because ^{18}F-FDG is taken up by activated macrophages, which are the predominant cell type present in the chronic phase of infection. High sensitivity and specificity for ^{18}F-FDG PET in the assessment of chronic osteomyelitis in the peripheral and axial skeleton also have been reported [104–107].

Fluorine-18-FDG has been reported to be both sensitive and specific for diagnosing implant-associated infections in trauma patients. Fluorine-18-FDG uptake in uninfected fractures and fracture nonunion is significantly lower than in infection and does not appear to be affected by the metallic implants used for fracture fixation [104, 105, 107–109].

Fluorine-18-FDG PET has been particularly useful for detecting osteomyelitis in the axial skeleton, an area where labeled leukocyte imaging is of limited value. It is especially useful for differentiating degenerative from infectious end-plate abnormalities, a distinction that is not always easily made with MRI [110]. In contrast to its utility in the spine, ^{18}F-FDG is not useful for diagnosing prosthetic joint infection. In a recent meta-analysis the sensitivity and specificity of ^{18}F-FDG PET for diagnosing prosthetic joint infection were 82 and 87 %, respectively, considerably lower than what has been reported by numerous investigators, over nearly 30 years, for labeled leukocyte/marrow imaging. Consequently, there appears to be little, if any role for this test in the evaluation of prosthetic joint infection [111, 112]. The data on ^{18}F-FDG imaging in the evaluation of diabetic foot infections are limited and contradictory, and at

the present time, it cannot be recommended as an alternative to labeled leukocyte imaging for diagnosing pedal osteomyelitis in diabetics [113, 114].

There are few published data on the use of ^{18}F-FDG in pediatric osteomyelitis (Fig. 24.19). Warmann et al. [115] performed ^{18}F-FDG PET/CT scans on six children, 4–13 years old, who after completing treatment for osteomyelitis were asymptomatic and had normal serum infection parameters but MRI findings suspicious for residual and/or additional abnormalities. In three of the six patients, there was no abnormal ^{18}F-FDG uptake, and in the other three ^{18}F-FDG uptake was less than what the authors anticipated would be indicative of osteomyelitis. On follow-up ranging from 4 months to more than 5 years, all six patients remained free of disease. In this investigation ^{18}F-FDG PET/CT was superior to MRI for differentiating infection from reparative processes in the skeleton, and the authors concluded that it is reasonable to terminate antibiotic therapy in children with osteomyelitis when laboratory parameters and clinical presentation are normal and when the ^{18}F-FDG PET/CT is

Fig. 24.19 Osteomyelitis of the right femur. Because of leukopenia, a 12-year-old patient with *Staphylococcus aureus* bacteremia and right knee pain was referred for an ^{18}F-FDG PET scan instead of a labeled leukocyte study. There is focal hypermetabolism (*arrows*) in the lateral condyle of right distal femur (SUV_{max}:2.5) on the coronal and sagittal images

not suspicious for active infection. Unfortunately baseline ^{18}F-FDG PET/CT imaging was not performed and none of the patients in the investigation had persistent infection, making it difficult to assess the true merit of the test.

Subperiosteal Abscess

The subperiosteal abscess results from extension of infection from the bony cortex into the subperiosteal space with subsequent elevation of the periosteum itself. On three-phase bone scintigraphy, the subperiosteal abscess presents as an area of hyperperfusion and hyperemia on early images with focal bony photopenia on the delayed bone images. Recognition of this entity is important because, even in the absence of other findings, it strongly suggests underlying osteomyelitis; moreover, it is best treated by surgery rather than antibiotics alone [116].

Septic Arthritis

Arthritis, or inflammation of a joint, may be infectious or noninfectious in origin and no radionuclide study currently available can differentiate one from the other. The classic presentation of acute arthritis on three-phase bone scintigraphy consists of hyperperfusion and hyperemia of a joint, on early images, with increased activity limited to the articular surfaces of the involved bones on delayed images. This presentation can be seen in both septic and aseptic arthritis. Furthermore, osteomyelitis and acute arthritis are not mutually exclusive, and bone scan findings consistent with septic arthritis can potentially mask underlying osteomyelitis. Neither gallium nor labeled leukocyte imaging is useful for separating infectious from noninfectious arthritis. In the case of leukocyte imaging, positive images have been reported in rheumatoid arthritis, acute gouty arthritis, and pseudogout (Fig. 24.20) [117–120]. Fluorine-18-FDG, like ^{67}Ga and labeled leukocytes, accumulates in joints affected by rheumatoid arthritis [121]. Consequently, its role in the evaluation of the septic joint, at least as a diagnostic tool, likely will be limited.

Chronic Recurrent Multifocal Osteomyelitis

Chronic recurrent multifocal osteomyelitis (CRMO) is a rare systemic inflammatory disorder that usually affects children between 5 and 15 years old and is twice as common in girls as in boys [122, 123]. Unlike hematogenous osteomyelitis, the onset of CRMO is insidious. While there is pain and swelling in the affected area, fever is present only in approximately one-third of patients. Most have an elevated erythrocyte sedimentation rate with normal white count and differential [124]. Any part of the skeleton may be affected, although the metaphyses of long bones are the most common sites. The medial ends of the clavicles, facial bones, spine, pelvis, and upper extremities also are frequently involved [83]. Although CRMO and infectious osteomyelitis share the common histopathological feature of chronic inflammation, cultures of the bone lesions in CRMO are sterile. The disease is characterized by intermittent bouts of exacerbations and remissions, over 5–8 years, which then gradually resolve over time. Most cases are erroneously diagnosed as septic osteomyelitis initially, but no microorganisms are identified [84]. The diagnosis, based on clinical, imaging, and pathologic findings, usually is established during recurrent episodes. Treatment is symptomatic; steroids and nonsteroidal anti-inflammatory drugs may offer some relief [83]. For refractory cases, surgical decortication has been performed. Up to 7 % of patients may suffer long-term sequelae including premature closure of the epiphysis, bone deformities, kyphosis, and thoracic outlet syndrome [124].

Active lesions are positive on all three phases of the bone scan, while quiescent lesions may be indistinguishable from adjacent normal bone. Scintigraphy facilitates early detection of the global distribution of the lesions and identifies lesions, which, together with radiographic correlation, may be recognized as characteristic of CRMO. Radionuclide bone imaging also identifies sites suitable for biopsy (Fig. 24.21) [122, 123].

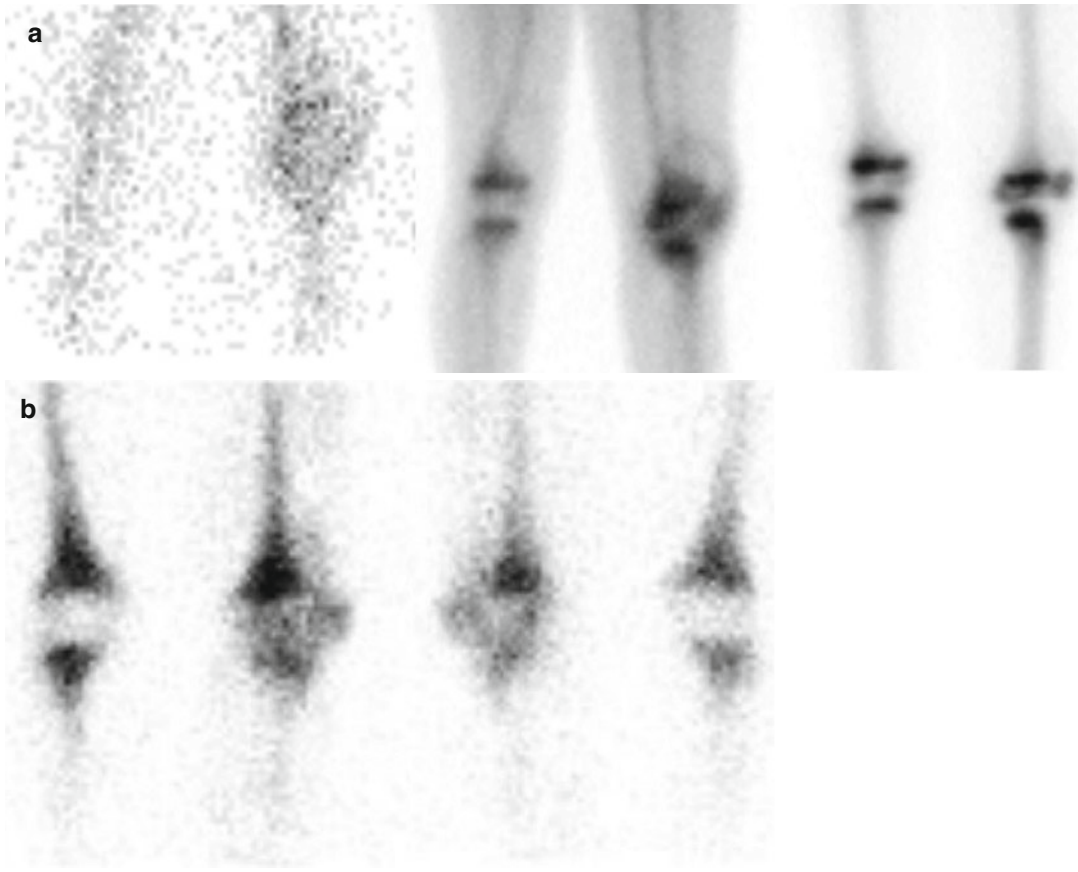

Fig. 24.20 (**a**) Three-phase bone scan performed on a 9-year-old child with septic arthritis of the left knee. This pattern also can be seen in aseptic arthritis. Increased tracer uptake involving the articular surfaces of the involved bones, moreover, can mask an underlying osteomyelitis. (**b**) The labeled leukocyte study of a 10-year-old child demonstrates increased activity in the left knee joint. This uptake pattern can be seen in both septic and aseptic inflammatory arthritis

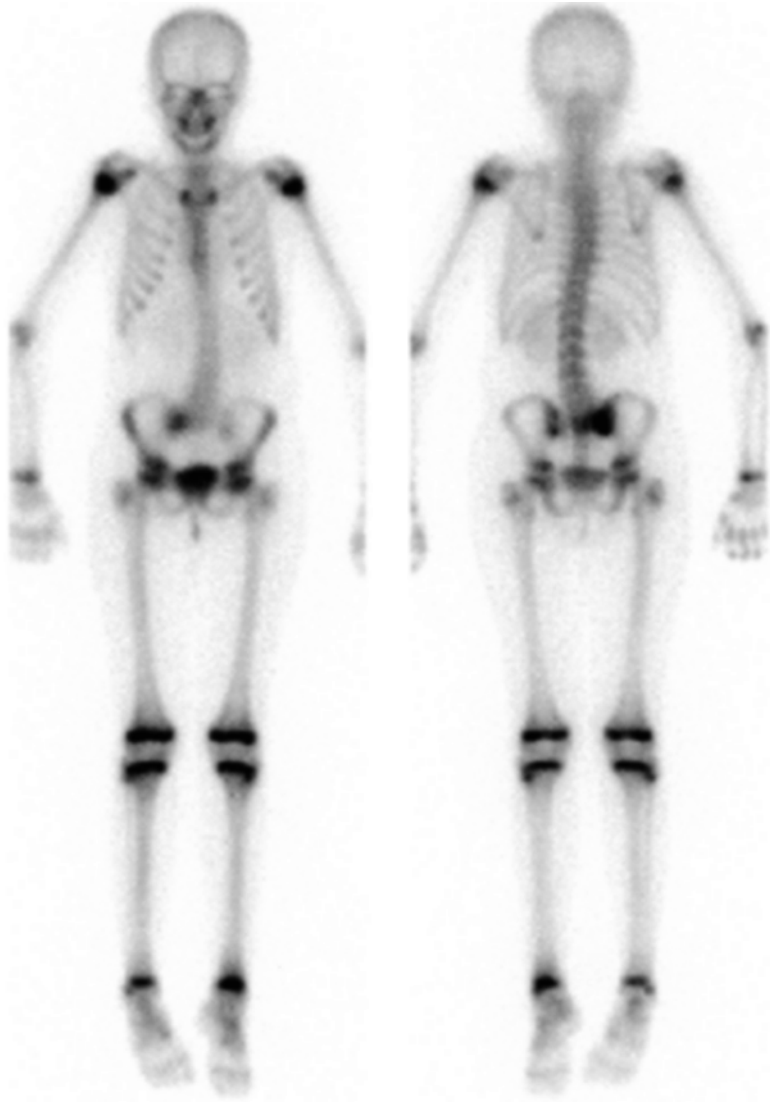

Fig. 24.21 Anterior and posterior whole-body images from a bone scan performed on an 11-year-old girl with CRMO. Note the focal areas of increased activity in the right sacroiliac region and in the distal left tibia

Conclusions

There are a myriad of radionuclide procedures from which to choose when evaluating the child suspected of harboring infection or inflammation. The practicing nuclear physician must, therefore, be cognizant of the tracers available, as well as the indications for which they are most useful, if the value of radionuclide imaging for diagnosing infection and inflammation in children is to be maximized.

References

1. Children's Infection Defense Center. St. Jude Children's Research Hospital.
2. Donohoe KJ, Brown ML, Collier D, et al. Society of Nuclear Medicine procedure guideline for bone scintigraphy. Society of Nuclear Medicine. 2003.
3. Love C, Din AS, Tomas MB, Kalapparambath TP, et al. Radionuclide bone imaging: an illustrative review. Radiographics. 2003;23:341–58.
4. Palestro CJ. The current role of gallium imaging in infection. Semin Nucl Med. 1994;24:128–41.
5. Palestro CJ, Malat J, Collica CJ, et al. Incidental diagnosis of pregnancy on bone and gallium scintigraphy. J Nucl Med. 1986;27:370–2.
6. Lopez OL, Maisano ER. Ga-67 uptake post cesarean section. Clin Nucl Med. 1984;9:103–4.
7. Desai AG, Intenzo C, Park C, et al. Drug-induced gallium uptake in the breasts. Clin Nucl Med. 1987;12:703–4.
8. Vasquez R, Oates E, Sarno RC, et al. Gallium-67 breast uptake in a patient with hypothalamic granuloma (sarcoid). J Nucl Med. 1998;19:118–21.
9. Engelstad B, Luks S, Hattner RS. Altered ^{67}Ga citrate distribution in patients with multiple red blood cell transfusions. AJR Am J Roentgenol. 1982;139:755–9.
10. Hattner RS, White DL. Gallium-67/stable gadolinium antagonism. MRI contrast agent markedly alters the normal biodistribution of Gallium–67. J Nucl Med. 1990;31:1844–6.
11. Palestro CJ, Brown ML, Forstrom LA, et al. Society of Nuclear Medicine procedure guideline for gallium scintigraphy in inflammation. 2004.
12. Love C, Palestro CJ. Radionuclide imaging of infection. J Nucl Med Tech. 2004;32:47–57.
13. Palestro CJ, Brown ML, Forstrom LA, et al. Society of Nuclear Medicine procedure guideline for In-111 leukocyte scintigraphy for suspected infection/inflammation. 2004.
14. Palestro CJ, Brown ML, Forstrom LA, et al. Society of Nuclear Medicine procedure guideline for Tc-99m Exametazime (HMPAO) labeled leukocyte scintigraphy for suspected infection/inflammation. 2004.
15. Palestro CJ, Love C, Bhargava KK. Labeled leukocyte imaging: current status and future directions. Q J Nucl Med Mol Imaging. 2009;53:105–23.
16. Ingbar DH. Mechanisms of lung injury. In: Bone RC, editor. Pulmonary and critical care medicine. St Louis: Mosby; 1998. p. 17–21.
17. Love C, Opoku-Agyemang P, Tomas MB, et al. Pulmonary activity on labeled leukocyte images: physiologic, pathologic, and imaging correlation. Radiographics. 2002;22:1385–93.
18. Saverymuttu SH, Peters AM, Danpure HJ, et al. Lung transit of ^{111}Indium-labelled granulocytes: relationship to labelling techniques. Scand J Haematol. 1983;30:151–60.
19. Roddie ME, Peters AM, Danpure HJ, et al. Inflammation: imaging with Tc-99 m HMPAO-labeled leukocytes. Radiology. 1988;166:767–72.
20. McAfee JG, Samin A. In-111 labeled leukocytes: a review of problems in image interpretation. Radiology. 1985;155:221–9.
21. Crass JR, L'Heureux P, Loken M. False-positive ^{111}In-labeled leukocyte scan in cystic fibrosis. Clin Nucl Med. 1979;4:291–3.
22. Fineman DS, Palestro CJ, Kim CK, et al. Detection of abnormalities in febrile AIDS patients with In-111-labeled leukocyte and Ga-67 scintigraphy. Radiology. 1989;170:677–80.
23. Palestro CJ, Padilla ML, Swyer AJ, et al. Diffuse pulmonary uptake of indium-111 labeled leukocytes in drug-induced pneumonitis. J Nucl Med. 1992;33:1175–7.
24. Powe JE, Short A, Sibbald WJ, et al. Pulmonary accumulation of polymorphonuclear leukocytes in the adult respiratory distress syndrome. Crit Care Med. 1982;10:712–8.
25. Love C, Tomas MB, Palestro CJ. Pulmonary activity on labeled leukocyte images: patterns of uptake and their significance. Nucl Med Commun. 2002;23:559–63.
26. Hangen DH, Segall GM, Harney EW, et al. Kinetics of leukocyte sequestration in the lungs of acutely septic primates: a study using ^{111}In-labeled autologous leukocytes. J Surg Res. 1990;48:196.
27. Malmros C, Holst E, Hansson L, et al. Dynamic accumulation of neutrophils in lungs and visceral organs during early abdominal sepsis in the pig. World J Surg. 1994;18:811–6.
28. Blomquist S, Malmros C, Martensson L, et al. Absence of lung reactions after complement depletion during dialysis: an experimental study in pigs. Artif Organs. 1991;15:397–401.
29. Palestro CJ, Love C, Tronco GG, et al. Fever in the postoperative patient: role of radionuclide imaging in its diagnosis. Radiographics. 2000;20:1649–60.
30. Love C, Tomas MB, Tronco GG, et al. Imaging infection and inflammation with ^{18}F-FDG-PET. Radiographics. 2005;25:1357–68.
31. Bell GI, Burant CF, Takeda J, et al. Structure and function of mammalian facilitative sugar transporters. J Biol Chem. 1993;268:19161–4.

32. Pauwels EK, Ribeiro MJ, Stoot JH, et al. FDG accumulation and tumor biology. Nucl Med Biol. 1998;25:317–22.
33. Zhuang H, Alavi A. 18-Fluorodeoxyglucose positron emission tomographic imaging in the detection and monitoring of infection and inflammation. Semin Nucl Med. 2002;32:47–59.
34. Mochizuki T, Tsukamoto E, Kuge Y, et al. FDG uptake and glucose transporter subtype expressions in experimental tumor and inflammation models. J Nucl Med. 2001;42:1551–5.
35. Kubota R, Yamada S, Kubota K, et al. Intratumoral distribution of fluorine-18-fluorodeoxyglucose in vivo: high accumulation in macrophages and granulation tissues studied by microautoradiography. J Nucl Med. 1992;33:1972–80.
36. Paik JY, Lee KH, Choe YS, et al. Augmented ^{18}F-FDG uptake in activated monocytes occurs during the priming process and involves tyrosine kinases and protein kinase C. J Nucl Med. 2004;45:124–8.
37. Gelfand MJ, Parisi MT, Treves ST. Pediatric radiopharmaceutical administered doses: 2010 North American consensus guidelines. J Nucl Med. 2010;52:318–22.
38. Palestro CJ, Goldsmith SJ. The use of gallium and labeled leukocyte scintigraphy in the AIDS patient. Q J Nucl Med. 1995;39:221–30.
39. O'Doherty MJ, Barrington SF, Campbell M, et al. PET scanning and the human immunodeficiency virus-positive patient. J Nucl Med. 1997;38:1575–83.
40. Hoffman JM, Waskin HA, Schifter T, et al. FDG-PET in differentiating lymphoma from nonmalignant central nervous system lesions in patients with AIDS. J Nucl Med. 1993;34:567–75.
41. Lorin MI, Feigin RD. Fever without localizing signs and fever of unknown origin. In: Feigin RD, Cherry JD, editors. Textbook of pediatric infectious diseases. 4th ed. Philadelphia: WB Saunders; 1998. p. 820–30.
42. Buonomo C, Treves ST. Gallium scanning in children with fever of unknown origin. Pediatr Radiol. 1993;23:307–10.
43. Haentjens M, Piepsz A, Schell-Frederick E, et al. Limitations in the use of indium-111-oxine-labeled leucocytes for the diagnosis of occult infection in children. Pediatr Radiol. 1987;17:139–42.
44. Williamson SL, Williamson MR, Siebert JJ, et al. Indium 111 white blood cell scanning in the pediatric population. Pediatr Radiol. 1986;16:493–7.
45. Steele RW, Jones SM, Lowe BA, et al. Usefulness of scanning procedures for diagnosis of fever of unknown origin in children. J Pediatr. 1991;119:526–30.
46. Blockmans D, Knockaert D, Maes A, et al. Clinical value of [^{18}F]fluoro-deoxyglucose positron emission tomography for patients with fever of unknown origin. Clin Infect Dis. 2001;32:191–6.
47. Meller J, Altenvoerde G, Munzel U, et al. Fever of unknown origin: prospective comparison of [^{18}F] FDG imaging with a double-head coincidence camera and gallium-67 citrate SPET. Eur J Nucl Med. 2000;27:1617–25.
48. Bleeker-Rovers CP, de Kleijn EM, Corstens FH, et al. Clinical value of FDG PET in patients with fever of unknown origin and patients suspected of focal infection or inflammation. Eur J Nucl Med Mol Imaging. 2004;31:29–37.
49. Lorenzen J, Buchert R, Bohuslavizki KH. Value of FDG PET in patients with fever of unknown origin. Nucl Med Commun. 2001;22:779–83.
50. Jasper N, Däbritz J, Frosch M, et al. Diagnostic value of [18F]-FDG PET/CT in children with fever of unknown origin or unexplained signs of inflammation. Eur J Nucl Med Mol Imaging. 2010;37:136–45.
51. Sturm E, Rings EH, Scholvinck EH, et al. Fluordeoxyglucose positron emission tomography contributes to management of pediatric liver transplantation candidates with fever of unknown origin. Liver Transpl. 2006;12:1698–704.
52. Ozen S, Fuhlbrigge RC. Update in paediatric vasculitis. Best Pract Res Clin Rheumatol. 2009;23:679–88.
53. Khubchandani RP, Viswanathan V. Pediatric vasculitides: a generalists approach. Indian J Pediatr. 2010;77:1165–71.
54. Basu N, Watts R, Bajema I, et al. EULAR points to consider in the development of classification and diagnostic criteria in systemic vasculitis. Ann Rheum Dis. 2010;69:1744–50.
55. Palestro CJ, Love C. Decreased sensitivity of 18F-FDG imaging in infection & inflammation. Semin Nucl Med. 2012;42(4):261–6.
56. Zerizer I, Tan K, Khan S, et al. Role of FDG-PET and PET/CT in the diagnosis and management of vasculitis. Eur J Radiol. 2010;73:504–9.
57. Bleeker-Rovers CP, Bredie SJ, van der Meer JW, et al. Fluorine 18 fluorodeoxyglucose positron emission tomography in the diagnosis and follow-up of three patients with vasculitis. Am J Med. 2004;116:50–3.
58. Brodmann M, Lipp RW, Passath A, et al. The role of 2-18F-fluoro-2-deoxy-d-glucose positron emission tomography in the diagnosis of giant cell arteritis of the temporal arteries. Rheumatology. 2004;43:241–2.
59. Blockmans D, De CL, Vanderschueren S, Knockaert D, et al. Repetitive 18F fluorodeoxyglucose positron emission tomography in giant cell arteritis: a prospective study of 35 patients. Arthritis Rheum. 2006;55:131–7.
60. Both M, Ahmadi-Simab K, Reuter M, et al. MRI and FDG-PET in the assessment of inflammatory aortic arch syndrome in complicated courses of giant cell arteritis. Ann Rheum Dis. 2008;67:1030–3.
61. Papathanasiou ND, Du Y, Menezes LJ, et al. 18F-Fluorodeoxyglucose PET/CT in the evaluation of large-vessel vasculitis: diagnostic performance and correlation with clinical and laboratory parameters. Br J Radiol. 2012;85(1014):e188–94.
62. Ulshen M. Inflammatory bowel disease. In: Behrman RE, Kliegman RM, Arvin AM, editors. Nelson textbook of pediatrics. 15th ed. Philadelphia: W.B. Saunders; 1996. p. 1080–4.
63. Shah DB, Cosgrove M, Rees JIS, et al. The technetium white cell scan as an initial imaging investigation for

evaluating suspected childhood inflammatory bowel disease. J Pediatr Gastoenterol Nutr. 1997;25:524–8.
64. Alberini JL, Badran A, Freneau E, et al. Technetium-99 m HMPAO-labeled leukocyte imaging compared with endoscopy, ultrasonography, and contrast radiology in children with inflammatory bowel disease. J Pediatr Gastoenterol Nutr. 2001;32:278–86.
65. Del Rosario MA, Fitzgerald JF, Siddiqui AR, et al. Clinical applications of technetium Tc 99 m hexamethyl propylene amine oxime leukocyte scan in children with inflammatory bowel disease. J Pediatr Gastroenterol Nutr. 1999;28:63–70.
66. Caobelli F, Panarotto MB, Andreoli F, et al. Is 99mTc-HMPAO granulocyte scan an alternative to endoscopy in pediatric chronic inflammatory bowel disease (IBD)? Eur J Pediatr. 2011;170:51–7.
67. Charron M, Del Rosario JF, Kocoshis S. Comparison of the sensitivity of early versus delayed imaging with Tc-99 m HMPAO WBC in children with inflammatory bowel disease. Clin Nucl Med. 1998;23:649–53.
68. Bhargava SA, Orenstein SR, Charron M. Technetium-99 m hexamethylpropyleneamine-oxime-labeled leukocyte scintigraphy in inflammatory bowel disease in children. J Pediatr. 1994;125:213–7.
69. Charron M. Inflammatory bowel disease in pediatric patients. Q J Nucl Med. 1997;41:309–20.
70. Charron M, del Rosario FJ, Kocoshis SA. Pediatric inflammatory bowel disease: assessment with scintigraphy with ^{99m}Tc white blood cells. Radiology. 1999;212:507–13.
71. Charron M. Pediatric inflammatory bowel disease imaged with Tc-99 m white blood cells [The Nuclear Medicine Atlas]. Clin Nucl Med. 2000;25:708–15.
72. Granquist L, Chapman SC, Hvidsten S, et al. Evaluation of ^{99m}Tc-HMPAO leukocyte scintigraphy in the investigation of pediatric inflammatory bowel disease. J Pediatr. 2003;143:48–53.
73. Davison SM, Chapman S, Murphy MS. ^{99m}Tc-HMPAO leucocyte scintigraphy fails to detect Crohn's disease in the proximal gastrointestinal tract. Arch Dis Child. 2001;85:43–6.
74. Bicik I, Bauerfeind P, Breitbach T, et al. Inflammatory bowel disease activity measured by positron-emission tomography. Lancet. 1997;350:262.
75. Skehan SJ, Issenman R, Mernagh J, et al. 18F-fluorodeoxyglucose positron tomography in diagnosis of paediatric inflammatory bowel disease. Lancet. 1999;354:836–7.
76. Lemberg DA, Issenman RM, Cawdron R, et al. Positron emission tomography in the investigation of pediatric inflammatory bowel disease. Inflamm Bowel Dis. 2005;11:733–8.
77. Loffler M, Weckesser M, Franzius C, et al. High diagnostic value of 18F-FDG-PET in pediatric patients with chronic inflammatory bowel disease. Ann N Y Acad Sci. 2006;1072:379–785.
78. Dabritz J, Jaspera N, Loeffler M, et al. Noninvasive assessment of pediatric inflammatory bowel disease with 18F-fluorodeoxyglucose–positron emission tomography and computed tomography. Eur J Gastroenterol Hepatol. 2011;23:81–9.
79. Spier BJ, Perlman SB, Reichelderfer M. FDG-PET in inflammatory bowel disease. Q J Nucl Med Mol Imaging. 2009;53:64–71.
80. Santiago-Restrepo C, Gimenez CR, McCarthy K. Imaging of osteomyelitis and musculoskeletal soft tissue infections: current concepts. Rheum Dis Clin North Am. 2003;29:89–109.
81. Carek PJ, Dickerson LM, Sack JL. Diagnosis and management of osteomyelitis. Am Fam Physician. 2001;63:2413–20.
82. Kim MK, Karpas A. Orthopedic emergencies: the limping child. Clin Pediatr Emerg Med. 2002;3:129–37.
83. Krogstad P, Smith AL. Osteomyelitis and septic arthritis. In: Feigin RD, Cherry JD, editors. Textbook of pediatric infectious diseases. 4th ed. Philadelphia: WB Saunders; 1998. p. 683–704.
84. McCarthy JJ, Dormans JP, Kozin SH, et al. Musculoskeletal infections in children: basic treatment principles and recent advancements. J Bone Joint Surg Am. 2004;86:850–63.
85. Kleinman PK. A regional approach to osteomyelitis of the lower extremities in children. Radiol Clin North Am. 2002;40:1033–59.
86. Schauwecker DS. The scintigraphic diagnosis of osteomyelitis. AJR Am J Roentgenol. 1992;158:9–18.
87. Ash JM, Gilday DL. The futility of bone scanning in neonatal osteomyelitis: concise communication. J Nucl Med. 1980;21:417–20.
88. Berkowitz ID, Wenzel W. "Normal" technetium bone scans in patients with acute osteomyelitis. Am J Dis Child. 1980;134:828–30.
89. Sullivan DC, Rosenfield NS, Ogden J, et al. Problems in the scintigraphic detection of osteomyelitis in children. Radiology. 1980;135:731–6.
90. Bressler EL, Conway JJ, Weiss SC. Neonatal osteomyelitis examined by bone scintigraphy. Radiology. 1984;152:685–8.
91. Nadel HR, Stilwell ME. Nuclear medicine topics in pediatric musculoskeletal disease: techniques and applications. Radiol Clin North Am. 2001;39:619–51.
92. Palestro CJ. Musculoskeletal infection. In: Freeman LM, editor. Nuclear medicine annual. New York: Raven Press; 1994. p. 91–119.
93. Rosenthall L, Lisbona R, Hernandez M, et al. ^{99m}Tc-PP and ^{67}Ga imaging following insertion of orthopedic devices. Radiology. 1979;133:717–21.
94. Lisbona R, Rosenthall L. Observations on the sequential use of 99mTc-phosphate complex and 67Ga imaging in osteomyelitis, cellulitis, and septic arthritis. Radiology. 1977;123:123–9.
95. Palestro CJ, Love C. Radionuclide imaging of musculoskeletal infection: conventional agents. Semin Musculoskelet Radiol. 2007;11:335–52.
96. Palestro CJ, Love C, Tronco GG, et al. Combined labeled leukocyte and technetium-99 m sulfur colloid marrow imaging for diagnosing musculoskeletal infection: principles, technique, interpretation, indications and limitations. Radiographics. 2006;26:859–70.

97. Palestro CJ, Roumanas P, Swyer AJ, et al. Diagnosis of musculoskeletal infection using combined In-111 labeled leukocyte and Tc-99 m SC marrow imaging. Clin Nucl Med. 1992;17:269–73.
98. Palestro CJ, Kim CK, Swyer AJ, et al. Radionuclide diagnosis of vertebral osteomyelitis: indium-111-leukocyte and technetium-99 m-methylene diphosphonate bone scintigraphy. J Nucl Med. 1991;32:1861–5.
99. Bar-Shalom R, Yefremov N, Guralnik L, et al. SPECT/CT using ^{67}Ga and ^{111}In-labeled leukocyte scintigraphy for diagnosis of infection. J Nucl Med. 2006;47:587–94.
100. Horger M, Eschmann SM, Pfannenberg C, et al. Added value of SPECT/CT in patients suspected of having bone infection: preliminary results. Arch Orthop Trauma Surg. 2007;127:211–21.
101. Filippi L, Schillaci O. Tc-99 m HMPAO-labeled leukocyte scintigraphy for bone and joint infections. J Nucl Med. 2006;47:1908–13.
102. Bruni C, Padovano F, Travascio L, et al. Usefulness of hybrid SPECT/CT for the 99mTc-HMPAO-labeled leukocyte scintigraphy in a case of cranial osteomyelitis. Braz J Infect Dis. 2008;12:558–60.
103. Moschilla G, Thompson J, Turner JH. Co-registered gallium-67 SPECT/CT imaging in the diagnosis of infection and monitoring treatment. World J Nucl Med. 2006;5:32–9.
104. Strobel K, Stumpe KDM. PET/CT in musculoskeletal infection. Semin Musculoskelet Radiol. 2007;11:353–64.
105. Guhlmann A, Brecht-Krauss D, Suger G, et al. Chronic osteomyelitis: detection with FDG PET and correlation with histopathologic findings. Radiology. 1998;206:749–54.
106. Guhlmann A, Brecht-Krauss D, Suger G, et al. Fluorine-18-FDG PET and technetium-99 m antigranulocyte antibody scintigraphy in chronic osteomyelitis. J Nucl Med. 1998;39:2145–52.
107. de Winter F, van de Wiele C, Vogelaers D, et al. Fluorine-18 fluorodeoxyglucose positron emission tomography: a highly accurate imaging modality for the diagnosis of chronic musculoskeletal infections. J Bone Joint Surg Am. 2001;83-A:651–60.
108. Kalicke T, Schmitz A, Risse JH, et al. Fluorine-18 fluorodeoxyglucose PET in infectious bone diseases: results of histologically confirmed cases. Eur J Nucl Med Mol Imaging. 2007;27:524–8.
109. Schiesser M, Stumpe KD, Trentz O, et al. Detection of metallic implant-associated infections with FDG PET in patients with trauma: correlation with microbiologic results. Radiology. 2003;226:391–8.
110. Gemmel F, Rijk PC, Parlevliet T, et al. Expanding role of ^{18}F-fluoro-D-deoxyglucose PET and PET/CT in spinal infections. Eur Spine J. 2010;19:540–51.
111. Kwee TC, Kwee RM, Alavi A. FDG-PET for diagnosing prosthetic joint infection: systematic review and metaanalysis. Eur J Nucl Med Mol Imaging. 2008;35:2122–32.
112. Love C, Marwin SE, Palestro CJ. Nuclear medicine and the infected joint replacement. Semin Nucl Med. 2009;39:66–78.
113. Familiari D, Glaudemans AW, Vitale V, et al. Can sequential 18F-FDG-PET/CT imaging replace WBC imaging in the diabetic foot? J Nucl Med. 2011;52:1012–9.
114. Palestro CJ, Love C. Nuclear medicine and diabetic foot infections. Semin Nucl Med. 2009;39:52–65.
115. Warmann SW, Dittmann H, Seitz G, et al. Follow-up of acute osteomyelitis in children: the possible role of PET/CT in selected cases. J Pediatr Surg. 2011;46:1550–6.
116. Allwright SJ, Miller JH, Gilsanz V. Subperiosteal abscess in children: scintigraphic appearance. Radiology. 1991;179:725–9.
117. Coleman RE, Samuelson CO, Bain S. Imaging with Tc-99 m MDP and Ga-67 citrate in patient with rheumatoid arthritis and suspected septic arthritis. J Nucl Med. 1982;23:479–82.
118. Uno K, Matsui N, Nohira K, et al. Indium-111 leukocyte imaging in patients with rheumatoid arthritis. J Nucl Med. 1986;27:339–44.
119. Palestro CJ, Vega A, Kim CK, et al. Appearance of acute gouty arthritis on indium-111-labeled scintigraphy. J Nucl Med. 1990;31:682–5.
120. Palestro CJ, Goldsmith SJ. In-111-labeled leukocyte imaging in a case of pseudogout. Clin Nucl Med. 1992;17:366–7.
121. Beckers C, Ribbens C, Andre B, et al. Assessment of disease activity in rheumatoid arthritis with (18) F-FDG PET. J Nucl Med. 2004;45:956–64.
122. Mortensson W, Edeburn G, Fries M, et al. Chronic recurrent multifocal osteomyelitis in children: a roentgenologic and scintigraphic investigation. Acta Radiol. 1988;29:565–70.
123. Iyer RS, Thapa MM, Chew FS. Imaging of chronic recurrent multifocal osteomyelitis: self-assessment module. AJR Am J Roentgenol. 2011;196(6 Suppl):WS62–5.
124. Schultz C, Holterhus PM, Seidel A, et al. Chronic recurrent multifocal osteomyelitis in children. Pediatr Infect Dis J. 1999;18:1008–13.

Pediatric Molecular Imaging

25

Heike Elisabeth Daldrup-Link
and Sanjiv Sam Gambhir

Molecular imaging technologies allow an in vivo detection, characterization, and quantification of cellular and molecular abnormalities that form the basis of disease. By contrast, traditional diagnostic imaging techniques detect morphologic-structural abnormalities that represent end effects of these biological alterations. The ability to image cellular and molecular alterations of target tissues in vivo, in patients, potentially allows for disease detection at an earlier stage of development, more specific characterization of the natural evolution of the underlying pathologic process (e.g., benign to malignant, low to high aggressiveness), and enable better tailored, individualized therapy approaches. While translational molecular imaging approaches are increasingly integrated into the clinical care of adult patients, clinical molecular imaging applications in pediatric patients are still limited due to safety considerations and regulatory and administrative hurdles. However, many diseases in children have specific molecular fingerprints that make them well-suited candidates for targeted imaging approaches. The clinical need for more specific information along with the continued success of molecular imaging techniques in adult patients will ultimately penetrate into pediatric imaging applications. New, child-adapted molecular imaging approaches are expected to improve our knowledge of the biology of pediatric disease and support the development of tailored diagnostic and therapeutic approaches. This chapter will provide an overview over current and emerging molecular imaging techniques for pediatric patients. We will elaborate upon specific considerations for child-adapted imaging tests and discuss emerging clinical applications. Future developments aim to integrate the advantages of several different molecular imaging tools towards the development of more comprehensive, quantitative readouts that can direct early decision making, guide individualized clinical care procedures, and ultimately, accelerate and improve positive treatment outcomes.

H.E. Daldrup-Link, MD, PhD (✉)
Department of Radiology, Pediatric Radiology Section,
Lucile Packard Children's Hospital,
Stanford School of Medicine, Stanford, CA, USA
e-mail: heiked@stanford.edu,
h.e.daldrup-link@stanford.edu

S.S. Gambhir, MD, PhD
Department of Radiology and Department of
Bioengineering, Molecular Imaging
Program at Stanford (MIPS),
Stanford University School of Medicine,
Stanford, CA, USA

Department of Materials Science and Engineering,
Stanford University School of Engineering,
Stanford, CA USA

Molecular Imaging Targets

Molecular imaging provides a dynamic and effective means of in vivo detection of cellular and molecular targets through real-time evaluation of spatiotemporal interactions with a designated

S.T. Treves (ed.), *Pediatric Nuclear Medicine and Molecular Imaging*,
DOI 10.1007/978-1-4614-9551-2_25,

imaging marker, generation of a topical map, and extraction of quantitative estimates of local target concentrations that are linked to the presence, aggressiveness, prognosis, and/or therapy response of the pathology of interest. The first step for molecular imaging approaches is to identify a clinically significant molecular target that adequately represents the process being studied. Examples of suitable molecular imaging targets of pediatric cancers include (i) extracellular proteins which have been secreted by cells of interest, such as matrix metalloproteinases (MMPs) in retinoblastoma [1]; (ii) cell membrane bound targets, such as Gd2, somatostatin, and CXCR4 chemokine receptors in neuroblastoma [2]; (iii) intracellular proteins, such as Yin Yang 1 (YY1) proteins in the cytoplasm of aggressive phenotypes of osteosarcoma cells [3]; (iv) specific mRNA profiles in rhabdomyosarcomas and neuroblastomas [4]; and (v) specific DNA alterations such as the MYC oncogene [5]. The next step is to select a clinically applicable molecular imaging probe that binds to the target molecule with a high degree of specificity. Desirable features of a molecular imaging marker is one that is biocompatible, possesses a tolerable toxicity profile, exudes a strong imaging signal, is quantifiable, maintains stability in vivo, has low background signal with selective target enhancement, should not dilute with cell divisions nor transfer to other cells, enable a reasonable time window for detection, and is finally completely eliminated from the body. Examples of such probes are provided in the clinical applications section below. Importantly, the selected probe has to be detectable with a clinically applicable imaging technology that provides adequate sensitivity and spatiotemporal resolution for its in vivo localization and quantification. Besides these biological considerations, practical aspects such as feasibility in the pediatric population, availability and cost will largely affect successful clinical translations of promising pediatric molecular imaging approaches.

Molecular Imaging Techniques

The rapid increase in knowledge of cellular and molecular targets for molecular imaging is accompanied by the development of novel, more specific and quantitative imaging technologies that facilitate disease detection, characterization, treatment monitoring, and posttreatment evaluation for disease recurrence [6–8]. Molecular imaging instrumentation encompasses numerous tools that enable visualization and quantification of particular cellular and molecular targets and pathways. Molecular imaging techniques require 2-dimensional or 3-dimensional imaging capabilities, high sensitivity, and quantitative information. Clinically applicable technological platforms include ultrasound, optical imaging, computed tomography (CT), magnetic resonance (MR) imaging, single-photon emission tomography (SPECT), and positron emission tomography (PET). It is important to understand the capabilities and limitations of these respective imaging tools, as they are being combined and integrated in hybrid imaging techniques, which are developing rapidly within the clinical realm (Fig. 25.1).

Ultrasound

Ultrasound is the screening modality of choice for a large variety of diseases in children. Advantages are the ease of use and wide availability, low cost, portability, no need for sedation, and lack of radiation exposure, thereby allowing quick and repetitive, noninvasive exams of the abdomen/pelvis, the neck, the heart, mediastinum and pleural space, the musculoskeletal system, and, in young children, the brain. Ultrasound is the only imaging technique that allows simultaneous integration with a clinical examination, e.g., correlation of ultrasound evaluations of the appendix with Mc Burney's sign. Ultrasound also allows for dynamic evaluations, e.g., of the stability of dysplastic hip joints in adduction-abduction or the motility of a thickened pylorus. Doppler ultrasound can add noninvasive information about vascular anatomy as well as the direction, velocity, and coherence of blood flow and organ perfusion. Limitations include primarily anatomical information, limited penetration depth in large/big patients, and dependence of image quality on well-trained personnel. Although much sought by the pediatric radiology community, there are few molecular imaging

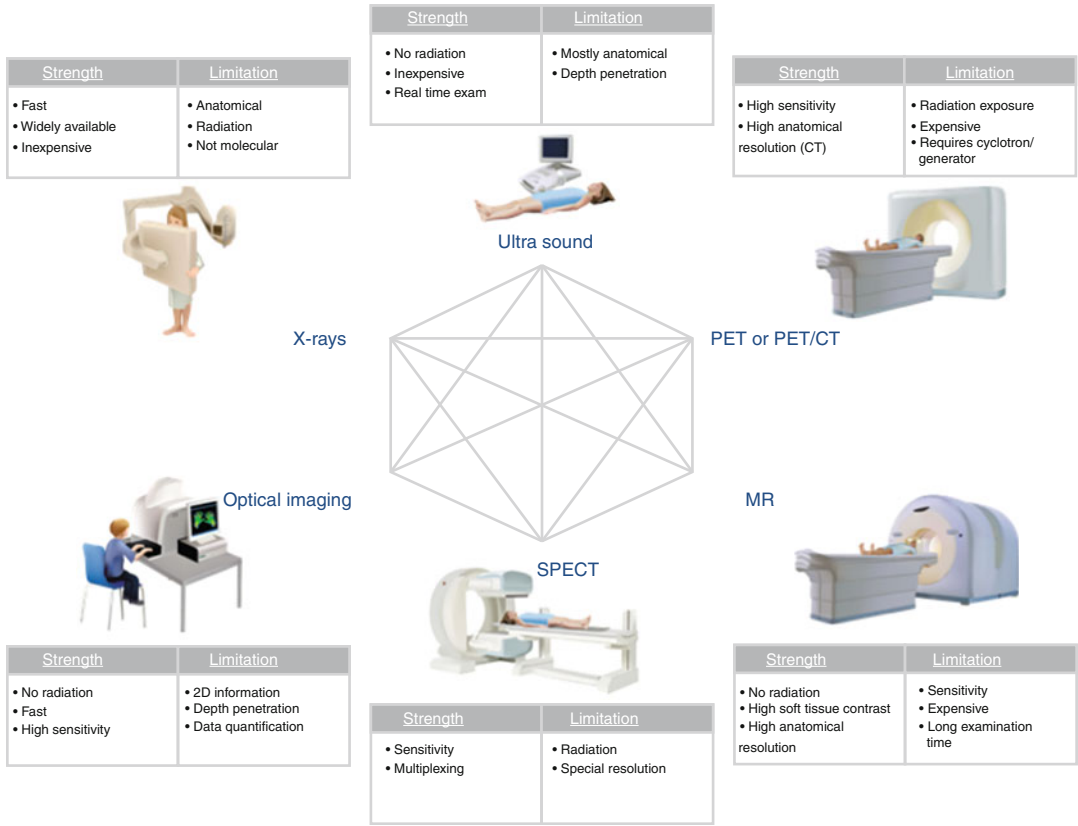

Fig. 25.1 Developments of hybrid molecular imaging technologies, as indicated by connections between the displayed cartoons and their respective strengths. Another evolving new imaging technology of specific interest for pediatric applications is photoacoustic imaging, which integrates both optical imaging and ultrasound technologies and which is currently entering clinical applications

applications available for ultrasound of children to date. Microbubble contrast agents, which are in the process of being introduced to the clinic, may provide a powerful platform to increase the specificity of ultrasound exams in children [9]. The use of microbubbles has been explored for improved detection of cancers and inflammations [10, 11], improved evaluation of brain ischemia [9, 12], echocardiography [13], and ultrasound-guided voiding cystourethrograms [14], among others [9, 10]. Targeted microbubbles may provide opportunities for more specific evaluations of tumors and inflammations [9–11, 15], although applications tailored to questions relevant for pediatric patients have not been described yet. Since the majority of μm-sized microbubbles stay in the intravascular space and do not extravasate, targets of molecular microbubble agents have to be present on the intraluminal vessel surface. Recognizing emerging cross-connections between imaging modalities, it is important to note that microbubbles can be also utilized as MR contrast agents [16], thereby opening opportunities for multiplexing on MR or PET/MR scans, e.g., via a combination of microbubble-mediated vascular imaging, Gd-chelate-mediated tissue enhancement, and FDG-mediated assessment of tissue metabolic activity. An integration of ultrasound probes and PET detectors is a relatively unexplored area, which could be of value for sedation-free tumor staging of small children and guided biopsies. A bimodal PET-US endoscopic probe combining in a miniaturized system a fully digital, 200 ps time resolution time-of-flight PET detector head (TOF-PET) coupled to a commercial ultrasound (US) assisted biopsy endoscope is currently being explored for targeted biopsies of pancreatic cancers in adults

(http://www-flc.desy.de/pet/projects/endotofpetus/index.php) and, if successful, could be similarly applied in children.

Optical Imaging

Optical imaging (OI) is based on the detection of light from various sources (fluorescence, bioluminescence, absorption, or reflectance). OI is very attractive for pediatric imaging applications because of its rapid (<1 min) and radiation-free image data acquisition. In addition, OI is inexpensive, noninvasive, and has molecular sensitivity, which is close to that of conventional radionuclide imaging techniques and several orders of magnitude greater than MRI [8, 17]. Limitations of OI include the lack of penetration depth, limited anatomical resolution, and complicated algorithms for data quantification. Biocompatible fluorescent probes and labels with emission wavelengths in the near-infrared (NIR) spectra (700–1,000 nm) are an important tool for optical imaging, and at least one fluorescent label, indocyanine green (ICG), is FDA-approved [18, 19]. Examples of clinical OI applications include the detection of inflamed joints of arthritic hands [19] (Fig. 25.2), detection of breast lesions [20], intraoperative detection of peritoneal metastases [21], and intraoperative brain tumor delineation combined with functional brain mapping [22]. Recent technical developments in instrumentation include dual-axes endoscopes fitted with a fluorescence confocal microendoscope for gastroscopic or colonoscopic lesion detection [23] and handheld probe-based optical imagers for intraoperative tumor delineation [24]. There are also a variety of hybrid imaging approaches, such as fusion of optical with x-ray data [25], ultrasound [26], MRI [27], and SPECT/PET [8, 28]. Multifunctional

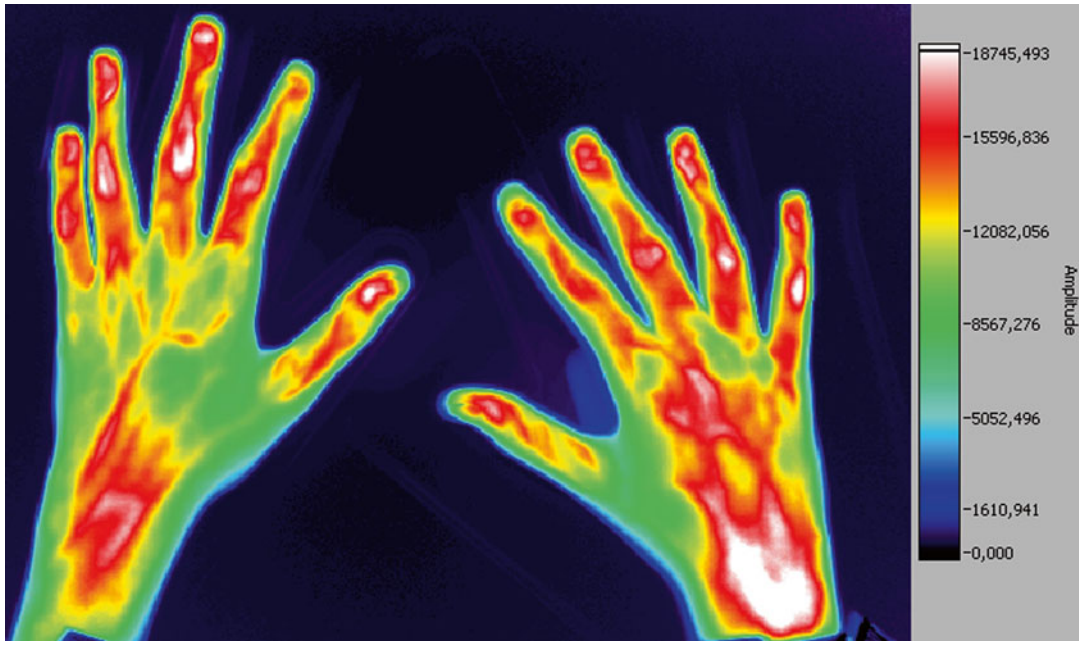

Fig. 25.2 Optical image (maximum intensity projection) of both hands of a 6-year-old girl with pain in the carpal area and finger joints of both hands and clinical signs of juvenile idiopathic arthritis. Optical images after intravenous injection of indocyanine green (ICG) show focal hyperperfusion in the radiocarpal joint, the carpal joints, the proximal carpophalangeal joint D5, and the metacarpophalangeal joints D2–4 of the right hand, as well as focal hyperperfusion of the radiocarpal joint and metacarpophalangeal joint D1–4 of the left hand, indicating active synovitis. Of note, this example shows a physiologic imaging application with the nonspecific blood pool agent ICG. Further applications of this novel, noninvasive and radiation-free imaging technology await introduction of more specific cellular and molecular fluorescent markers (Courtesy of Michel Eisenblätter, MD and Christoph Bremer, M.D., Department of Radiology, St. Franziskus Hospital, Münster, Germany)

contrast agents are developed for these hybrid technologies, which allow cross-validation of biomarker distribution [29] or biomarker activation [8]. For example, PET data could be used to track and quantify the concentration of a tumor-specific biomarker, whereas concomitant fluorescence labels could indicate enzymatic activation of a specific multifunctional probe [8].

Photoacoustic Imaging

Photoacoustic imaging is an emerging new imaging modality of specific interest for the pediatric imaging community because of its radiation-free, quick, and noninvasive nature [8]. The technique is based on delivery of non-ionizing, pulsed laser light into a tissue of interest. The incoming light is absorbed and converted into heat, leading to thermoelastic expansion of the target tissue and emission of ultrasound waves, which can be detected with an ultrasound transducer ("light in – ultrasound out"). The change in temperature (heat) in the target tissue(s) is extremely small and nonperturbing. A potentially important application for the pediatric population is photoacoustic measurement of tissue hemoglobin (Hb) concentrations and oxygen saturations based on differential absorption of light by oxygenated and deoxygenated Hb. This application could be utilized for noninvasive monitoring of brain and visceral organ oxygenation states in premature infants. In order to distinguish pathologies from normal organs, specific photoacoustic imaging agents may need to be administered [8]. Administration of molecular imaging agents that are targeted and are able to absorb light is potentially a powerful way to provide significant growth of this emerging modality. Furthermore, photoacoustics may also be useful as a modality when combined with ultrasound so that the information can be superimposed on a combined image. Advantages compared to optical imaging include deeper tissue penetration (up to 5 cm) and increased spatial resolution. Advantages compared to ultrasound include less image noise, ability to detect tissue oxygenation without any exogenous molecular imaging agents, and higher sensitivity for the detection of targeted probes (pictogram compared to microgram for US).

Computed Tomography (CT)

Computed tomography has limited utility for molecular imaging applications as a "stand-alone" technology because of its low sensitivity and low soft tissue contrast. However, CT is a well-established technology for providing "background" anatomical information for SPECT and PET/CT techniques. In the realm of pediatric imaging, the radiation exposure associated with CT is of high concern, and CT imaging tests are only performed if other modalities such as ultrasound or MR cannot be accommodated [30]. Therefore, the introduction and evaluation of alternative hybrid imaging techniques, such as PET/MR, should be carefully considered for the evaluation of children.

Single-Photon Emission Computed Tomography (SPECT)

SPECT imaging is well established for evaluation of a wide variety of pathologies in pediatric patients. SPECT imaging agents emit non-coincident gamma rays, as opposed to the coincident gamma rays associated with positron emitters for PET imaging. SPECT has the unique advantage, that it allows to detect single-photon radionuclides (e.g., ^{99m}Tc, ^{111}In, ^{123}I, ^{201}Tl, ^{133}Xe), which emit gamma rays at different energy levels, thereby potentially allowing simultaneous detection of multiple biochemical targets (multiplexing). Some examples of clinical SPECT imaging agents that target molecular processes include ^{123}I-metaiodobenzylguanidine (MIBG), a functional analogue of norepinephrine taken up by amine transporters on the cell surface of neuroblastomas, ^{111}In-DPTA-octreotide (DTPA = diethylenetriamine pentaacetate) for imaging the somatostatin receptor in neuroendocrine tumors [31], ^{99m}Tc TRODAT-1 ([2[[2-[[[3-(4-chlorophenyl)-8-methyl-8-azabicyclo[3,2,1]-oct-2-yl] methyl](2mercaptoethyl)amino]ethyl] amino] ethanethiolato(3-)-N2,N2',S2,S2]oxo-[1R-exo-exo)])-[^{99m}Tc]-technetium) for dopamine transporter imaging [32, 33], ^{99m}Tc-annexin V for imaging apoptosis [34], and xenon ^{133}Xe gas inhalation for the evaluation of pulmonary function

and regional cerebral blood flow (rCBF) assessment [35]. More recent technical developments include handheld gamma cameras for intraoperative detection of small tumors [36]. Limitations of SPECT include a lower sensitivity when compared to PET and lack of data quantification due to the need to estimate attenuation. However, the ongoing development of multi-detector CT coupled with SPECT in newer SPECT/CT devices [6, 8, 37] promises to significantly improve the quantitative precision of SPECT relative to PET in the future, with a resultant greater focus on the radiopharmaceutical, rather than the imaging device itself, in specific clinical applications.

Positron Emission Tomography (PET) and PET/CT

PET and PET/CT imaging have been established as a clinical tool for pediatric molecular imaging applications for many years. Advantages, which led to its clinical success, include its high sensitivity (detecting picomolar concentrations) and a high target-to-background contrast. Fluorine-18-2-fluoro-2-deoxy glucose (FDG) PET and PET/CT are being used for detection of a large variety of diseases, including pediatric malignancies, inflammatory disorders, and CNS disorders, particularly epilepsy and infantile spasms [8, 38] (Table 25.1). Additional appli-

Table 25.1 PET/CT applications for staging and restaging of pediatric malignant tumors: conclusions from clinical studies

Pathology	PET/CT applications for staging and restaging of pediatric malignant tumors: conclusions from clinical studies
Lymphoma	^{18}F-FDG PET/CT is more accurate than conventional imaging in detecting malignant lesions in childhood lymphoma and in predicting poor response to treatment [39–41]
	^{18}F-FDG PET/CT provides substantial complementary value to bone marrow biopsy in the initial diagnosis of pediatric lymphoma [42]
	^{18}F-FDG PET is more sensitive than bone scans for detection of osseous metastases [43]
	High doses of corticosteroids during induction of chemotherapy altered ^{18}F-FDG uptake patterns in children with lymphoblastic lymphoma [44]
	^{18}F-FDG PET/CT significantly influences radiation treatment target definition and field design in patients with Hodgkin's lymphoma [45]
	Limited WB ^{18}F-FDG PET/CT is appropriate for restaging under/after therapy when initial disease is confined to a limited WB FOV [46]
Sarcomas	Bone sarcomas: ^{18}F-FDG PET/CT is more accurate than conventional imaging in staging childhood primary bone tumors, excluding lung lesions [47, 48]
	Bone sarcomas: No added information from ^{99m}Tc-MDP bone scans compared to ^{18}F-FDG PET/CT [49]
	Bone sarcomas: Degree of tumor ^{18}F-FDG uptake allows for monitoring of therapeutic responses [49]
	^{18}F-FDG PET/CT useful in predicting therapy responses after only one course of neoadjuvant chemotherapy [50]
	Rhabdomyosarcomas: ^{18}F-FDG PET/CT valuable for initial staging (especially detection of lymph node and bone metastases) and prediction of outcomes [51, 52]
Wilms' tumor	Active Wilms' tumor is ^{18}F-FDG avid. ^{18}F-FDG PET/CT useful for defining tumor extent. Small pulmonary metastases better visualized with CT [53, 54]
	After chemotherapy, higher SUV was seen in histologically high-risk disease [53]
Head and neck cancer	^{18}F-FDG PET/CT more accurate than conventional imaging for tumor staging, recommended as first imaging modality [55]
Nasopharyngeal carcinoma	^{18}F-FDG PET/CT may underestimate tumor extent and regional lymphadenopathy compared with MRI at the time of diagnosis. ^{18}F-FDG PET/CT is sensitive and specific for follow-up and enables earlier determination of disease remission [56]
Neuroblastoma	^{68}Ga-DOTATATE can be used to image children with neuroblastoma and identify those suitable for molecular radiotherapy with ^{177}Lu-DOTATATE [57]
	^{18}F-DOPA PET/CT more accurate than CT/MR and MIBG in advanced-stage neuroblastoma [58, 59]
Neurofibromatosis I	^{18}F-FDG PET/CT useful for detecting malignant transformation in peripheral nerve sheath tumors [60]

cations in children using other radiotracers include ^{18}F-NaF for imaging of various traumatic causes of back pain [61], bone metastases [62], or non-accidental trauma [63] as well as ^{124}I-MIBG PET [64] and ^{18}F-DOPA PET/CT [58, 59] for staging of neuroblastoma, possibly replacing ^{123}I-MIBG SPECT. A main limitation with regard to molecular imaging applications is the inability for multiplexing (detection of more than one molecular target in one imaging session). PET radioisotopes emit positrons that lead to two gamma photons of the same energy (511 keV), thereby omitting parallel tracking of two different tracers. New PET/MR approaches may in part solve this issue and allow for simultaneous tracking of PET tracers and MR probes (Gd- and Fe-based labels).

The radiation exposure of PET/CT exams is of concern for the pediatric imaging community, and various "low dose" approaches are currently being pursued [65–69], such as eliminating duplicate diagnostic CT scans, performing low dose diagnostic contrast-enhanced CT scans as part of the PET/CT scan, using the diagnostic CT for attenuation correction of PET data (thereby eliminating a duplicate attenuation correction scan), lowering the dose of the applied radiotracer, and replacing the diagnostic CT by MR, as discussed in the next section.

Magnetic Resonance (MR) Imaging and PET/MR

MR imaging has the distinct advantage that it is not associated with any radiation exposure and that it provides a very high soft tissue contrast, thereby being the preferred imaging modality for staging and restaging of many primary tumors in children, including tumors of the CNS, abdomen, pelvis, and musculoskeletal system [70, 71]. MR imaging provides unique opportunities to interrogate specific physiologic processes noninvasively and repetitively without any radiation exposure. Examples include visualization and quantification of proton diffusion for tumor detection and characterization [70, 72–75], blood and tissue oxygenation for functional imaging applications [76, 77], and drug or metabolite concentrations in tumors or normal organs [78–80].

Hyperpolarized MR spectroscopic imaging is an exciting, relatively new area of molecular MR imaging, currently entering clinical applications in adult patients. For clinical applications, ^{13}C-labeled molecules are polarized into an antiparallel orientation, far beyond their thermal equilibrium, using a "dynamic nuclear polarization" (DNP) system outside of the MR magnet. The hyperpolarization of the probe decays rapidly, leaving a time window of a few minutes for transport of the probe to the patient, intravenous injection, and in vivo spectroscopic imaging of ^{13}C-containing metabolites in a clinical high field (≥3 T) MR scanner [8, 81]. Any delay in this process prevents acquisition of hyperpolarized MRI data, which is a major challenge for pediatric applications. Nevertheless, if completed successfully, hyperpolarized MRI enables rapid acquisition and dynamic mapping of fast biological processes in vivo. Specific applications include the use of [1-^{13}C]pyruvate hyperpolarized MRI for visualization of glycolytic processes during de novo tumor formation and therapy-induced regression [82] and the evaluation of the metabolism of [1-^{13}C]pyruvate to CO(2) relative to lactate as an indicator of preserved mitochondrial function in cardiac diseases [83]. Of note ^{13}C-hyperpolarized molecules are typically endogenous and have no known biological risks. However, they are injected at high concentrations, and possible side effects will need to be evaluated, particularly with regard to applications in children.

Another, immediately clinically applicable molecular MR imaging approach is the generation of whole body diffusion-weighted MR scans [73, 74], which provide a similar tumor-to-background contrast and improved anatomical resolution compared to ^{18}F-FDG PET scans (Fig. 25.3). These radiation-free whole body diffusion-weighted MR scans deserve close attention, since accumulating evidence suggests equivalent sensitivity for tumor detection compared to ^{18}F-FDG PET. The diffusion-weighted scans also provide a sensitive assessment of tumor response to therapy, which can be quantified based on the "apparent diffusion coefficient," a quantitative measure of the magnitude of water molecule diffusion (or Brownian motion) in target tissues [84] (Fig. 25.4, Table 25.2). Besides some technical challenges, which are currently being addressed, "biological" limitations of diffusion-weighted MR scans include a restricted diffusion in a variety of normal organs, such as the spleen, normal red marrow,

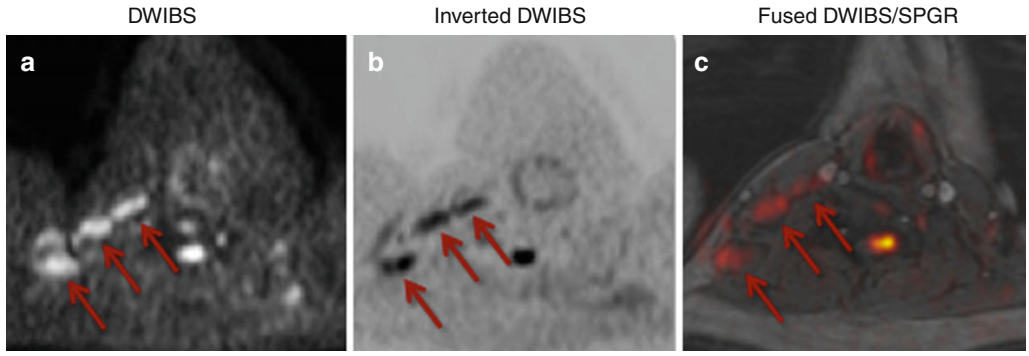

Fig. 25.3 Axial diffusion-weighed MR scan of the lower neck of a patient with malignant lymphoma: (**a**) original and (**b**) inverted diffusion-weighted MR scan (*DWIBS* diffusion-weighted imaging with background subtraction) shows three lymph nodes with restricted proton diffusion in the right lower neck (*arrows*). (**c**) The diffusion-weighted scans can be color-encoded and superimposed on a contrast-enhanced T1-weighted MR scan (*SPGR* spoiled gradient recalled echo sequence)

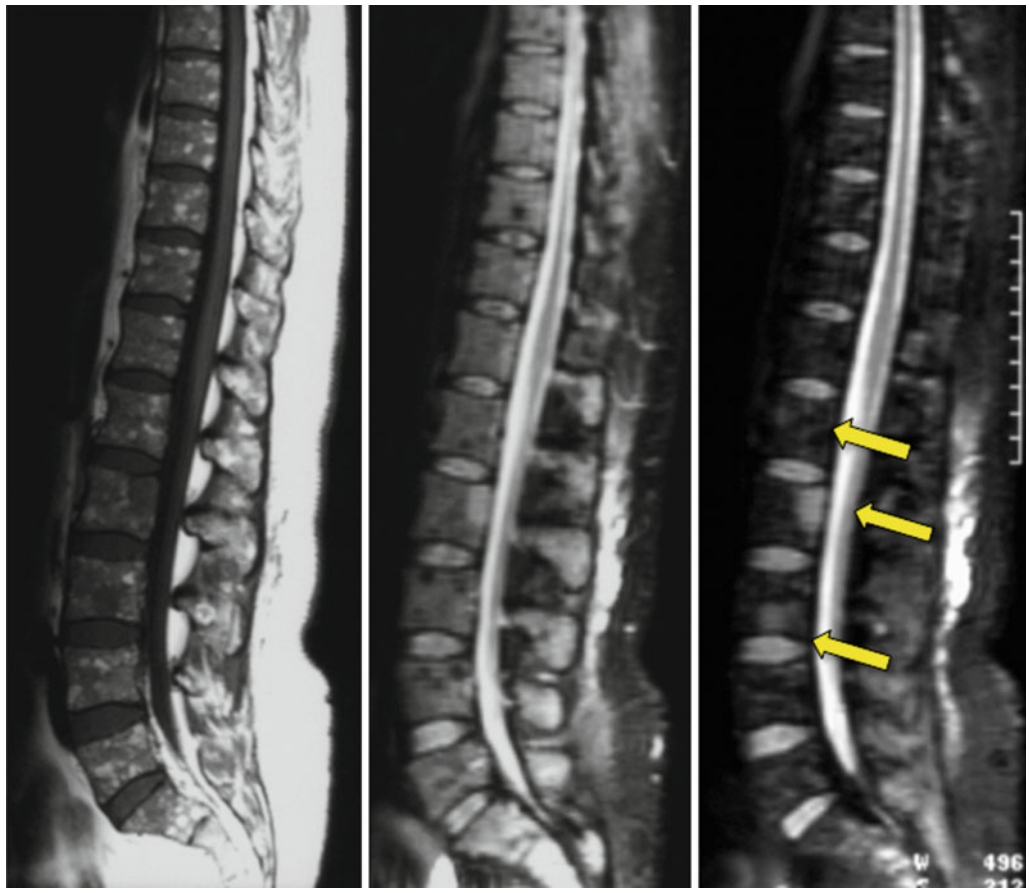

Fig. 25.4 Sagittal MR images of the spine of a patient with malignant lymphoma and multifocal bone marrow infiltration, status post chemotherapy and GCSF treatment. The reconverted, highly cellular hematopoietic marrow demonstrates low signal on plain T1-weighted MR images and high signal on STIR images, masking T1-hypointense and T2-hyperintense focal bone marrow lesions. Following intravenous injection of iron oxide nanoparticles, postcontrast STIR images demonstrate a decreased signal of the normal bone marrow due to iron oxide uptake by macrophages with persistent hyperintense signal of focal bone marrow lesions, thereby increasing the lesion-to-background contrast (From Daldrup-Link et al. [85] and Metz et al. [86])

Table 25.2 Current literature on diffusion-weighted MR imaging

Author, year	Number of patients	Site/pathology	MR parameters, field strength	Results and conclusion
Pediatric patients				
Ording Muller, 2011 [87]	42 children	Normal spine	DWIBS ($b=1{,}000$), 1.5 T	Restricted diffusion of the bone marrow is a normal finding in children, with an asymmetric distribution seen in 48 % of children
Alibek, 2009 [88]	29 children	CNS, chest, A/P, MSK tumors	DWI ($b=0$, 500, 1,000), 1.5 T	DWI is reliable for accurate detection and delineation of malignant pediatric tumors
Humphries, 2007 [89]	19 children	Abdominal tumors	DWI ($b=0$, 500, 1,000), 1.5 T	ADC values overlap between malignant and benign lesions. Correlation between cellularity and ADC, but cell count is not the sole determinant
Kato, 2011 [90]	56 children	Non-palpable testes	T2, DWI ($b=1{,}000$), 1.5 T	Both T2-FS and DWI facilitate sensitive detection of intra-abdominal testes
Adult patients				
Kyriazi, 2011 [91]	42	Ovarian cancer	DWI ($b=0$, 600, 900, 1,050), 1.5 T	*Tumor ADC values change in response to treatment*: DW MR imaging detects treatment response in patients with advanced ovarian cancer
Irie et al., 2011 [92]	23	Gall bladder	DWI (0, 1,000), 1.5 T	*High b-value DWI differentiate benign and malignant lesions*: (ADC – Benign gallbladder: lesions 2.26 ± 0.44 ; Malignant: 1.34 ± 0.50)
Razek, 2011 [93]	52	Renal	DWI ($b=0$, 800), 1.5 T	ADC of malignant tumors significantly different from benign tumors (Benign: 1.87 ± 0.5; Malignant: 1.56 ± 0.26; Cutoff 1.84)
Nagayama, 2011 [94]	45	Prostate	DWI ($b=0$, 800), 1.5 T	Cut off of 1.35×10–3 mm^2/s can differentiate malignant from nonmalignant zones (cancer 1.04 ± 0.31, noncancer peripheral zone 1.94 ± 0.31)
Kilickesmez, 2009 [95]	80	Renal and adrenal lesions	DWI ($b=0$, 500, 1,000), 1.5 T	Mean ADCs of renal pathologies significantly different from normal parenchyma. ADCs of benign lesions significantly different from renal clear cell carcinomas
Wang, 2011 [96]	21	Pancreas	DWI, ADC ($b=0$, 500), 1.5 T	Poorly differentiated pancreatic adenocarcinoma had lower ADC values (1.46 ± 0.17) than well differentiated carcinomas (2.10 ± 0.42)
Akduman, 2008 [97]	28	Abdominal lymph nodes	DWI ($b=600$), 1.5 T	Significant difference in ADC values of benign (2.38 ± 0.29) and malignant (1.84 ± 0.37) lymph nodes
Fujii, 2008 [98]	119	Ovarian tumors	DWI ($b=0$, 1,000), 1.5 T	No significant difference in ADC values of benign (1.47 ± 0.42) and malignant ovarian lesions (1.41 ± 0.34)
Kiliçkesmez, 2009 [99]	77	Liver lesions	DWI ($b=0$, 500, 1,000), 1.5 T	Mean ADCs of all focal liver lesions significantly different from normal liver parenchyma. No statistical significant difference between HCC and metastases
Soylu, 2010 [100]	55	Chronic hepatitis	DWI ($b=0$, 500, 1,000), 1.5 T	The ADC slightly lower in chronic hepatitis (1.46 ± 0.17) compared to normal liver (1.56 ± 0.16). No correlation between ADC values and fibrosis stages

(continued)

Table 25.2 (continued)

Author, year	Number of patients	Site/pathology	MR parameters, field strength	Results and conclusion
Rao, 2012 [101]	150	Abdominal organs	DWI (b=0, 50, 100, 200, 400, 800), 1.5 and 3 T	*No difference in ADC values at 1.5 and 3 T*: no difference in ADC values of normal abdominal organs at 1.5 and 3 T (19 volunteers, 150 patients)
Rosenkrantz, 2011 [102]	8	Normal abdominal organs	DWI(b=0, 500, 800),1.5 and 3 T	Compared with 1.5 T, SS EPI at 3.0 T provided generally similar ADC values, however, with worse image quality
Bilgili, 2011 [103]	11	healthy volunteers	DWI, (b=100, 500), 1.5 T	Significant differences in ADCs among locations and b values (P<.05), no significant differences in ADCs between repetitive imaging sessions
Saremi, 2011 [104]	13	Normal abdominal organs	DWI (b=50, 1,000), 1.5 and 3 T	Higher image quality and lower artifacts for breath hold DWI compared with free breathing. ADC not significantly different between 1.5 and 3 T (P>0.05)
Dale, 2010 [105]	16	Healthy volunteers	DWI (b=50, 400, 800) 1.5 and 3 T	Significant differences between ADC values at 1.5 and 3 T for liver (P<0.001), but not for pancreas or spleen
Satoh, 2011 [106]	130	Peritoneal metastases	DWI (b=1,000), 1.5 T	*Comparison with other imaging modalities*: ^{18}F PET/CT more sensitive than DWI. If PET/CT is not available, DWI can be used as a screening tool
Bozkurt, 2011 [107]	19	Ovarian, colon, GI, pancreatic	DWI (b=400, 800), 1.5 T	High b-value DWI improves the detection of peritoneal tumors when combined with conventional MRI
Yang, 2011 [108]	45	Liver	DWI (b=0, 50, 800), 1.5 T	DWI better than T2 w MRI for detection of 97 malignant hepatic lesions
Braithwaite, 2009 [109]	20	Abdomen	DW (b=0, 400), 3 T	No significant difference in ADC values between different imaging sessions, or on repeated sequences
Yang, 2008 [110]	56	Variety of primary tumors	DWI (b=NA), 1.5 T	Whole body DWI showed higher sensitivity and specificity for detecting skeletal metastasis when compared to CT, MRI and PET
Kiliçkesmez, 2008 [111]	50	Normal abdominal organs	DWI (b=0, 500, 1,000), 1.5 T	ADC values significantly different between four lobes of liver, between cortex and medulla of kidney but not between pancreatic head, body and tail
Tsushima, 2007 [112]	110	Abdomen	DWI (b=0, 1,000), 1.5 T	High b-value DWI has high sensitivity and specificity for detection of malignant tumors

DWIBS diffusion-weighted imaging with background suppression

salivary glands, bowel mucosa, some normal lymph nodes, and ovaries/testes, which limits tumor detection at these sites [84]. However, new MR imaging approaches, which suppress the false positive signal in these organs, are currently being developed and explored [84]. Thus, whole body diffusion-weighted MRI scans may replace ^{18}F-FDG PET scans for certain tumor staging indications in the near future, thereby necessitating more specific tracers for PET. Other new technological advances include intraoperative MR scanners, which allow image guided resection of CNS tumors [113], simultaneous fMRI and EEG scans for co-localization of epileptogenic foci [77], MR scanners integrated with high frequency focused ultrasound for targeted tumor ablations [114, 115], and integrated PET/MRI systems [116–118]. PET/MRI combines the high anatomical resolution and high soft tissue contrast of MRI with the high sensitivity of PET, thereby overcoming the limited sensitivity of traditional MRI contrast agents (10^{-3}–10^{-5} mol/L), overcoming the limited soft tissue contrast of PET or PET/CT scans, and providing significantly less radiation exposure compared to PET/CT. PET/MRI opens new opportunities to sequentially or simultaneously evaluate a large variety of physiologic processes (Table 25.3), which can be utilized to validate new biomarkers, to combine tracer quantification with functional assessment (e.g., tissue concentration and activation of an activatable tracer), or to investigate successive physiologic processes (e.g., receptor density and therapeutic drug uptake/activation). Combining whole body diffusion scans for tumor detection with "traditional" MRI scans for anatomical localization and tumor-specific PET tracers for functional assessment (e.g., ^{124}I-MIBG) could bring "one-stop-shop" local and whole body staging approaches to reality.

Clinical Molecular Imaging Applications with Future Perspectives

Disease detection, characterization, intervention, and monitoring are essential components for management and outcome of nearly every pediatric patient. Especially in the field of oncology, patients often undergo a multitude of diagnostic tests, which are collected and synthetized by the interpreting physician. Current and future trends aim towards integrated imaging approaches, described above, and coordinating them with workflows for other diagnostic tests, e.g., collection of blood samples after placement of a venous access for an imaging exam, collection of urine samples directly before a voiding cystourethrogram, or obtaining EEG and ECG data while the patient is waiting for an imaging test or even during an imaging scan. The ultimate goal is to provide a comprehensive evaluation and diagnosis with a single visit and diagnostic workup, which is not only convenient for the patient but also saves direct and indirect health-care costs by streamlining procedures, minimizing hospitalizations, and minimizing lost school or work time of children and their parents.

On the clinical side, genomics and molecular biomarkers are increasingly integrated in routine diagnostic workups of blood and tissue samples from patients with cancer or other complex multisystem disorders, in an effort to provide a more detailed understanding of the underlying disease process and to develop individualized therapy approaches. Examples include the determination of expression of the MYC oncogene for the diagnosis of neuroblastoma and medulloblastoma or the evaluation of α-fetoprotein and/or β-human chorionic gonadotropin (HCG) levels in germ cell tumors. The integration of this information with imaging data would further enhance our ability to align clinical care procedures towards individualized therapeutic and/or surgical interventions.

Molecular imaging biomarkers dynamically assess and quantify gene and protein function and resultant changes in tissue metabolism in vivo by interacting chemically with specific target cells or target molecules, and thereby, providing a specific imaging signal as a result of this interaction [8]. Thus, molecular imaging biomarkers provide more specific information about pathologic processes compared to traditional imaging approaches that rely on passive tissue accumulation and tracer density alone. In addition, molecular imaging biomarkers provide

Table 25.3 Overview of molecular imaging approaches for MR imaging and PET

Physiologic parameter	MRI	PET	Applications
Oncogene expression	Hyperpolarized ^{13}C-pyruvate MR spectroscopy [82] (and other HP agents)	Radiolabeled amino acids and peptides [119]	Early detection of cancer formation and regression, cancer characterization
Angiogenesis	Contrast-enhanced MR [120]	Radiolabeled RGD peptides [8]	Tumor detection and characterization
Microvascular permeability	Kinetic analyses of contrast-enhanced MR, preferably macromolecular contrast agents, nanoparticles [120]	Radiolabeled macromolecules, e.g., albumin [121]	Tumor characterization, tumor grading, estimating drug delivery to tumors
Blood flow	Contrast-enhanced MR, phase contrast sequences, ASL [122, 123], ^{17}O-Water bolus MR	^{15}O-Water [122, 124]	Tumor perfusion, tumor therapy response, myocardial ischemia, brain ischemia
DNA synthesis; amino/nucleic acid metabolism	MR spectroscopy: Cho, NAA, Cr [79, 80]	^{11}C-Methionine, ^{18}F-FET [125]	Brain tumor detection and grading, therapy response, tumor recurrence
Cell membrane synthesis	MR spectroscopy: Cho, NAA, Cr [79, 80]	^{11}C- and ^{18}F-Choline, ^{11}C-acetate [125]	Detection of bone metastases, therapy response (acetate: low grade liver cancers)
Tumor cell proliferation	MR spectroscopy: Cho/NAA and Cho/Cr ratios [79, 80], citrate MR	^{18}F-FLT [126]	Tumor grading, therapy response
Glucose consumption	GlucoseCEST after a Glc bolus	^{18}F-FDG [127, 128]	Tumor detection, tumor characterization, tumor therapy response, evaluation of inflammations and ischemia
Proton diffusion	Diffusion-weighted sequences [84]	–	Tumor detection, tumor characterization, tumor therapy response, evaluation of inflammations and ischemia
Mitochondrial function	Hyperpolarized ^{13}C-MRI [82]; $^{1-13}$C-pyruvate, $^{5-13}$C-glutamate, $^{2-13}$C-pyruvate	^{18}F-FDG [127, 128]	Noninvasive assessment of therapy effects that affect glycolysis and oxidative phosphorylation
Blood/tissue oxygenation, hypoxia	BOLD-MRI [76]	^{18}F-FMISO, ^{62}CU-ATSM [125]	Tumor therapy response, brain ischemia, myocardial ischemia, radiation therapy planning (overtreatment of hypoxic tumor areas)
Receptor density	Receptor-targeted nanoparticles [6]	For example, ^{18}F-DOPA, ^{124}I-MIBG, ^{68}Ga-DOTANOC [31]	Tumor detection, predict response to receptor-targeted therapy
Metabolite/drug concentration	MR spectroscopy, theranostic drugs [129]	Radiolabeled chemotherapeutics [130]	In vivo biodistribution, tumor accumulation, level of tracer/drug uptake, heterogenous intratumoral distribution, clearance from tumor
Cell death/apoptosis	Annexin-linked nanoparticles [7], diffusion-weighted sequences [84]	^{18}F-Annexin [7]	Tumor aggressiveness, therapy response
Macrophage phagocytosis	Iron oxide nanoparticle-enhanced MRI [85, 131, 132]	^{62}CU-labeled nanoparticles [133, 134]	Tumor detection, especially in RES, detection of tumor-associated macrophages, characterization of inflammations

ASL arterial spin labeling, *BOLD* blood oxygen-level dependent, *Cho* choline, *Cr* creatinine, *NAA* n-acetyl-aspartate, *RGD* arginine-glycine-aspartic acid, iron oxide nanoparticles

quantitative data, which can be utilized for early disease detection, prediction of overall disease aggressiveness, prediction and monitoring of therapy response, and to support the regulatory approval processes of novel diagnostic or therapeutic drugs [75]. A variety of molecular imaging biomarkers have been already evaluated in clinical trials while others are still emerging. They are generally categorized as diagnostic biomarkers, prognostic biomarkers, predictive biomarkers, as well as biomarkers of therapy response and biomarkers of disease recurrence. The NIH supports an online list of molecular imaging biomarkers for SPECT, PET, and MRI (MICAD, Molecular Imaging and Contrast Agent Database, http://micad.nih.gov), and the NIH biomarkers consortium supports systematic evaluations of new imaging biomarkers (http://www.biomarkersconsortium.org/projects_submit.php). The following sections will focus on imaging biomarkers for the diagnosis of solid malignant tumors in children, the most common clinical application. The development of imaging biomarkers for other indications, such as a variety of CNS disorders, MSK pathologies, autoimmune disorders, and inflammations, is also being actively pursued [7, 9].

Diagnostic Imaging Biomarkers

Diagnostic imaging biomarkers provide information about the presence or absence of disease. Some authors distinguish biomarkers for disease detection and biomarkers for disease staging. In the context of clinical imaging applications, these two aspects are almost always closely connected. Thus, we consider both, detection and staging, under this category.

A first application of diagnostic imaging biomarkers is screening for the presence of disease. Currently, we have limited preselections for imaging tests (e.g., nonselective screening of all patients with cancer susceptibility syndromes and all patients after tumor surgery) and apply low-cost technologies (e.g., ultrasound, x-rays) to screen a large patient population regarding the presence or absence of disease, being aware that these technologies have limited sensitivities and specificities. Future developments aim to improve prescreening procedures for patients at risk of developing a specific disease (e.g., p53 mutations, Li-Fraumeni syndrome, hemihypertrophy-related syndromes, neurofibromatosis 1), who could then be stratified to more advanced and better tailored imaging technologies [75]. For example, in patients with neurofibromatosis 1, who carry mutations of the *NF1* tumor suppressor gene leading to the development of both benign and malignant tumors, an increased metabolic activity of clinically symptomatic neurofibromas on ^{18}F-FDG PET/CT has shown a sensitivity of 89 % and a specificity of 95 % to indicate a malignant transformation to malignant peripheral nerve sheath tumors [135]. Oncogene expression can be detected with advanced imaging approaches, such as hyperpolarized ^{13}C-pyruvate MRI spectroscopy [82], via detection of an increased aerobic glycolysis and diminished oxidative phosphorylation (Warburg effect), which occurs before morphologic or other physiologic changes are apparent on conventional imaging tests. Of note, patients with cancer susceptibility syndromes include young patients who need anesthesia to undergo classical cross-sectional imaging studies. Advances in the development of quick, real-time molecular imaging tests, such as optical or ultrasound, would be highly beneficial for these children.

Once a tumor has been identified based on clinical examination, elevated tumor markers and/or ultrasound, an integrated imaging test is needed, which provides comprehensive staging of the primary tumor and potential metastases in one single session. PET/CT and PET/MR approaches may come close to this goal. Fluorine-18-FDG PET/CT has been established for staging and restaging of a number of malignant tumors in pediatric patients, including lymphoma [39, 42, 136], bone sarcomas [49, 137], rhabdomyosarcomas [49, 137], head and neck cancers [55], and Wilms' tumor [53]. Several studies demonstrated improved sensitivities and specificities of ^{18}F-FDG PET/CT compared to all collective standard staging procedures, specifically for patients with lymphomas, malignant sarcomas (bone and soft

tissue), and head and neck cancers [47, 51, 52, 55, 59, 137, 138]. While ^{18}F-FDG PET/CT applications for neuroblastoma staging remain controversial, ^{18}F-DOPA and ^{124}I-MIBG PET/CT have recently shown higher overall accuracy than ^{123}I-MIBG scintigraphy [59, 139].

Several recent studies have shown equivalent sensitivities and excellent agreement between ^{18}F-FDG PET/CT and whole body MRI for tumor detection in children [140–143] (Fig. 25.3). These studies were performed in small populations of pediatric patients and primarily focused on malignant lymphomas and sarcomas. Further direct comparisons between ^{18}F-FDG PET/CT and whole body diffusion MRI are critically needed to understand opportunities and limitations of this novel radiation-free staging technique. The combination of these two imaging technologies might eventually provide higher sensitivities and specificities than either technique alone.

A major challenge for both ^{18}F-FDG PET/CT and MRI is the detection of bone marrow metastases in highly cellular and metabolically active normal marrow in young children and/or after GCSF treatment. Solutions include ^{18}F-sodium fluoride (NaF)-PET/CT scans [144] and iron oxide nanoparticle-enhanced MRI scans [85, 86, 131]. Intravenously injected iron oxide nanoparticles are phagocytosed by macrophages in the reticuloendothelial system, i.e., liver, spleen, and bone marrow. In the early phase after contrast media administration, up to 1 h postinjection, there is no significant tumor uptake, leading to improved contrast between bone marrow and metastases [85, 86, 131] (Fig. 25.4). Delayed images provide more specific information about the tumor due to differential iron oxide uptake in different tumor types, benign versus malignant tumors, and tumors of different tumor grade [120, 132]. In the future, these approaches could be potentially combined for more specific evaluations of bone lesions with PET/MR.

Prognostic Imaging Biomarkers

Prognostic imaging biomarkers provide information about the natural history of a given disease prior to therapy. Prognostic biomarkers aim to identify patients with less aggressive tumors and a high likelihood of cure, treating them less aggressively, while those with more aggressive tumors and low likelihood of cure are stratified towards more aggressive therapeutic plans. Classically, therapy stratifications are mostly based on anatomical criteria, such as disease bulk, location, and distribution (local vs. systemic tumor spread). In the future, therapy decisions will be augmented by more detailed information about tumor genomics, proteomics, and related metabolic alterations [8, 75]. While histopathologic assessments have kept up with this development, related imaging approaches are largely behind in this arena.

Tumor size and volume, as determined by CT or MR, have been linked to overall survival for malignant lymphomas and sarcomas [39, 40, 145] and to distant metastases for bone sarcomas [146]. The metabolic activity of solid pediatric cancers, quantified by the standardized uptake value (SUV), can provide important additional information. The SUV represents the ratio of the radioactivity in a target tissue and the background radioactivity, assuming an even distribution of the injected radioactivity in the whole body. The SUV is measured as the tissue radioactivity concentration (e.g., in MBq/kg) at the time of image acquisition (corrected for physical decay of the radioisotope) divided by the injected activity per body weight (MBq/kg) at the time of injection. Instead of body weight, the SUV can be also normalized to body mass, lean body mass (SUL), or body surface area [147]. For evaluations of pediatric cancers with ^{18}F-FDG PET/CT, SUVs are usually calculated based on pixels representing the highest radioactivity in the tumor (SUVmax). The SUV value is affected by image noise, image resolution, user biased selection of measured area, and lesion size (SUV decreases for smaller lesions due to partial volume effects) [147]. Several authors reported a relation between pretherapeutic primary tumor SUV and outcome in pediatric patients. Baum et al. reported a shorter overall survival of pediatric patients with primary rhabdomyosarcomas with a ratio of tumor SUVmax to liver SUVmax >4.6 compared to

primary tumors with a lower ratio [51]. Gupta et al. reported higher baseline primary tumor SUV values in metastatic Ewing sarcoma (mean SUVmax = 11.31) compared to localized Ewing sarcoma (mean SUVmax = 6.84) [148]. And Begent et al. reported higher primary tumor SUVmax values (>5) in histologically high-risk Wilms' tumors compared to low-risk tumors (SUVmax <5) [53]. An interesting recent study in adult patients with breast cancer has shown that high SUVmax of local lymph nodes on pretreatment ^{18}F-FDG PET/CT correlated with disease recurrence [149]. While the general concept is known from histopathologic evaluations of local lymph nodes, the corresponding imaging concept would have to be evaluated for pediatric cancers.

Markers of tumor angiogenesis represent another important target for prognostic evaluations: for example, overexpression of VEGF indicated a poor prognosis in a wide variety of cancer types in both adult and pediatric patients [7, 146, 150]. In adult patients, the VEGF isoform $VEGF_{165}$ has been labeled with ^{123}I and used for imaging pancreatic carcinomas [7, 150]. However, the high radiation dose delivered to the thyroid via the ^{123}I radiotracer limits corresponding applications in children. Bevacizumab, a humanized FDA-approved anti-VEGF antibody, has been labeled with ^{111}In and applied for imaging of liver metastases in adult patients with colorectal cancer [7]. Bevacizumab is currently also applied in pediatric patients with malignant brain tumors and osteosarcomas [7, 151]. However, to the best of our knowledge, targeted imaging approaches in pediatric patients have not been pursued.

Predictive Biomarkers

Predictive imaging biomarkers provide information about the relative efficacy of a specific treatment BEFORE start of therapy. The aim is to identify those pathologies that will likely benefit from a specific therapy. Thus, patients could be stratified early to therapies with a high likelihood of inducing response while sparing them from toxic side effects to drugs that may not be effective against a given pathology. Examples include pretherapy ^{124}I-NaI PET studies to estimate tumor accumulation and radiation dose of ^{131}I-NaI treatment to thyroid cancers or pretherapy ^{124}I-MIBG PET studies to estimate tumor accumulation and radiation dose of neuroblastomas and pheochromocytomas prior to ^{131}I-MIBG treatment [152, 153]. Iodine-124-imaging (instead of ^{131}I-imaging) is needed because therapeutic ^{131}I emits photons with a peak of 364 keV, which cannot be efficiently collected by most gamma cameras [139].

Many other targeted therapies (e.g., monoclonal antibodies, transcription inhibitors, kinase inhibitors) are in need of specific predictive imaging biomarkers. Establishing noninvasive imaging approaches for predicting the efficacy of these targeted therapeutics in vivo will be essential for drug development and clinical applications. While small numbers of patients and high cure rates make the development of targeted diagnostic or therapeutic drugs for malignant germ cell tumors unlikely, these tumors have a signature production of α-fetoprotein and/or β-human chorionic gonadotropin (HCG) that could be in principle amenable to targeted imaging or therapy. Of note, treatment with monoclonal antibodies, such as rituximab, can lead to false-negative histopathologic assessments of residual disease, if they rely on the same tumor cell surface target. Thus, alternative antibodies are recommended for histopathologic evaluation of posttreatment samples (e.g., CD79a as a pan-B-cell antibody instead of CD20). The same concept would apply to mAb-based imaging approaches.

Biomarkers of Therapy Response

Biomarkers of therapy response can be also applied to monitor treatment effects DURING and AFTER therapy. Classical imaging criteria to determine treatment effects are based on morphologic observations, such as changes in tumor size (RECIST = Response Evaluation Criteria In Solid Tumors, WHO = World Health

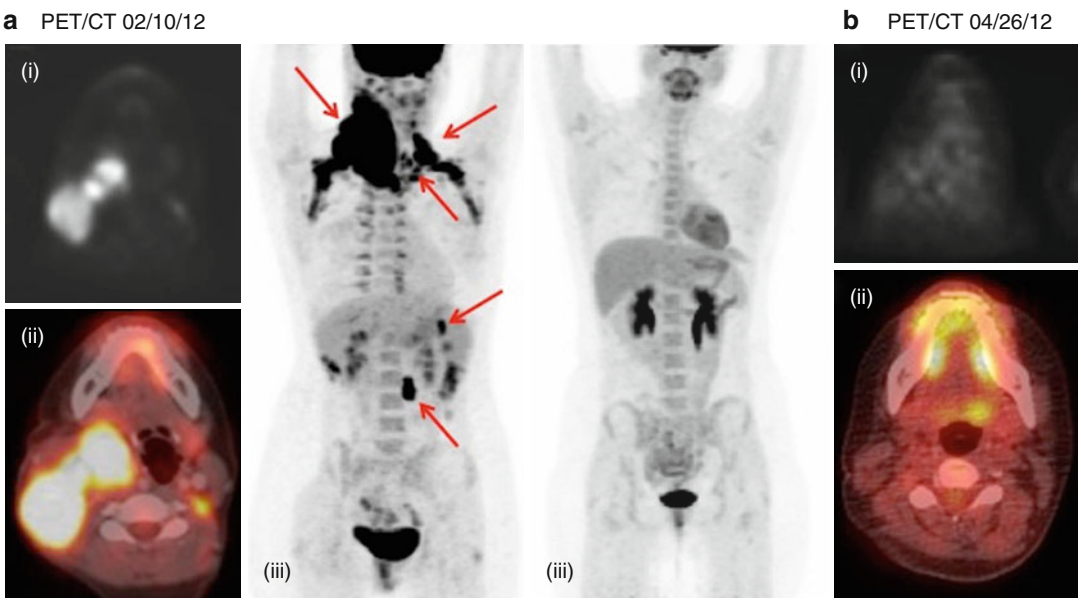

Fig. 25.5 Axial ^{18}F-FDG PET scan through the lower neck (*i*), corresponding integrated PET/CT (*ii*) and whole body minimum intensity projection (*iii*) of a 14-year-old girl with stage III A Hodgkin's lymphoma. (**a**) Pretreatment scans demonstrate bulky disease of the right neck, additional extensive lymphadenopathy of the left neck, bilateral supraclavicular areas and axillaries, as well as additional hypermetabolic lymph nodes at the splenic hilum and the left paraspinal retroperitoneum (*arrows*). (**b**) Follow-up scan after two cycles of chemotherapy demonstrates complete remission

Organization size criteria and COG = Children's Oncology Group criteria) [147]. More recently, physiologic criteria have been introduced for some tumors in adult patients based on a decline in ^{18}F-FDG tumor metabolism after two cycles of chemotherapy (PERCIST criteria = Positron Emission Tomography Response Criteria In Solid Tumors) [147]. In PERCIST, response to therapy is expressed as percentage change in SUL peak between the pre- and posttreatment scans. A complete metabolic response is defined as visual disappearance of all metabolically active tumor. A partial response is considered more than a 30 % decline in SUL peak, and progressive disease is classified as more than a 30 % increase in SUL peak or new lesions, if confirmed [147]. Accordingly, several studies in pediatric patients with malignant lymphomas and bone sarcomas have shown that a decline in tumor glucose consumption, as measured on posttreatment ^{18}F-FDG PET scans, correlates with chemotherapy response [39, 40, 145] (Fig. 25.5). Changes in tumor ^{18}F-FDG metabolism occurred before changes in tumor size were apparent. In patients with osteosarcoma, chemotherapy response could be predicted reliably on interim PET/CT scans and correlated well with tumor necrosis on histopathology [154]. Conversely, in pediatric patients with stage III or IV non-lymphoblastic NHL, only response at posttreatment PET/CT, but not interim PET/CT, could predict progression-free or overall survival [40]. Thus, the prognostic value of PERCIST criteria awaits systematic, tumor-specific validations in pediatric patients.

There appears to be a strong relationship between tumor cell number and glucose metabolism [147]. Consequently, diffusion-weighted MR scans demonstrate increasing proton diffusion in response to therapy (quantified as increasing ADC values, Fig. 25.6), which correlate to decreasing tumor ^{18}F-FDG uptake in some cancers [155, 156]. However, response assessment via ADC values is complex and not yet standardized for pediatric solid tumors, which are often inhomogeneous. Further studies are needed to systematically define and validate

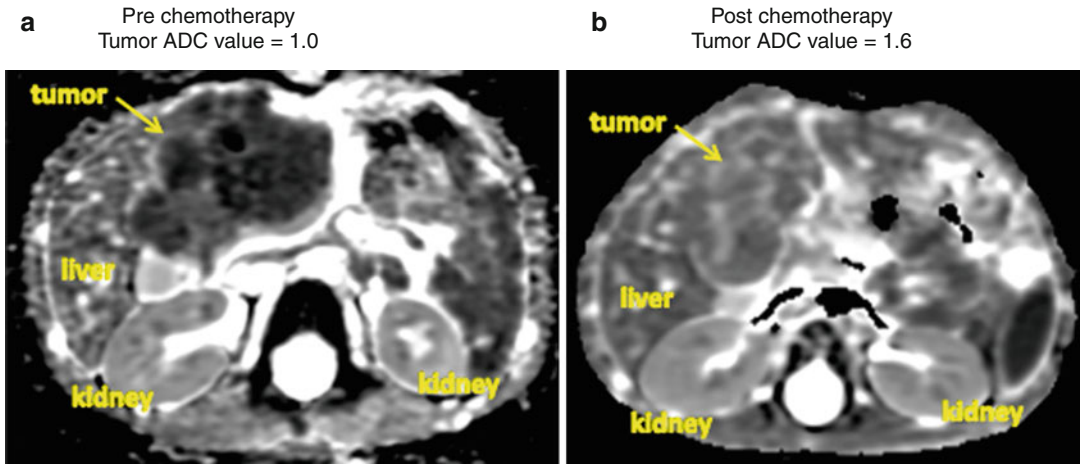

Fig. 25.6 ADC map of a hepatoblastoma before (**a**) and after (**b**) chemotherapy. ADC maps are calculated based on diffusion-weighted MR images and depict the rate of water diffusion for each image voxel as grey values (low signal = low ADC value = restricted diffusion; high signal = high ADC value = unrestricted diffusion). Tumor response to chemotherapy in this case is apparent by an increasing tumor signal and increasing ADC value on the posttreatment scan compared to the pretreatment scan

standardized acquisition parameters and related ADC measurements of pediatric cancers, to evaluate the reproducibility of treatment-induced ADC changes, to determine specific thresholds of ADC changes that indicate tumor response, and to correlate results with changes in ^{18}F-FDG metabolism. If diffusion-weighted scans can provide equivalent information regarding therapy response as compared to ^{18}F-FDG, this may open new opportunities to introduce other, more specific PET tracers (e.g., ^{124}I-MIBG), particularly for PET/MR approaches.

Fluorine-18-FDG PET imaging has been also explored as a potential biomarker of response to inhibition of insulin-like growth factor receptors (IGF-R) [157]. Insulin-like growth factors, IGF-1 and IGF-2, are small polypeptides involved in regulating cell proliferation, survival, differentiation, and transformation. IGF activities are mediated through binding and activation of IGF-1 or IGF-2 receptors (IGF-1R or IGF-2R). Overexpression of IGF-1R and IGF-2R has been reported in multiple types of cancer, including bone sarcomas (IGF-1R) and rhabdomyosarcomas (IGF-2R) (Fig. 25.7). In preclinical studies of IGF-1R/insulin receptor inhibitors, drug exposure impeded ^{18}F-FDG uptake in cells expressing IGF-1R, but not in cells that lack IGF-1R expression [157, 158]. This effect also correlated with direct measures of IGF-1R pathway inhibition.

Fluorine-18-deoxy-fluorothymidine (FLT), a thymidine analog, represents a marker of tumor cell proliferation, which can be used to monitor treatment response to chemotherapy and radiotherapy [159]. More specifically, FLT is linked to the expression and activity of cytosolic thymidine kinase-1 (TK-1), which is the first enzyme in the exogenous (salvage) pathway of DNA synthesis activated during the S-phase of the cell cycle [159]. In various tumors of adult patients, ^{18}F-FLT PET could accurately quantify therapy-induced changes in tumor growth rates [159]. However, data about applications in typical tumors of pediatric populations are scarce. In pediatric patients with primary brain tumors, ^{18}F-FLT PET was useful in primary staging and response assessment [126]. Conversely, in patients with metastatic germ cell tumors, Pfannenberg et al. could not find a significant correlation between ^{18}F-FLT tumor uptake and response to cisplatin-based chemotherapy [160].

Other approaches include measurements of therapy-induced tumor apoptosis. Apoptosis can occur via extrinsic, receptor-mediated or intrinsic, mitochondrial pathways. Both lead eventually to activation of caspases, which cleave specific intracellular proteins and cause formation of apoptotic

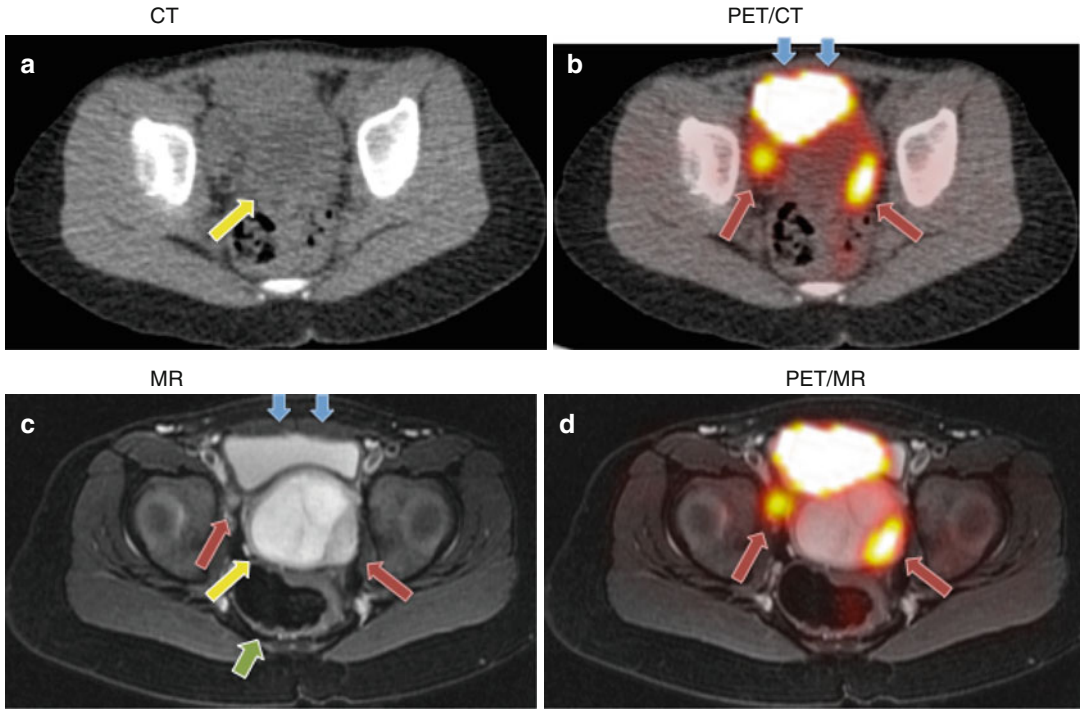

Fig. 25.7 Axial ^{18}F-FDG PET/CT and sequential ^{18}F-FDG PET/MR scans through the pelvis of a patient with a rhabdomyosarcoma: (**a**) The unenhanced CT scan shows a mass in the pelvis (*yellow arrow*). (**b**) Overlay of an ^{18}F-FDG PET scan improves delineation of the urinary bladder (*blue arrows*) and two hypermetabolic tumor nodules (*red arrows*). (**c**) T2-w MR scan provides further improved anatomical information, delineating a T2-hyperintense cystic, multiseptated tumor component (*yellow arrow*) between the bladder (*blue arrows*) and rectum (*green arrow*). (**d**) Fusion of the ^{18}F-FDG PET with the MR scan provides improved delineation of the hypermetabolic tumor nodules (*red arrows*), particularly the small nodule to the right of the mass. Note slight mismatch of urinary bladder shape due to sequential data acquisition

bodies, which are disposed by macrophages [7]. Clinically applicable radiotracers that can detect tumor apoptosis include ^{99m}Tc-annexin A5, which binds to phosphatidylserine residues on apoptotic tumor cells [7]. High ^{99m}Tc-annexin A5 tumor uptake has been correlated with therapy response in a number of malignant cancers in adults, but not pediatric cancers. In order to develop imaging approaches with higher anatomical resolution, corresponding ^{18}F-annexin A5- and annexin A5-labeled magnetofluorescent nanoparticles have been developed for PET and MRI, respectively, and were tested in animal models [7].

Multidrug resistance of cancers to chemotherapy is characterized by increased expression of the p-glycoprotein, which acts as an ATP-dependent drug-efflux pump. P-glycoprotein overexpression has been described in high-risk and advanced-stage neuroblastomas, malignant sarcomas, and hepatoblastomas, among others [161–164], and represents an important target for molecular imaging applications. P-glycoprotein overexpression has been measured with various PET tracers, including [^{11}C]verapamil [165] and [^{11}C]colchicine [166]. The pediatric oncology community awaits suitable applications for pediatric cancers.

Biomarkers of Disease Recurrence

The gold standard of therapeutic efficacy, and the efficacy of related imaging tests, is disease-free survival. Several studies have demonstrated that neither ^{18}F-FDG PET/CT nor MR can distinguish between minimal residual tumor versus no tumor [167]. Data suggest that the disappearance

of molecular clones of tumors (e.g., lymphomas) may lag behind the disappearance of morphologic evidence of disease [167]. The diagnosis of recurrent pediatric tumors with molecular imaging approaches remains a wide open area of investigation. It will likely require a combination of prescreening molecular genetic analyses and serum biomarkers, followed by molecular imaging of selected patients at risk for tumor recurrence. This approach may be facilitated by specific serum biomarkers of pediatric malignancies, which are either secreted by the tumor or generated by the host in response to the tumor and which can be utilized for both assessment of tumor therapy response and tumor recurrence [168]. Examples include alpha fetoprotein (AFP) serum levels in the majority of patients with hepatoblastomas as well as some patients with hepatocellular carcinoma (HCC) and non-seminomatous germ cell tumors (GCT); human chorionic gonadotropin (HCG) in patients with non-seminomatous GCT and a variety of other pediatric cancers; lactate dehydrogenase (LDH) in patients with GCT, neuroblastoma, lymphoma, and melanoma; and catecholamines, vanillinmandelic acid (VMA), and norepinephrine in 24 h urine of patients with neuroblastoma and pheochromocytoma [168]. An important additional aspect for tumor surveillance in pediatric patients is the potential risk for the development of secondary tumors later in life, which may require an integration of diagnostic biomarkers and biomarkers of disease recurrence. Imaging approaches for the detection of residual disease, recurrent disease, and secondary tumor development will have to be refined to integrate genetic testing and serum biomarkers into modern diagnostic workups.

Future developments will focus on further reducing radiation exposures, reducing unnecessary scans, and improving the yield from imaging tests [127, 169, 170]. Imaging today is like a traditional rotary phone that can fulfil only one function at a time. In the future, we will develop smarter approaches to integrate multiple diagnostic tests (potentially beyond imaging) into one single diagnostic test, which will consolidate anatomical, physiologic, and histopathologic information. The close interaction of basic science innovations and clinical advances along with the development of novel, cutting-edge imaging technologies will provide a unique platform to transform the field of pediatric radiology towards safer, more efficient, and more accurate diagnoses.

References

1. Adithi M, Nalini V, Kandalam M, Krishnakumar S. Expression of matrix metalloproteinases and their inhibitors in retinoblastoma. J Pediatr Hematol Oncol. 2007;29:399–405.
2. Zagozdzon R, Fu Y, Avraham HK. Csk homologous kinase inhibits CXCL12-CXCR4 signaling in neuroblastoma. Int J Oncol. 2008;32:619–23.
3. de Nigris F, Botti C, de Chiara A, et al. Expression of transcription factor Yin Yang 1 in human osteosarcomas. Eur J Cancer. 2006;42:2420–4.
4. Wei JS, Johansson P, Chen QR, et al. microRNA profiling identifies cancer-specific and prognostic signatures in pediatric malignancies. Clin Cancer Res. 2009;15:5560–8.
5. Slack A, Chen Z, Tonelli R, et al. The p53 regulatory gene MDM2 is a direct transcriptional target of MYCN in neuroblastoma. Proc Natl Acad Sci U S A. 2005;102:731–6.
6. Daldrup-Link HE, Hawkins RA, Meier R, Goldsby RE, Artemov D. Receptor imaging of pediatric tumors: clinical practice and new developments. Pediatr Radiol. 2008;38:1154–61.
7. Heneweer C, Grimm J. Clinical applications in molecular imaging. Pediatr Radiol. 2011;41:199–207.
8. James ML, Gambhir SS. A molecular imaging primer: modalities, imaging agents, and applications. Physiol Rev. 2012;92:897–965.
9. Kiessling I, Bzyl J, Kiessling F. Molecular ultrasound imaging and its potential for paediatric radiology. Pediatr Radiol. 2011;41:176–84.
10. Lindner JR. Microbubbles in medical imaging: current applications and future directions. Nat Rev Drug Discov. 2004;3:527–32.
11. Willmann JK, Cheng Z, Davis C, et al. Targeted microbubbles for imaging tumor angiogenesis: assessment of whole-body biodistribution with dynamic micro-PET in mice. Radiology. 2008;249:212–9.
12. Kern R, Diels A, Pettenpohl J, et al. Real-time ultrasound brain perfusion imaging with analysis of microbubble replenishment in acute MCA stroke. J Cereb Blood Flow Metab. 2011;31:1716–24.
13. Lindner JR. Molecular imaging with contrast ultrasound and targeted microbubbles. J Nucl Cardiol. 2004;11:215–21.
14. Mentzel HJ, Vogt S, Patzer L, et al. Contrast-enhanced sonography of vesicoureterorenal reflux in children: preliminary results. AJR Am J Roentgenol. 1999; 173:737–40.

15. Willmann JK, Paulmurugan R, Chen K, et al. US imaging of tumor angiogenesis with microbubbles targeted to vascular endothelial growth factor receptor type 2 in mice. Radiology. 2008;246:508–18.
16. Li L, Wei Q, Li HB, Wen S, Teng GJ. Evaluation of microbubbles as contrast agents for ultrasonography and magnetic resonance imaging. PLoS One. 2012;7:e34644.
17. Sutton EJ, Henning TD, Pichler BJ, Bremer C, Daldrup-Link HE. Cell tracking with optical imaging. Eur Radiol. 2008;18:2021–32.
18. Meier R, Krug C, Golovko D, et al. ICG-enhanced imaging of arthritis with an integrated optical imaging/X-ray system. Arthritis Rheum. 2010;62(8):2322–7.
19. Meier R, Thuermel K, Moog P, et al. Detection of synovitis in the hands of patients with rheumatological disorders: diagnostic performance of optical imaging in comparison to MRI. Arthritis Rheum. 2012;64:2489–98.
20. Roblyer D, Ueda S, Cerussi A, et al. Optical imaging of breast cancer oxyhemoglobin flare correlates with neoadjuvant chemotherapy response one day after starting treatment. Proc Natl Acad Sci U S A. 2011;108:14626–31.
21. Sheth RA, Upadhyay R, Stangenberg L, Sheth R, Weissleder R, Mahmood U. Improved detection of ovarian cancer metastases by intraoperative quantitative fluorescence protease imaging in a pre-clinical model. Gynecol Oncol. 2009;112:616–22.
22. Prakash N, Uhlemann F, Sheth SA, Bookheimer S, Martin N, Toga AW. Current trends in intraoperative optical imaging for functional brain mapping and delineation of lesions of language cortex. Neuroimage. 2009;47 Suppl 2:T116–26.
23. Liu JT, Mandella MJ, Ra H, et al. Miniature near-infrared dual-axes confocal microscope utilizing a two-dimensional microelectromechanical systems scanner. Opt Lett. 2007;32:256–8.
24. Zhao Q, Jiang H, Cao Z, Yang L, Mao H, Lipowska M. A handheld fluorescence molecular tomography system for intraoperative optical imaging of tumor margins. Med Phys. 2011;38:5873–8.
25. Meier R, Boddington S, Krug C, et al. Detection of postoperative granulation tissue with an ICG-enhanced integrated OI-/X-ray system. J Transl Med. 2008;6:73.
26. Bossy E, Sui L, Murray TW, Roy RA. Fusion of conventional ultrasound imaging and acousto-optic sensing by use of a standard pulsed-ultrasound scanner. Opt Lett. 2005;30:744–6.
27. Allard M, Cote D, Davidson L, Dazai J, Henkelman RM. Combined magnetic resonance and bioluminescence imaging of live mice. J Biomed Opt. 2007;12:034018.
28. Culver J, Akers W, Achilefu S. Multimodality molecular imaging with combined optical and SPECT/PET modalities. J Nucl Med. 2008;49:169–72.
29. Nahrendorf M, Keliher E, Marinelli B, et al. Hybrid PET-optical imaging using targeted probes. Proc Natl Acad Sci U S A. 2010;107:7910–5.
30. Goske MJ, Applegate KE, Bulas D, et al. Image gently: progress and challenges in CT education and advocacy. Pediatr Radiol. 2011;41 Suppl 2:461–6.
31. Vaccarili M, Lococo A, Fabiani F, Staffilano A. Clinical diagnostic application of 111In-DTPA-octreotide scintigraphy in small cell lung cancer. Tumori. 2000;86:224–8.
32. Chen YK, Liu RS, Huang WS, et al. The role of dopamine transporter imaging agent [^{99m}Tc]TRODAT-1 in hemi-parkinsonism rat brain. Nucl Med Biol. 2001;28:923–8.
33. Huang WS, Lin SZ, Lin JC, Wey SP, Ting G, Liu RS. Evaluation of early-stage Parkinson's disease with ^{99m}Tc-TRODAT-1 imaging. J Nucl Med. 2001;42:1303–8.
34. Belhocine T, Steinmetz N, Hustinx R, et al. Increased uptake of the apoptosis-imaging agent (99 m)Tc recombinant human Annexin V in human tumors after one course of chemotherapy as a predictor of tumor response and patient prognosis. Clin Cancer Res. 2002;8:2766–74.
35. Marks EC, Yonas H, Sanders MH, Love JT, Maxwell C, Schimmerman S. Physiologic implications of adding small amounts of carbon dioxide to the gas mixture during inhalation of xenon. Neuroradiology. 1992;34:297–300.
36. Van Haren RM, Fitzgerald TL. Intraoperative hand held gamma probe detection of a recurrent nonfunctional neuroendocrine tumor. JOP. 2008;9:704–7.
37. Filippi L, Manni C, Pierantozzi M, et al. 123I-FP-CIT semi-quantitative SPECT detects preclinical bilateral dopaminergic deficit in early Parkinson's disease with unilateral symptoms. Nucl Med Commun. 2005;26:421–6.
38. Newberg AB, Alavi A. PET in seizure disorders. Radiol Clin North Am. 2005;43:79–92.
39. Riad R, Omar W, Kotb M, et al. Role of PET/CT in malignant pediatric lymphoma. Eur J Nucl Med Mol Imaging. 2010;37:319–29.
40. Bakhshi S, Radhakrishnan V, Sharma P, et al. Pediatric nonlymphoblastic non-Hodgkin lymphoma: baseline, interim, and posttreatment PET/CT versus contrast-enhanced CT for evaluation–a prospective study. Radiology. 2012;262:956–68.
41. London K, Cross S, Onikul E, Dalla-Pozza L, Howman-Giles R. 18F-FDG PET/CT in paediatric lymphoma: comparison with conventional imaging. Eur J Nucl Med Mol Imaging. 2011;38:274–84.
42. Cheng G, Chen W, Chamroonrat W, Torigian DA, Zhuang H, Alavi A. Biopsy versus FDG PET/CT in the initial evaluation of bone marrow involvement in pediatric lymphoma patients. Eur J Nucl Med Mol Imaging. 2011;38:1469–76.
43. Shulkin BL, Goodin GS, McCarville MB, et al. Bone and [18F]fluorodeoxyglucose positron-emission tomography/computed tomography scanning for the assessment of osseous involvement in Hodgkin lymphoma in children and young adults. Leuk Lymphoma. 2009;50:1794–802.

44. Sharp SE, Gelfand MJ, Absalon MJ. Altered FDG uptake patterns in pediatric lymphoblastic lymphoma patients receiving induction chemotherapy that includes very high dose corticosteroids. Pediatr Radiol. 2012;42:331–6.
45. Robertson VL, Anderson CS, Keller FG, et al. Role of FDG-PET in the definition of involved-field radiation therapy and management for pediatric Hodgkin's lymphoma. Int J Radiat Oncol Biol Phys. 2011;80:324–32.
46. Sammer MB, Shulkin BL, Alessio A, Parisi MT. Role of limited whole-body PET/CT in pediatric lymphoma. AJR Am J Roentgenol. 2011;196:1047–55.
47. London K, Stege C, Cross S, et al. 18F-FDG PET/CT compared to conventional imaging modalities in pediatric primary bone tumors. Pediatr Radiol. 2012; 42:418–30.
48. Volker T, Denecke T, Steffen I, et al. Positron emission tomography for staging of pediatric sarcoma patients: results of a prospective multicenter trial. J Clin Oncol. 2007;25:5435–41.
49. Walter F, Czernin J, Hall T, et al. Is there a need for dedicated bone imaging in addition to 18F-FDG PET/CT imaging in pediatric sarcoma patients? J Pediatr Hematol Oncol. 2012;34:131–6.
50. Im HJ, Kim TS, Park SY, et al. Prediction of tumour necrosis fractions using metabolic and volumetric 18F-FDG PET/CT indices, after one course and at the completion of neoadjuvant chemotherapy, in children and young adults with osteosarcoma. Eur J Nucl Med Mol Imaging. 2012;39:39–49.
51. Baum SH, Fruhwald M, Rahbar K, Wessling J, Schober O, Weckesser M. Contribution of PET/CT to prediction of outcome in children and young adults with rhabdomyosarcoma. J Nucl Med. 2011;52:1535–40.
52. Ricard F, Cimarelli S, Deshayes E, Mognetti T, Thiesse P, Giammarile F. Additional benefit of F-18 FDG PET/CT in the staging and follow-up of pediatric rhabdomyosarcoma. Clin Nucl Med. 2011;36: 672–7.
53. Begent J, Sebire NJ, Levitt G, et al. Pilot study of F(18)-Fluorodeoxyglucose Positron Emission Tomography/computerised tomography in Wilms' tumour: correlation with conventional imaging, pathology and immunohistochemistry. Eur J Cancer. 2011;47:389–96.
54. Moinul Hossain AK, Shulkin BL, Gelfand MJ, et al. FDG positron emission tomography/computed tomography studies of Wilms' tumor. Eur J Nucl Med Mol Imaging. 2010;37:1300–8.
55. Boktor RR, Omar WS, Mousa E, et al. A preliminary report on the impact of (1)(8)F-FDG PET/CT in the management of paediatric head and neck cancer. Nucl Med Commun. 2012;33:21–8.
56. Cheuk DK, Sabin ND, Hossain M, et al. PET/CT for staging and follow-up of pediatric nasopharyngeal carcinoma. Eur J Nucl Med Mol Imaging. 2012;39: 1097–106.
57. Gains JE, Bomanji JB, Fersht NL, et al. 177Lu-DOTATATE molecular radiotherapy for childhood neuroblastoma. J Nucl Med. 2011;52:1041–7.
58. Lopci E, Piccardo A, Nanni C, et al. 18F-DOPA PET/CT in neuroblastoma: comparison of conventional imaging with CT/MR. Clin Nucl Med. 2012;37:e73–8.
59. Piccardo A, Lopci E, Conte M, et al. Comparison of 18F-dopa PET/CT and 123I-MIBG scintigraphy in stage 3 and 4 neuroblastoma: a pilot study. Eur J Nucl Med Mol Imaging. 2012;39:57–71.
60. Moharir M, London K, Howman-Giles R, North K. Utility of positron emission tomography for tumour surveillance in children with neurofibromatosis type 1. Eur J Nucl Med Mol Imaging. 2010;37:1309–17.
61. Drubach LA, Connolly SA, Palmer 3rd EL. Skeletal scintigraphy with 18F-NaF PET for the evaluation of bone pain in children. AJR Am J Roentgenol. 2011;197:713–9.
62. Li Y, Schiepers C, Lake R, Dadparvar S, Berenji GR. Clinical utility of (18)F-fluoride PET/CT in benign and malignant bone diseases. Bone. 2012;50:128–39.
63. Drubach LA, Johnston PR, Newton AW, Perez-Rossello JM, Grant FD, Kleinman PK. Skeletal trauma in child abuse: detection with 18F-NaF PET. Radiology. 2010;255:173–81.
64. Vaidyanathan G, Affleck DJ, Zalutsky MR. Validation of 4-[fluorine-18]fluoro-3-iodobenzylguanidine as a positron-emitting analog of MIBG. J Nucl Med. 1995;36:644–50.
65. Alessio AM, Kinahan PE, Manchanda V, Ghioni V, Aldape L, Parisi MT. Weight-based, low-dose pediatric whole-body PET/CT protocols. J Nucl Med. 2009;50:1570–7.
66. Chawla SC, Federman N, Zhang D, et al. Estimated cumulative radiation dose from PET/CT in children with malignancies: a 5-year retrospective review. Pediatr Radiol. 2010;40:681–6.
67. Gelfand MJ, Sharp SE, Treves ST, Fahey FH, Parisi MT, Alessio AM. Estimated cumulative radiation dose from PET/CT in children with malignancies. Pediatr Radiol. 2010;40:1712–3; author reply 4–5.
68. Kleis M, Daldrup-Link H, Matthay K, et al. Diagnostic value of PET/CT for the staging and restaging of pediatric tumors. Eur J Nucl Med Mol Imaging. 2009;36:23–36.
69. Tong S, Alessio AM, Kinahan PE. Image reconstruction for PET/CT scanners: past achievements and future challenges. Imaging Med. 2010;2:529–45.
70. Kaste SC. Imaging pediatric bone sarcomas. Radiol Clin North Am. 2011;49:749–65; vi–vii.
71. Brisse HJ, McCarville MB, Granata C, et al. Guidelines for imaging and staging of neuroblastic tumors: consensus report from the International Neuroblastoma Risk Group Project. Radiology. 2011;261:243–57.
72. Chavhan GB, Babyn PS. Whole-body MR imaging in children: principles, technique, current applications, and future directions. Radiographics. 2011;31:1757–72.
73. Kwee TC, Fijnheer R, Ludwig I, et al. Whole-body magnetic resonance imaging, including diffusion-weighted imaging, for diagnosing bone marrow involvement in malignant lymphoma. Br J Haematol. 2010;149:628–30.

74. Kwee TC, Takahara T, Vermoolen MA, Bierings MB, Mali WP, Nievelstein RA. Whole-body diffusion-weighted imaging for staging malignant lymphoma in children. Pediatr Radiol. 2010;40:1592–602; quiz 720–1.
75. Voss SD. Pediatric oncology and the future of oncological imaging. Pediatr Radiol. 2011;41 Suppl 1:S172–85.
76. Hyder F, Rothman DL. Quantitative fMRI and oxidative neuroenergetics. Neuroimage. 2012;62(2):985–94.
77. Jacobs J, Rohr A, Moeller F, et al. Evaluation of epileptogenic networks in children with tuberous sclerosis complex using EEG-fMRI. Epilepsia. 2008;49: 816–25.
78. Bendini M, Marton E, Feletti A, et al. Primary and metastatic intraaxial brain tumors: prospective comparison of multivoxel 2D chemical-shift imaging (CSI) proton MR spectroscopy, perfusion MRI, and histopathological findings in a group of 159 patients. Acta Neurochir (Wien). 2011;153:403–12.
79. Paldino MJ, Faerber EN, Poussaint TY. Imaging tumors of the pediatric central nervous system. Radiol Clin North Am. 2011;49:589–616, v.
80. Kim H, Catana C, Ratai EM, et al. Serial magnetic resonance spectroscopy reveals a direct metabolic effect of cediranib in glioblastoma. Cancer Res. 2011;71:3745–52.
81. Gallagher FA, Bohndiek SE, Kettunen MI, Lewis DY, Soloviev D, Brindle KM. Hyperpolarized 13C MRI and PET: in vivo tumor biochemistry. J Nucl Med. 2011;52:1333–6.
82. Hu S, Balakrishnan A, Bok RA, et al. 13C-pyruvate imaging reveals alterations in glycolysis that precede c-Myc-induced tumor formation and regression. Cell Metab. 2011;14:131–42.
83. Malloy CR, Merritt ME, Sherry AD. Could 13C MRI assist clinical decision-making for patients with heart disease? NMR Biomed. 2011;24:973–9.
84. Padhani AR, Koh DM, Collins DJ. Whole-body diffusion-weighted MR imaging in cancer: current status and research directions. Radiology. 2011;261:700–18.
85. Daldrup-Link HE, Rummeny EJ, Ihssen B, Kienast J, Link TM. Iron-oxide-enhanced MR imaging of bone marrow in patients with non-Hodgkin's lymphoma: differentiation between tumor infiltration and hypercellular bone marrow. Eur Radiol. 2002;12:1557–66.
86. Metz S, Lohr S, Settles M, et al. Ferumoxtran-10-enhanced MR imaging of the bone marrow before and after conditioning therapy in patients with non-Hodgkin lymphomas. Eur Radiol. 2006;16:598–607.
87. Ording Muller LS, Avenarius D, Olsen OE. High signal in bone marrow at diffusion-weighted imaging with body background suppression (DWIBS) in healthy children. Pediatr Radiol. 2011;41:221–6.
88. Alibek S, Cavallaro A, Aplas A, Uder M, Staatz G. Diffusion weighted imaging of pediatric and adolescent malignancies with regard to detection and delineation: initial experience. Acad Radiol. 2009;16:866–71.
89. Humphries PD, Sebire NJ, Siegel MJ, Olsen OE. Tumors in pediatric patients at diffusion-weighted MR imaging: apparent diffusion coefficient and tumor cellularity. Radiology. 2007;245:848–54.
90. Kato T, Kojima Y, Kamisawa H, et al. Findings of fat-suppressed T2-weighted and diffusion-weighted magnetic resonance imaging in the diagnosis of non-palpable testes. BJU Int. 2011;107:290–4.
91. Kyriazi S, Collins DJ, Messiou C, et al. Metastatic ovarian and primary peritoneal cancer: assessing chemotherapy response with diffusion-weighted MR imaging–value of histogram analysis of apparent diffusion coefficients. Radiology. 2011;261:182–92.
92. Irie H, Kamochi N, Nojiri J, Egashira Y, Sasaguri K, Kudo S. High b-value diffusion-weighted MRI in differentiation between benign and malignant polypoid gallbladder lesions. Acta Radiol. 2011;52:236–40.
93. Razek AA, Farouk A, Mousa A, Nabil N. Role of diffusion-weighted magnetic resonance imaging in characterization of renal tumors. J Comput Assist Tomogr. 2011;35:332–6.
94. Nagayama M, Watanabe Y, Terai A, et al. Determination of the cutoff level of apparent diffusion coefficient values for detection of prostate cancer. Jpn J Radiol. 2011;29:488–94.
95. Kilickesmez O, Inci E, Atilla S, et al. Diffusion-weighted imaging of the renal and adrenal lesions. J Comput Assist Tomogr. 2009;33:828–33.
96. Wang Y, Chen ZE, Nikolaidis P, et al. Diffusion-weighted magnetic resonance imaging of pancreatic adenocarcinomas: association with histopathology and tumor grade. J Magn Reson Imaging. 2011; 33:136–42.
97. Akduman EI, Momtahen AJ, Balci NC, Mahajann N, Havlioglu N, Wolverson MK. Comparison between malignant and benign abdominal lymph nodes on diffusion-weighted imaging. Acad Radiol. 2008;15:641–6.
98. Fujii S, Kakite S, Nishihara K, et al. Diagnostic accuracy of diffusion-weighted imaging in differentiating benign from malignant ovarian lesions. J Magn Reson Imaging. 2008;28:1149–56.
99. Kilickesmez O, Bayramoglu S, Inci E, Cimilli T. Value of apparent diffusion coefficient measurement for discrimination of focal benign and malignant hepatic masses. J Med Imaging Radiat Oncol. 2009;53:50–5.
100. Soylu A, Kilickesmez O, Poturoglu S, et al. Utility of diffusion-weighted MRI for assessing liver fibrosis in patients with chronic active hepatitis. Diagn Interv Radiol. 2010;16:204–8.
101. Rao RK, Riffel P, Meyer M, et al. Implementation of dual-source RF excitation in 3 T MR-scanners allows for nearly identical ADC values compared to 1.5 T MR scanners in the abdomen. PLoS One. 2012;7:e32613.
102. Rosenkrantz AB, Oei M, Babb JS, Niver BE, Taouli B. Diffusion-weighted imaging of the abdomen at 3.0 Tesla: image quality and apparent diffusion coefficient reproducibility compared with 1.5 Tesla. J Magn Reson Imaging. 2011;33:128–35.
103. Bilgili MY. Reproductibility of apparent diffusion coefficients measurements in diffusion-weighted MRI of the abdomen with different b values. Eur J Radiol. 2012;81:2066–8.

104. Saremi F, Jalili M, Sefidbakht S, et al. Diffusion-weighted imaging of the abdomen at 3 T: image quality comparison with 1.5-T magnet using 3 different imaging sequences. J Comput Assist Tomogr. 2011;35:317–25.
105. Dale BM, Braithwaite AC, Boll DT, Merkle EM. Field strength and diffusion encoding technique affect the apparent diffusion coefficient measurements in diffusion-weighted imaging of the abdomen. Invest Radiol. 2010;45:104–8.
106. Satoh Y, Ichikawa T, Motosugi U, et al. Diagnosis of peritoneal dissemination: comparison of 18F-FDG PET/CT, diffusion-weighted MRI, and contrast-enhanced MDCT. AJR Am J Roentgenol. 2011;196: 447–53.
107. Bozkurt M, Doganay S, Kantarci M, et al. Comparison of peritoneal tumor imaging using conventional MR imaging and diffusion-weighted MR imaging with different b values. Eur J Radiol. 2011;80:224–8.
108. Yang DM, Jahng GH, Kim HC, et al. The detection and discrimination of malignant and benign focal hepatic lesions: T2 weighted vs diffusion-weighted MRI. Br J Radiol. 2011;84:319–26.
109. Braithwaite AC, Dale BM, Boll DT, Merkle EM. Short- and midterm reproducibility of apparent diffusion coefficient measurements at 3.0-T diffusion-weighted imaging of the abdomen. Radiology. 2009;250:459–65.
110. Yang TH, Lin JZ, Wang X, Lu JH, Chen Z. Preliminary study of feasibility of whole body diffusion weighted imaging in diagnosis of metastasis of tumor. Chin Med Sci J. 2008;23:187–92.
111. Kilickesmez O, Yirik G, Bayramoglu S, Cimilli T, Aydin S. Non-breath-hold high b-value diffusion-weighted MRI with parallel imaging technique: apparent diffusion coefficient determination in normal abdominal organs. Diagn Interv Radiol. 2008; 14:83–7.
112. Tsushima Y, Takano A, Taketomi-Takahashi A, Endo K. Body diffusion-weighted MR imaging using high b-value for malignant tumor screening: usefulness and necessity of referring to T2-weighted images and creating fusion images. Acad Radiol. 2007;14:643–50.
113. Pamir MN, Ozduman K, Dincer A, Yildiz E, Peker S, Ozek MM. First intraoperative, shared-resource, ultrahigh-field 3-Tesla magnetic resonance imaging system and its application in low-grade glioma resection. J Neurosurg. 2010;112:57–69.
114. Auboiroux V, Petrusca L, Viallon M, Goget T, Becker CD, Salomir R. Ultrasonography-based 2D motion-compensated HIFU sonication integrated with reference-free MR temperature monitoring: a feasibility study ex vivo. Phys Med Biol. 2012;57:N159–71.
115. Sung HY, Jung SE, Cho SH, et al. Long-term outcome of high-intensity focused ultrasound in advanced pancreatic cancer. Pancreas. 2011;40:1080–6.
116. Drzezga A, Souvatzoglou M, Eiber M, et al. First clinical experience with integrated whole-body PET/MR: comparison to PET/CT in patients with oncologic diagnoses. J Nucl Med. 2012;53(6):845–55.
117. Samarin A, Burger C, Wollenweber SD, et al. PET/MR imaging of bone lesions – implications for PET quantification from imperfect attenuation correction. Eur J Nucl Med Mol Imaging. 2012;39(7):1154–60.
118. Schwenzer NF, Stegger L, Bisdas S, et al. Simultaneous PET/MR imaging in a human brain PET/MR system in 50 patients-current state of image quality. Eur J Radiol. 2012;81(11):3472–8.
119. Mukherjee A, Wickstrom E, Thakur ML. Imaging oncogene expression. Eur J Radiol. 2009;70:265–73.
120. Daldrup-Link HE, Simon GH, Brasch RC. Imaging of tumor angiogenesis: current approaches and future prospects. Curr Pharm Des. 2006;12: 2661–72.
121. Rygh CB, Qin S, Seo JW, et al. Longitudinal investigation of permeability and distribution of macromolecules in mouse malignant transformation using PET. Clin Cancer Res. 2011;17:550–9.
122. Henriksen OM, Larsson HB, Hansen AE, Gruner JM, Law I, Rostrup E. Estimation of intersubject variability of cerebral blood flow measurements using MRI and positron emission tomography. J Magn Reson Imaging. 2012;35:1290–9.
123. Gevers S, Nederveen AJ, Fijnvandraat K, et al. Arterial spin labeling measurement of cerebral perfusion in children with sickle cell disease. J Magn Reson Imaging. 2012;35:779–87.
124. Lubberink M, Wong YY, Raijmakers PG, et al. Myocardial oxygen extraction fraction measured using bolus inhalation of 15O-oxygen gas and dynamic PET. J Nucl Med. 2011;52:60–6.
125. Nanni C, Fantini L, Nicolini S, Fanti S. Non FDG PET. Clin Radiol. 2010;65:536–48.
126. Gilles R, Vogel WV, Gidding CE, Janssens GO, van der Vliet TM, Oyen WJ. (18)F-fluoro-L-thymidine-PET for the evaluation of primary brain tumours in children: a report of three cases. Nucl Med Commun. 2010;31:482–7.
127. Grant FD, Treves ST. Nuclear medicine and molecular imaging of the pediatric chest: current practical imaging assessment. Radiol Clin North Am. 2011;49:1025–51.
128. Purz S, Mauz-Korholz C, Korholz D, et al. [18F] Fluorodeoxyglucose positron emission tomography for detection of bone marrow involvement in children and adolescents with Hodgkin's lymphoma. J Clin Oncol. 2011;29:3523–8.
129. Cole AJ, Yang VC, David AE. Cancer theranostics: the rise of targeted magnetic nanoparticles. Trends Biotechnol. 2011;29:323–32.
130. Rottey S, Signore A, Van de Wiele C. Radiolabelled chemotherapeutics. Q J Nucl Med Mol Imaging. 2007;51:139–51.
131. Daldrup-Link HE, Mohanty A, Cuenod C, Pichler B, Link T. New perspectives on bone marrow contrast agents and molecular imaging. Semin Musculoskelet Radiol. 2009;13:145–56.
132. Daldrup-Link HE, Golovko D, Ruffel B, et al. MR imaging of tumor associated macrophages with

clinically-applicable iron oxide nanoparticles. Clin Cancer Res. 2011;17(17):5695–704.
133. Glaus C, Rossin R, Welch MJ, Bao G. In vivo evaluation of (64)Cu-labeled magnetic nanoparticles as a dual-modality PET/MR imaging agent. Bioconjug Chem. 2010;21:715–22.
134. Anderson CJ, Ferdani R. Copper-64 radiopharmaceuticals for PET imaging of cancer: advances in preclinical and clinical research. Cancer Biother Radiopharm. 2009;24:379–93.
135. Ferner RE, Golding JF, Smith M, et al. [18F]2-fluoro-2-deoxy-D-glucose positron emission tomography (FDG PET) as a diagnostic tool for neurofibromatosis 1 (NF1) associated malignant peripheral nerve sheath tumours (MPNSTs): a long-term clinical study. Ann Oncol. 2008;19:390–4.
136. Morimoto T, Tateishi U, Maeda T, Arai Y, Nakajima Y, Edmund Kim E. Nodal status of malignant lymphoma in pelvic and retroperitoneal lymphatic pathways: comparison of integrated PET/CT with or without contrast enhancement. Eur J Radiol. 2008; 67:508–13.
137. Tateishi U, Yamaguchi U, Seki K, Terauchi T, Arai Y, Kim EE. Bone and soft-tissue sarcoma: preoperative staging with fluorine 18 fluorodeoxyglucose PET/CT and conventional imaging. Radiology. 2007;245:839–47.
138. Tateishi U, Hosono A, Makimoto A, et al. Comparative study of FDG PET/CT and conventional imaging in the staging of rhabdomyosarcoma. Ann Nucl Med. 2009;23:155–61.
139. Lee CL, Wahnishe H, Sayre GA, et al. Radiation dose estimation using preclinical imaging with 124I-metaiodobenzylguanidine (MIBG) PET. Med Phys. 2010;37:4861–7.
140. Punwani S, Taylor SA, Bainbridge A, et al. Pediatric and adolescent lymphoma: comparison of whole-body STIR half-Fourier RARE MR imaging with an enhanced PET/CT reference for initial staging. Radiology. 2010;255:182–90.
141. Krohmer S, Sorge I, Krausse A, et al. Whole-body MRI for primary evaluation of malignant disease in children. Eur J Radiol. 2010;74:256–61.
142. Kwee TC, van Ufford HM, Beek FJ, et al. Whole-body MRI, including diffusion-weighted imaging, for the initial staging of malignant lymphoma: comparison to computed tomography. Invest Radiol. 2009;44:683–90.
143. Kwee TC, Takahara T, Ochiai R, et al. Whole-body diffusion-weighted magnetic resonance imaging. Eur J Radiol. 2009;70:409–17.
144. Lin FI, Rao JE, Mittra ES, et al. Prospective comparison of combined (1)(8)F-FDG and (1)(8)F-NaF PET/CT vs. (1)(8)F-FDG PET/CT imaging for detection of malignancy. Eur J Nucl Med Mol Imaging. 2012;39:262–70.
145. Bestic JM, Peterson JJ, Bancroft LW. Pediatric FDG PET/CT: physiologic uptake, normal variants, and benign conditions [corrected]. Radiographics. 2009; 29:1487–500.
146. Bakhshi S, Radhakrishnan V. Prognostic markers in osteosarcoma. Expert Rev Anticancer Ther. 2010; 10:271–87.
147. Wahl RL, Jacene H, Kasamon Y, Lodge MA. From RECIST to PERCIST: evolving considerations for PET response criteria in solid tumors. J Nucl Med. 2009;50 Suppl 1:122S–50.
148. Gupta K, Pawaskar A, Basu S, et al. Potential role of FDG PET imaging in predicting metastatic potential and assessment of therapeutic response to neoadjuvant chemotherapy in Ewing sarcoma family of tumors. Clin Nucl Med. 2011;36: 973–7.
149. Song BI, Lee SW, Jeong SY, et al. 18F-FDG uptake by metastatic axillary lymph nodes on pretreatment PET/CT as a prognostic factor for recurrence in patients with invasive ductal breast cancer. J Nucl Med. 2012;53:1337–44.
150. Cortes-Funes H. The role of antiangiogenesis therapy: bevacizumab and beyond. Clin Transl Oncol. 2009;11:349–55.
151. Aguilera DG, Goldman S, Fangusaro J. Bevacizumab and irinotecan in the treatment of children with recurrent/refractory medulloblastoma. Pediatr Blood Cancer. 2011;56:491–4.
152. Maraninchi D, Vey N, Viens P, et al. A phase II study of interleukin-2 in 49 patients with relapsed or refractory acute leukemia. Leuk Lymphoma. 1998;31:343–9.
153. Matthay KK, Weiss B, Villablanca JG, et al. Dose escalation study of no-carrier 131-MIBG for relapsed or refractory neuroblastoma: New Approaches to Neuroblastoma Therapy (NANT) Trial. J Nucl Med. 2012;53(7):1155–63.
154. Bajpai J, Kumar R, Sreenivas V, et al. Prediction of chemotherapy response by PET-CT in osteosarcoma: correlation with histologic necrosis. J Pediatr Hematol Oncol. 2011;33:e271–8.
155. Padhani AR, Liu G, Koh DM, et al. Diffusion-weighted magnetic resonance imaging as a cancer biomarker: consensus and recommendations. Neoplasia. 2009;11:102–25.
156. Afaq A, Andreou A, Koh DM. Diffusion-weighted magnetic resonance imaging for tumour response assessment: why, when and how? Cancer Imaging. 2010;10(Spec no A):S179–88.
157. Gao J, Chesebrough JW, Cartlidge SA, et al. Dual IGF-I/II-neutralizing antibody MEDI-573 potently inhibits IGF signaling and tumor growth. Cancer Res. 2011;71:1029–40.
158. McKinley ET, Bugaj JE, Zhao P, et al. 18FDG-PET predicts pharmacodynamic response to OSI-906, a

dual IGF-1R/IR inhibitor, in preclinical mouse models of lung cancer. Clin Cancer Res. 2011;17:3332–40.
159. Soloviev D, Lewis D, Honess D, Aboagye E. [(18)F] FLT: an imaging biomarker of tumour proliferation for assessment of tumour response to treatment. Eur J Cancer. 2012;48:416–24.
160. Pfannenberg C, Aschoff P, Dittmann H, et al. PET/CT with 18F-FLT: does it improve the therapeutic management of metastatic germ cell tumors? J Nucl Med. 2010;51:845–53.
161. Chan HS, Haddad G, Thorner PS, et al. P-glycoprotein expression as a predictor of the outcome of therapy for neuroblastoma. N Engl J Med. 1991;325:1608–14.
162. Chan HS, Thorner PS, Haddad G, Ling V. Immunohistochemical detection of P-glycoprotein: prognostic correlation in soft tissue sarcoma of childhood. J Clin Oncol. 1990;8:689–704.
163. Baldini N, Scotlandi K, Barbanti-Brodano G, et al. Expression of P-glycoprotein in high-grade osteosarcomas in relation to clinical outcome. N Engl J Med. 1995;333:1380–5.
164. Kucerova H, Sumerauer D, Drahokoupilova E, Piskova M, Bedrnicek J, Eckschlager T. Significance of P-glycoprotein expression in childhood malignant tumors. Neoplasma. 2001;48:472–8.
165. Hendrikse NH, Vaalburg W. Dynamics of multidrug resistance: P-glycoprotein analyses with positron emission tomography. Methods. 2002;27:228–33.
166. Levchenko A, Mehta BM, Lee JB, et al. Evaluation of 11C-colchicine for PET imaging of multiple drug resistance. J Nucl Med. 2000;41:493–501.
167. Cheson BD, Pfistner B, Juweid ME, et al. Revised response criteria for malignant lymphoma. J Clin Oncol. 2007;25:579–86.
168. Sandoval JA, Malkas LH, Hickey RJ. Clinical significance of serum biomarkers in pediatric solid mediastinal and abdominal tumors. Int J Mol Sci. 2012;13:1126–53.
169. Weckesser M. Molecular imaging with positron emission tomography in paediatric oncology–FDG and beyond. Pediatr Radiol. 2009;39 Suppl 3:450–5.
170. Gelfand MJ. Dosimetry of FDG PET/CT and other molecular imaging applications in pediatric patients. Pediatr Radiol. 2009;39 Suppl 1:S46–56.

Combined PET/MRI in Childhood

26

Thomas Pfluger and Wolfgang Peter Mueller

Magnetic resonance imaging (MRI) and positron emission tomography (PET) are diagnostic imaging modalities that allow visualization of morphological as well as functional features of different diseases in childhood. Both modalities are often used separately or even in competition. Some of the most important indications for both PET and MRI lie in the field of pediatric oncology. The most important malignant diseases in children are leukemia, brain tumors, lymphoma, Wilms' tumor, neuroblastoma, and soft tissue and bone sarcomas. Apart from leukemia, correct assessment of tumor expansion with modern imaging techniques, mainly consisting of ultrasonography, MRI (Fig. 26.1), and PET, is essential for cancer staging, for the choice of the best therapeutic approach, and for restaging after therapy or in recurrence [1, 2].

Basic Principles of Multimodality Imaging

Multimodality image fusion of functional and anatomical data can be performed by acquisition on dedicated hybrid imaging systems or by retrospective software co-registration of separate scans. Three basic components are required for PET/MR software registration: First is the acquisition of high-quality PET and MRI images and subsequent data storage. Second, there must be simple and prompt access to the corresponding images or image data sets. Adequate multimodal imaging requires a clinic-wide computer network, a digital archive of radiological and nuclear medical studies, multimodal image viewing workstations, and appropriate software for image correlation and fusion [3, 4]. Third and probably most important is the competence of the physician in evaluating nuclear medical and

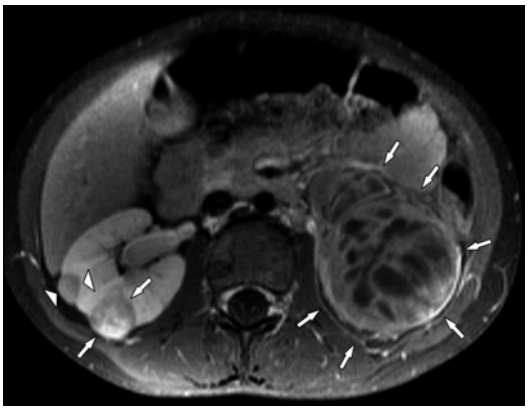

Fig. 26.1 A 4-year-old boy with bilateral Wilms' tumor and nephroblastomatosis. Transversal fat-suppressed T1-weighted image after contrast enhancement reveals bilateral nephroblastoma (*arrows*) and a right-sided nephroblastomatosis lesion (*arrowheads*). Exact detection of bilateral nephroblastoma and nephroblastomatosis lesions is essential for further surgical planning

T. Pfluger, MD (✉) • W.P. Mueller, MD
Department of Nuclear Medicine,
University Hospital of the LMU,
Ludwig-Maximilians-University of Munich,
Munich, Germany
e-mail: thomas.pfluger@med.uni-muenchen.de;
wolfgang.fendler@med.uni-muenchen.de

S.T. Treves (ed.), *Pediatric Nuclear Medicine and Molecular Imaging*,
DOI 10.1007/978-1-4614-9551-2_26, © Springer Science+Business Media New York 2014

radiological data sets. Because each individual modality can yield false-negative findings, a careful and time-consuming separate analysis of each individual modality prior to multimodal processing is essential. In combined multimodal image evaluation, there is a tendency to depend primarily on the findings of PET, which usually identifies pathological processes more rapidly. In doing so, one runs the risk of missing diagnoses that would be seen at MRI because of reliance on false-negative PET scans. Therefore, a mainly PET-guided analysis of MRI should be avoided.

Image Fusion

For images that were not acquired on a dedicated PET/MR hybrid system, the retrospective image fusion can be done using different approaches and algorithms, which, in general, are divided into feature- and volume (voxel)-based techniques. The image transformation can be static (displacement and rotation in all three spatial axes) or nonlinear (e.g., additional stretching or compression in order to compensate for spatial distortions such as those introduced by respiratory movements) [5].

The classical example of a feature-based method is the "surface matching" or Pelizzari algorithm, which uses organ surfaces as a property [6]. The disadvantages of this technique are the requirement for a potentially quite extensive segmentation of the organ surface in the different modalities and the fact that image registration is based only on the extracted portions of the image (surface pixels). Simply stated, volume-based techniques analyze similarities of pixel distribution in the two imaging modalities [5]. The representative of this algorithm group enjoying the widest current application is the "mutual information" algorithm in which two-dimensional grayscale histograms of the individual modalities and a combined histogram are analyzed and compared in various image transformations [7, 8]. Nonlinear approaches such as thin-plate spline (TPS) interpolation or hierarchical (pyramid) volume subdivision can be added to compensate for respiratory-induced soft tissue deformations in thorax and abdomen [9–11]. Advantages of the volume-based techniques include the fully automatic application, their robustness compared to a different "field of view," and the higher degree of precision in image registration [5].

A meta-analysis by Hutton and Braun quantified the exactness of software-based cerebral image registration at less than 3 mm [4]. For extracerebral applications, the PET and CT registration of pulmonary focal lesions showed a comparable exactness (average position of center of the lesion) of 6.2 mm for separate modalities [12] and of 7.6 mm for combined PET/CT scanners [13]. Furth et al. compared conventional imaging modalities (CIM, including thoracic CT and neck/abdomen/pelvis MRI) alone, PET alone, and side-by-side and voxel-based fusion of PET and CIM by using a normalized mutual information algorithm. In terms of disease staging and therapy assignment, voxel-based image fusion performed best with no false estimations compared to three underestimations for side-by-side images and 22 over- and underestimations for PET and CIM alone [14].

Image Presentation

The evaluation of multimodal imaging data consists of three stages. The first stage corresponds to the separate analysis of the multimodal data in nuclear medicine and diagnostic radiology with subsequent comparison of the reported findings. In case of discrepancies, a separate reevaluation of the imaging data is performed with comparison of the other imaging modality. This is the currently most widely used method, and it has the advantage of minimum requirements in terms of hardware and software, together with restricted logistic, temporal, and personnel requirements. A disadvantage is the lack of an exact anatomical-functional comparison of both methods. This disadvantage can be decisive in the recognition and delineation of physiological changes. The second stage consists of simultaneous interpretation of the multimodal data sets at the same site. Although this method enhances the capacity for morphological correlation, because of the associated significant increase in personnel, financial, and time requirements, it is advisable to progress

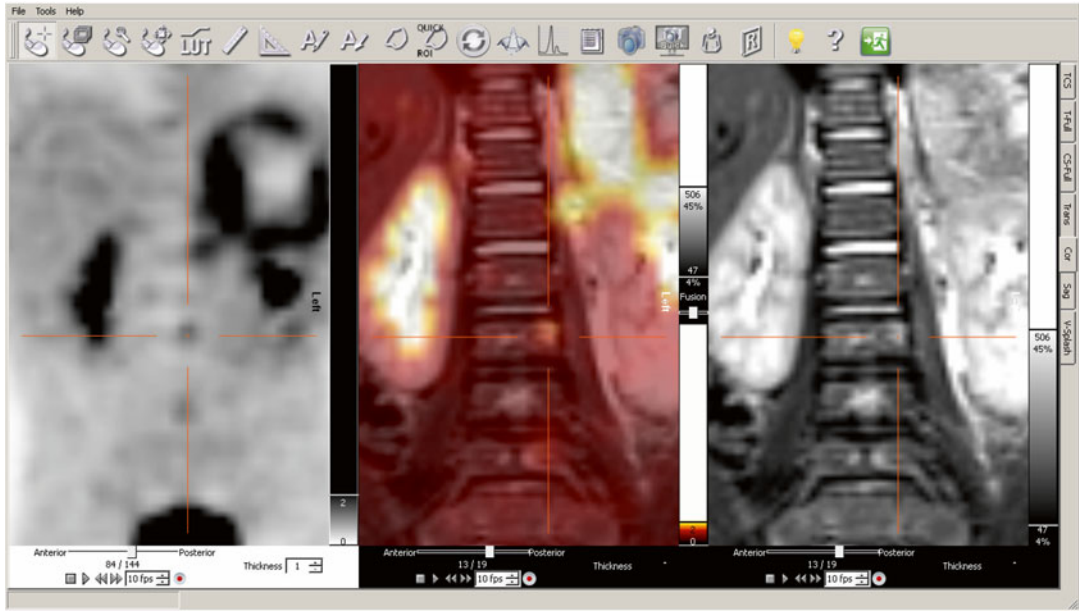

Fig. 26.2 Multimodality display on a Hermes workstation (Nuclear Diagnostics AB, Haegersten, Sweden) demonstrating a large left-sided paravertebral neuroblastoma in ^{18}F-FDG PET (*left image*) and T2-weighted MRI (*right image*). By synchronizing images, even small bone marrow metastases (crosshair) can exactly be correlated with a common cursor. By confirming the lesion in the fusion image (*middle image*), diagnostic accuracy as compared to single modalities alone can be increased

directly to the third stage. In the third stage, analysis of spatially synchronized image data is performed simultaneously at a single workstation (Fig. 26.2). Either synchronized data is acquired on a dedicated PET/MR device or synchronization is performed interactively and partially or fully automatic with help of a fusion algorithm [15]. These conditions provide for optimum spatial correlation of findings. Also useful is a common cursor that points to the corresponding location in both modalities, which are displayed side by side [5]. This exact synchronization of data sets with appropriate software provides the additional capacity for image fusion with superimposition of both sets of imaging data in one image (Fig. 26.3). In addition, a three-dimensional reconstruction of the fused imaging data can be used for therapy planning (Fig. 26.4). When using a fused image, it is important to note that original information from the two individual imaging modalities may be partially lost, meaning that the original images of each modality should also be simultaneously displayed [5] (Fig. 26.2).

Following image analysis comes the presentation of multimodal images to clinical colleagues, for whom the display of the fused imaging data sets moves to the foreground. Here, image fusion and three-dimensional reconstruction often represent decisive building blocks to understand the pathology and to facilitate further therapeutic planning (Fig. 26.4).

PET and MRI in Pediatric Oncology

Neuroblastoma

Neuroblastoma is the most common extracranial solid malignancy in pediatric patients (about 8 % of pediatric malignancies) and remains, despite treatment intensification, responsible for approximately 15 % of cancer deaths in children [16–19]. It is an embryonic tumor arising from the neural crest cells, which give rise to the adrenal medulla and the sympathetic nervous system [20]. The tumor is most frequently situated in the adrenal gland or

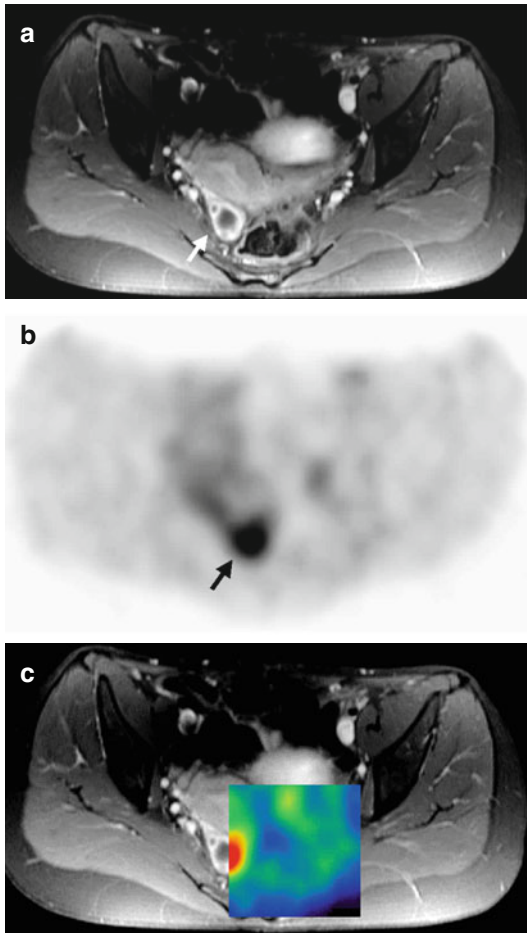

Fig. 26.3 Histologically proven non-affected cystic ovary in a patient with a recurrent yolk sack tumor. T1-weighted, fat-suppressed MR sequence after application of Gd-DTPA (**a**) depicts a physiological-appearing cystic ovary (*arrow*). Corresponding PET (**b**) revealed a false-positive finding with an increased glucose uptake (*arrow*) suspect of a recurrent disease. Multimodality display of registered images (**c**) shows exact spatial correlation between the cystic ovary in MRI and increased glucose uptake in PET

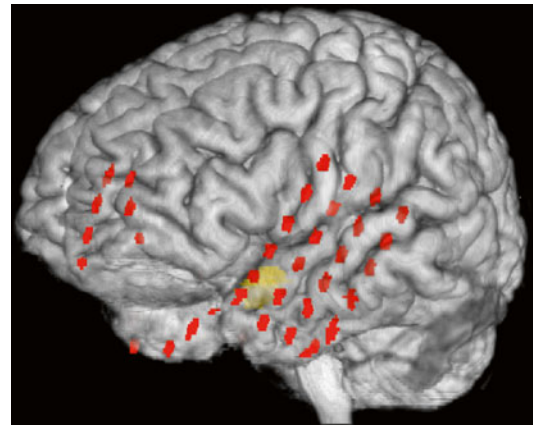

Fig. 26.4 3D reconstruction of a registered image data set. Cortical surface was rendered from MRI and *red dots* represent subdural EEG electrodes that were imaged with CT. The functional epileptogenic focus (*orange*) was defined by interictal ^{18}F-FDG PET and ictal ECD SPECT

elsewhere along the sympathetic nervous system chain [16]. At diagnosis, roughly 50 % of patients have distant hematogenous metastases [21]. There is strong evidence that initial staging of neuroblastoma remains decisive with respect to risk stratification in order to choose the most appropriate treatment option [18, 22]. Imaging of neuroblastoma consists of sonography, CT, MRI, and radionuclide examinations such as scintigraphic bone scanning, metaiodobenzylguanidine (MIBG) scintigraphy, PET with different tracers (fluorodeoxyglucose, ^{18}F-FDG; fluorodopa, ^{18}F-DOPA; somatostatin receptor agonists), as well as hybrid imaging (PET/CT, PET/MRI, and SPECT/CT) [23–34].

PET in Pediatric Neuroblastoma

Scintigraphy with ^{123}I- or ^{131}I-labeled MIBG has become a well-established method in the diagnosis and staging of neuroblastoma [35]. However, there are some limitations of this modality: limited spatial resolution, limited sensitivity for the detection of small lesions. Some of these limitations can potentially with PET due to its higher spatial resolution and the possibility of a whole-body tomography versus SPECT.

The use of ^{18}F-FDG PET in the evaluation of pediatric neuroblastoma is increasing, although its role remains less clear. Questions remain regarding when and in which patients ^{18}F-FDG PET is most useful. By comparing 113 paired ^{123}I-MIBG and ^{18}F-FDG PET scans, Sharp et al. concluded that ^{18}F-FDG should always be considered when ^{123}I-MIBG reveals less disease than suggested by clinical symptoms or conventional imaging modalities [26] (Fig. 26.5).

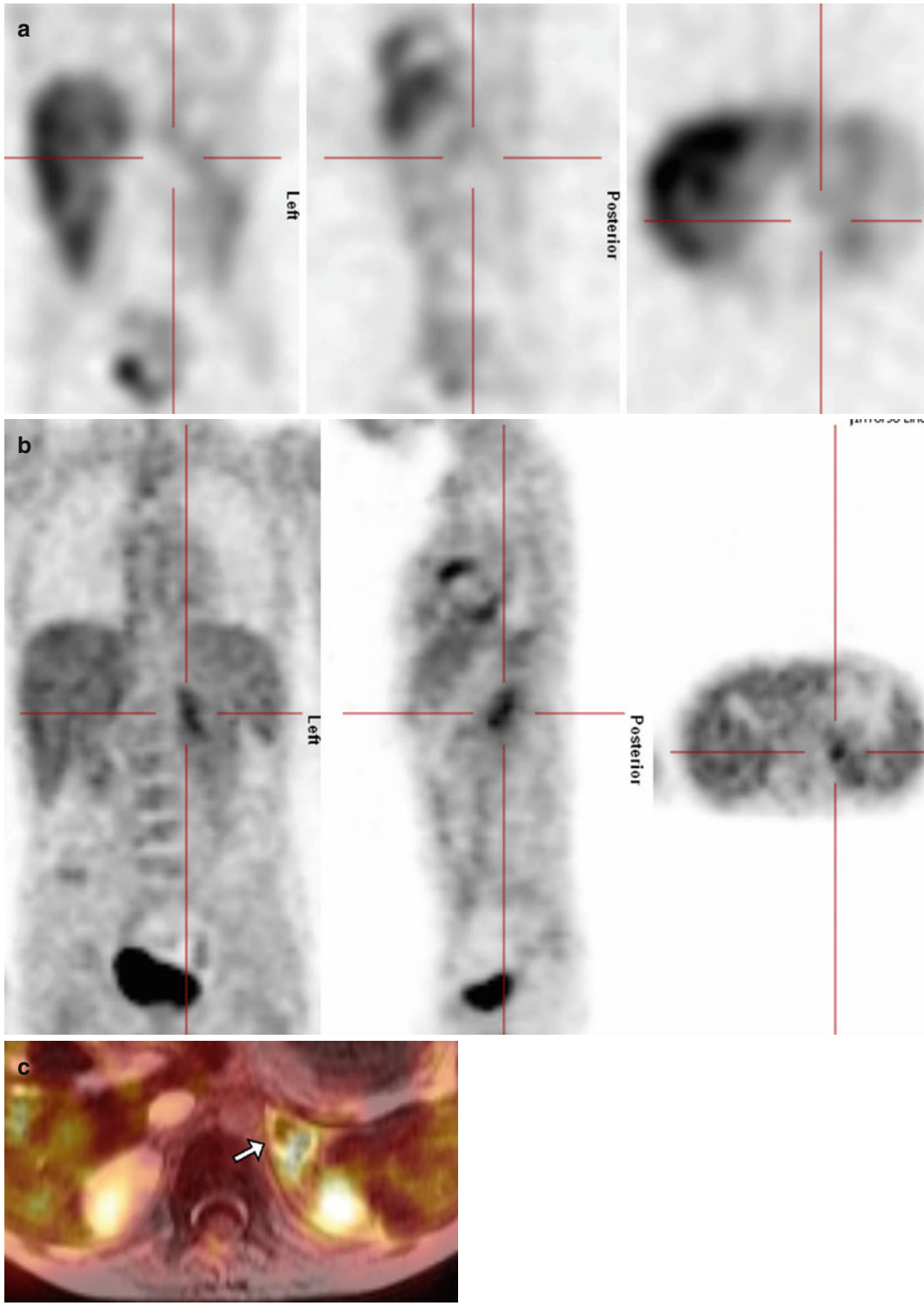

Fig. 26.5 A 7-year-old girl with a histologically proven recurrent neuroblastoma in the region of the left adrenal gland. Iodine-123-MIBG-SPECT does not show any pathological uptake in the left adrenal region (**a** – crosshair) leading to a false-negative result. Fluorine-18-FDG PET clearly demonstrates an increased glucose metabolism in the respective region (**b** – crosshair) suspect for recurrent disease. Image fusion between ^{18}F-FDG PET and MRI shows increased ^{18}F-FDG uptake within a contrast-enhancing soft tissue mass (**c** – *arrow*)

As ^{18}F-FDG is a marker for the viability of malignomas in general, more specific PET tracers have been developed for imaging the sympathetic nervous system like ^{11}C-hydroxyephedrine (HED) [36, 37]. This agent has been used to map the sympathetic innervation of the heart, and it has been shown that HED is highly concentrated in deposits of pheochromocytoma [38–40]. Franzius et al. showed that ^{11}C-HED PET/CT is feasible in tumors of the sympathetic nervous system [41]. However, tumor-to-background contrast of ^{11}C-HED in lesions can be higher, equal, or lower compared with ^{123}I-MIBG [41] and the relatively high physiological liver uptake of ^{11}C-HED may impair the detection of small liver metastases. Some of these shortcomings may be avoided by using PET/CT with ^{18}F-labeled tracers (half-life, 110 min), such as 6-^{18}F-fluoro-3,4-dihydroxy-2-phenylalanine (^{18}F-DOPA), which has been introduced for imaging a variety of neuroendocrine tumors [42–44]. Piccardo et al. compared the diagnostic value of ^{18}F-DOPA PET/CT with ^{123}I-MIBG on primary investigation and follow-up of neuroblastoma patients in a prospective pilot study. By using both a scan-based and lesion-based analyses higher sensitivities and comparable specificities of ^{18}F-DOPA versus ^{123}I-MIBG scintigraphy were seen [45].

Somatostatin receptor subtype 2 is expressed on the surface of some neuroblastomas [46–48]. Somatostatin analogues have been tested in small-scale studies for imaging and peptide-receptor radionuclide therapy (PRRT) of neuroblastomas. Gains et al. found abnormal ^{68}Ga-DOTATATE uptake in 6 out of 8 children with relapsed or refractory high-risk neuroblastoma [49]. All 6 patients received ^{177}Lu-DOTATATE treatment in 2–3 cycles. One patient showed progressive disease and 5 patients showed stable disease according to RECIST. Thus, besides ^{18}F-FDG, a variety of PET agents have been tested for neuroblastoma imaging and treatment; however, systematic evaluation of detection and response rates in larger-scale studies have yet to be performed.

MRI in Pediatric Neuroblastoma

MRI has several advantages in the diagnosis of neuroblastoma: high sensitivity in detecting bone marrow abnormalities [50], lack of ionizing radiation, high intrinsic soft tissue contrast resolution [24], depiction of internal structure [51], and exact definition of intraspinal tumor extension (Fig. 26.6) or diaphragmatic involvement of thoracic tumors [23, 52]. Furthermore MRI is the best modality to evaluate intracranial involvement or the extent of a possible vessel encasement [20, 23, 53–55]. All these factors are decisive, especially in primary diagnosis and for operative or biopsy planning [56].

Primary tumors usually appear heterogeneous and iso- to hyperintense compared to the liver with variable contrast enhancement on T1-weighted images [57]. T2 hyperintense cystic or necrotic areas may be seen within the tumor [57].

Metastatic disease shows a variety of different patterns [57]. Bone marrow metastases usually appear as low-intensity lesions on T1-weighted and as high-intensity area on T2-weighted images [57]. Liver involvement may be diffuse especially in stage 4S patients [57]. However, focal liver lesions with reduced contrast enhancement can be seen. CNS metastases are usually from tumor infiltration of the dura and neural crest (leptomeninges) [58]. Dural metastasis can be diffuse or nodular and tend to favor the external surface of the dura without involvement of the brain parenchyma [59].

Soft Tissue Sarcoma

Sarcomas are heterogeneous in terms of tumor biology, malignancy, and therapeutic options. Primary bone sarcomas occur in children up to the age of 19 years with an incidence of 8.9 per 1,000,000 according to SEER cancer incidence rates (2001–2004) [60]. They are divided into two larger groups: osteosarcomas and Ewing sarcomas. Soft tissue sarcomas in children originate from mesenchyme in the soft tissues and occur with an incidence of 12.0 per 1,000,000 [60]. The most common subtypes in children and adolescents are rhabdomyosarcoma, extraosseous Ewing sarcoma and peripheral neuroectodermal tumor, synovial sarcoma, neurofibrosarcoma, fibrosarcoma, and leiomyosarcoma.

Distant metastases are most often seen in lungs and bone marrow. The local tumor extent

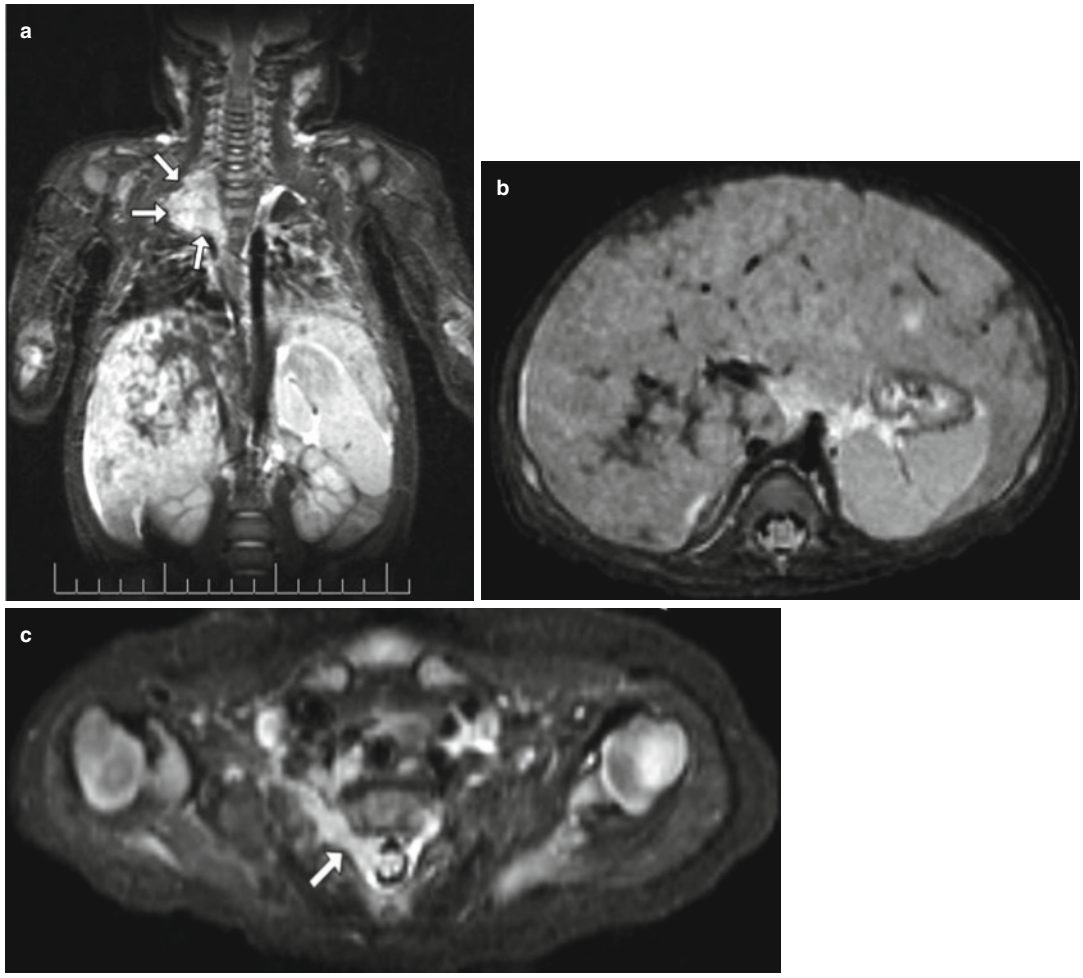

Fig. 26.6 A 2-month-old suckling with a stage IV neuroblastoma. Clinical and ultrasound findings did not demonstrate a primary tumor. Coronal T2-weighted MRI (**a**) clearly depicts a right paravertebral contrast-enhancing primary tumor (*arrows*). Transversal T1-weighted MRI of the abdomen (**b**) demonstrates diffuse liver metastases. Transversal T1-weighted MRI (**c**) shows the tumoral growth through intervertebral foramen (*arrow*) which is decisive for further therapy planning

and the presence of satellite lesions or distant metastases as determined by PET or MRI influence the treatment strategy.

PET in Pediatric Sarcomas

PET is competing with bone scans and CT for diagnostic value in detecting osseous tumor lesions. In retrospective and prospective studies, ^{18}F-FDG PET has shown greater sensitivity, specificity, and accuracy than bone scintigraphy in the detection of skeletal metastases from Ewing tumors [61–64]. For the detection of skeletal metastases from osteosarcoma, ^{18}F-FDG PET has not been shown to be superior to bone scans [61, 63, 65]. In a study with mixed series of bone and soft tissue sarcomas, PET had comparable sensitivity to CT in the detection of primary lesions and non-pulmonary metastases but a higher specificity. CT was superior for detecting pulmonary metastases [66, 67].

In primary bone sarcomas, multiple studies have shown that response to neoadjuvant chemotherapy can be evaluated using ^{18}F-FDG PET. It was demonstrated for both osteosarcomas and Ewing sarcomas that a decrease of ^{18}F-FDG uptake and a small posttherapeutic/pretherapeu-

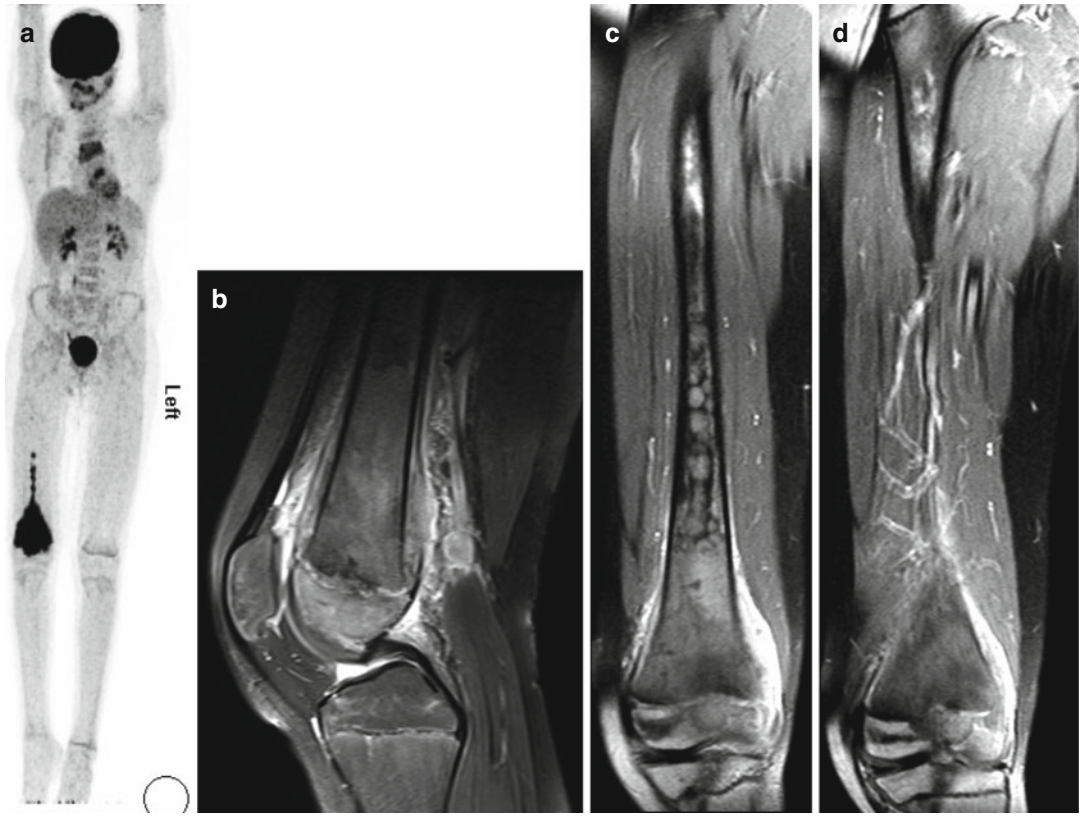

Fig. 26.7 A 13-year-old boy with an osteosarcoma of the right distal femur. 3D reconstructed ^{18}F-FDG PET (**a**) shows high glucose metabolism in the metaphysics and epiphysis of the right femur. Bone marrow extension can be seen up to the middle part of the femur. However, MRI (**b**–**d**) is indispensable for delineation of soft tissue involvement and bone marrow extension. Sagittal T2-weighted image (**b**) depicts exact soft tissue infiltration and epiphyseal involvement, decisive factors for operative planning. Fat-saturated T1-weighted images after contrast enhancement (**c**, **d**) demonstrate tumoral bone marrow extension far up to the proximal femur

tic SUV ratio showed a close correlation to the amount of tumor necrosis induced by chemotherapy [68–70]. The intensity of initial ^{18}F-FDG uptake of the primary tumor is further associated with a reduced overall and disease-free survival [71, 72].

There are only a few studies that investigated the diagnostic value of PET in staging of soft tissue sarcoma. In a retrospective analysis of 46 ^{18}F-FDG PET examinations in 25 young patients, ^{18}F-FDG PET demonstrated a sensitivity of 86 %, a specificity of 80 %, and a positive predictive value of 89 % [73]. The authors concluded that ^{18}F-FDG PET may be useful for the management of patients with soft tissue sarcoma [73].

MRI in Pediatric Sarcomas

MRI – compared to PET or bone scans – is the modality of choice for definition of local tumor extent and identification of skip lesions. By defining the relationship to surrounding soft tissue or neurovascular structures, surgical management is determined and possible target structures for needle biopsy are identified. MRI evaluation is essential to evaluate exact bony involvement in order to potentially preserve epiphyseal plate and joint function during surgical treatment [74] (Fig. 26.7).

Tumor appearance on MRI may be variable; however, typical patterns have been described: Osseous and soft tissue sarcomas usually have a low signal intensity on T1-weighted images, a high signal intensity on T2-weighted images, and

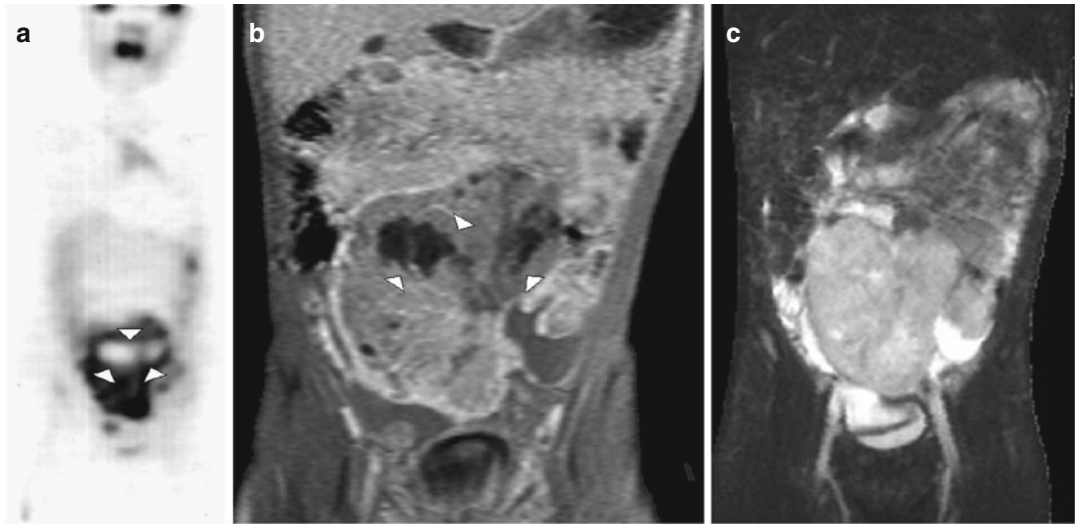

Fig. 26.8 Rhabdomyosarcoma of the lower abdomen in a 6-year-old boy. Fluorine-18-FDG PET demonstrates a large area with increased glucose uptake correlating to the primary tumor and a central photopenic defect (*arrowheads*) (**a**). This photopenic defect correlates well to central necrosis visible in the T1-weighted, contrast-enhanced MR sequence (*arrowheads*) (**b**). For operative planning, T2-weighted STIR sequence is necessary for the delineation of tumor borders and the course of vessels (**c**)

a heterogeneous enhancement after administration of gadolinium contrast agent [75, 76] (Fig. 26.8).

MRI features allow for better discrimination between benign and malignant lesions. For lesions with bone involvement, dense, wavy, and thick periosteal reactions indicate a slow-growing benign lesion, whereas rapid, malignant infiltration results in onion-skinned or lamellated periosteal patterns [75]. MRI characteristics of soft tissue sarcomas include heterogeneous T1/T2 signal and neurovascular encasement.

Changes in tumor volume and extent of necrosis are valuable information for response assessment [76]. Furthermore, MRI morphology in combination with functional ^{18}F-FDG PET was able to predict response to chemotherapy in osteosarcoma with high predictive values for good and poor responders [35].

Lymphoma

Malignant lymphoma and Hodgkin and non-Hodgkins disease are the most common forms of hematological malignancy in the developed world and comprise about 5.3 % of all cancers in the United States [77]. A number of various classification systems exist for lymphoma. The WHO classification, published in 2001 and updated 2008, is the latest system [78]. This classification attempts to divide lymphoma by phenotypic, molecular, or cytogenetic characteristics into three large groups (B cell, T cell, natural killer cell origin) with over 70 different subgroups. Once diagnosis has been established, evaluation of disease extent is important for appropriate treatment planning and determining prognosis. Staging of lymphoma is based on the Ann Arbor classification that classifies by the number of involved regions, the type of involvement (nodal or extranodal), and the distribution of the involved sites. In hematological malignancies, extensive disease involvement is not uncommon. Therefore, imaging modalities such as PET or MRI that can encompass the whole body are of great importance.

PET in Pediatric Lymphoma

Metabolic imaging is crucial in distinguishing disseminated disease from localized manifestations that might be treated by irradiation (Fig. 26.9). Fluorine-18-FDG PET alone is more sensitive than CT or MRI for detection of small

Fig. 26.9 A 7-year-old boy with back pain and a large prevertebral non-Hodgkin lymphoma. 3D reconstructed ^{18}F-FDG PET (**a**) gives an excellent overview of the lymphoma extension in the upper mediastinum and bone marrow involvement of the right scapula, right proximal humerus, and right proximal femur. On the other hand, MRI is indispensable for delineating tumor growth through intervertebral foramina (**b** – T2-weighted image in sagittal orientation), intraspinal involvement (**c** – T1-weighted image after contrast enhancement in sagittal orientation), and vessel involvement (**d** – T2-weighted image in axial orientation)

tumor foci such as lymph nodes <1.5 cm [79]. Fluorine-18-FDG PET further improves detection of occult splenic disease. By combining both functional imaging with ^{18}F-FDG, anatomical CT information, and adequate attenuation correction in PET/CT, even more precise lymphoma staging can be achieved [80].

One main advantage of metabolic imaging lies in response monitoring and prognosis stratification. Fluorine-18-FDG PET baseline and follow-up exams are strongly recommended for diffuse large B-cell lymphoma (DLBCL) and Hodgkin's disease. In both lymphoma entities, a negative interim ^{18}F-FDG PET has been linked to either event-free or progression-free overall survival [81–84]. PET has therefore been integrated into the revised IWG (International Working Group)

criteria at completion of first-line therapy and mid-therapy (interim) exam as powerful prognostic tool [81–83]. An ongoing EuroNet study (EuroNet-PHL-C1) will further show whether radiotherapy can be omitted in Hodgkin lymphoma patients that obtained a good early PET response after two cycles of chemotherapy without compromising the cure rate [85]. Early response monitoring by ^{18}F-FDG PET may be useful to minimize late toxicity of chemotherapy or radiotherapy in good responders and to identify nonresponders early in order to improve their prognosis by treatment modifications.

MRI in Pediatric Lymphoma

As whole-body MRI becomes more and more available, it is being evaluated for staging and treatment follow-up of pediatric lymphoma. Whole-body MRI using short tau inversion recovery (STIR) images proved to be more sensitive in bone marrow involvement than CT or bone scans at primary staging [86]. However, PET/CT remains the most accurate modality in lymph node staging [87, 88]. Recent techniques such as whole-body diffusion-weighted imaging detect lymphoma foci by restricted intralesional water motion and were shown to be useful for monitoring treatment response of bone marrow disease [89]. Intracerebral involvement can be seen by typical intra-axial single or multiple homogeneous contrast-enhancing lesions with marked surrounding edema and restricted diffusion [90]. Fluorine-18-FDG PET, however, is weak in detecting central nervous system disease.

MRI further enables frequent follow-up examinations without additional radiation exposure. MRI, therefore, helps to prevent long-term consequences of increased radiation burden in patients with an excellent prognosis compared to other pediatric malignancies.

Histiocytosis

Langerhans cell histiocytosis (LCH) refers to a group of disorders involving clonal proliferation of activated dendritic cells and macrophages. LCH usually affects children between the age of 1 and 15 years and is traditionally divided by number of lesions and lesion distribution into three groups: (1) unifocal eosinophilic granuloma, which is predominantly osseous or pulmonary; (2) multifocal Hand-Schüller-Christian disease with exophthalmus, lytic bone lesions (mostly in the base of the skull), and diabetes insipidus; and (3) multifocal multisystem Letterer-Siwe disease, which typically includes the abdominal viscera [91]. The main organs involved are bone, lung, skin, and lymph nodes; however, during the course of the disease, any organ system may be affected. Prognosis is determined by the involvement of risk organs and response to treatment which makes cross-sectional whole-body imaging the first choice for primary staging and posttherapy follow-up [92, 93]. PET/CT and MRI have been proven to reliably identify multifocal disease [94].

PET in Pediatric Histiocytosis

Fluorine-18-FDG PET is well established in evaluating pediatric Langerhans cell histiocytosis. In previous studies, PET showed a high sensitivity and specificity for LCH lesions and proved to be superior to bone scans and conventional radiography for overall lesion detection [95–97]. PET further allows for excellent lesion follow-up after chemotherapy and provides information on response earlier than plain film or CT [96–98].

Fluorine-18-FDG PET can be used to detect intracranial lesions or bone lesions of the skull; however, close proximity to brain uptake may lead to false-negative scan results (Fig. 26.10). Follow-up examinations have been described to be useful for monitoring CNS disease activity [99].

MRI in Pediatric Histiocytosis

MRI has become an integral part of LCH staging [100]. Bone lytic lesions are isointense to muscle on T1-weighted images and show enhancement after the addition of gadolinium contrast (Fig. 26.11). Hyperintense signal in histiocyte lesions, the surrounding bone marrow, periost, or soft tissue can be detected as a correlate of edema on T2-weighted images [101] (Fig. 26.11). MRI investigations detect bone marrow involvement or soft tissue mass in Langerhans cell histiocytosis with high sensitivity [102]. Fast whole-body inversion recovery imaging may be used to screen the entire body for bone involvement [103].

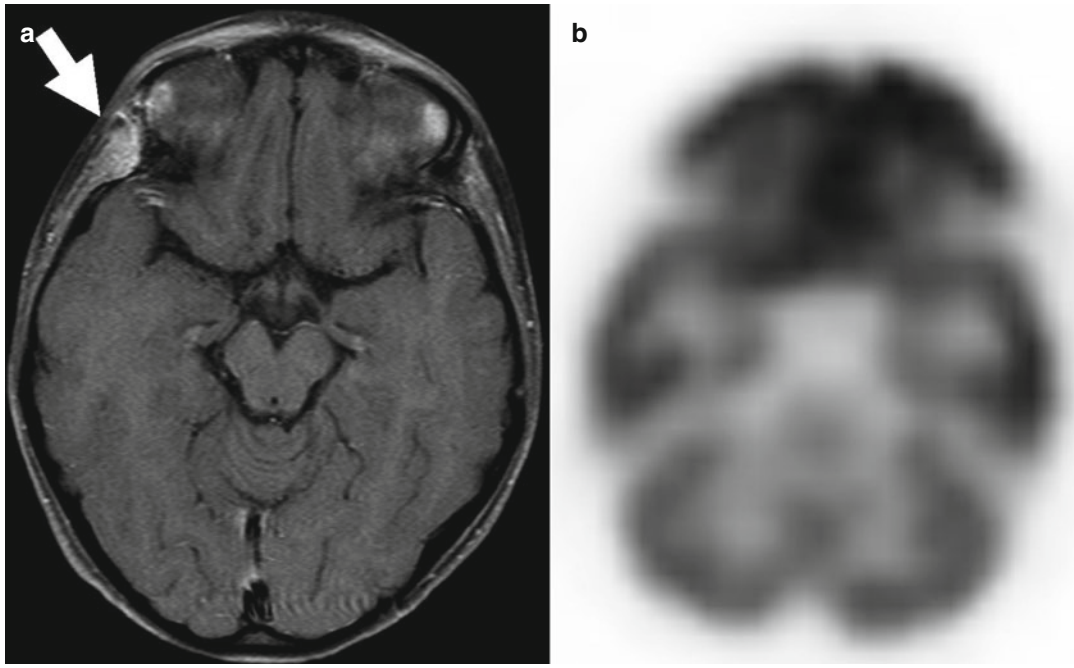

Fig. 26.10 Eosinophilic granuloma of the right frontal skull base in a 19-year-old boy on separate PET and MRI scans. A contrast-enhancing lesion of the right frontal skull base is seen on T1-weighted MRI images (*arrow*) (**a**). Corresponding PET images show normal uptake patterns (**b**). Cranial lesions may be missed on FDG PET as their metabolic activity often cannot be distinguished from physiological brain uptake. Active LCH was confirmed by biopsy

Previous reports underline the value of MRI for detecting skeletal as well as intracerebral involvement [102, 104, 105]. Image acquisition with a high spatial resolution further enables biopsy planning in complex anatomical sites.

Abnormalities on cranial MRI images can often be seen in intracerebral involvement of Langerhans disease. MRI changes include asymmetric T2 hyperintense lesions of the cerebellar medulla or the brainstem and less often hyperintense patterns of the cerebral white matter or the basal ganglia. Intracerebral LCH lesions are often hypointense on T1-weighted images and may show contrast enhancement. Furthermore infundibular enlargement as well as dural-based extraparenchymal masses may be seen [105].

Combined PET/MRI in Clinical Practice

In combined imaging, morphological information from MRI is complemented and extended by the functional information supplied by ^{18}F-FDG PET about glucose metabolism of the respective lesions. An important advantage of ^{18}F-FDG PET, especially in staging of malignant disease, is the capacity for examining the entire body or whole-body regions, while MRI is usually able to image only fractions of the same area during a single session (Fig. 26.9). Most publications of clinical applications and usefulness of multimodal diagnostic imaging concern oncological imaging or multimodal diagnosis of epilepsy [13, 106–115].

In oncological diagnostics the evaluation of glucose metabolism in the tumor by ^{18}F-FDG PET provides information on its viability. For this reason, PET in many cases has a higher specificity, sometimes even a higher sensitivity, than morphological imaging modalities (MRI and CT) [116–120]. Furthermore, a review of the literature shows ^{18}F-FDG PET imaging to be suitable for the majority of pediatric malignancies [1, 69, 71, 121–127]. Advances in these two anatomical and functional diagnostic imaging technologies have significantly influenced the staging and treatment approaches for

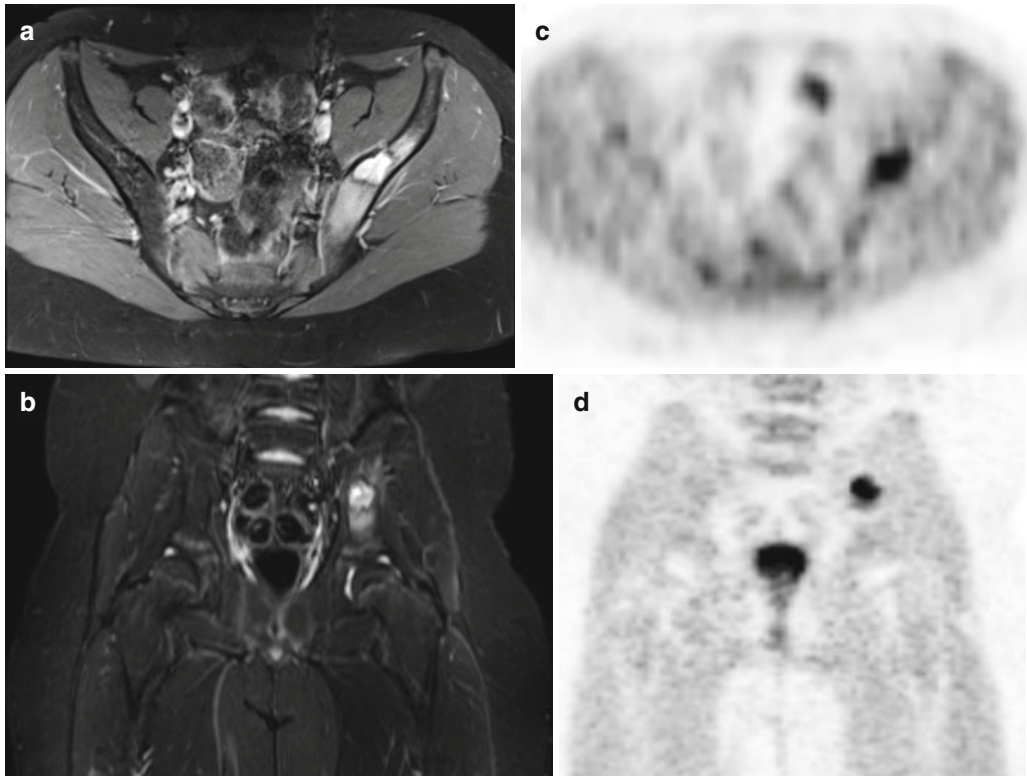

Fig. 26.11 Simultaneous MRI/PET acquisition of the pelvis in an 11-year-old boy with pain in the left hip. A contrast-enhancing lesion with surrounding bone marrow edema is seen on axial T1-weighted fat-saturated (**a**) and coronal T2-weighted (**b**) MRI images in the left iliac crest. Corresponding axial and coronal FDG PET images (**c** and **d**) confirm a hypermetabolic lesion. CT-guided biopsy of the lesion was performed and LCH histology was confirmed

pediatric tumors [123, 128]. The methods provide complementary information and have become essential in modern cancer therapy. Thus, anatomical and functional noninvasive technologies should be viewed as complementary rather than competitive. To identify a change in function without knowing accurately where it is localized or, equivalently, to know there is an anatomical change without understanding the nature of the underlying cause compromises the clinical efficacy of both anatomical and functional imaging techniques [123, 128, 129]. The combination of whole-body PET and state-of-the-art MRI offers accurate registration of metabolic and molecular aspects of a disease with exact correlation to anatomical findings, improving the diagnostic value of PET and MRI in identifying and characterizing malignancies and in tumor staging. PET can be used to detect areas of malignancies, tumor growth, therapeutic response, and recurrence. Malignancies with low or normal metabolic activity may clearly show positive or suspicious findings on MRI [130].

In a study on PET/MRI for staging and restaging in pediatric oncology, we compared the diagnostic value of single modalities with combined and registered PET/MRI analysis on 813 lesions from 132 pediatric patients [131]. In this comparative study, sensitivity and specificity in detecting viable tumor was significantly increased with combined analysis [132]. The main reasons for false-positive PET findings when looking at suspected solitary tumor lesions in children were inflammatory or reactive changes in lymph nodes without tumor infiltration (Fig. 26.12), normal bone marrow after chemotherapy, and physiological ^{18}F-FDG uptake of the muscle (Fig. 26.13), the intestine, the ovary (Fig. 26.3), the urinary tract, and brown adipose

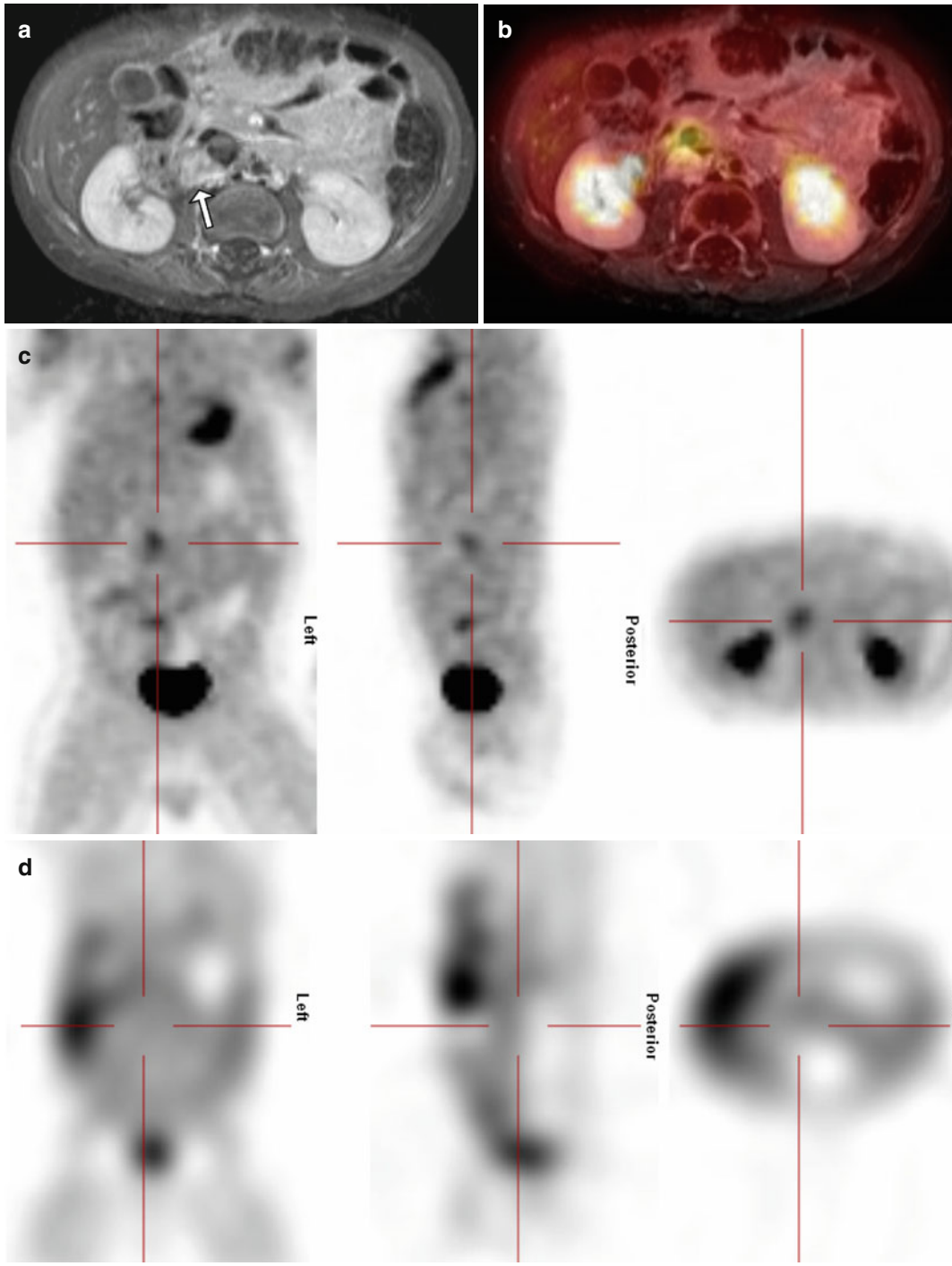

Fig. 26.12 A 9-month-old girl with stage IV neuroblastoma after chemotherapy. T1-weighted MRI shows a contrast-enhancing right-sided prevertebral lesion (*arrow*) (**a**). Fused MRI/PET (**b**) and PET (**c**) images demonstrate increased ^{18}F-FDG uptake of the lesion (crosshair). Iodine-123-MIBG scintigraphy (**d**) shows no increased uptake (crosshair). Biopsy confirms posttherapeutic reactive changes without evidence for tumor recurrence

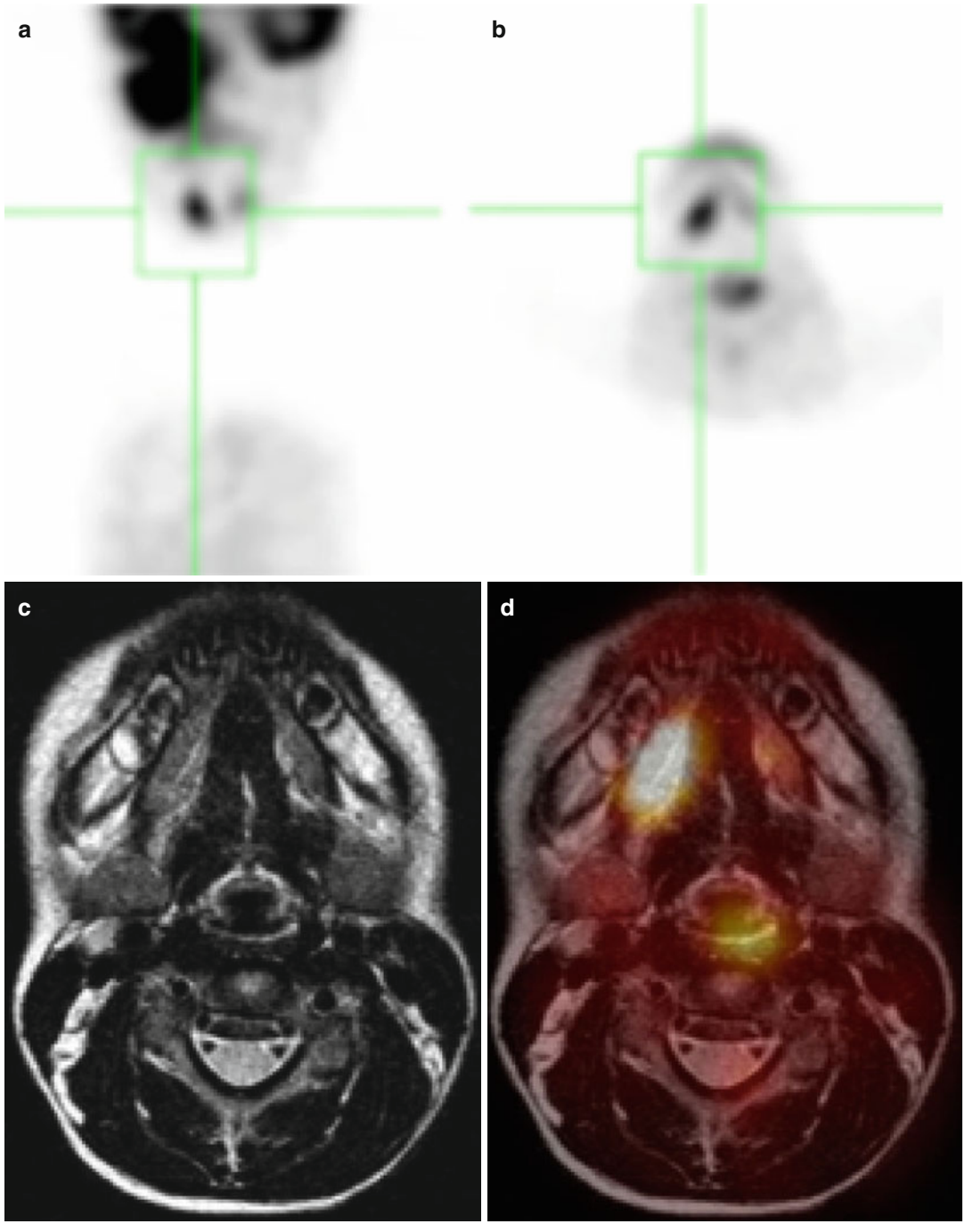

Fig. 26.13 A 5½-year-old girl with rhabdomyosarcoma – false positive on ^{18}F-FDG PET. At primary diagnosis, ^{18}F-FDG PET (**a**–**b**) shows an increased uptake in the submandibular region. A lymph node metastasis of the rhabdomyosarcoma was suspected. On the MRI (**c**: T2-weighted sequence, **d**: image fusion), no morphological changes are seen in this location. Therefore, the uptake corresponds to physiological muscle activity. The retromandibular primary tumor with its growth through the skull base is seen on the ^{18}F-FDG PET (**a**)

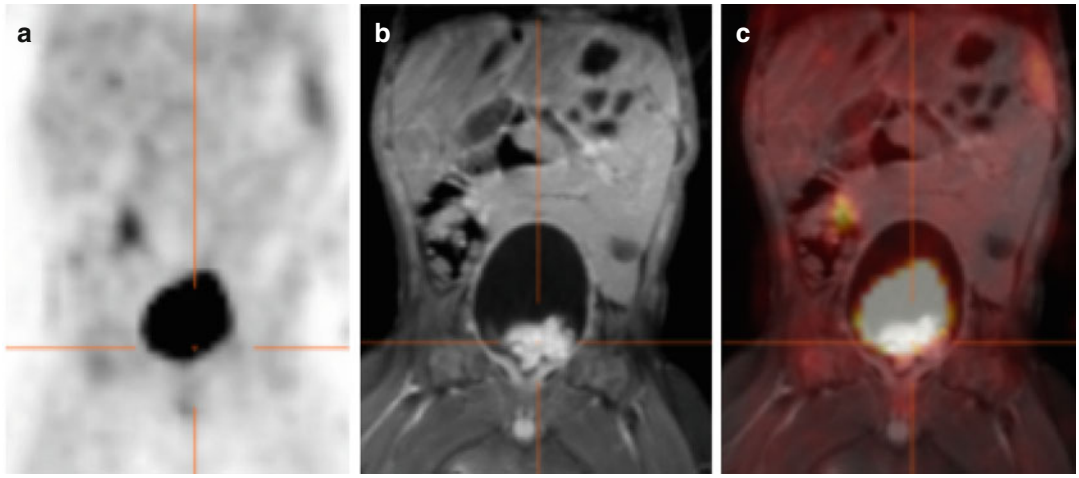

Fig. 26.14 A 1½-year-old boy with rhabdomyosarcoma of the urine bladder. False negative on ^{18}F-FDG PET. The lesion in the bladder is not visible on the ^{18}F-FDG PET (**a**) due to radiotracer accumulation in the urine bladder. Fat-suppressed T1-weighted MRI after contrast application (**b**) shows an intravesical tumor. On the registered image (**c**), the disconcordant location of the bladder is due to different filling at time of examination

tissue. False-negative findings in ^{18}F-FDG PET primarily occurred in bone metastases and tumor-affected lymph nodes due to low glucose metabolism or small size. One reason is the limited spatial resolution of PET leading to false-negative findings in very small lesions [133]. Another source for false-negative PET findings was a high physiological FDG uptake adjacent to the tumor lesion (Figs. 26.10 and 26.14). Under chemotherapy, active bone metastases may temporarily become PET negative (Table 26.1) [134]. In MRI, the main reasons for false-positive findings were enlarged lymph nodes and bone marrow edema without tumor involvement. On the other hand, small bone and lymph node metastases may account for false-negative findings (Fig. 26.15). Tumor lesions adjacent to normal bowel structures quite often cannot be distinguished from the bowel and consequently cannot be detected with MRI (Fig. 26.16). In the diagnosis of lymph nodes, a diameter of more than 1 cm is the leading parameter for the diagnosis of a metastasis. Therefore, lymph node metastases below this size and reactive lymph node enlargement are misinterpreted. Lesion size is not a reliable parameter for metastatic involvement [135]. After successful tumor therapy, bone marrow edema often persists for a long time in MRI and may be responsible for false-positive findings (Fig. 26.17). In summary, MRI is highly sensitive, but not very specific (Table 26.1) [133, 134, 136, 137]. In our study, ^{18}F-FDG PET alone showed superior specificity for disease follow-up when compared to MRI. We therefore suggested PET as method of choice for restaging when no further biopsy or surgery is intended. On the other hand, MRI is indispensable for primary staging and biopsy/surgery planning (Fig. 26.7) [131].

Table 26.1 Possible sources for false-positive and false-negative findings in MRI and ^{18}F-FDG PET

False positive – PET	Brown adipose tissue; physiological uptake in the muscles, bowel, ureter, and ovary; inflammatory changes (i.e., in lymph nodes); normal bone marrow after chemotherapy
False positive – MRI	Posttherapeutic changes (i.e., persisting bone marrow edema in treated metastases), enlarged lymph nodes without tumor affection
False negative – PET	Metastases with a small size and/or low glucose metabolism, tumor lesions under chemotherapy, lesion close to brain/muscle uptake
False negative – MRI	Small lymph node and bone metastases, lesions in the neighborhood of the bowel

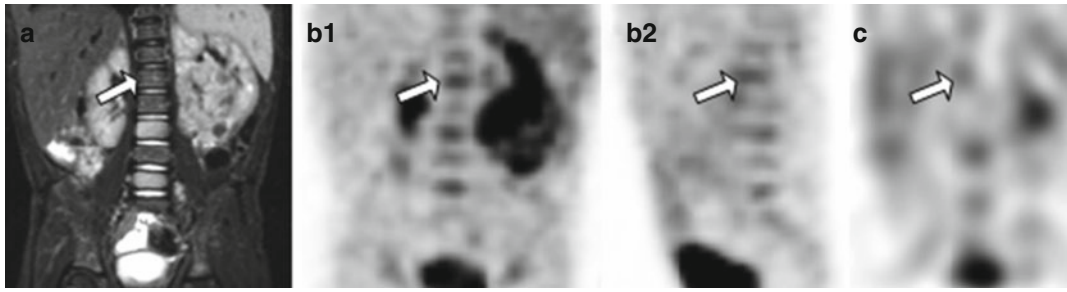

Fig. 26.15 A 4-year-old boy at primary diagnosis of a left-sided neuroblastoma with a false-negative finding on MRI. On the MRI (T2-weighted STIR sequence) suspect bone/bone marrow lesions were found in vertebral bodies L3 and L5. L1 (*arrows*) does not show pathological changes (**a**), whereas on the ^{18}F-FDG PET (**b1**, **b2**) and on the ^{123}I-MIBG scintigraphy (**c**), a suspicious lesion was found in L1. In addition, the primary tumor mass is demonstrated by all three imaging modalities

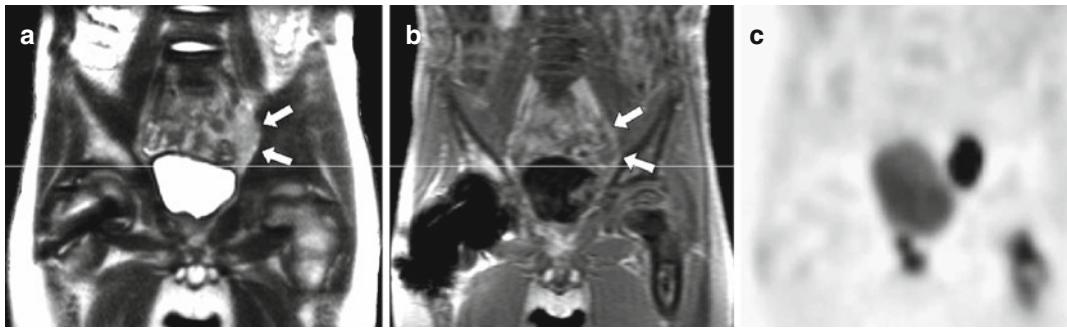

Fig. 26.16 Recurrent tumor of a rhabdomyosarcoma lateral and superior to the urine bladder (*arrows*) in a 6-year-old boy. This recurrent lesion cannot be distinguished from the adjacent bowel neither in T2-weighted MRI (**a**) nor in the T1-weighted sequence after application of Gd-DTPA (**b**), thereby leading to a false-negative finding. FDG PET clearly depicts an increased glucose metabolism in the corresponding region resulting in true-positive finding (**c**). Furthermore, postoperative metal artifacts in the right proximal femoral bone can be seen in MRI (**a**, **b**). In addition, PET and MRI show a metastasis of the left proximal femoral bone

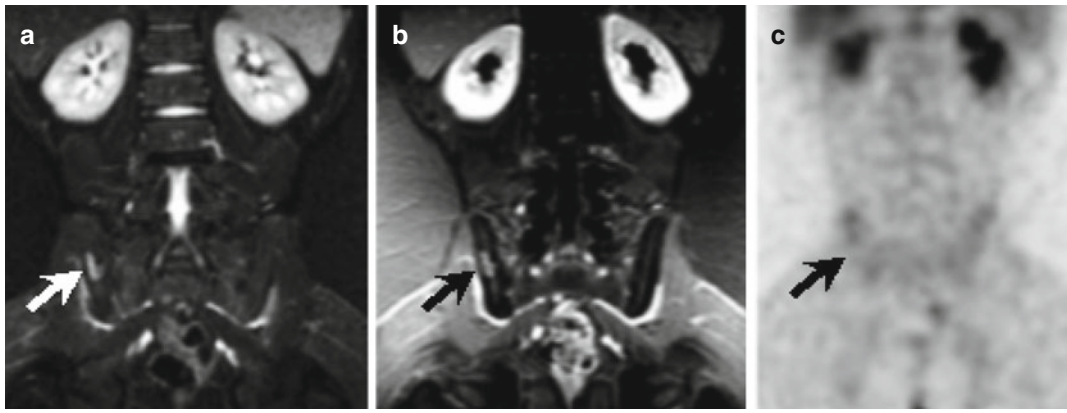

Fig. 26.17 A 9½-year-old boy with Hodgkin lymphoma: false-positive on the MRI. At follow-up, MRI (**a**: T2-weighted STIR; **b**: T1-weighted sequence after contrast application) shows residual bone marrow edema in the right iliac bone after chemotherapy (*arrow*). Fluorine-18-FDG PET (**c**) and follow-up examinations confirmed disease remission

When combining ^{18}F-FDG PET and MRI in pediatric oncology, PET as a whole-body imaging tool plays a major role in assessing MRI-positive lesions. The most important benefit of MRI is to distinguish PET-positive tumor lesions from physiologically increased glucose uptake. Combination of PET and MRI integrates the respective diagnostic values of both modalities in identifying and characterizing tumor tissue and therefore improves overall sensitivity and specificity [130, 131, 138, 139].

FDG PET is also used in the workup of inflammatory disease, though far less frequently than for oncological indications. It is the method of choice in the search for a focus of inflammation in a patient with fever of unknown origin and/or unclear sepsis [140–144]. Lesions detected with PET can be further delineated with MRI, which may also be useful for further therapy planning.

Furthermore, ^{18}F-FDG is very useful in the presurgical focus localization in the workup of epilepsy. An exact integration of the findings of morphological, electrophysiological, and nuclear medical examinations is of great importance in the planning of surgical procedures for the treatment of epilepsy and for determination of the borders of resection, again underscoring the role of integrative diagnostics [145, 146]. In these patients, functional diagnostic methods include EEG and nuclear medical methods for visualizing cerebral metabolism and perfusion. Frequently, ictal ^{99m}Tc-ethylcysteinate dimer (^{99m}Tc-ECD) SPECT is combined with interictal ^{18}F-FDG PET, which permits more exact identification of the seizure focus with typical hypometabolism seen on PET [147–150]. Beside conventional EEG leads, subdural electrodes may be implanted prior to the actual surgical procedure for direct measurement of the EEG signal from the cortical surface. These subdural electrodes can also be used for cortical stimulation. This permits delineation of functionally important areas that must be protected during a resective procedure. Knowledge of the exact position of the individual electrode points is important for demarcation of the resection boundaries. Because only CT can visualize these electrode points with sufficient accuracy, integration of CT information into the combined PET/MRI analysis is also necessary [146]. Demarcation of resection boundaries, therefore, requires integration of all four described modalities: MRI for brain morphology, CT to establish the position of the subdural EEG electrodes, PET for visualization of brain metabolism, and SPECT for visualization of hyperperfusion. This is best achieved with three-dimensional image fusion, which permits exact spatial integration (Fig. 26.4). Here, registration of images is possible within 1.5 mm, which is adequate for clinical application [151]. This method has also been shown to be superior to localization of electrodes using a conventional radiograph [146]. The resulting reconstructed three-dimensional data set provides the neurosurgeon with the information needed for exact preoperative planning, including functional information on the focus of the seizure and important (especially speech-related) brain areas, which must be protected during resection.

In conclusion, it is important to emphasize that MRI and PET are not competing modalities. Instead, these two methods in combination can produce a synergy between function and morphology. For planning of biopsies and resective surgery, the knowledge of function (i.e., tumor viability) provided by PET and of the exact morphology of the tumor provided by MRI is often crucial. In patients with cerebral lesions, the whole spectrum of digital image fusion with direct superimposition of several modalities with subsequent three-dimensional reconstruction should be applied. This provides the surgeon with the necessary tools for exact planning of approach and resection boundaries.

First Experience with Simultaneous PET/MRI

First integrated whole-body PET/MRI scanners have been introduced into research and clinical practice recently. Technical aspects of these hybrid scanners are discussed in Chap. 27. Image acquisition can be done within a reasonable time interval and algorithms for an adequate attenuation correction are being established [152]. First clinical experience in 32 adult patients with various

Fig. 26.18 Simultaneous MRI/PET acquisition in an 11-year-old boy with an LCH lesion in the left iliac bone. In contrast to PET/CT, real simultaneous data acquisition of PET and MRI facilitates delineation of increased physiological ^{18}F-FDG uptake in brown adipose tissue and the bowel (*arrows*)

oncological diseases has been collected [153]. Only two out of 80 lesions have been missed on PET/MR compared to PET/CT because of a lower lesion to liver SUV contrast [153]. However, neither the number of detected lesions nor the number of patients rated positive for suspected lesions has been significantly different for both modalities [153]. Examination times were comparable to PET/CT (15–25 min) and quantitative SUV measurements revealed a high correlation [153]. First clinical experience with pediatric patients indicates that true simultaneous PET/MRI acquisition has the potential to combine advantages of PET and MRI for pediatric oncology without additional radiation exposure of CT (Figs. 26.11 and 26.18). Especially in pediatric imaging, one PET/MR examination instead of two separate image acquisitions will hopefully improve patient comfort and reduce the number of sedations and associated complications in the future.

References

1. Connolly LP, Drubach LA, Ted Treves S. Applications of nuclear medicine in pediatric oncology. Clin Nucl Med. 2002;27(2):117–25.
2. Schmidt GP, Baur-Melnyk A, Tiling R, Hahn K, Reiser MF, Schoenberg SO. Comparison of high resolution whole-body MRI using parallel imaging and PET-CT. First experiences with a 32-channel MRI system. Radiologe. 2004;44(9):889–98.
3. Alyafei S, Inoue T, Zhang H, et al. Image fusion system using PACS for MRI, CT, and PET images. Clin Positron Imaging. 1999;2(3):137–43.
4. Hutton BF, Braun M. Software for image registration: algorithms, accuracy, efficacy. Semin Nucl Med. 2003;33(3):180–92.
5. Slomka PJ. Software approach to merging molecular with anatomic information. J Nucl Med. 2004;45 Suppl 1:36S–45.
6. Pelizzari CA, Chen GT, Spelbring DR, Weichselbaum RR, Chen CT. Accurate three-dimensional registration of CT, PET, and/or MR images of the brain. J Comput Assist Tomogr. 1989;13(1):20–6.
7. Maes F, Collignon A, Vandermeulen D, Marchal G, Suetens P. Multimodality image registration by maximization of mutual information. IEEE Trans Med Imaging. 1997;16(2):187–98.
8. Wells 3rd WM, Viola P, Atsumi H, Nakajima S, Kikinis R. Multi-modal volume registration by maximization of mutual information. Med Image Anal. 1996;1(1):35–51.
9. Meyer CR, Boes JL, Kim B, et al. Demonstration of accuracy and clinical versatility of mutual information for automatic multimodality image fusion using affine and thin-plate spline warped geometric deformations. Med Image Anal. 1997;1(3):195–206.
10. Bookstein F. Principal warps: thin-plate splines and the decomposition of deformations. IEEE Trans Pattern Anal Mach Intell. 1989;11(6):567–85.
11. Shekhar R, Walimbe V, Raja S, et al. Automated 3-dimensional elastic registration of whole-body PET

and CT from separate or combined scanners. J Nucl Med. 2005;46(9):1488–96.
12. Skalski J, Wahl RL, Meyer CR. Comparison of mutual information-based warping accuracy for fusing body CT and PET by 2 methods: CT mapped onto PET emission scan versus CT mapped onto PET transmission scan. J Nucl Med. 2002;43(9):1184–7.
13. Cohade C, Wahl RL. Applications of positron emission tomography/computed tomography image fusion in clinical positron emission tomography-clinical use, interpretation methods, diagnostic improvements. Semin Nucl Med. 2003;33(3):228–37.
14. Furth C, Denecke T, Steffen I, et al. Correlative imaging strategies implementing CT, MRI, and PET for staging of childhood Hodgkin disease. J Pediatr Hematol Oncol. 2006;28(8):501–12.
15. Stokking R, Zubal IG, Viergever MA. Display of fused images: methods, interpretation, and diagnostic improvements. Semin Nucl Med. 2003;33(3):219–27.
16. Belgaumi AF, Kauffman WM, Jenkins JJ, et al. Blindness in children with neuroblastoma. Cancer. 1997;80(10):1997–2004.
17. Kropp J, Hofmann M, Bihl H. Comparison of MIBG and pentetreotide scintigraphy in children with neuroblastoma. Is the expression of somatostatin receptors a prognostic factor? Anticancer Res. 1997;17(3B):1583–8.
18. Schmidt M, Simon T, Hero B, Schicha H, Berthold F. The prognostic impact of functional imaging with (123)I-mIBG in patients with stage 4 neuroblastoma >1 year of age on a high-risk treatment protocol: results of the German Neuroblastoma Trial NB97. Eur J Cancer. 2008;44(11):1552–8.
19. Taggart D, Dubois S, Matthay KK. Radiolabeled metaiodobenzylguanidine for imaging and therapy of neuroblastoma. Q J Nucl Med Mol Imaging. 2008;52(4):403–18.
20. Custodio CM, Semelka RC, Balci NC, Mitchell KM, Freeman JA. Adrenal neuroblastoma in an adult with tumor thrombus in the inferior vena cava. J Magn Reson Imaging. 1999;9(4):621–3.
21. DuBois SG, Matthay KK. Radiolabeled metaiodobenzylguanidine for the treatment of neuroblastoma. Nucl Med Biol. 2008;35 Suppl 1:S35–48.
22. Boubaker A, Bischof Delaloye A. MIBG scintigraphy for the diagnosis and follow-up of children with neuroblastoma. Q J Nucl Med Mol Imaging. 2008;52(4):388–402.
23. Hugosson C, Nyman R, Jorulf H, et al. Imaging of abdominal neuroblastoma in children. Acta Radiol. 1999;40(5):534–42.
24. Sofka CM, Semelka RC, Kelekis NL, et al. Magnetic resonance imaging of neuroblastoma using current techniques. Magn Reson Imaging. 1999;17(2):193–8.
25. Taggart DR, Han MM, Quach A, et al. Comparison of iodine-123 metaiodobenzylguanidine (MIBG) scan and [18F]fluorodeoxyglucose positron emission tomography to evaluate response after iodine-131 MIBG therapy for relapsed neuroblastoma. J Clin Oncol. 2009;27(32):5343–9.
26. Sharp SE, Shulkin BL, Gelfand MJ, Salisbury S, Furman WL. 123I-MIBG scintigraphy and 18F-FDG PET in neuroblastoma. J Nucl Med. 2009;50(8):1237–43.
27. Mc Dowell H, Losty P, Barnes N, Kokai G. Utility of FDG-PET/CT in the follow-up of neuroblastoma which became MIBG-negative. Pediatr Blood Cancer. 2009;52(4):552.
28. Kleis M, Daldrup-Link H, Matthay K, et al. Diagnostic value of PET/CT for the staging and restaging of pediatric tumors. Eur J Nucl Med Mol Imaging. 2009;36(1):23–36.
29. Shore RM. Positron emission tomography/computed tomography (PET/CT) in children. Pediatr Ann. 2008;37(6):404–12.
30. Rozovsky K, Koplewitz BZ, Krausz Y, et al. Added value of SPECT/CT for correlation of MIBG scintigraphy and diagnostic CT in neuroblastoma and pheochromocytoma. AJR Am J Roentgenol. 2008;190(4):1085–90.
31. Murphy JJ, Tawfeeq M, Chang B, Nadel H. Early experience with PET/CT scan in the evaluation of pediatric abdominal neoplasms. J Pediatr Surg. 2008;43(12):2186–92.
32. Colavolpe C, Guedj E, Cammilleri S, Taieb D, Mundler O, Coze C. Utility of FDG-PET/CT in the follow-up of neuroblastoma which became MIBG-negative. Pediatr Blood Cancer. 2008;51(6):828–31.
33. Roca I, Simo M, Sabado C, de Toledo JS. PET/CT in paediatrics: it is time to increase its use! Eur J Nucl Med Mol Imaging. 2007;34(5):628–9.
34. Franzius C, Riemann B, Vormoor J, et al. Metastatic neuroblastoma demonstrated by whole-body PET-CT using 11C-HED. Nuklearmedizin. 2005;44(1):N4–5.
35. Biasotti S, Garaventa A, Villavecchia GP, Cabria M, Nantron M, De Bernardi B. False-negative metaiodobenzylguanidine scintigraphy at diagnosis of neuroblastoma. Med Pediatr Oncol. 2000;35(2):153–5.
36. Rosenspire KC, Haka MS, Van Dort ME, et al. Synthesis and preliminary evaluation of carbon-11-meta-hydroxyephedrine: a false transmitter agent for heart neuronal imaging. J Nucl Med. 1990;31(8):1328–34.
37. Shulkin BL, Wieland DM, Baro ME, et al. PET hydroxyephedrine imaging of neuroblastoma. J Nucl Med. 1996;37(1):16–21.
38. Schwaiger M, Hutchins GD, Kalff V, et al. Evidence for regional catecholamine uptake and storage sites in the transplanted human heart by positron emission tomography. J Clin Invest. 1991;87(5):1681–90.
39. Schwaiger M, Kalff V, Rosenspire K, et al. Noninvasive evaluation of sympathetic nervous system in human heart by positron emission tomography. Circulation. 1990;82(2):457–64.
40. Shulkin BL, Wieland DM, Schwaiger M, et al. PET scanning with hydroxyephedrine: an approach to the localization of pheochromocytoma. J Nucl Med. 1992;33(6):1125–31.
41. Franzius C, Hermann K, Weckesser M, et al. Whole-body PET/CT with 11C-meta-hydroxyephedrine in tumors of the sympathetic nervous system: feasibility

study and comparison with 123I-MIBG SPECT/CT. J Nucl Med. 2006;47(10):1635–42.
42. Becherer A, Szabo M, Karanikas G, et al. Imaging of advanced neuroendocrine tumors with (18)F-FDOPA PET. J Nucl Med. 2004;45(7):1161–7.
43. Hoegerle S, Nitzsche E, Altehoefer C, et al. Pheochromocytomas: detection with 18F DOPA whole body PET–initial results. Radiology. 2002; 222(2):507–12.
44. Mamede M, Carrasquillo JA, Chen CC, et al. Discordant localization of 2-[18F]-fluoro-2-deoxy-D-glucose in 6-[18F]-fluorodopamine- and [(123) I]-metaiodobenzylguanidine-negative metastatic pheochromocytoma sites. Nucl Med Commun. 2006; 27(1):31–6.
45. Piccardo A, Lopci E, Conte M, et al. Comparison of 18F-dopa PET/CT and 123I-MIBG scintigraphy in stage 3 and 4 neuroblastoma: a pilot study. Eur J Nucl Med Mol Imaging. 2012;39(1):57–71.
46. O'Dorisio MS, Chen F, O'Dorisio TM, Wray D, Qualman SJ. Characterization of somatostatin receptors on human neuroblastoma tumors. Cell Growth Differ. 1994;5(1):1–8.
47. Albers AR, O'Dorisio MS, Balster DA, et al. Somatostatin receptor gene expression in neuroblastoma. Regul Pept. 2000;88(1–3):61–73.
48. Georgantzi K, Tsolakis AV, Stridsberg M, Jakobson A, Christofferson R, Janson ET. Differentiated expression of somatostatin receptor subtypes in experimental models and clinical neuroblastoma. Pediatr Blood Cancer. 2011;56(4):584–9.
49. Gains JE, Bomanji JB, Fersht NL, et al. 177Lu-DOTATATE molecular radiotherapy for childhood neuroblastoma. J Nucl Med. 2011;52(7):1041–7.
50. Lebtahi N, Gudinchet F, Nenadov-Beck M, Beck D, Bischof Delaloye A. Evaluating bone marrow metastasis of neuroblastoma with iodine-123-MIBG scintigraphy and MRI. J Nucl Med. 1997;38(9):1389–92.
51. Muller MF, Krestin GP, Willi UV. Abdominal tumors in children. A comparison between magnetic resonance tomography (MRT) and ultrasonography (US). Rofo. 1993;158(1):9–14.
52. Daldrup HE, Link TM, Wortler K, Reimer P, Rummeny EJ. MR imaging of thoracic tumors in pediatric patients. AJR Am J Roentgenol. 1998;170(6):1639–44.
53. Pfluger T, Czekalla R, Hundt C, et al. MR angiography versus color Doppler sonography in the evaluation of renal vessels and the inferior vena cava in abdominal masses of pediatric patients. AJR Am J Roentgenol. 1999;173(1):103–8.
54. Castellote A, Vazquez E, Vera J, et al. Cervicothoracic lesions in infants and children. Radiographics. 1999;19(3):583–600.
55. Slovis TL, Meza MP, Cushing B, et al. Thoracic neuroblastoma: what is the best imaging modality for evaluating extent of disease? Pediatr Radiol. 1997;27(3):273–5.
56. Kaste SC. Issues specific to implementing PET-CT for pediatric oncology: what we have learned along the way. Pediatr Radiol. 2004;34(3):205–13.
57. Lonergan GJ, Schwab CM, Suarez ES, Carlson CL. Neuroblastoma, ganglioneuroblastoma, and ganglioneuroma: radiologic-pathologic correlation. Radiographics. 2002;22(4):911–34.
58. Blatt J, Fitz C, Mirro Jr J. Recognition of central nervous system metastases in children with metastatic primary extracranial neuroblastoma. Pediatr Hematol Oncol. 1997;14(3):233–41.
59. D'Ambrosio N, Lyo JK, Young RJ, Haque SS, Karimi S. Imaging of metastatic CNS neuroblastoma. AJR Am J Roentgenol. 2010;194(5):1223–9.
60. Horner M, Ries L, Krapcho M, Neyman N. "SEER Cancer Statistics Review, 1975–2006". Surveillance Epidemiology and End Results (SEER). Section 29: Childhood Cancer ICCC. Bethesda: National Cancer Institute; 2009.
61. Franzius C, Sciuk J, Daldrup-Link HE, Jurgens H, Schober O. FDG-PET for detection of osseous metastases from malignant primary bone tumours: comparison with bone scintigraphy. Eur J Nucl Med. 2000;27(9):1305–11.
62. Gyorke T, Zajic T, Lange A, et al. Impact of FDG PET for staging of Ewing sarcomas and primitive neuroectodermal tumours. Nucl Med Commun. 2006;27(1): 17–24.
63. Kneisl JS, Patt JC, Johnson JC, Zuger JH. Is PET useful in detecting occult nonpulmonary metastases in pediatric bone sarcomas? Clin Orthop Relat Res. 2006;450:101–4.
64. Volker T, Denecke T, Steffen I, et al. Positron emission tomography for staging of pediatric sarcoma patients: results of a prospective multicenter trial. J Clin Oncol. 2007;25(34):5435–41.
65. Brenner W, Bohuslavizki KH, Eary JF. PET imaging of osteosarcoma. J Nucl Med. 2003;44(6):930–42.
66. Iagaru A, Chawla S, Menendez L, Conti PS. 18F-FDG PET and PET/CT for detection of pulmonary metastases from musculoskeletal sarcomas. Nucl Med Commun. 2006;27(10):795–802.
67. Iagaru A, Quon A, McDougall IR, Gambhir SS. F-18 FDG PET/CT evaluation of osseous and soft tissue sarcomas. Clin Nucl Med. 2006;31(12):754–60.
68. Schulte M, Brecht-Krauss D, Werner M, et al. Evaluation of neoadjuvant therapy response of osteogenic sarcoma using FDG PET. J Nucl Med. 1999;40(10):1637–43.
69. Hawkins DS, Rajendran JG, Conrad 3rd EU, Bruckner JD, Eary JF. Evaluation of chemotherapy response in pediatric bone sarcomas by [F-18]-fluorodeoxy-D-glucose positron emission tomography. Cancer. 2002;94(12):3277–84.
70. Hamada K, Tomita Y, Inoue A, et al. Evaluation of chemotherapy response in osteosarcoma with FDG-PET. Ann Nucl Med. 2009;23(1):89–95.
71. Franzius C, Bielack S, Flege S, Sciuk J, Jurgens H, Schober O. Prognostic significance of (18)F-FDG and (99m)Tc-methylene diphosphonate uptake in primary osteosarcoma. J Nucl Med. 2002;43(8):1012–7.
72. Costelloe CM, Raymond AK, Fitzgerald NE, et al. Tumor necrosis in osteosarcoma: inclusion of the

point of greatest metabolic activity from F-18 FDG PET/CT in the histopathologic analysis. Skeletal Radiol. 2010;39(2):131–40.
73. Mody RJ, Bui C, Hutchinson RJ, et al. FDG PET imaging of childhood sarcomas. Pediatr Blood Cancer. 2010;54(2):222–7.
74. Ferrone ML, Raut CP. Modern surgical therapy: limb salvage and the role of amputation for extremity soft-tissue sarcomas. Surg Oncol Clin N Am. 2012;21(2):201–13.
75. Brant W, Brant C. Fundamentals of diagnostic radiology, vol. 4. 3rd ed. Philadelphia: Lippincott, Williams & Williams; 2006.
76. Gilbert NF, Cannon CP, Lin PP, Lewis VO. Soft-tissue sarcoma. J Am Acad Orthop Surg. 2009;17(1):40–7.
77. Horner M, Ries L, Krapcho M, Neyman N. "SEER Cancer Statistics Review, 1975–2006". Surveillance Epidemiology and End Results (SEER). Table 1.4: age-adjusted SEER incidence and U.S. death rates and 5-year relative survival rates by primary cancer site, sex and time period. Bethesda: National Cancer Institute; 2009.
78. Jaffe ES, Harris NL, Stein H, Vardiman JW (Eds): World Health Organization Classification of Tumours. Pathology and Genetics of Tumours of Haematopoietic and Lymphoid Tissues. IARC Press: Lyon 2001.
79. Tatsumi M, Cohade C, Nakamoto Y, Fishman EK, Wahl RL. Direct comparison of FDG PET and CT findings in patients with lymphoma: initial experience. Radiology. 2005;237(3):1038–45.
80. Kasamon YL, Jones RJ, Wahl RL. Integrating PET and PET/CT into the risk-adapted therapy of lymphoma. J Nucl Med. 2007;48 Suppl 1:19S–27.
81. Haioun C, Itti E, Rahmouni A, et al. [18F]Fluoro-2-deoxy-D-glucose positron emission tomography (FDG-PET) in aggressive lymphoma: an early prognostic tool for predicting patient outcome. Blood. 2005;106(4):1376–81.
82. Hutchings M, Loft A, Hansen M, et al. FDG-PET after two cycles of chemotherapy predicts treatment failure and progression-free survival in Hodgkin lymphoma. Blood. 2006;107(1):52–9.
83. Dupuis J, Gaulard P, Hemery F, et al. Respective prognostic values of germinal center phenotype and early (18)fluorodeoxyglucose-positron emission tomography scanning in previously untreated patients with diffuse large B-cell lymphoma. Haematologica. 2007;92(6):778–83.
84. Mikhaeel NG, Hutchings M, Fields PA, O'Doherty MJ, Timothy AR. FDG-PET after two to three cycles of chemotherapy predicts progression-free and overall survival in high-grade non-Hodgkin lymphoma. Ann Oncol. 2005;16(9):1514–23.
85. Shankar A, Fiumara F, Pinkerton R. Role of FDG PET in the management of childhood lymphomas–case proven or is the jury still out? Eur J Cancer. 2008;44(5):663–73.
86. Kellenberger CJ, Miller SF, Khan M, Gilday DL, Weitzman S, Babyn PS. Initial experience with FSE STIR whole-body MR imaging for staging lymphoma in children. Eur Radiol. 2004;14(10): 1829–41.
87. Schmidt GP, Baur-Melnyk A, Herzog P, et al. High-resolution whole-body magnetic resonance image tumor staging with the use of parallel imaging versus dual-modality positron emission tomography-computed tomography: experience on a 32-channel system. Invest Radiol. 2005;40(12): 743–53.
88. Antoch G, Vogt FM, Freudenberg LS, et al. Whole-body dual-modality PET/CT and whole-body MRI for tumor staging in oncology. JAMA. 2003;290(24): 3199–206.
89. Ballon D, Watts R, Dyke JP, et al. Imaging therapeutic response in human bone marrow using rapid whole-body MRI. Magn Reson Med. 2004;52(6): 1234–8.
90. Yap KK, Sutherland T, Liew E, Tartaglia CJ, Pang M, Trost N. Magnetic resonance features of primary central nervous system lymphoma in the immunocompetent patient: a pictorial essay. J Med Imaging Radiat Oncol. 2012;56(2):179–86.
91. Hoover KB, Rosenthal DI, Mankin H. Langerhans cell histiocytosis. Skeletal Radiol. 2007;36(2): 95–104.
92. Minkov M, Grois N, Heitger A, Potschger U, Westermeier T, Gadner H. Response to initial treatment of multisystem Langerhans cell histiocytosis: an important prognostic indicator. Med Pediatr Oncol. 2002;39(6):581–5.
93. Gadner H, Grois N, Arico M, et al. A randomized trial of treatment for multisystem Langerhans' cell histiocytosis. J Pediatr. 2001;138(5):728–34.
94. Schmidt S, Eich G, Geoffray A, et al. Extraosseous Langerhans cell histiocytosis in children. Radiographics. 2008;28(3):707–26; quiz 910–701.
95. Phillips M, Allen C, Gerson P, McClain K. Comparison of FDG-PET scans to conventional radiography and bone scans in management of Langerhans cell histiocytosis. Pediatr Blood Cancer. 2009;52(1):97–101.
96. Kaste SC, Rodriguez-Galindo C, McCarville ME, Shulkin BL. PET-CT in pediatric Langerhans cell histiocytosis. Pediatr Radiol. 2007;37(7):615–22.
97. Blum R, Seymour JF, Hicks RJ. Role of 18FDG-positron emission tomography scanning in the management of histiocytosis. Leuk Lymphoma. 2002; 43(11):2155–7.
98. Binkovitz LA, Olshefski RS, Adler BH. Coincidence FDG-PET in the evaluation of Langerhans' cell histiocytosis: preliminary findings. Pediatr Radiol. 2003;33(9):598–602.
99. Buchler T, Cervinek L, Belohlavek O, et al. Langerhans cell histiocytosis with central nervous system involvement: follow-up by FDG-PET during treatment with cladribine. Pediatr Blood Cancer. 2005;44(3):286–8.
100. Meyer JS, De Camargo B. The role of radiology in the diagnosis and follow-up of Langerhans cell histiocytosis. Hematol Oncol Clin North Am. 1998; 12(2):307–26.

101. Kilborn TN, Teh J, Goodman TR. Paediatric manifestations of Langerhans cell histiocytosis: a review of the clinical and radiological findings. Clin Radiol. 2003;58(4):269–78.
102. Azouz EM, Saigal G, Rodriguez MM, Podda A. Langerhans' cell histiocytosis: pathology, imaging and treatment of skeletal involvement. Pediatr Radiol. 2005;35(2):103–15.
103. Kellenberger CJ, Epelman M, Miller SF, Babyn PS. Fast STIR whole-body MR imaging in children. Radiographics. 2004;24(5):1317–30.
104. Pavlik M, Bloom DA, Ozgonenel B, Sarnaik SA. Defining the role of magnetic resonance imaging in unifocal bone lesions of Langerhans cell histiocytosis. J Pediatr Hematol Oncol. 2005;27(8):432–5.
105. Grois N, Tsunematsu Y, Barkovich AJ, Favara BE. Central nervous system disease in Langerhans cell histiocytosis. Br J Cancer Suppl. 1994;23:S24–8.
106. Aquino SL, Asmuth JC, Alpert NM, Halpern EF, Fischman AJ. Improved radiologic staging of lung cancer with 2-[18F]-fluoro-2-deoxy-D-glucose-positron emission tomography and computed tomography registration. J Comput Assist Tomogr. 2003;27(4):479–84.
107. Coleman RE, Hawk TC, Hamblen SM, Cnmt, Laymon CM, Turkington TG. Detection of recurrent brain tumor. Comparison of MR registered camera-based and dedicated PET images. Clin Positron Imaging. 1999;2(1):57–61.
108. Dresel S, Grammerstorff J, Schwenzer K, et al. [18F] FDG imaging of head and neck tumours: comparison of hybrid PET and morphological methods. Eur J Nucl Med Mol Imaging. 2003;30(7):995–1003.
109. Keidar Z, Israel O, Krausz Y. SPECT/CT in tumor imaging: technical aspects and clinical applications. Semin Nucl Med. 2003;33(3):205–18.
110. Murphy M, O'Brien TJ, Morris K, Cook MJ. Multimodality image-guided epilepsy surgery. J Clin Neurosci. 2001;8(6):534–8.
111. Pfluger T, Schmied C, Porn U, et al. Integrated imaging using MRI and 123I metaiodobenzylguanidine scintigraphy to improve sensitivity and specificity in the diagnosis of pediatric neuroblastoma. AJR Am J Roentgenol. 2003;181(4):1115–24.
112. So EL. Role of neuroimaging in the management of seizure disorders. Mayo Clin Proc. 2002;77(11): 1251–64.
113. Tsai CC, Tsai CS, Ng KK, et al. The impact of image fusion in resolving discrepant findings between FDG-PET and MRI/CT in patients with gynaecological cancers. Eur J Nucl Med Mol Imaging. 2003;21:21.
114. Visvikis D, Ell PJ. Impact of technology on the utilisation of positron emission tomography in lymphoma: current and future perspectives. Eur J Nucl Med Mol Imaging. 2003;30 Suppl 1:S106–16.
115. Zhang W, Simos PG, Ishibashi H, et al. Multimodality neuroimaging evaluation improves the detection of subtle cortical dysplasia in seizure patients. Neurol Res. 2003;25(1):53–7.
116. Anderson H, Price P. What does positron emission tomography offer oncology? Eur J Cancer. 2000;36(16):2028–35.
117. Bar-Shalom R, Valdivia AY, Blaufox MD. PET imaging in oncology. Semin Nucl Med. 2000;30(3): 150–85.
118. Czech N, Brenner W, Kampen WU, Henze E. [Diagnostic value of positron emission tomography (PET) in clinical oncology]. Dtsch Med Wochenschr. 2000;125(18):565–7.
119. Delbeke D, Martin WH. Positron emission tomography imaging in oncology. Radiol Clin North Am. 2001;39(5):883–917.
120. Mankoff DA, Bellon JR. Positron-emission tomographic imaging of cancer: glucose metabolism and beyond. Semin Radiat Oncol. 2001;11(1):16–27.
121. Brisse H, Ollivier L, Edeline V, et al. Imaging of malignant tumours of the long bones in children: monitoring response to neoadjuvant chemotherapy and preoperative assessment. Pediatr Radiol. 2004;34(8):595–605.
122. Franzius C, Daldrup-Link HE, Sciuk J, et al. FDG-PET for detection of pulmonary metastases from malignant primary bone tumors: comparison with spiral CT. Ann Oncol. 2001;12(4):479–86.
123. Hudson MM, Krasin MJ, Kaste SC. PET imaging in pediatric Hodgkin's lymphoma. Pediatr Radiol. 2004;34(3):190–8.
124. Montravers F, McNamara D, Landman-Parker J, et al. [(18)F]FDG in childhood lymphoma: clinical utility and impact on management. Eur J Nucl Med Mol Imaging. 2002;29(9):1155–65.
125. O'Hara SM, Donnelly LF, Coleman RE. Pediatric body applications of FDG PET. AJR Am J Roentgenol. 1999;172(4):1019–24.
126. Shulkin BL. PET imaging in pediatric oncology. Pediatr Radiol. 2004;34(3):199–204.
127. Shulkin BL, Mitchell DS, Ungar DR, et al. Neoplasms in a pediatric population: 2-[F-18]-fluoro-2-deoxy-D-glucose PET studies. Radiology. 1995;194(2):495–500.
128. Czernin J. Clinical applications of FDG-PET in oncology. Acta Med Austriaca. 2002;29(5):162–70.
129. Townsend DW, Cherry SR. Combining anatomy and function: the path to true image fusion. Eur Radiol. 2001;11(10):1968–74.
130. Gaa J, Rummeny EJ, Seemann MD. Whole-body imaging with PET/MRI. Eur J Med Res. 2004;9(6): 309–12.
131. Pfluger T, Melzer HI, Mueller WP, et al. Diagnostic value of combined ^{18}F-FDG-PET/MRI for staging and restaging in paediatric oncology. Eur J Nucl Med Mol Imaging. 2013;39(11):1745–55.
132. Pfluger T, Vollmar C, Porn U, et al. Combined PET/MRI in cerebral and pediatric diagnostics. Der Nuklearmediziner. 2002;25(02):122–7.
133. Hueltenschmidt B, Sautter-Bihl ML, Lang O, et al. Whole body positron emission tomography in the treatment of Hodgkin disease. Cancer. 2001;91(2): 302–10.

134. Daldrup-Link HE, Franzius C, Link TM, et al. Whole-body MR imaging for detection of bone metastases in children and young adults: comparison with skeletal scintigraphy and FDG PET. AJR Am J Roentgenol. 2001;177(1):229–36.
135. Torabi M, Aquino SL, Harisinghani MG. Current concepts in lymph node imaging. J Nucl Med. 2004;45(9):1509–18.
136. Ilias I, Pacak K. Current approaches and recommended algorithm for the diagnostic localization of pheochromocytoma. J Clin Endocrinol Metab. 2004;89(2):479–91.
137. Korholz D, Kluge R, Wickmann L, et al. Importance of F18-fluorodeoxy-D-2-glucose positron emission tomography (FDG-PET) for staging and therapy control of Hodgkin's lymphoma in childhood and adolescence – consequences for the GPOH-HD 2003 protocol. Onkologie. 2003;26(5): 489–93.
138. Bredella MA, Caputo GR, Steinbach LS. Value of FDG positron emission tomography in conjunction with MR imaging for evaluating therapy response in patients with musculoskeletal sarcomas. AJR Am J Roentgenol. 2002;179(5):1145–50.
139. Popperl G, Lang S, Dagdelen O, et al. [Correlation of FDG-PET and MRI/CT with histopathology in primary diagnosis, lymph node staging and diagnosis of recurrency of head and neck cancer]. Rofo. 2002;174(6):714–20.
140. Blockmans D, Knockaert D, Maes A, et al. Clinical value of [(18)F]fluoro-deoxyglucose positron emission tomography for patients with fever of unknown origin. Clin Infect Dis. 2001;32(2):191–6.
141. Kapucu LO, Meltzer CC, Townsend DW, Keenan RJ, Luketich JD. Fluorine-18-fluorodeoxyglucose uptake in pneumonia. J Nucl Med. 1998;39(7): 1267–9.
142. Kresnik E, Mikosch P, Gallowitsch HJ, Heinisch M, Lind P. F-18 fluorodeoxyglucose positron emission tomography in the diagnosis of inflammatory bowel disease. Clin Nucl Med. 2001;26(10):867.
143. Meller J, Becker W. [Nuclear medicine diagnosis of patients with fever of unknown origin (FUO)]. Nuklearmedizin. 2001;40(3):59–70.
144. Weiner GM, Jenicke L, Buchert R, Bohuslavizki KH. [FDG PET for the localization diagnosis in inflammatory disease of unknown origin–two case reports]. Nuklearmedizin. 2001;40(4):N35–8.
145. Barnett GH, Kormos DW, Steiner CP, Morris H. Registration of EEG electrodes with three-dimensional neuroimaging using a frameless, armless stereotactic wand. Stereotact Funct Neurosurg. 1993;61(1):32–8.
146. Winkler PA, Vollmar C, Krishnan KG, Pfluger T, Bruckmann H, Noachtar S. Usefulness of 3-D reconstructed images of the human cerebral cortex for localization of subdural electrodes in epilepsy surgery. Epilepsy Res. 2000;41(2):169–78.
147. Carreras JL, Perez-Castejon MJ, Jimenez AM, Domper M, Montz R. [Neuroimaging in epilepsy. Advances in SPECT and PET in epilepsy]. Rev Neurol. 2000;30(4):359–63.
148. Matheja P, Kuwert T, Stodieck SR, et al. PET and SPECT in medically non-refractory complex partial seizures. Temporal asymmetries of glucose consumption, benzodiazepine receptor density, and blood flow. Nuklearmedizin. 1998;37(7):221–6.
149. Noachtar S, Arnold S, Yousry TA, Bartenstein P, Werhahn KJ, Tatsch K. Ictal technetium-99m ethyl cysteinate dimer single-photon emission tomographic findings and propagation of epileptic seizure activity in patients with extratemporal epilepsies. Eur J Nucl Med. 1998;25(2):166–72.
150. Oliveira AJ, da Costa JC, Hilario LN, Anselmi OE, Palmini A. Localization of the epileptogenic zone by ictal and interictal SPECT with 99mTc-ethyl cysteinate dimer in patients with medically refractory epilepsy. Epilepsia. 1999;40(6):693–702.
151. Pfluger T, Vollmar C, Wismuller A, et al. Quantitative comparison of automatic and interactive methods for MRI-SPECT image registration of the brain based on 3-dimensional calculation of error. J Nucl Med. 2000;41(11):1823–9.
152. Eiber M, Souvatzoglou M, Pickhard A, et al. Simulation of a MR-PET protocol for staging of head-and-neck cancer including Dixon MR for attenuation correction. Eur J Radiol. 2012;81(10): 2658–65.
153. Drzezga A, Souvatzoglou M, Eiber M, et al. First clinical experience with integrated whole-body PET/MR: comparison to PET/CT in patients with oncologic diagnoses. J Nucl Med. 2012;53(6):845–55.

Physical Aspects of Pediatric Nuclear Medicine Imaging

27

Frederic H. Fahey, Ruth Lim, and Georges El-Fakhri

Challenges in Pediatric Imaging

The value of nuclear medicine in children has been well established for practically all organ systems. In addition to the uses of nuclear medicine typically utilized in adults, there are a number of applications, specific to pediatrics, that are of great value as outlined in this monograph. Radionuclide therapy can also be very effective in children for a variety of diseases. The implementation of these therapies is covered in detail in other chapters in this book and will not be addressed here. But the application of diagnostic nuclear medicine in children presents unique challenges that need to be addressed in order to provide high-quality clinical information to our referring physicians. These may involve the acquisition of image data, the instrumentation to be used, or how best to process the data.

Many nuclear medicine protocols require a dynamic acquisition in order to analyze the temporal aspects of the uptake and clearance of the radiopharmaceutical, and thus the acquisition may take tens of minutes. Even static imaging can often take several minutes to acquire a sufficient number of counts for an interpretable image. Obviously, the time it takes to acquire a nuclear medicine study that provides adequate clinical information in children can be problematic, particularly in small children who may not be able to remain sufficiently still for duration of the study. For these reasons, standard approaches of immobilization may be inadequate, and the patient may need to be sedated or even anesthetized in order to perform the study. In the realm of dynamic imaging, it may also be necessary to understand the differences between the physiology of children and adults since there is the potential that the study should be acquired differently than the standard defined for the adult population. A complicating factor may be the difficulty in developing standards for the pediatric population. For static imaging, the study should be performed in a manner that provides the clinic with adequate information in the least

F.H. Fahey, DSc (✉)
Joint Program in Nuclear Medicine,
Department of Radiology, Harvard Medical School,
Boston, MA, USA

Division of Nuclear Medicine and Molecular Imaging, Department of Radiology,
Boston Children's Hospital, Boston, MA, USA
e-mail: frederic.fahey@childrens.harvard.edu

R. Lim, MD
Department of Radiology, Harvard Medical School,
Boston, MA, USA

Department of Radiology, Massachusetts General Hospital, Boston, MA, USA

G. El-Fakhri, PhD
Joint Program in Nuclear Medicine,
Department of Radiology, Harvard Medical School,
Boston, MA, USA

Division of Nuclear Medicine and Molecular Imaging, Center for Advanced Medical Imaging Sciences, Department of Radiology, Massachusetts General Hospital, Boston, MA, USA

S.T. Treves (ed.), *Pediatric Nuclear Medicine and Molecular Imaging*,
DOI 10.1007/978-1-4614-9551-2_27,

amount of time. Approaches that provide higher sensitivity or more efficient use of the acquired data can lead to a reduction in the duration of static nuclear medicine protocol. However, such modifications need to be balanced with the desire to keep the administered activity, and thus the radiation dose, to pediatric patients low in order to be prudent from a radiation safety point of view. The acquisition of the study also needs to be performed in such a way as to maintain spatial resolution as high as possible for optimal visualization of the organs of our smallest of patients.

The appropriate choice and use of instrumentation is essential for the proper practice of pediatric nuclear medicine. Using the right instrumentation that is maintained using a proper quality control program will be more likely to lead to an excellent study. This includes the appropriate choice of collimator for the specific diagnostic task at hand. In the pediatric setting, the need to acquire a high-resolution study as quickly as possible may demand a different collimator choice than what might be used for adults. Also, advances in instrumentation may have an impact when applied to children. Having a basic understanding of these advances allows one to take best advantage of them in the context of pediatric imaging.

The processing of nuclear medicine data may also vary for children. Variations in both anatomy and physiology as a function of patient age may require the study to be processed differently. In addition, the clinical questions being asked by a type of study may be different for children requiring a different approach to data processing. Lastly, advances in both image processing and tomographic reconstruction can lead to improvements in image quality and the efficient use of count information that may allow either shorter acquisition times or less administered activity to the patient or a combination of the two.

This chapter discusses physical aspects of the acquisition nuclear medicine studies, the equipment used, and the image processing that is applied to these studies in the context of pediatric nuclear medicine. Particular note will be made when the anatomy, physiology, or logistical considerations associated with imaging children may potentially lead to a modification to the approach typically used in adults.

Planar Imaging

Planar approaches to radionuclide imaging remain the most commonly performed nuclear medicine procedures in children, even with the advances in tomographic approaches such as SPECT and PET. Many essential clinical evaluations still rely on planar imaging including applications in the fields of gastroenterology, orthopedics, endocrinology, urology, and oncology. These studies may involve static or dynamic data acquisition as in the cases of a ^{123}I-MIBG scan for neuroblastoma or a ^{99m}Tc-MAG3 renal scan, respectively. Many of these procedures involve infants and neonates, our most vulnerable and challenging patients to image. Thus, special care should be taken with pediatric planar imaging to obtain high-quality clinical data as efficiently as possible. As discussed above, this includes particular consideration regarding data acquisition and instrumentation including collimation and data processing.

Acquisition

The acquisition of pediatric planar data must be given particular attention. In the first place, all planar protocols should be reviewed to assure that they are most appropriate given the state of the practice. For example, in ^{99m}Tc-MAG3 renal imaging, a perfusion phase with rapid framing may have been utilized in the past but may not be the current approach. In addition, as will be discussed, the instrumentation and data processing methods may have improved substantially since the time the protocol was developed. Therefore, acquisition protocols should be thoroughly reviewed and, if appropriate, modified in order to reflect the optimal approach for children in each study.

The imaging method may need to be adjusted for children, even in applications that are well established in the adult population. For small

children, adjustments may need to be made to allow for greater access to the patient. It may be necessary to provide extra space for ancillary, support apparatus. In other cases, the need for immobilization of the patient may require rearranging the gamma camera and other equipment. However, keeping the gamma camera as close to the patient as possible provides the images of highest spatial resolution which must be kept in mind even when making these adjustments for the sake of the patient.

Instrumentation

Both the use and choice of nuclear imaging instrumentation may vary when used in children. The need for high spatial resolution and efficiency must be balanced by the need to have quick and easy access to the patient mobilization. A standard, dual-detector gamma camera provides flexibility with respect to being able to perform planar imaging, whole-body scanning, and SPECT and can be used for pediatric imaging in a majority of cases. However, clinics that do a substantial amount of pediatric imaging may also consider that one of their system be a single-detector gamma camera. For example, performing a radionuclide cystogram in children suspected of urinary reflux can be difficult when using a dual-detector camera since the top head can restrict access to the patient.

There may be instances where intraoperative imaging may be desired and thus a mobile or handheld gamma camera may be appropriate. An example may be the surgical removal of osteoid osteomas. In advance of the surgery, ^{99m}Tc-MDP would be administered to the patient, and the patient and the mobile camera are brought to the operating room. The portion of the patient where the lesion is present is imaged to provide guidance to surgeon for its removal. Once the lesion is removed, the patient is imaged again to assure that it has been removed in its entirety. The camera needs to have the appropriate spatial resolution and sensitivity to properly localize the lesion and to assure its removal. In general, this requires either a high-resolution or an ultrahigh-resolution collimator. It is also necessary to be able to manipulate the unit around the operating room in order to image the pertinent region of the patient. Although mobile gamma cameras were once very popular in nuclear medicine clinics, few manufacturers continue to offer them. However, handheld cameras have been developed that can serve the same purpose. Again, this requires a system with high spatial resolution.

Collimation

The choice of collimation can be quite critical in pediatric nuclear medicine imaging and should be determined on a task-specific basis. In general, one must balance the need for excellent spatial resolution with need to complete the study in a time-efficient manner, and this may vary from protocol to protocol. For example, spatial resolution may be of most importance in the localization of abnormalities on a pediatric bone or renal scan, but sensitivity may be of primary concern when utilizing hepatobiliary imaging to diagnose biliary atresia. In addition, the use of collimators that provide magnification can be of significant value in special clinical cases.

Choice of Parallel-Hole Collimator

When acquiring a new gamma camera, the nuclear medicine practitioner is presented with a number of options with regard to parallel-hole collimators. When comparing low-energy collimators, the choice revolves around the aforementioned balance between spatial resolution and sensitivity.

In other cases, these choices are determined by the energy of the emissions from the radiopharmaceuticals used in the clinic since higher photon energies require thicker septa between collimator holes than for lower photon energies in order to minimize septal penetration. However, one must consider all photons emitted by the radiopharmaceutical and not just the primary photons utilized for imaging.

The low-energy collimators typically available to the nuclear medicine clinic are characterized as high sensitivity, general purpose, high

Table 27.1 Parallel-hole collimator parameters

	LEHS	LEHR	LEUHR	ME	HE
	Low-energy high-sensitivity	Low-energy high-resolution	Low-energy ultrahigh-resolution	Medium energy	High energy
Hole length (mm)	24	24	36	40	50
Hole diameter (mm)	2.5	1.1	1.1	2.9	3.4
Septal thickness (mm)	0.36	0.15	0.15	1.1	2
Sensitivity (cpm/μCi)	1,000	200	100	310	135
Collimator resolution @10 cm (mm)	14.6	6.4	4.6	10.8	12.6

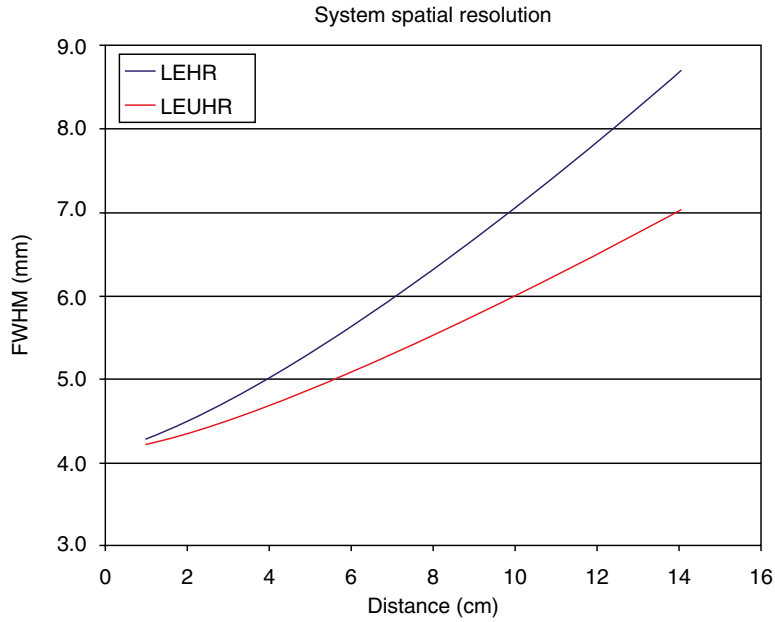

Fig. 27.1 System spatial resolution at a distance. The two graphs are for the low-energy high-resolution (*LEHR*) and low-energy ultrahigh-resolution (*LEUHR*) parallel-hole collimators. The design parameters as well as the sensitivities for these two collimators are listed in Table 27.1. The system spatial resolution is characterized by the full width at half maximum (*FWHM*) of the line spread function. All the system resolution is similar for the two collimators at distances less than 5 cm; the difference increases at distances greater than 10 cm

resolution, and ultrahigh resolution. It must be noted that the definition of these is not standardized across manufacturers, and thus one must consider the particular characteristics of the collimators associated with the camera of choice when making these comparisons. The specifications for these collimators from one manufacturer are presented in Table 27.1. The high-sensitivity collimator can be useful in pediatric imaging for applications that do not require specific localization of small features. For example, the evaluation of differential lung function from a perfusion lung scan can be well performed with such collimators. In these cases, the 5-fold gain in sensitivity can allow the imaging time to be substantially reduced. The utility of the general-purpose collimator in pediatric nuclear medicine is limited. In most cases where spatial resolution is not of primary importance, the high-sensitivity collimator is adequate.

However, one can still consider the appropriate collimator choice when spatial resolution is necessary, high or ultrahigh resolution. Figure 27.1 plots the system spatial resolution of these two collimators as a function of distance from the collimator face. As with all collimators, the spatial resolution of these degrades as the object is removed from the collimator. However, in cases where the collimator can be maintained close to the object of interest, as with certain

cases of planar imaging with children, the spatial resolution may not differ significantly. At a distance of 5 cm from the collimator face, the system spatial resolution is 4.8 and 5.3 mm for the ultrahigh- and high-resolution collimators, respectively. One might consider such a difference as minimal, particularly given the 2-fold difference in sensitivity between the two collimators. Therefore, one may consider the higher-sensitivity collimator when one can keep the object of interest within 5 cm or so to the collimator face. However, as the distance from the object is further removed from the collimator, the difference between the two collimators is more pronounced and thus the choice will depend on the diagnostic task at hand.

Iodine-123-labeled radiopharmaceuticals are often used in pediatric nuclear medicine such as ^{123}I for thyroid imaging and ^{123}I-MIBG for imaging children with suspected neuroblastoma. The primary emitted photon from ^{123}I has 159 keV, and so a low-energy collimator is often used with this radionuclide. However, 4 % of the photons emitted by ^{123}I have energies in the range 400 and 1,000 keV. Since the septal thickness usually utilized in low-energy collimators has limited effectiveness in stopping these high-energy photons, it is estimated that 40 % of the events detected in a ^{123}I study have resulted from the septal penetration of these high-energy photons. For these reasons, it may be more appropriate to utilize a medium-energy rather than a low-energy collimator when imaging ^{123}I since the thicker septa substantially reduces the septal penetration of the high-energy photons [1]. Figure 27.2 shows both phantom and patient images comparing the image quality using both medium-energy and low-energy collimators. In both cases, one can note the large number of the detected photons outside the phantom and patient boundary resulting from septal penetration.

Magnification Collimation

In many cases in pediatric nuclear medicine, one would prefer to have a higher-resolution image of a smaller anatomical region. In patients under 1 year of age with possible pyelonephritis, it may be necessary to acquire a high-resolution image of the renal cortex using ^{99m}Tc-DMSA in order to evaluate the extent of renal scarring. In another example, one might want to discern which bone in the foot has enhanced ^{99m}Tc-MDP uptake. The use of magnification collimation in instances like these can often provide the spatial resolution necessary to make the correct clinical interpretation. However, the distinction must be made between *optical* and *digital* magnification. In optical magnification, the acquired image is actually made larger through focusing and collimation. With respect to nuclear medicine, it is very difficult to focus gamma rays and thus collimation is the method used. Since a magnified image is projected onto the sodium iodide scintillation detector, the contribution on the intrinsic spatial resolution to the system spatial resolution is reduced by a factor equal to the magnification which leads to an overall improvement in the system spatial resolution. In digital magnification, the image is made larger post-acquisition without any real improvement in image quality. The image is merely made larger through the use of computational zoom. Although the digitally magnified image may be more visually pleasing, perhaps because it now takes up an appropriate amount of the computer display or is of a similar size as a companion, correlative image of the patient, it does not demonstrate improved image quality as can be the case with optically magnified images. Two types of collimation can provide optically magnified images, the pinhole and converging collimators; both of which will be discussed in this section.

The pinhole collimator (Fig. 27.3) is the simplest form of collimation used in nuclear medicine imaging. It consists of a single aperture or "pinhole" located at a distance from the detection material which allows the device to operate in a manner similar to a simple box-style photographic camera. Photons emitted from the object must pass through the pinhole in order to reach the detector. Thus the directionality of the detected photon is defined by the extension of the line connecting the loci of detection and the pinhole. The resultant image is reversed, and if the object-to-pinhole distance (b) is shorter than the

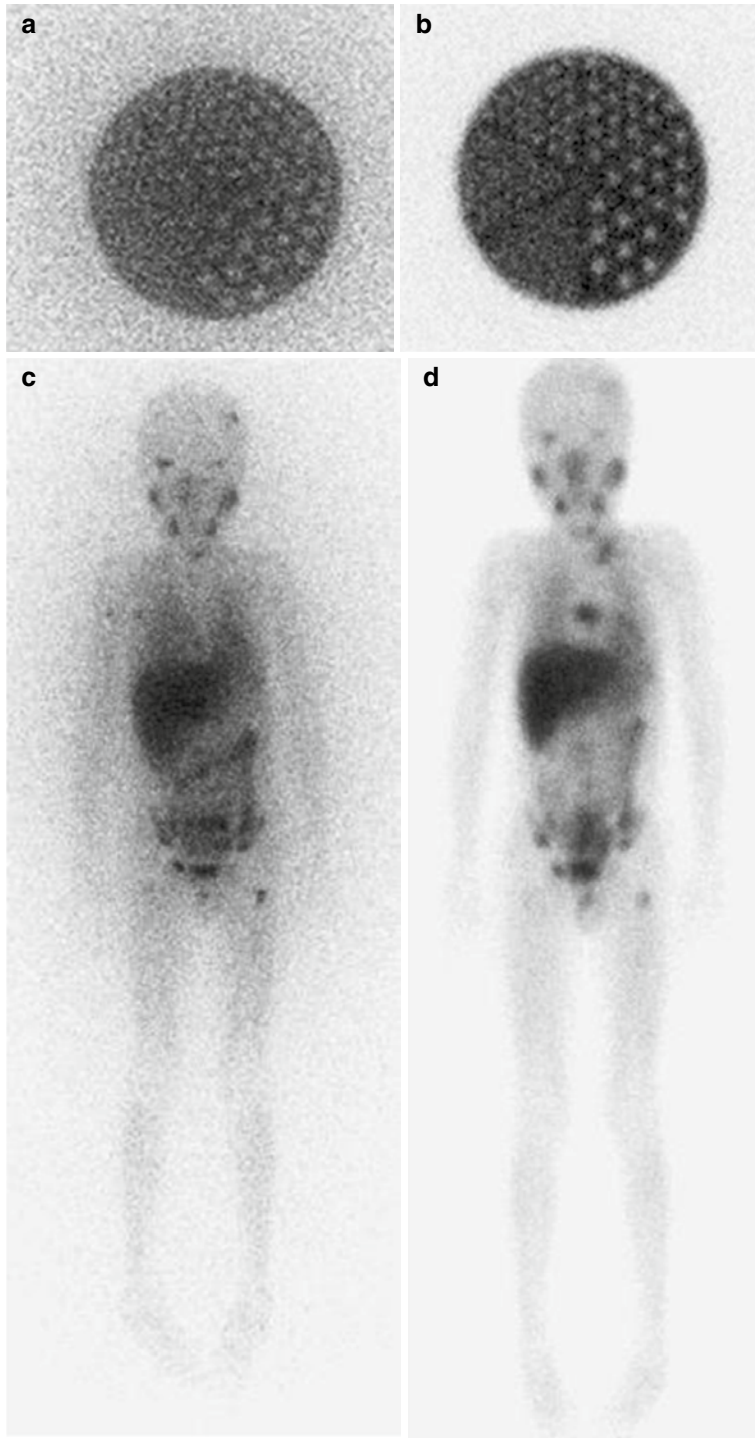

Fig. 27.2 Iodine-123 imaging with the medium energy (ME) and ultrahigh-resolution (LEUHR) collimators. The *top* images are planar image of ^{123}I in the Data Spectrum cylindrical phantom using (**a**) the LEUHR and (**b**) the ME collimators. The *bottom* images are whole-body scans of a 4-year-old patient with ^{123}I MIBG for neuroblastoma using (**c**) the LEUHR and (**d**) the ME collimators. Although the primary gamma energy for ^{123}I is 159 keV which would be considered low energy, 4 % of the emitted photons have energies over 400 keV. The use of the ME collimator significantly reduces the septal penetration leading to a substantial improvement in image quality

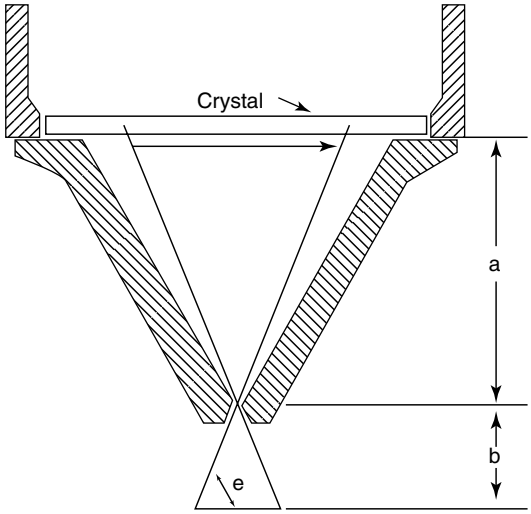

Fig. 27.3 Pinhole collimator. The relevant dimensions of the pinhole are the effective diameter, *d*, the crystal to pinhole distance, *a*, and the pinhole to object distance, *b*

detector-to-pinhole distance (*a*), the object is magnified. The degree of magnification (*M*) is determined by the ratio of these distances:

$$M = a / b$$

Thus the closer the object is to the pinhole, the greater the degree of magnification. The collimator spatial resolution (Rp) is given by

$$\mathrm{Rp} = d / a(a+b)$$

where *d* is the effective, pinhole aperture size. This equation indicates that the pinhole collimator resolution improves with smaller pinhole aperture size (note a smaller value of Rp is "higher resolution"). Typical aperture sizes are 4–6 mm in diameter although 1- or 2-mm apertures are sometimes used with very small children. The system spatial resolution (Gs) depends on both the collimator and intrinsic spatial resolution of the camera. However, as the image is magnified, the contribution of the intrinsic resolution is reduced by the magnification factor as shown below:

$$\mathrm{Gs} = \sqrt{\mathrm{Rp}^2 + (\mathrm{Ri} / M)^2}$$

This leads to an overall improvement in system spatial resolution as compared to similar collimator resolution values for parallel-hole collimation which does not provide magnification. Clinical examples that show the clear improvement in system spatial resolution from pinhole collimation as compared to parallel-hole collimator or parallel-hole collimation with digital zoom are provided in Chap. 15. In general, pinhole collimation provides the best system spatial resolution available in nuclear medicine imaging.

The pinhole collimator sensitivity is given by

$$\mathrm{Gp} = 1/16(d/b)^2 \cos^3\theta$$

where θ is the angle that defines how far off the central axis the source is located. Note that, unlike spatial resolution, collimator sensitivity degrades with smaller aperture size, and thus the use of very small apertures can require exceedingly long imaging times. The above equation indicates that sensitivity of a pinhole collimator drops off as the square of the object-to-aperture distance and is also reduced for locations off the central axis. This latter aspect is shown in Fig. 27.4 where the signal on the edge of the image is less intense than in the center.

As mentioned, the pinhole collimator provides magnification and the highest spatial resolution possible with the gamma camera. For these reasons, it can be very useful for imaging small organs such as the thyroid as well as for imaging very small patients or even small parts of larger patients. However, the pinhole collimator can introduce significant distortions into the imaging processes. Note that the magnification factor is a function of the object-to-aperture distance, and thus, for thicker organs, different portions of the object will be magnified by different amounts. In addition, the sensitivity also varies not only with object-to-aperture distance but also across the field of view.

In addition to the pinhole collimator, the converging collimator can also be used to provide optical magnification with enhanced image quality. The converging collimator consists of many holes all focused to a point some distance (approximately 50 cm) from the collimator face.

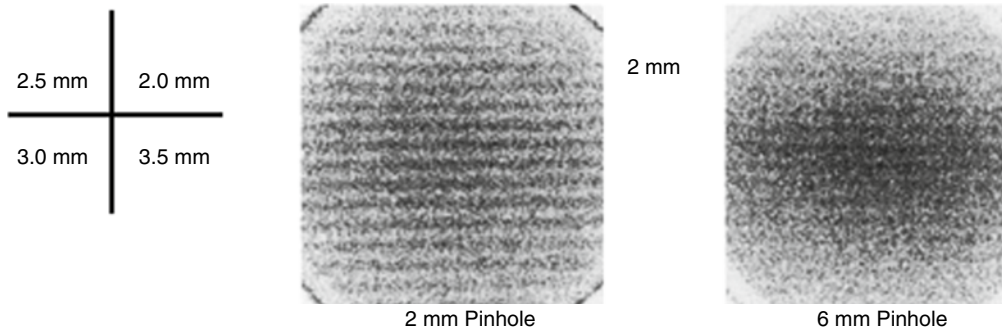

Fig. 27.4 Effect of off-axis imaging with pinhole collimator. Both images utilized a pinhole collimator, 2-mm on left and 6-mm aperture on right. Note the improved resolution and clarity using the 2-mm aperture compared to the 6-mm. Also note the higher sensitivity in the central part of the field of view

One advantage of the converging collimator is that its sensitivity increases with distance from the collimator face as one approaches the focal spot. Thereby, the converging collimator can provide higher spatial resolution without the subsequent loss of sensitivity relative to a parallel-hole collimator. On the other hand, the enhanced spatial resolution is not as striking as with the pinhole collimator. However, the use of converging collimators can provide notable clinical value when imaging children as demonstrated in Chap. 15.

Data Analysis and Image Processing

In many cases, planar nuclear medicine studies require quantitative data processing as part of the procedure irrespective of whether the study was acquired statically or dynamically. Such data processing often requires the definition of regions of interest (ROIs). For example, ROIs may need to be defined about each lung of a nuclear lung perfusion study using ^{99m}Tc-MAA in order to determine differential pulmonary function or about each kidney in a renogram using ^{99m}Tc-MAG3 to evaluate renal function. In these cases where data analysis is necessary, the quality of the quantitation in addition to image quality may determine the magnitude of the administered radiopharmaceutical dose that is required. For dynamic studies, the frame duration (i.e., number of seconds per frame) must also be considered. Therefore, these quantitative protocols should be reviewed periodically to assure that the quantitation is necessary and to determine whether any modification to the process should be considered given the current diagnostic requirements of the test. If, for example, one decides that either quantitation is no longer necessary or that the framing duration can be increased (e.g., from 30 to 60 s per frame), then one may be able to consider reducing the administered activity and, in turn, the radiation absorbed dose to the patient.

For a number of years, various approaches to image processing have been considered to either improve contrast or reduce quantum noise in planar nuclear medicine image [2]. In most cases, such approaches did not lead to substantial improvements in image quality. However, the recent advancement of adaptive filtering has been shown to enhance subjective image quality [3]. In these approaches, the size and nature of the filtering kernel is spatially modified depending on the local image content. Thus, areas of uniform activity are smoothed substantially whereas areas of varying spatial content such as those containing edges and fine detail much less smoothing is applied. In this way, the apparent noise level can be substantially reduced while preserving the sharpness of the image. In some cases, the processed image may be added to the original image to maintain familiar appearance of the clinical image. These approaches have been applied to both static and dynamic planar nuclear medicine images in a manner that can lead to significant image quality improvement without negatively affecting the accuracy of quantitative data analysis. Such image quality improvements can allow for substantial

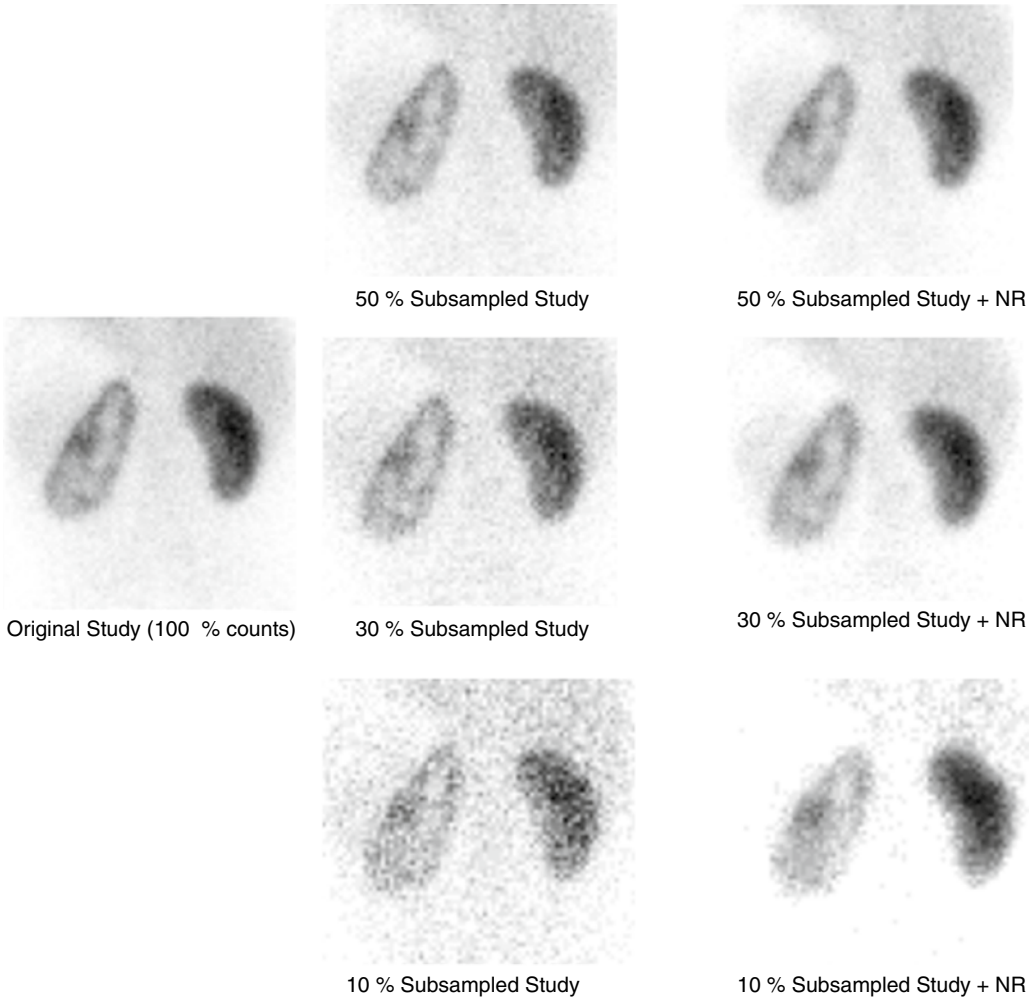

Fig. 27.5 Renal scan using ^{99m}Tc-MAG3 with and without noise reduction. The image on the *left* is the full dose study for comparison. The images in the *middle column* simulate using 50, 30 and 10 % of the full dose to perform the study. The images in the *right column* are the same three images, after the application of adaptive filtering noise reduction

reduction in the administered activity with subsequent reduction in the radiation absorbed dose to the patient as discussed in Chap. 31.

In Fig. 27.5, noise reduction through adaptive filtering has been applied to dynamic ^{99m}Tc-MAG3 renal study. MAG3 studies acquired with the amount of administered activity defined at the time by our clinical protocol were used as the base study referred to as the 100 % dose studies. Different amounts of administered activity were simulated from the base studies using binomial subsampling. The studies were then judged subjectively by a panel of experts in clinical nuclear medicine regarding their image quality and their adequacy for making clinical interpretation [4]. In the center column of Fig. 27.5, the deterioration in image quality with additional noise is evident. However, it was found that the administered dose could be reduced by 50 % without adversely affecting image quality. With the application of noise reduction through adaptive filtering, the administered activity could be reduced even further to 30 % of the full dose while maintaining adequate image quality. In addition, quantitative

ROI analysis was applied to the dynamic studies for the full dose, reduced dose, and reduced dose with noise reduction. It was found that the dose could be reduced to 10 % of the full dose without adversely affecting the quality of the quantitative analysis of these studies. A similar study was performed with scintigraphic hepatobiliary studies in infants for the diagnosis of biliary atresia [5]. All of the subjects in this study were under 1 year of age and thus they all received the minimum dose as defined by the North American Guidelines of 18.5 MBq [6]. Using binomial subsampling, studies were simulated where the patients received 50 and 25 % of the minimum dose prescribed by the guidelines. In addition, the dose was reduced according to the patients' body mass irrespective of the size of the patient. It was found that the minimum dose could be reduced to at least 25 % of its current value if noise reduction is utilized and in many cases much less than that. As advanced image processing techniques are further developed, these approaches can be applied to a wide variety of planar nuclear medicine studies with positive results leading to further opportunities for dose reduction in pediatric nuclear medicine.

SPECT

Single-photon emission computed tomography, or SPECT, was initially investigated in the 1960s prior to the development of computed tomography (CT) with the rotating gamma camera being developed in the late 1970s [7–9]. By the end of the 1980s, SPECT had become an essential clinical imaging modality, and practically all gamma cameras sold provided full SPECT capability. Almost immediately, SPECT was applied to children with positive effect, making what had been difficult diagnoses more straightforward through improved image contrast and localization of the deposited radiopharmaceutical. As with planar imaging, the application of SPECT to children requires specific considerations involving all aspects of the process including acquisition, reconstruction, and data processing. In addition, SPECT instrumentation must be reconsidered regarding the selection of the camera and collimators most suited for pediatric imaging. Also, newly developed high-sensitivity SPECT instrumentation for other uses such as cardiology may have applications in imaging children. Hybrid SPECT/CT applied to pediatrics will also be discussed.

Acquisition

The large majority of SPECT devices used in the clinic consist of rotating gamma cameras. Thus, this section will pertain to this technology unless otherwise specified. SPECT data acquisition is comprised of the collection of planar images at a set of specified viewing angles about the patient. These are referred to as projection images. In order to obtain these projection images, the camera rotates about the patient (Fig. 27.6). At all viewing angle, the camera face is parallel to the axis of rotation. Each detected event is typically assumed to have originated along the "line of origin." In general, more than 100 projection images are acquired about the patient in evenly spaced angular increments. In order to acquire a sufficient number of counts in a SPECT study, each projection is acquired for approximately 20 s, and, thus, the entire study takes between 15 and 30 min during which time the patient must remain stationary. This may make it difficult to perform SPECT in very small children without the use of sedation or anesthesia. If SPECT is acquired on the sedated or anesthetized patient, access to the patient may also be more challenging.

As discussed in the section on planar imaging, the highest spatial resolution is obtained when the patient is as close to the collimator as possible. Therefore, care must be taken in placing the patient within the scanner and setting up the acquisition. If the SPECT study is acquired with a circular orbit where the camera face is always a set distance from the axis of rotation, the camera may be quite far from the patient in certain projections, particularly in the anterior and posterior viewing angles. Therefore, noncircular, body contour orbiting capability is provided where the camera is moved radially as it rotates about the patient such that the camera is maintained within a few cm of the patient in each viewing angle.

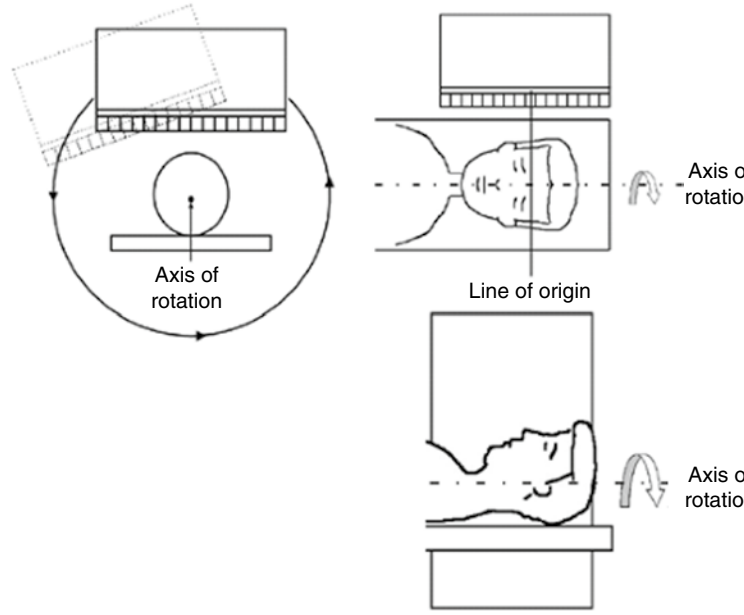

Fig. 27.6 SPECT acquisition using the rotating gamma camera. The gamma camera rotates about the patient keeping the camera face parallel to the axis of rotation. More than 100 projection images are acquired at even angular intervals over a 360° arc about the patient. A photon detected at a particular location is assumed to have come from the line of origin that intersects that point and is perpendicular to the crystal detector face

Maintaining the highest spatial resolution possible is always important but is particularly essential when imaging children. Therefore, body contour orbits are always recommended and special care must be spent on patient placement. The use of a thinner, pediatric imaging table for small children may also improve the ability to keep the rotating gamma camera close to the patient.

Most SPECT studies are acquired with dual-detector systems to improve the sensitivity of the system by a factor of 2. For most acquisitions, the two detector heads are located opposite each other so that two conjugate views of the patient are acquired simultaneously and the camera only rotates over 180°. This configuration is appropriate for many SPECT protocols including studies of the head, abdomen, and lumbar spine. However, in cardiac studies, the heart is located in the left anterior thorax, and thus acquiring data in the right posterior projections is of limited use. In these projections, the camera is at a substantial distance from the heart, and thus the spatial resolution is considerably reduced in these projections. Therefore, cardiac SPECT is typically acquired only from the right anterior to the left posterior projection views. If such studies are acquired with dual-detector SPECT systems, the two detectors are typically reconfigured to be at 90° to each other and the scanner is only rotated over 90°.

Instrumentation

Dual-detector rotating SPECT systems are recommended for use in children since they provide the high sensitivity necessary for outstanding image quality in these challenge patients. The choice of parallel collimation with pediatric SPECT requires some discussion. The use of very high-resolution collimators makes intuitive sense particularly when applied to small children, but one could also consider that a general-purpose collimator can acquire many more counts, perhaps more than a factor of 2, in the same imaging time. However, it has been shown that the use of higher spatial resolution collimators provides image quality relative to higher-sensitivity collimators even with substantially fewer counts [10]. In addition, higher spatial resolution collimators often have longer collimator holes that provide higher spatial resolution at greater depths within the patient which is of particular importance in SPECT since even a peripheral object within the patient is at some distance from the collimator, perhaps as much as 15–20 cm, at least in some

projections. As discussed previously, the spatial resolution of the ultrahigh- and high-resolution collimators is not very different within 5 cm of the collimator face, and in this region, the higher sensitivity of the HR may be more important. However, in SPECT, objects of interest are at some distance from the collimator, and at these distances, the difference in resolution is more striking, and thus the UHR may be more appropriate.

In the past 10 years, there have been a number of dedicated, high-sensitivity SPECT systems developed specifically for cardiac imaging [11]. In general, these devices are comprised of multiple scanning detector modules or the use of multiple pinhole collimators, all aimed at the heart. Initially, these devices were designed to provide faster throughput as they could provide comparable image quality to a conventional dual-detector SPECT system in a fraction of the imaging time. However, more recently there have been investigations to show that these devices can be used with less administered activity, leading to a reduction in patient radiation dose. Although these technologies were designed specifically for cardiac imaging, it may be reasonable to apply this same technology to pediatric imaging keeping in mind that these two, very different clinical situations may have varying imaging requirements with respect to resolution and sensitivity.

The use of focused collimation for SPECT has been considered practically from the time that SPECT was introduced to the clinic in the 1980s. For example, fan-beam or cone-beam collimation may provide sensitivity gains of about 1.5–3 times higher than parallel collimation with comparable resolution. Focused collimation leads to a field-of-view reduction, and thus, the technology has typically been applied to the imaging of smaller organs such as the brain or the heart. However, focused collimation may also be applicable to the imaging of small children. The issue has been the technical complication associated with these collimators. The collimators need to be calibrated and used at set imaging parameters. However, the introduction of sophisticated robotics associated with newer SPECT gantries can simplify the use of this technology by automatically driving the gantry appropriately and keeping the organ of interest within the sweet spot of the field of view. This newer approach has been applied to nuclear cardiology but could potentially also be applied to pediatric imaging. It may be possible, for example, to apply this technology to patients under 1 year of age scheduled to have a ^{99m}Tc-DMSA renal scan, thereby allowing the application and advantages of SPECT to even smaller patients.

Reconstruction

The acquired SPECT data is represented by a series of projection images taken at evenly spaced angles about the patient. In a typical 360° acquisition, 120 projection images are acquired every 3° about the patient. These data are then processed to generate a series of transaxial slices providing a 3D representation of the patient. The manner by which these projection data are processed into transaxial slices is referred to as *reconstruction* with similar methods being applied to other tomographic modalities such as PET and CT. In addition, absorption of emitted photons from deep within the patient is less likely to be detected than those emitted from the periphery of the patient due to self-absorption. Thus *attenuation correction* must be performed on SPECT studies to compensate for this effect, leading to data that more accurately reflects the in vivo distribution of the radiopharmaceutical.

The traditional approach to the reconstruction of tomographic data since the earliest days of SPECT has been *filtered backprojection*. In filtered backprojection, a detected event is assumed to have originated along the line of origin (Fig. 27.6). With parallel-hole collimation, the line of origin is perpendicular to the collimator face and intersects the locus of detection. Thus, the data from that location is *backprojected* through the object with no consideration for where along the line of origin the photon may have been emitted. In truth, the photon may have been emitted from a location slightly removed from the line of origin due to scatter or the limited spatial resolution associated with parallel-hole collimation. By backprojecting all of the

detected data in every projection, being mindful that the angle of backprojection depends on the angle at which each projection image was acquired, leads to a rather crude representation of the 3D object. In order to compensate for the uneven sampling of the data at different spatial frequencies, a filter that increases linearly with the spatial frequency known as the *ramp filter* must be applied to the backprojection process to make the resultant, reconstructed data interpretable. A second filter (e.g., Butterworth, Hamming, Hanning, or Shepp-Logan filter) is generally applied to de-emphasize the noise that results from the reconstruction process while accentuating the frequencies that best represent the object of interest. Since backprojection and filtering are linear processes, the order in which they are applied does not matter, in general, and thus different algorithms may apply the filtering at different stages in the process, i.e., before, during, or after the backprojection of the data. Filtered backprojection, as this approach is called, is fast, simple to implement, and robust.

For over a decade, iterative approaches to tomographic reconstruction have been developed [12]. In fact, iterative reconstruction is the most common approach used with PET data. Its application in SPECT and CT has only been considered in the last few years; however, it is expected to have considerable impact in these modalities in the near future. Iterative reconstruction starts with an initial naïve guess of the object. This guess could be a uniform image, a filtered backprojection, or some other reasonable first guess. An assumed model of the object is then applied to generate a set of projections that are consistent with current realization of the object. This assumed model could be very simple (e.g., similar to that used in simple backprojection) or very sophisticated, incorporating many of the aspects known about the image acquisition process including the presence of Poisson noise, Compton scatter, photon attenuation, or the variation of system resolution with distance from the collimator. In fact, one of the advantages of iterative reconstruction is this ability to incorporate such aspects directly into the reconstruction process potentially leading to a more accurate reconstruction.

The simulated projections are then compared to the real, acquired projections and any difference between the sets is typically characterized by the ratio of the 2 values at each sampling point. This divergence data is backprojected and added to the initial guess to obtain a second guess. The process is then repeated with the projection of the modeled data, the comparison to the acquired projections, backprojection of the divergence, and addition to the current guess. This process is iterated or repeated until an acceptable result is obtained. A statistical criterion can be set to determine when the projected modeled data adequately represents the real projection data when convergence has occurred. The approach most commonly used for iterative reconstruction is the maximum likelihood expectation maximization (MLEM) algorithm which maximizes the statistical definition likelihood generating the data set most likely to have resulted from the set of real projection data.

The MLEM algorithm may require as many as 30–100 iterations to converge to an acceptable answer which can take a considerable amount of time. An alternative algorithm that is substantially faster is the ordered subset expectation maximization (OSEM) algorithm. With OSEM, the projection data is divided up into a number of subsets of evenly spaced projections, and a new estimation of the object is generated after the processing of each subset rather than the entire set. Thus, for the example of N subsets, the estimation will be updated N times before all of the projections have been processed a single time. In general, the image quality using OSEM with N subsets and Xo iterations leads to similar image quality as the MLEM algorithm with the number (Xm) equal to the product the numbers of subsets and iterations of the OSEM algorithm ($Xm = N \times Xo$) but is obtained N times faster. For example, the image quality from OSEM with 3 iterations and 10 subsets is similar to that of the MLEM with 30 (3×10) iterations but will be reconstructed in 1/10 of the time.

As mentioned above, one of the advantages of iterative reconstruction is the ability to specify certain aspects of the reconstruction process potentially leading to a more accurate reconstruction.

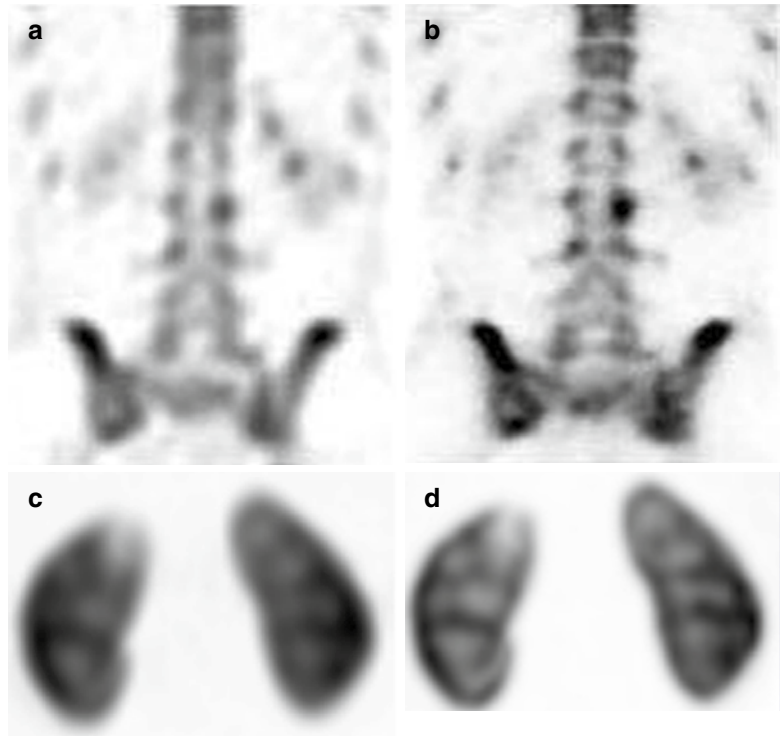

Fig. 27.7 Use of iterative reconstruction. The *top* images are two reconstructions of the same bone SPECT study using ^{99m}Tc MDP with (**a**) filtered back projection and full counts and (**b**) OSEM with resolution recovery with half of the counts. The *bottom* images are two reconstructions of the same renal SPECT study using ^{99m}Tc DMSA with (**c**) filtered back projection and full counts and (**d**) OSEM with resolution recovery with half of the counts

For example, knowledge of the variation of system spatial resolution with distance from a specific choice of collimator can be entered into the projection model leading to a sharpening of the reconstructed image, often referred to as *resolution recovery*. For resolution recovery to be effective, specific knowledge of the collimators being used and their performance characteristics is necessary. If applied across as well as within transverse planes, the process is referred to as 3D resolution recovery. In some cases, the resultant increase in image quality can allow for a reduction of image counts while maintaining acceptable image quality. This reduction in image counts may lead to either a reduction in administered activity and subsequent reduction in radiation dose to the patient or a reduction in imaging time which may be essential in order to complete a SPECT study in small children in a reasonable time with minimal use of sedation or anesthesia to limit patient motion.

We have investigated the potential for reducing the number of counts in pediatric bone and renal SPECT using OSEM iterative reconstruction with 3D resolution recovery [13, 14]. In these studies, the SPECT data for a number of pediatric patients were acquired with a dual-detector using a full 360° reconstructing with either both detectors or a single detector yielded data sets with full or half counts, respectively. This was done for both filtered backprojection and OSEM with resolution recovery. Observers with significant nuclear medicine experience blinded to the number of counts and the method of reconstruction reviewed the images and subjectively graded as to the image quality from a clinical interpretation point of view. For both bone SPECT with ^{99m}Tc-MDP and renal SPECT with ^{99m}Tc-DMSA, the data with half counts reconstructed with OSEM with 3D resolution recovery was deemed to have improved image quality relative to the data with full counts reconstructed with filtered backprojection (Fig. 27.7).

Hybrid SPECT/CT Imaging

At first, SPECT/CT incorporated a low-cost, low-power CT design that was utilized primarily

to provide a transmission scan for attenuation correction. It provided a crude version of a CT scan that, in some cases, could also be used for anatomical correlation. However, following the clinical success of PET/CT, state-of-the-art CT units were incorporated into SPECT/CT. Currently, all major gamma camera manufacturers provide a high-quality SPECT/CT option although some still offer lower cost options with moderate CT image quality. These lower cost options may involve the incorporation of flat panel detectors with a cone-beam CT acquisition approach. In practically all cases, the SPECT component of the device is located in front with the CT component posterior to it. Besides maintaining appropriate quality control programs for both SPECT and CT, it is essential to maintain close registration between the two modalities. Different manufacturers have implemented specific procedures for this calibration.

For the CT component, appropriate procedures for pediatric patients should be applied to keep the radiation dose to the patient as low as possible. In addition, SPECT/CT is applied in a limited region of the body and is often applied in a targeted fashion and only when necessary after the initial SPECT study has been acquired. For example, SPECT/CT may be applied in the lumbar spine region for studies for back pain in young athletes. This targeted approach will also tend to keep the radiation dose lower for SPECT/ CT.

The availability of SPECT/CT for most pediatric applications is still limited and potential for SPECT/MR is still years away. Thus, the application of software approaches to image registration continues to be very relevant. The registration of ^{123}I-MIBG and MR in a child with neuroblastoma or the correlation of ^{99m}Tc-MDP bone SPECT with CT can be very helpful. In addition, intramodality image registration as with ictal and interictal brain SPECT can be essential to make proper diagnosis. In these cases, the reconstructed data of the two modalities are loaded onto the same workstation. The widespread use of hospital-wide PACS and the DICOM image format standard has made this much simpler than it was even just a few years ago. One of the studies, often the one with higher resolution, is considered the "reference" image set and the other may be referred to as the "source" image set. The image registration algorithm has two basic components: one that applies a particular goodness-of-fit statistical criterion and the other is a search engine that looks through a defined set of possible configurations for the one that optimizes the statistical criterion. The statistical definition of mutual information is often used for the goodness-of-fit criterion. The search engine then seeks to find the best rotation, translation, and possibly scale combination such that the source image set is of the same size, location, and orientation as the reference set. The ratio of the pixel sizes stored in the file header of the two studies is often assumed to be the proper scale factor. The source set is then resampled along the same transverse planes with the same size and in the same location and orientation as the reference set. The multimodality reviewing tool will typically allow viewing of a merging of the two image sets with a blending slide that allows one to view either the reference set only, the resampled source set only, or any combination of the two. Even with the proliferation of hybrid imaging hardware, the ability to apply software-based image registration continues to be a very valuable clinical tool in pediatric nuclear medicine.

PET/CT

Following expanded reimbursement for oncologic PET and the introduction of PET/CT in the first part of the twenty-first century, the clinical application of PET expanded greatly. The number of clinical PET procedures in the USA increased by more than a factor of 5 between the years 2000 and 2010. The use of PET in children also increased dramatically during that period with the enhanced access to both PET instrumentation and radiopharmaceuticals such as ^{18}F-labeled fluorodeoxyglucose (FDG), leading to greater experience with the technology and a better definition of how it should be applied in children.

Besides the considerable increase in the application of PET, the other significant development

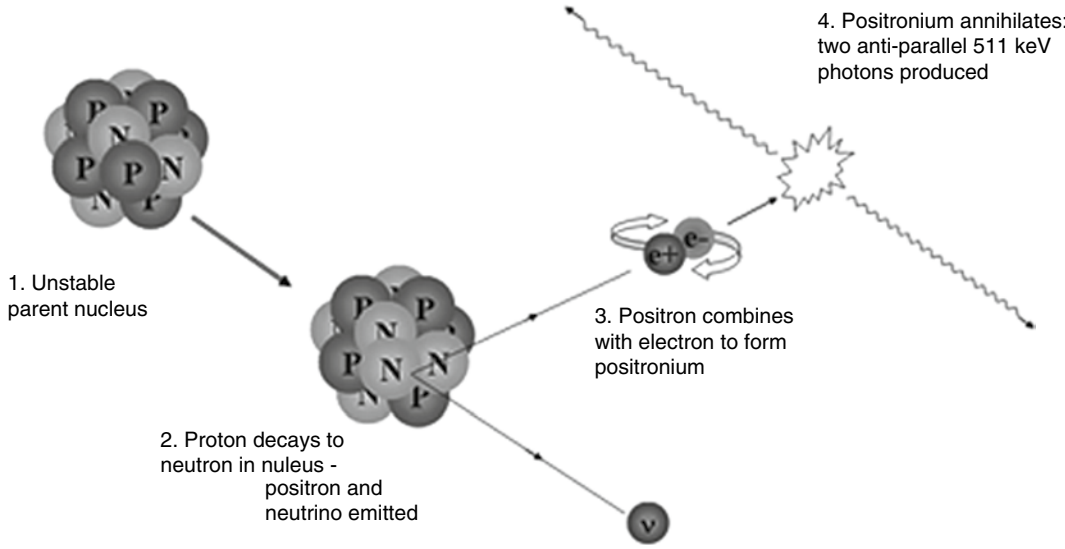

Fig. 27.8 Positron emission. (*1*) An unstable atom of a positron emitter (e.g., ^{18}F) is associated with a radiopharmaceutical such as ^{18}F FDG. (*2*) Upon de-excitation, a positron (e+) and a neutrino (ν) are emitted. (*3*) After traveling some distance, the positron joins with an electron (e−) to form positronium. (*4*) After a very short while, the positronium (or positron-electron pair) annihilates with all of their mass being converted into two 511 keV photons emitted back to back. If the two photons are detected, the event is assumed to have occurred on the line connecting the two detections, referred to as the *line of response* (LOR)

was the introduction and clinical acceptance of hybrid PET/CT. The combination of the functional/molecular data provided by PET with the high-quality anatomical imaging provided by CT has led a synergy yielding enhanced clinical information relative to the two modalities performed separately. This was particularly true for oncologic imaging where the emerging utility of PET was combined with the established value of CT. As a result, no PET-only devices have been marketed since 2006, only PET/CT. This section will review the acquisition, instrumentation, and reconstruction of PET/CT data, particularly in the context of pediatric imaging. In addition, the emerging technology of PET-MR will be discussed with respect to the potential for its use in children.

Acquisition

The acquisition of PET data is fundamentally different than planar nuclear imaging or SPECT. When a positron emitter such as ^{18}F decays, it emits a positron. The positron has the same mass as an electron, and its charge has the same magnitude as an electron but with positive rather than negative polarity. The emitted positron will travel some distance before it loses most of its kinetic energy at which point it will combine with an electron, its *antiparticle* (Fig. 27.8). After a very short time, the positron-electron pair *annihilates* with their mass being transformed into energy in the form of two photons emitted in opposite directions. The energy of each photon is 511 keV, the energy equivalent of the rest mass of either the electron or the positron according to the Einstein equation ($E=mc^2$). If the positron-electron pair is at rest when they annihilate, the two photons will be emitted at exactly 180° to each other, and if both photons are detected at the same time or in *coincidence*, it is assumed that they originated from the same annihilation event which occurred at a location somewhere along the line that connects the two detectors, referred to as the *line of response* (*LOR*). This approach to localizing a positron detection is referred to as *annihilation coincidence detection*. From a

physics point of view, the major advantage of PET over conventional nuclear imaging or SPECT is the ability to determine the directionality of detected events without the use of absorptive collimation. As a result, the sensitivity of PET can be a factor of 100 or more higher than that associated with SPECT.

The spatial resolution of PET is often better relative to SPECT although this need not be the case. To first order, the spatial resolution of PET is related to the size of the radiation detectors. Thus for a PET scanner with 5-mm detectors, the spatial resolution would be slightly higher than that considering the reconstruction process. However, there are two fundamental limitations to the spatial resolution of PET related to the positron range and the non-colinearity of the two annihilation photons. Even if the annihilation coincidence detection works perfectly, the locus being estimated would be that of the annihilation event whereas it is the point from where the positron was emitted that is of most interest since it best represents where the positron-emitting molecule was located. Depending on the initial kinetic energy of the positron, the distance from the point of emission to that of the annihilation, known as the positron range, may be several mm, perhaps as much as a cm, in soft tissue. In addition, if the positron-electron pair is not quite at rest at the time of annihilation, the two photons are not emitted at exactly 180° to each other, and thus, the LOR may not indicate the locus of annihilation exactly. In a whole-body PET system, these two fundamental factors limit the spatial resolution to about 3 mm regardless of how well the scanner is engineered including the size of the detectors. There are no such limitations in SPECT where it would be possible to make the collimator holes so small that one could acquire sub-mm SPECT. However, the sensitivity would be so low that one would either need to administer an inordinate amount of radioactivity to the patient or acquire for an unreasonable amount of time. Thus with current scanners, the spatial resolution parameters are about 6 mm for PET and 8–12 mm for SPECT.

In earlier versions of PET scanners, the PET acquisition data could be acquired in either two-dimensional (2D) or three-dimensional (3D) modes. In 2D mode, the acceptable LORs were limited to parallel transaxial planes by using absorptive, interplane septa. These septa did not act to resolve the data but instead were used to reduce interplane scatter (scatter fraction of less than 15 %) and random coincidences from out-of-plane radioactivity. In 3D mode, the septa were removed leading to an increase in sensitivity by about a factor of 4–5 but with an increase in the scatter fraction to greater than 35 % depending on the size of the patient and the distribution of the radioactivity. With the use of more sophisticated algorithms to compensate for scatter and faster scintillating material such as lutetium oxyorthosilicate (LSO) for PET detection, all new scanners acquire only in 3D mode.

Another advantage of the incorporation of faster scintillators into state-of-the-art scanners is the potential for acquiring the data in *time-of-flight* (TOF) mode. As described above, with annihilation coincidence detection, one can determine the LOR but not where along this line the event occurred. It is the combination of numerous LORs during the reconstruction process that eventually leads to the formation of a 3D representation of the PET radiopharmaceutical distribution. However, with faster detectors, one can determine the time difference between the detection of the two photons and, from this, make an estimate of where along the LOR the event occurred. Currently available scintillating materials have a temporal resolution of about 0.5–0.6 ns which corresponds to the ability to place the event to within about 7 cm along the LOR. Although this would not seem an accurate enough estimation to be practical, it provides the reconstruction algorithm with some additional localization information which can lead to a notable increase in the reconstructed signal-to-noise and subsequent improvement in image quality as well as quantitative accuracy, particularly in larger patients. Although the ability to localize an event to within 7 cm or so may be of limited value in smaller pediatric patients, the improvement in reconstruction algorithms and the development of faster scintillators may allow the extension of this technology to children.

CT data acquisition in the context of PET/CT includes many of the considerations of modern

helical, multi-detector CT. The CT component is comprised of a third-generation CT system where the x-ray tube continually rotates about the patient irradiating a fixed ring of x-ray sensitivity detectors. At the same time, the patient bed traverses through the gantry providing data acquisition over the selected volume of the patient. The x-ray rotation speed is quite fast, 0.3–1.0 s per rotation. The x-ray detection matrix consists of as few as 8 and as many as 64 rows of detectors of varying sizes extending 0.5–14 mm in the *z*-direction (into the scanner). The distance traversed by the imaging bed divided by the extent of the detector matrix is referred to as the pitch and can range from 0.5:1 to 1.5:1. Larger pitch values (e.g., 1.5:1) indicate faster bed speeds and shorter scan times for the same volume.

The x-ray tube voltage (in kVp) determines the energy of the electrons impinging the tube anode and, thereby, the maximum energy of the resultant x-ray spectrum. For example, a tube voltage of 120 kVp leads to a continuous spectrum of x-ray energies with a maximum of 120 keV. In addition, higher tube voltages yields more emitted x-rays and thus higher radiation dose to the patient as well. The tube current (in mA) defines the number of electrons traversing the x-ray tube and, thereby, the number of x-rays emitted per second. The number of emitted x-rays is directly proportional to both the tube current and the scan duration (in seconds), and thus the product of these two values is often reported as mAs. In helical CT, the tube current multiplied by the rotation speed divided by the pitch is often referred to as the *effective mAs*. For example, an acquisition utilizing a tube current of 210 mA with a rotation speed of 0.5 s per rotation and a pitch of 1.5:1 would be said to have an effective mAs of

$$\mathrm{mAs}_{\mathrm{eff}} = 210 \times 0.5 / 1.5 = 70 \ \mathrm{mAs}$$

The radiation dose to the patient can be altered by modifying the kVp, the effective mAs, or the portion of the patient that is scanned.

The CT acquisition parameters, particularly kVp and mAs, should be scaled for smaller patients. For example, if the same kVp and mAs are used in a small child as in large adult, the child would receive a radiation dose that was two to five times higher than the adult [15]. As a result, there are a number of schemes for reducing the dose from the CT component of PET/CT in children. Alessio et al. presented a scheme that scaled the mAs according to the Broselow-Luten color scale used in the emergency room to scale the administration of pharmaceuticals to children [16]. Using this scheme, they were able to reduce the radiation dose to smaller children by at least a factor of 2.

Instrumentation

All currently marketed, whole-body PET systems are hybrid PET/CT scanners. In general, these devices combine high-quality CT with state-of-the-art PET capability. In addition, the PET component acquires in 3D mode only. However, there are a number of other, optional features, on both the PET and CT sides, that one should consider when deciding on the best scanner for pediatric applications. In making this choice, one needs to consider the size and age of the patients to be scanned as well as the clinical applications to be utilized. Will the unit be used for neurology and cardiology as well as oncology? Will the unit be used for small children with epilepsy? Will high-speed cardiac CT imaging be necessary? Will the majority of the pediatric cases be 10–20-year-olds with lymphoma? Will the unit be used as a backup CT scanner when PET cases are not scheduled? The answers to any of these and other questions will affect the selection of the most appropriate scanner for a particular clinic planning PET/CT imaging of children.

For pediatric imaging, one hopes to be able to acquire the highest-quality image data possible in the shortest amount of time. Due to the patient's small size, one would like the highest spatial resolution possible. On the other hand, fast acquisition minimizes the potential patient motion while hopefully limiting the need for sedation or anesthesia during the image acquisition. Thus, there is the need for high spatial resolution and sensitivity. Fortunately, in PET, there is less of a tradeoff

between spatial resolution and sensitivity than there is SPECT or conventional nuclear medicine imaging. The spatial resolution is practically defined by the size of the detector elements. For a detector ring of a particular diameter, having smaller detectors typically means there are more of them which may lead to higher cost, but does not indicate lower sensitivity. One aspect of the scanner that can have significant impact on the sensitivity is the extent of the field of view in the z (or axial)-direction. The sensitivity for a PET scanner operating in 3D mode varies in the z-direction as a triangular (or, in some cases, a trapezoidal) function. Extending the z-direction field of view affects not only the base of the triangle but also the height, and thus extending the field of view by 30 % may increase the sensitivity by more than 40 %. As a result, for pediatric imaging, one may want to consider a scanner with the smallest detector elements available and the longest field of view.

As discussed above, time-of-flight PET improves image quality most significantly in larger patients, and thus its impact in smaller patients may be limited. However, it has been shown that TOF leads to some image quality improvement even in normal-sized adult patients. Therefore, having this capability may be reasonable if most of your patients are medium size teenagers or if the scanner is to be used for a mixed adult/children patient population.

Besides the conventional whole-body PET/CT scanners, there has also been the development of special PET devices for either imaging a particular portion of the body or for application in preclinical studies. The potential exists for applying the lessons learned from these developments to the imaging of very small children under special circumstances. The initial widespread application of FDG PET was in brain imaging, and as a result, dedicated units were developed for imaging the head with high resolution. In addition, the application of PET in experimental, small animals has grown substantially over the past 10 years. By using smaller detectors and reducing the diameter of the detector ring, one can significantly improve both the spatial resolution and sensitivity of the scanner. It is possible to extend this technology to a scanner than could be used under special circumstances such as within the neonatal intensive care unit. High-quality image data could be acquired on these very challenging patients in an acceptable imaging time. One limitation would be that these units would most likely be PET-only devices without the potential for hybrid imaging. However, software image registration could be applied between the PET and a separately acquired MR study, for example. Another emerging technology that could potentially be applied to pediatric imaging is the use of opposing flat panel detectors currently being investigated for dedicated PET devices for mammography often referred to as *positron emission mammography* or *PEM*. Expanding the size of these detectors may allow PET to be applied in infants or neonates. Keeping abreast of these advances in PET imaging may allow the application of this wonderful technology in even the smallest of children.

The CT component has a number of features that may be of considerable interest in pediatric imaging. In particular, there have been several features introduced in recent years in the context of CT dose reduction. One such dose reduction feature is tube current (mA) modulation which may be marketed under different trade names by the various manufacturers. In essence, the mA is varied during the acquisition of the helical CT study depending on the attenuating properties of the tissue within the field of view. The criteria used to determine an appropriate mA level may involve the exit exposure level or a statistical noise index in the acquired data. Within a single plane, the mA necessary to reach the selected criterion will be lower in the anterior/posterior direction where the patient is much thinner than in the lateral direction. Across planes, less mA would be necessary over the thorax than over the abdomen. Applying mA modulation both within and across planes can lead to as much as a 30–40 % reduction in radiation dose to the patient.

Shielding applied directly to the patient has been used to reduce the radiation dose to the breasts of young women. For example, the use of

bismuth shields has been shown to reduce the breast dose by as much as 30 % [17]. However, these must be used appropriately. Applying the shields directly to the patient's skin has been shown to cause artifacts in some cases, and thus, a foam spacer is often used to slightly offset the shields. In addition, the mA modulation map is often determined during the CT "scout" scan, and in these cases, the shields should be applied after the acquisition of the scout scan and prior to the CT acquisition.

Reconstruction

Iterative reconstruction has been the standard for PET for more than 10 years, leading to improved image quality, fewer artifacts, and a reduction in image noise. These improvements in image quality in conjunction with other technical advancements have allowed PET to be acquired with less administered activity in much shorter acquisition times. In the late 1990s, it was not uncommon to administer in excess of 740 MBq to the patient and image for up to 7 min per bed position. According to the North American pediatric dose guidelines [6], a 70-kg large teenage would receive 370 MBq and in many cases can be imaged in less than 3 min. Just as in SPECT, modeling the variation of spatial resolution across the field of view and incorporating this into the reconstruction algorithm can lead to further improvements in image quality. In the case of PET, this modeling most likely takes into account such issues as the depth-of-interaction effect which leads to a loss of spatial resolution at the periphery of the field of view. Further image quality improvements provided by the reconstruction algorithm has the potential for even further dose reduction.

Traditionally, CT data has been reconstructed using filtered back projection. Even though iterative approaches for the reconstruction of PET data were introduced into the clinic more than 10 years, the large size of CT data (typically, 100 s of slices using a 512×512 matrix as compared to 40 slices of 128×128 matrix for PET) delayed investigations of these algorithms in this arena. Such larger data sets led to long reconstruction times, and thus interactive reconstruction was not considered practical for clinical CT. As a result, filtered back projection remains the most commonly used CT reconstruction technique. More recently, more efficient algorithms, faster computers, and public concerns regarding radiation dose from CT have led to renewed interest in iterative approaches to CT reconstruction. Studies have shown that noise reduction by at least a factor of 2 is possible with the use of CT iterative reconstruction [18]. Post-processing iterative filtering techniques have also been investigated which may also afford some level of noise reduction without the loss of image quality. However, these post-processing approaches have only demonstrated modest noise reduction as compared to true iterative reconstruction approaches. This remains an emerging field, and it is expected that iterative reconstruction will become a standard approach to CT reconstruction in the near future leading to the opportunity for significant radiation dose reduction.

PET-MR

Simultaneous PET-MR is a novel and promising imaging modality that is generating substantial interest in the medical community while presenting many scientific challenges and opportunities. Unlike sequentially acquired whole-body PET/CT scans, the simultaneous acquisition of MR and PET data can be used to incorporate MR information (e.g., anatomical priors, motion, contrast enhancement, diffusion-weighted imaging, soft tissue characterization) with PET without the radiation dose associated with CT. In addition to halving the radiation dose associated with a PET/CT, simultaneous PET-MR offers another key advantage in the pediatric population: it obviates the need for separate (or longer) sedation/general anesthesia session that would be required for separately acquired PET and MR studies. We detail below some of the challenges and potentials of simultaneous PET-MR in the pediatric population.

PET-MR Instrumentation

Although proposed several years ago, the integration of PET and MR has remained, until recently, challenging due to the interference between the PET and MR components and due to the lack of space inside the MR bore. In order to overcome the effect of strong static magnetic field, gradient, and radiofrequency (RF) signals on the PET detectors, conventional photomultiplier tubes are replaced with avalanche photodiodes (APD), which are insensitive to strong magnetic fields and have good compactness. APDs measure the intensity of an optical signal and take advantage of the internal gain provided by ionization. The feasibility of using APDs for PET in a high magnetic field was first studied in 1998, and the first preclinical PET-MR scanner using LSO and APD detectors was reported in 2006.

One major disadvantage of presently available APDs is that they have two to three orders of magnitude lower gain than conventional PMTs and thus require sophisticated preamplifiers. APDs also suffer from limited timing resolution and cannot be used for time-of-flight (TOF) PET. In addition to modifications to PET instrumentation components, the advent of PET-MR has also required changes to some MR components to maintain PET image quality. For example, PET-compatible MR coils are configured to minimize attenuation of annihilation photons. An example is shown in Fig. 27.9. Sequential PET-MR systems have also been developed and are commercially available. Unlike the simultaneous PET-MR system, a sequential system does not require a major redesign of the PET system, as it is placed in line, adjacent to the MR system. This design does not allow simultaneous PET and MR acquisition; it allows for acquisition of co-registered PET and MR images acquired sequentially.

MR-Based Attenuation Correction

Accurate attenuation correction is critical to the introduction of PET-MR scanning of the abdomen. The full extent of the problem is seldom acknowledged, but experience has shown that even with PET/CT, it is difficult to obtain a valid attenuation correction in the face of subject movement. There are several active groups, exploring creative solution to the whole-body MR-based PET attenuation correction problems. One approach is to use atlas registration [19]. In order to obtain the attenuation map for an acquired MR image, a reference CT image can, in principle, be registered to the MR image using deformable inter-modality registration. Alternatively, a reference MR image, previously registered to a reference CT image, can be first registered to the MR image using deformable intra-modality registration followed by the same transformation of the reference CT image. Another approach, which may have potential for clinical use, is to segment an MR image into different tissue types and then assign the corresponding attenuation coefficients to them. This approach has been applied to both brain and whole-body imaging [20, 21]. Attenuation correction for MR coils can be achieved by co-registering a reference CT image of the coil to the MR image.

MR-Based Motion Correction

Contemporary whole-body PET cameras have an intrinsic spatial resolution of 3–4 mm. But as a practical matter, spatial resolution in pediatric body imaging is actually in the range of 6–10 mm, due to patient motion both voluntary and involuntary. Mechanical immobilization of pediatric patient helps, but voluntary movements on the scale of 1–5 mm still frequently occur. In body imaging, involuntary motion is substantial, with diaphragmatic excursion on the order of ~4 cm. Thus, the effects of respiration and organ motion are important sources of image degradation. This makes patient movement the most important cause of image degradation in PET body imaging. For example, hepatic lesions in the dome of the liver are easy to miss, due to respiratory motion. Even when detected, such lesions have an apparent standard uptake value (SUV) well below its true value. Simultaneous PET-MR offers an elegant solution to the motion problem. The motion field is used directly in the PET reconstruction, allowing nonrigid motion blurring to be completely removed without loss of SNR [22, 23].

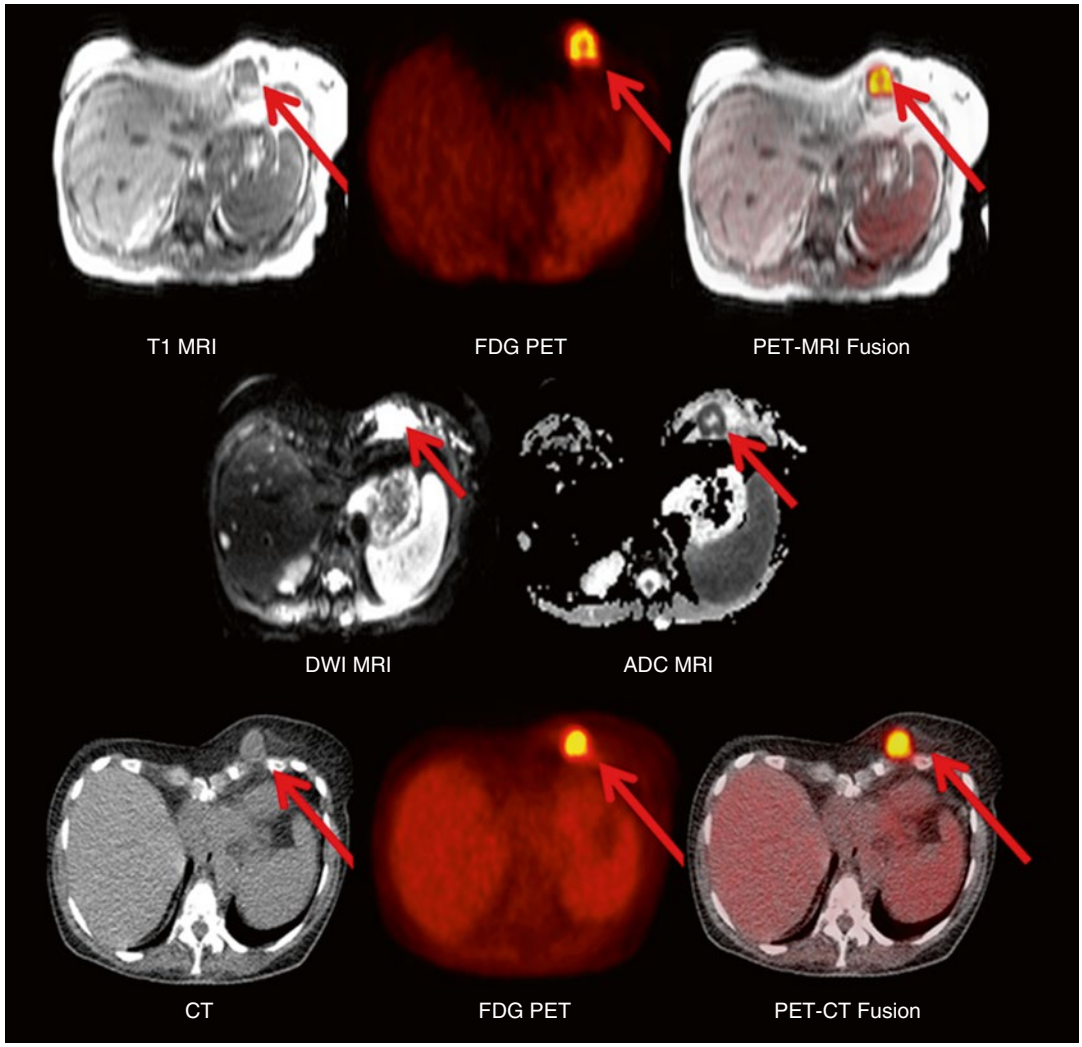

Fig. 27.9 PET-MR clinical example. *Top row* shows T1 MR and FDG PET of thorax acquired simultaneously using a hybrid PET-MR device. *Middle row* shows processed functional MR images. *Bottom row* shows PET study acquired in same patient

Summary

There have been a number of advances in nuclear medicine imaging in the past decade, particularly with regard to SPECT, PET, hybrid imaging, image processing, and tomographic reconstruction. Many of these advances can be applied to improve the quality of nuclear medicine imaging in children. Often this has led to imaging with higher sensitivity or image quality improvements with fewer counts allowing for the extension of advanced technologies to smaller children or the reduction of radiation dose to the patient while still providing high-quality clinical results. The application of nuclear medicine to children takes special care with respect to the approach to image acquisition, the choice of instrumentation including collimation, and the application of new processing and reconstruction techniques. A clear understanding of how these choices can enhance or hinder the quality of the nuclear medicine study is essential in these precious and challenging patients.

References

1. Snay ER, Treves ST, Fahey FH. Improved quality of pediatric 123I-MIBG images with medium-energy collimators. J Nucl Med Technol. 2011;39:100–4.
2. King MA, Doherty PW, Schwinger RB, Jacobs DA, Kidder RE, Miller TR. Fast count-dependent digital filtering of nuclear medicine images: concise communication. J Nucl Med. 1983;24:1039–45.
3. Wesolowski CA, Yahil A, Puetter RC, et al. Improved lesion detection from spatially adaptive, minimally complex, Pixon reconstruction of planar scintigraphic images. Comput Med Imaging Graph. 2005;29:65–81.
4. Hsiao E, Cao X, Zurakowsi D, Zukotynski K, Drubach L, Grant F, Yahil A, Vijay H, Davis RT, Fahey FH, Treves ST. Reduction in radiation dose in MAG3 renography by enhanced planar processing. Radiology. 2011;261:907–15.
5. Markelewicz R, Vitello M, Cao X, Zurakowski D, Zukotynski K, Drubach L, Grant F, Bar-Sever Z, Gelfand M, Treves ST. Dose reduction in newborns and infants undergoing hepatobiliary scintigraphy. Presented at Society of Nuclear Medicine annual meeting, Miami, FL, 2012.
6. Gelfand MJ, Parisi MT, Treves ST. Pediatric radiopharmaceutical administered doses: 2010 North American consensus guidelines. J Nucl Med. 2011; 52:318–22.
7. Kuhl DE, Edwards RQ. Image separation radioisotope scanning. Radiology. 1963;80:653–61.
8. Keyes Jr JW, Orlandea N, Heetderks WJ, Leonard PF, Rogers WL. The Humongotron – a scintillation-camera transaxial tomograph. J Nucl Med. 1977;18: 381–7.
9. Jaszczak RJ, Murphy PH, Huard D, et al. Radionuclide emission computed tomography of the head with Tc-99m and a scintillation camera. J Nucl Med. 1977;18:373–80.
10. Fahey FH, Harkness BA, Keyes Jr JW, et al. Sensitivity, resolution and image quality with a multihead SPECT camera. J Nucl Med. 1992;33:1859–63.
11. Garcia EV, Faber TL, Esteves FP. Cardiac dedicated ultrafast SPECT cameras: new designs and clinical implications. J Nucl Med. 2011;52:210–7.
12. Lange K, Carson R. EM reconstruction algorithms for emission and transmission tomography. J Comput Assist Tomogr. 1984;8:306–16.
13. Stansfield EC, Sheehy N, Zurakowski D, Vija AH, Fahey FH, Treves ST. Pediatric 99mTc-MDP bone SPECT with ordered subset expectation maximization iterative reconstruction with isotropic 3D resolution. Radiology. 2010;257:793–801.
14. Sheehy N, Tetrault T, Zurakowski D, Vija AH, Fahey FH, Treves ST. Pediatric 99mTc-DMSA SPECT using iterative reconstruction with isotropic resolution recovery: improved image quality and reduction in radiopharmaceutical administered activity. Radiology. 2009;251:511–6.
15. Fahey FH, Palmer MR, Strauss K, Zimmerman RE, Badawi R, Treves ST. Dosimetry and adequacy of CT-based attenuation correction for pediatric PET. Radiology. 2007;243:96–104.
16. Alessio AM, Kinahan PE, Manchanda V, et al. Weight-based, low-dose pediatric whole-body PET/CT protocols. J Nucl Med. 2009;50:1570–7.
17. Hurwitz LM, Yoshizumi TT, Goodman PC, Nelson RC, Toncheva G, Nguyen GB, Lowry C, Anderson-Evans C. Radiation dose savings for adult pulmonary embolus 64-MDCT using bismuth breast shields, lower peak kilovoltage, and automatic tube current modulation. AJR Am J Roentgenol. 2009;192:244–53.
18. Beister M, Kolditz D, Kalender WA. Iterative reconstruction methods in X-ray CT. Phys Med. 2012;28:94–108.
19. Beyer T, Weigert M, Quick HH, et al. MR-based attenuation correction for torso-PET/MR imaging: pitfalls in mapping MR to CT data. Eur J Nucl Med Mol Imaging. 2008;35:1142–6.
20. Martinez-Moller A, Souvatzoglou M, Delso G, et al. Tissue classification as a potential approach for attenuation correction in whole-body PET/MRI: evaluation with PET/CT data. J Nucl Med. 2009;50:520–6.
21. Schulz V, Torres-Espallardo I, Renisch S, et al. Automatic, three-segment, MR-based attenuation correction for whole-body PET/MR data. Eur J Nucl Med Mol Imaging. 2011;38:138–52.
22. Guérin B, Reese T, Cho S, Chun SY, Zhu X, Catana C, Alpert NM, El Fakhri G. Non-rigid PET motion compensation using tagged-MRI in simultaneous PET-MR imaging. Med Phys. 2011;38:3025–38.
23. Chun SY, Reese T, Guerin B, Catana C, Zhu X, Alpert N, El Fakhri G. MRI-based nonrigid motion correction in simultaneous PET/MRI. J Nucl Med. 2012;53: 1284–91. Featured cover article.

Radiation Exposures

28

Michael Stabin

The discoveries of radioactivity and ionizing radiation in the late nineteenth century created an unprecedented revolution in the medical sciences. The ability to noninvasively image internal structures of the body and the ability to treat diseases with radiation sources changed medicine forever, and the changes and improvements continue to this day. Soon after the discovery of the marvelous powers of radiation, we became aware of the possible deleterious effects on the human body of excessive radiation exposures. Effects on the eyes and skin were observed soon after protracted exposures, and in a short time, elevated leukemia rates were seen among radiologists [1]. Ionizing radiation is similar to electricity – its myriad of uses in our lives make it impossible to imagine a world without it, and when properly used it provides enormous benefits. Misuse, however, can result in injury or even death. As the majority of pediatric nuclear medicine studies are for diagnostic purposes, the levels of activity are low, and the risk of short-term ("nonstochastic") effects is not of concern. The focus is on the proper management of risks and benefits and avoidance of misadministrations. In therapeutic applications, the goal is to ensure effective treatment of disease while managing negative effects on normal tissues, often the active marrow. Chapter 31 deals specifically with dose reduction and optimization; this chapter will discuss methods and models for calculation of radiation dose for radiopharmaceuticals. Radiation dose from computed tomography (CT) will be briefly discussed as well, as positron emission tomography (PET) and single photon emission computed tomography (SPECT) studies are very commonly performed with a CT component, and the total radiation dose to the subject will be from both the nuclear medicine and CT components.

Dose Calculations

Radiation doses from internal emitters cannot be measured. Activity entering the body (in this case injected radiopharmaceuticals specially tailored to be taken up by particular organ systems) is widely distributed throughout the circulatory system and then deposits in particular organs, depending on the nature of the pharmaceutical (e.g., bone agents deposit in the skeleton and activity not taken up by bone is excreted fairly quickly in the urine). A few radiopharmaceuticals are administered orally or by inhalation, to image elements of the gastrointestinal (GI) or pulmonary regions. Due to both radioactive decay and biological removal, the activity in the organs of uptake decreases over time. At a given point in time, the dose rate to a

M. Stabin, PhD
Department of Radiology and Radiological Sciences,
Vanderbilt University Medical Center,
Nashville, TN, USA
e-mail: michael.stabin@vanderbilt.edu

S.T. Treves (ed.), *Pediatric Nuclear Medicine and Molecular Imaging*,
DOI 10.1007/978-1-4614-9551-2_28,

source organ with activity A_S can be calculated as [2]:

$$\dot{D}_T = \frac{k\, A_S \sum_i n_i\ E_i\ \phi_i\left(T \leftarrow S\right)}{m_T} \quad (28.1)$$

where $\dot{D}_T$ = absorbed dose rate in target organ T (Gy/s or rad/h)

A_S = activity in a source organ (MBq or μCi)

n_i = number of radiations with energy E_i emitted per nuclear transition

E_i = energy per radiation (MeV)

$\phi(T \leftarrow S)$ = fraction of energy emitted in a source that is absorbed in the target

m_T = mass of target region (kg or g)

k = some proportionality constant (Gy-kg/MBq-s-MeV or rad-g/μCi-h-MeV)

The radionuclide decays according to exponential processes:

$$A_S\left(t\right) = A_0 e^{-\lambda_p t} \quad (28.2)$$

where A_0 is the initial activity in the organ and λ_p = the *radiological* disappearance constant = $0.693/T_p$; T_p is the radionuclide half-life. Radiopharmaceuticals are removed from the body or certain organs also by exponential removal, in most cases. The rate of clearance of a *nonradioactive* substance that follows this rule can be shown as:

$$X\left(t\right) = X_0 e^{-\lambda_b t} \quad (28.3)$$

where $X(t)$ = the amount of the *nonradioactive* substance at time t

X_0 = the initial amount of substance X

λ_b = the *biological* disappearance constant = $0.693/T_b$

T_b = the *biological* halftime for removal

The biological halftime for removal is the same in concept as the radioactive (or physical) half-life; i.e., it is the time in which half of the material present at a given time is removed, but by biological clearance mechanisms, not radioactive decay. The two removal processes act in parallel, so the disappearance constants for the two processes can be added to give an "effective disappearance constant":

$$\lambda_e = \lambda_b + \lambda_p \quad (28.4)$$

where λ_e = effective disappearance constant

λ_p = radioactive (physical) decay constant

λ_b = biological disappearance constant

The "effective halftime" (T_e) is defined just as the other two halftimes, as $0.693/\lambda_e$; T_e is the time for half of the activity to be removed from the body or organ, by both physical decay and biological removal. Mathematically, the effective halftime is equal to the product of the two halftimes over their sum:

$$T_e = \frac{T_b \times T_p}{T_b + T_p} \quad (28.5)$$

To calculate the total dose over some time (usually from the time of administration to infinity) the time-activity curve for an organ must be integrated. The integral is often represented by the symbol $\tilde{A}$ (Fig. 28.1).

Common units for activity are Bq or MBq, and time may be given in seconds or hours, so $\tilde{A}$, the integral of the curve, will have units of, for example, Bq-s. One Bq-s is numerically equal to one nuclear transformation (or "disintegration"). For materials that cleared from the body or an organ by exponential processes, $\tilde{A}$ may be calculated as:

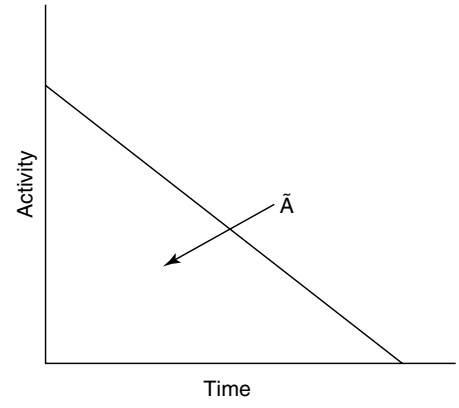

Fig. 28.1 A generalized time-activity curve for a radiopharmaceutical taken up in an organ. $\tilde{A}$ is the area under the curve ("cumulated activity")

$$\tilde{A}_S = \int_0^\infty A_S(t)\,\mathrm{d}t = \int_0^\infty A_0 \mathrm{e}^{-\lambda_e t}\,\mathrm{d}t = \frac{A_0}{\lambda_e} = 1.443 A_0 T_e \quad (28.6)$$

where A_0 is the initial activity in the organ, as above. The total dose over all time can then be given as:

$$D_T = \frac{k\tilde{A}_S \sum_i n_i\, E_i\, \phi_i(S \leftarrow T)}{m_T} \quad (28.7)$$

To complete the calculation, dose contributions from all source organs must be summed:

$$D_T = \frac{k \sum_S \tilde{A}_S \sum_i n_i\, E_i\, \phi_i(S \leftarrow T)}{m_T} \quad (28.8)$$

This looks like a complex math problem, but it can be considerably simplified. Everything in the equation except for $\tilde{A}$ can be combined into a term called the "dose factor" (DF) [2]. This factor contains all of the physics parameters needed for a calculation, and large compilations of these DFs are made available in Internet resources and software tools by the RAdiation Dose Assessment Resource (RADAR) Task Group of the Society of Nuclear Medicine and Molecular Imaging (SNMMI). Pharmaceutical kinetics are specific to each compound and must be determined via biokinetic studies using animals (preclinical) or human subjects (clinical). When the kinetics of each source organ (S) are determined, they may be combined with the appropriate DF values to calculate the dose to all target organs (T):

$$D_T = \sum_S \tilde{A}_S \times DF(S \leftarrow T) \quad (28.9)$$

There are no shortcuts to obtaining good data to determine the important organs of uptake and their kinetics. When a new radiopharmaceutical is developed, data must be obtained at several times after administration to observe the kinetics in the source organs (often there is more than one phase of clearance, a fast early phase with a short T_e, and one or more slower phases of clearance, each with their own T_e). For each phase, one needs a minimum of two data points to characterize the kinetic equation for that phase [3]; then the time integrals for all phases are added to obtain the total Ã. But once all of the data are obtained, they may be entered into the OLINDA/EXM personal computer software [4], which looks up the DF values and performs all of the repetitive calculations to provide dose values for all target organs.

Specialized Kinetic Models

For a few organs, typical biokinetic models employing simple exponential functions, as described above, are replaced with specialized models that define the unique behavior of these organs. Specifically, the urinary bladder and GI tract, involved in the elimination of radiopharmaceuticals from the body, are given special treatment. Activity eliminated from the body via the kidney-urine pathway is generally described by one or more exponential terms; however, the urinary bladder fills and empties at fairly regular intervals and thus has a complicated time-activity curve that cannot generally be characterized by fitting to a simple function. If the voiding intervals can be assumed to be regular, Cloutier et al. showed how a single equation could be used to estimate the number of disintegrations occurring in the bladder, based on the fractions of total body activity and biological halftimes with which they are removed [5]. This model is used in the OLINDA/EXM software [4], in a way that the user has to only enter this information and choose a bladder voiding interval. Bladder voiding is never completely regular, but a reasonable average interval of about 3.5 h may be assumed as a standard number, and experimentation can be done easily with the software to see how the bladder dose (and dose to other nearby organs) may change with more frequent assumed voiding intervals. For the GI tract, activity may be assumed to move through various defined compartments (stomach, intestines, and colon) with standard

rates. Activity excreted in the biliary pathway may enter the small intestine, while orally administered radiopharmaceuticals enter the stomach. The standard four-compartment model used for years in the OLINDA/EXM code has been recently updated to reflect more complexity (and thus realism) [6]. Explicit models are now given for adults and children, as well as for different types of materials (i.e., caloric and noncaloric liquids and solids). In these models, users need to cite a fraction of administered activity assumed to follow this pathway and choose the point of entry into the model (stomach or small intestine).

Effective Dose

Absorbed doses are calculated in Gy (or rad, 1 Gy = 100 rad). *Equivalent doses* (Sv or rem) are calculated easily as the absorbed dose multiplied by the appropriate *radiation weighting factor* (w_R). Radiation weighting factors are unity (1.0) for photons and electrons, so absorbed doses in Gy are numerically equal to equivalent doses in Sv. For alpha particles, however, the currently value of *w*R recommended by the International Commission on Radiological Protection (ICRP) is 20, so 1 mGy = 20 mSv [7]. Doses to individual organs are calculated for radiopharmaceuticals, to see which organs get the highest doses. Then an overall evaluation of the dose to all organs may be calculated with a quantity also defined by the ICRP, called *effective dose*. Certain organs or organ systems have been assigned dimensionless "tissue weighting factors," w_T, which are assumed to relate to their differing radiosensitivity for expressing stochastic effects (i.e., fatal cancers or genetic defects). The numerical values of these tissue weighting factors have been recommended three times by the ICRP, as new information about expressed radiation effects in human populations (most notably the survivors of the Japanese bombings) has become available (Table 28.1). Multiplying each organ's equivalent dose by its assigned weighting factor gives a "weighted dose equivalent." The *sum of weighted dose equivalents* for a given dose scenario gives the effective dose:

Table 28.1 Weighting factors recommended by the ICRPfor calculation of "effective dose"

Organ	ICRP 30 [8]	ICRP 60 [9]	ICRP 103 [7]
Gonads	0.25	0.20	0.08
Red marrow	0.12	0.12	0.12
Colon		0.12	0.12
Lungs	0.12	0.12	0.12
Stomach		0.12	0.12
Bladder		0.05	0.04
Breasts	0.15	0.05	0.12
Liver		0.05	0.04
Esophagus		0.05	0.04
Thyroid	0.03	0.05	0.04
Skin		0.01	0.01
Bone surfaces	0.03	0.01	0.01
Brain			0.01
Salivary glands			0.01
Remainder	0.30	0.05	0.12

$$E = \sum_T H_T \times w_T \qquad (28.10)$$

For example, calculation of the effective dose using the tissue weighting factors from ICRP 103 [7] and given individual organ equivalent doses (note that all weighting factors are not used and thus do not sum to 1.0) are shown in Table 28.2.

The effective dose is meant to represent the equivalent dose that, if received uniformly by the whole body, would result in the same total risk as that actually incurred by a given actual nonuniform irradiation. It is *not* the equivalent dose that one might calculate for the "whole body," using dose conversion factors for the total body, which average the energy absorbed in all organs over the mass of the total body; therefore this is not a very useful quantity in nuclear medicine applications. The design of radiopharmaceuticals causes them to be specifically concentrated in particular organs and to have fairly low uptake in most other tissues. For example, consider a case in which 35 % of ^{131}I is taken up in the thyroid, and assume the other 65 % is uniformly distributed in all other tissues. Assuming an effective halftime in the thyroid of 5 days, the cumulated activity is $1.443 \times 0.35 \times 5$ days $\times$ 24 h/day $\times$ 3,600 s/h = 2.18×10^5

Table 28.2 Calculation of the effective dose using the tissue weighting factors from ICRP 103and given individual organ equivalent doses

Organ	Weighting Factor	Equivalent Dose (mSv)	Weighted dose Equivalent (mSv)
Liver	0.04	0.50	0.020
Ovaries	0.08	0.25	0.020
Red marrow	0.12	0.40	0.048
Bone surfaces	0.01	0.55	0.0055
Thyroid	0.04	0.10	0.0040
Total (effective dose)			0.0975

s (Bq-s per Bq administered). The DF for thyroid ← thyroid for ^{131}I is 1.59×10^{-3} mGy/MBq-s, so the thyroid will get 3.47×10^{2} mGy/MBq administered. Administration of 3.7 MBq would result in 1.3×10^{3} mGy or 1.3 Gy to the thyroid. The other 65 %, uniformly distributed in the rest of the body will receive about 0.054 mGy. If we take all of the energy deposited in the thyroid and divide it by the mass of the tissues of the whole body, we get a "whole body dose" from this component of about 0.37 mGy. Adding it to the 0.054 mGy these tissues received from the 65 %, we get a "whole body dose" of 0.42 mGy, which is a factor of almost seven times what tissues other than thyroid actually received and is not meaningful, as it has no relation to the actual doses received by any real tissue in the body. The thyroid received about 1.3 Gy, and "other tissues" received about 0.054 mGy. If the body is more or less uniformly irradiated (e.g., from external irradiation fields, or for the few radionuclides that are uniformly distributed throughout the body, such as $^{3}H_2O$ or ^{137}Cs), all tissues and the body as a whole receive about the same level of dose, and "whole body dose" may be a useful number. This is almost never the case in nuclear medicine, so reporting of "whole body dose" is not useful and may be misleading, as shown above. We should consider the actual dose received by the organs receiving the highest doses and the effective dose for an overall dose number to express the total exposure. It is essential to note, however, that effective dose should (1) *never* be calculated for therapeutic applications of radiopharmaceuticals and (2) *never* be assumed to apply to any individual subject – it is intended to assess doses to populations, not individuals.

Anthropomorphic Models (Phantoms)

To obtain values of $\phi(T \leftarrow S)$ for photons, we need models of the body and its organs. We normally assume that all electron and alpha energy is absorbed where it is emitted (with a few special exceptions), so $\phi(S \leftarrow S) = 1$ and $\phi(T \leftarrow S)$ for all other values of T is set to zero. For photons, however, all values of $\phi(T \leftarrow S)$ will be between 0 and 1 for all sources and targets and are not easy to calculate. For several decades the stylized body models (Fig. 28.2, left) were used with Monte Carlo transport codes to calculate and tabulate values of $\phi(T \leftarrow S)$ for photons starting in all major organs of the body and the whole body. Now, the RADAR Task Group has defined a series of reference adult, pediatric, and pregnant female body models based on a surface rendering technique called Nonuniform Rational B-Splines (NURBS) that provide a much more realistic description of the body and its organs [10]. The numerical values of most absorbed fractions did not change dramatically, so overall dose estimates did not change profoundly, but the models are clearly superior in quality and realism.

Standardized Radiopharmaceutical Dose Estimates

When new radiopharmaceuticals are developed, new data must be developed to determine the radiation dosimetry of the agents, as part of the overall safety and efficacy evaluations required by the US Food and Drug Administration (FDA) [11]. Preclinical data obtained in some animal species may be extrapolated by various methods to obtain human dose estimates, and then data is gathered in human volunteers or patients to obtain clinical estimates of human radiation dose [11]. Doses are calculated using the standardized

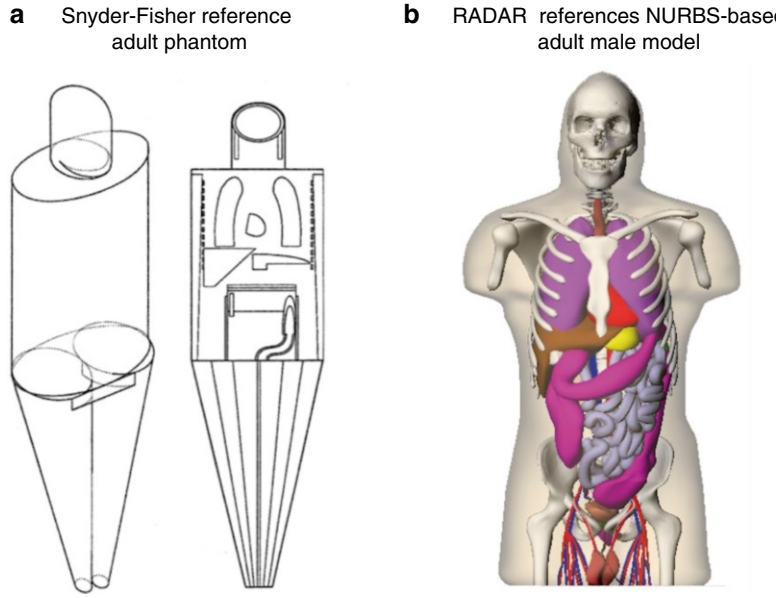

Fig. 28.2 (**a**) Snyder-Fisher reference adult phantom and (**b**) RADAR reference NURBS-based adult male model

anthropomorphic phantoms described in the previous section; the standard models defined for many years are for reference adults (male ~70 kg, female ~57 kg) and children of age 15 years, 10 years, 5 years, 1 year, and newborn. In many cases, there may be more than one study in which the kinetics were established. A radiopharmaceutical developer will typically engage several nuclear medicine centers in a multicenter clinical trial to develop the data needed for an FDA submission. These data may or may not ultimately be publicly released in open literature publications. Often, however, independent researchers may as well undertake studies in their own centers and publish the results independently. The Medical Internal Radiation Dose (MIRD) Committee of the SNMMI has published about 20 reports attempting to define standardized kinetics for individual radiopharmaceuticals [11]. The most definitive work, however, has been done by the ICRP Task Group on Radiopharmaceutical Dosimetry, which has published standardized dose estimates for hundreds of radiopharmaceuticals in a series of publications since 1988 [12–14]. They scan the published literature, including MIRD reports, if available, and in some cases unpublished data that they may have access to. They attempt to resolve possible conflicts in different reported values and present a standardized model that represents the best available understanding of the biokinetics of the compounds. They show the model for the data as initial fractions of uptake in important source organs, associated biological halftimes, and then develop tables of standardized organ dose estimates and effective doses for the reference adult and pediatric models. For example, the standard model for ^{99m}Tc-macroaggregated albumin (MAA) was given as shown in Table 28.3 [13].

Table 28.3 Standard model for ^{99m}Tc-macroaggregated albumin (MAA)

Source organ	F_S	T	a	$\tilde{A}_S/A_0$
Total body (excluding bladder contents)	1.0			7.61 h
Lungs	1.0	6 h 3 days	0.85 0.15	4.89 h
Liver	0.25	6 h 5 days	−1.0 1.0	1.04 h
Kidneys	1.0			1.07 min
Bladder contents	1.0			13.0 min

In this model, activity injected is assumed to pass first through the lungs, which exhibit a bi-exponential clearance curve, 85 % with a 6 h T_b and 15 % with a 3-day T_b. Then, 25 % of the activity is taken up by liver, which also exhibits a bi-exponential uptake and retention curve, the uptake

phase has a T_b of 6 h (the negating coefficient indicates that it is the uptake phase) and an elimination T_b of 5 days. The other 75 % is eliminated from the body with an assumed standard 0.25-day T_b; the kidneys and bladder content kinetics are determined from a special kinetic model (described above). Finally, the values of $\tilde{A}_S/A_0$ are given in units of time; really these are cumulated activity values per unit of administered activity (e.g., Bq-h/Bq administered). These values were referred to for many years as "residence time," but this caused considerable confusion for many, as "residence time" also means average time for a tracer in a system, and these normalized cumulated activity values do not reflect this. The MIRD Committee has adopted the term "time-integrated activity coefficient" to describe this term [15]; the RADAR Task Group refers to "normalized number of disintegrations" in source organs [2]. Standardized dose estimate tables in the ICRP publications are typically shown as in Table 28.4.

The RADAR web site (www.doseinfo-radar.com) has diverse and abundant data on standardized dose methods, models, and results. One page contains standardized dose estimates for the most important radiopharmaceuticals, usually based on the ICRP models, but sometimes using other sources of information if the ICRP models are not the most up to date. For adults, typical amounts of administered activity were chosen, and doses based on the best standard model are given for the first, second, and third highest-dose organs, gonads, and marrow and effective doses. For pediatric subjects, just effective doses are given (Table 28.5).

Table 28.4 Absorbed doses for ^{99m}Tc-labelled MAA, as shown in ICRP Publication 80

	Absorbed does per unit activity administered (mGy/MBq)				
Organ	Adult	15 years	10 years	5 years	1 year
Adrenals	6.8E–03	8.8E–03	1.3E–02	1.9E–02	3.1E–02
Bladder	8.7E–03	1.1E–02	1.4E–02	1.6E–02	3.0E–02
Bone surfaces	5.1E–03	6.4E–03	9.1E–03	1.4E–02	2.6E–02
Brain	9.2E–04	1.2E–03	2.0E–03	3.2E–02	5.5E–03
Breast	5.0E–03	5.6E–03	9.9E–03	1.4E–02	2.1E–02
Gall bladder	5.6E–03	7.0E–03	1.0E–02	1.6E–02	2.4E–02
GI–tract					
Stomach	3.7E–03	5.2E–03	8.0E–03	1.2E–02	2.0E–02
SI	2.0E–03	2.6E–03	4.3E–03	6.8E–03	1.2E–02
Colon	1.9E–03	2.6E–03	4.3E–03	6.9E–03	1.2E–02
(ULI	2.2E–03	2.9E–03	5.0E–03	8.3E–03	1.4E–02)
(LLI	1.6E–03	2.1E–03	3.3E–03	5.0E–03	9.5E–03)
Heart	9.6E–03	1.3E–02	1.8E–02	2.5E–02	3.8E–02
Kidneys	3.7E–03	4.8E–03	7.2E–03	1.1E–02	1.8E–02
Liver	1.6E–02	2.1E–02	3.0E–02	4.2E–02	7.4E–02
Lungs	6.6E–02	9.7E–02	1.3E–01	2.0E–01	3.9E–01
Muscles	2.8E–03	3.7E–03	5.2E–03	7.7E–03	1.4E–02
Oesophagus	6.1E–03	7.7E–03	1.1E–02	1.5E–02	2.2E–02
Ovaries	1.8E–03	2.3E–03	3.5E–03	5.4E–03	1.0E–02
Pancreas	5.6E–03	7.5E–03	1.1E–02	1.7E–02	2.9E–02
Red marrow	3.2E–03	3.8E–03	5.3E–03	7.2E–03	1.2E–02
Skin	1.5E–03	1.7E–03	2.7E–03	4.3E–03	7.8E–03
Spleen	4.1E–03	5.5E–03	8.3E–03	1.3E–02	2.2E–02
Testes	1.1E–03	1.4E–03	2.2E–03	3.3E–03	6.2E–03
Thymus	6.1E–03	7.7E–03	1.1E–02	1.5E–02	2.2E–02
Thyroids	2.5E–03	3.3E–03	5.7E–03	9.0E–03	1.6E–02
Uterus	2.2E–03	2.8E–03	4.2E–03	6.0E–03	1.1E–02
Remaining organs	2.8E–03	3.6E–03	5.0E–03	7.4E–03	1.3E–02
Effective dose (mSv/MBq)	**1.1E–02**	**1.6E–02**	**2.3E–02**	**3.4E–02**	**6.3E–02**

Table 28.5 Standardized effective dose values for pediatric subjects for selected radiopharmaceuticals

	15 years old		10 years old		5 years old		1 year old	
	mSv/MBq	rem/mCi	mSv/MBq	rem/mCi	mSv/MBq	rem/mCi	mSv/MBq	rem/mCi
Methyl-C-11 thymidine	0.0044	0.016	0.0068	0.025	0.011	0.041	0.020	0.074
2-C-11 thymidine	0.0034	0.013	0.0053	0.020	0.0084	0.031	0.016	0.059
O-15 water	0.0014	0.005	0.0023	0.009	0.0038	0.014	0.0077	0.028
F-18 fluorodeoxyglucose	0.024	0.089	0.037	0.14	0.056	0.21	0.095	0.35
Ga-67 citrate	0.130	0.48	0.20	0.74	0.33	1.2	0.640	2.4
Rb-82[a]	0.0017	0.0063	0.0036	0.013	0.0058	0.013	0.012	0.044
I-123 sodium iodide (0 % uptake)	0.016	0.059	0.024	0.089	0.037	0.14	0.067	0.25
I-123 sodium iodide (5 % uptake)	0.053	0.20	0.080	0.30	0.150	0.56	0.290	1.1
I-123 sodium iodide (15 % uptake)	0.11	0.41	0.17	0.63	0.35	1.3	0.65	2.4
I-123 sodium iodide (25 % Uptake)	0.17	0.63	0.26	0.96	0.54	2.0	1.0	3.7
I-123 sodium iodide (35 % uptake)	0.23	0.85	0.35	1.3	0.74	2.7	1.4	5.2
I-123 sodium iodide (45 % uptake)	0.29	1.1	0.44	1.6	0.94	3.5	1.8	6.7
I-123 sodium iodide (55 % uptake)	0.35	1.3	0.53	2.0	1.1	4.1	2.1	7.8
I-131 sodium iodide (0 % uptake)	0.088	0.33	0.14	0.52	0.21	0.78	0.4	1.5
I-131 sodium iodide (5 % uptake)	3.5	13	5.3	20	11	41	21	78
I-131 sodium iodide (15 % uptake)	10	37	15	56	34	130	62	230
I-131 sodium iodide (25 % uptake)	17	63	25	93	56	210	100	370
I-131 sodium iodide (35 % uptake)	24	89	36	133	78	290	140	520
I-131 sodium iodide (45 % uptake)	31	115	46	170	100	370	180	670
I-131 sodium iodide (55 % uptake)	37	137	56	210	120	440	220	810
In-111 DTPA – normal renal function	0.031	0.12	0.045	0.17	0.067	0.25	0.12	0.44
In-111 DTPA – abnormal renal function	0.059	0.22	0.088	0.33	0.13	0.48	0.23	0.85
In-111 platelets	0.93	3.4	1.4	5.2	2.1	7.8	3.7	14
In-111 white blood cells	0.79	2.9	1.2	4.4	1.8	6.7	3.2	12
In-111 pentatreotide also known as Octreoscan	0.071	0.26	0.10	0.37	0.16	0.59	0.28	1.0
Tc-99m disofenin also known as HIDA (iminodiacetic acid)	0.021	0.078	0.029	0.11	0.045	0.17	0.10	0.37
Tc-99m DMSA (dimercaptosuccinic acid) also known as succimer	0.011	0.041	0.015	0.056	0.021	0.078	0.037	0.14

Tc-99m exametazime also known as Ceretec and HMPAO	0.011	0.041	0.017	0.063	0.027	0.100	0.049	0.18
Tc-99m macroaggregated albumin (MAA)	0.016	0.059	0.023	0.085	0.034	0.13	0.063	0.23
Tc-99m medronate also known as Tc-99m Methylene diphosphonate (MDP)	0.0070	0.026	0.011	0.041	0.014	0.052	0.027	0.10
Tc-99m mertiatide also known as MAG3	0.0090	0.033	0.012	0.044	0.012	0.044	0.022	0.081
Tc-99m bicisate also known as ECD and Neurolite	0.0099	0.036	0.015	0.056	0.022	0.081	0.040	0.15
Tc-99m pentetate also known as Tc-99m DTPA	0.0062	0.023	0.0082	0.030	0.0090	0.033	0.016	0.059
Tc-99m pyrophosphate	0.0070	0.026	0.011	0.041	0.014	0.052	0.027	0.100
Tc-99m red blood cells	0.0089	0.033	0.014	0.052	0.021	0.078	0.039	0.144
Tc-99 sestamibi also known as Cardiolite (rest)	0.012	0.044	0.018	0.067	0.028	0.104	0.053	0.196
Tc-99 Sestamibi also known as Cardiolite (stress)	0.010	0.037	0.016	0.059	0.023	0.085	0.045	0.167
Tc-99m sodium pertechnetate	0.017	0.063	0.026	0.096	0.042	0.16	0.079	0.29
Tc-99m sulfur colloid	0.012	0.044	0.018	0.067	0.028	0.10	0.050	0.18
Tc-99m tetrofosmin also known as Myoview (rest)	0.0088	0.033	0.013	0.048	0.021	0.078	0.039	0.14
Tc-99m tetrofosmin also known as Myoview (stress)	0.0088	0.033	0.013	0.048	0.021	0.078	0.039	0.14
Tl-201 thallous chloride	0.20	0.74	0.56	2.1	0.79	2.9	1.3	4.8

[a]International Commission on Radiological Protection Task Group on Radiopharmaceutical Dosimetry, 2013, unpublished data

The Pregnant Patient

Pregnancy is of course less frequently encountered in pediatric populations than in the general adult population of nuclear medicine patients, but it may occur. Special anthropomorphic models for the pregnant woman in early pregnancy and at 3, 6, and 9 months' gestation were developed by Stabin et al. in 1995 [16], in the style of the Cristy/Eckerman phantom series, and were updated with realistic, image-based models by Xu et al. [17]. Table 28.6 gives standardized dose estimates for many radiopharmaceuticals calculated by Russell et al. [18] with the Stabin et al. phantom series.

Other Sources of Exposure

This book focuses on nuclear medicine examinations involving pediatric subjects: however, the care of individual subjects may involve exposure to other forms of ionizing radiation, including plain film x-ray imaging and computed tomography (CT). Assessment of radiation safety, risk, and dose reduction will be the subjects of other chapters in this book. A brief discussion of radiation doses from these other ionizing modalities was thought to be reasonable to put the entire radiation exposure of a pediatric subject in perspective. The effective dose values in Table 28.6 are given per unit administered activity of any given radiopharmaceutical. Often, administrations of radiopharmaceuticals to children are given on a per unit body weight basis, with some minimum amount of activity needed for a scan of reasonable quality. Treves et al. [19] surveyed a number of pediatric hospitals in North America and tried to characterize typical levels of administered activity for many pediatric examinations and the range of values that people may give. The ranges were surprising at times, but the median and mean values were helpful in understanding what reasonable levels of activity might be. For example, for ^{18}F-FDG they found minimum and maximum values of activity/mass to be 5.2–7.4 MBq/kg, with minimum and maximum activity values ranging from 18 to 74 and 370 to 555 MBq, respectively. So for a 10-year-old, for example, the lowest activity given might be around 40 MBq and the highest around 400 MBq, resulting in estimated effective doses of 0.037 mSv/MBq × 40 MBq = 1.5–0.037 mSv/MBq × 400 MBq = 15 mSv. Calculating effective doses from CT examinations is more complicated, as often only part of the body is imaged. The principal dose quantity in CT dose calculations is the computed tomography dose index (CTDI), given as:

$$\mathrm{CTDI} = \frac{1}{NT}\int_{-\infty}^{\infty} D(z)\,\mathrm{d}z$$

Here N is the number of tomographic sections imaged in a single axial scan, T is the width of the tomographic section along the axis of rotation imaged by one data channel, and $D(z)$ is the radiation dose profile along the axis of rotation (z). The CTDI may be converted into a "dose-length product" (DLP), and the American Association of Physicists in Medicine (AAPM) has provided factors that allow conversion of DLP values to effective dose [20]. Effective dose values quoted for typical CT exams vary from 1 to 2 mSv for head exams to around ~5 mSv for many exams of the body. The so-called "scout" CTs used prior to patient imaging are of very low dose and do not contribute substantially to a patient's overall dose history. However, if several PET, CT, and/or PET/CT scans are done on the same subject, doses can add up to levels that call for consideration of lowering radiopharmaceutical activity levels and CT examination settings. It is always prudent to keep radiation exposures as low as possible, for example, using lower mAs settings for smaller and thinner patients and limiting radiopharmaceutical dosages as possible [21]; this is discussed in Chap. 31 . On the other hand, one of the worst things for the patient is to administer *too little radiation*, so that no diagnostic benefit was received and the study has to be repeated. It is important to always remember that the direct benefits to the patient population significantly outweigh any theoretical cancer risks [22]. Understanding and communication of all risks and benefits of any medical procedure involving ionizing radiation is an essential part of the patient care process.

Table 28.6 Absorbed dose estimates to the embryo/fetus per unit activity of radiopharmaceutical administered to the mother (shading indicates maternal and fetal self-dose contributions)

	Early	3 months	6 months	9 months
Radiopharmaceutical	mGy/MBq	mGy/MBq	mGy/MBq	mGy/MBq
^{57}Co vitamin B-1, normal flushing	1.0×10^{0}	6.8×10^{-1}	8.4×10^{-1}	8.8×10^{-1}
^{57}Co vitamin B-12, normal – no flushing	1.5×10^{0}	1.0×10^{0}	1.2×10^{0}	1.3×10^{0}
^{57}Co vitamin B-12, PA – flushing	2.1×10^{-1}	1.7×10^{-1}	1.7×10^{-1}	1.5×10^{-1}
^{57}Co vitamin B-12, PA – no flushing	2.8×10^{-1}	2.1×10^{-1}	2.2×10^{-1}	2.0×10^{-1}
^{58}Co vitamin B-12, normal flushing	2.5×10^{0}	1.9×10^{0}	2.1×10^{0}	2.1×10^{0}
^{58}Co vitamin B-12, normal – no flushing	3.7×10^{0}	2.8×10^{0}	3.1×10^{0}	3.1×10^{0}
^{58}Co vitamin B-12, PA – flushing	8.3×10^{-1}	7.4×10^{-1}	6.4×10^{-1}	4.8×10^{-1}
^{58}Co vitamin B-12, PA – no flushing	9.8×10^{-1}	8.5×10^{-1}	7.6×10^{-1}	6.0×10^{-1}
^{60}Co vitamin B-12, normal flushing	3.7×10^{1}	2.8×10^{1}	3.1×10^{1}	3.2×10^{1}
^{60}Co vitamin B-12, normal – no flushing	5.5×10^{1}	4.2×10^{1}	4.7×10^{1}	4.7×10^{1}
^{60}Co vitamin B-12, PA – flushing	5.9×10^{0}	4.7×10^{0}	4.8×10^{0}	4.5×10^{0}
^{60}Co vitamin B-12, PA – no flushing	8.3×10^{0}	6.5×10^{0}	6.8×10^{0}	6.5×10^{0}
^{18}F FDG	2.2×10^{-2}	2.2×10^{-2}	1.7×10^{-2}	1.7×10^{-2}
^{18}F sodium fluoride	2.2×10^{-2}	1.7×10^{-2}	7.5×10^{-3}	6.8×10^{-3}
^{67}Ga citrate	9.3×10^{-2}	2.0×10^{-1}	1.8×10^{-1}	1.3×10^{-1}
^{123}I hippuran	3.1×10^{-2}	2.4×10^{-2}	8.4×10^{-3}	7.9×10^{-3}
^{123}I IMP	1.9×10^{-2}	1.1×10^{-2}	7.1×10^{-3}	5.9×10^{-3}
^{123}I MIBG	1.8×10^{-2}	1.2×10^{-2}	6.8×10^{-3}	6.2×10^{-3}
^{123}I sodium iodide	2.0×10^{-2}	1.4×10^{-2}	1.1×10^{-2}	9.8×10^{-3}
^{124}I sodium iodide	1.4×10^{-1}	1.0×10^{-1}	5.9×10^{-2}	4.6×10^{-2}
^{125}I HSA	2.5×10^{-1}	7.8×10^{-2}	3.8×10^{-2}	2.6×10^{-2}
^{125}I IMP	3.2×10^{-2}	1.3×10^{-2}	4.8×10^{-3}	3.6×10^{-3}
^{125}I MIBG	2.6×10^{-2}	1.1×10^{-2}	4.1×10^{-3}	3.4×10^{-3}
^{125}I sodium iodide	1.8×10^{-2}	9.5×10^{-3}	3.5×10^{-3}	2.3×10^{-3}
^{126}I sodium iodide	7.8×10^{-2}	5.1×10^{-2}	3.2×10^{-2}	2.6×10^{-2}
^{130}I sodium iodide	1.8×10^{-1}	1.3×10^{-1}	7.6×10^{-2}	5.7×10^{-2}
^{131}I hippuran	6.4×10^{-2}	5.0×10^{-2}	1.9×10^{-2}	1.8×10^{-2}
^{131}I HSA	5.2×10^{-1}	1.8×10^{-1}	1.6×10^{-1}	1.3×10^{-1}
^{131}I MAA	6.7×10^{-2}	4.2×10^{-2}	4.0×10^{-2}	4.2×10^{-2}
^{131}I MIBG	1.1×10^{-1}	5.4×10^{-2}	3.8×10^{-2}	3.5×10^{-2}
^{131}I sodium iodide	7.2×10^{-2}	6.8×10^{-2}	2.3×10^{-1}	2.7×10^{-1}
^{131}I rose bengal	2.2×10^{-1}	2.2×10^{-1}	1.6×10^{-1}	9.0×10^{-2}
^{111}In DTPA	6.5×10^{-2}	4.8×10^{-2}	2.0×10^{-2}	1.8×10^{-2}
^{111}In pentetreotide	8.2×10^{-2}	6.0×10^{-2}	3.5×10^{-2}	3.1×10^{-2}
^{111}In platelets	1.7×10^{-1}	1.1×10^{-1}	9.9×10^{-2}	8.9×10^{-2}
^{111}In red blood cells	2.2×10^{-1}	1.3×10^{-1}	1.1×10^{-1}	8.6×10^{-2}
^{111}In white blood cells	1.3×10^{-1}	9.6×10^{-2}	9.6×10^{-2}	9.4×10^{-2}
^{99m}Tc albumin microspheres	4.1×10^{-3}	3.0×10^{-3}	2.5×10^{-3}	2.1×10^{-3}
^{99m}Tc disofenin	1.7×10^{-2}	1.5×10^{-2}	1.2×10^{-2}	6.7×10^{-3}
^{99m}Tc DMSA	5.1×10^{-3}	4.7×10^{-3}	4.0×10^{-3}	3.4×10^{-3}
^{99m}Tc DTPA	1.2×10^{-2}	8.7×10^{-3}	4.1×10^{-3}	4.7×10^{-3}
^{99m}Tc DTPA aerosol	5.8×10^{-3}	4.3×10^{-3}	2.3×10^{-3}	3.0×10^{-3}
^{99m}Tc glucoheptonate	1.2×10^{-2}	1.1×10^{-2}	5.3×10^{-3}	4.6×10^{-3}
^{99m}Tc HDP	5.2×10^{-3}	5.4×10^{-3}	3.0×10^{-3}	2.5×10^{-3}
^{99m}Tc HEDP	7.2×10^{-3}	5.2×10^{-3}	2.7×10^{-3}	2.4×10^{-3}
^{99m}Tc HMPAO	8.7×10^{-3}	6.7×10^{-3}	4.8×10^{-3}	3.6×10^{-3}

(continued)

Table 28.6 (continued)

Radiopharmaceutical	Early mGy/MBq	3 months mGy/MBq	6 months mGy/MBq	9 months mGy/MBq
^{99m}Tc human serum albumin	5.1×10^{-3}	3.0×10^{-3}	2.6×10^{-3}	2.2×10^{-3}
^{99m}Tc MAA	2.8×10^{-3}	4.0×10^{-3}	5.0×10^{-3}	4.0×10^{-3}
^{99m}Tc MAG3	1.8×10^{-2}	1.4×10^{-2}	5.5×10^{-3}	5.2×10^{-3}
^{99m}Tc MDP	6.1×10^{-3}	5.4×10^{-3}	2.7×10^{-3}	2.4×10^{-3}
^{99m}Tc MIBI – rest	1.5×10^{-2}	1.2×10^{-2}	8.4×10^{-3}	5.4×10^{-3}
^{99m}Tc MIBI – stress	1.2×10^{-2}	9.5×10^{-3}	6.9×10^{-3}	4.4×10^{-3}
^{99m}Tc pertechnetate	1.1×10^{-2}	2.2×10^{-2}	1.4×10^{-2}	9.3×10^{-3}
^{99m}Tc PYP	6.0×10^{-3}	6.6×10^{-3}	3.6×10^{-3}	2.9×10^{-3}
^{99m}Tc RBC – heat treated	1.7×10^{-3}	1.6×10^{-3}	2.1×10^{-3}	2.2×10^{-3}
^{99m}Tc RBC – in vitro	6.8×10^{-3}	4.7×10^{-3}	3.4×10^{-3}	2.8×10^{-3}
^{99m}Tc RBC – in vivo	6.4×10^{-3}	4.3×10^{-3}	3.3×10^{-3}	2.7×10^{-3}
^{99m}Tc sulfur colloid – normal	1.8×10^{-3}	2.1×10^{-3}	3.2×10^{-3}	3.7×10^{-3}
^{99m}Tc sulfur colloid – liver disease	3.2×10^{-3}	2.5×10^{-3}	2.8×10^{-3}	2.8×10^{-3}
^{99m}Tc teboroxime	8.9×10^{-3}	7.1×10^{-3}	5.8×10^{-3}	3.7×10^{-3}
^{99m}Tc tetrofosmin	9.6×10^{-3}	7.0×10^{-3}	5.4×10^{-3}	3.6×10^{-3}
^{99m}Tc white blood cells	3.8×10^{-3}	2.8×10^{-3}	2.9×10^{-3}	2.8×10^{-3}
^{201}Tl chloride	9.7×10^{-2}	5.8×10^{-2}	4.7×10^{-2}	2.7×10^{-2}
^{127}Xe, 5 min rebreathing, 5 l spirometer volume	4.3×10^{-4}	2.4×10^{-4}	1.9×10^{-4}	1.5×10^{-4}
^{127}Xe, 5 min rebreathing, 7.5 l spirometer volume	2.3×10^{-4}	1.3×10^{-4}	1.0×10^{-4}	8.4×10^{-5}
^{127}Xe, 5 min rebreathing, 10 l spirometer volume	2.3×10^{-4}	1.4×10^{-4}	1.1×10^{-4}	9.2×10^{-5}
^{133}Xe, 5 min rebreathing, 5 l spirometer volume	4.1×10^{-4}	4.8×10^{-5}	3.5×10^{-5}	2.6×10^{-5}
^{133}Xe, 5 min rebreathing, 7.5 l spirometer volume	2.2×10^{-4}	2.6×10^{-5}	1.9×10^{-5}	1.5×10^{-5}
^{133}Xe, 5 min rebreathing, 10 l spirometer volume	2.5×10^{-4}	2.9×10^{-5}	2.1×10^{-5}	1.6×10^{-5}
^{133}Xe, injection	4.9×10^{-6}	1.0×10^{-6}	1.4×10^{-6}	1.6×10^{-6}

References

1. Ulrich H. Incidence of leukemia in radiologists. N Engl J Med. 1946;234:45–6.
2. Stabin MG, Siegel JA. Physical models and dose factors for use in internal dose assessment. Health Phys. 2003;85(3):294–310.
3. Siegel J, Thomas S, Stubbs J, Stabin M, Hays M, Koral K, Robertson J, Howell R, Wessels B, Fisher D, Weber D, Brill A. MIRD pamphlet No 16 – techniques for quantitative radiopharmaceutical biodistribution data acquisition and analysis for use in human radiation dose estimates. J Nucl Med. 1999;40:37S–61.
4. Stabin MG, Sparks RB, Crowe E. OLINDA/EXM: the second-generation personal computer software for internal dose assessment in nuclear medicine. J Nucl Med. 2005;46:1023.
5. Cloutier R, Smith S, Watson E, Snyder W, Warner G. Dose to the fetus from radionuclides in the bladder. Health Phys. 1973;25:147–61.
6. International Commission on Radiological Protection. Human alimentary tract model for radiological protection, ICRP publication, vol. 100. Oxford: Pergamon Press; 2007. p. 1–327.
7. International Commission on Radiological Protection. Recommendations of the ICRP. ICRP Publication 103, Annals ICRP. 2007;37(2–3).
8. International Commission on Radiological Protection. Limits for intakes of radionuclides by workers, ICRP publication, vol. 30. Oxford/New York: Pergamon Press; 1979.
9. International Commission on Radiological Protection. ICRP publication 60. Recommendations of the International Commission on Radiological Protection. Oxford/New York: Pergamon Press; 1990.
10. Stabin MG, Xu XG, Emmons MA, Segars WP, Shi C, Fernald MJ. RADAR reference adult, pediatric and pregnant female phantom series for internal and external dosimetry. J Nucl Med. 2012;53:1807–13.
11. Stabin MG. Fundamentals of nuclear medicine dosimetry. New York: Springer; 2008.
12. International Commission on Radiological Protection. Radiation dose to patients from radiopharmaceuticals. ICRP publication 53. Oxford, Pergamon Press. Ann ICRP. 1988;18(1–4).

13. International Commission on Radiological Protection. Radiation dose to patients from radiopharmaceuticals (addendum to ICRP publication 53). ICRP publication 80. Oxford, Pergamon Press. Ann ICRP. 1998;28(3).
14. International Commission on Radiological Protection. Radiation dose to patients from radiopharmaceuticals – addendum 3 to ICRP publication 53. ICRP publication 106. Oxford, Pergamon Press, Ann ICRP. 2008;38(1–2).
15. Bolch WE, Eckerman KF, Sgouros G, Thomas SR. MIRD pamphlet No. 21: a generalized schema for radiopharmaceutical dosimetry—standardization of nomenclature. J Nucl Med. 2009;50:477–84.
16. Stabin M, Watson E, Cristy M, et al. Mathematical models and specific absorbed fractions of photon energy in the nonpregnant adult female and at the end of each trimester of pregnancy. Oak Ridge: ORNL Report ORNL/TM-12907; 1995. p. i–ix. 1–140.
17. Xu XG, Taranenko V, Zhang J, Shi C. A boundary-representation method for designing whole-body radiation dosimetry models: pregnant females at the ends of three gestational periods: RPI-P3, -P6 and -P9. Phys Med Biol. 2007;52:7023–44.
18. Russell JR, Stabin MG, Sparks RB, Watson EE. Radiation absorbed dose to the embryo/fetus from radiopharmaceuticals. Health Phys. 1997;73(5): 756–69.
19. Treves ST, Davis RT, Fahey FH. Administered radiopharmaceutical doses in children: a survey of 13 pediatric hospitals in North America. J Nucl Med. 2008;49:1024–7.
20. AAPM, the American Association of Physicists in Medicine. The measurement, reporting, and management of radiation dose in CT. Report of AAPM Task Group 23 of the Diagnostic Imaging Council CT Committee. 2008.
21. Strauss KJ, Goske MJ, Frush DP, Butler PF, Morrison G. Image Gently Vendor Summit: working together for better estimates of pediatric radiation dose from CT. AJR Am J Roentgenol. 2009;192: 1169–75.
22. Zanzonico P, Stabin MG. Benefits of medical radiation exposures. Health Physics Society web site, http://hps.org/hpspublications/articles/Benefitsofmedradexposures.html.

Radiation Protection in Pediatric Nuclear Medicine

29

Frederic H. Fahey and William A. Lorenzen

The practice of pediatric nuclear medicine requires attention to detail with regard to radiation protection of the health professionals involved in acquiring the studies, the patients, and their families. Since performance of the studies may entail a more hands-on approach, particularly in very small children, those involved in acquiring the studies often need to be closer to the patient than would be the case in adult nuclear medicine. For example, a bone scan in a smaller child may require two technologists where one helps with the immobilization of the patient while the other acquires the study. In this instance, not only are two technologists involved with a single patient, but one may need to hold the radioactive patient in order to acquire the required view to make the clinical decision. In addition, if sedation or anesthesia is necessary to complete the study, other health professionals such as nurses and anesthesiologists may need to be in the imaging room with the radioactive patient. Lastly, there may be some studies such as ictal brain SPECT where the patient is injected remotely from the nuclear medicine clinic, which may present unique radiation protection considerations.

In addition, pediatric patients and their families require special consideration. According to the BEIR VII Phase 2 Report, children particularly young girls may be at higher risk than adults for adverse health effects from the exposure of ionizing radiation [1]. For these reasons, the nuclear medicine practitioner must utilize protocols that keep the administered activity (and thereby the radiation dose) to the patient as low as possible while maintaining the high quality of the clinical information. These considerations are discussed in detail in Chap. 31 regarding dose optimization in pediatric nuclear medicine. One must also consider the radiation protection of the patient's family including the parents but also importantly other siblings that may be exposed to the radioactive patient. This is particularly true for patients receiving radionuclide therapy.

This chapter will review radiation protection practice in a hospital setting, particularly with respect to pediatric nuclear medicine. This will include considerations of intrumentation, operations and training. As will be discussed, many of these will be very similar if not identical to that considered in a facility with mostly adult patients. However, the pediatric patient often presents unique challenges and these will be the focus of this chapter.

F.H. Fahey, DSc (✉)
Joint Program in Nuclear Medicine,
Department of Radiology, Harvard Medical School,
Boston, MA, USA

Division of Nuclear Medicine and Molecular Imaging, Department of Radiology,
Boston Children's Hospital,
Boston, MA, USA
e-mail: frederic.fahey@childrens.harvard.edu

W.A. Lorenzen, MS
Department of Radiation Safety,
Boston Children's Hospital, Boston, MA, USA
e-mail: william.lorenzen@childrens.harvard.edu

S.T. Treves (ed.), *Pediatric Nuclear Medicine and Molecular Imaging*,
DOI 10.1007/978-1-4614-9551-2_29,

Radiation Safety Roles and Responsibilities

The effective implementation of a nuclear medicine radiation protection program is an interdisciplinary endeavor involving the attention of radiation safety staff as well as practically all nuclear medicine practitioners including physicians, technologists, and physicists. In addition, other ancillary health professionals working with pediatric nuclear medicine patients including nurses, anesthesiologists, and child life professionals need to play an active role in radiation protection of themselves and their patients.

In the USA, radiopharmaceuticals are administered to patients under the direction of a physician who has been identified and recognized by the proper authorities as an "authorized user." The requirements necessary for a physician vary depending on nuclear medicine procedures to be performed. For example, if the clinic administers radionuclide therapy as well as perform diagnostic studies, there will be more stringent criteria placed on the physician. The authorized user is responsible for the appropriateness as well as for the proper performance of an indicated study. Prior to all nuclear medicine studies, the authorized user should conduct a review to assure that the study is indicated and, if so, whether the procedure should be modified for the particular patient. This latter part of the review is particularly important for pediatric patients that may provide unique challenges. If approved, the authorized user is ultimately responsible for all aspects of the performance of the procedure from the selection of the proper instrumentation, the administration of the radiopharmaceutical, the acquisition of the study, the analysis of the data and its interpretation, and dissemination of the results.

The radiation safety program is managed by the radiation safety officer (RSO) responsible for all aspects of the administration of the program. In particular, the RSO assures that a radiation protection program is maintained that is safe and compliant with all proper authorities. This includes the proper implementation and practice of all safety procedures, many of which will be described in this chapter. In larger programs the RSO may be a full-time position held by a health physicist or other properly credentialed radiation safety professional. However, in small outpatient clinics, the RSO may very well be a properly trained physician who also acts as the clinic's authorized user. Routine audits and proper recording of safety procedures are essential in order to track the successful and challenging aspects of the program. As previously mentioned, a successful radiation protection program requires cooperation of a diverse group of health professions. The RSO is often the individual that provides this coordination.

Depending on the size of the clinic or the institution within which the clinic resides, the institution may have either a limited or broad scope radioactive material license. A limited scope license is appropriate for small clinics, and, in this case, the entire radionuclide handling and safety program is specified within the submitted license. Larger programs can apply for a broad scope radioactive material license which provides the institution with more flexibility in its radiation safety management. In the context of a broad scope license, the institution assigns a Radiation Safety Committee (RSC) that sets policy and provides oversight for the institution's radiation safety program.

The clinic's technical staff is on the front line with regard to radiation safety implementation from accepting the delivery of the radiopharmaceuticals, the preparation of the dose and its administration, and the performance of the study. This can be particularly challenging when imaging children where it may be necessary to modify the standard protocol in order to complete the study. Close communication between the technologist, the physician, and the RSO can minimize radiation safety complications resulting from such modifications. In addition to good radiation safety practice, the technologist must maintain records to help track these practices in order to identify program aspects that are challenging. In instances where certain aspects of the current radiation safety program present significant considerations in the context of pediatric nuclear medicine, close communication between the authorized user, the technical staff, and the

RSO, in most cases, can lead to a sound operational solution that maintains high-quality clinical work that is safe and compliant.

Radiation Safety Management Commitment and Structure

The Nuclear Regulatory Commission (NRC) is the main regulatory body in the US that promulgates rules and guidance documents regarding the use of radioactive materials including the practice of nuclear medicine. The most pertinent of these regulations are published in the US Title 10 of the Code of Federal Regulations Parts 20 and 35 (10 CFR 20 and 10 CFR 35), respectively [2, 3]. In some states the regulatory responsibility has been delegated to the state by the NRC provided that the rules, guidance, and licensing process of that Agreement State are consistent with the requirements of the NRC but they may not be identical to the NRC. In all cases the licensee should refer to the regulatory requirements of the agency under which that facility operates.

Over the years, the NRC has published a number of guidance documents that are necessary reading for those establishing a nuclear medicine radiation protection program. Since Hospital Health Physics was published in 1993, the NRC has updated Regulatory Guide 10.8 with a more recent version, NUREG-1556, Volume 9, *Program-Specific Guidance About Medical Licensees*, which provides extensive licensing guidance for medical facilities [4]. Broad scope medical licensees should also refer to NUREG-1556, Volume 11, *Program-Specific Guidance About Licenses of Broad Scope* [5].

The regulatory licensing agencies often expect and may require applicants to use and follow the licensing guidance in Volume 9, which is very extensive. A valuable supplemental guidance document is *A Guide for Diagnostic Nuclear Medicine* by Jeffrey Siegel, Ph.D., and published by the Society of Nuclear Medicine [6]. This document focuses on diagnostic nuclear medicine applications and discusses some alternative calculations and industry viewpoints that may be useful.

Licensing

In reviewing radioactive material licenses, all regulators will refer to the contents as a means to ensure that licensees understand and comply with the applicable regulations. However, it is not a means of ensuring an effective radiation safety program for all licensees. A specific program may be considered compliant when following the pragmatic language discussed in the license application, but the key is that license applications that include overly prescriptive and specific program details and commitments do not guarantee functional compliance. In many cases, it can be to the detriment of a licensee to specify in too much detail how one will achieve compliance rather than a broader and more general statement of approach committed to the assurance of safety and compliance. In either case the bottom line is the need for the licensee to achieve compliance, and crafting license commitment language in broad terms can provide the flexibility necessary for establishing and managing a safe and compliant program. This is particularly true in the practice of pediatric nuclear medicine where such flexibility may be the difference between success and failure in the implementation of a particular procedure.

It is important to recognize that statements made in the license application will become commitments to which one must adhere. Typically the last condition on a medical license reads as follows:

> "Except as specifically provided otherwise in this license, the licensee shall conduct its program in accordance with the statements, representations, and procedures contained in the documents, including any enclosures, listed below. The Nuclear Regulatory Commission's regulations shall govern unless the statements, representations, and procedures in the licensee's application and correspondence are more restrictive than the regulations."

The most common items of noncompliance cited by regulators result from statements made in the license application that are not followed exactly as stated, and therefore, overly detailed commitments should be avoided. An established radiation protection program can always

evoke more controls and requirements than what is stated in a license, but it can never perform less.

General Guidelines

NUREG-1556 Volume 9 provides detailed instructions for filing a license application. One thing to keep in mind is that the clinic or institution must be able to effectively implement and operate under the provisions in the license application. It is important to know when to accept the guidance from NUREG-1556 Vol. 9 and when it might be beneficial to deviate from it. When preparing a license application, one should provide the least amount of specificity necessary while giving the information being requested. In addition, information should not be included that is not required. As an example, it is not required that an applicant provides the institution's radiation safety manual as part of the license application. Submission of such an internal program document may lead to the institution's commitment to follow every aspect and procedures described. In addition, any change or modifications made to this document would require the submission and subsequent approval of a license amendment. Submitting a license application with such specificity may reduce the flexibility necessary to effectively practice pediatric nuclear medicine.

During the license application process, the documentations and statements provided should reflect the institution's commitment to following the regulations. The regulations provide adequate measures for safety in the use of radioactive material. Overly committing to information contained in Volume 9 can result in an unnecessary burden on an operational radiation safety program without producing tangible benefits other than showing compliance with a license application commitment.

In deciding whether to subscribe to the language contained in NUREG-1556 Volume 9, there is a tendency to offer a commitment to follow the "model procedures" it contains. From Section 1.2 of Volume 9:

"Use of the word "should" implies "may" and is not intended to mean "must" or "shall;" the procedures provided in this guidance are intended to serve only as examples."

The decision to accept a model procedure should only be done with the use the term "should" and not "must" or "shall."

Radiation Safety Committee

The RSC consists of a chair, the RSO, as well as representatives of each type of authorized user and the nursing service. A representative of the institution's administration also serves on the committee. In addition, the institution can assign any other individuals to the committee it deems appropriate. The RSO and the RSC work very closely together as the RSO implements safety procedures and audits based on policies established by the RSC. The size of and breath of an institution's request to possess and use radioactive material will dictate the need for the establishment of a RSC. The licensee should be careful to not overstate the details of how its committee will operate. Some specific items to consider:

- If specific names are included, a license will need to be amended if someone leaves or is replaced. Instead of stating "The committee consists of Drs. Smith, Jones and Brown," an alternatively statement would be "The committee currently consists of Drs. John, James, and Johnson." This demonstrates the establishment of a committee and leaves the determination of its appropriate constituency to regulatory review. The use of words like "currently" implies that there may be changes in the future. This approach can be used in many licensing areas, e.g., waste management and dosimetry providers.
- Establish a meeting quorum that is below your "normal" attendance. If members are absent, the required meeting can still be held without concern from violating a license condition mandating a meeting take place at a specified interval.

- Do not establish a specific meeting frequency that could result in a violation of a license condition. One method to avoid this is to provide application language that commits to meeting and states an expectation on frequency: "The Radiation Safety Committee (RSC) will meet periodically to review the Radiation Safety Program. Typically, the RSC will meet quarterly."

Radiation Safety Officer

The RSO is the only position that is identified by name on all licenses issued. The position will typically be held by someone who has demonstrated the fulfillment of the qualification specified in 10 CFR Part 35 through both education and experience requirements for that position. The RSO is typically the person who manages the radiation safety program and oversees the conduct of the required compliance-related activities mandated by regulation and the license conditions. A critical element in the success of the radiation safety program is through the support and performance of the RSO. Inherent to this is the direct reporting of this position to upper management and its ability to identify and correct programmatic deficiencies effectively. The RSO position can be hampered through either lack of adequate resources or management obfuscation that may lead to citations of regulatory noncompliance. The RSO should have clear lines of authority and be responsible for all aspects of the program. In many hospital programs, the RSO is established by identifying who has the qualification necessary to satisfy regulatory requirements, and the location within the organization where this person resides is often overlooked and not adequately considered.

Authorized Users

An authorized user (AU) is a position identified by training and experience to the administration of radioactive material under a radioactive material license. The AU designation requires the submission of training, experience, and attestation for the specific area in which he or she is looking to practice. In many cases, a physician certified by a national board in the practice of nuclear medicine and radiology will be recognized in meeting these requirements. Depending on the license category, the submission of an applicant's documents and request to serve as an AU will be either to the institution's RSC or directly to the regulatory agency. In either case the demonstration of the requirements is identical with details found in 10 CFR Part 35.

Training

Training for personnel who work with or around radioactive material is a regulatory requirement and can be found in Title 10 of the Code of Federal Regulations Part 19 [7]. Training is not a onetime event but an ongoing process. Training in the regulatory context is often demonstrated through a syllabus, a classroom, a proof of attendance, and possibly a test. It is essential to determine who should be trained and with what frequency. The regulations define the educational content that must be covered. 10 CFR 19.12 requires instructions for "All individuals who in the course of employment are likely to receive in a year an occupational dose in excess of 100 mrem (1 mSv)…" It should be noted that some have questioned the extent of this list of workers because of 10 CFR 19.12(b) which also states that "In determining those individuals subject to the requirements of paragraph (a) of this section, licensees must take into consideration assigned activities during normal and abnormal situations involving exposure to radiation from radioactive material which can reasonably be expected to occur during the life of a licensed facility. The extent of these instructions must be commensurate with potential radiological health protection problems present in the work place." The operational program through the RSO and RSC (when one exists) should identify the personnel that are subject to the training requirements which should

Table 29.1 Maximum permissible exposure levels, quarterly guidelines, and examples of ALARA I and ALARA II action levels

	Maximum permissible annual exposure levels[a]	Quarterly guidelines[b]	ALARA I action levels[c]	ALARA II action levels[c]
Whole body (total effective dose equivalent)	50	12.5	1.25	3.75
Extremity	500	125	12.5	37.5

All exposure values are in mSv
[a]According to US 10CFR 20
[b]Determined by dividing the maximum permissible annual exposure levels by 4
[c]Examples of ALARA I and ALARA II action levels were set at 10 and 30 % of the quarterly guideline values, respectively

depend on the employee's duty, the location of work assignments, and a facilities' operating history. In most cases the determinations result in the exposure being far less than 1 mSv. A training program can always include as many employees needed to ensure a satisfactory level of comfort and awareness within a program. However, it would not be suggested that that level of training be required as part of a licensing process and thus be mandatory.

Occupational Dose

An essential aspect of any radiation safety program is the assessment of the radiation dose that employees receive. This provides assurance that none of the employees have received a radiation dose above the maximum permissible levels specified by appropriate regulatory authorities. The maximum permissible dose levels as specified by 10 CFR 20 are listed in Table 29.1. In addition, it is important to identify abnormal or exceptional personnel exposures, even if such are clearly less than regulatory levels, that might indicate areas of clinical practice that need to be reconsidered. Fundamental components of dosimetric estimation of employees are a monitoring program consisting of the use of personnel dosimeters and the estimation of internal dosimetry.

The regulations (10 CFR 20.1502) clearly state that it is necessary to ensure, at a minimum, the monitoring of employees in adherence to these regulations. The determination of who is likely to get exposures at or above these levels is the licensees' responsibility and subject to review by the governing regulatory authority. The inclusion of others into the monitoring program may have advantages or reasons beyond meeting the regulatory requirements, but these will have impact on the overall cost and operations of the radiation safety program that need to be considered.

External

With respect to the regulations, it is reasonable to consider whole-body and extremity monitoring. There has been recent concern regarding radiation dose to the lens of the eye of employees given that the threshold for this deterministic effect may be somewhat lower than previously thought [8, 9]. However, within nuclear medicine radiation dose to the lens of the eye should not be considerably different than that to the whole body, and thus the whole-body dosimeter is most likely adequate for both.

For those who manually handle radiopharmaceuticals they can receive significantly higher radiation dose to the fingers than to the whole body, and thus the extremity dose must be monitored. In a pediatric nuclear medicine clinic, practically all radiopharmaceutical doses may have to be adjusted for patient size requiring manipulation, and thus extremity monitoring of the technical staff is most appropriate. It is important to evaluate where on the body dosimetry should be worn as well as what type and how many should be worn. There has been recent investigation where nuclear medicine technologists have worn multiple small dosimeters on different locations on multiple fingers on both hands [10]. These studies indicate that the radiation dose to different locations on different fingers

can vary greatly. It is not surprising that the highest dose is from the tips of the index fingers of both hands. However, the study also indicated that a single ring monitor on the dominant hand provides a reasonable, conservative dose estimate to both hands. That being said, there may be special situations where the use of multiple finger dosimeters may be considered. For example, when a clinic introduces a new procedure such as an approach to radionuclide therapy, it may be very instructive to utilize multiple dosimeters early on in order to gain a better understanding of the radiation dose associate with the technology.

Typically the issuance of dosimetry for monitoring exposure is managed through a third party. It is advantageous to only commit to the use of a dosimetry provider that meets the requirements of 10 CFR §20.1501(c) and not provide unnecessary details regarding function or service. This statement provides the regulator the generic information needed to ensure the requirements of the regulation are met. Most personnel dosimeters are analyzed periodically, perhaps monthly or quarterly. For example, once a month the dosimeters are collected from all monitored employees and sent to the vendor who provided them for analysis, and a subsequent report is generated within several weeks. In practically all cases, this approach works very well.

Within pediatric nuclear medicine, it is rare that one needs to monitor personnel dosimetry within a different time course than monthly or quarterly. However, there may be some occasions where it would be helpful to better understand the radiation dose contributions of certain parts of the procedure. This may be particularly true for new procedures or those that are suspected to deliver a reasonable dose to the employee. In these cases, it may be helpful to use dosimeters that can be read in real time. For example, one may want to know what aspect of PET/CT performed in children leads to the highest dose to the technologist. And so, a real-time dosimeter is issued to the technologists performing these studies, and they are instructed to maintain a "dose log" where they record the dose during the different stages of the procedure, i.e., dose preparation, dose administration, patient preparation, data acquisition, and procedure completion. If such data are recorded for a number of similar procedures, the radiation safety program can develop a dose profile of the procedure. In this example, the fact that the majority of the radiation dose the technologist receives is during the dose preparation and administration may allow for modifications of the procedure that help to reduce the radiation dose to the technologist.

Another application of real-time dose monitoring may be when questions arise regarding the radiation dose to ancillary health professionals who may not be routinely monitored but are nevertheless concerned about their radiation dose. Allowing such individuals to wear real-time dosimeters and recording the dose for several procedures may provide the employee with a better comprehension of the radiation dose to which they are exposed. This may also be helpful with parents and other family members who want to stay close to their children during their procedures but are concerned about the radiation dose they may personally receive. In most cases, staying with their children will expose the parents to only a few μSv at most, but specific knowledge regarding the exposure may be well appreciated.

Internal

Historically, internal monitoring was only a regulatory requirement for those individuals handling therapeutic doses of ^{131}I sodium iodide (NaI). As the volatility and stability of these radiopharmaceuticals are now better controlled, the likelihood of an intake has decreased dramatically. Therefore, the specific thyroid bioassay requirement was deleted from the last regulatory modification of 10 CFR 35. However, the perception that this requirement exists is still prevalent in the nuclear medicine community.

The regulatory requirement for internal monitoring mirrors the requirement for external monitoring: those individuals likely to exceed 10 % of the annual limit on intake (ALI). The probability of this occurring at a medical facility is unlikely. The license commitment should reflect this fact. A licensee can monitor anyone they choose but that should be a program decision not a license commitment.

Dose Limits for Family Members

Sometimes the regulations can be problematic for a particular institution and asking for a variance during the licensing process is needed. For example, limiting the time a parent can spend with their child who has undergone a nuclear medicine therapeutic procedure because of the public dose rule (10 CFR 20.1301) may be unnecessary. Nevertheless, the rule exists and a variance should be sought. The NRC has granted an exemption up to 20 mSv under certain circumstances involving children, while at least one Agreement State has allowed the occupational dose limit of 50 mSv. An example of the request would be:

> "Adults providing care to minors undergoing treatment with byproduct material during confinement may receive up to 20 mSv in a year. The following conditions will apply:
>
> - The exemption will apply only to adult family members providing care to minors undergoing treatment with byproduct material during periods of hospital confinement.
> - Training to adult family caregivers shall be provided commensurate with the risks and instructions normally provided to workers in accordance with 10 CFR Part 19. Training shall include instructions in maintaining exposures as low as reasonably achievable.
> - Adult family caregivers shall be monitored for radiation exposure and a program of controls using standard radiation protection practices to minimize time, maximize distance, and use of shielding in maintaining exposures as low as reasonably achievable shall be implemented.
> - The exemption shall not apply to pregnant adult family caregivers."

Because of the possibility of an "overexposure" involving a family member visiting a patient, the NRC has been sensitized to this issue and has instituted some policies for expedited license amendments to accommodate such requests. It may be more prudent to have an amendment in place before it is needed.

Surveys and Monitoring

For medical licensees, surveys and monitoring became a licensing issue with the revision of 10 CFR 35 in 2002. Previously, the regulations were very detailed and prescriptive on this topic leaving little room for license flexibility. However, much of the prescriptive requirements have been removed. Nevertheless, facilities usually continue to survey in the same manner as before: daily surveys in areas of preparation and administration, weekly wipes in these same areas, and weekly surveys in areas of waste storage. There are at least two issues with making this older regulatory model a part of the current program: Weekly wipes are ineffective when most radiopharmaceuticals used in the clinic have half-lives of 6 h or less, and weekly surveys in your waste area may be insufficient. Although perhaps more sensitive than meter surveys, weekly wipes blindly taken in a department are unlikely to yield contamination results that wouldn't have been picked up by careful meter surveys. However, weekly wipe surveys may be useful in dose preparatory areas where meter backgrounds may be too high to yield useful results. Likewise, waste areas should be surveyed when new waste is added to the area or waste is moved around to ensure dose limits in an unrestricted area are not exceeded. Dose levels in a medical facility waste area typically do not increase on a weekly basis.

Effluents

Medical facilities rarely release even minute quantities of airborne radioactive material unless they have a medical cyclotron for producing PET radiopharmaceuticals onsite. The management of a cyclotron facility is beyond the scope of this chapter. As previously mentioned, due to historical volatility issues, ^{131}I-NaI is the most probable source for released airborne radioactive material. Monitoring the hood stack from a nuclear medicine department may have been necessary and routine practice when volatility was a greater concern. However, since this is no longer the case, committing to an effluent sampling program would be an unjustified burden to the radiation protection program. As allowed by the NRC Regulatory Guide 4.20, calculation using the Environmental Protection Agency (EPA) computer code, COMPLY, is a better means

of demonstrating compliance with applicable effluent regulations.

Waste

Because most isotopes used in a medical facility that routinely generate radioactive waste are short lived, the storage and decay of this waste makes disposal fairly easy. 10 CFR 35.92 was revised to eliminate the need for storing waste for ten half-lives and allows for the final survey as the determining factor in decayed waste. Although you may continue to store your waste for ten half-lives before performing the final survey, compliance with 10 CFR 35.92 should be the license commitment. If your facility has a nonclinical component, you should request to store all your waste in accordance with 10 CFR 35.92. It is unreasonable to store and dispose of ^{131}I generated in a clinic in a different manner than if the ^{131}I came from a research laboratory.

When acquiring and managing longer-lived radioactive sources with half-lives of months or years for quality control measurements or calibrations, it is prudent to ensure that the vendor from whom the purchase is made agrees to accept the return of the source when it is no longer needed. This will eliminate the costly disposal of these sources.

10 CFR 35.1000 Procedures

The NRC has offered some guidance on new modality treatments (e.g., SIR-Spheres and GliaSite). One topic of discussion is which physician group should be the authorized user. Although such procedures are not routinely performed in children currently, it is reasonable to review this information in the event a pediatric application is developed in the future. While some of the products have been registered as devices and therefore indicate radiation oncology as the preferred choice, some of the physical characteristics of the products may be more similar to a radiopharmaceutical, and therefore, the consideration may lean toward nuclear medicine. Collaborative working relationships would eliminate most of the problems.

It is important to remember that there is no one right way to pursue an emerging technology. By its very nature, there is no documented track record on which to base a final decision. If local regulations favor a particular physician group as the de facto authorized user group and your particular situation differs from the de facto group, you should request a variance if you are a specific licensee or if a Broad Scope licensee have your Radiation Safety Committee approve your desired group. It will be important to document the training and experience of the physician or physician group as well as your rationale for deviating from the traditionally "approved" group.

Radiation Protection Principles

The establishment of a radiation safety program is centered on the core understanding of basic radiation safety principles. This will typically involve the creation of a radiation safety manual that describes specific aspects of radiation safety that govern the licensee's control and management of radiation and radioactive material. The purpose of a radiation safety manual is typically twofold: It satisfies regulatory requirements regarding the licensee's program in radiation safety and it also serves as the reference document by which all levels of the organization can learn and understand the specific aspects of the institution's radiation safety program. Although the details of each institution's radiation safety manual are unique to its specific needs and uses of radioactive material, they do commonly address the application of some basic radiation protection principles used in managing the safe use of radioactive material. These principles will be discussed in this section in the context of pediatric nuclear medicine.

Time, Distance, and Shielding

These three fundamentals of radiation safety are part of every radiation safety program. From the

receipt of radioactive material through its disposal as waste, the application of one or more of these basics of guiding radiation safety will be employed in the overall management and control of radiation exposure to staff, patients, families, and the general public.

Time

The time spent by individuals near radioactive sources should be minimized. However, the patients are themselves a source of radiation; thus, special care needs to be taken to minimize exposure while performing the clinical task at hand without making the patient feel as if they are being left alone. This is particularly important in the pediatric setting. Therefore, the nuclear medicine staff need to learn to work quickly, efficiently, and accurately. Repeating one's work may be annoying to the staff, patient, and physician, but it also increases the amount of exposure time and thereby the radiation dose to staff. It is important to perform procedures correctly the first time. When it is practical, the staff should rehearse new or infrequently performed tasks before working with the radioactivity.

Distance

Although the duties of the nuclear medicine staff require proximity to radioactive sources, they should maximize the distance from these sources as much as possible. When required to handle radioactive materials, staff should use forceps, tongs, vial racks, or any other suitable instruments to increase the distance between themselves and the source of radioactivity. Radioactive materials should be stored in more remote areas of the laboratory away from high traffic or areas where duties typically not associated with radioactive materials are performed. Most pediatric nuclear medicine procedures require the technologist and other support staff to be close to the radioactive patient. The staff should seek to maximize that distance if possible while still attending to the needs of the patient. An additional step or two away from the patient will dramatically reduce one's exposure. Putting distance between the source of radioactivity and the technologist is extremely effective because, according to the inverse square law, exposure decreases as the square of the distance. Thus, doubling the distance from a source decreases the exposure by a factor of 4, and tripling the distance decreases the exposure by a factor of 9. This is also true for parents who accompany their child during a nuclear medicine imaging procedure. Parents should be instructed to stay as far from their child as they feel comfortable. If they can stay 2 m away, that is 4 times better than 1 m.

Shielding

Shielding is one of the most effective methods for minimizing radiation exposure to patients and staff. Regulations require that all syringes be shielded during kit preparation and patient administration. Likewise, all vials containing radioactive material must also be appropriately shielded. All ^{99}Mo/^{99m}Tc generators are required to be shielded beyond the device's inherent shielding. That is, the inherent shielding of generators may satisfy the Department of Transportation safety requirements but is not adequate for laboratory use. Almost all radiopharmaceuticals are required to be kept behind lead shielding during storage and patient dose preparation.

It is important that the appropriate shielding material be selected for the radioactive material being used. Most shielding devices are made of lead, leaded glass, tungsten, or some combination of such high-Z (Z is the number of protons per atom) materials. However, this type of shielding is not appropriate for all circumstances. When using beta emitters such as ^{32}P and ^{89}Sr, it is necessary to use Lucite or other appropriate low-Z material as a shield to minimize the production of bremsstrahlung radiation (low-energy x-rays). If dense shielding materials are used with beta emitters, the staff may actually receive measurable photon radiation exposure due to the bremsstrahlung radiation.

When using shielding for gamma radiation, one must also consider the energy of the radioactive emissions. For example, the amount of lead shielding needed to attenuate the 140-keV photon of ^{99m}Tc may not be sufficient for ^{131}I (364-keV gamma rays) or positron emitters such as ^{18}F (511-keV photons). Although it is not in the

day-to-day duties of the nuclear medicine staff to calculate appropriate shielding, it can be very useful to understand the rationale behind these calculations. Each commonly used radioisotope in nuclear medicine has a half-value layer (HVL) associated with different shielding materials indicating the thickness of the particular material that would be required to attenuate the number of photons from a radioactive source by half. The half-value layer can be derived by dividing the number 0.693 by the linear attenuation coefficient, μ. Both for the HVL and μ are unique for the specific material and the photon energy, and either can be used to determine the thickness of shielding needed to attenuate the photons to the desired level.

ALARA

A fundamental concept of occupational radiation protection is the notion of ALARA or "as low as reasonably achievable." The spirit of ALARA is that merely being within the regulatory guidelines is not sufficient for a radiation safety program. One must operate the program is such a manner that employees and the public are exposed to the least amount of radiation possible while still maintaining a reasonable approach to the operations of the facility. For example, it is not acceptable for a facility that uses ionizing radiation for all employees to receive 90 % of the maximum permissible whole-body radiation exposure if one could limit the exposure to less than 10 %. An analysis of the operations should be performed that leads to an optimization of the benefits of procedures relative to the radiation risk to personnel and the public that may result as a consequence. However, such dose reduction should always be considered in the context of the benefit of the particular operation. In the nuclear medicine clinic, this might mean that procedures are evaluated and implemented in a manner that will keep the exposure to the technical staff "as low as reasonably achievable." In reviewing the personnel monitoring records for the laboratory, not only should those close to regulatory limits be noted but also any exposures that seem to be exceptional for a particular employee.

As a consequence of the ALARA philosophy, facilities using ionizing radiation including nuclear medicine clinics must establish action levels below the regulatory limits of personnel exposure. The personnel monitoring records are reviewed regularly (e.g., quarterly). Individuals exceeding these action levels are notified and, in some cases, interviewed to determine if there was a certain circumstance that led to these higher exposure levels and whether operations should be modified. It is common practice to divide the annual maximum permissible doses by four to establish quarterly guidelines and then to reduce these further. Two levels are typically set referred to as ALARA I, often set at 10 % of the quarterly guideline, and ALARA II, set at 40 %. Table 29.1 lists the annual whole-body and extremity limits set by 10 CFR 20 with quarterly guidelines (1/4 of the regulatory limit) as well as examples of ALARA I (10 %) and ALARA II (30 %) action levels. If an employee exceeds a quarterly ALARA I level, a notification may be sent to the individual, perhaps with a reminder of good radiation safety practice. If the ALARA II level is exceeded, the situation should be reviewed by the RSO to identify any circumstances that may have led to the higher exposures and whether any further action is warranted.

Other Principles of Protection

Activities that would enhance the likelihood of internal radiation exposure are not allowed in areas where radioactivity is handled including eating, drinking, chewing gum, or applying cosmetics or lip balms. Regulators have assessed noncompliance by observing empty and discarded food containers, cups, chewed gum, food remnants, or other items to indicate that these activities are occurring in areas where they are not allowed. The use and storage of radioactive gases and volatile radioactive materials can also lead to internal exposure because they can be inhaled or absorbed through mucous membranes or the skin. Xenon gas should be used with closed breathing systems in negative pressure rooms. However, many experienced technologists will affirm that these precautions may not serve their

protective function unless the patient is cooperative. Hence, perhaps the most effective way to minimize one's exposure to xenon gas is to make sure the patient is familiarized with the procedure and clearly understands the technologist's expectations particularly in pediatric patients.

Radioiodine poses a special problem because it is a volatile material that tends to become easily airborne. Complicating matters is that radioiodine is easily absorbed through the skin or mucous membranes and ultimately taken up by the thyroid gland. To minimize risk from accidental breakage or spillage, packages or containers of radioiodine should be opened under a fume (exhaust) hood. Similarly, radioiodine should be stored behind shielding within a fume hood. When handling radioiodine, gloves are required, but technologists should also consider wearing disposable protective sleeves. Any physician or technologist administering radioiodine therapy or handling open vials of liquid radioiodine should undergo thyroid survey following the therapy to check for internal radioiodine contamination.

Radioiodine therapy constitutes a number of potential risks to many individuals including staff, family members, and other members of the public. According to the ALARA concept, the staff needs to minimize the exposure by the patient to themselves and other persons incidentally exposed to the patient. Because radioiodine-treated patients will return home either right after the therapy or after a short hospitalization, physicians and the radiation safety staff must educate patients and their families regarding ways to minimize incidental radiation exposure [11, 12]. Radioiodine therapy with ^{131}I presents a dual challenge because it is a beta emitter that also emits a 364-keV gamma ray. The beta particle contributes to internal exposure if ingested or inhaled, and the energetic 364-keV gamma emission is capable of radiation exposure at a distance. The patient and family need to be aware that radioiodine can be passed through sweat, saliva, urine, and stool. The patient's eating utensils should be disposable or washed and kept separately from those used by others. Close contact with other individuals should be minimized for several days post therapy. The patient should sleep alone; kissing, holding, and intimacy should be discouraged until approved by the nuclear medicine physician. Breastfeeding should be discontinued, and contact with other children should be minimized. Patients must diligently wash their hands, and care must be taken to flush the toilet after each use. In addition, with young children undergoing nuclear medicine therapeutic procedures with ^{131}I, care must be taken to ensure caregivers have an appropriate method for the disposal of diapers and other potentially radioactive material once they return home. It is prudent to consult with the RSO regarding other potential home/life conditions that may expose others to the radiation from the child.

Nuclear medicine technologists and other occupationally exposed workers find themselves constantly exposed to low levels of radioactivity. The overall effects of this exposure are still uncertain as discussed in Chap. 31. However, unless future research proves otherwise, the technologist should assume that all radiation exposure, no matter how small, has potential deleterious effects. With this in mind, staff should diligently apply what they know regarding time, distance, shielding, and the ALARA principle to minimize radiation exposure to themselves, fellow workers, patients and their families, as well as other incidentally encountered individuals.

Pregnancy

Pregnant staff should take special precautions as developing cells are more radiosensitive than mature, developed cells. In order to protect the developing embryo/fetus, lower exposure limits have been adopted. Female employees who work with radiation that become pregnant can choose to officially declare their pregnancy to the RSO. Currently, the exposure limit for the embryo/fetus for the entire pregnancy is 5 mSv for women who have officially declared their pregnancy. Guidance on this matter can be found in the NRC Regulatory Guide 8.13 *Instructions Concerning Prenatal Radiation Exposure* [13].

Individual institutions may take different precautions for the pregnant worker. However, when it is possible, the pregnant worker should be

excused from those procedures that yield the most exposure. Some of these might include patient administration of higher-dose procedures and radiopharmacy tasks. Pregnant staff should also take extra precautions against airborne radiopharmaceuticals. In addition, they should wear two monitoring badges: The usual location to estimate the workers' typical exposure, and the second badge should be worn near the waist to determine the potential exposure to the developing fetus. This approach provides a more accurate estimate of the fetal exposure.

The institution should also take precautions to avoid performing nuclear medicine procedures on pregnant patients. All female patients of childbearing age should be asked whether they are pregnant prior to the administration of the radiopharmaceutical. A nuclear medicine clinic that images children should have a policy as to what is meant by "childbearing age." Such a policy may include female patients older than 12 years of age or after their first menstrual period. With teenage girls, the technologist may want to ask this question in a discrete manner.

The clinic may decide that there are certain procedures for which pregnancy should be confirmed or denied medically. These may be procedures with the potential for a reasonable dose to be received by the embryo. In these cases, a pregnancy test can be ordered and the procedure delayed until after the results are known.

If the patient knows that she is pregnant or may possibly be, the referring physician should be consulted and decision should be made whether the procedure should still be performed or whether it should be cancelled or postponed. There may be instances where it is determined that the procedure is necessary for the health of the patient, and in these cases, informed consent should be obtained.

Instrumentation

In addition to the equipment necessary for the clinical operation, a nuclear medicine laboratory will also need some equipment specific for radiation safety. Also, the dose calibrator, well counter, and thyroid probe may be used for both clinical and safety purposes. The dose calibrator is a pressurized gas-filled ionization chamber that is used to assay the activity to be administered to the patient. The device, which is typically filled with argon at ten times atmospheric pressure, can accurately measure amounts of activity from 0.7 MBq up to 37 GBq. A dose log must be maintained of the date, time, and amount of radioactivity administered to each patient as well as the individual who performed the administration, and the dose calibrator is essential for the quality of this record. A standard quality control program of the dose calibrator that includes evaluation of the chamber's constancy, linearity, accuracy, and geometric variations must be maintained to ensure the integrity of the measurements.

The sodium iodide well counter can be used for the counting of radioactive biological samples such as for the evaluation of glomerular filtration rate (GFR), but it can also evaluate wipe assays of removable activity for protection purposes. Unlike the dose calibrator, the well counter is based on a solid sodium iodide crystal and thereby is used for measuring less than 20 kBq of activity. In the context of radiation safety in nuclear medicine, the well counter can measure activities as low as 10 Bq and thus is useful for measuring very small amounts of radioactivity, significantly less than regulatory limits for both accepting packages shipped from the radiopharmacy (0.04 kBq) and sealed sources used for calibration (0.2 kBq). The quality control for the well counter includes energy calibration, the chi square test, as well as determination of the efficiency and the minimum detectable activity (MDA).

Two different types of survey meters are utilized in the nuclear medicine clinic, a Geiger-Mueller (G-M) meter and an ionization (or "ion") chamber. The G-M meter is used for surveying items and areas for the presence of contamination. Thus, they are used for surveying packages received from the radiopharmacy as well as areas in the clinic where radioactivity has been handled at the end of each working day. The G-M meter can also be used to survey any areas where one

suspects there might be contamination. Lastly, the G-M meter is used to survey radioactive trash prior to its disposal. It should be noted that the G-M meter only detects events with no specific information regarding the energy deposited, and, thus, it is not the device of choice for estimating exposure or air kerma levels from which radiation dose can be inferred.

The ion chamber is based on the collection of ionization in a gas (often air) and thus makes measurements directly related to the radiation quantity *exposure* (in roentgens, R) and air kerma (in gray, Gy). These measurements at some location can be used to directly infer the radiation dose that would be received by an individual at that location. This can be very useful for measuring the air kerma rate at a set distance from a patient who has received ^{131}I therapy to assure that it is safe to allow the patient to leave the hospital without exposing family members and other members of the general public to unacceptable levels of radiation as discussed in other sections of this chapter.

Patient and Family Safety

As discussed in Chap. 31, children are considered to be at a higher, potential risk from radiation than adults. At the same time, the practice of nuclear medicine in children can be of great clinical value but can also be quite challenging as discussed extensively in this book. Therefore, careful attention to detail in pediatric nuclear medicine is very important. Being able to perform the procedure correctly and in a timely fashion often can be the difference between success and failure. With very small or otherwise challenging patients, there may be only one opportunity to get the procedure done right.

Chapter 28 describes radiation dosimetry in the context of pediatric nuclear medicine. As discussed, the primary determining factor for the radiation dose is the administered activity to the patient and can be considered the primary dose index for nuclear medicine. The radiation dose received by any of the patients' organs is directly related to the administered activity. Nuclear medicine clinics that perform procedures in children only on occasion may have questions regarding the proper administered activity for different size patients. As described in Chap. 31, several organizations have developed guidelines in this regard. In particular, the Image Gently program in conjunction with the Society of Nuclear Medicine and Molecular Imaging (SNMMI), the Society of Pediatric Radiology, and the American College of Radiology issued the North American Guidelines for Administered Doses in Adolescents and Children [14]. The European Association of Nuclear Medicine (EANM) has also published what is referred to as the EANM Pediatric Dose Card to also provide guidance in this regard [15]. More recently, the SNMMI and the EANM have worked to bring these two sets of guidelines into harmonization. In addition, advances in instrumentation, image processing, and reconstruction can provide an opportunity for dose reduction as described in Chaps. 27 and 31.

It is natural for the parents of young children undergoing nuclear medicine procedures to want to understand the benefits and potential risks associated with the procedure. In addition, teenagers may have their own questions as they may have discussed radiation and its effects in school. Therefore, the nuclear medicine professional should be well prepared to discuss these issues with the parents or to put them in contact with an expert in radiation protection who can best answer their questions and concerns [16]. Much of the background information for this discussion is covered in Chaps. 28 and 30 along with the listing of many excellent references.

A discussion with patients and their families may include the following: During the procedure, the patient will be administered a small amount of radioactivity that emits radiation similar to that given off by x-ray machines, and this exposure may carry a very small potential risk that the patient may contract cancer sometime in their remaining life. The amount of radiation that the patient will receive is similar to that from other radiologic exams such as CT scans or that received from background radiation in 1–2 years. If asked, one can provide a radiation effective dose estimate to folks receiving similar

procedures, but one should be clear that their individual radiation dose may vary significantly from these estimates.

References

1. Committee to Assess Health Risks from Exposure to Low Levels of Ionizing Radiation, National Research Council. Health risks from exposure to low levels of ionizing radiation: BEIR VII phase 2. Washington, DC: National Research Council of the National Academies; 2006.
2. U.S. Nuclear Regulatory Commission. Code of Federal Regulations. Standards for protection against radiation. Washington, DC: U.S. Government Printing Office: 10 CFR Part 20; 2002.
3. U.S. Nuclear Regulatory Commission. Code of Federal Regulations. Medical use of byproduct material. Washington, DC: U.S. Government Printing Office: 10 CFR Part 35; 2002.
4. Consolidated Guidance About Materials Licenses: Program - Specific Guidance About Medical Use Licenses. U.S. Nuclear Regulatory Commission. NUREG-1556, Volume 9, Rev.1 - Program Specific Guidance about Medical Licensees. 2005.
5. Consolidated Guidance About Materials Licenses: Program-Specific Guidance About Licenses of Broad Scope. U.S. Nuclear Regulatory Commission. NUREG-1556, Volume 11 - Program-Specific Guidance About Licenses of Broad Scope. 1999.
6. Siegel JA. A guide for diagnostic nuclear medicine. Reston: Society of Nuclear Medicine; 2001.
7. U.S. Nuclear Regulatory Commission. Code of federal regulations. Notices, instructions and reports to workers: inspection and investigations. Washington, DC: U.S. Government Printing Office: 10 CFR Part 19; 1973.
8. ICRP Statement on Tissue Reactions, ICRP ref 4825-3093-1 464, International Commission on Radiation Protection, Ottawa. 2011.
9. Bouffler S, Ainsbury E, Gilvin P, Harrison J. Radiation-induced cataracts: the health protection agency's response to the ICRP statement on tissue reactions and recommendation on the dose limit for the eye lens. J Radiol Prot. 2012;32:479–88.
10. Sans Merce M, Ruiz N, Barth I, Carnicer A, Donadille L, Ferrari P, Fulop M, Ginjaume M, Gualdrini G, Krim S, Mariotti F, Ortega X, Rimpler A, Vanhavere F, Baechler S. Extremity exposure in nuclear medicine: preliminary results of a European study. Radiat Prot Dosimetry. 2011;144:515–20.
11. Guidelines for Patients Receiving I-131 Radiotherapy Treatment. Society of Nuclear Medicine and Molecular Imaging. http://interactive.snm.org/index.cfm?PageID=11220. 2011.
12. Sisson JC, Freitas J, McDougall IR, Dauer LT, Hurley JR, Brierley JD, Edinboro CH, Rosenthal D, Thomas MJ, Wexler JA, Asamoah E, Avram AM, Milas M, Greenlee C. Radiation safety in the treatment of patients with thyroid diseases by radioiodine ^{131}I: practice recommendations of the American Thyroid Association. Thyroid. 2011;21:335–46.
13. Instructions Concerning Prenatal Radiation Exposure. U.S. Nuclear Regulatory Commission. NUREG-18.3. 1999.
14. Gelfand MJ, Parisi MT, Treves ST. Pediatric radiopharmaceutical administered doses: 2010 North American Consensus guidelines. J Nucl Med. 2011;52:318–22.
15. Lassmann M, Biassoni L, Monsieurs M, Franzius C, Jacobs F. The new EANM paediatric dosage card. Eur J Nucl Med Mol Imaging. 2008;35:1748.
16. Fahey FH, Treves ST, Adelstein SJ. Minimizing and communicating risk in pediatric nuclear medicine. J Nucl Med. 2011;52:1240–51.

Radiation Risk

30

S. James Adelstein

The practitioner of pediatric nuclear medicine should have some knowledge of radiation effects and the potential hazards that may result from low-level radiation exposures. There are several reasons such information is essential. First, specialists should ensure that the exposure of patients to radiation from diagnostic or therapeutic procedures is not excessive. Although all current radiopharmaceuticals deliver radiation doses within a readily acceptable range, such was not the case 40 years ago when the radionuclides employed were generally longer-lived and emitted significant particulate radiation, e.g., iodine-131 (^{131}I) and strontium-87m (^{87m}Sr). As a result, before 1970 at Boston Children's Hospital, radionuclides were administered only to patients with advanced neoplastic diseases. Today, as new agents are introduced, it is imperative to understand the details of their distribution and the resulting radiation doses delivered to various organs. Moreover, for those who participate in clinical trials with new radiolabeled agents, an estimation of the absorbed radiation dose is required by institutional review boards, as is some assessment of the potential hazard (see also Chap. 28).

Second, patients and particularly the parents of young patients are frequently concerned about the radiation risks associated with nuclear medical procedures. It is important to convey these potential risks clearly, placing them in the context of radiologic and other risks as well as the benefits to be gained.

Third, nuclear medical specialists are often asked their advice about the potential harm that may result from nuclear accidents such as those at Three Mile Island, Chernobyl, and Fukushima. It serves the practitioner well to respond to such requests in an authoritative and intelligible fashion.

The increased use of medical imaging procedures in general, but especially in children, has sensitized the pediatric community to the concomitant increase in radiation exposure, particularly from CT examinations but from nuclear imaging studies, as well [1]. In response, a nationwide program aimed at reducing medical radiation exposure in children, *Image Gently*, has been established (www.imagegently.org).

This chapter presents some of the radiobiologic consequences of irradiation as well as conclusions from several epidemiologic studies of radiation exposure. How the radiation protection community thinks about low-dose and low-dose-rate exposure is considered. A final section discusses how to explain potential risks to others.

S.J. Adelstein, MD, PhD
Joint Program in Nuclear Medicine,
Department of Radiology, Harvard Medical School,
Boston, MA, USA

Department of Radiology,
Brigham and Women's Hospital,
Boston, MA, USA
e-mail: james_adelstein@hms.harvard.edu

S.T. Treves (ed.), *Pediatric Nuclear Medicine and Molecular Imaging*,
DOI 10.1007/978-1-4614-9551-2_30,

Effects of Radiation Exposure

Radiobiologic Consequences

We are now aware that damage to the genome is the basis for most radiation action on cells; this is the case particularly for late effects—cancer production in somatic cells and mutagenesis in germ cells—although all of the mechanistic details have not been worked out. At the molecular level, ionizing radiation causes base damage, single-strand breaks and double-strand breaks (DSBs) in DNA, as well as cross-linking between DNA strands and between DNA and nuclear proteins. Of particular significance are DSBs, which are susceptible to misrepair. They are induced with radiation doses as small as 1 mGy, and their frequency arises linearly with dose [2]. Molecular damage leads to point mutations, partial and complete gene deletions, disrepair, translocations, and other genetic changes. These changes, in turn, result in inheritable disorders in germ cells and, through the interplay of oncogenes, tumor suppressor genes, and clonal selection, in cellular transformation and carcinogenesis in somatic cells.

Of relevance to nuclear medicine is the observation, in cell cultures, that fractionation of radiation dose or reducing the dose rate decreases the frequency of carcinogenic transformations. Thus a given dose from beta particles or gamma photons, such as that produced by extended radioactive decay, results in a lower transformation frequency than the same dose delivered acutely by x-ray or electron generators [3].

Chromosomal aberrations are the most obvious of the cytogenetic changes produced by irradiation. Of these changes, chromosome and chromatid breaks and structural rearrangements are the most common. When two breaks are produced in a cell and the ends joined other than in their original sequence, stable and unstable structural anomalies occur. As two electron tracks are generally needed to produce these aberrations, the dose–response relation, taking into account the occasional single track that produces two breaks, is a linear–quadratic one [4].

Exposure of rodents and other animals to increasing doses of radiation leads to an increased incidence of cancers and inheritable genetic abnormalities. In the case of cancers, the incidence rises with dose to reach a maximum at about 3–5 cGy. Decreasing the dose rate or fractionating the dose reduces the incidence of animal cancers—with its obvious relevance to internally deposited radionuclides [5].

The main source of genetic information about the effects of radiation on the germ cells of mammals comes from experiments with mice. Increasing rates of mutation are found with increasing doses. Again, a reduction in dose rate has a significant effect on mutational frequency. In the male mouse, radiation sensitivity is reduced by a factor of three when the dose rate goes from 1,000 to 10 mGy/min, whereas in the female mouse low-dose rates produce few if any mutations. From these experiments, the doubling dose (i.e., that quantity of radiation required to double the mutation rate to twice its spontaneous value) is estimated to be approximately 1 Gy. As no direct information on the production of radiation-induced, inheritable human disorders is available, risk estimates are based on mouse experiments. The children of persons exposed acutely to radiation in Hiroshima and Nagasaki have been carefully examined, and no evidence for genetic change above the baseline has been found. Hence, it has been assumed that humans are no more sensitive to inheritable mutations than mice, and, in the case of chronic irradiation, may be considerably less so [6].

Epidemiologic Studies

In a number of instances, exposure to ionizing radiation has produced cancer in humans. Early radiologists, who performed fluoroscopic examinations with bare hands and high-dose sources, developed skin cancers. Radium-dial painters, who pointed brushes with their tongues, developed sarcomas of the bone. Patients receiving thorium by injection to make the liver opaque to x-rays developed liver tumors. These observations alerted the medical community to the proposition that high-dose exposure could produce human cancer at some later time.

More recent studies have been concerned with quantifying the dose–response relationship in populations exposed to various doses of

radiation in the range of 0.1–3 Sv. These populations include survivors of the atomic bomb detonations in Japan, patients treated by x-rays for ankylosing spondylitis, patients with tuberculosis and thoracoplasties who were followed for long periods with multiple fluoroscopies, patients treated with radiation for mastitis, and children who underwent irradiation of the scalp and thymus with concomitant irradiation of the thyroid. In addition, children who ingested ^{131}I following the Chernobyl disaster have been followed. All of these studies have shown an increase in cancer incidence with increasing doses of radiation for a number of organs including the bone marrow, breast, thyroid gland, lung, stomach, colon, and ovary.

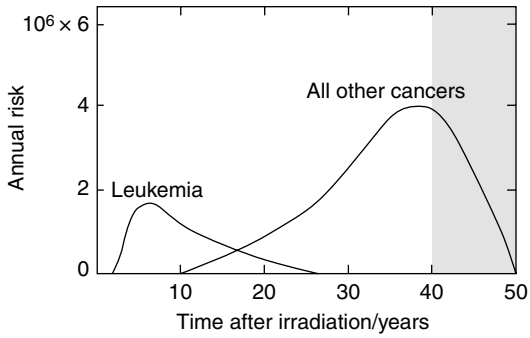

Fig. 30.1 Nominal risk of cancer mortality versus time following 2-mSv uniform whole-body irradiation (From Sinclair [19], adapted with permission of the National Council on Radiation Protection and Measurements)

Although among these studies there are some variations in the dose–response relationship, several generalities have emerged [4]:

1. The response of bone marrow differs significantly from that of solid organs. Leukemias appear earlier after exposure than do other cancers; they reach a peak incidence within 5–10 years and decline slowly thereafter (Fig. 30.1). Childhood forms, such as acute lymphocytic leukemia, differ from adult forms, such as acute and chronic myelogenous leukemia. The dose–response curve for leukemia appears to be linear–quadratic in shape with a possible threshold [7]. For solid tumors there is a latent period of at least 10 years, and the dose–response curves appear to be approximated by straight lines (Fig. 30.2) [8]. Not all tissues are equally sensitive to radiation carcinogenesis. In the Hiroshima–Nagasaki life-span study, breast and bladder were more so and rectum, pancreas, and uterus less.
2. Children are more susceptible than adults [9]. Moreover, there seems to be an increase in childhood cancers, particularly leukemia, of the same magnitude in children exposed in utero. The incidence of additional cancer cases increases with age in parallel with the increase in cancer of solid organs seen in an unexposed population.
3. Exposure of the thyroid gland to external radiation results in an increased incidence of thyroid nodules and thyroid cancer,

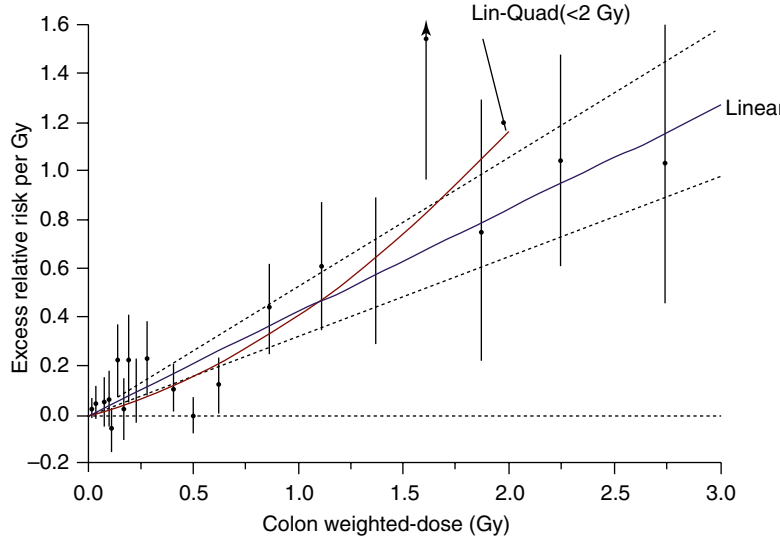

Fig. 30.2 Dose–response for radiation-induced solid cancers from life-span study of atomic bomb survivors (From Ozasa et al. [8], with permission)

as would be expected. Childhood thyroid cancer has increased early and markedly in areas subject to radioiodine fallout from the Chernobyl nuclear accident [10]. The marked sensitivity and rapid onset may be due to the relative iodine deficiency in these areas. Notwithstanding, this observation suggests that caution should be used in treating children and young adolescents before the age of 15 with ^{131}I. The oncogenic pathway RET–RAS–BRAF–MAPK may be involved in the pathogenesis of these juvenile papillary thyroid cancers. Rearrangement of the RET/PTC gene following the induction of DSBs seems particularly to be implicated [11].

Moderate to high doses of radiation *in utero* also produce developmental defects and functional losses in certain organs. Unlike carcinogenesis, these responses have a clear threshold above the levels provided by most nuclear medical procedures. For this reason they are not described here but can be found in a number of sources [12]. As for inheritable diseases following radiation of gametes, so far none have been observed in humans at low doses and are, therefore, not considered to be of significance [13].

Low-Dose and Low-Dose-Rate Exposure

Most nuclear medical exposures and most nonoccupational accidental radiation exposures are at equivalent doses from 5 to 25 mSv (see Chaps. 28 and 31). Ideally, estimates of the risk would be derived from definitive epidemiologic studies performed in this dose range. Although there are many such studies, none is conclusive. Several populations have been examined: atomic bomb survivors, persons exposed to nuclear sources such as fallout from weapon tests, those exposed as workers in nuclear facilities, medically irradiated populations, and persons who have lived in high-background areas. Some studies have shown increases in cancer incidence with low doses, and others have not; a few have indicated a decrease in cancer incidence with doses slightly above background levels. All have suffered from small sample size, inadequate controls, incomplete dosimetry, or a range of confounding factors. As the statistical restraints on studies of small populations are so much greater than those on large ones, it is easy to see why these investigations shed little light on the question of a threshold for radiation effects and provide an uncertain estimate of radiation risks at low doses [14].

In addition, there is experimental evidence that low doses of radiation do produce paradoxical biologic effects, but whether these are detrimental or protective is a matter of contention. Chronic, low-dose exposure (1 mSv per week for mice; 0.8 mSv per day for rats) increases the life span of rodents, an effect that has been ascribed to enhanced immune responsiveness. Similarly, a decreased incidence of thymic lymphoma has been found in mice as a result of chronic, fractionated low-dose total-body x-irradiation [15]. Furthermore, exposure of some cells and organisms to low-dose radiation produces an adaptive response to higher doses of radiation; that is, certain biologic changes occur with less frequency at higher levels of radiation exposure than are found in previously unexposed cells [16]. These changes include survival, chromosome aberrations, and gene mutations. The increased radiation resistance has been ascribed to radical scavenging, stimulated DNA repair mechanisms, or the production of protective stress proteins.

On the other hand, there is now evidence that irradiated cells may produce biologic effects in their unirradiated neighbors, a response called the bystander effect. This phenomenon seems to rely on a transmissible factor(s). It has been shown in an in vitro cell system that the adaptive response may cancel out the bystander effect, which would make it difficult to predict the importance of the latter at low-dose exposures [17].

National and international bodies, taking a prudent approach, have adopted the stance that all radiation exposure is potentially harmful, with even the lowest doses producing some damage at the molecular and cellular levels [4]. Thus, considerable effort has been expended in estimating the risks at low doses and low-dose rate by

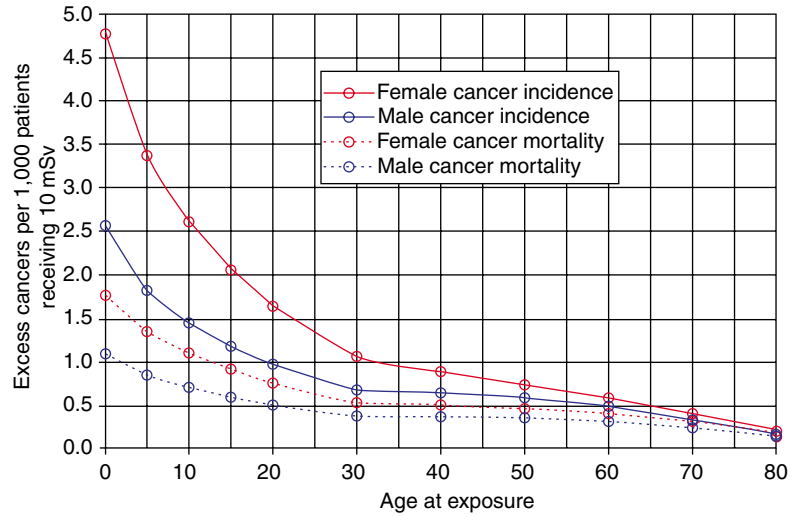

Fig. 30.3 Radiation-induced cancer risk estimation for 10-mSv exposure as a function of age (From Sodickson et al. [20], with permission of RSNA)

extrapolation from moderate- and high-dose epidemiologic data. The principal arguments have focused on the correct form for the dose–response curve. The curve for leukemia, which appears to be of the linear–quadratic form, agrees with the shape of responses across a wide variety of biologic end points. In the case of solid organs, extrapolation has proved more difficult; the data fit a linear relationship but there is considerable uncertainty at low doses (Fig. 30.2). On the other hand, a linear–quadratic response can appear linear at high and moderate doses. To take into account this possibility and the fact that progressively lowering the dose rate incrementally reduces the slope of the dose–response curve in experimental systems, a dose and dose-rate effectiveness factor has been introduced to approximate the limiting slopes at low-dose rate. The value of this factor has been estimated to be 1.5–10, but most agencies have used a value of approximately 2 to be on the conservative side. From all these adjustments, the carcinogenic risk from 10-mSv exposure is estimated at ~5 in 10,000 for adults and about l in 1,000 for children (Fig. 30.3).

Despite the uncertainty of estimates at low doses, national and international agencies advise that the most prudent estimate of risk is based on extrapolation from the linear non-threshold relationship. Thus, it is incumbent on practitioners to minimize these risks without compromising clinical care. Three general approaches can be employed. First, minimize the dose from imaging procedures that use ionizing radiation without compromising image fidelity; second, replace procedures based on ionizing radiation (e.g., CT and nuclear studies) with those that are not (e.g., MRI and ultrasound) when appropriate; third, order CT and nuclear images only when indicated by clinical decision rules and appropriateness criteria. When such guidelines have been followed, significant reduction in radiation exposure has been observed. The "Image Gently" campaign championed by the Alliance for Radiation Safety in Pediatric Imaging has taken the lead in promoting these, and much useful information for patients, families, and medical practitioners can be found on their website (see www.imagegently.org).

Explaining the Risks to Others

Effective Dose

To estimate the radiation risk from any diagnostic procedure or accidental exposure, it is necessary to relate a dose quantity to a risk quantity. For nuclear medical procedures in which, by design, the dose to different organs varies, it is useful to combine the doses into a single metric that can be used for comparative purposes. This is best done

Table 30.1 Assessment of radiation risk from ^{99m}Tc-MAG3

	Administered activity (MBq)	Effective dose (mSv)	Risk (%)	
			Female	Male
Newborn	4.4	1.41	0.04	0.02
5-year-old	55.5	0.78	0.04	0.02
10-year-old	104.0	1.56	0.04	0.01
Adult	370.0	4.44	0.04	0.02

Note that although the risk per unit of exposure increases with decreasing age, the scaling of administered activity with body surface area evens out the relative risk

by employing the effective dose (E), the dose to each organ for a given procedure multiplied by a weighting factor and then summed:

$$E = \Sigma H_T W_T,$$

where H_T is the dose to organ T and W_T is the weighting factor for organ T. The weighting factor is proportional to the radiation sensitivity of each organ as determined from epidemiologic studies of carcinogenesis and, in the case of the gonads, from experimental studies of inheritable disorders. Thus the effective dose is a risk surrogate that is corrected for the heterogeneity of absorbed organ doses obtained in most nuclear medical procedures or from accidental exposure to radionuclides. Some representative effective doses from nuclear medical procedures are given in Chap. 28.

It should be appreciated that the effective dose has been calculated for healthy adults and does not take into account either the age or the life expectancy of sick children. It should be used only to compare the radiation risk of one procedure with another and as a basis for comparison with other hazards. Nonetheless, it is possible to estimate the radiation risk from common nuclear medical procedures; for example, that for ^{99m}Tc-disodium [*N*-[*N*-*N*-(mercaptoacetyl)glycyl]-glycinato(2-)-N,N′,N″,S]oxotechnetate(2-) (^{99m}Tc-MAG3) (Table 30.1) has been assessed using the results from Fig. 30.3 and Chap. 31.

Institutional Review Boards

The institutional review process that is required before new or experimental procedures are introduced is greatly facilitated by having a uniform radiation risk standard with which the new procedures may be compared. Of course, review boards are also interested in the relative benefit and effectiveness of the new procedure in relation to its hazard; introduction of the procedure to the clinic, after all, is based on efficacy. In pediatric nuclear medicine, these questions are especially important as many new procedures and agents are first tested in adult patients and then extended to children on a trial basis. We have found that a good comparison is with equivalent doses from well-established radiologic and nuclear medical procedures. (Keep in mind that the background equivalent dose, excepting radon exposure, is about 1 mSv per year.) Some representative equivalent doses are chest radiograph, 0.1 mSv; i.v. urogram, 3 mSv; and abdominal CT, 8 mSv.

Patients and Their Families

When providing information to patients who are to undergo a diagnostic nuclear medical procedure or to those inadvertently exposed to radiation releases, as well as to their families, the goal should be to reduce anxiety by conveying a realistic and comprehensible estimate of the projected harm. This is not always an easy task. As described above, the long-term consequences of radiation exposure are frightening in their potential prospect: cancers and genetic defects. Moreover, the perception of risk is often contextual with the fear of radiation exposure from a nuclear accident being greater than that from medical and natural sources [18].

There are several ways to facilitate the discussion of these matters with patients. First, the time course for the late effects of radiation can be described with the help of a diagram such as that shown in Fig. 30.1. The risk of leukemia starts after a latent period of 2 years, peaks at 6–7 years, and is generally exhausted after 25 years. The risk of a solid tumor begins after 10 years and may peak after 40 years. The lifetime attributable risk of a 10-mSv exposure in children is shown in Table 30.2 and Fig. 30.3. One way of expressing

Table 30.2 Additional lifetime attributable risk of all forms of cancer from 10 mSv of radiation exposure relative to the general population (baseline)

Age at exposure	% Cancer incidence		% Cancer mortality	
	Males	Females	Males	Females
Baseline	45.5	36.9	22.1	17.5
8 years	+0.2	+0.3	+0.1	+0.1
20 years	+0.1	+0.2	+0.1	+0.1

this risk is to compare it with the ordinary risk of dying of cancer—a probability of approximately 20 %. The incremental risks are small and are outweighed by the benefits.

A similar approach can be taken for inheritable genetic risks. It is important to convey that the uncertainty is greater in this instance because estimates are based on animal data, although we are fairly certain that humans are less sensitive than mice. In humans the probability of an offspring having a genetic abnormality, which includes genetic and chromosomal diseases as well as constitutional diseases and anomalies, is about 6 %. Following a radiation exposure of 10 mSv, it is projected that there is an additional probability of 0.0004 %, so the total probability becomes 6.0004 %, hardly a significant increment [6].

Another approach is to compare these risks to other hazards of everyday living. With an average fatal accident rate of 6 per 10,000 per year, over a 50-year period, this risk is approximately 3 %, or the equivalent of an exposure to 600 mSv or 120 average nuclear medical procedures. Fatal accidents also provide a useful spectrum of risks (Table 30.3). The analogy, however, can be faulted as these accidents are generally immediately fatal in comparison with the long-term consequences of radiation exposure. In contrast, the frightening aspects of radiation risk are the uncertainty of outcome and relatively long period of latency.

No conversations with patients and families concerning the risks of exposure from imaging studies should omit their benefits. This should include the reasons for the study, be it for diagnostic accuracy, for its impact on decisions as to treatment and hospitalization, to measure therapeutic response, etc. The discussion should make it clear that the decision to employ a nuclear or CT study is based on a benefit that exceeds any perceived risk. Although most patients and parents generally assume such logic, it is reassuring for them to hear that those caring for the health of children do so as well.

Table 30.3 Lifetime risk of death from everyday activities compared with medical radiation exposures, e.g., 1 out of 304 Americans will die as a result of an accident while riding in a car during his/her lifetime

Activity	1/risk	Examination	1/risk
Riding in car	304		
Crossing street	652	CT abdomen (10 years old)	1,600
Choking	894	CT abdomen (40 years old)	2,900
Drowning	1,127	^{18}FDG-PET (10 years old)	1,515
Falling on stairs	2,024	^{18}FDG-PET (40 years old)	2,700
Riding bike	4,734	^{99m}Tc-MDP (10 years old)	2,560
Airplane crash	7,058	^{99m}Tc-MDP (40 years old)	4,760
Hit by lightning	84,388		

From Fahey et al. [18], with permission

Conclusion

Practitioners of pediatric nuclear medicine should have a firm understanding of the risks of radiation, particularly at low doses and low-dose rates. We have an obligation to look at the absorbed doses from standard procedures with these risks in mind and to convey the risks of new ones to institutional review boards in a fashion that compares them with the risks of other medical tests. We must be able to present these risks to patients and their families in a manner that allows them to appreciate the hazards and benefits in a realistic way and in relation to the risks of other activities.

References

1. Fazel R, Krumholz HM, Wang Y. Exposure to low-dose ionizing radiation from medical imaging procedures. N Engl J Med. 2009;361(9):849–57.
2. Rothkamm K, Löbrich M. Evidence for a lack of DNA double-strand break repair in human cells

exposed to very low x-ray doses. Proc Natl Acad Sci U S A. 2003;100:5057–62.
3. Dale RG. Dose-rate effects in targeted radiotherapy. Phys Med Biol. 1996;41:1871–84.
4. National Research Council of the National Academies. Health risks from exposure to low level of ionizing radiation: BEIR VII, phase 2. Washington, DC: The National Academies Press; 2006.
5. Ullrich RL, Storer JB. Influence of γ irradiation on the development of neoplastic disease in mice. III. Dose-rate effects. Radiat Res. 1979;80:325–42.
6. Sankaranarayanan K. Estimation of the hereditary risks of exposure to ionizing radiation: current status, and emerging perspectives. Health Phys. 2001;80(4): 363–9.
7. Shore RE, Shimizu Y, Kasagi K, et al. Japanese a-bomb survivor data and studies of low-dose effects. In: Ninth Annual Gilbert W. Beebe Symposium: scientific advances in radiobiology and radiation epidemiology, implications for radiation exposure regulation. Washington, DC: The National Academies; 2010.
8. Ozasa K, Shimizu Y, Suyama A, et al. Studies of the mortality of atomic bomb survivors, report 14, 1950-2003: an overview of cancer and noncancer diseases. Radiat Res. 2012;177:229–43.
9. Brenner DJ. Estimating cancer risks from pediatric CT: going from the qualitative to the quantitative. Pediatr Radiol. 2002;32:228–31.
10. United Nations Scientific Committee on the Effects of Atomic Radiation. Sources and effects of ionizing radiations. UNSCEAR 2000 report to the General Assembly with scientific annexes, vol. II: effects. New York: United Nations; 2000.
11. Fagin JA. Editorial: challenging dogma in thyroid cancer molecular genetics–role of RET/PTC and BRAF in tumor initiation. J Clin Endocrinol Metab. 2004;89:4264–6.
12. Schull WJ, Otake M. Cognitive function and prenatal exposure to ionizing radiation. Teratology. 1999;59: 222–6.
13. Fujiwara S, Suyama A, Cologne JB, et al. Prevalence of adult-onset multifactorial disease among offspring of atomic bomb survivors. Radiat Res. 2008;170(4): 451–7.
14. Boice Jr JD. Lauriston Taylor lecture: radiation epidemiology – the golden age and future challenges. Health Phys. 2011;100(1):59–76.
15. Ishii K, Hosoi Y, Yamada S, et al. Decreased incidence of thymic lymphoma in AKR mice as a result of chronic, fractionated low-dose total-body X irradiation. Radiat Res. 1996;146:582–5.
16. Johansson L. Hormesis: an update of the present position. Eur J Nucl Med Mol Imaging. 2003;30:921–33.
17. Mitchell SA, Marino SA, Brenner DJ, et al. Bystander effect and adaptive response in C3H 10T1/2 cells. Int J Radiat Biol. 2004;80:465–72.
18. Fahey FH, Treves ST, Adelstein SJ. Minimizing and communicating radiation risk in pediatric nuclear medicine. J Nucl Med. 2011;52:1240–51.
19. Sinclair WK. Proceedings of the twentieth annual meeting of the National Council of Radiation Protection and Measurements, Apr 1984. Proceedings No. 6, Bethesda: NCRP; 1985. p 227.
20. Sodickson A, Baeyens PF, Andriole KP, et al. Recurrent CT, cumulative radiation exposure, and associated radiation-induced cancer risks from CT of adults. Radiology. 2009;251:175–84.

Dose Optimization in Pediatric Nuclear Medicine

31

S. Ted Treves and Frederic H. Fahey

Diagnostic nuclear medicine studies provide invaluable information in the diagnosis and follow-up of many disorders in children. These studies are physiologic, highly sensitive, and minimally invasive. It is generally agreed that when performed appropriately, nuclear medicine studies carry low radiation exposures and pose no demonstrable risk to patients. To date, there have not been documented risks to the patient with such low doses of radiation from nuclear medicine studies.

During the past few years, there has been an increased level of interest and concern over the potential health risks to children from diagnostic imaging studies that utilize ionizing radiation. Reported risks from CT in children include the development of cancers and, in the case of CT radiation exposures to the head in early life, an effect on cognitive function. These concerns have been a source of extensive coverage both in the scientific literature and in the public press. These communications are too many to cite in this chapter. Even with such a wealth of published literature, controversy still exists regarding what the real or potential risks are from low radiation exposures in diagnostic imaging in children. This topic is likely to remain a source of ongoing discussion and further research for some time to come [1, 2].

Although radiation doses in pediatric nuclear medicine are low, it is considered prudent and good practice to perform these studies using the lowest amounts of radioactivity that preserves the procedure's diagnostic value. When considering nuclear medicine imaging in children, it is important to balance the real benefit to the patient and referring physicians with the potential risk of low radiation exposure. The Society of Nuclear Medicine and Molecular Imaging (SNMMI) and the Society of Nuclear Medicine Technologist Section (SNMTS) have published a joint statement (June, 2012) in this regard that states: "The SNMMI and SNMTS believe that the right test with the right dose should be given to the right patient at the right time. When nuclear medicine and molecular imaging procedures are performed correctly on appropriate clinical indications in

S.T. Treves, MD (✉)
Joint Program in Nuclear Medicine,
Department of Radiology,
Harvard Medical School,
Boston, MA, USA

Division of Nuclear Medicine and Molecular Imaging, Department of Radiology,
Boston Children's Hospital,
Boston, MA, USA

Division of Nuclear Medicine and Molecular Imaging, Department of Radiology,
Brigham and Women's Hospital, Boston, MA, USA
e-mail: ted_treves@HMS.harvard.edu

F.H. Fahey, DSc
Joint Program in Nuclear Medicine,
Department of Radiology,
Harvard Medical School, Boston, MA, USA

Division of Nuclear Medicine and Molecular Imaging, Department of Radiology,
Boston Children's Hospital, Boston, MA, USA
e-mail: frederic.fahey@childrens.harvard.edu

S.T. Treves (ed.), *Pediatric Nuclear Medicine and Molecular Imaging*,
DOI 10.1007/978-1-4614-9551-2_31,

patients, the real benefits of the procedure significantly outweigh any potential risks. The procedure that provides the most useful clinical information is the one that should be performed." Please see Chap. 30 [3–9].

The benefits of nuclear medicine to the care of pediatric patients are described in several chapters in this book. Radiation exposures from pediatric nuclear medicine procedures and potential risks from radiation exposures in nuclear medicine are discussed in Chaps. 28 and 30, respectively. This chapter focuses on ways and means to achieve reduction in radiation exposures in these patients without adversely affecting the diagnostic quality of the studies.

Factors that can lead to reduction in radiation exposure in children undergoing nuclear medicine studies include the following:

1. Lowering radiopharmaceutical administered doses
2. Appropriateness of clinical indications and utilization
3. Optimization of imaging protocols
4. Application of advanced imaging processing and display
5. New and advanced instrumentation
6. Education and communication

Radiopharmaceutical Administered Activities

The most influential factor in controlling radiation exposure in nuclear medicine is the amount of radiopharmaceutical activity administered to the patient. While pediatric applications of nuclear medicine have been used extensively for many decades, radiopharmaceutical administered activities in children traditionally have not been standardized until very recently [6, 7].

Historically, pediatric administered radiopharmaceutical doses have been determined by a combination of factors including practitioners' experience and preference, available instrumentation, patient size, desired image quality, photon flux examination time, and the patient's ability to cooperate. Over the years, individual institutions have developed their own approach towards determining pediatric doses in their practices. As a consequence, pediatric radiopharmaceutical administered doses have varied over a rather broad range with the consequent wide variation of patients' radiation exposures. High doses (which may not result in improved diagnostic sensitivity or accuracy) or low doses (which do not permit adequate examination) should be considered unnecessary radiation exposures and should therefore be avoided whenever possible.

Contributing to this large variability of radiopharmaceutical administered doses in children has been the fact that with very few exceptions, most radiopharmaceutical package inserts have not provided guidance on pediatric doses. Instead most contain what has been known as the "orphan clause" that states something like this: "Pediatric Use: Safety and effectiveness in children have not been established."

Lack of information on pediatric administered doses and absorbed doses, the desire of some physicians or technologists to obtain a study in the shortest possible time, combined with inexperience in handling pediatric patients are all factors that can contribute to radiopharmaceutical overdose in children [3].

Dose estimations for pediatric patients based on adult dose corrected for body weight, body surface area or other expressions of size have been considered adequate general guides for children over 1 year of age. However, premature infants and newborns require special consideration, and the concept of minimum total dose should be considered. *Minimum total dose* may be defined as the minimum dose of a radiopharmaceutical below which the study will be deemed inadequate regardless of the patient's body size [4].

In 2008, we conducted a survey of pediatric radiopharmaceutical dose protocols among 13 premier children's hospitals in North America. These institutions have modern imaging systems and their staffs have an excellent understanding of the pediatric patient. However, even under those circumstances, our review indicated that the administered dose ranges varied rather widely. The information gathered in this survey showed that the values for *maximum activity* and activity calculated as a function of *body weight*

varied by an average factor of 3 and as much as 10. Importantly, radiopharmaceutical doses given to the *smallest children* (minimum administered dose) varied by an average factor of 10 and as much as 20 in some procedures. These findings suggest that a refined approach to determine optimal radiopharmaceutical doses in newborns and infants is needed. Our survey did not include institutions that were not exclusively dedicated to children, so one would speculate that the actual variation in administered doses might be even greater across adult institutions that also image children. Publication of the results of this survey elicited considerable interest among imaging specialists including pediatric nuclear medicine practitioners.

The 2010 North American Guidelines for Administered Radiopharmaceutical Doses list recommended doses based on maximum doses, doses by body weight, and also minimum doses for a number of agents. These guidelines are approved by the Society of Nuclear Medicine and Molecular Imaging (SNMMI), the Society for Pediatric Radiology (SPR), and the American College of Radiology (ACR) and are endorsed by the Image Gently Campaign (IG). The guidelines were distributed widely on the IG and SNMMI websites and in the form of pamphlets with the dose guidelines that were distributed within professional journals and also mailed to nuclear medicine departments in North America. This group continues to meet to update these guidelines [5–7].

The European Association of Nuclear Medicine (EANM) has also developed a pediatric dose card. Using this lookup table, administered dose can be determined based on which radiopharmaceutical is being used and on patient weight [10].

Appropriateness of Clinical Indications, Utilization Criteria, Sequencing of Studies

One way to reduce radiation exposures in pediatric nuclear medicine is to ensure that the requested procedure is the most appropriate approach to the specific diagnostic question and that the administered dose is appropriate to the specific clinical task. Therefore, it is important to review each request and obtain sufficient clinical information in each case before proceeding with a study. When multiple imaging studies are contemplated for one patient, it is helpful to determine in what order these tests should be obtained to assure that one can achieve the desired diagnosis in the most efficient way and with the lowest patient radiation exposure possible. From the vantage point of nuclear medicine, we offer some examples on how to reduce exposures based on certain diagnostic objectives.

Consider the case of radiographic voiding cystourethrography (VCUG) and radionuclide cystography (RNC). One way to reduce radiation exposure to patients is to obtain an RNC instead of a VCUG for the initial detection of vesicoureteral reflux and also for follow-ups. Depending on the equipment and the technique, RNC gives 20–100 times lower dose than VCUG, it continuously monitors filling and voiding, and it high contrast and a high sensitivity for the detection and assessment of vesicoureteral reflux. Although the spatial resolution of RNC is inferior to VCUG, RNC is more sensitive, and in many instances, even with the relatively poor spatial resolution, it can serve to answer whether reflux is present or not (Fig. 31.1).

During the investigation of recurrent urinary tract infections, some practices indicate a cystogram first to determine if the patient has vesicoureteral reflux or not. In this approach, if the patient doesn't have reflux, the evaluation for renal parenchymal damage is not usually pursued. This is known as the "bottom-up" approach. However, it is important to consider that renal damage from pyelonephritis can exist without detectable vesicoureteral reflux. Other practices employ a so-called "top-down" approach. This approach begins with the initial assessment of renal cortical damage with ^{99m}Tc-DMSA scintigraphy. This approach reduces the need for an initial VCUG or RNC. In this setting, reflux studies are reserved for patients in whom the DMSA scan reveals renal damage. Reducing the number of necessary voiding studies in patients who are asymptomatic can reduce patients' gonadal dose (Fig. 31.2).

Fig. 31.1 Selected images of a radionuclide cystogram (RNC) from a 6-month-old girl showing severe bilateral reflux

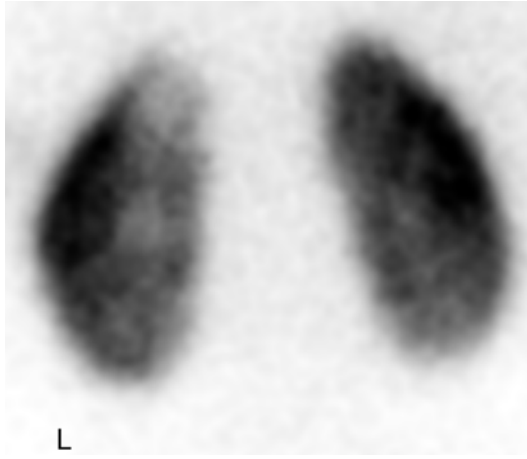

Fig. 31.2 ^{99m}Tc-DMSA renal scan in an 8-month-old boy with recurrent fever. There is a focal reduction of tracer uptake in the left upper pole, presumably due to pyelonephritis in the patient without vesicoureteral reflux

Pulmonary Aspiration and the Salivagram

In the diagnosis of pulmonary aspiration, the early use of the salivagram in some cases may be preferable to barium swallow studies. The salivagram is highly physiologic, noninvasive, and very sensitive and delivers a very low radiation exposure to the patient. Obviously, this test does not give detailed anatomic information compared to a barium swallow (such as the evaluation of the swallowing dynamics), but in some patients the information derived by the salivagram may provide sufficient information to help in the management of the patient (Fig. 31.3).

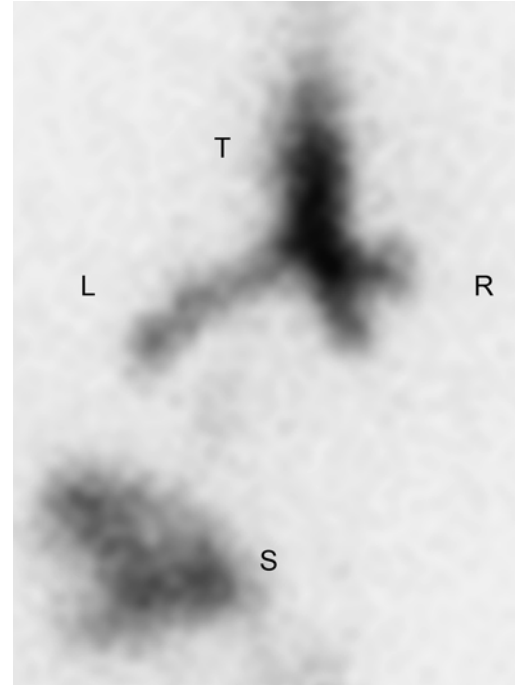

Fig. 31.3 Bilateral aspiration demonstrated by a salivagram in a 4-month-old boy with recurrent pulmonary infections. *T* trachea, *S* stomach, *L and R* left and right main bronchi

Evaluating the Skeletal Origin of Back and Extremity Pain

Localization of a skeletal cause of back or extremity pain in young children can be challenging. Patient or parent reports of the location of pain may be unreliable including the presence of referred pain. Frequently, these patients initially

undergo plain radiography or even CT to the region suspected of being the origin of pain. It is possible that an X-ray or even a CT may focus on the wrong region of the body, missing the true region of interest. In this setting, one advantage of skeletal scintigraphy to be considered is that a large area of the body can be evaluated in one imaging session. In one example, the child's mother reported that the young child had developed ankle pain following a fall. Radiographs of the area were normal and the orthopedic surgeon prescribed "high-top" sneakers in an attempt to provide support to the patient's ankle. As the patient didn't improve, the surgeon indicated a bone scan. The scan revealed a spiral fracture of the tibia that was later confirmed by a plain radiograph. The patient's symptoms improved after placement of a cast. In retrospect, the diagnosis of tibial injury could have been obtained with a bone scan that would have directed the therapy quickly and more precisely (see Fig. 15.15 in Chap. 15).

In another example, a young male with persistent lower back pain was relieved by analgesics. Over several weeks, the patient had two sets of X-rays of the lumbosacral spine. One of these examinations suggested mild scoliosis. As the patient's symptoms persisted, a CT of the lower lumbar spine was obtained which was normal. The referring physician indicated a bone scan. This study revealed an intense, focal area of very high uptake at the level of T12 in the region of the posterior elements. Scintigraphically, this appearance suggested an osteoid osteoma. A repeat CT including the region of T12 revealed a characteristic finding of an osteoid osteoma (see Fig. 15.3 in Chap. 15).

These two cases exemplify the usefulness of large area imaging provided by skeletal scintigraphy in the evaluation of children with back pain or extremity pain. Once a lesion is detected by scintigraphy, focused imaging with an X-ray or CT can help add specificity to the finding.

Optimization of Imaging Protocols: Acquisition and Display

Standard imaging protocols can be modified, adapted, or optimized in ways such that the diagnostic information is maintained, but at a lower radiation exposure to the patient. For example, one way to reduce pediatric administered doses is to consider the type of study (dynamic or static, etc.) and the diagnostic goal or task. For example in some centers, it is routine to acquire a dynamic renal study with ^{99m}Tc-MAG3 in two framing rates: the first 60 s of the study for 1–2 frames/s for a radionuclide angiogram followed by a "slower" framing rate of 0.25–0.30/s for approximately 20–30 min. However, in most patients the study is viewed and evaluated in sequential 0.5–1.0 min frames. Since the information gathered by the radionuclide angiogram very rarely adds to the diagnosis, the MAG3 study can be obtained with a lower dose than that needed to obtain radionuclide angiogram. This concept can also be applied to other procedures such as hepatobiliary scintigraphy.

Application of Advanced Image Processing

Using advanced image processing in both planar scintigraphy and SPECT, it is possible to achieve significant reductions in radiopharmaceutical administered doses and therefore radiation exposures without loss of diagnostic information. The use of enhanced planar processing (EPP) helps to either reduce the radiopharmaceutical dose or reduce imaging time [11].

In planar imaging spatially adaptive filtering can be useful in static and dynamic studies. Such an approach can provide similar image quality with fewer acquired counts. In static imaging, adaptive filtering can either allow a reduction in the amount of activity administered to the patient given the same acquisition time or alternatively while using the standard administered activity reduce the imaging time. For example a whole body bone scan that would normally take approximately 20–30 min to acquire could be completed in 10–15 min which may alleviate the need for sedation in small patients. Alternatively, reduction of both image acquisition time and of administered activity could be achieved by reducing both factors proportionately. Reduction of imaging time can increase patient comfort and reduce immobilization time. In the case of dynamic

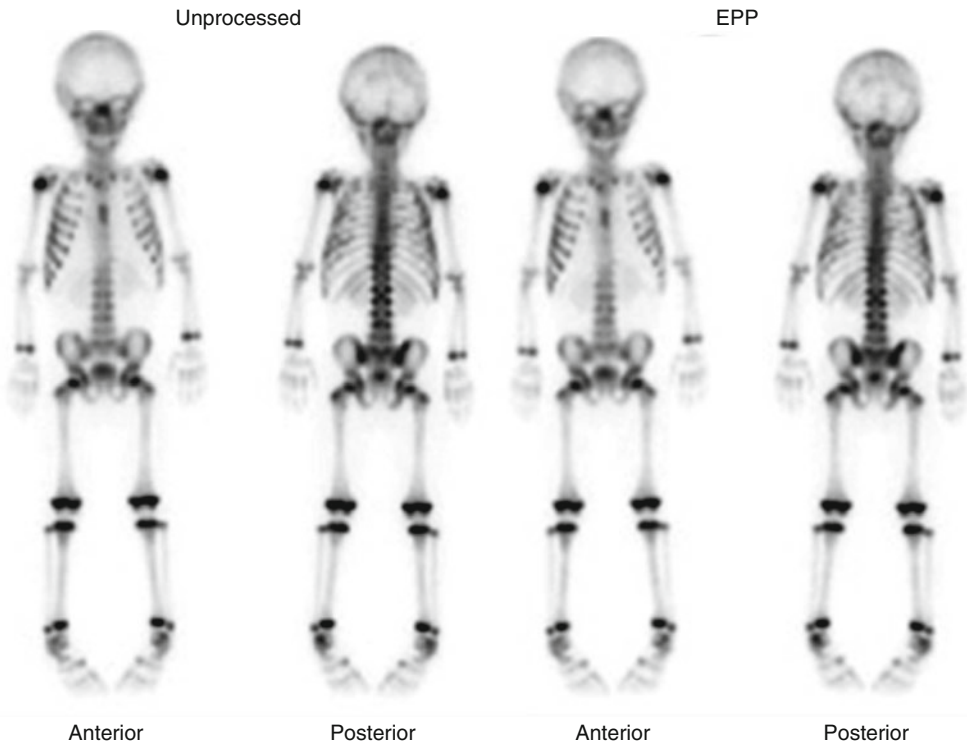

Fig. 31.4 Use of enhanced planar processing (EPP) to reduce imaging time while preserving diagnostic information. Technetium-99m-MDP planar whole body scintigraphy in a 3 year-old boy that received 3.7 mCi [136.9 MBq] of ^{99m}Tc-MDP. Left panel: The total imaging time was 14 minutes. Right panel: with EPP, the total imaging time was only 3.5 minutes. Alternatively, the patient could receive 25% of the original amount of tracer and be imaged for 14 minutes

studies, while EPP cannot reduce the imaging time (as acquisition time is governed by the radiopharmaceutical kinetics), it allows for a reduction of administered activity. These approaches aim to reduce the random noise in the image without degrading the spatial resolution by varying the degree of filtration depending on the image content of the local region of the image (Figs. 31.4 and 31.5).

We have applied this method on previously acquired ^{99m}Tc-MAG3 renal studies as well as in hepatobiliary studies and have demonstrated that images of diagnostic quality can be achieved with a 50–60 % reduction in radiopharmaceutical administered activity (Figs. 31.6 and 31.7).

Application of advanced image processing in SPECT can achieve both improvements in image quality with significant reduction of administered activity. As an example, ordered subset expectation maximization (OSEM) with 3D resolution recovery can achieve these goals. These reconstruction algorithms can make SPECT more feasible in small patients. Since SPECT was first introduced in the clinic, filtered back projection (FBP) has been the standard method of image reconstruction. In the past few years, iterative reconstruction approaches have been introduced in SPECT. Unlike FBP, these approaches can incorporate both the noise properties of the projection data and other physical parameters such as how the collimator resolution varies with distance leading to a more accurate reconstruction. Iterative reconstruction techniques have been shown to provide at least similar but most often improved image quality with significantly less counts needed to achieve the diagnostic task. Therefore, high-quality studies can be obtained with either much lower radiation exposure to the

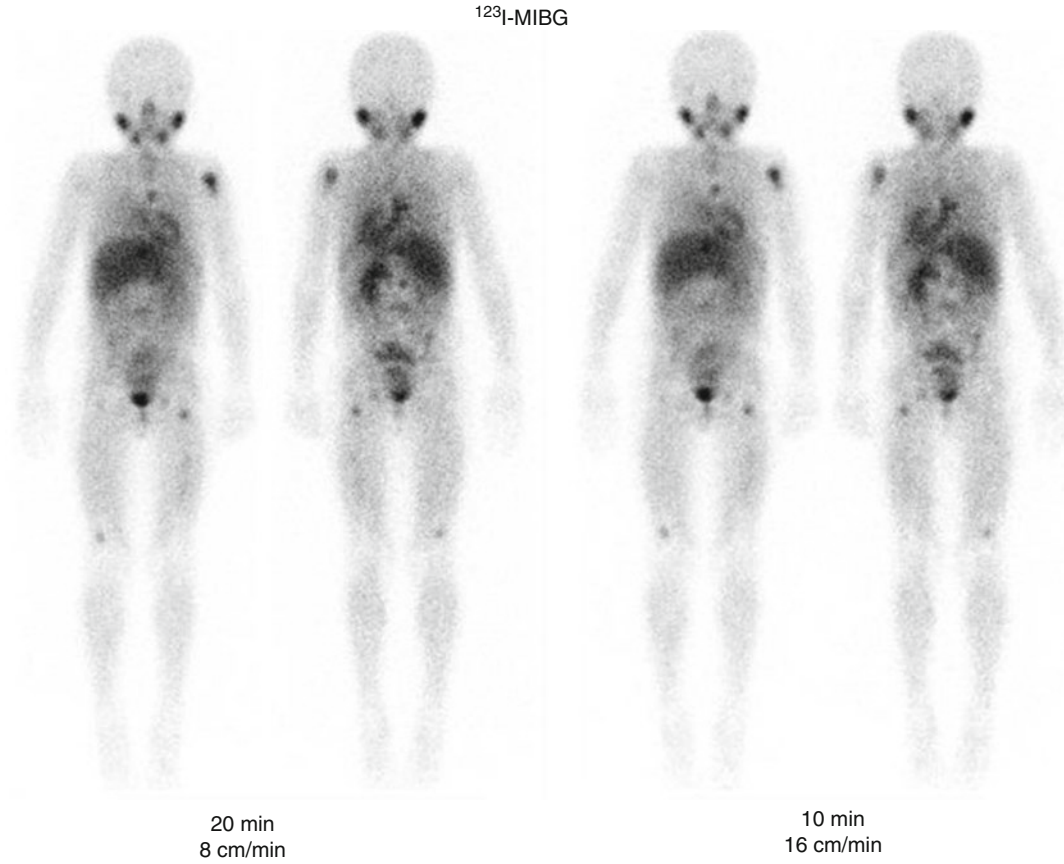

Fig. 31.5 Iodine-123 MIBG whole body scan from a 7-year-old male with neuroblastoma. *Left panel*: 100 % of the administered dose scanned at 8 cm/min for 20 min. *Right panel*: Same dose acquired for 10 min at 16 cm/min using EPP. Scanning time was reduced in half. Alternatively, dose can be reduced in half with a 20-min acquisition

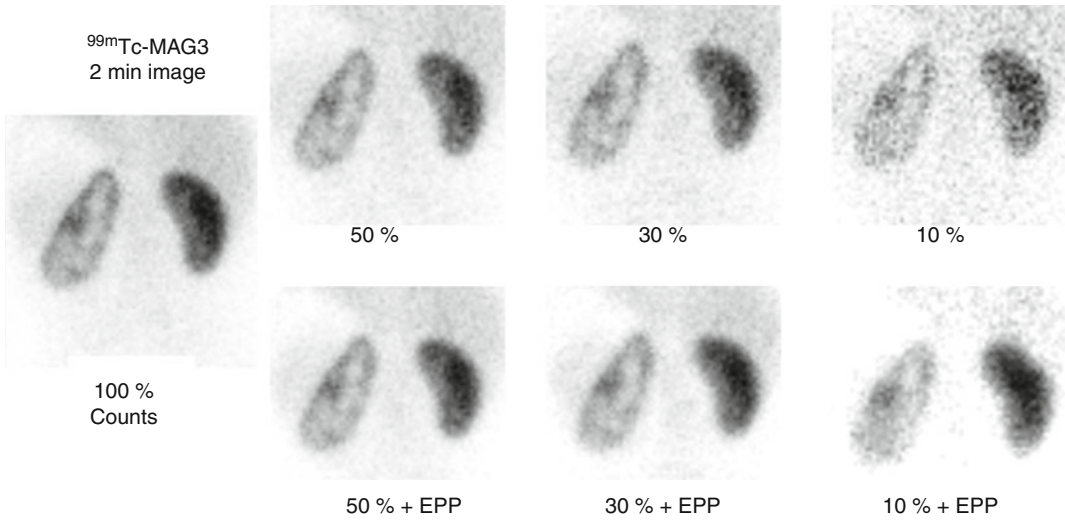

Fig. 31.6 Technetium-99m-MAG3 study from an 8-month-old boy, 2-min image. *Left*: 2-min image with the full counts. *First row*: Same image subsampled to 50, 30, and 10 %, respectively. *Second row*: Same images after application of enhanced planar processing (*EPP*) shows that the dose of MAG3 can be reduced to 30 % of the standard dose without loss of diagnostic value

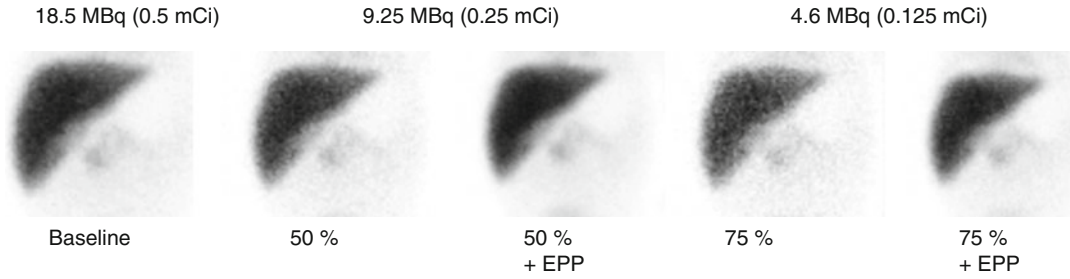

Fig. 31.7 Hepatobiliary scintigraphy and dose reduction. Selected image from a 60-min study from an infant with conjugated bilirubinemia. Using enhanced planar processing (*EPP*), the dose can be reduced by 75 % of the recommended minimum dose from the North American Guidelines of 0.5 mCi. The effective dose is reduced from 0.185 to 0.046 rem (1.85–0.46 mSv) without loss of diagnostic information

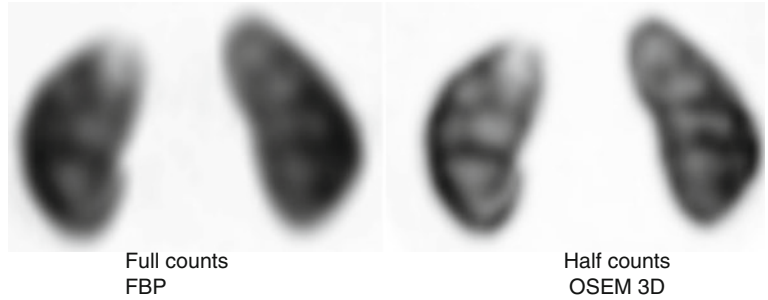

Fig. 31.8 Technetium-99m-DMSA SPECT. *Left panel*: Reconstruction using filtered back projection (*FBP*) with 100 % counts. *Right panel*: Same study with half the counts reconstructed with OSEM 3D, showing improved spatial resolution at half the dose

patient or shorter imaging times, or a combination of both. In other words, it is possible that ordered subset expectation maximization (OSEM) with 3D resolution recovery methods will allow for a significant reduction of the time necessary to acquire SPECT, making it possible to acquire a high-quality SPECT of an infant in only a few minutes. We have used ordered subset expectation maximization with 3D resolution recovery (OSEM-3D) in renal (^{99m}Tc-DMSA) and skeletal (^{99m}Tc-MDP) SPECT.

Application of OSEM-3D on SPECT data in both cases showed that administered doses of the radiopharmaceuticals can be reduced to at least 50 % with a significant improvement in image resolution. With this approach it is possible to reduce administered doses using the same acquisition times or reduce imaging time by 50 % or so, or a combination of these two advantages can be applied (e.g., reduce the administered dose by 25 % and the imaging time also by 25 %) (Figs. 31.8, 31.9, 31.10, and 31.11) [12–16].

Instrumentation

Instrumentation, Adaptation, Collimator Use, Detectors
(See also Chap. 27)

Recent advances in nuclear medicine instrumentation have the potential to contribute towards a reduction of radiopharmaceutical administered doses while maintaining diagnostic image quality. With conventional gamma cameras, clearly, utilizing dual detector systems instead of single detector systems can help reduce the administered dose with the same image acquisition time. 3D PET enables the acquisition of a larger number of photons while enabling more rapid imaging times than with 2D PET. Most, if not all modern PET systems have improved imaging in 3D with greater acquisition sensitivity compared to the 2D approach. Even with the increased susceptibility to scatter and random coincidences with 3D acquisition, this may not be an important

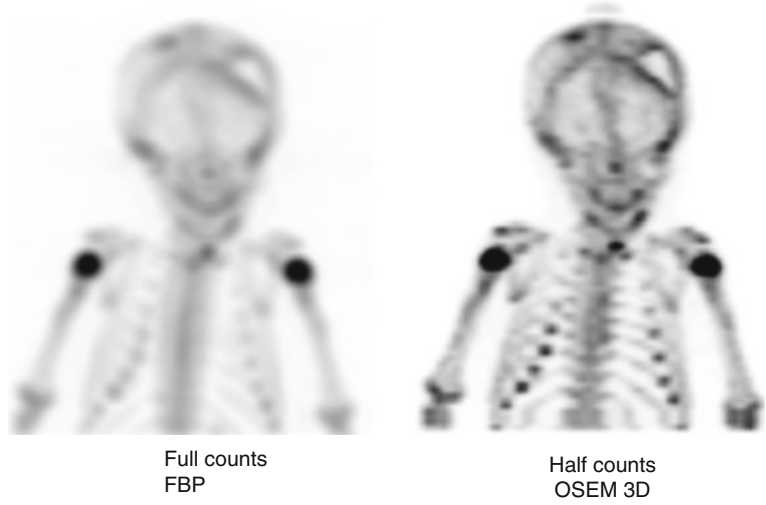

Fig. 31.9 Technetium-99m-MDP bone SPECT from an 18-month-old boy with Langerhans cell histiocytosis. *Left panel*: SPECT with the standard dose reconstructed using filtered back projection (*FBP*). *Right panel*: Same study reconstructed with half the counts of the original reconstructed with OSEM 3D. The spatial resolution with the OSEM 3D method, even at half the counts, is clearly superior to the FBP image

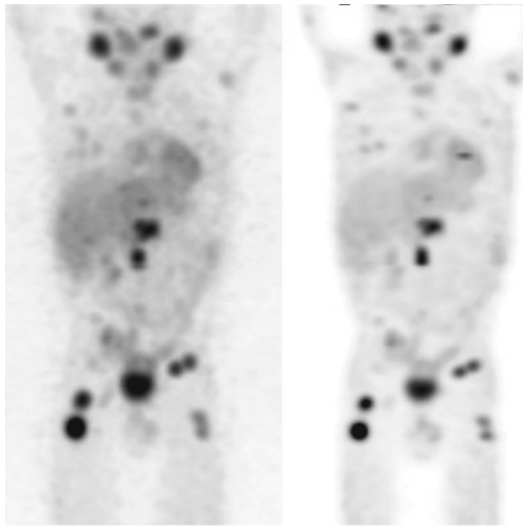

Fig. 31.10 Iodine-123 MIBG SPECT. A 12-year-old male with relapsed neuroblastoma. *Left panel*: MIP of the full MIBG dose reconstructed with filtered back projection (*FBP*). *Right panel*: Same study with half the counts reconstructed with OSEM 3D with resolution recovery. Image quality is improved with OSEM 3D even with half the counts

factor in imaging children. Thus, less administered activity can be given to patients without adverse effect on clinical imaging.

Most studies in pediatric nuclear medicine are obtained using conventional gamma cameras. During the past few years, new systems have been designed specifically to optimize myocardial perfusion SPECT. Several designs have become available with special geometry optimized to image the heart, and some are equipped with newer detectors such as CdZn, CZT which provide improved energy resolution, improved geometry and spatial resolution, faster acquisition times, and improved processing. They can complete studies in as short a time as one-fourth of the time of conventional gamma camera systems. These systems allow imaging at a lower administered radiopharmaceutical dose. These systems could potentially be adapted for imaging children with the obvious advantages of higher sensitivity and resolution (see Chap. 27 – Physical Aspects of Pediatric Nuclear Medicine Imaging).

Although changing collimators is time consuming, it is possible to optimize and even reduce the radiopharmaceutical administered dose needed in relation to the patient size and the clinical task. Here there are opportunities for dose reduction. Obviously, the size of pediatric patients varies greatly. In babies with a rather small body cross section, it is possible to effectively use a collimator with shorter holes (high-sensitivity collimator) than in a patient with a relatively large cross section. Therefore, radiopharmaceutical administered doses can be adapted to the diagnostic task considering the sensitivity and resolution of the collimator so that the desired diagnostic information can be

Fig. 31.11 A 7-month-old boy with the heterotaxy syndrome. Spleen SPECT with heat denatured ^{99m}Tc-labeled red blood cells. *Left panel*: the spleen is imaged with filtered back projection using the full counts. *Right panel*: using OSEM 3D with only half the counts, the image is of obvious higher spatial resolution

obtained. An ultrahigh-resolution collimator has a sensitivity of 100 counts per minute per microcurie, while a high-resolution collimator is twice as sensitive at 200 counts per minute per microcurie. A high-sensitivity collimator has a sensitivity of 1,000 counts per minute per microcurie. The spatial resolutions expressed as full width at half maximum (FWHM) are 6, 7.4, and 15.6 mm at 10 cm, respectively. The spatial resolution varies with distance from the collimator and thus may not be as divergent at 5 cm. If the patient is very small, such as a baby undergoing a hepatobiliary scan, it may be possible to use a high-resolution collimator if the objective of the study is simply to identify if tracer migrates to the bowel. Using a high-resolution collimator can reduce the dose by half compared to an ultrahigh-resolution collimator. Even more dose reduction can be achieved using a high-sensitivity collimator. However, if the patient to be imaged is larger, such as a teenager or a young adult, it may be better to use a high-resolution collimator to achieve better resolution at a greater depth.

With the wider availability of PET/CT and SPECT/CT or hybrid imaging, the radiation dose from CT needs to be considered as an important factor contributing to patient radiation exposure. With the increased concern about radiation exposures from CT, several manufacturers of hybrid equipment have developed improvements leading to a reduction of CT dose in these systems. This is a work in progress. At the time of this writing, there has been no uniform agreement about the most appropriate approach to address this. It is generally agreed, however, that in many cases where hybrid imaging is performed, the need to utilize full-dose diagnostic CT or not must be considered. It is possible to obtain appropriate attenuation correction with CT at doses much lower than diagnostic levels. Depending on the specific case, one can develop three approaches: (1) If attenuation correction is all that is needed, a very low-dose CT can be sufficient. This may be enough in most cases for anatomic localization of PET lesions. (2) If precise anatomic localization is needed, then a CT with a low dose, but sufficient to provide the desired anatomical information, can be used. (3) If the patient needs both the PET and the CT in one imaging session, this can be done using diagnostic levels of CT that can be used both for attenuation correction and for CT diagnosis. One may consider that a "menu" can be developed for each individual case so the appropriate protocol could be used depending on the specific diagnostic task.

Reduction of CT Exposure

Another example on how to reduce radiation exposure is the avoidance of redundant or unnecessary CT studies. For example, if a patient with

Hodgkin's disease is referred for an FDG PET/CT who had a diagnostic CT a few days earlier, it is not necessary to obtain another high-resolution CT. If the quality of the externally obtained CT is adequate, this CT can be fused electronically with the PET. The PET/CT can then be obtained with very low CT exposure only for the purpose of attenuation correction if needed, therefore avoiding an additional diagnostic CT exposure to the patient. Certain strict oncology protocols rely primarily on tumor size as an indication of the effectiveness of therapy, and these have required multiple CT examinations over the course of therapy. On the other hand, reduction in the uptake of certain radiotracers such as FDG in tumors has been shown to reflect early effectiveness of therapy even though tumor size may not have shown a concomitant decrease in size on CT. This is frequently seen in patients with lymphoma. Therefore, there is the potential to reduce the number of CT examinations needed to follow the effect of therapy on these patients with a more timely use of FDG PET as a biomarker. With this approach, the overall radiation exposure to these patients can be significantly reduced. In some cases, it would be desirable to obtain a low-dose CT as part of the PET/CT acquisition and, as needed, obtain a diagnostic CT of the area(s) of interest based on a PET finding that may need clarification with fine anatomical detail (PET-guided CT) [17–21].

Education and Communication

Perception about radiation varies quite widely among the public and physicians, scientists, and other members of care teams. The word "nuclear" in nuclear medicine has traditionally elicited concern. Therefore, it is essential that members of the nuclear medicine team be able to communicate effectively with referring physicians, patients, parents, and other members of the patient's care team about nuclear medicine and radiation exposures within the context of the examination at hand. It is no longer sufficient to indicate that nuclear medicine procedures are safe. In addition, it is useful to prepare procedure-specific brochures or pamphlets that can also be posted on the Internet to provide information to patients and families that are scheduled to undergo nuclear medicine examinations. These informational tools should contain explanations about the procedures as well as radiation exposures in the context of the clinical question being asked. Also, patients and families should be assured that every precaution has been taken to ensure that the appropriate test which is most likely to provide the information desired at the lowest possible radiation exposure is being selected.

As new information about advances in pediatric nuclear medicine, radiation exposures, and potential risks become available, it is important that such information is shared and communicated among professionals, patients, and the public.

The Image Gently Campaign (IGC), developed by the Alliance for Radiation Safety in Pediatric Imaging, is a very useful source of information. The IGC counts as members the Society for Pediatric Radiology (SPR), the American College of Radiology (ACR), the American Association of Physicists in Medicine (AAPM), the Society of Nuclear Medicine and Molecular Imaging (SNMMI), and the SNM Technologist Section. The Image Gently Campaign encouraged and supported the formation of a pediatric nuclear medicine group to work on radiopharmaceutical administered doses with the objective to achieve expert consensus, improve communications, and develop new guidelines. This group that consists of pediatric nuclear medicine physicians, technologists, and physicists conducted several expert consensus workshops at the annual meetings of the SNMMI and the SPR from 2008 through 2013. The IGC seeks to increase awareness about lowering radiation exposures from imaging studies and to provide information to patients and caregivers. The first initiative produced by this group was a patient and parent information brochure about pediatric nuclear medicine's value and explanation of radiation exposures with these procedures. The nuclear medicine group of the IGC produced the "2010 North American Guidelines for Pediatric Radiopharmaceutical Administered Doses"

which were published in 2011 [6, 7, 22–27]. More recently the North American Group and the European Association of Nuclear Medicine and Molecular Imaging have developed updated joint guidelines that incorporate consensus between the two expert groups. These new guidelines are called Harmonization Guidelines and will be published shortly in the European Journal of Nuclear Medicine and in the Journal of Nuclear Medicine and Molecular Imaging.

References

1. Ernst M, Freed ME, Zametkin AJ. Health hazards of radiation exposure in the context of brain imaging research: special consideration for children. J Nucl Med. 1998;39(4):689–98.
2. Pearce MS, Salotti JA, Little MP, et al. Radiation exposure from CT scans in childhood and subsequent risk of leukaemia and brain tumours: a retrospective cohort study. Lancet. 2012;380(9840):499–505.
3. Treves ST, Baker A, Fahey FH, et al. Nuclear medicine in the first year of life. J Nucl Med. 2011;52(6): 905–25.
4. Treves ST. Pediatric nuclear medicine/PET. 3rd ed. New York: Springer; 2007.
5. Treves ST, Davis RT, Fahey FH. Administered radiopharmaceutical doses in children: a survey of 13 pediatric hospitals in North America. J Nucl Med. 2008;49(6):1024–7.
6. Gelfand MJ, Parisi MT, Treves ST. Pediatric radiopharmaceutical administered doses: 2010 North American consensus guidelines. J Nucl Med. 2011;52(2):318–22.
7. Treves ST, Parisi MT, Gelfand MJ. Pediatric radiopharmaceutical doses: new guidelines. Radiology. 2011;261(2):347–9.
8. Brenner D, Elliston C, Hall E, Berdon W. Estimated risks of radiation-induced fatal cancer from pediatric CT. AJR Am J Roentgenol. 2001;176(2):289–96.
9. Hall P, Adami HO, Trichopoulos D, et al. Effect of low doses of ionising radiation in infancy on cognitive function in adulthood: Swedish population based cohort study. BMJ. 2004;328(7430):19.
10. Lassmann M, Biassoni L, Monsieurs M, Franzius C, Jacobs F. The new EANM paediatric dosage card. Eur J Nucl Med Mol Imaging. 2007;34(5):796–8.
11. Mawlawi O, Yahil A, Vija H, Erwin W, Macapinlac H. Reduction in scan duration or injected dose in planar bone scintigraphy enabled by Pixon(R) post-processing. J Nucl Med Meeting Abstr. 2007; 48(MeetingAbstracts_2):13P-b.
12. Sheehy N, Tetrault TA, Zurakowski D, Vija AH, Fahey FH, Treves ST. Pediatric 99mTc-DMSA SPECT performed by using iterative reconstruction with isotropic resolution recovery: improved image quality and reduced radiopharmaceutical activity. Radiology. 2009;251(2):511–6.
13. Stansfield EC, Sheehy N, Zurakowski D, Vija AH, Fahey FH, Treves ST. Pediatric 99mTc-MDP bone SPECT with ordered subset expectation maximization iterative reconstruction with isotropic 3D resolution recovery. Radiology. 2010;257(3):793–801.
14. Hsiao EM, Cao X, Zurakowski D, et al. Reduction in radiation dose in mercaptoacetyltriglycerine renography with enhanced planar processing. Radiology. 2011;261(3):907–15.
15. Romer W, Reichel N, Vija HA, et al. Isotropic reconstruction of SPECT data using OSEM3D: correlation with CT. Acad Radiol. 2006;13(4):496–502.
16. Vija AH, Yahil A, Hawman EG. Adaptive noise reduction and sharpening of OSEM-reconstructed data. IEEE Nucl Sci Symp Conf Rec. 2005;5: 2583–7.
17. Gelfand MJ. Dose reduction in pediatric hybrid and planar imaging. Q J Nucl Med Mol Imaging. 2010; 54(4):379–88.
18. McCollough CH, Primak AN, Braun N, Kofler J, Yu L, Christner J. Strategies for reducing radiation dose in CT. Radiol Clin North Am. 2009;47(1):27–40.
19. Chawla SC, Federman N, Zhang D, et al. Estimated cumulative radiation dose from PET/CT in children with malignancies: a 5-year retrospective review. Pediatr Radiol. 2010;40(5):681–6.
20. Alessio AM, Kinahan PE, Manchanda V, Ghioni V, Aldape L, Parisi MT. Weight-based, low-dose pediatric whole-body PET/CT protocols. J Nucl Med. 2009;50(10):1570–7.
21. Accorsi R, Karp JS, Surti S. Improved dose regimen in pediatric PET. J Nucl Med. 2010;51(2):293–300.
22. Goske MJ, Applegate KE, Boylan J, et al. Image Gently(SM): a national education and communication campaign in radiology using the science of social marketing. J Am Coll Radiol. 2008;5(12):1200–5.
23. What you should know about pediatric nuclear medicine and radiation safety. http://www.pedrad.org/associations/5364/files/Im_Gen_.NucMed_youngeraud.pdf. Accessed 26 May 2011.
24. Fahey FH, Treves ST, Adelstein SJ. Minimizing and communicating radiation risk in pediatric nuclear medicine. J Nucl Med. 2011;52(8):1240–51.
25. Goske MJ, Applegate KE, Bulas D, et al. Approaches to promotion and implementation of action on radiation protection for children. Radiat Prot Dosimetry. 2011;147(1–2):137–41.
26. Sgouros G, Frey EC, Bolch WE, Wayson MB, Abadia AF, Treves ST. An approach for balancing diagnostic image quality with cancer risk: application to pediatric diagnostic imaging of 99mTc-dimercaptosuccinic acid. J Nucl Med. 2011;52(12):1923–9.
27. Wayson M, Lee C, Sgouros G, Treves ST, Frey E, Bolch WE. Internal photon and electron dosimetry of the newborn patient–a hybrid computational phantom study. Phys Med Biol. 2012;57(5):1433–57.

Index

S.T. Treves (ed.), *Pediatric Nuclear Medicine and Molecular Imaging*,
DOI 10.1007/978-1-4614-9551-2, © Springer Science+Business Media New York 2014

D

I